2002

Solid-State Sensors, Actuators, and Microsystems Workshop

www.hh2002.org

Sponsored by the
Transducer Research Foundation, Inc.
Additional support provided:
Defense Advanced Research Projects Agency

Hilton Head Workshop
June 2 - 6, 2002 • Hilton Head, South Carolina
Editors: Robert Sulouff & Martin W. Schmidt

TRF Catalog Number: 02TRF-0001
Library of Congress Control Number: 2002104282
ISBN Number: 0-9640024-4-2
ISSN 1539-2058 (Print) • ISSN: 1539-204X (Electronic)
DOI 10.31438/trf.hh2002.0

2002

Solid-State Sensors, Actuators, and Microsystems Workshop

Hilton Head Island, South Carolina • June 2 - 6, 2002

All opinions expressed in this digest are those of the authors and are not binding on Transducer Research Foundation, Inc.
Copies of available volumes of this digest may be obtained from the Transducer Research Foundation, Inc., c/o 307 Laurel Street, San Diego, California 92101-1630 USA (+1-619-232-9499)

Copyright and Reprint Permission: Abstracting is permitted with credit to the source. Libraries are permitted to photocopy beyond the limit of U.S. copyright law for private use of patrons those articles in this volume that carry a code at the bottom of the first page, provided the per-copy fee indicated in the code is paid through Copyright Clearance Center, 222 Rosewood Drive, Danvers, MA 01923. For other copying, reprint or republication permission, contact Transducer Research Foundation, Inc., c/o 307 Laurel Street, San Diego, California 92101-1630 USA, info@transducer-research-foundation.org. All rights reserved. Copyright ©2002 by the Transducer Research Foundation, Inc. Personal use of this material is permitted. However, permission to reprint/republish this material for advertising or promotional purposes of for creating new collective works for resale or redistribution to servers or lists, or to reuse any copyrighted component of this work in other works must be obtained from the Transducer Research Foundation, Inc.

TRF Catalog Number: 02TRF-0001
Library of Congress Control Number: 2002104282
ISBN Number: 0-9640024-4-2
ISSN 1539-2058 (Print) • ISSN: 1539-204X (Electronic)
DOI 10.31438/trf.hh2002.0

This product contains Adobe Acrobat software. Copying this product's instructions and/or designs for use on future CD-ROMs or digital products is prohibited without written permission from The Printing House and Adobe Systems Incorporated. The Printing House or its suppliers are not liable for any direct, indirect, special, incidental, or consequential damages to your hardware or other software arising out of the use–or the inability to use–the material on this CD-ROM. This includes, but is not limited to, the loss of data or loss of profit. Adobe, Acrobat and the Acrobat logo are trademarks of Adobe Systems Incorporated or its subsidiaries and may be registered in certain jurisdictions.

If you have questions regarding the installation, please contact:

The Printing House
Phone: +1-608-873-4500
Hours: Monday through Friday, 8 am - 5 pm CST
E-mail: graphics@printinghouseinc.com

Greetings from the General Chairman

It is my pleasure to welcome you to the 2002 Solid-State Sensor, Actuator and Microsystems Workshop, or as we often call it, *The Hilton Head Workshop*. This is the tenth in a biannual series of regional workshops, held since 1984 on Hilton-Head Island, and dedicated to a scientific exchange of ideas in the areas of micro and nanofabricated devices and systems. This workshop is scheduled to be on alternate years from the International Conference on Solid-State Sensors, Actuators, and Microsystems (Transducers Conference). While the biannual Transducers Conference is a large, international, multi-session meeting, the Hilton Head Workshop is designed to be highly interactive and smaller. Consequently, this regional workshop restricts attendance to residents of the Americas in order to keep the size manageable. The overall organization of the workshop is modeled somewhat after the Gordon Conference, leaving plenty of time for extensive Q&A, free time in the afternoons for interaction amongst the participants, and a significant number of evening events. This structure has helped to promote a highly collegial and collaborative group of researchers in this region. In addition, the meeting has often served as an important venue for new researchers (graduate students, young professionals) to immerse themselves in the field.

The technical program was planned beginning in the Fall of 2001 with the selection of our four invited speakers. Following this, the Technical Program Committee met in early January to select the contributed oral and poster presentations. As in the past, this was a highly competitive process, with well less than 50% of the submissions ultimately being selected for the program.

Perhaps the most significant change for this year has been an increased attention to late news submissions. The program has 4 oral presentation slots for late news, and these submissions, as well as the late news posters are being included in the technical digest of the meeting for the first time this year. We hope these changes will give researchers the chance to feature their latest work in a quality format.

I would like to thank all the individuals and organizations that have contributed to this workshop. The Technical Program Chair, Bob Sulouff, did an outstanding job of organizing the program committee, steering the committee in the selection of papers, and organizing the technical program. The Technical Program Committee members generously donated both their time and their organization's travel funds to participate in the paper selection meeting and review the more than 200 abstracts. Chip Spangler helped organize the corporate sponsorship and student travel support. The Transducers Research Foundation (TRF) and DARPA are both contributing to the student travel support. The rest of the organizing committee included Tom Kenny (Technical Program), Mark Allen (Local Arrangements), and Joe Giachino (Finances). Finally, professional management of the conference was provided by Katharine Cline and the team at Preferred Meeting Management, Inc (PMMI).

I'd like to say thanks to all the authors and participants for making the Hilton Head Workshop such a special event.

Martin A. Schmidt
General Chairman

Organizing Committee

General Chairman	**Martin A. Schmidt** Massachusetts Institute of Technology
Technical Program Chairman	**Robert Sulouff** Analog Devices
Technical Program Vice-Chairman	**Thomas W. Kenny** Stanford University
Treasurer	**Joseph M. Giachino** University of Michigan
Local Arrangements	**Mark G. Allen** Georgia Institute of Technology
Publications	**David S. Eddy** Delphi
Student Travel Grants	**Leland "Chip" Spangler** Aspen Technologies

Technical Program Committee

David Arch
Honeywell Laboratories

Susanne C. Arney
AT&T Bell Laboratories

David Beebe
University of Wisconsin at Madison

James Bustillo
Georgia Institute of Technology

Philip Congdon
Consultant

Harold Craighead
Cornell University

Gary Fedder
Carnegie Mellon University

Leslie Field
MEMSInsight, Inc.

John R. Gilbert
Coventor, Inc.

Jay Jakubczak
Sandia National Laboratories

Jack Judy
University of California at Los Angeles

Thomas W. Kenny
Stanford University

Wen Ko
Case Western Reserve University

Peter Krulevitch
Lawrence Livermore National Laboratory

Dorian Liepmann
University of California at Berkeley

Carlos Mastrangelo
Corning Intellisense

Clark T.-C. Nguyen
University of Michigan

M. Allen Northrup
MicroFluidic Systems, Inc.

Martin A. Schmidt
Massachusetts Institute of Technology

Robert Sulouff
Analog Devices, Inc.

James Walker
Tellium, Inc.

Jacob White
Massachusetts Institute of Technology

Acknowledgements

Special acknowledgements to the Transducers Research Foundation, Inc. and the Defense Advanced Research Projects Agency (DARPA) MTO/MEMS and Bio Flips Programs for their educational grant support of this conference.

The Transducers Research Foundation, Inc. would also like to thank the following companies for their financial support, encouragement, and involvement in the 2002 Solid State Sensor, Actuator, and Microsystems Workshop.

Applied MEMS
Ardesta LLC
MEMS Industry Group
MEMSCAP
Sensors Magazine

Solid-State Sensor, Actuator and Microsystems Workshop
June 2 - 6, 2002
Crowne Plaza Resort
Hilton Head Island, South Carolina

Program and Table of Contents

Sunday, June 2

Monday, June 3

Session 9
Session Chair - David Arch

Contributed Posters

Late News Posters

TECHNICAL PAPERS

Solid-State Sensors, Actuators, and Microsystems
Workshop

2002
Hilton Head Island, South Carolina
June 2 - 6

OPTICAL MEMS DESIGN FOR TELECOMMUNICATIONS APPLICATIONS

Vladimir A. Aksyuk, Maria E. Simon, Flavio Pardo, Susanne Arney
Lucent Technologies, Bell Labs
Murray Hill, NJ 07479

Daniel Lopez
Agere Systems
Murray Hill, NJ 07479

Anita Villanueva
Massachusetts Institute of Technology
Cambridge, MA 02139

ABSTRACT

As optical telecommunication networks become more complex, there is an emerging need for systems capable of very complex switching and manipulation of large numbers of optical signals. MEMS enable these systems by combining excellent capabilities and optical properties of macroscopic optomechanics with dense integration of multiple actuators on a single chip. Such optical MEMS present common design and process challenges, such as multiple electrical and optical IO, optical surface quality, optical integration density (fill factor) and actuator performance and reliability. We have used general design approaches such as pure-flexure design, electrostatic actuation and residual stress engineering in addressing these challenges. On several examples in this paper we illustrate these approaches along with underlying design tradeoffs and process requirements. We also describe specific numerical techniques useful for electrostatic actuator optimization and for analyzing the effects of residual stress.

INTRODUCTION

Even during the current slowdown in the telecommunication industry the drive towards growth and sophistication continues in both core and metropolitan optical networks. With hundreds of wavelength channels being transmitted through a single fiber at ever-higher bit rates, flexibility and the ability to reconfigure, provision and restore connections through a network are critical. Many of the light manipulation tasks associated with such networks are cheaper and easier if performed optically. These applications are not limited to optical switching, but also include tasks such as dynamic gain equalization and dispersion compensation. These tasks have to be performed with very little optical penalty.

The individual operations can be performed very well by conventional optomechanical components. However, they are bulky, expensive and slow. More importantly, the number of signals that need to be manipulated is very large, often hundreds or even thousands. MEMS allow integration densities sufficient to deal with this large number of signals. Most optomechanical components can be scaled down using MEMS technologies without an increase in optical loss or other optical penalties. This technology enables new lightwave systems for larger, more flexible and more complex optical networks of the future.

The designer is typically challenged to achieve the densest integration in the optical domain (highest “fill factor” in a 1D or 2D array of MEMS devices). This requirement is universal for applications ranging from large optical switches to adaptive optics, from tunable gratings to WDM gain equalizers and Add-Drop multiplexors. While increasing the density of optical elements one has to continue to provide ways of individually actuating the devices.

The individual devices may be provisionally divided into an actuator and an optical element. Many optical elements have been demonstrated previously, including mirrors, filters, refractive and diffractive lenses, and polarization control elements [1-3]. In this paper instead of considering various optical elements, which are often specialized for a particular application, we will concentrate on actuators, specifically the aspects of actuator design common to a variety of optical MEMS.

For the dense integration and the large number of degrees of freedom that have to be independently controlled on a single chip, electrostatic actuation presents significant advantages over other actuation principles. It provides very low power dissipation, allowing more devices to be put closer together. The electric fields can be highly localized by design, leading to very low cross-talk between neighboring devices. Requiring no special materials, it is suitable for a variety of fabrication processes. The higher actuation voltage typically associated with electrostatic actuation is usually a reasonable price to pay for the benefits. Besides, unconventional electrostatic design approaches can provide ways to further reduce the driving voltages, as discussed below.

Although beyond the scope of this paper, integrated sensors and feedback can further improve electrostatic actuators, increasing range and decreasing voltage at the expense of the additional complexity of the sensor and the feedback electronics. This is in most cases feasible only if electronic circuits are closely integrated with the MEMS devices.

In this paper we will use several examples of optical MEMS devices to illustrate the common recurrent themes in device design. These are elastic elements and pure-flexure design (with no mechanical surface contact between moving parts), electrostatic actuation principle and residual stress engineering. We will attempt to show different ways these themes can manifest themselves and different approaches that can be used in understanding, modeling and utilizing them.

Very often a MEMS designer is confronted by nonlinear phenomena. Stress, residual or induced, leads to nonlinear mechanics, such as buckling. In fact, for both deforming beams and plates, the linear, small-displacement theory is valid only as long as the tension or compression along the beam or within the plate is small [4]. In the vast majority of cases capacitances in electrostatic actuators are nonlinear functions of displacements, producing position-dependent actuation forces and thus nonlinear equations of motion.

In some cases these nonlinearities are to be avoided, e.g., by strain-relieving elastic suspensions. In others they have to be dealt with, such as in designing electrodes for a tilting mirror. They can also be put to productive use and even enable new types of mechanisms. In all cases numerical modeling becomes very useful and necessary in analyzing the effects.

In our first example below we consider a simplified model of a beam-steering micromirror with an elastic suspension and

0-9640024-4-2/hh2002/$20©2002TRF
DOI 10.31438/trf.hh2002.1

Solid-State Sensors, Actuators, and Microsystems Workshop
Hilton Head Island, South Carolina, June 2-6, 2002

electrostatic actuation by a fixed electrode. We describe a combination of numerical and analytical techniques useful in predicting the actuator performance characteristics. We also illustrate the modeling of residual stress effects on the mirror suspension, and show a useful analytical approach for spring optimization. Although the model we use to illustrate the techniques is very simple, the same techniques are applicable to a whole class of much more complex devices.

In another example of a tilting mirror a small displacement is transduced into comparably large tilt of a reflector. Achieving the required angle with a pure-flexure design presents a certain challenge. This device provides another example for the spring optimization.

The next part of the paper illustrates how residual stress can be used to an advantage. First, we show a mechanical part with deliberately built-in residual stress employed to create self-assembling devices, and then show residual stress enabling a completely different type of a tilting mirror device. This interesting device illustrates where the previously described analysis techniques are no longer applicable. It also takes the next step beyond the pure-flexure micromachines. The concept behind this device allows decoupling of actuation range and voltage, showing a way to a significant actuation voltage reduction.

Finally we consider the effects of the residual stress on the shape of 2D plates. Here we consider bimorph plates with large stress mismatch between layers. Such structures present an interesting case of geometrical mechanical nonlinearity and can be used for building a new type of a bi-stable (latchable) actuator.

SIMPLE MIRROR – NUMERICAL ANALYSIS

In this section a self-consistent approach to solve the mechanical and electrostatic behavior of certain types of MEMS devices is presented. The approach combines numerical simulation with analytical formulas in order to reduce the total numerical simulation time. It works well and provides significant computational advantage when electrostatic and mechanical problems can be effectively decoupled.

Suppose we can postulate *a priori* that electrostatic forces influence only a few mechanical degrees of freedom (DOF). This is the case when several parts connected by springs move as separate rigid bodies (without deformation) under the influence of electrostatic forces, and the electrostatic forces are not acting on the springs. Such electrostatic forces can be calculated for all values of mechanical DOF and then the simple mechanical problem can be solved in the presence of these applied position-dependent forces. Moreover, when changes in some DOF are small, they can be treated as a perturbation.

We will illustrate the technique on a simple example below. Later in this paper we will give another example of an electromechanical system which is strongly coupled and for which this technique cannot be applied.

Figure 1 shows a typical 1-axis tilting mirror design. The electrically grounded mirror tilts around the $\hat{y}$ axis as a voltage V is applied to the electrode. We will assume all the mechanical deformation occurs in the springs, the mirror is assumed rigid. The mechanical energy is given by,

$$E_M = \sum_i \frac{1}{2} K_i (r_i)^2 + \frac{1}{2} \tau \theta^2, \qquad \text{Eq. 1}$$

where r_i is the displacement of the center of mass of the mirror from equilibrium *(i=x,y,z),* θ is the mirror tilting angle, τ and K_i are the torsional and linear spring stiffnesses respectively.

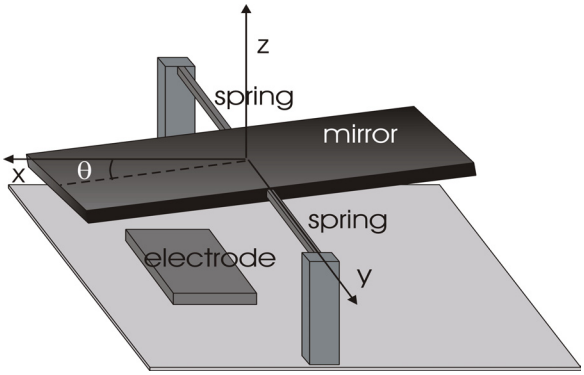

Figure 1. *Schematic of a 1-axis tilting mirror.*

The mirror is designed to have the torsional stiffness much smaller than the linear ones, in other words the lowest vibration eigenmode of the model is rotation. In this limit the linear terms (first term in Eq. 1) can be treated as a perturbative correction of the pure torsional model (last term in Eq.1).

The electrostatic energy is given by $E_E = \frac{1}{2} V^2 C$,

where C is the capacitance and V is the applied voltage on the electrode, and any other conductor is grounded. As the mirror was assumed rigid, the capacitance depends only on the mirror coordinates, $C(\theta, \vec{r})$. This capacitance can be obtained using any finite element electrostatic solver, such as the commercial CoventorWare™ software package. From the mechanical and electrostatic energies, the following set of equilibrium equations can be derived:

$$\tau\theta = \frac{1}{2} V^2 \frac{\partial C}{\partial \theta} \qquad \text{Eq. 2}$$

$$K_i r_i = \frac{1}{2} V^2 \frac{\partial C}{\partial r_i} \qquad \text{Eq. 3}$$

For the known function $C(\theta, \vec{r})$ these equations determine the equilibrium voltage $V(\theta)$ at which a given angle is attained.

The problem can be solved by a perturbative approach. The solving mechanism is:

1. Solution of the unperturbed system. Only the pure torsional model (last term in Eq.1) is considered. Numerical simulations are performed to get $C^0(\theta,0)$. Eq. 2 is solved to get the unperturbed solution $V^0(\theta)$.

2. Correction of the trajectory $\vec{r}^0(\theta)$. This correction is obtained solving Eq.3 using the unperturbed V^0 and C^0. To solve Eq.3, more numerical simulation is needed in order to evaluate the derivatives: $C^0(\theta, \delta_x)$ is needed to obtain

$$\frac{\partial C}{\partial x}(\theta,0) = \frac{C^0(\theta,\delta_x) - C^0(\theta,0)}{\delta_x} .$$

3. Correction of the voltage $V^1(\theta)$. Numerical simulations are performed to get $C^1(\theta, \vec{\rho}^0(\theta))$. Eq.2 is solved to get $V^1(\theta)$.

4. Iteration of steps 2 and 3 until the trajectories converge. V^1 and C^1 are used to recalculate $\vec{\rho}^1(\theta)$ (step 2). These new trajectories can be used to recalculate V and C (step 3) and so on. This procedure can be repeated until $\vec{\rho}^n \approx \vec{\rho}^{n+1}$.

Figure 2 shows voltage vs. tilt angle curves for a mirror, as calculated using this procedure. The voltage V^0 of a pure rotation and the voltage of a corrected model including displacements in z are shown. The solution shown by the second curve took only a few iterations to converge. The modeled device was built, and experimental data are also shown. The corrected solution reproduces the experimental data very well. Voltages and angles are normalized to the snap-down values.

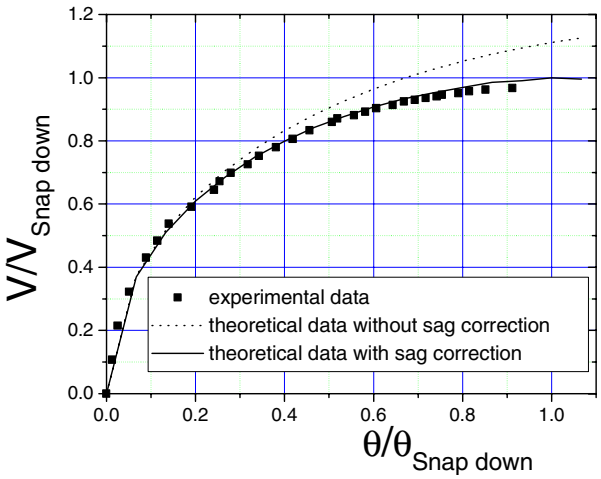

Figure 2. *Voltages vs. angle curves. The dotted line corresponds to the unperturbed solution and the solid line corresponds to the corrected solution. The squares are the actual experimental data.*

This method is most useful for more complex mechanical models with more degrees of freedom. For example it is very useful in analyzing gimbaled mirror models with 2 movable rigid bodies (mirror and gimbal ring) and 4 spring elements. The model contains 8 mechanical degrees of freedom – two tilt angles and 6 translations for the two bodies. For any given trajectory in the 2D angle space the two voltages can be calculated, taking into account the x, y and z displacements as perturbations. The same technique can also be easily adapted to analyze the effects of low-frequency mechanical vibrations on the device.

The technique provides significant computational savings for these types of problems since only a few capacitance calculations are required to obtain a trajectory. To compare, if standard iterative fully coupled electrostatic-mechanical method were used, multiple iterations of electrostatic and mechanical calculations would have been required for each point. Moreover, the number of iterations required usually diverges at the instability points, while our technique is completely insensitive to this issue.

SIMPLE MIRROR – STRESS EFFECTS

The previous analysis assumed that the suspension springs are elastic with certain stiffness for rotation and displacement. However, the designer has to make sure those numbers are well-defined. Processing, packaging and thermal mismatch are only a few sources known to introduce stress in the mirror layer. A robust design should be insensitive to such stresses.

The design in Fig. 1 uses straight torsion members rigidly fixed on the sides. It is not strain-relieved. A compressive stress with such a suspension will lead to buckling. Buckling is a situation when the mechanical structure deforms, spontaneously breaking its symmetry even when no external forces are applied.

Almost any elastic-mechanical solver that can calculate the resonance modes and frequencies can easily predict the stress level, at which such deformation occurs. Fundamentally, a resonance frequency is a measure of energy required for a deformation of a particular shape. When spontaneous deformation occurs, such as in case of buckling, that means no energy is required for such deformation, and consequently the corresponding resonance frequency reaches 0 at this point.

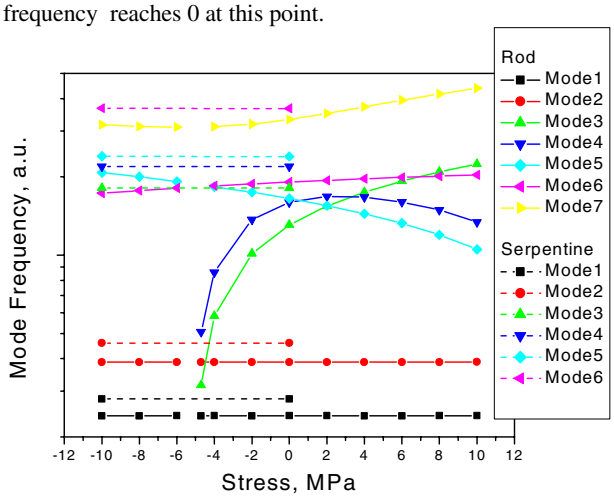

Figure 3. *Computer-simulated resonance mode frequencies for double-gimbaled mirrors as a function of residual stress. "Serpentine" spring design is insensitive to stress, while "Rod" design exhibits buckling at –5 MPa. Compressive stress is negative.*

Figure 3 shows a set of resonance frequencies of a 2D beam-steering micromirror device as a function of residual stress. Two sets of curves are shown. One set is for a device with properly designed, strain relieving "serpentine" torsional springs. This set shows resonance frequencies completely independent of the residual stress value. The other set of curves shows the same device when simple straight torsion "rods" with similar torsional spring constants were substituted for the original springs.

One can observe that frequencies for two mechanical resonance modes (both corresponding to in-plane translations) turn to 0 at about –5MPa. This means that above this stress level the mirror would buckle, i.e., spontaneously shift in the plane from its symmetrical configuration. This quite clearly undesirable effect can be easily experimentally observed. It can result in significant spread of the device characteristics and sensitivity to mechanical vibration.

The serpentine spring design effectively solves this problem. In fact, much higher residual stress levels, up to at least 100 MPa compressive, do not show any appreciable effect in simulations and no degradation attributable to stress was ever observed experimentally in these devices.

Design of serpentine and other periodic springs can be easily accomplished. Their stiffness, both torsional and translational, can

be calculated based on the standard small displacement beam theory [4].

DOUBLE HINGE TILTING MIRRORS

In the types of mirrors discussed above, electrostatic force is applied directly to the moving element. This imposes limitations on the actuation range and the drive voltage. It is sometimes more efficient to decouple the force-producing element from the moving element and connect them with a type of a transmission mechanism. This allows more flexibility in designing the force mechanism. For example, the voltage can be lowered by using a small-gap parallel-plate actuator and then converting the small displacement into the required large tilt. A "double-hinge" tilting mirror device shown in Fig 4 uses this actuation approach.

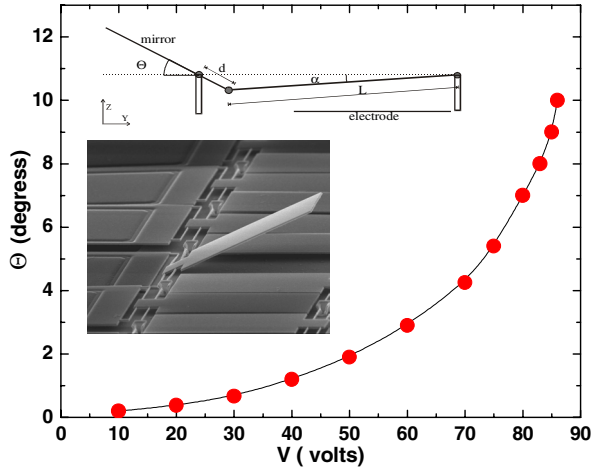

Figure 4. *Double Hinge tilting mirror. Mechanical tilt angle as a function of applied voltage. Bottom shows a micrograph of the device in the snap-down position. Top schematic illustrates the angle amplification principle.*

This approach relies on the effectiveness of the transmission mechanism, in this case the "double-hinge" connecting the actuator to the tilting reflector. Such mechanisms commonly require elements with significant difference in stiffness with respect to different deformations. Here torsional deformation in the hinges should be much easier to produce than linear displacement. More specifically $\tau / d < K$ where τ is the torsional stiffness, K is the vertical stiffness and d is the length of the lever arm. Note that d should be kept small since it determines the degree of amplification.

This disparity in stiffness is easier to accomplish by a rocking-type mechanical contact point, which effectively has very low τ but a very large K. Mechanical contact effectively allows one to design extremely non-linear mechanical suspensions: there is a sharp discontinuity in the displacement as a function of force when contact occurs. In particular this allows one to design mechanical links (springs) soft for some deformations and very hard for others.

In MEMS actuator design however, the best performance and reliability is achieved with pure flexure elements, without rubbing mechanical joints or other surfaces in contact. Considering the pure flexure suspension, one is tempted to try and replicate the nonlinearities of the mechanical contact with designs like straight rods, similar to the one shown in Fig. 4. But such nonlinearities fundamentally come at a price of increased sensitivity to residual stress, since the nonlinear behavior manifests itself exactly when the stress (e.g., tension) is induced within the beam. As we have shown before, such designs may not be sufficiently robust to stress variations.

It is possible to design strain-relieved, linear elastic springs which possess the required stiffness ratio. Such springs are preferable from the standpoint of performance (repeatability, robustness) and reliability (wear). We have used the periodic serpentine spring analysis mentioned above to design the linear elastic type of the "double-hinge" joint. We have successfully fabricated such devices. Their performance is illustrated in Fig. 4. Large tilting angles are achieved at moderate voltages while operating in the highly repeatable, reliable and stable pure-flexure regime.

The implementation of such designs is critically dependent upon the availability of the process that can accurately create features much smaller than the characteristic feature size of the rest of the device, such as beams with high aspect ratio cross-sections.

SELF-ASSEMBLY

While in the previous examples the effects of the residual stress had to be minimized, the next few examples show how the residual stress can be creatively utilized. Similarly to the way thermally induced stress powers thermal actuators, residual stress can produce useful work.

In surface micromachining and other processes many complex devices can not be produced in their final shape or form. Instead they have to be assembled – individual parts have to be moved to their final position and locked there. For example a shutter has to be locked in a vertical position, or a tilting mirror has to be positioned at a given height above the electrodes. The residual stress can be used to perform this assembly automatically. Such self-assembly is incorporated in a micromirror shown in Fig. 5. [5]

The self-assembly is accomplished during the release step of the processing sequence on all mirrors simultaneously without either human intervention or external power supply. The mechanical energy is stored during deposition in the special high-stress layer, which is put on top of the four assembly arms. Immediately after the assembly arms are released, the tensile stress in this layer causes them to bend up and push the mirror frame, lifting it in place above the Si substrate. The tapered cuts in the

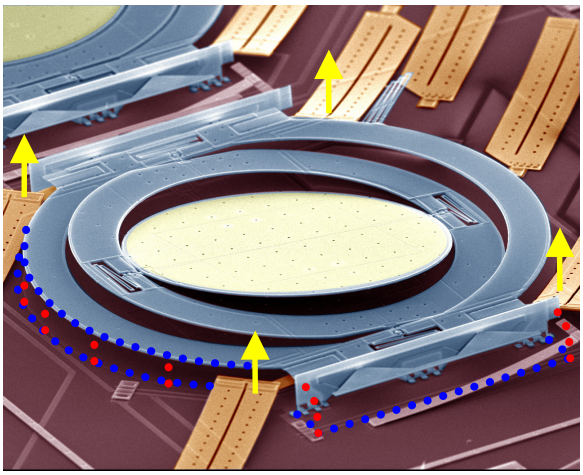

Figure 5. *Self-assembling beam-steering micromirror.*

hinged sidewalls are engaged with the dovetail structures at the frame edge, and as the frame is raised, the sidewalls are rotated 90 degrees out of their initial position within the substrate plane. In their final, vertical position, the sidewalls provide a lithographically defined accurate stop, locking the frame precisely in place.

To ensure stability of the frame and mirror position above the electrodes, the self-assembly holding force exceeds by a large margin any electrostatic and g-shock forces the device can be subjected to. A freestanding, unloaded bimorph self-assembly arm will assume the shape of an arc of radius R, given by the arm's layer thicknesses, elastic moduli and the residual stress of the materials. When the arm is loaded at the tip with a force F, its shape for small displacements is given by the superposition of the initial arc and the deformation due to the load:

$$z(x) = \frac{x^2}{2R} - \frac{Fx^2(3L-x)}{6EI} \quad ,$$

where z is the position of the point on the arm at distance x from the origin, L is the length of the arm, E is the beam Young's modulus and I is the crossection moment of inertia.

If the assembly arm lifts the mirror to a height h, the holding force is given by:

$$h = z(L) \quad \Rightarrow \quad F = 3EI\frac{L^2/2R - h}{L^3},$$

which dependence is illustrated in Fig. 6.

For our self-assembling mirror the holding force produced by the four arms is in excess of 70uN, corresponding to the weight of the mirror structure during a ~2000g mechanical shock test. The maximum possible electrostatic force applied to the mirror does not exceed 10uN. Thus our design is quite stable.

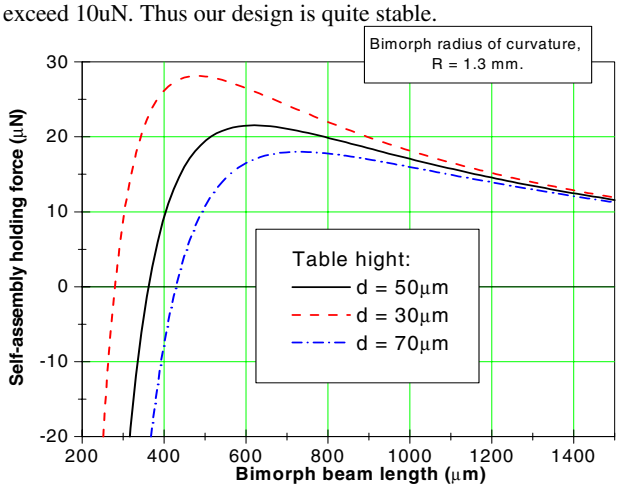

Figure 6. *Forces produced by a single self-assembly arm for different lifting heights and arm lengths.*

PARTY-FAVOR TILTING MIRRORS

The device shown in Fig. 7 combines residual stress engineering with yet another electrostatic approach and functions as a piston-tilt micromirror. The residual stress is used to modify the shape of the actuator elements and position the optical device initially away from and at an angle to the substrate. The curled arm itself is used as a movable, elastic element of the actuator, uncurling itself gradually as voltage is increased on the fixed electrode directly beneath. As the arm uncurls, the legs with dimples at their edge come in contact with the grounded landing pads at the sides of the fixed electrode. The dimples on the legs protrude downward, lower than the bottom surface of the arm itself, defining the final minimum gap between the arm and the electrode underneath and preventing the arm from touching and

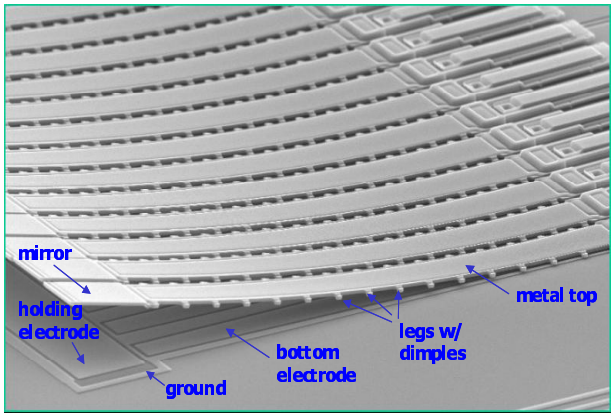

Figure 7. *"Party-favor" tilt-piston devices.*

shorting to the electrode.

This device is an example of a strongly coupled electrostatic-mechanical system, as the shape of a conductor rather than just its position, changes as a result of the applied electrostatic force. It also uses mechanical contact during operation. This is a static contact with normal load. When contact can not be avoided, the order of preference for design is first a fixed contact point with normal load, a fixed contact point with normal and lateral load and the last is a contact point sliding under normal and lateral load.

As shown in Fig. 8, these devices achieve tilt angles comparable to the ones attained by the Double Hinge devices at about the same actuation voltage. But here no fine lithography is required, and the actuation voltage is independent of the amplitude of motion (defined by the arm's length), allowing a significant voltage reduction.

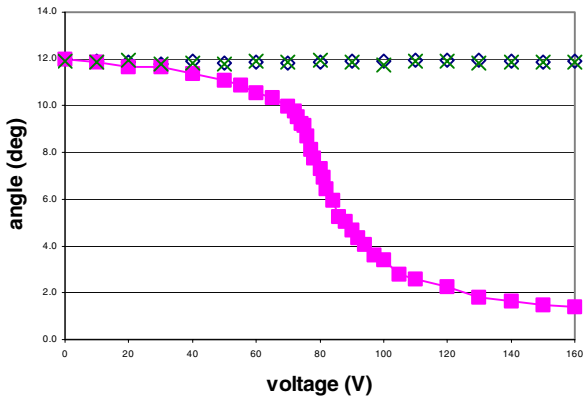

Figure 8. *"Party-favor" mirror tilt as a function of applied voltage. Curved line- device with voltage applied, straight lines- two nearest-neighbor devices, showing no crosstalk.*

Indeed, for a rough estimate we can neglect electrostatic forces where separation is large and only consider the region in the vicinity of the point of contact. The voltage required to start uncurling the arm is dependent only upon the arm stiffness and curvature, electrode width and the *smallest* gap between the electrode and the arm (defined by the dimple height). For example if the dimple height is reduced, the actuation voltage required for

the same amplitude of motion is reduced in proportion with the gap. If the electrode is of a uniform width, the device shows a threshold behavior – when the voltage reaches the "uncurling" voltage, the device will uncurl completely. To make the uncurling motion gradual (~70V to ~100V in Fig. 8), the electrode is tapered, so that larger voltage is required to uncurl the last portion of the device than the first portion. Alternatively, the electrode can be made uniform and the curvature of the arm increasing toward the free end to achieve the same effect.

The slope of the curve from 0 to 70V is explained by the far-field part of the electrostatic force, and the slope above 100V by the fact that the electrode does not extend all the way under the free end on the arm.

STRESS IN BIMORPH PLATES BI-STABLE ACTUATOR

The curvature arising in mirrors consisting of two or more material layers due to dissimilar stress is a widely discussed topic. Small isotropic stresses in uniform layers lead to spherical distortions in thin plates. Various ways of reducing such unwanted curvature have been demonstrated, from better stress control to stiffening the plates to stress compensation in multiple layer stacks.

It is interesting to take a look at the other limit, where the stress and the distortion are large. Unlike beams where the small displacement linear theory is applicable for displacements smaller than the beam length (with a few exceptions), for plates the problem becomes nonlinear at displacements comparable to the plate *thickness*. Indeed, such deformations generally cannot occur without considerable in-plane stress. For example a disc can be deformed to become spherical, but cannot form a complete sphere without being significantly stretched or compressed. An exception to the rule is the cylindrical deformation, which requires only bending and no in-plane stretching or compression.

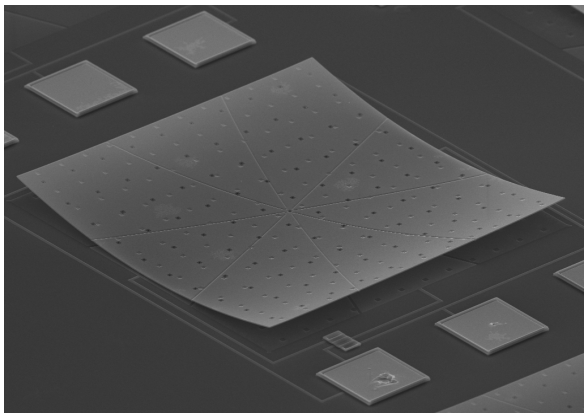

Figure 9 *Bi-stable actuator plate.*

If we consider a square bimorph plate with dissimilarly stressed materials, for small stresses the equilibrium shape of the plate is spherical. If we increase the stress, the radius of the sphere will linearly decrease up to a point when the deformation of the plate becomes comparable to plates thickness. If the stress is increased further, the deformation shape starts to deviate from a sphere until a point where a bifurcation occurs and the symmetry is spontaneously broken. As the stress is further increased the plate assumes cylindrical shape, as shown in Fig. 9.

Note however that there are two equivalent directions in which the axis of the cylinder may be pointing – along either of the edges of the plate. Thus this mechanical structure is bi-stable, with two equivalent equilibrium shapes. It is at the same time effectively strain relieved – its shape would not change if the substrate were stretched or compressed.

The plate in the figure can be switched between stable positions by pulling on it electrostatically with sets of electrodes underneath, similar to the "party-favor" device above. This device can be used for building pure-flexure latchable low voltage out of plane actuators.

CONCLUSIONS

Although the examples above mostly are tilting micromirrors of various types, different optical elements and actuators can be and have been used to create a wide variety of optical MEMS devices. Scaling down of existing macromechanical optics provides a way toward cheaper, smaller and faster optical components, while maintaining excellent optical performance: low insertion loss, high contrast, low polarization and low wavelength dependence, etc. More importantly, dense integration of MOEMS devices on a single chip enables completely new optical subsystems, where large numbers of optical signals can be switched or manipulated simultaneously.

For such applications electrostatic actuation principles provide low power dissipation, low crosstalk, excellent performance and design flexibility and ease of fabrication. Although with conventional approaches actuation voltage tends to increase with increased mechanical range, unconventional types of actuators allow circumventing the problem without compromising speed or mechanical robustness.

Design of elastic elements and residual stress engineering are the other two important themes in actuator design for optical MEMS, detailed understanding and use of which leads to robust, reliable, high-performance devices.

Nonlinear phenomena, mechanical, electrostatic and coupled, are abundant in MEMS actuators. Such phenomena can be effectively avoided or harnessed for productive purposes using various sorts of analytical and numerical analysis techniques.

REFERENCES

1. D. J. Bishop, C. R. Giles, and S. R. Das, "The Rise of Optical Switching", *Scientific American*, Jan 2001, pp. 88-94.
2. A. Neukermans, 'MEMS devices for all optical networks' *Proc. SPIE* Vol. 4561 *MOEMS and Miniaturized Systems II*, pp.1-10, 2001.
3. V. Aksyuk, B. Barber, C.R. Giles, R. Ruel, L. Stulz, and D. Bishop, "Low Insertion Loss Packaged and Fiber-connectorized Si Surface-Micromachined Reflective Optical Switch," *Solid-State Sensor and Actuator Workshop*, pp. 79-82, Hilton Head Island, South Carolina, June 8-11, 1998.
4. L. D. Landau and E. M. Lifshitz, *Theory of Elasticity, volume 7 of the course of Theoretical Physics,* translated by J. Sykes and W. Reid (Addison-Wesley Publishing Company, Inc., Reading, Massachusetts, 1959).
5. V. A. Aksyuk, F. Pardo, D. J. Bishop, "Stress-induced curvature engineering in surface-micromachined devices", Proc. SPIE, vol. 3680, p. 984, March 1999.

A MECHANICALLY-BALANCED, DRIE ROTARY ACTUATOR FOR A HIGH-POWER TUNABLE LASER

Hal Jerman and John D. Grade
iolon, Inc.
1870 Lundy Ave, San Jose, CA 95131

ABSTRACT

A DRIE actuator has been developed to allow tuning of a 20-mW output power, external-cavity laser operating over the entire C- or L-band for long-haul telecommunications applications. This actuator has the ability to rotate a large, externally-fabricated mirror about a point in space selected to achieve the desired continuous tuning range. The actuator has been designed to be mechanically balanced and therefore relatively immune to accelerations in the plane of the device.

APPLICATION BACKGROUND

Long-haul telecommunications systems have traditionally used fixed wavelength lasers to transmit data over fiber optic links. Systems currently in operation can multiplex light from as many as 100 fixed wavelength lasers, each modulated at up to 10 Gb/s, at wavelengths around 1550 nm on a single optical fiber. Optical channels have been assigned by the International Telecommunications Union (ITU) at regular intervals, which in current systems are at 100 GHz (0.8 nm) or 50 GHz spacing, although the trend is to move to 25 GHz channel spacing in the near future. There is an inventory problem associated with supplying so many different fixed wavelength devices and current systems employing fixed wavelength lasers cannot be rapidly configured to provision new optical links in the network. Tunable lasers solve these problems if they can provide optical performance equal to or better than the current fixed wavelength lasers at an acceptable price.

OPTICAL DESIGN

The optical design of this laser is a modification of the classic Littman-Metcalf arrangement, Fig. 1, where a Fabry-Perot laser diode chip includes one AR-coated facet [**1**]. Light from that facet is collimated and strikes a diffraction grating at grazing incidence. Light of different wavelengths is diffracted at different angles, thus the diffraction grating serves as an optical filter in the cavity. A beam at the angle associated with the desired output wavelength is retro-reflected by a mirror mounted on a microactuator, sending the light back to the diode thus supporting lasing at that wavelength in the cavity. Changing the angle of the retro-reflecting mirror varies the wavelength of the laser light.

The phase of the light in the cavity must also be controlled to eliminate mode hops, or abrupt changes in wavelength of light, as the laser is tuned. The cavity length and mirror angle must be simultaneously changed so that there are always an equal integer number of waves in the cavity. The geometrical arrangement to achieve this was originally described by Metcalf and Liu [**2**], where the tuning mirror rotates about a proscribed point in space. In traditional tunable lasers of this design, rotation is controlled by having a mechanical bearing at that location, although it is difficult to insure that the mechanical pivot is in the correct location for a given set of optical components.

Alternative designs for external cavity lasers including micromechanical elements for tuning have included vertical-cavity, surface-emitting lasers (VCSEL's) [**3**,**4**] and Fabry-Perot lasers including a moving rear-facet reflector [**5**], but these designs have not yet achieved the combination of power, tuning range, and optical performance needed for long-haul telecommunications applications.

In our design, a flexural suspension has been designed to place a virtual pivot point for a rotating mirror remote from the actuator device itself, to achieve the required phase control [**6**]. A pivot set by a flexural suspension is inherently free from friction and hysteresis effects common in mechanical bearings and tends to be reproducible and easy to adjust with a closed-loop control system.

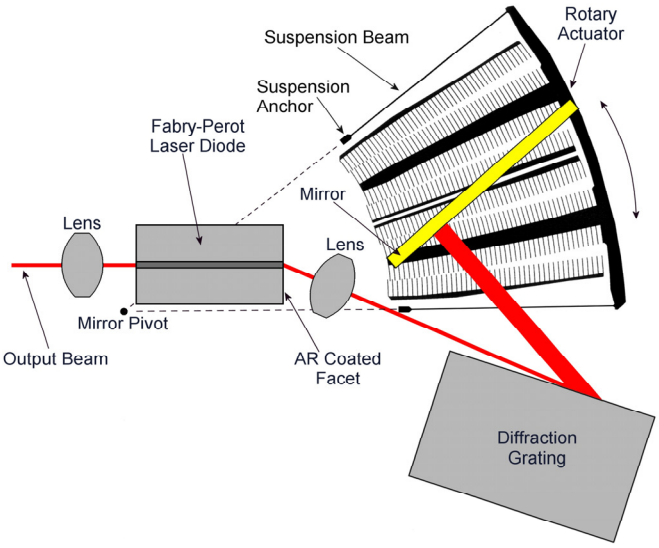

Figure 1. *Schematic view of a modified Littman-Metcalf external cavity laser. Laser is tuned by rotating a mirror mounted on a MEMS actuator about a virtual pivot point selected to maintain the correct phase relationship in the cavity.*

A separately fabricated mirror with a high-reflectivity gold coating is attached to mounting pads on the actuator and extends 600 µm out-of-plane to intercept the light. The range of motion of the mirror required to tune over a given range of wavelengths is set by the line spacing of the grating and the operating wavelength. In this case, with 1200 line/mm grating period, the wavelength changes about 7.5 nm for each degree of rotation around the mirror virtual pivot. Thus to tune over a 38 nm wavelength range, the mirror must rotate a total of almost 5 degrees, and the distal end of the mirror must travel over 300 µm during full range tuning.

The individual optical elements are mounted on a temperature-controlled ceramic substrate. Controlling the

0-9640024-4-2/hh2002/$20©2002TRF
DOI 10.31438/trf.hh2002.2

temperature to about 25°C improves the output power of the diode, increases diode life, and provides a stable cavity geometry.

In addition, an etalon wavelength locker assembly is included which is needed both to insure that the laser is accurately tuned to the desired ITU channel, and also to allow rapid closed-loop servo tuning of the laser. These lockers use the periodic transmission spectrum of a Fabry-Perot etalon, where the etalon thickness and angle are adjusted so that a specified transmission intensity (e.g. 50%) corresponds to sequential ITU channel wavelengths.

By including this locker on the same temperature-controlled platform as the laser, the stability of the etalon used to set the channel wavelength is improved. The frequency can be held to an absolute accuracy of about +/-0.7 GHz at a channel frequency of about 195 THz over temperature and the lifetime of the device, which represents a maximum frequency error of about +/-3.5 ppm. The laser must be controlled to a resolution of about 0.1 GHz in order to meet this specification, or about 1 part in 50,000 of the full-scale range of the actuator. The laser and locker are hermetically sealed in a conventional hybrid butterfly package. A schematic view of the package configuration is shown in Fig. 2.

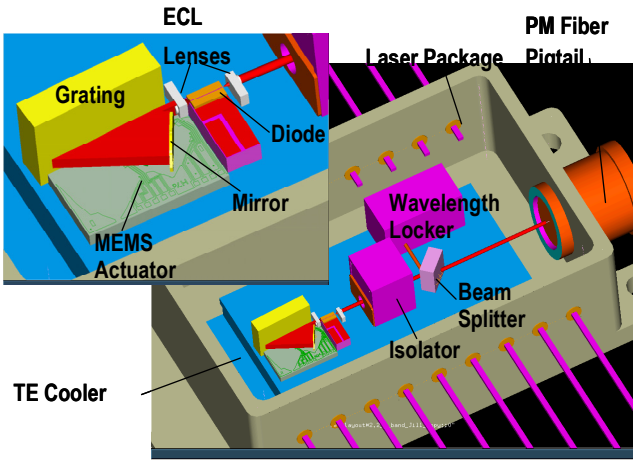

Figure 2. *Schematic view of the packaged external cavity laser including the optical isolator, wavelength locker section, and fiber pigtail assembly. The 19x26 mm butterfly package is hermetically sealed.*

ACTUATOR DESIGN

The fabrication of this actuator is identical to that used for an optical switch described at HH2000 [**7**]. A cavity is formed in an oxidized substrate, whose extent will define which parts of the structure are fixed to the substrate and which are free to move. A second wafer is fusion-bonded to this etched surface and ground and polished to a thickness of 85 µm. After contact holes and aluminum bonding pads are defined, the 85-µm thick Si layer is DRIE etched to form the suspended electrostatic actuator, substrate attachment areas, bonding pads, and electrical interconnect. With currently available etching tools, 4-µm wide suspension elements and 10-µm comb gaps are reliably obtained. A plan view of one actuator design is shown in Fig. 3, showing the actuator in relation to the laser diode chip, collimating lens, and a portion of the diffraction grating.

This and similar actuators have been designed to use separately fabricated optical elements, such as mirrors, thin-film optical filters, lenses, and diffraction gratings. This results in a relatively simple actuator process, with correspondingly high yield, and optical elements that can be fabricated in a variety of material systems with no concern about how their fabrication process would need to be integrated with the actuator.

This actuator requires 150V to rotate a 600-µm tall x 1.7-mm long mirror through 5° about a remote pivot point, resulting in more than 300 µm of total mirror motion.

The actuator design incorporates a unique mechanically-balanced approach. Many other electrostatic rotary sensors and actuators have been symmetric about their center of rotation [**8,9**] and thus have been inherently balanced. From an optical design standpoint it would have been difficult to assemble a practical laser system with a symmetric actuator rotating about the desired mirror pivot point, so an alternative approach was taken to design an actuator which rotates a mirror about the desired pivot point but also includes features to mechanically balance the device.

A virtual pivot can be made by attaching two adjacent ends of a pair of flexural beams to the moveable frame and anchoring the other two ends to the substrate [**10**]. If the beams cross in an X-shape, then for small deflections the center of rotation of the flexure is at the center of the X [**11**]. If the beams are arranged in a V-shape or do not physically cross, then for small deflections the center of rotation is at the base of the V or at the intersection of lines passing through the beams.

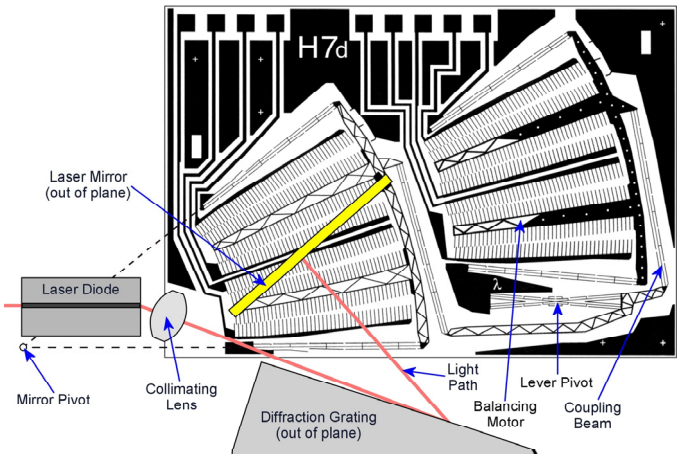

Figure 3. *Plan view of laser mirror actuator, laser die, collimating lens and diffraction grating. The actuator chip is 4.3 mm x 3.0 mm. The laser mirror is driven, e.g. clockwise, by its motor while the balancing motor is driven counter-clockwise. The motion is constrained by the pivoting lever and the associated coupling beams to minimize response to external vibration.*

To make a laser mirror rotator, two similar rotary actuators with virtual pivots are coupled via a lever with an X-type flexural pivot and driven in a push-pull configuration. A photograph of a mirror motor chip is shown in Fig. 4. The mass of the right-hand motor is designed to be nearly identical to the mass of the left-hand motor and mirror. External accelerations in the plane of the actuator then cause equal and opposite torques on the pivoting lever, eliminating any significant rotation of that lever or the motors it connects. It is feasible to realize a 600× reduction in mirror rotation due to in-plane acceleration compared to a similar single motor and mirror without this balancing arrangement. Any residual motion of the part is due to slight imbalances between the right-hand and left-hand masses and flexing of the lever due the imposed torques. The response to out-of-plane accelerations is

reduced by the large out-of-plane stiffness provided by the high aspect ratio of the suspension. This mechanical-balancing concept can also be applied to linear actuators by arranging a similar pivoting lever between two linear actuators of equal mass.

The suspension beams, coupling beams, and flexural pivot include protection fins to improve the sidewall profile during etching [**6**,**7**]. These protection features are attached locally on or near the structures, for example, along the length of a suspension beam. Thus while the narrow suspension beams are being etched, ions tend to be channeled in the etch direction, and stray ions from adjacent open areas are blocked by the fins.

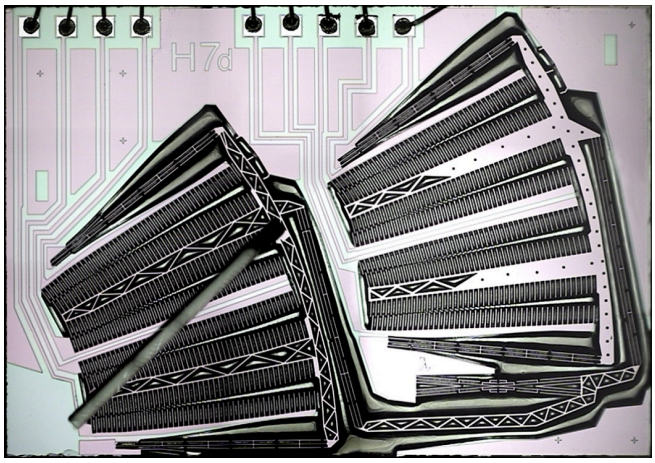

Figure 4. *Photograph of laser mirror actuator die after the externally-fabricated mirror is attached. Protection fins are fabricated on the suspension and connector beams to control the sidewall etch profile.*

ACTUATOR RESPONSE

For a closed-loop system it is important to design the actuator to have a transfer function that is monotonic, and have as linear a response as possible. A conventional comb-drive actuator provides a force that is nearly independent of position as long as the combs are interdigitated, but that force is quadratic in applied voltage. For a given maximum drive voltage, the actuator range can be doubled by providing combs that can either "push" or "pull", however the drive circuitry must be designed so that there is no dead-zone or hysteresis in the center of the range. Differential drive can be employed with fully interdigitated combs to linearize the response [**8**], but for this actuator, that would result in combs more than 400 μm long. To resist the side electrostatic forces imposed on them, such long combs would need to be quite wide. However, as the width of the combs is increased to make them stiffer, the motor mass and the comb pitch are increased, reducing the resonant frequency and electrostatic force. Instead, the lengths of the individual combs have been adjusted to substantially linearize the response over the operating range while limiting the maximum comb length to 125 μm. A graph of rotation vs. drive voltage is shown in Fig. 5 for a typical actuator with a resonant frequency of about 300 Hz.

With a transfer function similar to that in Figure 5, the laser system, including a wavelength-locking servo, can maintain wavelength accuracy of better than 10 pm (1.25 GHz) with an applied acceleration of 5 g at 50 Hz.

The reliability of the actuators and laser is critically important in a telecommunications application, where a 20 year lifetime is required. The use of purely flexural suspension elements insures that there are no friction or stiction issues during operation. A set of actuators has been collectively cycled over 60 billion times with no measurable change in performance.

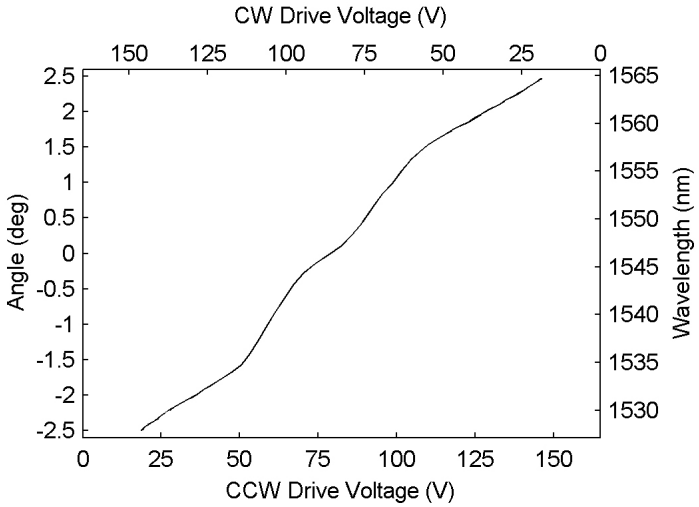

Figure 5. *Angular response of the mirror actuator vs. differential drive voltage. The response has been linearized by adjusting the lengths of the individual combs.*

LASER PERFORMANCE

The laser can be tuned and locked on 25 GHz ITU channels over a wavelength range of 38 nm with greater than 20 mW (+13 dBm) of single-mode, fiber-coupled output power, and it has supported transmission of data at 40 Gb/s over distances exceeding 800 km and 10 Gb/s over distances exceeding 3000 km. The laser can be tuned to another channel and locked in less than 15 ms. A plot of 100 superimposed optical spectra showing the laser locked to sequential, 25 GHz-spaced channels is shown in Fig. 6.

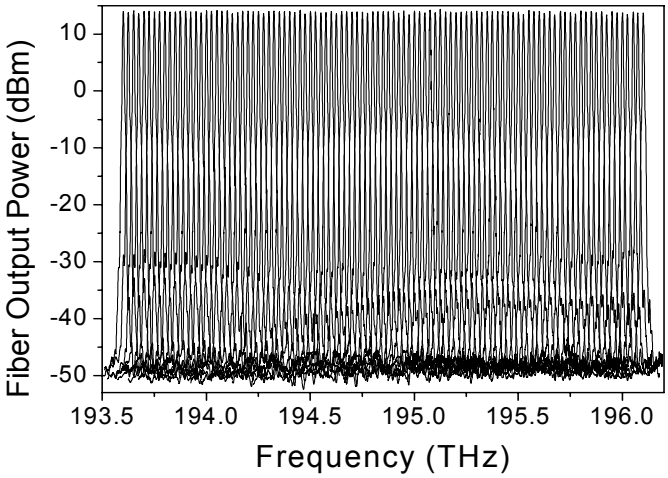

Figure 6. *Superimposed optical spectra of laser locked to 100 consecutive 25 GHz ITU optical channels. Fiber-coupled output power is >20 mW (+13 dBm) and side mode suppression is > 50 dB. These optical signals have been used to transmit data at 10 Gb/s over 3000 km.*

With appropriate optical components, similar performance can be obtained in both the C-band (1529-1561 nm) and L-band

(1566-1607 nm) and with channels spaced by 25, 50 or 100 GHz. The optical performance of the laser is improved by having a relatively long, external cavity and a highly dispersive diffraction grating. The laser has relative intensity noise (RIN) of less than -145 dB/Hz from 10 MHz to 10 GHz, polarization extinction ratio better than 20 dB, and spontaneous emission background more than 50 dBc/nm below the laser peak value. The fundamental, spontaneous-emission-induced linewidth is less than 1 MHz, narrower than that of a typical DFB laser. Such superior optical performance is required to support high data rates over long distances in an optical link.

Very small mechanical fluctuations of the mirror on the actuator in the range of 5-50 kHz kilohertz broaden the observed time-averaged optical linewidth, and a homodyne measurement with a 25 μs delay gives a time-averaged 3 dB linewidth of about 2 MHz. This represents an average displacement of the mirror over the 25 μs measurement interval of about 0.12 nm.

PERFORMANCE UNDER VIBRATION

As described above, the mirror rotator consists of two identical counter-rotating actuators, coupled in a counterweighted configuration so that the net moment of the device is zero. The balanced actuator design is important for minimizing excitation of the fundamental resonant mode. The residual low-frequency vibrational sensitivity is suppressed with servo control of the actuator. At higher frequencies, conventional viscous damping tends to minimize the coupling between external vibrations and the laser, however some modes are damped more than others. Fig. 7 shows the transfer function of case acceleration to laser frequency variation, as the vibration frequency is swept from 10 Hz to 10 kHz. The upper graph shows the sensitivity without the wavelength locker servo activated. The lower graph shows the effect of the wavelength locker servo, reducing the laser frequency sensitivity to 15 MHz per applied G of case acceleration at 10 Hz vibration frequency.

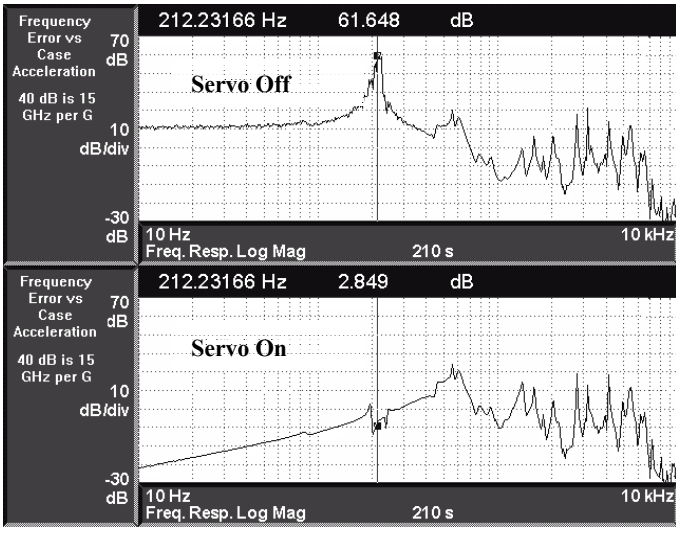

Figure 7. *The transfer function in MHz/G as the laser is subjected to vibrational excitation from 10 Hz to 10 kHz. The fundamental in-plane response of this actuator at about 212 Hz has been reduced by about 35 dB by the servo system.*

CONCLUSIONS

Silicon DRIE microactuators have enabled a small form factor, tunable laser source ideal for many data transmission applications. The performance of the laser meets the optical power, side mode suppression, polarization extinction ratio, relative intensity noise, and linewidth requirements for transmitting 10 Gb/s over distances greater than 3000 km. Frequency accuracy of ±1.25 GHz is obtained with closed loop control of the actuator drive voltage. Substantial immunity of the laser system to vibrations is achieved through a combination of mechanical design and active servo control.

ACKNOWLEDGEMENTS

The authors would like to thank the iolon development team for their help in preparing this paper, including Kathy Jackson for preparing and testing the actuator devices, Jill Berger and Jeff Hutchins for providing the optical data and Al Fennema and Ken Cheung for the servo response data.

REFERENCES

1. M. G. Littman and H. J. Metcalf, “Spectrally narrow pulsed dye laser without beam expander”, *Applied Optics*, Vol. 17 No. 14, (1978) 2224-2227.
2. K. Liu and M.G. Littman, “Novel geometry for single-mode scanning of tunable lasers”, *Optics Letters*, Vol. 6 No. 3, (1981) 117-118.
3. D. Vakhshoori, P. Tayebati, Chih-Cheng Lu, M. Azimi, P. Wang, Jiang-Huai Zhou and E. Canoglu, “2 mW CW single mode operation of a tunable 1550 nm vertical cavity surface emitting laser with 50 nm tuning range,” *Eletronic. Let.*, **35**, 1-2 (1999).
4. F. Sugihwo, M.C. Larson, and J.D. Harris, “Micromachined widely tunable vertical cavity laser diodes”, *J. Microelectro-mechanical Systems*, Vol. 7, No. 1. (1998) pp. 48-55.
5. X.M. Zhang, A.Q. Liu, V.M. Murukesham, and F.A. Chollet, “Integrated micromachined tunable lasers for all-optical network applications, *Proceedings Transducers 2001*, June 2001, pp. 1314-1317.
6. J.H. Jerman, J.D. Grade, J.D. Berger, and J.F. Heanue, “Tunable laser with microactuator”, International Publication number WO 01/43241, WIPO, June 2001.
7. J.D. Grade, H. Jerman, and T.W. Kenny, “A large-deflection electrostatic actuator for optical switching applications,” *Technical Digest of the 2000 Solid State Sensor and Actuator Workshop*, Hilton Head, SC, June 2000, pp. 97-100.
8. L.S. Fan, S.J. Woodman, R.C. Moore, L. Crawford, T.C. Reiley, and M.A. Moser, "Batch-Fabricated Area-Efficient Milli-Actuators," *Technical Digest of the 1994 Solid State Sensor and Actuator Workshop*, Hilton Head, SC, June 1994, pp 38-42.
9. D.A. Horsley, A. Singh, A.P. Pisano, and R. Horowitz, "Angular Micropositioner for Disk Drives", *Proceedings of the Tenth International Workshop on Micro Electro Mechanical Systems*, 1997, pp 454-458.
10. J.D. Grade and J.H. Jerman, “MEMS electrostatic actuators for optical switching applications”, *Technical Digest, Optical Fiber Communication Conference*, March 2001, paper WX2-2.
11. S.T. Smith and D.G. Chetwynd, *Foundations of Ultraprecision Mechanism Design*, Gordon and Beach Science Pub., Amsterdam, 1992, p. 119.

LOW VOLTAGE MEMS ANALOG MICROMIRROR ARRAYS WITH HIDDEN VERTICAL COMB-DRIVE ACTUATORS

Dooyoung Hah, Sophia Huang, Hung Nguyen, Hsin Chang, Jui-Che Tsai, and Ming C. Wu
Department of Electrical Engineering, University of California, Los Angeles
Los Angeles, CA 90095-1594

Hiroshi Toshiyoshi
Institute of Industrial Science, University of Tokyo
Tokyo, Japan 153-8505

ABSTRACT

We report on a novel, polysilicon surface-micromachined one-dimensional (1-D) analog micromirror array. Large continuous DC scan angle (23.6° optical) and low operating voltage (6V) have been achieved using vertical comb-drive actuators. The actuators and torsion springs are placed underneath the mirror (137 × 120 μm^2) to achieve high fill-factor (91%). The measured resonant frequency of the mirror ranges from 3.4 kHz to 8.1 kHz. The static scanning characteristics show good uniformity (<±3.2%) for a 1 × 10 array with a mirror pitch of 150 μm. The measured DC scanning characteristics and resonant frequencies agree well with theoretical values. This micromirror array has applications in optical wavelength-division multiplexed (WDM) routers and wavelength-selective crossconnect (WSXC).

INTRODUCTION

The advance of photonic communication networks towards optical layer networking has created a great demand for many new functional optical network elements. Microelectromechanical-systems (MEMS) is a key enabling technology for many of these new devices. Optical MEMS devices for dynamic optical add-drop multiplexers (OADM) [1], 2-D [2-3] and 3-D optical crossconnects (OXC) [4] have been reported. Previously, we have reported a novel wavelength-division-multiplexed (WDM) router that employs a 1-D array of analog micromirrors [5]. Large continuous scan range and high fill factor are required to achieve high channel count and flat spectral response. In addition, low voltage, low power actuation is desired to reduce power consumption of drive electronics.

Most of the micromirrors reported to date employ parallel-plate type electrostatic actuators. The pull-in phenomena in such actuators, however, limit the useful range of continuous scanning. The vertical comb-drive actuator reported recently [6, 7] offers several inherent advantages for actuating micromirrors. It can be designed to avoid pull-in effect and utilize the entire range of rotation. The large force density of vertical comb drives also lead to low voltage operation. However, the bulk-micromachined structures are not suitable for implementing high fill factor micromirror arrays where actuators are hidden underneath the mirrors. The surface-micromachining technique offers more flexibility for designing such multi-layer structures.

In this paper, we report on a novel surface-micromachined analog micromirror array with hidden vertical comb drive actuators. High fill factor (91%), flat mirror surface (137x120 μm^2), low operating voltage (6 V), and large continuous scan angle (23.6° optical) are successfully achieved. This device is made possible by exploiting the chemical-mechanical planarization (CMP) processes in SUMMiT-V offered by Sandia National Laboratory.

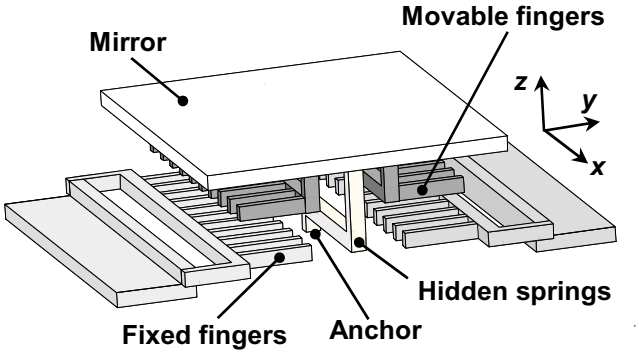

Figure 1. *The schematic structure of the proposed micromirror.*

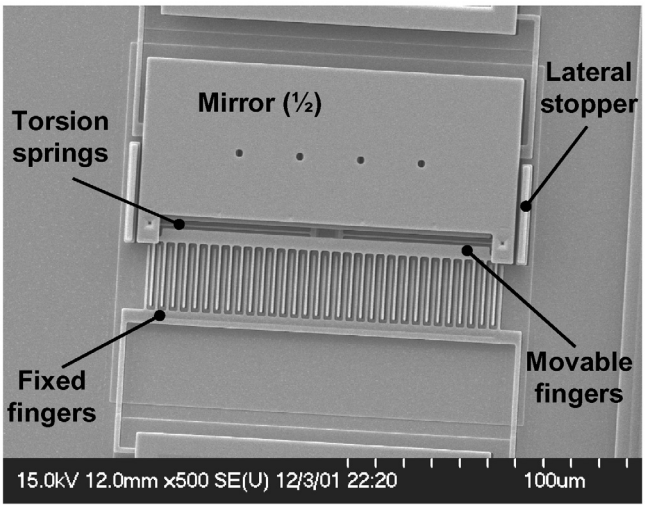

Figure 2. *The SEM micrograph of the fabricated micromirror. The lower half of the micromirror was removed intentionally to reveal the underlying comb structures.*

THEORY

The schematic of the analog micromirror is shown in Fig. 1. The vertical comb-drive actuators and the torsional springs were placed underneath the mirror to achieve high fill-factor, which is required for flat-top frequency response. Figure 2 shows the scanning electron microscope (SEM) image of the fabricated micromirror. Half of the mirror was intentionally removed to reveal the underlying structures. The height difference between the movable and the fixed fingers is illustrated by different contrast.

0-9640024-4-2/hh2002/$20©2002TRF
DOI 10.31438/trf.hh2002.3

Lateral stoppers are incorporated to constrain in-plane rotation caused by lateral instability.

In contrast to parallel-plate actuators, the analysis of the vertical comb-drive actuators is more complicated due to strong fringe field, especially when there is no overlap between the comb fingers. We have developed a hybrid model that combines analytical formulation with two-dimensional finite element solutions. This model is much faster than full three-dimensional finite element method, and can be used as a design tool.

The total capacitance (C_t) as a function of the mirror angle, θ, can be calculated by integrating the sheet capacitance of a unit cell, C_{unit}, as indicated by the dotted box in Fig. 3(a):

$$C_t(\theta) = 2N_f \cdot \int_{L_{over}} C_{unit}(h_0 - y \cdot \theta)dy \quad (1)$$

where N_f, h_0, y, and L_{over} are the number of fingers, initial mirror height, distance from rotation axis, and overlapped finger length, respectively. C_{unit} is a function of the mirror height and is computed by a 2-D finite element method (FEM) to account for the fringe field. Figure 3(b) shows the calculated distributions of electric potentials in a unit cell when a voltage (V) is applied to the fixed fingers. The mirror, the movable fingers, and the shielding electrode are grounded. The mirror and the movable fingers are attracted towards fixed fingers by the electrostatic torque (T_e) until it is balanced by a mechanical restoring torque (T_r):

$$T_e = \frac{V^2}{2}\frac{\partial C_t}{\partial \theta} \quad (2)$$

$$T_r = \frac{mG_{poly}W_sT_s^3}{3L_s}\left(1 - \frac{192}{\pi^5}\frac{T_s}{W_s}\tanh\left(\frac{\pi}{2}\frac{W_s}{T_s}\right)\right)\cdot\theta \quad (3)$$

where, m is number of springs with dimension of T_s (thickness) × W_s (width) × L_s (length), assuming $W_s > T_s$, and G_{poly} is the shear modulus of polysilicon. At sufficiently large angle, pull-in could occur due to the parallel plate capacitances between the mirror and the top surface of the fixed electrode. Previously, we have proved that the pull-in angle (θ_{pi}) for any electrostatic actuator is only a function of the capacitance [8], and can be found by solving the following equation:

$$\frac{\partial C_t}{\partial \theta} - \theta \cdot \frac{\partial^2 C_t}{\partial \theta^2} = 0 \quad (4)$$

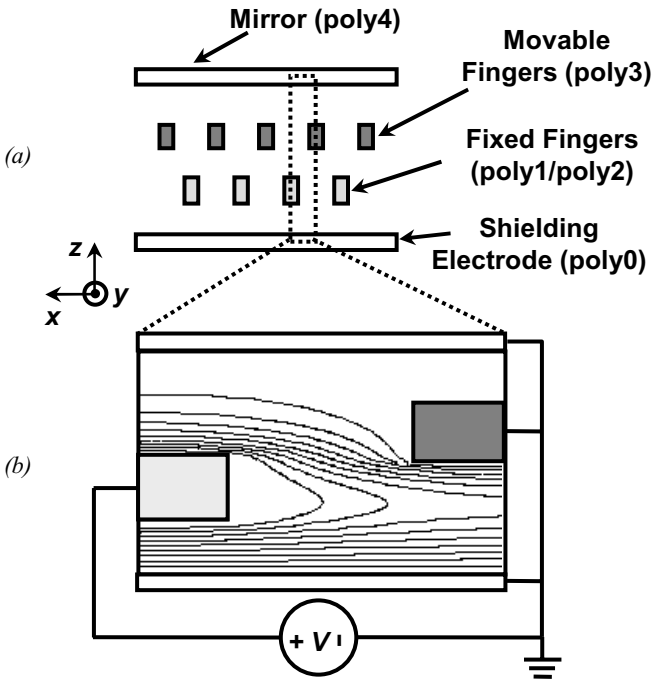

Figure 3. *(a) The cross-section and (b) the calculated electric potential distribution of the proposed micromirror.*

DESIGN

Our design is based on the SUMMiT-V (Sandia ultra-planar multilevel MEMS technology-V) process. SUMMiT-V consists of five polysilicon layers (one is fixed and four are movable) and is ideal for implementing our devices. There are two chemical-mechanical planarization processes in SUMMiT-V: one before deposition of the poly3 layer and the other before deposition of poly4 layer. We use laminated poly1 (1 μm thick) and poly2 (1.5 μm thick) layers for fixed bottom fingers, and poly3 (2.25 μm thick) for movable top fingers. The first CMP process provides a vertical offset between the fixed and movable combs and keep the movable fingers flat and straight. The mirror is fabricated on the top polysilicon layer, poly4 (2.25 μm thick). Thanks to the second CMP process, the mirror surface is smooth and flat. A shielding electrode (poly0) is added below the fixed comb to prevent any unexpected interaction between the mirror and substrate. The cross-section of the device is shown in Fig. 3(a).

The minimum spacing between fixed and movable combs allowed in SUMMiT-V is 0.5 μm. The narrow gap spacing greatly increases the capacitance and therefore the force density, which can be utilized to reduce the operating voltage. The minimum finger width is 1 μm. The narrow finger and spacing also allow us to increase the number of fingers underneath the mirror, whose width of 137 μm is fixed by the system requirement.

Our main design trade-off is reducing voltage while maintaining high enough threshold for lateral instability. It is known that narrow gap spacing in comb drive actuator can lead to lateral instability at high voltages [9]. We need to have sufficiently large safety margin to prevent lateral instability even in the presence of imperfect fabrication (e.g., misalignment between fixed and movable comb fingers). To investigate this trade-off, finger spacing ranges from 0.5 to 3 μm were included in the design. The finger length (Lf) was varied from 15 to 30 μm. Three types of springs as shown in Fig. 4 are employed in our layout. An important criterion for the spring design is that the ratio of the spring constants for in-plane rotation (about z-axis), k_z, to out-of-plane rotation (about x-axis), k_x, should be as large as possible. From this point of view, Type *B* spring is better than Type *C* because the former has smaller k_x and larger k_z. The length of the

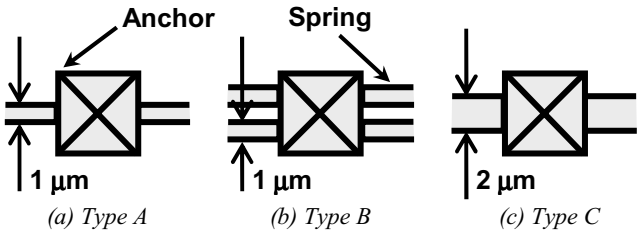

Figure 4. *Top-view schematics of the three types of torsion springs used in our design.*

spring was designed to be 55 μm. The mirror pitch of 150 μm is determined by the system requirement. With lateral stoppers, the maximum mirror width (in *x* direction) allowed by SUMMiT-V design rule is 137 μm. Therefore the linear fill-factor along the array direction is 91%. The mirror length (in *y* direction) is 120 μm.

EXPERIMENTAL RESULTS

The fabrication of the analog micromirror array is performed at Sandia National Lab. After SUMMiT-V process was completed, the chip was released in HF and dried. Cr/Au is deposited on the whole wafer by maskless e-beam evaporation to enhance the mirror reflectivity. Electrical isolation between electrodes was achieved by incorporating overhang structures. The radius of curvature of the mirror was measured to be 135 mm before metallization. The stress in metal reduces that to 23 mm after metallization. The DC scanning characteristics of the micromirrors for various finger gap spacing, finger lengths, and torsion springs are measured by WYKO, a non-contact interferometric surface profiler. The measured results (symbols) are shown in Fig. 5, together with the calculated results (lines) obtained using our hybrid finite element method and our pull-in model [8]. The measured results agreed very well with theory. For Type A spring with 0.5 μm finger spacing, a scan angle of 5.9° is obtained at 6 V (Fig. 5(a)). The maximum angle is limited by the pull-in effect, which occurs due to the residue parallel-plate capacitances in the structure. As finger gap spacing increases (Fig. 5(a)) or finger length increases (Fig. 5(b)), the maximum angle decreases because of earlier occurrence of pull-in. In all cases, the measured pull-in angles are slightly lower than the calculated values. This is attributed to the narrow gaps (1 μm) between the finger tips and the bases. The largest scan angle (6.9° at 18.1 V) is realized by short comb fingers (L_f = 15 μm). The resonant frequencies of the micromirrors were characterized using a Polytech Microscan laser Doppler vibrometer. The resonant frequencies for various spring types are summarized in Table I. The measured results agree very well with the theoretical values. The ratio of the measured resonant frequencies is

$$f_{R,A} : f_{R,B} : f_{R,C} = \sqrt{k_A} : \sqrt{k_B} : \sqrt{k_C} = 1 : 1.5 : 2.4 . \quad (5)$$

Fig. 6 shows the scanning electron micrographs (SEM) of the 1 × 10 micromirror array. The finger gap and length are 1 μm and 30 μm, respectively. Type *A* was used for the torsion spring. It is shown that the mirror surface remains flat in spite of the complicated topography underneath the mirror. The measured pull-in angle is 6.1°, which is occurred at 8.8 V. Good uniformity in the angle-versus-voltage characteristics (<±3.2%) across the array was

***Table I**. The measured and the calculated resonant frequencies of the micromirror.*

Spring type	Measured [kHz]	Calculated [kHz]
A	3.4	3.5
B	5.1	5.0
C	8.1	8.0

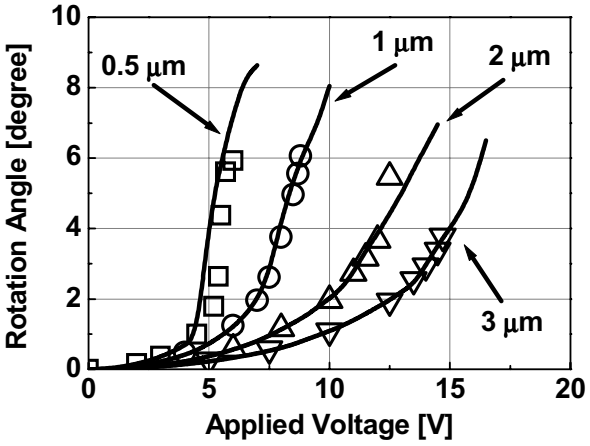

(a) For various finger gap spacing, finger length: 30 μm, type A spring.

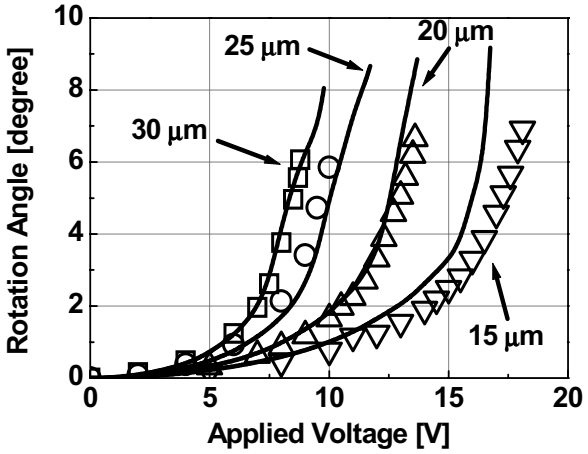

(b) For various finger length, finger gap spacing: 1 μm, type A spring.

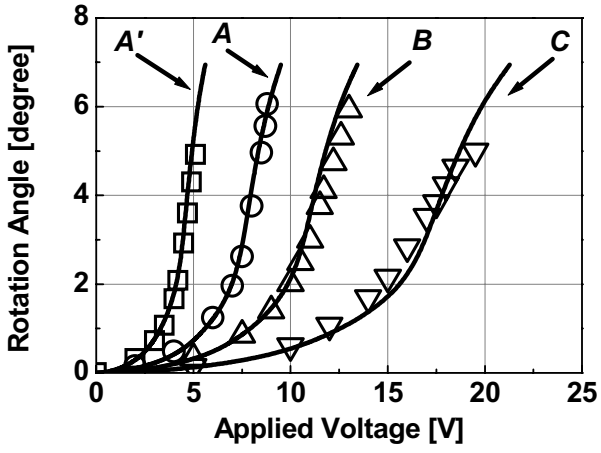

(c) For various types of springs (defined in Fig. 4), finger gap spacing: 1 μm, finger length: 30 μm. Type A' is same as type A except that it is three times longer than type A.

***Figure 5.** The measured (symbols) and the calculated (lines) DC scanning characteristics of the fabricated mirrors.*

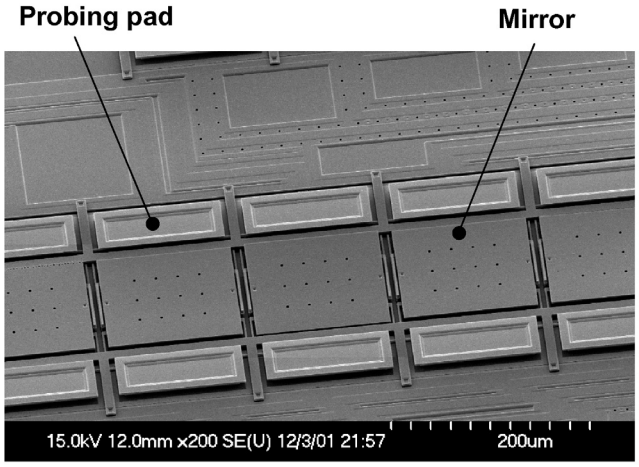

Figure 6. *The SEM image of the micromirror array.*

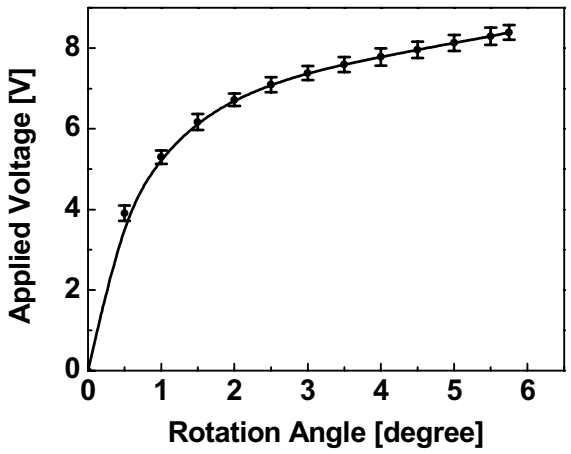

Figure 7. *Uniformity of DC scanning characteristics in the 1 × 10 analog micromirror array.*

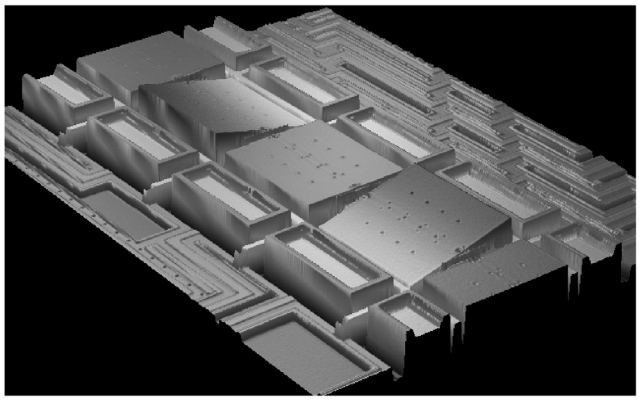

Figure 8. *The WYKO image of the fabricated micromirror array. Two of the mirrors are tilted by biasing the actuators.*

obtained (Fig. 7). Fig. 8 shows the optical interferometric image of the fabricated micromirror array. Two of the mirrors have been tilted by the actuators.

CONCLUSIONS

We have successfully designed and tested a 1-D analog scanning micromirror array with hidden vertical comb-drive actuators. Low operating voltage (6 V), wide scan range (23.6º optical), high fill-factor (91%), moderate resonant frequency (3.4 kHz), and good uniformity (< ±3.2%) have been demonstrated. The experimental results agree very well with our model. This micromirror array is very useful for WDM routers and WSXC.

ACKNOWLEDGEMENTS

The authors would like to thank Pamela R. Patterson, Wibool Piyawattanametha, and Erwin K. Lau of UCLA for technical assistance. This project is supported by DARPA/SPAWAR under contract N66001-00-C-8088.

REFERENCES

1. J. E. Ford, V. A. Aksyuk, David J. Bishop, and J. A. Walker, "Wavelength add–drop switching using tilting micromirrors," *J. Light. Technol*., vol. 17, pp. 904-911 (1999).

2. L. Y. Lin, E. L. Goldstein, and R. W. Tkach, "Free-space micromachined optical switches for optical networking," *IEEE J. Select. Topics Quantum Electron.: Special Issue on Microoptoelectromechanical Systems (MOEMS)*, vol. 5, pp. 4-9 (1999).

3. A. Husain, "MEMS-based photonic switching in communications networks," *Technical Digest of the OFC 2001*, Anaheim, CA, 3/17-22/01, Paper WX1.

4. R. Ryf, et al., "1296-port MEMS transparent optical crossconnect with 2.07Petabit/s switch capacity," *Technical Digest of the OFC 2001*, Anaheim, CA, 3/17-22/01, Postdeadline Paper PD28.

5. D. Hah, S. Huang, H. Nguyen, H. Chang, H. Toshiyoshi, and M. C. Wu, "A Low Voltage, Large Scan Angle MEMS Micromirror Array with Hidden Vertical Comb-Drive Actuators for WDM Routers," *2002 Optical Fiber Communication (OFC) Conference*, Anaheim, California, March 17-24, 2002

6. J.-L. A. Yeh, H. Jiang, and N. C. Tien, "Integrated polysilicon and DRIE bulk silicon micromachining for an electrostatic torsional actuator," *J. Microelectromech. Syst*., vol. 8, pp. 456-465 (1999).

7. R. A. Conant, J. T. Nee, K. Lau, and R. S. Muller, "A flat high-frequency scanning Micromirror," *Technical Digest of the 2000 Solid-State Sensor and Actuator Workshop*, Hilton Head, SC, 2000, pp. 6-9.

8. D. Hah, H. Toshiyoshi, and M. C. Wu, "Design of electrostatic actuators for MOEMS," *Technical Digest of the Symposium on Design, Test, Integration and Packaging of MEMS/MOEMS 2002*, Cannes-Mandelieu, France, 5/6-8/02, will be presented.

9. T. Hirano, T. Furuhata, K. J. Gabriel, and H. Fujita, "Design, fabrication, and operation of submicron gap comb-drive microactuators," *J. Microelectromech. Syst*., vol. 1, pp. 52-59 (1992).

MICROMIRROR ARRAY PHASE MODULATOR FOR ULTRASHORT OPTICAL PULSE SHAPING

Kebin Li, Uma Krishnamoorthy, Jonathan P. Heritage
Department of Electrical Engineering, University of California Davis, Davis, CA 95616
Olav Solgaard
Department of Electrical Engineering, Stanford University, Stanford, CA 94035

ABSTRACT

A linear phased array of programmable micromirrors provides dual mode motion. The micromirrors can be individually rotated about an axis through a mirror, and the whole mirror can be translated perpendicular to the mirror surface. Rotational motion adds the flexibility of constructing piecewise linear approximations to a desired phase modulation profile, enabling spatial phase modulation with higher diffraction efficiency than achievable with only translation. A new interferometer using on-chip stationary reference micromirror to calibrate the motion of the movable micromirror is presented. The coherent behavior of the micromirror array is also demonstrated. Applications include spatial scanning, and ultrashort-pulse shaping.

INTRODUCTION

Over the past decade powerful optical waveform synthesis (or pulse shaping) methods have been developed which allow generation of complicated ultrafast optical waveforms according to user specification. Coupled with the recent advances and resulting widespread availability of femtosecond lasers, as well as improvements in femtosecond pulse characterization techniques, femtosecond pulse shaping is poised to impact many diverse applications. Those areas include quantum control with light, laser selective chemistry, particle acceleration, coherent control over ultrafast physical processes, high field physics and optical communication.

Pulse shaping using reflective spatial light phase modulator (SLPM) is shown in Fig. 1. An ultrashort laser pulse is incident on a simple grating and lens apparatus, separated by the focal length of the lens, which spatially decomposes the pulse into individual optical frequency components at the focal plane of lens. One can insert spatially patterned masks or a programmable SLPM at the focal plane in order to manipulate the amplitude and the phase of the spatially dispersed optical frequency components. After the various frequencies are reflected and reassembled into a single

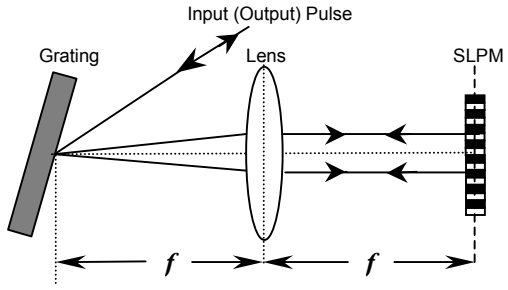

Figure 1. *Reflective ultrashort pulse-shaping apparatus.*

collimated beam by the lens and grating, one obtains a shaped pulse. In the high resolution limit, the pulse shape is determined by the Fourier transform of the amplitude and phase pattern imposed on the spectrum by the masks. The pulse shaper is dispersion free, so that in the presence of a flat mirror, the output and input pulses are identical.

Programmable SLPM are a key component in a femtosecond pulse shaper [**1**] and are thus under intense investigation recently because of its potential applications. Existing linear SLPMs, fall into two categories; deformable continuous thin membrane mirrors [**2**], and pixilated arrays of liquid crystal phase shifters [**3**].

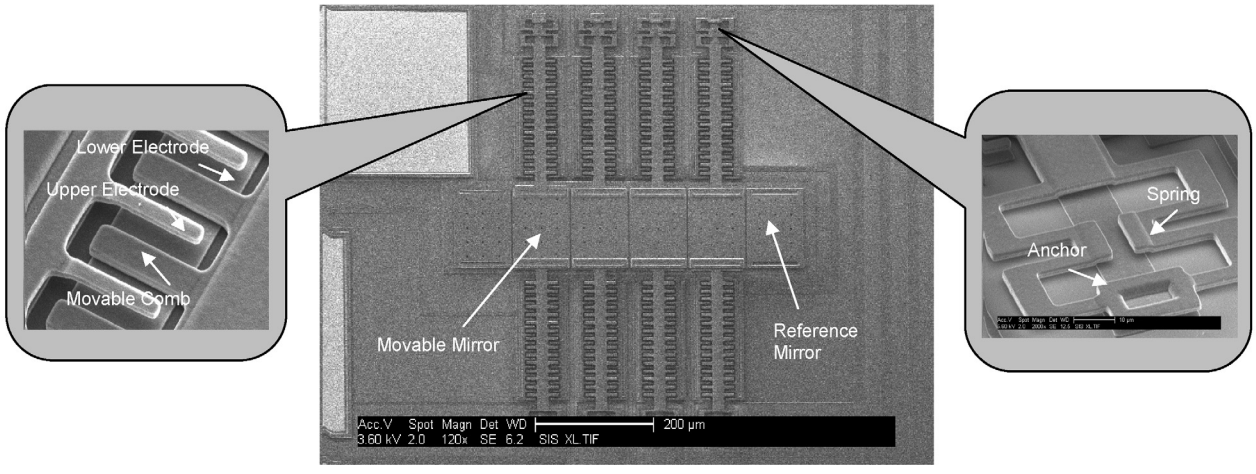

Figure 2*. SEM photographs of the micromirror array showing four movable mirrors and two stationary reference mirrors. The left blowup shows the details of the upper comb electrode and the lower planer capacitive electrode. The right blowup shows the tether and spring that support the mirror.*

Travel support has been generously provided by the Transducers Research Foundation and by the DARPA MEMS and DARPA BioFlips Programs

Deformation of a continuous membrane produces smooth spectral phase variations and a corresponding, high quality optical pulse but membranes are not capable of producing localized rapid spectral phase changes. Pixilated arrays of phase modulators can produce rapid phase changes between pixels. However, the phase shift for each pixel is constant and the resulting discrete approximation to smooth phase variations results in undesired energy in the pulse wings.

Here we introduce a new coherent micromirror-array SLPM (Fig.2), which is fabricated by the MUMPS process. The mirrors of the array have both rotational motion and elevation control [**4**] enabling high fidelity phase modulation. Vertical elevation (modulo π) of the mirror introduces the desired phase shift for each pixel, while mirror tilt allows a much-improved *piecewise linear* approximation to the local phase variation compared to commercially-available SLPMs, such as liquid crystal and thin membrane mirror phase modulators.

MICROMIRROR DESIGN AND FABRICATION

In order to achieve both rotation and linear motion of the micromirror, we designed an actuator with two upper vertical comb drives and two lower planar capacitive drives. Figure 2 shows an SEM micrograph of an array fabricated in the MUMPS surface micromachining process. In our SLPM design, each mirror is 100 x 120 microns and has four stationary electrodes on each side. A pair of vertical comb drives emanating from each mirror, are tethered their far ends. They act as springs to support a freely floating mirror. Applying the same potential to each of the fixed upper vertical combs raises a mirror with out applying a torque. A mirror may be similarly depressed by applying the same potential on each of four lower planar conductors. A mirror is rotated by applying a potential to one comb (on both sides of the mirror) with another equal potential is on the diagonally opposing planar electrode. Ideally, the applied potentials are arranged such that the forces on the torsion bar are equal and opposite and then no vertical motion accompanies the rotation. Unbalanced forces result in both vertical motion and rotation.

Surface flatness of the micromirror is very important for the optical applications. We use a Zygo system to measure the surface planarity of our micromirror array. Figure 3 shows surface plots of two micromirrors in the array. The phase change across each mirror is less than one hundredth of 2π for 1.6 micron input pulse

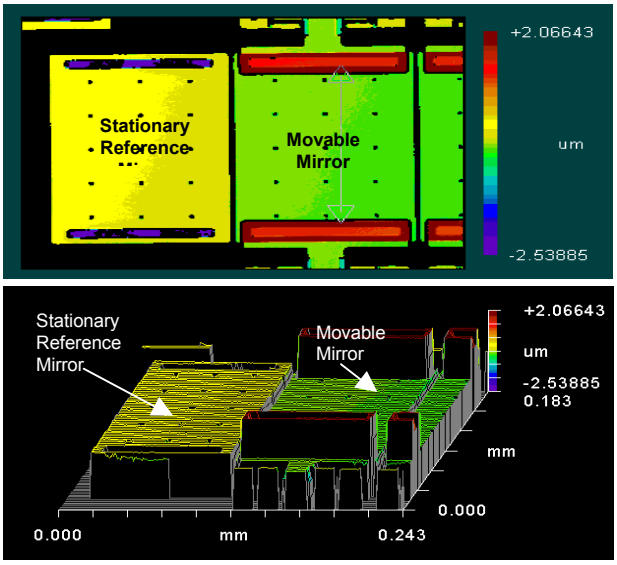

Figure 3. *Micromirror surface flatness measurement using Zygo system, radius of curvature reaches as much as 4.8 m for 100 μm× 120 μm mirrormirror*

central wavelength. The radius of curvature perpendicular to the comb drive direction is 0.41 meter, and 4.8 meter in the direction of the drives. These polysilicon micromirrors, which are not coated, have 40 percent reflectivity. Although with gold coating, much higher reflectivity can be reached however, mirror flantens will be affected.

ON-CHIP REFERENCE MIRROR INTERFEROMETER

We designed a simple interferometer in order to calibrate the motions of the micromirrors. Reflections off the movable mirror under test and off an on-chip stationary reference mirror generate an interference pattern in the far field. Using a thin glass plate we split a laser beam into two coherent beams, which are focused on the two mirrors separately. The reflected far field interference pattern contains the information of movable micromirror position. This interferometer is less sensitive to vibrations than more

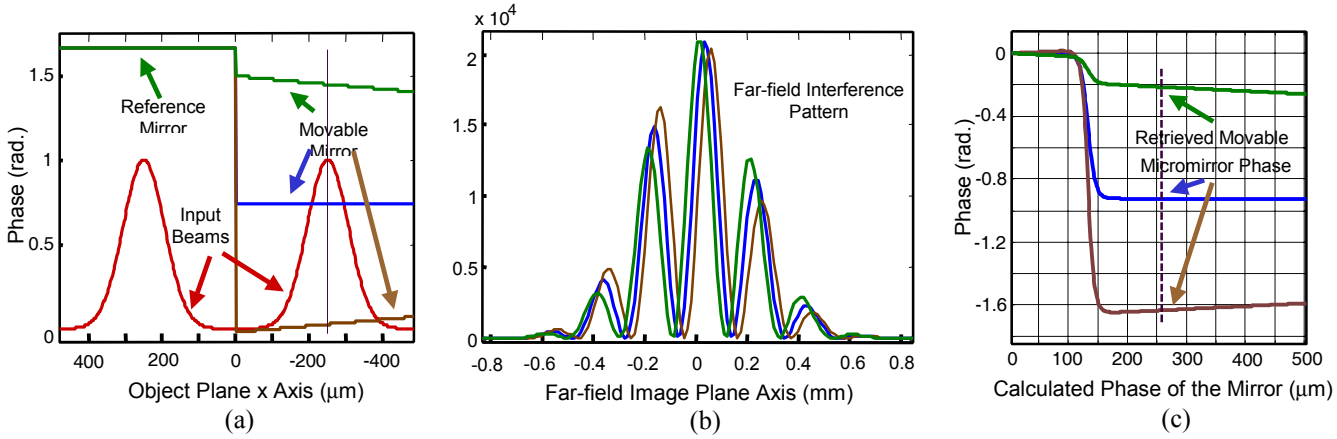

Figure 4. *Simulation of the phase retrieval from the far field interference pattern created by the reflections from the reference and movable mirrors. (a) The three different states of the mirrors with the two coherent inputs overlaid. (b) Three interference patterns corresponding to the three positions of the movable mirror. (c) Movable-mirror phase calculated from the interference pattern.*

complicated interferometers with off-chip reference arms and is easy to operate.

This Fourier-transform method can be proved and simulated as shown in the following discussion. Assume two Gaussian coherent beams are focused, one on the reference mirror and the other on the movable micromirror. The spacing is $2x_0$. The movable mirror tilts with a slope of f_0. The output field amplitude from the micromirrors is:

$$g(x) = Ae^{-a(x+x_0)^2} + Ae^{-a(x-x_0)^2} e^{i2\pi f_0 (x-x_0)}. \quad (1)$$

The far field interference pattern field amplitude is the Fourier transform of the Eq.(1). The corresponding intensity is then found. Next, take the Fourier transform of the *intensity* profile of the interference pattern and make use of the positive component of the spectrum:

$$C\{\cos[2\pi f_0 (x-2x_0)] + i\sin[2\pi f_0 (x-2x_0)]\}, \quad (2)$$

C is a constant. It is easy to see now that if we divide the imaginary part by the real part and take the inverse tangent of that, one retrieves the slope, f_0, for the movable micromirror, when x is near $2x_0$.

We developed a simulation program to illustrate the process of phase retrieval. The simulation results in Fig.4 show how the spatial phase variation of the movable mirror (Fig. 4a) leads to a shift and intensity change of the far-field interference pattern (Fig. 4b), from which the vertical displacement and tilt of the mirror under test can be retrieved (Fig. 4c).

MICROMIRROR MOTION CALIBRATION

The micromirror motion calibration can be put into three categories. There are, elevation or depression, tilt angle, and general motion with respect to applied voltage. An experimental measurement for the first two cases is shown in Fig. 5.

We previously reported **[5]** a special case of our interfrometer, which uses only one optical beam, and thus can only measure tilt and elevation change in separate measurements. Using a single spot, which covers two adjacent mirrors, an interference dip appears in the far field diffraction pattern. Changes its position are in proportion to the optical phase difference between the optical paths. When the mirrors are at the same height, constructive interference produces a single broad spot as is displayed in the far-left image in Fig. 5(a). When the mirror is elevated by $h = \lambda/4$, the optical path length difference between the two mirrors results in destructive interference, as is displayed in the far right hand image in Fig. 5(a). The corresponding optical phase difference is then

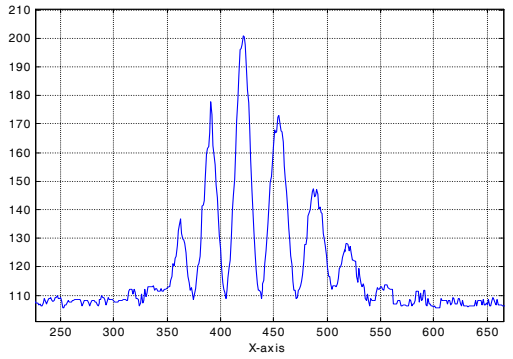

(a)

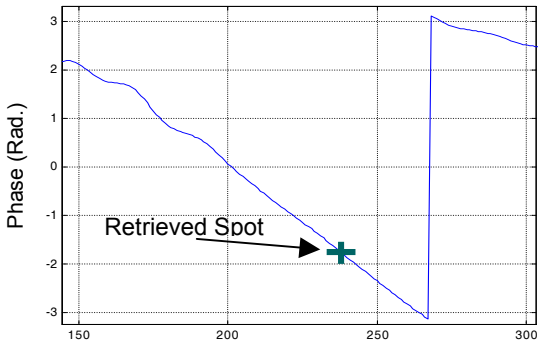

(b)

Figure 6. *Experimentally measured far-field interference pattern and the retrieved phase of the movable mirror. (a) The far field interference fringe pattern generated by movable mirror and reference mirror. (b) Retrieved phase of the movable mirror. Both the vertical displacement and tilt angle can be calibrated. For example: The phase difference of the retrieved spot relative to the reference mirror is 4.75 radians, and the micromirror tilt angle is* 0.33^0

$4\pi h/\lambda$. The phase shift for an arbitrary h produces an off center interference dip as is displayed in the middle image of Fig. 5(a). Figure 5(b) shows the levitation displacement versus the applied potential to upper and lower electrodes. The lower electrodes, in

(a)

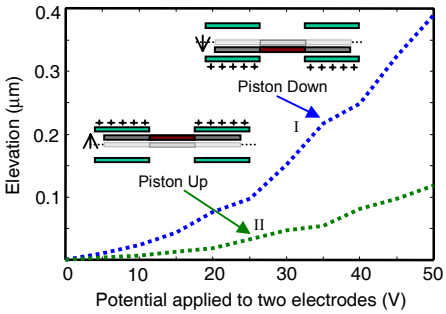

(b)

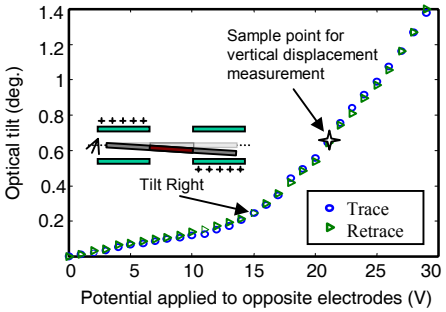

(c)

Figure 5. *Measured micromirror motion. (a) CCD images of far field diffraction pattern obtained when both a movable mirror and a reference mirror are illuminated. Elevation increases from zero to λ/4 from left to right. (b) Elevation vs. applied potentials for downward (curve I) and upward (curve II) displacements. (c) Tilt vs. applied potentials. The same potential is applied to the diagonally opposing electrodes.*

this design, provide greater force per unit applied potential than the comb structure. Reduction of electrode size allows design of symmetric, or alternatively, symmetric comb drives could be fabricated.

Figure 5(c) shows mirror tilt when the same potential is put on opposite electrodes. The measured useable static range of angular and vertical motions was 1.4 degrees (optical) and 1.2 microns, respectively. Because of the asymmetry of the electrodes, an elevation change occurs in this situation as well. We pick a sample point shown in Fig. 5(c) to measure the vertical shift caused by this asymmetry using our general Fourier-transform approach discussed before. Figure 6(a) shows the intensity profile of far field interference pattern measured by CCD camera when movable mirror is under this sample condition, 21.5 volts on opposite electrodes. The retrieved phase of the mirror is shown in Fig. 6(b). From that we get mirror tilt angle 0.33^o that matches well with the optical tilt 0.65^o in Fig. 5(c) using simple beam shift method.

We also retrieve vertical down shift 4.75 radians from the plot. It is shown in Fig. 3 that the stationary reference micromirror is 0.2 μm higher than the resting movable mirror due to the design. Since the coherent light source is $\lambda = 0.632$ μm, the phase delay in this case is 3.98 radians. So the actual mirror vertical down shift is 0.39 radians or 0.04 μm. Referring to the Fig. 5(b), we see that the actual elevation lies between curves II and I. This is the expected result which demonstrates the important capability to obtain both rotation and elevation in a single measurement.

COHERENT PHASED ARRAY DEMONSTRATION

To demonstrate the operation of the coherent micromirror array, we displayed the far field diffraction when illuminated with a monochromatic line source ($\lambda = 632$ nm). This configuration is formally analogous to high-resolution femtosecond pulse shaping. We investigated three arrangements of the mirror array that illustrate coherent control of the diffracted wave front. Figure 7(a) shows three different mirror position patterns. Pattern 1 (light gray outline) is for free floating mirrors with no applied potential. This establishes the system diffraction limit as shown in Fig. 7(b), dotted peak. In pattern 2 (hashed diagonals) all the micromirrors tilt the same angle as a reference bulk mirror. This configuration produces a four-micromirror array, which is now a blazed diffraction grating. Figure 7(c) shows four diffraction orders plus the specular reflection. In sharp contrast, if we adjust each mirror height as shown in Fig. 7(a) the grating becomes the equivalent of a single, large tilted reference bulk mirror, except now, it is pixelated. Pattern 3, (gray fill) reflects only into a new specular direction, as shown in Fig. 7(b). Higher order diffraction is effectively suppressed. This operation can only be accomplished with a coherent array of mirrors that have simultaneous tilt and elevation.

CONCLUSIONS

In summary, we propose and demonstrate a new type of digitized programmable SLPM using MEMS technology. We have designed, fabricated, and calibrated array of micromirrors with independent tilt and elevation control, and demonstrated that our arrays can perform coherent phase modulation. These devices, when expanded to larger array sizes, will find applications in femtosecond pulse shaping.

REFERENCES

1. A.M. Weiner, J.P. Heritage and E. M.Kirschner, "High-resolution femtosecond pulse shaping," *J. Opt. Soc. Amer.,* vol. B5, p.1563, 1988.
2. C. Dorrer, F. Salin, F. Verluise and J.P. Huignard, "Programmable phase control of femtosecond pulses by use of a nonpixelated spatial light modulator," *Opt.Lett.,* vol. 23, (no.9), p709. May 1, 1998.
3. A.M. Weiner, D.E. Leaird, J.S. Patel and J.R. Wullert, "Programmable femtosecond pulse shaping by use of a multielement liquid-crystal phase modulator," *Opt. Lett.,* vol. 15, p.326, 1990.
4. U. Krishnamoorthy, K.Li, K. Yu, D. Lee, J.P. Heritage and O. Solgaard, *11th International Conference on Solid-State Sensors and Actuators* (Transducer '01), Munich, Germany, June 10-14, 2001.
5. K. Li, U. Krishnamoorthy, J. P. Heritage, and O. Solgaard, "Coherent Micromirror arrays," *Opt. Lett*., vol 27, p.366, 2002.

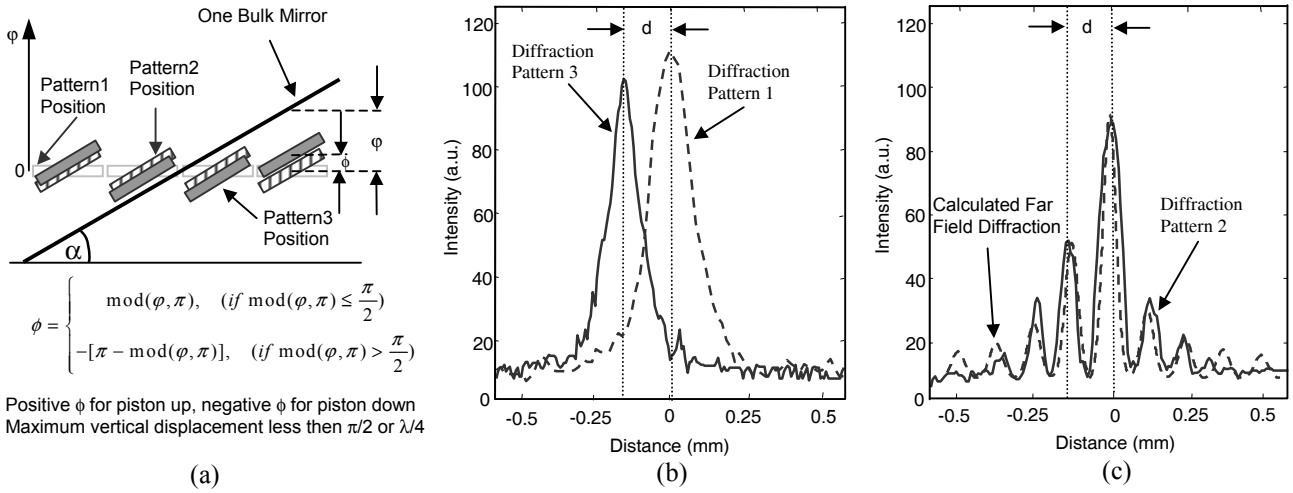

Figure 7. *Coherent phased array far field diffraction patterns. (a) Three different mirror array position patterns and minimum ϕ calculation, (b) Diffraction limit for pattern 1 mirror array position and shifted beam for pattern 3 position with both tilt and vertical levitation motions, (c) Diffraction pattern of tilt only pattern 2 position, which forms a coarse brazed grating.*

AN ELECTROSTATIC, ON/OFF MEMS VALVE FOR GAS FUEL DELIVERY OF A MICROENGINE

Xue'en Yang, Alexander Hölke, and Martin Schmidt
Microsystems Technology Laboratories
Massachusetts Institute of Technology
Cambridge, MA 02139

ABSTRACT

An electrostatic, on/off silicon valve designed to control gaseous fuel combustion by an array of such valves in a micro gas turbine engine was fabricated and fully characterized. Tested with nitrogen under room temperature, the valve opened against 10 atmospheres of pressure at 136 V and delivered a flow rate of 45 sccm (cm^3/min). At the same pressure, the helium leak-rate was expected to be less than 0.03 sccm, 0.07% of the open flow rate. The valve showed no sign of failure after more than 10^5 cycles.

INTRODUCTION

MIT is developing a MEMS gas turbine generator for high power density output in applications such as portable power sources and micro air vehicles [**1**]. Figure 1 shows the cross-sectional view of the microengine in a 5-wafer stack. The valve is to be place on top of the fuel manifold, modulating the fuel flow from the tank to the combustion chamber. Table 1 lists the design specifications for the engine valve. In addition, during fabrication, the valve needs to survive wafer-bond anneals at 1100ºC, and during operation, it needs to open against 10 atm upstream pressure under a high-temperature operating environment (400ºC), and deliver a maximum flow rate of 600 sccm. Engine proportional flow control can be accomplished with an array of valves (designed to have 20 elements). However, the operation requirements cannot be met by previously reported MEMS valves, many of which are designed for lower-temperature, lower-pressure or lower-flow rate applications, e.g., by thermal [**2**], electromagnetic [**3**], or piezoelectric [**4**] actuations. Reported electrostatic valves did not meet the specifications because they used metals for actuation [**5**], used soft material for sealing surface [**6**], designed for low-pressure flow control [**7**], or designed for normally-open flow control [**8**].

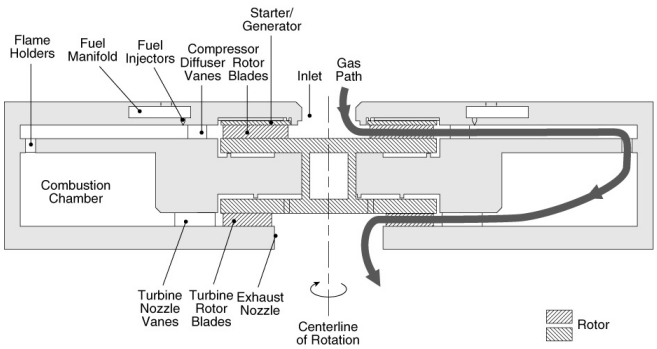

Figure 1. Cross-sectional view of the microengine. The fuel valve structure will be placed on top of the stack, between a fuel tank and the supply plenum.

Table 1. Fuel Valve Specifications for the microengine.

	Fuel Valve
Fuel	Gaseous
Temperature	0ºC - 400ºC
Flow Rate (maximum)	45 g/h (600 sccm)
Flow Rate (one valve)	1.5 g/h (30 sccm)
Fuel Pressure	1 Mpa (10 atm)
Allowed Pressure Loss	0.7 Mpa (7 atm)
Leak Rate	< 0.03 cm^3/min He
Power Consumption	< 10mW
Time Response	10^{-1}s
Size	2.5cm

DESIGN AND FABRICATION

Using fusion bonding of multiple Silicon-On-Insulator (SOI) wafers and Deep Reactive Ion Etch (DRIE), we were able to design and fabricate an electrostatic valve that demonstrated feasibility at room temperature. The prototype valve is comprised of three fusion-bonded wafers. Figure 2 shows the design concept using a 3-D bisected schematic. The valve is normally closed when the tank is pressurized. When voltage is applied between the top electrode and the boss, electrostatic force lifts up the boss and opens the valve, allowing gas fuel to flow past the top wafer and the tethers, then radially inward through the valve seat, and finally exit through the bottom of the die. The flow was designed to choke at the exit of the valve seat.

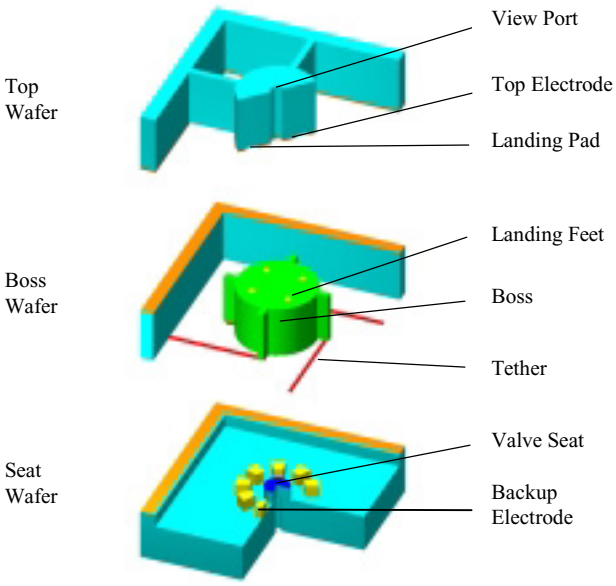

Figure 2. 3-D cross-sectional schematic of the micro valve.

Travel support has been generously provided by the Transducers Research Foundation and by the DARPA MEMS and DARPA bioflips programs

A 2-D schematic of the three bonded layers is shown in Figure 3. As seen from the figure, the top wafer is prepared from a SOI wafer and it contains the view-port (for testing purpose), the top electrode and the landing pads. The top electrode is etched on a SOI layer, and the buried oxide layer is used as the insulation from the substrate, which is grounded during operation. The landing pads are cylindrical openings etched through the SOI and oxide layers. They are used as mechanical stops to prevent the boss from colliding on the top electrode during opening. The boss wafer, also prepared from a SOI wafer, features a silicon boss actuator supported on four straight tethers in a pinwheel configuration. The tethers are etched from a SOI layer to ensure uniform thickness. During operation, the tethers are grounded, and as a result, the boss is electrically floating. However, because of the dominant capacitance distribution in the buried oxide, the voltage drop between the boss and the tethers is not significant. During pull-in, the landing feet on top of the boss will move up and stop at the landing pads and thus make electrical contact with the grounded top substrate. By doing so, a minimum air gap is formed between the two electrodes and electric shorting is avoided. The bottom wafer, prepared from a double-sided polished (DSP) wafer, has the valve outlet, the valve seat and the backup electrode (used for testing purpose). The valve seat contains a polysilicon surface, which prevents bonding to the boss under high temperature contact because of its roughness.

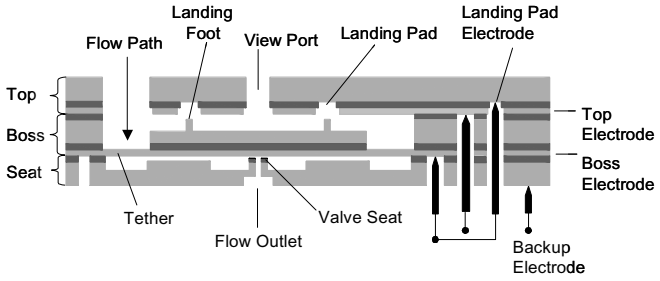

Figure 3. Schematic cross-section of the fuel valve.

A brief description of the fabrication sequences is as follows. A SOI wafer with 0.34 µm SOI/ 1 µm SiO_2/ 500 µm Si substrate thickness was used as the top wafer. The SOI layer was first plasma etched to define the top electrode area (1.1 mm diameter) as well as the landing pad, and the oxide layer was HF etched using a different mask to avoid undercut. The wafer was then DRIE etched through from the bottom to form the inlet paths. The boss wafer used a SOI wafer with 17 µm SOI/ 0.4 µm SiO_2/ 380 µm Si substrate thickness. The wafer was first oxidized to form a 1.5 µm thick oxide. Four landing feet, targeted for 3.4 µm deep, were then plasma etched on the electrode area. Subsequently, the wafer was flipped and etched from the back using DRIE to form the 17 µm thick, 60 µm wide, and 800 µm long tethers. DRIE was then used again to etch from the top, using the buried oxide as the etch stop. Finally, the boss was released using an ultrasonic HF bath to etch away the oxide layer. Fabrication of the seat wafer was a little more complicated. A DSP wafer was first oxidized (for 0.7 µm thick). 0.95 µm of LPCVD polysilicon was then deposited at 625 C (as the valve seat). The wafer was subsequently oxidized again (for 1 µm thick). After a series of DRIE etches, a flow channel of inner diameter 36 µm and 200 µm depth connected to an outlet of 100 µm diameter and 250 µm depth was formed. The valve seats were flat and two geometries were used: diameter 34 and 42 µm, on a total of six dies. After the three wafers were fabricated, they were fusion bonded together and annealed at 1100 C for 1 hour. The wafer stack was then die-sawed into 1.54 cm × 1.54 cm square chips. Figure 4 shows the SEM photos of the three wafers as fabricated as well as the pictures of the valve chip.

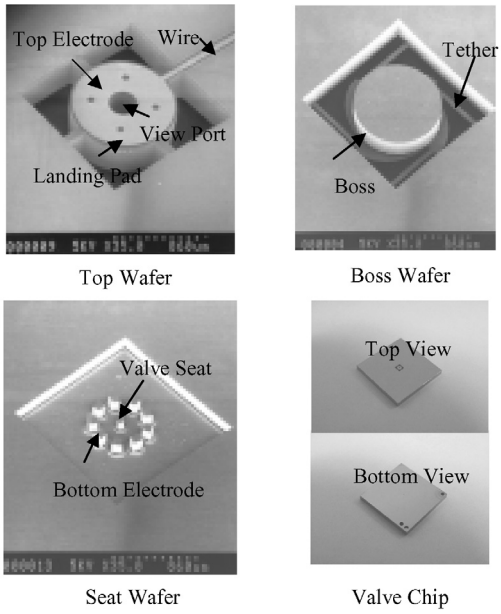

Figure 4. SEM photos of the three wafers as fabricated, as well as pictures of valve chip.

PACKAGING AND EXPERIMENTAL SETUP

The prototype valve was tested under room temperature using nitrogen. The package for the fuel valve was designed to withstand at least 10 atm and support a maximum voltage of 300V. We used *plexiglass* for the flow housing, and pogo pins for electrical connection. Figure 5 shows the package assembly. The valve chip is placed at the center of the aluminum spacer. Fluid connection is achieved by fitting *Scanivalve* stainless steel tubes into the side openings of the top and bottom plates and sealing them with epoxy. Pogo pins are fixed into the pinholes of the pin holder, delivering electrical potentials from a voltage source to the different layers of the valve chip.

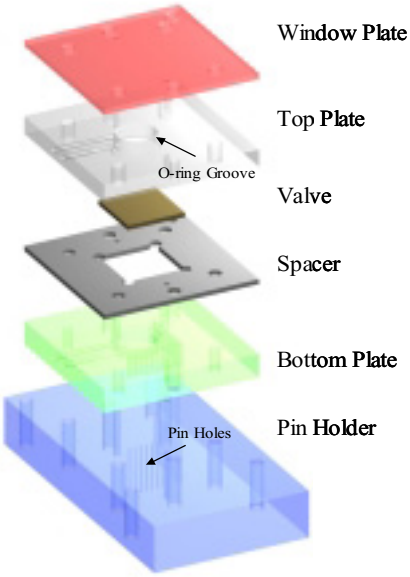

Figure 5. Package assembly for valve testing.

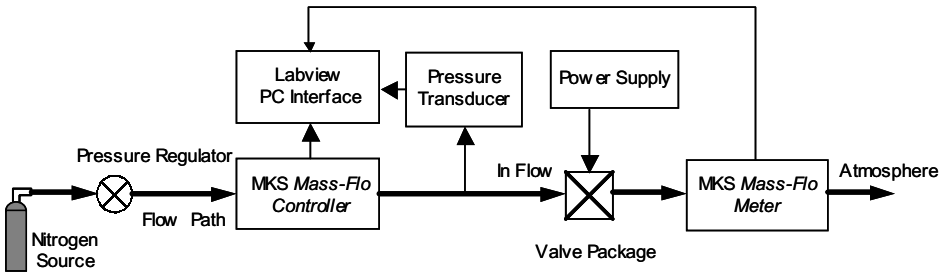

Figure 6. A chart representation of the flow test setup.

A schematic representation of the flow test setup is shown in Figure 6. A *Mass-Flow* Controller by *MKS Instruments* was used to measure the flow rate. A *Honeywell* pressure transducer was used to measure the upstream pressure. Data acquisition was done via a *NI* GPIB board and a LabVIEW interface was used for data display. For measuring the leak rate, a helium leak detector was used.

TESTING AND RESULTS

With no external pressure applied, the experimental quasi-static pull-in voltage of the valve was 38±2 V, which matched with the calculations. The results following were obtained from a die with 34 µm diameter valve seat. For gas supplied at the specific pressures, the steady state flow rate as a function of voltage is plotted in Figure 7, showing pull-in instability at different levels. The voltage that initiated a steady flow rate is the minimum DC voltage required to switch on the valve. This switch-on voltage is plotted against the upstream pressure in Figure 8. The flow rates at such pressures are plotted in Figure 9, which illustrates close match with the results of numerical simulation using FLUENT, confirming that at higher pressure (> ~1.5 atm), the flow chokes at the exit of the valve seat. At 10 atm, the opening voltage was 136 V, resulting in a flow rate of 45 sccm, higher than 30 sccm as designed. This is because the valve diameter as fabricated is larger than designed on the mask. Flow rates can be better controlled by considering the undercut effect of DRIE in the mask design.

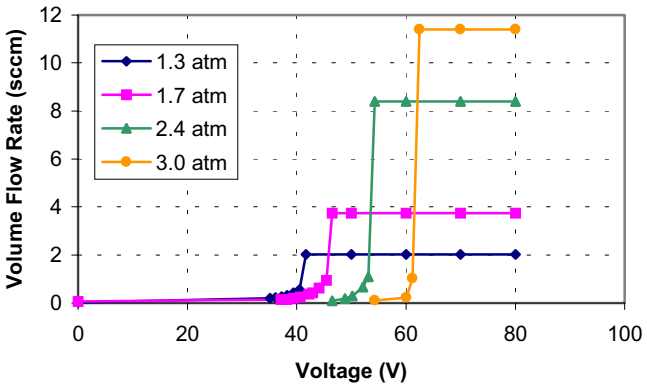

Figure 7. Steady volume flow rate as a function of applied voltage at given pressures.

Leak rates for two dies having different valve seat diameters are plotted in Figure 10. Because of the upper limit of

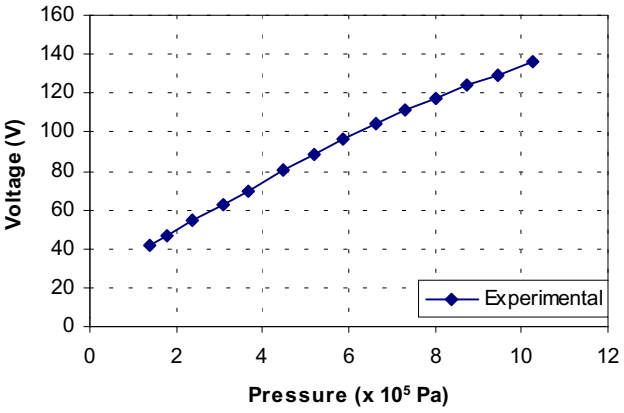

Figure 8. Opening voltage as a function of absolute upstream pressure.

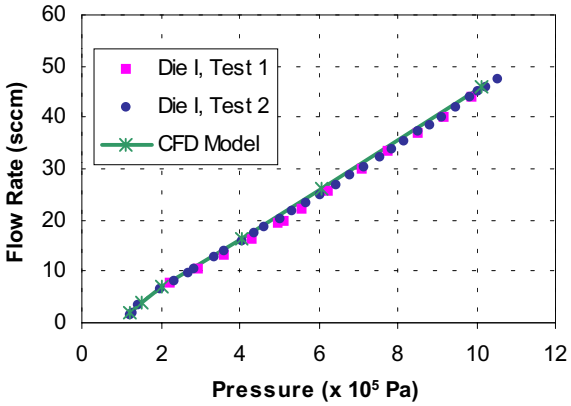

Figure 9. Comparison of steady flow rate vs. absolute upstream pressure with experiment and CFD model.

the detector, leak rates at higher upstream pressure were not available. Using the linear relation as observed from Figure 9, we predicted that the leak rate at 10 atm upstream pressure would be less than 0.03 sccm for the smaller valve seat case (34 µm diameter). Smaller leak rates were observed with larger valve seats, suggesting that sealing could be improved by altering the valve seat geometry.

A fiber optic sensor was used to detect the motion of the boss during the opening operation (because of the window plate of the flow package, a concave lens had to be used in order to enhance the output signal). At 10 atm, with a step voltage of 136V, the step response of the valve is shown in Figure 11,

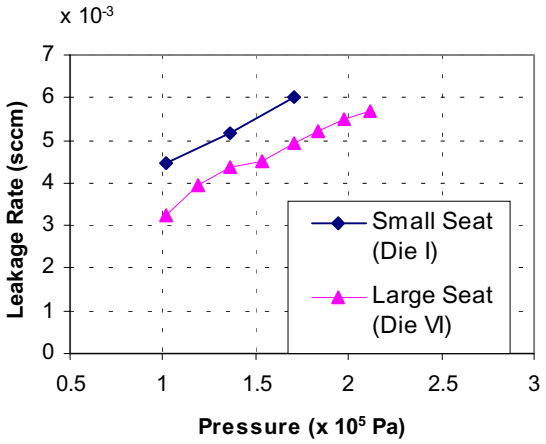

Figure 10. Helium leak rate as a function of the upstream pressure.

revealing a rise time of about 20 ms. Note that oscillations in the plot were caused by the noise in the fiber optic system. The valve was also subjected to cyclic tests using a simulated square waveform. It was demonstrated that at the 10 atm condition, the valve operated without any sign of failure after more than 10^5 cycles.

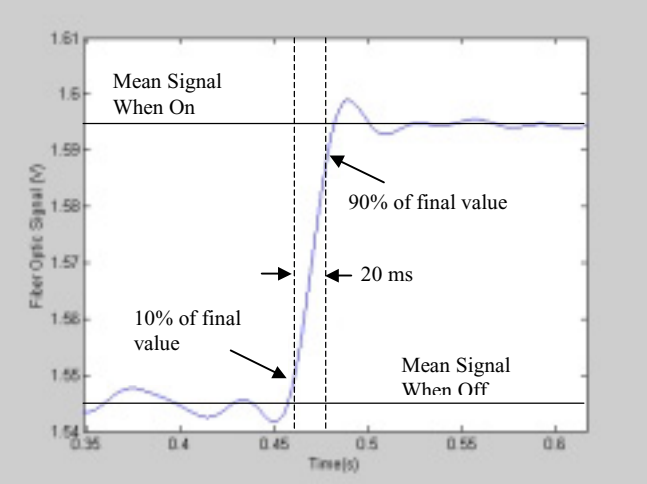

Figure 11. Demonstration of the rise time when the valve was subjected to a step response. The upstream pressure was 10 atm, and the opening voltage was 136 V.

CONCLUSIONS AND FUTURE WORK

The MIT microengine prototype valve has been fabricated, assembled, and tested. The valve employs electrostatic actuation and uses polysilicon as the valve seat. Design of the valve is made possible using SOI wafers and the DRIE process. The valve has been tested with nitrogen under room temperature. Results demonstrated feasibility of the design of a MEMS valve for the micro gas turbine engine.

In order to modulate the flow and accomplish the control scheme, an array of such valves (designed to be 20) will need to be incorporated into the microengine in the future. Operation at high temperature must also be demonstrated.

ACKNOWLEDGEMENTS

This work was supported by DARPA TTO, Dr R. Rosenfield manager. The authors would like to thank Prof. A. Epstein, Prof. J. Lang , Dr. A. Ayon, Dr. S. Jacobson, and Dr. S. Umans for their contributions. Travel support has been generously provided by the Transducers Research Foundation and by the DARPA MEMS and DARPA bioflips programs.

REFERENCES

1. A. H. Epstein *et al.*, "Micro-Heat Engine, Gas Turbine, and Rocket Engines – The MIT Microengine Project", AIAA 97-1773, *28th AIAA Fluid Dynamics Conference*, Snowmass Village, CO, June 1997.

2. A. R. Collin, D. W. Kensall, "A Thermopneumatically-Actuated Microvalve with Improved Thermal Efficiency and Integrated State Sensing", *Solid-State Sensor and Actuator Workshop*, Hilton Head Island, South Carolina, June 4-8, 2000, pp. 234-237.

3. D. J. Sadler, W. O. Kwang, H. A. Chong, et al, "A New Magnetically Actuated Microvalve for Liquid and Gas Control Applications", *Transducers'99*, June 7-10, 1999, Sendai, Japan, pp. 1812-1815

4. W. C. Chakraborty, D. P. Bame, T. K. Tang, "MEMS Micro-Valve for Space Applications", *Transducers'99*, June 7-10, 1999, Sendai, Japan, pp. 1820-1823

5. K, Sato, et al, "An Electrostatically Actuated Gas Valve with an S-Shaped Film Element", *Journal of Micromechanics and Microengineering*, 4(1994), pp. 205-209.

6. M. L. Philpott, D. J. Beebe, et al, "Switchable Electrostatic Micro-Valves with High Hold-Off Pressure", *Solid-State Sensor and Actuator Workshop*, Hilton Head Island, South Carolina, June 4-8, 2000, pp. 226-229.

7. N. Vandelli, D. Wroblewski, M Velonis, T. Bifano, "Development of a MEMS Microvalve Array for Fluid Flow Control", *Journal of Microelectromechanical Systems*, Vol. 7, No. 4, December 1998,pp. 395-403.

8. L. Yobas, M. A. Huff, F. J. Lisy, D. M. Durand, "A Novel Bulk-Micromachined Electrostatic Microvalve with a Curved-Compliant Structure Applicable for a Pneumatic Tactile Display", *Journal of Microelectro-mechanical Systems*, Vol. 10, No. 2, June 2001, pp. 187-196.

DESIGN, FABRICATION AND TESTING OF THE P^3 MICRO HEAT ENGINE

J. Skinner, M. Thompson, S. Whalen, R. F. Richards, D. F. Bahr and C.D. Richards
School of Mechanical and Materials Engineering
Washington State University
Pullman, Washington 99164-2920

ABSTRACT

The development and testing of a micro heat engine is presented. The P^3 micro heat engine is an external combustion engine, in which thermal power is converted to mechanical power through the use of a novel thermodynamic cycle that approaches the ideal vapor Carnot cycle. Mechanical power is converted into electrical power through the use of a thin-film piezoelectric membrane generator. This design is well suited to photolithography-based batch fabrication methods, and is unlike any conventionally manufactured macro-scale engine.

INTRODUCTION

There is a pressing need for high energy density micro power generation systems. The energy densities of existing electrochemical batteries are too low (around 1 kJ/g) to sustain the power needs of MEMS devices for long periods **[1]**. An attractive alternative to batteries are hydrocarbon fuels, currently the most successful means yet developed to transport and store energy compactly. A typical liquid hydrocarbon fuel holds around 50 kJ/g in its chemical bonds **[2]**. However, the development of a micro-scale device that can efficiently convert this chemical energy into useful electrical power is challenging. Among the micro-scale concepts to generate electrical power using the chemical energy of hydrocarbon fuels now being explored are fuel cells, static heat engines and dynamic heat engines.

On the macro-scale, dynamic heat engines have achieved greater success than either fuel cells or static heat engines. This success is in large part because dynamic heat engines are more fuel flexible than fuel cells and have achieved higher conversion efficiencies than static heat engines. For these reasons, a variety of designs for micro-scale dynamic heat engines have been advanced. These include a gas turbine (Brayton cycle) engine**[3,4]**, a micro rotary internal combustion (Otto cycle) engine**[5]** and a micro heat engine based combustion driven reciprocating liquid piston (Otto/Diesel cycle)**[6]**. Each of these dynamic heat engines are internal combustion engines.

Work at WSU has been directed toward the development of a MEMS power system based on a dynamic heat engine that is driven by an external heat source, the P^3 micro heat engine **[7]**. Since micro-manufacturing methods excel at producing many identical copies of two-dimensional structures, the engine design is a modular, two-dimensional architecture. The P^3 micro engine produces electrical power by employing a three-part strategy. First, thermal power is conducted into the P^3 engine from an external heat source. Second, thermal power is converted to mechanical power through the expansion and compression of a two-phase working fluid by the oscillation of a flexible membrane. Third, mechanical power is converted into electrical power through the use of a thin-film piezoelectric generator.

DESIGN

The design of the P^3 micro heat engine is based on a two-dimensional modular architecture. An individual module or unit-cell engine consists of a cavity filled with a saturated, two-phase working fluid, and bounded on the top and bottom by thin membranes. The top membrane of the cavity is a thin film piezoelectric membrane generator.

Heat is alternately conducted in and out of the two-phase working fluid, through the thin membranes capping the cavity at top and bottom. As heat is conducted first into and then out of the working fluid, the quality and volume of the saturated mixture first increases and then decreases. As a consequence, the upper membrane, which is fabricated of a piezoelectric thin film, acts like a piston in a conventional large-scale engine. Instead of sliding in and out, however, the piezoelectric thin film membrane flexes in and out. In this way, the piezoelectric membrane acts alternately as a generator/expander and as an actuator/compressor during the engine cycle. The useful output of a unit cell engine is the electrical power generated by the piezoelectric membrane as it is strained during expansion of the two-phase working fluid, minus the power consumed by the membrane during the compression of the working fluid.

The working cycle of the micro heat engine may be approximated with four ideal processes: (1) compression, (2) isothermal, isobaric high temperature heat addition, (3) expansion and (4) isothermal, isobaric low temperature heat rejection. The capability to expand and compressed a saturated two-phase working fluid enables the engine's thermodynamic cycle to approach the ideal Carnot vapor cycle **[8]**.

A power supply can be constructed of a single unit-cell engine or an array of many unit cell engines combined together. This modularity gives great flexibility in the assembling of energy conversion devices. Combined in parallel, the unit cell engines would be driven by the same temperature difference. Combined in series, the unit cell engines would form a cascade so that each unit cell engine would be driven by a fraction of the total temperature difference across the entire cascade.

FABRICATION

A prototype unit-cell heat engine is fabricated of three components: a silicon membrane with thin-film piezoelectric generator, a middle spacer in which the engine cavities are defined, and a silicon membrane with resistance heater. Figure 1 shows a cross-section. A two-phase mixture of the working fluid, Fluorinert, fills the engine cavities. The piezoelectric material used in the thin-film membrane generator is lead zirconate titanate or PZT.

The generator and heater membrane wafers are fabricated from (100) Silicon wafers. First an oxide layer is grown through a dry thermal process. Photolithography is used to define the square

0-9640024-4-2/hh2002/$20©2002TRF
DOI 10.31438/trf.hh2002.6

membrane geometries on the back side of the wafers. An anisotropic wet etch in EDP creates square pyramidal cavities in the (100) silicon wafer. Membranes are created in the generator and heater wafers, with membrane thickness controlled with a Boron-doped etch stop. Membranes with thickness from 2.0 to 0.5 microns and side lengths from 2000 to 4000 microns have been fabricated.

The engine cavity is defined through the use of a spacer between the generator and heater wafers. Presently that spacer is fabricated out of semiconductor tape. The diameter of the engine cavity is determined by the size of the hole cut in the tape. The cavity depth is determined by stacking up multiple layers of tape. Since the tape is ~90 microns thick, nominal cavity depths of 90 and 180 microns are used.

The wafer containing the heater membranes is completed, by fabricating gold resistance heaters on the front side of the membranes. In the prototype engine, these heaters are used as a controllable heat source to run the engine. The heaters take the form of a ring with a radius equal to the engine's vapor bubble radius. To fabricate the resistance heaters, gold is sputtered on the wafer, and the ring heater geometry is defined by photolithography.

Thin-film piezoelectric membrane generators are fabricated on the front side of the membranes on the generator wafer. First, a common bottom electrode is formed by sputtering 20 nm of titanium followed by 200 nm of platinum. The wafer is then spin coated with PZT solution in a sol-gel process **[9]**. Presently, final PZT thin film thickness can be tailored from 0.25 to 2.0 microns. Top electrodes are formed by sputtering 200 nm of gold on top of the PZT thin film. Electrode pads are defined by photolithography. Figure 2 shows a top view of a membrane generator.

The engine is assembled, by sealing a two-phase working fluid into a cavity formed by a semiconductor tape spacer between the heater and generator membranes. The cavity is filled with liquid working fluid from a syringe, and the membrane generator is then aligned face down on the spacer and centered above the resistance heater. A vapor bubble is nucleated in the engine cavity by applying an electric current to the heater. Once the vapor bubble is in place, the assembled engine is clamped together to seal in the two-phase working fluid. Figure 3 shows a top view of a back-lit engine after assembly. The vapor bubble and ring heater are clearly visible in the photograph.

MEMBRANE GENERATOR TESTING

Dynamic testing of membrane generators is performed with a bulge tester designed to generate a cyclic pressure wave to excite the membrane. An interferometer is used to measure membrane deflection. Interferograms of the membrane generators are captured at any position in the membrane oscillation during dynamic testing with a timing circuit that controls the laser pulse and camera shutter **[10]**.

Results of the dynamic testing of a 2.5 micron thick, 1.45 mm square membrane generator are given in Fig 4. In the figure, the bulge tester applies a sinusoidal pressure wave, oscillating between 0 and 13.8 kPa, at the resonant frequency of the membrane, 1300 Hz. This excitation causes the membrane generator to deflect between – 8 microns and +16 microns, and produces an open circuit voltage of 60 mV (peak-to-peak).

Increases in generator output over that seen in Fig. 4 have been achieved by improvements in membrane generator design

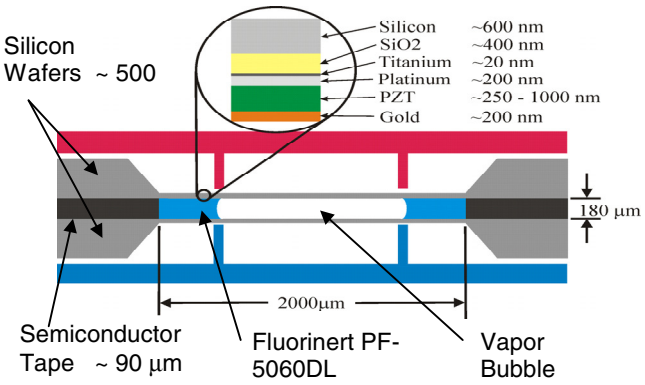

Figure 1. *Cross-section of P^3 unit cell engine.*

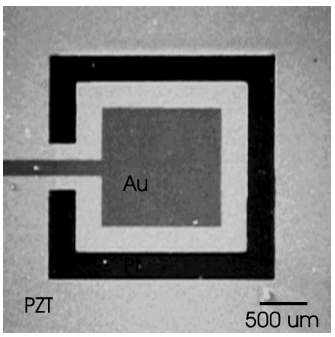

Figure 2. *Top view of a membrane generator.*

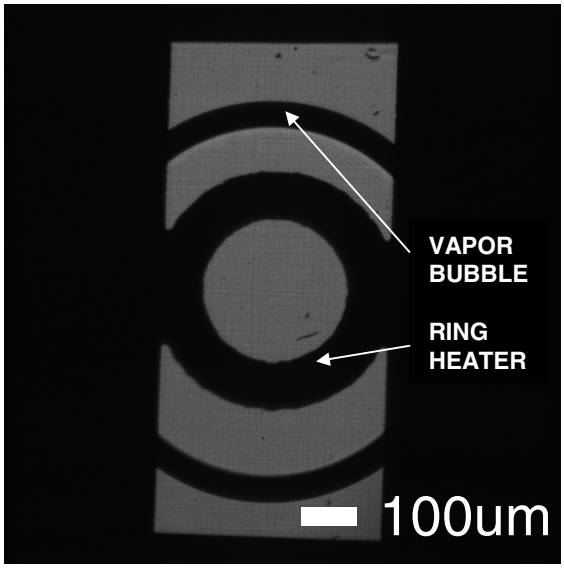

Figure 3. *Top view of a back-lit engine.*

and fabrication **[11]**. Figure 5 shows a plot of open circuit voltage versus membrane deflection, as produced by a second-generation membrane generator (2.5 mm thick, 2.5 mm square). This improved membrane generator has a resonant frequency of 482 Hz and produces 1.6 V at a deflection of just under 60 microns.

The power produced by a membrane generator can be determined by dissipating the electrical output of a membrane generator through a known resistance. Figure 6 shows power versus load resistance curves acquired at different operating frequencies for a second-generation membrane generator. The maximum power produced by the membrane generator increases by nearly two orders of magnitude from 1 microwatt to nearly 50 microwatts as the driving frequency rises from 100 Hz to 482 Hz (the membrane generator's resonant frequency).

HEAT ENGINE TESTING

Dynamic testing of the micro heat engine is performed by electrically pulsing the engine's resistance heater to periodically heat the two-phase working fluid. A square wave with duty cycle between 1 and 25% is used to power the resistance heater. The engine cycle speed is determined by the frequency of this square-wave heating function. Membrane deflection is measured using the holographic interferometer described in the previous section. Typical results from dynamic tests of the micro heat engine are shown in Figs. 7, 8 and 9.

In Fig. 7 measured membrane deflections are plotted versus time for a micro engine driven at 100 Hz. The generator membrane is seen to deflect between 4 and 12 microns.

Open circuit voltages produced by an engine running at five cycle speeds between 100 and 200 Hz are shown in Fig. 8. In the figure, voltage is plotted against the energy dissipated as heat in the resistance heater during each cycle. Voltages between 10 and 60 millivolts are produced when the engine is driven with heat pulses between 1 and 16 millijoules.

The electrical power produced by the engine can be determined by dissipating the electrical output of the membrane generator through a known resistance. Figure 9 shows power produced versus load resistance for an engine running at 100 Hz. Maximum power produced is 0.6 microwatts. Recall from Fig. 8, that this power is similar in magnitude to the maximum power produced by the membrane generator driven by the bulge tester at 100 Hz. In that figure, the power produced by the membrane generator increased nearly two orders of magnitude as the cycle speed of the membrane generator increased from 100 Hz to its resonant frequency. A similar increase in power production is expected as the cycle speed of the micro engine is increased from 100 Hz to its resonant frequency. For this reason, current efforts are focused on increasing the cycle speed of the micro engine.

CONCLUSIONS

The development of a micro heat engine, has been described. The design, fabrication and testing of the engine and its membrane generator have been discussed. Membrane generators have been shown to be capable of producing open circuit voltages of over 1.5 Volts and a peak power of nearly 50 milliwatts. Prototype micro engines have been run at cycle speeds of 100 to 200 Hz, with membrane deflections on the order of 10 microns. The micro engines produce an open circuit voltage of 60 millivolts and a peak power of 0.6 milliwatts. Running the micro engines at

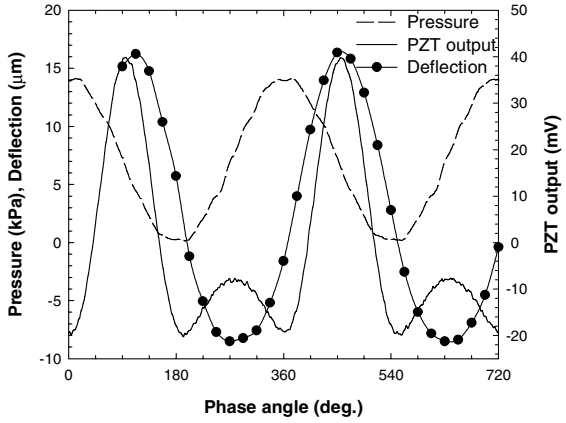

Figure 4. *Pressure, deflection and PZT membrane generator output voltage versus driver phase angle.*

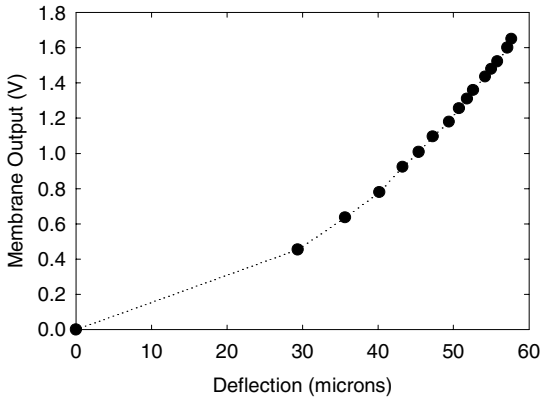

Figure 5. *PZT membrane generator output voltage versus membrane deflection.*

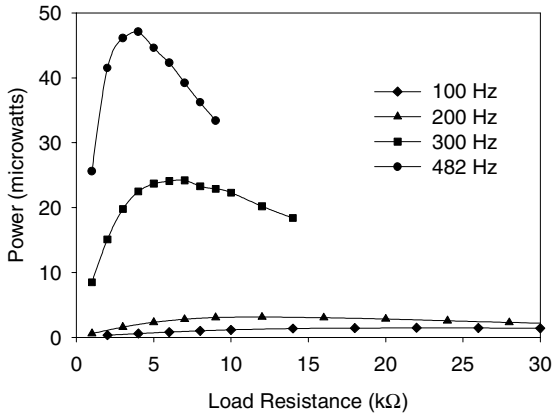

Figure 6. *PZT membrane generator power versus load resistance at driving frequencies of 100, 200, 300 and 482 Hz.*

their resonant frequency is expected to significantly increase their output.

ACKNOWLEDGMENT

We gratefully acknowledge the support of the National Science Foundation under the "XYZ on a Chip" program, award number 9980837

REFERENCES

1. Land Warrior Power Requirements, Institute of Defense Analysis, U.S. Army Soldier Systems Center, Natick, MA (2000).

2. R.A. Strehlow, Combustion Fundamentals, McGraw-Hill, New York (1984).

3. A.H. Epstein, et. al., "Micro-Heat Engines, Gas Turbines and Rocket Engines – The MIT Microengine project" *Proc. 28th AIAA Fluid Dynamics Conf.*, Snowmass, Colorado (1997).

4. A. Mehra, X. Zhang, A.A. Ayon, I.A., Waitz, M.A., Schmidt and C.M. Spadaccini, "A Six-Wafer Combustion System for a Silicon Micro Gas Turbine Engine," J.MEMS, Vol.9, No. 4 (2000)

5. K. Fu, A. J. Knobloch, F.C. Marinez, D.C. Walther, C. Fernandez-Pello, A.P. Pisano, D. Liepmann, "Design and Fabrication of a Silicon-Based MEMS Rotary Engine," *Proc. ASME IMECE 2001*, Paper No. MEMS-23925, New York (2001).

6. W. Yang, "Liquid Piston Chip Engine," *Proc. DARPA/MTO MEMS/MPG/NMASP Principal Investigators' Meeting*, Bloomington, CO, (2001).

7. C-G.Xu,C., J.Hall, C. Richards, D. Bahr, and R. Richards, "Design of a Micro Heat Engine," *Proc. ASME IMECE*, MEMS-Vol.2 (2000), pp.261-268.

8. C.D. Richards, D.F. Bahr, C-G Xu & R.F. Richards, "MEMS Power: The P^3 System," *Proc. of IECEC 2001, 36th Intersociety Energy Conversion Engineering Conference*, Savannah, Georgia (2001).

9. D.F. Bahr, J.C. Merlino, P. Banerjee, C.M. Yip and A. Bandyopadhyay, "Reliability And Properties Of PZT Thin Films For MEMS Applications" *Proc. Materials Research Society, Materials Science of MEMS Devices*, vol. 546, (1999) pp. 153-185.

10. J. D. Hall, N. E. Apperson, B. T. Crozier, C. Xu, R. F. Richards, D. F. Bahr, and C. D. Richards, "A facility for characterizing the dynamic mechanical behavior of thin film membranes for microelectromechanical systems devices," To appear in *Review of Scientific Instruments*, May 2002.

11. D.F. Bahr, K.R. Bruce, B.W. Olson, L.M. Eakins, C.D. Richards, and R.F.Richards, "Electro-Mechanical Coupling And Power Generation In A PZT Micro-Engine," *Proc. Materials Research Society, Materials Science of Microelectromechanical Systems (MEMS) Devices IV*, vol. 687, (2002) pp. 4.3.1-6

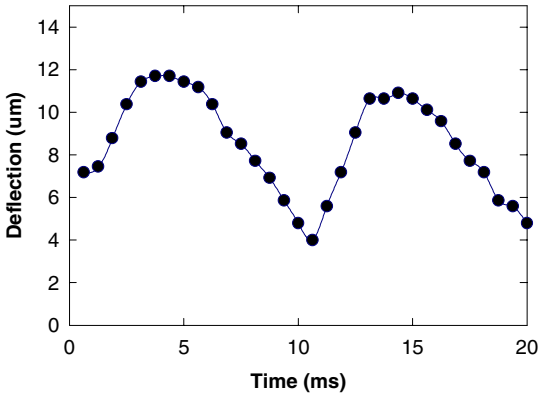

Figure 7. *Membrane deflection versus time for a micro engine cycling at 100 Hz.*

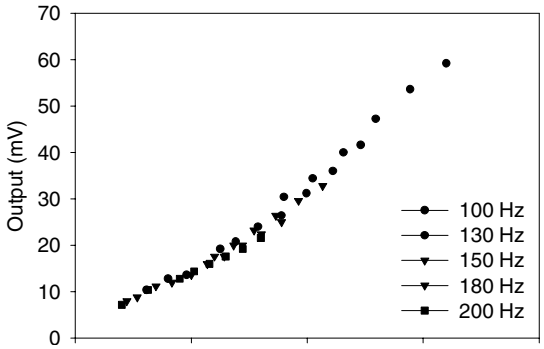

Figure 9. *Membrane generator power versus load resistance for a micro engine cycling at 100 Hz.*

Figure 8. *Membrane generator output voltage versus energy into engine per cycle.*

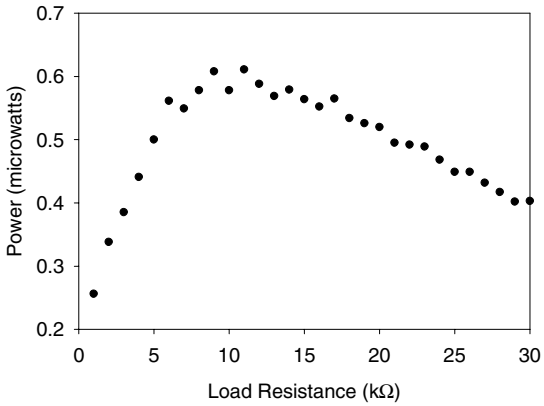

HIGH-TEMPERATURE MICROCOMBUSTION-BASED AMMONIA MICROCHEMICAL HYDROGEN GENERATOR REACTORS FOR PEM FUEL CELLS

Mark A. Shannon[1], Gabriel V. Moore, Jason Ganley, Craig Miesse, Cynthia Rice, Edmund G. Seebauer, and Richard I. Masel
University of Illinois at Urbana-Champaign
Urbana, IL 61801

ABSTRACT

A high-density source of hydrogen for proton exchange membrane (PEM) fuel cells is being actively pursued in order to create a MEMS-based micro-power-generator (MPG). The approach presented is to generate hydrogen and power by decomposing ammonia (NH_3) in a high-temperature microchemical system. Three critical components of this MPG have been fabricated and tested: (i) a high-temperature microcombustor and (ii) a decomposition microreactor, and (iii) a PEM fuel cell. The critical breakthroughs to achieve this MPG hydrogen generator are a *sub-millimeter* critical length scale microcombustor and a high surface area microchemical reactor.

INTRODUCTION

The development of MEMS-based micro-power-generators (MPG) can enable a new class of portable electronics. Micro-fabricated proton exchange membrane (PEM) fuel cells can supply electrical power with a power density that exceeds lithium ion batteries, provided a high-density source of hydrogen is supplied. There has been a great deal of work on creating high-density source of hydrogen, including metal hydrides, and reforming of liquid hydrocarbon fuels to hydrogen, such as methanol. However, only liquid H_2 (@ 20K) and CH_4 (@ 147K) have a higher hydrogen density than liquid ammonia (NH_3). Moreover, NH_3 remains liquid at ambient temperatures and pressure (9.6 atm @ 300K), which is also useful since the higher pressure eliminates the need for liquid pumping. A key issue, therefore, is how to convert NH_3 to H_2 efficiently and completely, so that NH_3 poisoning of the PEM anode catalyst is minimized.

One viable approach to convert NH_3 to H_2 is to thermally decompose ammonia, by

$$2\ NH_3 + \text{heat} \rightarrow N_2 + 3\ H_2\ . \qquad (1)$$

The hydrogen from the reactor is then fed into a PEM fuel cell to generate electricity. The minimum amount of heat to spontaneously thermally decompose NH_3 at the minimum temperature (T_{crit} = 183.04ºC) required is remarkably small (7.92 {kcal/(mol H_2 produced)}). However, the kinetics are extremely slow, making decomposition at that low a temperature impractical, particularly in a microscale reactor with small residency times. To increase the kinetics high enough that nearly 100% of NH_3 can be converted to N_2 and H_2, a high temperature, catalytic microreactor is needed. However, operating a microreactor at high temperatures present a new set of challenges: (i) producing a high-temperature source at the microscale, (ii) loss of efficiency due to heating losses, and (iii) catalyst degradation.

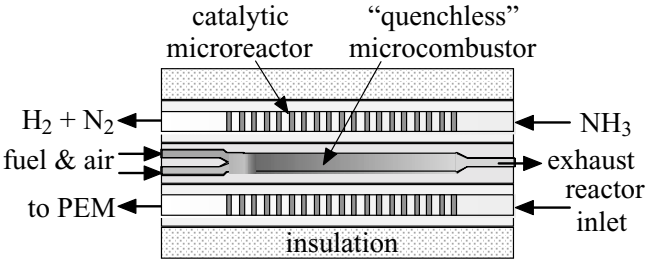

Figure 1. *Concept of counterflow heat exchange 600°C microchemical ammonia (NH_3) decomposition reactor, sandwiched about a high-temperature (>1000°C) microcombustor. Reactor area and size is far larger than the microcombustor, in order to maximize high-temperature efficiency of burner and match heat output of the burner to heat input to the reactor.*

Presently, several reactors for ammonia decomposition have already been proposed. Many use electrical energy to heat the reactor to high temperatures, satisfying challenge (i), since resistive heaters can be relatively easily integrated into a micro-fabricated reactor. However, the use of electrical energy to generate heat lowers the overall efficiency of the system, making (ii) even more difficult to achieve. As heat losses tend to be significant for microscale systems, and must be supplied for steady-state operation, electrical power must also be supplied for the losses as well as any pump power needed, which non-linearly decreases the overall efficiency with increasing losses. Therefore, the conversion of NH_3 to H_2 in an electrically heated MPG system can consume more electrical energy to heat the reactor than is produced by the H_2 in the fuel cell.

To supply sufficient heat for both decomposition and heat losses, we utilize a high-temperature microcombustor that can burn hydrocarbon fuels, such as butane, methane, and acetylene. In addition to not using H_2 to supply the heat energy, the direct heating content of hydrocarbon fuels even exceeds that from H_2 due to 50% conversion efficiency in the PEM to electrical power. Therefore, the overall fuel load of both NH_3 and a fuel such as butane is smaller than with NH_3 alone. To realize a NH_3 to H_2 converter, a microcombustor is coupled to the ammonia decomposition reactor, as shown schematically in Figure 1. Fuel is consumed in a microcombustor to provide heat for the microreactor, which sandwiches the heater to reduce losses. The only electricity needed to run the device is the electricity to run an air pump. The critical breakthroughs to achieve this MPG hydrogen generator are a *sub-millimeter* critical length scale microcombustor and a high surface area microchemical reactor.

[1] Submitting author. Address: 1206 West Green Street, Urbana, IL 61801, USA. Email: mas1@uiuc.edu

0-9640024-4-2/hh2002/$20©2002TRF
DOI 10.31438/trf.hh2002.7

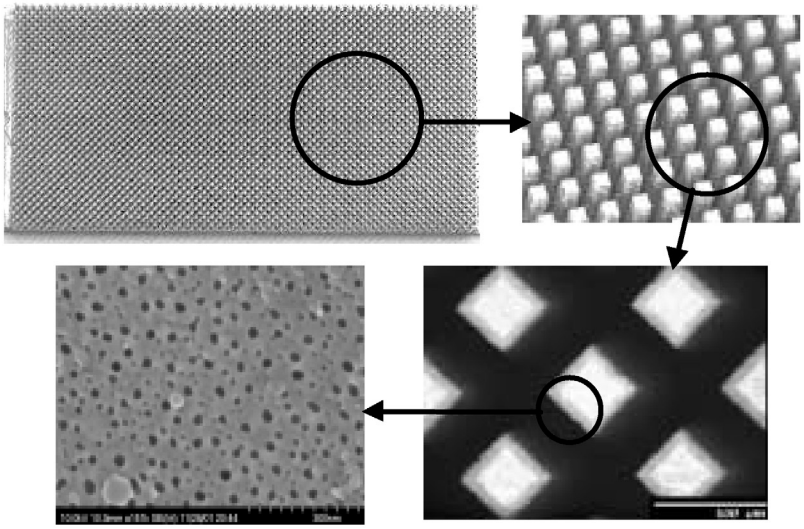

***Figure 2**. Photograph of an anodized aluminum reactor bed with the upper right inset showing 300 by 300 μm square posts 3000 μm long forming the high surface area reactor. The surfaces of the posts shown in the lower right inset are anodized to a thickness ~ 1/6th of the post. The anodized surface, shown in the lower left inset, is impregnated with platinum, utilizing the monodisperse 30 to 60 nm diameter pores.*

FABRICATION

The microreactors tested in this study were fabricated by electrical discharge machining (EDM) of 1100 aluminum alloy bar stock. Two different reactor bodies were fabricated. As shown in Fig. 2, one had an array of 3350 posts arranged in an area 25x50 mm. The second, as shown in Fig. 3 had an array of approximately 250 square posts 300 μm on a side, and 3 mm high. The posts were arranged over a square area 9.5 mm on a side. The posts (insets of Fig. 2) were then anodized to yield a high surface area alumina with an average pore size of 30-60 nm. To do so, the reactors were degreased in acetone and potentiostatically anodized in a 0.16 M solution of oxalic acid for a period of 24 hours. The anodization voltage was varied to test the effect on the anodic alumina. Finally, the microreactor was impregnated with catalyst via treatment with platinum hexafluoroacetylacentonate [Pt-$(hfac)_2$] or Ruthenium hexafluoroacetylacentonate [Ru-$(hfac)_2$] in 2-pentanedione.

The microcombustors were fabricated in two ways. The first combustor was fabricated from polished polycrystalline sintered silicon carbide (SiC) wafers that were diced to 2.5 by 5 cm rectangles. Longitudinal slots 1 cm wide were made various depths ranging from 300 to 800 μm deep in one wafer. The micro-combustion chamber was formed by bonding a slotted and unslotted wafer together, as shown in Fig. 4(a). Before bonding, the surfaces were coated with multiple layers of silica and alumina, approximately (140 Å/100 Å)$_n$ for each set, alternatively deposited by e-beam evaporation, until the total thickness of the coating was approximately 0.5 μm. The coated wafer was then annealed at 1550ºC. The second burners were fabricated by molding green alumina sheets with a 300 μm deep slot by 5 mm wide, and then sintering together. Both burners were then surface treated to remove impurities. The completed combustors were placed in holders that delivered fuel and air to the slot, premixed in a small (O(1 mm)) chamber immediately before the slot.

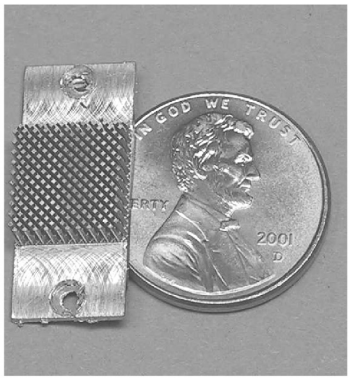

***Figure 3.** A picture of the smaller microreactor. This reactor can produce 8 sccm (i.e. about 2 watts) of 99% pure hydrogen when run at 650°C.*

(a)

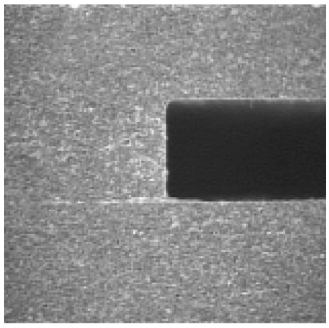

(b)

***Figure 4**. Close-up in (a) of a 600 μm deep etched slot in aluminosilicate coated and bonded SiC burner shown in Fig. 7. A monolithic, treated alumina microcombustor is shown in (b) with slot depth of 300 μm, which also sustained gas-phase combustion.*

RESULTS and DISCUSSION

The key goal for this NH_3-based MPG is to extract more electrical energy than heat energy supplied, by utilizing the high chemical potential of the H_2 in the PEM vs. the relatively low dissociation energy of the NH_3 in the catalytic microreactor. For the microreactor, several issues were addressed, including heat transfer, pressure drops, and most importantly, stationary catalyst structures that are not subject to degradation at high temperatures.

The reactor structures shown in Figs. 2 and 3 allow easy flow of reactants and products due to the relatively large passageways, thus pressure drops were negligible. Since the reactor body was made from an aluminum alloy, and the core of the posts, as seen in the inset in Fig. 2 remained metallic with relatively large aspect ratio of about $1/10^{th}$ cross-sectional area to length, the reactor structures and posts were essentially isothermal. This would not necessarily be the case for smaller posts made entirely from anodized alumina. When anodized at the conditions described above, the size of the posts did not change upon anodization. However, the resultant structure is porous as shown in the lower left inset in Figure 2. The surface area for reaction greatly increases during the anodization process, thereby increasing the conversion rate within the reactors. For example, the penny sized microreactor shown in Figure 3 has an internal surface area of 0.82 m^2, about 1000 times its physical surface area. In addition to high area, the anodized alumina structure with the platinum immobilized onto the posts by impregnation, calcination and reduction is stable at elevated temperatures and does not degrade.

The first ammonia reforming results are shown in Fig. 5. During this experiment 92 sccm of ammonia was fed into the reactor in Fig 2, and the conversion was measured as a function of temperature. The figure shows that 99% pure hydrogen is produced in the reactor at 650ºC. A mass balance shows that 140 standard cm^3 of hydrogen gas/min is produced by the reactor under these conditions. This is enough hydrogen to produce 20 watts of electricity in a 50% efficient fuel cell. More importantly, the reformate stream does not contain CO to poison the hydrogen PEM fuel cell downstream. However, the remaining NH_3 can also poison the anode catalyst of the PEM. Therefore, further work is needed to reduce the NH_3 to negligible amounts by increasing catalyst area and increasing the reactor temperature above 650ºC, which requires a higher temperature substrate than the aluminum alloy used. In addition, an ammonia trap is needed to scavenge any trace amounts of NH_3 remaining.

The thermal losses from the reactor to the surroundings, as well as the fluid flow design has a large impact on the amount of heating power that needs to be supplied to the microreactor. A poorly insulated device might consume 17 watts of fuel and only produce a net of 4 watts of electricity. However, due to supplying heat via combustion, there is still a net production of electricity by the MPG. But it is still important to design for optimum thermal management to reduce losses to a minimum. By employing counter flow heating fluids and reactor products, enthalpy losses can be minimized. By sandwiching the micro-combustor between reactors, heat losses from the burner to the surroundings are minimized. In addition, placing the lower temperature reactors on the outer surfaces, and separating the reactors from the surroundings using vacuum insulation and radiative shielding, combined with high quality aerogel insulation can reduce heat losses to less than 1 W for each 4 to 5 W of electricity produced.

To efficiently generate the high-temperature heat required, we utilize gas-phase combustion of hydrocarbon fuels, due to their very high energy density and operating temperatures. However, to supply the desired heating rate and > 650ºC temperatures to the reactor, the microcombustor needs to be much smaller than the reactor: sub-millimeter in size for low power (< 1 W) applications. MIT has developed high-temperature silicon-based combustors [**1-2**], but it is about 1 order of magnitude larger than we require for the MPG. Simply reducing its size, though, is a major issue, since steady-state homogeneous combustion flames thermally and chemically quench below a critical length scale. Figure 6 shows our measured quench lengths for various materials with hot and cold walls. When the walls are "cold" (below about 400ºC), all materials quench around 2.5 mm. However, for hot walls, the surface material strongly matters, with quench lengths down to 100 microns possible. By using burner walls coated with alumina-magnesia-silicates, we have fabricated and tested SiC and alumina microcombustors (Fig. 4) with quench lengths far below 1 mm [**3**].

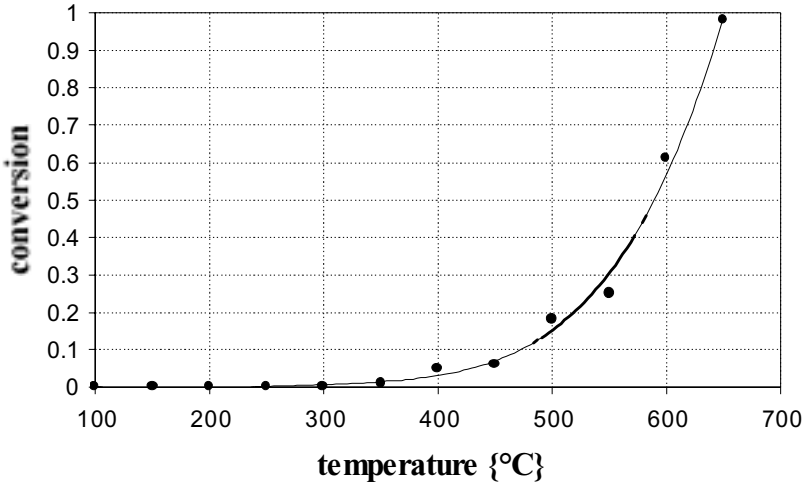

Figure 5. *Results for the conversion of ammonium to hydrogen and nitrogen via decomposition in the anodized catalytic microreactor shown above as a function of temperature, with a NH_3 flow rate of 92 sccm.*

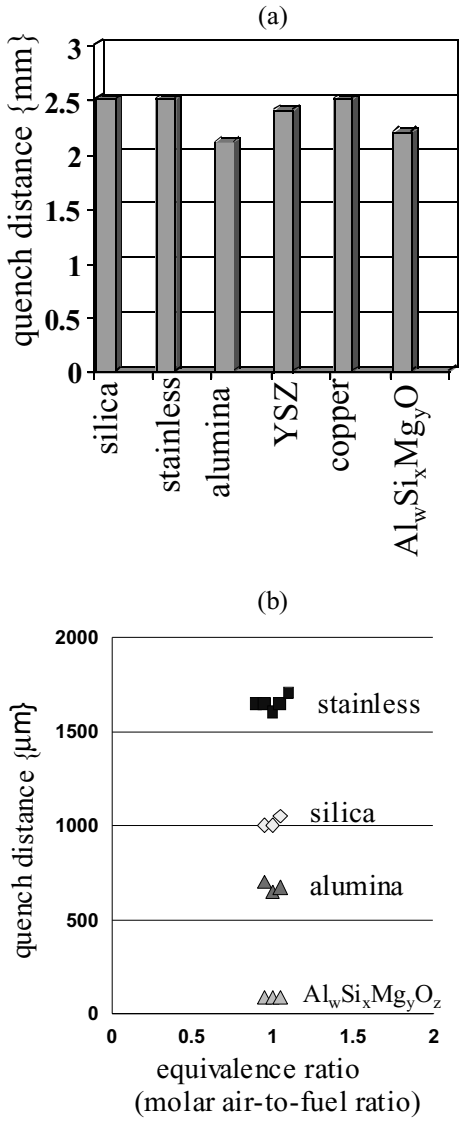

***Figure 6**. Data for quench lengths for different wall materials for (a) cold walls at 300°C and (b) hot walls at 1000°C. Note that for cold walls, the quench lengths are approximately the same for all materials, in agreement with values reported in the literature, due to dominant thermal quenching of the flame. However, for hot walls, wall composition has a very strong effect, and treated compounds of alumina/silica/magnesia have quench lengths of < 100 μm, an order of magnitude below silica alone.*

Figure 7 shows a SiC burner producing watts of steady-state heat energy at high temperatures (>1000ºC) without quenching. The ability to burn hydrocarbon fuels in air in a sub-millimeter critical quench length combustor allows very small, high-efficiency burners to directly deliver the high-quality heat needed to drive the NH_3 to H_2 conversion efficiency to near 100%. The high heating value of gas-phase combustion of hydrocarbon fuels, such as butane, also allows the overall size of the combustor to be much smaller than if lower energy fuels were used, or if lower temperature catalytic combustion was employed, although both these techniques are also possible. The key benefit to having the burner much smaller than the reactor is that the overall fuel use is lower. Thus, both the microcombustor and fuel supply are smaller, minimizing the overall system size.

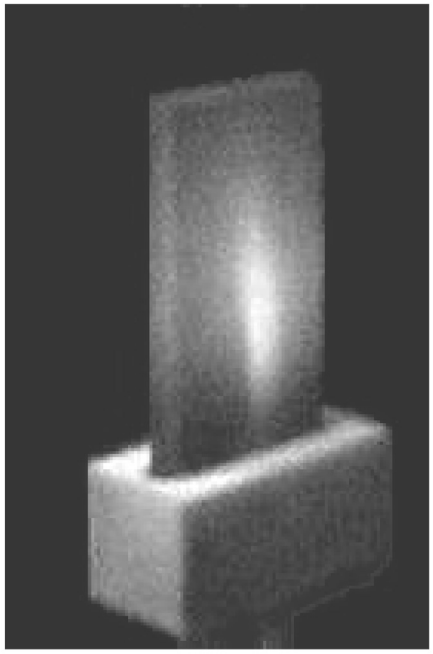

***Figure 7.** Self-sustained gas-phase combustion of CH_4 and air in a coated SiC microcombustor with a slot depth of 600 μm, with a critical quench length of 300 μm. Flame ignited at around 550°C, and walls reached over 1000°C.*

CONCLUSIONS

The goal for this work is to generate pure hydrogen gas from ammonia, a high-hydrogen density source, for PEM fuel cells for micro-power and larger, electrical generators. We have been able to thermally decompose 99% NH_3 feedstock at 650ºC to H_2 in first generation aluminum micromachined reactors with anodized alumina supported catalysts. Further work is needed to increase the reactor temperature and effective catalyst area to approach 100% conversion efficiency. The reactor is directly heated via combustion of hydrocarbon fuels in air in a high-temperature microcombustor. Two types of microcombustors have been demonstrated that achieve greater than 1000ºC temperatures with critical quench lengths well below 1 mm to provide the heat source for the next generation of ammonia microreactor.

ACKNOWLEGEMENTS

This work is supported by ARO under the MURI program, grant number DAAD 19-01-1-0582.

REFERENCES

1. A. Mehra and I.A. Waitz, "Development of a hydrogen combustor for a microfabricated gas turbine engine," *Technical Digest of the 1998 Solid-State Sensor and Actuator Workshop*, Hilton Head Isl., SC, Transducer Research Foundation, Cleveland OH (1998), pp. 35- 40.

2. A. Mehra, X. Zhang, A.A. Ayon, I.A. Waitz, M.A. Schmidt, C.M Spadaccini, "Six-wafer combustion system for a silicon micro gas turbine engine", *Journal of Microelectromechanical Systems 9 (4),* 517-27 (2000).

3. R.I. Masel and M.A. Shannon, "Microcombustor having submillimeter critical dimensions," U.S. Patent Oct. (2000).

MEMS AND Si MICROMACHINING FOR HIGH FREQUENCY APPLICATIONS

Linda P.B. Katehi
Purdue University
West Lafayette, IN 47907

ABSTRACT

RF micromachining and MEMS technology promise to provide an innovative approach in the development of effective and low-cost circuits and systems, and is expected to have significant application in the development of low-cost antenna arrays and re-configurable apertures. This paper presents a brief history and the state of the art in the development of RF MEMS devices, with primary emphases on switches, and of Si micromachined circuit components for use in high-performance, high-density, on-wafer packaged circuits.

SUMMARY

a) RF MEMS Switches

RF Micro Electrical Mechanical Structures (MEMS) has been identified as a technology, that has the potential to provide a major impact on existing RF architectures in sensors(radar) and communications by reducing weight, cost and size, and power dissipation. The impact of this technology to communication system cost, size and volume is expected to be a few orders of magnitude. Key MEMS devices for current RF architectures are switches in radar systems and filters in communications systems. From a system's standpoint, RF MEMS is enabling new RF System architectures. Future communications require increasing functionality and performance endurance requirements that can be addressed by the successful insertion of new highly integrated MEMS sensors and instruments.

In the last ten years, MEMS as applied to microwave and millimeter wave circuits have experienced an exponential growth. In 1991, Larson et al. described rotary MEMS switches with good performance at RF frequencies [1, 2]. C.T. Nguyen demonstrated the successful development of MEMS HF filters in 1993-1994 [3] and Yao et al. demonstrated a surface micromachined series switch for telecommunications applications in 1995 [4]. Recently, shunt microwave switches have been developed in the X to K/Ka band [5], [6] and [8]. These switches are usually electrostatic in nature and commonly driven by bias voltages in the 30-80 V range. Most recently, low actuation voltage switches requiring 9 Volts of DC actuation have been demonstrated [7], [9], [10] and have opened new directions in system implementation and development of communication systems architectures. These MEMS devices are primarily designed for low-loss applications that do not require fast rates such as airborne and/or deep space communication. The advantage of MEMS switches over their solid state counterparts such as FETs or PIN diodes is their extremely low series resistance and low drive power requirements.

For MEMS switches to become appropriate for wireless hand-held communications systems, actuation voltages less than 6 Volts are required. The primary goal of this section is to demonstrate the design, fabrication and DC as well as RF characterization of low-actuation-voltage electrostatic shunt microwave switches. Ultra low-loss, low actuation voltage RF MEMS switches have been successfully fabricated at the University of Michigan as shown in Figure 4. These switches are designed for use with finite ground coplanar waveguide, but the design methodology and fabrication approach are very general and can be utilized towards the development of any low-actuation voltage switch architectures. In order to lower the pull-in voltage of the structure, three different design goals may be pursued: (1) increasing the area of actuation, (2) diminishing the gap between the switch and bottom electrode, and (3) designing a structure with low spring constant. In the first case, the area can only be increased by so much before compactness becomes a prevailing issue. In the second case, the return loss associated with the RF signal restricts the gap. The third design goal is the one with the most flexibility, since the design of the springs does not considerably impact the size, weight, and/or RF performance of the circuit. Figure 1 shows a scanning electron micrograph (SEM) of a shunt switch design appropriate for operation with a Finite Ground CPW (FGCPW) interconnect. The development of RF MEMS devices continues at present in government laboratories, industry and academia with substantial emphasis on packaging and reliability.

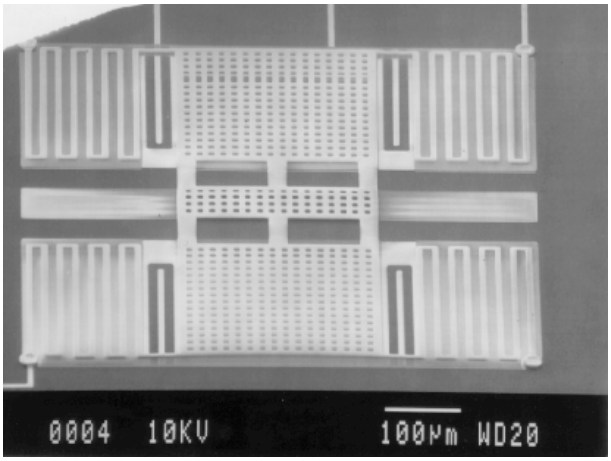

Figure 1: Low-Activation Voltage Switch Designed and Fabricated at the University of Michigan

b) Three Dimensional Integration and Packaging Using Si Micromachining

Emerging military, space, and commercial communications systems, as well as unique military applications in radar and missile seekers, are placing a high premium on low cost, small, light weight RF electronic components, while at the same time increasing demands for higher functionality. Systems are using higher and higher frequencies, in part for size considerations and in part for bandwidth. Commercial and military satellite, some commercial terrestrial, and space borne communications systems are operating in or being designed for the Ka-band (25-40 GHz).

0-9640024-4-2/hh2002/$20©2002TRF
DOI 10.31438/trf.hh2002.8

On these satellite systems, electronic packaging can account for up to 30% of the overall spacecraft mass while the telecommunication subsystem can account for 15% or more of the dry mass. At the same time external organizational considerations are driving space agencies to reduce mission cost and failure probability (and hence reduce system complexity). Innovative approaches to the integration and packaging of RF systems are keys to achieving these goals.

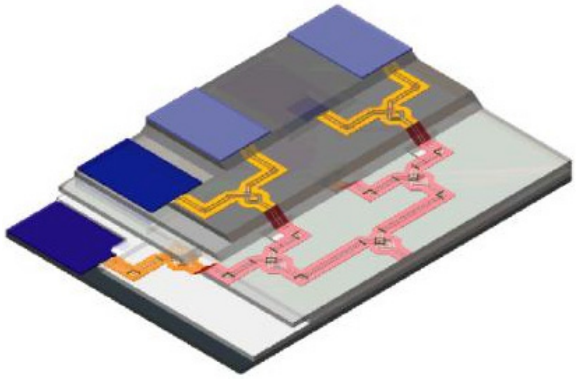

Figure 2: Three Dimensional Interconnect Network

The framework of the micromachined integrated circuit is the collection of interconnects offered by this technology, each appropriate for specific applications. Micromachining techniques enable the fabrication of coplanar waveguide with the semiconductor material etched out between the conductor elements, thus substantially reducing dielectric loss and surface wave modes in the substrate. Layers of substrate can be added to the micromachined structure, with cavities cut to fit over the surface elements of the adjoining layer, providing shielding for the enclosed circuit elements. Metallization can be applied to the enclosure structure to further electromagnetically isolate the circuit elements. Isolations of 40 dB or better between transmission lines similar to those in Figure 2 and separated by 100 μm have been demonstrated [11,12], providing an additional 20-30 dB greater than the isolation between conventionally fabricated lines, due to the micromachining of the substrate.

These shielded and micromachined circuit elements can then be geometrically laid out in a much denser circuit architecture. Using these approaches, radiation and substrate losses can be essentially eliminated, leaving only the ohmic loss of the metal. At higher frequencies, finite ground plane coplanar waveguide (FGC) and variations of it have been found to be most useful due to its ability to transition easily vertically through the wafers. However, depending on the applications, finite ground microstrip line could be the interconnect of choice.

c) Lumped Passive Components

At microwave and millimeter-wave frequencies (up to Ka band), a novel technology has been developed to design and realize high performance lumped passive components such as Wilkinson power dividers and hybrid couplers leading to substantial reduction in size. The basis of this novel technology is the development of high Q, micromachined lumped components such as spiral inductors, metal-insulator-metal (MIM) capacitors and thin-film-resistors (TFRs). For example, by removing the Si wafer around a spiral inductor through selective etching as shown in Figure 7, inductors with a high resonant frequency (38 GHz for a 1.5 nH inductor), high Q-factor (~30) and high linearity are possible. These micromachined spiral inductors can then be used to design dividers, hybrids and couplers at X-, K- and Ka-band with almost two orders of magnitude reduction in size, in addition to improved electrical performance in terms of insertion loss and bandwidth, with respect to standard printed circuit technology. Recent work has demonstrated, for the first time, X- and K-band power dividers with low loss (0.6 dB) and wide bandwidth (25% bandwidth for 15 dB return loss) [13,14]. Due to the use of high-Q spiral inductors, the loss introduced by the lumped Wilkinson power divider is even lower than some distributed designs. One of the most important reasons for using lumped design is the smaller chip size.

Using lumped components to replace transmission lines, the chip size of the X-band design is reduced by a factor of six (to 0.3 mm x 0.5 mm). These lumped components can be fabricated on a variety of III-V substrates and are expected to provide similar size reduction and performance improvement to a multistage MMIC module. Besides the narrow application to forming the basis for the RF power distribution network of the small sized MCMs, this component technology has the general potential to revolutionize high frequency RF circuit design and to lead to tremendous reductions in systems cost and size.

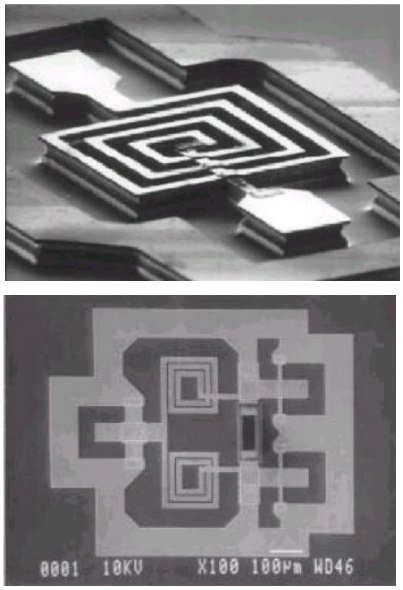

Figure 3: Micromachined Inductor and Whilkinson Power Divider

d) Wafer-to-wafer Bonding

The bonding of silicon wafers is a well-established commercial technology for applications such as power devices, silicon on insulator (SOI), MEMS sensors, die attachments, sealing, and other MEMS components [15]. Thermocompression bonding of gold-to-gold intermediate layers is the bonding method selected for the multi-layer architecture of Figure 4 because it can be achieved at a sufficiently low temperature that metalization and interconnects of the circuits on the various layers are undisturbed. This type of wafer-to-wafer bonding can be hermetic, so that the final multi-layer structure forms a complete hermetically sealed package. This wafer bonding technique is used for vacuum

cavities in MEMS pressure sensors, and shows exceptional promise for RF circuits as well. This is the same technique used to form the RF bump electrical transitions described above, and these RF bump bonds form part of the mechanical bonding of the wafer layers as well as an electrical connection.

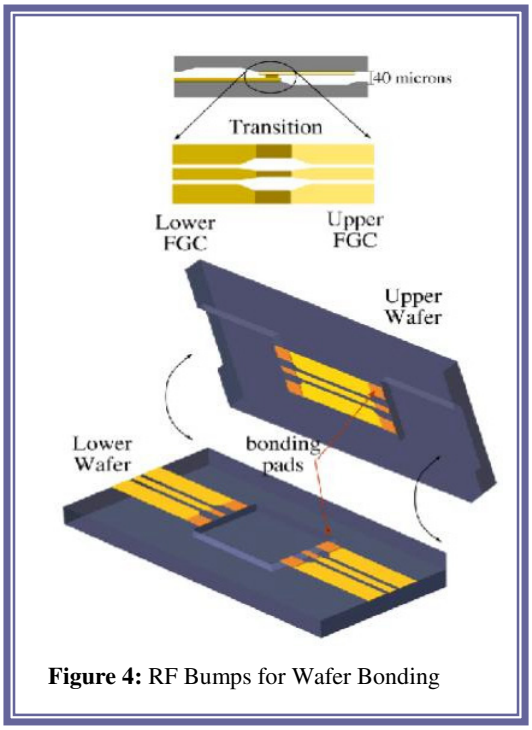

Figure 4: RF Bumps for Wafer Bonding

CONCLUSIONS

The micromechanical switch is without doubt the paradigm RF MEMS device. Within the last decade the RF community has experienced a growing plethora of MEMS switch designs. These designs have achieved a high level of RF performance, while maintaining ultra-low-power dissipation and large-scale integration. Due to the above characteristics, such RF MEMS devices should enable a wide variety of new system capabilities. With the ability to support any combination of electrical and micromechanical devices on a single chip, RF MEMS open an endless horizon of tantalizing possibilities for future designs and systems. In addition, the continual research on new design tools and methodologies, ensures that MEMS holds a tremendous promise in contributing heavily to the next generation of RF-based applications.

On the other hand, Si micromachining can provide on-wafer packaging and excellent performance. On-wafer *S*-parameter measurements of a 20 GHz low noise amplifier with an integrated conformal package have been demonstrated. These measurements confirm that integration of a conformal package can be achieved in MMIC applications through the use of silicon micromachining techniques. The conformal package offers the benefit of RF shielding and isolation without detriment to the performance of the amplifier.

ACKNOWLEDGEMENTS

This work has been funded by DARPA MAFET II (under Raytheon) and by the Army Research Office.

REFERENCES

1. R. H. Hackett, L. E. Larson, and M. Melendes, "The Integration Of Micro-Machine Fabrication With Electronic Device Fabrication On III-V Semiconductor Materials," in Transducers Proceedings, pp.51-54, 1991.
2. C. T.-C. Nguyen, Micromechanical Signal Processors. PhD Thesis, University of California at Berkeley, 1994.
3. J. J. Yao and M. F. Chang, "A Surface Micromachined Miniature Switch For Telecommunications Applications With Signal Frequencies From Dc Up To 4 Ghz," in The 8th International Conference on Solid-State Sensors and Actuators Digest, pp. 384-387, 1995.
4. C. Goldsmith, T. H. Lin, B. Powers, W. R. Wu, and B. Norvell, Micromechanical Membrane Switches For Microwave Applications, IEEE MTT-S International Microwave Symposium Digest, pp. 91-94, 1995.
5. C. Goldsmith, J. Randall, S. Eshelman, and T. H. Lin, Characteristics Of Micromachined Switches At Microwave Frequencies, IEEE MTT-S International Microwave Symposium Digest, pp. 1141-1144, 1996.
6. Sergio Pacheco, Clark T. Nguyen, and Linda P. B. Katehi, "Micromechanical Electrostatic K-Band Switches," IEEE MTT-S International Microwave Symposium Digest, pp. 1569-1572, 1998.
7. C.L. Goldsmith, A. Malczewski, Z.J. Yao, S. Chen, J. Ehmke and D. H. Hinzel, RF MEMS Variable Capacitors for Tunable Filters, Special Issue on RF Applications of MEMS Technology, RF and Microwave Computer-Aided Engineering, v. 9, n. 4, pp. 362-374, July 1999.
8. Sergio P. Pacheco, Linda P. B. Katehi, and Clark T.-C. Nguyen, "Design of Low Actuation Voltage RF MEMS Switch," IEEE MTT-S International Microwave Symposium Digest, pp. 165-168, 2000.
9. Yongming Cai and Linda P.B. Katehi, "Wide Band Series Switch Fabricated Using Metal As Sacrificial Layer," European Microwave Conference, Paris, France, October 2000.
10. Jeremy B. Muldavin and Gabriel M. Rebeiz, "30 GHz Tuned MEMS Switches", IEEE MTT-S International Microwave Symposium Digest, pp. 1511-1514, 1999.
11. Katherine J. Herrick, Tom Schwarz and Linda P.B. Katehi, "Si-Micromachined Coplanar Waveguides for Use in High Frequency Circuits," IEEE Transactions on Microwave Theory and Techniques, Special Issue on Millimeter-Wave Technologies, Vol. 46, No. 6, June 1998, pp. 762-768.
12. Accuglass 512 Spin-on-Glass (SOG), Product Bulletin, Allied-Signal Inc., Planarization and diffusion products, 1090 S. Milpitas Blvd., Milpitas, California 95035.
13. D. Kother, B. Hopf, Th. Sporkman and I. Wolf, "MMIC Wilkinson Couplers for Frequencies up to 110 GHz," 1995 IEEE MTT-S, pp. 663-666.
14. T. M. Weller, R.M. Henderson, K. J. Herrick L.P.B. Katehi, Three-Dimensional High Frequency Distribution Networks -Part I Optimization of CPW Discontinuities, accepted for publication in Transactions on Microwave Theory and Techniques, Oct. 2000.
15. Katherine J. Herrick and Linda P.B. Katehi, "RF W-Band Wafer-to-Wafer Transition," accepted for publication in IEEE Microwave Theory and Techniques, August 2000.

POLY-SIGE: A HIGH-*Q* STRUCTURAL MATERIAL FOR INTEGRATED RF MEMS

Sunil A. Bhave[1], Brian L. Bircumshaw[2], Wing Zin Low[1], Yong-Sang Kim[1,†], Albert P. Pisano[2,1], Tsu-Jae King[1], and Roger T. Howe[1,2]

Department of Electrical Engineering & Computer Sciences[1] and Department of Mechanical Engineering[2]
Berkeley Sensor & Actuator Center, 497 Cory Hall, University of California, Berkeley, CA 94720-1774

ABSTRACT

This paper presents new material data for single- and multi-layer CMOS compatible poly-SiGe films, including mechanical quality factor (*Q*), Young's modulus, and strain gradient. Using audio frequency folded-flexure comb-drive resonators, the mechanical quality factor of poly-SiGe was determined at 2μTorr pressure. As-deposited poly-SiGe has Q = 20,000 – 31,000. CMOS compatible rapid thermal annealing (RTA) at 525°C for 60 seconds results in a quality factor between 40,000 and 44,000. We have measured the highest *Q* factor yet reported for poly-SiGe ($Q \approx 61{,}100$), as a result of RTA at 600°C for one minute. The measured resonant frequencies of the resonators were used to back-calculate the Young's modulus of poly-SiGe: $E = 155 \pm 5$GPa. The calculated elastic modulus is significantly higher than the metallurgical Young's modulus of 146GPa. The as-deposited strain gradient of the tri-layer poly-SiGe film was found to be $1.75 \cdot 10^{-4}$μm^{-1} (curl-up). RTA at 600°C for one minute drops the tri-layer strain gradient to $2.67 \cdot 10^{-5}$μm^{-1} (curl-up). The graded Ge content multi-layer film was observed to induce a larger normalized strain gradient.

I. INTRODUCTION

Polycrystalline silicon-germanium (poly-SiGe) is a promising material for surface micro-machined MEMS (Micro-Electromechanical Systems) applications. Conformal deposition is possible using chemical vapor deposition techniques at temperatures below 425°C **[1,2]**. Consequently, poly-SiGe can be micro-machined directly on top of modern foundry CMOS. Moreover, research by Sedky *et al.* has shown that thermal annealing of CMOS devices at 525°C for up to 90 minutes leaves the underlying electronics largely unaffected **[3]**.

Micromachined resonators can exhibit very high mechanical quality factors. Indeed, poly-Si MEMS resonators have been reported to have *Q*'s in excess of 80,000 **[4]**. Due to their high *Q*'s, MEMS resonators have superior frequency-selectivity compared to electronic active filters. Also, micromachined resonators are promising as replacements for discrete filters and oscillators in wireless communications systems **[5,6]**. Integrating RF MEMS directly with CMOS promises to drop parasitic capacitances and inductances, as well as reduce fabrication and integration costs, and the form factor of telecommunications devices.

Using low-temperature poly-SiGe, it is our aim to make the MEMS CMOS integration process straightforward and modular, particularly for RF applications. This paper lays the groundwork for this goal by characterizing single- and multi-layer poly-SiGe films with processes relevant for RF MEMS applications. Section II presents the fabrication method used to micromachine the poly-SiGe test structures. Section III summarizes *Q* data collected from audio frequency poly-SiGe resonators. For MEMS microresonator filters and oscillators, *Q* is of prime importance. In Section IV, the measured resonant frequencies and geometric dimensions are used to back-calculate the Young's modulus of poly-SiGe. Finally, strain gradient and the effects of RTA are discussed in Section V.

II. FABRICATION

All devices were fabricated using a single-mask, timed-release process with silicon dioxide as the sacrificial layer. Single crystal silicon wafers were used as the starting substrate. Two microns of low temperature oxide (LTO) was then deposited at 400ºC. The LTO acts as both the sacrificial layer and the mechanical anchor. LTO was used as opposed to a polycrystalline germanium (poly-Ge) sacrificial layer **[1,2]** because of the need for electrical isolation between the mechanical anchors and the substrate.

Four structural films were studied: 1μm thick poly-SiGe films containing 62%, 65%, or 68% Ge, and a 3μm tri-layer sandwich (Figure 1). All films were deposited by LPCVD at 425ºC and *in-situ* boron-doped (using B_2H_6), yielding a deposition rate of roughly 80Å per minute. The as-deposited RMS surface roughness of the films is 50Å for the tri-layer sandwich and under 30Å for the single-layer films. The tri-layer film was used to investigate whether films with different average stresses can be combined to cancel out the residual strain gradient **[7]**.

The resonators and strain gradient test structures used for this paper were defined using a single-mask photolithography step, followed by a standard anisotropic HBr plasma etch using a poly-Si etch recipe. A timed dip in concentrated HF was used to release the structures while leaving SiO_2 pedestals for mechanical anchoring of the test devices.

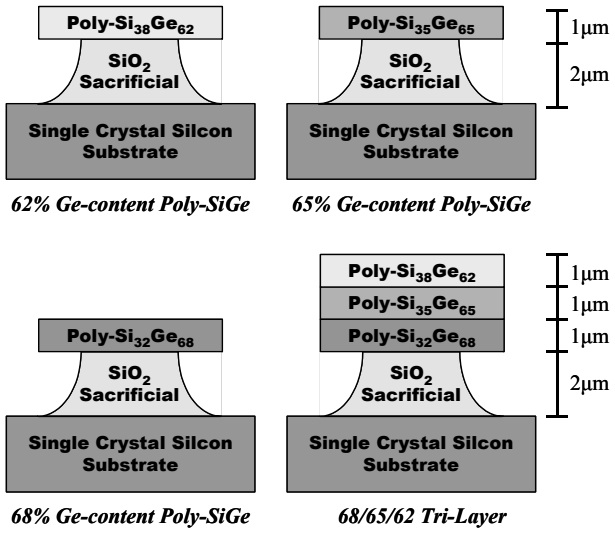

Figure 1. *Cross-sectional views of the four types of structural films studied in this paper (depicted after HF release).*

† Current address: Department of Electrical Engineering, Myongji University, Kyongki, Korea.

Travel support has been generously provided by the Transducers Research Foundation and by the DARPA MEMS and DARPA BioFlips programs.

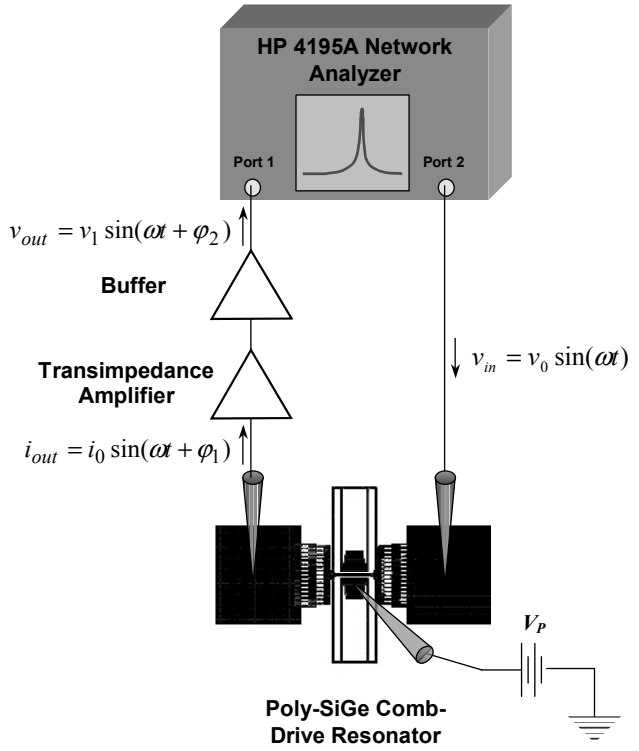

Figure 2. *Schematic of the experimental test setup used for* Q *measurements.* V_p *= 15V and* v_0 *= 1V for the* Q *data presented in this paper. Higher offset voltages,* V_P*, result in non-linear, Duffing behavior. All tests were conducted at an ambient pressure of 2μTorr at room temperature.*

III. *Q* MEASUREMENT

Quality factors were measured for 10.5kHz and 20kHz folded-flexure comb-drive resonators fabricated from the single- and tri-layer films mentioned above. The test setup is shown in Figure 2. Tests were conducted in an MMR vacuum probe station with conventional feedthroughs. The substrate was biased to V_P to prevent the shuttle of the comb-drive resonators from being pulled down onto the substrate.

An HP 4195A network analyzer was used to determine the frequency response of the resonators. From the frequency response, the resonant frequency and mechanical *Q* were determined.

As-deposited poly-SiGe has a *Q* between 20,000 and 31,000 (Figure 3). After 1 minute RTA at 600ºC in nitrogen ambient, the quality factor of all films increases by a factor of roughly 2.2 to 2.6. The tri-layer film had a *Q* of 61,100, the largest *Q* measured to date for poly-SiGe (Figures 4 and 5). RTA reduces the defect density of the poly-SiGe films, thereby increasing the *Q*. As a result, the internal dissipation for all films decreases and, in turn, *Q* increases. There was no discernable alteration in the resonant frequency due to RTA. Figure 6 clearly indicates that the tri-layer film consistently exhibits a higher quality factor than all of the other films. This could be due to the tri-layer resonators having larger volumes, which tends to yield higher *Q*'s **[8]**.

Ideally, all MEMS processing steps should be performed at CMOS compatible temperatures: deposition below 425ºC, followed by annealing up to 525ºC. Linear interpolation of Figure 3 indicates that CMOS compatible poly-SiGe has a $Q \approx 40{,}000 - 44{,}000$, which is 1.6X – 1.9X better than that of as-deposited films.

RTA was carried out beyond 525ºC to establish an upper bound on *Q*. The positive linear trend of Figure 3 is evidence that the intrinsic *Q* of poly-SiGe is higher than 61,000. To obtain *Q*'s greater than 44,000 and still remain CMOS compatible, longer anneal times can be used at temperatures around 525ºC.

It should be noted that determination of *Q* was complicated by resonant-frequency drift. Accurate measurements of *Q* take roughly 40 minutes on the HP 4195A network analyzer. We observed a downward frequency drift of roughly 1 to 4Hz over this time span. Resistive heating of the resonators is negligible. Adsorption of residual oxygen, however, could be significant. Assuming the gas in the chamber is composed of 21% O_2, formation of an oxygen monolayer takes only 3 seconds at 1μTorr (assuming a densely packed monolayer and 100% stiction rate). Therefore, absorbed gases might be causing a mass-loading affect **[9]**, accounting for the downward drift in resonant frequency. The observed drift artificially increases or decreases the measured *Q* depending on the sweep direction. Furthermore, for high-resolution frequency measurements, the network analyzer takes multiple measurements and averages the results, which tends to smooth the resonant peak and decrease the measured *Q*. Based on the large data sets obtained, the *Q* values presented are estimated to have an uncertainty of about ±5%.

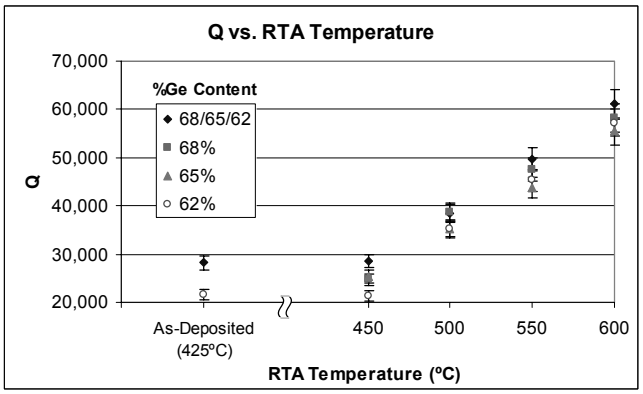

Figure 3. *Graph of* Q *versus RTA Temperature. Notice that* Q *is unaltered for RTA temperatures up to approximately 450ºC. Above 450ºC,* Q *is roughly linear with respect to RTA temperature. All RTA was done for 1 minute at the specified temperature in nitrogen ambient.*

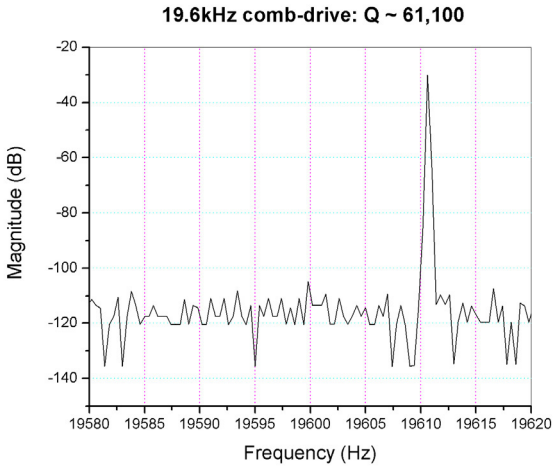

Figure 4. *The magnitude (dB) versus frequency for a tri-layer poly-SiGe, 20kHz (design) comb-drive resonator. The peak occurs around 19.6 kHz.*

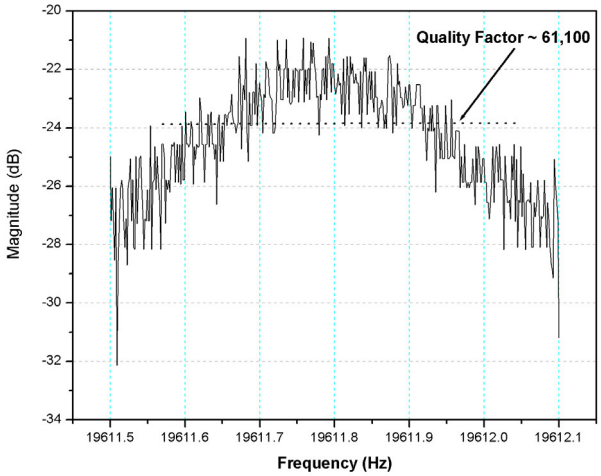

Figure 5. *Close-up of the resonant peak presented in Figure 4.* Q *was measured from a 3Hz frequency sweep near resonance.*

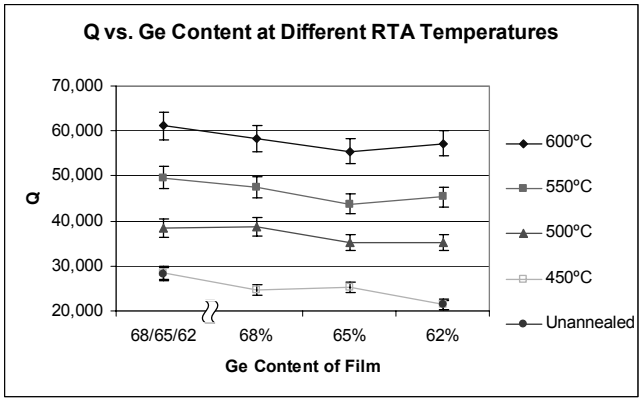

Figure 6. *Graph of* Q *versus %Ge content at different RTA Temperatures. The* Q*'s for all films are comparable for any given set of anneal conditions.*

IV. YOUNG'S MODULUS

Young's modulus, E, was back-calculated from the frequency equation:

$$\textbf{(1)} \qquad f_r = \frac{1}{2\pi}\left[\frac{2E(W/L)^3}{\rho(A_p + 0.3714A)}\right]^{\frac{1}{2}}$$

where f_r, the resonant frequency of the resonator, is estimated by Rayleigh's Energy Method **[10]**. A_p and A are the layout areas of the shuttle/comb fingers and the folded-flexure spring suspension, respectively. W and L are the width and length of the folded-flexures, and ρ is the mass density of the poly-SiGe film.

Rutherford back scattering (RBS) was used to verify the mass ratio of Si and Ge in the various poly-SiGe films to within ±2.0%. This is an extreme upper bound, as the Si/Ge ratio is also verified by deposition conditions. A ±2.0% error in the Si/Ge ratio results in a ±1.4% uncertainty in mass density ρ.

W, L, A_p, and A were all measured to within ±30nm or ±900nm^2 using a Wyko confocal white-light interferometer. The uncertainty in W is thus approximately ±1.5%. Uncertainties in L, A_p, and A are negligible. The resonant frequency, f_r, of 10.5kHz (design) folded-flexure resonators was determined to within ±2Hz with the network analyzer. Combining the measured values of f_r, ρ, W, L, A_p, and A with Equation **(1),** E was found to be 155GPa, with a normalized uncertainty of ±3.0%. The metallurgical elastic modulus for a poly-$Si_{35}Ge_{65}$ film is 146GPa (i.e., the E interpolated from the Young's modulii of Si and Ge based on the mass ratio of a poly-$Si_{35}Ge_{65}$ film). There is no discernable trend between E and Ge content (Table 1).

V. STRAIN GRADIENT

Strain gradient was determined by measuring the out-of-plane tip deflection of 10µm wide, 300µm long cantilevers. The deflection was determined using the Wyko white-light interferometer. The strain gradient in as-deposited films decreases with increasing Ge content (Table 2). Rapid thermal annealing for one minute at 600ºC improves the single layer strain gradients by as much as a factor of 4.7, while the tri-layer strain gradient improves by a factor of 6.5 (Figure 7). The results indicate that the strain gradient is most effectively reduced by a modest anneal. Both as-deposited and annealed films curl up.

The strain gradient of the annealed tri-layer film ($2.67 \cdot 10^{-5}$ µm^{-1}) is 15 times higher than that of the high-temperature annealed poly-Si in Analog Devices' BiCMOS process ($1.78 \cdot 10^{-6}$ µm^{-1}, **[11]**). High-frequency RF devices and, in particular, MEMS RF resonators tend to have small dimensions, rendering strain gradient of lesser importance. For such small devices, the strain gradients exhibited by the poly-SiGe films are acceptable. However, their high strain gradients make these poly-SiGe films unsuitable for many larger micromachined devices.

Table 1. *Young's modulii calculated from the measured resonant frequencies of as-deposited, folded-flexure resonators with 10.5kHz & 20kHz (design) resonant frequencies. The calculated Young's modulii have a normalized uncertainty of ±3.0%.*

%Ge Content	f_r (kHz)	E (GPa)	f_r (kHz)	E (GPa)
68/65/62	10.4	149	20.7	158
68	10.6	156	20.6	159
65	10.5	152	19.8	154
62	no data	no data	no data	no data

Table 2. *Measured and normalized strain gradients for the various poly-SiGe films before and after RTA. RTA for 1 minute at 600ºC reduces the curl-up of a 300µm tri-layer cantilever beam from 7.9µm to 1.2µm. The tri-layer's strain gradient is, in general, lower than the single layer samples because of its greater thickness. The normalized strain gradient is simply the measured strain gradient multiplied by the film's thickness. All tip deflections were measured to within ±5nm. Hence, all strain gradients have uncertainties less than ±0.5%.*

%Ge Content	Strain Gradient (µm^{-1})		Normalized Strain Gradient	
	As-Deposited	RTA @ 600°C	As-Deposited	RTA @ 600°C
68/65/62	$1.75 \cdot 10^{-4}$	$2.67 \cdot 10^{-5}$	$5.25 \cdot 10^{-4}$	$8.01 \cdot 10^{-5}$
68	$2.95 \cdot 10^{-4}$	$6.89 \cdot 10^{-5}$	$2.95 \cdot 10^{-4}$	$6.89 \cdot 10^{-5}$
65	$3.54 \cdot 10^{-4}$	$7.60 \cdot 10^{-5}$	$3.54 \cdot 10^{-4}$	$7.60 \cdot 10^{-5}$
62	$4.68 \cdot 10^{-4}$	$1.87 \cdot 10^{-4}$	$4.68 \cdot 10^{-4}$	$1.87 \cdot 10^{-4}$

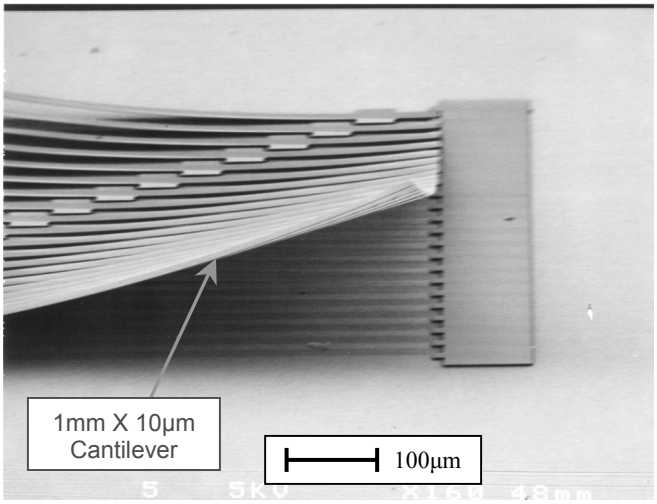

(a) *As-deposited tri-layer strain gradient.*

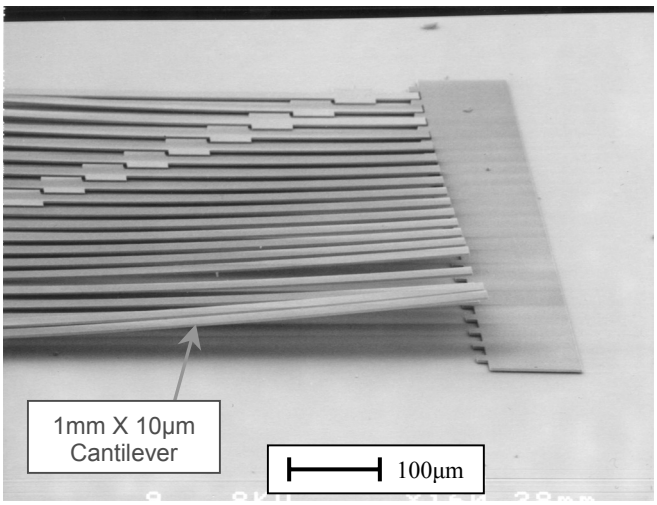

(b) *Tri-layer strain gradient after one minute RTA at 600ºC.*

Figure 7. *Poly-SiGe strain gradient test structures as-deposited* ***(a)*** *and after RTA* ***(b)****. As is apparent from the figure, RTA significantly reduces the strain gradient. Note: the discontinuity in tip deflections in* ***(b)*** *is due to the fact that one of the long cantilevers was caught under another one.*

To first order, we can normalize the strain gradient by multiplying the measured strain gradient by the film's thickness. Table 3 indicates that the tri-layer film does not have improved strain gradient. Indeed, the tri-layer film exhibits higher normalized strain gradient than each of the single films. RBS data confirms that inter-layer diffusion of Ge nullified the graded Ge distribution in all but the top half-micron of the film, thereby canceling any positive effect that such a grading might have.

VI. CONCLUSIONS

The $Q \approx 42{,}000$ and elastic modulus, $E \approx 155$GPa, of poly-SiGe are of sufficient quality so as to make poly-SiGe attractive for integrated RF MEMS applications. For small nanoelectromechanical systems (NEMS) resonators (where large strain gradients are not overly detrimental), poly-SiGe is particularly attractive. The capability of poly-SiGe to be micromachined directly on top of modern foundry CMOS enables lower parasitics, less feedthrough, and, ultimately, lowers the cost of wireless communications devices.

The large observed strain gradient of poly-SiGe currently limits the material's application to large MEMS devices. However, the RTA results presented herein indicate that the strain gradient can be reduced significantly with modest annealing. Our group is continuing to develop methods for bringing down the strain gradient.

ACKNOWLEDGEMENTS

The authors wish to thank the DARPA MEMS program, whose generous grant (#N66001-00-1-8955) has made this research possible. We thank Dr. Kin Man Yu at LBL for the RBS results, Marilyn Kushner for making masks at short notice, and Charley Williams for helping us fix the MMR probe station.

REFERENCES

1. A. E. Franke, Y. Jiao, M. T. Wu, T.-J. King and R. T. Howe, "Post-CMOS Modular Integration of Poly-SiGe Microstructures using Poly-Ge Sacrificial Layers," *Solid-State Sensor and Actuator Workshop*, Hilton Head Island, South Carolina, June 4-8 (2000), pp. 18-21.

2. A. E. Franke, "Polycrystalline Silicon-Germanium Films for Integrated Microsystems," *PhD Dissertation*, Dept. of Electrical Engineering and Computer Sciences, UC Berkeley (2000).

3. S. Sedky, A. Witvrouw, H. Bender and K. Baert, "Experimental Determination of the Maximum Post-Process Annealing Temperature for Standard CMOS Wafers," *IEEE Transactions of Electron Devices*, Vol.48 (no.2) (2001), pp. 377-85.

4. M. Biebl, G. T. Mulhern, and R. T. Howe, "In Situ Phosphorus-Doped Polysilicon for Integrated MEMS," *8th International Conference on Solid-State Sensors and Actuators and Eurosensors IX*, Stockholm, Sweden (1995), pp. 198-201.

5. C. T.-C. Nguyen, "High-Q micromechanical oscillators and filters for communications," *Proceedings of 1997 IEEE International Symposium on Circuits and System,* Hong Kong (1997), pp. 2825-8.

6. J. R. Clark, W.-T. Hsu, and C. T.-C. Nguyen, "High-Q VHF Micromechanical Contour-Mode Disk Resonators," *Technical Digest, IEEE Int. Electron Devices Meeting*, San Francisco, California (2000), pp. 399-402.

7. J. Yang, H. Kahn, A-Q. He, S.M. Philips and A. H. Heuer, "A new technique for producing large-area as-deposited zero-stress LPCVD polysilicon films: the MultiPoly process," *JMEMS* December (2000), pp. 485-494.

8. M. L. Roukes, "Nanoelctromechanical Systems," *Solid-State Sensor and Actuator Workshop*, Hilton Head Island, South Carolina, June 4-8 (2000), pp. 367-376.

9. C. T.-C. Nguyen, "Micromechanical Signal Processors," *PhD Dissertation*, Dept. of Electrical Engineering and Computer Sciences, UC Berkeley (1994), pp. 138-155.

10. W. C. Tang, C. T.-C. Nguyen, R. T. Howe, "Laterally Driven Polysilicon Resonant Microstructures," *Proceedings IEEE MEMS*, February (1989), pp. 53-59.

11. K. Nunan, G. Ready, and J. Sledziewski, "LPCVD & PECVD Operations designed for iMEMS Sensor Devices," *Journal of Vacuum Technology and Coating*, January (2001), pp. 27-37.

A LOW TEMPERATURE BI-CMOS COMPATIBLE PROCESS FOR MEMS RF RESONATORS AND FILTERS

Jennifer L. Lund, Christopher V. Jahnes, Hariklia Deligianni, L. Paivikki Buchwalter, John M. Cotte, Panayotis Andricacos, David E. Seeger, and John H. Magerlein
IBM T. J. Watson Research Center
Yorktown Heights, NY 10598

ABSTRACT

A low temperature, Bi-CMOS compatible process for the fabrication of MEMS resonators and filters has been developed. These devices hold the promise of reducing cost and power requirements in IC's for communications applications. The devices were fabricated on 200mm wafers in standard production tools using materials and processes routinely employed for on-chip interconnect in a typical CMOS line. The maximum processing temperature for the MEMS devices is 400C.

Simple cantilever and fixed beam structures were fabricated and tested. Un-encapsulated devices were measured in a low-pressure system to determine frequency response and quality factor (Q). Devices were typically actuated with DC biases between 4-5 V; useful tuning range is from ~3-7 V, corresponding to a 1% shift in frequency for the devices measured here. Frequency responses from 3-45 MHz have been recorded. Under vacuum, average device Q's were around 2000, although values above 10,000 have been measured. The devices maintain peak Q up to a pressure of approximately 100 mT. Temperature effects were also studied.

INTRODUCTION

The potential for MEMS devices to have a great impact on the communications industry has been widely discussed recently [**1**]. MEMS RF switches, reference oscillators, filters, and varactors are a few of the devices that could replace expensive and bulky off-chip passive components. It has even been proposed that MEMS filters could dramatically alter today's typical RF front-end architecture [**2**].

For resonators and filters aimed at replacing passive components in RF communications circuitry, the most critical design factors are ability to reach the frequencies of interest (~900MHz-2.1GHz), low power and/or bias voltages, size, and cost. To meet these needs, high-modulus/low-density materials must be used, aggressive scaling of both beam and gap dimensions is required, and straightforward integration with analog IC processes is desirable. A wide variety of materials have been used to form MEMS resonators, including polysilicon [**3,4**], single crystal silicon [**5,6**], SiO_2 [**7**], Si_3N_4 [**8**], Ni, poly-SiGe [**9**], and a variety of piezoelectric films. Similarly, there are a number of means of exciting and detecting resonance; electrostatic actuation is most common but magnetic [**8**], thermal [**7**], and optical [**10**] methods have been used. Finally, the varied geometries of MEMS resonators include comb-drives, which typically resonate in the kHz range, diaphragms, simple bridge and cantilever beams, torsional elements, and circular disks, which have been reported at frequencies as high as 156 MHz [**11**].

The MEMS resonators and filters demonstrated here are simple cantilever and fixed beam structures that use electrostatic actuation. Our preliminary design goals included low actuation voltages (< 6V), intermediate frequencies (~few 100 MHz), and the use of fabrication techniques that would allow the devices to be seamlessly integrated with the interconnect levels of high-speed CMOS or Bi-CMOS processes. The latter constraint leads to a maximum processing temperature of 400C and a somewhat limited set of materials. The resulting process was developed and run at the IBM Semiconductor Research and Development Center, where IBM's SiGe Bi-CMOS processes are qualified.

PROCESS DEVELOPMENT

Device fabrication begins with the lower metal level, which forms the drive and sense electrodes for the resonator, as well as the physical anchor points for and electrical contact to the beam. This metal level may be shared with other interconnect levels, such as a copper wiring level or a local interconnect level using a refractory metal (e.g., tungsten). The next step is the formation of a cavity for device encapsulation. The cavity serves two functions: to physically protect the device, and to assist in providing a low-pressure ambient for device operation. It has been repeatedly demonstrated that pressure is the greatest limiting factor on the achievable quality factor (Q) for MEMS resonators. This cavity may be comprised of one or more of the inter-layer dielectric (ILD) films used in the chip interconnect levels. Next, the sacrificial layer that forms the gap between resonator and electrode is deposited. Gaps between 300-3000Å were fabricated; nominal thickness of 1000Å was used in the process. The sacrificial material is patterned to allow contact between beam and lower metal (beam anchors). Then the beam materials, which consist of a thin metal layer followed by a thick dielectric layer, are deposited and patterned. Beam thicknesses from 0.6–1.0μm were used in this process, although thicker beams may be made. Fig. 1 shows a schematic of these process steps; Fig. 2 and Fig. 3 show SEM cross-sections of a cantilever beam resonator at this stage.

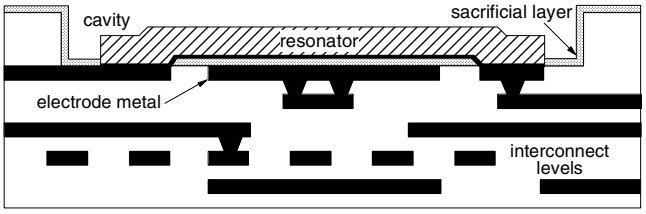

Fig. 1. *Initial process steps include formation of lower metal electrode layer and cavity for device encapsulation, followed by deposition and patterning of sacrificial layer and beam materials.*

The cavity is then refilled with additional sacrificial material, planarized, and sealed with a dielectric membrane, as shown in Fig. 4 and Fig. 5. The target thickness of the "upper" gap was 2500Å; however, planarity of the sacrificial material within the cavity was challenging to control and depended on the sizes of both the beam and the cavity. To solve this problem in subsequent runs, we reversed the order of formation of the beam and "cavity". This change allows us to planarize the additional ILD material

0-9640024-4-2/hh2002/$20©2002TRF
DOI 10.31438/trf.hh2002.10

rather than the sacrificial material (a process which is well known and practiced), and has the additional advantage of making the formation of thicker beams easier.

The sacrificial material must now be removed from the bulk of the cavity and from beneath the beam. Small vias are etched through the top membrane, and the sacrificial material is removed with a dry release process. Using this process, we have been able to easily undercut beams with gap thicknesses of as little as 300A (Fig. 6, left), and also to evacuate very large, deep cavities. Fig. 8 shows a FIB cross-section of a resonator beam after this procedure.

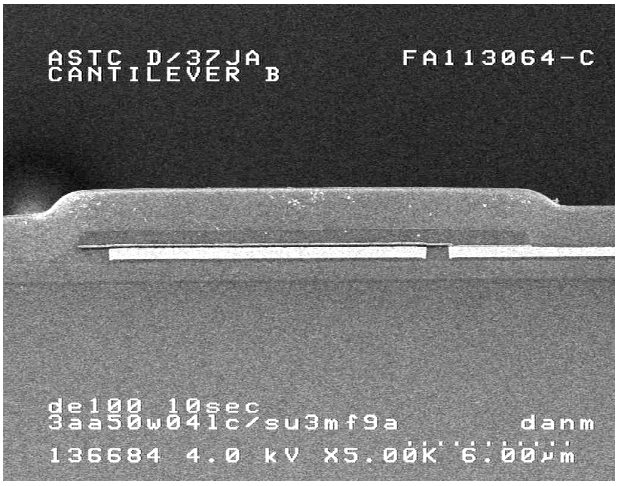

Fig. 2. *SEM cross-section of an un-encapsulated cantilever beam resonator prior to release (the material coating the beam is quartz deposited during SEM sample preparation).*

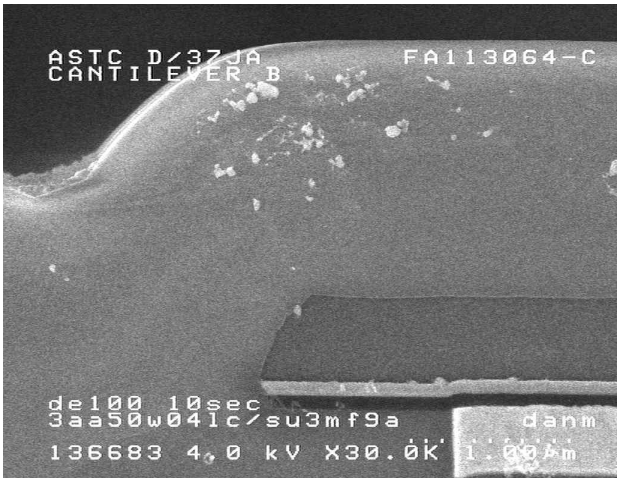

Fig. 3. *Expanded view of the tip of the cantilever beam of Fig. 2, more clearly showing the metal and dielectric layers of the beam, the gap, and the lower electrode. The total beam thickness is approximately 6500Å; the gap spacing is 1000Å.*

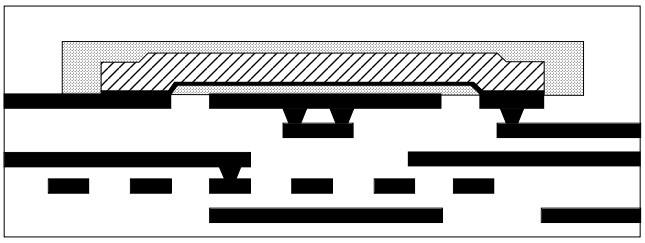

Fig. 4. *The device is surrounded with additional sacrificial material, and sealed inside a planarized cavity.*

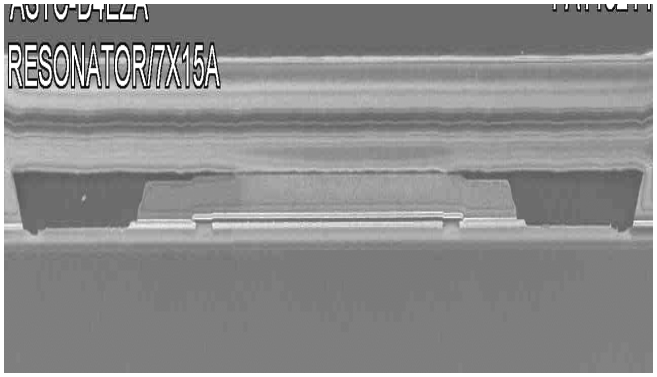

Fig. 5. *SEM cross-section of an encapsulated fixed beam resonator prior to release. The photo has been expanded in the z-direction to emphasize the gaps above and below the beam.*

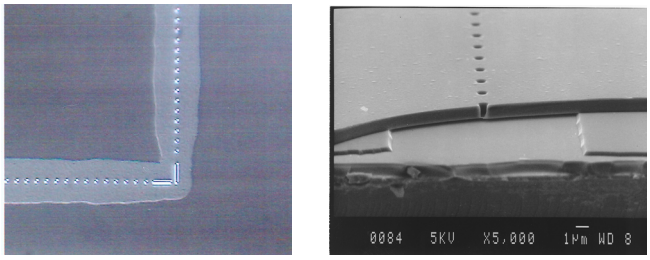

Fig. 6. *Demonstration of release of sacrificial layer through vias for a 300Å thick film (left, optical top-down photo) and a 2700Å thick film (right, SEM cross-section).*

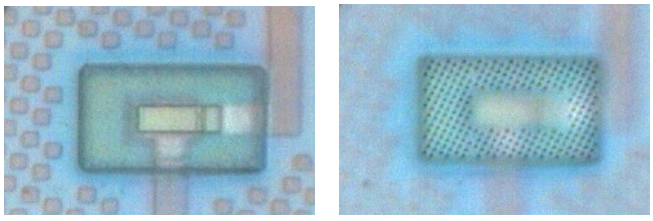

Fig. 7. *Optical photograph of a cantilever beam resonator after release through vias. On the left, focus is on the beam; on the right, focus is on the vias holes in the cavity membrane.*

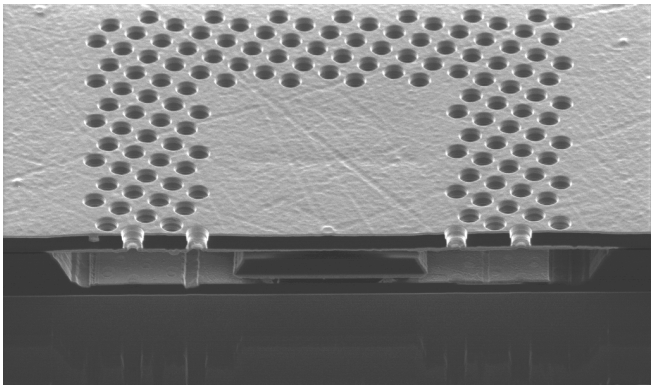

Fig. 8. *FIB cross-section showing evacuated cavity and freestanding fixed beam resonator after release through vias.*

Following release, the vias are re-sealed with an additional plasma-enhanced chemical vapor deposited (PECVD) film (Fig. 9 and Fig. 10). These two steps (release and sealing) can be done in a single tool, allowing a low pressure ambient within the device cavity. The "pinch-off" process can also be started in a PECVD tool and finished in a UHV tool such as a sputtering system if

lower initial cavity pressures are desired. For limiting re-deposition inside the cavity during the pinch-off process, the size of the release vias is relatively unimportant as long as the aspect ratio remains above 4 (see Fig. 11). We selected 0.25µm vias with a depth of 1.0µm. To further limit effects of re-deposition on beam mass, release vias are not placed within 1.0µm of the device.

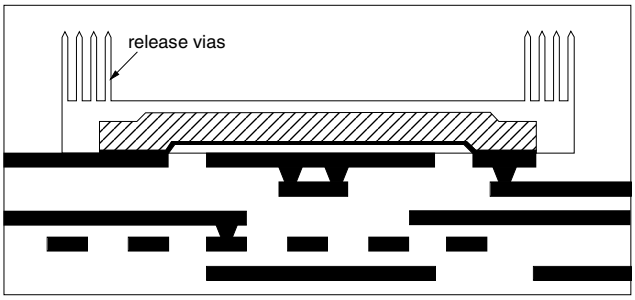

Fig. 9. *Release vias are etched in the cavity ceiling, and the sacrificial material is removed through the vias using a dry process. The vias are then sealed with an additional dielectric deposition.*

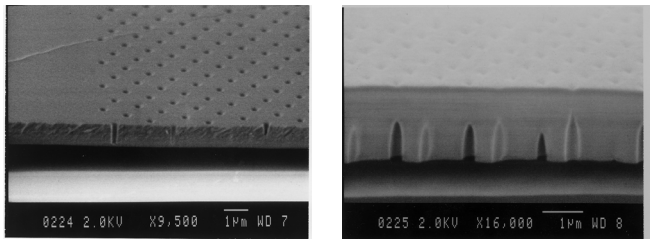

Fig. 10. *SEM cross-sections showing removal of a 1µm thick sacrificial layer through vias, and pinch-off of those vias with a second dielectric deposition. Note the cleanliness of the cavity floor beneath the vias.*

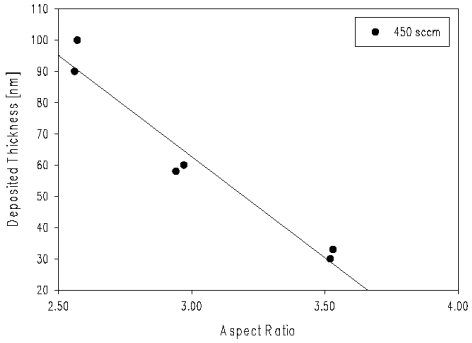

Fig. 11. *To limit re-deposition inside the cavity, release via aspect ratios should be kept above 4.*

RESULTS

Two basic beam sizes and configurations were characterized for frequency response and Q: 4µm x 10µm and 7µm x 15µm fixed beams and cantilever beams. Smaller beams were also fabricated but have not been successfully measured. Un-encapsulated devices were characterized so that the measurement pressure could be known and controlled. Except where specifically noted otherwise, the measurements reported here are for typical pressures of 30-50 µTorr and at room temperature. Measurements were taken on-wafer using microwave probes and an HP8753B network analyzer. Generally, DC bias and input power were applied to the beam, and transmitted power was measured from the grounded lower electrode. The plots below give S_{21} log magnitude vs. frequency; typical input power is –20 dBm and bias voltages are noted.

Fig. 12 and Fig. 13 show typical frequency responses for the fixed beam and cantilever beam resonators. While we have only been able to detect the fundamental mode for the fixed beam resonators, the cantilever beams reliably exhibit frequency responses corresponding to two different modes. Simple theory can predict these frequencies. Using:

$$f_i = \frac{\xi_i^2}{4\pi\sqrt{3}} \sqrt{\frac{E}{\rho}} \frac{t}{l^2}$$

where $\xi_1 = 1.875$, $\xi_2 = 4.694$ for the cantilever beam and $\xi_1 = 4.730$ for the fixed beam [12], and assuming $t = 0.65\mu m$, $\rho = 3.1$ gm/cm^3, and $E = 160$ GPa, this yields:

		Predicted [MHz]		Measured [MHz]	
		1st mode	2nd mode	1st mode	2nd mode
Cantilever Beam	15µm	3.35	21.01	3.05	21.35
	10µm	7.54	47.27	7.32	45.15
Fixed Beam	15µm	21.33	-	21.83	-
	10µm	48.00	-	42.32	-

Table 1. *Predicted and measured values of f_0 for fixed and cantilever beams.*

Note that the values of E and ρ used in the calculation are fitted parameters; 3.1 gm/cm^3 is a typical value for ρ and nanoindentation measurements of the dielectric layer of the beam gave values of ~190 GPa for E. A more accurate means of determining the material properties of the composite beams will be desirable.

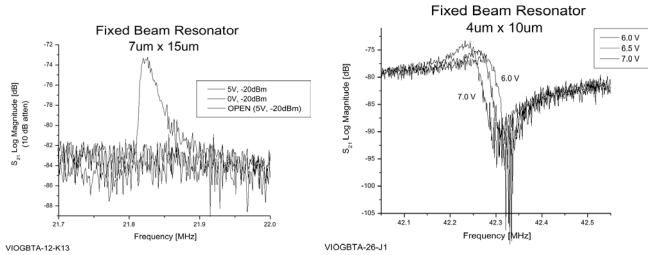

Fig. 12. *Frequency response of fixed beam resonators. For the 15µm beam (left), measurements at 0V DC bias and an open circuit are shown for reference. For the 10µm beam (right), voltage tuning is demonstrated.*

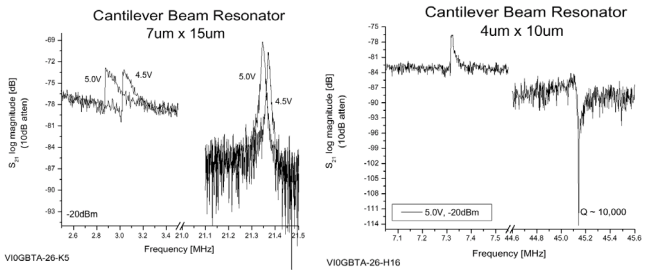

Fig. 13. *Frequency responses of cantilever beam resonators. Cantilevers reliably show responses that correspond to more than one mode. Voltage tuning is also shown for the device on the left.*

Figs. 13, 14, and 15 also demonstrate an important property of MEMS resonators: voltage tuning. In order to achieve target frequency and stability specifications for resonators in communications circuits, extraordinary process control will be

required, particularly as the beams are scaled to smaller dimensions. Given process and, more importantly, material property variability, it is unlikely that these specs can be met without some method of actively tuning the resonant frequency. Although not yet completely characterized, we see here (Fig. 14) a 1% change in frequency over the range of 3.2-5.0V DC bias.

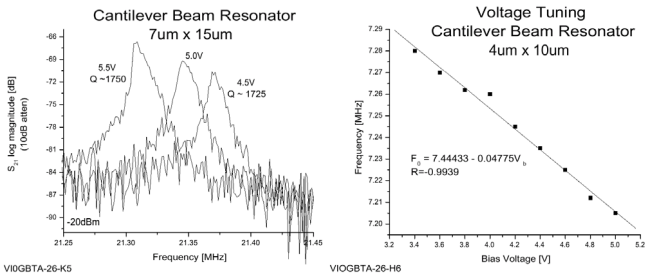

Fig. 14. *Effect of bias voltage on center frequency and Q for a cantilever beam resonator.*

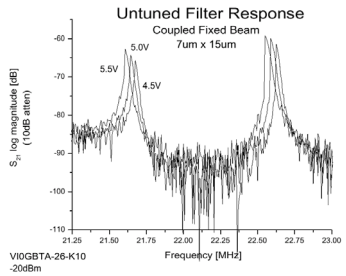

Fig. 15. *Two peaks are exhibited by a coupled fixed beam filter structure. The bias voltages were not tuned independently in this measurement.*

The effects of pressure and temperature on resonant frequency are displayed in Fig. 16 and Fig. 17. As expected, Q decreases with increasing pressure, although peak Q is maintained up to about 100 mT. It is possible that the on-chip encapsulation method may not be able to maintain a long-term partial pressure in the mT range. Temperature variation from 25C to 85C yielded less that 0.15% change in center frequency for the fixed and cantilever beams in Fig. 17. This is well within the 1% tuning range noted above, and indeed is somewhat less than the device-to-device and day-to-day measurement variability that was typically found.

Finally, reliability data is anecdotal at this point. Several devices have been left operating overnight with no ill effects; the longest has been left for 18.5 hours at 22 MHz (over 10^{12} cycles).

CONCLUSIONS

MEMS resonators have been fabricated using processes and materials that are commonly found in the interconnect levels of CMOS and BiCMOS IC's. The maximum processing temperature for these devices is 400C, making it possible for them to be integrated directly on-chip without affecting the existing analog circuitry. These devices operate in the intermediate frequency range and exhibit the very high Q-factors characteristic of mechanical resonators. The ability to excite higher-order modes has been demonstrated. Voltage tuning, which can compensate for process and temperature variations, has also been shown.

The long-term efficacy of the wafer-level encapsulation process described here has not yet been assessed. Even if it should prove to be insufficient for maintaining a low pressure ambient without additional packaging solutions, wafer-level encapsulation is still critical for physical protection of the devices.

Scaling of MEMS resonators to achieve higher frequencies remains a distinct challenge. Very low signal-to-noise ratios will make driving and sensing these beams difficult. Furthermore, the very high impedance and effective Q of very small beams make their practical utility in analog circuit design an open question.

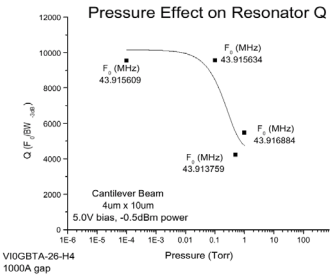

Fig. 16. *Resonator damping increases with increasing pressure, although peak Q is maintained up to about 100mT.*

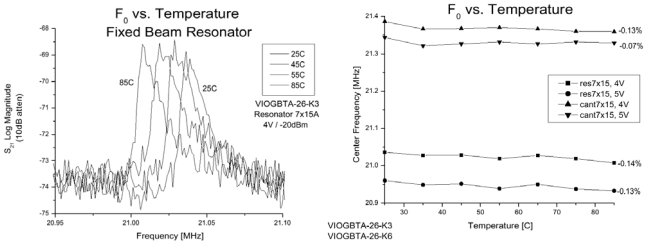

Fig. 17. *Effect of temperature on frequency response for fixed beam and cantilever beam resonators.*

ACKNOWLEDGEMENTS

The authors wish to thank the members of the ASTL and ASTC laboratories who contributed to this work, particularly R. Acosta, J. Yoon, I. Babich, J. Treichler, M. Carasso, A. Mahorowala, V. Patel, and A. McDonald. Thanks also to K. Jenkins for RF measurement assistance, and D. Dove for helpful discussions.

REFERENCES

1. P. Gelsinger, remarks at Intel Developer Forum, 28 Feb. 2002.
2. C. Nguyen, A.-C. Wong, and H. Ding, "Tunable, switchable, high-Q VHF MEMS bandpass filters," *Dig. ISSCC*, (1999) pp. 78-79.
3. F. Bannon, J. Clark, and C. Nguyen, "High frequency micro-electromechanical IF filters," *Proc. IEDM*, (1996) pp. 773-776.
4. K. Wang, A.-C. Wong, and C. Nguyen, "VHF free-free beam high-Q microelectromechanical resonators," *MEMS '99*, (1999) pp. 453-458.
5. R.A. Buser and N.F. de Rooij, "Capacitively activated torsional high-Q resonator," *Proc. MEMS '90*, (1990) pp. 132-135.
6. J. Weigold, *et al.*, "A merged process for thick single-crystal Si resonators and BiCMOS circuitry," *J. MEMS, 8*, 3 (1999), pp. 221-228.
7. O. Brand *et al.*, "Thermally excited silicon oxide beam and bridge resonators in CMOS technology," *IEEE Trans. on Electron Devices, 40*, 10 (1993), pp. 1745-1753.
8. D. Greywall, "Micromechanical RF filters excited by the Lorentz force," *J. MEMS, 9*, 1 (1999), pp. 78-84.
9. A. Franke, *et al.*, "Post-CMOS modular integration of poly-SiGe microstructures using poly-Ge sacrificial layers," *Tech. Dig. 2000 Solid State Sensor and Actuator Workshop*, (2000), pp. 18-21.
10. T. Lammerink, M. Elwenspoek, and J. Fluitman, "Optical excitation of micro-mechanical resonators," *Proc. MEMS '91*, (1991), pp. 160-165.
11. J. Clark, W.-T. Hsu, and C. Nguyen, "High-Q VHF micromechanical contour-mode disk resonators," *Proc. IEDM*, (Dec. 2000), pp. 493-496.
12. W. Weaver, S. Timoshenko, and D. Young, *Vibration Problems in Engineering*, John Wiley & Sons, New York, 1990.

MICROMACHINED MAGNETICALLY RECONFIGURABLE FREQUENCY-SELECTABLE SURFACES

Joe Zendejas, John Gianvittorio, Bongyoung Yoo, Yahya Rahmat-Samii, Ken Nobe, and Jack W. Judy
Electrical Engineering Department, University of California, Los Angeles
Los Angeles, CA, 90095 USA

ABSTRACT

Reconfigurable frequency-selective surfaces have been realized by integrating an array of batch fabricated magnetic microactuators into an array of conductive dipole elements. The microactuators in the array consist of a 896×168×30 μm^3 ferromagnetic plate made of 40Co-60Ni attached to a pair of 400×30×1 μm^3 polysilicon torsion bars. The remanent magnetization in the hard ferromagnetic material allows relatively small magnetic fields (~1750 A/m or 22 Oe) to induce significant angular deflections (~45°). By rotating the dipole elements from 0° to more than 45°, the filtering response of the frequency-selective surface can be tuned over a range of 5 GHz at frequencies over 60 GHz.

INTRODUCTION

The expanding needs of RF and mm-wave system designers are pushing the limits of MEMS development [1-2]. Switchable and tunable RF and mm-wave systems are of great interest because they offer the potential to expand the functionality and capability of high-frequency communication systems.

Frequency-selective surfaces (FSSs) are periodic structures in two dimensions that can provide frequency filtering to incoming electromagnetic waves (Figure 1a). A common FSS example is the mesh screen on the door of a microwave oven. The mesh screen blocks electromagnetic radiation from the inside of the microwave oven while allowing the operator to see inside safely. Although FSSs have long been studied, they have experienced tremendous growth in the last ten years with new applications emerging (e.g., frequency filters or diplexers in high performance reflector antenna systems, advanced radome designs, and smart surfaces for stealth applications). These FSSs are typically designed with static elements for a specific frequency response (Figure 1b). The size and spacing of the periodic cells in an array of elements controls the overall frequency response and bandwidth of the surface (Figure 2) [3].

Although prior work on FSSs has only been on arrangements of static in-plane elements [4], in many applications it would be highly advantageous to adaptively reconfigure the frequency and bandwidth response of an FSS. However, a fundamental challenge has been achieving significant high-speed reconfigurability without compromising filtering performance. The frequency and bandwidth response of FSSs can be adjusted by reconfiguring the size, spacing, or orientation of the elements in the array.

Simulations performed using two methods developed at UCLA (*i.e.,* a periodic moment method analysis technique and a finite difference time domain technique FDTD), have shown that the frequency response of an FSS is a strong function of dipole element tilt [5-7]. Rotating conductive elements in an array through an angle of 0° to 30°, can significantly shift its overall frequency response. To enable the efficient control of mm-wave signals, single devices or arrays of microactuators are needed that can travel relatively large distances (~1 mm) with a high degree of control and reliability.

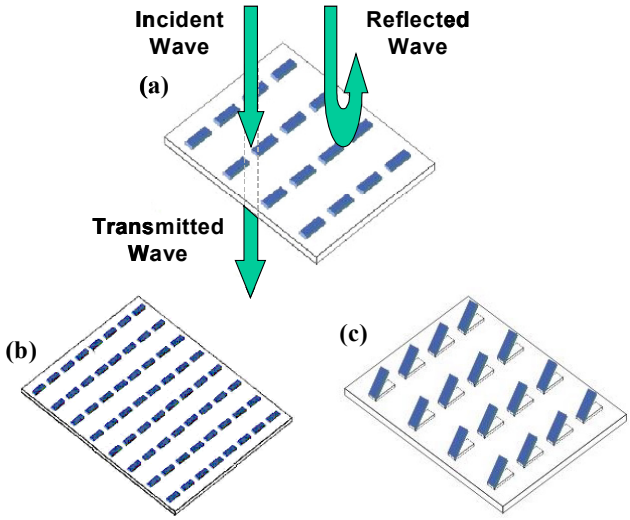

***Figure 1**. Frequency selective surfaces: (a) incident, reflected, and transmitted waves through an FSS; (b) an FSS with a different frequency response; (c) an FSS with rotating dipoles.*

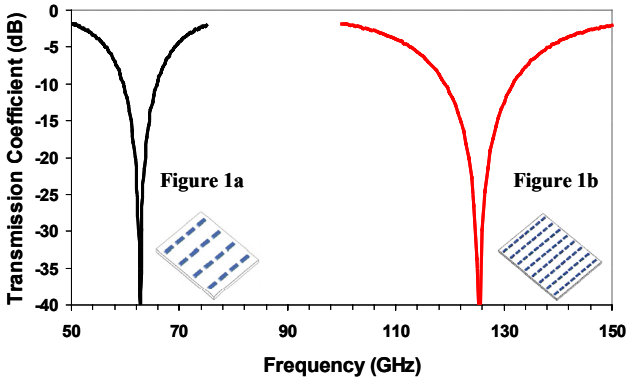

***Figure 2**. Simulated frequency responses of different static arrays as a function of element size and periodicity.*

ANALYSIS

An attempt to look at the effect of a non-planar FSS was performed in [4]. In that work, the authors investigated a discrete number of non-planar configurations (of the periodic scatterer). Rigorous simulations in [5] have been used to show the effects of having the periodic elements rotated such that they are no longer confined to the periodic plane. An illustration of the concept of rotated dipoles is shown in Figure 1c. Even though the dipoles are tilted, the reflected field remains normal to the *x-y* plane because the reflected wave is the fundamental Floquet mode, which depends on the angle of incidence, not the orientation of the periodic dipole.

0-9640024-4-2/hh2002/$20©2002TRF
DOI 10.31438/trf.hh2002.11

Solid-State Sensors, Actuators, and Microsystems Workshop
Hilton Head Island, South Carolina, June 2-6, 2002

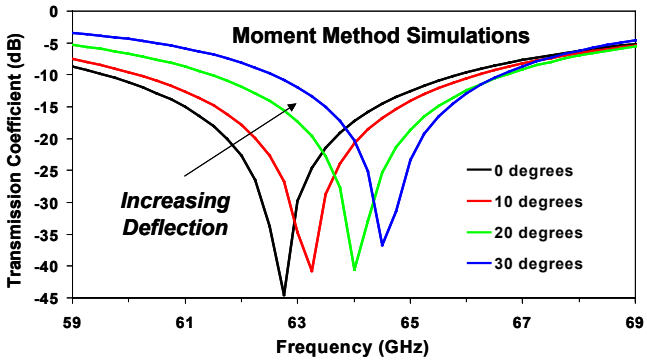

***Figure 3**. Simulations of the effect of angular deflection on the frequency response of an array of dipoles (896×168 μm^3). Note the prominent shift upwards and to the right with increasing angular deflection.*

Figure 3 shows the normal incidence transmission coefficient of an FSS composed of thin dipoles, as a function of dipole rotation (φ = 0° to 30°). The φ = 0° curve shows a resonance when λ/2 is approximately the length of the dipole element. Since the incident field is normal to the *x*-*y* plane, in the limit φ = 90° (*i.e.,* dipoles parallel to the *z*-axis) no currents can be excited on the dipoles. An observation from Figure 3 is that the resonant frequency is shifted as the dipole tilt is increased. The shift in the resonant frequency is due to the mutual coupling between the dipoles. Since in this case the length of each dipole is 80% of the periodicity, the spacing between the dipoles is small. As the dipoles are tilted, the spacing between them increases, which changes the coupling. The change in the mutual coupling shifts the λ /2 resonance.

DESIGN

Advances and developments in micromachining and MEMS technology can be used to fabricate an FSS array with elements capable of rotation, thereby enabling the tuning of the frequency response. Particularly well suited for this application is a ferromagnetic microactuator consisting of a ferromagnetic plate and non-magnetic torsional flexures (Figure 4). The device is actuated by an off-chip source for the magnetic field. The microactuation principle is essentially that of a compass needle – the integrated magnetic microelements rotate with the applied magnetic field.

This microactuation technology combines the excellent mechanical robustness of polysilicon flexures with the large forces that can be generated by ferromagnetic materials in a magnetic field. The ability of microactuators made with technology to rotate through large out-of-plane deflections (>90º) has been previously demonstrated [9-10]. Accurate models for the static and dynamic behavior of this microactuation technology have also been developed and reveal that high-speed tuning of the dipole array is feasible [8-10].

The unique features that make this microactuator technology well suited for this application include: (1) no individual interconnects that might otherwise interfere with the frequency response and bandwidth of the surface are needed, and (2) dense arrays of actuators can all be driven simultaneously to the same angular deflection by changing only one parameter – the driving magnetic field (Figure 5).

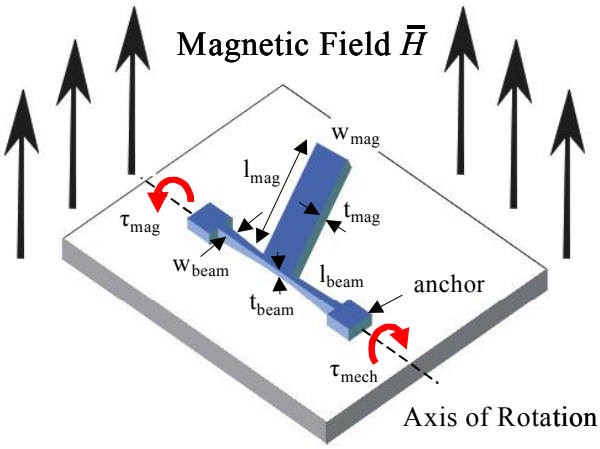

***Figure 4**. Ferromagnetic microactuators with torsional flexure driven by an off-chip source of magnetic field.*

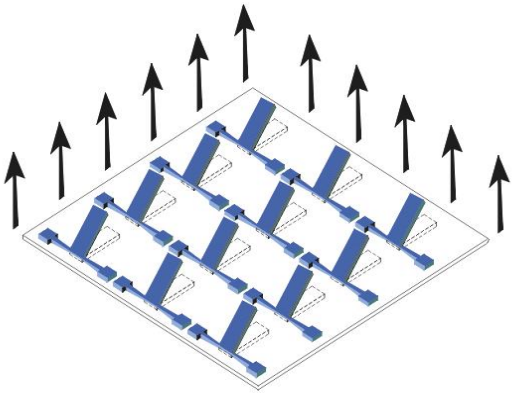

***Figure 5**. Array of actuators being driven by a magnetic field.*

As shown in [10], the appropriate material for this microactuator technology is a hard magnetic material (*i.e.,* one with a large coercivity and remanent magnetization). In this work we have developed a process for electroplating 40Co-60N as the ferromagnetic material with the magnetic properties described in Figure 6, with coercivity 6000 A/m (75 Oe) and magnetic saturation 1.0 T.

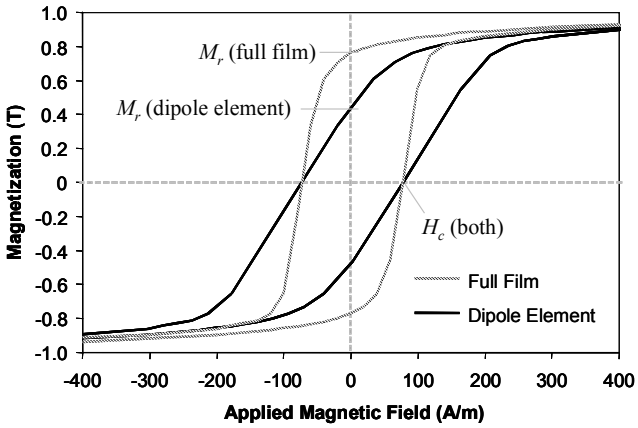

***Figure 6**. Measured B-H loop for 30-μm-thick films of electroplated 40Co-60Ni with no demagnetizing field (dashed) and with the effects of a calculated demagnetization field from a 896×168×30 μm^3 element (solid).*

Since the FSS was designed with an array of 896×168 μm^2 elements, the demagnetization coefficients are $N_a = 0.012$, $N_b = 0.14$, and $N_c = 0.835$ (*i.e.,* assuming a magnetic film thickness of 30 μm) [9]. The result being that the *B-H* loop of an individual microactuator element (*i.e.,* solid line in Figure 6) will be sheared relative to the *B-H* loop measured in a sample with negligible demagnetization coefficients in the plane of the sample (*i.e.,* $N_a \approx 0$, $N_b \approx 0$, and $N_c \approx 1$ and illustrated with the dashed line in Figure 6). Thus the maximum remanent magnetization in an individual element will be ~0.45 T. If the torsional flexure is made of polysilicon and has the following dimensions 400×30×1 μm^3, the mechanical deflection as a function of magnetic field directed normal to the surface of the wafer is given in Figure 7. The magnetic drive field required for a 45º deflection is only 1750 A/m (22 Oe), as compared to 7000 A/m (88 Oe) in previous work [9-10]. The much higher remanent magnetization of the 40Co-60Ni alloys provides a tremendous boost in performance that allows for smaller driving fields and low-power operation.

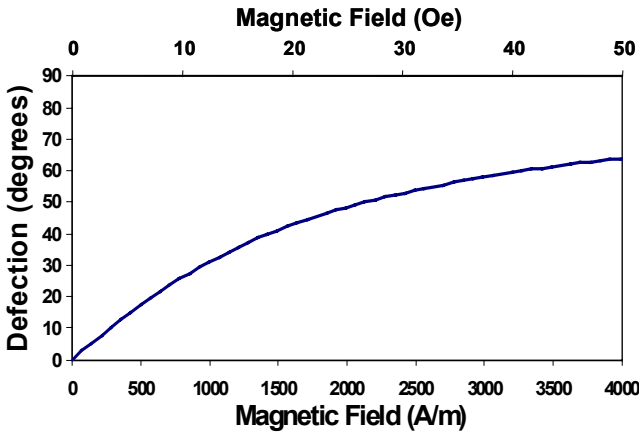

Figure 7. *Theoretical angular deflection of a 896×168×30 μm^3 40Co-60Ni plate attached to a pair of 400×30×1 μm^3 polysilicon torsional beams.*

FABRICATION

There are many important considerations when designing the fabrication process for a micromachined magnetically reconfigurable FSS: substrate loss, magnetic material, and process integration. In order to achieve the highest Q response, a low-loss substrate is required that minimizes the amount of attenuation contributed from the substrate. In this work, a <100> p-type silicon wafer with 30-60 Ω-cm was used. To achieve a large angle of deflection for a low external magnetic field, a thick film of hard magnetic material with substantial remanent magnetization is needed.

The fabrication process starts for devices reported here with the deposition of a 2-μm-thick layer of low-temperature oxide (LTO). Anchors for the torsion beam pads are then patterned into the LTO sacrificial layer. A 1-μm-thick film of undoped polysilicon is then deposited using low-pressure chemical-vapor deposition (LPCVD). The mechanical structures are then patterned into the polysilicon (Figure 8a). An adhesion layer of chrome and a seed layer of nickel are evaporated onto the polysilicon plates. Then a 0.2-μm-thick layer of titanium is evaporated onto the entire surface to act as the conduction layer between elements during plating. A 48-μm-thick photoresist mold (Shipley, STR 1045) is then patterned on the Ti conduction layer and around the Cr-Ni seed layer where the electroplated magnetic material is deposited (Figure 8b). The Co-Ni alloy is electroplated from a chloride bath with dc plating. The stress in the deposit is a minimum at an alloy composition of 40Co-60Ni when saccharin is added as a stress reducer. A 1-μm-thick layer of Au is deposited to add a high conductivity surface to the dipole element. After plating the photoresist plating mold is stripped (Figure 8c) and the excess conduction layer is removed. The final release is performed in 49% HF for 60 min to release the microstructures, which are then dried by CO_2-supercritical drying to complete the fabrication process (Figure 8d). An image of a typical microfabricated dipole element is given in Figure 9.

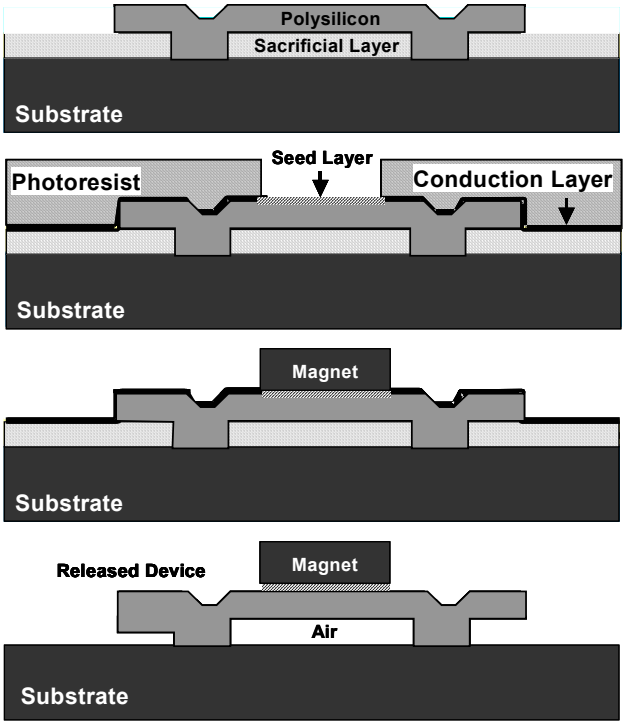

Figure 8. *Fabrication process for FSS elements: (a) deposition and etching of sacrificial and microflexure layers; (b) deposition of adhesion, seed, and conduction layers with formation of plating mold; (c) plated Co-Ni alloy and stripped plating mold; (d) removal of seed layer and the sacrificial layer to release the device.*

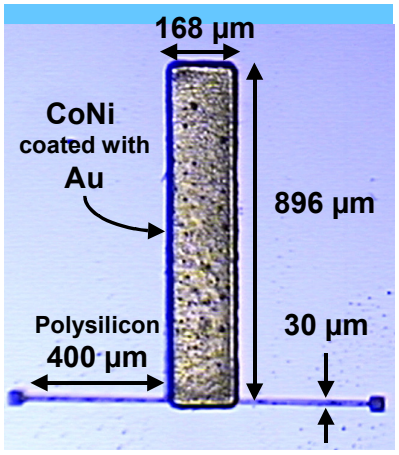

Figure 9. *Image of a single dipole with a pair of 400×30×1 μm^3 polysilicon torsion beams and a 896×168×31 μm^3 dipole.*

TESTING

The frequency response of an FSS, consisting of a 25×25 element array of 896×168×31 μm^3 elements made of 1 µm of Au on 30 µm of 40Co-60Ni on 1 µm of undoped polysilicon (Figure 9), is measured using an HP8510 network analyzer with a millimeter-wave source setup (Figure 10). The FSS is uniformly illuminated with a horn antenna and microwave-absorbing material is used to decrease edge diffraction and noise. Experimental results of the effect of angular deflection on frequency response, reveals the trend predicted by simulations (*i.e.,* the frequency shift upwards with increasing angle of deflection shown in Figure 3).

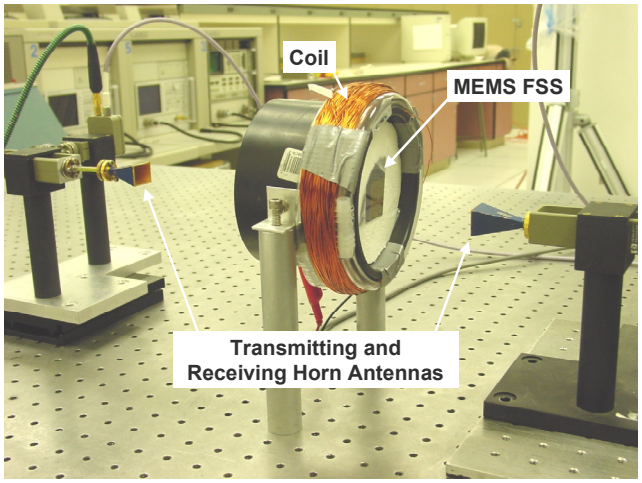

Figure 10. *Experimental setup for characterizing the frequency response of the MEMS-enabled reconfigurable FSS.*

From the measured results (Figure 11), it can be seen that as the elements are tilted, the blocked frequency band shifts higher. However, the rejection of the filter is gradually reduced.

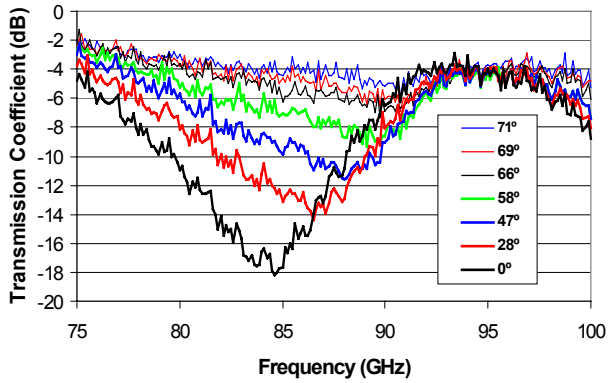

Figure 11. *Measured frequency response of rotated MEMs FSS for normal incidence.*

CONCLUSIONS

Rotating the dipole elements in a FSS can tune its frequency response at high frequencies (e.g., > 60 GHz) over a wide range (~5 GHz). Micromachining and MEMS technologies, specifically arrays of ferromagnetic microactuators with polysilicon torsional flexures, can be used to realize reconfigurable FSSs. Initial results indicate that substrate losses limit the Q of the filter response. Future implications of this work include new agile high-frequency communication systems and stealth technology.

ACKNOWLEGMENT

The authors would like to thank that staff of the UCLA Nanoelectronics Research Laboratory and the staff of the UCLA Center for High Frequency Research. This work was funded in part by NSF XYZ #0089095 and an AT&T Fellowship.

REFERENCES

[1] Clark C.-T. Nguyen, L. P. B. Katehi, G. M. Rebeiz, "Micromachined devices for wireless communications", *Proceedings of the IEEE*, vol. 86, no. 8, pp. 1756-1768.

[2] Clark C.-T. Nguyen, "Frequency-selective MEMS for miniaturized low-power communication devices", *IEEE Transactions on Microwave Theory and Techniques*, vol. 47, no. 8, pp. 1486-1503.

[3] Y. Rahmat-Samii and A. N. Tulintseff, "Diffraction analysis of frequency selective reflector antennas", *IEEE Transactions Antennas Propagation*, vol. AP-41, no. 4, pp. 476-487, 1993.

[4] B. Irvine, W. L. Ko, and R. Mittra, "A comparative study of angular scattering characteristics of a class of nonplanar frequency selective surfaces", *Electromagnetics*, vol. 15, no. 6, pp. 649-663, 1995

[5] Alon Barlevy and Yahya Rahmat-Samii, "Control of Resonant bandwidth in frequency selective surfaces by tilting the periodic elements", *Microwave and Optical Technology Letters*, vol. 21, no. 2, pp. 114-117, 1999.

[6] Alon Barlevy, and Yahya Rahmat-Samii. "*Characterization of Electromagnetic Band-Gaps Composed of Multiple Periodic Tripods with Interconnecting Vias: Concept, Analysis, and Design*." *IEEE Transactions on Antennas and Propagation*, vol. 49, no. 3, pp. 343-353, 2001.

[7] Yahya Rahmat-Samii and H. Mosallaei. "*Electromagnetic Band-gap Structures: Classification, Characterization, and Applications." Proceedings of 11th International Conference on Antennas and Propagation*, April 2001, vol. 2, pp. 560-564.

[8] Jack W. Judy, Richard. S. Muller, and Hans. H. Zappe, "Magnetic microactuation of polysilicon flexure structures," *IEEE Journal of Microelectromechanical Systems*, vol. 4, no. 4, pp. 162-169, 1995.

[9] Jack W. Judy and Richard. S. Muller, "Magnetic microactuation of torsional polysilicon structures," *Sensors and Actuators A (Physical)*, vol. A53, no. 1-4, pp. 392-396, 1996.

[10] Jack W. Judy and Richard. S. Muller, "Magnetically Actuated, Addressable Microstructures" *IEEE Journal of Microelectromechanical Systems*, vol. 6, no. 3, pp. 249-256, 1997.

MICROMACHINED JET ARRAYS FOR LIQUID IMPINGEMENT COOLING OF VLSI CHIPS

Evelyn N. Wang, Lian Zhang, Linan Jiang, Jae-Mo Koo, Kenneth E. Goodson, and Thomas W. Kenny
Mechanical Engineering, Stanford University
Stanford, CA 94305-4085

James G. Maveety and Eduardo A. Sanchez
Intel Corporation
Santa Clara, CA 95052-8119

ABSTRACT

Two-phase cooling of VLSI chips with microjet heat sinks promises a new, effective heat removal method. Microjet arrays can achieve improved temperature uniformity in the presence of chip hotspots. This paper describes the development and assesses the performance of micromachined single and multi-jet arrays with orifice diameters less than 100 μm. The devices were tested in a confined geometry with a dedicated heater test chip, as well as in an open geometry with a standard 1 cm^2 Intel test chip. In the confined geometry, a 76 μm diameter four-jet array at a flow rate of 8 ml/min removed over 90 W/cm^2. Experimental comparisons of microjet and microchannel performance show that microjets have improved thermal uniformity, offer a significantly more stable two-phase region, and do not exhibit superheating. These advantages suggest that microjet arrays are the preferred micro heat sinks for effective device cooling.

INTRODUCTION

The continuing increase in the power density of VLSI chips necessitates the development of novel heat removal technology. Thermal resistances less than 0.1 °C/W for heat sinks will be required in the next few years **[1]**. Micromachined heat sinks such as microchannels and microjets are compact and offers low thermal resistances **[2]**. However, microjet impingement has been of particular interest because the direct cooling onto the chip surface eliminates conduction resistances associated with the packaging and promises high heat removal rates. Furthermore, with microjet arrays, greater surface temperature uniformity can be achieved.

Past microjet research has focused on single-phase air impingement, which provides relatively low heat removal rates. Single and multi-air jet arrays with orifice diameters ranging from 50-800 μm have been studied **[3-6]**, including integration with heat sink modules **[5]** and actuation by magnetically driven membranes **[6]**. Heat transfer coefficients of 2500 W/m^2K were achieved with 1.3E7 ml/min air flow rate **[4]**.

Two-phase liquid microjet impingement is advantageous because the latent heat associated with phase change of the working fluid can be utilized to yield higher heat transfer coefficients. Macro scale jets with diameters greater than 0.28 mm using two phase heat transfer has been extensively studied in the past with several liquids, including water, R-113, and RC-72 **[7]**. Our past work characterized single microjet liquid impingement with orifice diameters less than 50 μm in an open geometry, and demonstrated removing over 40 W/cm^2. Heat transfer coefficients of 2200 W/m^2K at 2-3.5 ml/min water flow rate were attained **[8]**.

In this paper, heat transfer performance of single and multi-jet arrays with orifice diameters less than 100 μm is examined in confined and open geometries. The characterization of these microjets allows comparison with past microchannel research to investigate the advantages of using microjet heat sinks for future chip cooling. This work aids in developing an optimal design for micro heat sinks in closed-loop, pumped cooling systems.

DESIGN AND FABRICATION

The fabricated single and multi-jet arrays have circular orifice diameters ranging from 40 μm to 76 μm. The lengths of the jets are 300 μm. The fabricated test heater chip emulates a high power VLSI chip with an effective heating area of 1 cm^2. As shown in Figure 1, seven polysilicon doped resistance thermometers are defined along the centerline to measure the one-dimensional chip surface temperature profile. Because the resistance of doped polysilicon changes as a function of temperature, the surface temperature can be monitored as a function of the resistance change through calibration. The heater has a resistance of 500 Ω and the thermometers have a resistance of 7 kΩ each, with a temperature sensitivity of ranging from –6 Ω/°C to –20 Ω/°C. On the other side of the heater chip, a 1 cm^2, 200 μm deep reservoir collects the impinging water from the jets.

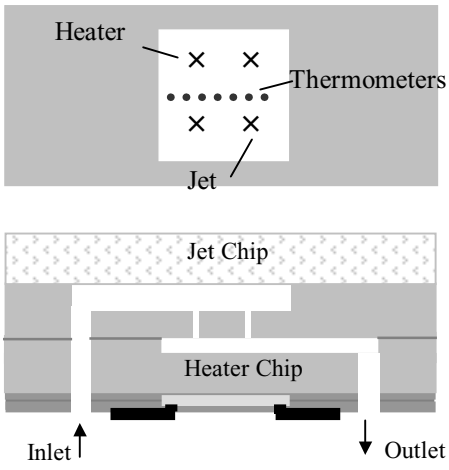

Figure 1. *Schematics of the top and cross-sectional views of a bonded confined jet impingement test chip, consisting of a four-jet array and a heater chip. The crosses on the top view show the configuration for the four-jet array.*

0-9640024-4-2/hh2002/$20©2002TRF
DOI 10.31438/trf.hh2002.12

The design and fabrication for both the jet and heater devices are similar to the ones described in **[8]**. However, the previous devices were only tested in an open geometry, where the fluid was not contained. The configuration is not practical for realistic microelectronic applications due to electrical shorting problems. In this study, the heater and jet chips described above are bonded together to form a confined geometry test chip. The chip fully encloses the impinging liquid and there are clear fluidic inlet and outlet paths. Figure 1 shows a schematic of the bonded test chips. The fluid enters the inlet to the jet chip, and after jet formation, fluid impinges onto the heater surface, and the heated fluid is collected from the outlet. The jet orifice to the heater surface separation is 200 μm.

Detailed fabrication procedures for these jet and heater chips are described in **[8]**, so the steps will be discussed briefly here. For the jet chips, the jets are first formed by deep reactive ion etching (DRIE) into single crystal silicon substrates. From the backside, a deep reservoir and inlet are then plasma etched. Finally, to seal the inlet and reservoir, a Pyrex glass slide is anodically bonded to the silicon substrate. For the heater chips, the outlet and reservoir are plasma etched with DRIE into single crystal silicon substrates. A nitride insulation layer is deposited. Polysilicon is then deposited, doped with Boron, and annealed to form the resistors. Finally, aluminum is deposited to form electrical contacts to the resistors. Once the jets and heater chips are fabricated, they are bonded together using 5-minute cure epoxy to make confined geometry test chips.

EXPERIMENTAL SETUP

The experimental setup for testing the microjet heat sinks is shown in Figure 2. The syringe pump continuously delivers deionized water to the test fixture. Water was chosen because it has a high latent heat of evaporation. A pressure sensor at the entrance to the test fixture monitors the pressure drop across the jets.

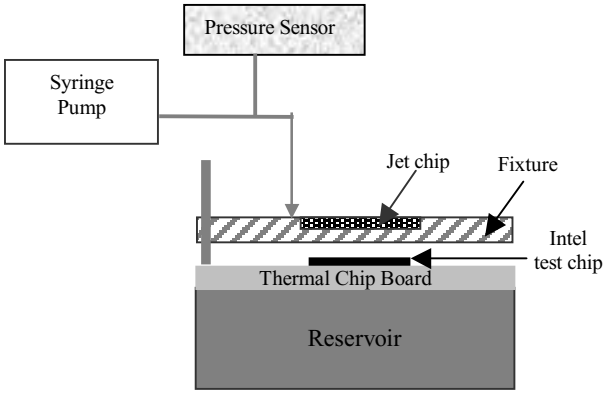

Figure 2. *Schematic of the experimental setup with the Intel standard test chip board. For the confined geometry jet experiments, the jet test fixture and thermal chip board are replaced with the bonded chip and fixture.*

Measurements were performed using a dedicated fixture for the confined geometry test chips that fully encloses the impinging liquid, as well as with another fixture for the open geometry experiments with a 1 cm^2 Intel test chip. In both cases, the fixture clamps the jet test chip, and an O-ring seals the inlet.

Figure 3(a) is a picture of the bonded test chip with its designated fixture. A small printed circuit board is glued onto the resistor side of the heater chip, so that electrical connections can be made from the aluminum contacts on the chip to a breadboard, where the resistances are measured. The heated water from the outlet is collected into a reservoir. Figure 3(b) shows the open geometry test fixture to which the microjet array is attached. The Intel test chip board is placed directly under the fixture. Because the experiments are performed in an open geometry, slots on the chip board allow the excess fluid to flow into a reservoir below the board. The Intel 30 W thermal chip with an area of 1 cm^2 has a temperature sensor at the chip center, which measures the average surface temperature. This test chip is analogous to a Pentium 4 processor chip and is a standard test chip currently used for experiments with metal heat sinks.

The data from these experiments are collected by a 16-bit 16-channel PCMCIA A/D card through a signal conditioning circuit. The measurements are recorded by LabView.

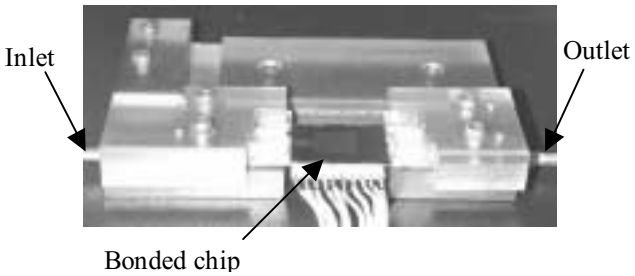

(a). *Fixture for bonded jet experiments. The jet chip is on top, and the heater chip is on the bottom with the wire-bonded printed circuit board to make electrical contacts to the resistors.*

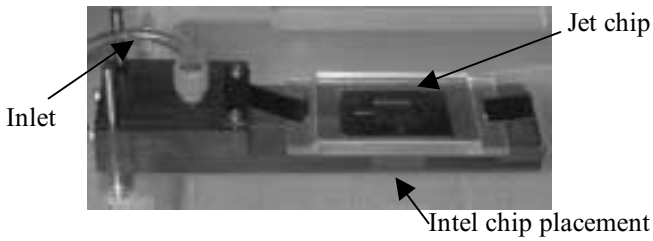

(b). *Fixture for Intel setup, which is placed directly on top of the Intel thermal chip board.*

Figure 3. *Pictures of test fixtures for confined and open geometry experiments.*

EXPERIMENTAL RESULTS

The effects of using a single and a four-jet array to distribute cool fluid over the hot surface in the confined geometry were examined. Data are provided for varying levels of power and as a reference, for the case of no liquid impingement. Figure 4(a) clearly shows a distinct temperature drop at the impingement point on the chip surface, located at 5mm. For the case of the jet array, as shown in Figure 4(b), with the same liquid flow rate per jet (2 ml/min), the temperature profile along the centerline of the chip is more uniform. These confined jets use a combined cooling effect of both jet impingement and forced convective flow. As a

result, the fluidic removal route introduces the asymmetry in both of the temperature profiles because the heated water flows toward the outlet. The outlet is located on the right end of the graphs, which results in the chip surface temperatures to be the highest near that region.

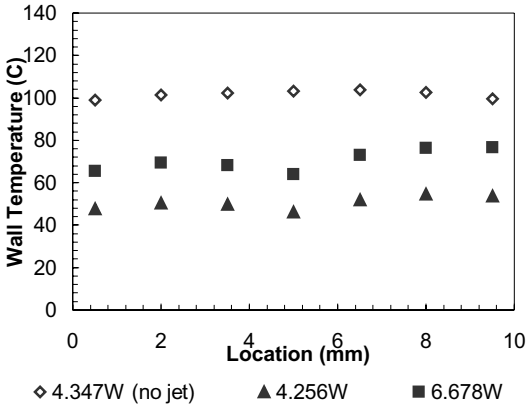

(a). *Temperature profile for a single jet. The impingement point is located at 5 mm. The data are for a flow rate of 2ml/min with a pressure drop of 5.4 psi.*

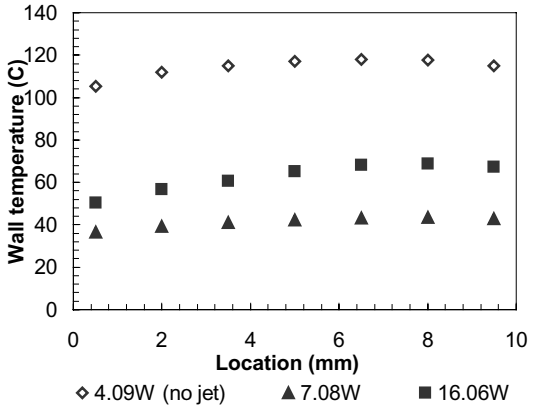

(b). *Temperature profile for a jet array. The data for flow rate of 8ml/min with a pressure drop of 6.9 psi.*

Figure 4. *One dimensional temperature profiles for a single and an array of four 76μm diameter jets. The data with no jet is taken for comparison.*

In Figure 5, the average temperature rise of a single jet and the four-jet array are compared as a function of the applied power. The experimental results confirm the anticipated surface temperature behavior. There is an initial linear temperature rise indicating a combination of forced convection and jet impingement single-phase heat transfer. The temperature plateau signifies the two-phase heat transfer region where the latent heat is being used. The final sharp temperature rise is due to dry out. The flow rates for the single jet and jet array could not be directly compared, because each jet requires a certain flow rate in order to form a jet stream **[8]**. However, the results show that as the flow rate is increased, more power can be removed. The 76 μm diameter four-jet array removes 92 W/cm^2 with an 80^{o}C temperature rise at a flow rate of 8 ml/min and 6.9 psi pressure drop. The estimated heat transfer coefficient for the four-jet array is over 10,000 W/m^{2}K at 8ml/min. Higher flow rates and a more optimized heat sink design will facilitate even higher heat flux removal and heat transfer coefficients.

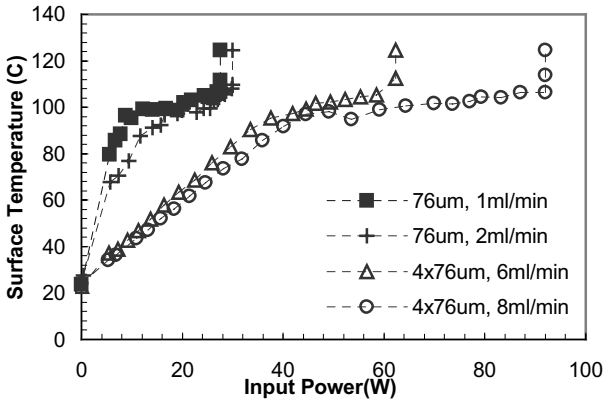

Figure 5. *Comparison of average chip surface temperature with increasing power for a single 76 μm diameter jet to a 76 μm diameter four-jet array in a confined jet configuration.*

COMPARISONS TO MICROCHANNEL PERFORMANCE

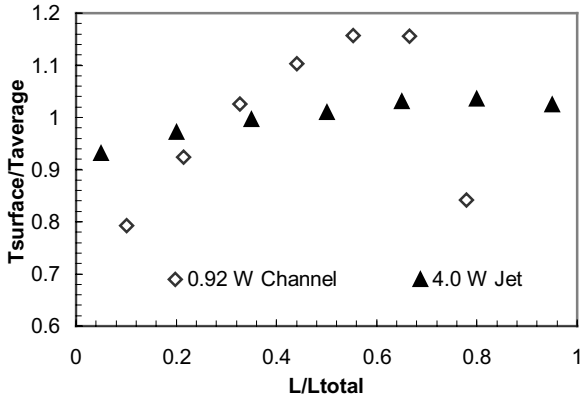

Figure 6. *Comparison of temperature uniformity for a single channel and a four-jet array. The single channel is 74 μm wide, 52 μm deep, 76 μm hydraulic diameter tested at 0.1ml/min flow rate **[9]**. The jet array consists of four 76μm jets tested at 8ml/min.*

To assess the advantages of microjet heat sinks, the performance of single jets and multi-jet arrays is compared with the results of our past microchannel research **[9, 10]** using our own heater chips with integrated thermometer and a standard Intel test chip. Figure 6 compares the temperature uniformity along the length of the heated area for a single 61 μm hydraulic diameter microchannel and a four 76 μm diameter jet array. The channels and jets were not fabricated and tested with the intention of a direct comparison, so the scaling is normalized to account for the differences in power levels and thermometer placement of the heated area. Steeper temperature gradients are present in the microchannels than in the jet array and maximum temperature difference of 47 ^{o}C at 2.6 W is recorded due to the lateral fluid motion in the channels.

Figure 7 compares the performance of forty parallel microchannels with a hydraulic diameter of 100 μm **[10]** to a single 70 μm diameter jet at similar flow rates using the standard Intel test chip. The microchannels are placed directly on top of

the thermal chip with thermal grease. The results show that microjets are more effective because they can remove larger heat fluxes at lower surface chip temperatures. Also, the surface temperature plateau observed in microjet impingement is more stable and more easily attainable, indicating better chip temperature uniformity. The temperature fluctuations in the two phase region are a result of the open geometry, and can be eliminated with confinement. In addition, wall superheating of almost 30°C is apparent in the microchannels, which is not present in the microjets.

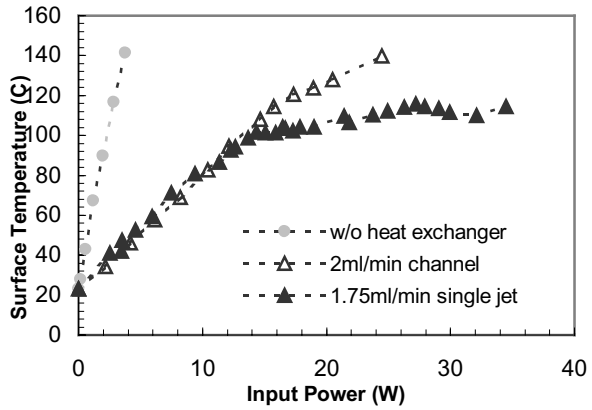

Figure 7. *Average surface temperature measured with increasing power for microchannels and microjets at comparable flow rates. A single 70μm diameter jet has a pressure drop of 6.7psi pressure drop. Forty parallel microchannels have dimensions of 100μm width, 100μm depth, and 15 mm in length.*

CONCLUSIONS

This paper presents new heat transfer measurements with microfabricated jet arrays in a confined geometry. Heater chips with thermometers are fabricated to measure the local temperature distribution and to study the effects of using single jets and multi-jet arrays in two-phase liquid impingement cooling. A careful comparison of uniformity and heat transfer in microchannels and microjets shows clear advantages for the microjets, including a stable two-phase region and the absence of superheating. Removal of 90 W/cm^2 is demonstrated at a flow rate of 8 ml/min using a microjet array, extending our performance to meet most upcoming industrial requirements for microprocessor packaging.

ACKNOWLEDGEMENTS

This work is supported by DARPA HERETIC Program under DARPA Contract F33615-99-C-1442, National Defense Science and Engineering Graduate Fellowship (Evelyn Wang), and Stanford Graduate Fellowship (Lian Zhang). The project made use of the National Nanofabrication Users Network facilities funded by the National Science Foundation under award number ECS-9731294. Travel support has been generously provided by the Transducers Research Foundation and by the DARPA MEMS and DARPA BioFlips programs.

REFERENCES

1. C. D. Patel, "Enabling Pumped Liquid Loop Cooling: Justification and the Key Technology and Cost Barriers," *Proceedings of 2000 International Conference on High-Density Interconnnect and Systems Packaging*, Denver, CO, USA, April 25-28, 2000, pp.145-152.

2. D. B. Tuckerman and R. F. W. Pease, "High-Performance Heat Sinking for VLSI," *IEEE Electron Device Letter*, *EDL-2*, 126-129, (1981).

3. S. Wu, J. Mai, Y. C. Tai and C. M. Ho, "Micro heat exchanger by using MEMS impinging jets," *Proceedings of the IEEE Micro Electro Mechanical Systems (MEMS)*, 171-176, (1999).

4. Q. Lin, S. Wu, Y. Yuen, Y. C. Tai and C. M. Ho, "MEMS Impinging-Jet Cooling," *Proceedings of 2000 ASME International Mechanical Engineering Congress and Exposition*, Orlando, FL, USA, Nov. 2000, pp.137-142.

5. S. Stefanescu, M. Mehregany, J. Leland and K. Yerkes, "Micro jet array heat sink for power electronics," *Proceedings of the IEEE Micro Electro Mechanical Systems (MEMS)*, pp.165-170.

6. D. J. Coe, M. G. Allen, B. L. Smith and A. Glezer, "Addressable micromachined jet arrays," *International Conference on Solid-State Sensors and Actuators, and Eurosensors IX, Proceedings*, *2*, 329-332, (1995).

7. D. Wolf, F. P. Incropera and R. Viskanta, "Jet Impingement Boiling," *Advances in Heat Transfer*, Academic Press, New York, 23, pp.1-132, (1993).

8. L. Zhang, et al, "Microscale Liquid Impingement Cooling," *Proceedings of 2001 ASME International Mechanical Engineering Congress and Exposition*, New York, NY, USA, November 11-16, 2001, pp.23820.

9. L. Zhang, et al, "Enhanced Nucleate Boiling in Microchannels," *Fifteenth IEEE International Conference on Micro Electro Mechanical Systems*, Las Vegas, Nevada, U.S.A, January 20-24, 2002, pp.89-92.

10. L. Jiang, J.-M. Koo, S. Zeng, J. Mikkelson, L. Zhang, P. Zhou, J. Maveety, A. T. Quan, T. W. Kenny, J. G. Santiago and K. E. Goodson, "Two-phase microchannel heat sinks for an VLSI cooling system," *Seventeenth Annual IEEE Semiconductor Thermal Measurement and Management Symposium*, San Jose, CA USA, March 20-22, 2001, pp.153-157.

HYDRAULIC AMPLIFICATION DEVICES FOR MICROSCALE ACTUATION

J.L. Steyn , H.Q. Li, D.C. Roberts, K.T. Turner, O. Yaglioglu, Y.-H. Su,
M.A. Schmidt, S.M. Spearing, N.W. Hagood
Massachusetts Institute of Technology
Cambridge, MA 02139
R. Mlcak
Boston MicroSystems, Inc.
Woburn, MA 01801

ABSTRACT

Hydraulic amplification devices for stroke amplification in MEMS devices have been designed, fabricated and evaluated experimentally. This work investigates the feasibility of using the concept of hydraulic amplification as a means of increasing the actuation stroke of a piezoelectric actuator in a microfabricated actuation system. The important aspects relating to the design of these devices are presented. This paper further provides a brief overview of the fabrication process used and then proceeds to address the topics related to the successful filling and sealing of small-scale hydraulic couplers. Both static and dynamic sealing techniques were used. Static tests were performed and stroke amplification ratios as high as 50:1 were obtained, with the peak-to-peak amplified stroke being approximately 25µm. Results from a piezoelectrically driven hydraulic amplifier are also presented and show resonant behavior at approximately 5kHz, proving that high-frequency, high-force, large-stroke actuation can be performed on the microscale using piezoelectric hydraulic amplification.

INTRODUCTION

Relying on Pascal's law, hydraulic amplification can be seen as a conceptually elegant means of increasing either the stroke or the force of an actuator. No mechanical linkages or mechanisms are used, and there are only two moving parts - the two pistons. The actuator can take any form, but in this work we are primarily concerned with a piezoelectric actuator requiring stroke amplification.

The work presented here forms part of a larger program at the Massachusetts Institute of Technology to develop piezoelectric MicroHydraulic Transducer (MHT) technologies. The goal of MHT technology is to use hydraulics in conjunction with piezoelectric materials to produce hydraulic pumps or generators for actuation and power generation applications. It is beneficial to operate the piezoelectric material at high frequencies for maximum power output [1]. High frequency operation requires mechanical systems with high natural frequencies if quasi-static operation is desired. The use of fabrication technologies associated with MicroElectroMechanical Systems (MEMS) presents the opportunity to build small hydraulic machines capable of operating quasi-statically at high frequencies. In addition, the small scale results in increased power densities.

A 3-dimensional section view of the full MHT device being developed is shown in Figure 1. This device has a piezoelectrically driven piston and two piezoelectrically driven active valves. The use of so-called "active" valves instead of the typical "passive" check valves used in pumps allows for bi-directional operation, enabling this device to operate as both a pump and a generator. Both the main piston and the two valves employ a piezoelectric micro-actuator as described by Roberts *et al* [2].

The active valves (see [3]) require large stroke operation in the kHz range of frequencies. In addition, the device shown in Figure 1 is designed to operate at pressures as high as 2MPa, and therefore the valves should also be able to operate at these pressures. Piezoelectric materials have sufficient actuation force and bandwidth to drive these valves, but are lacking in stroke. For this device, hydraulic amplification was chosen as the most feasible means of increasing the uniaxial actuation of a piezoelectric element.

Macroscale examples of hydraulic amplifiers exist. (See, e.g. [4,5]). This work proceeds to present, for the first time, hydraulic amplification as a general means of stroke amplification for use in MEMS, with the use of the basic principle extending beyond that of piezoelectric valve operation. The relevant issues pertaining to the development of such devices are discussed, and experimental results are presented.

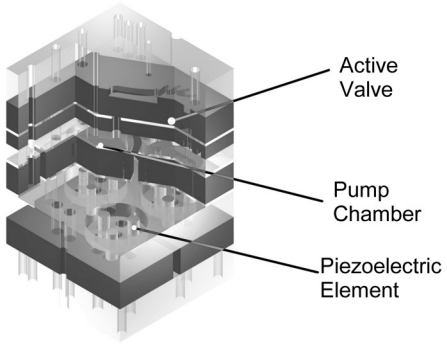

Figure 1. *A 3D section view of the full MicroHydraulic Transducer device with two hydraulically amplified piezoelectrically driven active valves and a piezoelectrically driven main piston.*

DEVICE LAYOUT AND DESIGN CONSIDERATIONS

Figures 2 and 3 schematically show the layout of the devices that were evaluated. Figure 2 depicts a pressure operated hydraulic amplifier, and Figure 3 a piezoelectrically driven one.

Travel support has been generously provided by the Transducers Research Foundation and by the DARPA MEMS and DARPA BioFlips programs.

Both devices consist of nine layers - five layers, L2, L4, L5, L7 and L8, are silicon layers, and the other four, L1, L3, L6 and L9, are borosilicate glass. In both devices, a short stroke motion of the large piston in layers 4 and 5 is amplified to a large stroke motion of the small piston in layer 7. All pistons are formed using Silicon On Insulator (SOI) substrates, where the SOI device layer is used as an annular membrane tether to attach the piston to the device structure and to act as a flexural seal.

In the process of the designing these devices, the following aspects were considered: (a) The stiffness and strength of the membrane tethers. Within the constraints of available SOI thicknesses, device area available, manufacturing capabilities and the required deflections, the membranes were designed for maximum strength and minimum added compliance to the hydraulic amplification chamber (HAC). (b) The added compliance of the remaining device structure. By use of finite element analysis, suitable dimensions for the silicon and glass support structures were defined to enable a compact yet stiff device. (c) The height of the HAC. This chamber, formed in L6, was designed for minimum volume without introducing unnecessary squeeze film damping with a chamber height that is too low.

The results of both a pressure-operated, as well as a piezoelectrically driven hydraulic amplifier are presented here. Both devices had a large piston of diameter 6.8mm with a tether width of 225µm, and a small piston diameter of 0.51mm with corresponding tether width of 442µm. This gives a theoretical stroke amplification ratio of between 40:1 and 50:1, when taking into account all the relevant compliances in the system. Due to geometric nonlinearities in the small piston structure, the amplification ratio is not constant for the full range of travel of the two pistons.

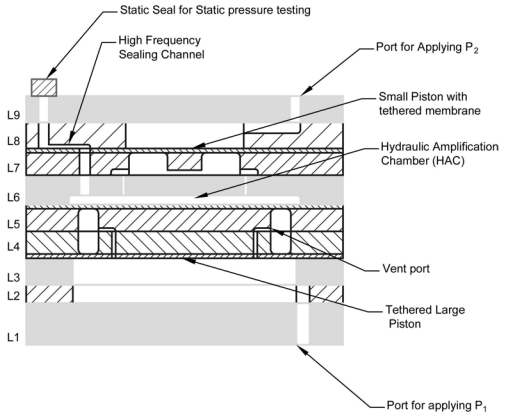

Figure 2. *Static, pressure operated hydraulic amplifier.*

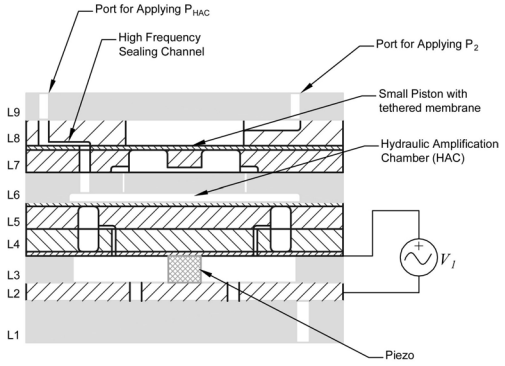

Figure 3. *Dynamic, piezoelectrically driven hydraulic amplifier.*

FABRICATION OVERVIEW

The silicon layers were bulk micromachined using Deep Reactive Ion Etching (DRIE). All glass layers (Pyrex ™ 7740) were ultrasonically machined, on the wafer scale. In the case of Layer 6, a 200µm deep recess was made to form the HAC.

Wafer-level Si-Si fusion bonding was used to bond L4 to L5, as well as L7 to L8. Wafer-level anodic bonding was used to bond L6 to the L4-5 stack and also to bond L1 to L2. All other bonds were anodic bonds performed on the die level. For the piezoelectric device shown in Figure 3, a small bulk piezoelectric element was integrated in the final anodic bonding step, as described in [2].

Figure 4 shows the device subassemblies, with Figure 5 showing a completed device. The final device is a nine-layer Si-glass sandwich structure and has dimensions of 20x20x10mm.

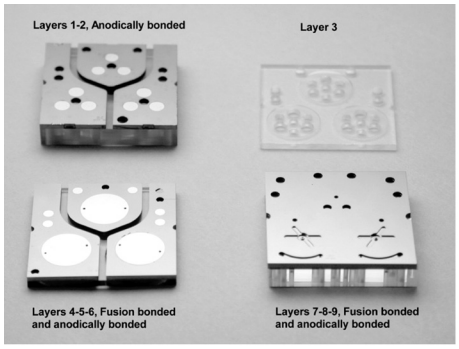

Figure 4: *Subassemblies of the nine-layer hydraulic amplification device. Various unique fabrication techniques were used to produce these dies.*

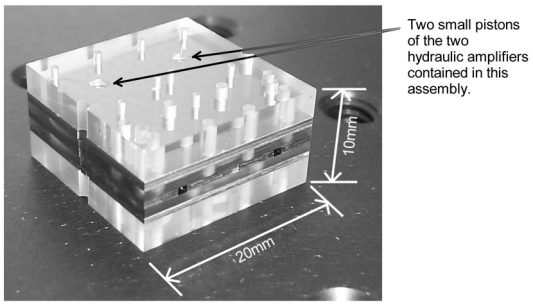

Figure 5: *Assembled hydraulic amplification device. Each such stack contains two independent hydraulic amplifiers.*

FILLING TECHNIQUES

Effective hydraulic amplification relies on bubble-free filling of the HAC. To achieve this, a process was developed where the HAC is first evacuated and purged with the vapor of the hydraulic fluid. Afterwards, the chamber is filled with the fluid itself. This process ensured that any entrapped gases in the HAC would mostly consist of the vapor of the hydraulic fluid.

This method of vapor purging prior to filling required that the hydraulic fluid itself had a sufficiently high vapor pressure. The fluid of choice was hexamethyldisiloxane, with a viscosity at room temperature of ~0.65cst, and a vapor pressure of 6.7kPa. Using this silicone oil, bubble free filling of the HAC was attained through a 10µmx10µm by 1000µm long filling channel.

SEALING TECHNIQUES

Two methods were used for sealing the hydraulic amplifier. The first method, used for the pressure operated "static" devices, relied on a 125μm thick PTFE film backed by a brass plate and preloaded with an o-ring. This seal was placed over the filling hole in Layer 9. Minimal seal compression and creep was observed, and therefore the pressure inside the HAC remained unaffected.

For the piezoelectrically driven dynamic hydraulic amplifier, a "dynamic seal" was used. This seal consisted of a small (10μmx10μm cross section, 1000μm long) channel that acted as a fluid low pass filter. By using this sealing technique, it was possible to set the steady-state pressure inside of the HAC to a desired value using an outside pressure source, whilst maintaining high-frequency pressure fluctuations due to the piezoelectric actuation inside the HAC. Figure 6 illustrates the effectiveness of this channel. When driving the large piston, and observing the motion of the small piston, rolloff is detected at a frequency of 0.1Hz, well below the kHz operating frequencies of the device.

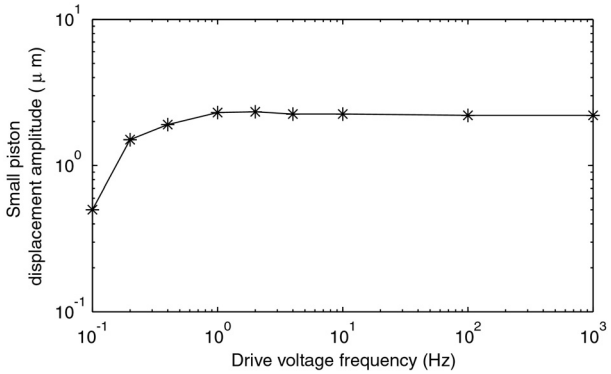

Figure 6: *Frequency response of the dynamic seal. This seal acts as a low pass filter to the HAC.*

STATIC HYDRAULIC AMPLIFICATION

Static, pressure-operated hydraulic amplification tests were performed to evaluate the ability of the hydraulic amplification chamber to couple the motion of the two pistons. Pressures were applied to the large piston (P_1) and the small piston (P_2). P_1 was varied from 0 to 200kPa for preset pressures of P_2 = 0, 53, 105, 153, 206 and 253kPa. Loading the HAC in this manner made it possible to prove the stiffness of the coupler. Using a laser vibrometry system, the displacements of the small and large pistons were measured. The results of these tests are shown in Figures 7 and 8. From these results, one can calculate the amplification ratio (Figure 9), defined as the ratio of the difference in displacement of the small piston versus that of the large piston.

Figure 7 shows discrepancies between the predicted and actual motion. This is due to additional compliance in the HAC, which could be caused by a small bubble in the fluid in this particular case. The good agreement on the results in Figure 8, for the small piston, can be explained by the fact that the differential pressure across the large piston is not very large for the deflections seen. Therefore, the pressure on the large piston, P_1, is approximately equal to the pressure in the HAC, P_{HAC}. Therefore, Figure 8 is almost equivalent to a series of pressure-deflection tests on the small piston structure alone. Figure 9 shows similar

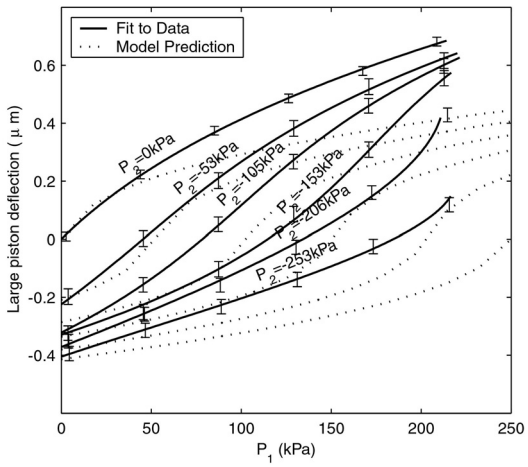

Figure 7: *Motion of the large piston under applied pressure on both the large piston (P_1), and the small piston (P_2).*

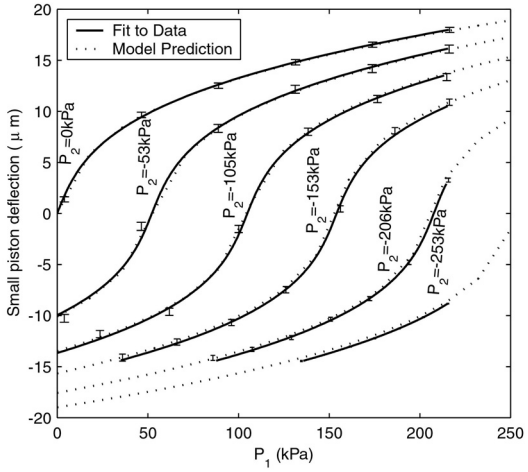

Figure 8: *Motion of the small piston under applied pressure on both the large piston (P_1), and the small piston (P_2).*

trends for both the predicted and measured amplification ratios, with the exception being the case where P_2=0kPa.

VERIFICATION OF DYNAMIC OPERATION

To prove that the hydraulic amplifier can function as intended - that is, to amplify the stroke of a piezoelectric actuation element - tests were performed on a piezoelectrically driven hydraulic amplifier as was shown schematically in Figure 3. Figure 10 is an amplitude spectrum of the motion of the small piston, when excited using a sweep excitation on the piezoelectrically driven large piston. A first resonance of approximately 10kHz was observed when using gas to pressurize the small piston. When liquid was used on top of the small piston, this frequency reduced to approximately 5kHz due to the added mass effect of the fluid on the small piston.

Figure 11 shows the behavior of the small and large pistons for various excitation voltages at 1kHz sinusoidal excitation
In this case, the voltage replaces the applied large piston pressure used to create Figures 7 and 8. In the case of the dynamic hydraulic amplifier, much better correlation is seen between the predicted and measured results, most likely due to improved filling of the HAC. The same holds for the amplification ratio, depicted

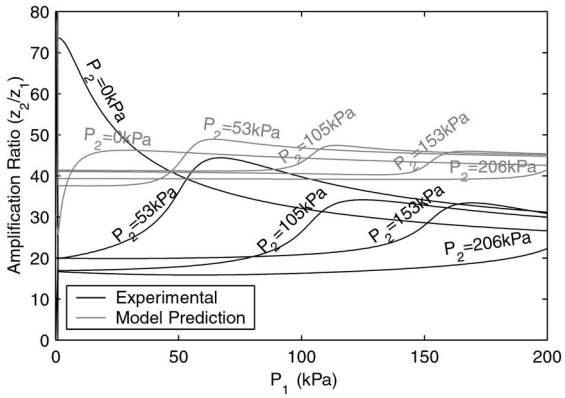

Figure 9: *Amplification ratio for the static hydraulic amplifier.*

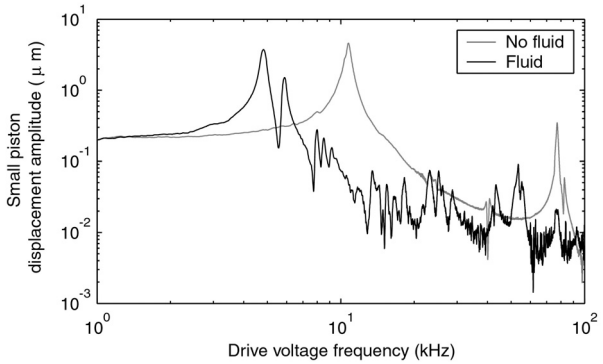

Figure 10: *Displacement spectrum of the small piston. Excitation was 5Vp-p.*

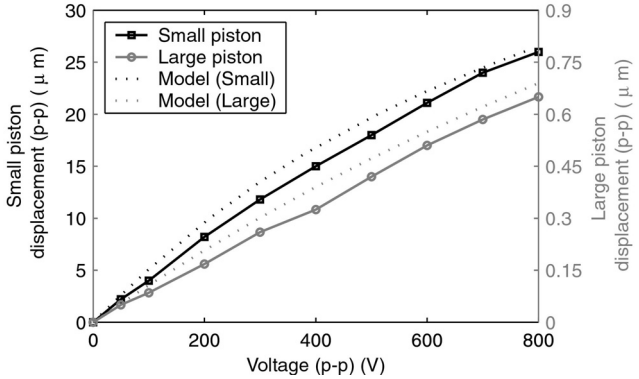

Figure 11: *Displacement of the small and large pistons of the dynamic hydraulic amplifier for various excitation voltages. Sinusoidal excitation at 1kHz.*

in Figure 12. Note that there is acceptable agreement between the amplification ratios observed during static and dynamic actuation.

CONCLUSIONS

In this work we have developed and evaluated microfabricated hydraulic amplification devices. The important issues relating to the design of such devices on the microscale have been addressed. We have also demonstrated that filling and sealing of microfabricated dead volumes with hydraulic fluid is feasible, and stiff hydraulic couplers can be produced using the techniques described here. The experimental results show that microfabricated hydraulic amplification devices can have

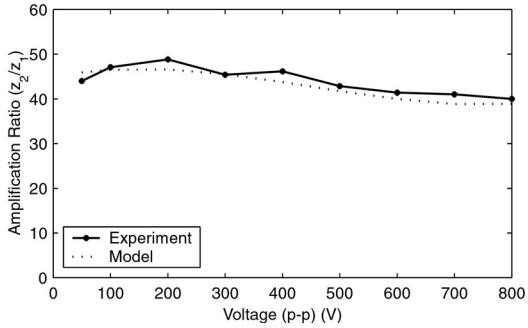

Figure 12: *Amplification ratio results for the piezoelectric hydraulic amplifier.*

sufficient stiffness and actuation authority for application in high-pressure microvalves and other types of micropositioning devices. It has also been shown that these devices can have sufficient bandwidth to allow for high frequency operation, with large amplification ratios.

ACKNOWLEDGMENTS

All microfabrication was performed at the MIT Microsystems Technology Laboratories (MTL). The authors also wish to acknowledge the group of Prof. Liou at the University of Nebraska for all the Au-Sn sputter deposited films used to incorporate the piezoelectric elements. This work was performed under ONR grants N00014-01-1-0857 and N00014-97-1-0880 and DARPA grant DAAG55-98-1-0361.

REFERENCES

1. N.W. Hagood IV, *et al*. "Micro-hydraulic Transducer Technology for Actuation and Power Generation", *SPIE 7th International Symposium on Smart Structures and Materials*, Newport Beach, CA, March 5-9, 2000.

2. D.C. Roberts *et al*, "A High Frequency, High Stiffness Piezoelectric Micro-Actuator for Hydraulic Applications," Proceedings of the 11th International Conference on Solid-State Sensors and Actuators, Munich, Germany, June 10-14, 2001, pp. 686-689.

3. D.C. Roberts *et al*, "Modeling, Design, and Simulation of a Piezoelectrically Driven Microvalve for High Pressure, High Frequency Applications," *Proceedings of the SPIE 8th International Symposium on Smart Structures and Materials, Newport Beach, CA*, March 5-8, 2001, Vol. 4327, pp. 366-380.

4. P. Tang, *et al*. "Combined Piezoelectric-Hydraulic Actuator Based Active Vibration Control for Rotordynamic System", *Trans. of the ASME - Journal of Vibration and Acoustics*, July 1995, Vol. 177, pp285-293

5. J. Garcia-Bonito, *et al*. "A novel high-displacement piezoelectric actuator for active vibration control", *Smart Materials and Structures*, Vol 7 1998, pp31-42, IOP

6. H.Q. Li, *et al*, "A High Frequency, High Flow Rate Piezoelectrically Driven MEMS Micropump", *Technical Digest of the 2000 Solid-State Sensor and Actuator Workshop*, Hilton Head, SC, June 2000

7. J.L. Steyn, "Hydraulic Amplification for Actuation in MicroElectroMechanical Systems", Master's Thesis, MIT, 2002

8. D.C. Roberts, "Design, modeling, fabrication and testing of a piezoelectric microvalve for high pressure, high frequency hydraulic applications", PhD Thesis, MIT, 2002

Robot Leg Motion in a Planarized-SOI, 2 Poly Process

Seth Hollar[1], Anita Flynn[2], Sarah Bergbreiter[1], K.S.J.Pister[1]
[1]Berkeley Sensor and Actuator Center, University of California, Berkeley 94720
[2]Micropropulsion Corporation, Berkeley, CA 94704

ABSTRACT

With the ultimate goal of creating autonomous microrobots, we have developed a new five-mask process that combines two polysilicon structural layers with 35 µm thick SOI structures and a backside substrate etch. The polysilicon layers provide 3D hinged structures, high compliance structures, and electrical wiring. The SOI structural layer yields much stronger structures and large-force actuators. On an 8mm x 3mm robot, we have demonstrated polysilicon hinges with SOI electrostatic inchworm motors. This combination allowed us to demonstrate 200 µm out-of-plane motion of a hinged SOI robot leg. Using an off-chip controller, the robot leg was actuated through almost 30°. In addition, we have completed static friction tests of polysilicon flaps to more accurately model the frictional forces of the linkages.

INTRODUCTION

Until recently, one of the greatest challenges in designing autonomous microrobots has been finding actuators that are efficient and capable of large forces and displacements. Shimoyama, et al. have suggested providing external actuation and power through vibratory or magnetic fields [1,2]. Kladitis [3] and Ebefors [4] have both demonstrated walking microrobots using electro-thermal actuation and off-chip power supplies. While thermal actuators achieve the large forces and displacements necessary for a microrobot, the large power requirements prevent these robots from becoming autonomous.

In an effort to design lower power actuators, Yeh et al. developed an electrostatic inchworm motor that could be fabricated with a single mask SOI process [5]. Inchworm motors combine large forces from gap closing actuators (GCAs) with large displacements by continually repeating small steps.

A second challenge of microrobots has been to combine the aforementioned actuators with compliant structures to create out-of-plane motion. Yeh suggested various hinged structures which could be folded to create an articulated microrobot [6]. However, these linkages were not easily combined with a means of low-power actuation.

To this end, we have developed a process in which electrostatic inchworm motors in thick SOI can be fabricated with thinner polysilicon structures on top. This process combined with solar cells and digital electronics provides us with a basis for designing autonomous walking microrobots. Figure 1 shows a conceptual rendering of our current design. A CMOS controller chip generates signals to drive the motors. A chip with solar cells and high voltage buffers provides power and converts the low voltage CMOS signals to the 30 volts needed to drive the actuators.

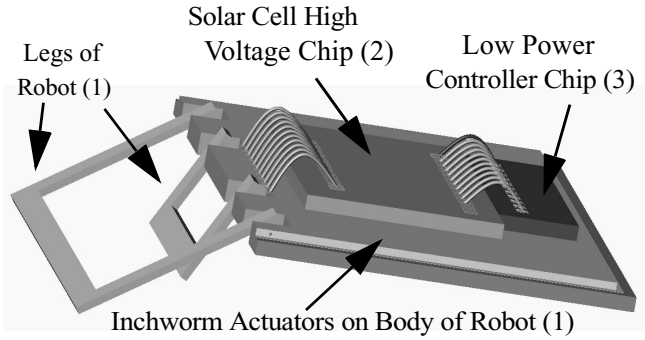

Figure 1. Computer modeled rendering of walking robot. The 3-chip hybrid is composed of 1) Legs and Motor process, 2) Solar Cells and High Voltage process and 3) Low Power CMOS process.

FABRICATION PROCESS

We designed a new process that combines low power, high force actuators in SOI with hinged structures and linkages from traditional polysilicon micromachining. An SEM of a typical hinge is shown in Figure 2 and a flow diagram of the five mask process is shown in Figure 3.

We started with an SOI wafer that had a device layer thickness of 20-40 µm (Figure 3a). The top layer was patterned and etched using the Bosch ASE process (Figure 3b).

A key challenge of the process was adding structural polysilicon after the primary SOI etch. This was accomplished using Yasseen's method of thick glass planarization. Following [7], we spun on a glass slurry (Figure 3c), burnt out the organic (Figure 3d), and reflowed the glass at 890 C, where

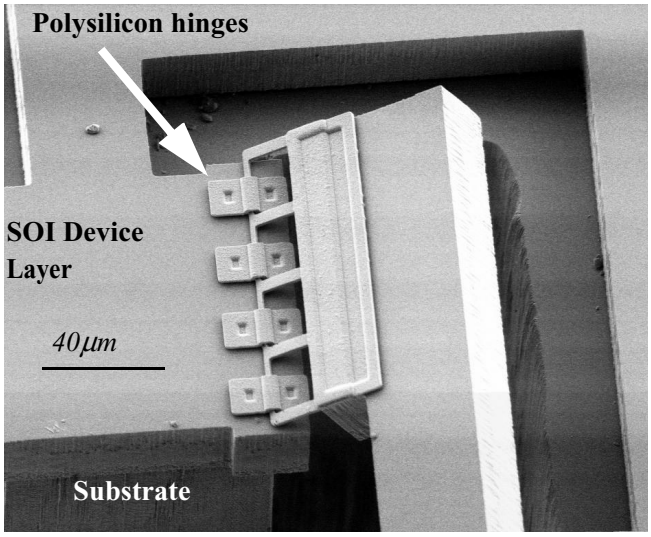

Figure 2. Polysilicon hinges attached to SOI device layer. The substrate is also seen in this SEM.

0-9640024-4-2/hh2002/$20©2002TRF
DOI 10.31438/trf.hh2002.14

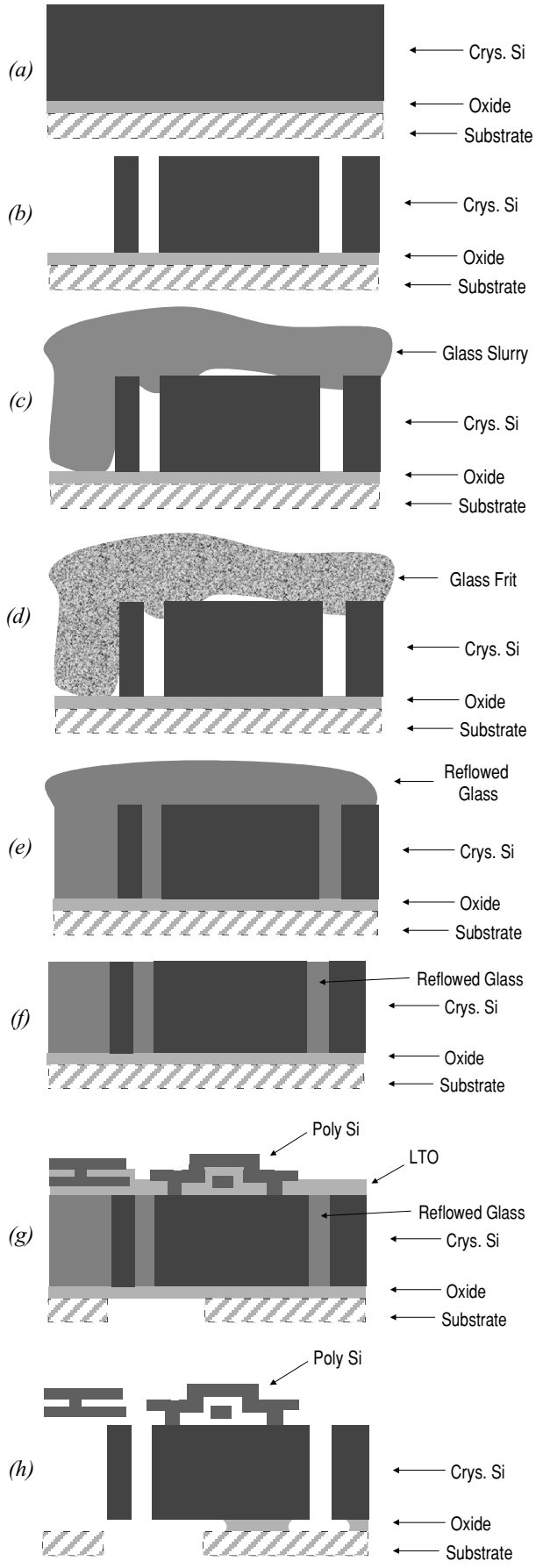

Figure 3. Process Flow.

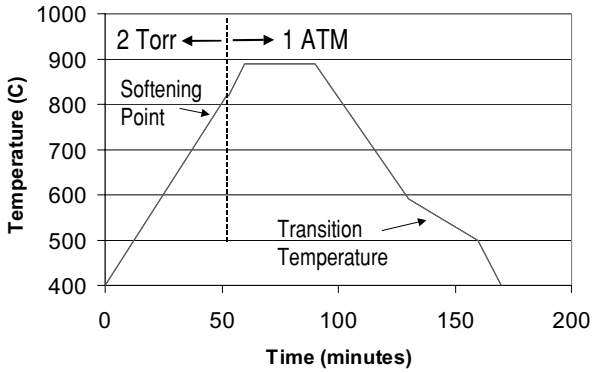

Figure 4. Firing profile of glass. The glass was heated in an oxygen ambient at 2 Torr to allow the glass to flow into deep trenches. Any remaining bubbles were then minimized during the pressurization stage from 2 Torr to 1 ATM.

the frit coalesced to form a single glass network (Figure 3e). The wafers were fired in a low pressure furnace to minimize the occurrence of bubbles. However, we found that simply firing in low pressure did not completely remove bubbles. As a deviation from [7], we heated the glass to just below the firing temperature in an oxygen ambient at 2 Torr to allow the glass to flow into deep trenches. Any remaining bubbles were then minimized during the pressurization stage from 2 Torr to 1 ATM. The firing profile is shown in Figure 4. Finally, the glass was chemically mechanically polished (CMP) to the SOI/glass interface (Figure 3f) to provide a planarized surface.

After planarization, wafers underwent standard polysilicon micromachining. Three masks were used to define 2 structural polysilicon layers (fine-line lithography: 2 μm). 0.6 μm of PSG was first deposited on the planarized SOI surface, followed by a 2 μm thick layer of patterned polysilicon. After another 0.6 μm PSG deposition, the wafer was patterned with a contact mask used for anchoring the following polysilicon layer. Next, 2 μm of the second and final polysilicon layer was deposited. Finally, a backside substrate etch was performed using the same Bosch ASE process as before (Figure 3g).

For the release, a solution of HCl, HF and H_2O was used in a timed etch on the planarized glass, buried thermal oxide, and PSG. The goal was to etch long enough to remove the PSG and reflowed glass, but not so long as to remove all of the bur-

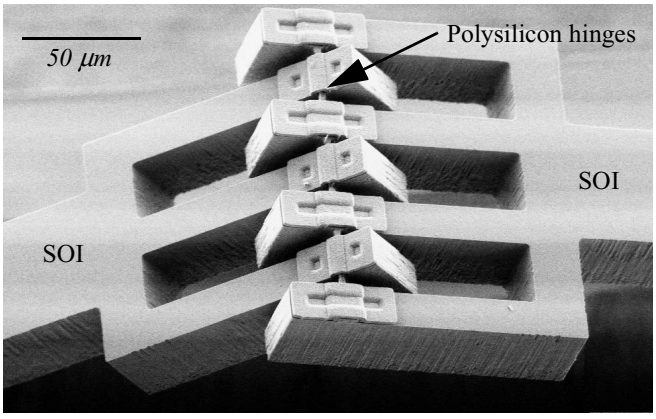

Figure 5. Polysilicon hinge structure with interdigitated device layer SOI.

ied oxide. The reflowed glass etches approximately 30 times faster than the buried oxide, so tight tolerances in the undercut of the thermal oxide were maintained. Narrow SOI blocks were fully undercut while wide SOI blocks were still anchored to the substrate via the thermal oxide (Figure 3h).

An unfortunate by-product of the release was that alumina particles were scattered across the wafer. Since the glass frit was created at Ferro Corporation using an alumina ball mill for an extended period of time, alumina flakes on the order of 0.5 µm were present in the glass mixture. To remove the alumina particles, the devices were placed in a heated bath (50^{o} C) of NH_4OH and H_2O_2. Critical point drying was performed to avoid damage from water surface tension.

ROBOT LEG DESIGN

Using the five-mask process described above, we designed an 8mm x 3mm robot that uses inchworm motors and hinged SOI legs. We used pin hinges (Figures 2 and 5) in a 1 DOF leg whose linkages are depicted in the kinematically equivalent 2D diagram in Figure 6. The robot design incorporates a number of design advantages from the process and remedies some problems associated with Yeh's original inchworm motor.

Since both the SOI and polysilicon act as conductors, the motor wiring is not constrained to any particular layer. This allowed us to draw connections from the motors into a set of bond pads in the back of the robot. An example of a polysilicon jumper is shown in Figure 7. However, wiring over long distances was problematic. Since both the SOI and polysilicon are susceptible to pull-in after the PSG and thermal oxide layers are removed, SOI anchors were placed periodically along the wire. These anchors provided enough mechanical stiffness to withstand electrostatic forces between the SOI wiring and robot substrate.

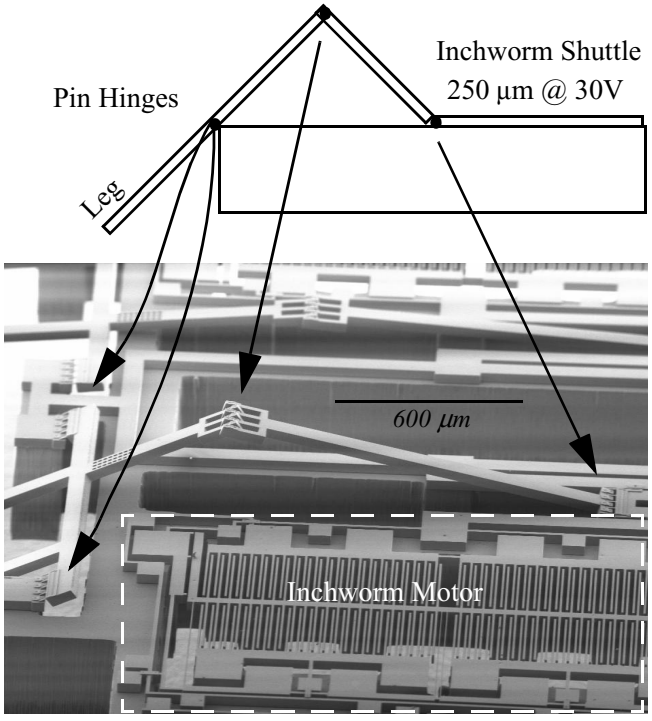

Figure 6. Kinematic diagram of robot leg and SEM of linkage structure. Arrows are used to show the position of hinges relative to the diagram. In the lower right hand corner of the SEM, one of the drive GCAs of the inchworm motor is visible.

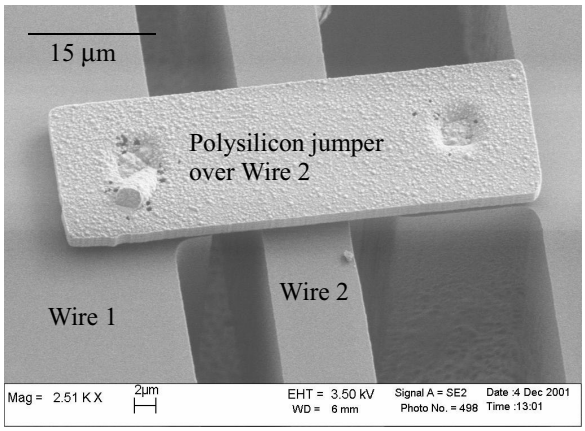

Figure 7. A polysilicon jumper bridges Wire 2.

The improved inchworm motors also utilized flaps to constrain the motion of the shuttle to the plane of the device. As seen in Figure 8, the flap attached to the shuttle on the left prevents the shuttle from falling through the wafer, and the flap over the shuttle on the right prevents the shuttle from popping up out-of-plane. With the inclusion of flaps, the shuttle is no longer constrained by parallel flexures as in [5].

The backside etch yielded several advantages over the original inchworm motor process and for the robot in general. Removing the substrate underneath movable structures in the inchworm motors prevented substrate stiction and reduced the chance particulate matter would get stuck between the gap closing actuators. Additionally, backside removal provided a lightened skeletal frame, which reduced the amount of force required from the motors.

Preset structures can be set so as to maximize mechanical advantage during the initial actuation. Without preset structures, the out-of-plane moment arm is limited to the thickness of the SOI. As shown in Figure 9, a preset structure can be translated and latched into place with a manual probe. Guided by the preset structure, the shuttle is also repositioned.

EXPERIMENTAL RESULTS

Finally, we tested the robot motors and legs. Motors were actuated using a programmable Atmel AVR microcontroller whose I/O pins interfaced to an Analog Devices AD8600 16 Channel DAC. Amplifiers on the channels converted the 5 V maximum outputs of the DAC to the 30V signals needed for the motors. The programmability of the test setup allowed us to troubleshoot the inchworm motors and characterize the speed of individual steps of the inchworms.

Each motor we tested measured 700µm x 4mm in area. A stand-alone motor actuated reliably over 300 µm of displacement at speeds up to 200µm/s, an almost 4x improvement in travel from [5]. A simple flexural spring attached to the shuttle exhibited a calculated reaction force of 45µN under maximum extension. The motor's maximum range was limited by physical stops on the shuttle itself, not by the output

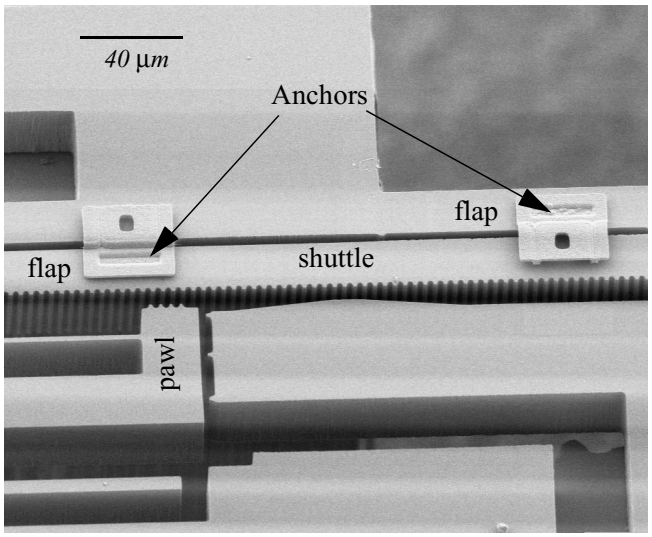

Figure 8. The inchworm motor shuttle and pawl. The flaps are used to constrain the motion of the shuttle. Flap anchors are labeled to show the direction of the flap constraint.

force of the motors. The motor was calculated to maintain a force of at least 120 μN at 30V.

To test the leg, we had to preset the shuttle by 150 μm using the latch structure in Figure 9. This gave the leg an initial starting angle of 34^o relative to the plane of the motor (Figure 10).

An additional complication arose, however, because of a design flaw in the motors. Gap stops used to prevent electrical shorting of the GCAs were drawn too small. The resulting fabricated motors exhibited shorting of the gap fingers when the clutch was actuated.

This limited the range of speeds the motor could operate at from 8μm/s to 32μm/s. Nevertheless, we were able to actuate the robot leg from 34^o to 63^o with a shuttle sweep range of 250μm (Figure 11). Future designs with larger gap stops will prevent electrical shorting and yield higher performance leg actuation.

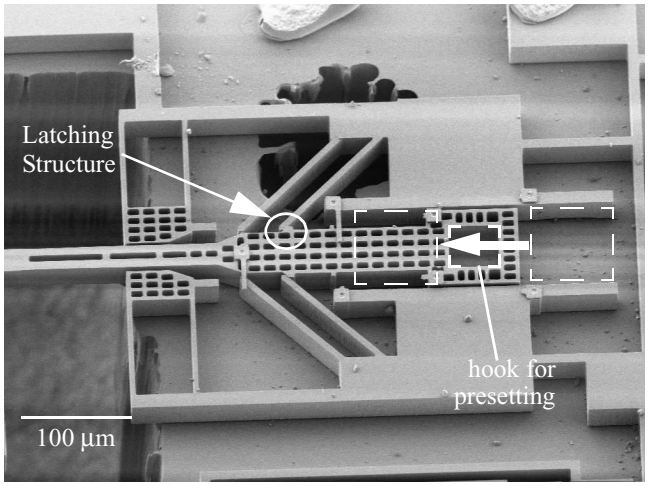

Figure 9. SEM of latch structure midway between starting position and latched position. Probe tip is used to move structure into place.

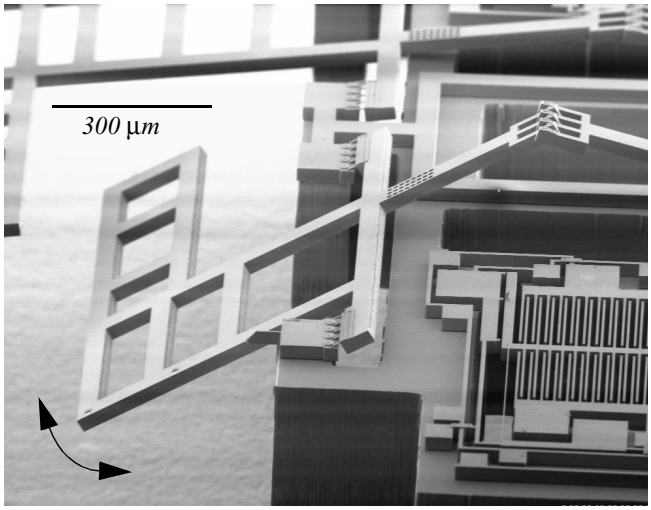

Figure 10. SEM of robot leg in preset condition. Leg was actuated through almost 30^o of angular deflection

By adding polysilicon flaps to constrain the motor shuttle, we introduced a possible source of adhesion and friction to the motor design. Yeh demonstrated in friction tests of polysilicon on nitride that the force required to slide a shuttle along the substrate and rotate an unloaded hinge required between 1-43 μN, values much greater than the weight of the lever arm (3.2 nN) [8].

To test the amount of static friction an inchworm actuator must overcome to move the shuttle, we designed simple SOI sliding test structures attached to polysilicon vernier springs (Figure 12). The test structures were designed both with and without substrate underneath. This allowed us to compare sliding polysilicon flaps along SOI to sliding an SOI beam along the silicon substrate.

A histogram of the force required to overcome static friction and adhesion in each of the test structures is shown in Figure 13. Force required to move the SOI beam ranged from

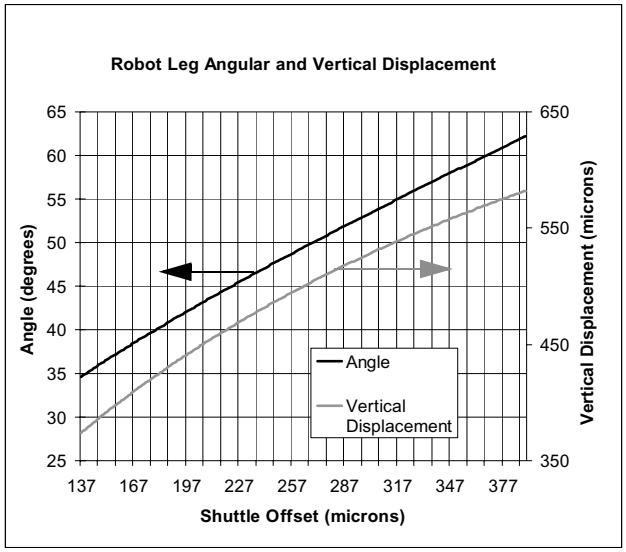

Figure 11. Angular deflection and vertical displacement of leg tip as a function of shuttle travel of inchworm motor. Shuttle actuated over 250 μm in this example.

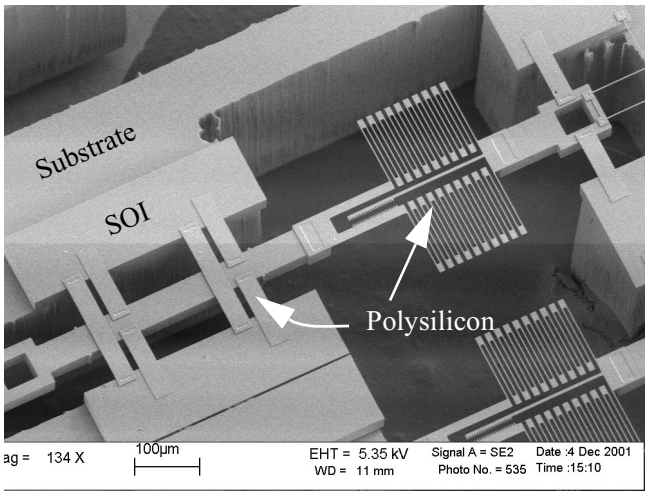

Figure 12. SEM of the sliding test structure. A vernier spring was used to measure the force required to move polysilicon flaps over the SOI device layer.

0.5-13 µN with substrate and 0.5-15 µN without substrate. Peak value recurrence for both sliding structures was between 1-3 µN.

It is important to note that there are several data points not included in this graph. After storing the test structures in normal laboratory conditions for approximately one month, sliders with polysilicon flaps required forces much greater than the vernier springs could measure (>>25 µN). This was probably due to adhesive forces from ambient moisture and will likely need to be addressed in future robot design and testing.

These frictional forces were included in the overall robot model. In order to provide enough force to lift the robot, we designed the inchworm actuators to output a calculated 120 µN of force. This figure takes into account the approximate weight of the robot (~70 µN), the mechanical advantage of the linkages (~1), and the maximum possible frictional and adhesive forces of the flaps and hinges (~20 µN).

CONCLUSIONS AND FUTURE WORK

Autonomous microrobots are quickly becoming a reality. One of the last steps is combining a robot leg with efficient, high force actuators. Our process seeks to bridge the gap by integrating electrostatic SOI actuators with high compliance polysilicon structures. The enabling step of the process is planarization of the SOI device layer via reflowed glass. The process allows key improvements to the electrostatic inchworm actuators, including a backside etch underneath the actuators, polysilicon flaps to constrain the shuttle motion, complex wiring, and the ability to preset structures to increase mechanical advantage out-of-plane. Different robot legs, including those with torsional hinges and 2 DOF legs are also being designed for future experiments. Ultimately, we intend to combine legs and actuators from this process with solar cells and a digital CMOS chip to form a complete autonomous microrobot.

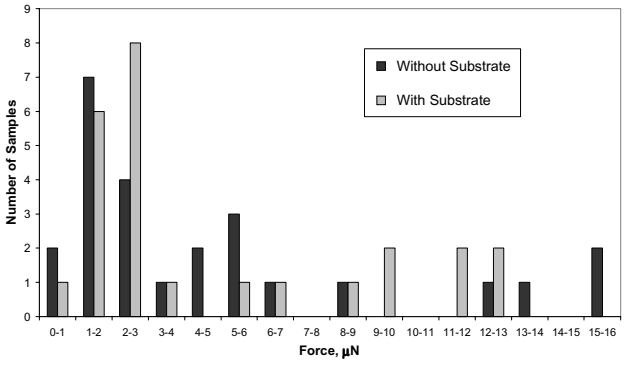

Figure 13. Force measurements taken from the sliding friction test structures in Figure 12. A mean force of 4.6 µN and median of 2.5 µN were the same for sliders with and without a substrate.

It should be noted, however, that this process can be used for more than just designing walking robots. Microtweezers, microoptical scanning systems, and micromanipulators are just a few promising candidates for this process.

ACKNOWLEDGEMENTS

Chris Keller from MEMS Precision Instruments (http://www.memspi.com), UC Berkeley Microlab, especially Bob Hamilton and Joe Donnelly, James Wu from Lawrence Livermore Labs, Dimitry Kousminov from Accurel Systems. Research sponsored by DARPA/ITO SDR.

REFERENCES

[1] N. Miki, I. Shimoyama, “Flight performance of micro-wings rotating in an alternating magnetic field”, *Technical Digest of MEMS 99*, Orlando, FL, (1999), pp. 153-8.

[2] T. Yasuda, I Shimoyama, and H. Miura, “Microrobot locomotion in a mechanical vibration field”, *Advanced Robotics*, 9, 2 (1995).

[3] P.E. Kladitis, V.M. Bright, “Prototype microrobots for micro-positioning and micro-unmanned vehicles”, *Sensors and Actuators A: Physical*, 80 (2000), pp.132-7.

[4] T. Ebefors, J. Mattsson, E. Kalvesten, and G. Stemme, “A micromotion system based on polyimide joint actuators”, *Eurosensors XII* (1998), pp. 391-4.

[5] R. Yeh, S. Hollar, and K.S.J. Pister, “A Single Mask, Large Force, and Large Displacement Electrostatic Inch-worm Motor”, *Technical Digest of MEMS 01*, Interlaken, Switzerland (2001), pp. 260-4.

[6] R. Yeh, E. Kruglick, and K.S.J Pister, "Surface-Micromachined Components for Articulated Microrobots", *J. Microelectromechanical Systems*, 5, 1 (1996), pp. 10-17.

[7] A. Yasseen, J. Cawley, and M. Mehregany, “Thick Glass Film Technology for Polysilicon Surface Micromachining,” *J. Microelectromechanical Systems*, 8, 2 (1999), pp. 172-9.

[8] R. Yeh and K.S.J. Pister, “Measurement of Static Friction in Mechanical Couplings of articulated microrobots”, *Proceedings of SPIE*, Austin, TX (1995), pp. 40-50.

A MINIATURIZED MICROBIAL FUEL CELL

Mu Chiao, Kien B. Lam, Yu-Chuan Su and Liwei Lin
Berkeley Sensor and Actuator Center
Department of Mechanical Engineering, 1113 Etcheverry Hall
University of California at Berkeley, Berkeley, CA 94720-1740
Email: muchiao@me.berkeley.edu Phone: 510-642-8983

ABSTRACT

This paper presents a miniaturized microbial fuel cell as an energy source for MEMS. A microorganism, *Saccharomyces cerevisiae*, is used to catalyse glucose and electricity is produced by the overall redox reaction. The fabricated miniaturized microbial fuel cell has an electrode area of 0.07 cm^2. The bio-electrical responses of the miniaturized microbial fuel cell are characterized. The open-circuit potential is measured as 300 mV and lasts for 2 hours. The current density is measured as 286 nA/cm^2 and lasts for 30 minutes under a 100 ohm load.

INTRODUCTION

Miniaturized, portable power sources are important for the realization of MEMS. Previous approaches including micro turbine engines and micro batteries[1, 2] have been proposed. In this paper, we have demonstrated the feasibility of a miniaturized microbial fuel cell as an energy source for MEMS.

Figure 1 shows the operation principle of a microbial fuel cell. In the anode compartment, microorganisms, such as *Saccharomyces cerevisiae*, are put into a buffer solution. Glucose is fed to the microorganisms and the hydrogen protons, electrons and carbon dioxide are generated during the fermentation process[3]. The electrons are transferred to the electrode and protons are diffused through a proton-exchange membrane(PEM). In order to increase the electron transfer efficiency, an electron transfer *mediator* is needed in the anolyte suspension[4]. In the cathode compartment, oxidizing materials such as potassium ferricyanide can be used to accept the electrons and reduce to ferrocyanide. The reduced ferrocyanide is oxidized by oxygen and returns to ferricyanide and water. The wastes produced in the microbial fuel cell are carbon dioxide and water.

FABRICATION PROCESSES

Figure 2(a) shows the close-up diagram of the PEM with Cr/Au electrode. Filter papers with 0.2μm porosity are used as the electrode support and Cr/Au is thermal evaporated on to the support. After the electrodes with porous supports are fabricated, they are thermal compression bonded to the PEM, Dupont Nafion-117. Figure 2(b) shows

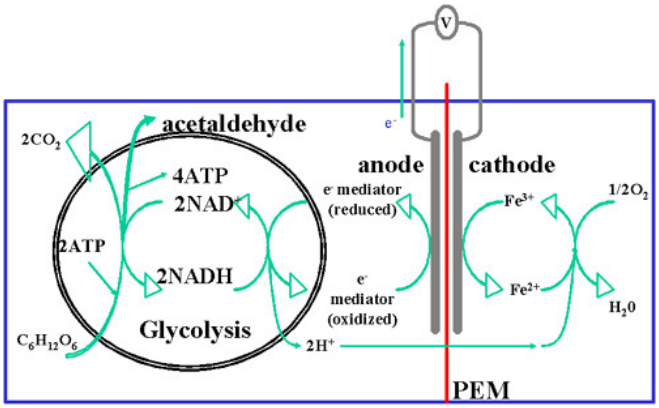

Figure 1: Operational principle of a microbial fuel cell.

the explode diagram of of the miniaturized microbial fuel cel. The electrode area is 0.07 cm^2 and the fluid ports are made of plastic with o-ring seal to minimize leakage. In the final assembly step, the fluid ports and the electrode/PEM assembly are glued together and ready for testing.

EXPERIMENTAL PROCEDURES AND RESULTS

The anolyte is prepared as the following: microorganism culture (*Saccharomyces cerevisiae*) is mixed with glucose in a 0.1 M phosphate buffer(pH 7.0). An electron transfer mediator, methylene blue of 0.01 M is then added in to promote the bio-electrical reaction efficiency. Moreover, a sufficient aeration is provided to enhance the fermentation process. On the cathode side, a 0.02 M potassium ferricyanide solution is prepared in a 0.1 M phosphate buffer(pH 7.0). The bio-electrical responses are measured by dropping a drop(volume 0.16 c.c.) of each corresponding solutions into the anode and cathode compartments and the electrical signals are measured chronically. Figure 3 shows the measurement results of the open-circuit voltage response of a microbial fuel cell. The voltage goes up to 300 mV and lasts for more than 2 hours. The final voltage drop after 2 hours is identified as solution dried out in air. The fuel cell discharge experiment is also carried out and the result is shown in Fig. 4 for two loading conditions. In the first loading condition, a bare conduction wire with resistance of 0.18 ohm is used. As shown in Fig. 4, the voltage goes up

0-9640024-4-2/hh2002/$20©2002TRF
DOI 10.31438/trf.hh2002.15

Solid-State Sensors, Actuators, and Microsystems Workshop
Hilton Head Island, South Carolina, June 2-6, 2002

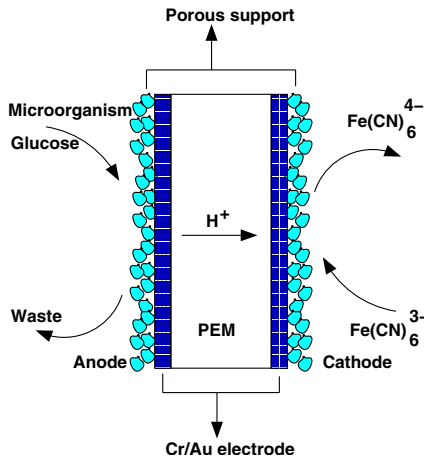

(a)

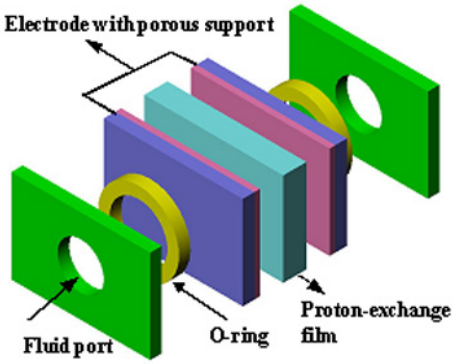

(b)

Figure 2: Design of a miniaturized microbial fuel cell. (a): A close-up schematic diagram of the PEM, Cr/Au electrodes and porous support. (b): Final assembly of the fuel cell.

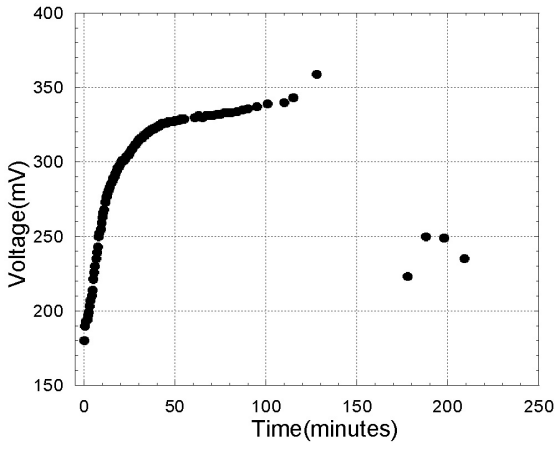

Figure 3: Open-circuit voltage measurement results.

to 13 μV in 10 minutes. In the second loading condition, a resistor of 100 ohm is used, the voltage maintains at 2μV for 30 minutes. The current density of 286 nA/cm^2 is then calculated by dividing the current with the electrode area.

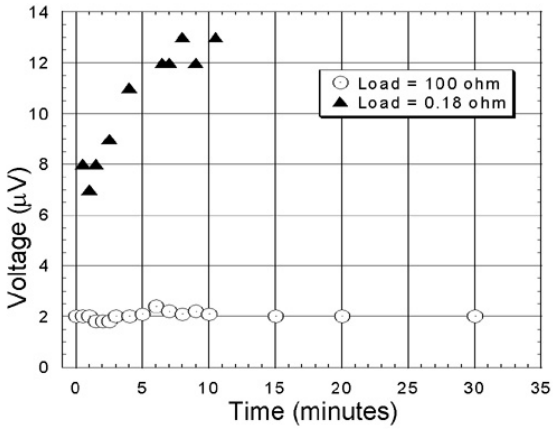

Figure 4: Microbial fuel cell discharge measurement results.

CONCLUSIONS

In this paper, we have demonstrated a miniaturized microbial fuel cell as a power source for MEMS. *Saccharomyces cerevisiae* is used to catalyse glucose and generate electricity. The wastes in the fuel cell are water and carbon dioxide. The fuel cell electrode area is 0.07 cm^2 and the current density is measured as 286 nA/cm^2 under 100 ohm and remains stable for 30 minutes. The open-circuit voltage goes up to 300 mV and lasts for 2 hours.

ACKNOWLEDGEMENTS

The authors would like to thank Mr. K.S. Teh and Ms. K. Cheung at UCB for valuable discussions on bacteria culturing. Theses devices are fabricated at the UCB Microfabrication Laboratory. This work is supported in part by an NSF CAREER award(ECS-0096098) and a DARPA MTO/MEMS grant (F30602-98-2-0227).

REFERENCES

[1] C. L. Tsai and A. K. Henning. Surface micromachined turbines. *Proc. of 9th IEEE Int'l Conference on Solid-State Sensors and Actuators*, pages 829–832, 1997.

[2] K. B. Lee and L. Lin. Electrolyte based on-demand and disposable microbattery. In *Technical Digest of IEEE Micro Electro Mechanical Systems*, pages 236–239, Jan 2002.

[3] H. A. Videla and A. J. Arvia. The responses of a bioelectrochemical cell with saccharomyces cerevisiae metabolizing glucose under various fermentation conditions. *Biotechnology and bioengineering*, XVII:1529–1543, 1975.

[4] T. Akiba, H. P. Bennetto, J. L. Stirling, and K. Tanaka. Electricity production from alkalophilic organisms. *Biotechnology Letters*, 9:611–616, 1987.

HIGH-*Q* MICROMECHANICAL RESONATORS IN CH_4-REACTANT-OPTIMIZED HIGH ACOUSTIC VELOCITY CVD POLYDIAMOND

Jing Wang, James E. Butler*, D. S. Y. Hsu*, and Clark T.-C. Nguyen
Center for Integrated Wireless Microsystems (WIMS), Dept. of EECS
University of Michigan, Ann Arbor, Michigan 48109-2122 USA
*Gas/Surface Dynamics Section, Code 6174, Naval Research Laboratory, Washington DC 20375
TEL: (734)647-1782, FAX: (734)763-9324, email: jingw@engin.umich.edu

ABSTRACT

Vibrating micromechanical resonators with *Q*'s greater than 30,000 have been demonstrated in CVD polydiamond material with an acoustic velocity of 14,252 m/s—the highest to date among surface-micromachinable materials for micromechanical resonators—achieved via exhaustive modifications to a CVD polydiamond deposition recipe that identify low CH_4 reactant concentration as the key to attaining high acoustic velocity. As a result of these modifications, folded-beam comb-transduced micromechanical resonators made in CVD polydiamond have now been measured with resonance frequencies 1.77X higher than that of identical polysilicon counterparts, 1.20X higher than achievable by SiC (another high acoustic velocity material contender [1]), and 1.53X higher than a previous attempt at using CVD polydiamond as a resonator structural material [2].

Keywords: wireless communications, RF MEMS, diamond, resonator

I. INTRODUCTION

Spurred by increasing interest in RF communication applications of MEMS technology [3], the frequencies of vibrating micromechanical resonators have seen dramatic increases in recent years, through which frequencies in the hundreds of MHz have now been demonstrated [4][5]. Among strategies for further extending frequencies past 1 GHz, the use of alternative structural materials with higher acoustic velocities than polysilicon, such as silicon carbide [1][4], have been particularly successful. Of the presently available set of thin-film-depositable materials, diamond potentially offers the largest acoustic velocity, with *single crystal* values on the order of 18,076 m/s [6], which is 2.24X higher than that of polysilicon and 1.50X higher than that of silicon carbide. Unfortunately, however, recent attempts to use CVD *polydiamond* as the structural material for micromechanical resonators have thus far yielded an acoustic velocity on the order of only 9,320 m/s, far lower than potentially achievable [2].

This paper reports for the first time micromechanical resonators in CVD polydiamond material with an acoustic velocity of 14,252 m/s, achieved via exhaustive changes made to the CVD polydiamond deposition recipe that identify low CH_4 reactant concentration as the key to high acoustic velocity. As a result of these changes, folded-beam comb-transduced micromechanical resonators made in CVD polydiamond are now demonstrated with resonance frequencies 1.77X higher than that of identical polysilicon counterparts, and with similar *Q*'s.

II. CVD POLYDIAMOND RECIPE VARIATIONS

The fabrication process that achieves CVD polydiamond devices with the final cross-section of Fig. 1 is similar to that of [2], except that doped LPCVD polysilicon (rather than metal) is used as the interconnect layer, and a 920°C LPCVD oxide (HTO) is utilized as the sacrificial layer (rather than PECVD oxide). These adjustments were made mainly to allow a wider variance in diamond deposition and etch recipes during the search for the right recipe.

As in [2], CVD polydiamond was deposited by first establishing a seed layer of diamond with a sufficient nucleation density, then depositing and *in situ* boron doping the diamond material via a microwave PECVD process, still using 2.45 GHz microwaves, but this time changing the substrate temperature and the concentrations of the CH_4 and B_2H_6 reactants, in search of an optimum recipe that yields high acoustic velocity while retaining high-*Q*, low stress, and low surface roughness. Table I presents a listing of four representative recipe variations.

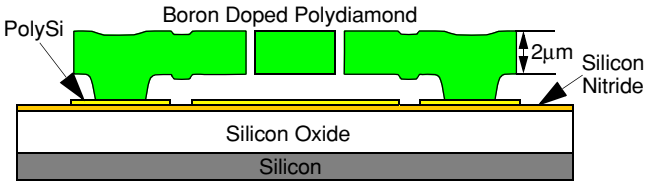

Fig. 1: Final cross-section of a CVD polydiamond micromechanical device in the process technology used for this work.

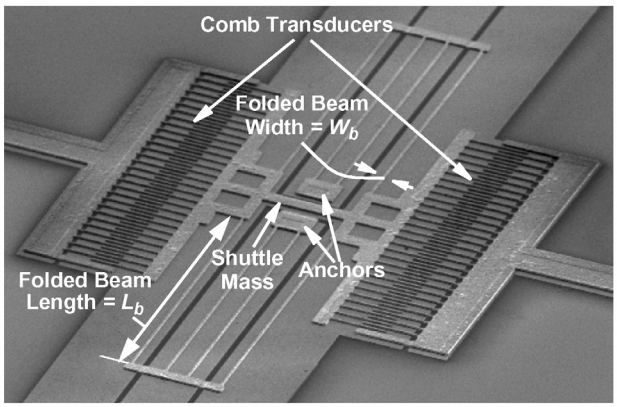

Fig. 2: SEM of a fabricated TypeD folded-beam, comb-transduced CVD polydiamond micromechanical resonator.

III. EXPERIMENTAL RESULTS

Figure 2 presents the wide-view SEM of a fabricated TypeD (c.f., Table I) CVD polydiamond folded-beam micromechanical resonator. Figures 3 and 4 present measured frequency characteristics using the inset circuits under 50μTorr vacuum for a TypeC and a TypeD device, both with identical dimensions, but showing widely disparate resonance frequencies of 19.893 kHz and 27.345 kHz, respectively. As summarized in Table I, and assuming a constant density of 3,500 kg/m^3 for CVD polydiamond deposited with CH_4 concentrations less than 1% [9], these frequencies correspond to acoustic velocities of 10,419 m/s and 14,252 m/s, with the TypeD material showing a 1.37X higher acoustic velocity than the TypeC. The TypeD device also exhibits a much higher *Q* of 36,460 than the 19,892 of the TypeC.

From Table I the main difference between these two devices is in the CH_4 concentrations used during CVD diamond deposition, which was much smaller (0.33%) for the higher frequency TypeD device than for the TypeC device (0.9%). This, together with the observation that lower deposition rates attained with low CH_4 reactant concentrations lead to smaller deposits of non-diamond carbon

Travel support has been generously provided by the Transducers Research Foundation and by the DARPA MEMS and DARPA BioFlips programs.

Table I: CVD Polydiamond Properties vs. Deposition Conditions

Parameter	TypeA*	TypeB†	TypeC‡	TypeD‡	Units
Pretreatment? [2]	no	yes	yes	yes	yes/no
Temperature	575	750	750	800	°C
CH_4 Concentration	0.33	0.33	0.9	0.33	%
Power	800	800	600	800	W
B_2H_6 Concentration	6.7	6.7	6.7	11.1	10^{-5}%
H_2 Flow Rate	900	900	900	900	sccm
Deposition Time	2,400	1,200	480	1,200	min
Thickness	1.4	2.11	1.86	2.56	µm
Surface Roughness	145	80	60	50	nm
Resonance Frequency, f_o	2938	35.82	19.893	27.352	kHz
Quality Factor, Q	6,225	19,500	19,892	36,460	—
Young's Modulus, E	305	654	380	711	GPa
Density, ρ [9]	3,500	3,500	3,500	3,500	kg/m^3
Acoust. Vel. ($=\sqrt{E/\rho}$)	9,320	13,670	10,419	14,252	m/s

* Clamped-clamped beam resonator with length L_r=55µm, width W_r=8µm, thickness h_r=1.1µm.

† Folded-beam, comb-transduced resonator with L_b=160µm, W_b=2μm, shuttle mass m_s=9.03×10^{-11}kg.

‡ Folded-beam resonator with the design of Figs. 3 and 4.

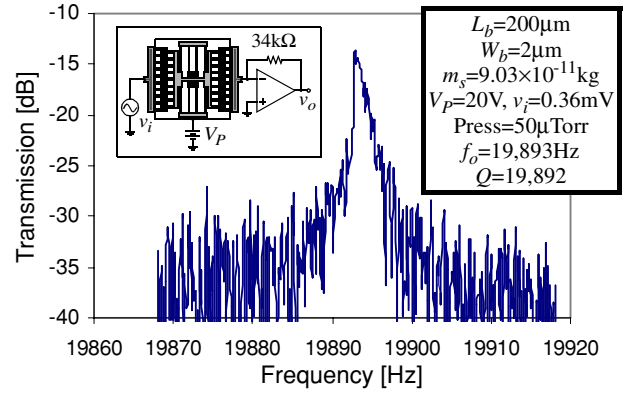

Fig. 3: Measured frequency characteristic (under 50 µTorr vacuum) for the TypeC polydiamond folded-beam resonator.

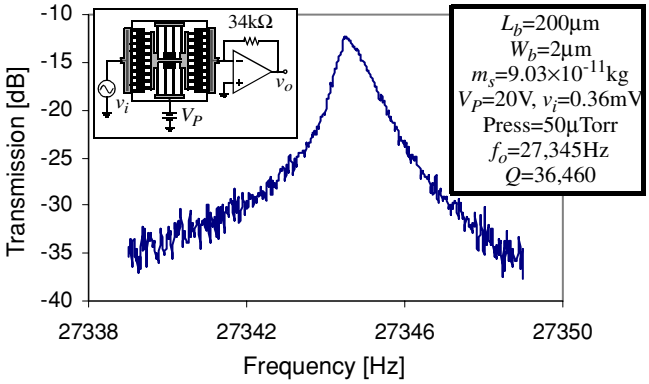

Fig. 4: Measured frequency characteristic (under 50 µTorr vacuum) for the TypeD polydiamond folded beam resonator.

and a smaller density of micropore defects [7][8][9], suggests that the modulus of elasticity E of the deposited CVD diamond material is strongly dependent upon the amount of non-diamond carbon, voids, and defects, present in the final film. In addition, since larger grain sizes reduce the boundary areas where non-diamond carbon resides, and given that grain size generally increases with film thickness, a higher E is expected for thicker films, as verified in Table I. Since acoustic velocity goes as $\sqrt{E}$, thicker films with fewer voids and defects should also exhibit higher acoustic velocity.

A mechanism where film quality plays a significant role in setting E is clearly supported by Fig. 5, which presents close-in SEM shots of TypeC and TypeD devices, showing a substantially smoother, porous-free surface for the better performing TypeD device. The surface roughness seen for the TypeD device is, in fact, comparable to that attainable in previous polysilicon counterparts [10]. On the other hand, pores and voids are clearly visible in the TypeC material, and these then likely contribute to a smaller Young's modulus. As evidence of the degrading impact of non-diamond carbon in the final film, the TypeA recipe lacks a plasma pretreatment step [2], and thus, suffers from poor nucleation and carburization over the substrate before deposition, leading to the lowest acoustic velocity of all recipes in Table I.

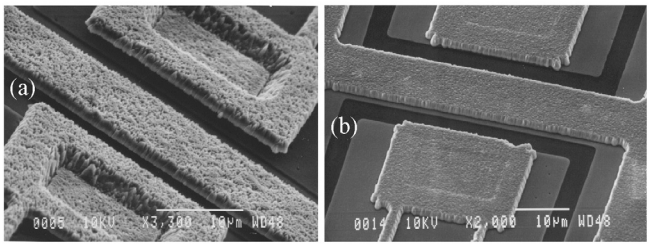

Fig. 5: Close-in SEMs of the etched edges on (a) a TypeC device; and (b) a TypeD device.

In summary, in order to maximize the acoustic velocity of CVD diamond material, the CH_4 reactant concentration should be reduced during deposition, and the temperature increased to maintain a reasonable deposition rate, as was done for the TypeD device en route to the highest reported acoustic velocity so far in a surface-micromachinable material for micromechanical resonators.

IV. CONCLUSIONS

CVD polydiamond with an acoustic velocity as high as 14,252 m/s has been achieved via a low CH_4-concentration deposition recipe and used to demonstrate micromechanical resonators with Q's greater than 30,000 and frequencies substantially higher than those of equivalently sized devices in any other material to date. These results now establish CVD polydiamond as one the strongest contenders among high acoustic velocity materials potentially capable of extending vibrating micromechanical resonance frequencies past 1 GHz for RF communication applications [3].

***Acknowledgment*:** This work was supported in part by DARPA Grant No. F30602-01-1-0573 and an NSF ERC on WIMS.

References.

[1] M. Mehregany, *et al.*, *Proc. IEEE,* vol. 86, pp 1594-1609, Aug. 1998.

[2] J. Wang, *et al.*, *Tech. Digest*, 2002 IEEE MEMS Conf., Las Vegas, Jan. 20-24, 2002, pp. 657-660.

[3] C. T.-C. Nguyen, *Dig. of Papers*, Topical Mtg on Silicon Monolithic IC's in RF Systems, Sept. 12-14, 2001, pp. 23-32.

[4] M. L. Roukes, 2000 Solid-State Sensor and Actuator Workshop, June 4-8, 2000, pp. 367-376.

[5] J. R. Clark, *et al.*, 2000 IEEE Int. Electron Devices Mtg (IEDM), Dec. 11-13, 2000, pp. 399-402.

[6] M. D. Whitfield, *et al.*, *Diamond and Related Materials*, vol. 8, pp. 732-737, 1999.

[7] E. D. Nicholson, *et al.*, *Diamond and Related Materials*, vol. 6, pp. 817-821, 1997.

[8] E. Kalaugher, *et al.*, *Diamond and Related Materials*, vol. 6, pp. 826-829, 1997.

[9] R. Kuschnereit, *et al.*, *Thin Solid Films*, vol. 312, pp. 66-72, 1998.

[10] C. T.-C. Nguyen and R. T. Howe, *IEEE J. Solid-State Circuits,* vol. 34, no. 4, pp. 440-455, April 1999.

MICROMECHANICAL FORCE SENSING WITH APPLICATIONS IN BIOLOGY

Thomas W. Kenny, Yiching Liang, Su-Wen Ueng, Michael Bartsch and Robert Rudnitsky

Departments of Mechanical Engineering and Applied Physics, Stanford University,
Stanford, CA 94305, Kenny@mems.stanford.edu

ABSTRACT

In recent years, MEMS devices have been developed for a wide variety of applications. Many of the signals that these sensors are intended to detect are expressed as forces that stress or deflect the micromechanical structure. As sensors are miniaturized, these forces naturally become smaller, and techniques for detection are required to improve. As the force sensing capabilities of MEMS devices have improved, it has become possible to apply these devices to interesting scientific experiments on biological systems.

INTRODUCTION

Since the 1970s, silicon fabrication tools have been adapted and extended to allow fabrication of micromechanical structures [**1**]. In recent years, this field has grown to include a bewildering variety of resonators, pumps, gear trains, inertial sensors, optical switches, and many other devices. And, the fabrication tool set has expanded to include use of thick photoresists, high aspect ratio plasma etching, and materials such as acrylic. The expansion of the tools and applications can be expected to continue as interest in bioanalytical systems, and telecommunications applications grows. Sensors make up a significant subset of all micromechanical devices. Most of these devices operate by sensing forces derived from the signal of interest. As examples, pressure sensors detect forces on diaphragms, inertial sensors detect forces on test masses, magnetometers detect torque on magnets, and so on.

Before the development of micromechanical devices, macroscopic force sensors were used in many instruments. Bonded strain gauges, optical deflectors, differential capacitors, and other instrumental means were used to convert macroscopic physical signals into electrical signals. MEMS devices enabled a completely new approach to many common instruments, and the opportunity for miniaturization of these instruments enables force sensing to become important in many new applications. In general, miniaturization of the dimensions of a force sensor imposes a reduction in the force to be detected. For example, the force available for a pressure sensor is necessarily proportional to the area of the diaphragm. The force available for inertial sensors generally scales as the mass, which scales as the cube of the dimension. Therefore, miniature sensors are generally required to detect smaller forces than macrosensors.

Using micromechanical structures and integrated sensors, it is possible to detect forces over a very wide range. In this paper, the sizes of the forces that are detected in a variety of existing micrometer and nanometer scale devices will be outlined. It will be seen that forces ranging from milli-Newtons to atto-Newtons are detectable using appropriately-designed devices. This paper will discuss work in this area and opportunities for important measurements and applications, particularly in the area of biological science.

FORCE-SENSING IN PIEZORESISTIVE MEMS DEVICES

Before discussing custom-force sensors, some examples of force sensing in commercial MEMS devices will be presented. This discussion will illustrate some of the basic methods for force sensing, and the very impressive performance achieved with "conventional" low-cost MEMS devices.

The first example is a standard piezoresistive pressure sensor, such as the Lucas Novasensor NP301 [**2**]. This sensor is fabricated by standard etching of silicon, wafer bonding (to form a sealed vacuum cavity), and ion implantation (to form piezoresistive strain gauges on the diaphragm). These devices are manufactured in quantities of millions annually, sold for a few dollars (plus packaging costs), and are a well-established example of simple, but profitable MEMS devices.

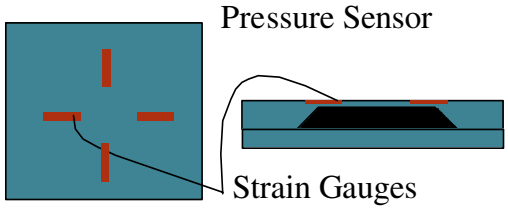

Figure 1 *Drawing of a Piezoresistive Pressure Sensor, such as the Lucas Novasensor NP301. The piezoresistive strain gauges act as resistors whose resistance is a function of the pressure-induced strain in the thin silicon diaphragm. An off-chip wheatstone bridge readout circuit allows straightforward measurement of the pressure difference between the outside and the sealed reference cavity.*

This particular micromachined sensor has a diaphragm area of about $(1\text{mm})^2$, and can detect pressures up to 15 PSI. This corresponds to a maximum force of 25 mN. These devices are specified to an accuracy of 0.5% of the full-scale signal, corresponding to a force accuracy of 100 μN. Individual devices may be calibrated to an accuracy of about 20-50x better then the lot specification, so individual mm-scale micromachined pressure sensors are capable of force detection from 25 mN down to 5 μN. If the noise of a pressure sensor is measured with a simple, off-chip instrumentation amplifier, the voltage fluctuations correspond to forces as small as 10 nN [**3**].

This is a very impressive performance capability. For contrast, the standard instrument for measuring small forces in one axis is the conventional load cell. There are many commercial suppliers of load cells, some of whom specialize in load cells for relatively small forces. In order to measure down to 1 mN with a commercial load cell, it is necessary to spend more than $400, and the purchased devices suffer from drift so that offset adjustments are constantly required. The piezoresistive pressure sensor is more than 100x more accurate for small forces, and is available at about 100x less cost.

0-9640024-4-2/hh2002/$20©2002TRF
DOI 10.31438/trf.hh2002.17

Piezoresistive sensors have been used for many other MEMS applications, including accelerometers [**4,5**], gyroscopes [**6**], and AFM cantilevers [**7**]. The primary advantage of this approach is that the sensor impedance is relatively low (a few KΩ), and it is possible to extract small signals without interference from noise with off-chip integrated circuits. Therefore, low-cost, two-chip hybrid systems can be built without the need to develop an integrated MEMS/Electronics process.

There has been recent interest in the development of ultrathin piezoresistive cantilevers for various applications. The main reason for this approach is that the sensitivity should improve dramatically as the thickness is reduced. However, it is also necessary to confine the piezoresistor into a fraction of the beam thickness, and this becomes a challenge for beam thickness less than 2 μm. Growth of very thin films of doped epitaxial silicon has allowed development of piezoresistive cantilevers thinner than 0.1 μm, and these cantilevers have been shown by Harley and Liang to be capable of detecting forces as small as 1 fN. [**8,9**]

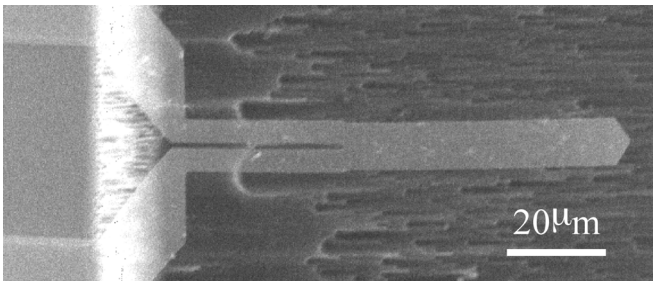

Figure 2 *SEM micrograph of an ultrathin piezoresistive cantilever. This cantilever is 70 nm thick, and includes a 20 nm n-type piezoresistor. This cantilever has force resolution of 1.6 fN/√Hz at 1 kHz at room temperature.* ***[9]***

FORCE SENSING IN A CAPACITIVE ACCELEROMETER

Our second micrometer-scale MEMS example is a surface micromachined accelerometer, the ADXL202 [**10**]. This device is a member of the Analog ADXL family, in which 2μm-thick polysilicon masses are suspended above a surface in the middle of an integrated circuit. The deflection of this small proof mass is detected by differential capacitance measurement between arrays of fingers on the edge of the mass and mounted on the surrounding substrate. Because of the small total capacitance involved (<0.2 pF), an integrated circuit with a preamplifier positioned as close as possible to the capacitor is required.

The micromechanical structure consists of a layer of polysilicon with thickness of 2 μm, mass of 10^{-10} kg, suspension stiffness of about 1 N/m. The minimum detectable acceleration (in a 1 Hz bandwidth) is approximately 0.5 mg (where 1g = 9.8 m/s^2). For this device structure, this acceleration corresponds to a displacement of about 0.005 Angstroms (0.5 pm), and results in a force on the proof mass of about 0.5 pN. This is a phenomenal performance level for an off-the-shelf component that is widely sold for as little as $10. This performance level is very close to thermodynamic limits for force detection, and represents a very impressive accomplishment within a large scale production environment.

There are various noise sources to be concerned with in miniature accelerometers, many of which will impose some limit on the minimum detectable signal. At a fundamental level, there is a thermomechanical noise mechanism to be concerned with. This mechanism is the mechanical analog of Johnson Noise in resistors, in which energy dissipation necessarily introduces fluctuations through thermodynamics. For the case of accelerometers, this fluctuation may be represented as a 'Noise force' applied to the proof mass. This noise source has been analyzed for accelerometers [**11**], and results in a minimum detectable acceleration of

$$A_{\min} = \sqrt{\frac{4k_B\omega_o\Delta F}{mQ}}, \qquad [1]$$

where k_B is Boltzmann's constant, ω_o is the resonant frequency of the suspension for the proof mass, m is the mass value, and Q is the Quality Factor of the resonance (approximately equal to the number of free oscillations that will occur before damping causes the oscillation amplitude to decay by 1/e). This thermodynamic limit cannot be avoided, and this limit becomes significant where m becomes very small.

It is possible to work around this issue through the use of feedback control. In most cases, the sensitivity (V/g) of an accelerometer is proportional to $1/\omega_o^2$, so it is useful to select a low value of resonant frequency. In addition, this helps reduce the thermomechanical noise. However, the resonance frequency also determines the bandwidth of the accelerometer. Feedback control can be used to modify the apparent dynamics of the device by imposing force feedback to "stiffen" the suspension. For an accelerometer, this can allow operation above the open-loop resonance without the responsivity and noise issues that would accompany an increased resonance. This method is used in conventional seismometers [**12**] and conventional inertial navigation accelerometers [**13**], and has been adapted to a MEMS accelerometer with a tunneling transducer [**14**].

In the ADXL accelerometer example discussed here, the minimum detectable acceleration (assuming Q=0.7) is 0.3 mg in a 1-Hz bandwidth. This is less than a factor of two smaller than the specified performance for these accelerometers, and represents a final limit to the performance of accelerometers based on a surface-micromachined architecture. Nevertheless, this MEMS device is operating by detecting forces smaller than 1 pN, reflecting what is possible with highly-integrated differential capacitive sensing.

FORCE SENSING IN GYROSCOPES

There has been significant recent interest in the use of gyroscopes to detect errors in automobile orientation, and to trigger corrective differential braking to achieve active skid control. Bosch manufactures a miniature Coriolis Force gyroscope for this application, and it represents another impressive example of the detection of small forces.

In this device, a proof mass of less than 0.01 mg is excited into resonant oscillation at frequency of 500 Hz with amplitude of approximately 10 μm. Rotations of the sensor about an axis perpendicular to the motion of the mass cause an oscillating Coriolis force with amplitude :

$$F_{Coriolis} = m\omega xV,$$

where "x" is the vector cross-product between the rotation vector and the velocity vector. The velocity of the mass is

oscillating with amplitude equal to the product of the amplitude and oscillation frequency. For a rotation of 1 degree/sec, this oscillating Coriolis force has amplitude of 6 pN. One advantage for detection of this force is that it appears as an oscillating signal, rather than as a DC signal. Unfortunately, there are many error sources to be overcome in a Coriolis gyro, including cross-coupling between the lateral modes, and thermally-enhanced cross-coupling. Thermal noise also imposes a fundamental limit for force detection in a gyroscope [**15**].

$$\Omega_{\min} = \frac{1}{4C_g Amplitude}\sqrt{\frac{4k_B T}{\omega_o m Q}}$$

For the parameters described above, thermal noise limits detection to signals greater than 0.1 degree/sec in a 1 Hz bandwidth. These issues were discussed at greater length by Geen at Hilton Head '98 [**16**].

FORCE SENSING IN OTHER MEMS DEVICES

In addition to piezoresistive sensing and capacitive sensing, it is possible to use optical transducers. AFM cantilever deflection is typically sensed by detecting the deflection of a reflected optical beam with a split photodetector. With low stiffness cantilevers (1 N/m), AFM instruments typically are capable of detecting forces as small as 10 pN.

Interferometric detection of cantilever deflection is also possible [17]. For cantilevers with stiffness of 1 N/m, interferometric detection allows force sensing at or below 1 pN. For ultrathin cantilevers, this capability can be extended to better than 1 aN [**18**].

Tunneling displacement transducers have also been explored by many researchers for sensing applications [**19-22**]. These sensors are capable of detecting displacements of pm. Because of limitations imposed by van der waals attraction, tunneling transducers use stiffness of 1 N/m or more to detect forces as small a 1 pN.

In summary, MEMS devices have been described which are based on a wide variety of displacement transducers. Briefly, it has been shown that piezoresistive, optical, capacitive, and tunneling transducers are all capable of force detection ranging from mN to pN, and some are capable of extension to fN or aN with some effort. This very broad force measuring capability is central to the broad array of applications for MEMS devices.

FORCE SENSING IN BIOLOGY

There has been great and increasing interest among Biological scientists in the mechanical behavior of molecules, cells, and larger structures. Theoretical and experimental studies of "folding", "sticking", and "stretching" of molecules and cellular structures are widespread. Research into the fundamentals of muscle actuation, cell adhesion, protein folding, and other fundamental aspects of micro and macro Biology produces much of the most interesting contributions to Nature and Science. From our perspective, these are all questions that are very familiar to the discipline of Mechanical Engineering. In some ways, much of modern biology is beginning to look like applied mechanical engineering.

The tools that biological scientists have developed for research are not always appropriate for these applications. Centrifuges, Microscopes, X-ray crystallography and others are not well suited to the study of the interesting structures in situ.

What is needed is a new set of custom tools for interacting with these biological systems. These tools must have the right size scale to interface to molecules, cells, or larger structures, and must have the appropriate sensitivities for extraction of interesting signals. MEMS provides a tool fabrication technology that can be adapted to many of these problems. The following list of examples shows the breadth of opportunity :

- Measurements of the binding forces of the DNA double helix show that it should be possible to distinguish the bonds and sequence DNA with resolution of 10 pN [**23**]
- The forces exerted on actin filaments by single myosin "molecular motors" is between 5 and 100 pN [**24**]
- The molecules responsible for cell adhesion are capable of maintaining adhesion forces of 10-100 pN [**25**]
- The forces at work in the process of protein folding have been characterized energetically and shown to be in the 0.1-100 pN range. [**26**]
- Individual muscles in small insects (cockroaches) have been studied as examples of efficient microactuators, and are known to exert forces in the μN-mN range [**27**].

There are many other examples, but we easily see that the range of biological force sensing applications maps to the range of forces that can be detected by MEMS devices. In addition, it is possible to design MEMS force sensors with dimensions that are compatible with the physical geometries of these biological science applications.

CELL ADHESION EXPERIMENTS

The adhesion of individual cells is mediated by Cadherin Molecules, which extend from the actin filament structure inside of cells through the cell membrane. The ends of Cadherin molecules consist of a number of extra-cellular domains that can become attached to complimentary molecules from adjacent cells. The interactions between cadherin molecules cannot be directly detected using conventional biological science instrumentation, but it is possible to use the AFM and custom AFM cantilevers for these studies. Based on studies with whole cells, the adhesion forces for individual molecules are expected to be near 30 pN [**28**]. AFM studies of molecular interactions have been carried out by many researchers [**29,30**].

We have adapted a commercial AFM for experiments on individual cadherin molecules. The AFM must allow operation of the cantilever underwater, and the AFM cantilever and substrate must be prepared with an appropriate coating of cadherin molecules. In practice, this preparation is complicated, because it is not sufficient to simply coat the surface with cadherin molecules. In order to achieve binding that is similar to the interaction in a cellular system, it is necessary to build a surface that will cause the cadherin molecules to extend vertically. We accomplish this by coating the surface with a sequence of biotin, neutravadin, biotinalyted proteins, and then with cadherins that are initiated from a complimentary protein. This chain of support material must all feature binding strength that is greater than the adhesion forces expected from the cadherins. Experiments using fluorescent tags are carried out at each stage of the assembly to verify selective adhesion with known densities.

In order to produce a surface with a known area that will be close enough to the opposing surface for molecular interaction, we attach known-diameter polystyrene beads to the ends of the cantilever prior to the molecular preparations.

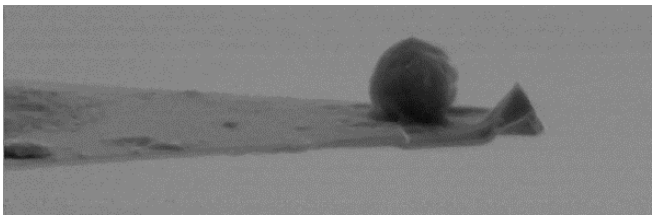

Figure 3 *SEM micrograph of a 2µm diameter polystyrene bead attached to the end of a microfabricated cantilever for Cadherin Adhesion experiments.*

After preparation of the cantilever and substrate, adhesion experiments are carried out under control of the AFM. The tip of the cantilever is brought into contact with the surface, and the deflection is measured as the cantilever is retracted. A typical retraction curve is shown in figure 4. Starting from the upper right, the cantilever is backed away from the surface. As the deflection is reduced, the measured force also reduces. As we pass the neutral deflection point, the cantilever tip remains attached to the surface because of the adhesive force of the Cadherin molecules. After some overshoot, some or all of the adhesion force breaks free, and the cantilever deflection is reduced. These "steps" in the cantilever retraction curve are understood to represent breaking of individual molecular adhesions. In some cases, the entire attachment is broken in a single step. In other cases, such as the example shown in Figure 4, there appears to be at least 2 distinct detachment events. In the data shown in this figure, these two events each appear to be about 70 pN in magnitude. This experiment is repeated many times (hundreds to thousands), and histograms of attachment force are gathered to identify the values of attachment force for single molecules.

This work is in progress in our group, and we have already begun to observe variations in adhesion behavior as a function of Cadherin density, solution pH and calcium content, and are exploring the behavior as a function of contact force and duration. One significant advantage of this approach is that studies as a function of controllable dynamical parameters are possible, allowing a variety of interesting experiments. As a result, there is a rapidly-growing community of researchers utilizing AFM-based instruments and standard or custom cantilevers to carry out molecular biology experiments. New cantilevers with integrated heaters, multiple-axis force sensing, or other unique sensitivities will enhance this research field, and will provide continuing opportunities for MEMS researchers.

INSECT BIOMECHANICS EXPERIMENTS

Insects provide interesting examples of miniature system operation, as well as high-performance locomotion. For example, cockroaches are able to navigate complicated environments at high speed without difficulty. In contrast, the best man-made miniature robots are generally slow, and are easily trapped within complicated terrain. Sophisticated measurements of the terrain and high-level robotic maneuvering algorithms are required to function reliably. The contrast in these two examples has led researchers in "biomimetics" projects to try to learn more about cockroach biomechanics so that small man-made robots can acquire the same features.

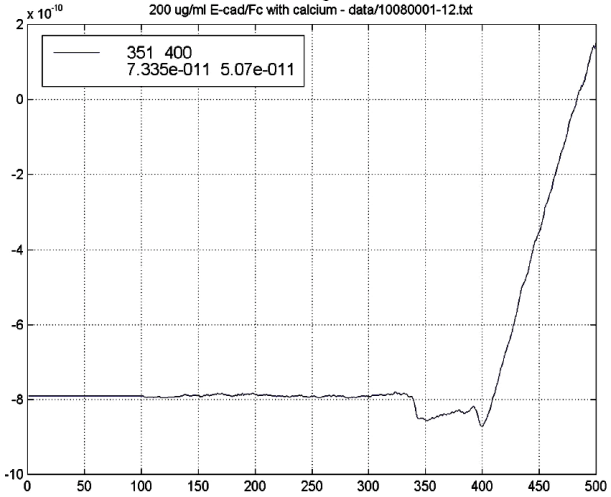

Figure 4 *Plot of cantilever contact force as a function of handle displacement. In this curve, the units on the vertical axis are Hundreds of pN, and the units on the horizontal axis are angstroms of displacement. The glitches at the lower right of the figure represent single molecule detachment events.*

The first step in such a program is to carry out measurements of cockroach biomechanics. This is difficult because cockroaches are too small and too fast for macroscopic instrumentation. Load cells and force platforms cannot resolve the small forces from real cockroaches, and the dynamic response of such instruments is too slow to capture some of the more important elements of the roach behavior. Since the interesting forces can be as large as mN, and the details are in the µN range, custom MEMS instrumentation.

Our group has been developing MEMS force platforms with integrated multiple-axis piezoresistive force sensors. Because of the relatively large forces involved (for MEMS), these structures are based on relatively thick (40 µm) flexures, and required adaptation of our fabrication processes for such thick structures. SEMs of the MEMS force plate are shown in Figure 5 below. Each corner of the force plate is supported by a thin flexure with a 2-axis piezoresistive force sensor.

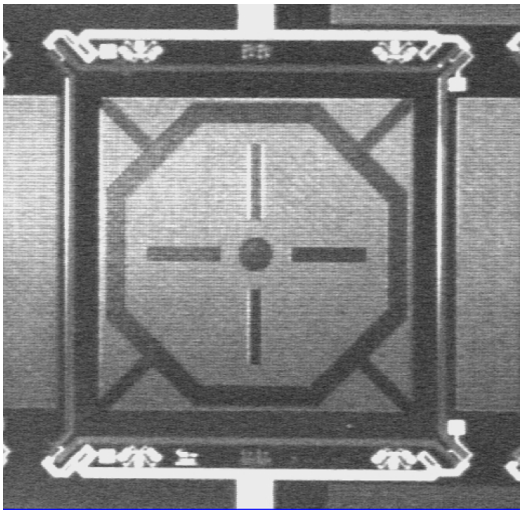

Figure 5 *SEM Micrograph of the MEMS force plate*

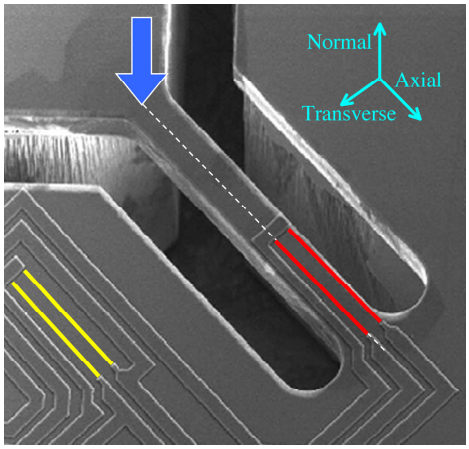

Figure 6 *Close-up SEM of flexure supporting the force plate.*

These microfabricated force plates are capable of resolving 10 nN force signals in the vertical and lateral directions, and have been used for measurements on live, free-running American cockroaches and carpenter ants. These measurements are the first ever performed on cockroaches lighter than 1 gm, and the first ever performed on ants of any kind by any means. A series of representative force measurements for a running cockroach are shown in Figure 7, and for a walking ant in figure 8. In each of these measurements, there is a distinct "double -bump" in the normal force signal, which is consistent with observations on much larger animals. The two "bumps" are r due to heel-strike and toe-push-off in normal walking, with the dip inbetween attributed to flexing of the "knee". From this data, we see that these insects walk in a manner that is very much like the walking of much larger creatures. Perhaps we should make robots which walk this way!

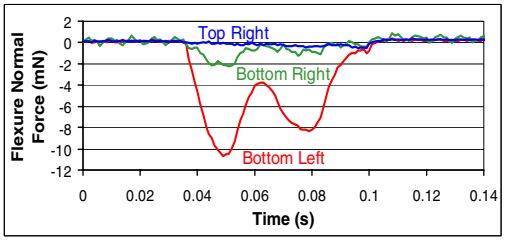

Figure 7 *Time trace of the leg forces measured for an American cockroach running across the force platform.*

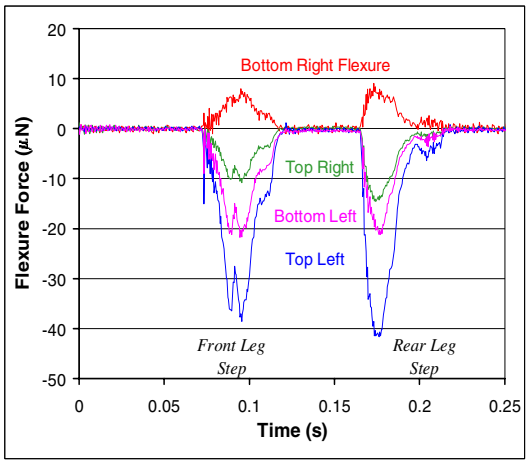

Figure 8 *Time traces of the leg forces measured for a carpenter ant walking across the force platform.*

MEASUREMENT OF GECKO ADHESION

Geckos are remarkable creatures, primarily for their unusual ability to cling to vertical and inverted surfaces. The adhesion mechanism has been the subject of speculation for more than 100 years [**31**], but definitive measurements have been difficult to carry out because of the microscopic origin of these adhesion forces. Figure 9 shows a SEM micrograph of one of the hairs on the foot of a Tokay gecko, and a close-up of the end of this hair. This hair terminates in a dense patch of sub-micron spatula that are crucial to the adhesion. Our hypothesis is that the adhesion process is due to van der waals force between the flattened ends of these spatula and the irregular shape of the opposing surface.

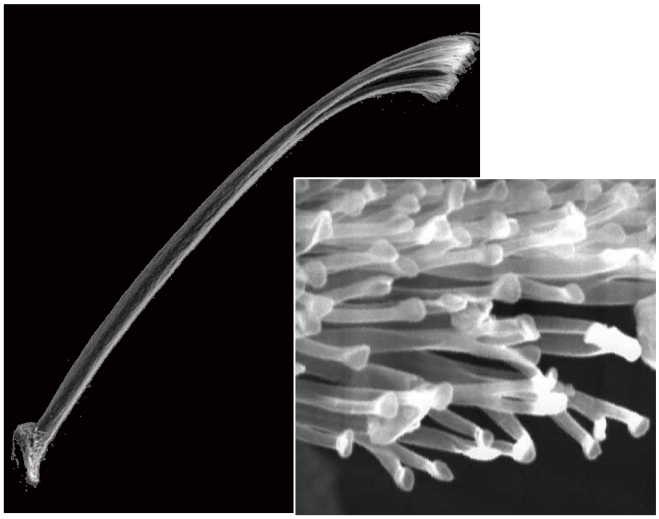

Figure 9 *SEM Micrograph of a Setae from the toe of a Tokay Gecko. The microstructures on the end of the toe are shown in the inset. The flattened ends of these microstructures are less than 1 μm in area, and a Tokay has more than 1 million such hairs on its feet. (SEM courtesy of Kellar Autumn)*

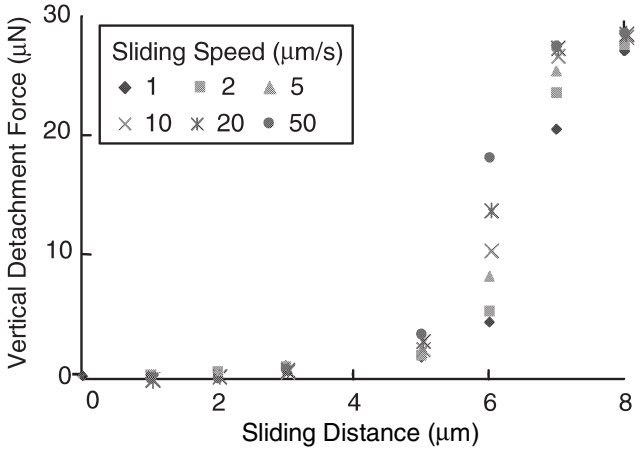

Figure 10 *Plot of the measured adhesion force as a function of the lateral sliding distance recorded at a series of different sliding velocities.*

At Hilton Head '00, we reported on some preliminary measurements of adhesion of individual Setae on a custom 2-axis micromechanical force sensor [**32**], which showed that the magnitude of the adhesion force is consistent with what should be expected for van der waals force. We also saw that the adhesive force is enhanced by lateral sliding across the

opposing surface. More recently, we have measured the amplitude of the adhesion force as a function of lateral sliding distance and for a variety of different sliding velocities, and determined that sliding of about 5 µm leads to a significant increase in adhesion, independent of the sliding speed. This data is shown in Figure 10 We believe that this result indicates that the sliding produces a kind of "combing" effect on the microstructure, and that the absence of a speed dependence shows that this effect is not related to the dynamic properties of the structure.

CONCLUSIONS

In this paper, the force sensing capabilities of MEMS devices have been discussed, and related to opportunities for measurements in biology. We've presented examples of measurements at the molecular level, at the whole-insect level, and an exploration of nano-scale adhesion mechanisms. There are many more opportunities for MEMS to contribute to biological science measurements.

ACKNOWLEDGEMENTS

The authors acknowledge collaborative support from R. Full, W. Heberle, and T. Hsieh at UC Berkeley, K. Autumn at Lewis and Clark, and J, Nelson, J. Spudich, M. Cutkosky, and their groups at Stanford. This work was supported by MURI/ONR Biomimetics Program (N-00014-98-1-0669), and by NSF XYZ on a Chip Program (CMS-9980838-002).

REFERENCES

1. K.E. Petersen, "Silicon as a Mechanical Material," *Proc. IEEE*, 70, 420-457 (1982).
2. Lucas Novasensor NP301, Fremont, CA.
3. J.K. Reynolds, D.C. Catling, R.C. Blue, N. Maluf, T.W. Kenny, "Packaging a Piezoresistive Pressure Sensor for Pressure and Temperature Stability in a Martian Environment," *Sensors and Actuators* 83, 142-149 (2000).
4. See Lucas Novasensor, ICSensors, Endevco for examples.
5. A. Partridge, et. al. "A High-Performance Planar Piezoresistive Accelerometer," *JMEMS* 9, 58-66 (2000).
6. F. Gretillat, M. Gretillat, and N.F. de Rooij, "Improved Design of a Silicon Micromachined Gyroscope with Piezoresistive Detection and Electromagnetic Excitation," *JMEMS* 8, 243 (1999).
7. M. Tortonese, "Force Sensors for Scanning Probe Microscopy," PhD Thesis, Stanford University (1993).
8. J.A. Harley, and T.W. Kenny, "High Sensitivity Piezoresistive Cantilevers under 1000Å Thick," *Appl. Phys. Lett*. 75, 289 (1999).
9. Y. Liang, S-W Ueng, T.W. Kenny, "Performance Characteristics of Ultra-Thin n-Type Piezoresistive Cantilevers", *Proceedings Transducers '01*, Munich Germany, p. 998 (2001).
10. Analog Devices ADXL202 Data Sheet, Cambridge, MA.
11. T. B. Gabrielson, "Mechanical-thermal Noise in Micromachined Acoustic and Vibration Sensors," *IEEE Electron Devices*, 40, 903 (1993).
12. Guralp CMG-40T, Guralp Systems Limited, Berks, UK.
13. QA3000, Honeywell Inertial Products, Redmond, WA.
14. C.H. Liu, and T.W. Kenny, A High-Precision, Wide-Bandwidth Micromachined Tunneling Accelerometer, *JMEMS*, 10,425 (2001)
15. F. Ayazi and K. Najafi, "A HARPSS Polysilicon Vibrating Ring Gyroscope", *JMEMS* 10, 169 (2001).
16. J.A. Geen, "A Path to Low-Cost Gyroscopy", *Proceedings 1998 Hilton Head Workshop on Solid State Sensors and Actuators*, 51 (1998).
17. D. Rugar, H.J. Mamin, and P. Guethner, "Improved Fiber-Optic Interferometer for Atomic Force Microscope," *Appl. Phys. Lett*. 55, 2588 (1989).
18. H.J. Mamin and D. Rugar, "Sub-Attonewton Force Detection at Millikelvin Temperatures", *Appl. Phys. Lett*. 79, 3358 (2001).
19. T.W. Kenny, et.al., "Micromachined Infrared Sensors using Tunneling Displacement Transducers," *Rev. Sci. Instrument*. 67, 112 (1996).
20. R.L. Kubena, D.J. Vickers-Kirby, R.J. Joyce, and F.P. Stratton, "A New Tunneling-based Sensor for Inertial Rotation Rate Measurements," *JMEMS* 8, 439 (1999).
21. C. Yeh, and K. Najafi, "Micromachined Tunneling Accelerometer with a Low-Voltage CMOS Interface Circuit," in *Proceedings 1997 International Conference on Solid State Sensors and Actuators* 1213 (1997).
22. J. Wang, B. McClelland, P.M. Zavracky, N.E. McGruer, and R.H. Morrison, "Study of Tunneling Noise Using Surface-Micromachined Tunneling Tip Devices," *1997 International Conference on Solid State Sensors and Actuators* 467 (1997).
23. Lee, G.U., Kidwell, D.A., Colton, R.J., "Sensing discrete streptavidin-biotin interactions with atomic force microscopy," *Langmuir*, 10, 354 (1994).
24. Moores, S.L., Sabry, J.H., and Spudich, J.A. "Myosin dynamics in live Dictyostelium cells (green fluorescent protein)", *Proc. Natl. Acad. Sci*. 93, 443-446 (1996).
25. C.L. Adams, Y-T Chen, S.J. Smith, W.J. Nelson, "Mechanisms of Epithelial Cell-Cell Adhesion and Cell Compaction Revealed by High-resolution Tracking of E-Cadherin-Green Fluorescent Protein," *The Journal of Cell Biology* 142, 1105 (1998).
26. M. Rief et.al. "Reversible unfolding of individual titin immunoglobulin domains by AFM," *Science* 276 (5315) : 1109 (1997).
27. K. Autumn, et.al., "How Gecko Feet Work", *American Zoologist* 39, 621 (1999).
28.A.S. Yap, W.M. Brieher, M. Pruschy, B.M. Gumbiner, "Lateral clustering of the adhesive ectodomain: A fundamental determinant of cadherin function", *Current Biology* 7, 308 (1997)
29. T. Hugel, et.al., "Elasticity of single polyelectrolyte chains and their desorption from solid supports studied by AFM based single molecule force spectroscopy", *Macromolecules* 34, 1039 (2001).
30. W. Baumgartner, et.al., "Determination of the unbinding force of hemophilic interaction of vascular endothelial cadherin by atomic force microscopy", *Biophysics Journal* 76, A351 (1999).
31. H.R. Schmidt, "Zur Anatoomie und Physiologie der Geckopfote", *Jena Z. Naturw* 39, 551 (1904).
32. K. Autumn, Y. Liang, W.P. Chan, T. Hsieh, R. Fearing, T.W. Kenny, and R. Full, Dry Adhesive Force of a Single Gecko Foot-Hair, *Nature.* 405: 681-685 (2000).

A WATER-POWERED MICRO DRUG DELIVERY SYSTEM

Yu-Chuan Su, Liwei Lin, and Albert P. Pisano
Department of Mechanical Engineering and Berkeley Sensor & Actuator Center
University of California at Berkeley
Berkeley, CA 94720-1740

ABSTRACT

This paper presents a plastic micro drug delivery system that draws power directly from water without using any electrical power and delivers liquid drugs with pressure up to 25 MPa to overcome possible blockages from microorganisms. The system consists of an osmotic micro-actuator, a drug reservoir, a microfluidic channel to control the diffusive flow of drug, and a drug delivery port. The actuating membrane has an initial diameter of 800 µm and the length of the microfluidic channel is 1 cm with a cross section of 30 x 100 μm^2. Using oxygen plasma to activate polymer surfaces, simultaneous sealing (in the presence of water) and encapsulation of liquid are accomplished. Employing the net water flow induced by osmosis, this prototype drug delivery system has a measured, constant delivery rate at 0.2 µl/hr for an operation period of 10 hours with a delivery volume of 2 µl. The delivery rate and volume can be designed to target specific disease for the treatment period of hours up to years. As such, this micro drug delivery system has strong potential in biomedical applications.

INTRODUCTION

In recent years, MEMS (Microelectromechanical Systems) techniques have been applied to a variety of medical research to both improve the performance of existing devices and to explore new territories that realized by the advanced micro-machining technologies. Drug delivery, which covers a broad range of techniques for transporting therapeutic agents into the human body, remains an important challenge in medicine and the applications of MEMS techniques may have open up new research opportunities.

Implantable, controlled-release drug delivery systems offer benefits over repetitive administration of conventional drug therapy by providing unattended continuous delivery within the therapeutic window. Avoiding highly variable peak concentrations often seen after immediate release of doses, constant drug concentration delivery systems as the one presented in this paper can result in enhanced drug efficacy and minimized side effects [1]. Furthermore, these systems have the potential to provide alternative paths to deliver special drug components such as proteins and peptides, which are often difficult to administrate due to rapid degradation and poor absorption in the gastrointestinal tract. Another example is macromolecule, which is difficult to deliver by other techniques [2].

Osmotic drug delivery systems have been used for both oral and implantable constant-rate drug delivery for decades [3]. Previously, we have demonstrated an osmotic micro-actuator by means of microfabrication [4]. This work presents the advances in an all-plastic, micro drug delivery system. Three technical accomplishments have been achieved in this work: (1) bonding of PDMS with barrier polymers by introducing an intermediate elastomer layer for system integration; (2) direct liquid encapsulation and sealing at room temperature in the presence of water; and (3) delivery rates up to 20 times faster than previous achieved in microscale osmotic actuation. Powered by osmosis, this micro drug delivery system has the potential as an implantable drug delivery system to provide constant-rate drug release profiles.

PRINCIPLES AND THEORETICAL MODELS

A schematic diagram of the micro drug delivery system is illustrated in Figure 1. The system is composed of two major parts: the osmotic actuator at the bottom and microfluidic components including the drug storage reservoir and the delivery channel at the top. The details of the micro osmotic actuator have been reported previously [4] while the top part is made of Polydimethylsiloxane (PDMS) to form the drug reservoir and the delivery channel. Induced by the concentration difference across the semipermeable membrane at the bottom of the osmotic actuator, water from aqueous environment is drawn through the semipermeable membrane into the chamber filled with osmotic driving agent to power the drug delivery system. By virtue of the incompressibility of water, the top actuating membrane, which is hundreds of times more flexible than the bottom semipermeable membrane, expands to drive and release the liquid drug stored in the reservoir. The convective flow rate of drug driven out of the reservoir can be represented as follows:

$$Q_{dc} = C_d \cdot Q_c \qquad (1)$$

where Q_{dc} is the convective flow rate of drug, C_d is the concentration of drug in the formulation within reservoir, and Q_c is the overall convective flow rate of drug and its diluents, which is equal to the expansion rate of the actuating membrane.

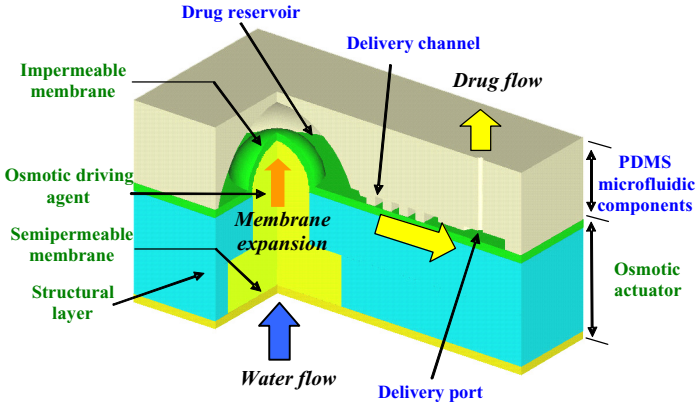

Figure 1. *A schematic diagram of the micro drug delivery system. The integration of PDMS microfluidic components and osmotic actuator is achieved by plasma-activated bonding.*

In addition to convective flow, drug is also released to outside environment by diffusion. The diffusive flow rate of drug through the delivery channel can be simplified as follows:

$$Q_{dd} = DA\Delta C_d / L \qquad (2)$$

where Q_{dd} is the diffusive flow rate of drug, D is the diffusivity of drug through the delivery channel, A is the cross-sectional area of the delivery channel, ΔC_d is the difference of drug concentration between inside reservoir and outside environment, and L is the length of delivery channel. Generally, the drug concentration in

0-9640024-4-2/hh2002/$20©2002TRF
DOI 10.31438/trf.hh2002.18

Solid-State Sensors, Actuators, and Microsystems Workshop
Hilton Head Island, South Carolina, June 2-6, 2002

the inside reservoir is much higher than the drug concentration in the outside environment such that ΔC_d can be approximated by C_d. It is desired to keep the diffusive flow rate of drug much less than the convective flow rate of drug such that the release rate of drug will be constant and controlled by osmosis. A performance index can be defined as follows [2]:

$$I_c = \frac{Q_{dd}}{Q_{dc}} = \frac{DA}{Q_c L} \qquad (3)$$

where I_c is the ratio of diffusive flow rate to convective flow rate of drug, which defines the consistency of drug flow and lower values indicate better consistency. With specified drug diffusivity and delivery rate, smaller cross-sectional area and longer length of the delivery channel will improve the consistency but also increase the pressure drop across the delivery channel, which can be represented as follows [5]:

$$\Delta P = \frac{12 Q_c \mu L}{w h^3}\left[1 - \frac{h}{w}\left(\frac{192}{\pi^5}\sum_{n=1}^{\infty}\frac{1}{n^5}\tanh\left(\frac{n\pi w}{h}\right)\right)\right]^{-1} \qquad (4)$$

where ΔP is the pressure drop across the delivery channel, μ is the viscosity of the formulation within reservoir, w is the width of the delivery channel, and h is the height of the delivery channel. The pressure drop should be kept under less than 10% of the driving pressure the actuator can provide to assure normal operation of the overall system.

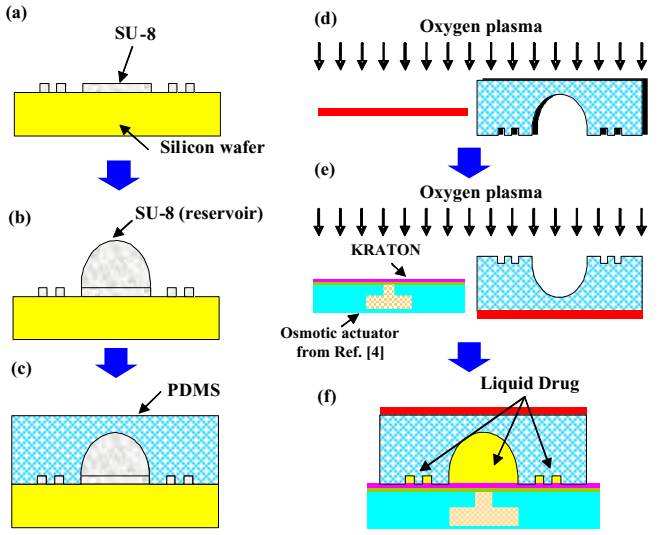

Figure 2. *Fabrication process of the micro drug delivery system.*

FABRICATION PROCESS

Figure 2 shows the fabrication process of the micro drug delivery system. A layer of 100 µm thick negative photoresist (MicroChem SU-8 100) is spin-coated and patterned on top of a clean silicon wafer to create a mold for duplicating microfluidic components in the following polymer casting process as shown in Figure 2(a). Placing a droplet of SU-8 on top of the designated spot naturally forms the dome-shape mold of drug reservoir as shown in Figure 2(b). Because of its high viscosity, the SU-8 dome can be more than 1 mm tall and the actual height can be controlled by temperature. After the SU-8 mold is fully UV cured, it is placed in a desiccator under vacuum for 2 hours with a vial containing a few drops of tridecafluoro-1,1,2,2-tetrahydrooctyl-1-trichlorosilane to silanize the surfaces [6]. Silanization of the mold facilitates the removal of the polymeric replica after casting. Figure 3 shows the SEM micrograph of the SU-8 mold where the drug reservoir is 1.8 mm in diameter and 800 µm in height.

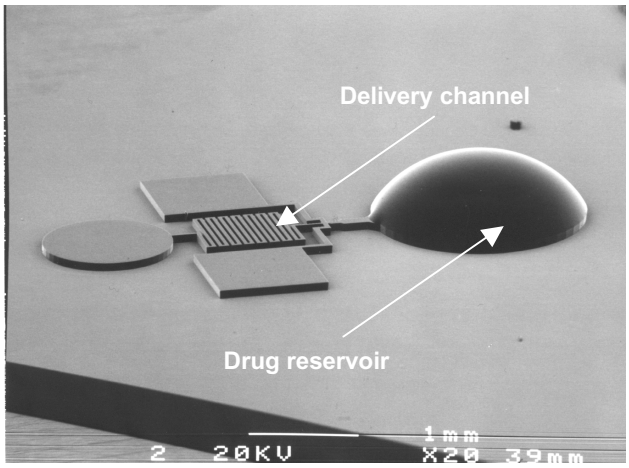

Figure 3. *SEM micrograph of SU-8 mold for PDMS casting (process step b in Figure 2).*

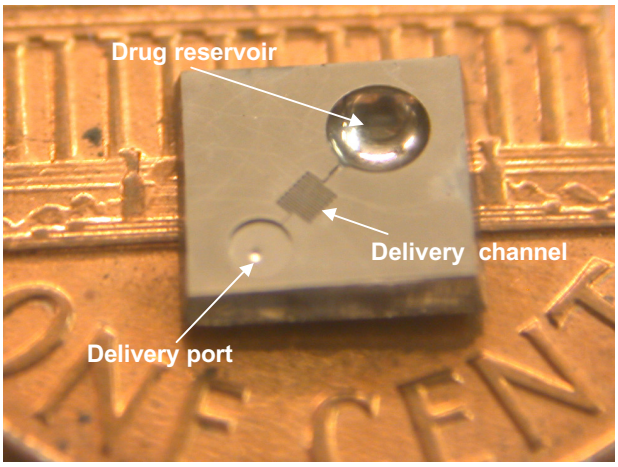

Figure 4. *The water-powered drug delivery system pictured with a one-cent coin showing the drug reservoir, delivery channel, and delivery port.*

A mixture of 10:1 PDMS prepolymer and curing agent (Dow-Corning Sylgard 184) is stirred thoroughly and then degassed under vacuum. The prepolymer and curing agent mixture is then poured onto the mold, degassed, and cured for 1 hour at 75 °C as shown in Figure 2(c). Before PDMS is fully cured, a needle is inserted to form a delivery port (for flow rate measurement, not shown in the figure). After thoroughly curved, this PDMS replica is then peeled off from the mold and the needle is removed. Figure 4 is the molded PDMS replica containing microfluidic channel with a one-cent coin. Because PDMS is permeable to vapor, a 15 µm thick barrier film (DuPont Mylar M45) is added on back of the replica as shown in Figure 2(d) to prevent liquid in the reservoir from evaporating and diffusing into outside environment. Native PDMS has low surface energy and cannot form strong enough bonding with Mylar. To prepare surfaces to achieve reliable bonding, both PDMS and Mylar surfaces are treated by oxygen plasma. These treated surfaces finally form strong bonding.

Figure 5 shows the SEM micrograph of the bonding interface between PDMS and Mylar.

The major challenge of the integration process of a micro osmotic actuator (process details described previously [4]) and the PDMS replica is the bonding process. The top layer of the osmotic micro-actuator is a flexible and impermeable membrane made of vinylidene chloride and acrylonitrile copolymer (Dow Saran F-310) that cannot form strong bonding with PDMS even after plasma treatment [6]. For polymers cannot be directly bonded with PDMS by plasma treatment, we spin-coat an intermediate layer to facilitate bonding. Styrene-isoprene-styrene (S-I-S) copolymer (KRATON D-1193) is dissolved in toluene and spin-coated on top of the Saran membrane to form a 30 μm thick intermediate layer. Both KRATON and PDMS are then exposed to oxygen plasma to activate the bonding surfaces (Fig. 2e) using a parallel-plate plasma etching system (Technics PE-IIA). Strong bonding can be achieved once two surfaces are brought to conformal contact. It has been reported that treated PDMS surface becomes hydrophilic and remains active for bonding if it is placed under liquid immediately after treatment [6,7]. Because the actuating membrane only moves in one direction, additional efforts are required to feed liquid drug into the drug reservoir and microfluidic channel. For aqueous drugs, since both treated surfaces are hydrophilic and the appearance of liquid around the bonding interface will not disturb the bonding process, liquid drug can fill microfluidic channel spontaneously and be encapsulated by employing the plasma-activated bonding process (Fig. 2f). The extra liquid drug in the gap between two bonding surfaces will eventually evaporate and strong bonding will be achieved once two surfaces are in contact. The cross-sectional view of the assembled micro drug delivery system is shown in Figure 6 where the thickness of the PDMS layer is 1.5 mm.

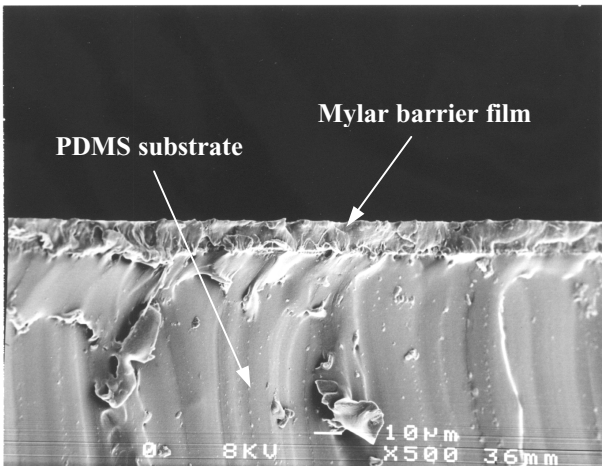

Figure 5. *Cross-sectional SEM micrograph of the bonding interface between PDMS substrate and Mylar barrier film.*

MEASUREMENT RESULTS

Flow rate measurement is conducted to verify the operation principles and design concepts. The released liquid flow from the fabricated micro drug delivery system is directed to a transparent polymer tube and the flow rate is estimated by tracing the movement of liquid-air interface in the tube. Polyimide tube of 310 μm in outer diameter, 275 μm in inner diameter, and 5 cm in length is inserted to the delivery port as shown in Figure 7 (the tube is cut to show its cross section). The gap between tube and delivery port is filled by pouring and curing additional PDMS prepolymer mixture around the connection. This will prevent the measurement error caused by leak. Another measurement error may come from the loss of liquid to outside environment by evaporation and diffusion. To estimate the loss of evaporation and diffusion along the tube, the following equation is used [8]:

$$Q_{dv} = \frac{D_v P M_w A}{R_0 T L} \ln \frac{P_{A_2}}{P_{A_1}} \qquad (5)$$

where Q_{dv} is the rate of liquid loss by evaporation and diffusion, D_v is the diffusivity of vapor along the tube, P is the total pressure, M_w is the molecular weight of liquid, A is the cross-sectional area of the tube, R_0 is the universal gas constant, T is the absolute temperature, L is the length of tube, and P_{Ai} is the partial pressure of air at each end. Using tubes with small area to length ratios, the loss by evaporation and diffusion can be reduced. Considering water evaporating in a tube of 5 cm in length and 275 μm in diameter at room temperature, this loss by evaporation and diffusion is 0.00256 μl/hr, which is 1.3% of the overall convective flow rate. Figure 8 shows the measured total delivery volume with respect to time. The delivery rate is observed at 0.2 μl/hr for an operation period of 10 hours.

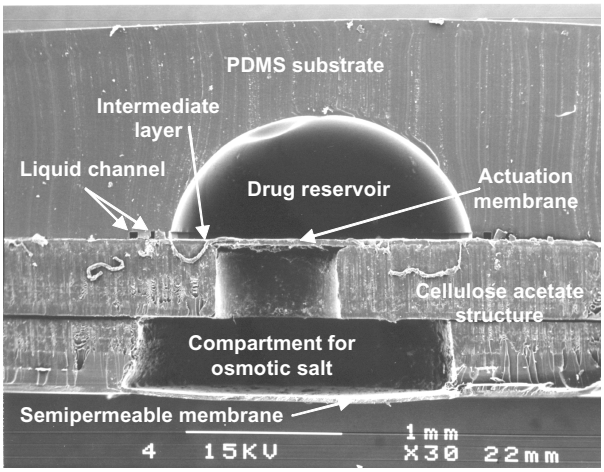

Figure 6. *Cross-sectional SEM micrograph of the assembled micro drug delivery system.*

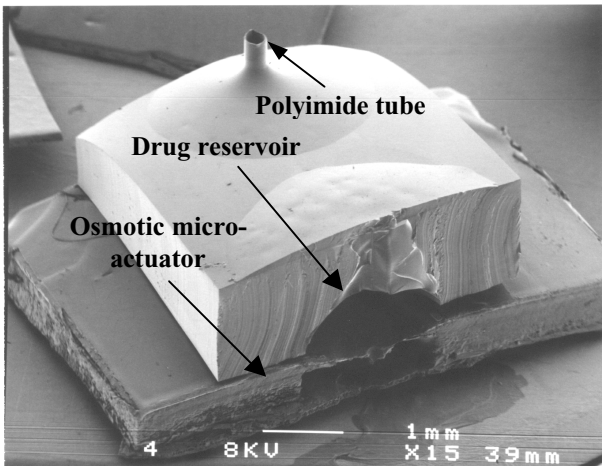

Figure 7. *SEM micrograph of the micro drug delivery system with polyimide tube inserted for flow rate measurement.*

DISCUSSIONS

The length and cross-sectional area of the delivery channel are chosen to make sure that: (1) the diffusive flow rate of exiting drug is much lower than the convective flow rate of exiting drug such that the total drug delivery rate will keep consistent; and (2) the diffusive flow rate of entering fluid is much lower than the convective flow rate of exiting drug such that contamination, destabilizing, and diluting is minimized. To verify our current design, the following real values are used: L = 1 cm, Q_c = 0.2 µl/hr, D = 2x10^{-10} m^2/s, μ = 500 centipoise, w = 30 µm, h = 100 µm, and A = 30 µm x 100 µm. Applying Equation 3 and 4, the calculation indicates that I_c = 0.00108 and ΔP = 873 Pa. Even though the flow resistance across the delivery channel is high (~10^{16} kg/m^{4}s), the resulted pressure drop is negligible compared to the driving pressure an osmotic actuator can provide because of the low drug flow rate.

Pressure drop will increase significantly if highly viscous drugs such as suspensions are delivered. Considering a suspension with viscosity (μ) equal to 50,000 centipoise being driven through the same microchannel with the same flow rate as the previous example, the pressure drop ΔP in this case will increase to 87 kPa while I_c remain around 0.001. In order to keep the flow consistent and stable, it is desired to minimize both I_c and ΔP. For example, by increasing both cross-sectional area and length of the delivery channel to 4 times of the previous values, pressure drop will be reduced to 22 kPa while I_c remain the same value. For designing delivery channel in demand of transporting high viscosity drugs, another performance index can be defined as follows:

$$I_s = \frac{I_c}{(\Delta P)^{-1}} \propto \frac{D\mu}{A} \qquad (6)$$

where I_s defines the efficiency of simultaneously minimizing I_c and ΔP and lower values indicate higher efficiency. With specified drug diffusivity and viscosity, cross-sectional area is the dominant factor for improving the overall performance considering both pressure drop and diffusive flow.

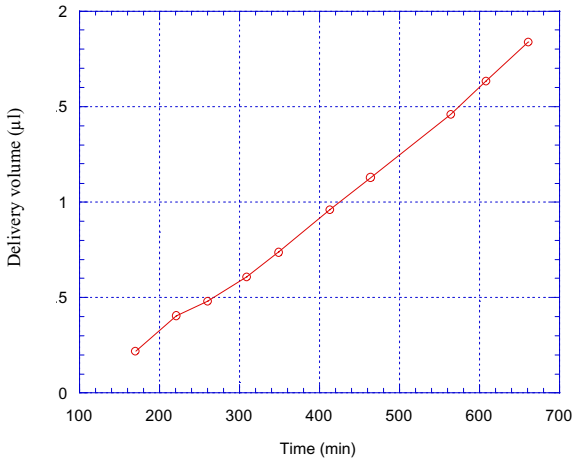

Figure 8. *Measured delivery volume with respect to time of the micro drug delivery system.*

Osmotic systems for the delivery of drugs to animals are well known. For implantation applications, larger drug reservoirs are preferred because their long working period will make replacement surgery less frequently. The current design of the micro drug delivery system can be modified to increase the delivery volume by increasing the area of the impermeable actuating membrane on top of the osmotic actuator as well as increasing the volume of the drug reservoir. The drug delivery rate can also be altered to be faster or slower by changing the area, thickness, and permeability of the semipermeable membrane. Biocompatibility, durability, reliability, and reactivity to drugs of the micro drug delivery system are major criteria for its potential implantation applications. Further investigation and improvement are required.

CONCLUSIONS

A plastic micro drug delivery system that draws power directly from water without any electrical power consumption is demonstrated. The system delivers liquid drugs with pressure up to 25 MPa and the prototype design that utilizes a system volume of about 2.5 x 2.5 x 2 mm^3 can deliver fluid drugs of 2 µl with a constant delivery rate at 0.2 µl/hr for an operation period of 10 hours. Furthermore, the micro drug delivery system is made of biocompatible polymers including cellulose acetate and PDMS for biomedical applications. Three technical accomplishments have been achieved in this work: (1) bonding of PDMS with barrier polymers by introducing an intermediate elastomer layer for system integration; (2) direct liquid encapsulation and sealing at room temperature in the presence of water; and (3) delivery rates up to 20 times faster than previously reported results. In order to precisely control the drug delivery rate, it is found that the design of the drug delivery microchannel is critical and a performance index is proposed with respect to the cross-sectional area of the microchannel and the properties of the liquid drug.

ACKNOWLEGEMENTS

The authors would like to thank Alza, Dow, DuPont, and Kraton for providing testing samples. These devices are fabricated in the UC-Berkeley Microfabrication Lab. (silicon and SU-8 molds) and Microsystem Lab. (plastic parts). This work is supported in part by DARPA/MTO/BioFlips Grant F30602-00-2-0566.

REFERENCES

1. C.L. Stevenson, F. Theeuwes, and J.C. Wright, "Osmotic Implantable Delivery Systems", Chapter 11, Handbook of Pharmaceutical Controlled Release Technology, Marcel Dekker, 2000.
2. U.S. Patent 6,156,331 (Dec. 5, 2000), Peery et al., (to Alza Corporation).
3. S. Venkatraman, N. Davar, A. Chester, and L. Kleiner, "An Overview of Controlled Release Systems", Chapter 22, Handbook of Pharmaceutical Controlled Release Technology, Marcel Dekker, 2000.
4. Y-C. Su, L Lin, and A.P. Pisano, "Water-Powered, Osmotic Microactuator", IEEE MEMS2001 Conference, pp. 393-396, 2001.
5. K. Foster and G.A. Parker, Fluidics: Components and Circuits, Wiley, 1970.
6. D.C. Duffy, J.C. Mcdonald, Olivier, J.A. Schueller, and G.M. Whitesides, "Rapid Prototyping of Microfluidic Systems in Poly(dimethylsiloxane)", Analytical Chemistry, Vol. 70, pp. 4974-4984, 1998.
7. B-H. Jo, L.M.V. Lerberghe, K.M. Motsegood, and D.J. Beebe, "Three-Dimensional Micro-Channel Fabrication in Poly-dimethylsiloxane (PDMS) Elastomer", IEEE Journal of Micro-electromechanical Systems, Vol. 9, pp. 76-81, 2000.
8. J.P. Holman, Heat Transfer, McGraw-Hill, 1992.

DERMAL THERMO-PORATION WITH A PDMS-BASED PATCH FOR TRANSDERMAL BIOMOLECULAR DETECTION

M. Paranjape[1,2], J. Garra[2], S. Brida[2], T. Schneider[2,4], R. White[2,4], J. Currie[1,2,3]

[1]Department of Physics, Georgetown University, Washington D.C. 20057
[2]Georgetown Advanced Electronics Laboratory (GAEL), Washington D.C. 20057
[3]Department of Pharmacology, Georgetown University, Washington D.C. 20057
[4]Science Applications International Corporation (SAIC), McLean, VA 22102

ABSTRACT

This paper describes the fabrication of an adhesive bandage, consisting of a stack of compliant polydimethylsiloxane (PDMS) microfluidic elements, to perform controlled and non-invasive transdermal (through the skin) sampling of bio-molecules. The patch-like device will be worn on the skin, and has two PDMS component layers that form vertically oriented micro-fluidic channels and reservoirs. In addition, micro-heaters are integrated onto the PDMS layer that will be in contact with the skin, and are used sequentially to thermally ablate tiny micro-pores through only the dead skin layer, allowing for easier diffusion of the normally trapped bio-molecules to the skin surface. The micro-channels and fluid-filled reservoirs assist in transporting these bio-molecules from just beneath the dead skin layer to a colorimetric absorbent paper detector situated on top of the bi-layer PDMS patch. This paper will focus on the fabrication of the prototype PDMS patch. A brief introduction to the operation of the patch microsystem is first presented.

INTRODUCTION

A means of non-invasive and real-time sampling of specific bio-molecules from the interstitial fluid would provide an important and convenient means for monitoring individuals prone to high health risks, such as those exposed to environmental, chemical, or biological hazards, have predisposed health conditions, or need to be closely monitored following illness. The polydimethylsiloxane (PDMS) based skin patch being presented in this paper is a novel bioMEMS device relying on the advances made in microfabrication technologies related to both PDMS and thick SU-8 photoresist mold processing **[1-3]**. The prototype of the PDMS patch will be used to sample glucose however the development of this microsystem will provide an enabling technology for transdermal sampling of other bio-molecules that do not normally diffuse across the skin **[4]**. Due to the large size of many bio-molecules of medical relevance, they are unable to penetrate the densely packed layers of dead skin (stratum corneum, or SC) cells to reach the skin surface. The dead skin layer, in an unbroken state, acts as a very effective seal against interstitial fluid leakage and bio-molecular containment. When the seal is compromised, the interstitial fluid and the bio-molecules contained therein become available on the skin surface.

The method by which large bio-molecules, such as glucose, can reach the skin surface for subsequent analysis by the PDMS patch is by opening a microscopic region of the stratum corneum to allow the glucose (and other bio-molecules) to diffuse naturally to the skin surface. By locally applying a high temperature in proximity to the skin surface, the dead skin cells can be thermally ablated, or vaporized, using micro-heaters integrated on the PDMS layer closest to the skin surface. By regulating the current through a resistive heater and its time duration, the generated heat pulse can be controlled to such an extent that neither living tissue nor nerves are affected by the momentary elevation in temperature.

A cross-sectional view of the PDMS adhesive patch is shown in Fig. 1, comprising of a micro-fluidic sampling system coupled with a thermal ablation system allowing body analyte sampling at the Stratum Corneum (SC)/Viable Epidermis (VE) interface without invasive extraction of interstitial fluid. Upon creation of a micro-pore opening in the dead skin layer (SC), perfusion of the bio-molecules will be used in a non-inflammatory collection strategy. On-patch reservoirs encapsulating physiological fluid are used for bio-molecule perfusion, while capillary channels enable fluid transfer between the skin surface and the glucose detector. These components are illustrated in Fig. 1 (not to scale), showing three separate analysis systems, each in different states of transdermal transfer operation, described later. Each analysis system can be addressed individually and on-demand, as dictated by the use of the PDMS patch.

From Fig. 1, the microfluidic system can be viewed as three distinct PDMS levels rather than two: 1. the capillary level that forms the reservoir and transport capillaries, 2. the dermal interface, which provides the bottom seal to the reservoir and contains the thermal micro-ablation heaters, and 3. the detector interface that is in contact with the detector patch and provides the top seal for the reservoir. The operation of the device and the function of each level will be described in the following sections.

PDMS PATCH OPERATION

The PDMS-based patch is a macro-sized device approximately 1 cm^2 in dimension, containing 25 individually addressable analysis systems for programmed or on-demand use. Both back and front sides of the prototype biomolecular detection bandage have been shown in Figs. 2 and 3. The colorimetric detection patch, produced by Dermal Systems International (DSI, San Francisco, CA) situated above the capillary channels changes color depending on the concentration of glucose being sampled. A representative color dot (boxed area of Fig. 3) has been magnified in Fig. 4. Additionally, the gray-scale gradient with corresponding glucose concentrations has been given.

The patch operates at the micron level to transport and detect bio-molecules from the host's interstitial fluid. This is accomplished by enhancing transdermal transfer of bio-molecules to a physiological sampling fluid, which is released by the PDMS patch during a sampling operation. The physiological fluid is normally encapsulated in a reservoir but is released using a bubble drive mechanism through electrolysis that forces this liquid out of the reservoir. The physiological fluid bathes the ablated micro-pore region and the bubble-driven fluid, in conjunction with capillary action, allows for fluidic mobility towards the glucose detector. Fig. 1 depicts the three possible (controllable) states of the individual micro-capillary systems. The leftmost micro-capillary system (#1) shows an exhausted capillary-reservoir pair that has already been used for an analysis procedure. The SC has

0-9640024-4-2/hh2002/$20©2002TRF
DOI 10.31438/trf.hh2002.19

Solid-State Sensors, Actuators, and Microsystems Workshop
Hilton Head Island, South Carolina, June 2-6, 2002

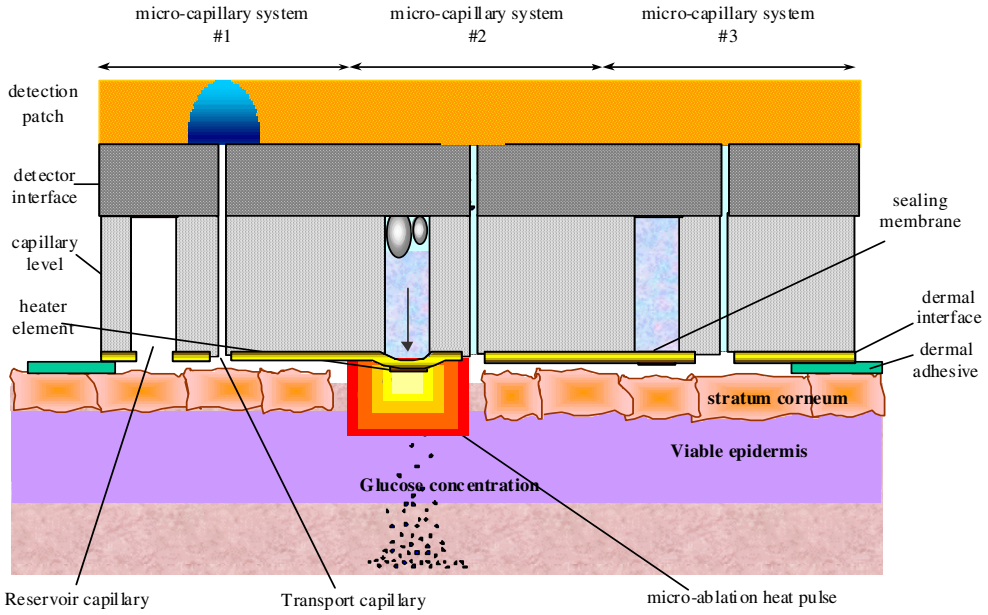

Fig. 1. *The PDMS-based patch prototype located on the skin surface showing the Stratum Corneum (SC) and Viable Epidermis (VE). The microfluidic system is separated into three levels comprising the capillary level, the dermal interface, and the detector interface. The topmost layer uses colorimetric glucose detection paper. The figure also illustrates a concentration gradient of glucose.*

restored itself some time after thermal ablation, the reservoir has emptied, and capture of glucose from the interstitial fluid has occurred, indicated by the stain on the glucose detector paper on the upper surface of the chip. The middle micro-capillary system

Fig. 2. *PDMS patch prototype (backside)*

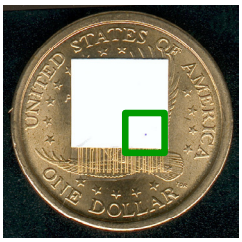

Fig. 3. *PDMS patch prototype (topside)*

(#2) is performing an on-demand analysis. The rightmost capillary system is ready for future use. The remainder of the paper is dedicated to the fabrication process involved in producing the bi-layered PDMS patch.

PDMS Patch Design Considerations

PDMS technology makes use of standard silicon-based processing yet allows for rapid, cost effective fabrication of microfluidic systems that are flexible and compliant. This is an important design consideration for a dermal patch. Furthermore, by using the transparent PDMS, alignment of the two-layer patch becomes easier using standard optical microscopes and visually aligning each level independently. The PDMS (Dow Corning, Midland, MI) structures are created using SU-8 (MicroChem Corp. Newton, MA) as the mold form. In the design of the patch, the thickness of the PDMS for both the capillary/dermal layer and detector interface is nominally 200 µm. All metal electrodes, interconnects, bonding pads and heating elements are deposited directly on the PDMS surface and patterned using sputter deposition and a selective etch **[5]**.

To facilitate ease in processing the PDMS layers, the silicone was molded onto SU-8 on glass handling-wafers. These handle wafers allow the PDMS to be placed in standard fabrication and test equipment, and more importantly, allows for simple alignment of the two levels required in the patch design. Therefore, when bonding multiple layers of PDMS together using oxygen plasma

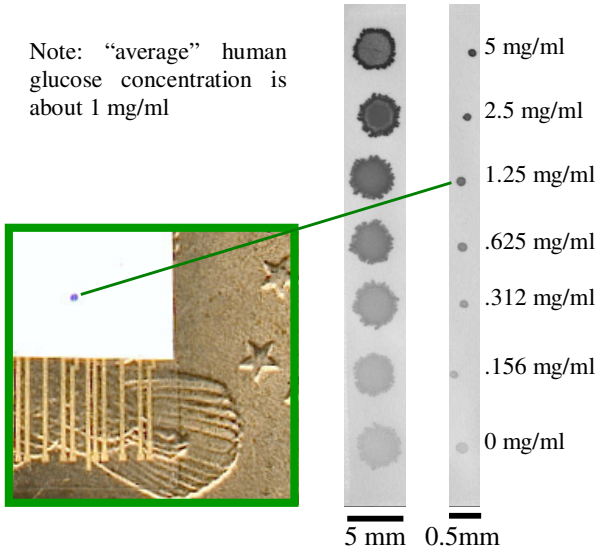

Fig. 4. *Colorimetric detector patch that gives the glucose concentration.*

treated surfaces **[6]**, it is imperative that one handle wafer remains attached to the PDMS structure. Upon completion of the final device, the last step would be to release the multi-level PDMS

stack from the remaining handle wafer. In order to process a particular side of a PDMS layer, a strategy was developed to allow for the selective removal of only one handle wafer over another. Otherwise, during a release procedure, no control would exist with regards to which handle wafer is removed. The basis of the selective release mechanism relies on a thin sacrificial layer being deposited directly onto the SU-8 mold prior to forming the PDMS structure **[7]**. Selective release is accomplished by dissolving only the sacrificial layer in a chemical etchant that does not attack any other sacrificial layer nor the structural PDMS and metalization.

FABRICATION

Microfluidic channels are typically formed in PDMS by casting a relatively thick layer of uncured polymer in a patterned SU-8 mold, as shown in Fig. 5. The SU-8 heights can range from 50-200µm, while the PDMS is usually much thicker. The channels formed in this way direct fluid flow along the surface plane of the PDMS.

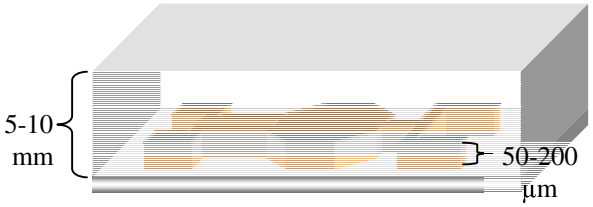

Fig. 5. *Thick PDMS layer cast in an SU-8 mold for a typical microfluidic application with channels on the surface of the PDMS.*

For the PDMS patch, precisely defined *vertical* capillary microchannels and fluid reservoirs need to be formed through the entire thickness of the PDMS layer, as shown in Fig. 6. This requires inserting the handle wafer, mold, and un-cured silicone elastomer into a specially devised mechanical jig that ensures planarity of the PDMS surface while removing excess elastomer so that the cured PDMS thickness is approximately equal to the mold relief height of the SU-8.

Fig. 6 *PDMS cast in the SU-8 mold with vertical microchannels. The large reservoir is 500µm x 500µm while the two smaller capillary channels are 100µm x 100µm. The small capillaries are separated by 100µm from each other, and from the large reservoir.*

A limitation to the mechanical jig, which presses the PDMS and mold tightly together, is that it always tends to leave behind a thin residual PDMS layer on top of the mold features, which effectively seals the top end of the channels formed by the mold. Increasing the applied force can effectively eliminate the residual layer, but too much pressure can cause the finer mold features to fracture and become lodged in the PDMS layer upon release from the mold. The layer can also be etched away in a solution of tetrabutylammonium fluroride in n-methyl-2-pyrrolidinone **[8]**. For the PDMS patch, RIE processing was used **[3]** to selectively remove the residual sealing layer above the capillary mold feature while leaving the seal intact above the reservoir region. Thus, the limitation of the press has, in fact, become an advantage since it offers a means to have the reservoir sealed on one end while rendering fluidic-vias (or *f-vias*) after dry etching the capillary region. Fig. 7 presents an optical picture and an SEM micrograph of the reservoir sealed on one side and the *f-via* capillaries running through the 200µm thick PDMS after the RIE process.

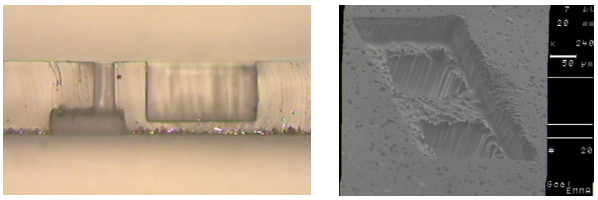

(a) (b)

Fig. 7. (a) *Cross-section of the PDMS layer showing the sealed reservoir on the right and the f-via capillary on the left. The dry etched region was designed to be larger than the capillary dimension, and* ***(b)*** *SEM showing PDMS texture after RIE processing and the oversized etch area with respect to the f-vias.*

The process flow for the two levels of the PDMS patch has been illustrated in Figs. 8 and 9. The former figure illustrates the processing on the two separate layers while the latter shows the process on the bonded microsystem. The required bonding operation of the two individual PDMS layers is accomplished by exposing the two surfaces to an oxygen plasma. In order to avoid instantaneous bonding without proper alignment, methanol is used as a surfactant to allow optical alignment of the two layers. Once aligned, the methanol is evaporated by elevated temperature **[9]**. The process flow does not illustrate the selective removal of the glass handle wafers nor are the release layers shown. Information on these techniques can be found in **[7]**.

DISCUSSION

The two-level PDMS patch was fabricated in a 5 x 5 array yielding 25 individually addressable sampling cells in a 1cm^2 area. Since this is only a prototype device, the dimensions of capillaries, reservoirs, and metalization traces were not minimized.

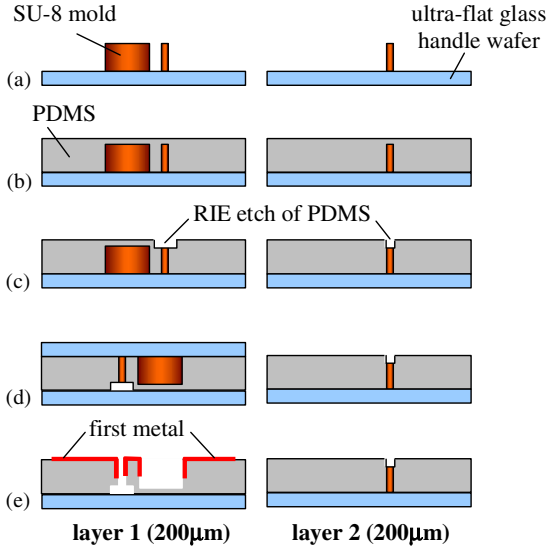

Fig. 8. *(a) Original three-level (no RIE) SU-8 mold set made on glass substrates, with heights indicated. (b) Cast PDMS in SU-8 molds. (c) Perform selective RIE to open holes in capillary regions only. (d) Bond glass substrate to top of layer 1 and turn device upside down to selectively release other glass substrate. (e) Removal of glass substrate and SU-8 from layer 1 followed by metalization of layers 1 and 2 for interconnect.*

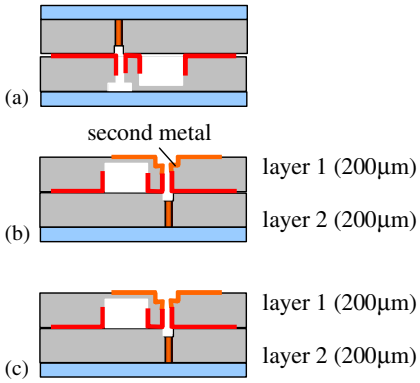

Fig. 9. *(a) Layer 2 capillary is aligned and bonded onto layer 1. (b) Turning device upside down, glass substrate from layer 1 is released and metal traces deposited, including ablation micro-heaters. (c) Re-invert to perform final glass substrate release from layer 2.*

Although fabricating bioMEMS or microfluidic systems in PDMS is a relatively simple process with fast turnaround times and low material costs, there are some limitations in working with this material. Literature suggests that typical applications of PDMS are those when routing relatively large microfluidic channels parallel to the silicone surface, as was shown in Fig. 5. In these cases, any internal stresses that may be present in the PDMS, either during curing or after release from the SU-8 mold, are not critical. In the case of the PDMS patch, stress is an important factor for two important reasons. First, since the patch is a bi-layer, any stresses must be accounted for in view of the alignment of the two layers. Secondly, the PDMS has metalization traces that should not be compromised or deformed during the curing phase of the process.

The problem of PDMS stress has produced several fabrication challenges, but most problematic is that PDMS shrinks as it is cured into a solid state. When the silicone material is cast in an SU-8 mold, internal stresses build during the curing process. The polymer wants to shrink, but it remains stretched and held in place by the SU-8 features and by its attachment at the interface to the mold substrate. Once released, the polymer is allowed to relax and contract. This is a problem for the batch fabrication of devices in PDMS because the distance between cells or individual devices decreases when the layer is released from the mold. Subsequent processing steps including photolithographic patterning of metals and alignment to other device layers is impossible because the interdevice spacing has changed. Furthermore, the stresses in the PDMS layer are not necessarily isotropic, so shrinkage percentage can vary depending on the direction.

As shown in Figs. 9 and 10, the patch prototype fabrication sequence required metalization and lithography to be performed after releasing the PDMS from the mold since the process required access to the sidewalls of the microchannel features. Metalization on a tensile PDMS substrate that is still in its mold can be problematic due to difficulties with adhesion, so the surface must be treated prior to deposition **[5]**. However, when the PDMS is finally released from the SU-8 at the end of the fabrication process, it relaxes, and the metal is subjected to strong compressive stress. The PDMS contracted as expected and more often than not, caused the metal pattern to be compromised. This buckling often caused the metal traces to detach at least partially from the PDMS substrate despite the good adhesion observed in the metal film after deposition.

CONCLUSIONS

A fabrication process for a bi-layer PDMS patch was developed for use in a dermal thermo-poration microsystem for transdermal sampling of bio-molecules. PDMS allows for rapid prototyping of compliant devices, ideal for an adhesive bandage. A 5 x 5 array of sampling cells was fabricated and tested for thermal characterization of the micro-ablation heater. Tests were conducted on surrogate (cloned) human skin, which mimics real skin in many ways including the stratum corneum thickness. Some limitations of the PDMS process include its shrinkage after removal from the SU-8 mold, resulting in misalignment and registry issues throughout the array. The compressive stresses also caused metal adhesion problems, metal and standard photoresist cracking, and PDMS delamination. Some of these problems may be resolved in the second iteration where PDMS will be replaced by silicon or SU-8 as a structural material. Such a solution may render a patch that is not as flexible as PDMS.

ACKNOWLEDGMENTS

The authors would like to thank Mr. Paul Goldey and Mr. Leon Der for their invaluable assistance in device fabrication and technical support. The assistance and contributions by the DSI staff is also gratefully acknowledged. This work is supported through a BioFlips DARPA-MTO contract (BAA 00-11, Program Manager: Dr. Michael Krihack).

REFERENCES

1. Y. Xia, G. M. Whitesides, “Soft Lithography”, Angew. Chem. Int. Ed. Engl., **37**, pp. 550-575, 1998.
2. D. C. Duffy, J. C. MacDonald, O. Schueller, G. M. Whitesides, “Rapid Prototyping of Microfluidic Systems in Polydimethylsiloxane”, Anal Chem, **70**, pp. 4974-4984, 1998.
3. J. Garra, T. Long, J. Currie, T. Schneider, R. White, M. Paranjape, “Polydimethylsiloxane (PDMS) Dry Etching for the Fabrication of Fluidic Microsystems”, Journal of Vacuum Science Technology – A, *to be published*.
4. M. Paranjape, J. Currie, C. Peck, T. Schneider, R. White, “The B-FIT Microsystem Concept”, BioMEMS and Biomedical Nanotechnology World 2000 Conf., Columbus, OH, 2000.
5. J. Garra, S. Brida, T. Schneider, J. Currie, M. Paranjape, “Metal Deposition on PDMS and SU-8 Surfaces”, 2nd DARPA Annual Progress Rep., 2001.
6. B. H. Jo, L. M. V. Lerberghe, K. M. Motsegood, and D. J. Beebe, “Three-dimensional Micro-channel Fabrication in Polydimethylsiloxane (PDMS) Elastomer”, Journal of Microelectromechanical Systems, **9**, pp. 76-81, 2000.
7. C. Luo, J. Garra, M. Cheng, S. Brida, T. Schneider, R. White, J. Currie, M. Paranjape, “Sacrificial Release Layers for PDMS and SU-8 Structures”, 2nd DARPA Annual Progress Rep., 2001.
8. S. Takayama, E. Ostuni, X. Qian, J. C. MacDonald, X. Jiang, M. Wu, P. Leduc, D. E. Ingber, G. M. Whitesides, “Patterning the Topographical Environment for Mammalian Cell Culture Using Laminar Flows in Capillaries”, IEEE-EMBS Special Topic Conference on Microtechnologies in Medicine and Biology, Lyon, France, pp. 322-325, 2000.
9. J. A. Davis, S. Raty, D. T. Eddington, I. K. Glasgow, H. C. Zeringue, M. B. Wheeler, D. J. Beebe, “Development of Microfluidic Channels for the Culture of Mammalian Embryos”, IEEE-EMBS Special Topic Conference on Microtechnologies in Medicine and Biology, Lyon, France, pp. 307-310, 2000.

DESIGN, FABRICATION AND TESTING OF A MEMS SYRINGE

Boris Stoeber, and Dorian Liepmann
Berkeley Sensor and Actuator Center, University of California at Berkeley
Berkeley, Ca 94720-1774

ABSTRACT

Drugs can be delivered effectively and painlessly into the epidermal layer under the stratum corneum above the capillary bed into which the drug diffuses. This approach has even been demonstrated for lyophilized compounds that are advantageous for many situations because of their long-term stability. For this purpose a disposable syringe has been developed and fabricated using a combination of standard silicon MEMS technology and soft lithography. The MEMS syringe is based on an array of hollow pointed silicon microneedles and a deformable PDMS (polydimethylsiloxane) reservoir for a suspension of lyophilized drug. The associated phenomenon of clog formation in the needle channel due to shear-induced particle sedimentation is described in terms of its impact on system design. The complete system has been successfully tested on a model tissue.

INTRODUCTION

The need for a technology that produces disposable devices, such as MEMS, could provide an ideal platform for the widespread distribution of pharmaceuticals such as vaccines without the need for environmentally-controlled storage. MEMS technology could also provide a means to administer a pharmaceutical compound without requiring trained personnel to prepare or give the shot. A very simple concept for a disposable syringe is shown in Fig.1. A deformable reservoir on the backside of an array of microneedles contains a lyophilized drug suspended in a non-aqueous fluid. Merely pressing the device against the skin delivers the medicine or vaccine. Such a device would be ideal for wide-spread distribution of vaccines in third-world situations where the lack of storage and trained personnel are significant problems.

Many therapeutic agents including most antibiotics are unstable in aqueous solution, which is the usual formulation for delivery. Either the medication has to be prepared just before use or the prepared formulation has to be kept cool to prolong its efficacy. Dehydrated or lyophilized compounds are significantly safer. In addition, lyophilized medications have been shown to be bio-available when injected between the stratum corneum and the capillary bed. An additional advantage is that the injection will be painless at these depths (20 – 100 ìm) in the epidermis because the needles do not reach the upper nerve cells. The drug, however, is able to diffuse deeper into the skin and is absorbed into the capillaries of the dermis.

Microneedles have been an active area of research for almost a decade [**1-11**] for biomedical applications including µTAS (micro Total Analysis Systems), yet integration of such needles into complete microsystems has not been performed mainly because of process compatibility problems. The device presented here uses two different materials, silicon and PDMS, that can be photolithographically defined to be the micro-needle array and the drug reservoir.

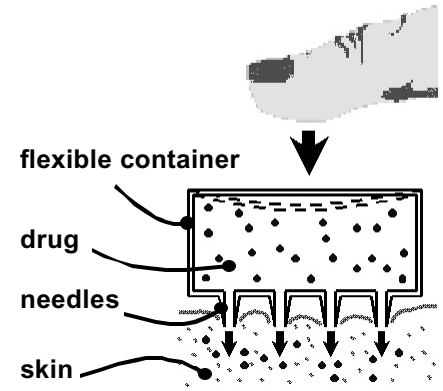

Figure 1. *Concept of a disposable MEMS syringe.*

NEEDLE DESIGN AND FABRICATION

Needles fabricated using MEMS technology can be divided into two major groups; in-plane needles where the needle shaft is fabricated in a plane parallel to the substrate [**1-5**], and out-of-plane needles, which have their shafts perpendicular to the wafer plane [**6-11**]. Some of the in-plane needle designs allow for integration of electronics, but they can only be arranged in single rows, and mainly problems associated with interconnects have prevented them from being integrated into complete micro systems. The major advantage of out-of-plane needles is the possibility to arrange them in arrays so that fluid can be delivered or sampled over a wider area making the system more stable and robust [**9**]. These considerations make arrays of hollow pointed out-of plane needle the most adaptable for a MEMS syringe, since these needles are rigid, easily penetrate the skin and have multiple orifices so that the syringe cannot be plugged unexpectedly.

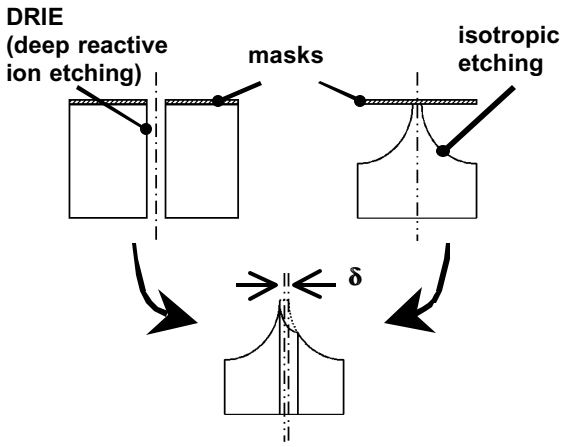

Figure 2. *Design of a pointed hollow out-of-plane needle.*

Travel support has been generously provided by the Transducers Research Foundation and by the DARPA MEMS and DARPA BioFlips programs. Research support by Becton-Dickinson and the DARPA Simbiosys program is also gratefully acknowledged. Simulations were performed using CFD ACE+ software provided by CFD Research Corporation, Huntsville, AL.

The design shown in Fig.2 has been fabricated using the Bosch process [**12**] for DRIE (deep reactive ion etching) to etch the needle channel through the substrate, while the outer shape of the needle is obtained through under-etching of a circular mask with isotropic etching techniques while the sidewalls of the needle channel is protected by a passivation layer. An offset δ of the center lines of the two corresponding etch masks results in a needle with a sharp tip on the circumference of its shaft.

Figure 3 shows an electron micrograph of such an array of needles. The design permits a density of 600 needles / cm^2 for shaft lengths of 200 µm. Figure 4 allows size comparison of such silicon needles with a conventional 26 gauge stainless steel needle.

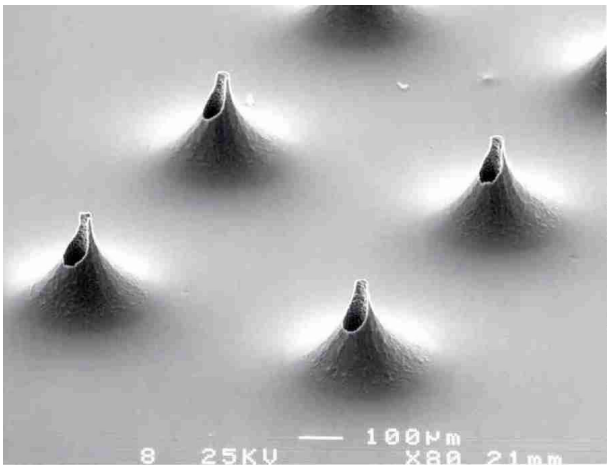

Figure 3. *Array of pointed hollow out-of-plane silicon needles with height of 200 ìm and channel diameter of 40 ìm.*

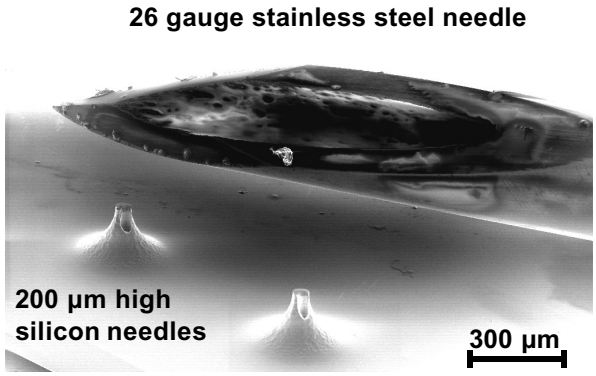

Figure 4. *Size comparison of a 26 gauge stainless steel needle and an early version of silicon needles.*

FLUID MECHANICAL DESIGN

The nature of suspension flow into contractions in the flow field sets an important design criterion for a MEMS syringe because we anticipate its use with a lyophilized drug. A model suspension of 0.7 µm large polystyrene beads in water have been shown to agglomerate at the inlet region of a D = 50 µm wide flow channel at surprisingly low flow rates q = 0.1 µl / min and particle concentrations Φ = 0.1 % as shown in Fig.5. In a short time the channel inlet completely clogs as shown in Fig.6 for 2-D suspension flow into a contraction. For any drug delivery system it is critical that the needle channnels stay open until the end of the injection process.

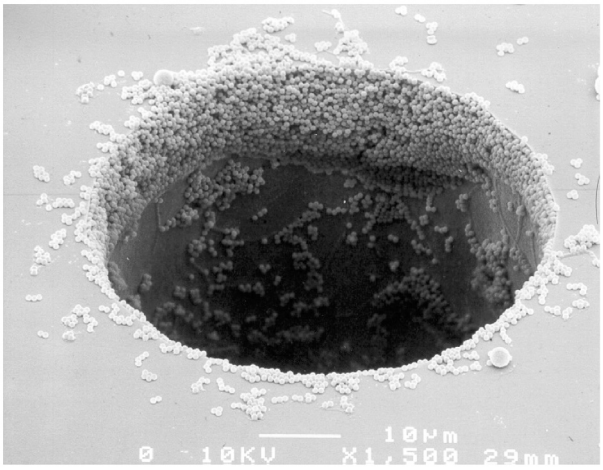

Figure 5. *0.7 µm large polystyrene beads start to agglomerate at the inlet of the flow channel.*

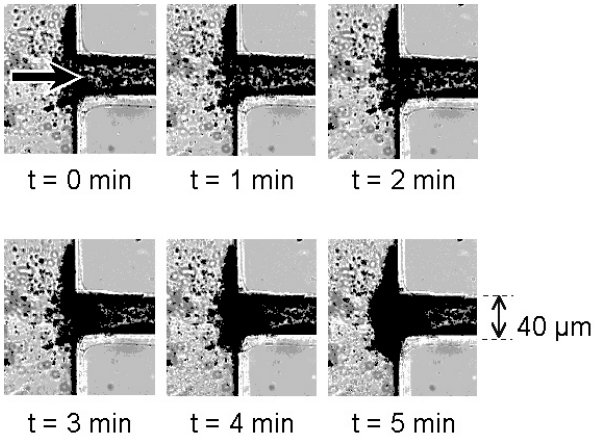

Figure 6. *Sequential video images of polystyrene beads (0.92 µm) agglomerating and finally blocking the inlet of a 2-D channel. The particles appear as dark shadows.*

Recent results based on the dimensional analysis in [**13**] show that the critical nondimensional number for this phenomenon

$$\Pi = \frac{q \cdot d^3 \cdot \tau \cdot \Phi}{D^6} \qquad (1)$$

can be used to determine a typical time scale τ for clog formation for suspension flow into a flow channel. The most critical parameter of this fluid mechanical problem is the diameter of the flow channel D, related to Eq.(1) through the size parameter D / d to the third power and through the nondimensional shear rate [**13**] $q\ \tau / D^3$. In the case where this time scale needs to be reduced and the size of the particles d is fixed the most effective adjustment can be achieved by increasing the channel diameter. However, increasing the channel diameter reduces the sharpness of the needle tip and widens the opening along the needle shaft that could result in leakage during injection. Instead of widening the entire channel, an easily fabricated two-step channel inlet can reduce the overall shear rate in the flow as shown in Fig. 7 if appropriate scaling is maintained. If the difference in diameters for these two steps is too large, the shear rate at the second contraction is identical to the shear rate in the case of a simple contraction, so that the same typical timescale for clogging can be expected. These simulations were performed using CFD ACE+ software from CFD Research Corporation.

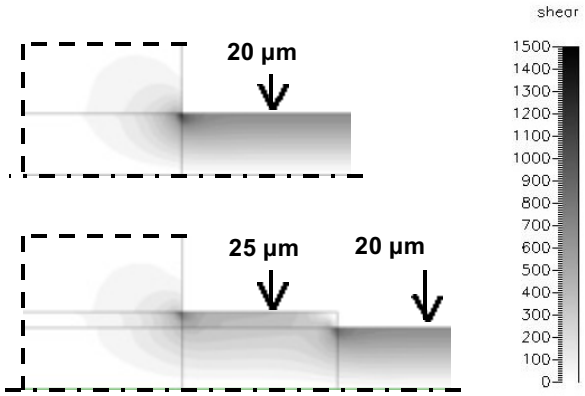

Figure 7. *Computational results showing the reduction of the maximum shear rate [1/sec] for a fluid flowing into a 40 µm wide channel at a flow rate of 2 µl / min.*

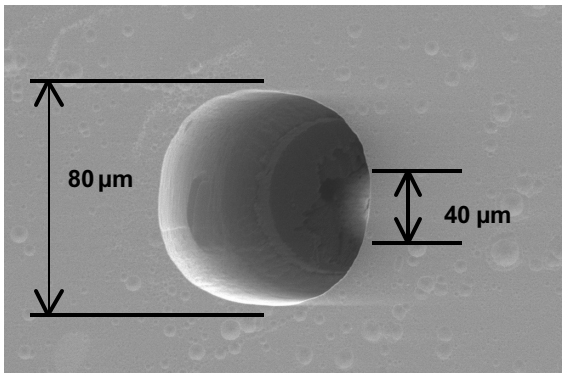

Figure 8. *2-Step channel inlet.*

CONTAINER FABRICATION AND INTEGRATION

The flexible container for the drug suspension has been fabricated out of PDMS that is chemically bonded to silicon as outlined in Fig.9. Coating a silicon mold with a monolayer of HMDS facilitates the removal of the PDMS from this mold after the casting and hardening steps as shown in Fig.10. The surface of the PDMS is then activated in a low power oxygen plasma, so that contact with the backside of the silicon micro-needle array chemically bonds these two devices together [**14**]. This process is suitable for batch fabrication of MEMS syringes because an entire wafer size PDMS sheet can be bonded to the backside of a silicon wafer. The PDMS can then be cut along silicon dye cleavage lines with a sharp blade, while these cleavage lines need to be cut into the wafer backside prior to the isotropic etching step.

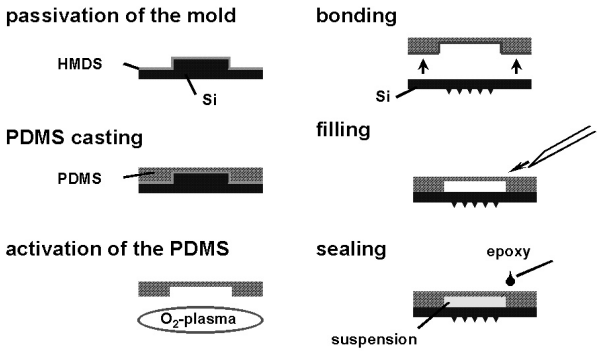

Figure 9. *Process flow for reservoir fabrication and device integration.*

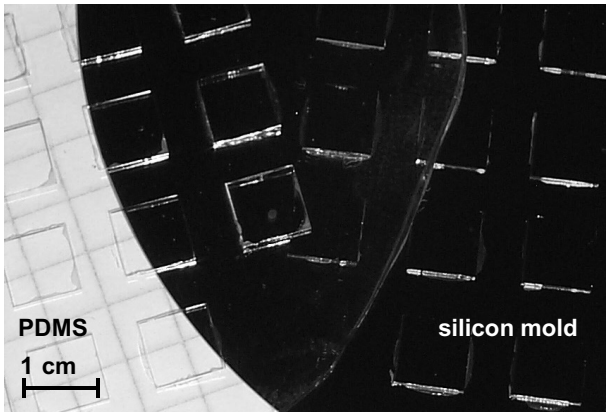

Figure 10. *PDMS sheet with container grooves peeled off its silicon mold.*

The PDMS container of the assembled MEMS syringe shown in Fig.11 has been filled with a suspension of blue polystyrene microbeads in water. Its 8 needles are spaced 1 mm apart from each other, however much larger and denser arrays of needles are possible. The PDMS container volume of 20 µl can be easily varied using different silicon molds.

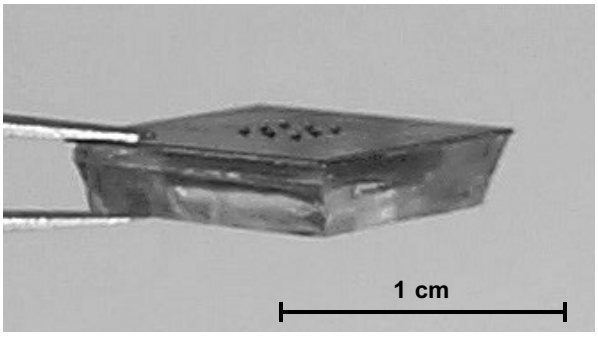

Figure 11. *A MEMS syringe with 8 microneedles and a PDMS container filled with a suspension of blue microbeads.*

TESTING OF THE MEMS SYRINGE

Aqueous suspensions of blue and fluorescent polystyrene beads were injected using a MEMS syringe into chicken breast as a model tissue. The surface of chicken flesh in Fig.12 shows the 8 injection marks of the 2x4 needle array of the syringe.

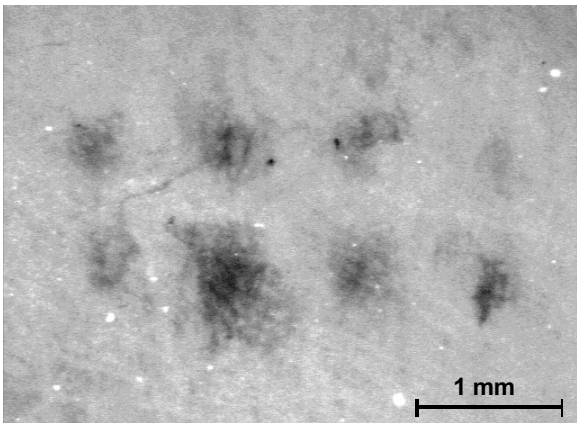

Figure 12. *Injection marks of a MEMS syringe with an array of 2x4 needles on the surface of chicken breast.*

The delivery depths of fluorescent particles have been investigated using confocal microscopy (Fig.13). These results indicate that the maximum particle concentration occurred about 20 µm under the surface, while a strong signal could still be detected at 70 µm.

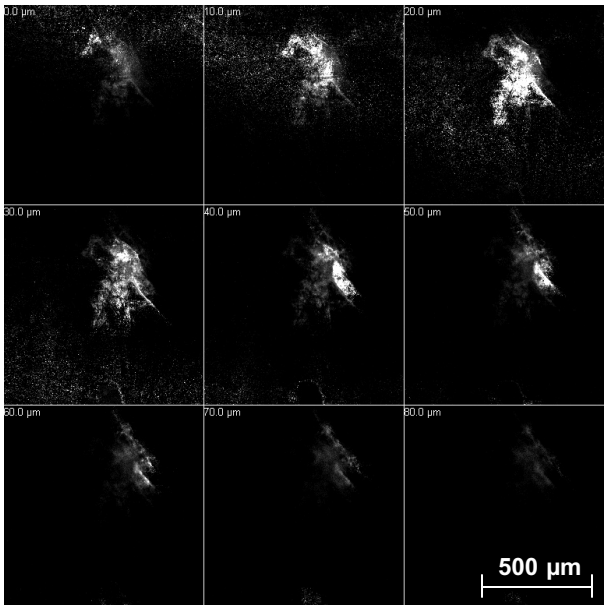

Figure 13. *Confocal microscopic images of 0.7 µm large fluorescent polystyrene beads at different depths in chicken tissue.*

Thus the injection of a suspension of microscale particles with a MEMS syringe was successfully delivered into a model tissue at the target depth.

CONCLUSIONS

A disposable syringe has been fabricated in MEMS technology, and it has been successfully tested for injection of a sample suspension into a model tissue. The micro-particles were delivered at an appropriate depth for human skin, below the stratum corneum and above the nerves, which exist deeper in the dermal layer. Design solutions have been proposed to avoid the possibility of clog formation in the needle channels due to shear induced sedimentation of the solid phase of a drug suspension.

These results indicate that the MEMS syringe is a very promising and potentially very useful biomedical tool. However, further experiments to directly monitor drug absorption by the body would be necessary for a final validation of this drug delivery concept. In addition to delivery efficiency of the device, it will also be critical to determine how much of drug in the reservoir is delivered and its reproducibility accounting for person-to-person variability. For this reason we see this device as a tool for vaccines and antibiotics where over-dosing is not a significant problem.

REFERENCES

1. L. Lin, A.P. Pisano, and R.S. Muller, "Silicon Processed Microneedles", Proceedings ot the 7th International Conference on Solid-State Sensors and Actuators (Transducers'93)*, Yokohama, Japan , 06/07-10/93, Institute of Electrical Engineers of Japan, Tokyo (1993), pp. 237-240.*

2. J. Chen, K.D. Wise, "A Multichannel Neural Probe for Selective Chemical Delivery at the Cellular Level", ", Technical Digest of the 1994 Solid-State Sensor and Actuator Workshop*, Hilton Head Isl., SC, 06/13-16/94, Transducer Research Foundation, Cleveland (1994), pp. 256-259.*

3. N.H. Talbot, A.P. Pisano, "Polymolding: Two Wafer Polysilicon Micromolding of closed Flow Passages for Microneedles and Microfluidic Devices", Technical Digest of the 1998 Solid-State Sensor and Actuator Workshop*, Hilton Head Isl., SC, 06/8-11/98, Transducer Research Foundation, Cleveland (1998), pp. 265-268.*

4. K.S. Lebouitz, and A.P. Pisano, "Microneedles and Microlancets fabricated using SOI wafers and isotropic etching", Proceedings of the Symposium on Microstructures and Microfabricated Systems IV*, Boston, MA, 11/1-6/98, Electrochemical Society, Pennington, NJ (1998), pp. 235-244.*

5. J. Brazzle, D. Bartholomeusz, R. Davies, J. Andrade, R.A. Van Wagenen, and A.B. Frazier, "Active Microneedles with Integrated Functionality", Technical Digest of the 2000 Solid-State Sensor and Actuator Workshop*, Hilton Head Isl., SC, 06/04-08/00, Transducer Research Foundation, Cleveland (2000), pp. 199-202.*

6. S. Henry, D.V. McAllister, M.G. Allen, and M.R. Prausnitz., "Microfabricated Microneedles: A Novel Approach to Transdermal Drug Delivery", Journal of Pharmaceutical Sciences, 87*, 8, pp. 922-925, (1998).*

7. D.V. McAllister, F. Cros, S.P Davis, L.M. Matta, M.R. Prausnitz, and M.G. Allen, "Tree-Dimensional Hollow Microneedle and Microtube Arrays", Proceedings of the 10th International Conference on Solid-State Sensors and Actuators (Transducers'99) *, Sendai, Japan 06/7-10/99, Institute of Electrical Engineers of Japan, Tokyo (1999), pp. 1098-1101.*

8. K. Chun, G. Hshiguchi, H. Toshiyoshi, H.Fujita, Y. Kikuchi, J. Ishikawa, Y. Murakami, and E. Tamiya, "An Array of Hollow Microcapillaries for the Controlled Injection of Genetic Materials into Animal/Plant Cells", Proceedings of 12th International Workshop on Micro Electro Mechanical Systems*, Orlando, FL, 01/17-21/99, IEEE, Piscataway (1999), pp. 406-412.*

9. B. Stoeber, and D. Liepmann, "Fluid Injection Through Out-Of-Plane Microneedles", Proceedings of 1st Annual International IEEE-EMBS Special Topic Conference on Microtechnologies in Medicine and Biology, Lyon, France, 10/12-14/00, IEEE, Piscataway (2000), pp. 224-228.

10. J.G.E. Gardeniers, J.W. Berenschot, M.J. de Boer, Y. Yeshurun, M. Hefetz, R. van 't Oever, and A. van den Berg, "Silicon Micromachined Hollow Microneedles for Transdermal Liquid Transfer", Proceedings of 15th International Conference on Micro Electro Mechanical Systems*, Las Vegas, NV, 01/20-24/02, IEEE, Piscataway (2002), pp. 141-144.*

11. P. Griss, G. Stemme, "Novel, Side Opened Out-of-Plane Microneedles for Microfluidic Transdermal Interfacing", Proceedings of 15th International Conference on Micro Electro Mechanical Systems*, Las Vegas, NV, 01/20-24/02, IEEE, Piscataway (2002), pp. 467-470.*

12. F. Lärmer, and P. Schilp, German Patent DE 4241045 (1994).

13. B. Stoeber, and D. Liepmann, "Operational Limits of Suspension Flow through Sudden Contractions", Proceedings of the 2001 ASME international Mechanical Engineering Congress and Exposition*, New York, NY, 11/11-16/01, ASME (2001), disc set vol.2, IMECE2001/MEMS-23878.*

14. D.C. Duffy, J.C. McDonald, O.J.A. Schueller, and G.M. Whitesides, "Rapid Prototyping of Microfluidic Systems in Poly(dimethylsiloxane)", Anal. Chem, 70*, pp. 4974-4984 (1998).*

A WAFER-LEVEL VACUUM PACKAGING PROCESS BY RTP ALUMINUM-TO-NITRIDE BONDING

Mu Chiao and Liwei Lin
Berkeley Sensor and Actuator Center
Department of Mechanical Engineering
University of California at Berkeley
Berkeley, CA 94720-1740 E-mail: muchiao@me.berkeley.edu

ABSTRACT

This paper presents a wafer-level MEMS vacuum packaging process by using RTP (Rapid Thermal Processing) aluminum-to-nitride bonding. The measured quality factor of a vacuum-packaged comb-resonator is 1800±200 corresponding to a 200mTorr vacuum inside the packaged micro cavity. Both long-term and accelerated vacuum stability tests are conducted to characterize the durability of the packages. It is found that the vacuum quality has not degraded over a period of 9 weeks under regular environment and over a period of 24 hours under a harsh environment(130^{o}C, 2.7atm and 100% RH) in the autoclave test. In an effort to address the issue of post-packaging frequency tuning, a pulsed laser deposition method is developed by using either indium or aluminum as the deposition material for frequency tuning. A maximum of 18.1% reduction in frequency has been achieved and a first-order, linear model is found adequate to explain the frequency tuning results.

INTRODUCTION

Vacuum packaging is an enabling technology for MEMS resonators to ensure high precision performances. For example, MEMS resonators have the advantages over conventional microelectronics for narrow bandwidth (high quality factor) applications in wireless communications[1]. Since the dominant energy loss of mechanical resonators in the micro scale is the air damping effect[2], vacuum packaging is key to achieve high quality factor. For example, the quality factor of comb-shape resonator is around 20-40 as measured in air and can be as high as 50000 in a 10^{-7}Torr vacuum[2].

Various vacuum packaging processes have been reported and drawbacks for practical implementation can be identified in previous approaches. For example, extra lithography and processing steps are required in a wafer-level, silicon nitride vacuum encapsulation process[1]. In the approach of localized resistive heating and bonding process, difficulty in wafer-level packaging[3] is identified. Recently, wafer-level RTP(Rapid Thermal Processing) bonding process for MEMS packaging applications is proven to be effective and easy for implementation with proven long-term stability [4, 5]. This paper advanced the RTP bonding technology further by demonstrating the feasibility of MEMS vacuum packaging.

In another packaging related issue, post-packaging trimming by means of pulsed laser deposition (PLD) is addressed. The background of the work comes from process variations in making microstructures, such as local geometrical variations and local mechanical property variations. As a result, it is difficult to precisely control the dynamic characteristics of micro resonators and post-fabrication tuning is required. Several researches in the area of MEMS resonator tuning have been reported on two resonator components: spring and mass. In the spring tuning mechanisms, either thermal joule heating[6, 7] or electrostatic force pulling[8] have been proposed. In the mass tuning mechanisms, the MEMS resonator mass can be modified by localized CVD deposition[9]. A new approach for frequency tuning by using PLD(Pulsed Laser Deposition) is demonstrated in this paper. It has the advantages of precise process control, versatility and can be easily implemented into the packaging process as compared with previously demonstrated methods.

VACUUM PACKAGING PROCESS AND RESULTS

Figure 1(a) shows the schematic illustration of the RTP MEMS vacuum packaging process. Comb-shape microresonators are chosen as the vacuum packaging examples in this paper and a standard surface-micromachining process is used to fabricate these microresonators. One major design addition is that an integrated sealing ring using silicon nitride as the topmost layer in incorporated for the purpose of aluminum-to-nitride bonding[5]. The glass cap wafer is deposited and patterned with 4 μm-thick aluminum sealing rings. The aluminum ring width ranges from 100 to 250 μm and bonding area ranges from 600x600 to 1000x1000 μm^2. Before the vacuum packaging process, both the device and cap wafers are baked in vacuum at 300^{o}C for various periods to dry out water and gas species adhere at the surface. Afterwards, the device and cap wafers are flip-chip assembled immediately and loaded into a quartz chamber as shown in Fig. 1(b). and put into a RTP chamber. The

0-9640024-4-2/hh2002/$20©2002TRF
DOI 10.31438/trf.hh2002.21

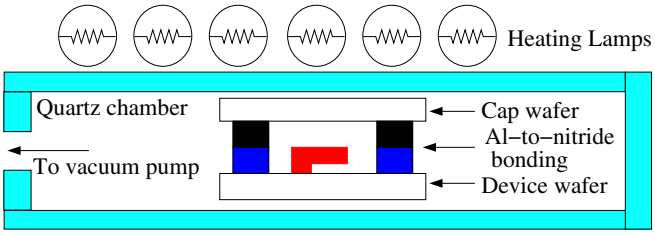

(a)

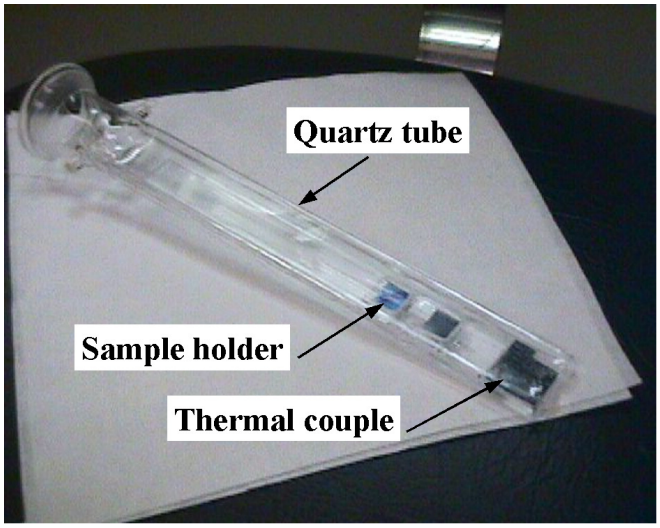

(b)

Figure 1: Experimental setup for RTP vacuum packaging. (a): The schematic diagram of the vacuum packaging process using RTP Al-to-nitride bonding. (b): Quartz chamber for RTP vacuum packaging.

base vacuum estimated at 10 mTorr inside the quartz chamber is achieved by using a mechanical pump. After heating for 10 seconds at 750^{o}C, the aluminum-to-nitride bond is formed.

Figure 2 shows the measured spectrum of a vacuum-packaged, double-folded beam comb-drive resonator by using a micro-stroboscope[10]. The central resonant frequency is at about 18625 Hz and the quality factor is extracted as 1800±200 corresponding to a pressure level about 200 mTorr inside the package[1]. In order to monitor the long-term stability of the vacuum packages, the quality factors of various devices are recorded up to 9 weeks, as shown in Fig. 3. Three vacuum-packaged micro resonators are tested. The quality factors of the resonators are 1800, 400 and 200, corresponding to different pre-baking time in vacuum of 12, 4 and 0 hours, respectively. It can be observed in Fig. 3 that the quality factor increases when the pre-baking time period in vacuum increases. Furthermore, the vacuum levels hold up well under the regular operation environment because the value of the quality factor remains

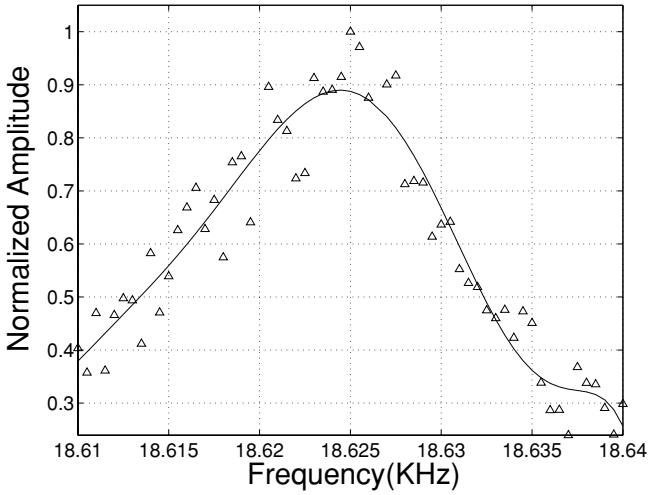

Figure 2: The spectrum of a vacuum packaged comb-resonator measured by a microstroboscope. The quality factor is extracted as 1800±200 corresponding to a pressure of 200 mTorr inside the package.

the same within experimental error bars. However, in order to determine an optimal pre-baking procedure, further investigations are necessary.

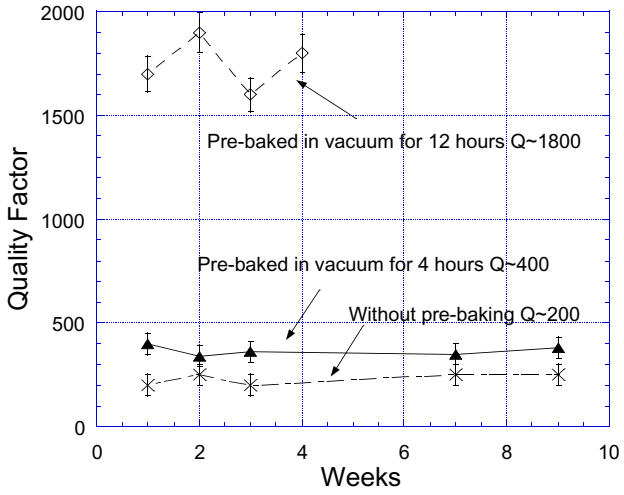

Figure 3: Long-term stability tests up to 9 weeks. Three sets of vacuum packaged resonators with different pre-baking procedures are tested. The resulting Q inside the package increases with pre-baking time.

In addition to the regular operation environment, it is important to characterize the vacuum quality under harsh environment. Vacuum-packaged comb-resonators are put into harsh autoclave testing environment(130^{o}C, 2.7 atm and 100%RH) for accelerated testing. The high pressure, high temperature and steam conditions could raise corrosion against the bonding interface and accelerate the gas diffusion process into the vacuum cavity. The spectrum of a comb resonator before and after a 24-hour continu-

ously harsh environment testing are shown and compared in Fig. 4. In this case, the quality factor maintains at 200 after 24 hours of storage in the autoclave testing chamber. Since the slight differences between the two spectrum are within the normal experimental errors, a conclusion may be drawn that this harsh environment test does not affect the vacuum seal.

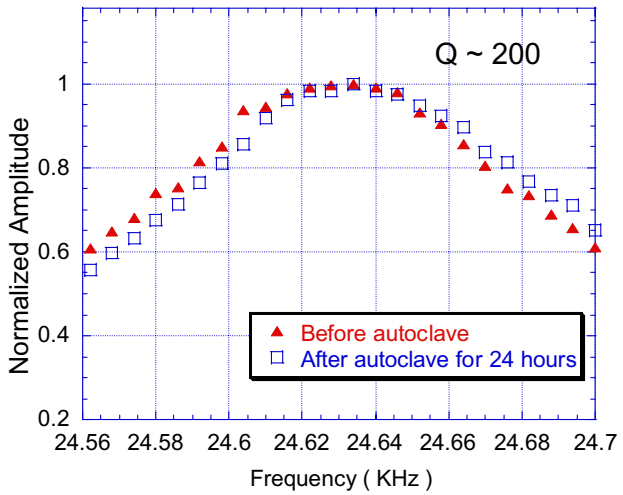

Figure 4: Accelerated testing results of a vacuum-packaged comb-resonator. The quality factor stays at 200 after 24 hours in the autoclave chamber under 130^{o}C, 2.7atm and 100% RH.

To further characterize the bonding quality, 60 MEMS packages formed by RTP Al-to-nitride bonding were sent to Sandia National Laboratory for MIL-STD-883E hermeticity testing[11]. The packaged devices are first tested using the gross leak check by using a combination of mass-increase and bubble-check testing methods. Samples are immersed into 60 psi FC-72 fluid for 3 hours and weighted afterwards. An increase in weight will confirm a leakage into the packages. The samples are also heated over the FC-72 boiling temperature and the observation of bubble formation inside the packages will also confirm the leakage. After the packages have passed the gross leak tests, helium fine leak tests are performed. The packaged devices are first baked at 150^{o}C for 2 hours to dry out water and put into a chamber with pressurized 60 psi helium for 2 hours. The packages are tested using a helium detector of a 10^{-8} atm-cc/sec scale. All 60 packages have passed the MIL-STD-883E gross and fine leak tests. The helium fine leak rate was found less than 5×10^{-8} atm-cc/sec. The examination on the quality of the bonding interface is conducted under SEM. Figure 5 shows the SEM photo of the silicon substrate where the bonding interface is examined after forcefully breaking the aluminum-to-nitride bond. It is observed that the glass debris is attached to substrate and fractures are formed in the silicon bulk. Part of the glass wafer is also fractured and attached to the silicon substrate as a strong bond is accomplished.

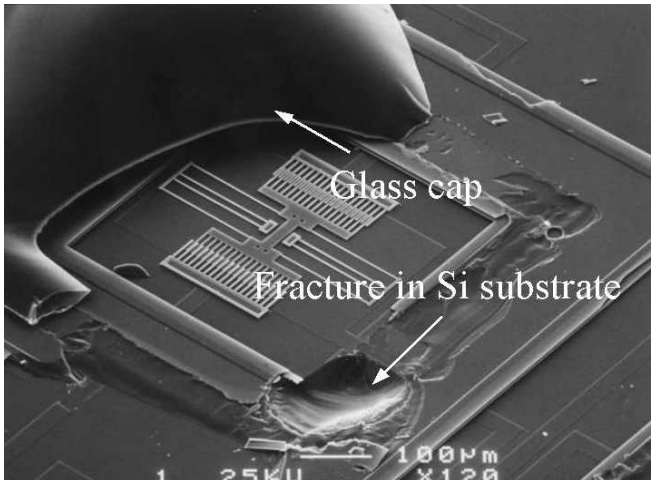

Figure 5: SEM microphoto of the silicon substrate after the Al-to-silicon nitride bond is forcefully broken. Bulk glass is found on the silicon substrate.

POST-PACKAGING FREQUENCY TUNING BY PLD

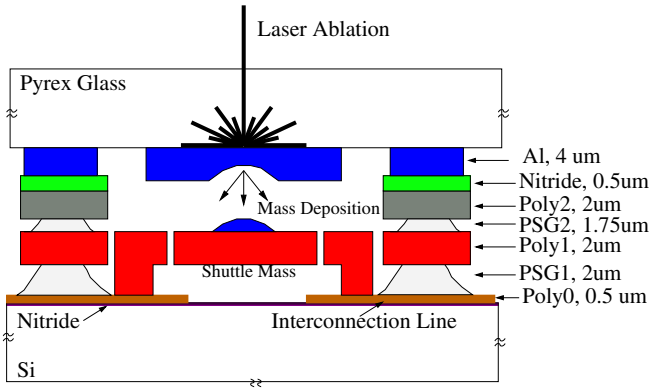

Figure 6: Schematic diagram showing the frequency tuning process by post-packaging PLD.

The working principle of the PLD frequency tuning process is illustrated in Fig. 6. After the MEMS packaging process is completed by using RTP Al-to-nitride bonding, a pulsed laser(6 nano-second, 532nm, 0.6mJ) is introduced to locally vaporize the metal thin film that was deposited on the Pyrex-glass packaging cap. The same bonding ring material such as aluminum can be used as the PLD deposition material. A shuttle plate is designed as part of the resonator to allow the re-deposition of the donor metal such that a reduction in resonant frequency is expected. Under a high intensity and short pulse laser irradiation, the metal vapor can be built up at the metal film-glass interface [12, 13]. Before the metal film layer is melted through-out, the vapor pressure is high enough to push and separate the rest of the metal film for deposition on to the accepting substrate as in the illustration.

Both indium and aluminum have been used as the frequency tuning donor metal materials in this work. Figure.7 shows the SEM micrograph of a resonator after the PLD process by using indium as the deposition material. A chunk of indium is deposited on to a shuttle plate of a modified comb-shape resonator that has one side of the folded-beam structure replaced with a shuttle plate. Figure 8 shows the measured spectrum of a resonator before and after the PLD tuning process and a -1.2% of frequency change is observed. The quality factor after the PLD process seems to increase as shown in this figure and further investigation is required to understand the fundamental mechanism. It can be shown from a linear spring-mass vibration model that frequency change, Δf, m_o and m has the following relation,

$$\Delta f = \frac{f - f_o}{f_o} = \sqrt{\frac{m_o}{m_o + \Delta m}} - 1 \qquad (1)$$

where f_o and f are the natural frequency of the microresonator before and after PLD, respectively. In this work, m_o, the original mass, is calculated using comb-resonator layout and Δm, the mass increment, is estimated by using an image processing software and SEM microphotos to estimate the deposition area and thickness. As shown in Fig. 9, a linear correspondence is observed as predicted by a the linear undamped spring-mass model(dashed line). A maximum frequency change of -18.1% is achieved.

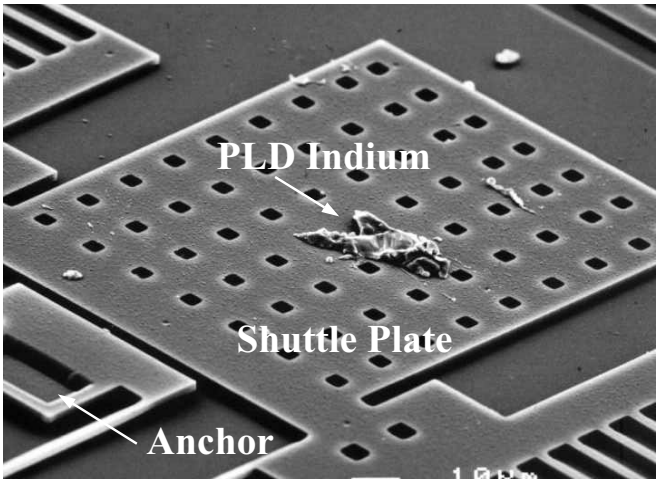

Figure 7: SEM microphoto of a MEMS resonator with mass deposited by PLD indium.

CONCLUSIONS

In this paper, MEMS vacuum packaging process based on RTP aluminum-to-silicon nitride bonding has been described. The quality factor of a vacuum-packaged comb-resonator has been measured as 1800±200 corresponding to a pressure about 200mTorr inside the package. The effect of pre-baking period in vacuum prior to bonding has been

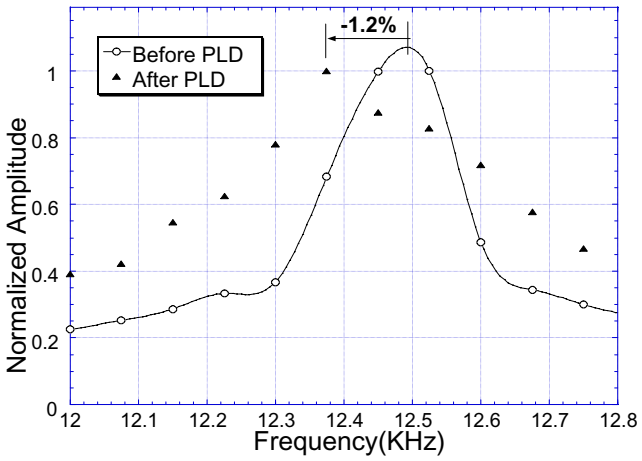

Figure 8: Spectrum measured by a microstroboscope of a resonator before and after PLD frequency tuning process.

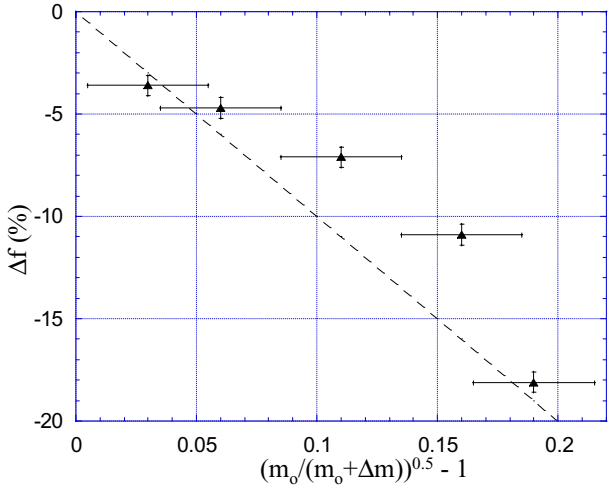

Figure 9: Experimental results showing a linear correspondence of frequency shift(Δf, in %) with respect to $(m_o/(m_o + \Delta m))^{0.5} - 1$ as predicted by an undamped spring-mass model.

shown to have great effects on the vacuum encapsulation level. It is found that the quality factor increases with increasing pre-baking time under vacuum environment. The long-term stability tests of the vacuum packages have been carried out for up to 9 weeks. The Q remains stable over time and it indicates the vacuum quality has not degraded. Furthermore, vacuum-packaged comb-resonators have been placed in an autoclave chamber(130^{o}C, 2.7 atm and 100%RH) for 24 hours for accelerated testing. It is found that the quality factor stays at 200 and the the vacuum quality inside the package has not been affected by the harsh environment.

A post-packaging frequency tuning technique by PLD has been demonstrated by using either indium and or aluminum as the donor material. The spectrum of a MEMS

resonator is measured before and after the PLD frequency tuning process and a maximum resonant frequency reduction of 18.1% on a modified comb-shape resonator is demonstrated. It is found that a first-order, undamped spring-mass vibration model explains well for the PLD tuning experimental results.

ACKNOWLEDGEMENTS

The authors would like to thank Dr. A. D. Oliver of Sandia National Laboratory for MIL-STD-883E hermeticity testing and discussions on leak tests , Mr. S. Avadhanula and Prof. R. Fearing of EECS, UC-Berkeley on their laser equipment for the PLD work and Dr. X. Meng of Cryogenic group at UCB for the vacuum apparatus. Theses devices are fabricated at the UCB Microfabrication Laboratory. This work is supported in part by an NSF CAREER award(ECS-0096098) and a DARPA MTO/MEMS grant (F30602-98-2-0227).

REFERENCES

[1] L. Lin, R. T. Howe, and A. P. Pisano. Microelectromechanical filters for signal processing. *Journal of Microelectromechanical Systems*, 7(3):286–294, Sept. 1998.

[2] W. C. Tang. *Electrostatic Comb Drive for Resonant Sensor and Actuator Applications*. PhD thesis, University of California at Berkeley, 1990.

[3] Y.T. Cheng, W. T. Hsu, L Lin, C. T. Nguyen, and K Najafi. Vacuum packaging technology using localized aluminum/silicon-to-glass bonding. In *Proceedings of IEEE Micro Electro Mechanical Systems*, pages 18–21, Jan 2001.

[4] M. Chiao and L. Lin. Hermetic wafer bonding based on rapid thermal processing. *Sensors and Actuators A-Physical*, 91:398–402, 2001.

[5] M. Chiao and L. Lin. Accerlerated hermeticity testing of a glass-silicon package formed by RTP aluminum-to-silicon nitride bonding. In *11th Int. Conference on Solid-State Sensors and Actuators, Transducer's 01 , Technical Digest*, pages 190–193, Munich, Germany, 2001.

[6] K. Wang, A. C. Wong, W. T. Hsu, and C. T.-C. Nguyen. Frequency trimming and Q-factor enhancement of micromechanical resonators via localized filament annealing. In *Transducers'97*, pages 109–112, 1997.

[7] T. Remtema and L. Lin. Active frequency tuning for microresonators by localized thermal stressing effects. In *Technical Digest of Solid-State sensor and actuator workshop*, pages 363–366, 2000.

[8] K. B. Lee and Y. H. Cho. Frequency tuning of a laterally driven microresonator using an electrostatic comb array of linearly varied length. In *Transducers'97*, pages 113–116, 1997.

[9] D. Joachim and L. Lin. Localized deposition of polysilicon for MEMS post-fabrication processing. In *Proceedings of ASME International Mechanical Engineering Congress and Exposition-MEMS*, pages 37–42, 1999.

[10] D. M. Freeman and C. Q. Davis. Using video microscopy to characterize micromechanics of biological and man-made micromachines. In *Technical Digest of Solid-State sensor and actuator workshop*, pages 161–167, June 1996.

[11] A.D. Oliver and C.M. Matzke. 100% foundry compatible packaging and full wafer release/die seperation technique for surface micromachined devices. In *Late News Digest of Solid-State sensor and actuator w orkshop*, pages 5–6, 2000.

[12] R. J. Harrach. Analytical solutions for laser heating and burnthrough of opaque solid slabs. *Journal of Applied Physics*, 48(6):2370–2383, June 1977.

[13] J. Bohandy, B. F. Kim, F. J. Adrian, and A. N. Jette. Metal deposition st 532 nm using a laser transfer technique. *Journal of Applied Physics*, 63(4):1158–1162, Feb. 1988.

A ROBUST GOLD-SILICON EUTECTIC WAFER BONDING TECHNOLOGY FOR VACUUM PACKAGING

Yuhai Mei, G. Roientan Lahiji, and Khalil Najafi

Center for Wireless Integrated Microsystems
The University of Michigan
1301 Beal Ave., Ann Arbor, MI 48109

ABSTRACT

A uniform, high-yield, reproducible, gold-silicon eutectic bonding technology for wafer-level MEMS vacuum packaging has been successfully demonstrated. A device wafer containing a polysilicon layer is eutectically bonded to a silicon cap wafer containing an electroplated gold bond ring. The soft eutectic flows over non-planar surfaces containing insulated feedthroughs of polysilicon (1.2µm-thick,). The two wafers are first baked in vacuum at 300°C for 60 minutes, brought into intimate contact under a pressure of 1MPa, and subsequently bonded at ~400°C for 30 minutes in a vacuum of ~0.25mTorr. A bond yield of >95% is achieved across 4" wafers, and excellent reproducibility is achieved from wafer to wafer. The low-pressure inside the vacuum-sealed cavity is monitored using a thin (~2.5µm-thick) diaphragm of insulated polysilicon. After bonding and diaphragm release, the diaphragm buckles under the one atmosphere of pressure by > 27µm. The buckling in the diaphragms has been maintained for more than 14 weeks. Vacuum sensors are being fabricated to more exactly monitor the pressure inside the package.

INTRODUCTION

Low-cost, simple, and reproducible hermetic/vacuum packaging technologies are required for many microsystems, including resonant devices and RF MEMS. Several groups, including ours, are developing new techniques for implementing small packages [**1**-**5**]. Most of these involve bonding of two wafers, a package (cap) silicon/glass wafer, and a device silicon wafer. Several wafer bonding techniques, including adhesive, glass frit, solder, eutectic, silicon fusion/direct and anodic bonding have been used. Of these, eutectic bonding is one of the most attractive because it is easy to use, it forms a soft eutectic to allow bonding over non-planar surfaces, it can be done at slightly above the eutectic temperature (363°C), and it does not out-gas.

Although Au-Si eutectic has long been used for wafer bonding and packaging [**1**-**3**], few have reported its successful use in vacuum packaging. There are several reasons for this, including non-uniform eutectic flow, void formation, insufficient eutectic material in between wafers causing non-uniform bonding, oxidation of bond surfaces, and poor surface contact/adhesion. Furthermore, few published reports have presented data showing full wafer-level bonding [**2**]. The main problem with Au-Si eutectic bonding has been a lack of uniformity over an entire wafer, and lack of reproducibility from wafer to wafer. This paper presents a uniform, high-yield, reproducible, silicon-gold eutectic wafer-level bonding technology used for vacuum encapsulation of MEMS. The paper presents a detailed description of the bonding process and the steps necessary to ensure a uniform and reproducible bond. The vacuum inside packaged cavities is monitored using a thin flexible diaphragm that is fabricated on one side of the packaged cavity. This wafer-level bonding technology can be applied to a variety of MEMS devices which require a prescribed level of vacuum or pressure, excellent bonding strength, low fabrication cost, and high reliability and yield.

GOLD-SILICON EUTECTIC BONDING

Gold-silicon eutectic formation occurs at 363°C for 19 atomic % Si, as shown in the phase diagram in Fig. 1. The eutectic can be used to bond two wafers, or be used for hermetic and vacuum packaging. To form the eutectic, silicon and gold have to be provided to the bond interface. Typically, the gold is deposited on one of the wafers to a desired thickness, and the silicon is provided either from the bulk of one of the wafers, or from thin films deposited on one or both wafers. Figure 2, for example, shows two wafers, a device wafer containing feedthroughs and a top poysilicon layer, and a cap wafer containing the package cavity and an electroplated gold bond ring. When the two wafers are brought into contact and heated to above 363°C, silicon is supplied from both the cap wafer (underneath the gold ring) and the device wafer (the polysilicon layer), and will react with gold to initiate the eutectic liquid formation. Upon cooling, the bond consists of Au-Si hypereutectic phase and represents a typical strong diffusional bond [**6**]. We will present additional detail and discussion on the bonding mechanisms, and different bond interfaces and materials later in the paper.

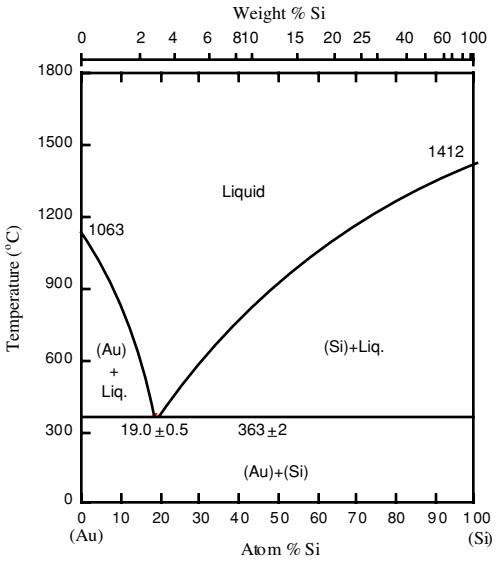

Figure 1. Binary phase diagram of Au-Si alloy.

0-9640024-4-2/hh2002/$20©2002TRF
DOI 10.31438/trf.hh2002.22

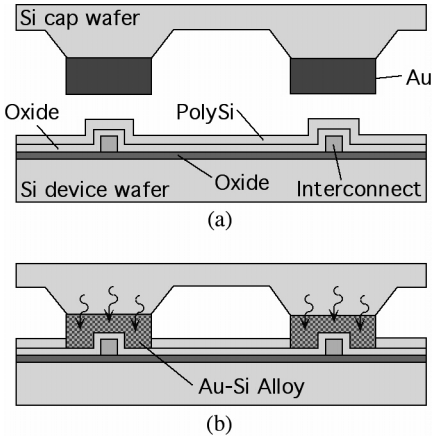

Figure 2. Schematic diagram of Au-Si eutectic bonding: at (a) room temperature, (b) >363°C.

TEST DEVICES AND FABRICATION

To develop and characterize the bonding process, a set of test wafers and devices were fabricated. The experiments involved two wafers, a device wafer which supports the required bonding layers, and a silicon cap wafer that contains the gold bond ring and the package cavity. Silicon is used as the cap wafer because it can be easily machined, matches the thermal expansion of the device wafer, is low cost, and has excellent mechanical characteristics. In the following, the fabrication process for each of these wafers is first described, and the details of wafer bonding process are then presented.

Figure 3 shows the fabrication process of the cap wafer. Thermal oxide (0.5µm) is first grown on the backside of the cap wafer in order to protect the wafer during the following KOH wet etching process. Next, the bonding layer is formed on the front surface. It consists of a layer of Ti (200Å), followed by a seed layer of Au (1000Å), and a top layer of Cr (500Å). The chromium is patterned in areas where the thick gold bond ring is to be formed. The bond ring is typically 200µm wide. Gold is now electroplated to a thickness of 4-8µm through a thick photoresist mask. The plating mask and the underlying Ti/Au/Cr layer are now removed and the wafer is etched in KOH for 60 minutes to form a ~50µm deep recess to create the package cavity. This completes the processing of the cap wafer.

Figure 4 shows the fabrication process of the device wafer. In these initial experiments, the device wafer simply supports a multi-layer of thin dielectric and polysilicon films. These films eventually form a thin diaphragm that can be used to monitor the pressure inside the package. Thermal oxide (2µm) and LPCVD Si_3N_4 (1800Å) and SiO_2 (2300Å) are first deposited on a silicon substrate for electrical insulation followed by the deposition of 1.2µm LPCVD polysilicon. The polysilicon is then phosphorus-doped and patterned to form electrical interconnects and feedthroughs. In order to prevent the diffusion of Au into this interconnect layer during the bonding process, a LPCVD SiO_2 (2300Å)/ Si_3N_4 (1800Å) barrier layer is deposited. Next, a second layer of LPCVD polysilicon (0.5µm) is deposited; this polysilicon film forms the bonding layer on the device wafer. The wafers are now ready to be bonded. Note that the diaphragms are released after the two wafers are bonded together. Diaphragm release is performed by etching the device wafer from the back side in a DRIE as illustrated in Fig. 4(b).

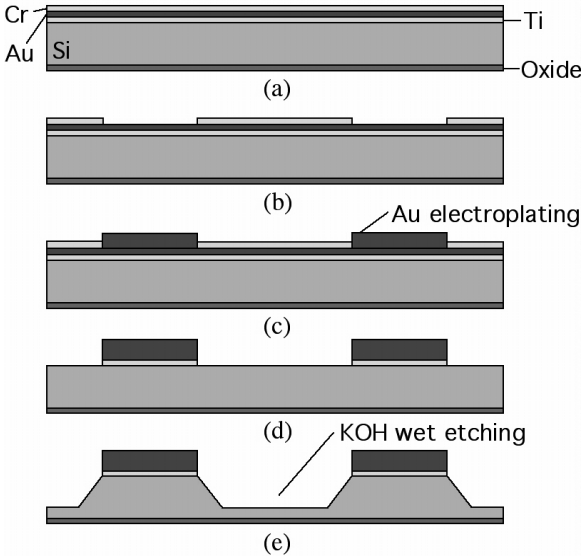

Figure 3. Fabrication process flow of the silicon cap wafer.

The cap and device wafers are now aligned, and then bonded. The most critical step in the process is the exact bonding sequence. Bonding is performed in an Electronic Vision EV-420 bonder, where the temperature and pressure can be controlled. After placement in the bonding chamber, the chamber is pumped down to a vacuum level of about 0.25mTorr. The wafers are then baked at 300°C for about 60 minutes to release any residual materials off of the surfaces of the package cavity. Note that this baking is performed at 300°C, which is far below the eutectic point. The wafers are now brought into intimate contact under an applied pressure of 1MPa, and the wafer stack is heated to the desired bonding temperature. Most of our bonds were performed at a temperature of 400°C for about 20-30 minutes. The applied pressure helps distribute the eutectic throughout the bond interface. Now, the wafers are cooled down to room temperature and removed from the bonder. It should be noted that it is desirable to *rapidly* cool down the wafer stack after bonding in order to obtain a fine microstructure for the gold-silicon alloy after it solidifies.

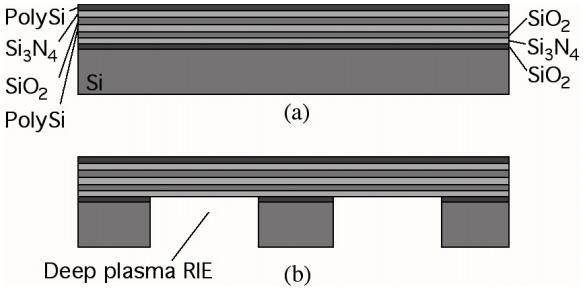

Figure 4. Process flow of the device wafer, containing a 2.52µm multilayer diaphragm used for vacuum monitoring.

EXPERIMENTAL RESULTS

As stated above, the diaphragms are released in a DRIE etcher after the wafers are bonded together. Figure 5(a) shows the photograph of a full bonded wafer pair. Inspection of the wafer shows a yield of more than 95% of the packaged diaphragms deflecting down across the wafer. Figures 5(b,c) show close-ups of the buckled diaphragms over the vacuum-sealed cavity. Note that the thin diaphragm bends by a large

amount and still survives the one atmosphere of pressure difference across it. Figure 6 shows a SEM photograph of the cleaved bond interface, showing the eutectic region. Figure 7 shows a photograph of a device where the cap wafer is forcefully broken and removed, leaving behind silicon in the bond areas. This illustrates a very uniform and strong bond.

The pressure in the sealed cavity can be grossly monitored by monitoring the deflection of the diaphragm as a function of pressure and time. When the bonded wafer is placed inside a vacuum chamber, the diaphragms begin to move up as the chamber is pumped down and the differential pressure across the diaphragm decreases. Several wafers have been bonded and tested in this fashion. The longest wafer has been tested for more than 14 weeks, and the diaphragms are still deflected in ambient pressure. The above technique is not the most accurate to measure and monitor the pressure inside the cavity. To do this, one needs vacuum sensors. We are currently fabricating a set of packages with integrated vacuum sensors that should allow us to directly measure the package pressure down to 1mTorr.

In addition to bonding cap wafers to flat device wafers without any feedthroughs, we have also bonded the cap wafer to a device wafer with 1.2μm thick feedthroughs. As previously mentioned, the advantage of the eutectic is that it flows over these feedthroughs. The wafers bonded with these feedthroughs also show excellent uniformity and reproducibility.

DISCUSSION

In order to characterize and understand the wafer boning process, we have also bonded many different wafers with different set of materials and bonding layers. The material sets which were bonded and tested included: Si/Ti/Au to Au/Ti/Si; Si/Ti/Au to Si; Si/Ti/Au to PolySi/Si; Si/Ti/Au to Oxide/Si; and Si/Ti/Au to Nitirde/Si. Of these wafers, we have found that the bond quality and uniformity between Au-Au, Au-Si, and Au-PolySi is the best. In particular, it is noted that the bond quality is best when the gold and silicon are supplied from two different wafers, instead of from the same wafer. Test wafers where the Au-Si eutectic was bonded to a substrate covered with either oxide or nitride produced very non-uniform and poor bonds. The reasons for this are not exactly known at this point, but the following discussion explains what we believe is occurring in the bonding process.

To help illustrate this, we refer to Figure 8. Let's consider the case of a cap wafer with a gold-silicon eutectic ring being bonded to a silicon oxide surface. The surface of the oxide is generally terminated by $-OH$ groups. During eutectic bonding, silicon atoms from the cap wafer diffuse through the gold layer, and arrive at the top surface of the oxide, where they either establish a weak chemical bond with $-H$, or react with $-OH$ groups to form a $Si-O$ bond. This results in the generation of hydrogen, which in turn forms micro- or nano- voids along the bond interface. These are the cause of a weak bond between the eutectic alloy and the oxide.

If LPCVD polysilicon or silicon is used as bonding material on the device wafer, a strong bond is obtained. The polysilicon layer is deposited immediately after the deposition of a LPCVD oxide layer on the device wafer; a strong chemical bond exists between silicon and oxygen atoms along the interface between the oxide and the polysilicon (Fig. 9(a)). When the surface of the polysilicon (or Si) is exposed to air and water, a layer of $-OH$ group forms on the surface (Fig. 9(a)). A very thin layer of oxide is also formed. This very thin native oxide and $-OH$ layers are consumed by Si atoms that diffuse through the Au layer and reach the interface, thus forming a strong diffusional bond at the interface of Au and polysilicon. Although in some regions Au atoms arrive at the interface between the polysilicon and the oxide, the strong bond between $Si-Si$ is not affected (Fig. 9(b)) therefore there still remain a large number of $Si-Si$ bonds along the interface. Consequently a very strong and uniform bond establishes across the entire interface. The above mechanisms can also be applied to both nitride and poly/nitide.

We have also studied the effect of the cooling rate on the quality of the eutectic bond. It is well-known that the physical properties of a metal alloy, such as gas diffusivity, depends on the microstructure which depends on such variables as the

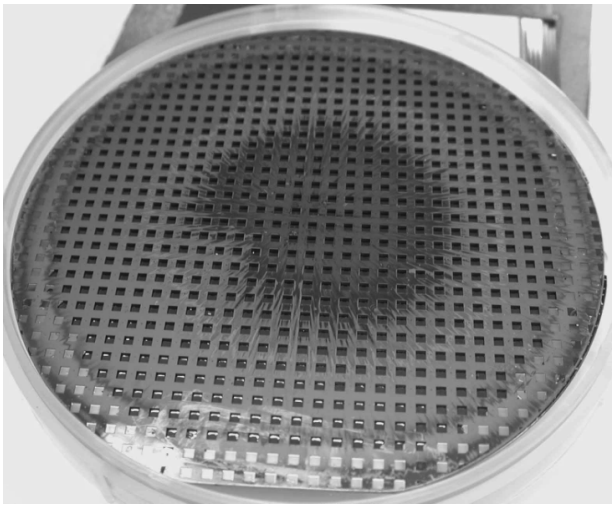

Figure 5(a): Photograph of two bonded Si wafers with cavities covered by thin diaphragms. The yield is >95%.

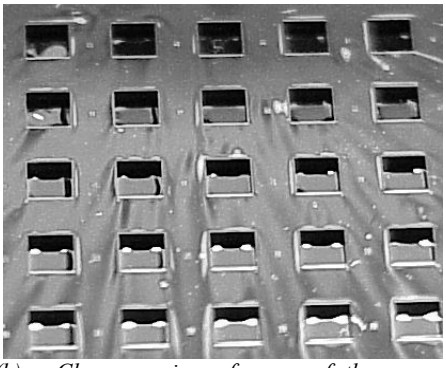

Figure 5(b): Close-up view of some of the vacuum sealed cavities, showing buckled diaphragms.

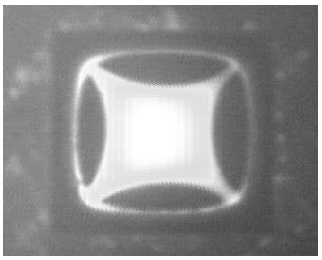

Figure 5(c): Close-up with of a bucled diaphragm covering a sealed cavity. The diaphragm has bucked down by ~28μm.

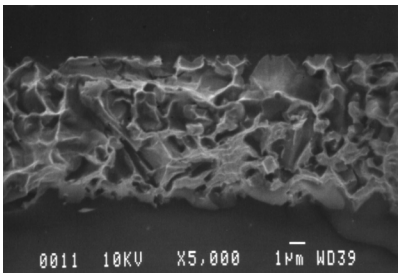

Figure 6. SEM of cross-section of the bond interface.

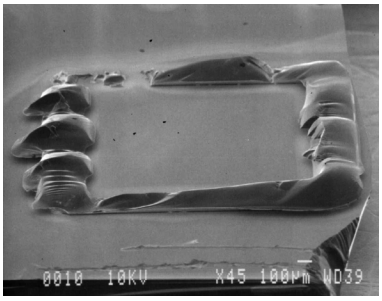

Figure 7. SEM of broken bond region showing excellent uniformity.

alloying elements present, their concentrations, and the heat treatment of the alloy. As shown in Fig. 1, at >363°C, the Au-Si alloy is completely liquid (of composition 19% Si). At the eutectic point, the solidification process starts and solids of Au and Si begin to form. For packaging applications, one needs a fine (uniform) microstructure in the alloy because smaller grains are more impervious to gas diffusion. Fast cooling (quenching) of the eutectic results in a fine microstrucrture, and is therefore preferred. We have analyzed the microstructure of both quenched and slowly-cooled Au-Si eutectic, and observed that the quenched eutectic has a finer microstructure.

The above proposed Au-Si eutectic bonding experiments indicate that the Au-Si eutectic bond must be conducted: (a) in a vacuum or inert gas ambient to avoid further oxidization at high temperature; (b) LPCVD polysilicon must be deposited immediately after LPCVD oxide deposition to achieve a clean and strong interface between silicon and oxide; (c) some contact force must be applied on the wafers to provide an intimate contact between the bonding materials (Au and polysilicon); (d) the bonded wafers should be cooled down as fast as possible around the eutectic temperature; (e) the thickness of the eutectic material should be several microns in order to provide sufficient Au-Si eutectic, so when the wafers are pressed together, the eutectic can cover over non-planar surfaces; and (f) the wafers should be properly baked to minimize out-gassing.

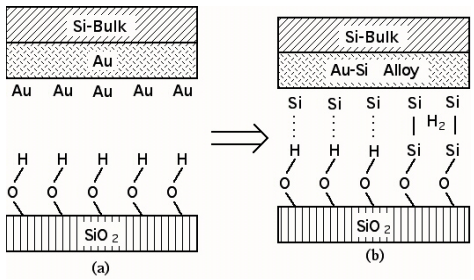

Figure 8. Schematic drawing of atomic configurations at bonding interfaces with LPCVD oxide only.

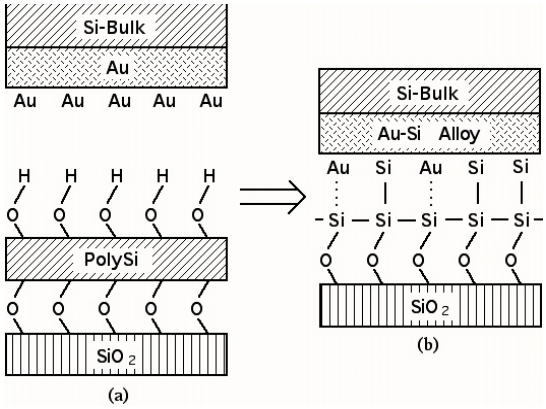

Figure 9. Schematic drawing of atomic configurations at bonding interfaces with LPCVD oxide and polysilicon.

CONCLUSIONS

We have successfully demonstrated a uniform, high-yield, reproducible, gold-silicon eutectic wafer-level bonding technology and its application to MEMS vacuum packaging. Uniform bonding has been achieved across 4" silicon wafers with better than 95% yield on both flat wafers and wafers with feedthroughs. The best bonds are achieved on wafer pairs where the cap wafer is made of silicon with an electroplated layer of gold, and a device wafer with a polysilicon bond ring deposited over insulated feedthroughs. Vacuum-sealed cavities have been tested by monitoring the deflection of thin flexible diaphragms covering the sealed cavities, and show stable pressure inside the sealed cavity after 14 week.

ACKNOWLEDGEMENTS

The authors acknowledge the support of Integrated Sensing Inc. (ISSYS) for wafer testing. This research is supported by the Engineering Research Centers Program of the National Science Foundation under Award Number EEC-9986866.

REFERENCES

1. R.F. Wolffenbuttel, "Low-Temperature Intermediate Au-Si Wafer Bonding: Eutectic or Silicide Bond", *Sensors and Actuators,* A-62 (1997) , pp. 680-686.
2. F. Ohara, et al., "Method for Manufacturing a Semiconductor Acceleration Sensor Device," *U.S. Patent* 5668033, 1997
3. M .B. Cohn, K. F. Bohringer, J. M. Noworolski, A. Singh, C. G. Keller, K. Y. Goldberg, R. T. Howe, "Microassembly Technologies for MEMS", *Proceeding of SPIE*, 3512 (1998), pp. 2~16.
4. B. Ziaie, J. A. V. Arx, M.R. Dokmeci, and K. Najafi, "A Hermetic Glass-Silicon Micropackage with High-Density On-Chip Feedthroughs for Sensors & Actuators", *JMEMS,* Vol. 5, No. 3, September (1996), pp. 166-179.4.
5. Y. T. Cheng, W.T. Hsu, Liwei Lin, C.T. Nguyen, and K. Najafi, "Vacuum Packaging Technology Using Localized Aluminum/Silicon-To-Glass Bonding", *MEMS 2001*, Interlaken, Switzerland, Jan. (2001), pp.18-21.
6. R. K. Shukla and N.P. Mencinger, "A Critical Review of VLSI Die-Attachment in High Reliability Applications", *Solid State Technology,* July (1985), pp. 67-74.

A BAROMETRIC PRESSURE SENSOR WITH INTEGRATED REFERENCE PRESSURE CONTROL USING LOCALIZED CVD

Patty P. L. Chang-Chien, and Kensall D. Wise

Engineering Research Center for Wireless Integrated MicroSystems
Department of Electrical Engineering and Computer Science
University of Michigan, Ann Arbor, MI 48109-2122, U.S.A.

ABSTRACT

This paper reports a barometric pressure sensor with integrated reference pressure control. The device was packaged in a cavity, which was created using anodic bonding and subsequently vacuum sealed using localized CVD (Chemical Vapor Deposition) at near ambient temperature. A post-packaging pressure control system, which consisted of in-cavity pressure monitoring and pressure control units, was incorporated with the barometric pressure sensors. The sensor modules, with embedded comb resonators and gettering heaters, were fabricated using a double-polysilicon dissolved-wafer process. The wafers were anodically bonded, thinned, and then released in EDP. Localized CVD was then used to seal the cavity and to react away the residual gas within it using the getters to create the desired reference pressure, as measured using the in-cavity resonators. This implementation required very little extra design space, and only one additional mask compared to the sensor alone. Process improvements have reduced the sealing time and power by a factor of four compared to that previously reported [1]. Sensors capable of resolving 25mTorr pressure changes with a sensitivity of ~60fF/Torr were obtained.

Keywords: Hermetic Packaging, Pressure Sensor, Vacuum Control, localized CVD.

INTRODUCTION

Silicon-based capacitive pressure sensors have been studied extensively in recent years. They are attractive due to their high sensitivity to pressure, low temperature coefficients, and low power consumption compared to their piezoresistive counterparts. Two of the major challenges for absolute pressure sensors are hermetic vacuum sealing and subsequent long-term stability (i.e., outgassing) into the cavity. Both of these lead to a change of pressure in the reference cavity, significantly degrading the sensor accuracy. Accuracy in the absolute pressure sensor cannot be achieved without a knowledge of the reference pressure.

A batch vacuum-sealed barometric pressure sensor capable of resolving 25mTorr over a 300Torr dynamic range [2] has been reported. However, the accuracy of these devices was limited by outgassing into the reference cavity. To improve sensor accuracy, both for as-fabricated and for long-term in-field use, titanium passive getters used for oxygen gettering had been implemented with the absolute pressure sensors [2]. Cavity pressures from 500mTorr to 10Torr were observed for sensors packaged in a sub-mTorr environment. Corman [3] reported similar results from cavities in which neither gettering nor gas evacuation were implemented. Pressures on the order of 1mbar (~1.3Torr) were measured from cavities anodically bonded at a background pressure of 10^{-5}mbar (1.33×10^{-2}mTorr). Despite that the residual pressure in the sealed environment depends on the amount of gas generated in a given cavity volume, these results suggest that the implementation of a passive getter (such as titanium film) alone is not sufficient. In addition, a minor drift in sensor output (a possible indication of vacuum degradation in the cavity) had also been observed in the absolute barometric pressure sensors [4]. This indicates that an active in-cavity pressure control is necessary for high performance, high-accuracy applications.

We recently demonstrated that localized-CVD can be used to seal wafer cavities at low overall temperature, achieving residual pressures less than 50mTorr as measured with an in-cavity microresonator [1]. This paper significantly extends this previous work to report the first pressure sensor with integrated vacuum sensing/control capability and a localized-CVD seal.

PACKAGING APPROACH

A post-packaging pressure control system has been designed and demonstrated previously [1]. The general approach is to create the vacuum cavity using an anodic bond, to seal the cavity in a low-pressure CVD environment, and to subsequently monitor the internal cavity pressure and maintain it below a critical level with an active getter. Thus, the three main system components are the first-level package, a pressure-monitoring unit, and an in-chamber pressure control unit. All of the components in this system can be integrated at wafer-level. This produces a significant cost advantage over many active pressure control systems. In addition, an accurate reading of the pressure inside the cavity is not required as long as the pressure is below a critical level. For high-performance pressure sensors and resonators, this critical level is on the order of a few tens of mTorr.

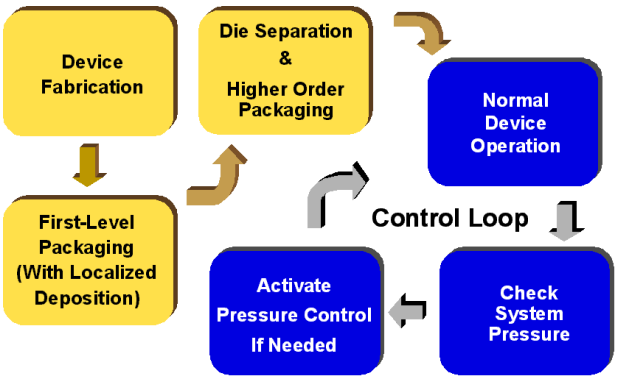

Fig. 1: *Post-packaging pressure control system flow chart.*

The system flow chart for an active post-packaging pressure control module is shown in Figure 1. After fabrication, wafer-level packaging by localized deposition is performed, followed by

0-9640024-4-2/hh2002/$20©2002TRF
DOI 10.31438/trf.hh2002.23

Solid-State Sensors, Actuators, and Microsystems Workshop
Hilton Head Island, South Carolina, June 2-6, 2002

any higher-level packaging as required. Once packaged, the device operates in its normal mode and cavity pressure is monitored periodically. In the event of vacuum degradation higher than some desired level, pressure control is activated to restore the vacuum back to an acceptable level.

A wafer-level packaging technique that combines anodic bonding and localized heating [1] is utilized to provide a low and predictable pressure in the packaged cavity. The cavity is formed by a recess in the silicon substrate, an incomplete polysilicon ring, and a glass wafer. With this design, oxygen and other gases generated during the bonding process can be pumped out of the cavity through the opening of the polysilicon ring (i.e., the sealing channel). The bonded wafers are then placed in a low-vacuum silane environment to seal the cavity by localized CVD. With this approach, the cavity can be sealed at a controlled pressure near ambient temperature. For simplicity and process compatibility, comb-drive micro-resonators and suspended polysilicon gettering heaters are chosen as the pressure monitoring and pressure control units of the post-packaging pressure control system, respectively.

SYSTEM DESIGN

The post-packaging pressure control system described above was incorporated into Chavan's barometric pressure sensor design [2]. An optical photograph showing the top view of the pressure sensor module is shown in Figure 2. The reference cavity is formed using an anodic bond between glass and an incomplete polysilicon ring with a sealing heater at the ring opening. The recessed area is composed of a center cavity for the pressure sensor and four side cavities housing two comb resonators and two polysilicon gettering heaters, which are components of the post-packaging pressure control system. The side cavities are linked to the main chamber via connecting channels. The channels are located symmetrically about the main chamber to minimize any geometric imbalance of the diaphragm induced by the openings. The channels are 50μm wide, 45μm long, and 3.5μm tall. The calculated conductance of a channel in SiH_4 at room temperature is $5.438mm^3/s$. At this flow rate, the side cavity pressure reaches equilibrium with the main chamber in a fraction of a second.

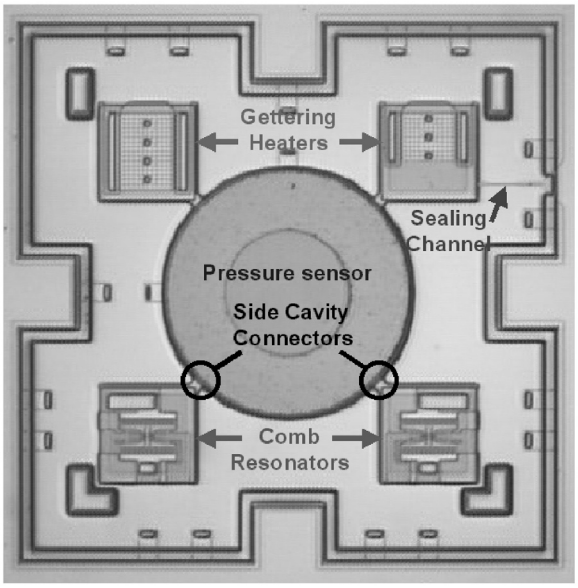

Fig. 2: *Optical photograph of a pressure sensor module before anodic bonding showing its system components.*

Each side cavity is 420μm by 420μm by 8μm. These side cavities take up very little additional chip space since they are located at the four coroners of the circular sensor. It is a great advantage to integrate post-packaging pressure control into the sensor for performance enhancement, with very little overhead cost and only one additional mask compared to the sensor alone. The embedded resonators, which serve as the in-cavity pressure monitoring units, have 2μm wide, 2μm thick, and 20μm long fingers with an overlap of 10μm. The spacing between two adjacent fingers was 2μm, and the doubly-folded support springs were 50μm long. The gettering heaters, which are the pressure control units, have a resistance of about 250Ω each. The sealing heater, located at the opening of the sealing channel is 10μm wide and was designed to have a resistance of ~300Ω. The sealing channel shown in Figure 3 is 2μm by 2μm by 125μm at the narrow region. The wider regions, designed to increase the channel conductance, have the dimensions of 11μm by 2μm by 90μm, and 11μm by 2μm by 40μm. The effective calculated channel conductance is $9.54\times10^{-3}mm^3/s$. The entire cavity has an approximate volume of $1.12\times10^{-2}mm^3$, which can be filled with SiH_4 in 2sec via the sealing channel.

Pressure sensors with unbossed (regular), bossed, and pedestal-plate diaphragms were implemented. The bossed diaphragm limits the displacement of the sensor and hence improves the linearity at some cost in sensitivity. The sensor with the suspended polysilicon electrode is designed to increase the sensor sensitivity by increasing the effective surface of the sensing area while simultaneously improving linearity.

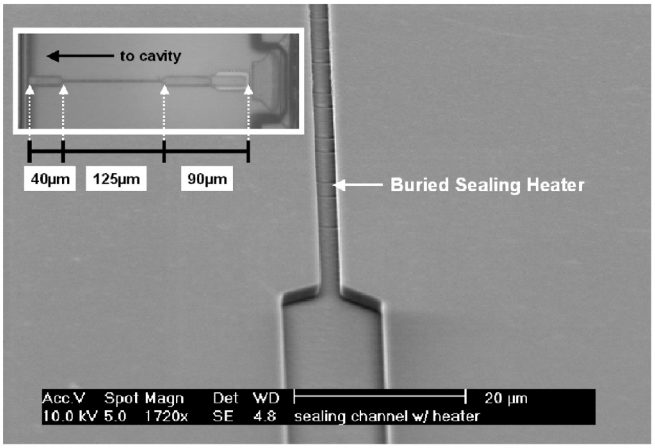

Fig. 3: *A SEM showing the sealing channel region, and an insert showing the channel design.*

DEVICE FABRICATION

The silicon wafer was fabricated using a double-polysilicon dissolved-wafer process [2]. Fabrication began with a 7μm KOH cavity recess followed by 10μm and 4μm-deep boron diffusions to form the boss and the diaphragm, respectively. An oxide/nitride layer was deposited for substrate isolation and was patterned to form the poly electrode anchors. The first layer of polysilicon was deposited, doped, and patterned to form device leads, sealing heaters, and electrodes. A second dielectric layer was then patterned to form anchors for the resonators and gettering heaters. Low-stress polysilicon was then deposited and doped, followed by a CMP (Chemical Mechanical Polishing) step. The resonators, heaters, and bonding ring were patterned, followed by an HF

release. LTO was deposited and patterned, and Cr/Au was deposited to form the contacts. The glass wafer was first recessed to form the four side cavities. A layer of Ti/Pt/Au was then deposited to form the electrodes, and the glass was partially diced. Anodic bonding was performed on the two wafers at 400ºC and 1000V. The Si wafer was then thinned to speed up the release process, and the devices were released in EDP.

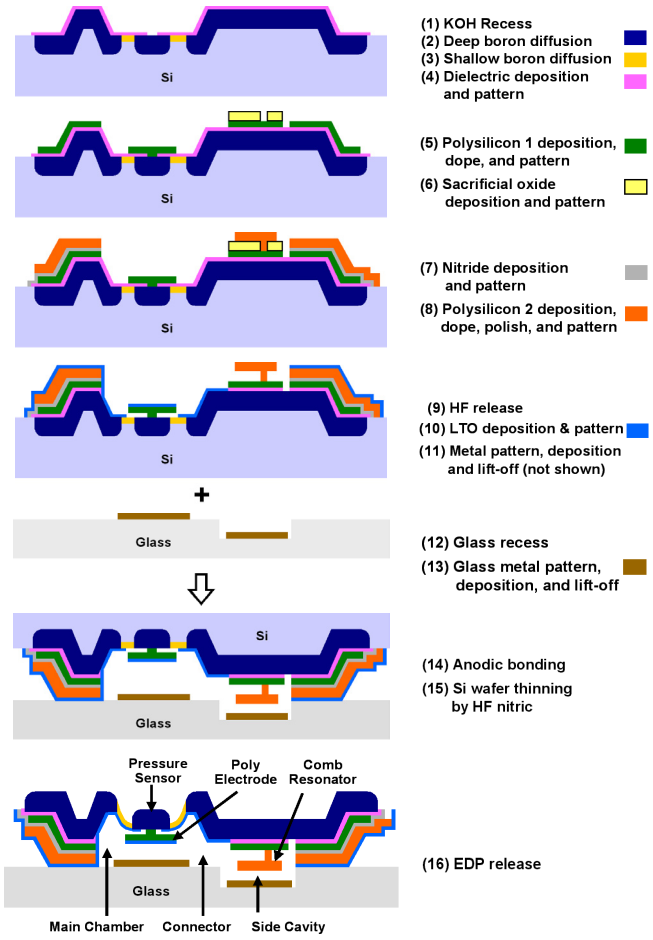

Fig. 4: *Simplified schematic diagram showing the process flow of a barometric pressure sensor with the polysilicon electrode. (Layers not drawn to scale)*

EXPERIMENTAL RESULTS

A fabricated array of the sensor modules is shown in Figure 5. Each device is 5mm by 5mm on a side. An optical photograph taken from the backside of the module (looking through the glass wafer) is shown in Figure 6. There are total of five different diaphragm dimensions; each is sensitive to a specific pressure range with a total range of 300Torr. The bossed areas for the different boss dimensions are ~0.259mm^2, ~0.242mm^2, ~0.228mm^2, ~0.218mm^2, and ~0.203mm^2. Figure 7 is a photograph taken from a module with poly electrode prior to anodic bonding. The individual components are shown in Figures 7 (a) through (e). The poly electrode, as shown in Figure 7 (a), is suspended 2µm above the diaphragm. It is connected physically and electrically to the boss via four small anchors at the center. The small release holes are designed to speed up the release process. The poly electrode has an area of ~0.511mm^2 for all boss dimensions, a substantial increase in usable sensing area over any of the bossed diaphragms.

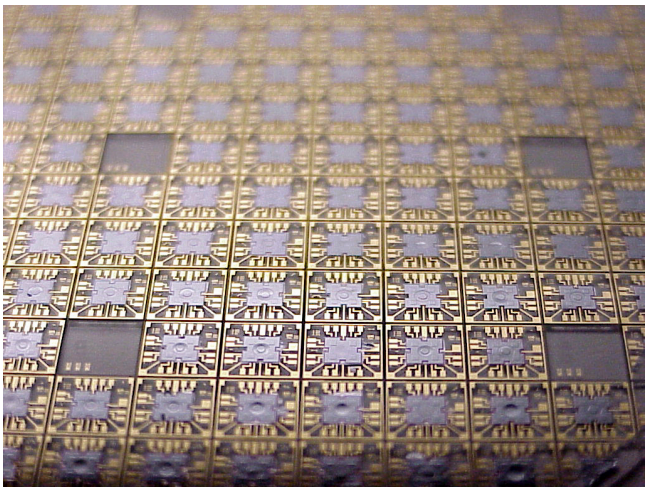

Fig. 5: *A fabricated array of barometric pressure sensors.*

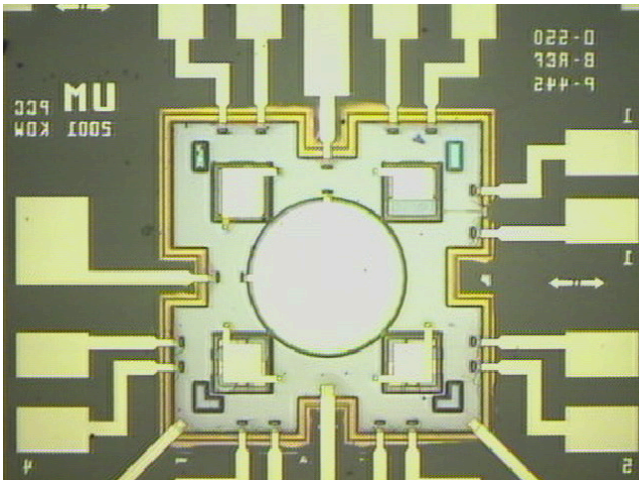

Fig. 6: *An optical photograph of the pressure sensor module looking through the glass wafer.*

The gettering heaters (Figures 7b, c) are suspended 2µm above the substrate as well. The large gettering heater has a surface area of ~0.070mm^2, and the small one has an area of ~0.044mm^2. Both heaters are anchored below to small islands of the first layer polysilicon for structur-al support. The small gettering heater is designed such that the path of the sealing channel entrance to the main cavity is cleared of structures in order to ease the gas transport to the other side cavities. The channel has a lid at its opening to seal the entire module during EDP. The channel is later opened by undercutting the lid with an isotropic dry etch.

After fabrication, the sensors are placed in a PECVD chamber for sealing. The individual dies are separated by physically breaking the glass wafer along the pre-diced lines. The dicing lines are only about half-wafer deep so the entire wafer can be handled during the anodic bonding process. The PECVD chamber is used only as a SiH_4 supply chamber. The module is sealed by activating the sealing heater. The electrical connections to the heater are provided by an outside power source via electrical feedthroughs.

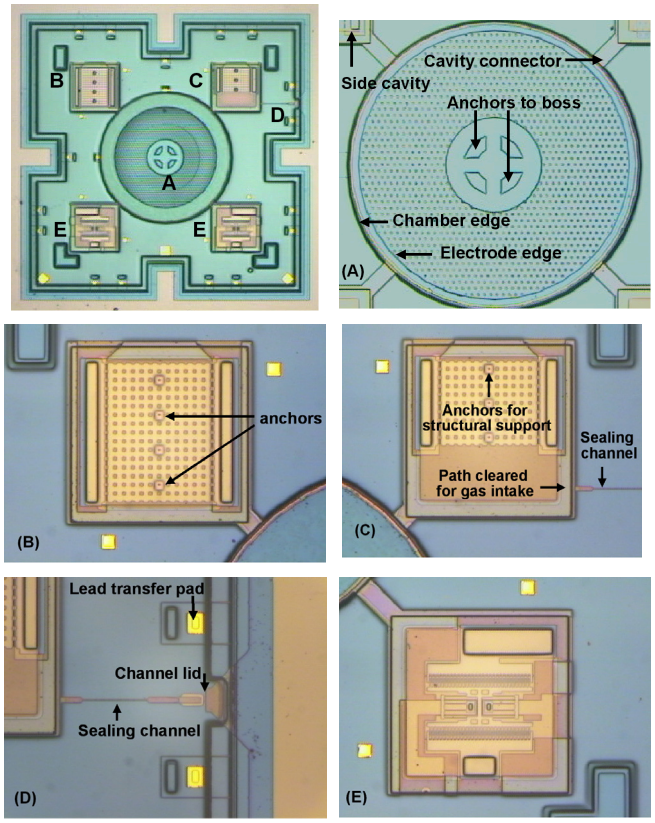

Fig. 7: *Optical photographs of a barometric pressure sensor module and its contents. (a) polysilicon electrode, (b) large gettering heater, (c) small gettering heater, (d) sealing channel region, and (e) one of the comb resonators.*

The devices are sealed at 200mTorr of SiH_4 at a flow rate of 80sccm. The performance of the sealing heater was dramatically improved compared to the ones reported previously [1]. The sealing power required was reduced by about a factor of four (~620mW instead of ~2.2W), and the sealing time was reduced to about 40min for an adequate seal. The estimated local deposition temperature is 600ºC. Figure 8 is an optical photograph of a sealed channel taken through the glass wafer. This improvement in heater performance is a result of process optimization and the removal of the most of the bulk substrate. After sealing, one of the gettering heaters is activated at atmospheric pressure to further reduce the cavity pressure. The estimated sealed pressure after getter activation is 30mTorr.

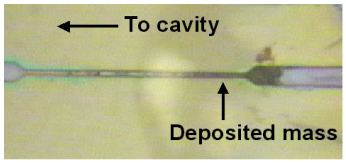

Fig. 8: *Optical photograph of a sealed channel (looking through the glass wafer).*

The barometric sensors were tested in a pressure chamber and the changes in capacitances were measured as a function of applied pressure. Some of the pressure vs. capacitance characteristics are shown in Figure 9. Sensitivities as high as ~60fF/Torr, which corresponds to a pressure resolution <25mT, were obtained from the sensors. The measured capacitances of the sensors vary between 8pF and 11pF depending on the design.

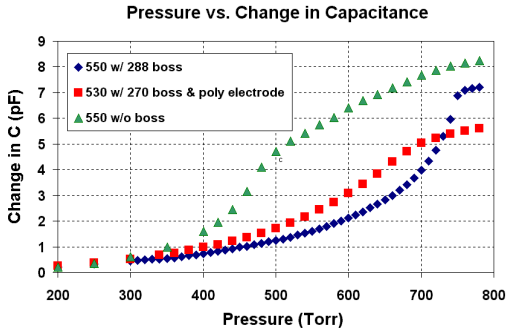

Fig. 9: *Pressure vs. change in capacitance data taken from some of the pressure sensors.*

CONCLUSIONS

In this paper, a pressure sensor module with integrated reference pressure control was designed and fabricated. This device was sealed using localized CVD, subsequently reacting any residual gas within the cavity using the getters to decrease the desired reference pressure, as measured using the in-cavity resonators. To incorporate the internal reference cavity control, only one additional mask was necessary compared to the sensor alone. With design and process improvements, the sealing power and sealing time required for the localized CVD were both reduced by about a factor of four compared to that previously reported [1]. The chamber condition during sealing was optimized at a SiH_4 pressure of 200mTorr at a flow rate of 80sccm. The higher silane flow rate sped up the deposition process and the lower overall pressure ensured a lower after sealing pressure in the cavity. The estimated pressure in the cavity is approximately 30mTorr after gettering heater activation. A sensitivity as high as 60fF/Torr was obtained from a sealed barometric pressure sensor.

ACKNOWLEDGMENTS

This work is supported by DARPA under the contract number F30602-98-20227, this work made use of ERC shared facilities supported by NSF under award number EEC-0096866.

REFERENCES

1. P. Chang-Chien, and K. D. Wise, "Wafer-Level Packaging Using Localized Mass Deposition", *International Conference on Solid State Sensors and Actuators, Transducers 01,* pp. 182-185, 2001.

2. A. V. Chavan and K. D. Wise, "A Multi-Lead Vacuum-Sealed Capacitive Pressure Sensor," *Digest Solid-State Sensor and Actuator Workshop,* Hilton Head, pp. 212-215, June 1998.

3. T. Corman, P. Enoksson, and G. Stemme, "Low-pressure-encapsulated resonant structures with integrated electrodes for electrostatic excitation and capacitive detection", *Sensors and Actuators,*A66, pp.16 0-166, 1998.

4. A.V. Chavan, An integrated high resolution barometric pressure sensing system, Doctoral Dissertation, University of Michigan, 2000.

5. H. Henmi, S. Shoji, Y. Shoji, K. Yosimi, and M. Esashi, "Vacuum package for microresonators by glass-silicon anodic bonding", *International Conference on Solid State Sensors and Actuators, Transducers 93*, pp. 584-587, 1993

6. Y. T. Cheng, L. Lin, and K. Najafi, "Fabrication and hermeticity testing of a glass-silicon packaging formed using localized aluminum/silicon-to-glass bonding", *International MEMS Conference*, pp. 757-762, 2000.

7. H. Guckel, "Surface micromachined pressure transducers", *Sensors and Actuators*, A28, pp. 133-146, 1991.

OPTICAL FIBER TIP FABRICATED BY SURFACE TENSION CONTROLLED ETCHING

Pak Kin Wong, Tza-Huei Wang, and Chih-Ming Ho
Mechanical & Aerospace Engineering, University of California, Los Angeles
Los Angeles, CA 90095

ABSTRACT

This paper presents a chemical etching method for fabricating probe tips used in scanning near-field optical microscopy. The fiber tip is sharpened by the gradual reduction of the etchant meniscus height that is associated with the decrease of the tip diameter during etching. Control of final tip geometry by adjusting the physical properties of the etching medium is discussed. In addition, we report a novel parallel-etching technique that allows control of the final tip angle by modifying the boundary condition of the meniscus. Tip angle can be adjusted from 7° to 22° by simply controlling the gap distance between fibers and number of fibers etched.

INTRODUCTION

Scanning near-field optical microscopy (SNOM) is a promising imaging technique that is not limited by diffraction since it's probe works in close proximity to the surface and images the sample point-by-point with resolution that cannot be achieved by classical optical microscopy. The technique not only allows high spatial resolution but also maintains useful contrast mechanisms, such as fluorescence and polarization, in optical microscopy. After the first demonstration of SNOM in 1984 [**1**], the technique has been applied to various areas, such as photopatterning of monomolecular films [**2**] and detection of single fluorescence molecules [**3**].

As in other forms of scanning probe microscopy, the probe tip is the main factor that determines the quality of the images. The probe tip has to be precisely formed in order to optimize the system performance according to their applications [**4**]. Presently, the fiber probe tips are fabricated by i) chemical etching in a bulk etchant or at the etchant-solvent interface [**5**] or ii) a heating and pulling method with a commercial micropipette puller [**6**]. The heating and pulling method generally produces long tips with small tip angles, which is often undesirable due to low optical transmission [**7**]. The chemical etching method is undoubtedly the simplest and the most inexpensive optical fiber tip sharpening method, while still allowing for high optical transmission. However, the relationship between the tip angle and etching parameters (e.g. nature of etchant, choice of organic solvent and etching temperature) is not clear, and there is no technique that is both simple and effective that can control the final tip angle over a large range.

In this report, we present a technique based on a theoretical model that can be used to fabricate optical fiber tips with desired geometries. A capillary rise experiment was performed to measure the surface tension and contact angle at the interface to verify the model. Adjustment of the fiber tip angle by controlling the physical properties of the etching medium is discussed. Moreover, control of final tip geometry was demonstrated by etching multiple fibers in parallel with different gap distances between fibers and the number of fibers etched at the same time.

Travel Support has been generously provided by the Transducers Research Foundation and by the DARPA MEMS and DARPA BioFlips Programs.

PRINCIPLE OF TIP FORMATION

The typical chemical etching process for fiber tip formation at the interface is shown in figure 1. The fiber is immersed into a stack solution of etchant and etchant-insoluble organic solvent. The etchant wets the fiber surface with an initial meniscus height. As etching proceeds, the upward pulling force resulting from surface tension decreases due to the reduction of the fiber radius in contact with the etchant. Consequently, the meniscus height reduces progressively until the portion of the fiber below the oil is completely etched, forming the tip.

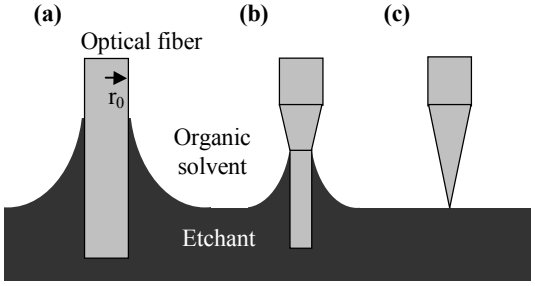

***Figure 1**. Schematics illustrating the formation of a fiber tip.*

Therefore, the final tip profile can be determined according to the relationship between fiber radius and meniscus height, which can be derived by solving the Young-Laplace equation (equation 1) in the axisymmetric case with appropriate boundary conditions (equation 2) (figure 2).

$$\frac{d^2y}{dx^2} = \left[1+\left(\frac{dy}{dx}\right)^2\right]\left\{\frac{\Delta\rho g}{\sigma}y\left[1+\left(\frac{dy}{dx}\right)^2\right]^{\frac{1}{2}} - \frac{1}{x}\frac{dy}{dx}\right\} \qquad (1)$$

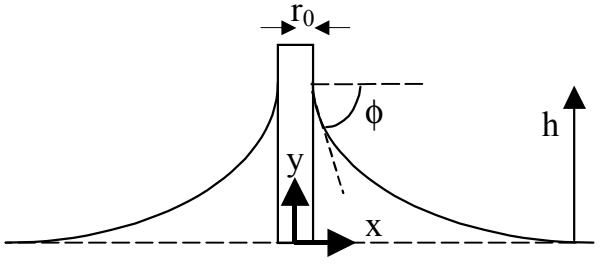

***Figure 2**. The static meniscus on a circular cylinder immersed into a solution.*

$$\frac{dy}{dx} = -\tan\phi \quad \text{at } x = r_0$$
$$y \to 0 \text{ as } x \to \infty \tag{2}$$

The equation has been solved both numerically [**8**] and analytically [**9**]. Equation 3 shows the first order approximate solution of the meniscus profile solved by the matched asymptotic expansions method [**10**]. The normalized meniscus height is given by equation 4:

$$z(r,\varepsilon) = -c\ln\varepsilon + c(2\ln 2 - \gamma) - c\ln[r + (r^2 - c^2)^{1/2}] + o(1) \tag{3}$$

$$z(r=1) = \sin\phi\left\{\ln\frac{4}{\varepsilon\ (1+\cos\phi)} - \gamma\right\} \tag{4}$$

where x and y are the coordinates, $\Delta\rho$ is the density difference between etchant and solvent, g is gravity, σ is surface tension, ϕ is the angle between the meniscus and x axis (π - contact angle) ($c = \sin\phi$), r_0 is the fiber radius, $z = y/r_0$ and $r = x/r_0$ are normalized parameters describing the geometry, $l_0 = (\sigma/\rho g)^{0.5}$ is the capillary length, $\varepsilon = r_0/l_0$ is the perturbation parameter for solving the equation, and γ is the Euler's constant (0.5772). Figure 3 shows meniscus profiles for different fiber radii. The final tip geometry can be estimated by joining the upper ends of the meniscus profiles.

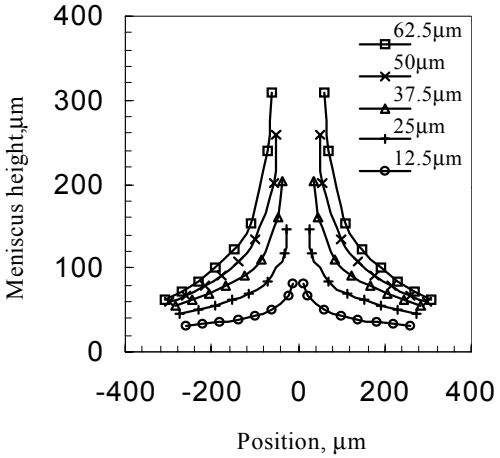

***Figure 3**. Meniscus profiles for different fiber radii.*

TIP ETCHING

Optical fiber tips were fabricated by etching single mode optical fibers with cladding diameters of 125μm (F-SA, Newport Corporation). Roughly 2cm of the polyacrylate coating at the distal end was stripped away and the fiber was cleaned with acetone and DI water. The fiber probe was perpendicularly immersed into the etchant-solvent stack solution. The etchant and organic solvent used in the experiment were hydrofluoric acid (49%) and silicone oil, respectively. All the etching experiments were carried out at room temperature.

Figures 4a shows a series of fibers at intermediate stages during etching. The taper region gradually extends as the etching proceeds until formation of the fiber tip. Etching rate of fiber cladding in 49% HF can be estimated from figure 4b, which gives a value of 3.3μm/min. A typical etching process required less than 40min.

It is clear that the final tip shape is governed by the density difference, surface tension and contact angle at the interface. Density difference can be easily obtained, but the surface tension and contact angle are not available. To verify the model, we measured the surface tension by performing a capillary rise experiment and directly observed the contact angle at the interface (Fig. 5). Surface tension at HF-silicone oil interface and the contact angle were estimated to be 0.047N/m and 17°, respectively. Figure 6 shows the predicted tip profile based on the theoretical model using the aforementioned surface tension and contact angle measured values. Good agreement was obtained when the predicted tip profile was compared to an etched fiber tip.

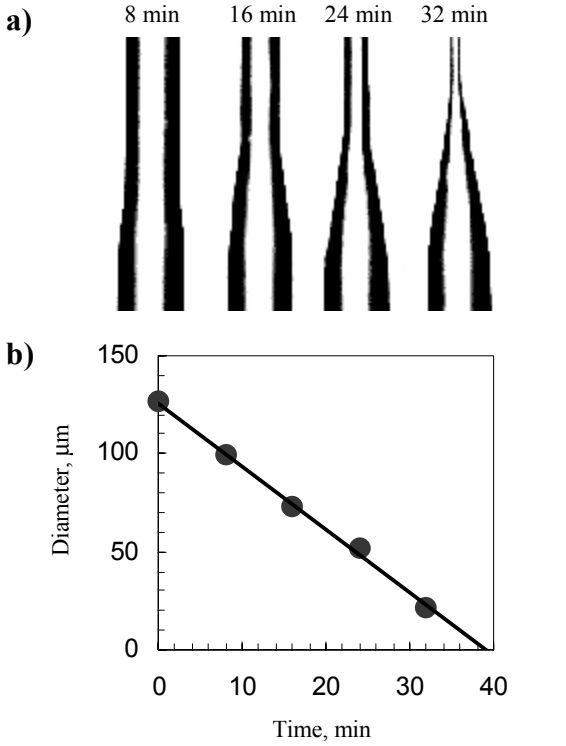

***Figure 4**. (a) Fibers at intermediate stages during tip formation. (b) Diameter of fiber end as a function of time.*

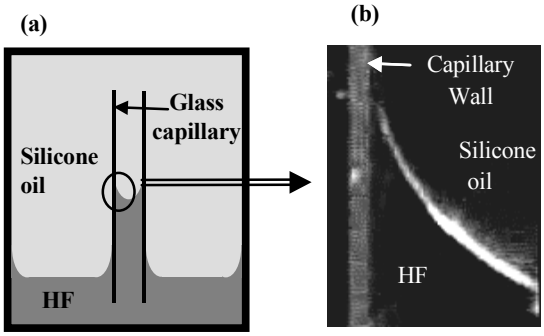

***Figure 5**. (a) Schematic of the capillary rise experiment. (b) Meniscus inside a glass capillary.*

TIP ANGLE CONTROL

From equation 4, it is found that a dramatic change in surface tension and the density difference has minimal effect on the meniscus height because of the logarithm in the equation. The physical reason is that the meniscus height is governed by the force balance between the surface tension force and the weight of the etchant fluid entrained along the fiber surface. A slight rise of the meniscus height results in a rapid increase in the volume and

weight of the etchant fluid that must be balanced by a dramatic rise in surface tension force. Conversely, a small increase in surface tension and density difference has little effect on the meniscus height due to the relationship between height and weight. The meniscus height is sensitive to the change in contact angle at the interface. This is because the contact angle directly affects the meniscus profile and the volume and weight of the etchant. Hence the meniscus height and the final tip profile critically depend on only the contact angle.

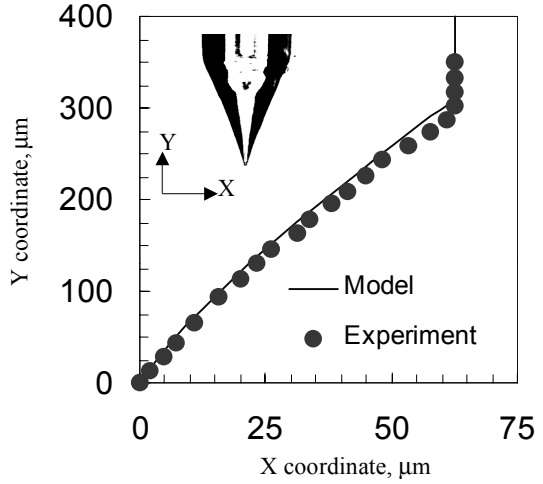

Figure 6. *Comparison of tip profiles. — Profile calculated based on the theoretical model with surface tension and contact angle determined in the capillary rise experiment. • Profile measured from an etched fiber tip. Insert: Photography of an optical fiber tip.*

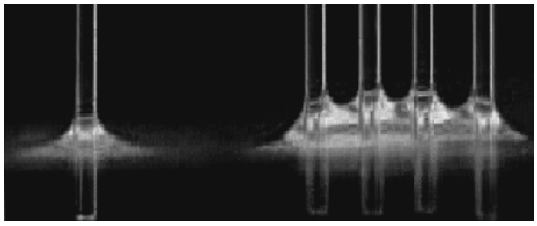

Figure 7. *Illustration of meniscus profiles under different boundary conditions.*

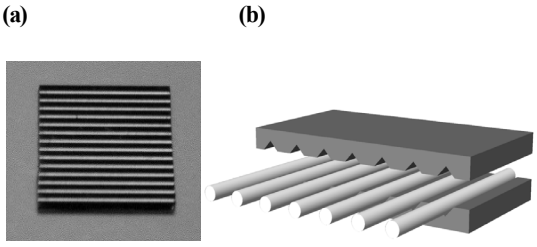

Figure 8. (a) *V-groove for parallel-etching experiment. (b) Schematic showing alignment of fibers by v-groove.*

Based on the model, optical fiber tips can be fabricated with desired geometries by adjusting the physical parameters that determine the force balance in the system, such as surface tension, density difference of etchant and solvent, and the contact angle of the liquid-liquid interface. These parameters can be altered by changing the organic solvent [**5**], HF concentration [**11**], or etching temperature [**12**]. Replacing the organic solvent allows for a relatively large range of achievable tip angles; however, there is no general rule for the choice of organic solvent to fabricate an optical fiber with specific tip angle. The contact angles at such solvent-etchant interfaces are generally not available. On the other hand, more control of the fiber tip angle can be accomplished by fine-tuning the etchant concentration and etching temperature. To the first order approximation, the change in fiber tip geometry can be estimated by only the change in contact angle. Consequently, one can use the model to predict the fiber tip profile under different etching conditions, such as an increase in etching temperature or etchant concentration. The dependence of surface tension under such conditions is given by thermodynamic theory and the relationship between surface tension and contact angle is related by Young's equation. These relationships can be used to estimate the effect of varying the etching conditions on the final tip geometry.

PARALLEL-ETCHING

Although our model allows for predictable fabrication of fiber tips, the tip characteristics are sensitive to variations in the experimental conditions. It is valuable if we can have a simple, repeatable and controllable method to fabricate fiber tips with a large range of tip angles. Insight can be obtained by reconsidering the Young-Laplace equation. There are two boundary conditions for the ordinary differential equation. Adjusting the contact angle by changing the etching conditions represents modification of the first boundary condition at the three phase interfacial region. On the other hand, the second boundary condition assumes that the meniscus extends to infinity without interacting with the other boundary. We propose to alter the meniscus profile and meniscus height by introducing a second physical boundary. This opens new opportunity for controlling the tip angle through an easy and efficient method.

Figure 7 illustrates the effect of immersing multiple glass tubes into a solution on the meniscus profile. The meniscus profile was modified and a larger meniscus height was observed. To implement the idea for fiber tip etching, multiple fibers were aligned and etched in parallel. The fibers are positioned with precise gap distances by using v-groove structures etched by KOH (figure 8).

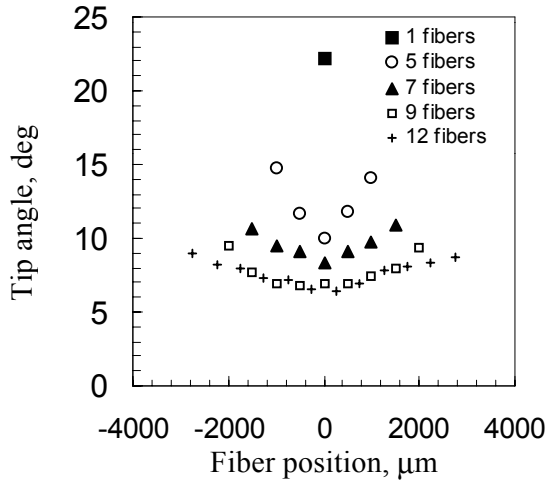

Figure 9. *Position dependence of tip angle in parallel-etching.*

In parallel-etching, meniscus height is governed by the force balance of surface tension and the weight of the etchant pulled up on the fiber surface. The upward pulling force is proportional to the number of fibers immersed into the stack solution while the weight of the pulled etchant depends on the number of fibers and gap distance. In general, reducing the gap distance and increasing the number of fibers increases the meniscus height. It is also observed that there is a moderate dependence of fiber position on the tip angle (Figure 9). This is because there are only a finite number of fibers immersed in the solution and the meniscuses on the end-most fibers have different boundary conditions than those in between fibers. By using parallel-etching, the cone angle can be adjusted from 7° to 22° by simply changing the number of fibers and gap distance (Fig. 10 and 11). Compared to other fiber tip fabrication methods, this novel parallel-etching technique is simple and reproducible.

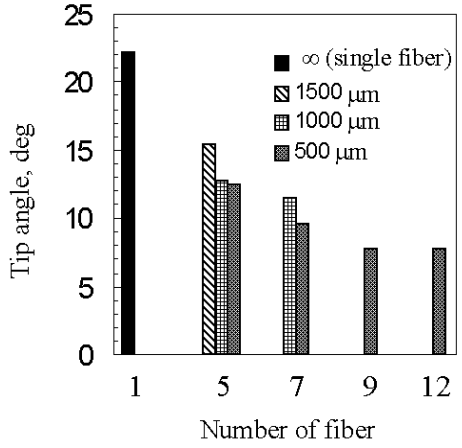

Figure 10. *Tip angles of fibers etched under different conditions.*

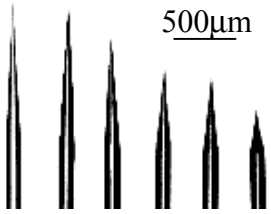

Figure 11. *Photographs of optical fiber tip etched under different conditions.*

CONCLUSIONS

A chemical etching technique was developed for fabricating scanning near-field optical microscope probes. The mechanism of the etching process was verified with an independent experiment. We also described a novel technique for controlling the tip angle by etching multiple fibers in parallel. It is foreseeable that the method will extend to other configurations such as array-etching and concentric-etching with other boundary materials. A large selection of materials with different surface properties will generate opportunities for fabricating fiber tips with superior performance for new applications.

ACKNOWLEDGMENTS

The authors would like to thank Sylvain Masset for his valuable insight and Linda Chun for her technical assistance. This work is supported by DARPA MTO under a Contract N66001-00-c-8092 managed by SPAWAR and NSF NIRT program.

REFERENCES

1. D. W. Pohl, W. Denk, M. Lanz, "Optical Stethoscopy: Image Recording with Resolution λ/20", *Applied Physics Letters, 44*, 651 (1984).

2. A. Naber, T. Dziomba, U. C. Fischer, H.-J. Maas, H. Fuchs, "Photopatterning of a Monomolecular Dye Film by Means of Scanning Near-Field Optical Microscopy", *Applied Physics A, 70*, 227 (2000).

3. E. Betzig, R. J. Chichester, "Single Molecules Observed by Near-Field Scanning Optical Microscopy", *Science, 262*, 1422 (1993).

4. M. N. Libenson, G. S. Zhdanov, "Optimisation of Near-field Optical Probes", *Proceeding of IEEE Lasers and Electro-Optics Society 1996 Annual Meeting*, Boston, MA, 11/18-11/96, (1996), pp. 36-37.

5. P. Hoffmann, B. Dutoit, R. Salathé, "Comparison of Mechanically Drawn and Protection Layer Chemically Etched Optical Fiber Tips", *Ultramicroscopy, 61,* 165 (1995).

6. B.A.F. Puygranier, S. Montgomery, J. Ashe, R.J. Turner, P. Dawson, "Imaging Tip Formation in Single-mode Optical Fibres", *Ultramicroscopy, 86,* 233 (2001).

7. T. Held, S. Emonin, O. Marti, O. Hollricher, "Method to Produce High-resolution Scanning Near-field Optical Microscope Probes by Beveling Optical Fibers", *Review of Scientific Instruments, 71*, 3118 (2000).

8. C. Huh, L. E. Scriven, "Shapes of Axisymmetric Fluid Interfaces of Unbounded Extent", *Journal of Colloid and Interface Science, 30*, 323 (1969).

9. D. F. James, "The Meniscus on the Outside of a Small Circular Cylinder", *Journal of Fluid Mechanics, 63*, 657 (1974).

10. L. L. Lo. "The Meniscus on a Needle – a Lesson in Matching", *Journal of Fluid Mechanics*, *132*, 65 (1983).

11. A Sayah, C. Philipona, P. Lambelet, M. Pfeffer, F. Marquis-Weible, "Fiber Tips for Scanning Near-Field Optical Microscopy Fabricated by Normal and Reverse Etching", *Ultramicroscopy, 71,* 59 (1998).

12. S.I. Hosain, Y. Lacroute, J. P. Goudonnet, "A Simple Low-Cost Highly Reproducible Method of Fabricating Optical Fiber Tips for a Photon Scanning Tunneling Microscope", *Microwave and Optical Technology Letters, 13,* 243 (1996).

LOW-VOLTAGE HIGH-SPEED ULTRASONIC CHROMATOGRAPHY FOR MICROFLUIDIC ASSAYS

Chung-Hoon Lee and Amit Lal
*Sonic*MEMS Laboratory
Department of Electrical and Computer Engineering
University of Wisconsin-Madison
Madison, WI 53706

ABSTRACT

A novel ultrasonic microfluidic device for polystyrene bead separation is presented. A bead mixture of different size beads are first focused at the pressure nodes in the capillary, and then separated by an inertial nonlinear force generated by capillary transverse vibrations. The separations occur within seconds enabling high speed sample replacement and separations. The bead separation is demonstrated at 1 V_{pp} drive at 165 kHz enabling battery powered assays.

INTRODUCTION

A great potential of integrated microfluidic systems is to handle microscale amounts of liquid that bears essential benefits of sample preparation integration, device miniaturization for ambulatory applications, power reduction for battery operation, and lower cost of bioassays. These features can lead to fast diagnostic bio-analytical systems. We present a portable micro analysis system using ultrasonic radiation forces in this paper that promises to fulfill the aforementioned qualities. Cells, proteins, and DNA can all be bound to polystyrene and latex beads. Hence, any system that can separate beads can potentially separate the bio-entities enabling bead based assays. The bead separation technology presented here requires sub five volt operation for CMOS control, and consumes $\sim$ 10 milliwatts, and takes less than 10 seconds to separate beads by size.The small platform and low cost of fabrication holds the promise of disposable assay systems.

Figure 1 and Figure 2 describe the acoustic separation system. A glass/polyimide capillary is either wrapped or bonded onto a piezoelectric PZT (lead-zirconate-titanate oxide) plate. The PZT plate stretches the capillary in the length direction which excites the longitudinal mode of the liquid in the capillary leading to bead focusing at pressure nodes in the capillary as discusses later. The PZT can also excite the transverse vibrations of the capillary that separate the focused beads. The focusing and separations occur at locations within the capillary that are highly predictable. Furthermore, the separation occurs over a distance of 100 microns within the capillary enabling easy viewing using a CCD chip as shown in Figure 2. The separation is controlled electronically by tuning the frequency at the PZT making electronic control of the entire assay.

How does the system proposed in this paper compare to other separation methods? Some other techniques for microscale separation in microfluidic systems include electro-osmotic flow, magnetic separations, dielectrophoretic separations, and electrophoretic separations, diffusion-based separations, cantilever-binding mass-sensing assays. A typical electro-osmotic microfluidic assay system for separation utilizing differential mobility in a high electric field for beads/molecules requires a conducting medium and usually high voltages. Magnetic bead separation can require the use of high currents for sufficient magnetic field production or require external magnetics that need to be moved. Dielectrophoretic separations require electrical connections to the fluid and can require non-conducting medium and high voltages. Binding to cantilever and detecting the resulting mass or strain change are also attractive but requires coating of the cantilevers with specific binding molecules.

ACOUSTIC RADIATION FORCE

Particle manipulation with projected acoustic field has been investigated by many researchers. Acoustic radiation forces generated by concave transducers have been used to concentrate particles at pressure nodes [1]. Previous attempts for focusing beads at pressure nodes using ultrasonic radiation force have led to increased detection limit of agglutination assays [2]. However, to our knowledge, separation of beads by size using the acoustic radiation force has not been demonstrated so far.

The basic principle of the particle manipulation using the acoustic radiation force is that the diffracted acoustic field from a particle leads to a nonsymmetric acoustic field around the particle. The nonsymmetric field results in a net force to move the particle. The 2^{nd} order pressure integrated over the particle surface results in a net force pulling the particles to acoustic nodes or antinodes depending on the acoustic contrast constant,

$$\mathcal{A}(\alpha,\sigma) = \frac{\alpha + 2(\alpha-1)/3}{1+2\alpha} - \frac{1}{3\alpha\sigma^2} \tag{1}$$

where α is the ratio of the bead density to the medium density and σ is the ratio of the speed of sound. For standing waves, the radiation force has been derived by Yosioka and Kawasima [3] as,

$$F_{ac} = -4\pi k d^3 \bar{\mathcal{E}} \sin(2kx)\mathcal{A}(\alpha,\sigma) \tag{2}$$

where k is the acoustic wave number, d is the radius of a sphere, $\bar{\mathcal{E}}$ is the mean total energy-density, x is the distance from the pressure node and $\mathcal{A}(\alpha,\sigma)$ is the density-compressibility factor that is given by Eq. 1. This expression is valid with $d/\lambda << 1$, where d is the diameter of the bead and λ is the wavelength, a condition easily satisfied in experiments. The radiation force F_{ac} has been experimentally evaluated by K. Yasuda and T. Kamakura [4] and found by measuring velocity

0-9640024-4-2/hh2002/$20©2002TRF
DOI 10.31438/trf.hh2002.25

versus time of particles subjected to acoustic pressure. Since the contrast factor $\mathcal{A}$ of polystyrene beads is positive, the density of polystyrene and speed of sound are 1.05 g/cm^3 and 2170 m/s, respectively, the beads are expected to move toward the pressure nodes ($x = n\lambda/2$, where $n = 0, 1, 2, \ldots$) of the standing wave.

In addition to radiation pressure, the volume uptake of the particles in finite space of a glass capillary will lead to the non-linear bands formed by the beads. Since the force is proportional to the cube of the particle diameter (d^3), one predicts that the large particles will move towards the nodes with a higher force, leading to particle separation. Additionally, there is the shear viscous acoustic field near the wall of the glass capillaries that can cause localized streaming and radiation forces but is not important in the effect studied in this paper.

THE GLASS CAPILLARY/PZT ACTUATOR

A schematic drawing of the glass capillary/PZT transducer is shown in Figure 1. A polyimide coated glass capillary (ID = 100 μm, OD = 200 μm, coated polyimide thickness = 12 μm) is folded around the PZT plate (10 mm $\times$ 2.5 mm $\times$ 0.5 mm). For intimate contact between the PZT plate and glass capillary, a 300 μm deep trench was made on the both ends of the PZT plate and glass capillary is adhesively bonded to the trenches of PZT plate ends using cyanoacrylate. The intimate contact ensures controlled boundary conditions for repeatable results. The bent shape was chosen to ensure easy access to a CCD to image the inside of the capillary. This setup also decouples the acoustic boundary conditions of the separator from those of other components such as the acoustic pump. A typical hand-assembled device is shown in Figure 2. Two electrodes are soldered at the center of the PZT plate since a node of the displacement of PZT plate is at the center.

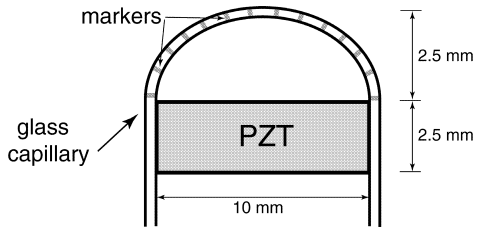

Figure 1. Schematic drawing of the capillary/PZT transducer. The actual device (Figure 2) has a 300 μm deep trench at each end of the PZT plate to secure the glass capillary.

The $\lambda/2$ mode along the PZT plate length is weakly coupled to bending modes as shown in Figure 3. The resonance frequency of this mode can be approximated as

$$f = \frac{c}{2L_{eff}} \tag{3}$$

where c ($\sim$ 3200 m/s) is the speed of sound in the PZT plate and L_{eff} is the effective length or width of the PZT plate. From Eq. 3, half-wavelength resonance frequencies for the length mode is $\sim$ 160 kHz. Measured electrical impedance from an HP4194 impedance analyzer is shown in Figure 3.

THE GLASS CAPILLARY MOTION ANALYSIS

The exact analysis for the capillary motion requires consideration of the finite radius of curvature of the bent

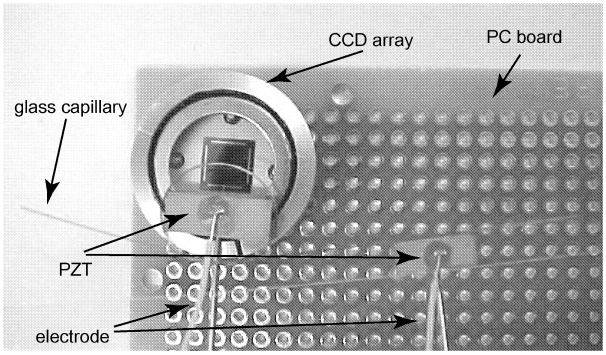

Figure 2. The capillary/PZT transducer with electrodes on a circuit board. There are lithographically defined evenly spaced titanium thin film markers on the capillary to assist velocity measurements and to monitor bead location in the capillary.

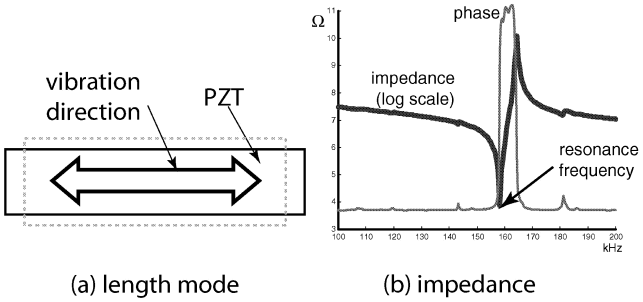

Figure 3. Measured impedance of the glass capillary/PZT transducer using an HP4194 impedance analyzer (The resonance frequency of the length mode is slightly different from the PZT plate resonance. This is due to the glass capillary loading effect).

beam. Instead we choose to model the bent capillary as a straight beam, which leads to results that reconfirmed by finite element analysis and experimental data. The bending motion of a straight beam can be modelled by

$$EI\frac{\partial^4 u}{\partial x^4} = \rho A\frac{\partial^2 u}{\partial t^2} \tag{4}$$

where E is the Young's modulus of the glass capillary, I is the moment of inertia, ρ is the density, A is the cross section area, and u is the displacement. The standing wave solutions to Eq. 4 can be written as

$$\begin{aligned} u(x) &= C_1\sinh(kx) + C_2\cosh(kx) \\ &\quad + C_3\sin(kx) + C_4\cos(kx) \end{aligned} \tag{5}$$

For the clamped-clamped beam, the $\sin(kx)$ dominates while the $\sinh(kx)$ satisfies boundary conditions at the clamped edges. Here we approximate the solution as $\sin(kx)$ for simplicity. In addition to capillary bending modes, the motion of the PZT plate is superposed on the capillary mode. As shown in Figure 4, if the capillary is not resonated, the PZT plate motion induces the following approximate motion to the capillary,

$$v_x \sim x/L - 1/2 \tag{6}$$

$$v_{y,dc} \sim -x\cdot(x - L) \tag{7}$$

where L is the length of the capillary and PZT plate edge is located at $x = 0$. However, if the capillary is resonated at its bending mode resonance frequencies, an AC motion of the glass capillary will be induced as mentioned above (Eq. 5) and can be written as

$$v_{y,ac} \sim \sin(kx) \tag{8}$$

Hence, the total glass capillary velocity in the y direction may be written as,

$$v_{y,total} = A_1 \cdot x \cdot (x - L) + B_1 \cdot \sin(kx) \tag{9}$$

where A_1 and B_1 are constants determined by device dimensions, material properties and driving frequency.

The total velocity profile of the capillary in the x and y directions are shown in Figure 4 for A=6 and B=1.

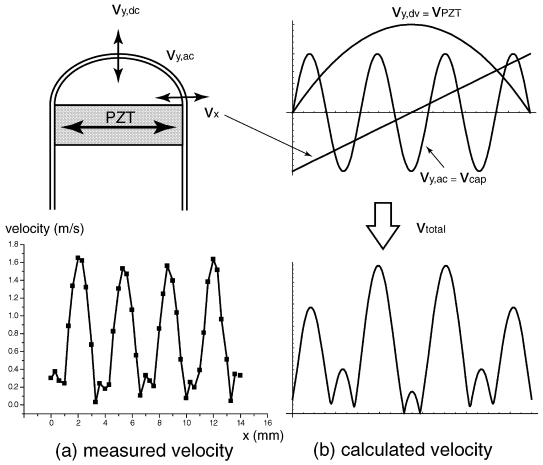

Figure 4. Measured v_{total} and analytical profile of v_x, v_y and v_{total} using straight-beam approximation.

The capillary displacement and velocity were measured using a Polytec-PI interferometer. The measured velocity of the capillary excited at 160 kHz (corresponds to PZT $\lambda/2$ mode) are shown in Figure 4 (a). This measured velocity profile matches well with the calculated data. ANSYS analysis was also done to calculate the capillary transverse motion, for comparison with the measured data as shown in Figure 5. The calculated velocity is well matched with the measured data and the simple model except near the capillary-PZT plate joint. It is believed that this discrepancy was due to pre-existing tension of the bent capillary that was not included in the analysis. Modal analysis revealed that there are several resonance modes which correspond to capillary resonance and total system resonance (Figure 6). As we can clearly see in Figure 6 the capillary resonance (for example, $\sim$ 139 and 166 kHz) is close to the total system resonance ($\sim$ 159 kHz) as also verified by experiments.

PRINCIPLE OF OPERATION

Given the motion analysis, we can focus on how the acoustic system separates particles. The transverse motion of the capillary is excited over a wide range of frequencies as shown in Figure 6. This motion induces a force given by

$$F_{inertial} = \frac{\pi^2}{4} M u_0^2 \omega^2 k_{cap} \sin(2k_{cap}x) \tag{10}$$

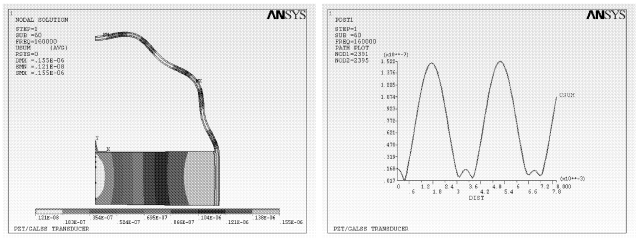

Figure 5. ANSYS harmonic analysis. (a) The motion of the actuator. (b) The displacement profile along the capillary.

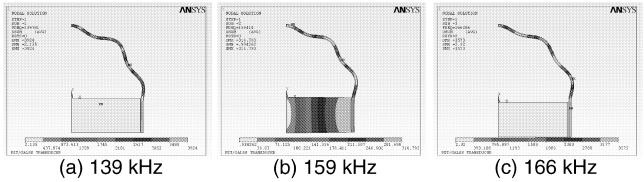

Figure 6. ANSYS modal analysis results. (b) indicates glass capillary/PZT coupled resonance. Other modes are PZT motion exciting eigen modes of capillary.

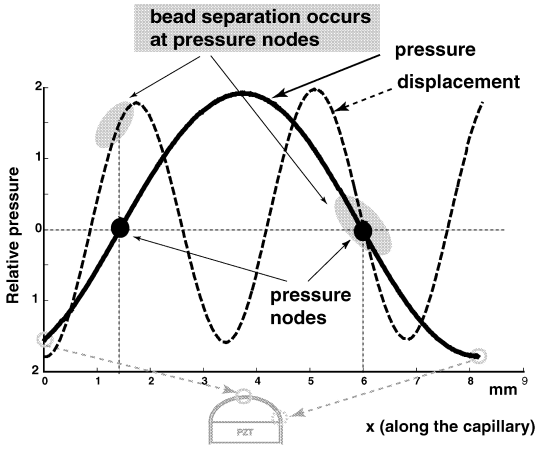

Figure 7. ANSYS derived the pressure profile inside the capillary: The displacement profile of the capillary was overlapped onto the pressure profile. the polystyrene beads were focused at the pressure nodes and separated.

where M (= $\frac{4\pi}{3} d^3(\rho_{bead} - \rho_{water})$) is the mass difference between the bead and water, u_0 is the transverse displacement amplitude, ω is the radian frequency, and k_{cap} is the wavenumber corresponding to the capillary mode. The derivation of this force is beyond the scope of this paper. The inertial force alone randomizes the bead motion and separation is not achieved. To separate, the radiation force along the capillary is needed. The x-directed velocity in Figure 4 is a approximated as a straight line. The PZT stretches the capillary exciting the symmetric acoustic pressure standing waves inside the capillary. This pressure wave is shown as the pseudo-half wavelength pressure shown in Figure 7. This pressure wave is responsible for focusing the beads at the pressure nodes as predicted by Eq. 2. At PZT resonance, this force is sufficient to overcome the inertial forces described by Eq. 10. Then as the frequency is changed slightly around the resonance frequency, the radiation force is reduced and the inertial force acting

in different directions separates the beads at different angles as shown in Figure 8. Hence,bead separation is enabled by application of radiation and inertial forces acting in different directions with controlled amplitudes. As shown in Figure 7, the inertial force is maximized at the points of maximum slope of the capillary transverse motion, close to the points of stable points of radiation force. Two such points are shown in Figure 7, which were verified by experiments.

SEPARATION EXPERIMENTS

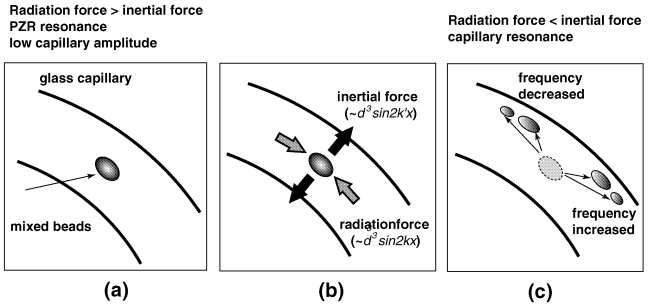

Figure 8. (a) The radiation force acting axially focuses all the beads together overcoming the inertial forces. (b) The radiation force reduction and the separation of particles. Note that as the frequency is increased or decreased, the inertial force vector changes giving separated beads in two different angles as shown in (c).

Although different bead sizes ranging from $0.5\mu m$ to $10\mu m$ were separated, the methodology is displayed for 3 and 10 μm beads is shown in Figure 9. Figure 9 (a) shows uniformly distributed bead mixture in the capillary before the actuation, (b) shows the beads moving to a node when the actuator is driven at the PZT plate length mode (159 kHz @ $1V_{pp}$) resonance resulting focusing of the beads at the pressure nodes. After the beads moved to the node, the frequency is changed to 165 kHz resulting in bead separation due to the intertial force acting in orthogonal directions to the radiation force (c), and then 3 seconds later the bead mixture was totally separated, (d). Such beads separations could be used to perform ratiometric assays if beads are coated by different antibodies. Another application of separation is to separate white cells from red blood cells for diagnosis. Figure 10 shows the left over white blood cells after red blood cells were lysed away in the bead focus areas.

CONCLUSIONS

A novel structure for bead separation for assays using radiation pressure and inertial forces has been demonstrated. An analysis of capillary motion that agrees with the measured data leads to pressure nodes where the beads move into and the radiation force and the gradient of the radiation force separate different size beads. The driving voltage was less than 1 V_{pp}, which can be operated by traditional CMOS circuits. The glass capillary/PZT actuator was successfully integrated onto a CCD/LCD (with a portable computer) for a portable microfluidic assay system.

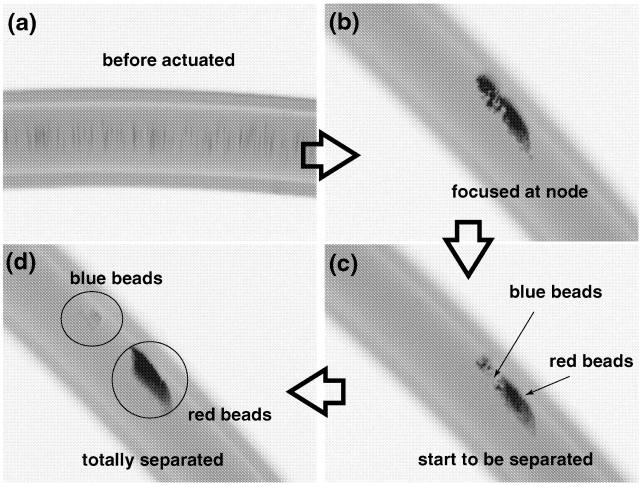

Figure 9. Bead separation at a pressure node: the size of the beads on top-left side is 3 μm and on bottom-right side is 10 μm in (d). These pictures are taken on a fluorescence microscope to distinguish the beads by color.

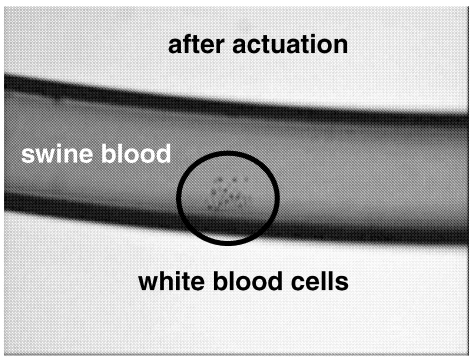

Figure 10. A portable glass capillary/PZT actuator assay system: Swine white cell separation.

ACKNOWLEDGEMENTS

We would like to thank Wisconsin Center for Advanced Microelectronics (WCAM) for technical support. This reserach was supported in part by DARPA-MTO under the BioFlip program, contract #F30602-00-2-0572.

REFERENCES

1. T. Kozuka et al., "Non-contact micromanipulation using an ultrasonic standing wave field," *IEEE, The Ninth Annual International Workshop on Micro Electro Mechanical Systems*, pp. 435–440, 1996.
2. G. Whitworth and W. T. Coakley, "Particle column formation in a stationary ultrasonic field," *Journal-of-the-Acoustical-Society-of-America*, vol. 91, no. 1, pp. 79–85, 1992.
3. K. Yosioka and Y. Kawasima, "Acoustic radiaotion pressure on a compressible sphere," *Acustica*, vol. 5, pp. 167–173, 1955.
4. K. Yasuda and T. Kamakura, "Acoustic radiation force on micrometer-size particles," *Appl. Phys. Lett.*, vol. 71, no. 13, pp. 1771–1773, 1997.

THERMOELASTICALLY ACTUATED ACOUSTIC PROXIMITY SENSOR WITH INTEGRATED THROUGH-WAFER INTERCONNECTS

Venkataraman Chandrasekaran[1], Eugene M. Chow*[2], Thomas W. Kenny*[1], Toshikazu Nishida[2], Louis N. Cattafesta[1], Bhavani V. Sankar[1] and Mark Sheplak[1]

[1]Department of Aerospace Engineering, Mechanics and Engineering Science
[2]Department of Electrical and Computer Engineering
University of Florida
Gainesville, FL 32611-6250

*[1]Department of Mechanical Engineering
*[2]Department of Electrical and Computer Engineering
Stanford University
Stanford, CA 94305-4085

ABSTRACT

This paper presents the development of a micromachined acoustic sensor/actuator for real-time cavity monitoring for high-speed, supercavitating vehicles (HSSV). Low-resistance polysilicon through-wafer electrical interconnects have been integrated with the sensor to enable backside contacts for drive and sense circuitry. The sensor and interconnects were fabricated in a CMOS compatible process using a deep reactive ion etch (DRIE), producing a 1 *mm* diameter, 10 μm thick diaphragm and 20 μm diameter high aspect ratio through-wafer vias on a SOI wafer. The diaphragm incorporates a central resistive heater for thermoelastic actuation and diffused piezoresistors for sensing acoustic pressure perturbations. Measured results indicate an acoustic transmitting sensitivity of 22 *mPa/V* at a distance of 10 *mm* and a frequency of 60 *kHz*, a receiving sensitivity of 0.98 $\mu V/(V.Pa)$, a flat frequency response over the measured range of 1-20 *kHz*, a linear response from 60-140 *dB*, negligible leakage current for the junction-isolated diffused piezoresistors (<2 *nA* at –10 *V*), low interconnect resistance of 14 Ω, and a noise floor of $\approx 1.4 \times 10^{-16}\ V^2/Hz$ at a bias of 9 *V*, in the frequency range of operation.

INTRODUCTION

Our goal is to develop a real-time cavity monitoring system for a high-speed, supercavitating underwater vehicle. The high velocity of the vehicle is made possible by supercavitation, which results in the entire vehicle being encapsulated in a gaseous cavity or bubble, thus greatly reducing wetted friction drag **[1]**. There are several methods to measure the cavity distance, all involving the radiation of energy from the hull towards the cavity interface, the subsequent reflection of the incident wave at the gas/water interface, and the detection of the reflected pulse (Figure 1). The unstable nature and poor electromagnetic (EM) reflection coefficient of the air/water interface are some of the disadvantages of using laser or EM-based techniques. Acoustic techniques possess good signal-to-noise characteristics due to the sound hard boundary at the interface **[2]**. In addition, as the cavity structure begins to degrade and the interface possesses waviness or bubbly regions, the specular reflection assumption is strongly dependent on the interface roughness relative to the wavelength (λ) of the radiated energy. If the wavelength is on the order of the interface roughness or smaller, the incident radiation will be scattered at the wavy interface and may not be redirected to the fixed receiver location. In these regions, acoustic-based techniques provide an advantage because it is possible to fabricate compact devices to radiate acoustic energy possessing wavelengths on the order of a millimeter **[3]**. Thus acoustic techniques present a potentially efficient way of measuring the interface proximity as well as discerning the nature of the interface. The harsh seawater environment necessitates a sensor possessing a hydrophobic barrier and backside electrical connections (Figure 1).

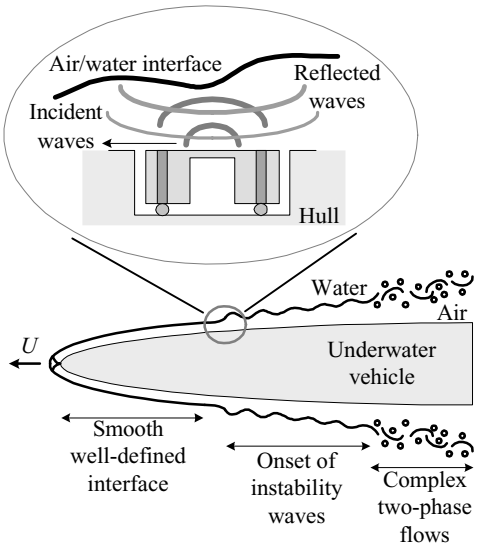

Figure 1: *Bump-bonded sensor package placed on the hull of an underwater supercavitating vehicle for monitoring the state and thickness of the air/water interface.*

Acoustic proximity sensors based on various operating principles have been reported including thermoelastic **[3]**, capacitive **[4]** and piezoelectric **[5]**, but these do not meet all the requirements of a real-time cavity monitor in terms of operating frequencies and packaging suitable for harsh environments.

ACOUSTIC PROXIMITY SENSOR

The acoustic transceiver structure integrates diffused resistors for thermoelastic actuation and piezoresistive detection and boron-doped polysilicon electrical through-wafer interconnects (ETWI). Figure 2 shows a top view microscopic image of the sensor/actuator, and a cross-sectional schematic is shown in Figure

Travel support has been generously provided by the Transducers Research Foundation and by the DARPA MEMS and DARPA BioFlips programs.

3. The device structure consists of a 1 *mm* diameter, 10 μm thick circular composite diaphragm. Two semicircular diffused heaters (60 μm diameter) are located in the center for electrothermal actuation of the diaphragm. Four diffused p-type silicon piezoresistors are located at the edge of the diaphragm for piezoresistive detection of the membrane vibrations.

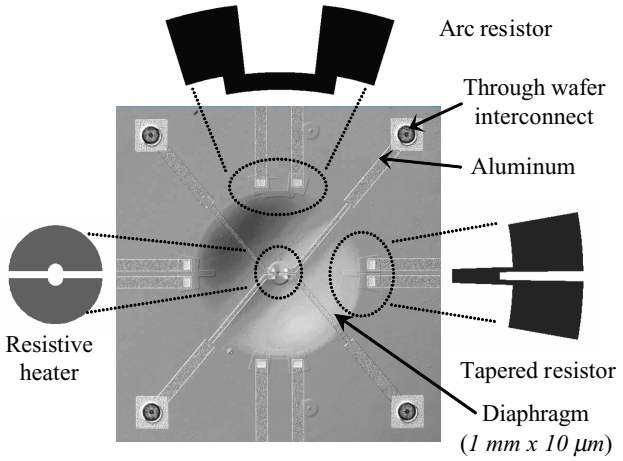

***Figure 2**: Top view microscopic (diffraction interference contrast) image of the acoustic proximity sensor with integrated through-wafer interconnects.*

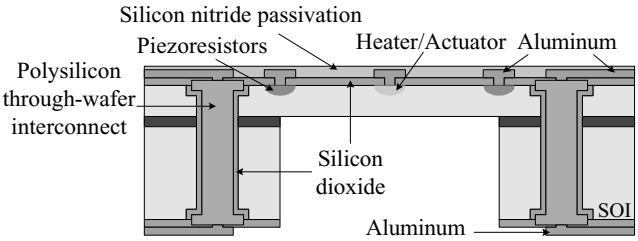

***Figure 3:** Cross-sectional schematic of the proximity sensor.*

The intended application of the sensor necessitates a rugged package capable of withstanding the harsh seawater environment. Therefore, polysilicon ETWI measuring 20 μm in diameter have been integrated with the sensor/actuator **[6,7]**. The use of p-type ETWI enables direct ohmic contact to p-type piezoresistors employed for the acoustic sensor. The ETWI thus enables an integrated "bump-bonded" sensor package with the drive and sense circuitry hidden from the environment. We have previously integrated ETWI with released piezoresistive sensors for cantilever arrays **[8]**. The heater for thermoelastic actuation and piezoresistors are connected to the ETWI via 75 μm wide, 1.4 μm thick aluminum traces. A 7000 $\AA$ thick silicon dioxide film is thermally grown on top of the silicon layer to provide compressive stress to the diaphragm in addition to serving as a dielectric passivation for the piezoresistors. A 3500 $\AA$ low-stress, PECVD silicon nitride passivation layer provides a protective moisture barrier on the top surface of the device.

OPERATING PRINCIPLES

Thermoelastic Actuation

Dynamic Joule heating of the resistor causes the formation of a temperature gradient across the diaphragm cross-section. This non-uniform temperature distribution produces a thermal moment that results in out-of-plane bending of the diaphragm. The asymmetrical composite lay-up of the diaphragm (see Figure 3) further enhances the coupling between in-plane forces generated by the heating and the transverse deflection **[9]**. Thus, by applying a time-varying instantaneous voltage signal, the diaphragm is forced into vibration. The temperature distribution in the diaphragm is a function of the driving frequency of the signal and depends on the depth of penetration of the thermal wave, governed by Fourier's law of heat conduction **[10]**. The harmonic heating excites the diaphragm at the driving frequency, ω, but also at twice that frequency, 2ω, and at dc. This is due to the non-linear nature of thermoelastic actuation, where the input power has a quadratic dependence on the excitation voltage, causing the power to be redistributed into two frequency bins (i.e., 0 and 2ω). By adding a conditioning dc voltage **[3]** the ratio of power between the two frequencies can be controlled as shown by the following equation,

$$\left(\bar{V} + V' \sin \omega t\right)^2 = \bar{V}^2 + \frac{V'^2}{2}\left(1 - \cos 2\omega t\right) + 2\bar{V}V' \sin \omega t.$$

However, adding an offset voltage to the harmonic signal adds a static temperature distribution, which consequently changes the in-plane stress field and the resonant frequency of the diaphragm.

Piezoresistive Detection

Electromechanical transduction of the membrane vibration is achieved via four diffused silicon piezoresistors located at the edge of the diaphragm in a Wheatstone bridge configuration **[11]**. The arrangement consists of two tapered and two arc-shaped piezoresistors. The piezoresistors are designed such that they possess the same nominal resistance. An acoustic wave impinging on the diaphragm causes it to deflect and changes the stress in the diaphragm. The change in resistance of the piezoresistors due to a change in the stress field is equal but opposite for the arc and tapered resistors due to the nature of the stress being detected. Thus for an undeflected diaphragm, the output of the Wheatstone bridge is zero, but a deflection caused by an acoustic wave produces a differential voltage output across the bridge.

FABRICATION

The fabrication process begins with the creation of the ETWI **[6,7]**. After the wafer with ETWI is planarized, the ETWI wafer provides the substrate for the subsequent backend CMOS process to fabricate the acoustic proximity sensor. Figure 4 outlines the overall fabrication sequence.

Electrical Through-Wafer Interconnects

The fabrication process begins with a 450 μm thick double side polished n-type silicon-on-insulator wafer. A 2 μm thick thermally grown silicon dioxide acts as the mask for the through-wafer via DRIE. The front and the backsides of the wafer were etched for approximately equal durations (**4A**). Etching through both sides of the wafer was done to maintain a high aspect ratio for the structure. To achieve smooth sidewalls and a straight via profile, a 30 minute timed overetch from the front side of the wafer was performed using an etch recipe with higher passivation. The oxide used as a mask was then stripped using a buffered oxide etch (BOE). After the via formation, the interconnect were dielectrically isolated from the bulk silicon substrate by growing a 2 μm thermal oxide (**4B**). Electrical conduction was achieved through the deposition of 2 μm LPCVD polysilicon over the oxide (**4B**). This was followed by boron diffusion doping of the polysilicon for 2 hours at $1000^{o}C$ and then a drive-in anneal at $1000^{o}C$.

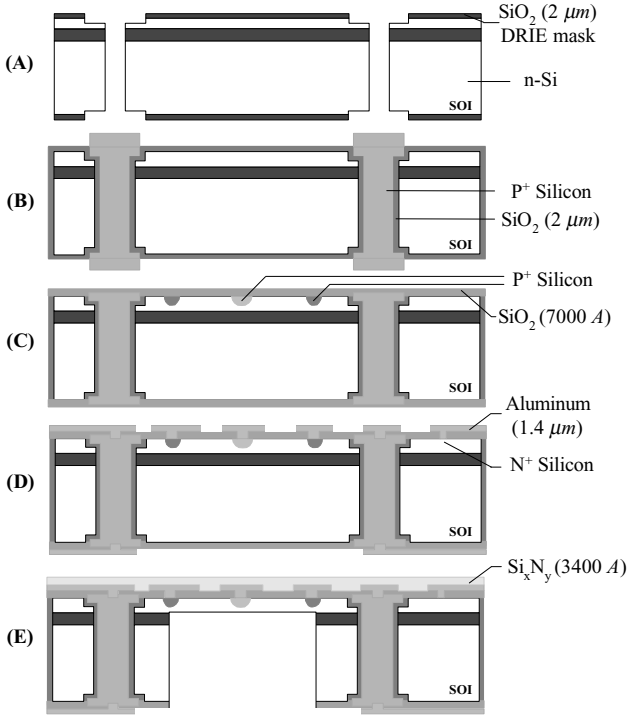

Figure 4: *A schematic of the fabrication sequence.*

The boron diffusion process results in the formation of a non-conducting borosilicate glass that is not easily etched by hydrofluoric acid. However, a wet oxidation at 1100^{o}C for 30 minutes, followed by a 60 minute etch using (6:1) BOE effectively removes the non-conducting glass. The process of polysilicon deposition and boron diffusion doping was repeated 2-3 times to achieve a low-resistance pETWI. Further details of the ETWI fabrication process can be found in *Chow et. al* **[6]** and *Chandrasekaran et. al* **[7]**. After patterning the ETWI, an isotropic plasma etch was performed on the doped polysilicon to planarize the interconnects and produce a gradually sloping sidewall on the front and back of the wafer (**4C**). This is critical for the integration of the ETWI with the sensor/actuator since it ensures proper metal coverage over the ETWI.

Acoustic Sensor/Actuator

A thin layer of oxide was then grown and patterned for the heater implantation. Boron was implanted to achieve P^{++} regions with a concentration of 1E-20 cm^{-3} (**4C**). After implantation, the wafers were annealed at 1100 ^{o}C for 30 minutes to create a junction depth of 0.75 μm. The wafers were then patterned with the piezoresistors mask and again implanted with boron to form P^{++} regions of similar concentration (**4C**). A silicon dioxide layer 7000 $\AA$ thick was thermally grown at 950 ^{o}C to passivate the resistors and provide a compressive stress to the diaphragm (**4C**). The diffusion of the heater resistors and piezoresistors were simulated using FLOOPS **[12]** to account for the entire thermal budget of the process flow. A 1.4 μm thick aluminum (Al/1%Si) layer was sputtered and patterned once the contact cuts in the oxide dielectric layer were made (**4D**). Low stress PECVD nitride (3500 $\AA$) was then deposited to form a moisture barrier (**4E**). The wafers were then patterned on the backside with front to back alignment to create the diaphragm. The relative alignment of the piezoresistors and the diaphragm is critical to ensure piezoresistor placement at the edge of the diaphragm. DRIE was performed from the backside of the wafer up to the buried oxide layer (BOX) (**4E**). Once the diaphragm was created, the buried oxide layer was removed using 6:1 BOE.

RESULTS AND DISCUSSION

Experimental characterization of the sensor/actuator was conducted in the Interdisciplinary Microsystems Laboratory at the University of Florida. The experimental details and results of the electrical and acoustic characterization of the sensor/actuator are described in this section.

Electrical Characterization

Current versus voltage (I-V) characterizations were performed on the sensors to extract the resistance of the diffused piezoresistors and the ETWI. In addition, I-V measurements were also obtained across the p-n junction formed between the diffused resistors and the silicon substrate to obtain its forward and reverse bias characteristics. The reverse bias characteristics of this p-n junction determines the leakage current from the resistors into the substrate. Minimal leakage is essential for effective Joule heating of the diaphragm and low piezoresistor noise floor. All measurements were made using a Hewlett Packard 4155B semiconductor parameter analyzer and a wafer level probe station.

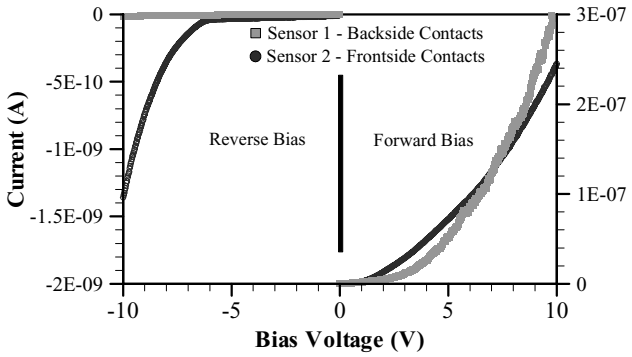

Figure 5*: Forward and reverse bias characteristics of the diffused piezoresistors, indicating negligible leakage current (< 2 nA at -10 V).*

Results of the I-V characterization indicate negligible leakage current up to a reverse bias voltage of 10 V (Figure 5). The forward and reverse bias characteristics of the p-n junction measured through the ETWI was compared to another sensor with front-side contacts. As indicated in Figure 5, the interconnects do not affect the bias characteristics. The results also indicate deviations from the ideal diode behavior due to a large series resistance of the lightly doped silicon substrate. The average resistance was found to be around 2200 Ω for the actuating heater, 5500 Ω for the arc resistor and 7500 Ω for the tapered resistor. The average ETWI resistance was measured to be around 14 Ω.

Diaphragm Surface Velocity Measurements

Transverse velocity measurements were made on the diaphragm surface using a Polytec scanning laser vibrometer fitted onto an Olympus microscope producing a laser spot size of 2 μm. The diaphragm was excited using a periodic chirp signal with a specified dc offset. The response of the diaphragm was obtained at specific scan points on the surface. This velocity information measured over the entire surface is then integrated to obtain displacement mode shapes.

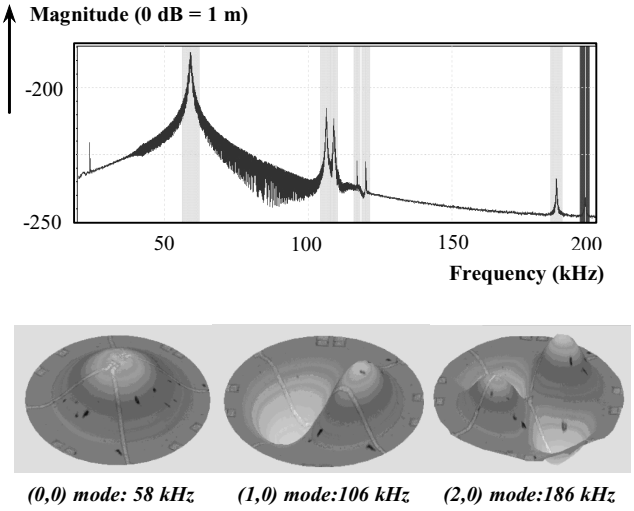

Figure 6: *Average spectrum and visualization of the vibrating diaphragm mode shapes using a scanning laser vibrometer.*

Figure 6 shows the average spectrum of the diaphragm surface response to the excitation signal and also illustrates the first three vibration modes.

Acoustic Characterization - Receiver

The dynamic response of the sensor to acoustic pressure perturbations was characterized in a plane wave tube (PWT). The PWT consists of a rigid-walled duct that supports planar (0,0 mode) acoustic waves propagating along the length of the duct. Thus, sensors placed at the same axial location from the acoustic driver sense the same acoustic pressure field.

The sensors were calibrated in two different PWTs, a 25.4 *mm* x 25.4 *mm* normal incidence PWT and an 8.5 *mm* x 8.5 *mm* grazing incidence PWT. The sensor and a reference microphone (Brüel and Kjær Type 4138) were flush mounted at the same axial distance from the acoustic driver. The sensor was biased at 9 *V*, and the differential output of the Wheatstone bridge was connected to a SR560 preamplifier. The amplified signal was then fed into a SR785 dynamic spectrum analyzer for data processing.

The low-frequency cut-off for the first non-planar (1,0), (0,1) mode is 20 *kHz* for the grazing incidence PWT and 6.7 *kHz* for the normal incidence tube. Thus, the useable bandwidth is limited to 20 *kHz* and 6.7 *kHz* respectively. A low frequency limit of 1 *kHz* is imposed by the compression driver, which becomes excursion limited at low frequencies.

Linearity

The normal incidence PWT was used to measure the linear response of the sensor to varying sound pressure levels. A 1 *kHz* tone at varying amplitudes, monitored by the reference microphone, was used to excite the sensor, which was biased at 9*V*. The rms output voltage of the sensor at each sound pressure level was recorded. The output voltages are shown in Figure 7 for sound pressure levels up to 140 *dB* (ref 20 *μPa*). The results indicate a linear response to acoustic pressure perturbations over four orders of magnitude (60 - 140 *dB*). The calculated sensitivity at 1 *kHz* is 1.415 ± 0.0002 *μV/(V.Pa)*, or equivalently, –117 *dB* re 1 *V/(V.Pa)*.

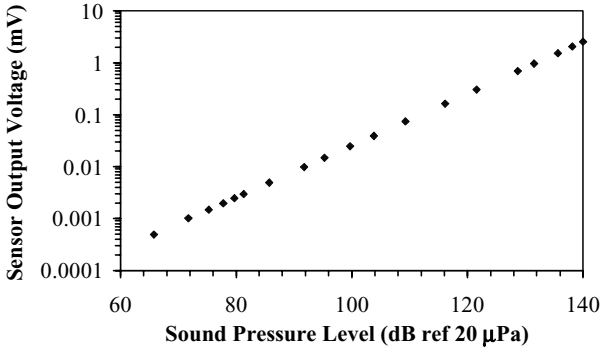

Figure 7: *Plot illustrating the device linearity in sensing acoustic pressure perturbations (up to 140 dB) at a frequency of 1 kHz.*

Frequency Response

Figure 8 shows the magnitude frequency response of the sensor calibrated in the grazing incidence PWT, as well as the normal incidence tube using a constant amplitude tone of 110 *dB*. The plot indicates a flat frequency response with an average sensitivity of 0.98 *μV/(V.Pa)* or equivalently –120.2 *dB* re 1 *V/(V.Pa*) with a standard deviation of 1 *dB* over measured frequency range.

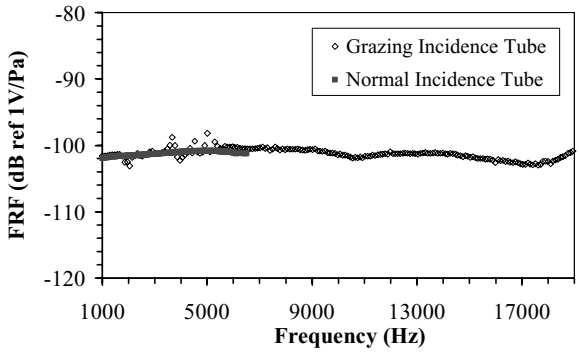

Figure 8: *Magnitude of the sensor frequency response function to a constant sound pressure level of 110 dB.*

The results obtained from the grazing incidence PWT indicate data scatter at low frequencies. These variations may be attributed to the non-ideal propagation characteristics of the tube, including a compliant boundary condition and an area change at the tube termination. The same frequency range (1-6 *kHz*) tested in the normal incidence tube indicates a flat sensor response.

Acoustic Characterization - Transmitter

The end application requires an array of sensors to be used in a network to monitor the state of the entire cavity. When used as an array, minimal cross-talk between the sensors is required for efficient real-time monitoring. The directional behavior of the generated acoustic field and the spacing between the sensors will determine the cross-talk. The acoustic field generated by the vibration of the thermoelastically actuated diaphragm was characterized in a free-field environment. In order to characterize the transmitted acoustic field, two sets of measurements were obtained. In both cases, the transmitting sensor was fixed and oriented such that the diaphragm surface is vertical. The transmitter was excited with a combination of harmonic ac voltage (9 *Vpk*) and a dc (9 *V*) voltage. The acoustic field was measured using a Brüel and Kjær Type 4138 condenser microphone. To measure the directionality of the generated acoustic field, the microphone was positioned at a fixed radial distance of 25 *mm*

from the transmitter and a jig was constructed that allowed the microphone to be revolved around the transmitter at the fixed radius. Sound pressure measurements were made at 2^o intervals, from 0^o (on axis) to 90^o, averaged, and recorded.

To obtain the variation of sound pressure level with distance from the transmitter, the microphone was positioned directly opposite the transmitter on a single axis traverse with a precision of 1 *micron*. The initial position was set at 3 *mm* from the transmitting diaphragm and then varied to 50 *mm* along the axis of the diaphragm. At each position, sound pressure measurements were obtained using a SR785 dynamic spectrum analyzer.

Figure 9 shows the normalized directional response of the generated acoustic field, which indicates a drop in sound pressure level with increasing angle from the diaphragm axis. At an angle of 90^o the sound pressure level is reduced to 40% of the maximum on-axis value. Theoretically, a sensor with Helmholtz number $ka<1$ should exhibit omni-directional radiation pattern, where k is the wave number given by ω/c and a is the diameter of the diaphragm. The observed difference between theory and experiment may be attributed to the packaging of the sensor, which is recessed in a square depression of 0.5 *mm*, or the statically deflected diaphragm, which may also have some effect on focusing the sound field. The oscillations in sound pressure level with changing angle may be the result of scattering from the sensor package.

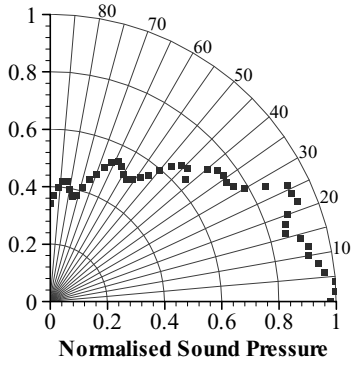

Figure 9: *Directivity of the generated acoustic field at a frequency of 60 kHz.*

Sound pressure measurements versus distance from the diaphragm surface are plotted in Figure 10.

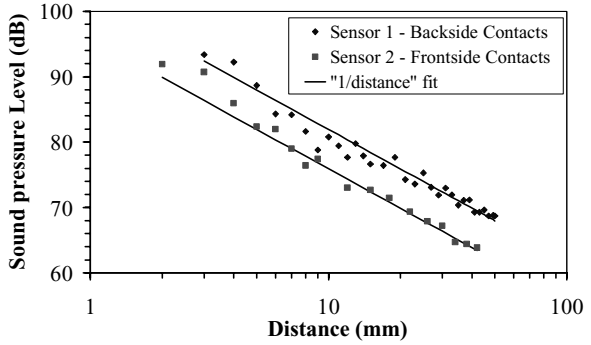

Figure 10: *Sound pressure level of generated acoustic field as a function of radial distance, at a frequency of 60 kHz.*

The graph indicates a transmitting sensitivity of 22 *mPa/V* at a distance of 10 *mm* and an operating frequency of 60 *kHz*. The plot also shows the inverse relation between sound pressure level and distance. The oscillations in the data are due to scattering from the microphone surface resulting in the formation of a standing wave between the transmitter and the microphone. The scattering effect is reduced with increasing distance from the transmitter.

The effect of varying static and dynamic power used to excite the sensor at a fixed frequency (55 *kHz*) was also investigated.

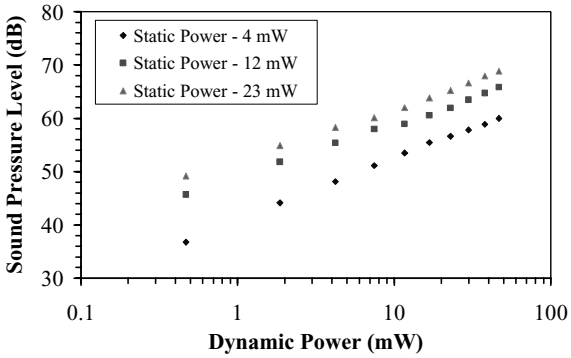

Figure 11: *Variation in sound pressure level with change in static and dynamic input power.*

The results are plotted in Figure 11 and indicate a direct dependence on the dynamic power. The sound pressure level also increases with increasing static power for a given dynamic power. The low sound pressure level observed even at high excitation voltage is due to the operating frequency. The device has a high quality factor (see Figure 6) and exhibits appreciable response only near its resonant frequency.

Noise Floor Spectra

The study of the electrical noise floor of a device is required to determine the minimum detectable signal (MDS). Measurements of the noise power spectral density (PSD) were made in a Faraday cage using low-noise test equipment. The aim of the experimental setup is to isolate the random physical noise of the device under test (DUT) from deterministic interference. Deterministic sources arise from capacitive coupling of electromagnetic interference (EMI) to the device and cabling, with the ac power line being the major contributor (60 *Hz* and its harmonics). The Faraday cage considerably reduces the interference, permitting analysis of the noise PSD.

The sensor was configured similar to the operating conditions with a 9 *V* bias across the Wheatstone bridge. A battery powered Stanford Research Systems SR560 differential amplifier with specified noise voltage of 4 $nV/\sqrt{Hz}$ was used to amplify the differential voltage from the bridge with a gain of 10,000. After proper grounding of all measurement equipment, the noise PSD was measured using a SR785 dynamic spectrum analyzer using 500 averages. In order to maintain sufficient resolution at low frequencies, a low frequency range of 0-1.6 *kHz* with a 2 *Hz* bin was used. This frequency resolution effectively isolates the 60 *Hz* power line interference. Larger frequency ranges of 25.6 *kHz* with 8 *Hz* bin were used for the higher frequencies. In order to extract the device noise floor, the set-up noise PSD was measured by shorting the differential outputs of the bridge and was subtracted from the total noise PSD. The MDS (per $\sqrt{Hz}$) was then calculated by taking the square root of the noise PSD and dividing with the sensitivity of the device to obtain pressure.

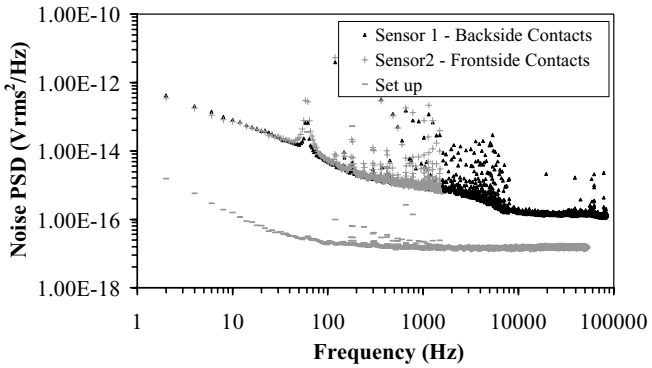

Figure 12: *Noise power spectral density of the sensor at a bridge bias of 9 V (set-up noise included).*

The voltage noise PSD of the sensor is plotted in Figure 12. As indicated**,** the voltage noise PSD is dominated by *1/f* noise at low frequencies. Additional plots of the set-up noise from the amplifier and EMI and a sensor with front-side contacts are also shown for comparison. The results indicate a negligible noise contribution from the interconnect. The *1/f* noise intersects the thermal noise ($\approx 1.4 \times 10^{-16}$ V^2/Hz) at approximately 10 *kHz*, making the device only Johnson noise limited at the operating frequencies. The "spikes" in the data are due to the deterministic interference at 60 *Hz* and 20 *kHz* and their harmonics.

PROXIMITY SENSING

To demonstrate the use of the device as a proximity sensor, two sensors were placed 20 *mm* apart and oriented towards each other. The transmitting sensor was electrothermally excited using a 9 *Vpk* ac signal over a 10 *kHz* frequency range. The generated acoustic signals were detected using a second sensor as the receiver. The receiver was selected such that its first resonance is higher than that of the transmitter. Figure 13 shows the normalized frequency response of the receiver compared to the response of the reference microphone (Brüel and Kjær Type 4138). The plot indicates good agreement between the sensor and the reference microphone. The deviation in response beyond 62 *kHz* is due to the fact that the receiving sensor is approaching its own resonance near 70 *kHz*.

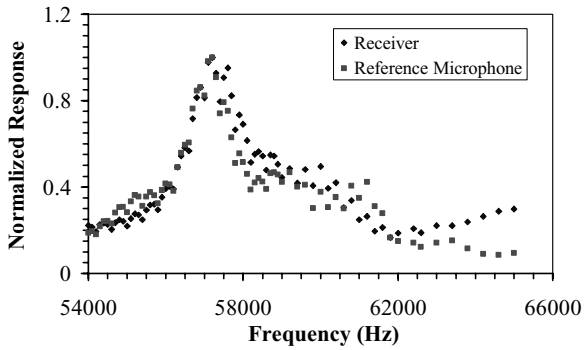

Figure 13: *Plot illustrating the frequency response of the receiver compared to a reference microphone.*

CONCLUSIONS AND FUTURE WORK

An acoustic proximity sensor with integrated through-wafer electrical interconnects has been developed. Preliminary characterizations indicate a flat frequency response, good acoustic receiving sensitivity and a low noise floor (1.34 *mPa/√Hz* - MDS).

Future work will focus on a more thorough characterization of the sensor and the development of an optimized 2nd generation transmitter/receiver based on a non-linear, composite, dynamic model of the diaphragm. The sensor will be implemented with different proximity sensing algorithms developed for real-time monitoring of the cavity surrounding the HSSV. Also, detailed characterization of the diaphragm surface response to various excitation signals using the scanning laser vibrometer will be performed. This information will be used to project the acoustic field generated by the diaphragm via Rayleigh's integral and compared to the acoustic measurement of the radiation pattern.

ACKNOWLEDGEMENT

This work is supported by the Office of Naval Research (contract #N00014-00-1-0343) monitored by Dr. Kam Ng. The sensors were fabricated in the Stanford nanofabrication facility at the Center for Integrated Systems, Stanford.

REFERENCES

1. D. J. Warner, "Technology Assessment of Hydrodynamic/ Supercavitating Technologies," Alliant Techsystems Inc. Final Report, June 1998.
2. M. Rossi, "Acoustics and Electroacoustics," Artech House, 1988.
3. M. R. Hornung, and O. Brand, "Micromachined Ultrasound-Based Proximity Sensors," Kluwer Academic Publishers, Boston, 1999.
4. X. Jin, I. Ladabaum, F. L. Degertekin, et. al., "Fabrication and Characterization of Surface Micromachined Capacitive Ultrasonic Immersion Transducers" *JMEMS*, vol. 8, No. 1, pp. 100-14, 1999.
5. J. Bernstein, K. Houston, L. Niles, et. al., "Micromachined Ferroelectric Transducers for Acoustic Imaging, "*Transducers '97*, pp. 421-4, 1997.
6. E. M. Chow, A. Partridge, C. F. Quate, et. al., "Through-Wafer Electrical Interconnects Compatible with Standard Semiconductor Processing," *Solid State Sensors and Actuator Workshop*, pp.343-6, 2000.
7. V. Chandrasekaran, E. M. Chow, T. W. Kenny, et. al., "Through Wafer Electrical Interconnects For MEMS Sensors," *ASME 2001*, New York, 2001.
8. E.M. Chow, H.T. Soh, and H.C. Lee, "Integration of through-wafer interconnects with a two-dimensional cantilever array," *Sensors and Actuators A*, vol. A83, pp.118, 2000.
9. J. N. Reddy, "Mechanics of Laminated Composite Plates: Theory and Analysis," CRC Press, Boca Raton, FL, 1997.
10. M. Ozisik, "Heat Conduction," Wiley-Interscience Publication, pp. 2, 2000.
11. M. Sheplak, K. S. Breuer, and M. A. Schmidt, "Dielectrically-Isolated, Single-Crystal Silicon, Piezoresistive Microphone," *Solid-State Sensor and Actuator Workshop*, pp. 23-6, 1998.
12. M. E. Law and S. Cea, "Continuum Based Modeling of Silicon Integrated Circuit Processing: An Object Oriented Approach," *Computational Materials Science*, vol. 12, No. 1, pp. 289-308, 1998.

GaAs-BASED WAVEGUIDE MOEMS

O. Blum Spahn, T. Bakke, C. P. Tigges, J. Johnson, G. Grossetete, F. R. Gass, E. M. Ochoa*, J. L. Reno, J. F. Klem, G. M. Peake, C. T. Sullivan

Sandia National Laboratories, MS0603, Albuquerque, NM 87185
Phone: (505) 844-3458, Fax: (505) 844-8985, Email: oblum@sandia.gov

*Air Force Institute of Technology, Wright-Patterson AFB, OH

ABSTRACT

We describe our work on GaAs-based waveguide switch that is also a mechanical cantilever. Several types of 1xn switches have been fabricated and performance of a 1x2 device is presented. Switching voltages between 6V and 13V volts and switching speeds as low as 32 μsec have been measured.

INTRODUCTION

Recently MOEMS have undergone a period of explosive growth, both in terms of academic and commercial interest. While silicon has played a dominant role, there is an increasing interest in compound semiconductor approaches, driven largely by emerging broadband communication and sensor applications.

Use of compound semiconductors for realization of MEMS and MOEMS has several advantages. Due to epitaxial growth, they are monocrystalline, atomically flat and have extremely well controlled thickness and stress. Furthermore, use of direct band gap semiconductors allows for incorporation of optical functionality into mechanical structures, for example truly monolithic integration of lasers, MEMS and detectors. In addition, there are numerous combinations of materials and release etches which can result in MEMS/MOEMS structures [**1**]. Finally, the zinc blende structure allows for piezoelectricity as a result of lack of center of symmetry (in contrast to silicon), which leads to interesting sensing applications. In this paper we describe 1x2 and 1x4 switch consisting of a waveguide embedded in a cantilever, fabricated in GaAs-based materials. Possible applications include a true-time delay for low power, wide-bandwidth, space-borne phased array antenna, nonvolatile mechanical memory with latching waveguide switches and a number of sensing applications, such as 3-axis accelerometer. f integrated with active sources and detectors, such devices can be used for detection of small displacements, as well as implementation of integrated multi-wavelength laser sources for wavelength division multiplexing (WDM).

EXPERIMENTAL DETAILS

The 1x2 switch layout and layer cross section of the waveguide are shown schematically in Figure 1a and b. Fabrication process consists of contact metal patterning, waveguide patterning and dry etch, wet chemical release etching and sublimation drying. Scanning electron micrograph of a completed waveguide is shown in Figure 2. Actuation is accomplished by electrostatic means, by application of bias between the movable waveguide and static electrodes. This results in 4 μm (12 μm) deflection of the 1x2 (1x4) cantilevered waveguide in the plane of the wafer, which lines it up with one of the two output waveguides.

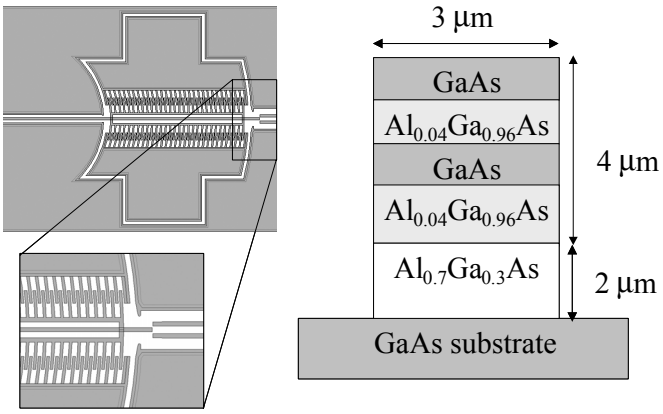

Figure 1 a) schematic layout of a 1x2 switch with the input/output section shown in the inset b) layer structure of the 3 μm wide and 4 μm tall waveguide

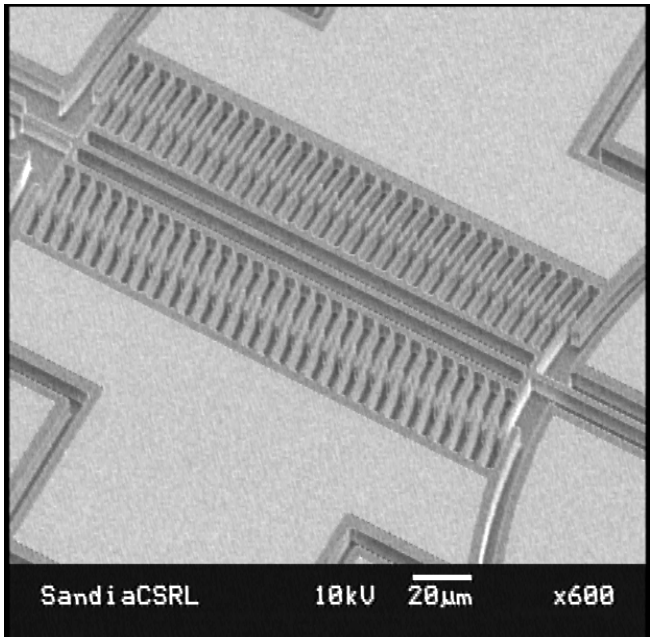

Figure 2 A scanning electron micrograph (SEM) of a top view of fabricated 1x2 switch.

0-9640024-4-2/hh2002/$20©2002TRF
DOI 10.31438/trf.hh2002.27

We also have fabricated a 1x8 waveguide with a 28 μm deflection. 1x2 waveguide cantilevers switch at 6-13 V with resonant frequencies between 2 kHz and 4 kHz for beam lengths between 450 μm to 700 μm as shown in Figure 3. Resonant frequency and Q were measured by DC biasing the movable cantilever to a point where one half of the maximum optical power is observed in the corresponding output waveguide. Then the AC perturbation was applied and temporal power oscillations were a measured at the output waveguide. Resonant frequency and Q were obtained from the frequency of the oscillations and their damping.

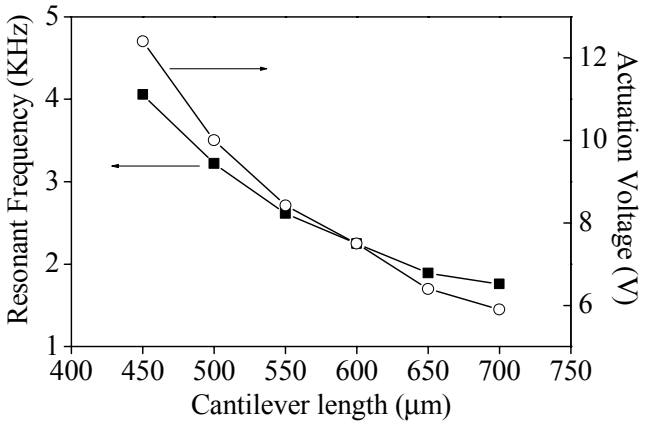

Figure 3 Actuation voltages (voltage for maximum coupling into the output waveguide) for a 1x2 switch for as a function of the cantilever length.

Measured Q values fall between 9 and 4. All measurements are taken in ambient atmosphere. Figure 4 shows optical power measured at the output waveguide as a function of applied voltage for a 1x2 and a 1x4 switch as the cantilever is deflected in one direction.

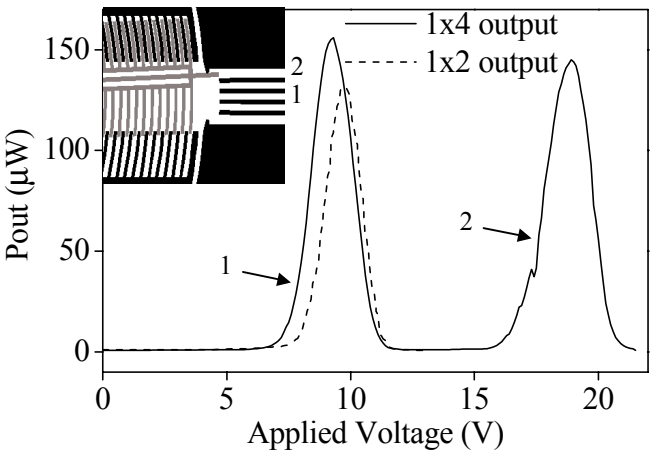

Figure 4 Optical power for a 1x4 (solid line) and 1x2 (dashed line) switch at the output waveguide as a function of bias voltage which deflects the input cantilever waveguide in and out of alignment with the fixed output waveguides (in one direction). Inset shows a schematic of a 1x4 switch deflected in one direction past the output waveguide #1 and #2. Output power in these waveguides is indicated on the plot with a waveguide number.

Waveguides are designed for single mode operation at 1.32 μm, which has been confirmed experimentally for appropriate launch conditions. Experimentally measured end-to-end loss was found to be on the average 0.8 dB/cm excluding fiber to waveguide insertion loss. Major contributors to the loss consist of cross through loss ~0.3 dB and undercut interface loss < 0.05 dB (loss due to transition from undercut region of the waveguide to the anchored region). These optical results were obtained from a previous generation of waveguides [**2**] using thermally detuned Fabry-Perot method. Optical measurements on the current generation are ongoing. It should be noted that the air gap between the movable cantilever waveguide and the fixed output waveguide is designed to be resonant and thus to minimize transmission losses. Dependence of loss on the size of the air gap is described elsewhere [**3**].

Switching speed of these types of waveguides has been predicted to be less than 100 μsec. In fact, previous generation of device was measured to switch at 44 μsec for a 350 μm long cantilever. Use of an appropriate accelerate-brake voltage scheme on the opposite stator electrodes further reduced the switching speed to 32 μsec.

CONCLUSIONS

While there have been reports of silicon-based MOEMS waveguides [**4**], our work represents a novel approach in utilization of compound semiconductors which through their unique properties allow for innovative applications, particularly in the area of monolithically integrated MEMS and photonics

ACKNOWLEDGMENTS

Sandia National Laboratories is a multiprogram laboratory operated by Sandia Corporation for the United States Department of Energy under contract No. DE-AC04-94AL85000.

REFERENCES

1. K. Hjort, "Sacrificial etching of III-V compounds for micromechanical devices", *J. Micromech. Microeng, 370*, 6 (1996)

2. O. B. Spahn, C. T. Sullivan, T. Bakke, A. Allerman, J. Reno, G. Grossetete, J. Lean, C. Fuller, **"**Promise and progress of GaAs MEMS and MOEMS**",** *2001 International Conference on Compound Semiconductor Manufacturing Technology*, 21-24 May 2001, Las Vegas, NV, USA **,** p.77-80

3. T. Bakke, C. P. Tigges, J. J. Lean, C. T. Sullivan and O. B. Spahn, "Planar Microoptomechanical Waveguide Switches", *IEEE J. Select. Topics in Quantum Electron." 64*, 8(2002)

4. E. Ollier, P. Mottier "Integrated electrostatic micro-switch for optical fibre networks driven by low voltage", *Electron. Lett*., *2007*, 32 (1996)

MEMS-Based Flow Controller for Flow Cytometry

Eugen Cabuz, Jay Schwichtenberg, Bob DeMers, Ernie Satren, Aravind Padmanabhan, & Cleo Cabuz
Honeywell Intl.
12001 State Highway 55, Plymouth, MN 55441, aravind.padmanabhan@honeywell.com

ABSTRACT

The paper reports a highly miniaturized, low-power/low-cost micro flow controller capable of producing pressure-driven, pulse-free liquid flows in the nL/sec to mL/sec range. The system operates in closed-loop and relies on two high speed, low power microvalves and a newly developed, highly sensitive liquid flow sensor. A manually pressurized chamber is used as the pressure source. The system has been developed for providing the flows required in a portable flow cytometer [1] using hydrodynamic focusing but it can also be used as a general-purpose flow-driving module in a variety of microfluidic applications where small size, low-cost and low-power are essential. Point-of-care medical microinstruments, highly parallel processing in drug discovery applications, micro dosing system for drug delivery, on-line process monitoring in food/chemical industry are just some areas that would benefit from the described system. The flow controller is also ideally suited for operation in corrosive and biological fluids.

INTRODUCTION

Existing precision fluid delivery systems are bulky, expensive, and typically employ high-power syringe pumps (one order of magnitude larger power) [2]. Such systems are not suitable for use in low-cost portable instruments. The existing electroosmosis/electrophoresis-based pumping systems require high voltages, tend to be invasive and are typically useful only for very low flow rates. The peristaltic (thermal/electrostatic) pumps generate pulses and do not result in precise flow rate control. A recently published pressure-based mass flow controller [3] is about the same size (per channel) as our controller but the lowest flow it can control is two orders of magnitude higher and it consumes five times more power than our controller. There is therefore a need for a miniaturized, pulse-free, and low-power pumping system for controlling flow rates in the µL/s and nL/s regimes. The new flow controller that is reported in this paper addresses this need.

DESCRIPTION

The micro flow controller employs two key MEMS-based technologies that have been developed at Honeywell (Figure 1): electrostatically-actuated silicon microvalves [4], and glass-based thermal microbrick™ flow sensors [5].

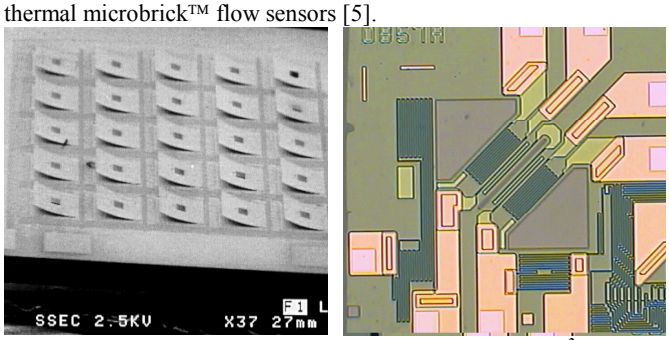

Figure 1. SEM photographs of the 6 x 6 x 0.4 mm³ silicon microvalve and 1.7 x 1.7 x 0.5 mm³ microbrick™ liquid flow sensor chips.

Figure 2 shows a schematic structure of the proposed micro flow controller. The key elements/features of each channel of the controller are:

- an unregulated primary high pressure source (P_d = 0.2 psi gage; P_{max} = 1.0 psi gage; Vol_{max} = 2 cm^3 = 4x6x0.08 cm^3) which, for portable applications can be manually pressurized. A low power mesopump can be used to generate desired pressure in other cases [6];
- a regulated secondary pressure source (0.1–1 psi gage), with the pressure drawn from the primary pressure source and controlled through two low-power (< 1 mW) & fast (~ 1 ms)/high impedance microvalves;
- a short response time (~ 1 ms) flow sensor capable of measuring liquid flows in the nL/sec – mL/sec range;
- a closed loop circuit including the flow sensor and the valves that maintains a constant flow in each channel;
- a pneumatic-to-hydraulic interface realized with a porous plug;
- a very good seal between the flow controller and the fluidic channel;
- the overall response time for the flow controller is about 10 milliseconds.

SIMULATION

A SPICE system model has been developed to predict the operation of the flow controller and to study the effect of compliance in a miniaturized pneumatically driven pumping system. For the chosen microcytometer cartridge design, the model showed that the effect of vibrations on core formation and flow stability were either minimal or non-existent. This SPICE modeling result was confirmed by experimental work done with the flow controller. Detailed results of the simulation work will be reported at the conference.

EXPERIMENTAL RESULTS

The flow controller has been extensively characterized for different types of microvalves and different operation regimes. Flow rate pulsatility of less than 3% (Figure 3) has been demonstrated for the microcytometer application.

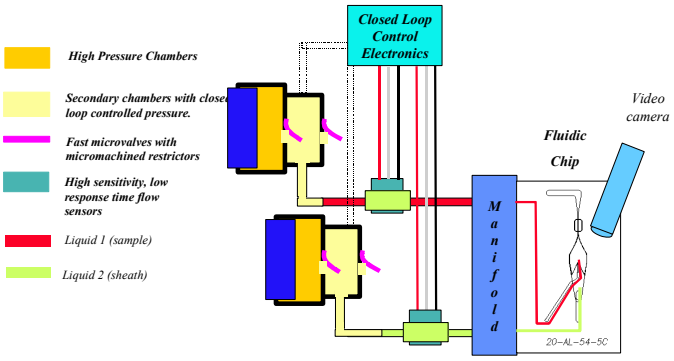

Figure 2. Schematic diagram of a 2-channel micro flow controller based on MEMS-based microvalves and flow sensors.

0-9640024-4-2/hh2002/$20©2002TRF
DOI 10.31438/trf.hh2002.28

Solid-State Sensors, Actuators, and Microsystems Workshop
Hilton Head Island, South Carolina, June 2-6, 2002

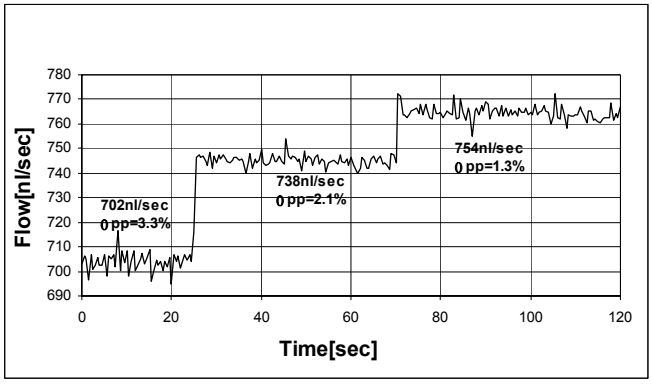

Figure 3. Experimental results showing excellent flow rate control (1.3 to 3.3 % peak-to-peak rate variation) obtained by pneumatically driving the liquid from a manually pressurized source, through closed-loop control. Each closed-loop channel comprises of two silicon micromachined microvalves and a microbrick™ liquid flow sensor.

This measured pulsatility is more than *one order of magnitude better* than what can be obtained using commercially available precision syringe pumps. A figure of merit defined as: *size* x *cost* x *pulsatility* for the proposed flow controller would be more than *two orders of magnitude better* than that for currently available, state-of-the-art open-loop fluid pumping systems.

Figure 4 shows a cross-sectional view through the five modules of the flow controller: pressure source module, microvalve module, reagent reservoir module, interface module, and flow sensor module.

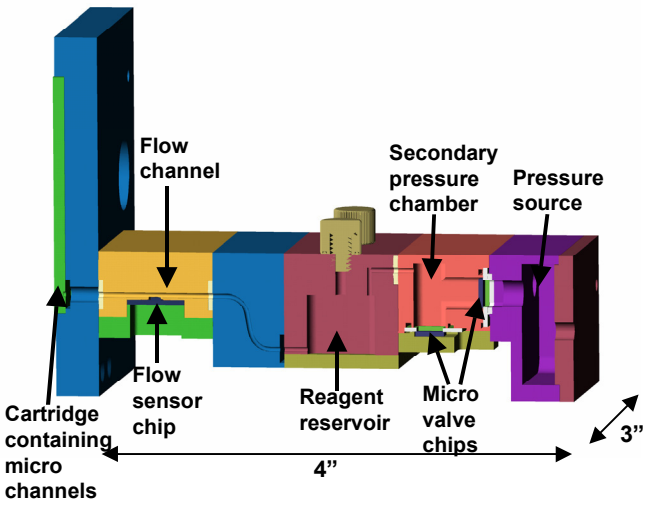

Figure 4. Cross-sectional view of the micro flow controller showing the various modules. The modules interface with each via custom-built polymer seals.

Figure 5 shows a photograph of the flow controller. This system was used to generate a 15 µm wide core flow in the flow channel of the Honeywell microcytometer. Figure 6 shows the core widths that were generated for various sheath-to-core flow rate ratios. Stable, and repeatable core formation was demonstrated with the flow controller.

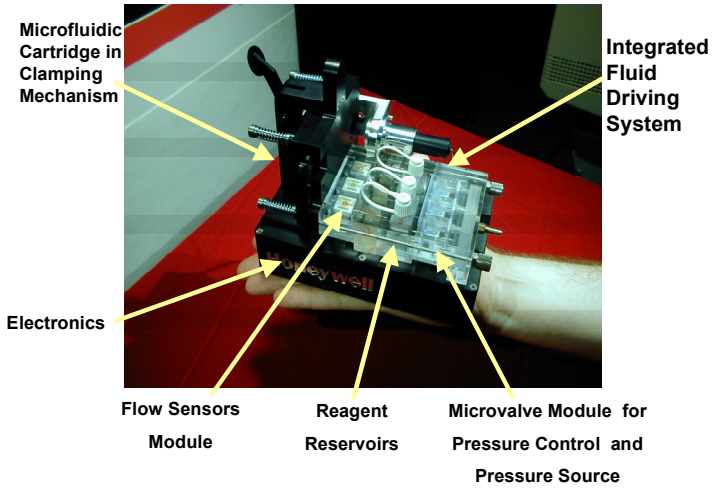

Figure 5. Photograph of the integrated version of the 3-channel micro flow controller showing its various components. The integrated flow controller is 4” x 3” x 1” in size.

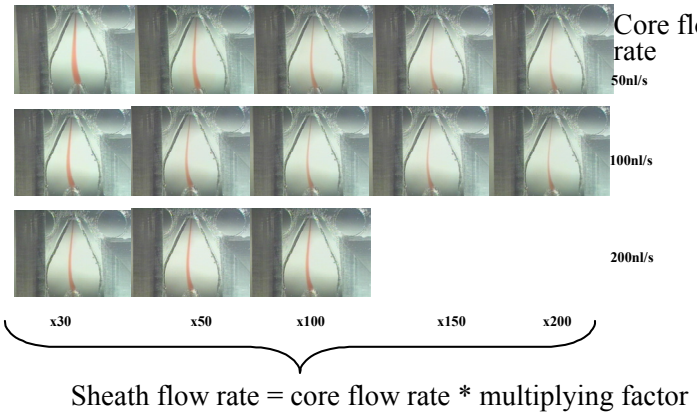

Figure 6. Optical images taken in the hydrodynamic focusing chamber of the flow cytometer showing the core flow (dark color) within the external sheath flow (colorless) for various sheath to core flow rate ratios. The flow controller produces a stable, pulse-free core flow for a range of sheath to core flow ratios.

ACKNOWLEDGMENTS

This work, done in collaboration with Micronics Inc., was supported by DARPA Contract MDA972-00-C-0029. Micronics designed/fabricated the microfluidic cartridges. We are grateful for the assistance of Curtiss Hella and the entire Micronics team.

REFERENCES

[1].[http://www.darpa.mil/MTO/bioflips/presentations/2001-1/index.html [DARPA BioFlip Program]

[2]. http://www.instechlabs.com/syringe.html [Harvard Apparatus Syringe Pump]

[3] Fitch, J., et al., “Pressure-based mass flow control using thermopneumatically actuated microvalves”, *Proceedings Sensors & Actuators Workshop*, Transducer Research Foundation, OH, pp. 162-165, 1998.

[4]. Ohnstein, T, et al., “Micromachined Silicon Microvalve”, *Proceedings of MEMS 1990*, Napa Valley, CA, pp. 95-98, 1990.

[5]. Bonne, U., et al., “Microsensor Housing”, *US Patent 6,322,24,* Issued November 27, 2001.

[6]. Cabuz et al, “Mesoscopic Sampler”*, Transducers’99, June 7-12, 1999, Sendai Japan*

CAPILLARY ARRAY ELECTROPHORESIS BIOPROCESSORS

Richard A. Mathies, Eric T. Lagally, Toshihiro Kamei, William H. Grover, Chung N. Liu and James R. Scherer
Department of Chemistry, University of California, Berkeley, CA 94720
Robert A. Street
Palo Alto Research Center, Palo Alto, CA 94314

ABSTRACT

Microfabricated capillary array electrophoresis devices have been developed that provide unprecedented analysis speed and throughput. The next challenge is the development of integrated arrays of valves, vents, pumps and reactors to provide nanoliter volume sample preparation and the development of integrated detectors to facilitate portable devices. This paper presents our current work on the development of integrated pneumatic valves and pumps that operate on the nanoliter scale, microfabricated resistive heaters and temperature sensors for integrated sample preparation, and integrated hydrogenated amorphous Si photodiode detectors that enable point-of-analysis devices.

INTRODUCTION

MEMS technologies are now being applied with great success to the development of microfabricated "lab-on-a-chip" chemical and biochemical analysis devices. The earliest successful devices consisting of single channels etched in silica substrates were used to perform rapid capillary electrophoretic (CE) analyses of fluorescent dyes and amino acids [**1**]. This work rapidly spawned the application of microfabricated CE devices to DNA fragment sizing [**2**], DNA sequencing [**3, 4**], protein analyses [**5**], and clinical measurements [**6**]. Virtually all classes of chemical and biochemical analyses can be reduced to a chip-based format. However, the power of MEMS is not just its ability to make a compact device for rapid analyses. Microfabrication importantly and uniquely enables the production of dense arrays of analysis devices providing high throughput and low analysis cost.

The development of arrays of chemical and biochemical analysis systems integrated into wafer-scale devices presents unique opportunities and challenges. Our early work presented rectilinear arrays of 12 and 48 separation channels that were detected by mechanical and galvoscanning confocal fluorescence [**7**, **8**]. However, we found that these formats were not optimal because the devices were hard to layout, they contained deleterious turns, extension to larger channel numbers was not facile, and each new chip layout required a new scanner configuration. The transition to radial channel layouts effectively addressed all of these limitations. Radially arrayed channels are easily designed in groups of from 2 to 4 separation channel-injector modules that are replicated by exploiting the radial symmetry. Detection is accomplished with the Berkeley rotary confocal fluorescence scanner that is easily adapted to wafers of different diameters, and can detect from one to 384 channels in its current configuration.

A typical microfabricated capillary array electrophoresis (μCAE) wafer layout is presented in Figure 1 along with an expanded view of one channel-injector module. 96 Channels are arrayed radially with the cathode end of the separation channels on the perimeter and the common anode at the center, providing a 5.5 cm separation distance on the 150-mm diameter wafer. Two samples are introduced in adjacent sample reservoirs and then loaded through the cross channel injector by applying electrophoretic potential between the sample reservoirs and the common waste reservoir. Once the intersection is charged with analyte, the analyte is separated by applying a potential from the common cathode to the central anode, driving the analyte through a sieving gel for size-based separation.

The analyte is detected as it migrates to the anode by the rotary confocal fluorescence scanner depicted in Figure 1C. Light at 488 nm is introduced into the optical system at a dichroic beamsplitter and passed up through a rotating rhomb prism and microscope objective so that the focused exciting light scans in a 1-cm radius circle about the central anode. The fluorescence emitted when the labeled analyte passes this "finish line" is gathered by the objective, descanned by the rhomb prism, and passed to a four-color confocal fluorescence detector. The scanner operates at rates from a few to 20 Hz, and it collects four 16-bit data points every 20 microns about the 6.28 cm circumference detection circle. The detection sensitivity of this scanner is typically in the picomolar range.

This chip and detection format have now been used for a wide variety of biochemical analyses. Using noncovalent intercalation dyes for 2-color labeling, Shi et al. analyzed 96 human genomic samples for genetic variations in the methylenetetrahydrofolate reductase gene in only 120 s [**9**]. Medintz et al. performed human identity determination on 96 genomic samples by analyzing multiplexed short tandem repeats in under 8 minutes [**10**]. Paegel et al. recently presented the development of a novel folded channel DNA sequencing microchannel plate and demonstrated its utility by performing DNA sequencing to 500 bases per lane on a 96-lane device [**11**]. Finally, recent work by Emrich et al. presented the fabrication of a 384-lane μCAE device on a 200-mm diameter wafer and demonstrated its utility by typing human genomic samples for a common genetic variation associated with hereditary haemochromatosis [**12**]. Figure 2 summarizes progress in the development and application of μCAE systems. Our first analyses on single

0-9640024-4-2/hh2002/$20©2002TRF
DOI 10.31438/trf.hh2002.29

Solid-State Sensors, Actuators, and Microsystems Workshop
Hilton Head Island, South Carolina, June 2-6, 2002

channels detected a single sample in 120 s [**2**]. The throughput has rapidly climbed over the years. Our most recent results using 200 mm dia. wafers with 384 separation channels produced throughputs of 2 samples per second of operation - an increase of nearly 300-fold in only 8 years.

The dramatic advances in analytical capabilities of microfabricated electrophoretic analysis systems along with the equally dramatic advances in the number of analyses that can be performed on a given wafer, present important new challenges for the field. While the promise of large numbers of high-speed analyses has been dramatically met by

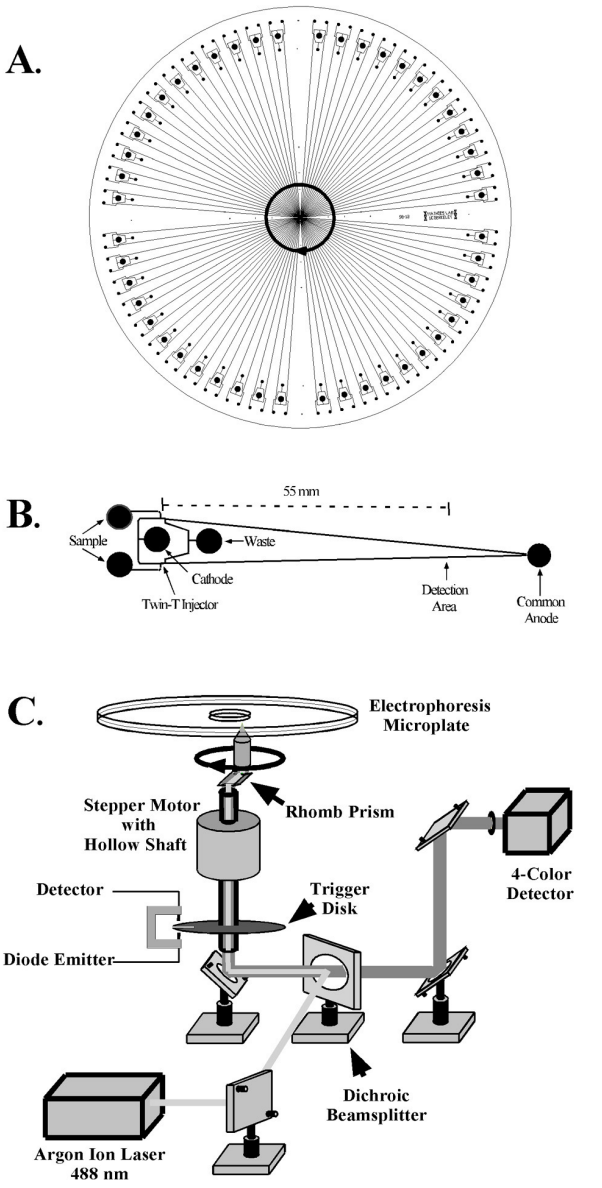

Figure 1. *(A) Design of a 96-channel microfabricated radial capillary array electrophoresis microchannel plate. (B) Expanded view of a pair of separation channels showing the common cathode and waste reservoirs and the twin-T injector. (C) Design of the Berkeley confocal fluorescence rotary scanner. Adapted from Shi et al.* [**9**].

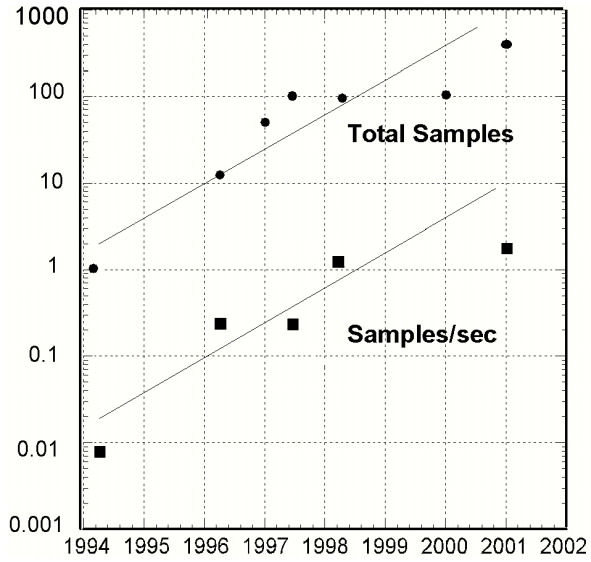

Figure 2. *Performance advances of microfabricated capillary array electrophoresis devices over the past 8 years.*

μCAE systems, the promise to reduce sample volumes and hence costs from microliters to nanoliters has not been delivered. The use of microfluidic channels provides in principle the ability to transport nanoliter volumes, to react nanoliter volumes, to clean-up and concentrate these small volumes, and load them on analysis channels. No one has yet presented a convincing general paradigm for accomplishing this important goal. Achieving this goal is critical if we are to have a facile, low-cost, and rapid way to introduce samples into the high-throughput analyzers described above. The purpose of this paper is to present current work in our lab directed toward the development of fully integrated microdevices for manipulating, reacting and detecting chemical and biochemical analytes.

INTEGRATED VALVE STRUCTURES

A key challenge in the development of integrated nanoliter sample preparation is the facile production of low dead-volume valves. The utility of pneumatically driven membrane flex valves for μL fluidics [**13**] encouraged us to develop a nanoliter version of this valve. Figure 3 presents the fluidic characteristics of the latex membrane valves that we have developed [**14**]. Figure 3A plots the external pressure required to force sample through a valve closed with the indicated valve pressure. The valves are capable of withstanding only a small forward pressure of ≤20 kPa. The breakdown pressure, defined as the inflection point in Figure 3A, occurs at approximately 10 kPa. Figure 3B presents the flow rate of water through the valve at different valve positions. All flow rates were determined using a 14 kPa forward pressure. The flow rate rapidly surpasses 300 nL/s at very small membrane deflections; the maximum flow rate is 360 nL/s. Despite the simple

fabrication procedure, these valves have demonstrated their utility through the performance of nL PCR coupled to CE analysis on a chip [**15, 16**].

While these discrete pneumatic valves have worked well, their fabrication is problematic for high density devices. Thus, we desired a more routine and transferable fabrication method. We therefore developed a PDMS membrane valve composed of four components: a channel layer, a fluidic port layer, a polydimethylsiloxane (PDMS) membrane and a drilled access layer. Figure 4 presents a cross-sectional schematic of the PDMS membrane valve.

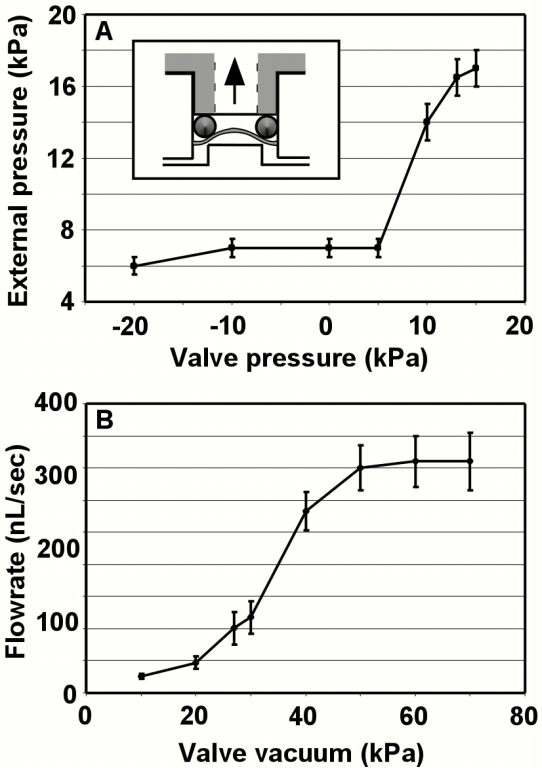

Figure 3. *(A) Breakdown pressure of the latex membrane valve. (B) Flow rate of water through the latex membrane valve as a function of the activation vacuum with a pressure head of 14 kPa. The inset presents the design of the latex membrane valve.*

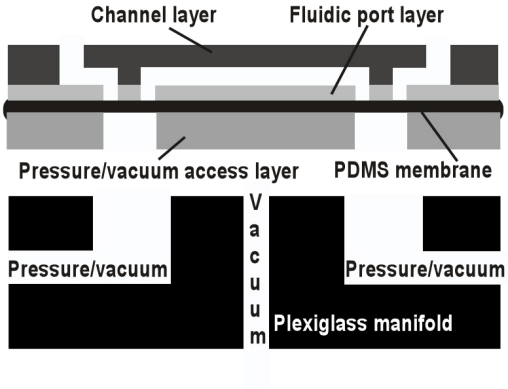

Figure 4. *Schematic of the PDMS membrane valve with plexiglass manifold.*

The channel layer is formed by bonding a 550- with a 210-µm 10-cm diameter glass wafer. 0.01" Diameter holes were drilled in the 210-µm glass wafer to act as fluidic ports for the valve. By using a thin 210-µm glass wafer and drilled holes of 254-µm in diameter, valves with extremely small dead volumes (~20 nL) can be produced. The pressure/vacuum access layer was made of a 1.1-mm, 10 cm diameter glass wafer. 1.5-mm holes were drilled on the wafer to deliver vacuum/pressure from an external Plexiglass manifold. The PDMS membrane valve is formed by sandwiching a 0.007" thick PDMS membrane between the channel layer and the access layer. Reproducible and leak-free bonding was obtained with this method.

The performance of the PDMS membrane valve was characterized by determining the breakdown pressure of the valve, the flow rate of water across the valve, and membrane durability testing. The breakdown pressure of valve is defined as the minimum external pressure needed to force liquid to leak through the valve when the valve is set under various pressure and vacuum levels. Figure 5 presents the valve breakdown pressure of the PDMS membrane valves. The breakdown pressure is as high as ~75 kPa with an applied valve pressure of 40 kPa. It is very important to have such a high breakdown pressure to ensure a reliable and leak-free valve.

The flow rate of water through the valve was determined by measuring the time it takes to fill a channel of known volume. Figure 5B presents the flow rate

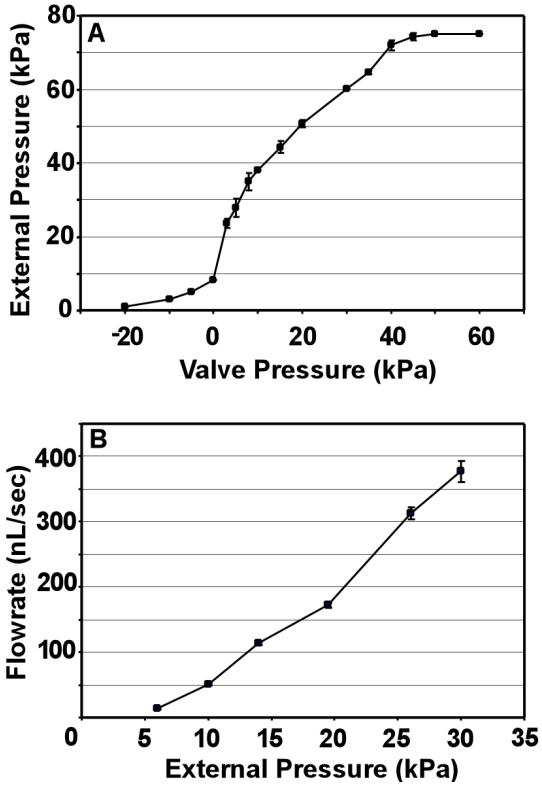

Figure 5. *(A) Valve breakdown pressure vs. applied pressure for the PDMS membrane valve. (B) Flow rate of water vs. applied pressure for the PDMS membrane valve.*

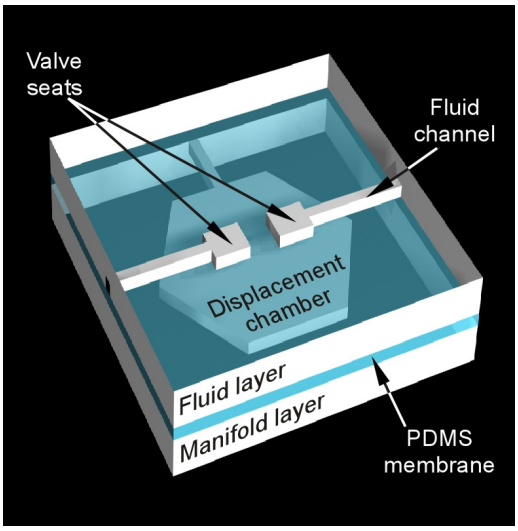

***Figure 6**. CAD view of an integrated valve.*

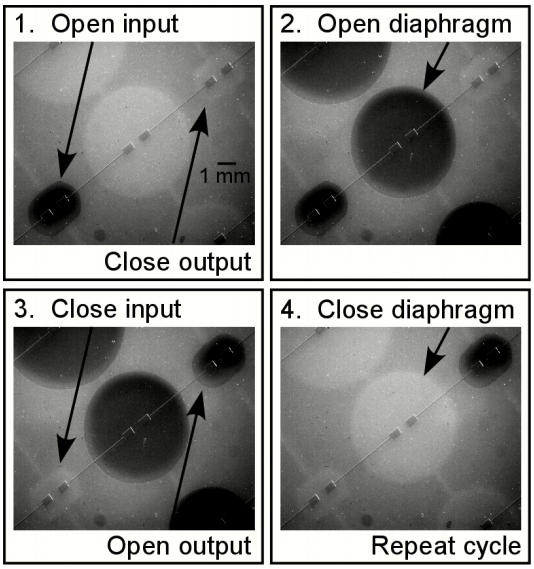

***Figure 7**. Actuation of a microfabricated PDMS diaphragm pump.*

through the PDMS valve as a function of applied pressure. The flow rate was linear in the applied pressure, and flow rates as high as ~380 nL/s are achieved by applying an external pressure of 30 kPa. No significant changes of deflection have been observed with more than 100 actuations. This demonstrates that the PDMS membrane valve is very durable and reliable for long-term use.

VALVE ARRAYS AND PUMPS

We have also developed methods to make arrays of integrated valves. In this design, pneumatic connections are integrated into the device, allowing many more valves to be operated in parallel. The three-layer design of the integrated valve is shown in Figure 6. The manifold layer contains etched channels that distribute vacuum or pressure to valves in the device; the etched channels on the fluidic layer contain the fluid to be routed or pumped. The three-layer topology of integrated valves allows several valves to be controlled by the same vacuum/pressure line, thereby maximizing the number of valves on the device while minimizing the number of pneumatic connections. In an integrated valve, the membrane deflects away from the fluid layer and into an etched displacement chamber in the manifold layer. The volume of the displacement chamber determines the volume of fluid that can be drawn into the valve.

We have demonstrated that a novel microfluidic diaphragm pump can be constructed by placing three integrated valves in series. The pumps are operated by actuating the constituent valves according to the cycle shown in Figure 7. Reversing the actuation cycle reverses the direction of fluid pumping. All 48 pumps are controlled by only nine pneumatic connections placed at the edge of the device. The volume pumped per actuation was determined by counting the actuations required to pump a known volume of solution; pumps were found to range from 94 nL to 7.1 µL per actuation depending on the displacement chamber volume. A series of five circular-shaped pumps were used to quantify the relationship between diaphragm valve size and volume pumped per actuation. These results suggest that a circular diaphragm pump will pump approximately 72% of the volume of the displacement chamber of its diaphragm valve, and that the relationship between the volume pumped and the displacement chamber volume is linear. This work demonstrates that diaphragm pumps may be designed to accurately and reproducibly pump specific volumes in applications where nanoliter to microliter-scale control of fluids is required.

INTEGRATED HEATERS AND TEMPERATURE SENSORS

We have also developed fully integrated heaters and Pt resistance temperature detectors (RTDs) for our genomic analysis microdevices. The heaters are fabricated on the backside of the device, and consist of parallel sets of Ti/Pt resistors with gold leads to the edge of the device for electrical contact. The leads are electroplated gold to decrease their resistance, which allows for localized heating at the chamber of interest. The Ti/Pt RTDs are fabricated within the glass microreactors, and are of a four-wire design, which minimizes noise and systematic error due to self-heating effects. Figure 8A presents a scanning electron micrograph of a completed RTD. Electrical current is applied through the two outside leads, and voltage as a function of temperature is sensed on the inside leads. The dependence of voltage on resistance is expected to be linear for a Pt RTD over our narrow temperature range. Figure 8B presents a typical calibration curve for our Ti/Pt RTDs. The figure indicates a nearly perfectly linear dependence of measured voltage on applied current, although the actual fitted function is the Calendar Van Dusen Equation, which for temperatures above 0ºC assumes a quadratic form:

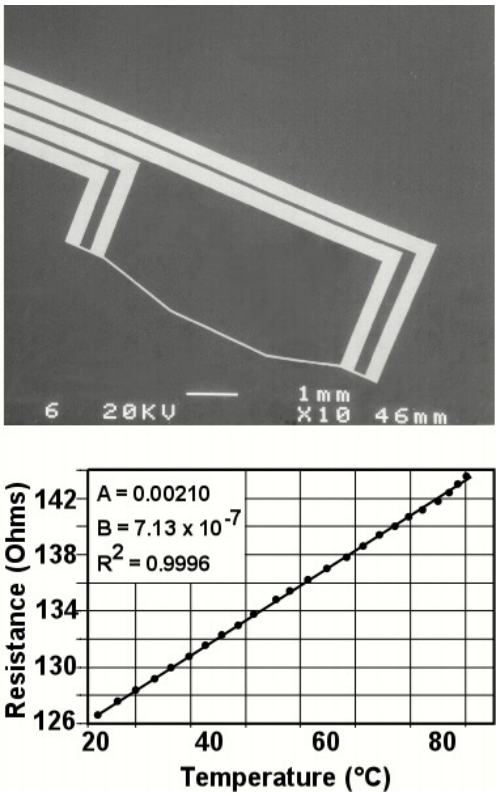

Figure 8. *(A) Scanning electron micrograph of an integrated Ti/Pt RTD used for sensing temperature within microfabricated reactors. (B) A typical calibration curve for our RTDs.*

$$R_t = R_0(1 + AT + BT^2)$$

where R_t is the resistance at temperature T and R_0 is the RTD resistance at 0ºC.

INTEGRATED DETECTORS

The miniaturization and on-chip integration of the fluorescence detection system is a fundamental challenge that will enable the development of portable point-of-analysis devices. Conventional crystalline Si photodiodes have been proposed as integrated detectors [**17**]. Our work has been directed toward the use of hydrogenated amorphous silicon (a-Si:H) PIN photodiodes to fashion an integrated fluorescence detector. High sensitivity a-Si:H photodiodes can be fabricated by plasma enhanced chemical vapor deposition at a very low temperature of ~200^{O}C. This permits the direct fabrication of a-Si:H photodiodes on inexpensive substrates such as glass or plastics. Moreover, many advantages of a-Si:H in manufacturing, patterning, and low production cost will be important in making arrays of photodiodes [**18**] and in making disposable devices.

Figure 9 presents our design for an integrated a-Si:H photodiode detector and optical system for μCAE devices. The annular shape of the a-Si:H detector allows us to use vertical laser excitation (e.g.. from a VCSEL) to keep laser light from directly impinging on the optical filter and the

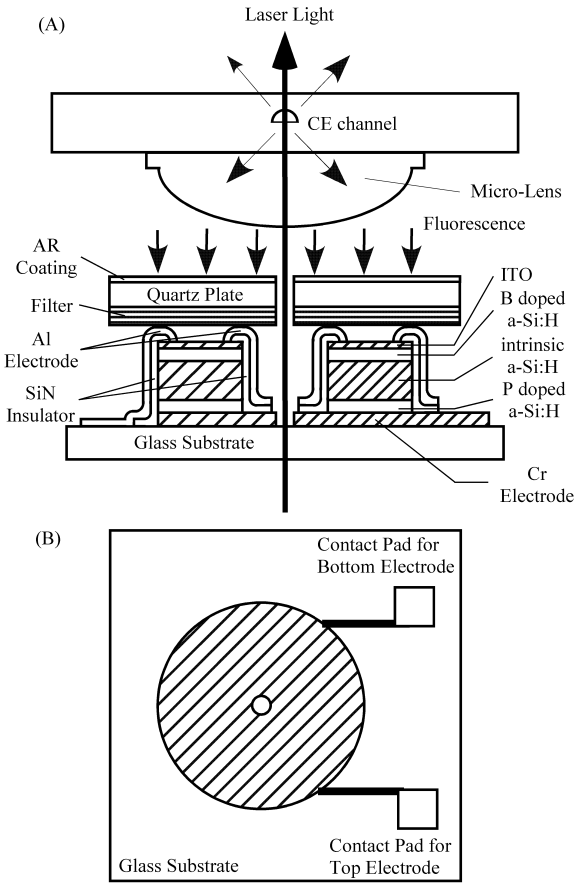

Figure 9. *Design of an integrated a-Si:H photodiode and optical system for detecting analytes in microfabricated capillary electrophoresis channels. (A) Cross-sectional view. (B) Top view of annular a-Si:H photodiode detector.*

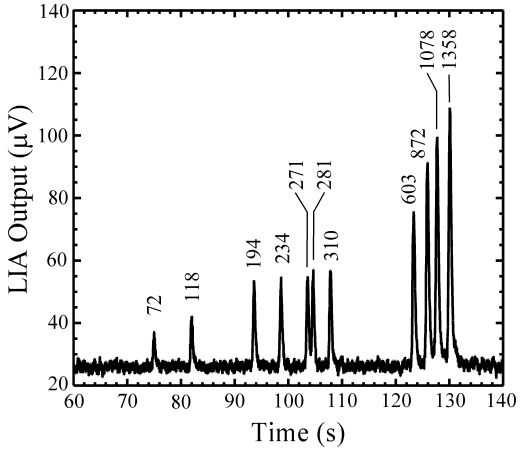

Figure 10. *Electrophoretic separation of a ϕX174 Hae III digest of DNA labeled with thiazole orange fluorescent dye and detected with an a-Si:H photodiode detector.*

detector. First, laser light at 488 nm is introduced normal to the μCAE plate through pinholes in the detector and optical filter. The fluorophore in the channel is illuminated by the laser light, producing fluorescence. The fluorescence is collected by a micro-lens such as a half-ball lens or aspheric

lens, and transmitted by a long-pass filter such as a multi-layer ZnS/YF3 interference filter that simultaneously eliminates the excitation light. Finally, fluorescence reaches the a-Si:H detector and a photocurrent is generated.

To explore the feasibility of this design, DNA fragment sizing was performed and detected with an a-Si:H detector. Fluorescence labeling of the 25 ng/μl sample of ϕ174 HaeIII DNA digest ladder was accomplished with 1 μM of an intercalating dye (thiazole orange). The DNA samples were injected by the plug injection method and electrophoresis was carried out at 300 V/cm. A reverse bias voltage of 1 V was applied to the a-Si:H diode, and the photocurrent synchronized to chopped laser light (Ar ion laser, 488 nm, 7 mW) was detected by a lock-in amplifier. The chopping frequency was 27 Hz, while the time constant was 100 ms. Figure 10 shows that all 11 peaks of this DNA ladder are successfully observed with a good S/N ratio.

Further integration of the laser and detector is possible. Because of the compatibility of a-Si:H diodes with glass, it is feasible to monolithically integrate the detector with these glass wafer electrophoretic devices. The combination of a blue-green VCSEL with this detector module should lead to a simple "contact lens" type of excitation and detection module for microfabricated CE chips. Therefore, a-Si:H photodiodes are promising for use as integrated detectors, because they are easy to manufacture and pattern, should dramatically reduce production costs, and should facilitate the development of portable point-of-analysis devices.

SUMMARY AND CONCLUSIONS

The development of fully integrated chemical and biochemical microprocessors will depend on the development of facile reliable integrated sample preparation technologies as well as detection methods. We have presented a variety of methods for producing pneumatic valve structures, characterized their operation, and shown that they can be used to make PCR reactors, valve arrays and pumps. The fabrication of integrated temperature sensors and heaters is also presented. When combined with the development of integrated a-Si:H photodiode detectors and chip VCSEL sources, it is evident that portable point-of-analysis lab-on-a-chip devices are now feasible.

REFERENCES

1. D. J. Harrison, K. Fluri, K. Seiler, Z. Fan, C. S. Effenhauser, and A. Manz, "Micromachining a miniaturized capillary electrophoresis-based chemical analysis system on a chip", *Science, 261*, 895-897 (1992).

2. A. T. Woolley and R. A. Mathies, "Ultra-high-speed DNA fragment separations using microfabricated capillary array electrophoresis chips", *Proc. Natl. Acad. Sci. U.S.A., 91*, 11348-11352 (1994).

3. S. Liu, Y. Shi, W. W. Ja, and R. A. Mathies, "Optimization of high-speed DNA sequencing on microfabricated capillary electrophoresis channels", *Anal. Chem., 71*, 566-573 (1999).

4. D. Schmalzing, N. Tsao, L. Koutny, D. Chisholm, A. Srivastava, A. Adourian, L. Linton, P. McEwan, P. Matsudaira, D. Ehrlich, "Toward real-world sequencing by microdevice electrophoresis", *Genome Res., 9*, 853 (1999).

5. C. Colyer, D. Shakuntala, D. Mangru, and D. J. Harrison, "Microchip-based capillary electrophoresis of human serum proteins", *Journal of Chromatography A, 781*, 271 (1997).

6. H. J. Tian, L. C. Brody, S. J. Fan, Z. L. Huang, and J. P. Landers, *Clinical Chemistry, 47*, 173-185 (2001).

7. A. T. Woolley, G. F. Sensabaugh, and R. A. Mathies, "High-speed DNA genotyping using microfabricated capillary array electrophoresis chips", *Anal. Chem., 69*, 2181 (1997).

8. P. C. Simpson, D. J. Roach, A. T. Woolley, T. Thorsen, R. Johnston, G. F. Sensabaugh, and R. A. Mathies, "High-throughput genetic analysis using microfabricated 96-sample capillary array electrophoresis microplates", *Proc. Natl. Acad. Sci. U.S.A.*, *95*, 2256-2261 (1998).

9. Y. Shi, P. C. Simpson, J. R. Scherer, D. S. Wexler, C. Skibola, M. T. Smith, and R. A. Mathies, "Radial capillary array electrophoresis microplate and scanner for high-performance nucleic acid analysis", *Anal. Chem., 71*, 5354-5361 (1999).

10. I. Medintz, L. Berti, C. A. Emrich, J. Tom, J. R. Scherer, and R. A. Mathies, "Genotyping energy-transfer cassette labeled short tandem repeat amplicons with capillary electrophoresis microchannel plates", *Clinical Chemistry,* 47, 1614-1621 (2001).

11. B. M. Paegel, C. A. Emrich, G. J. Wedemayer, J. R. Scherer, and R. A. Mathies, "High-throughput DNA sequencing with a 96-lane capillary array electrophoresis bioprocessor", *Proc. Natl. Acad. Sci. U.S.A.*, *99*, 574-579 (2002).

12. C. A. Emrich, H. Tian, I. L. Medintz, and R. A. Mathies, "Microfabricated 384-lane capillary array electrophoresis bioanalyzer for ultra high-throughput genetic analysis", *Nature Biotechnology,* submitted (2002).

13. R. C. Anderson, X. Su, G. J. Bogdan, and J. Fenton, "A miniature integrated device for automated multistep genetic assays", *Nucleic Acids Research, 28*, e60 (2000).

14. E. T. Lagally, P. C. Simpson, and R. A. Mathies, "Monolithic integrated microfluidic DNA amplification and capillary electrophoresis analysis system", *Sensors and Actuators B, 63*, 138-146 (2000).

15. E. T. Lagally, I. Medintz, and R. A. Mathies, "Single-molecule DNA amplification and analysis in an integrated microfluidic device", *Anal. Chem., 73*, 565-570 (2001).

16. E. T. Lagally, C. A. Emrich, and R. A. Mathies, "Fully integrated PCR-capillary electrophoresis microsystem for DNA analysis", *Lab-on-a-Chip, 1*, 102-107 (2001).

17. J. R. Webster, M. A. Burns, D. T. Burke, and C. H. Mastrangelo, "Monolithic capillary electrophoresis device with integrated fluorescence detector", *Analytical Chemistry, 73*, 1622-1626 (2001).

18. R. A. Street and L. E. Antonuk, "Amorphous silicon arrays develop a medical image", *IEEE Circuits and Devices Magazine, 9 (4) July*, 38-42 (1993).

ELECTROCHEMICAL MICROSENSORS FOR DNA MUTATION DETECTION

Xing Yang, Chunnian Shi, R. Erik Holmlin, Shana O. Kelley, Michael G. Hill
GeneOhm Sciences, Inc.
6146 Nancy Ridge Drive, Suite 101
San Diego, CA 92121

Donald M. Crothers
Department of Chemistry
Yale University
225 Prospect Street
New Haven, CT 06511

Jacqueline K. Barton
Department of Chemistry
Mail Code 127-77
California Institute of Technology
Pasadena, CA 91125

ABSTRACT

We have developed a new electrochemical microsensor for DNA mutation detection. It is based on the unique properties of DNA-mediated electron transfer. Gold microelectrode arrays have been designed and fabricated on silicon substrates. Densely packed double-stranded DNA thin films on gold surfaces have been prepared and characterized. It has been shown that the redox-active intercalators bound to the DNA films exhibit well-resolved electrochemical responses. More importantly, it has also been demonstrated that DNA-mediated reduction of the bound intercalator depends critically on stacking within the double helical array. *Based on difference in charge transport through double-stranded DNA rather than hybridization energy*, we have demonstrated detection of point mutations in DNA duplexes irrespective of the DNA sequence composition, mutation position in the DNA duplexes, or mutation identity.

INTRODUCTION

The success of the human genome project (HGP) provides a starting point for understanding basic human genetic makeup. It is agreed that genetic variations, with SNP (single nucleotide polymorphisms, single-base variations in genetic codes) being the most common one, are not only responsible for human diversity but also carry significant medical differences in disease susceptibility and drug response. Reliable detection of such genetic mutations is critical for the study, diagnosis, and treatment of many human diseases.

To date, most assays proposed for large-scale genetic analysis rely on molecular recognition events associated with DNA hybridization [**1**,**2**] to catalogue sequence information. Applied to mutation detection, hybridization assays are inherently limited in specificity, especially in the case of SNPs when only one base in the DNA strand is mutated. Detection of a SNP in the test sequence requires a distinguishable difference in pairing energies between the probe sequence and a completely complementary versus mutated target strand. With only a single mutation in an extended oligonucleotide, these differences can be very small. Moreover, duplex stabilities for oligonucleotides of a fixed length can vary considerably as a function of base content, with GC-rich sequences significantly more stable than AT-rich analogues. As a consequence, detection of point mutations with libraries of immobilized oligonucleotides (where duplex-binding energies for adjacent probe sequences may vary significantly more than the differential binding energies of a particular probe with its complementary versus mutated test sequences) requires extensive manipulation of hybridization conditions as well as sophisticated deconvolution algorithms.

Monitoring charge transport through double-stranded DNA offers an alternative approach to the detection of point mutations. Photoinduced electron transfer through donor/acceptor-labeled duplexes has been observed in a variety of systems [**3**]. Significantly, DNA-mediated reactions show a weak dependence on distance but are exceptionally sensitive to the perturbations in the base stack: intervening bulges inhibit long-range photochemical guanine oxidation, and single-base mismatches markedly reduce photoinduced electron-transfer yields [**3**]. Thus, while single-base mismatches may cause only subtle changes in duplex stability and structure, they appear to induce significant perturbations in the electronic structure of the base-pair stack. This sensitivity of electron transfer to perturbation in the DNA duplex provides a complementary signaling mechanism for mutation detection.

Based on DNA-mediated electron transfer, here we present electrochemical microsensors for accurate, rapid, and low-cost detection of genetic mutations.

DNA-MEDIATED ELECTRON TRANSFER

Electrochemistry has been used extensively to investigate the kinetics of electron transfer through self-assembled monolayers on solid surfaces. Systems that feature redox-active head groups held at various distances by aliphatic alkanethiols or conjugated linkers have yielded important information regarding the ability of different media to promote long-range electronic coupling. To investigate DNA-mediated electron transfer, we have applied these methods to study redox-active intercalators bound at discrete sites within the individual helices of a DNA monolayer on gold.

We have previously developed techniques for assembling DNA duplexes derivatized at the 5' end with thiol-terminated linkers onto gold surfaces [**4**]. Electrochemical assays, radio active tagging experiments, and atomic force microscopy (AFM) all indicated that the duplexes form densely packed monlayers oriented in an upright position with respect to the gold surface [**4**] as shown in Figure 1. An average of surface coverage of 50

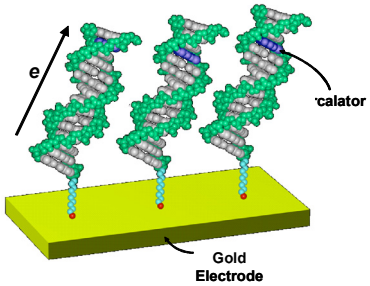

Figure 1. *DNA-Modified Gold Electrode.*

0-9640024-4-2/hh2002/$20©2002TRF
DOI 10.31438/trf.hh2002.30

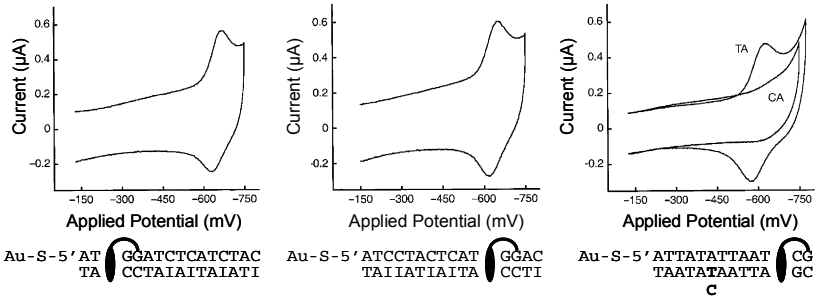

(a) *(b)*

Figure 2. *Voltammograms of Gold Electrodes Modified with DM-Cross-Linked Duplexes.*

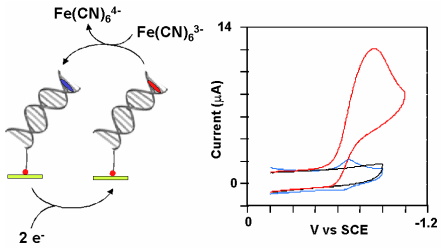

Figure 4. *Electrocatalysis.*

pmol/cm^2 has been reported. Our work showed several unique features of double-stranded DNA films. Densely packed thiol-modified duplexes readily adsorb to gold with a high and apparently uniform surface coverage. Moreover, as long as electrochemical experiments are conducted at sufficiently negative potentials, the DNA duplexes are oriented in an upright position with respect to the metal surface. This arrangement helps direct charge transport through the double helix.

DNA modified electrodes exhibit very high affinities for DNA-binding substrates, and promote efficient electron transfer between the electrode and redox-active intercalators. To investigate charge transfer through DNA as a function of distance, we have site-specifically cross-linked a redox-active intercalator, daunomycin (DM), into the DNA films. DM undergoes a reversible reduction within the potential window of the monolayers. The site of intercalation was controlled in the duplexes by incorporating a single GC base step in otherwise A-T or inosine(I)-C sequences; as daunomycin requires the N-2 of guanine for covalent cross-linking, the intercalator is constrained to these positions. Moving the GC-step along the duplex therefore provided a systematic variation in the location of the DM-binding site relative to the thiol-terminated linker. Cross-linking DM to the DNA in solution, and then depositing the labeled duplexes onto gold afforded a series of films in which the intercalator was linked quantitatively at a known separation from the electrode surface.

In the first experiment, films with 15-base-pair DM-labeled DNA duplexes were formed on gold electrodes (0.02 cm^2, MF-2014 from Bioanalytical Systems, Inc.) As shown in Figure 2 (a), with the controlled position of the GC base pair in the duplexes, the distance of DM from the gold surface was significantly different between the two duplexes (15 Å versus 45 Å). However, efficient reduction of DM was observed regardless of its position along the 15 base-pair sequence. Not only were the intensities of the DM signals the same for each of the duplexes studied, but the

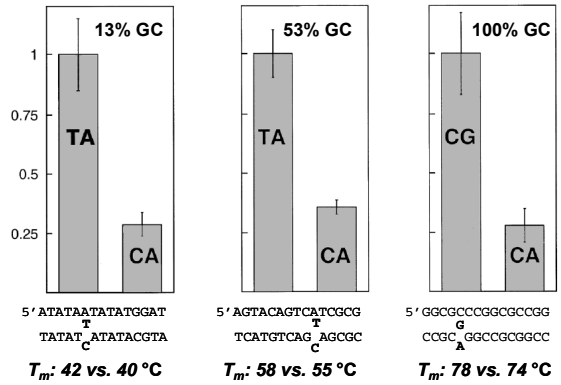

Figure 3. *Sequence Independence.*

characteristic splitting between the catholic and anodic waves as a function of scan rate were essentially invariant throughout the entire series. Clearly within the time resolution of this experiment, increasing the through-helix DM/gold separation did not substantially affect the rate of electron transfer.

In the second experiment, a single site within the 15-base-pair duplex was mutated to produce a CA mismatch between the intercalated DM and the gold electrode surface. Although CA mismatches are known to cause only local disruptions in the DNA base stack with the base remaining intrahelical, the presence of this one-base change switched off the electrochemical response entirely, as shown in Figure 2 (b). In the related control experiment, sequences in which the positions of DM and CA mismatch were reversed (such that the mismatch was located above the DM relative to the gold) showed no diminution in the electrochemical response. Moreover, AFM images of the CA-mutated sequences were indistinguishable from those of the fully base-paired analogues, revealing that the bulk structure of the DNA films was not significantly altered by the presence of the mismatch.

It is determined in the next experiment that the characteristic drop in coulometric signals for DM bound to DNA films containing CA mismatch compared to fully paired films is essentially invariant across AT-rich to GC-rich sequences tested under identical conditions. As shown in Figure 3, DNA duplexes with varied percentage of GC content were either fully base-paired or contain a single CA mismatch. Regardless of the sequence composition, and therefore over a wild range of duplex stabilities (ΔT_m=40°C), the CA mismatches contained with these duplexes were accurately detected.

Finally, although duplexes containing mismatches can be distinguished by direct voltammetry of redox-active intercalators, the absolute electrochemical signals are limited by the surface concentration of the intercalators (~50 pmol/cm^2). In order to increase the inherent sensitivity of this assay, we coupled the direct electron transfer to an electrocatalytic process involving a species freely diffusing in solution (Figure 4 (a)). Methylene blue (MB) was chosen as the intercalated catalyst with potassium ferricyanide as the solution substrate. Shown in Figure 4 (b), addition of micromolar MB to a 2.0 mM ferricyanide solution caused a pronounced electrochemical signal at the DNA-modified electrode. Notably this signal comes at the reduction potential of MB and is completely irreversible: electrons flow from the Au electrode to the intercalated MB and then are accepted by ferricyanide in solution (thus no electrochemical oxidation peak is observed). Chemical oxidized MB is again available for electrochemical reduction and the catalytic cycle continues as long as the potential of the gold electrode is sufficiently negative to MB. This electrocatalysis process effectively amplifies the intercalator signal and improves the discrimination between signals obtained for mismatched versus base-paired duplex films.

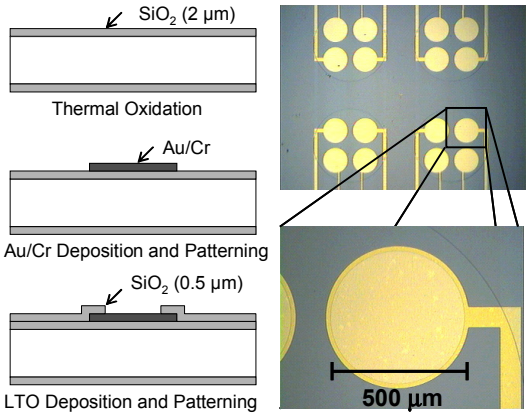

(a) *(b)*

Figure 5. *Sensor Fabrication Process.*

Taken together, these experiments have established the basic understanding of DNA-mediated electron transfer and provided the foundation for developing chip-based electrochemical microsensors for DNA mutation detection.

SENSOR DESIGN AND FABRICATION

Fabricated on a silicon substrate, the sensor consists of an array of gold microelectrodes sandwiched between two layers of silicon dioxide. Microelectrodes with varied dimensions ranging from 0.1 mm to 1 mm in diameter and 500 Å to 6500 Å in thickness were designed and fabricated.

Shown in Figure 5 (a), the fabrication process started with 4 inch <100> silicon wafers. First, a layer of 2 µm silicon dioxide was thermally grown on the wafer at 1100 °C. Then, a thin layer of 100 Å chromium followed by a layer of gold were deposited by thermal evaporation. The thin chromium layer improved the adhesion of gold to the silicon oxide surface. In order to investigate its effect on sensor performance, the thickness of the gold layer was varied from 100 Å to 6500 Å. Finally, another layer of 5000 Å LPCVD silicon dioxide was deposited at 450 °C and patterned to expose the Au electrodes.

Figure 5 (b) shows an array of fabricated gold microelectrodes.

EXPERIMENTS AND RESULTS

Gold Surface Preparation and Characterization

Electrochemical cleaning – cyclic voltammetry of oxidation and reduction of the gold electrode in sulfuric acid – was used to remove any contaminant adsorbed physically or chemically on the gold surface and also qualitatively characterize the gold surface.

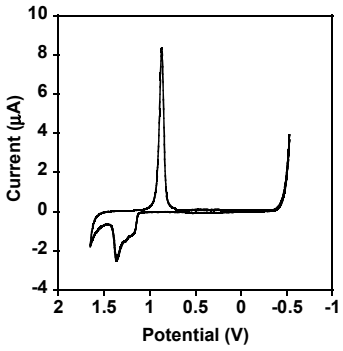

Figure 6. *Electrochemical Cleaning of Gold Electrode.*

Cyclic voltammetry was carried out in an electrochemical cell using a Bioanalytical Systems (BAS, Model CV-50W) electrochemical analyzer. A normal three-electrode configuration consisting of a modified gold-disk working electrode, a saturated calomel reference electrode (SCE, Fisher Scientific), and a platinum wire auxilliary electrode was used. The working compartment of the electrochemical cell was separated from the reference compartment. Potentials were reported versus SCE. Volumes of 30 ml were typically employed. Figure 6 shows a typical cyclic voltammogram obtained on a gold microelectrode (1 mm in diameter) in 1 M H_2SO_4 upon cycling the potentials between +1.65 V and -0.5 V at a scan rate of 100 mV/s. The sharp rise in anodic current to a peak near +1.1 V, a single oxide stripping peak near +0.9 V, and reproducible cyclic voltammograms on successive scans indicated that the gold surface was very clean and ready for DNA monolayer formation.

DNA Film Formation

15- to 21-base oligonucleotides immobilized on a controlled pore glass resin were first synthesized according to automated solid-phase techniques on an ABI 394 DNA/RNA Synthesizer and then treated in succession with carbonyldiimidazole and 1,6-diaminohexane at the 5'-hydroxy terminus before cleavage from the resin. After deprotection, the free amine was treated with 2-pyridyldithiopropionic acid *N*-succinimide ester to produce a disulfide. Sequences were purified by reverse-phase HPLC, converted to free thiols using dithiothreitol, and repurified before hybridization to their complements. Gold microelectrodes were modified by incubation in 0.1 mM solutions of derivatized DNA duplexes in 5 mM phosphate/50 mM NaCl/0.1 M Mg^{2+} (pH 7) for 12-24 hours at ambient temperature.

Comparison of cyclic voltammetry of ferricyanide at bare and DNA-modified gold microelectrodes provides a convenient and qualitative way to monitor the surface coverage of DNA duplexes. The negatively charged ion $[Fe(CN)_6]^{4-}$ is repelled from the surface of the modified microelectrode by the polyanionic DNA, and should exhibit essentially no response when the surface is well covered. Figure 7 shows a typical cyclic voltammogram of a DNA modified gold microelectrode (0.5 mm in diameter) in 1 mM $[Fe(CN)_6]^{4-}$/2.5 mM phosphate/25 mM NaCl. Indeed, the microelectrode well covered with DNA duplexes showed no electrochemical response whereas the bare electrode gave well-resolved redox peaks of ferricyanide.

Mismatch Detection

To demonstrate mutation detection, DNA-mediated electron transfer on gold microelectrodes was studied using cyclic voltammetry and chronocoulometry experiments. Single-base mismatches were incorporated into two different DNA duplexes

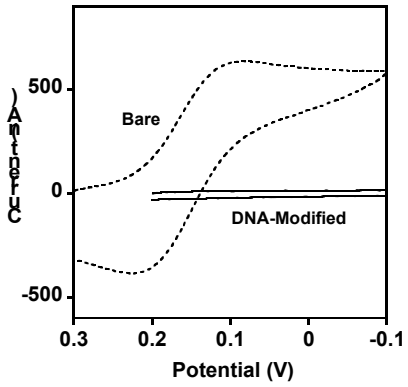

Figure 7. *Blocking of Ferricyanide Redox by DNA Duplexes.*

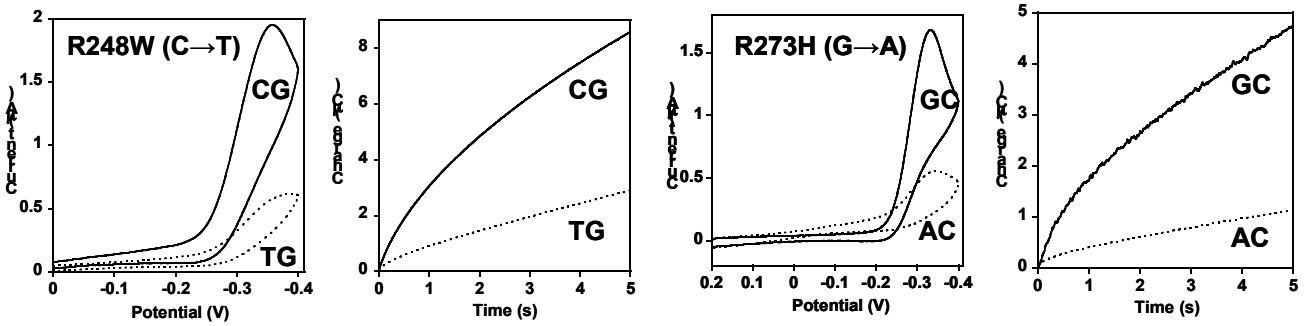

*(a) 5'-ATGAAC**C**GGAGGCCC-3' (**C→T**)*
Detection Condition: 0.25 μM MB, 2 mM Ferricyanide

*(b) 5'-GAGGTGC**G**TGTTTGT-3' (**G→A**)*
Detection Condition: 0.5 μM MB, 1 mM Ferricyanide

***Figure 8.** Detection of Mismatches in p53 Gene.*

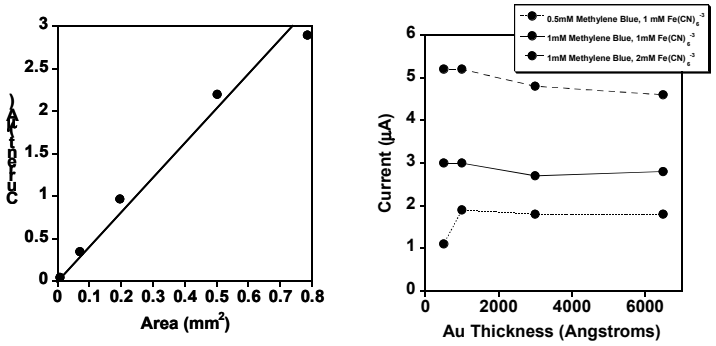

***Figure 9.** Dependence of Peak Current on Electrode Dimensions.*

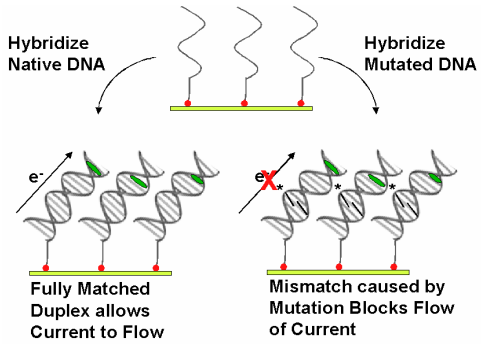

***Figure 10.** Electrochemical Microsensors for Mutation Detection.*

(Figure 8). Gold microelectrodes modified with these duplexes were interrogated by cyclic voltammetry (potential between +0.2 to -0.4 V and scan rate of 100 mV/s) and chronocoulometry (potential at -0.35 V) with MB as the intercalated catalyst and ferricyanide as the solution substrate. The experimental results shown in Figure 8 clearly demonstrate the remarkable sensitivity of this electrocatalytic assay. Indeed, incorporation of a mismatch into the duplex significantly attenuated the electrocatalytic response. In both cases, the peak current and the measured charge at the fixed potential for base-paired duplexes were almost four times the ones for mismatched duplexes. It should be noted that because the charge transfer-based assay features a catalytic reaction whose rate depends on the degree of complementarity within the individual duplexes, the measured charge resulting from the reduction of MB at base-paired versus mismatched films increases disproportionately with longer integration time. Increased integration times continue to increase the differentiation of signals obtained with mismatched versus paired complements.

The effect of dimensions of gold microelectrodes on the electrocatalytic assay was also studied. Cyclic voltammetry of DNA-modified gold microelectrodes with different diameters (0.1 mm, 0.3 mm, 0.5 mm, 0.8mm, and 1 mm) and different thicknesses (500 Å, 1000 Å, 3000 Å, and 6500 Å) were performed. Figure 9 shows that the peak current is linearly proportional to the area, but shows no dependence on the thickness of the gold microelectrodes when the thickness is above 1000 Å.

Electrochemical Microsensors

Based on these results, we are developing microsensors for diagnosing mutations in individual patients (Figure 10). DNA duplexes are formed on the sensor electrode surface. The composition of the duplexes positions them to determine if DNA from a patient contains a mutation. One strand of the duplex - the strand linked to the electrode - is chemically synthesized with sequence pre-programmed to be a portion of a gene that is known to contain a mutational hot-spot. The second strand of the duplex is processed from a patient sample (e.g. blood sample or tumor biopsy). The duplexes form by hybridization (in 100% yield) when the DNA-modified electrode is exposed to a solution of the patient's DNA duplexes. The readout of the mutation is performed using chronocoulometry with MB and ferricyanide. The amount of measured charge at a fixed potential determines the existence of a mismatch in the film which is caused by the mutation in the patient's sample.

CONCLUSIONS

We have demonstrated that DNA-mediated electron transfer reactions are exquisitely sensitive to the stacking of the intervening bases. Because of its insensitivity to mismatch position, mismatch identity, and sequence content, this electrochemical assay provides an accurate, rapid, and inexpensive solution to mutation analysis. Based on these results, we have developed microfabricated electrochemical sensors for detecting mutations in DNA duplexes.

REFERENCES

1. S.P.A. Fodor, "Massively Parallel Genomics," *Sciences,* 277, 393 (1997).
2. E.M. Southern, "DNA Chips – Analyzing Sequence by Hybridization to Oligonucleotides on a Large Scale," *Trends in Genetics*, 12, 110 (1996).
3. S.O. Kelley, R.E. Holmlin, E.D.A. Stemp, and J.K. Barton, "Photoinduced Electron Transfer in Ethidium-Modified DNA Duplexes: Dependence on Distance and Base Stacking," *Journal of the American Chemical Society*, 119, 9861 (1997).
4. S.O. Kelley, J.K. Barton, N.J. Jackson, L.D. McPherson, A.B. Potter, E.M. Spain, M.J. Allen, and M.G. Hill, "Orienting DNA Helices on Gold Using Applied Electric Field," *Langmuir*, 14, 6781 (1998).

IMPROVEMENT OF DNA MICROARRAY BIOCHIPS USING MICROFLUIDIC MIXING TECHNIQUE

Robin H. Liu, Ralf Lenigk, Dale Ganser, Justin Bonanno, and Piotr Grodzinski
Microfluidics Lab, PSRL, Motorola Labs
Tempe, AZ 85284

Bobbi Sanchez and Pankaj Singhal
Motorola Life Science
Tempe, AZ 85284

Steve Dai
SSRC, Motorola Labs
Tempe, AZ 85284

ABSTRACT

Conventional DNA microarray hybridization relies on the diffusion of targets to surface-bound probes, and thus is a rate-limited process. In this paper, a micromixing technique based on cavitation microstreaming principle was developed to accelerate hybridization process. Fluidic experiments showed that the time to fully mix a 20 μL chamber using microstreaming was significantly reduced from hours (a pure diffusion-based mixing) to tens of seconds. Cavitation microstreaming was implemented to enhance DNA hybridization in both fluorescent detection based and electro-chemical detection based microarray chips. Hybridization results showed that microstreaming results in up to 5 folds signal enhancement and kinetics acceleration, and signal uniformity is also significantly improved, compared to conventional diffusion-based biochips. Acoustic microstreaming has many advantages over most existing mixing techniques for hybridization enhancement, including simple apparatus, ease of implementation, low power consumption (2 mW), and low cost.

INTRODUCTION

DNA microarray is one of the most promising analytical techniques in molecular biology. DNA hybridization is a heterogeneous bimolecular reaction, involving mixing and binding of the target DNA in a free solution and the DNA probes immobilized on a surface. The hybridization rate depends on a number of parameters, among which mass transfer in the bulk (3D) as well as on the surface (2D) is playing an important role. In most conventional microarray biochips, hybridization solely relies on diffusion, and thus is a lengthy rate-limiting process (6 ~ 20 hrs) [1]. This greatly limits the throughput of sample analyses. Various methods have been developed to accelerate the hybridization process, including electric hybridization [2], dynamic hybridization using paramagnetic beads [3], and the Flow-Thru approach [4]. It is believed that introduction of micromixing technique can accelerate hybridization kinetics and improve uniformity of hybridization.

A few interesting mixing techniques to facilitate mixing of various fluids within a DNA hybridization chamber have been reported in recent years. Of particular interest is "rotational mixing" that involves a rotatable body having a rotational axis [21]. This technique generally works better in macro-scale fluidic chambers since the mixing relies on the inertial force of the fluid. However, when the reaction chamber is shallow (e.g., ~200 μm or less), viscous force dominates fluidic behavior due to low Reynolds number (~1). It is believed that mixing in microfluidic environment cannot be significantly enhanced by mechanical agitation means, such as rotation or shaking.

Ultrasonic mixing using a piezoelectric element was also reported to achieve hybridization enhancement [5]. Other similar works on ultrasonic mixing were reported in [6] and [7]. The former used ultrasonic traveling waves generated by a pieozoelectric film to the liquid in a mixing chamber. The latter used loosely-focused acoustic waves generated by an electrode-patterned pieozoelectric film. Both devices require a complicated fabrication process (e.g., Si bulk etching). Other mixing approaches to enhance hybridization include bubbling gas through the chamber and "drain and fill" method [8]. Both mixing schemes require system setups with in-line flowing and pumping, and possibly a precise flow control.

In this paper, we will describe the phenomenon of cavitation microstreaming, which provides a mechanism for achieving rapid and homogeneous mixing in a hybridization chamber. An air bubble trapping design using micromachined air pockets, coupled with a commercially available piezoelectric (PZT) disk, is presented. Fluidic experiments to demonstrate utilization of cavitation microstreaming to achieve a high degree of fluid transport and mixing enhancement in a hybridization chamber will be described. DNA hybridization experiments to demonstrate improvement of hybridization kinetics and signal uniformity using cavitation microstreaming will be discussed.

THEORY

An air bubble in a liquid medium can act as an actuator when the bubble undergoes vibration within a sound field. The behavior of bubbles in sound fields is determined largely by their resonance characteristics. For frequencies in the range considered here (~ kHz), the radius of a bubble at resonant frequency f (Hz) is given by the equation:

$$2\pi af = \sqrt{3\gamma P_o / \rho} \qquad (1)$$

where a is the bubble radius (cm), γ is the ratio of specific heats for the gas, Po is the hydrostatic pressure (dynes/cm2) and ρ is the density of the liquid (g/cc). Using this equation with the parameter values f = 5000 Hz, one finds a for resonance to be approximately 0.3 mm.

When the bubble undergoes vibration within a sound field, the frictional forces generated at the air/liquid interface induce a bulk fluid flow around the air bubble, called cavitation microstreaming or acoustic microstreaming [9]. It was found that cavitation microstreaming is orderly at low driving amplitudes when the insonation frequency drives the bubbles at their resonance frequency for pulsation and when the bubbles are situated on solid boundaries. The bubble-induced streaming is strongly dependent on

0-9640024-4-2/hh2002/$20©2002TRF
DOI 10.31438/trf.hh2002.31

Solid-State Sensors, Actuators, and Microsystems Workshop
Hilton Head Island, South Carolina, June 2-6, 2002

frequency for a given bubble radius, and on bubble radius for a given frequency. Acoustic microstreaming arising around a single bubble excited close to resonance produces strong liquid circulation flow in the liquid chamber. This liquid circulation flow can be used to effectively enhance mixing. Although cavitation microstreaming has been reported and studied since 1950s [9], we have not found the use of this phenomenon to enhance micromixing. One challenge here is to precisely control the size of the air bubbles. In this work, we have developed a design to engineer the air bubbles for mixing enhancement.

EXPERIMENTAL DETAILS

Fluidic experiments with dye were implemented to visualize and study cavitation microstreaming in a hybridization chamber. As shown in Fig.1, the chamber was constructed by sealing a conventional DNA microarray glass chip with a polycarbonate cover layer using a double-side adhesive tape (3M, St. Paul, MN). The adhesive tape with thickness of 100 µm serves as a spacing gasket to define the shape and dimension of the chamber. The cover layer has a desired number of air pockets uniformly distributed above the chamber (12 x 15 x 0.1 mm). The air pockets (500 µm in depth and 500 µm in diameter) that were milling machined were used to trap air bubbles in the reaction solution. A PZT disk (15 mm diameter, APC Inc., Mackeyville, PA) was glued on the outer surface of the cover layer. The chamber contents were irradiated by the sound that came from the PZT. Visual observations were made from above using a stereoscope. One half of the chamber was filled with DI water and the other half with a red dye solution that was used to depict motion of fluid elements in the chamber. The frequencies employed were 3 kHz (sinusoidal wave) with 10 Vpp.

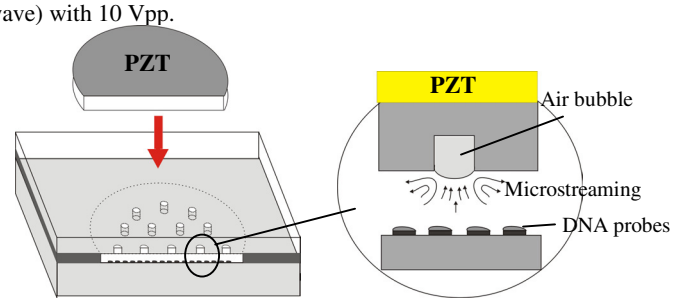

Fig.1 Schematic of the mixing chamber with DNA probes.

High-density DNA microarray hybridization was performed to evaluate mixing enhancement in improving hybridization efficiency and uniformity over conventional diffusion-based hybridization. A fluorescent detection based microarray biochip that consists of a high-density array of oligonucleotide probes dispensed on a 1x3 inch pre-treated glass slide was used. The oligonucleotide probes that consist of two types of oligonucleotides (NEO and YJEK) and a positive control were arranged in a uniform pattern across the entire slide. A 1 x 3 inch double-side adhesive tape (3M, St. Paul, MN), which was cut into four 12 x 15 mm windows, was used to bond a polypropylene cover layer with the glass slide and serves as a spacing gasket to define the shape and dimension of the chambers on the glass slide. The polypropylene cover layer consists of a number of air pockets (500 µm in depth and 500 µm in diameter) on the side facing the DNA array. The air pockets are uniformly distributed across the cover layer with a pitch of 2 mm. A PZT disk (15 mm diameter) was glued on the outer surface of one chamber, in which cavitation microstreaming was implemented while static hybridization (i.e., diffusion-only) was performed as a control in one of the other three chambers on the same chip. During hybridization, a fluorescently labeled oligonucleotide target solution (with a volume of 18 µL), which has 50% formamide, 6xSSPE, and 10 nM Cy3 labeled targets that have complements to the NEO and YJEK sequence on the slide, was loaded into each detection chamber. The PZT was driven at 5 kHz and 10 Vpp. Hybridization was carried out for 2 hr. Following the hybridization, the polypropylene layer was removed from the array glass slide, which was subsequently washed with TNT for 30 minutes at 42 °C and then 3x water. The glass slide was scanned using a microarray scanner (Axon Instruments, Inc., Union City, CA).

An assay for single nucleotide polymorphisms (SNP's) associated with hematochromatosis was performed in a Motorola eSensor™ device with microstreaming. The eSensor™ devices allow for continuous measurement of DNA hybridization during the reaction due to the homogenous nature of the assay, thus allowing hybridization kinetics study. Each device consists of a plastic cover layer assembled with a printed circuit board (PCB) chip that has 16 detection electrodes. Four electrodes contain identical oligonucleotide probes for HFE-H. The plastic cover layer has 4x4 air pockets (500 µm in depth and 500 µm in diameter) facing the DNA probes. A PZT disk was glued on the outer surface of the cover layer to induce microstreaming during the hybridization. The DNA target solution containing HFE-H polymorphism (210 bp) was amplified from human genomic DNA characterized for HFE genotype. The PCR product was prepared by asymmetrical amplification of 100 ng of human genomic DNA using a set of three primers with a final concentration of 0.5 µM per primer, 400 µM dNTP, 50 mM KC, 10 mM Tris-HCL (pH 8.3), 2 mM MgCl2, 0.05 U / µl Taq polymerase, and 100 µg / ml bovine serum albumin. Cycling parameters were: 95°C (3 min) to denature human DNA, followed by 40 cycles (94°C for 45 sec, 58 °C for 55 sec, 72°C for 60 sec), and ending 72 °C for 6 min to extend all unfinished DNA strands. Following PCR, the amplicon solution was mixed with a hybridization solution in a ratio of 1:2. The hybridization buffer is composed of 0.85 M sodium perchlorate, 18.4 % v/v Qiagen Lysis buffer AL, 10 mM tris HCl pH 7.5, 1 mM 6-mercaptohexnol and 10 % v/v fetal bovine serum. The hybridization cocktail was then filled into an eSensorTM chip with an internal volume of 65 µL. Hybridization was performed at 35 °C. During the hybridization process, the PZT was driven at 5 kHz and 10 Vpp. The signals were read out using a Motorola Hydra®600 instrument. For comparison purpose, hybridization reaction was also implemented in a conventional diffusion-based eSensor™ chip using the same amplicon mixture. Study of hybridization kinetics as a function of cavitation microstreaming amplitude (Vpp) was also performed using 5 Vpp and 40 Vpp, as compared to 10 Vpp.

RESULTS AND DISCUSSION

Fluidic dye experiments showed that sonic irradiation caused little motion of the liquid if air bubbles were excluded from the chamber. However, with air bubbles that have a resonant frequency matching the PZT frequency, a gross liquid motion was seen to take place around individual bubble. Since the top pockets are distributed above the chamber, the resulting acoustic streaming dominates the mixing in the whole chamber within a few seconds.

As shown in Fig. 2, when the PZT was turned on (5 kHz and 10 Vpp), the streaming occurred around each air bubble and the microstreaming fields began to interfere with each other. Churning motion in the liquid was seen at the air-liquid interface. Fluidic elements were focused into a narrow stream and move rapidly toward the bubble surface, then decreases as the elements spread out and leave the bubble region. As streaming continued and fluid elements moved rapidly, the dye eventually completely filled the chamber. Fluidic experiment (Fig. 2) shows that complete mixing was achieved across the whole chamber within 1 min and 45 sec, while the mixing based on pure diffusion (i.e., without acoustic mixing) took about 12 hrs for the same chamber. Dye experiments were also performed to investigate the relationship between the mixing rate and acoustic parameters. It was found that square sound wave gives faster mixing than sinusoidal sound wave. Higher amplitude also results in faster mixing. For example, complete mixing in the same chamber was achieved within 35 sec if a 5 kHz and 40 Vpp sinusoidal wave was employed.

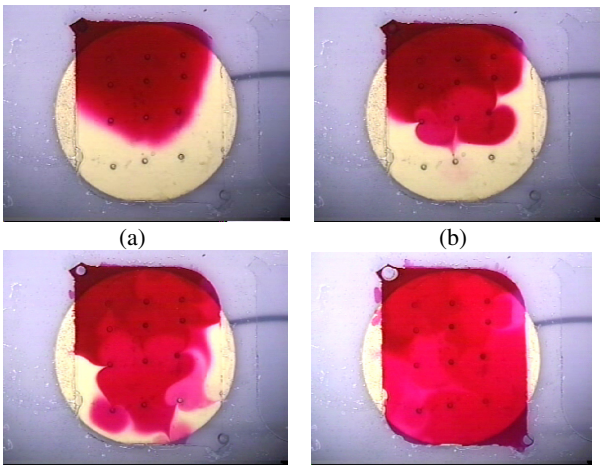

(a) (b) (c) (d)

Fig.2: Images showing cavitation microstreanming in a 12 x 15 x 0.1 mm chamber at (a) time 0; (b) 28 sec; (c) 1 min 7 sec; (d) 1 min 46 sec.

Fig. 3 shows fluorescent scanning images of a microstreaming enhanced array and a diffusion-based array. Fluorescent intensity data for both arrays were analyzed. As shown in Fig.4, the average intensity of the mixing array is five times more than that of the static hybridization array, and signal uniformity (co-variance) is greatly improved by implementing microstreaming. These results indicate that hybridization reactions in oligonucleotide array formats can generally be affected by the level of mixing of the target ligand. Efficient and effective cavitation microstreaming can ensure maximal presentation of the sample targets to the array, and thus significantly improve hybridization efficiency and quality.

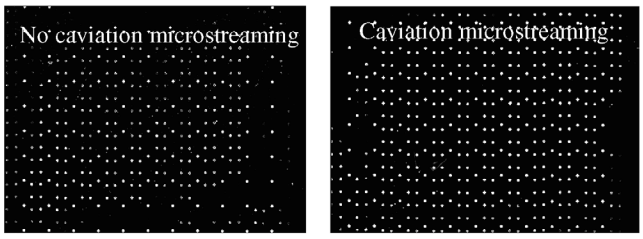

Fig. 3: Fluorescent images of hybridization assay in a HD array chip.

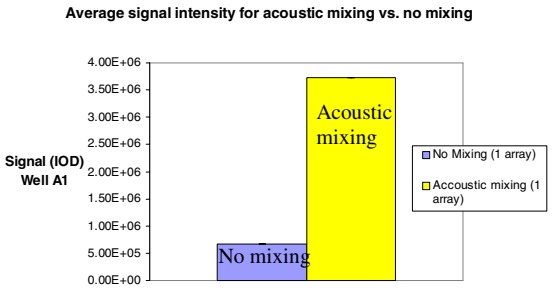

(a)

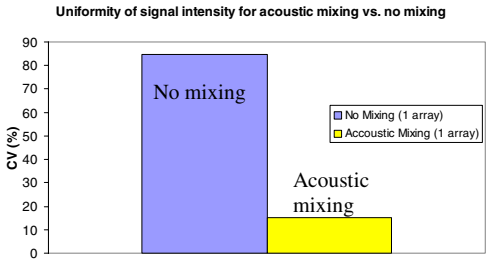

(b)

Fig.4: (a) Averaged fluorescent intensity. (b) Intensity uniformity (note: 0% CV = fully uniform).

Kinetic data of the genotyping experiments using target DNA obtained by PCR amplification from human genomic DNA to bind to the sensor electrodes on Motorola eSensor™ chips were collected by measuring electrochemical signal as a function of time. Fig. 5 summarizes the hybridization kinetics results for a mixing-enhanced device and a diffusion-based device. Each data point is the mean value obtained from four electrodes with identical DNA capture probes in the same device. Note that the y-axis in the figure is the measurement of the Faradaic current from the electrodes. The Faradaic current is directly proportional to the number of ferrocene moieties immobilized at the electrode surface that in turn is proportional to the number of target nucleic acid molecules. The results show that for diffusion-based hybridization, hybridization signal evolves slowly and exhibits linear increase. This steady-state behavior indicates the attainment of equilibrium for the hybridization reaction is not achieved within the time frame of the experiment. Moreover, the standard deviation of each data point shows that the pure diffusion-based hybridization has relatively large electrode-to-electrode variation. For the hybridization assay coupled with cavitation microstreaming, the signal increased rapidly, showing additional acceleration and much uniform signal distribution (small standard deviations) compared to the diffusion-based device. After 40 minutes of hybridization, the sample in the mixing-enhanced device reached a saturated Faradaic current value with a signal-to-background ratio of 30, which is 5 times that of the sample in the diffusion-based device. It took approximately 6 hrs for the diffusion-based sample to reach the saturated level (not shown here).

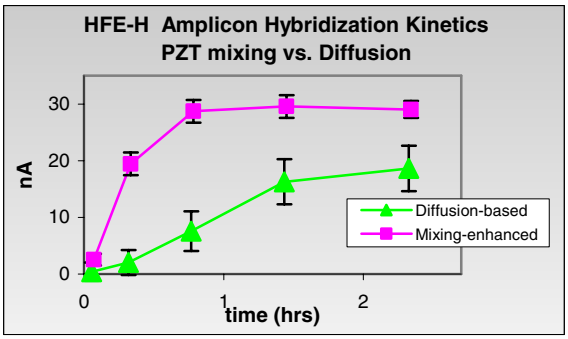

Fig. 5: Hybridization kinetics measurement for acoustic mixing vs. diffusion in eSensor™.

From fluidic experiments with dye, it has been found that higher acoustic amplitude (i.e., peak-to-peak voltage) gives faster mixing enhancement. To evaluate hybridization enhancement as a function of acoustic amplitude, HFE-H hybridization was also performed in eSensor™ devices with different amplitudes. As shown in Fig. 6, 40 Vpp results in faster hybridization kinetics and more uniform signals than 10 and 5 Vpp.

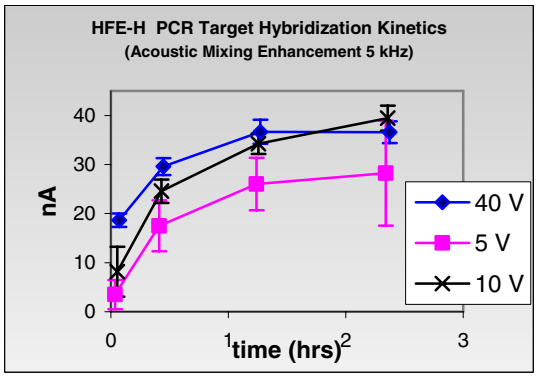

Fig. 6: Hybridization kinetics for chips using different acoustic amplitudes (V peak-to-peak).

Both fluidic and hybridization experiments demonstrated that cavitation microstreaming not only provides rapid lateral mass transport of fluidic elements (thus ensures a homogenous mixture of targets across the ship) but also enhances the vertical mass transport of target DNA in the solution to the probes on the surface. The rapid lateral fluidic movement allows uniform hybridization signals to be achieved across the large surface area on the chip. Uniformity of hybridization is critical especially for detection of low-abundance targets. Lack of lateral flow convection could lead to non-homogeneous array performance and hybridization differences that are independent of differences in target concentration.

The fast vertical mass transport of target DNA in the solution to the surface-bound probes gives rise to hybridization kinetics acceleration. Cavitation microstreaming in a shallow hybridization chamber reduces the thickness of the stagnant (diffusion) boundary layer of fluid on the chip surface, and thus decreases depletion effect. Targets are in close proximity to the surface-bound probes, resulting fast mass transport due to short diffusion length. The combination of rapid lateral and vertical mass transport allows continuous replenish of fresh DNA targets around the probes that has been depleted of complementary targets. As a result, the hybridization rate is greatly increased. Although this hybridization enhancement is not as significant as compared to the flow-thru approach [4] and the electronic DNA hybridization [10], the distinct advantage that cavitation microstreaming has over the above two methods is its rapid lateral mass transport that significantly enhances uniformity of hybridization. Moreover, cavitation microstreaming requires very limited and simple mixing apparatus, and thus can be easily implemented in most existing biochip devices including conventional high-density or low-density DNA/RNA array chips.

CONCLUSIONS

We have developed a microfluidic mixing technique that is based on the principle of cavitation microstreaming. We demonstrated that rapid and homogeneous dye mixing was achieved in a shallow chamber device. Hybridization experiments in high-density microarray chips and eSensor™ devices showed that cavitation microstreaming results in 5-fold increase in hybridization rate and significantly enhanced signal uniformity due to significant convective current in both lateral and vertical directions, compared to conventional diffusion-based hybridization.

ACKNOWLEDGEMENT

The authors would like to express their thanks to Dr. Gary Olsen from Motorola Life Science for useful discussion on hybridization kinetics. This work has been sponsored in part by DARPA contract #MDA972-01-3-0001 and NIST ATP contract #1999011104A.

REFERENCES

1. Schena, M., *Microarray BiochipTechnology*. 2000, Natick, MA: Eaton Publishing.
2. Sosnowski, R., *et al.*, *Rapid Determination of Single Base Mismatch Mutations in DNA Hybrids by Direct Electric Field Control.* Proc. Natl. Acad. Sci., 1997. **94**: p. 1119-1123.
3. Fan, Z.H., *et al.*, *Dynamic DNA hybridization on a chip using paramagnetic beads.* Anal. Chem., 1999. **71**: p. 4851-4859.
4. Cheek, B.J., *et al.*, *Chemiluminescence Detection for Hybridization Assays on the Flow-Thru Chip, a Three-Dimensional Microchannel Biochip.* Anal. Chem., 2001. **73**: p. 5777-5783.
5. US patent No. 6,168,948 B1, Anderson, R. C., et al., "Miniaturized Genetic Analysis Systems and Methods", 2001
6. Moroney, R.M., R.M. White, and R.T. Howe. *Ultrasonically induced microtransport*. in *MEMS '95*. 1995. The Netherlands.
7. Zhu, X. and E.S. Kim, *Microfluidic Motion Generation with Acoustic Waves.* Sensors and Actuators: A. Physical, 1998. **66 (1-3)**: p. 355-360.
8. US Patent No. 6,114,122, Besemer, D., et al., "Fluidics Station With a Mounting System and Method of Using", 2000.
9. Elder, S.A., *Cavitation Microstreaming.* J. Acoust. Soc. Am., 1959. **31**: p. 54-62.
10. Edman, C., *et al.*, *Electric Field Directed Nucleic Acid Hybridization on Microchips.* Nucl. Acids Res., 1998. **25**: p. 4907-4914.

An Immunoassay Platform Based on CMOS Hall Sensors

Turgut Aytur, P. Robert Beatty[1], Bernhard Boser
Dept. of Electrical Engineering & Computer Sciences, [1]Dept. of Molecular & Cellular Biology
University of California, Berkeley, CA 94720

Mekhail Anwar
Dept. of Electrical Engineering and Computer Sciences
Massachusetts Institute of Technology
Cambridge, MA 02139

Tomohiro Ishikawa
System Technology Research Center
Sharp Corporation
Chiba, Japan

ABSTRACT

We describe an immunoassay utilizing standard CMOS technology. An array of Hall sensors is used to detect the magnetic beads that serve as the assay signal. Electrical and magnetic modulation is employed to improve the sensitivity of the sensors. The devices receive two post-processing steps to improve sensitivity and biocompatibility. We have fabricated prototype devices using a 0.25-μm BiCMOS process, and have successfully detected anti-Hu IgG antibody at a concentration of 200pM.

INTRODUCTION

Diagnosis is an essential tool in the health care industry. The role of diagnosis is expanding, particularly within the context of screening and prevention. Infectious diseases are a major cause of death in the world, with HIV/AIDS, tuberculosis, and malaria responsible for approximately 5.7 million deaths in 1998 **[1]**. Rapid diagnosis is essential during epidemics for fast treatment and containment.

A dominant technology in diagnostics is the Enzyme-Linked Immunosorbent Assay (ELISA). Immunoassays, such as ELISA, are diagnostic tools that rely on the highly specific interaction of antibody binding to cognate antigen. In the ELISA, the detection of unknown antibody or antigen is signaled through an enzymatic label that activates a dye. ELISAs can be administered in a doctor's office or hospital environment, allowing for cost effective diagnosis of a broad range of diseases. However, most ELISA tests require a basic laboratory environment and some staff training. For many infectious diseases, a rapid, precise quantitative measurement is required for accurate diagnosis, which is rarely possible in the field. Therefore, improvements in diagnosis should focus on rapid, cost-effective in-field or point-of-care testing.

Magnetically-Labeled Assays

The limitations in ELISA for quantified point-of-care diagnostics stem mostly from the enzymatic label. Recently, the use of micron-scale magnetic beads as labels has been described **[2,3,4]**. There are many advantages gained from using a magnetic label. First, there are no comparable sources of magnetic signal in biology, so the background is intrinsically low. Second, magnetic beads can be used to manipulate biological systems The beads are specifically superparamagnetic, as they have very low remnance. When placed in a magnetic field, however, they generate an induced magnetic field. The magnetic beads can be made biologically active by coating the polystyrene encapsulation.

Travel support was generously provided by the Transducers Research Foundation, and the DARPA MEMS and DARPA BioFlips Programs.

The magnetic label requires a different detection system than ELISA. The first reports of assays utilizing magnetic labels employed superconducting quantum interference devices as sensors **[2]**. These devices are highly sensitive to magnetic fields, but are not portable. More recently, a device has been developed based on giant magneto resistor (GMR) technology **[3,4]**. GMR devices are highly sensitive, and are now in mass production in computer disk-drive read heads. A simplified protocol for an assay involving this device is shown in Figure 1.

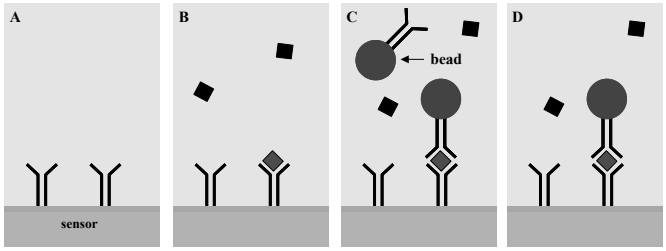

Figure 1. *Simplified magnetically-labeled assay.*

The gold surface received a coating protein. The test liquid was added (Figure 1b). Next, magnetic beads coated with an appropriate antibody against the target antigen were added (Figure 1c). Magnetic beads far from the sensor but still in solution will not affect the result. This assay used magnetic washing, where unbound beads were pulled from the sensor by a magnetic field (Figure 1d). An external magnetic field normal to the sensor surface was then applied. The induced field generated by bound beads was measured as a resistance change in the GMR sensor. The amount of change in resistance corresponds to the number of beads bound. This device has single magnetic bead sensitivity.

Improvements in cost and manufacturability of the magnetic sensors may broaden the applicability of magnetically-labeled assays. CMOS is the most widely manufactured semiconductor technology. It is an attractive substrate for MEMS devices due to manufacturing ease and potential as an intelligent substrate. The sensor can be easily integrated with other functionality. The small size of the sensor chips described in this paper implies that the microfabrication costs will not dominate the assay expense. It is therefore beneficial to utilize CMOS for the sensing technology.

THEORY

Hall sensors can be operated in current or voltage mode. A particular example of a current-mode device that exploits the MOS transistor structure is the dual-drain Hall FET. The differential output current of this device can be expressed as **[5]**,

$$i_d = \frac{L}{2W}\mu_H G B_z I_{DS} \qquad (1)$$

0-9640024-4-2/hh2002/$20©2002TRF
DOI 10.31438/trf.hh2002.32

where W and L are the channel width and length, respectively, of the device, μ_H is the Hall mobility, and G is a geometric constant that accounts for current confinement at the device boundaries. In the low magnetic fields of this application, the Hall mobility is well represented by the carrier mobility. For a long-channel device operating in saturation, Eq. 1 can be rewritten as,

$$i_d \cong {\mu_{eff}^2}/{4}\; GB_z C_{ox}\left(V_{gs} - V_t\right)^2 \qquad (2)$$

where μ_{eff} is the effective carrier mobility.

Device Scaling

In the analysis above, the applied field is assumed to be uniform and normal to the sensor surface. Magnetic beads produce a local, non-uniform field when placed in an external field. This field is well modelled by a magnetic dipole equation. The peak signal decays with cubic dependence on the height from the sensor plane. A simulation of the induced magnetic field, measured normal to a plane 5µm below the center of a 5–µm bead, is shown in Figure 2.

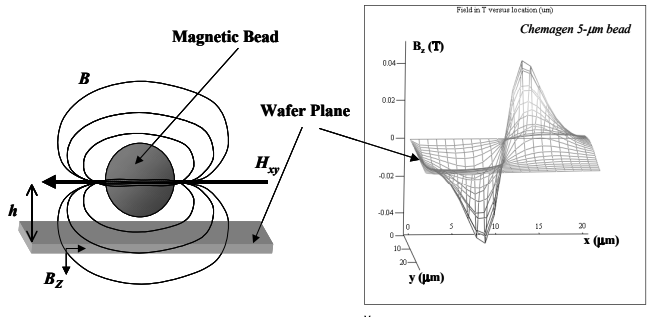

Figure 2. *Simulated magnetic field for a 5-µm magnetic bead in a 35-kA/m field, 5-µm for the surface.*

The total field integrates to zero, since the field strength is anti-symmetric about the y-axis. Therefore, a hall-sensor device that is much larger than the bead will have a smaller signal than a correctly scaled device. Consider the hypothetical situation shown in Figure 3. In these devices, the magnetic field is zero outside the shaded strip, and finite in it. The current bends in the region with field, as predicted, but tends to redistribute in the no field region. From this illustration, it is clear that the Hall sensor device size should be scaled according the bead size. The minimum size of the sensor is limited by lithographic constraints.

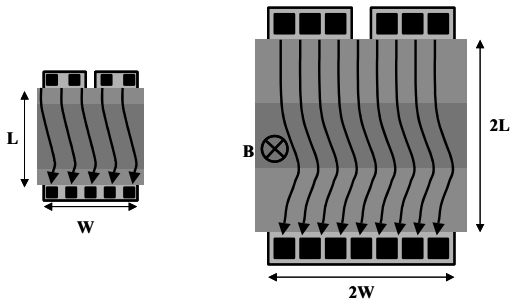

Figure 3. *Illustration of current lines for two device sizes in the same non-uniform magnetic field. The larger device has a reduced output signal due to charge redistribution.*

Flicker Noise

CMOS devices have poor low-frequency noise properties due to flicker or 1/f noise. The noise spectral density, as the name suggests, is inversely proportional to frequency. The consequence of this is that signals at DC do not benefit from narrowing of the noise bandwidth, eliminating the trade-off between bandwidth and Signal-to-Noise Ratio (SNR). Thus, there exists a minimum detectable signal, independent of noise bandwidth.

For conventional magnetic sensing applications, the signal frequency is either not known or assumed to be at DC. However, in this application the excitation frequency of the external magnetic field is limited only by practical constraints of electromagnets. This improves the signal detection in two ways: First, a band-pass filter can be employed to restore the trade-off between bandwidth and SNR. Second, the signal can be moved to a frequency of lower spectral noise density. Unfortunately, there is still approximately one order of magnitude difference between the flicker noise corner frequency of the MOS hall device and the maximum frequency to practically operate the electromagnetic excitation. To overcome this, we combine electrical modulation and magnetic modulation, as represented in Figure 4.

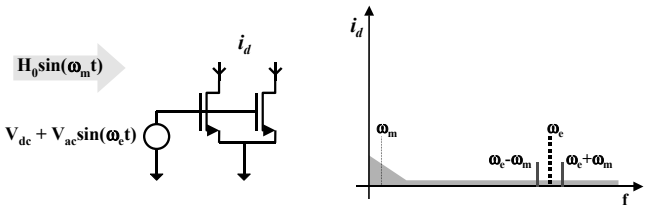

Figure 4. *Illustration of magnetic and electrical modulation applied to the dual-drain NMOS sensor device. The modulated output signal appears at frequencies* $\omega_e \pm \omega_m$ *,*

The gate-to-source voltage and magnetic field are applied as:

$$V_{gs}(t) = V_{DC} + V_{AC}\sin(\omega_e t) \qquad (3)$$

$$H_{xy}(t) = H_0\sin(\omega_m t) \qquad (4)$$

Where ω_e and ω_m are the electrical and magnetic modulation frequencies, respectively. Combining eq. (2) with eqs. (3) and (4) defines the modulated output spectrum. In addition to DC and higher order terms, the differential drain current will contain the term:

$$i_d \propto \sin(\omega_e \pm \omega_m) \qquad (6)$$

The electrical modulation frequency can be selected such that thermal noise, rather than flicker noise, dominates. The magnetic modulation is desirable to separate the wanted signal from carrier leakage (dashed line in Figure 4). Carrier leakage results from a variety sources, including device leakage and parasitic coupling, and results in a limit on the minimum detectable signal.

DESIGN AND FABRICATION

Sensor Chip

The sensor chips were fabricated in Agere Systems (formerly Lucent Technologies-Microelectronics) 0.25-µm single-poly 5-

metal BiCMOS process. Each Hall device is implemented as a 6-µm x 6-µm dual-drain NMOS device. The drains are separated by a 1-µm x 1-µm field-oxide region. Each sensor consists of two matched devices that source current in opposite directions (Figure 5), so that uniform magnetic fields are rejected.

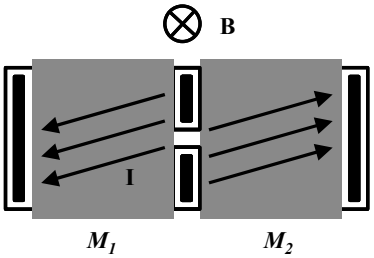

Figure 5*. Two Hall devices source current in opposite directions, reducing uniform fields by 30-40 dB.*

This reduces the leakage signal from the excitation field by 30-40dB. This leakage signal occurs due to misalignment of the excitation field with the sensor surface.

The sensor array consists of 32 x 8 sensor elements. Figure 6 shows a portion of the sensor array.

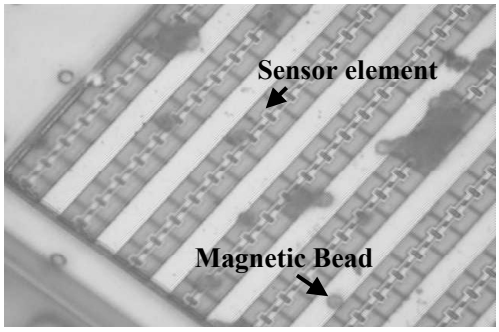

Figure 6. *A Portion of the sensor array with 3-µm magnetic beads. The Cr/Au layer was not applied to allow viewing of sensor detail.*

Each element is addressable via a shift register. The drain current of the selected sensing device is converted to a voltage before being amplified by a bipolar tranconductance amplifier. This balanced, current-mode output is sent off chip.

Due to a chip area restriction of 1mm x 1mm, additional metalization post-processing was necessary to move bond pads away from the sensing area. This allows wire bonding to the chip outside of the fluid vessel. This part of the post-processing will not be described, as future prototypes will accomplish this with the standard metallization.

Devices are post-processed in subsections of the initial 8" wafer. First, the silicon dioxide above the sensor area is thinned by plasma etching. This reduces the distance from a magnetic bead to the sensor surface, increasing the signal. The etch depth is controlled by comparison with etch reference marks implemented in the standard metallization, resulting in a final oxide thickness of approximately 2µm. Next, a thin layer (50nm/150nm) of Cr/Au is patterned over the sensor area using lift-off. Other materials were tested for protein adsorption, including Ti and Cu, but were found to be less effective than Au. However, Cu may represent a significant advantage in processing simplicity for CMOS processes that use Cu for metalization.

Packaging and Experimental Setup

Processed chips, including metallization extension, are assembled as drawn in Figure 7.

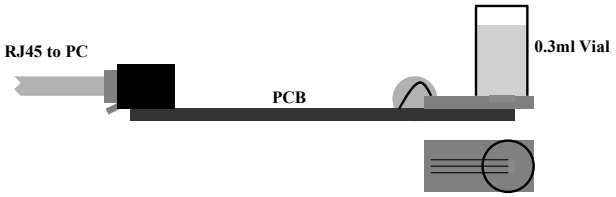

Figure 7. *Simplified assembly diagram of sensor chip with fluid container and printed circuit board.*

9mm x 15mm chips are mounted on a 15-cm long PCB. A 300-µL polystyrene vial is inverted and epoxied to the silicon chip. A small hole is predrilled in the vial to allow fluid entry. The PCB connects to an analog processing board via RJ45 connector. A 1-kHz, 30-kA/m magnetic field is applied parallel to the sensor surface by a custom C-core electromagnet (Figure 8).

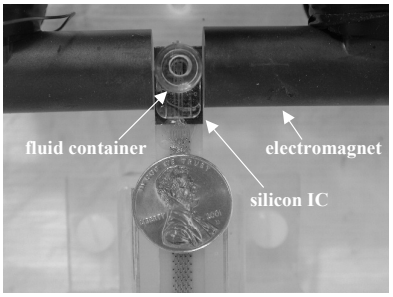

Figure 8. *Sensor chip and assembly mounted in the C-core electromagnet.*

This magnet is mounted on rubber bushings so that it can be adjusted to reduce leakage normal to the sensor surface. The 250-kHz electrical modulation signal is sinusoidal and is applied to both the gate of the active sensing device and the input of the mixer IC. The balanced, current-mode output of the post amplifier is converted to a voltage on the analog processing PCB and amplified by instrumentation amplifiers. A simplified diagram of the signal processing is shown in Figure 9. Data is processed automatically in Matlab (The Mathworks, Natick, MA). The signal is digitally demodulated into in-phase and quadrature baseband components. These baseband signals are filtered by a FIR low-pass filter before reconstruction into polar form.

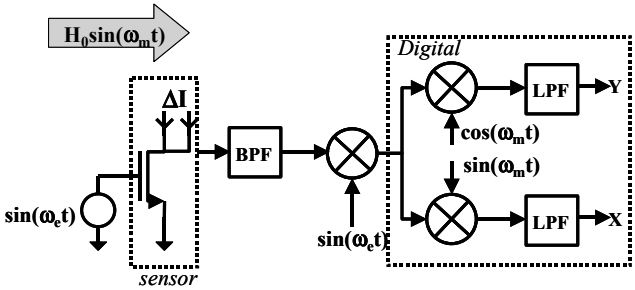

Figure 9. *Simplified diagram of the signal processing path. Digital signal processing is performed in software.*

The noise bandwidth can be adjusted by controlling the FIR filter bandwidth.

RESULTS

Anti-Hu IgG Assay

The sensor chip surfaces were coated overnight with 10 µg/ml human IgG diluted in phosphate buffered saline (PBS). Surfaces were blocked with 3% Non-Fat Dry Milk for 1 hour and washed 3 times in PBS with 0.5% Tween-20 (PBS-T). Either biotinylated goat anti-human IgG (200pM) or biotinylated goat anti-mouse IgG (as a control) (Sigma Aldrich, St. Louis, MO) was added to separate vials and incubated for 30 minutes. The samples were then washed 3 times with PBS and streptavidin-coated magnetic beads (5-8um diameter, Chemegen, Germany) diluted 1:200 to 125ug/ml were added and allowed to settle for 20 minutes. A rare-earth magnet was placed approximately 8mm above the sensor surface for 60 seconds before measurement. The magnet position was determined empirically. The sample was then placed in the measurement system. Figure 10 shows the response from the first 96 sensor elements for the goat anti-human IgG shown in grey and the goat anti-mouse IgG shown in black.

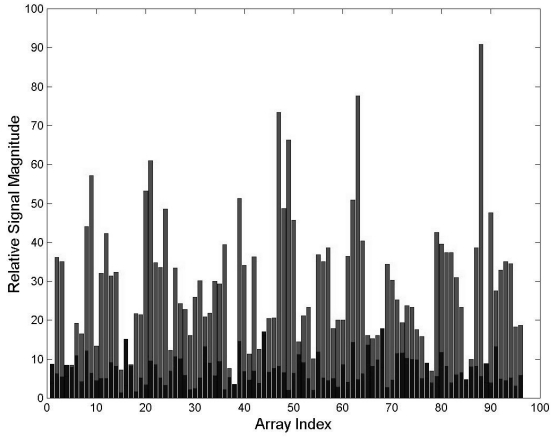

Figure 10. *Relative output signal magnitude vs. array element index for anti-Hu IgG target protein (grey) and control (black). The average signal-to-noise ratio is approximately 13dB.*

This data was collected prior to the use of electrical modulation. Recent experiments indicate that use of electrical modulation improves SNR by approximately 10-20dB. This improvement in SNR can be used to reduce the scan time for the array. Scanning all 256 elements takes approximately 2 minutes. The scanning time for the array becomes important if the device is scanned repeatedly while the magnetic washing force is ramped. This washing method may provide additional information about assay binding characteristics.

CONCLUSIONS

We have demonstrated an immunoassay platform with clinically relevant sensitivity, fabricated in a CMOS process. The noise and sensitivity limitations that traditionally limit the applicability of CMOS Hall sensors have been mitigated through architectural and signal processing techniques. With these improvements, the CMOS substrate may provide a cost-effective and easily manufactured platform for diagnostics. Furthermore, the proposed assay platform is potentially compact and automated, making it applicable to in-field applications.

ACKNOWLEDGEMENTS

The authors would like to thank Agere Systems for microfabrication support and Prof. Eva Harris for discussion and laboratory resources.

REFERENCES

1. World Health Organization Infectious Disease Report, 1999.
2. R. Kotitz, et al, "SQUID based remnance measurements for immunoassays", *IEEE Trans. on Applied Superconductivity*, 7, 36 (1997).
3. D. Baselt, et al, "A biosensor based on magnetoresistance technology", *Biosensors and Bioelectronics,*13, 791 (1998).
4. R.L. Edelstein, et al, "The BARC biosensor applied to the detection of biological warfare agents", *Biosensors and Bioelectronics*, 14, 805 (2000).
5. R. S. Popovic, *Hall Effect Devices,* New York, IOP ltd, 1991.

A MICROMACHINED HYDROGEL-GATED SMART FLOW CONTROLLER

Yuandong Gu [1], Antonio Baldi [2], Babak Ziaie [2,3], and Ronald A. Siegel [1,3]
Department of Pharmaceutics[1], Electrical and Computer Engineering[2], and Biomedical Engineering[3]
University of Minnesota, Minneapolis, MN 55455

ABSTRACT

In this paper, we report on the design concept, fabrication, characterization, and testing of a micromachined, hydrogel-gated smart flow controller (HFC) that responds to different environmental stimuli. The HFC is composed of two components, a 3-dimensional crosscut structure and a loaded stimuli-sensitive hydrogel. The free swelling behaviors of glucose- and temperature-sensitive hydrogels were characterized. A gating mechanism of the HFC was postulated, and verified by microscopy. For the temperature-sensitive HFC, temperature cycling between 25 and 40 °C resulted in a flow rate change between 0 and 12 ml/minute with a 10 second response time. The flow rate through the device at 40 °C increases almost linearly with pressure across the structure. Flow through the HFC loaded with a glucose-sensitive hydrogel is shown to respond to changes in glucose concentration in the external solution. The response time is, however, as long as 2 hours.

INTRODUCTION

Environmentally sensitive hydrogels undergo a volume change in response to different physiological stimuli [**1-3**]. Integration of microelectromechanical systems (MEMS) with such gels offers unique opportunities in the field of microfluidics [**3, 4**]. However, entrapment and polymerization of such gels in small cavities and channels are challenging. Beebe *et al* have demonstrated *in situ* photopolymerization of a pH-sensitive hydrogel around microposts to prevent the gel from being dislodged by the flow [**4**]. With this approach, control of *in plane* flow, i. e. a flow in microchannels running along the surface, was achieved. In this paper, we report on the design concept, fabrication, characterization, and testing of a micromachined, hydrogel-gated flow controller (HFC) for the control of perpendicular flow through the device. This structure permits control at higher flow rates.

THEORY

The design concept of the HFC is shown in Figure 1-a. The HFC consists of a 500 μm-thick Pyrex glass plate with two sets of parallel trench cuts on either side. Each parallel set is 300 μm deep and 120 μm wide. The parallel cuts on the two sides intersect perpendicularly. Since they are deeper than half plate thickness, the cuts form 120 μm × 120 μm holes at the cross points that span the thickness of the plate. This unique 3-D structure allows the hydrogel to be polymerized inside the interconnected trenches, anchoring it to the structure and providing flow control at the cross points.

Figure 1-b shows a photograph of the HFC where the transparent temperature-sensitive hydrogel has been dyed for visualization purposes. Figures 2-a,b demonstrate the working principle of the HFC. When the hydrogel is in the shrunken state, the gate opens and the liquid (vertical to the device plane) flows through the gaps in the cross points between the hydrogel and the trench walls, with high flow rate (Figure 2-b). When the hydrogel is swollen, the gaps between the hydrogel and the trench walls narrow and the liquid flows more slowly (Figure 2-a).

EXPERIMENTAL DETAILS

Fabrication of the 3-D structure: A 500 μm-thick Pyrex glass wafer was first silanized to render the surface hydrophobic. Then, the first set of trenches was cut into the Pyrex wafer with a wafer-dicing saw. The wafer was turned over, and the second set of trenches was cut into the opposite side of the wafer by the same means, but 90° in orientation to the first set of trenches. All the trenches were 300 μm deep, 120 μm wide, and 180 μm apart.

Loading of the hydrogels: The fabricated 3-D structure was sandwiched between two glass slides. The pregel solution was then introduced into the structure by capillary action at 4 °C. The 'sandwich' was brought to room temperature and left overnight to initiate and complete the polymerization and gelation. The hydrogel-loaded 3-D structure, HFC, was then removed from the sandwich, and subsequently equilibrated in phosphate buffered saline (PBS) solution for further use. Two kinds of hydrogels, temperature- and glucose-sensitive hydrogels, were used in this study. The recipes for their corresponding pregel solutions are listed below.

1) Temperature-sensitive: 100 mg isopropylacrylamide (NIPA), 1 mg N,N'-methylenebisacrylamide (Bis), 5 μl N,N,N',N'-tetramethylethylenediamine (TEMED), and 1 mg ammonium persulfate (APS). All dissolved in 1 ml deionized water.
2) Glucose-sensitive: 80 mg acrylamide (AAm), 52 mg 3-methylacrylamidophenylboronic acid (MPBA), 0.5 mg Bis, 5 μl TEMED, and 0.5 mg APS. All dissolved in 0.7 ml deionized water.

Testing: Cylindrical hydrogels, with the same compositions as those that were polymerized in the HFC, were polymerized in glass capillaries with I. D. = 1.2 mm. The free swelling profile of the hydrogels was studied in pH 7.4 PBS solutions. The equilibrated HFC was mounted between two tubes, and an external hydraulic pressure was applied across it. The flow rate was monitored under different temperatures, glucose concentrations, and different external pressure. After measuring the flow rate, the temperature-sensitive HFC was disassembled and observed under the microscope at 25 and 40°C, respectively, to verify the proposed working principle.

Travel support has been generously provided by the Transducers Research Foundation and by the DARPA MEMS and DARPA BioFlips programs.

RESULTS AND DISCUSSION

Silanization and hydrogel loading: Pre-silanization of the Pyrex wafer before fabricating the 3-D structure creates an environment that is hydrophobic everywhere except in the newly cut trenches, which are hydrophilic. Such an environment benefits the HFC in two aspects: 1) it helps to retain the hydrophilic hydrogels inside the trenches, and 2) it facilitates the removal of HFC from the sandwiching glass slides, which were also silanized to be hydrophobic.

The pregel solution contains a redox polymerization system. At room temperature, the pregel solution gels in less than 10 minutes. Prechilling the pregel solution to 4 ˚C slows down the polymerization rate, allowing enough time for hydrogel loading. Due to the hydrophilicity of the trenches and hydrophobicity of the surroundings, the pregel solution is preferentially drawn into the trenches without air bubbles.

Free swelling of hydrogels: Figure 3 shows the free swelling behavior of the temperature-sensitive and glucose-sensitive hydrogels in pH 7.4 PBS solution. For temperature-sensitive hydrogel, the diameter increases to 1.7 mm at 25˚C and shrinks to about 0.7 mm at 40 ˚C, showing a clear volume phase transition between 32-34 ˚C. It is interesting to notice that when the gel is swollen, its diameter exceeds the diameter at the time of formation, which was 1.2 mm; when the gel shrinks, its diameter drops below 1.2 mm. For the glucose-sensitive hydrogel, diameter shrinks 25% compared to the time of formation when equilibrated in glucose-free pH 7.4 PBS solutions [**2**]. However, at pH 7.4, the gel swells monotonically with increase in glucose concentration.

Proposed working principle: The proposed working principle of the HFC is illustrated in Figure 2 a-b. When the hydrogel is in the swollen state (Figure 2-a), it completely fills the trenches. No flow is allowed through the crosspoints, and the gate is closed. When the hydrogel is shrunken (Figure 2-b), however, it can no longer occupy the whole trench space, and gaps at the crosspoints are formed between the hydrogel and the trench walls. These gaps allow the liquid (vertical to the device plane) to flow through. Light microscopy on a temperature-sensitive HFC supports the proposed working principle. When the hydrogels are polymerized *in situ*, they fill the trenches. Since the hydrogel swells at 25 ˚C in the free-swelling geometry (Fig. 2c), we expect that at hat temperature the hydrogel in the device will exert pressure against the trench wall and effectively seal off fluid transport. At 40 ˚C (Figure 2-d), the hydrogels shrink to a size that is smaller than the trenches; creating gaps between the hydrogels and the trench walls. These gaps are identified in Figure 2-d by the arrow. The free swelling data correlates with the volume changes in the photographs and flow rate measurements. For the glucose-sensitive HFC, in the absence of glucose, the gel has the smallest diameter, i.e., the HFC has the largest gap between the hydrogel and the trench walls, resulting in a high flow rate. Upon addition of glucose, the gel swells, the gap gets smaller, and the flow rate drops. However, it is worthwhile to notice that the shrunken hydrogel, instead of sitting in the center of the crosspoint, adheres to one side of the trench wall. We attribute this unexpected observation to the inhomogeneity of hydrogels and the unbalanced forces on both sides of the hydrogel. The reason for this discrepancy needs to be clarified, although it does not seem to affect the behavior of the HFC.

Flow rate measurement: Figure 4 shows flow rate measurements for the temperature and glucose sensitive HFCs. As can be seen, for the temperature sensitive HFC, flow rate changes between 0-12 ml/min for a temperature swing of 15 ˚C. For the glucose sensitive HFC the change is between 5-26 µl/min in response to a 20 mM change in glucose concentration. The difference in the flow rates magnitudes between the two HFCs is due to different swelling behaviors of the hydrogels. Figure 5 shows the flow rate through the temperature-sensitive HFC as a function of external pressure drop at 40˚C. Flow rate increases almost linearly with external pressure applied across the HFC. For an external pressure of 3.43 kPa, a flow rate as high as 10.18 ml/minute is achieved. The slight increase in the slope of the curve at higher pressure may imply small deformation of the hydrogel under higher pressure.

Response time: The response time (the time required to sense a change in flow rate after external conditions are changed) for the temperature-sensitive HFC is about 10 seconds (Figure 4-a). However, for glucose-sensitive hydrogels, the response time is as long as 2 hours (Figure 4-b). This is due to the fact that heat transfer is much faster than the diffusional mass transfer of glucose. The flow rate reaches the plateau in 50 seconds in the case of swelling and 120 seconds in the case of shrinking with the temperature-sensitive HFC.

CONCLUSIONS

In this paper, we presented the design concept and fabrication of a unique 3-D structure that allows anchoring of hydrogels for active flow controlling. Such a structure is easy to fabricate and load in hydrogels. Integration of such a structure with stimuli-sensitive hydrogels, such as temperature-sensitive and glucose-sensitive hydrogels enables control of flow which is perpendicular to the surface of the HFC. The hydrogel-integrated structure, HFC, has been shown to modulate the flow rate in response to external stimuli, such as temperature and glucose. A glucose-sensitive HFC can be envisioned potentially for closed-loop insulin delivery for diabetes. However, the prolonged response time for the glucose-sensitive HFC is the major drawback in applying the HFC to closed-loop insulin delivery. Work is in progress to decrease the thickness of the structures in the device in order to decrease the response time.

REFERENCES

1. T. Tanaka *et al.*, " Phase transitions in ionic gels", *Phys. Rev. Lett.*, *1936*, 45(1980).
2. Y. Gu, and R. A. Siegel, "Swelling behavior of phenylboronic acid hydrogel in glucose solution", *28th International Symposium on Controlled Release of Bioactive Materials*, San Diego, 6/23-27/2001.
3. Q. Yu *et al.*, " Responsive biomimetic hydrogel valve for microfluidics", *App. Phys. Lett., 2589*, 78(2001)
4. D. J. Beebe *et al*., " Functional hydrogel structures for autonomous flow control inside microfluidic channels" *Nature, 588*, 404(2000)

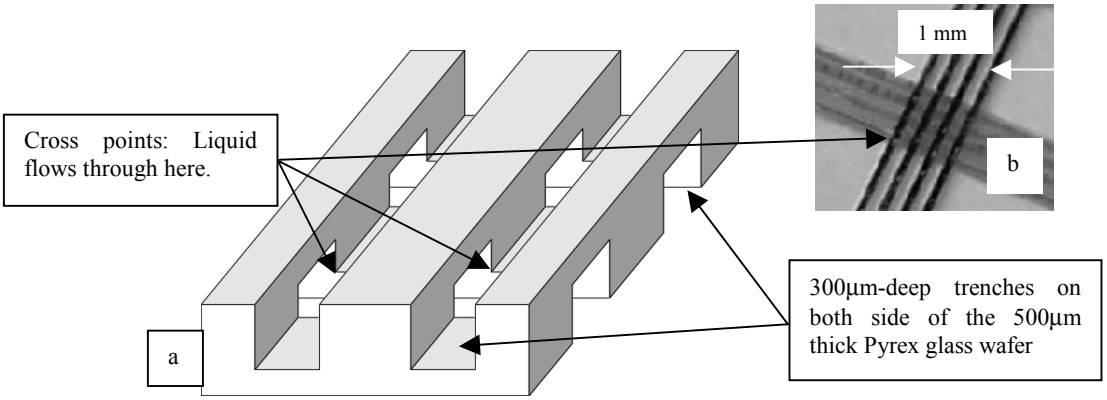

Figure 1. *a) Design concept of the 3-D structure. b) HFC loaded with temperature-sensitive hydrogel.*

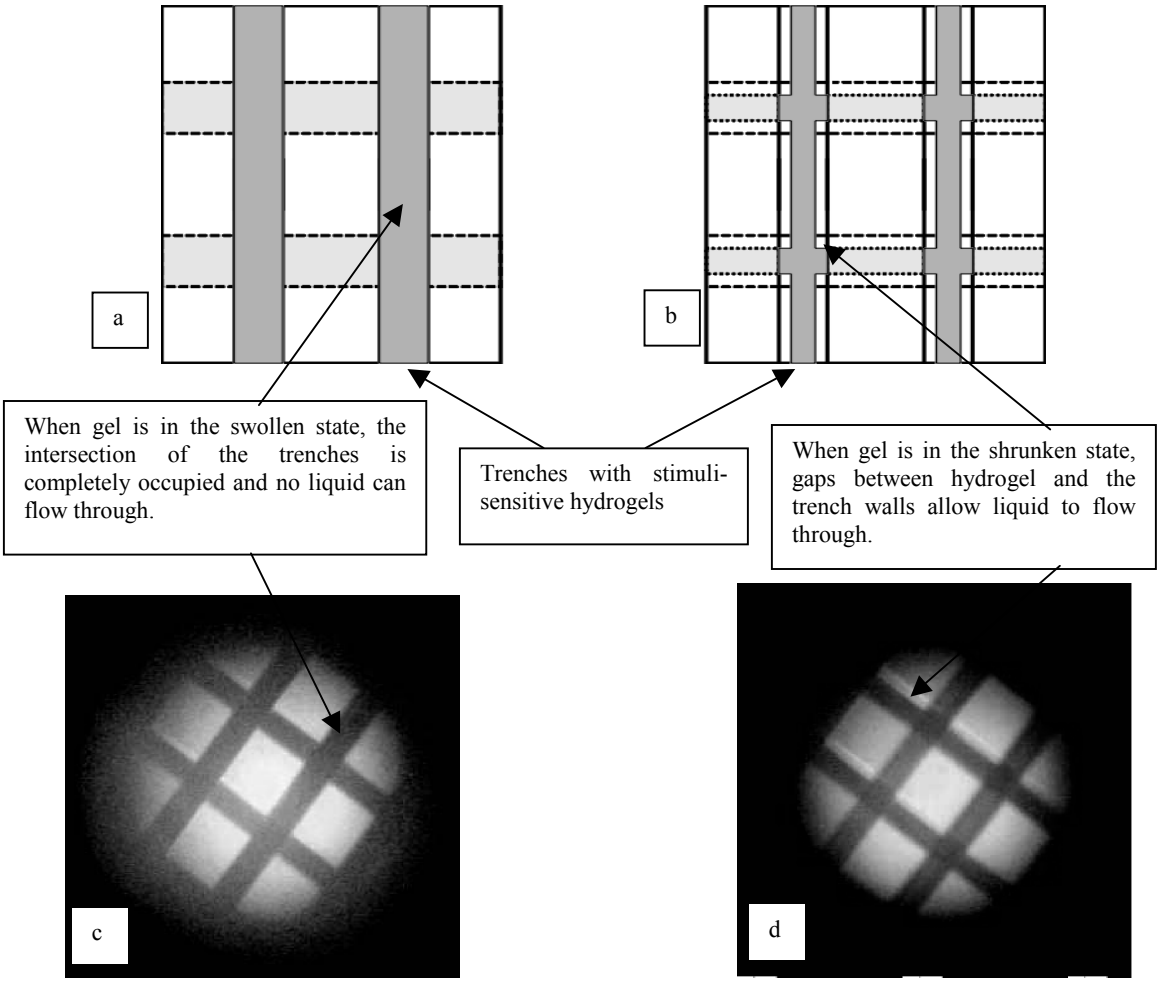

Figure 2. *Proposed working principle and photomicrograph of a temperature-sensitive HFC. a, c) Closed gate when the hydrogel is swollen. b, d) Opened gate when the hydrogel is shrunken. Arrow in d) shows the gap between the shrunken hydrogels and the trench walls.*

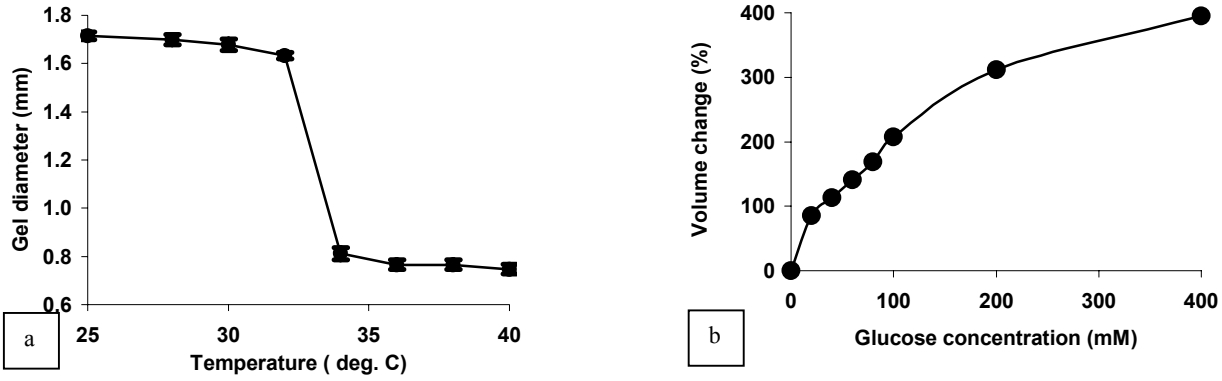

Figure 3. *Free swelling behavior of the a) temperature-sensitive, and b) glucose-sensitive hydrogels in pH 7.4 PBS solution. Temperature-sensitive hydrogel swells at 25˚C and shrinks at 40˚C, with volume phase transition between 32-34˚C. The glucose-sensitive hydrogel swells with increase in glucose concentration.*

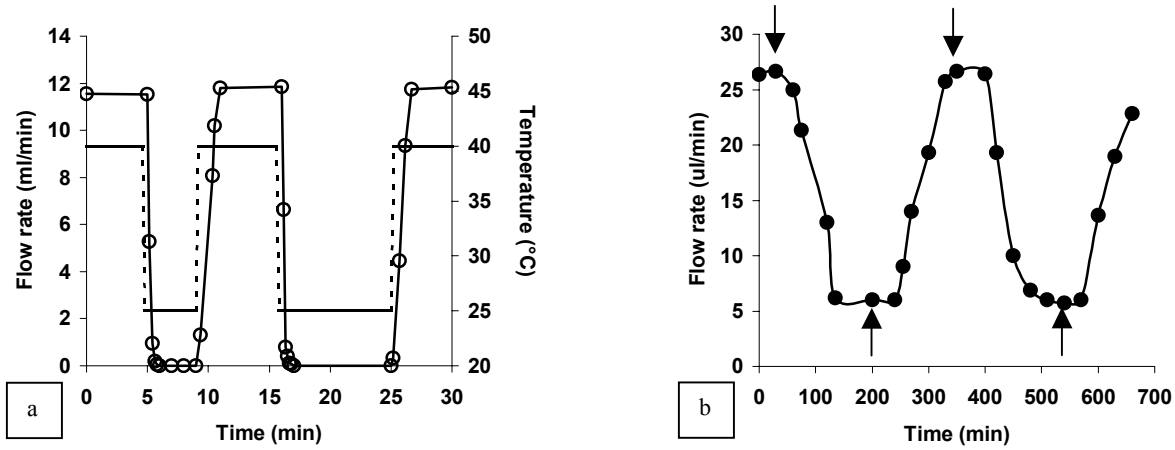

Figure 4. *a) Response of the flow rate (solid line) through a temperature-sensitive HFC to temperature change (dashed line). b) Response of a glucose-sensitive HFC to glucose concentration change. Down arrows indicate addition of 20mM glucose, and up arrows indicate removal of glucose.*

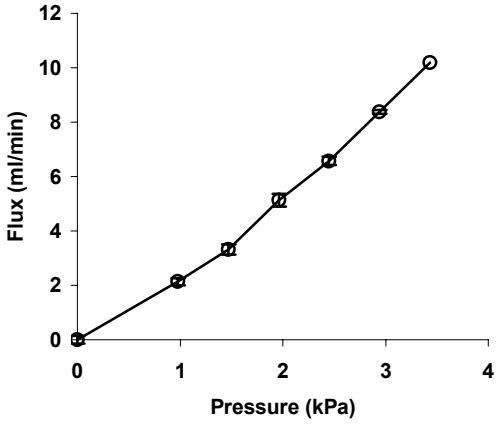

Figure 5. *Flow rate vs. external pressure through a temperature-sensitive HFC at 40˚C. The flow rate increases almost linearly with external hydraulic pressure.*

EWOD Driving of Droplet on NxM Grid Using Single-Layer Electrode Patterns

Shih-Kang Fan*, Peter-Patrick de Guzman, and Chang-Jin "CJ" Kim
Mechanical and Aerospace Engineering Department University of California, Los Angeles (UCLA)
Los Angeles, CA 90095-1597

ABSTRACT

This paper demonstrates 2-D droplet movement implementing electrowetting-on-dielectric (EWOD) for actuation. Experimentation on different electrode configurations reveals certain requirements and flexibilities for EWOD device design. The current device has a single layer of rectangular electrode rows-one set of rows on top and the other set on bottom plate, orthogonally oriented. The innovation lies in the use of only N+M electrodes to control NxM different positions of a droplet on a 2-D grid without requiring fabrication of multi-layer electrodes.

INTRODUCTION

Recently, our group has reported how to create (from reservoir), drive, divide, or merge droplets, all using electrowetting-on-dielectric (EWOD) actuation [1]. EWOD is an actuation mechanism that is based on electrically controlling a surface's wettability to aqueous liquids [2,3]. With these four functions on individual droplets in hand, the next major challenge to realizing 2-D reconfigurable digital microfluidic circuits (Fig. 1) [4,5] is how to drive individual droplets on a NxM array of possible droplet positions.

An obvious approach to drive droplets with EWOD on a NxM array is to have one drive electrode for every designated position in the array. Taking this approach, although certainly feasible and common in integrated circuits (IC), calls for physical connection to each individual electrode within the array independently. However, the desire to minimize fabrication complexity and the uncertainties about EWOD mechanism on non-planar surfaces motivated our search for a simpler solution.

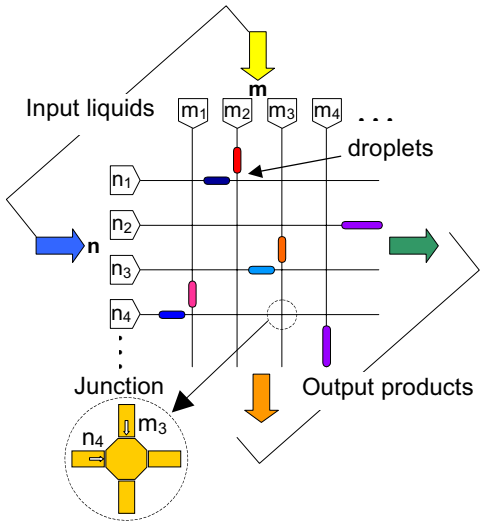

Figure 1. Conceptual description of reconfigurable digital microfluidic circuits [5].

* *Travel support has been generously provided by the Transducers Research Foundation and by the DARPA MEMS and DARPA BioFlips programs.*

TECHNICAL BACKGROUND

Fig. 2 shows the cross section and top view of an EWOD device with a single-layer of electrodes on both top and bottom glass plates [1]. A liquid droplet is placed in the gap between these two plates. *Driving electrodes* are patterned on one glass plate (shown bottom) subsequently coated with a dielectric layer and a thin hydrophobic coating (e.g., Teflon). The other plate has an unpatterned *reference electrode* layer covered with a thin hydrophobic coating. For clarification, we define the electrode providing the reference electric potential (usually ground) as a *reference electrode* (shown on top plate in Fig. 2) in a *reference state* and the electrode supplying the driving electric potential as the *driving electrode* in a *driving state*. Although the reference electrode and the driving electrode can be situated on the same plate, (i.e., the other plate has no electrode) we found that vertically opposing the reference electrode and the driving electrode induces more efficient EWOD actuation. Note, a smaller space "D" (Fig. 2(b)) between two drive electrodes is desirable to have smooth droplet movement with lower driving electric potential.

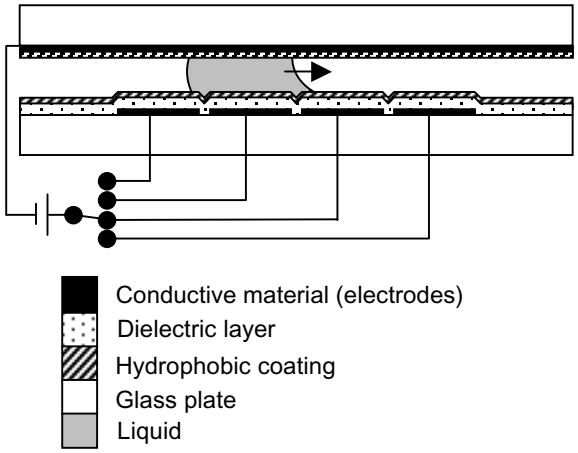

(a) Cross sectional view

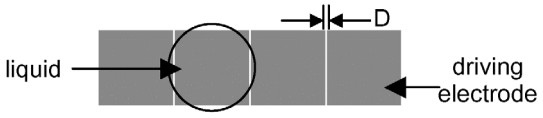

(b) Top view. The blank reference electrode on top plate is not shown.

Figure 2. Single-layer electrode EWOD device.

To reduce fabrication complexity and sustain predictable EWOD actuation, a single conductive layer patterned for electrodes and conduction lines currently presents the most desirable approach. Fig. 3 shows the top view of a possible digital microfluidic circuit applying the electrode configuration previously described in Fig. 2 into the conceptualization depicted in Fig. 1. As the number of electrode increases, the number of conduction lines connecting the outside control circuits to the inner electrodes, likewise increase. These lines must run through

the small spacing "D" between electrodes with single conduction layer architecture. Since “D” is limited for efficient droplet actuation, the number of drive electrodes is also limited. Moreover, if each drive electrode is controlled by an individual control signal, the complexity of the electric circuit escalates when dealing with a large electrode grid.

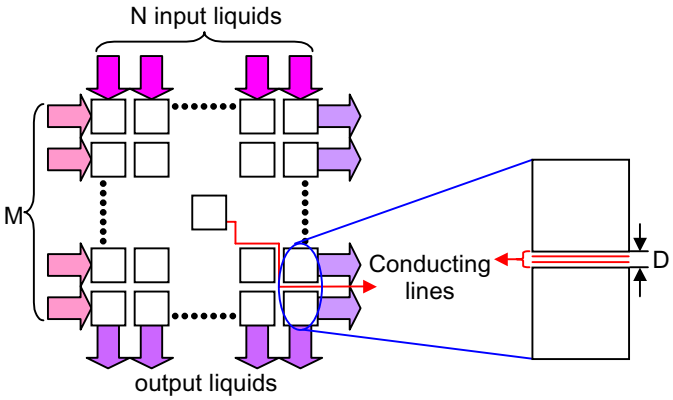

Figure 3. Top view of digital microfluidics circuit with N+M input liquids.

THEORY

Observation of a droplet moving on a 2-D grid, as shown in Fig. 4, revealed the possibility of dividing the movement into two components: (1) X-direction and (2) Y-direction. Therefore, our approach is to position the droplet by using two groups of electrodes. One set of electrodes control the X position of the droplet, while the other set controls the Y position. This concept is similar to a XY table with two drive motors.

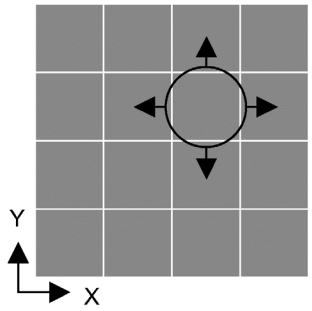

Figure 4. Droplet movement in a 4×4 electrode array

To achieve this concept, two sets of orthogonal electrode rows are required, one row of electrodes on each top and bottom plate. As shown in Fig. 5, each row is responsible for one direction movement. For example, movement in the X-direction can be made by the rows of electrodes on bottom plate and movement in the Y- direction by the rows of electrodes on top plate. As described previously in Fig. 2, one reference electrode is kept grounded while potential is applied to the individual drive electrodes to drive the droplets. The same driving scheme is conserved in this configuration. Since we can independently control the potential of each electrode, we can switch between reference and driving states for each electrode. Electrode(s) within an electrode row on either top or bottom plates are then assigned reference or driving states depending on the direction of movement. The beauty of this configuration lies in the reduced number of control signals. Only N+M control signals are necessary to create a virtual NxM grid.

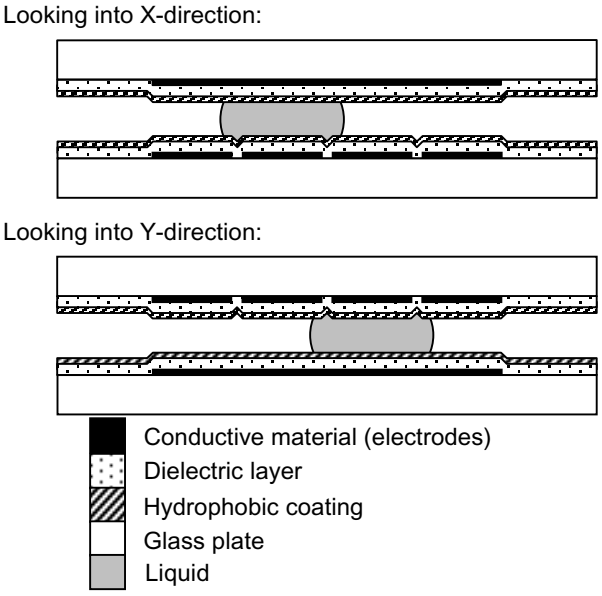

Figure 5. Cross sections of an EWOD device with driving electrodes on both top and bottom channel surfaces.

Note that Figure 2 shows an EWOD device with an asymmetric cross section, while Figure 5 shows one with a symmetric cross section. The contact angle versus applied electric potential measurements of these two situations is discussed in [6]. Experimentally, we verified that EWOD actuation occurs on both asymmetric and symmetric devices.

DESIGN OF ELECTRODE ROWS

Design I

Fig. 6 shows the first design. Fig. 6(a) is the top view of a set of electrode rows, which can drive the droplet in the X-direction. These electrode rows consist of vertical major electrodes (four shown) and minor horizontal fingers. Each major electrode branches out to minor electrodes of fingers interdigitating with neighboring electrode fingers. With this design, a droplet sitting on a minor electrode moves only in the X-direction to another minor electrode when activating an adjacent major electrode. This occurs because of the minimized wettable surface above and below each minor electrode. Using the same electrode design in the Y-direction should generate a similar effect (Fig. 6(b)). Initial experiments on the same configuration as in Fig. 2(a) to test EWOD actuation with this electrode row design proved successful. Unidirectional droplet movement was observed when using electrodes within the electrode row (either Fig. 6(a) or 6(b)) as driving electrodes and an unpatterned conductive layer as the reference electrode on the top plate. To test droplet movement in both X and Y directions, another set of electrode rows was patterned on separate glass plates and were combined as in Fig. 6(c). However, the anticipated 2-D droplet movement was not obtained. Further investigation revealed that the electric ground through the electrode fingers generated insufficient driving forces. It was found to be important to fill all empty spaces with electrode surface to provide more area for grounding when the corresponding drive electrode is energized.

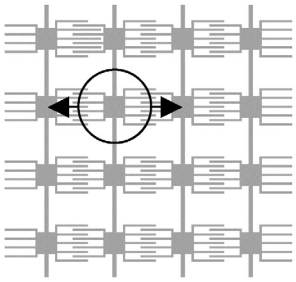

(a) Bottom electrode rows: X-direction movement.

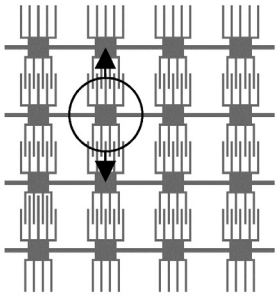

(b) Top electrode rows: Y-direction movement.

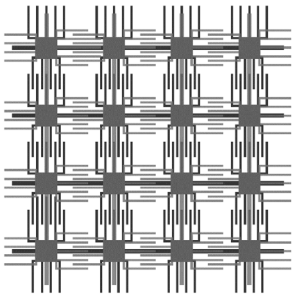

(c) left: Orthogonal top and bottom electrode rows: X-Y movement.

Figure 6. Design I: divide driving electrodes into two directions to decrease control signals. X-Y movement is not achieved because of insufficient electric ground.

Design II

Consequently, an extra *surrounding electrode*, as shown in Fig. 7, was placed within the area between electrodes in Design II. When the droplet is driven in the X-direction, the actuation scheme is as follows: vertically oriented major electrodes, shown in Fig. 7(a), work as driving electrodes, while all horizontally oriented major electrodes (Fig. 7(b)) on the top plate and the surrounding electrode provide sufficient electric ground. Movement in the Y-direction simply involves reversing this actuation scheme. Later actuation tests successfully demonstrated 2-D droplet movement.

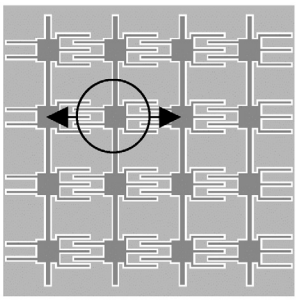

(a) Bottom electrode rows: surrounding electrode is placed to fill between the electrodes. Electrode row is used to drive the droplet along the arrows.

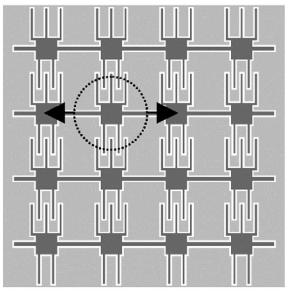

(b) Top electrode rows: both the electrode row and surrounding electrode provide electric ground when droplet moves in the arrow direction

Figure 7. Design II: surrounding electrode is added to provide sufficient electric ground; actuation scheme for droplet movement in X-direction.

By adding a surrounding electrode, we increased the reference electrode area and fulfilled 2-D EWOD actuation. However, the surrounding electrode also decreased the number of fingers between minor electrodes, comparing Fig. 6 and 7. When the number of electrode fingers decreases, the length of the droplet meniscus that contributes to actuation also decreases, resulting in a reduction of EWOD actuation force.

Design III

The fingers in Design I and II were designed for facilitating droplet movement. The finger design was first introduced by Pollack *et al.* [7]. However, it was proven (to be reported elsewhere) that, in most cases, droplets can be driven more effectively without the presence of overlapping fingers. Fig. 8 shows redesigned major electrodes with minor electrodes free of fingers. This design maximized overlapping meniscus length thereby theoretically increasing the EWOD actuation force. Testing on this third electrode design indeed resulted in a lower initial driving voltage or higher droplet velocity, compared with Design I and II.

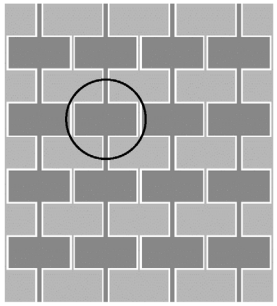

(a) Bottom electrode rows: X-direction movement

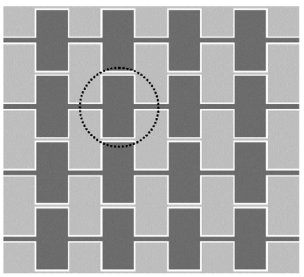

(b) Top electrode rows: Y-direction movement

Figure 8. Design III: electrodes without fingers to provide more electrowetting force. Lower applied voltage or higher moving speed is achieved.

Design IV: Current design (rectangular electrode rows)

Using the knowledge accumulated through the previous experiments and electrode designs, the current electrode design became elegantly simple. From previous designs, we observed two important factors to design the driving electrode: (1) electrode fingers are not required, (2) maximize length of meniscus overlapping neighboring electrode. The current design, shown in Fig. 9 with rectangular electrodes, is the extreme case with these two factors. It may first appear, with this design, that it will be difficult to confine the droplet movement along a well-define line (Fig 9(a)). However, if only the rectangular electrode right above the droplet is grounded (dash lined in Fig. 9(b)), the movement in the X-direction follows the ground electrode. In short, when one plate (e.g., bottom plate) is used to drive the droplet (e.g., to X-direction), one of the electrode rows on the other plate (e.g., top plate) can be used to maintain the movement in course (e.g., against Y-direction).

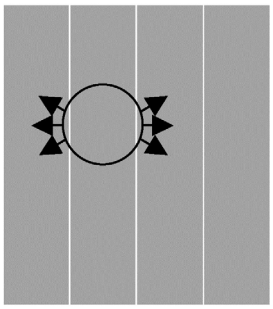

(a) Bottom electrode row: changing the X position of the droplet. The X-direction movement is not ideal.

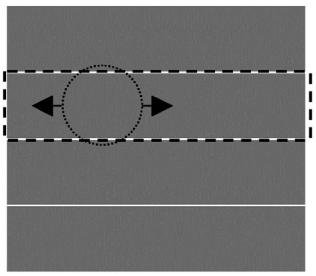

(b) Top electrode row: selectively apply electric ground can keep the Y position of the droplet.

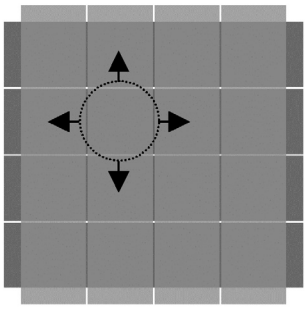

(c) left: 2-D movement of droplet between two electrode sets can be driven by the lowest voltage and the least control signals.

Figure 9. Design IV: Current design using rectangular electrodes.

FABRICATION

The device for each design consisted of two glass plates with a single layer of patterned electrodes. The electrode top view for each device was shown in the previous figures. Although each design has different electrode shapes, all these designs have the same cross section, as shown in Fig. 5. Since electrodes are placed on both the top and bottom plates, to observe the droplet movement, we required the use of ITO (indium tin oxide), a transparent conductive material deposited and patterned on the top plate. The fabrication processes are as follows: (1) Deposit and pattern ITO (top plate) and Cr/Au (bottom plate). (2) Deposit and pattern wire soldering pads on ITO. (3) Deposit dielectric material on both plates. (4) Spin Teflon on both plates. (5) Solder wires to soldering pads.

RESULT

Fig. 10(a) shows a frame of video recording, which verifies the proposed driving scheme, along with the schematic interpretation of the device. The droplet had a velocity of 30 mm/s at 80 V_{AC}. Higher driving speed is obtainable by applying higher voltage. In this experiment, our goal was to verify the device design; thick (~ 0.5 m) dielectric layer is used. By using thinner dielectric layers, driving voltage can be decreased [8].

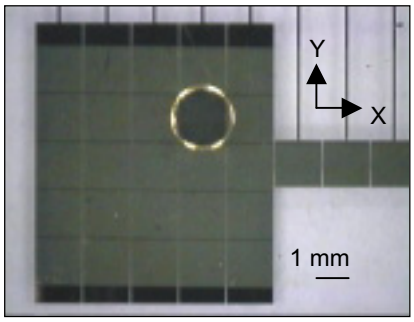

(a) Droplet is moving on a 5×5 grid.

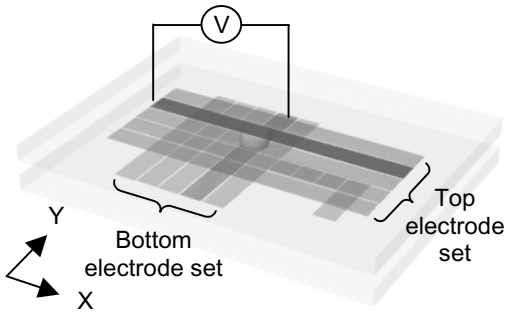

(b) The corresponding activated electrodes of (a) are highlighted.

Figure 10. Testing of the current design.

To demonstrate the programmability, we have driven the droplet to follow alphabets. Fig. 11 shows overlapping images of a droplet traveling along the paths of characters HH02.

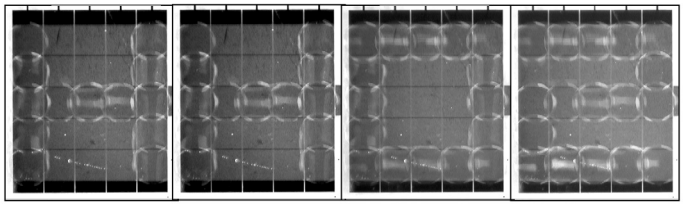

Figure 11. A droplet following characters HH02, demonstrating the programmability for arbitrary continuous path of a droplet on a NxM grid.

CONCLUSION

EWOD actuation of droplets on a virtual NxM grid using only N+M control signals was presented. The current rectangular electrode row design requires only a single conduction layer, thereby simplifying fabrication and minimizing complexity of electrode wiring. The rectangular electrode design improved actuation efficiency by increasing the droplet meniscus length. The result is a major step toward full realization of programmable digital microfluidic circuits.

ACKNOWLEDGEMENT

This work was supported by the National Science Foundation (NSF) CAREER Award, NSF Engineering Microsystems: "XYZ on a chip" Program, and Defense Advanced Research Projects Agency (DARPA) BioFlips Program. The authors would like to thank the members of Dr. Robin Garrell's group and Sung Kwon Cho, Jesse Fowler, and Hyejin Moon for valuable discussion.

REFERENCES

1. S. K. Cho, S.-K. Fan, H. Moon, and C.-J. Kim, "Towards Digital Microfluidic Circuits: Creating, Transporting, Cutting and Merging Liquid Droplets by Electrowetting-based Actuation", *Proc. IEEE Conf. Micro Electro Mechanical Systems*, Las Vegas, NV, Jan. 2002, pp. 32-35.

2. M. Vallet, B. Berge, and L. Vovelle, "Electrowetting of water and aqueous solutions on poly(ethylene terephthalate) insulating films", *Polymer*, vol.37, (no.12), June 1996. p.2465-70.

3. H. J. J. Verheijen and M. W. J. Prins, "Contact angles and wetting velocity measured electrically," *Review of Scientific Instruments*, vol.70, (no.9), Sept. 1999. p.3668-73.

4. J. Lee, H. Moon, J. Fowler, C.-J. Kim, and T. Schoellhammer, "Addressable Micro Liquid Handling by Electric Control of Surface Tension," *Proc. IEEE Conf. Micro Electro Mechanical Systems*, Interlaken, Switzerland, Jan. 2001, pp. 499-502.

5. C.-J. Kim "Micropumping by Electrowetting", *Proc. MEMS, ASME IMECE*, New York, NY, Nov. 2001.

6. S. K. Cho, H. Monn, J. Fowler, and C.-J. Kim, "Splitting a Liquid Droplet for Electrowetting-Based Microfluidics," *Proc. MEMS, ASME IMECE*, New York, NY, Nov. 2001.

7. M. G. Pollack and R. B. Fair, "Electrowetting-based Actuation of Liquid droplets for Microfluidic Applications", *Applied Physics Letters*, Vol. 77, No. 11, pp. 1725-1726.

8. H. Moon, S. K. Cho, R. L. Garrell, and C.-J. Kim, "Low Voltage Operation of Contact Angle Modulation by Electrowetting-On-Dielectric (EWOD) Principle", being submitted.

A MICROBUBBLE-POWERED BIOPARTICLE ACTUATOR

Rebecca A. Braff, Antimony L. Gerhardt, and Martin A. Schmidt
Microsystems Technology Laboratories, Massachusetts Institute of Technology
Cambridge, MA 02139
Martha L. Gray
Division of Health Sciences and Technology, Harvard-MIT
Cambridge, MA 02139
Mehmet Toner
Center for Engineering in Medicine, Mass. Gen. Hosp., and Health Sciences and Technology, Harvard-MIT
Boston, MA 02114

ABSTRACT

In this paper, we present the results of a device that uses controllable microbubble actuation to manipulate bioparticles. The goal of this project was to design a device that can capture bioparticles (e.g. cells) in predetermined locations and then selectively release them. We use a thermal bubble actuation method to accomplish this goal. In this paper we describe two specific accomplishments: 1) the use of micromachined nucleation cavities and specialized coatings to precisely localize thermal bubbles and to achieve controllable bubble formation temperatures, and 2) the demonstration of controllable microbubbles in a new device for particle sorting.

INTRODUCTION

Microelectromechanical systems (MEMS) have great potential in the biomedical field **[1]**. Microscale devices can be used for clinical applications such as drug or blood testing, and also for basic biological research into cells and DNA sequencing. While these devices can take advantage of small sample sizes and high throughput that are not possible on the macroscale, there are still significant obstacles that must be overcome to make MEMS devices feasible for most biomedical applications. One of the most critical issues for biological MEMS is the movement and control of fluids and particles in fluids on the microscale.

There are several methods of microfluidic actuation that are currently in use**[2-4]**. Examples include thermopneumatic pumping**[5, 6]**, electrostatic actuation **[7, 8]**, piezoelectric actuation**[9]**, bimetalic structures **[10]**, electromagnetic actuation **[11, 12]**, and stimuli-responsive hydrogels**[13]**.

Recently, microfabricated devices have been proposed that employ thermally formed microbubbles as actuators, valves, and pumps **[5, 14-19]**. Microbubble powered devices have the advantage that they can run using relatively uncomplicated electronics, resulting in simple yet robust MEMS. These devices have no moving mechanical parts, and have relatively simple electronics.

The earliest use of bubble formation to create a jet of fluid was in the inkjet printer industry **[20-23]**. By using a thin-film heater to form a vapor bubble, thermal inkjet pens fire drops of ink out of chambers due to the volume expansion created by the bubble.

Evans et al. used vapor bubbles as valves and pumps in their micromixer**[16]** and in their 'bubble spring and channel valve'**[24]**. However, the group reports that the valve may only be opened once because of difficulties removing the initial bubble from the confinement region. This case illustrates some of the problems with the use of microbubbles; namely that bubbles do not always dissipate when the heat is turned off, and that devices are unable to properly manipulate the bubbles to place them in desired locations. This group later used electrochemical bubbles instead of vapor bubbles in a device **[25]**.

Vapor bubbles have also been used as a means of mechanical actuation. Lin et al. **[17, 18]** used microfabricated polysilicon resistive heaters to boil Fluorinert liquid and form a vapor bubble underneath a microfabricated paddle.

A similar application of bubbles in the literature is in a bubble jet that ejects a solution of DNA onto a glass surface**[26]**. Using this technique, precise volumes of DNA solution may be applied to a surface in order to form a DNA microarray for biological screening.

These examples illustrate the potential of bubble actuation. The explosive vaporization used in the inkjet printing industry has already been proven as an effective, reliable fluid actuation mechanism. Problems still impede the use of controllable microbubbles for fluidic actuation, but if they can be solved, the resulting technology could be very powerful. There has not previously been an experimental or theoretical framework for design and implementation of bubble systems with robust operation characteristics. For microbubbles to be a useful tool for MEMS devices, it is necessary to be able to form bubbles in predetermined locations while minimizing the power necessary to do so, and to be able to do this in a controllable way. A second important issue is that when the heater used to form a bubble is turned off, the bubble often remains due to dissolved gas that has come out of solution into the bubble. This can severely impede the performance of a microbubble-powered device.

In this paper, we present a resistive heater that can form bubbles in predetermined locations, repeatably, and at a reduced superheat from conventional thin-film heaters. We then demonstrate the operation of this heater in a novel bioparticle manipulation device.

DEVICE OVERVIEW

To establish proof of principle, our goal is to create a device capable of capturing and releasing bioparticles in a controlled fashion, and more specifically to have the potential of scaling it up into a large-scale array. Figure 1 shows our design of the microbubble-powered bioparticle actuator.

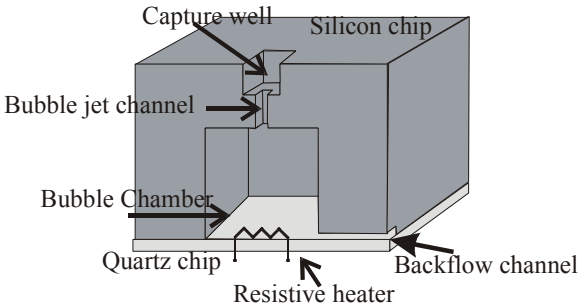

Figure 1: *Schematic of the microbubble bioparticle actuator.*

Travel support has been generously provided by the Transducers Research Foundation and by the DARPA MEMS and DARPA Bioflips programs.

In Figure 2 the operation of the device is shown. When a back flow is applied, a bioparticle may be drawn into a capture well (a). The well can be sized to accommodate only one particle. Then, when a bulk flow is applied over the top of the device, all the uncaptured particles are swept away (b). In order to release the particle, a voltage is applied to the resistive heater in the bubble chamber below and a bubble forms (c). The volume expansion in the bubble chamber pushes out a jet of fluid that ejects the bioparticle from the capture well where it may be entrained in the flow and carried out of the chamber (d). In this paper, we first present the fabrication processes, then discuss the control of the bubble formation process, and finally move on to present the implementation of the microbubble-powered bioparticle actuator.

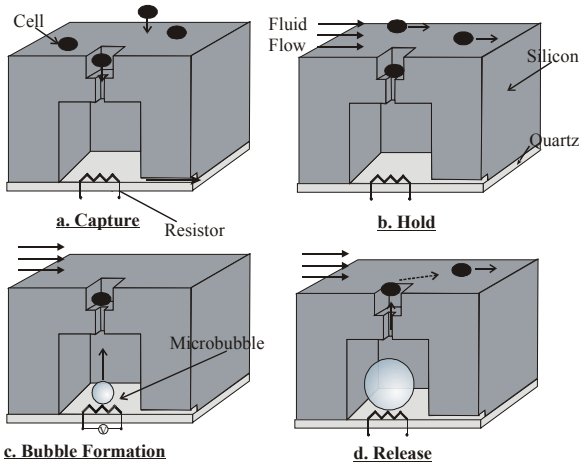

Figure 2: *Operation of the microbubble bioparticle actuator.*

EXPERIMENTAL

As discussed above, the goals of this work are to first accomplish controllable microbubble formation, and then to demonstrate this bubble actuation in a bioMEMS device.

In order to better control microbubble formation, it is necessary first to understand the bubble nucleation process. When liquid is heated in the presence of a solid surface, heterogeneous nucleation usually occurs. In this regime, bubbles typically nucleate in cavities (surface defects) on the heated surface. The degree of superheat necessary to nucleate a bubble in a cavity is inversely dependent on the cavity radius, as shown in Equation 1.

$$T_w - T_{sat} = \frac{2\sigma T_{sat}}{h_{lv}\rho_v r_c} \quad (1)$$

Where T_w is the surface temperature, T_{sat} is the saturation temperature (100°C for water), σ is the surface tension, h_{fg} is the latent heat of vaporization, ρ_v is the vapor density, and r_c is the cavity radius. For example, the surface temperature necessary to nucleate bubbles in water with a surface that has a 1µm cavity radius is about 133°C. For a 0.1µm cavity radius the temperature to nucleate a bubble is about 432°C, well above the thermodynamic superheat limit of water, which is about 270-320°C. Above this limit, bubbles will spontaneously form and do not need a surface cavity for nucleation. This is called homogeneous bubble nucleation.

Accordingly, for surfaces with cavity sizes well below 1µm, it is likely that homogeneous nucleation will occur since the liquid will reach the superheat limit before a bubble nucleates in a cavity. Micromachined surfaces tend to have very smooth surfaces. For instance, for platinum resistors that are only 3-6µm wide, and 0.1µm thick, it is unlikely that cavities will exist on the surface that are large enough for heterogeneous nucleation to occur.

For this reason, a process was developed whereby cavities approximately 6µm wide and twice as deep could be formed in the middle of platinum thin film heaters on quartz wafers. These cavities could then act as nucleation sites for bubble formation. The process we developed to etch cavities(5µm square, 10-20µm deep) in quartz wafers and then deposit thin-film platinum resistors over the top is shown in Figure 3. We start with 4 inch quartz wafers and deposit 0.5µm of polysilicon on top of them. We then pattern the cavities using standard photolithography, and etch the pattern into the polysilicon using a plasma etch. Next the quartz is etched, using the polysilicon as a hard mask, with a CHF_3 plasma for 75-130 minutes depending on the desired depth. After this the polysilicon mask is stripped in SF_6 plasma and the resistors are patterned with photoresist for a lift-off process. A 100Å adhesion layer of titanium followed by 1000Å of platinum is deposited by an electron beam tool, then the metal is lifted off in acetone. The final step is to anneal the wafers at 600°C in nitrogen for one hour.

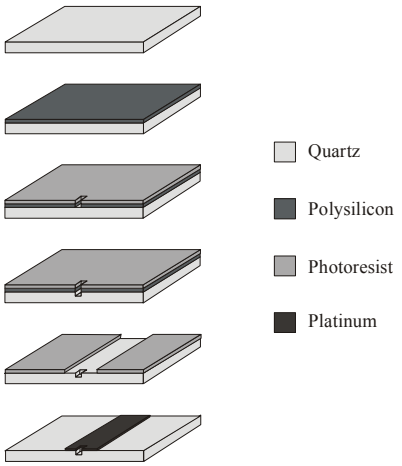

Figure 3. *Quartz wafer process.*

These quartz resistor wafers were tested using a probe station and a semiconductor parameter analyzer to ramp up the voltage while measuring the current in the resistor. The platinum resistors were calibrated to determine the temperature/resistance characteristic so that the temperature of the resistors could be determined from the resulting I-V curves. Resistor wafers were fabricated with and without bubble nucleation cavities and then some of them were coated with CYTOP™ **[27]** or silanized to render the surfaces hydrophobic. Testing was then carried out using a thin layer of deionized water which had been degassed just prior to testing by boiling it for several minutes. A glass cover slip was placed over several drops of this water during testing, in order to prevent evaporation. Voltage was ramped up a half volt at a time, every 1 millisecond until a bubble was formed, and then immediately turned off.

The second phase of testing took place using the full device. The microbubble bioparticle actuator is comprised of two wafers: the quartz resistor wafer described above, and a silicon device wafer, which are bonded together using CYTOP™. The silicon device wafer fabrication process is shown in Figure 4. The wafer is etched with a nested mask to define the capture well and bubble jet channel on one side, then the heater chamber is etched from the back. Afterwards the wafers are diced into chips and bonded to the quartz resistor chips using CYTOP™. The method for CYTOP™ bonding is to prebake a quartz chip on a hotplate at 90°C for 30

minutes, then spin on the CYTOP™ at 2000rpm for 30 seconds, then postbake on a hotplate at 90°C for 30 minutes**[29]**. Immediately afterwards, the silicon chip is bonded to the CYTOP-coated quartz chip using an aluminum jig on top of a hotplate at 160°C. The chips are aligned and bonded in the jig with a 10Kg weight on top for 2 hours, then cooled for another hour before removal from the jig.

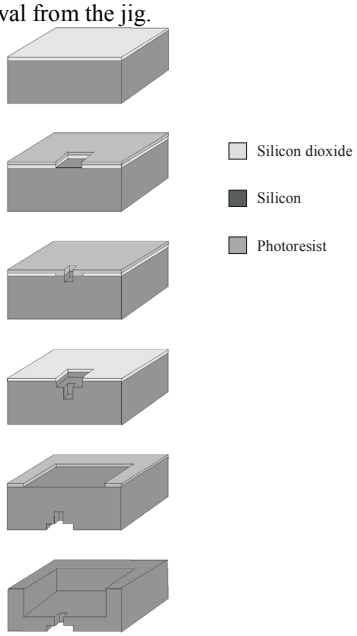

Figure 4. *Silicon fabrication process.*

A flow chamber was machined to test the devices and is shown in Figure 5. In addition to the inlet and outlet for fluid across the top of the chip, there is an additional port that can be used to fill the heater chambers or alternately, to provide a pressure drop to draw particles into the capture wells via the backflow channel. An aluminum block (a) machined with inlets and an outlet, and a depression in which the chip can sit. A PDMS gasket (b) rests in the depression. The quartz resistor chip (c) bonded to the silicon chip (d) sits on top of the gasket. Another PDMS gasket (e) is placed on top, which is covered by a glass slide (f). The top aluminum cap (g) is screwed down into the aluminum base to create a fluidic seal.

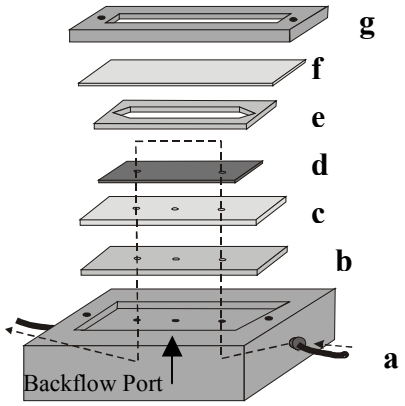

Figure 5. *Flow chamber and package.*

To test the device, it was first vacuum-filled **[28]** with 0.05% Triton X-100 surfactant solution and then placed in the flow chamber. A solution of 10µm diameter polystyrene beads flows over the top of the device, using a syringe pump. Electrical contact is made using probes on a probe station, and bubbles are formed in the bubble chamber using the same method described above for the resistor wafer testing.

RESULTS AND DISCUSSION

An experiment was run to determine the effect of having cavities in resistive heaters, as well as the effect of the different surface treatments, using resistor wafers prepared six different ways: bare quartz with no cavities, bare quartz with cavities, silanized quartz with no cavities, silanized quartz with cavities, CYTOP-coated quartz with no cavities, and CYTOP™ -coated quartz with cavities. Testing was carried out as described above. The bubbles formed in cavities on every trial with the two hydrophobic surface preparations (Figure 6), but did not often form in cavities on the bare, untreated quartz. The bubble formation temperature results are shown below in Figure 7. 44 resistors were tested on each wafer to comprise the data shown below.

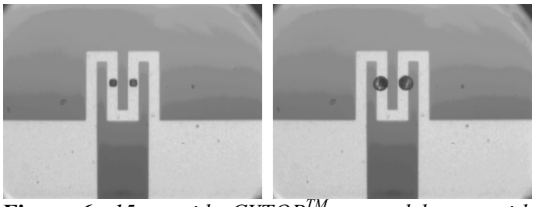

Figure 6: *15µm wide CYTOP™ -coated heater with 10µm wide cavities, before and after voltage applied.*

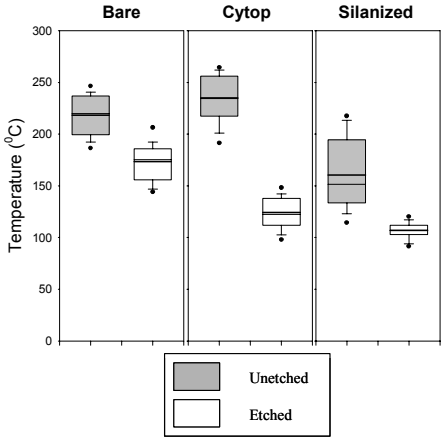

Figure 7: *A plot comparing the average bubble formation temperature of bare resistor wafers with and without etched cavities, silanized wafers with and without etched cavities, and CYTOP™ -coated resistor wafers with and without cavities. The boxes represent the 25th through 75th percentiles of data. The lines span the 5th through 25th and 75th through 95th percentiles of the data and the points represent outlying data. Lines in the boxes represent mean and median data.*

In all cases, the temperature of bubble formation of a wafer with cavities was lower than the temperature of bubble formation for a wafer prepared the same way with no cavities. As the bubbles formed in holes for the two treated wafers, it makes sense that they formed at lower temperatures. Since the CYTOP™ layer is 1µm thick, considerably thicker than the effect of silanization, it makes sense that this added thermal resistance would result in a higher bubble formation temperature for the etched wafers coated with CYTOP™ than for the etched silanized wafers.

The photographs of device operation are shown in Figure 8. In (A) and (B) a small backflow pulls a bead into a well and it is

then held there against the bulk flow in the chamber (C) (t=0). In (D) the bead is ejected from the well when a bubble is formed in the chamber below (t=0.77sec), and In (E) and (F) the bead is entrained in the bulk flow and carried away (t=0.87, t=2.66 sec).

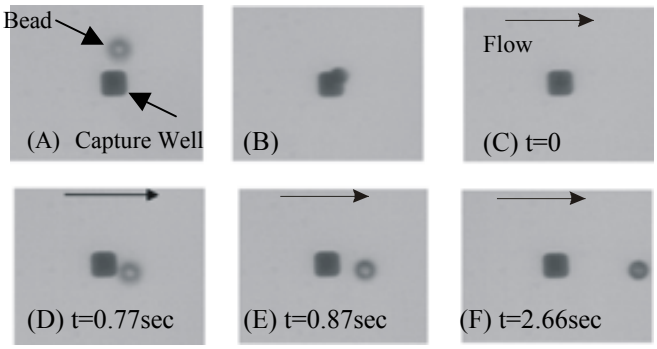

Figure 8: *Sequential photos of device operation.*

CONCLUSION

This actuator demonstrates the potential of microbubbles for fluidic actuation. The device has also successfully manipulated yeast cells. The next step will be to create a small array of wells and complete testing with biological cells.

ACKNOWLEDGEMENTS

This work was carried out with funding from the Alliance for Cellular Signaling project(NIGMS). Fabrication was completed at the MIT Microsystems Technology Laboratories. The authors would also like to thank Professor B. Mikic for many useful discussions about bubble formation. Travel support has been generously provided by the Transducers Research Foundation and by the DARPA MEMS and DARPA bioflips programs.

REFERENCES

1. Voldman, J., M.L. Gray, and M.A. Schmidt, "Microfabrication in Biology and Medicine." *Annual Review of Biomedical Engineering*, 1999. *1*: p. 401-425.
2. Shoji, S. and M. Esashi, "Microflow Devices and Systems." *Journal of Micromechanics and Microengineering*, 1994. *4*: p. 157-171.
3. Ho, C.-M. and Y.-C. Tai, "Micro-Electro-Mechanical-Systems (MEMS) and Fluid Flows." *Annual Review of Fluid Mechanics,* 1998. ***30***: p. 579-612.
4. Gravesen, P., J. Branebjerg, and O.S. Jensen, "Microfluidics- A Review." *Journal of Micromechanics and Microengineering*, 1993. *3*: p. 168-182.
5. Elwenspoek, M., et al., "Towards Integrated Microliquid Handling Systems." *Journal of Micromechancs and Microengineering,* 1994. *4*: p. 227-245.
6. Grosjean, C. and Y.-C. Tai. "A Thermopneumatic Peristaltic Micropump." *Transducers '99*. 1999.
7. Zengerle, R., et al. "Performance Simulation of Microminiaturized Membrane Pumps." *Transducers '93*. 1993.
8. Zengerle, R., et al., "A Bidirectional Silicon Micropump." *Sensors and Actuators A*, 1995. *A50*: p. 81-86.
9. Koch, M., et al., "A Novel Micromachined Pump Based on Thick-Film Piezoelectric Actuation." *Sensors and Actuators A*, 1998. *70*: p. 98-103.
10. Jerman, H. "Electrically-Activated, Micromachined Diaphragm Valves." *IEEE Solid State Sensor and Actuator Workshop*. 1990.
11. Miller, R.A., et al. "Electromagnetic MEMS Scanning Mirrors for Holographic Data Storage." *Solid State Sensor and Actuator Workshop*. 1996.
12. Yanagisawa, K., H. Kuwano, and A. Tago. "An Electromagnetically Driven Microvalve." *Transducers '93*. 1993.
13. Liu, R.H., Q. Yu, and D.J. Beebe, "Fabrication and Characterization of Hydrogel-Based Microvalves." *Journal of Microelectromechanical Systems*, 2002. *11*(1): p. 45-53.
14. Choi, B.K., et al. "Electrolytic and Thermal Bubble Generation Using AC Inductive Powering." *Transducers '99*. 1999. Sendai, Japan.
15. Donald, D.K., "Thermal Optical Switches for Light." 1998, Hewlett Packard Company: US Patent 5,732,168.
16. Evans, J., D. Liepmann, and A.P. Pisano. "Planar Laminar Mixer." *MEMS '97*. 1997.
17. Lin, L., A. Pisano, and A. Lee. "Microbubble Powered Actuator." *Transducers '91*. 1991.
18. Lin, L. and A. Pisano, "Bubble Forming on a Micro Line Heater," *ASME Microechanical Sensors, Actuators, and Systems*, D. Cho, et al., Editors. 1991. p. 147-163.
19. Lin, L., "Microscale Thermal Bubble Formation: Thermophysical Phenomena and Applications." *Microscale thermophysical Engineering,* 1998. **2**: p. 71-85.
20. Beatty, C.C. "A Chronology of Thermal Ink-Jet Strucures." *Solid-State Sensor and Actuator Workshop*. 1996. Hilton Head, S.C.
21. Asai, A., "Application of the Nucleation Theory to the Design of Bubble Jet Printers." *Japanese Journal of Applied Physics*, 1989. *28*: p. 909-915.
22. Allen, R.R., J.D. Meyer, and W.R. Knight, "Thermodynamics and Hydrodynamics of Thermal Ink Jets." *Hewlett-Packard Journal,* 1985. *36*: p. 21-27.
23. Nielsen, N.J., "History of Thinkjet Printhead Development." *Hewlett-Packard Journal,* 1985. *36*: p. 4-10.
24. Evans, J.D. and D. Liepmann. "The Bubble Spring and Channel (BSAC) Valve: An Actuated, Bistable Mechanical Valve for In-Plane Fluid Control." *Transducers '99*. 1999. Sendai, Japan.
25. Papavasiliou, A.P., D. Liepmann, and A.P. Pisano. "Electrolysis-Bubble Actuated Gate Valve." *Solid-State Sensor and Actuator Workshop*. 2000.
26. Okamoto, T., T. Suzuki, and N. Yamamoto, "Microarray Fabrication with Covalent Attachment of DNA Using Bubble Jet Technology." *Nature Biotechnology*, 2000. *18:* p. 438-441.
27. Matsumoto, Y., K. Yoshida, and M. Ishida, "A Novel Deposition Technique for Fluorocarbon Films and its Applications for Bulk- and Surface-Micromachined Devices." *Sensors and Actuators A*, 1998. *66*: p. 308-314.
28. Monahan, J., A.A. Gewirth, and R.G. Nuzzo, "A Method for Filling Complex Polymeric Microfluidic Devices and Arrays." *Analytical Chemistry,* 2001.*73*: p.3193-3197.
29. Lu, H., Schmidt, M.A., Jensen, K.F., "Photochemical Reactions and On-Line Detection in Microfabricated Reactors." *Lab on a Chip*, 2001 1:p.22-28.

WAFER LEVEL ANTI-STICTION COATINGS WITH SUPERIOR THERMAL STABILITY

W. R. Ashurst, C. Carraro and R. Maboudian
Department of Chemical Engineering
University of California
201 Gilman Hall, Berkeley, CA 94720, USA
tel 510.643.3489, fax 510.642.4778
ashurbr@uclink4.berkeley.edu

W. Frey
Robert Bosch Corporation
Research and Technology Center
4009 Miranda Ave., Palo Alto, CA 94304, USA
tel 650.320.2903, fax 650.320.2999
wilhelm.frey@bosch.com

ABSTRACT

This paper describes a processing method which allows for the application of a dichlorodimethylsilane (DDMS) anti-stiction monolayer to MEMS on a wafer scale from the vapor phase. This processing method represents significant advantages over the existing liquid based coating technologies (e.g., OTS and FDTS self assembled monolayers (SAMs) [**1**]) for a variety of reasons. Earlier SAMs, especially FDTS, are susceptible to high levels of particulate contamination. Additionally, SAMs based on OTS or alkene (e.g., octadecene) chemistries suffer from low thermal stability (up to about 225°C in air)[**2**]. However, monolayers formed using DDMS have the unique combination of low particle susceptibility *and* high thermal stability (upwards of 425°C in air) [**3**]. By utilizing vapor phase (dry) processing, the problems associated with liquid processing such as scale-up, chemical and substrate handling and process control, can be overcome.

We have designed and built a reactor system that allows for the vapor phase deposition of a variety of monolayer systems on both die and wafer levels. Primarily, this system has been used to study the deposition of DDMS monolayers. First, released microstructures are introduced to the vessel. Then *in situ* cleaning of the microstructures (as well as the reactor vessel) with a down-stream water (or oxygen) plasma is performed. The reactive precursor is dosed and the surface reaction is carried out. The structures are then ready to be removed from the system and tested.

We have evaluated vapor deposited DDMS films in a number of ways. Contact angle analysis, X-ray photoelectron spectroscopy (XPS) and atomic force microscopy (AFM) have been used to characterize the film on Si(100). Film properties such as work of adhesion and coefficient of static friction were measured from coated micromachine test structures. It is shown that the DDMS monolayer deposited from the vapor phase is quite effective at reducing adhesion and friction.

INTRODUCTION

One major factor that limits the widespread use and reliability of microelectromechanical systems (MEMS) is adhesion [**4**]. Adhesion is a result of the dominance of surface forces, such as capillary, hydrogen bonding, electrostatic, or van der Waals, over body forces at the micro-scale. When internal restoring forces of microstructures cannot overcome surface adhesive forces, the devices are said to suffer from stiction. Stiction, which can involve both adhesion and friction, can be categorized into two types. The first type, termed release stiction, results from the method used to release the microdevice from the sacrificial layers needed during fabrication. In this case, structures released in liquid etchants, and subsequently oxidized, are dried in such a way that liquid capillary forces, due to the hydrophilic nature of the oxidized surface, are sufficient to draw compliant microstructure surfaces into contact. Once this occurs, the high energy hydrophilic surfaces remain adhered if the microdevice cannot generate enough restoring force to overcome the adhesion. The second type of stiction, called in-use stiction, refers to adhesion that occurrs after the release stage, such as when the device is in operation, in storage or improperly handled. As we shall see, it is the in-use stiction that poses the greatest threat to MEMS reliability.

Engineering solutions to the problem of release stiction, reviewed elsewhere [**5,6**], include novel processing techniques such as critical point drying (CPD), freeze sublimation drying and vapor phase etching of sacrificial layers. Other approaches include surface modification techniques such as roughening the structure surfaces to reduce the contact area and changing the water meniscus shape by surface modification.

While the above techniques can be quite effective at the elimination of release stiction, they generally do not prevent in-use stiction. In-use stiction can be quantified by determining the work of adhesion, employing the cantilever beam array (CBA) technique [**7**]. Approaches to reduce in-use stiction fall under two categories, physical and chemical modifications of surfaces [**5,6**]. In the physical approach, the surfaces are roughened to reduce the effective contact areas [**8**]. With this approach, a factor of 20 reduction in apparent surface tension of the roughened polysilicon is reported.

Various types of chemical modifications have been explored as possible anti-stiction treatments, and have been reviewed elsewhere [**6**]. It is well known that the application of hydrocarbon or fluorocarbon chlorosilane-based SAMs can greatly improve the adhesion properties of micromechanical surfaces. Although these monolayer systems provide many favorable characteristics, they also possess qualities that limit their applicability. Such qualities can be grouped into two types, those that arise due to the chemistry involved, and those that are due to the solution based SAM formation processes. Although chemistry related limitations can be significant, the issues related to the SAM deposition *process* are what generally limit the widespread application of the SAMs as anti-stiction methods in industry [**6**]. One limitation is that the coating process is cumbersome because the SAM solution must be freshly made and appropriately conditioned immediately before each coating. This is due to the sensitivity of the SAM solution to ambient humidity, and the ability of the SAM precursors to polymerize. Another difficulty related to the coating process is one of "portability." The large number of process variables, varying expertise and care of operators, as well as the lack of standardized wafer level coating equipment make the success rate of SAM coating processes vary considerably from run to run and laboratory to laboratory. Perhaps the greatest limitation is that of scaling up the process from single dies to whole wafers and eventually multi-wafer cassettes. Much of the work up to this stage has consisted of releasing dies 1×1 cm^2. Scaling up the release and coating process to full-wafer level and eventually to multi-wafer cassettes poses substantial engineering challenges.

Recent developments in the chlorosilane-based monolayer technology address some of these issues by performing the coating process in the vapor phase. Vapor phase processing eliminates the use of organic solvents and greatly simplifies handling of the samples. Moreover, the stoichiometry of the precursor molecules can be more precisely controlled. It has been demonstrated that monolayer films that are produced from the precursor tridecafluoro-1,1,2,2-

Travel support has been generously provided by the Transducers Research Foundation and by the DARPA MEMS and DARPA BioFlips programs.

0-9640024-4-2/hh2002/$20©2002TRF
DOI 10.31438/trf.hh2002.36

tetrahydrooctyltrichlorosilane ($CF_3(CF_2)_5(CH_2)_2SiCl_3$, FOTS) in a low-pressure CVD style reactor exhibit low adhesion energies [**9,10**]. Additionally, *in-situ* plasma cleaning of the sample as well as *in-situ* measurement of the film growth provide excellent process uniformity, reproducibility and monitoring capability [**10**].

The dimethyldichlorosilane ($(CH_3)_2SiCl_2$, DDMS) monolayer has also been proposed as a promising anti-stiction surface coating for MEMS. Recently, it was found that the DDMS monolayer was quite effective at reducing friction and adhesion, although not quite as effective as OTS [**3,11**]. This precursor has several other properties that make it an attractive candidate for vapor phase processing. The DDMS precursor has a lower tendency to polymerize, it has a vapor pressure at room temperature that is much greater than any other chlorosilane precursor used in anti-stiction processes, and for every DDMS molecule that gets hydrolyzed, only two molecules of HCl will result, as opposed to three from OTS or FDTS. Perhaps the most compelling distinction that DDMS has over OTS is that it has a much greater thermal stability in an oxidizing ambient. In fact, the DDMS films can withstand upwards of 400°C whereas OTS films begin to degrade at about 225°C.

The goal of this work is to develop a dry process which allows for the deposition of an anti-stiction monolayer at the wafer level. The monolayer must survive other post processing steps, such as packaging, and not impede such processes. The coating process must be one that can easily be adapted to industrial settings, have the potential for automatic control, and satisfy uniformity constraints. To accomplish this goals, and in light of the facts above, we turn our attention to the DDMS precursor deposited from vapor phase and build a process around these constraints.

EXPERIMENTAL

The deposition system consists of a mechanical pump (base pressure $\sim 2\times10^{-3}$ torr) connected to a glass-based reaction chamber, which is connected to a reactant delivery subsystem. The chamber is constructed out of glass (or quartz) so that it is easy to modify and clean, and is rather inexpensive. This is a significant departure from earlier efforts. A convectron pressure gauge and thermocouple are used to measure process parameters. Currently, we have designed and constructed two interchangeable custom chambers for this work. The smaller chamber, which measures about 2 inches in diameter, is useful for coating a few dies at the time, while the larger chamber is used for coating a whole 6 in. wafer. The chambers are equipped with perforated electrodes that can be biased to create an *in situ* DC plasma. The liquid reactants (in this case deionized water, 18 MΩ-cm and DDMS, Gelest 99+%) are loaded into small glass tubes connected by valves to the chamber. A simplified schematic of this system is shown in Fig. 1 and a photograph of the large reactor is shown in Fig. 2. The reactants are degassed before use with three or more freeze–pump–thaw cycles. Results presented in this paper are from samples prepared in both chambers, and we find that the film quality does not depend on the chamber used.

The Si(100) samples are rinsed in acetone and then cleaned by exposure to ultraviolet light and ozone (UVO) for 15 minutes. Then the samples are treated with concentrated HF for 10 minutes and UVO cleaned again before introduction to the vapor deposition chamber. Micromachine samples are released by etching for 90 minutes in a 1:1 (v/v) mixture of concentrated HF and HCl. The etchant mixture is rinsed away using a funnel aparatus described elsewhere [**1**] with deionized water until the pH of the effluent was 7. The water is similarly displaced with isopropanol (IPA). The structures are transported in IPA and dried in a Tousimis Autosamdri 815-B CPD system. The dried micromachine test structures are then introduced to the deposition chamber.

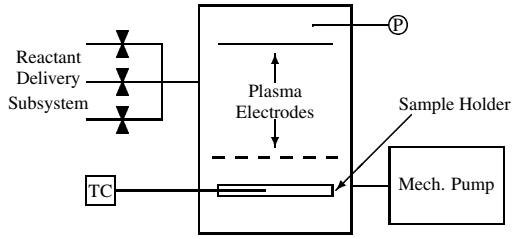

Figure 1. *The basic diagram for the vapor-phase anti-stiction film deposition reactor. The sample rests on an aluminum sample holder, and can be heated from below. The plasma electrodes (upper solid, lower perforated) allow for the in situ cleaning of the structures. (P = pressure gauge, TC = thermocouple)*

Figure 2. *A photograph of the large reactor system.*

The samples are placed into the chamber on a large aluminum sample holder that is placed underneath the lower (ground) perforated electrode. The aluminum stage is fitted with a thermocouple near the surface so that temperature can be monitored. Once inside the chamber, micromachine and Si(100) samples are treated identically, as follows. First, the system is evacuated to a pressure of less than 10 mtorr. Then the samples are cleaned of any organic contamination that usually results from the CPD process by *in situ* plasma cleaning. This is accomplished by first creating a background of oxygen (O_2) gas in the chamber by performing purge–pump cycles with O_2. Then, O_2 is admitted into the chamber so that the pressure of O_2 is about 300 mtorr. Next, a downstream plasma is struck by applying a DC bias (about -700V) to the top electrode while the bottom electrode is held at ground. It is very important that micromechanical structures are not placed inside the plasma discharge—they must be placed downstream of the plasma to avoid detrimental side effects such as curling of structural layers. While the O_2 plasma is on, water gas is dosed into the chamber (about 500 mtorr) which, over time, effectively displaces the O_2. Exposure of silicon to a water plasma is known to leave the surfaces hydroxyl (-OH) terminated [**12**]. The entire plasma treatment takes about 15 minutes, after which the samples are ready for surface reaction.

The surface reaction is carried out by first dosing the water. Water gas is admitted to the chamber until the pressure is in excess of 5 torr. Then the chamber is evacuated down to the desired pressure of water, between 1 to 1.3 torr, and isolated from the pump. Next, the DDMS precursor is dosed to the chamber until the total pressure is in the range of 2.5 to 3 torr. The reaction is carried out for 10 to 15 minutes, after which time the chamber is pumped out and vented with nitrogen. The samples are removed and ready for testing.

Static contact angle data are taken with DI water (resistivity

18 MΩ-cm) and spectroscopic grade hexadecane (Aldrich Chemical Co.) according to the sessile droplet method with a Ramé Hart 100 A goniometer. A Digital Instruments Nanoscope III atomic force microscope is used in tapping mode to image the surfaces. All micromachine actuation is done under normal laboratory ambient conditions, 20°C and 40% relative humidity.

Adhesion tests are carried out using the cantilever beam array method described elsewhere [**7**]. Some of the test structures used for adhesion measurements are treated in the large reactor, placed about the chamber so that the spacing would resemble a 6 in. wafer. Coeficient of static friction tests are carried out on sidewall friction testers, coated in the smaller reactor. The details regarding the fabrication and actuation of these devices can be found elsewhere [**3**]. All liquid phase samples were prepared according to the methods outlined in Ref. [**3**].

To test the performance of the coating after packaging, some 6 in. wafers containing test devices are processed. The 6 in. silicon cap wafer has structured cavities and bond frames. A low temperature melting seal glass paste is screen printed onto the bond frames, followed by drying and prebaking. Alignment of cap and sensor wafer followed by heating to 430°C under 1000 N bonding force for a couple of minutes leads to hermetic sealing with enclosed application specific pressure adjustable from <5 torr through >1000 torr.

RESULTS AND DISCUSSION

In order to test the deposition system and to find the correct process conditions, Si(100) samples were treated under varying process conditions and examined by contact angle. In the experimental setup described previously, the process variables that could be independently manipulated were substrate temperature, partial pressure of water and DDMS, and time. Early experimentation showed that increasing substrate temperature (over the range of 20°C to 50°C), all other parameters being equal, resulted in films that had decreasing water contact angle. It is speculated that this effect is due to a decrease in the adsorption of DDMS and/or water at the reactive surface at higher temperatures. The main result of such temperature experiments is that there is no need to heat the sample.

Other preliminary experiments included process sequences where the reactive precursors were dosed to a given set of partial pressures, evacuated, then dosed again to the same set of partial pressures. It was found that there was virtually no effect of the number of dosing cycles on the contact angle so long as the total time for reaction was the same. In other words, four 2.5 minutes doses are *equivalent* to a single 10 minute dose. This implies that there is not a substantial amount of depletion of the reactive precursors as the reaction proceeds. Depletion of the reactive precursor was a concern, since the surfaces of the glass reactor (and most of the internal components) are also coated by the DDMS, and thus represent a parasitic loss of reactive precursor.

Through other sets of experimentation, it was found that there were optimum conditions for this process. Various early experiments showed that increasing the pressure of the precursor and water resulted in films with higher contact angles. Also increasing the reaction time resulted in films with higher contact angles. However, the partial pressures and time cannot be increased without bound, as an unfortunate side reaction can occur. The DDMS and water can react to produce a type of viscous liquid, presumably a silicone oil. This liquid can therefore be deposited in a very thin and uniform manner, and cannot be seen on Si(100) test chips. This thin liquid film has a water contact angle of about 104° to 106°. If cantilever beams are treated under conditions which generate this liquid, severe adhesion results upon actuation. Indeed, the work of adhesion for beams coated with this liquid is so much greater than that of oxide coated beams that it could not be accurately determined. After peeling up the beams with a probe tip, small patches of a liquid-like substance were found underneath the structures. It therefore became clear that the process window in which a high quality film with no residue could be produced was fairly small, and that a set of optimization experiments were needed. Hence, through a series of such experiments, the parameters described in the experimental section were found to give the best results on Si(100) and micromachines.

Once suitable deposition conditions were found, coating of microstructures was carried out. Early experimentation with cantilever beam arrays yielded inconsistent results. These inconsistencies were traced to the CPD step. It was found that clean oxide samples (water contact angle ∼0°) which entered the CPD aparatus had a water contact angle of anywhere between 50°and 80°after the drying process, indicating that some contamination had occurred. Also, cantilever beams which entered the CPD aparatus with oxide surfaces emerged with varying adhesion properties which were not oxide-like. With this observation, it was clear that a post drying cleaning step was needed. Keeping in mind the requirements for dry and conformal processing, the plasma cleaning step described in the previous section was chosen and implemented. After treatment of the contaminated samples, the water contact angle was again near 0°, and cantilever beams showed oxide-like adhesion behavior. An additional benefit to the plasma cleaning step is that the reactor walls, and other surfaces, are cleaned of any residue from previous coating runs.

With proper and repeatable deposition methods in place, determination of the film properties began. Water contact angle results on treated Si(100) can be found in Table 1. The data show that the DDMS films produced either by solution methods or vapor methods are similar in wetability. XPS shows no difference in the chemical make-up of films deposited from solution versus vapor methods. AFM, however, reveals an important difference between the two methods. Figure 3 shows AFM images of solution and vapor deposited DDMS films on Si(100). It is interesting to note the substantial reduction in particles present on the vapor processed sample with respect to the solution processed sample.

Coating	θ_{H_2O}	θ_{HD}	l_d (μm)	$\mathcal{W}$ (μJ/m^2)
DDMS vapor	102°	38°	510	62
DDMS liquid	103°	38°	550	45
OTS	110°	38°	750	12
Oxide	0–30°	0–20°	<150	20,000

Table 1. *Selected properties of the DDMS monolayer deposited from vapor phase versus liquid phase. OTS and oxide values are given for comparison. Property data are water contact angle, hexadecane contact angle, detachment length, apparent work of adhesion, and coeficient of static friction (sidewall), respectively.*

The large size reactor was used to determine the uniformity of the deposition process. A bare 6 in. Si(100) wafer was placed in the reactor and treated (using optimum conditions) with DDMS. The wafer was cleaved through the center and contact angle measurements were performed on a cross wafer strip. Of 18 uniformly spaced measurements, the variation in water contact angle across the 6 in. strip was much less than 1°. This was an encouraging result, since it means that scaling the process to accomodate larger samples is a simple matter of creating a larger reaction chamber.

Some 6 in. processed wafers were also coated. Due to the uni-

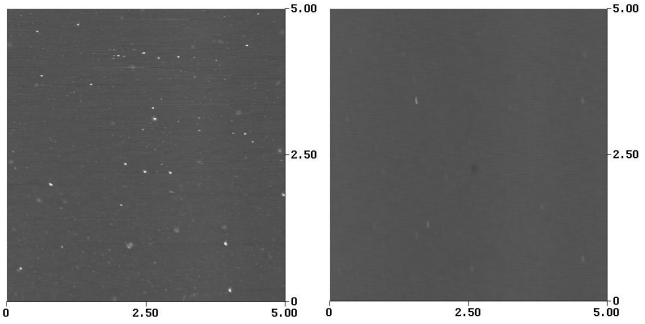

Figure 3. *AFM images (5 × 5 μm) of liquid processed (left) and vapor processed (right) DDMS films on Si(100). The particles evident on the liquid processeed sample are not present on the vapor processed sample. The z-range (10 nm) is the same for both scans.*

form coating of the entire wafer, the bonding frames were coated as well. X-ray inspection of bonded wafers show uniform bonding interfaces. A standard process characterization, including leak testing, was performed and showed that the coated wafer exhibited no significant deviation from uncoated wafers. This hermetic bonding through the SAM layer indicates that the monolayer on the bond frame is removed via the lead oxide content of the seal glass. Preliminary stiction behavior characterizations of the packaged test structures qualitatively show substantial reduction in sticking probability. Quantitative statistical characterization is currently underway.

In CBA structures, all beams were found to be free standing after the CPD and DDMS vapor coating process. After actuation, beams of length 450 μm or less were consistently free standing, and the detachment length for our test structures, averaged over 20 arrays, was found to be 510 μm. Using a calculation based on detachment length and other physical parameters [**3**], the apparent work of adhesion is found to be about 62 μJ/m^2. This value compares well (although slightly higher) with the apparent work of adhesion found for the solution deposited film. Both studies used test structures of the same design from the same wafer, and were actuated in the same manner. In another experiment, several chips containing CBAs were placed at different locations in the large reactor and processed to simulate the full wafer properties. After testing the CBA structures, it was found that the variation of the apparent work of adhesion was no more than that which is present across liquid coated samples.

Sidewall friction testers [**3**] were used to quantify the coefficient of static friction of the DDMS films. The coated devices were tested, and an average value of 0.35 was found. This value is slightly higher than that for the solution deposited film, but is consistent with the vapor deposited film having lower water conatact angle and higher apparent work of adhesion. Unlike the CBA results, however, the coefficient of static friction showed marked variation from sample to sample, with extremum values at approximately 0.3 to 1.5 times the mean. This was not expected, since all other measurements showed remarkable uniformity. Currently, the reason for this variation is under study.

CONCLUSIONS AND FUTURE WORK

Based upon the data presented here, a viable vapor phase method for the deposition of the DDMS anti-stiction film has been delveloped. The adhesion and friction properties determined for the vapor phase deposited film are found to be similar to those determined for solution deposited films. However, AFM confirms that fewer particles are generated during the dry coating process than the solution based coating process. Moreover, the scaling issues associated with solution based SAMs are avoided when dealing with dry processes. Also, uniformity tests confirm the process to be quite uniform over an area comparable to a 6 in. wafer. Further plans for the vapor deposition system include investigations on other monolayer systems.

ACKNOWLEDGEMENTS

The authors wish to thank the NSF (grant DMII-0099765) and Robert Bosch Corporation via the UC-SMART program for project funding. The authors also wish to thank Sandia National Labs for providing test structures. Additional financial support from the National Science Foundation in the form of a graduate fellowship (WRA) is gratefully acknowledged.

REFERENCES

1. R. Maboudian, W. R. Ashurst, and C. Carraro, "Self-assembled monolayers as anti-stiction coating for mems: Characteristics and recent progress," *Sensors and Actuators A*, vol. 82, pp. 219–223 (2000).

2. W. R. Ashurst, *et al*., "Alkene based monolayer films as anti-stiction coatings for polysilicon MEMS," *Technical Digest, Proceedings of the 2000 Solid-State Sensor and Actuator Workshop, Hilton Head*, pp. 320–323 (2000).

3. W. R. Ashurst, *et al*., "Dichlorodimethylsilane as an anti-stiction monolayer for MEMS: A comparison to the octadecyltrichlorosilane self assembled monolayer," *Journal of Microelectromechanical Systems*, vol. 10, no. 1, pp. 41–49 (2001).

4. R. Maboudian and R. T. Howe, "Critical review: Adhesion in surface micromechanical structures," *J. Vac. Sci. Technol. B*, vol. 15, pp. 1–20 (1997).

5. R. Maboudian, "Surface processes in MEMS technology," *Surface Science Reports*, vol. 30, pp. 207–269 (1998).

6. R. Maboudian, W. R. Ashurst, and C. Carraro, "Tribological challenges in micromechanical systems," *Tribology Letters*, vol. 12, no. 2, pp. 95–100 (2002).

7. C. H. Mastrangelo, "Adhesion-related failure mechanisms in micromechanical devices," *Tribology Letters*, vol. 3, no. 3, pp. 223–238 (1997).

8. K. Komvopoulos, "Surface engineering and microtribology for microelectromechanical systems," *Wear*, vol. 200, pp. 305–327 (1996).

9. J. Sakata, *et al*., "Anti-stiction silanization coating to silicon microstructures by a vapor deposition process," *Transducers '99* (1999).

10. T. M. Mayer, *et al*., "Chemical vapor deposition of fluoroalkylsilane monolayer films for adhesion control in microelectromechanical systems," *Journal of Vacuum Science and Technology B*, vol. 18, pp. 2433–2440 (2000).

11. B. H. Kim, *et al*., "A new organic modifier for anti-stiction," *Journal of Microelectromechaincal Systems*, vol. 10, pp. 33–40 (2001).

12. P. R. McCurdy, *et al*., "A modified molecular beam instrument for the imaging of radicals interacting with surfaces during plasma processing," *Review of Scientific Instruments*, vol. 68, no. 4, pp. 1684–1693 (1997).

JPL's MEMS Gyroscope Fabrication, 8-Electrode Tuning, and Performance Results

Sam Y. Bae, Ken J. Hayworth, Kirill V. Shcheglov, Karl Y. Yee, and Dean V. Wiberg.
Jet Propulsion Laboratory
Pasadena, CA 91109
http://mems.jpl.nasa.gov

ABSTRACT

In this paper, we present JPL's 8-electrode MEMS gyroscope, which allows for full electrostatic tuning of the resonant structure. It has shown a sufficient electrostatic tuning range needed to fully correct the native frequency mismatches of our current fabrication process. Test data shows that this gyroscope design has Q's averaging 30,000 (measured via ring-down time method) and native frequency mismatch on the order of 0.4%. The electrostatic tuning of the mismatched frequencies has successfully demonstrated 0.02% matching for the test batch and down to 0.003% (10mHz at 3000Hz) repeatable frequency matching during specific tuning experiments. As a result, we can report angle random walk (ARW) value of 0.1deg/rthr and 2°/hr bias instability (Allan variance 1/f floor estimated). A third party, Honeywell Inc., tested one of the earlier designed 4-electrode gyroscopes, which achieved frequency degeneracy through a mechanical ion-milling of the springs, and reported 1°/hr bias instability.

INTRODUCTION

The Jet Propulsion Laboratory (JPL) has an ongoing effort to develop a silicon based miniaturized vibratory gyroscope for space navigation applications. Manufacturing of the gyroscope follows established standard technologies used in the silicon batch fabrications of MEMS devices, permitting the gyroscope to be batch-produced, thereby available to a larger market at lower cost. At the same time, the JPL gyroscope has incorporated features designed to stretch its performance to a navigation-qualified sensor as described in previous publications. [1, 2]

Figure 1 is a SEM photo of a JPL MEMS gyroscope. Figure 2 delineates its components.

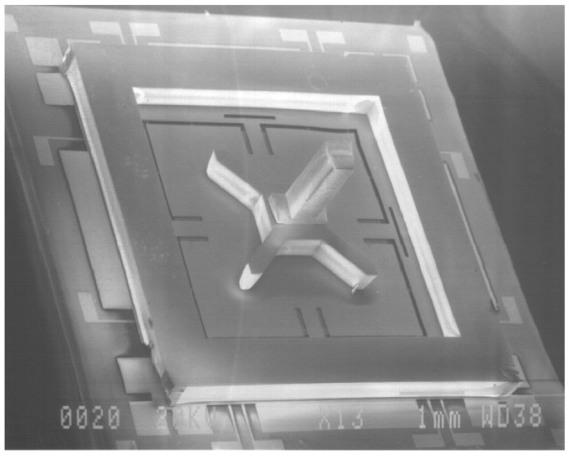

Figure 1. (Left) An SEM photo of a fabricated JPL MEMS gyroscope

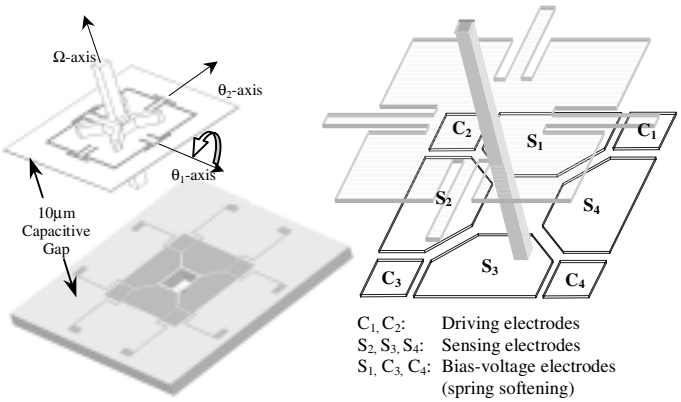

Figure 2. (Left) A sketch of JPL MEMS gyroscope's cloverleaf (top) and electrode-plate (bottom) **(Right)** 8-Electrode layout. 4-petal membrane drawn semi-transparently on top of the electrodes.

A gyroscope consists of three parts: 1) a two degree-of-freedom 4-petal clover membrane, suspended by two-fold symmetric 4 T-springs at each mid-edge, 2) a post, the main inertial element, runs perpendicular to θ_1-θ_2 plane (hereon we call the first two components the "cloverleaf"), 3) 8-electrode plates that drive and sense the capacitive changes of the cloverleaf's membrane (hereon call the "electrode-plate"). The total dimensions of the assembled MEMS gyroscope are 9 x 9 x 6mm.

The 4-petal clover membrane 2 degrees-of-freedom which exhibit two closely matched natural modes. These have the shape of plate rocking modes. While a positive voltage is applied to the cloverleaf, Electrodes C_1 and C_2 (Figure 2 right) drive the cloverleaf's 4-petal membrane sinusoidally with respect to the θ_1-axis to one of the rocking modes (this is the "drive-mode"). When the gyroscope rotates around the Ω-axis, the energy in the drive-mode is transferred to the other rocking mode, the "sense-mode," inducing a skew motion with respect to the θ_2-axis. Then, the Electrodes S_2, S_3, and S_4 pick up the capacitive changes, and attached transimpedance amplifiers convert this varying capacitance into a voltage. Finally, the sense signal is demodulated by multiplying with the drive signal; the demodulated signal produces a baseband signal proportional to the inertial rate of the gyroscope in the direction of the Ω-axis. In practice, an automatic gain control (AGC) loop tracks the natural frequency of the gyroscope, and a force rebalance (FRB) loop damps the transient energy transferred to the sense-mode, ensuring fast and stable rate response of the overall signal. The rest of the electrodes, C_3, C_4, and S_1, are used for electrostatic tuning; properly biasing the three with respect to the resonator causes the unmatched frequencies to become closely matched and aligned to the preferred modal axis by softening the 4 T-springs. (See

0-9640024-4-2/hh2002/$20©2002TRF
DOI 10.31438/trf.hh2002.37

Electrostatic Tuning Section) In the perfect case, the rocking modes have two equal frequencies (i.e. degenerate, $f_1 = f_2$) and only Q and electronic noise would limit the performance. Note in many other gyroscope designs, the springs are either trimmed or ablated mechanically through a laser or ion-etcher to achieve modal degeneracy; however, the JPL gyroscope's 10µm gap and large electrode area allow simple electrostatic tuning to replace the mechanical tuning of gyroscopes.

FABRICATIONS

Electrode-plate fabrication starts with a 500µm thick, 100mm diameter, (100) oriented, double side polished, resistance as low as 10Ω-cm and P-type doped wafer. Cloverleaf fabrication start with a 26micron thin SOI, 500µm thick, 100mm diameter, double side polished, resistant as low as 10Ω-cm wafers and p-type doped wafer.

Table 1. Cross-sections of the JPL MEMS gyroscope fabrications.

Electrode-plate	Cloverleaf
a. 8micron Pillar Etch	**a.** Bottom side metalization (Bias- voltage contacts and bond-metal)
b. 4micron Oxide Growth. Electrical insulation from the base.	**b.** Bottom side STS-etch
c. Oxide Openings (Indicated with arrows)	**c.** Topside STS through etched. 4 cloverleaf and springs release)
d. Bottom side Metalization (Bond-metal)	**d.** SOI Insulation layer etched
e. Top side Metalization (Electrodes and Bond-metal)	
f. STS Through Etch	Cloverleaf and electrode-plate bonded and post inserted

PERFORMANCE TUNING

The performance of a vibratory gyroscope depends crucially on the physical properties of the resonant structure. In our case, the gyroscope performs optimally when 1) the 4-petal membrane has low dampening (high Qs), 2) the two rocking modes are closely matched in frequency, and 3) the first two properties are stable over both time and temperature [3].

To achieve high Q's, we chose a ceramic substrate mount (Figure 3) that provides a relatively large mass for stable and rigid mounting and tested in a low vacuum environment ($<10^{-3}$Torr). Operation in vacuum is required because this type of large electrode area, a thin gap resonator is highly damped by squeeze film dampening in air. A rigid mounting to the package was required since the JPL gyroscope's cloverleaf was not balanced in its rocking modes unlike balanced tuning fork gyro designs. In other words, a fraction of the energy of a rocking mode contained in the package was subject to varying loses to the environment. The current substrate helped resolve this problem by brut force, the ratio of energies being proportional to the ratio of resonator mass to package mass. As a result, we attained Qs as high as 76,000. The Qs were measured by noting the ring down time of an un-driven mode with no electronics attached.

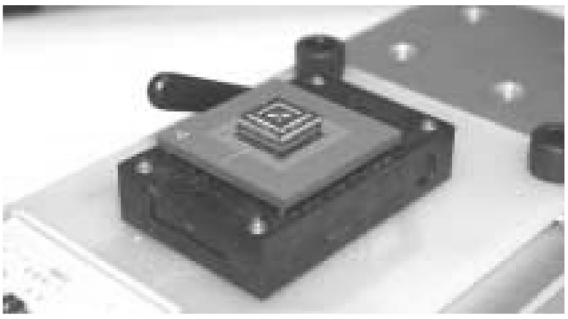

Figure 3. JPL MEMS Gyroscope mounted on a ceramic substrate then on zero-insertion-force socket (standard quad package).

ELECTROSTATIC TUNING

Like all other Coriolis force based gyroscopes, when the gyroscope is first assembled, imperfections in fabrications result in mismatched frequencies. (See Table 2 for statistics) The mismatched frequency was mainly due to uneven stresses received from a thermal compression bonding. The top of figure 4 shows a gyroscope having an 18.75Hz frequency split, a 0.6% mismatch, and would have resulted in poor gyroscope performance or not even operating control loops. The bottom of figure 4 shows the same gyroscope after DC voltages had been placed on the Electrodes C_3, C_4, and S_1. The modes were then split only by 200mHz. (Later, we had gone further narrowing the splits to zero.) This condition is called modal degeneracy. At this state, the resonator behaves like a Foucault pendulum with no preferred rocking directions, and this gives maximum sensitivity of the device.

The gyroscope's resonator can be modeled as a 2 degree-of-freedom torsional oscillator. Its rocking-mode is characterized by inertia, dampening, and stiffness matrices. The asymmetries in the inertia and stiffness matrices determine the frequency mismatch. The electrostatic tuning is based on the non-linear force equation applied in a biased capacitor. Applying this principle, we were then able to soften the springs of the resonator utilizing an ideal proportional feedback loop. Using a minimum of two bias electrodes, we aligned the stiffness matrix with the inertia matrix's asymmetries, thereby giving rise to the degenerate modes. We derived a set of tuning equations using a redundant set of 4 bias electrodes. We then implemented these non-linear equations to create three virtual "tuning knobs," using a DSP program. These "knobs" separate the tuning process into three parts: knob#1) alignment of modes, knob#2) setting of frequency f1, knob#3) setting of frequency f2. Each of these steps is completely separate from the others and can thus be automated into control loops. Tuning of a gyroscope is thus accomplished by driving the

resonator in a particular direction and tweaking Knob#1 until only one natural mode is excited, as known as "quadrature nulling." The drive loop is now locked onto driving only a single mode with frequency f1. Knob#2 is now tweaked to set f1 to a desired target frequency. Finally, the drive control loop is switched to driving the orthogonal rocking direction, locking onto that mode at frequency f2. Knob#3 is now tweaked to set f2 also to the target frequency. Because knob #1,#2 and #3 are implemented to simultaneously change voltages on all 4 bias pads using the non-linear tuning equations, they ensure that the tweaking of knob#3 only affects f2 and does not disturb f1 or modal alignment.

This technique was not fully developed at the time of testing the 7 gyroscopes in Table 2, which is why they have tuned frequencies listed that are still relatively large. We now run all our gyroscope with tuned splits in the range of 10mHz and are developing algorithms that will continuously tune our gyroscope during operation using the virtual "tuning knobs" described above. This will eventually allow for automatic frequency tuning compensating for time and temperature effects.

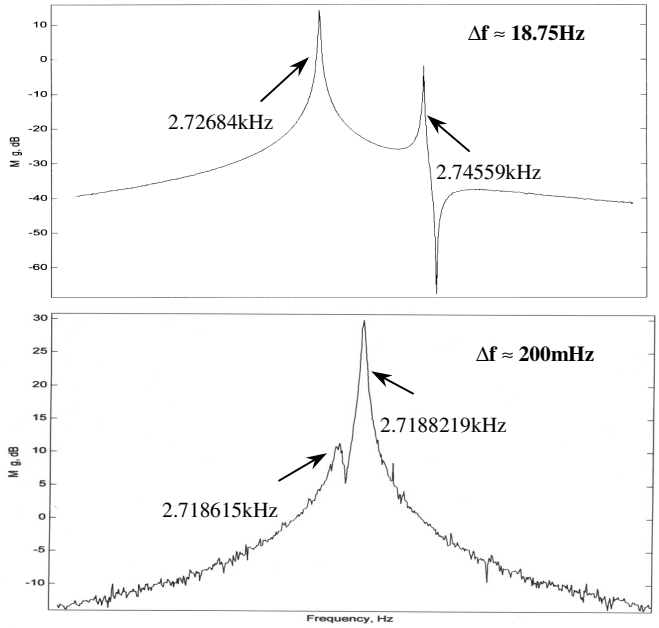

Figure 4. Micro-gyroscope #8.
(Top) Native frequency split at rocking mode, Δf ≈ 18.75Hz
(Bottom) After applying electrostatic bias voltages on 3 of the 8 electrodes, Δf ≈ 200mHz

RESULTS

As shown in Table 2, we tested 7 gyroscopes in house. The measured bias instability performance for each is given in the table. Rate table testing statistics for one gyrocope (gyroscope #8) is shown in Figure 5. These include a rate linearity and repeatability test over the ±1°/sec range, a plot of rate bias and rate drift over a 10 minute period, and a standard gyroscope Green chart analyzing this 10 minutes of drift data for its standard deviation statistics at various integration times. The bias instability figure is approximated as the minimum on this graph and the ARW as 1/60 the value of the initial –1/2 slope line at 1 second integration time. Statistics for this particular gyroscope are 2°/hr bias instability and 0.1deg/rthr ARW.

Table 2. Test results of the 7 JPL MEMS Gyroscopes

Gyro	Q (high)	Q (low)	Unmatched Native Frequency	Tuned frequency (Δf= f1-f2)	Performance °/hr.
5	32,000	4,700	8.30	1.0	5
6	19,000	9,300	8.50	1.0	2.0
8	76,000	42,000	18.8	0.20	2.0
9	30,000	12,000	10.6	0.50	25
13	48,000	29,000	8.00	0.50	6.0
14	19,000	17,000	12.0	0.26	10
18	60,000	54,000	11.0	0.50	2.0
avg.	41,000	24,000	11.0	0.57	10

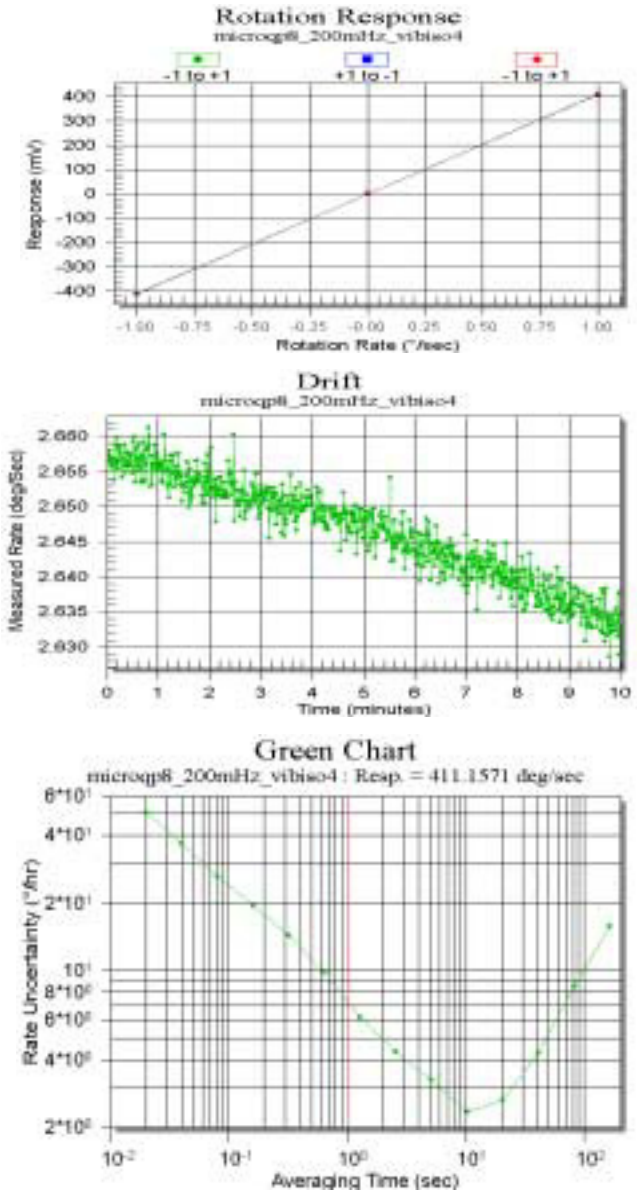

Figure 5. MEMS gyroscope #8 (Top) Rotation response **(Middle)** Drift data **(Bottom)** Green chart;

Figure 6 shows a Green Chart measured by a third party test of one of our gyro designs. Honeywell Inc. tested a 4-electrode gyroscope, not having extra biasing electrodes seen in 8-electrode gyroscope, and reported bias instability (flicker floor estimate) of 1°/hr.

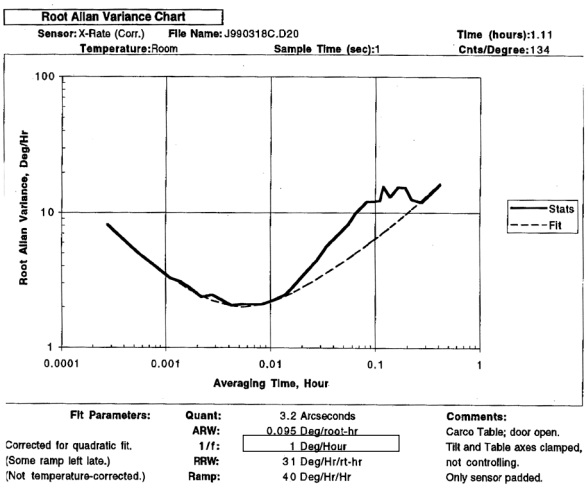

Figure 6. Honeywell Inc. tested a JPL micro-gyroscope, reported bias instability (1/f floor fit) of 1degree/hour (boxed)

CONCLUSIONS

Several unique attributes of the JPL gyroscope design account for its high performance marks. First, it is manufactured using a bulk silicon process with relatively large dimensions giving it high relative manufacturing precision. This also means the resonator (minus the post) is made of a single piece of high Q silicon. Second, the resonator wafer is wafer bonded to the electrode wafer giving a thin, repeatable 10um capacitive gap with large surface area for sensing, driving, and electrostatic tuning of the resonator. Third, the symmetric electrode design and large electrostatic tuning range in the device, combined with the native precision above, allows for tuning to modal degeneracy in a majority of devices in a wafer. Fourth, the large inertial mass of the vertical post provides strong Coriolis coupling between these degenerate modes. These combined attributes have lead to a sensitive rate sensor.

ACKNOWLEDGEMENT

Funding for this work was provided by the Jet Propulsion Laboratory, Center for Integrated Space Microsystems and The National Aeronautics and Space Administration (NASA) Code R, UPN 755.

The JPL MEMS Team would like to thank Mr. Dorian Challoner for his full support during this project and valuable comments reflecting his in-depth knowledge of the subject.

[1] T. K. Tang, R. C. Gutierrez, J. Wilcox, C. Stell, V. Vorperian, R. Calvet. W. Li, I. Charkaborty, R. Bartman, W. Kaiser, "Silicon Bulk Micromachined Vibratory Gyroscope", Tech Digest, Solid-State Sensor and Actuator Workshop, Hilton Head, S. C. pp. 288-293, June 1996

[2] T. K Tang, R. C Gutierrez, C. B. Stell, V. Vorperian, G. A. Arakaki, J. T. Rice, W. J. Li, I. Chakrabory, K. Shcheglov, J. Z. Wilcox, W. J. Kaiser, "A packaged silicon MEMS vibratory gyroscope for microspacecraft", in *Proc. IEEE Micro Electro Mechanical Systems Workshop (MEMS '97)*, Japan, 1997, pp. 500-505

[3] K. Shcheglov, C. Evans, R. Gutierrez, T. K. Tang, "Temperature dependent characteristics of the JPL silicon MEMS gyroscope", *in Proc. IEEE Aerospace Conference 2000,* Volume 1, pp. 403-411,

LIQUID PHASE CONSTRUCTION OF MICROSTRUCTURES

Joseph M. Bauer[1,3], Taher A. Saif[2], and David J. Beebe[3]
[1]Theoretical and Applied Mechanics Department
University of Illinois at Urbana-Champaign
Urbana, IL 61801
[2]Department of Mechanical and Industrial Engineering
University of Illinois at Urbana-Champaign
Urbana, IL 61801
[3]Biomedical Engineering Department
University of Wisconsin-Madison
Madison, WI 53706

ABSTRACT

The controlled formation of curved, three-dimensional microstructures can be accomplished through solidification from a liquid phase. As a demonstration, we have placed objects in contact with the interface of a photopolymerizable liquid and air to create various liquid menisci that were subsequently solidified with ultraviolet radiation. Geometric control is achieved through variation of physical and environmental parameters; for example, solidified menisci formed at 25°C were 300μm taller than those formed at 7°C. Comparisons between the polymerized structures and theoretical predictions for liquid menisci indicate that the polymerization process results in repeatable changes in contact angle and meniscus size.

INTRODUCTION

The creation of microscale structures using methods borrowed from the integrated circuit industry has led to the development of Micro Electrical Mechanical Systems (MEMS)**[1, 2]**. These methods are largely limited to the creation of two-dimensional or pseudo three-dimensional (orthogonal) structures**[3, 4]**. Unfortunately, methods to construct non-orthogonal shapes (smooth curves, etc.) at the microscale are limited. Curved microstructures are desirable, as they would have different mechanical responses to loading and different fluid flow patterns around them as compared to orthogonal structures. In this paper, we demonstrate a liquid phase construction process that allows for the rapid construction of smooth three-dimensional microstructure geometries.

Our process is based on the interactions between solids, liquids, and gases that give rise to smooth curves. For example, if a solid is brought into contact with a gas/liquid interface such as air and water, and then moved either into the liquid or pulled away from the liquid surface, the interface will form a smooth, curved shape (Figure 1). The interface between two immiscible liquids of different density will react in a similar way. Both hydrophilic and hydrophobic objects can be positioned at relative heights with respect to the interface, simultaneously forming multiple structures of varying complexity. If the liquid is solidified in this configuration, the result is a solid three-dimensional structure with curved features.

Although the solidification of the liquid will cause the solid objects to adhere to the solid three-dimensional structures, removal of the solid objects is possible through various schemes. For example, the solidification could be partially completed, the object removed, and the solidification completed or the solid object could be constructed from a sacrificial material that would be dissolved after the solidification was complete. Alternatively, the solid object could become part of the completed device. A compliant bottom surface facilitates the final release of the solidified structures as well as allowing the deformed compliant surface to serve as a mold as shown in Figure 1 (far right). Electrical, fluidic, and pneumatic connections could then be established by means of holes created with the various solid objects.

THEORY

Control over the liquid meniscus prior to solidification can be accomplished by using different solid objects and heights, or by varying the interfacial surface tension or density of the liquid. For example, consider the curvature of a one-dimensional gas-liquid interface in contact with a solid (Figure 2). For an arbitrarily curved interface with one principal radius of curvature, R_1, the pressure increase, ΔP, on the concave side of the interface is given by the Young-LaPlace equation, $\Delta P = \gamma(1/R_1 + 1/R_2)$, where γ is the interfacial surface tension and $R_2 = \infty$. The hydrostatic pressure difference between the two fluids is $\Delta P = \Delta\rho g(H_0\text{-}Y)$, where $\Delta\rho = |\rho_1 - \rho_2|$ is the density difference between the fluids, g is gravity, H_0 the meniscus height, and Y is the vertical coordinate. Equating these two expressions gives

$$\gamma \frac{d\theta}{dS} = \Delta\rho g (H_0 - Y)$$

at any point, S, on the meniscus. This can be solved analytically for the x and y coordinates of each point on the meniscus:

$$X = \sqrt{\frac{\gamma}{\Delta\rho g}}\left\{ \ln\left[\frac{\tan(\beta_0/2)}{\tan(\beta/2)} \right] + 2(\cos\beta_0 + \cos\beta) \right\}$$

$$Y = \sqrt{\frac{\gamma}{\Delta\rho g}}\{2(\sin\beta_0 - \sin\beta)\}$$

where $\beta = \pi/4 - \theta/2$, $\theta_0 \le \theta \le \pi/2$, and $\beta_0 = \pi/4 - \theta_0/2$**[5]**. Thus, the curvature of the meniscus is a function of the interfacial surface tension, the relative weight density of the fluids, and the contact angle, θ_0. In general, surface tension increases faster than density as temperature is lowered, allowing a larger meniscus to be formed at lower temperatures. At a given temperature, careful selection of the density of an immiscible upper fluid, and thus $\Delta\rho$, also allows the size of the meniscus to be modified. Lastly, by varying the height, shape, or surface roughness of the solid, the contact angle can be changed, resulting in a different curvature of the meniscus. The contact angle can also be modified through evaporation of the liquid or prior wetting of the solid object. Three-dimensional shapes produced by this technique have two principal radii of curvature, and the solution must be computed numerically, but the same parameters control the meniscus shape as in the one-dimensional case.

EXPERIMENTAL SETUP

The experimental apparatus is depicted in Figure 3. An xyz manipulator positioned the solid objects with respect to the liquid surface. Norland Optical Adhesive No. 61 (a UV-curable adhesive) was chosen as the liquid to solidify due to its commercial

0-9640024-4-2/hh2002/$20©2002TRF
DOI 10.31438/trf.hh2002.38

availability, low degree of volume shrinkage, and known values of surface tension and density. A compliant surface of polydimethylsiloxane (PDMS) supported by a glass platform held the adhesive. Both the glass and the PDMS are transparent to UV light, allowing the UV lamp to be located below the adhesive. This configuration permitted free motion of the xyz manipulator and unobstructed placement of the solid objects. At a distance of several centimeters, the UV intensity at 365nm from the lamp was approximately 2 mW/cm^2. This produced cure times of several minutes to one hour, depending on the thickness of the adhesive layer. Shorter cure times—on the order of a minute—could be achieved with a more powerful UV lamp.

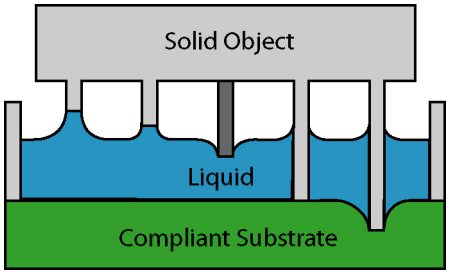

Figure 1. A solid object in contact with a liquid interface forms smooth, curved menisci. *The middle solid object is hydrophobic, while the others are hydrophilic.*

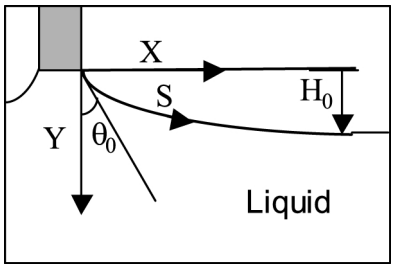

Figure 2. Definition of variables.

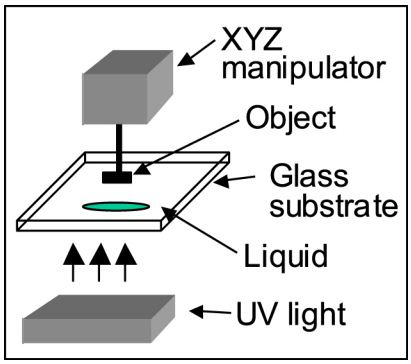

Figure 3. A schematic of the experimental setup.

RESULTS

A variety of curved, three-dimensional microstructures were created at 25°C using this technique (Figure 4). Figure 4a & b shows various "drawn" structures that were created by placing an object in contact with the adhesive and then drawing the object away from the surface and holding it at a constant height during polymerization. Moving the solid objects into the interface creates "molded" structures that assume the shape of the mold, with edges defined by the characteristics of the interface (Figure 4c & d). Finally, moving the solid object through the interface until it deforms the lower compliant surface creates a shape in the compliant surface that acts as a mold to govern the lower surface of the polymerized layer (Figure 4e & f). Deforming the compliant surface has the advantage of producing a structure that perfectly conforms to the deformation in the compliant layer, as the compliant layer is unaffected by the characteristics of the polymerizable liquid. Since the mold is compliant, it can easily be removed (peeled off) from the polymerized structure. For the images shown in Figure 4e and f, a 60µm diameter glass fiber deformed the PDMS surface. Upon removal of the fiber, a 60µm diameter hole was created that allowed fluid to be pumped through the resulting "needle" structures.

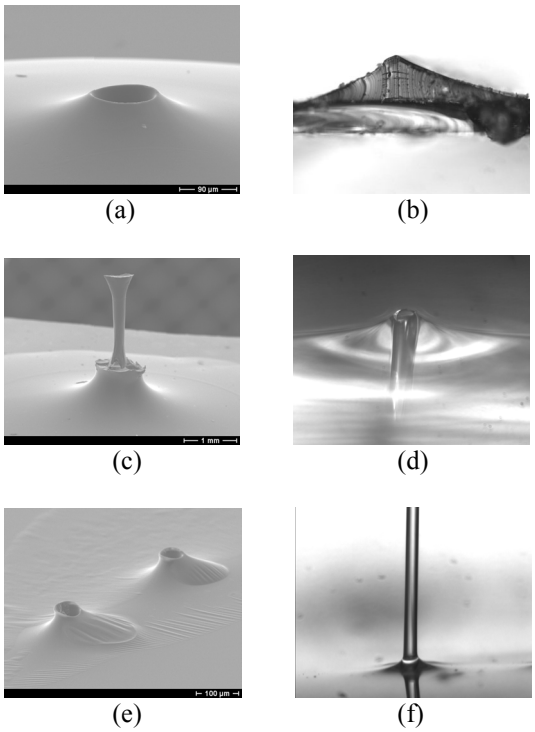

Figure 4. Examples of various polymerized structures. *(a) SEM image of a "volcano" with a cone-shaped interior formed using a drawn glass capillary; (b) Optical image of a "wall" created with a 50µm thick sheet of transparency plastic; (c) SEM image of a "column" created with tubing; (d) An optical image of a "needle" formed by penetrating the entire depth of the fluid with a 60µm diameter glass fiber. Backlighting allows the hole to be seen; (e) SEM image of two "needles" created by deforming a PDMS surface with 60µm diameter glass fibers; (f) Optical image of a "needle" pumping fluid. A reflection of the fluid can be seen in the lower half of the image.*

The fabrication of the devices in Figure 4 was accomplished with several different release schemes. The structures in Figure 4a and b were formed by pulling the solid object away from the solidified structure after polymerization. Teflon was found to be a suitable material for this type of release. As seen in Figure 5, the Teflon object can be pulled away from the polymerized structure without damaging the structure. Another method that we have employed is to coat the solid objects with surfactants for ease of

removal after polymerization. This is the release scheme used in forming the structures in Figure 4d and e. Shape memory (or shape changing) solid objects can also facilitate release. For the "column" shown in Figure 4c, tubing that expanded to its original diameter with the application of heat was used to remove the tubing mold from the polymerized structure.

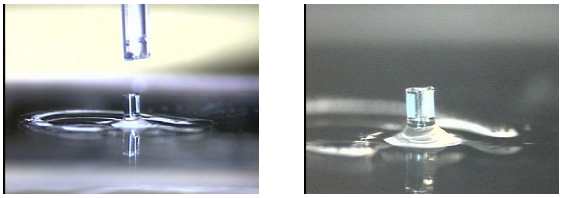

(a) (b)

Figure 5. A release scheme using Teflon. *(a) A Teflon tube and the resulting polymerized structure after release; (b) The polymerized cylindrical structure (diameter=300μm).*

While the structures in Figures 4 and 5 were fabricated at 25°C, we have observed changes in meniscus size and shape in accordance with the theory presented above. Specifically, menisci polymerized at 25°C were 300μm taller than those formed at 7°C. For a constant contact angle, this decrease in temperature should produce a larger meniscus, as surface tension increases faster than density when temperature is lowered. However, the contact angle did not remain constant, and increased to an amount that produced the observed decrease in meniscus size at the lower temperature**[6]**.

CONCLUSION

The combination of various solid objects, photopolymerizable liquids, polymerization conditions, and temperatures allows structures of various sizes and shapes to be created within the limitations of surface tension driven construction. Placing multiple solid objects in contact with the liquid surface prior to polymerization forms complex connected structures. In addition, research on the formation of drops has identified other relevant parameters that influence liquid meniscus formation, providing designers with additional control over geometry**[7]**. Thus, a liquid phase construction technique will enable the formation of diverse, curved, three-dimensional microstructures.

ACKNOWLEDGEMENTS

This work was supported under a grant from DARPA-MTO, BioFLIPS program. We would also like to thank Glenn M. Walker for helpful discussions.

REFERENCES

1. M. Madou, *Fundamentals of Microfabrication*. Boca Raton, FL: CRC Press LLC (1997).

2. G. T. A. Kovacs, *Micromachined Transducers Sourcebook*. Boston: WCB McGraw-Hill (1998).

3. H. Guckel, T. R. Christenson, K. J. Skrobis, D. D. Denton, B. Choi, E. G. Lovell, J. W. Lee, S. S. Bajikar, and T. W. Chapman, "Deep X-Ray and UV Lithographies for Micromechanics," Solid State Sensor and Actuator Workshop, Hilton Head, SC (1990).

4. J. M. Bustillo, R. T. Howe, and R. S. Muller, "Surface micromachining for microelectromechanical systems," *P. IEEE*, vol. 86, pp. 1552-1574 (1998).

5. M. T. A. Saif, "A study on the Interaction Force Between Two Small Bodies on a Liquid for Micro Self Assembly and Separation," ASME Winter Annual Meeting, Orlando, Florida (2000).

6. J. M. Bauer, T. A. Saif, and D. J. Beebe, "Liquid Phase Construction of Microstructures," *Submitted to Appl. Phys. Lett.* (2002).

7. J. Eggers, "Nonlinear Dynamics and Breakup on Free-Surface Flows," *Rev. Mod. Phys.*, vol. 69, pp. 865-929 (1997).

SELECTIVE AND LOCALIZED BONDING USING INDUCTION HEATING

Andrew Cao, Mu Chiao & Liwei Lin
Department of Mechanical Engineering
University of California at Berkeley
Berkeley Sensor And Actuator Center
Berkeley, CA, 94720, acao@me.berkeleyedu

ABSTRACT

Selective and localized bonding using induction heating has been successfully demonstrated for MEMS (Microelectromechanical Systems) packaging and fabrication applications. Eddy current is generated when a closed metal bonding ring is placed under an alternating magnetic field. The metal bonding rings function both as the heating source and bonding solder. Both Pyrex-to-Pyrex and Pyrex-to-polycarbonate bonding processes have been achieved. The heating cycle needed to complete the bonding process is 100ms and 60 seconds for the polymer and Pyrex bonding processes respectively. The low thermal budget allows water to be encapsulated inside a cavity without evaporating. Experimentally, Pyrex substrates can be hermetically bonded using gold bonding rings. The gold bonding ring can be used as a solder that bonds the substrates, or it can be used as a heat source to locally meld the glass and facilitates direct Pyrex-to-Pyrex bonding. In either case, the bond was very strong and managed to maintain a hermetically sealed cavity.

INTRODUCTION

Hermetic sealing and packaging is vital in MEMS device applications for long-term stability. It is well known that hermetic packaging in the chip level is expensive and can contribute to a major portion of the overall cost of a device. Wafer-level packaging can substantially reduce the price of packaging and overall manufacturing cost. Therefore, many researchers have worked on various approaches for hermetical sealing processes either with or without enclosed MEMS devices. For example, an LPCVD (Low Pressure Chemical Vapor Deposition) silicon nitride sealing process has been used to encapsulate micro-resonators in vacuum environment [1,2]. A resistive joule heating method has been used to seal sensors and resonators in hermetic and vacuum environments [3-5]. A RTP (Rapid Thermal Processing) bonding process has been applied to MEMS packaging for hermetic and vacuum applications [6-7]. The introduction of selective and localized bonding using induction heating takes the advantages of the above processes, including localized and selective bonding. Induction heating is suitable for parallel processing and it is relatively easy to implement. As such, this new class of bonding method may have potential for MEMS packaging applications.

Induction heating is commonly used in industry for applications ranging from welding, heat treatment of metals and bottle sealing. In microelectronics processing, induction heating has been proposed for whole-wafer bonding process [8]. Previously, induction heating has been demonstrated to remotely and selectively applied heat to micro bonding rings [9]. This paper uses induction heating to perform hermetic bonding of glass wafers and plastic wafers and demonstrates the feasibility of encapsulating liquid.

THEORY

Selective and localized induction heating is based on Faraday's law. Electric field and eddy current are generated on metal rings by placing the ring inside a changing magnetic field. Joule heating is generated remotely and selectively on localized areas. Figure 1 shows the schematic diagram of this concept. With proper design and process control, the heating area can be confined selectively and locally for the purpose of bonding applications. In the prototype demonstration, a cavity drilled in the center of the bonding ring is shown in Fig. 1, and is filled with water to test the feasibility of localized heating without vaporizing the water. If the heating causes the water to evaporate, the steam created would interfere with the bonding process, making encapsulation impossible.

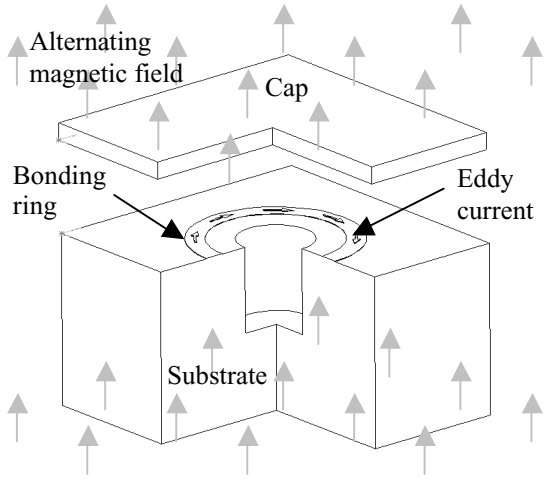

Figure 1. Induction heating and bonding concept. Using externally applied alternating magnetic field to induce eddy currents and resistive heating in a metallic bonding ring.

It is believed that modifications to the macroscopic induction heating theory was necessary, because some of the assumptions that were made while deriving those theorymight no longer hold in the microscopic scale. The gold bonding rings used is 6μm thick, has a 1mm inner diameter and a width of 100-200μm. The electric field generated in the bonding ring is

$$E = -\frac{d\Phi_B}{dt} = -K\mu A\frac{dI}{dt} \quad (1)$$

Where E is the electromotive force (EMF) generated, Φ_B is the magnetic flux, μ is the permeability, A is the cross sectional area, I is the current powering the coil, and K is the coil constant, which governs the strength of the magnetic field created for a given coil current. Given the small cross sectional area of the bonding rings, it is very difficult to generate a high EMF. As Eq. 1 implies, adequate heating requires a large high frequency current running through a coil that could generate a strong magnetic field for the bonding ring.

The induction bonding setup is shown in Fig. 2. The bonding sample is placed in the center of an 8 turned helical coil, which has a 12mm inside diameter, 18mm outer diameter, 3mm tube diameter and a 5mm gap between the top and bottom four turns.

0-9640024-4-2/hh2002/$20©2002TRF
DOI 10.31438/trf.hh2002.39

Solid-State Sensors, Actuators, and Microsystems Workshop
Hilton Head Island, South Carolina, June 2-6, 2002

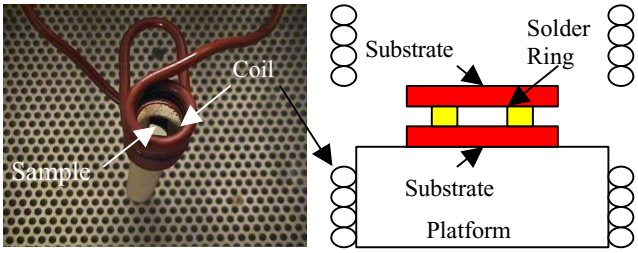

Figure 2. Induction heating setup using an 8 turned helical coil driven between 10-15MHz.

The magnetic intensity applied to the bonding ring could be calculated by modeling the coil as 8 current loops each with a 7.5mm radius and an axial distance z away from the bonding ring. The magnetic intensity contribution of each loop can be calculated using Eq. 2, which is derived from Ampere's law [10].

$$H(z) = \frac{r^2 I}{2(r^2 + z^2)^{3/2}} \qquad (2)$$

Where I stand for the current running through the coil. With the coil geometry above, the magnetic intensity generated is approximately 150I(A/m). Up to 180 Amps can be generated in the coil, creating a magnetic intensity as high as 27,000 (A/m) in our current setup.

During an induction heating operation, the coil and the heated work piece, e.g. a metal cylinder, are magnetically linked. The magnetic field generated by the coil induces an EMF and eddy current in the cylinder. As the current flows in the cylinder, it too creates a magnetic field. According to Lenz's law, the field the cylinder generates is opposite to the original magnetic field that was generating the eddy current. Hence as the incoming magnetic field travel towards the center of the cylinder, it is cancelled by the opposing magnetic field the induced eddy current generates. Therefore, less and less eddy current can be induced radially towards the center of the cylinder. The depth where the eddy current density reaches 1/e of the surface density is called the skin depth, defined as

$$\delta = \sqrt{\frac{\rho}{f\pi\mu}} \qquad (3)$$

Where δ is the skin depth, ρ is resistivity, and f is the frequency. The above macroscopic induction heating theory [11-13] holds when the induced eddy current is large and the opposing magnetic field generated is sufficient to cancel the incoming magnetic field. In this case, most of the eddy current travels circumferentially in the first radial skin depth and generate resistive heating there. However, when the bonding ring is very small and thin, the induced voltage is low, and the resistance to eddy current flow is high. In this case, the induced eddy current and the opposing magnetic field created is low, therefore, the incoming magnetic field can penetrate deeper into the radial direction, inducing more eddy currents and more heating.

EXPERIMENTAL RESULTS

The prediction of induction heating modified for small thin bonding rings was tested using several different metal rings patterned on Pyrex substrates. Temperature indicating paint was used to determine the location of heat generation, as well as the temperature reached by the rings. Once the paint reaches its indicating temperature, it turns from opaque to clear; this process can take less than 10ms.

Several experiments confirmed that heat could be generated beyond the radial skin depth as defined by Eq. 3. Figure 3 shows pictures of concentric tungsten rings covered in 150°C temperature indicating paint heated under induction power.

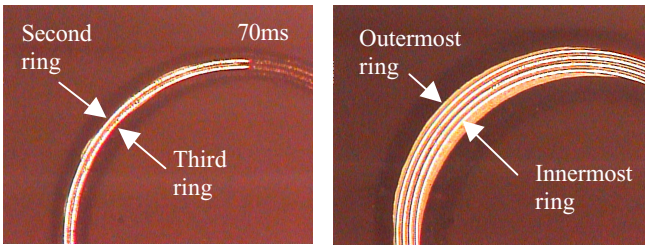

(a) (b)

Figure 3. Tungsten bonding rings painted with 150°C temperature indicating paint and heated under induction power

The four rings are approximately 2mm in diameter, 2μm thick, 20μm wide with a 20μm gaps between each ring. At 150°C, the radial skin depth of tungsten calculated using Eq 3. is 40μm. If the macroscopic skin depth theory holds, the outermost ring should produced the most heat, the second ring that is 40μm away from the outermost skin should have little resistive heating, and the innermost ring should have virtually no heating at all. Judging by Fig. 3, the paint started to melt from the center rings and spread equally to both sides of the innermost and outermost rings. It can be concluded that approximately equal heating originated from all of the rings. The center two rings heated up first because it was harder for the heat generated in those rings to be conducted away.

Heat generation between 6μm thick, 1mm diameter gold rings with widths of 200μm and 50μm were compared. Induction power was applied to the gold ring until they started glowing at roughly 900°C. The calculated skin depth of gold at this temperature is 45μm. It was observed that 200μm wide rings required 400W of coil power to sustain glowing while the 50μm ring required 1000W. Therefore, heat must be generated beyond the 45μm radial skin depth, otherwise the extra width of the gold ring would act as a heat sink to dissipate heat thus it should require more coil power to attain glowing. The fact that heat can be generated beyond the theoretical radial skin depth is important because more heating power can be couple into the metal rings than predicted by macroscopic theory [11-13]. It should be noted that at this small scale, metal rings with lower resistance, either made thicker, wider or made from more conductive metals tends to generate more heat. Figure 4 shows the temperature reached by a gold bonding ring with varying power level and heating time. When the coil power is at 100W, the temperature of the metal ring can only reach 400°C in 0.5 second. When the coil power is above 500W, the ring temperature reaches more than 1000°C in 0.5 second. However, increasing the coil power above 500W show less dramatic increase in the temperature-time plot.

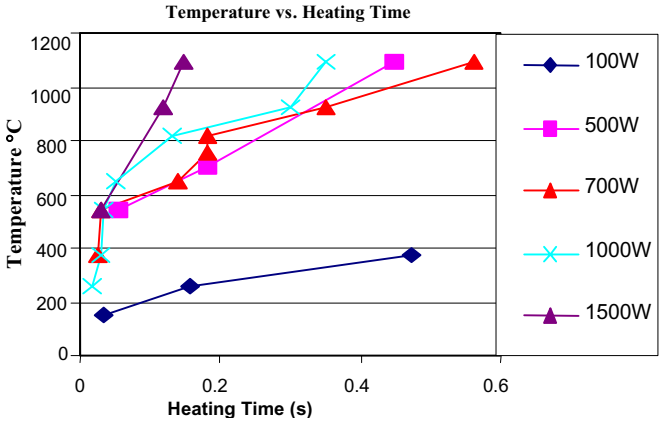

Figure 4. Measured temperature with respect to time of 6 μm thick, 200μm-wide and 1mm diameter gold bonding ring under various induction heating power.

Polycarbonate substrate has been bonded to glass substrate using gold bonding rings. The time needed to achieve bonding is 100ms. The adhesion strength of these bonds is limited by the adhesion strength of the gold bonding ring to the glass substrate. Forcefully breaking one of these bonds usually result in the gold bonding ring being peeled off from the glass substrate while adhering to the polycarbonate substrate. Due to the low thermal budget requirements of the bonding cycle, it is possible to encapsulate water using this bonding setup. Figure 5 shows picture of a polycarbonate cavity bonded with a glass cap encapsulating liquid water. The gold bonding ring is 1mm across, 100µm wide, and 6µm thick. Since the bonding process only takes 100ms and the thermal budget is low, the water droplet was expected to stay very close to its initial ambient temperature.

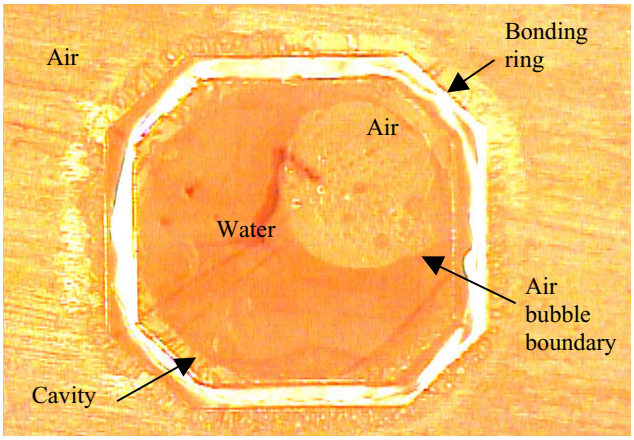

Figure 5. Water encapsulated between a cavity drilled in polycarbonate substrate and a glass cover plate

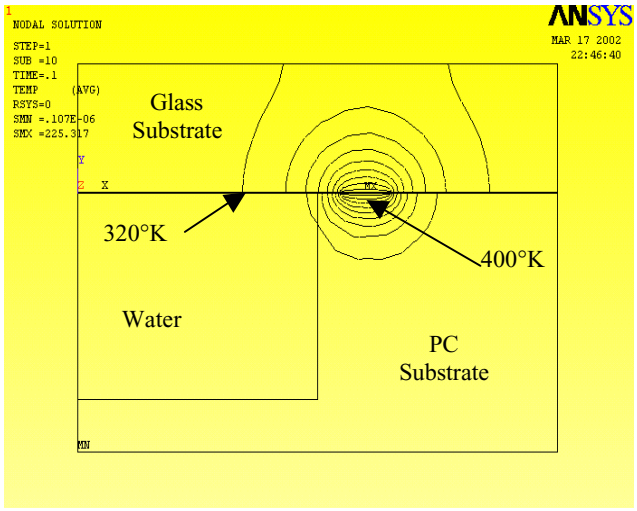

Figure 6. Finite element simulation of 100ms Pyrex to Polycarbonate (PC) bond. Water encapsulated in the cavity will receive minimal heating

Figure 6 show a finite element analysis of the glass to polycarbonate bond at 100ms, which indicates the heat which originates from the bonding ring will not warm the water originally at 300°K, encapsulated in the polycarbonate cavity. This is an important requirement for encapsulating bio-fluids, which can be damaged just few degrees above body temperature. This process may have potential application in sealing or encapsulating drugs, chemicals or bio-medical materials.

Pyres-gold-Pyrex bonding was accomplished using gold bonding rings 1.2 mm across, 6µm thick and either 100µm or 200µm wide. The gold rings, which were patterned on a Pyrex substrate, were kept in contact with another bare Pyrex substrate. Bonding was achieved using 750W of coil power, heating the ring to a bright red glow at approximately 900ºC for 60 seconds.

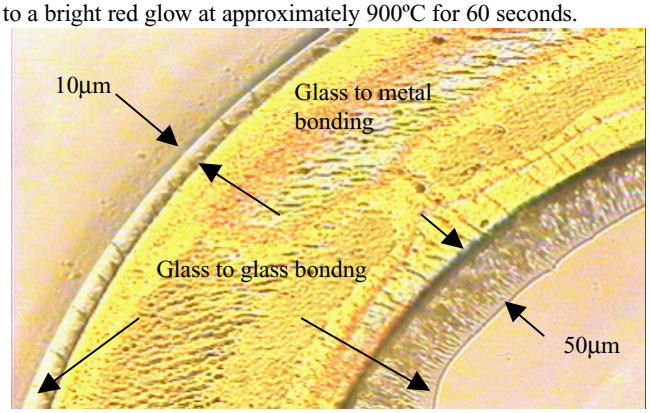

Figure 7. Pyrex-to-Pyrex bonding using 1mm diameter, 200µm wide and 4µm thick gold solder.

Direct Pyrex-to-Pyrex bonding can be achieved by applying higher temperature and pressure to the glass-gold-glass bond system. The higher temperature softens the glass, and the applied pressure forces the molten glass to flow around the gold ring and bond to the molten glass on the opposing substrate. Figure7 show a direct Pyrex-to-Pyrex bond on both the inner and outer boundaries of the gold bonding ring. This bond was achieved in 3 seconds using 1500W of coil power.

Both the Pyres-gold-Pyrex, and direct Pyres-to-Pyrex bonds were very strong, they are comparable to the bulk strength of Pyrex substrate. Forcefully breaking one of these bonds usually resulted in tearing of the bulk substrate as shown in Fig. 8.

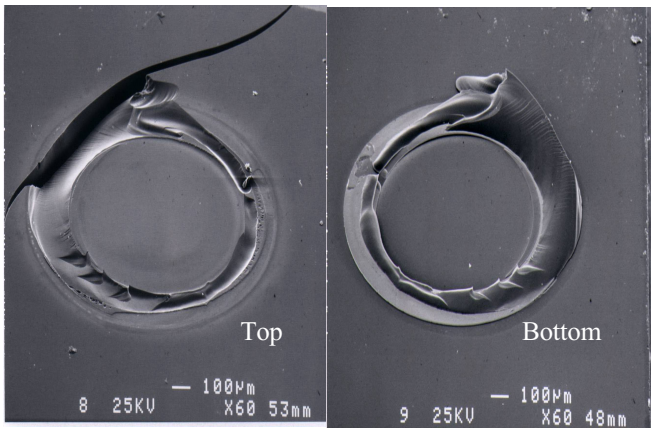

Figure 8. Two halves of a forcefully broken Pyrex-to-Pyrex bond.

Both types of bonds were tested for hermetic sealing using dyed isopropyl alcohol. Alcohol has a very low surface tension hence it can easily seep into a non-hermetic seal. The bond interface was flooded with alcohol for approximately 1 minute before the alcohol starts to evaporate away. Figure 9 show a Pyrex-gold-Pyrex bond that was once submerged in alcohol, now approximately half the alcohol evaporated away from the interface. The bonds were also tested in a 100% humidity, 2 atmosphere autoclave chamber for 30 minutes. Both kinds of bonds were able to keep moisture out of the enclosed cavity.

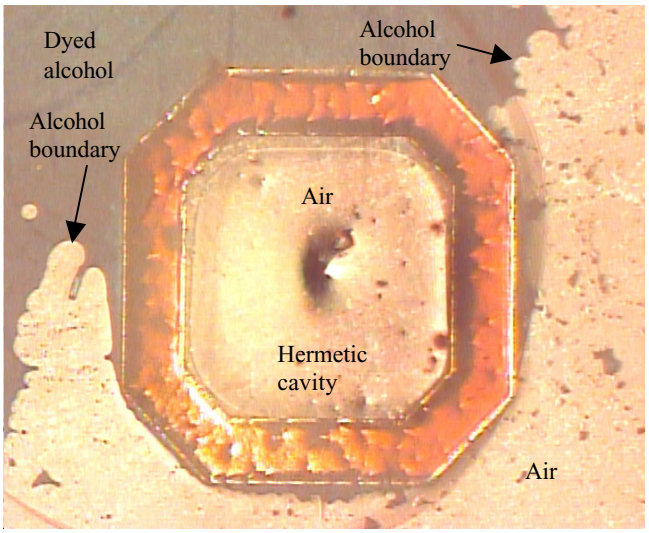

Figure 9. Alcohol cannot seep into the Pyrex-gold-Pyrex bonded cavity.

It is highly desirable to reduce the bonding time. Short heating cycles reduces the heat-affected zone, decreases the amount of energy needed for bonding, and increases production rate. Using induction heating, it is theoretically possible to achieve bonding very quickly. However short heating cycles like the 3 second Pyrex-to Pyrex bond mentioned earlier often suffer from localized burnouts. These failures are the result of uneven heating of the metal bonding rings. The electrical resistivity of most metals increases quickly with increasing temperature. Since the same amount of eddy current has to travels around the bonding ring with a constant cross sectional area; once a hot spot develops, the resistivity will locally increase, causing even more heat generation than its neighboring area. This effect can quickly lead to localized melting, vaporization, or oxidation of the bonding ring.

There are three methods to reduce the occurrence of burnouts. 1) Increase the heating power gradually. This allows the heat to conduct from the hot spots to its neighboring region, hence evening out the heat generated. 2) Use thicker bonding rings, hence process variations would not be as noticeable. 3) perform the bonding in an inert environment, this prevent oxidation of the heated metal ring. 4) Use metal that has a high melting temperature and is relatively inert. This is the reason why gold was chosen to make high temperature glass to glass bonding rings. Even though gold does not easily oxidize, hot spots can cause localized melting, and surface tension wicks the molten gold to the solid gold region and break the current loop. This effect can be seen in Fig 10.

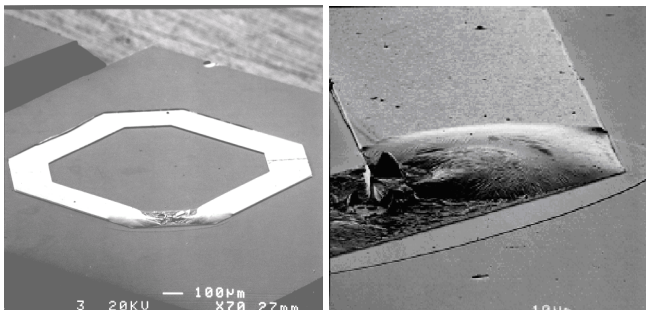

Figure 10. Localized melting of gold bonding ring a) one corner of the bonding has melted and broke the current loop. b) detailed view of melted region shows the melted region has a thicker and rounder cross sectional area than the original loop.

CONCLUSION

A modified theory of induction heating for MEMS scaled parts has been proposed and verified. It has been shown that for small thin parts, eddy current heating can be generated beyond the theoretical radial skin depth derived for macroscopic induction heating. In the micro-scale, metal rings with less resistance; either made wider, thicker, and of more conductive material can generate more heating.

Induction heating has been applied to perform strong, hermetic bonding in the microscale. The bonding temperature is approximately 900°C or above, and the bonding time ranged from 3 second to 60 seconds. Slow bonding cycles achieves hermetic bond on a more controllable and consistent basis. Rapid hermetic bonding is more prone to burnouts hence it has lower success rate. Future research will focus on sub-second induction bonding and encapsulation of MEMS devices

ACKNOWLEDGEMENT

These devices were fabricated in the UC Berkeley microfabrication laboratory. This work is supported in part by an NSF Career award (ECS-00960098) and a DARPA/MTO/MEMS grant

REFERENCES

[1] Liwei Lin, K. McNair, R.T. Howe and A.P. Pisano, "Vacuum Encapsulated Lateral Microresonators", 7th Int. Conference on Solid State Sensors and Actuators, pp 170-273, Yokohama, Japan, June, 1993.

[2] Liwei Lin, "selective Encapsulation of MEMS: Micro Channels, Needles, Resonators, and Electromechanical Filters", Ph. D. Theses, UC Berkeley, 21, 1993

[3] Y.T Cheng, Liwei Lin, and Kahlil Najafi, "Localized Bonding with PSG or Indium Solder as intermediate Layer," Proceedings of IEEE Micro Electro Mechanical Systems Workshop, pp. 285-289, Orlando, Florida, 1999

[4] Y. T. Cheng, L. Lin, K. Najafi, "localized silicon fusion and Eutectic Bonding for MEMS Fabrication and Packaging", Technical Digest of the 1998 Solid State Sensor and Actuator Workshop, Hilton Head, pp 233-236, 1998

[5] Y. T. Cheng, W. T. Hsu, L. Lin, C. T. Nguyen, and K. Najafi. "Vacuum Packaging Technology Using Localized Aluminum/Silicon-to Glass Bonding", Technical Digest of the 2001 Micro Electro Mechanical System. Interlaken, Switzerland, pp18-21.

[6] Mu Chiao and Liwei Lin, "Hermetic Wafer Bonding Based On Rapid Thermal Processing. Solid State Sensor and Actuator Workshop. Hilton head, pp 347-350

[7] M. Chiao and Liwei Lin, "A Wafer-Level Vacuum Packaging Process by RTP Aluminum-to-Nitride Bonding", to appear in this workshop.

[8] Thompson K. , Gianchandani Y. B, Booske J. , Cooper R. Si-Si Bonding Using RF and Microwave Radiation. The 11th International Conference on Solid-State Sensors and Actuators, Munich, Germany, June 10-14, 2001. p226-229

[9] Andrew Cao and Liwei Lin "Selective Induction Heating for MEMS Packaging and Fabrication". Proceedings of 2001 ASME International Mechanical Engineering Congress and Exposition, Nov 11-16, 2001, New York, NY

[10] Lieu, D. U.C Berkeley, ME 219 reader. Spring 2001

[11] Davies, J. Simpson. P. "Induction Heating Handbook". McGraw-Hill Book Company (UK) limited. 1926

[12] Zinn, S. and Semiatin S. L. Elements of Induction heating. Carnes Publication Services, Inc. 1991

[13] Curits, F. W. High-frequency Induction heating, second edition. McGraw Hill Book Company, Inc. 1950

ELECTRICAL THROUGH WAFER INTERCONNECTS WITH 0.05 PICO FARADS PARASITIC CAPACITANCE ON 400 μM THICK SILICON SUBSTRATE

Ching H. Cheng, Arif S. Ergun, and Butrus T. Khuri-Yakub
Edward L. Ginzton Laboratory, Stanford University
Stanford, CA 94305-4085

ABSTRACT

This paper presents a technology for high density and low parasitic capacitance electrical through-wafer interconnects (vias) to an array of micromachined transducers on a silicon wafer. Vertical wafer feedthroughs (interconnects) connect an array of sensors or actuators from the front side (transducer side) to the backside (packaging side) of the wafer. A 20 to 1 high aspect ratio 400 μm long and 20 μm diameter interconnect is achieved by using deep reactive ion etching (DRIE). Reduction of the parasitic capacitance to the substrate is achieved using reverse-biased pn-junction diodes operating in the depletion region. A parasitic capacitance of 0.05 pF has been demonstrated by this approach. This three-dimensional architecture allows for elegant wafer-level packaging through simple flip-chip bonding of the chip's backside to a printed circuit board (PCB) or a signal processing wafer.

INTRODUCTION

In micro-electro-mechanical-systems (MEMS) applications, it is advantageous to have electronic circuitry as near the sensor/actuator as possible. However, integrating both the MEMS devices with electronics on the same wafer often leads to a compromise between the performance of either or both systems. An excellent solution to this problem is to construct the optimum MEMS devices and electronics on separate wafers, provide a through wafer interconnect with minimum resistance and capacitance on the MEMS wafer, then flip-chip bond the two wafers (Fig. 1). In this fashion, the MEMS wafer can be fully populated such as in applications of infra-red (IR) focal plane arrays or three-dimensional ultrasound imaging [**1-5**]. Finally, since the MEMS and electronics wafers can be fabricated in different facilities, the overall yield of the manufacturing process is enhanced.

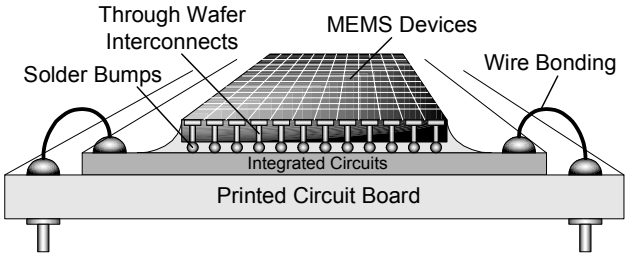

Figure 1. *Packaging schematic of through-wafer interconnects.*

The architecture of achieving this hybrid integration with high density is based on through-wafer vertical interconnects with high aspect ratio. Many processes have been previously used to fabricate through-wafer interconnects [**6**][**7**] including dry etched polysilicon filled interconnects by Chow et al [**8**]. In previous work, we integrated similar interconnects into an active sensor arrays and made improvements on parasitic capacitance from 2 pF to 0.28 pF [**1**].

To further reduce the parasitic capacitance, we propose to use a through wafer interconnect as shown in Fig. 2. The interconnect presents a parallel capacitance and a series resistance to the input impedance of the MEMS device. Thus, for operation that is not limited by the interconnect, both the capacitance and resistance have to be very small. We will present a technology where the parasitic capacitance is reduced to 0.05 pF in a silicon wafer that is 400 μm thick with a resistivity of 1000 Ω-cm and with a via that has a diameter of 20 μm.

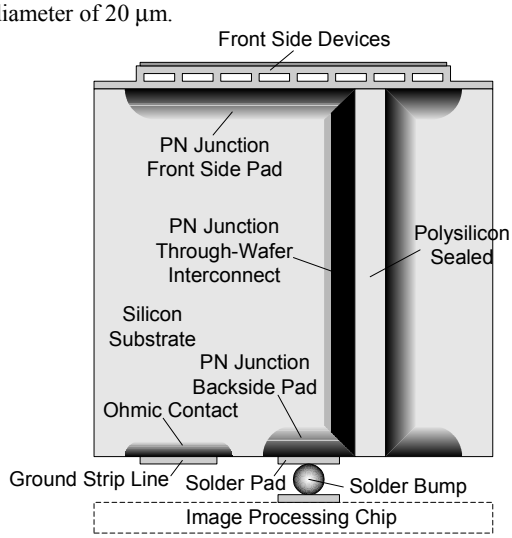

Figure 2. *Schematic of the through-wafer interconnect.*

For our current application, the through-wafer interconnect is used for integration of two-dimensional ultrasonic transducer arrays with electronic dies. In an ultrasonic transducer array operation, the parasitic capacitance of the interconnect between an array element and its transmit/receive electronics is the limiting factor for the dynamic range and bandwidth. Therefore, it is always best to put the electronics as close to the array elements as possible. In this work, we demonstrate a method to integrate a 128 x 128 capacitive micromachined ultrasonic transducer (CMUT) array with the electronic circuit without sacrificing the performance of either while minimizing the parasitic capacitance. To do this, an electrical through-wafer interconnect is employed to address the array elements individually, where the front side of the wafer is fully populated with the ultrasonic array elements, and the backside is solely dedicated to bond pads for the flip-chip bonding to the printed circuit board (PCB) or the integrated circuits (Fig. 1). In this manner, the parasitics due to any interconnection cable are avoided. To further improve the device performance, the parasitic capacitance of the through-wafer interconnects to the silicon substrate needs to be reduced to a much lower level than the device capacitance.

Travel support has been generously provided by the Transducers Research Foundation and by the DARPA MEMS and DARPA bioFlips Programs.

0-9640024-4-2/hh2002/$20©2002TRF
DOI 10.31438/trf.hh2002.40

PARASITIC CAPACITANCE REDUCTION

The via can either have a metal-insulator-semiconductor (MIS) or a PN junction diode relationship with the silicon. In order to reduce the capacitance of the via, it is best to have a reversed biased pn junction because the depletion region can be made very large, as shown in Fig. 3. Hence, the parasitic capacitance can be reduced to about 0.05 pF. Two-sided deep reactive ion etching (RIE) is used to make through wafer holes with an aspect ration of 20:1. In previous work [**1**], we made vias with MIS junctions that had a parasitic capacitance of 0.28 pF. However, in this work, we report vias with PN junction diodes that have a measured parasitic capacitance of 0.05 pF at a reverse bias more than 10V as seen in Fig. 11. This will allow operation of MEMS devices at very high frequencies and without a loss of dynamic range due to the interconnect. The parasitic capacitance can be further reduced by reducing the thickness of the wafer, the diameter of the via, and increasing the resistivity of the silicon wafer.

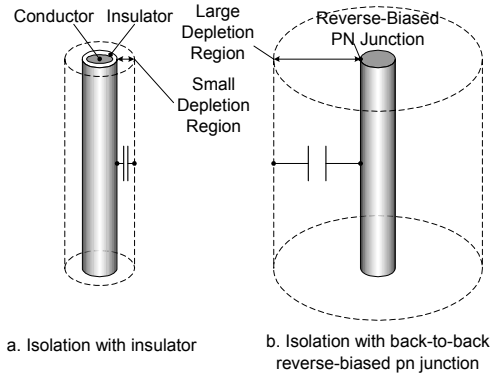

Figure 3. *Schematic of the MIS and PN junctions.*

Parasitic capacitance has a detrimental effect on the performance of the CMUT. For each array element, there are three sources contributing to the parasitic capacitance: the front side 400 µm x 400 µm pad for the bottom electrode of the transducers; the backside 200 µm x 140 µm pad for bonding; and the through-wafer interconnect with 400 µm length and 20 µm diameter (Fig. 4). The optimum solution for parasitic capacitance reduction is to implement reverse-biased pn-junction diodes on the front and backside pads of the wafer and inside the interconnects as shown in Fig. 3. When the pn junction is reversed biased (DC), the high resistivity (> 1000 ohm-cm) silicon substrate is fully depleted, thus a low parasitic capacitance is achieved.

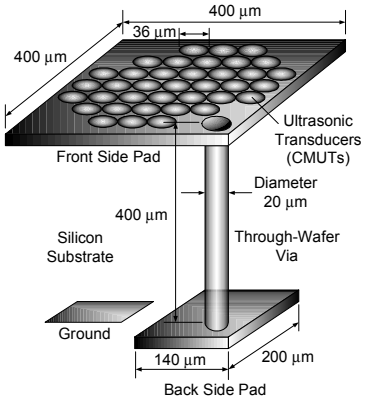

Figure 4. *Schematic of the MIS and PN junctions.*

EXPECTED PARASITICS

Based on simulation, a silicon substrate with resistivity of 1000 ohm-cm is used. A reversed bias voltage is applied to drive the pn junction diodes into the depletion region. The expected capacitance-voltage (CV) relationship is shown in Figure 5. We expect the total parasitic capacitance to be lower than 0.06 pF for a reverse bias voltage of more than 10 volts. This includes capacitance of the front and backside pads and a single through-wafer interconnect, which is a substantial improvement over previously reported results [**1**]. The predicted series resistance is 434 Ω which assumes that the doping profile is the same for the surfaces on top of the wafer and inside the via holes.

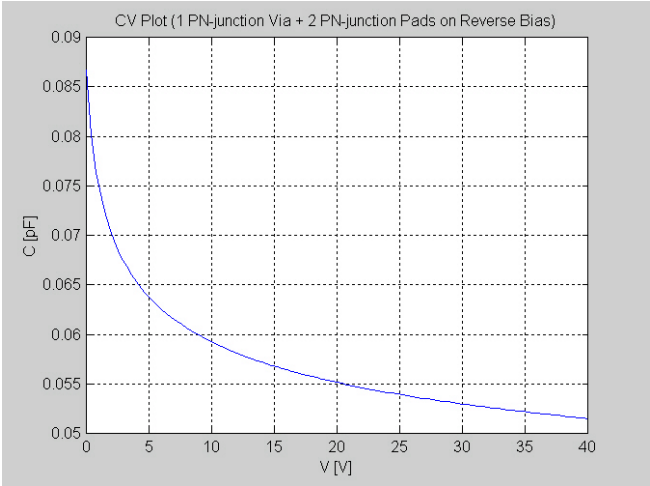

Figure 5. *Expected parasitic capacitance*

THROUGH WAFER INTERCONNECT PROCESS

The process flow is shown in Fig. 6. We start with a 400 µm thick double-sided polished n-type <100> Si wafer which is thermally oxidized to 2 µm thick to serve as a hard mask for the deep etch. Both sides are then patterned with 20 µm diameter openings for each interconnect (Fig. 6a). The through-wafer deep etch is done by etching half way from both sides of the wafer (Fig. 6b). By this means, a 20 to 1 high aspect ratio via hole can be achieved. When the interconnect is etched through, the helium flow used for cooling goes through the etched holes, and the etching will be slowed down, serving as an etch stop. The wafer is then heavily doped with boron to build the pn junction diode inside the holes (Fig. 6c). The interconnect holes are then filled with polysilicon (Fig. 6d). The polysilicon on both sides is then etched back and stopped on the oxide (Fig. 6e). It is ready to be etched for the front and back side oxide opening (Fig. 6f). The wafer is then doped with boron which makes up the pn junctions for the front and backside pads. The oxide is etched and the backside is patterned with photoresist for phosphorous ion implantation for ohmic contact (Fig. 6g). After this step, the transducers can be built on top of the front side pn-junction pad (Fig. 8). At the very end, the backside metal pads for flip-chip bonding are formed by lift-off (Fig. 6h). The SEM pictures show the cross section of a finished interconnect in Fig. 7. The wafer is ready for flip-chip bonding to a circuit chip or PCB (Fig. 9).

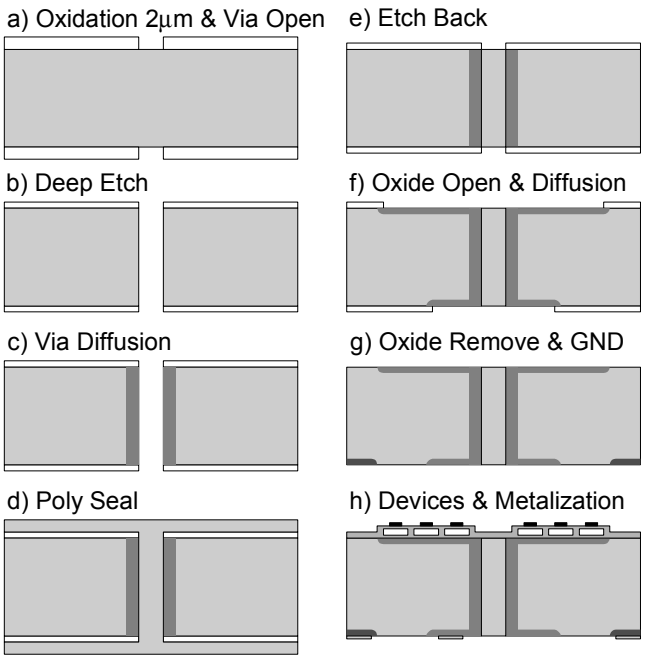

Figure 6. *Fabrication process for through wafer interconnects.*

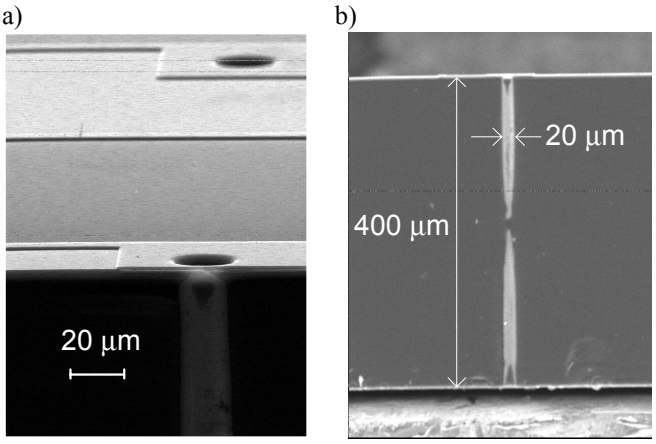

Figure 7. *SEM pictures of the cross section of the interconnects.*

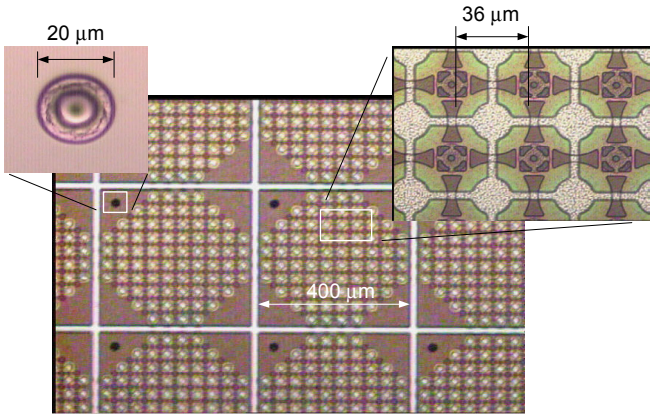

Figure 8. *Photographs of CMUT array elements with through - wafer interconnects.*

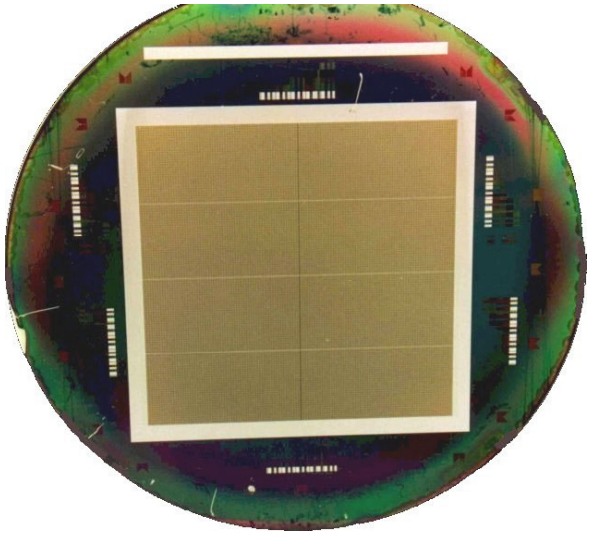

Figure 9. *Photograph of a finished 128 x 128 CMUT array on a 4" silicon wafer.*

TEST RESULTS

As shown in Fig. 10, a testing device with a through-wafer interconnect connected with both front side and back side pads and a ground to the substrate is employed to measure the C-V characteristic at 1 MHz frequency. A reversed DC bias is applied to drive both pn-junction pads into the depletion region. The total capacitance is the capacitance of the through-wafer interconnect plus both pads. The series resistance for each via is 900 Ω which is more than our prediction of 434 Ω. This discrepancy comes from the non-uniform doping profile throughout the via hole. However, we assumed a uniform doping profile for our calculation. Compared with the top wafer surface, there is less dopant getting into the via hole. The doping profile inside the via hole depends on the uniformity during the boron diffusion process which is hard to achieve without a special simulation tool [**9**]. The leakage current coming from both pads and the via is 7nA.

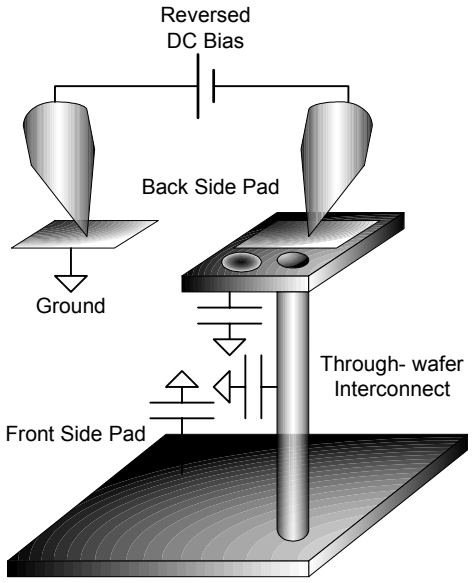

Figure 10. *Capacitance measurement set-up.*

Fig. 11 shows a C-V characteristics at 1 MHz frequency. By applying a reverse bias for more than 10 volts the capacitance will decrease to 0.055 pF because of depletion into the substrate. This experimental result is very close to what we expected from the simulation (Fig. 12).

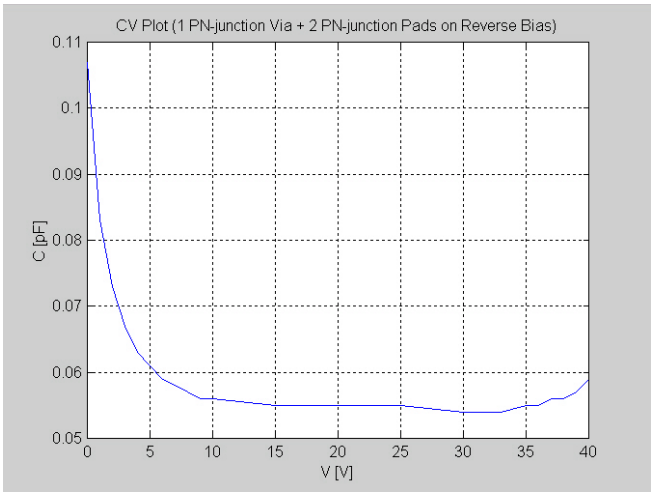

Figure 11. *Measured capacitance-voltage relationship (CV) of a reversed biased pn junction through wafer interconnect.*

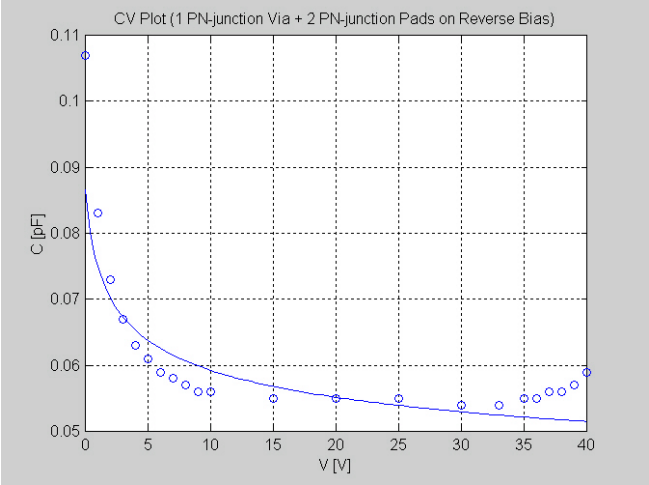

Figure 12. *Comparison of capacitance-voltage relationships (CV) of a reversed biased pn junction through wafer interconnect.*

CONCLUSIONS

The C-V measurements reveal that electrical through-wafer interconnects with parasitic capacitance of 0.05pF have been achieved. This makes possible of its application to more devices with lower capacitance. Although the series resistance of the through-wafer interconnects is not very serious for the CMUT application, it stands as a problem for the future. This series resistance can be substantially reduced by employing doped polysilicon or metal to seal the via holes which will be shown in a future work.

ACKNOWLEDGEMENT

This work is sponsored by the Office of Naval Research.

REFERENCES

1. C. H. Cheng, A. S. Ergun, B. T. Khuri-Yakub, " Electrical Through-Wafer Interconnects with Sub-PicoFarad Parasitic Capacitance," *MEMS Conference 2001*, Berkeley, California, 8/24-26/2001.

2. C. H. Cheng, E. M. Chow, A. S. Ergun, and B. T. Khuri-Yakub, "An Efficient Electrical Addressing Method Using Through-Wafer Vias for Two-Dimensional Ultrasonic Arrays," *Proceedings of 2000 IEEE International Ultrasonics Symposium*, San Juan, Puerto Rico, 10/22-25/2000, pp. 1179-82.

3. B. T. Khuri-Yakub, C. H. Cheng, F. L. Degertekin, S. Ergun, S. Hansen, X. C. Jin, and O. Oralkan, "Silicon Micromachined Ultrasonic Transducers," presented at the *Fifth European Conference on Underwater Acoustics*, Lyon France, July 10-13, 2000.

4. S. Calmes, C. H. Cheng, F. L. Degertekin, X. C. Jin, and B. T. Khuri-Yakub, "Highly Integrated 2-D Capacitive Micromachined Ultrasound Transducers," presented at the *1999 IEEE International Ultrasonics Symposium*, Lake Tahoe, Nevada, Octobor 17-20, 1999; in Ultrasonics Symposium Proceedings, pp. 1163-6.

5. X. C. Jin, C. H. Cheng. O. Oralkan, S. Calmes, F. L. Degertekin, and B. T. Khuri-Yakub, "Recent Progress in Capacitive Micromachined Ultrasonic Immersion Transducer Array," presented at the *8th International Symposium on Integrated Circuits, Devices and Systems*, Singapore, September 8-10, 1999; in ISIC-99 Proceedings, pp.159-162.

6. H. T. Soh, C. P. Yue, A. McCarthy, et al., "Ultra-Low Resistance, Through-Wafer Via (TWV) Technology and Its Application in Three Dimensional Structures on Silicon," *Japanese Journal of Applied Physics*, Part I 38(4B), 2393-6 (1999).

7. T. R. Anthony, "Forming Electrical Interconnections through Semiconductor Wafers," *Journal of Applied Physics*, 52(8) 5340-9 (1981).

8. E. M. Chow, A. Partridge, C. F. Quate, T. W. Kenny, "Through-Wafer Electrical Interconnects Compatible with Stanford Semiconductor Processing," *Solid-State Sensor and Actuator Workshop*, Hilton Head Island, South Carolina, June 4-8, 2000, pp. 343-6.

9. R. Rumpf, K. Suzuki, "Modeling of Irregular Boron Diffusion Profiles over Varied Surface Topologies," *Digest of Papers. Microprocesses and Nanotechnology '99*, pp. 198-9.

NANOSCALE GAP FABRICATION AND INTEGRATION OF CARBON NANOTUBES BY MICROMACHINING

Jaehyun Chung, Junghoon Lee, Rodney S. Ruoff, and Wing Kam Liu
Mechanical Engineering, Northwestern University
Evanston, IL, 60208

ABSTRACT

This paper presents new techniques for fabricating nanoscale gaps based on micro-lithography and the assembly of carbon nanotubes(CNTs) across these gaps. A sharp nanoscale gap was fabricated by the controlled over-etching of an Al thin film. The etching process was monitored by measured resistance to fabricate a nanoscale gap (~20nm) was fabricated. It was found that the fluctuation of the etching rate during the final minutes was so uniform that we could rely on timed etching to obtain the nanoscale gap. A round-shaped gap was also created by reversing a bridge pattern with a lift-off process. The smallest gap created by this method was 150 nm. AC electrophoresis was used to deposit CNTs dispersed in a liquid across the prepared gaps. A highly oriented deposition was obtained across a round gap. Compared with chemical vapor deposition (CVD) methods, the suggested deposition steps can be performed at a room temperature in an open environment, thus providing more process freedom. Various configurations for device application and fundamental experiments can be conceived using the proposed method.

INTRODUCTION

Since their discovery in 1991[**1**], carbon nanotubes (CNTs) have been studied for many applications due to their unique characteristics. For example, some CNTs are a few micrometers long with the diameter of 1~25nm. A remarkably robust nanoscale composition with such a high aspect ratio can enable high strength structures [**2**]. Also, the outstanding electrical, mechanical, and chemical characteristics create possibilities for various applications in nanoscale sensing and actuation [**3-6**]. For device applications, highly ordered nanoscale structures of CNTs often need to be integrated with microscale systems for input/output functions. Material testing, for example, requires a movable stage fabricated by micromachining [**7**]. Figure 1 shows an example configuration for chemical sensing by electromechanical transduction. The CNT deposited in the gap is driven into resonance by either an electrostatic or electromagnetic force. The resonance characteristic can be readily altered by an extremely small amount, e.g, countable number, of molecular deposits by reaction with a functionalized surface. For these kinds of device applications, nanoscale gaps (50-500nm) are essential to mechanically support CNTs, to provide actuation, and to receive the electro-mechanical response of CNTs.

It has been shown that CNTs could be positioned by growing them across a gap [**8**]. This process, however, needed very accurately patterned catalyst sites and a high temperature over 900°C. Also, an electric field had to be provided to control the direction of deposition, which raises the issue of providing a voltage on a sample inside a high-temperature, closed chamber. This paper presents new techniques for fabricating nanoscale gaps based on micro-lithography and assembling CNTs across these gaps at a room temperature in an open environment. Unlike serial process such as electron beam lithography, the proposed nano-gap fabrication method can be readily combined with current micromachining techniques, and applied to batch production. CNTs dispersed in a solution were directionally deposited across these gaps guided by an electric field.

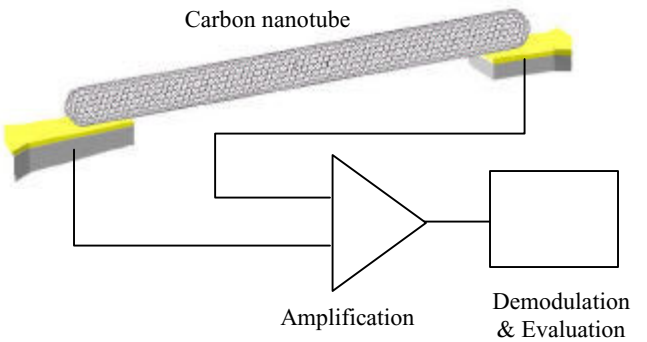

Figure 1. *Carbon-nanotube-based sensor*

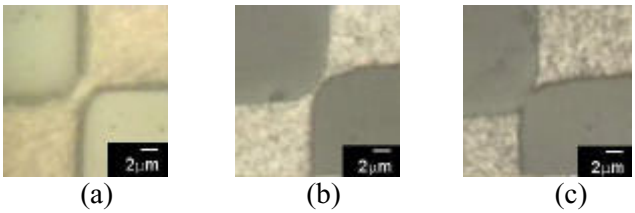

Figure 2. *Sharp gap fabrication by Al etching (a) initial etching (b) additional etching (c) necking and gap creation*

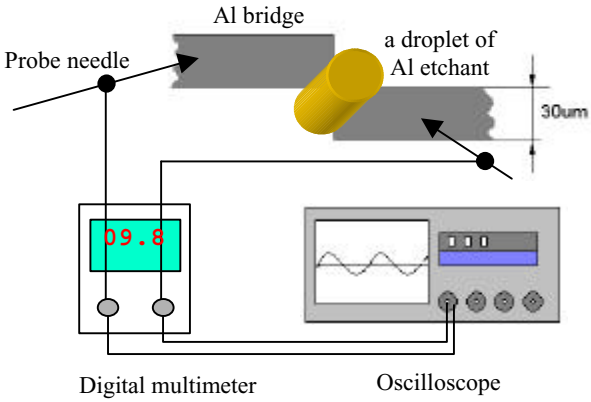

Figure 3. *The monitoring of Al etching*

*Travel support has been generously provided by the Transducers Research Foundation and by the DARPA MEMS and DARPA BioFlips programs.

FABRICATION PROCESS

Two kinds of gaps - a sharp gap and a round gap - were fabricated in this paper. A sharp gap was fabricated by a two-step etching of Al, and a round gap was made by reversing an Al bridge pattern with a lift-off process.

Figure 2 shows the two-step etching process used to create a sharp gap. Al (1200Å) was deposited on a SiO_2 layer and patterned after lithography with ~4μm pattern overlap. The Al layer was initially etched by a wet etchant at 23 °C until a ~2μm wide pattern remained due to undercutting (a). After the initial etching and rinsing, a drop of Al etchant was used to further etch the bridge-shaped pattern (b). Figure 3 shows an experimental setup to monitor the etching rate with an ohm-meter. Subsequent necking occurred, and a sharp gap was created (c).

It was found that even though the total etching time to create a gap may vary much, the fluctuation of etching rate during the final ten minutes is relatively small. We speculate that this is attributed to the reaction-limited process due to the decrease in etching product shortly before the gap is opened. Figure 4 shows the reciprocal of the etching rate (rate of decreasing resistance) determined by measured resistance. The etching rate was not consistent until the value was over 5min/Ω, but its variation afterward was small enough to be considered uniform.

The gap size thus could be controlled by the etching time

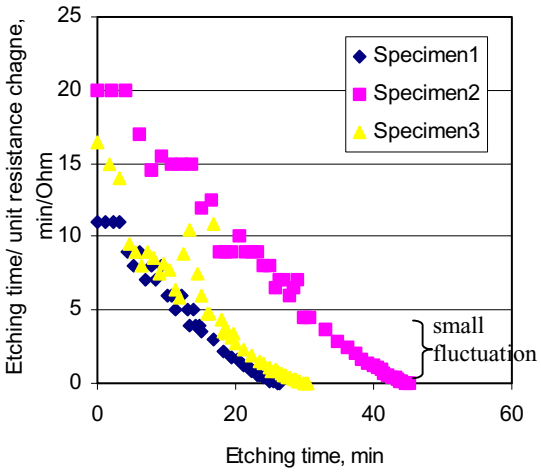

Figure 4. *Etching time vs. etching time/unit resistance change (R^{-1})*

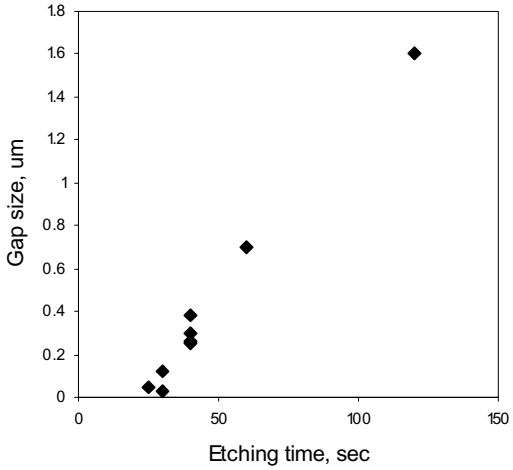

Figure 5. *Terminal etching time vs. the size of a sharp gap*

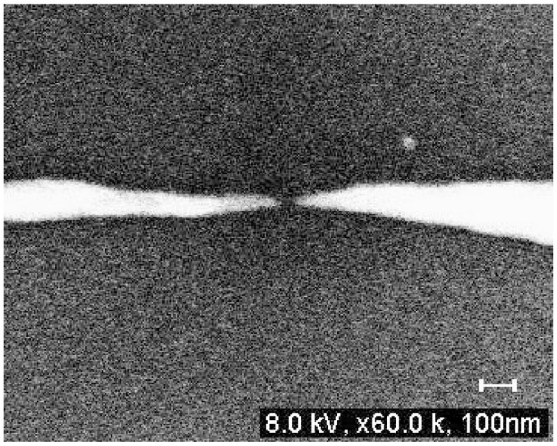

Figure 6. *The sharp gap of 50 nm*

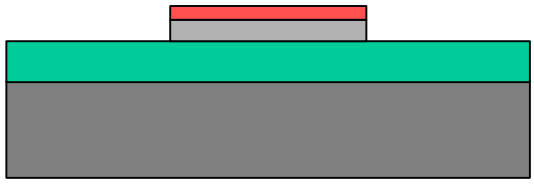

(a) LPCVD Si_3N_4 and Al patterning

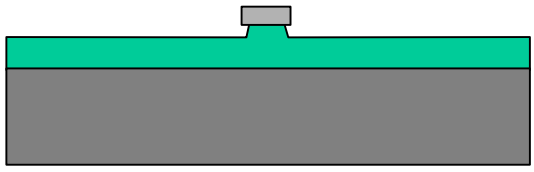

(b) Al horizontal etching and Isotropic RIE

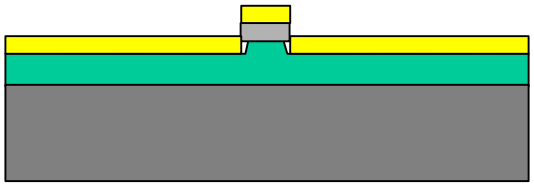

(c) Cr deposition

(d) Al lift-off in Al etchant

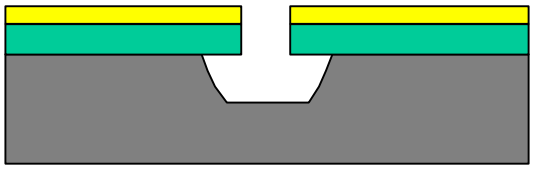

(e) Anisotropic RIE and HNA etching

Figure 7. *Round gap fabrication process*

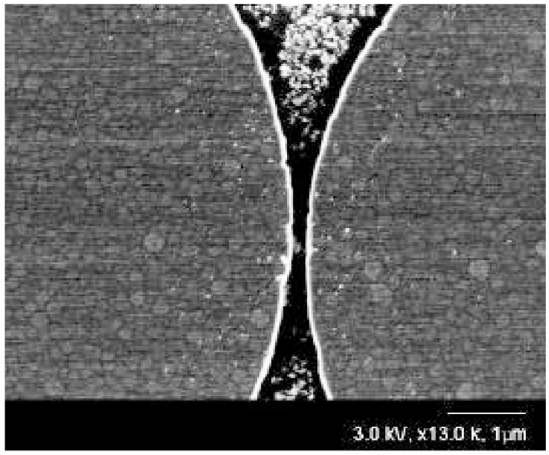

Figure 8. *The round gap of 150 nm*

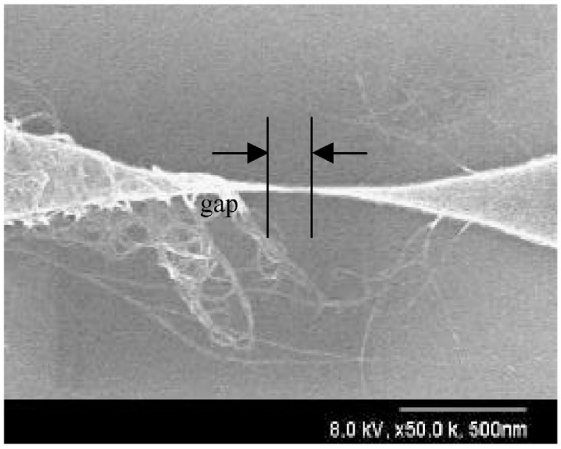

Figure 9. *Carbon nanotube deposition in a sharp gap by AC electrophoresis*

measured from the moment when the resistance of the Al bridge went to infinity. Figure 5 shows the relationship between the etching time after the gap opening and the gap size. Under 50 seconds of etching time, gap sizes smaller than 500nm were obtained. The smallest sharp gap fabricated by this method was 20nm, and a 50nm gap is shown in Figure 6.

A round gap was also fabricated to test different types of electric fields. For example, a relatively straight electric field could be formed between the round electrodes for more highly ordered deposition of CNTs.

The round gap was fabricated with the pattern reversal of Al bridge shape as shown in Fig. 7. On top of the low stress Si_3N_4 (4000Å), Al (1200Å) was deposited and a bridge (immediately before a gap was formed) shape was created by the method described previously. Reactive ion etching (RIE) was used to undercut Si_3N_4, and Cr (500 Å) was then non-conformally deposited. The Al was removed together with the overlying Cr layer in Al etchant at 50°C (lift-off). Finally a round gap was created by the RIE of Si_3N_4 and etching of Si in HNA ($HF+HNO_3+CH_3COOH$).

The gap size was determined by the width of Al bridge prior to Cr deposition. The smallest gap size obtained by this method was ~150nm, shown in Figure 8. The depth of the trench between electrodes is 1.5μm.

CNT DEPOSITION

For the assembly of CNTs over a gap, either a growth method or a deposition method can be used. A CVD growth method has been proposed to fabricate a free standing SWCNTs between the posts [**9**]. Recently, an electric field was applied to align CNTs during their growth on electrodes, since thermal vibration and gas flow can randomize the orientation of CNTs [**8**]. However, this method can limit the freedom of device fabrication by the growing conditions. Electrodes with high melting temperature metal were needed, and catalysts should be precisely patterned on top of electrodes. Also, specimens require extremely clean experimental conditions to prevent the generation of amorphous hydrocarbons.

On the other hand, CNT deposition can also be accomplished by dispersing CNTs in a solution and applying an electric field to attract CNTs between electrodes [**10**]. In the solution, CNTs as well as other particles may be attracted by a dipole moment, $p=ql$, where q is electric charge and l is the length of a CNT. However, it was found that CNTs are slowly attracted by a DC electric field and many unwanted particles in the CNT solution are more easily deposited. CNTs could be easily attracted by a high-frequency (~ 5MHz) AC field. In this case, round particles, such as catalysts and amorphous carbon debris, were not attracted, and could be excluded in the deposition process [**11**].

In our process, SWCNTs were dispersed and suspended in a dichloro-benzene solution. Subsequently, the solution was sonicated for several hours in order to untangle the CNT ropes. After sonication, one drop of CNT solution was placed on the gap and an electric field of 5kV/cm @10MHz was applied. The electric field was applied until the solution was completely evaporated, and images were taken by scanning electron microscopy (SEM).

Figure 9 shows a bundle of entangled CNTs deposited across the sharp gap. Since a round electric field was formed around the electrodes, a bundle of CNTs was deposited along the electric field. Small particles were gathered by stronger electric fields between sharp electrodes. It is believed that the sharp gap is not suitable for CNT deposition, but is better for nanoscale particle deposition.

Figure 10 shows the deposited CNTs across the round gap. In this case, CNTs were deposited with a more regular pattern, and were suspended across the gap. Compared with CVD methods, the suggested deposition steps can be performed at a room temperature in an open environment, thus providing more process freedom. A more refined process to deposit a single CNT is being developed. Various configurations for device application and fundamental experiments can be conceived by the proposed method.

CONCLUSION

New techniques for fabricating nanoscale gaps based on micro-lithography were proposed. A sharp gap was fabricated by two-step wet etching of an Al thin film. A round gap was created by reversing an Al bridge pattern with lift-off. The smallest gaps fabricated by this method were 20nm for a sharp gap and 150nm for a round gap. The fabrication steps yielded consistent results.

CNTs dispersed in dichloro-benzene were deposited across the fabricated gaps by AC electrophoresis. A bundle of entangled CNTs were deposited across the sharp gap, and more ordered CNTs were deposited across the round gap. The proposed method can be used for various device applications and fundamental experiments.

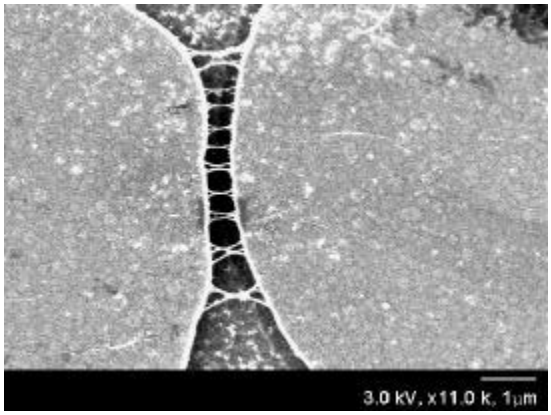

(a) top view

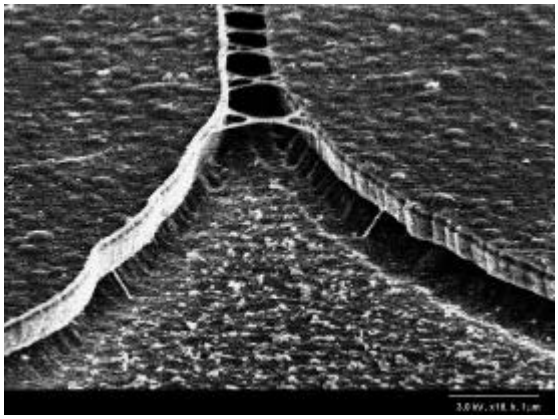

(b) side view

Figure 10. *Carbon nanotube deposition on a round gap by AC electrophoresis*

REFERENCES

1. S. Iijima, "Helical microtubules of graphite carbon", *Nature*, 354, 56 (1994)

2. S. Akita, Y. Nakayama, S. Mizooka, Y. Tkano, T. Okawa, Y. Miyatake, S. Yamanaka, M. Tsuji, and T. Nosaka, "Nanotweezers consisting of carbon nanotubes operating in an automic force microscope", *Appl. Phys. Lett.* 79(11), 1691 (2001)

3. Y. Ren and D. L. Price, " Nuetron scattering study of H_2 adsorption in single walled carbon nanotubes", *Appl. Phys. Lett.* 79, 3684 (2001)

4. P. G. Collins, K. Bradley, M. Ishigami and A. Zettl, "Extreme oxygen sensitivity of electronic properties of carbon nanotubes", *Science* 287, 1801 (2000)

5. J. Kong, N. R. Franklin, C. Zhou, M. G. Chopline, S. Peng, K. Cho and H. Dai, "Nanotube molecular wires as chemical sensors", *Science*, 287, 622 (2000)

6. M. F. Yu, O. Lourie, M. J. Dyer, K. Moloni, T. F. Kelly, and R. S. Ruoff, "Strength and Breaking Mechanism of Multiwalled Carbon Nanotubes Under Tensile Load", *Science*, 287, 637 (2000)

7. M. F. Yu, M. J. Dyer, G. D. Skidmore, H. W. Rohrs, X. K. Lu, K. D. Ausman, J. R. Von Ehr, and R. S. Ruoff, "Three-dimensional manipulation of carbon nanotubes under a scanning electron microscope", *Nanotechnology*, 10, 244 (1999)

8. Y. Zhang, A. Chang, J. Cao, Q. Wang, W. Kim, Y. Li, N. Morris, E. Yenlimez, J. Kong, and H. Dai, "Electric-field-directed growth of aligned single-walled carbon nanotubes", *Appl. Phys. Lett*., 79(19), 3155 (2001)

9. A. M. Cassell, N. R. Franklin, T. W. Tombler, E. M. Chan, J. Han, and H. Dai, "Directed growth of free-standing single-walled carbon nanotubes", *J. Am. Chem, Soc*, 121, 7975 (1999)

10. K. Yamamoto, S. Akita and Y. Nakayama, "Orientation and purification of carbon nanotubes using ac electrophoresis", *Appl. Phys*. 31, L34, (1998)

11. X. Q. Chen, T. Saito, H. Yamada, and K. Matsushige, "Aligning single-wall carbon nanotubes with an alternating-current electric field", *Appl. Phys. Lett*., 78(23), 3714 (2001)

ACKNOWLEDGEMENT

The authors appreciate support from the Office of Naval Research (ONR) Miniaturized Intelligent Sensors Program (MIS).

A PASSIVE-TELEMETRY-BASED PRESSURE SENSING SYSTEM

Andrew DeHennis and Kensall D. Wise

NSF Engineering Research Center for Wireless Integrated MicroSystems
Department of Electrical Engineering and Computer Science
The University of Michigan, Ann Arbor, MI 48109-2122

ABSTRACT

This paper presents a wireless battery-free pressure sensing system. The system utilizes a bulk micromachined capacitive pressure sensor along with a capacitive interface circuit implementing passive absorption telemetry. The pressure transducer is based on the dissolved wafer process and has been designed to test the scalability of polysilicon-to-glass anodic bonding. The sensors have been fabricated realizing a 100μm-wide bonding ring sealed at wafer level. The sensor interface implements a capacitance-to-frequency converter with a sensitivity of 377Hz/pF for readout of the capacitive pressure sensor and reference capacitors. The wireless system utilizes inductively coupled power and frequency-encoded backscatter modulation for transmission of sensor readout data.

INTRODUCTION

Wireless data gathering systems have the potential to restructure the instrumentation used in a variety of industries, including security, health care, and transportation. In looking at the possibilities for the implementation of telemetry, we find two methods: active telemetry and passive telemetry. Active telemetry provides two-way communication over a long range [1]; however, systems usually consume a relatively large volume and have a finite lifetime due to battery limitations. Passive telemetry reduces the transmission distance; however, it does allow the implementation of battery-free wireless devices. There are currently two methods of implementing passive telemetry systems. One method uses a fully passive sensing device that shifts the resonant frequency of an LC tank and can be monitored through a wireless link [2]. Implementing circuitry with the wireless device, passive telemetry can modulate a reflected load to the remote powering transceiver [3,4]. Radio Frequency Identification (RFID) devices have commercialized passive telemetry systems for the readout of wireless, battery-free tags for applications in tracking and security, among others [5]. Extending this technology in its integration with sensors and actuators then begins to allow a whole range of applications. MEMS technology is laying the groundwork for the practical realization of such devices in its development of fabrication processes that allow for full integration of the system at the wafer level [6]. Wireless passive telemetry systems based on the integration of MEMS and RF backscatter modulation have been realized for neural recording [7] and intraocular pressure monitoring [8]. A passive wireless system that provides sensing capability needs not only the implementation of passive telemetry circuitry but also the realization of both the sensor interface circuitry and the sensors themselves. Current work on the integration of passive telemetry with sensing systems aims to define the size/range/power tradeoffs for such devices.

THEORETICAL ANALYSIS

The two essential parts of passive telemetry systems are the ability to couple power to the wireless system and the ability to recover the modulated backscattered signal. Previous work has presented the theory governing the power transmission through inductive coupling [2,5,7,9]. This investigation has focused on an analysis of the modulated backscattering transmission technique, looking at an inductively coupled parallel LCR tank (representing the wireless monitoring system) and the remote powering and data-receiving antenna [3]. The equivalent circuit model for this system is shown in Fig. 1. The modulated backscattering technique is

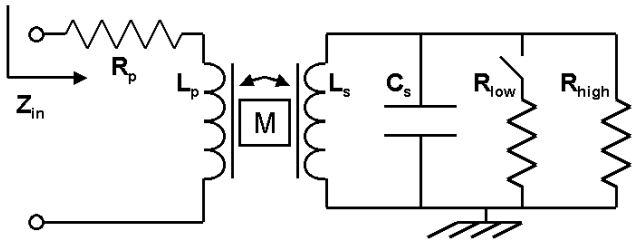

Fig. 1: *Equivalent circuit model for passive absorption telemetry, generating a modulated load for the primary antenna.*

implemented by switching between an equivalent high-Q LCR tank and an equivalent low-Q LCR tank. Analysis of the input impedance of the coupled primary inductor at the resonant frequency of the secondary LC tank reveals

$$Z_{in}(\omega_0) = R_P + \omega_0 L_P\left(i - ik^2 + k^2 Q_{\text{tank}}\right) \qquad (1)$$

where R_p and L_p are the respective resistance and inductance of the primary antenna, k is the coupling coefficient between L_P and L_S [2,5], and Q_{tank} is the quality factor of the parallel LCR tank defined at resonance by

$$Q_{\text{tank}} = R_{load}\sqrt{\frac{C_S}{L_S}} \qquad (2)$$

where R_{load} represents the load for the coupled wireless system defined by R_{high} when the loading switch is open and R_{low} when the loading switch is closed. The backscattered signal can be found by the difference between the two states such that

$$\Delta Z_{in}(\omega_0) = \left|Z_{in}(\omega_0, Q_{high})\right| - \left|Z_{in}(\omega_0, Q_{low})\right| \qquad (3)$$

where Q_{high} and Q_{low} are the quality factors (Q_{tank}) of the loaded and unloaded parallel LCR tanks, respectively. When applied to a passive telemetry system, the primary inductor is also responsible for inductively coupling power to the wireless system. Thus, a high-powered AC signal is generated into L_p through the external circuitry [7,9]. The modulated loading of the parallel LCR tank reflects an amplitude modulation (AM) on the carrier. The received signal can be defined by the percent modulation of the carrier by

0-9640024-4-2/hh2002/$20©2002TRF
DOI 10.31438/trf.hh2002.42

$$\frac{\Delta V_{AM}}{V_{carrier}} \cong \frac{\Delta Z_{in}(\omega_0)}{\left|Z_{in}(\omega_0, Q_{high})\right|} \quad (4)$$

where V_{AM} is the modulation voltage and $V_{carrier}$ is the amplitude voltage of the carrier waveform, thus defining the received AM signal at the readout antenna for modulated backscattered data transmission. Eq. (4) realizes the signal received by the remote powering antenna is a function of the carrier frequency defined by the resonance of the wireless device and the external transmitter, the coupling coefficient, k, the passive loading resistance, R_{low}, and the power consumption of the circuit represented by R_{high} and defining Q_{high}.

SYSTEM DESIGN

The system-level implementation of this wireless device has been designed to simplify the on-chip functionality needed, providing only readout and transmission of the sensor and reference information. This approach minimizes both the power consumption and the die area needed to implement the interface circuit for the wireless system. A block diagram for the passive telemetry system is shown in Fig. 2. The pressure

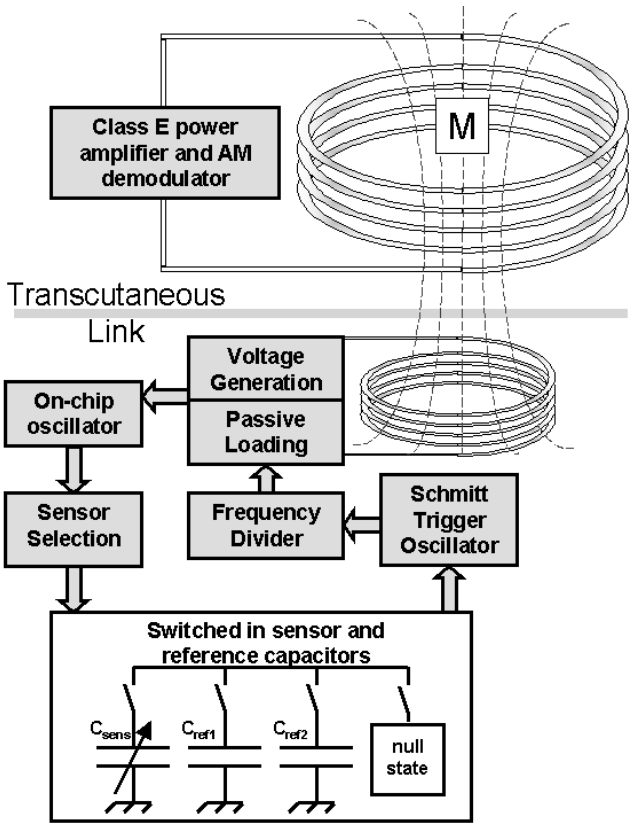

Fig. 2: *Block diagram of the wireless pressure sensing system*

sensors used in this system are capacitive transducers. The capacitive signal from the transducer is digitized by the use of a capacitance-to-frequency (C-F) converter, which is implemented with a Schmitt-input ring oscillator with complimentary pass gates to provide the switching between the sensor, the reference capacitors, and the null state. The switchable C-F conversion and frequency-division circuitry is shown in Fig. 3. The oscillation frequency of the C-F converter can be found by [10]

$$f_{osc} = \frac{I_o}{2V_h C_{sens}} \quad (5)$$

where V_h is the hysteresis of the Schmitt input stage, C_{sens} is the sensor capacitance, and I_o is the charging current determined by the output impedance of the drive transistors and the regulated power supply voltage. In passive telemetry applications, the regulated power supply can suffer from a high level of ripple due to rectified carrier feedthrough [3]. The implementation of the

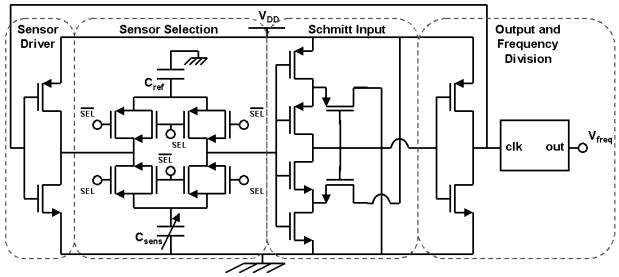

Fig. 3: *A schematic of the switchable Schmitt trigger oscillator used for capacitance to frequency conversion.*

Schmitt trigger oscillator provides a sensor interface that will not suffer from V_{dd} ripple sensitivity as long as the ripple is kept below the V_h hysteresis of the Schmitt input. The output of the oscillator is then used as the input to a frequency divider that generates a 50% duty-cycle digital square wave.

There is a second on-chip oscillator, which is fed into a frequency divider and a 4-bit decoder. The decoded signal is used to select the C-F readout to read one of four states: sensor readout, reference high, reference low, and a null state [11]. These four states are essential for wireless communication with the system. Reading of the two reference capacitors is necessary in order to compensate the system for temperature drift [12] and fluctuations in the availability of power for the wireless device [8,11]. Since switching between these states is done through an on chip oscillator, the null state is used to synchronize the coupled systems. The digital frequency-encoded information for the sensor and reference capacitors can then be sent to the RF front end of the system for transmission via absorption modulation. For battery-free operation, a remote power source must be nearby in order to generate the RF carrier. The wireless system includes a resonant LC tank at the front end followed by a full-bridge rectifier. There is an added diode to protect the regulated signal from any power fluctuations caused by the actively loaded LC tank. The RF front end of the system is shown in Fig 4. The absorption modulation is done using the digital frequency output of the C-F converter to actively load the LC tank of the wireless system in controlling the switching of the shunting transistor M_{load}, which is the absorption modulation loading transistor. When the M_{load} transistor is open, the system couples rectified power through the blocking diode,

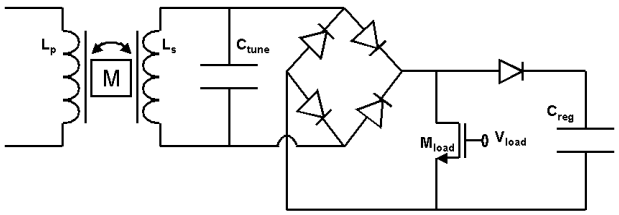

Fig. 4: *Schematic of the RF front end showing the rectification and load modulation implementation*

charging up C_{reg}, which is the capacitor that provides power to all of the on-chip circuitry through the entire AC cycle and through

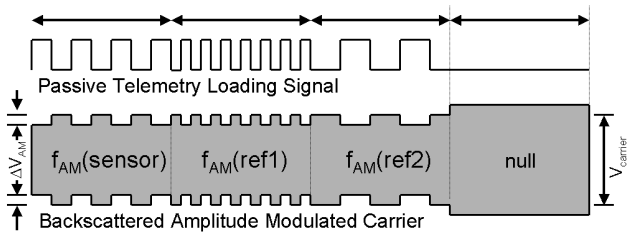

Fig. 5: *AM frequency-encoded waveforms for the sensor readout of the wireless microsystem*

the entire loading state. When the transistor is in the on state, the LC tank of the wireless system is shunted, which then generates a reflected load on the remote powering antenna. The transmission of the sensor and reference data is encoded in the amplitude modulation frequency. A visualization of the transmission protocol for the modulated backscattered signal is shown in Fig. 5. The system uses a Class E power amplifier [7,9] to generate the RF remote carrier with an added AM demodulator for decoding of the reflected loading signal [5]. The bandpass demodulator is set to filter out the high frequency carrier and the DC offset of the resonant power amplifier. The signal is then digitized for further filtering and digital signal processing. An initial hardware filter is needed due to the relatively large voltage levels on the resonant node of the transmitter.

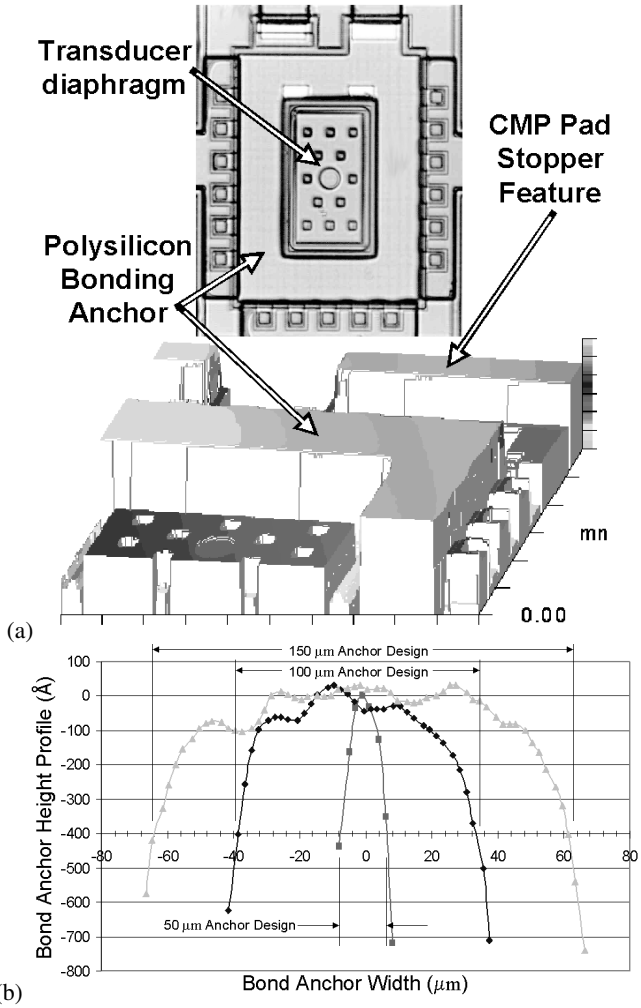

Fig. 6: *(a) Silicon side of the capacitive pressure sensor before anodic bonding, (b) the effects of CMP on three different size anchor widths*

TRANSDUCER DESIGN AND FABRICATION

The pressure transducers were fabricated using an anodically bonded silicon-on-glass process. The structure utilizes a two-layer polysilicon process to form hermetic feedthroughs to a sealed cavity [6,12] and a 4μm-thick boron-doped diaphragm. A polysilicon-bonding ring is utilized to seal the cavity during the anodic bonding process. Chemical Mechanical Polishing (CMP) is used to decrease the surface roughness of the polysilicon to below 500Å, which is needed to provide a uniform bond [12,13]. The CMP process has width scaling limitations due to the rounding of edges caused when polishing structures that have high topology, such as the recessed-cavity pressure sensors. The transducers were designed to allow an investigation of the experimental limitations in scaling the bonding anchor width using this process. Pad stopper features were used to minimize the rounding effect that the CMP process had on the bonding ring [14]. The pre-bonded capacitive pressure transducer is shown along side an optical plot of the anchor areas and pad stopper features in Fig. 6(a). The pressure transducer has been fabricated with a surface micromachined plate inside the cavity to increase the sensitivity per unit area of the diaphragm [6]. A contour map was developed using optical spectroscopy across the polysilicon anchor areas before deposition of low temperature oxide [12], from which the CMP rounding effect is shown in Fig. 6(b). Anodic bonding tolerates a step height of no more than 50nm [13], which decreases the effective bonding width of the three anchor designs. The 150μm, 100μm and 50μm anchor widths decreased to approximately 125μm, 70μm, and 15μm, respectively, due to CMP. Uniform bonding rings around the anchors were only realized with the 100μm and 150μm designs. A uniform bond ring around the cavity was not achieved with the 50μm design, most likely due to the high amount of rounding on that design. The final design dimensions of the transducer diaphragm are 300μm x 500μm. This design achieved a 0.5mm x 0.75mm x 0.5mm pressure sensor, sealed at wafer level. The sensor has a sensitivity of 0.2fF/mmHg, operating over a pressure range from 600 to 1000mmHg.

RESULTS

The passive telemetry interface circuit was fabricated using a 3μm BiCMOS process (Fig. 7). On-chip poly-to-poly power

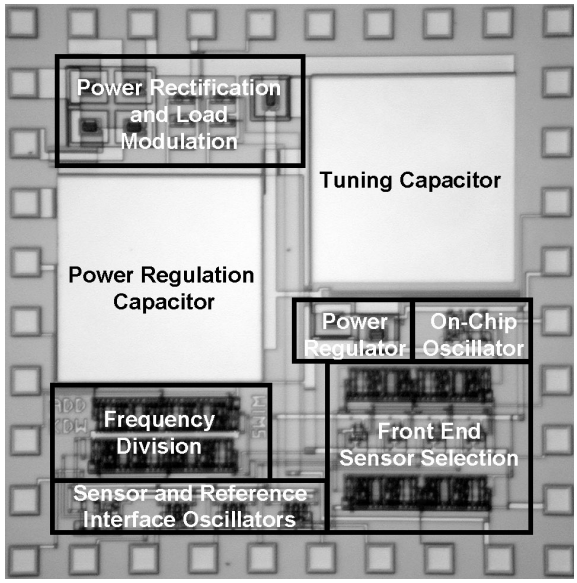

Fig. 7: *Photograph the 2mmx2mm passive-telemetry capacitive interface circuit realized using a 3μm 2P/1M BiCMOS process*

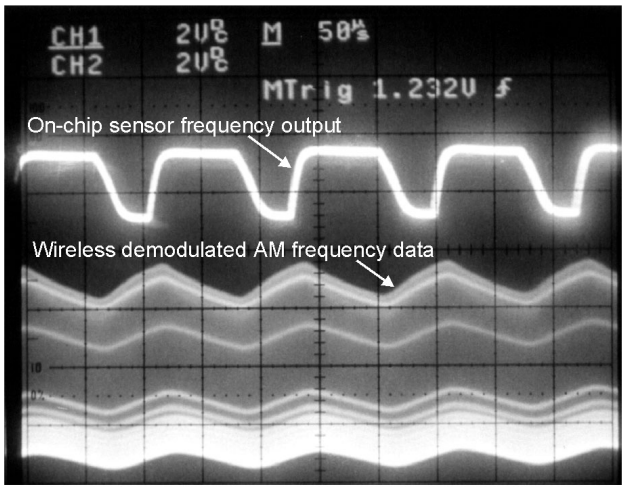

Fig. 8: *Wireless system testing showing internal frequency output of the wireless system as well as the wirelessly received, first-order demodulated reverse telemetry signal.*

regulation capacitors have been fabricated on-chip to allow for continuous functionality of the interface circuitry though the loaded and unloaded states of the system. Results from wireless testing using a Class E amplifier running at 800kHz are shown in Fig. 8. Testing has shown the power consumption of the interface circuit to be 1mW running at 3V, which sets R_{high}=18kΩ for the high-Q state of the passive telemetry. The measured low-Q state for this system finds R_{low}=433Ω. An analysis of the percent modulation of this system predicted by Eq. (4) for a configuration with coupling coefficients scaling from k=0.05 to k=0.025 results in 17% to 2% amplitude modulation of the carrier, respectively. Characterization of the C-F converter (Fig. 9) shows a pressure sensitivity of 377Hz/pF. At close coupling distances, the dominant noise source in the received wireless data is carrier feedthough, which sets the frequency resolution to approximately 30Hz per cycle, without averaging. A higher performance version of this system can be configured using devices designed for higher sensitivity and lower dynamic range [2,12], obtaining a resolution less than 3mmHg.

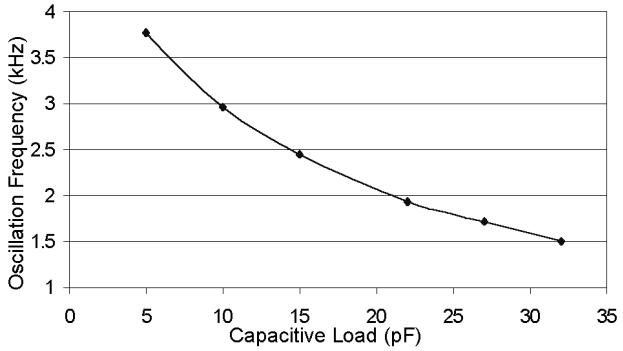

Fig. 9: *Capacitance-to-frequency conversion characteristic of the interface chip with a 3V regulated supply.*

CONCLUSIONS

The design and realization of a battery-free pressure sensing system that utilizes remote inductive powering and passive telemetry has been presented. The theory governing the design of backscattered modulation telemetry devices has been developed. Capacitive pressure transducers have been fabricated realizing 100µm-wide polysilicon-to-glass bonding anchors sealed at wafer level. A passive telemetry interface that provides wireless frequency-encoded sensor readout has been implemented using a capacitance-to-frequency readout from the sensor. The realized circuit has a sensitivity of 377Hz/pF and can wirelessly resolve a capacitance change of less than 80fF at the transducer.

ACKNOWLEDGMENTS

This work is supported by the Engineering Research Centers Program of the National Science Foundation under Award Number EEC-9986866 and by a gift from Ms. Polly Anderson. The authors would like to thank Katharine Beach for her fabrication of the circuit.

REFERENCES

[1] A. M. Leung, *et. al*, "Intracranial Pressure Telemetry System Using Semicustom Integrated Circuits," *IEEE Transactions on Biomedical Engineering*, vol. BME-33, April 1986, pp. 386-395.

[2] A. DeHennis and K. D. Wise, "A Double-Sided Single-Chip Wireless Pressure Sensor," *IEEE Conference on Micro-ElectroMechanical Systems*, Las Vegas, NV, Jan. 2002, pp. 252-255.

[3] Q. Huang and M. Oberle, "A 0.5mW Passive Telemetry IC for Biomedical Applications," *IEEE Journal of Solid State Circuits*, Vol. 33, No. 7, July 1998, pp. 937-946.

[4] Stavros Charzandroulis *et al*, "A Miniature Pressure System with a Capacitive Sensor and a Passive Telemetry Link for Use in Implantable Applications," *Journal of MicroElectroMechanical Systems*, Vol. 9, No. 1, March 2000, pp. 18-23.

[5] K. Finkenzeller, RFID Handbook, John Wiley & Sons Ltd., Chichester, England, 1999.

[6] A. V. Chavan and K. D. Wise, "A Monolithic Fully-Integrated Vacuum-Sealed CMOS Pressure Sensor," *IEEE Conference on Micro-ElectroMechanical Systems*, Jan 2000, pp. 341-346.

[7] T. Akin, K. Najafi, and R. M. Bradley, "A Wireless Implantable Multichannel Digital Neural Recording System for a Micromachined Sieve Electrode," *IEEE Journal of Solid State Circuits*, Vol. 33, No. 1, January 1998, pp. 937-946.

[8] K. Stangel, *et al*, "A Programmable Intaocular CMOS Pressure Sensor System Implant," *IEEE Journal of Solid-State Circuits*, Vol. 36, No.7, July 2001, pp. 1094-1100.

[9] P. Troyk and M. Schwan. "Class E Driver for Transcutaneous Power and Data Link for Implanted Electronics Devices," *Medical and Biological Engineering & Computing*, January 1992, pp. 69-75.

[10] Y. Matsumoto and M. Esashi, "Integrated Silicon Capacitive Accelerometer with PLL Servo Technique," *Sensors and Actuators A*, Vol. 39, 1993, pp 209-217

[11] J. Ji, S. Cho, Y. Zhang, K. Najafi, K. Wise, " An Ultraminiature CMOS Pressure Sensor for a Multiplexed Cardiovascular Catheter," *IEEE Transactions on Electron Devices*, Vol 39, No 10, Oct. 1992, pp. 2260-2267.

[12] A. V. Chavan and K. D. Wise, "A Multi-Lead Vacuum-Sealed Capacitive Pressure Sensor," *Digest Solid-State Sensor and Actuator Workshop*, Hilton Head, June 1998, pp. 212-215

[13] S. Mack, H. Baumann, U. Gosele, "Gas Tightness of Cavities Sealed by Silicon Wafer Bonding," *IEEE Conference on Micro-ElectroMechanical Systems*, Nagoya, Japan, pp. 488-493, Jan. 1997.

[14] A. Chavan, An Integrated High Resolution Barometric Pressure Sensing System, Doctoral Thesis, University of Michigan, 2000

DEVELOPMENT OF ARTIFICIAL LATERAL-LINE FLOW SENSORS

Zhifang Fan, Jack.Chen, Jun Zou, Junjun Li, Chang Liu and Fred Delcomyn*
Micro Actuators, Sensors and Systems Group
Micro and Nanotechnology Laboratory
* Department of Entomology
University of Illinois at Urbana-Champaign, Urbana, IL 61801

SUMMARY

We report the development of an underwater flow sensor that is based on biological inspiration – the biological lateral line sensors. The design, fabrication process and initial testing results for an artificial lateral line sensor are reported. The fabrication is based on a highly efficiently three-dimensional assembly process, used in conjunction with silicon micromachining techniques.

BACKGROUND

Evolved over hundreds of millions of years, many fish species rely on lateral line sensors to monitor surrounding flow fields for maneuvering and survival under water [1]. It is conjectured that fish is equipped with distance touch sense of underwater obstacles, predators, and prey. A lateral line system, shown in Fig. 1, consists of an array of distributed sensor nodes (so called neuromasts) that span the length of the fish body. Each sensor node, in turn, consists of a cluster of *hair cells* embedded in protective, gel-like domes. In certain fish species, the lateral line sensor nodes may be directly exposed at the surface of the skin. In others, the sensor nodes may be hidden in subdermal channels in order to minimize wear and damage. An individual biological hair cell is called a mechanoreceptor. It consists of a vertical cilium attached to a neuron. The fundamental principle of a single haircell is as follows. When the cilium of the haircell is bent by the local fluid flow, the neuron attached to the cilium stretches and produces action potentials.

An array of haircells with different length and hence frequency characteristics reside at each sensor node. This slows fish to extend the dynamic range and frequency spectrum of the environmental awareness.

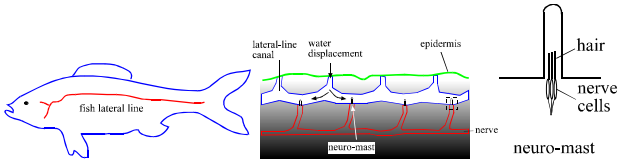

Figure 1: Schematic diagram of fish lateral line sensor system. The lateral line is distributed through the fish body surface. A lateral line consists of many neuronal nodes, called neuro-masts. Each neuromast consists of an array of haircells embedded in a protective dome.

Engineered flow sensors have been developed in the past based on a number of sensing principles, including thermal (hot-wire) anemometry [2], Doppler frequency shift, and indirect inference from pressure differences [3-4]. Hot-wire anemometers use fine heating elements that double as temperature sensors. The local flow rate is inferred from the extent of forced convective heat transfer from the hot wire. The majority of existing hot-wire anemometers are manufactured using macroscopic machining methods. Micromachined hot-wire anemometers have also been developed in recent years [5]. Sensors based on Doppler frequency shifts consist of an acoustic launcher and a receiver. The speed of fluid in between the launcher and the receiver is interpreted using Doppler frequency shift. The overall size of the device is generally large. Existing flow sensors based on pressure distribution measurements also have large sizes and are generally not suitable for forming distributed arrays.

In the past two decades, several research groups have developed micromachined flow sensors that are based on a variety of sensing principles including the three principles mentioned above [6-13]. Microfabrication offers the benefits of high spatial resolution, fast time response, integrated signal processing, and potentially low costs. In addition to flow sensors, boundary-layer shear stress sensors have been realized using floating element methods [14] and thermal transfer principles [15]. However, shear stress sensors are located directly on the fluid-solid boundary and do not provide adequate information about mean stream flow velocity.

This work offers an alternative method for underwater flow sensing. The sensor is uniquely based on biological inspiration. Each sensor covers small footprint and therefore high density integration is possible. The vertical cilium extends into the boundary layer flow instead of residing at the non-slip interface, allowing greater flow sensitivity.

SENSING PRINCIPLE

The schematic diagram of the artificial lateral line sensor is shown in Fig. 2. Each sensor consists of an in-plane fixed-free cantilever with a vertical artificial cilium attached at the distal, free end. External flow parallel to the sensor substrate imparts upon the vertical cilium. Due to rigid connection between the in-plane cantilever and the vertical cilium, a mechanical bending moment is transferred to the horizontal cantilever beam, inducing strain at the base of the cantilever beam. The magnitude of the induced strain can be sensed by many means, for example by using integrated piezoresistive sensors. The overall sensor system may use an array of individual sensory nodes with systematically varying positions, height of cilia, and orientation. Such a distributed sensor array can provide information about flow structure evolution and increase the accuracy of flow field interpretation.

In this paper, we focus on the development and characterization of individual hair-cell-like sensors.

0-9640024-4-2/hh2002/$20©2002TRF
DOI 10.31438/trf.hh2002.43

Solid-State Sensors, Actuators, and Microsystems Workshop
Hilton Head Island, South Carolina, June 2-6, 2002

A comprehensive understanding of the relation between the output (relative change of resistance) and the mean flow velocity must take into consideration many possible flow conditions. For complex situations, it may be necessary to use the finite-element numerical method to estimate the sensor output precisely. A comprehensive treatment on the fluid mechanics aspect is beyond of the scope of this paper, which focuses on the discussion of new design and fabrication methods. Nonetheless, the relationship can be analytically expressed if the flow condition is simple and well defined [16].

As a first-order approximation, the magnitude of the output signal is proportional to u_0^2.

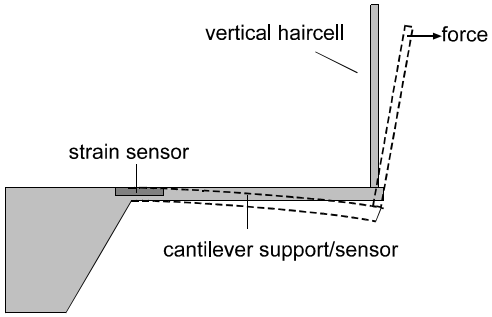

Figure 2: Schematic diagram of a single artificial haircell sensor consisting of a horizontal cantilever with a vertical cilium attached at the free end. We sense the bending of the vertical cilium using the strain sensor located at the base of the horizontal cantilever.

FABRICATION PROCESS

Flow sensors based on flow moment transfer have been reported in the past. The previously reported devices fall into two categories. A first type utilizes monolithic cantilever beams fabricated within the plane of the wafer by using bulk micromachining methods [6]. Such a sensor is not applicable for large array formation, as each sensor must be discretely packaged. A second type utilizes a vertical, high-aspect-ratio cilium that is connected to micromachined force-sensing components [17, 18]. The overall yield and repeatability of the sensor are generally low because the fabrication process is not monolithic.

The PDMA Three-Dimensional Assembly Process

In this study, we leverage a recently developed, efficiently three-dimensional assembly process to realize the vertical cilium, a key component of the hair cell. The vertical cilium is realized using a three-dimensional assembly technique called plastic deformation magnetic assembly (PDMA) [19].

Hair Cell Fabrication Process

The overall fabrication process of the artificial hair cell is discussed in the following and illustrated in Fig. 3. The process begins with deposition of a silicon dioxide layer by thermal oxidation. The oxide layer is patterned and selectively removed to provide openings for forming piezoresistive sensors by the diffusion doping process. Boron pre-deposition is performed at 950°C for 15 min. It is followed by oxidation drive-in at 1100°C for 2 hours, reaching an oxidation thickness of 500 nm (Fig. 3c).

The targeted sheet resistivity of the doped resistor is 100 $\Omega/\square$. The gauge factor of such a doped piezoresistive sensor is a function of the doping concentration and the substrate orientation [20-21]. At such a doping level, the gauge factor is optimized. In addition, the relatively high sheet resistivity allows a relatively large resistance value (on the order of 2-5 kΩ) to be realized within a small device footprint.

The wafer is etched from the backside using wet anisotropic etching or deep reactive ion etching until a silicon membrane with desired thickness is achieved (Fig. 3e). Structures that are pertinent to the PDMA process are then deposited and patterned. We deposit a layer of thin-film copper (300 nm thick) and pattern it photolithographically. A 600-nm-thick gold thin film is deposited by using the lift-off technique. This ensures good step coverage over the boundary of the sacrificial material and minimizes stress concentration. The subsequently electroplated Permalloy material is 10 μm (Fig. 3f) in thickness.

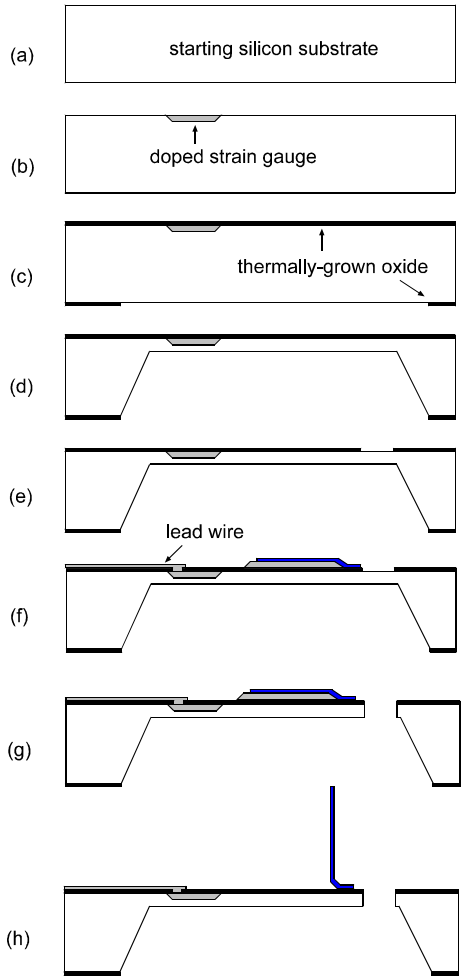

Figure 3: Fabrication process of an artificial lateral line sensor with integrated signal processing units. In the final step, the vertical cilium is assembled into three-dimensional position. It can be further protected and insulated by uniform, conformal deposition of Parylene thin film.

The wafer is then etched from the front side to define the cantilever beams (Fig. 3g). Following this step, the wafer is immersed in diluted HCl solutions to remove the copper

sacrificial layer and to free the cantilever beam. The PDMA process is performed, followed by drying of the wafer (Fig. 3h). The SEM micrograph of a representative device is shown in Fig. 4. The length, width, and thickness of the in-plane cantilever are 1100 μm, 180 μm, and 17 μm, respectively. The height, width and thickness of the vertical cilium are 820 μm, 100 μm, and 10 μm, respectively.

Improvement has been made to the original PDMA process to increase the yield of assembly. The cross-sectional view of the bending region according to the original PDMA assembly method introduces two problems. First, the beam has been prone to breaking during the assembly process due to excessive stress concentration at the step caused by the edge of the sacrificial layer. Secondly, the exact location of bending is uncertain, being between points A and B. This affects the uniformity of the angle of assembled hair-cell cilia.

A structural modification has been proposed and validated (Fig. 5). An extended patch made of 10-μm-thick electroplated Permalloy is electroplated to overlap with the edge of the sacrificial layer. This produces two noticeable improvements. First, the exact location of bending is much more easily controlled. Wse confirmed that the bending occurs at point C. Secondly, bending will not involve the step-coverage region and therefore the stress-induced fracture is removed.

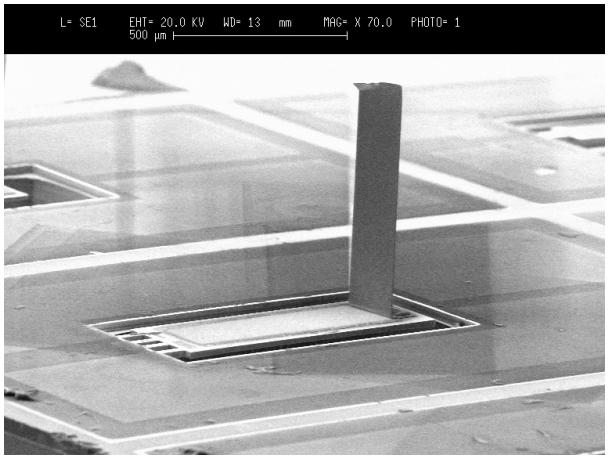

Figure 4: SEM of a single artificial hair cell sensor. The cilium is 820 μm tall.

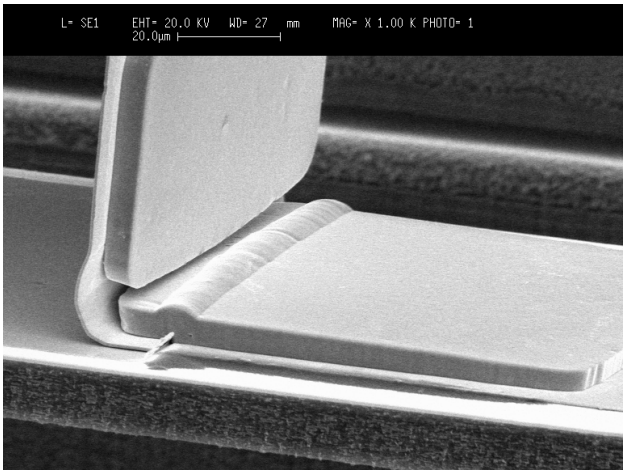

Figure 5: SEM of the plastically bent region at the base of the vertical cilium.

We have demonstrated that it is possible to strengthen the plastically deformed joint of the vertical cilium by using localized electroless plating methods. First, circuit elements and wire leads are protected from shorting by an organic insulator such as the photoresist. A thin layer of electrolessly-plated gold is grown onto the exposed vertical cilium at 95^{o}C for 10 min with the growth rate being approximately 0.3 μm/min.

The fabricated device is coated with 300-nm-thick uniform Parylene deposition for increasing strength and electrical insulation (Fig. 6). The insulating coating allows sensors to operate in conducting fluids. The deposited material, however, increases the force constant of the cantilever beam. The thickness must be optimized with respect to two competing concerns, electrochemical protection and sensitivity.

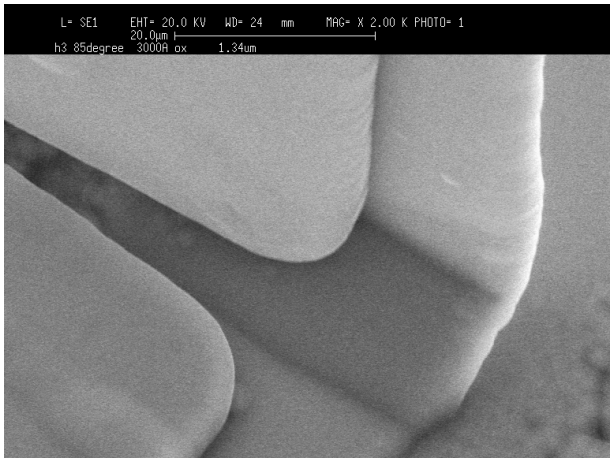

Figure 6: Enlarged view of the plastically bent region coated with Parylene thin film for strengthening and electrical insulation.

RESULTS AND DISCUSSIONS

The sensors are mounted on a thin glass plate, which is placed within a laminar flow water tunnel. One edge of the glass is polished to present a sharp profile facing the flow. The sensor is located 1 mm from the leading (sharp) edge. The flow rate of the water tunnel is varied manually. Laminar flow with u_0 ranging from 0 to 1 m/s passes the sensor element. The flow impacts the cilium at its broad side, i.e., parallel to the long axis of the substrate cantilever. The sensor is biased under constant voltage (1 V) and the output current is monitored. The output response is shown in Fig. 7. The best-fit curve follows a second-order polynomial expression.

We are currently developing arrayed sensors to characterize the response of the sensors with respect to the orientation to the flow and to the height of the artificial cilium. It is believed that in order to increase the sensitivity, one can increase the height of the cilium or reduce the thickness of the in-plane cantilever. However, the vertical cilium should not be excessively tall as this may increase the chance of damage. For long cilia and higher flow rates, the interpretation of flow is more challenging as multiple flow regimes (laminar, transition, or turbulent) may be applied through the length of the cilium. To understand the exact nature and profile of local flow would require multiple-sensor clusters much like the biological sensors.

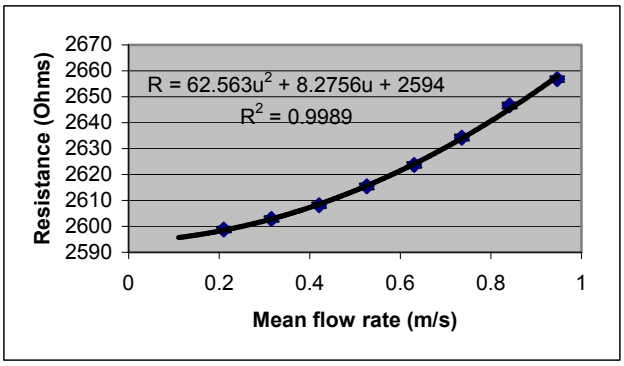

Figure 7: Measurement results showing output current vs. flow rate of a representative sensor under constant voltage biasing.

CONCLUSIONS

We have developed the design and fabrication process of an individual micromachined artificial lateral-line sensor for flow sensing applications. The sensor is realized using combined bulk micromachining methods and an efficient three-dimensional assembly method. Sensors can be strengthened using electroless plating and Parylene conformal coating. They can be realized monolithically using combined bulk micromachining and three-dimensional assembly methods.

ACKNOWLEDGMENTS

The authors wish to thank the sponsors of this research work – AFOSR BioInspired Concepts (BIC) Program, NSF Career Award and NASA.

REFERENCES

1. C.E. Bond, Biology of fishes, 2nd Ed., Saunders (1996).
2. A.E. Perry, Hot wire anemometry, Claredon Press (1982).
3. M. Richter, M. Wackerle, P. Woias, B. Hillerich, "A novel flow sensor with high time resolution based on differential pressure principle," *Proc. 12th Int. Conf. On Micro Electro Mechanical Systems,* Orlando, FL, pp. 118-123 (1999).
4. O.K. Rediniotis, E. Johansen and T. Tsao, "MEMS-based probes for velocity and pressure measurements in unsteady and turbulent flowfields," *Proc. 37th Aerospace Sciences Meeting,* Reno, Nevada (1999).
5. F. Jiang, Y.C. Tai, C.M. Ho, K. Rainer, M. Garstenauer, "Theoretical and experimental studies of micromachined hot-wire anemometer," *Digest IEEE Int. Electron Devices Meetings (IEDM)*, pp. 139-142, San Francisco (1994).
6. N. Svedin, E. Stemme, G. Stemme**,** "A static turbine flow meter with a micromachined silicon torque sensor," Technical Digest (MEMS 2001) *14th IEEE International Conference on Micro Electro Mechanical Systems*, pp.208-11, Interlaken, Switzerland (2001).
7. L. Lofdahl, E. Kalvesten, T. Hadzianagnostakis, G. Stemme, "An integrated silicon based wall pressure-shear stress sensor for measurements in turbulent flows," *Proc. 1996 International Mechanical Engineering Congress and Exposition*, pp. 245-51, New York, NY, USA (1996).
8. N. Svedin, E. Kalvesten, E. Stemme, G. Stemme, "A new silicon gas-flow sensor based on lift force," *Journal of Microelectromechanical Systems,* vol.7, no.3, pp.303-8, (1998).
9. T. Ebefors, E. Kalvesten, G. Stemme, "Three dimensional silicon triple-hot-wire anemometer based on polyimide joints," *Proc. Eleventh Annual International Workshop on Micro Electro Mechanical Systems*, pp.93-98 (1998).
10. E. Kalvesten, C. Vieider, L. Lofdahl, G. Stemme G, "An integrated pressure-flow sensor for correlation measurements in turbulent gas flows," *Sensors & Actuators A-Physical*, Vol. A52, No.1-3, pp. 51-8 (1996).
11. P. Enoksson, G. Stemme, E. Stemme, "A Coriolis mass flow sensor structure in silicon," *Proceedings. The Ninth Annual International Workshop on Micro Electro Mechanical Systems*, Machines and Systems, pp.156-61 (1996).
12. L. Lofdahl, G. Stemme, B. Johansson, "Silicon based flow sensors used for mean velocity and turbulence measurements," *Experiments in Fluids*, Vol.12, No.4-5, pp.270-6 (1992).
13. G.T.A. Kovacs, Micromachined transducers sourcebook, McGraw-Hill (1998).
14. Padmanabhan, H. Goldberg, K.D. Breuer, M.A. Schmidt, "A wafer-bonded floating-element shear stress microsensor with optical position sensing by photodiodes," *J. Microelectromechanical systems*, Vol. 5, No. 4, pp. 307-15 (1996).
15. Y. Xu, F. Jiang, Q. Lin, J. Clendenen, S. Tung and Y.C. Tai, "Under water shear stress sensor," *Fifteenth IEEE International Conference on Micro Electro Mechanical Systems (MEMS '02)*, Las Vegas, USA, (2002).
16. F.M. White, Fluid mechanics, 4th Edition, McGraw-Hill (1999).
17. J. Ayers, P.M. Zavracky, N. McGruer, D. Massa, V. Vorus, R. Mukherjee, S. Currie, "A modular behavioral-based architecture for biomimetic autonomous underwater robots," *Proc. of the Autonomous Vehicles in Mine Countermeasures Symposium. Naval Postgraduate School*, CD ROM (1998); world-wide-web site http://www.cis.plym.ac.uk/cis/InsectRobotics/biomimetics.htm.
18. Y. Ozaki, T. Ohyama, T. Yasuda, I. Shimoyama, "An air flow sensor modeled on wind receptor hairs of insects", *Proc. MEMS 2000*, pp. 531-6, Miyazaki (2000).
19. Jun Zou, J. Chen and C. Liu, "Plastic deformation magnetic assembly (PDMA) of out-of-plane microstructures: Technology and application," *IEEE/ASME Journal of MEMS*, Vol. 10, No. 2, pp. 302-309 (2001).
20. W.G. Pfann and R.N. Thurston, "Semiconducting stress transducers utilizing the transverse and shear piezoresistance effects," *J. Appl., Phys.*, Vol. 32, No. 10, pp. 2008-19 (1961).
21. S.V. Spoutai, "Practical model for electrical properties of highly doped p-type polysilicon," *4th International Conference on Actual Problems of Electronic Instrument Engineering Proceedings. APEIE-98*, pp. 27-29, Novosibirsk, Russia (1998).

THEORY, EXPERIMENTAL REALIZATION, AND PROPERTIES OF MINIATURE BRAGG FIBERS

J.G.Fleming, Shawn-Yu Lin, and Ronald Hadley
MEMS and Novel Silicon Technologies, Sandia National Laboratories
Albuquerque, NM, 87185-1080

ABSTRACT

This paper outlines our work on the theory, experimental realization and properties of miniature Bragg fibers. These structures were proposed over 20 years ago and consist of hollow tubes in which light is guided in a low index media (air) and confined by surrounding Bragg mirror stacks. The thicknesses of high and low index layers making up the mirror stacks have been determined theoretically. Structures with internal diameters from 5 to 30 microns have been fabricated and much larger structures should also be possible. We have demonstrated the fabrication of these structures with short wavelength band edges ranging from 400 to 1600nm. There may be potential applications for such structures in the fields of integrated optics and BioMEMS.

INTRODUCTION

The propagation of long wavelength, millimeter scale radiation through hollow waveguides is well known. Less well know are proposals in the 1960's to used hollow metal structures to propagate short wavelength light [1]. This field died out with the development of glass optical fibers. There is also interest in various coated hollow metal fibers for the propagation of 10-micron radiation for medical applications [2-6]. The inside hollow diameter of these metallic structures is typically on the order of a millimeter. Yariv and coworkers first proposed Bragg fibers in 1978 [7]. Several other groups have recently revisited the idea of Bragg fibers [8-10]. In most cases the application being considered is that of optical fibers. Such fibers potentially have very low losses, in theory considerably less than that of standard silica fibers. However, this extremely low loss behavior is only exhibited by a particular mode, the TE_{01}, which does not propagate in standard fibers. In our work we are interested in the development of miniature Bragg fibers with inner diameters in the order of 1-200 microns. These fibers are fabricated in the plane of the wafer using modifications of standard silicon processes. We are interested not in the very low loss applications associated with optical fiber communications, but rather applications associated with integrated optics and BioMEMS where losses on the order of 1-5dB/cm may be acceptable. Potential advantages of this approach in the field of integrated optics include: elimination of end facets, ease of integration with index matching and other fluids and possible development of novel thermo-optical structures. Potential advantages in the area of BioMEMS include the guiding of light and liquids in the same platform.

THEORY

Typical waveguides guide light as the result of a difference in refractive index between two low loss optical media. Light is confined in such structures to the higher index media. The greater the index contrast between the low and high index media the greater the level of confinement. The greater the confinement the smaller the radius of curvature which can be defined without loss of light from the guide. The smaller the radius of curvature the smaller the size of the final part. However when light is tightly confined, its mode in the waveguide is very small and it becomes difficult to couple light into and out of the low index contrast optical fibers, which are the backbone of optical communications. The guiding principle of Bragg fibers is fundamentally different. In this case light propagates in a low index material, air, and is confined by a dielectric mirror. Compact bends can be realized using dielectric mirrors. The mode size for single mode propagation is on the order of a micron. However, in certain cases these structures can be made effectively single mode [9]. The efficiency of the mirror stacks used to confine the light is dependent on the index contrast between the high and low index materials making up the mirror. In the case of high index contrast systems such as silicon (n~3.5) and silicon dioxide (n~1.46) only three pairs of layers result in reflectivity's greater than those of metals over a very large range of wavelengths. Also, in the case of these high index contrast systems, the mirrors are effective for all angles of incidence. The thickness of higher refractive index layers making up the mirror stack is very similar to those given by that of a 1/4-wave stack, the wavelength divided by four times the index of refraction. Optimal layer thickness targeted at a wavelength of 1.5 microns lower wavelength band edge, are 0.36 microns for SiO_2, 0.11 microns for Si and 0.21 microns for SiN. Such an arrangement results in low losses in the TE mode, but high losses for TM modes. TM mode losses can be reduced without greatly increasing TE mode losses by doubling the thickness of the inner most layer. Losses for these dimensions at 1.5 micron wavelengths for a 4 pair Si/SiO2 mirror stack are predicted to be on the order of 3dB/cm for TM and 0.2 dB/cm for TE. Losses can be reduced by increasing the number of layers and can be greatly reduced by propagating only the TE_{01} mode in a ~13 micron diameter circular Bragg fiber [9].

EXPERIMENTAL DETAILS

The structures were fabricated on 6-inch silicon wafers using widely available silicon processing tools. The process steps can generally be classified as the creation of an undercut trench, the sealing of the top of the trench, and the deposition of the mirror stack, Figure 1. The materials making up the mirror stack are introduced into the trench through periodic openings along it's length. The openings are widely enough spaced that they do not seem to effect the propagation of light along the trench to first order. The process relies on low sticking constant (high step coverage) of CVD (chemical vapor deposition) and diffusion processes, in particular the deposition of Si from silane, SiN from dichlorosilane and ammonia and the thermal oxidation of silicon. Combinations of processes enable the creation of Si, SiN and SiO_2 mirror layers. In Bragg fibers, the range of wavelengths propagated depends on the layer thickness. Since the thickness is determined by a CVD process we have very tight control over these parameters and it is readily possible to create waveguides which propagate short wavelength radiation. It is also noteworthy that no fine

0-9640024-4-2/hh2002/$20©2002TRF
DOI 10.31438/trf.hh2002.44

Solid-State Sensors, Actuators, and Microsystems Workshop
Hilton Head Island, South Carolina, June 2-6, 2002

feature lithography is required to generate the structures. Relatively simple additions to the process can be employed to modify the tube shape, Figure 2. Since the mirror levels are on the internal surfaces of the channel it is also possible to remove the opaque layers surrounding the structure, Figure 3.

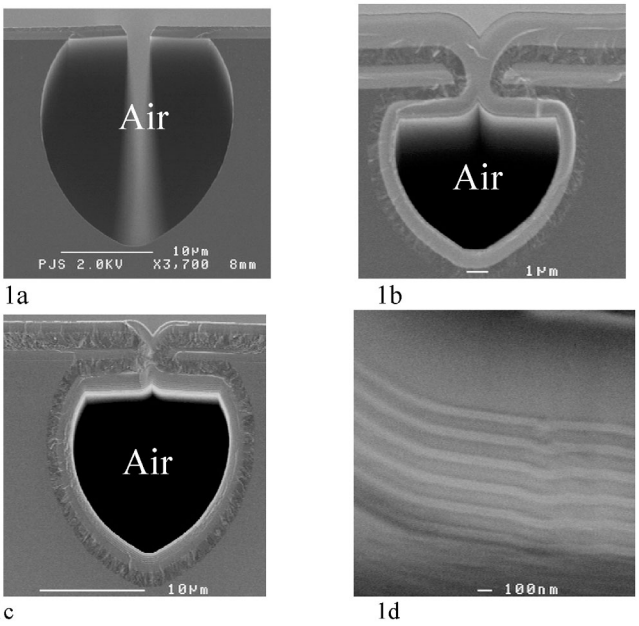

Figure 1. Scanning electron micrograph cross sections outlining the steps in the fabrication of miniature Bragg fibers. 1a shows the formation of the undercut trench. It is formed by isotropically etching the Si substrate through an open line in a low stress SiN layer. The isotropic etch is F based. Figure 1b shows the filling of the opening in the silicon nitride. This is achieved by first depositing 2 microns of polysilicon and then growing a 1-micron thermal oxide. Figure 1c shows the structure after the deposition of the mirror stack. Figure 1d shows a magnified image of a mirror stack consisting of SiO_2 and SiN targeted at 400nm. The reactants needed for the deposition of the mirror stacks enter the trenches through periodic, larger openings not shown in this view, which are not closed off by the polysilicon and oxidation processes of step b.

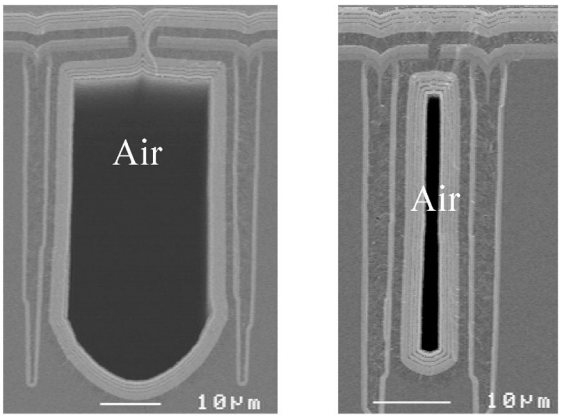

Figure 2. By adding a second mask level which is used to form oxide-lined trenches it is possible to control the lateral dimension of the trench. By controlling the width of the trench opening and the etch time it is possible to control the depth of the trench.

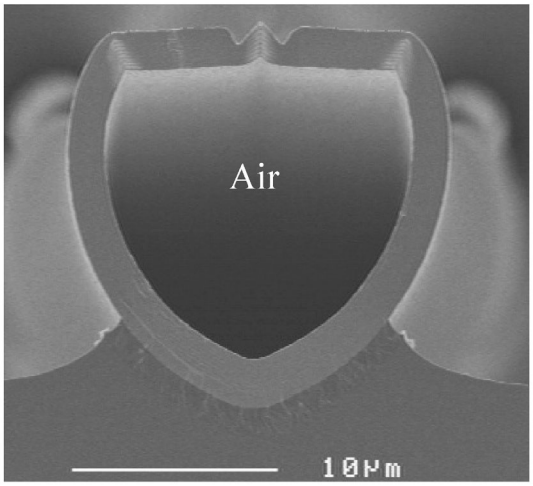

Figure 3. Since the mirror stack is located on the internal surfaces of the tube it is possible to blanket etch back the top layers to remove the optically opaque polysilicon layer used to close the top seam of the trench and, if desired, silicon from the trench edges. This will enable the propagation of light outside the "bandgap" of the mirror stack through the structure.

TESTING

The optical properties of the structures were tested by the free space coupling of laser light into them. Tunable laser modules were used to investigate the wavelength dependence of light propagation through the channels. Losses were determined by investigating the variation of light intensity through various lengths of Bragg fiber. In the case of structures designed to propagate visible light, simple experiments were performed in which light from a tungsten white light source was propagated through the channels and the resulting image was captured on film. In all cases, the lengths of channel investigated ranged from 100's of microns to millimeters.

RESULTS AND DISCUSSION

Figure 4 demonstrates the propagation of visible light through miniature Bragg fibers designed to have a short wavelength cutoff of 400nm. The light source was a white light tungsten bulb and the length of channel was roughly 6 millimeters.

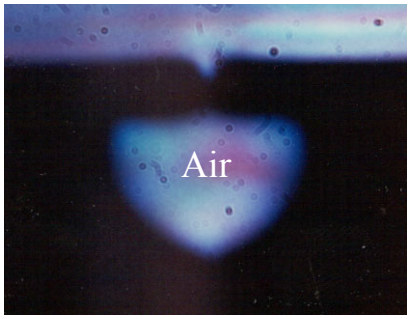

Figure 4. Optical image of visible light propagating through roughly 6 millimeters of a miniature Bragg fiber. The magnification is 1000 times. The Bragg fiber was targeted to have a lower wavelength cutoff at 400nm. The mirror stack consisted of SiN and SiO_2.

Figure 5 shows a plot of light intensity as a function of wavelength for two different lengths of Bragg fiber with a lower wavelength edge at ~1550nm. In this case the mirror layers were Si and SiN and the diameter was roughly 15 microns and there were 4 mirror pairs.

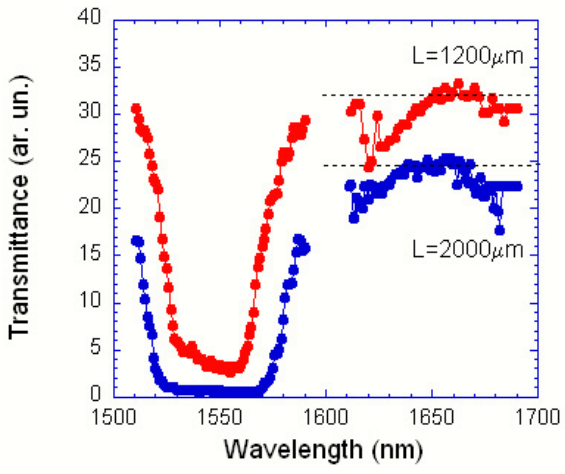

Figure 5. Transmission as a function of wavelength for two different lengths of Bragg fiber. The lower band edge is at~1550nm. The discontinuity at ~1600nm is the result of changing laser modules. The exact long wavelength cutoff is unknown since the series of laser modules available did not extend further than 1680nm.

From data similar to that presented in Figure 5 we estimate the losses in these structures to be on the order of 2-5db/cm. This is in good agreement with that predicted by theory. The losses of the shorter wavelength structures of Figure 4 have not yet been measured, however, we believe the losses will be considerably lower. Modeling indicates that much of the loss in Si/SiN mirror stacks is the result of adsorption by the polysilicon in the mirror stack. The value of polysilicon adsorption used in the theory was 10 dB/cm. The adsorption coefficients of silicon dioxide and silicon nitride are much lower.

Since the range of transmission of the structures exceeded the range of the available turnable laser modules we were unable to accurately identify the full bandwidth of the Bragg fibers tested in Figure 5. However, the 100nm demonstrated is more than adequate for many applications. It is also notable that the drop off of intensity at ~1550nm evident in Figure 5 is very sharp.

Since the light in these structures is propagating in air there is no discontinuity in index as the light from the laser enters and leaves the Bragg fiber. As a result the Fabry-Perot resonant features typically present are, in this case, entirely absent.

We have observed experimentally that the coupling of laser light into the miniature Bragg fibers is relatively insensitive to the alignment of the beam with the centerline of the fiber, making laser coupling to the Bragg fibers relatively straightforward. Theory predicts that, for the Bragg fibers to be single mode, the diameter of the tube should be on the order of a micron. While this should be possible it may be relatively difficult to achieve with the current fabrication process. The roughly 15 micron diameter structures fabricated to date are multimode. It has been theoretically predicted that circular structures with similar dimensions could be made to be effectively single mode. Losses of the TE_{01} mode are predicted to be significantly less than that of other modes [9]. Thus during propagation over long distances all the other modes will dissipate leaving only the TE_{01} mode. It should be possible to fabricate quite circular miniature Bragg fiber structures; however, this mode is not typically generated by light emitting devices. While the integrated mode size of the miniature Bragg fibers can be made to match that of a single mode fiber the actual mode shape will be different. This may be an issue for integrated optics applications. We are in the process of experimentally determining what effect this has on the input and output coupling of such structures to fibers and whether or not it is possible to geometrically come up with structures which will only support a single mode.

We have also investigated the formation of both splitters and bends, which will be important building blocks of any real device. Both have been demonstrated. Bends with radii of 40 microns have less than 0.4 dB loss per 90-degree bend. Mirror bends taking up roughly the same area have similar performance.

The presence of the gas inlet ports along the structure at intervals ranging from 400 to 1600 microns did not appear to have a major influence on loss. This is not unexpected since the openings are well spaced and the "air gaps" are roughly the same size as the hollow tubes.

POTENTIAL APPLICATIONS

While these structures are still being evaluated, we believe that they may have many potential applications to integrated optics and BioMEMS. One of the major issues in large optical switching arrays is the divergence of light as it propagates in air. This leads to large mirror sizes and requires collection, focusing, alignment and collimator schemes. In miniature Bragg fibers, light also propagates in air, however the light is confined by the Bragg fiber. It may be possible to integrate an array of crossing Bragg fibers with a series of movable, two-position mirror MEMS devices. The MEMS mirrors could fit into the gas inlet ports. In this N^2 structure the light would be confined to the Bragg fiber. The mirrors would therefore only need to be on the order of the diameter of the fiber, 5-10 microns. It may even be possible to fabricate very large, ~125 micron diameter, Bragg fibers into which the optical fiber can be inserted. The fibers can then be adiabatically tapered down to 5 micron in diameter. This approach would eliminate the need for collimators, lensing and other fiber alignment structures. Components of such a system are currently in development.

At present, we have only demonstrated the propagation of light in "air-filled" Bragg fibers. However, it should also be possible to introduce low index liquids into such structures. Many potentially interesting fluids exist. For example, certain fluids exhibit changes of index with temperature, which are an order of magnitude greater than those of solids [11]. It may be possible to integrate fluid filled Bragg fibers with heaters to make more efficient thermo-optical devices such as switches and attenuators.

Finally, we believe that it may be possible to fill such structures with biological fluids. In these structures both light and liquids would be guided within a single platform. At present there exist conventional structures where light, confined in dielectric waveguides, is evanescently coupled into fluorescently tagged biological samples [12-13]. Light emitted from the tags is then

evanescently coupled back into the waveguide. Both of these evanescent coupling processes are relatively inefficient. On the other hand if light and fluid could be confined to a single channel the interaction of light with the liquid and the trapping of the emitted light in the channel could be much more efficient.

SUMMARY AND CONCLUSIONS

Miniature Bragg fibers have been demonstrated for the first time. The structures are fabricated using standard silicon processing tools on 6-inch wafers. A wide range of different geometry of structure has been demonstrated as have a number of different mirror stack configurations. Guiding of light from ~400 to 1700nm has been demonstrated as have bends and splitters. Losses are 2-5 dB/cm and potentially can be many orders of magnitude lower. There are many potentially interesting applications for these novel structures.

ACKNOWLEDGEMENTS

The authors gratefully acknowledge the efforts of their coworkers at Sandia National Laboratories Microelectronics Development Laboratory and the Compound Semiconductor Research Laboratory, especially Melanie Tuck and James Bur. Sandia is a multiprogram laboratory operated by Sandia Corporation, a Lockheed Martin Company, for the United States Department of Energy.

REFERENCES

1. E.A.J. Marcatili and R.A. Schmeltzer, "Hollow Metallic and Dielectric Waveguides for Long Distance Optical Transmission and Lasers", Bell System Tech. J., *July* (1964), 1783.

2. M. Miyagi and S. Kawakami, "Design Theory of Dielectric-Coated Circular Metallic Waveguides for Infrared Transmission", J. Lightwave Tech., *LT-2*, 116 (1984).

3. N. Croitoru, J. Dror and I. Gannot, "Characterization of hollow fibers for the transmission of infrared radiation", Appl. Optics, *29*, 1805 (1990).

4. Y. Kato and M. Miyagi, "Modes and Attenuation Constants in Circular Hollow Waveguides with Small Core Diameters for the Infrared", IEEE Trans. Microwave Theory and Tech., *40*, 679 (1992).

5. F.E. Vermeulen, T. Wang C.R.James and A.M. Robinson, "Propagation of Infrared Radiation in Hollow Microstructural Cylindrical Waveguides", J. Lightwave Tech., *11*, 1956 (1993).

6. R. L. Kozodoy, A.T. Pagkalinawan and J. A. Harrington, "Small-bore hollow waveguides for delivery of 3-υm laser radiation", Appl. Optics, *35*, 1077 (1996).

7. P.Yeh, A. Yariv and E. Marom, "Theory of Bragg fiber", J. Opt. Soc. Am. *68*, 1196 (1978).

8. Y. Xu, R.K. Lee and A. Yariv, "Asymptotic analysis of Bragg fibers", Optics Lett., *25*, 1756 (2000).

9. S.G. Johnson et-al, "Low-loss asymptotically single-mode propagation in large-core OmniGuide fibers", Optics Exp., *9*, 748 (2001).

10. T. Kawanishi and M. Izutsu, "Coaxial periodic optical waveguide", Optics Exp., *7*, 10 (2000).

11. M.B.J. Diemeer, J.J. Brons and E.S. Trommel, "Polymeric optical waveguide switch using the thermooptic effect", J. Lightwave Tech., *7*, 449 (1989).

12. T.R.E. Simpson, D.J. Revell, M.J. Cook and D.A. Russell, Evanescent Wave Exited Fluorescence from Self-Assembled Phthalocyanine Monolayers", Langmuir, *13*, 460 (1997).

13. H.P. Kao and J.S. Schoeniger, "Hollow cylindrical waveguides for use as evanescent fluorescence-based sensors: effect of numerical aperture on collected signal", Appl. Optics, *36*, 8199 (1997).

MEASUREMENT OF CHANGES IN TISSUE METABOLISM USING A CLARK-TYPE OXYGEN SENSOR

Benjamin Franc, Nathalia Peixoto*, Laurent Giovangrandi*,**
Glen McLaughlin*, and Gregory T.A. Kovacs*
Department of Electrical Engineering* and Department of Nuclear Medicine**
Stanford University, Stanford, CA 94305-4075

ABSTRACT

This paper presents data characterizing the ability to measure metabolic activity at a tissue interface using a Clark-type oxygen concentration sensor consisting of a microfabricated thin-film electrode matrix overlaid with a solid-state proton conductive matrix and encapsulated in a bio-inert polytetrafluoroethylene film. HL-1 atrial myocytes were cultured onto the sensor surface. Cyclic voltammetry was utilized to characterize the sensor response over 30 minutes while the overlying tissue was subjected to either triiodothyronine or verapamil, drugs known to upregulate or downregulate, respectively, the metabolic activity of myocardial cells. Levels of percent of baseline current were calculated for both drugs, as well as for controls. The change of measured oxygen concentration was considered inversely proportional to the change in metabolic activity. Each of the drugs exerted a significant metabolic effect on the tissue, as evidenced by changes in the sensor current, thus confirming the ability to measure cellular metabolic changes at the tissue surface using the Clark-type oxygen sensor. Verapamil at 25µg/L was found to increase oxygen concentration to 135±4% as compared to control values (95±8%). Triiodothyronine at 2.5µg/L, on the other hand, decreased oxygen levels in the extracellular space to 85±9%, as compared to baseline oxygen (98±6%). The recorded metabolic effects of the tested drugs were consistent with their known physiologic effects. This sensor has possible applications in drug screening or toxicological detection.

INTRODUCTION

During the last few years, miniaturization has enabled more accurate modeling of drug effects on human tissues by means of *in vitro* testing with cultured tissue and has decreased the need for large populations of animal experiments. A large proportion of drug screening is based on binding affinity of the drug to a receptor of interest. However, much can be gained from knowledge of the actual physiologic effect of the drug on the cell of interest, especially in the case of screening metabolic depressants for organ preservation, anti-metabolites for the immune system, and chemotherapeutics.

Similarly, toxicological testing no longer requires extensive sample transport and processing times. Cell-based biosensors have demonstrated their usefulness in toxicity monitoring in the field and a cell-based biosensor system utilizing extracellular electrical recording from chick cardiac myocytes has been demonstrated [**1**]. More elaborate systems **[2]** to better classify analytes and general purpose hardware and software platforms also based on extra-cellular recordings have made the emergence of biosensors as toxicological analyzers in the field imminent **[3]**. However, these applications could benefit from the measurement of effects on cell physiology instead of those on electrical activity alone.

Characterization of cell physiology can be achieved by multiple means. The utilization of oxygen by the tissue is a function of cellular metabolism and the use of an oxygen sensor as a means of monitoring drug effects on cellular metabolism *in vitro* has been previously demonstrated by optical techniques. For example, an oxygen sensor utilizing fluorescence quenching has been used to monitor cellular metabolic response of tissue cultivated in a hollow fiber bioreactor to various drugs and toxins. Changes in oxygen concentration in the space adjacent to the cell were demonstrated to be a direct indication of metabolic demands of the cell. Drawbacks to this approach have included severe temperature sensitivity and the time required to attain stability **[4]**. In addition to these problems, oxygen sensors used in the medical and biotechnology fields have not yet been miniaturized for metabolic drug and toxicity screening. The size, inconsistent performance and short shelf life limit the utility of today's aqueous-based oxygen sensors [**5**]**.**

In order to show the ability to detect toxic or metabolically active substances utilizing a microfabricated Clark-type oxygen sensor, a highly metabolically active cell line was sought. Cells utilized on such a metabolic sensor do not need to be electrically active, thus any type of robust, anchorage-dependent and metabolically active tissue may be used. Myocardium has very high oxygen demands; in the human body, resting myocardial tissue may extract as much as 75% of the oxygen from the arterial circulation whereas other tissues extract only 20-25% [**6**]. Furthermore, an easily cultured cell line exists, the HL-1 from the AT-1 mouse atrial cardiomyocyte tumor lineage, and is capable of maintaining its contractile, morphological, and electro-physiological characteristics when cultured [**7**].

In addition to high oxygen utilization of the myocardium, there are many well-characterized drugs that affect myocyte metabolism, making it an ideal candidate tissue for a metabolic sensor. In particular, triiodothyronine (thyroid hormone, T3) is known to regulate oxygen consumption and oxidative phosphorylation, and has known inotropic and chronotropic effects. Nongenomic-based effects of T3 on cardiac tissue occur rapidly; within four minutes of cardiac myocyte exposure to T3, slow-inactivating sodium channels are recruited and calcium movement across the cell membrane is stimulated, resulting in more rapid and sustained contractions [**8,9**].

Verapamil, a calcium channel blocker, has the opposite effect on myocardial tissue metabolism as thyroid hormone. Verapamil acts at specific binding sites associated with potential-dependent calcium channels and thereby interferes with the slow inward calcium current, preventing the trigger current for myocardial contraction [**6**]. This, in turn, decreases the work done by the heart and the metabolic demand. Clinical studies have demonstrated electrophysiologic effects of verapamil within 1-2 minutes, with peak effect seen at 10 minutes and residual effects observed up to 6 hours following intravenous administration **[10**].

METHODS

Clark-type integrated oxygen sensors were fabricated as previously described [**11**]. Briefly, they consist of a micro-

Travel support has been generously provided by the Transducers Research Foundation and by the DARPA MEMS and DARPA BioFlips programs.

0-9640024-4-2/hh2002/$20©2002TRF
DOI 10.31438/trf.hh2002.45

Solid-State Sensors, Actuators, and Microsystems Workshop
Hilton Head Island, South Carolina, June 2-6, 2002

fabricated thin-film electrode matrix overlaid with a solid-state proton conductive matrix (NafionTM:PVP-360) and coated with a polytetrafluoroethylene (PTFE) film, as is shown schematically in Figure 1. Fabrication of the electrode array was followed by integration into a standard dual in-line package. A cell culture dish with a 1cm hole in the bottom was mounted over the chip, such that the surface of the sensor formed part of the floor of the culture dish. Inlet and outlet ports were provided through the top of the culture dish to allow physiological medium to flow through the chamber. Perfusion was maintained at 1mL/min by a peristaltic pump.

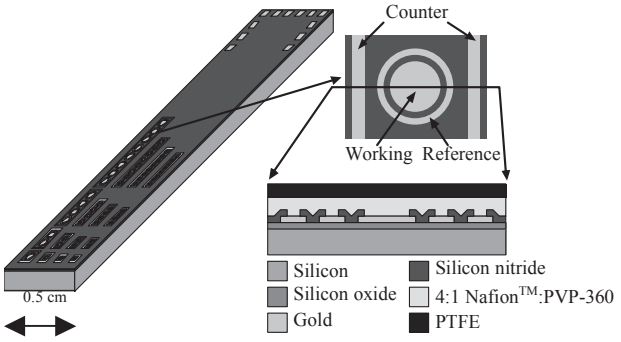

*Figure 1. Single element cross-section of the dissolved gas sensor test matrix [**11**].*

The oxygen arrays used for the experiments had either four elements with a working electrode diameter of 80μm or eight elements with working electrode diameter of 40 μm. An example of a fabricated sensor is shown in Figure 2.

A calibration curve was taken for each of the oxygen sensors by plotting the current obtained at the diffusion-controlled voltage against the oxygen concentration measured utilizing a standard handheld dissolved oxygen monitor (Oakton pH/DO 300 series, Oakton Instruments, Vernon Hills, Illinois), plotting it over three points, and curve fitting with a linear regression model. Linearity had been previously demonstrated in [**11**].

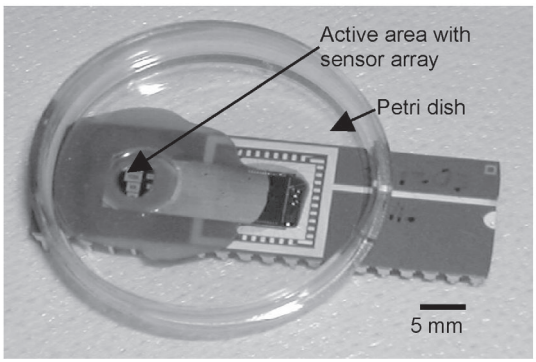

Figure 2. Fabricated sensor array, integrated into a petri dish and bonded to a DIP package, ready for use. Cells are cultured on the active area with sensor array.

As for the cell culture procedures, HL-1 atrial myocytes were plated on fibronectin coated sensors at a density of 50,000 cells/dish and cultured in serum-containing media (Claycomb media with the addition of penicillin, streptomycin, norepinephrine, fetal bovine serum, and glutamine). After reaching confluency, spontaneous beating of the cultured tissue was visually noted and the tissue was considered ready for pharmacologic testing. A single experiment utilizing one drug was performed on the tissue cultured on the oxygen sensor each day after beating was observed, thus preventing overlap from drug effects.

Physiologically relevant doses of verapamil and triiodothyronine were chosen from average serum concentrations available in published clinical studies [**10,13**]. Solutions of media were prepared containing the following drugs at the respective concentrations: triiodothyronine at 2.5μg/L (3.1×10^{-4} mM), and 25 μg/L (3.1×10^{-5} mM) and verapamil at 2.5 (5.5×10^{-6} mM), 25 (5.5×10^{-5} mM), and 100μg/L (2.2×10^{-4} mM). Control solution (placebos) consisted of Claycomb media [**7**] without drug added but prepared in the same manner as the other drug solutions (i.e., mixed and heated in a water bath). Solutions were heated to 37°C just before entering the chamber and intra-chamber temperatures were monitored and maintained at 36±1°C. Voltammetric curves with excitation voltages varying from -0.2V to -0.8V were recorded at 30 second intervals for a total of 240 time points. Unless otherwise noted, experiments were run using the following procedure: after perfusing the culture for 20 min and obtaining a baseline, the low concentration of the drug (or placebo) was perfused for 30 min, the first washout phase Claycomb media was perfused for 20 min, and finally this same schedule was repeated for the high dose concentration and final washout. A typical response of an experimental run following this schedule is presented in Figure 3.

All recordings were performed using a potentiostat (Electrochemical Workstation CH600A, CH Instruments, Austin, Texas) connected to a laptop computer. Six experiments were performed for each of the two drugs as well as for the control group. The current value at a particular voltage for each time point was extracted from the data set for each experiment. Student's t-test was applied for each data set. Voltages were typically analyzed at 0.6V or 0.7V, depending on the particular sensor and the range of voltages at which the current fell in the diffusion-governed region as determined by the calibration curves.

During analysis, the current signal representing the oxygen concentration recorded during the 20 minutes prior to introduction of the drug-containing solution was used as a baseline. Subsequent measurements were evaluated as a percentage of this baseline. A sustained change in signal from baseline appearing after perfusion with the drug was considered to be a drug effect. The average signal over the time course of the drug effect was utilized as a representation of the effect of the drug on oxygen concentration during that period. An inversely proportional relationship between metabolism and oxygen concentrations at the interface between the tissue and sensor was assumed.

Besides calibration with three oxygen levels, temperature dependence of the oxygen sensor was characterized by gradually heating the perfusion media in the appropriate temperature range over the course of 30 minutes and monitoring the response of the current. Sensor response without cells showed exponential behavior with temperature increase, as predicted by the Nernst equation [**12**]. Other parameters investigated included signal response of the sensor to the same drugs without a cell culture overlaying the sensor and with a dead cell culture overlaying the sensor over the course of 30 minutes, the response of the sensor system to the introduction of fresh media independent of drug response every 5 minutes over 30 minutes, and the effect of vigorous mixing on the concentration of oxygen within a solution and the resulting effect from the metabolic sensor set-up.

RESULTS

Regression analysis of calibrations of the oxygen sensors produced linear fits with correlation coefficient values of 0.78 to 0.95. These calibrations were utilized in quantifying oxygen concentration versus time during the experiments. Thyroid hormone's effects on tissue metabolism began over 30 minutes

following initial perfusion with the drug while the effects of verapamil were seen more rapidly, typically around 10 minutes following the beginning of drug perfusion.

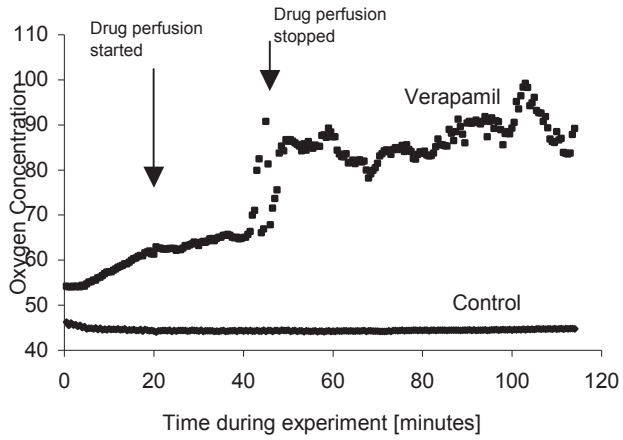

Figure 3. Example of oxygen concentration changes for control condition and under the effect of verapamil (25µg/L). Either verapamil (upper curve) or placebo (bottom curve) was perfused from 20 to 50 min, and again from 70 to100 min. Claycomb solution was perfused from 0 to 20, 50 to 70, and 100 to 120 min. The exact cause of the upward drift of the baseline oxygen concentration during the first 20 minutes has not been elucidated.

The percentage of oxygen concentration present within the cell-sensor interface during various phases of the experiment was plotted for each drug. Verapamil demonstrated a statistically significant increase in oxygen concentration compared to the control solution. As presented in Figure 3, the drug effect is clearly observed after the initial perfusion with verapamil (low dose, initiated at 20min), but after the first washout phase (from 50 to 70 min) and subsequent application of the high dose (from 70 min on), it is not straightforward to analyze the compound effect of both drug applications. The dose dependent nature of the verapamil response could not be verified, although the decrease in metabolism by the HL-1 cells can be undoubtedly shown. For the 2.5µg/L dose, the relative increase in oxygen concentration as compared to baseline was 8%. At the high dose of 25µg/L, the increase was 35±4%. A bar plot of these results is shown in Figure 4, where the data for the control experiments as well as the triiodothyronine responses are summarized.

We also tested a higher dose of verapamil, 100µg/L, in order to compare tissue response to the previously proposed drug administration schedule. In this case, only one dose was used, as opposed to the low and high sequential doses, but the same results were obtained. Oxygen concentration increased to 110±9% (n=5experiments, 20 data points/experiment).

Thyroid hormone (T3) produced a statistically significant decrease in the oxygen concentration present at the cell sensor interface as compared to the placebo solution; although the trend of this response appeared to be dose dependent, this behavior was not proven statistically significant in these experiments. The low dose of T3 decreased extracellular oxygen concentration to 85±9% as compared to baseline (98±5). The high dose, 25µg/L, produced a decrease to 77±12%. These results were obtained as means and standard deviations of six independent experimental runs. Figure 4 summarizes these results.

A commercially available glucometer was utilized to confirm either increases or decreases in metabolism from the effluent stream every 10 minutes during all experiments. A summary of all experimental data is contained in Figure 5.

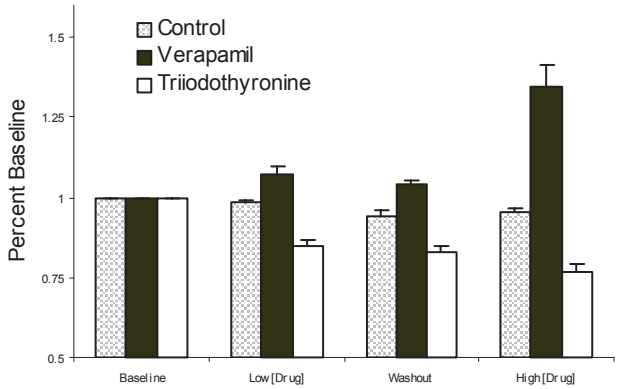

Figure 4. Relative response of oxygen concentration for control condition (placebo), verapamil and triiodo-thyronine application. The first set of columns refer to baseline (20min, n=40 data points/experiment), the second set refers to the applied low-dose (30min, n=60 data points/experiment), the third presents washout (20min), and the fourth shows the response for the high dose (30 min).

Although temperature-dependent responses were characterized with and without cells, in order to exclude any temperature-related variation, either by the electrochemical reaction or by the cellular metabolism itself, the cell culture dish was maintained at a constant temperature during data acquisition. In order to achieve temperature stability, perfusion was maintained at the same flow rate throughout the experiment. Control experiments in which no cells were used show an absence of response to drug application or solution exchange between used and new media. A 30 min period was usually required to attain sensor stability, either in experiments with or without cells, as can be observed in the initial phase of the control curve in Figure 3.

	Dose	EME	OME	Avg n	SE (%)	Dose Dep	Gluc Verify
T3	2.5µg/L (N=6)	↑	↑ (15.3±9.0% p=0.005)	44	4.2	Yes (trend)	Yes
	25µg/L (N=6)	↑	↑ (23.3±13% p=0.007)	34	3.3	P=0.12	Yes
VP	2.5µg/L (N=6)	↓	↓ (7.48±10% p=0.04)	49	4.2	No	Yes
	25µg/L (N=7)	↓	↓ (34.7±4.3% p=0.02)	33	3.3		Yes
	100µg/L (N=5)	↓	↓ (11.2±9.4% p=0.007)	--	--		--

Figure 5. Effects of drugs on myocardial tissue. "T3"= triiodothyronine. "VP"=verapamil."EME"=expected theoretical effect of drug on tissue metabolism. "OME"= effect on metabolism inferred from increase/decrease in oxygen consumption during application of drug compared to baseline. Statistical significance is calculated with comparison to the observed effect of control. "Avg n"=average number of time points at which the observed drug effect was measured in each experiment. SE=average standard error as determined by unpooled analysis of experiments expressed in percent. Dose dependency ("Dose dep") is based upon varying responses of doses representing separate means. "Gluc verify" denotes whether the observed increase/decrease in metabolism as measured by the oxygen sensor was verifiable with a standard glucose assay. "—" = analysis was not performed.

DISCUSSION AND CONCLUSION

Dissolved gas sensors operate by electrochemically reducing oxygen dissolved in solution and measuring the resulting current. The main advantage of the presented sensor is that the electrodes are contained within an oxygen permeable PTFE membrane, which prevents signals from other electroactive species from interfering with the measurement of oxygen concentration.

The experiments described here used this advantage to measure changes in oxygen concentration at the surface of cultured myocardial tissue as the tissue was perfused with various metabolically altering drugs. Metabolic changes were inferred from this data assuming that metabolism was directly proportional to oxygen utilization and, thus, inversely proportional to oxygen concentration measured at the extracellular space.

The metabolic activity, as reflected by the concentration of oxygen at the tissue surface, was augmented by thyroid hormone (triiodothyronine, T3) which is consistent with T3's role in increasing cellular metabolism. The effects of this medication typically occurred after thirty minutes, during the washout phase of the experiment, which was expected, given its known mechanism of action.

Decreases in metabolic activity of the tissue were observed following exposure to verapamil and these effects were seen more rapidly than the metabolic effects of T3. These observations are consistent with both the mechanism and expected time course of action of this medication. Although it seems that the metabolic responses to drugs are dose-dependent, this could not yet be shown statistically. Factors that may have contributed to the variance in the magnitude of the drug effect include the dependence of the absolute level of metabolic activity on the location of the sensor relative to the tissue itself, the influence of oxygen availability and level of contractility on the measured drug effect.

The Nernstian behavior of the electrochemical reduction of oxygen explains part of the observed temperature dependence of the sensor responses. Temperature stability was maintained throughout the experiments in order to assure that the oxygen reduction currents in the diffusion region of measured voltammetric curves were consistent throughout experiments.

Both increases and decreases in metabolism were confirmed by changes in glucose concentration. However, the relative changes in glucose concentration were too small to be precisely measured with the device used in this study, thereby precluding any significant analysis of this data (not shown).

In conclusion, these experiments demonstrated the feasibility of monitoring metabolic changes using a recently developed Clark-type oxygen sensor. This type of measurement has many conceivable uses such as toxin detection and drug discovery. The ability to couple any type of metabolically active cell with the oxygen sensor allows for versatility. In addition, the detection of a wide variety of biologically active substances, including those that act at the cellular as well as the genetic levels, may be performed with a single type of cell because changes in cellular metabolism are a common endpoint for most drug interactions. Further sophistication in drug screening or toxin detection is possible by combining the sensitivity of such a metabolic sensor with other more specific analyzing sensors, such as those that measure the binding affinity of drugs to specific target receptors.

Though promising data was observed and statistically significant changes in metabolism were measured during the application of each of the drugs investigated, rigorous investigation of signal variability remains to be performed. This variability may occur at different levels and may involve 1) minute-to-minute variability in cellular metabolism; 2) environmental changes such as temperature drift or protein deposition; 3) inherent sensor variability. Further work will focus on quantitative approaches to correlate levels of metabolism with measured oxygen concentrations. Future experiments will make use of an independent confirmation of metabolism, such as an in-line glucometer, and will focus on cells in which the use or production of an easily measured variable has a one-to-one relationship with metabolism. At that point, the resolution and repeatability of metabolic changes detectable by this oxygen sensor system may be determined.

ACKNOWLEDGMENTS

This work is funded by DARPA under contract N666001-96-C-8631 and Medtronic Corporation (Minneapolis, MN, USA).

REFERENCES

1. S.A. Gray, J.K. Kusel, K.M. Shaffer. "Design and demonstration of an automated cell-based biosensor" *Biosensors and Bioelectronics*, 16:7-8 535-42 (2001).
2. A.M. Aravanis, B.D. DeBusschere, A.J. Chruscinski, et al. "A genetically engineered cell-based biosensor for functional classification of agents" *Biosensors and Bioelectronics,* 16:7-8 571-7 (2001).
3. K.H. Gilchrist, V.N. Barker, L.E. Fletcher et al. "General purpose, field-portable cell-based biosensor platform." *Biosensors and Bioelectronics*, 16:7-8 557-564 (2001).
4. H.K. Maerz, R. Buchholz, F. Emmrich, et al. "Applicating fiber optical methods for toxicological testing *in vitro*" *Proceedings of SPIE – The International Society for Optical Engineering*, 3603: 228-236 (1999).
5. L.C. Clark, "Monitor and Control of Blood and Tissue Oxygen Tension" *Transactions of the American Society of Artificial Internal Organs*, 2:144-56 (1956).
6. G.A. Langer (Ed.), The Myocardium. Academic Press, San Diego, (1997).
7. W.C. Claycomb, N.A. Lanson, B.S. Stallworth, et al, "HL-1 cells: a cardiac muscle cell line that contracts and retains phenotypic characteristics of the adult cardiomyocyte" *Proceedings of the National Academy of Science*, 195:2979-84 (1998).
8. A.J. Drake-Holland, MIM Noble (Ed), Cardiac Metabolism, John-Wiley and Sons. Chichester (1983).
9. W.H. Dillman. "Thyroid hormone influences on the cardiovascular system: molecular and clinical studies" *Thyroid Today*, 24:3-4 (2001).
10. M.J. Antonaccio (Ed.). Cardiovascular pharmacology. Raven Press, New York (1990).
11. G.W. McLaughlin, K. Braden, B. Franc, G.T.A. Kovacs, "Solid-state dissolved oxygen sensor test matrix using a pulsed-plasma deposited PTFE film" *Transducers '01*, 2:1692-95 (2001).
12. A.J. Bard, L.R. Faulkner (Ed). Electrochemical Methods, Fundamentals and Applications. John Wiley and Sons, New York, (2001).
13. J. Morganroth, E.N. Moore (Ed). "The Evaluation of beta blocker and calcium antagonist drugs" Proceedings M. Nijhoff, Boston (1982).

A 0.8µm CMOS INTEGRATED SURFACE MICROMACHINED CAPACITIVE PRESSURE SENSOR WITH EEPROM TRIMMING AND DIGITAL OUTPUT FOR A TIRE PRESSURE MONITORING SYSTEM

B.P. Gogoi, S. Jo, R. August, A. McNeil, M. Fuhrmann, J. Torres, T. F. Miller, A. Reodique, M. Shaw, K. Neumann, D. Hughes Jr. and D. J. Monk
Motorola Semiconductor Products Sector, 2100 East Elliot Road, MD EL311,
Tempe, Arizona 85284, USA

ABSTRACT

The development of an integrated process for the merging of a surface micromachined capacitive pressure sensor with a 0.8 µm CMOS double metal, double polysilicon process is reported in this paper. A number of innovative pressure sensor designs with improved pressure linearity have been fabricated with this process. Designs with internal anchors and an optimum signal processing algorithm have demonstrated significant improvements in pressure linearity over more conventional designs. The system architecture and circuit implementation using EEPROM for pressure and temperature calibration are described. The results of the pressure and temperature behavior of the integrated sensors are described.

INTRODUCTION

The National Highway Transportation Safety Administration (NHTSA) is in the process of drafting a regulation (as of March, 2002) that will mandate some form of tire deflation monitoring, in response to the TREAD act, signed in 2000. The mandate is for this sensing capability to be in place by 2003. It is not yet clear whether differential wheel speed sensing in the ABS system or direct tire pressure monitoring (TPM) will prevail; however, it may be that both are needed for the near future (5-10 years). The direct TPM application is truly a micro-electro-mechanical *system*. Figure 1 shows an example of a microsystem with micromachined sensor, interface electronics, microcontroller, and rf output device. Motorola has developed a micromachined sensor device that is a CMOS-integrated (0.8µm) surface micromachined pressure and temperature sensor with digital output and is already in production with the MCU+RF in a single package. Furthermore, this package has an integrated harsh media compability packaging scheme built-in to provide protection from the tire environment.

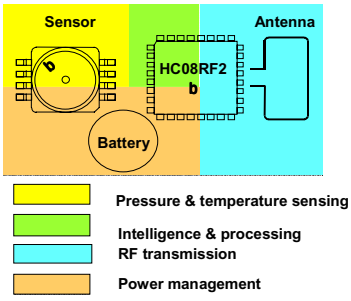

Figure 1. Example of a tire pressure monitoring microsystem with micromachined sensor, interface electronics, microcontroller, and rf output device.

The TPM application, and drive to migrate from bipolar integrated pressure sensors to CMOS integrated pressure sensors, has prompted this development effort. The project is a system-level (MEM*S*) development. It includes the development of an integrated surface micromachined pressure sensor.

Other companies also have products that are targeted for the tire pressure monitoring market. Details of their product offerings can be found on their respective web-pages. Similar surface micromachined, CMOS integrated pressure sensor technology can be found for BiCMOS flows and CMOS technology [**1-7**]

In this paper, the CMOS integration of a surface micromachined capacitive pressure sensor into a 0.8µm double poly, double metal process is described [**8**]. The design and development of capacitive pressure sensors with considerably improved pressure linearity performance is also described [**9**]. The interface circuit for this capacitive sensor was designed to perform the calibration of the measured pressure and temperature using EEPROM. The interface circuit generates an output digital code for both the pressure and temperature sensor. The system configuration to form a TPM System is also described using a block diagram.

SYSTEM AND INTERFACE CIRCUITRY DESIGN

The system is designed for low power and low voltage operation. The supply range is from 3.6 to 2.1 V and is ratio metric. Low current consumption is used to allow battery operation for 10 years. In Standby mode only the low frequency oscillator runs to send a wake-up pulse to the MCU. Temperature measurement and DAC mode use less than 500µA. Pressure sampling consumes the most current at 1.5 mA, but uses high frequency bandwidth sampling to quickly return to sleep mode. This creates a larger noise bandwidth and shows the system constraints of power, noise, and speed. Algorithms can be used by the MCU to alleviate the design tradeoffs.

The control circuit function is to measure and calibrate pressure and temperature. The device performs an 8-bit A/D conversion of either signal. The MCU monitors the output and sets the control circuit's threshold for the conversion of the pressure or temperature to a digital signal or the detection of a specific threshold.

The pressure signal conditioning begins with a capacitance-to-voltage conversion using a nonlinearity reduction scheme in a switched capacitor amplifier. An EEPROM trim register is used to trim offset, gain, and temperature coefficients of the analog signal. Temperature is measured through a diffused resistor, with a positive temperature coefficient, using the same 8-bit current source that sets the threshold for the comparator. The EEPROM trim register trims the offset and gain. The pressure, temperature, and DAC signals are multiplexed to a sample

0-9640024-4-2/hh2002/$20©2002TRF
DOI 10.31438/trf.hh2002.46

capacitor, which stores the value for A/D conversion. The wakeup pulse is multiplexed to the output pin with a parity check and the digital pressure or temperature output. A reset pin is used to hard reset the MCU and provide test vectors for circuit analysis. A block diagram representation of the system and the interface circuit is shown in Figure 2

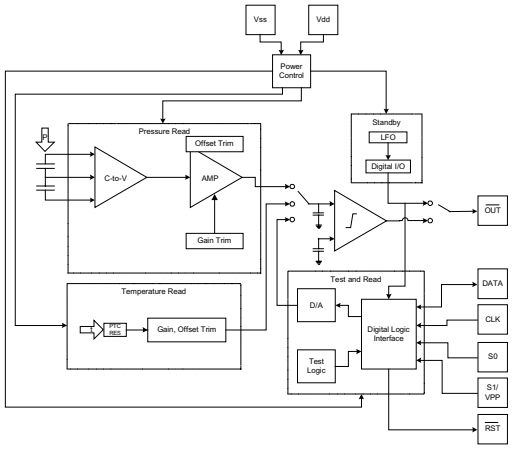

Figure 2. Block diagram representation of interface circuit

TRANSDUCER DESIGN

The primary goals of the transducer design were the following: 1) Produce a sufficient base capacitance 2) Minimize pressure linearity errors 3) Maximize pressure sensitivity 4) Minimize the die area 5) Minimize temperature errors 6) Minimize the parasitic capacitance to the substrate

Perhaps the major design challenge for capacitive sensors is achieving a low linearity error, sufficient pressure sensitivity, and a small die size.

Traditionally, there has always been a trade-off between items 2 and 3; greater sensitivity usually produces larger linearity errors. Although linearity errors can be improved with reduced pressure sensitivity, more circuit gain is required, and circuit noise and other errors can increase. Thus, there is a desire to have a high pressure sensitivity and a low pressure linearity error, and therefore, other approaches were investigated to reduce linearity errors.

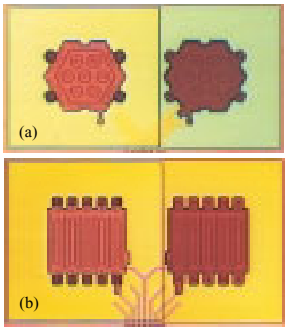

Figure 3. Figure 3 (a) Transducer using an internal post diaphragm design. (b) Transducer using a rectangular diaphragm design.

It is well known that first order linearization can be achieved by using a signal processing algorithm based on 1/Cs, with Cs being the pressure sensitive capacitor element [**1-2**]. The signal processing algorithm used produces an output proportional to the quantity 1- Cr/Cs, with Cr being a fixed reference capacitor element. For an ideal Cr and Cs, i.e., Cr constant and Cs behaving as a parallel plate capacitor with a linear pressure dependent gap, the linearity error can be substantially reduced. Using this algorithm, one major source of linearity error is non-uniform diaphragm deflection. Actual diaphragms are constrained at the edges, and this produces non-uniform deflection. As an example, a square diaphragm clamped at its perimeter and subjected to pressure has non-uniform deflection, with deflection greatest at the center, and zero at the perimeter. For this case the average deflection is only about 30% of the maximum deflection.

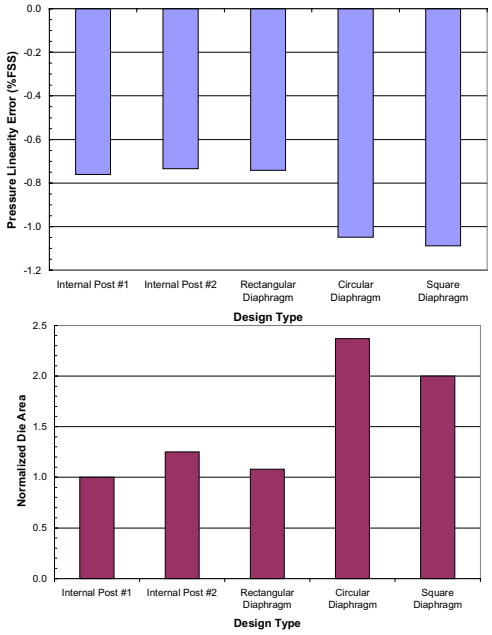

Figure 4. The pressure linearity error and normalized die area for several designs.

Finite element simulations were used to evaluate candidate diaphragm shapes for uniformity of diaphragm deflection. In addition to previously used shapes, such as circles and squares, "internal post" configurations were evaluated. Internal post designs anchor the diaphragm both at its perimeter and at internal locations. Simulations showed that some configurations of internal posts could produce more uniform diaphragm deflection, and significantly reduce linearity error at a given sensitivity level [**7**]. Figures 3(a). and (b). show photographs of an internal post design and a rectangular diaphragm design. Figure 4 shows the measured linearity error for several different design types. All designs have the same pressure sensitivity. The relative die area for the various designs normalized to the size of the Internal Post #1 design is also shown in this figure. The advantages of the internal post and the rectangular diaphragm designs are clear from the improved pressure linearity error and relatively small size.

PROCESS INTEGRATION

The process integration and fabrication of the CMOS integrated pressure sensor is described in this section. The details of the CMOS processing that are not relevant to the sensor integration have been omitted.

The methodology used in the insertion of the sensor module into the CMOS process was based on the requirements that there is no impact, either thermally or topographically, on the CMOS fabrication. This is done by insertion of the micromachining steps before the temperature sensitive process steps of the CMOS process. It was identified that the source/drain

implants and the subsequent thermal processing were the temperature sensitive steps. In addition, the process integration was designed to reuse, as much as possible, the fabrication steps of the CMOS process. The cross-section of the CMOS and sensor devices is shown in Figure 5 illustrating the key features of the process integration.

The fabrication process starts with the standard CMOS fabrication process in which the active areas are defined using an isolation field oxide using a LOCOS process. In addition to defining the active area of the CMOS devices, the field oxide is used as the area where the sensor is to be formed. The next step is the formation of the floating gate of the EEPROM. The required extension implant of the EEPROM is completed followed by the deposition of the thin tunnel oxide. The EEPROM floating gate is then deposited using a doped LPCVD polysilicon film. The floating gate polysilicon is patterned and etched so that it also forms the bottom fixed plate of the capacitive pressure sensor. The isolation of the fixed electrode to the substrate is provided by the CMOS field oxide isolation. The CMOS transistor gate oxide is then deposited followed by the gate polysilicon deposition.

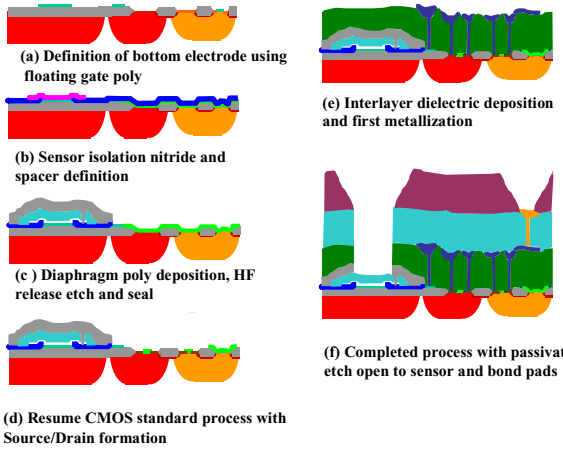

Figure 5. Selected cross-sections of CMOS integrated capacitive pressure sensor process flow.

At this stage, the CMOS fabrication is suspended and the sensor fabrication steps are inserted. The first step is the deposition of a layer of PECVD oxide to protect the CMOS gate Poly from future sensor processing. The next step is the removal of the PECVD oxide, gate polysilicon and the gate oxide from the sensor area. This is done in such a way that the bottom polysilicon plate is not affected by the etching process. After the gate oxide is removed, an isolation layer of low stress silicon rich nitride is deposited using an LPCVD process. The silicon rich nitride is chosen for its excellent etch resistance to HF based chemistries. The silicon nitride is used to isolate the top and bottom plates of the pressure sensor and also protect the CMOS area from subsequent micromachining steps.

The sacrificial layer of the sensor is next deposited using a phosphorus-doped glass. The thickness of this layer defines the spacing between the bottom fixed electrode and the moveable diaphragm. The spacer layer is also patterned for transducer designs, which utilize internal support posts for improved pressure linearity.. The sensor diaphragm is then formed by deposition of a LPCVD polysilicon layer. The polysilicon is then doped, patterned and etched to define the diaphragm.

The pressure sensitive diaphragm is then released by removing the sacrificial layer below the diaphragm polysilicon. Etch ports located at the periphery allow the HF based chemistry to completely remove the phosphorus-doped glass. The etch ports are then sealed using a line of sight sealing with a PECVD deposited oxide layer. The thickness of the PECVD oxide is chosen to ensure that the etch holes are plugged and the cavity between the fixed plate and the diaphragm is sealed at the deposition pressure of the PECVD oxide. This completes the formation of the sensor module.

The next step is the resumption of the CMOS fabrication process. This is done by first removing the sealing oxide, isolation nitride and protective oxide over the CMOS device area. The CMOS device formation is then resumed with the formation of the source/drain regions, and the subsequent thermal treatment to provide the activation anneal and definition of the junctions. This thermal treatment also serves to activate the dopants and provide the stress relief anneal in the sensor polysilicon film.

The first interlayer dielectric layer is next deposited, patterned and etched to allow for the subsequent first metal layer to contact the various CMOS devices as well as provide the interconnect for the sensor to the circuit. The second interlayer dielectric layer is then deposited, patterned and etched to form vias for the second metal to contact the first metal with the routing required for the circuit blocks. Finally, the passivation layer is deposited over both the CMOS and sensor device area. The passivation layer is then patterned and etched to expose the bond pads. In addition, the passivation layer, second, and first dielectric layers are then removed over the pressure sensitive element but not from the reference sensor element. This exposes the polysilicon diaphragm of the sensitive element leaving it free to deflect under an applied pressure. The reference element has very little deflection since it has a very thick composite diaphragm. Both the pressure sensitive element and the reference elements are used by the circuit to generate the output of the sensor. This completes the description of the process integration of the capacitive pressure sensor with the CMOS devices. Figure 6 shows a die picture of a typical CMOS integrated pressure sensor.

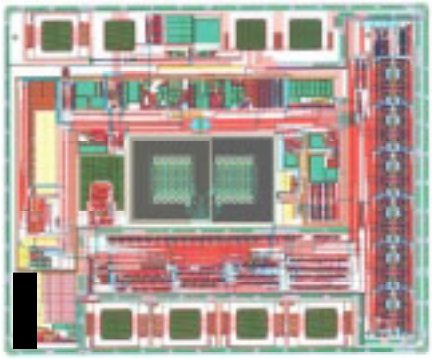

Figure 6. Microphotograph of CMOS Integrated pressure sensor

EXPERIMENTAL RESULTS AND DISCUSSION

The stand-alone pressure sensors designed for the tire pressure monitoring system were tested using a capacitive readout test setup. The capacitance vs. pressure characteristics were obtained for a large number of devices. A family of curves of Capacitance vs. Pressure for one of the designs is shown in Figure 7. The pressure sensitive devices a good linearity behavior with pressure while the reference devices do not show any pressure sensitivity as designed.

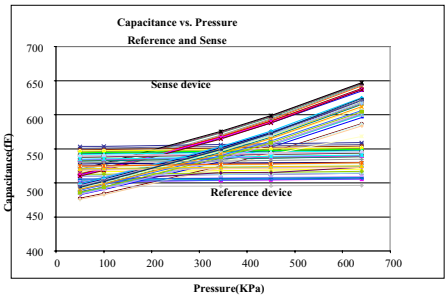

Figure 7. Family of capacitance versus pressure characteristics for pressure sensitive and reference devices.

The digital output data for the integrated devices were also obtained for a variety of designs over a wide range of temperature.

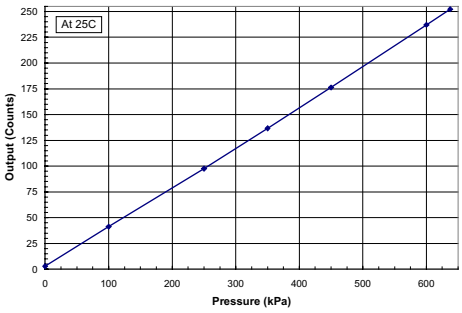

Figure 8. Digital output of a typical sensor with applied pressure at 25C.

Figure 8 shows a typical plot of the digital output count of a typical device as a function of the applied pressure at room temperature. The linearity, temperature coefficient of offset and sensitivity of the integrated devices were also measured. A summary of the performance of a typical device is given below in Table 1.0

Table 1.0 Performance summary of a typical device

Pressure Range	Temperature Range	Full Scale Output	Pressure Linearity Error	TC Offset	TC Sensitivity	Thermal Hysteresis
[kPa]	[C]	[Counts]	[%FSS]	[Counts/C]	[%FSS/C]	[%FSS]
0 to 637.5	-40 to 125	0 to 255	-1.5	0.01	-0.005	0.04

CONCLUSIONS

The development of a CMOS integrated surface micromachined capacitive pressure sensor for a tire pressure monitoring system has been reported in this paper. The design of pressure sensors with improved pressure linearity as well as a block diagram description of the interface circuitry has been described. The process integration steps for inserting the pressure sensor into a double poly, double metal CMOS process was described. The performance of the pressure sensor devices itself was presented. In addition, the digital output behavior of the interface circuit for both the pressure sensor and temperature sensor was presented.

REFERENCES

1. H. Dudaicevs, M. Kandler, Y. Manoli, W. Mokwa, and E. Spiegel, "Surface Micromachined Pressure Sensors with Integrated CMOS Read-Out Electronics," *Sensors and Actuators A*, 43 (1994) 157-163.
2. D. Weiler, O. Machul, D. Hammerschmidt, J. Amelung, and B. J. Hosticka, "A Single-Chip Smart Pressure Sensor Family with 2 Dimensional Calibration," *Advanced Microsystems for Automotive Applications 2000,* Eds. S. Krüger and W. Gessner (Springer: 2000) 289-295.
3. T. Lisec, M. Kreutzer, and B. Wagner, "Surface Micromachined Piezoresistive Pressure Sensors with Step-Type Bent and Flat Membrane Structures," *IEEE Trans. On Electron Devices*, vol. 43, no. 9, 9 September, 1996, pp. 1547-1552.
4. K. Shimaoka, O. Tabata, M. Kimura, and S. Sugiyama, "Micro-Diaphragm Pressure Sensor Using Polysilicon Sacrificial Layer Etch-Stop Technique," *The 7th International Conference on Solid-State Sensors and Actuators: Transducers '93,* Yokohama, Japan, 632-635.
5. T. Scheiter, H. Kapels, K.-G. Oppermann, M. Steger, C. Hierold, W. M. Werner, and H.-J. Timme, "Full Integration of a Pressure-Sensor System into a Standard BiCMOS Process," *Sensors and Actuators* A 67 (1998) 211-214.
6. C. Hierold, "Intelligent CMOS Sensors," *The Thirteenth Annual International Conference on Micro Electro Mechanical Systems (MEMS200)*, Miyazaki, Japan, 23-27 January, 2000, 1-6.
7. H.K. Trieu, M. Knier, O. Köster, H. Kappert, M. Schmidt, and W. Mokwa, "Monolithic Integrated Surface Micromachined Pressure Sensors with Analog On-Chip Linearization and Temperature Compensation," *The Thirteenth Annual International Conference on Micro Electro Mechanical Systems (MEMS200),* Miyazaki, Japan, 23-27 January, 2000, 547-550.
8. B. Gogoi, K. Neumann, D. Hughes Jr., D. Odle, D. J. Monk, R. August, A. McNeil, J. Schmiesing, and J. Foerstner, "Integrated CMOS Capacitive Pressure Sensor," Patent Pending, 2000.
9. A. McNeil, D.J. Monk and B. Gogoi, "Method of manufacturing a sensor" US patent 6,352,874 B1, 2002

INFRARED DIAGNOSTICS FOR MEASURING FLUID AND SOLID MOTION INSIDE MEMS

Gengxin Han, James C. Bird, K. Johan A. Westin & Kenneth S. Breuer
Division of Engineering, Box D Brown University
Providence, RI 02912. USA

ABSTRACT

A new velocimetry system has been developed for use in microdevices that incorporate silicon as their structural material. The system is designed to illuminate and measure particle and surface motions using infrared wavelengths, taking advantage of the fact that silicon is largely transmissive to light with wavelength above 1 micron. The system allows us to observe motion *inside* silicon-based microdevices, which are otherwise opaque to light at visible wavelengths. By analyzing these images using both time-of-flight and phase-locked techniques, we can make quantitative measurements about the position and speed of internal surfaces and the motion of fluids inside complex microfabricated devices.

INTRODUCTION

The rapid growth and significant progress in the development of microfluidic devices has revealed a need for measurement techniques to measure the flow inside microdevices with micron-scale resolution. Non-invasive diagnostics, such as Particle Image Velocimetry (PIV) [**1**] are well-suited to this task and in recent years, micro-PIV techniques have been described [**6,8**] which press conventional methods to the limits of optical resolution. PIV is one example of a *time-of-flight* measurement, in which the velocity of an object is inferred by measuring its displacement during a known time period. The displacement is computed from two images, each exposed with a short laser pulse and taken in rapid succession. If the objects of interest are small particles suspended in a fluid, the velocity field can be measured. However the technique is not restricted to suspended particles and can also be used on any feature that can be tracked in a pair of images. A second mode of measuring motion is by stroboscopic illumination of an object in harmonic motion. In general, this technique cannot be used for fluid motion, because, even if the flow is harmonic, suspended particles are unlikely to follow closed paths. However, this *phase-locked* technique has been used to great success in the measurement of the motion of harmonically-forced MEMS devices such as accelerometers, etc. [**4**].

As the complexity of the microdevices increases, the ability to provide optical access through a transparent surface becomes increasingly difficulty to ensure. The use of transparent materials (glass, Pyrex, plastic, etc.) often represents a compromise to the fabrication sequence, as these materials are not as structurally or thermally robust as single-crystal silicon or silicon carbide and cannot be processed with as much flexibility as is available for silicon-based substrates. In addition, the fabrication methods for these materials tend to be less precise, compromising precision fabrication. Lastly, as multi-layer microfabricated silicon structures become increasingly common, the requirement to incorporate a glass window for visualization purposes is often impossible to accommodate without further complication to the fabrication sequences – a complication that is usually unacceptable.

Although visible light is no longer suitable as an illumination source for a micro-PIV system, the absorption coefficient of silicon falls sharply in the near infrared regime, and is effectively transparent at wavelengths between 1.1 and 2.5 microns. This property implies that infrared (IR) light might be a desirable illuminating source for PIV system if one would like to visualize motion *inside* a silicon-based microdevice. The present paper explores the idea of using IR illumination to measure motion inside silicon devices.

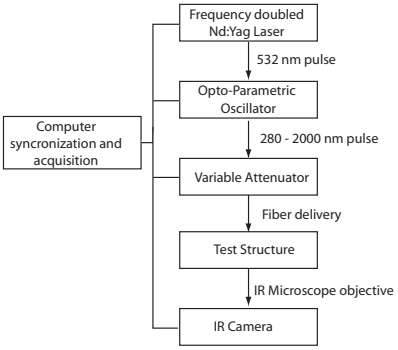

Figure 1. Overall schematic of IR micro motion system.

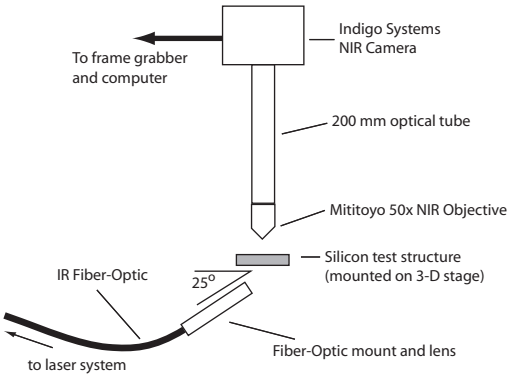

Figure 2. Schematic of the optical configuration for micro-motion measurement.

BACKGROUND THEORY

The general optical system is outlined in Figure 1 and Figure 2. The device is illuminated using a twin Nd:YAG laser system which emits a pair of 4.5 ns pulses at 1064 nm. Although we could use this wavelength, the transmissivity of silicon is not optimal here, and higher wavelengths are more desirable. To achieve this, the beam is frequency-doubled to 532 nm and then directed through an Opto-Parametric-Oscillator (OPO) - a nonlinear crystal system that enables the laser pulse to be tuned to a wavelength anywhere between 300 nm and 2000 nm. In the present case, we typically tune the laser to 1200 nm, where silicon reaches a high level of transparency. The pulse is then coupled to a fiber-optic delivery system and directed to the target, which is flood-illuminated by the two laser pulses. The angle at which the light hits the target is quite important, and depends on what is being

0-9640024-4-2/hh2002/$20©2002TRF
DOI 10.31438/trf.hh2002.47

illuminated. For solid surface measurement, we have found that illumination in pure transmission mode is the most effective, in which case the laser is positioned directly below the sample, at ninety degrees to the focal plane. For small particle illumination typical of PIV, a shallow angle of approximately 25 degrees with respect to the focal plane was found to be optimal, although the precise dependence of this is still being quantified more closely.

The scattered light is collected by a Near Infrared (NIR) microscope objective mounted on a 200 mm corrected tube and imaged using an Indigo Systems Indium Gallium Arsenide (InGaAs) NIR camera. This camera has a 320x256 pixel array (30 micron pixel size) with excellent sensitivity between 900 and 1700 nm. Different microscope objectives have been used for different studies. For PIV measurements, a 50x 0.42NA Mititoyo objective has been used. This optical arrangement gives a field of view of 192 by 154 microns, which although small, gives good resolution of the small particles that are imaged in PIV measurements. For the solid surface motion study described in this paper, a 20x 0.3 NA objective was used to achieve a larger field of view (at the cost of spatial resolution).

The resultant images are transferred at 60 Hz to a data acquisition computer. Although the NIR camera is a video-rate device and cannot be triggered, as can most modern CCD systems, the laser pulses are synchronized to the video sync signal and can be adjusted to fall anywhere within the video frame. In the case of phase-locked operation, the position of the laser pulse in the frame is not important, as long as it doesn't fall on the inter-frame boundary, in which case a dead image will result. However, in the case of time-of-flight measurements, the laser timing is adjusted so that the two laser pulses straddle adjacent video frames. For the Indigo camera, this inter-frame boundary is 0.12 ms in duration, so that the separation between the two laser flashes can be no shorter than 0.12 ms –more than adequate for most low-speed motions. Higher speed activity can be captured either with dual-illumination of a single frame or by using two cameras externally synchronized to be out of phase. Triggered IR cameras or interline cameras which can store two images in quick succession may be available in the near future to ease this concern.

FLUID VELOCITY MEASUREMENTS

A significant difference between visible micro-PIV and the IR micro-PIV system is the particle scattering technique used. In a visible PIV system, one can use an inelastic technique, such as epi-fluorescence, to image submicron particles. This has the advantage that background reflections at the excitation wavelength can be filtered out by the use of a dichroic filter, greatly enhancing the sensitivity of the image-gathering optics and enables the use of small particles, which can track the flow very accurately. In contrast, in the IR system, fluorescent particles with both absorption and emission bands in the IR regime do not exist (to our knowledge), and this mandates the use of elastic scattering techniques to image the particles. Laser scattering from small particles is highly dependent on the particle size and wavelength, and the scattered intensity (I) varies like [**2**]:

$$I \propto d^6 / \lambda^4 ,$$

where d is the particle diameter and λ is the wavelength of the recording light. From which we see, there is a tradeoff between higher wavelengths to achieve greater silicon transmissivity, and greater sensitivity in the NIR camera, (which also increases at higher wavelengths), and using lower wavelengths to maximize the scattering intensity and to improve the point spread function size. A compromise wavelength of 1200nm was found to work well, although some results in this paper were also obtained at 1064nm (before the OPO was fully operational). The intensity penalty due to wavelength can also be offset by using particles of larger diameter, d.

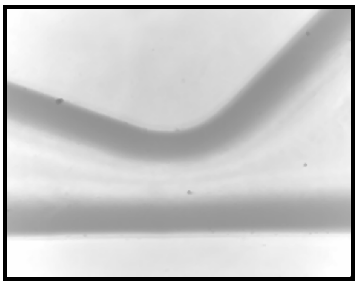

Figure 3. IR image of micronozzle throat using broad band illumination without flow. The shadows are due to the diffraction in the silicon-air transition.

The geometry tested was a converging-diverging flow inside a silicon micronozzle, shown in Figure 3. The device was fabricated by etching the nozzle geometry 300 microns deep into a 500 micron-thick silicon wafer. A second silicon wafer was fusion-bonded to the first in order to cap the structure. The device is thus opaque to visible light. The nozzle shown in Figure 3 has a throat width of 40 μm. The measurements reported here were taken downstream of the throat where the flow expands to a channel 300μm deep by 1000μm wide.

The water flow was seeded (0.06% by volume) with 1 micron uncoated polystyrene particles with a refractive index of 1.56 at 589 nm. The relative refractive index is 1.17 (compared to water). Smaller particles would be preferable, but the intensity increases strongly with particle diameter (see above), and this was found to give good particle visibility.

In a micro-PIV system, the spatial resolution of the system is given by the diameter of the diffraction-limited point spread function, ds, in the image plane, which is given by:

$$d_s = 2.44M \frac{\lambda}{2NA}$$

where M is the total magnification of the microscope, and NA is the numerical aperture of the objective lens [**2,6**]. At a wavelength of 560 nm, with a 1.4 NA 60x objective, Meinhart *et al*. report $d_s = 29.3\ \mu m$ [**8**]. For the same lens system (which will operate in the Near IR, as long as it is not anti-IR coated), but using light at 1.2 microns, this is degraded to 62 microns. For the 50x, 0.42 NA objective used in the current study, the point-spread diameter is 174 microns. This is considerably larger than the optimal lens system and is primarily due to the low NA of the current lens. However, the low NA has a significant advantage – it has a large working distance, which is important for imaging inside thick silicon devices, and convenient for this preliminary study.

If we track a 1-micron particle, then, following Adrian [**1**] and Meinhart *et al.* [**6**], the effective diameter, d_e, projected on the image plane can be expressed as

$$d_e = (M^2 d_p^2 + d_s^2)^{1/2} ,$$

which yields $d_e = 181$ microns, compared with approximately 30 microns reported by Meinhart *et al.* for visible light micro-PIV. The spot size is dominated by the diffraction point spread. However, since the NIR camera has large pixel sizes (30 microns), this is not as bad as it seems, and the imaged particle is only six pixels wide – close to ideal for PIV sub-pixel interpolation. Assuming that we can achieve $1/10^{th}$ pixel accuracy in the PIV algorithms, this gives a spatial resolution of 360 nm.

In the current experiment, by using two pulse separation times, (δt = 0.125 ms and 17.5 ms) we measured the velocity in two flow conditions: a) a high flow rate regime where the average nozzle throat velocity is 62 mm/s and b) a low flow rate regime where the average nozzle throat velocity is 250 μm/s. The interrogation areas chosen were a region close to the wall (for the high speed flow condition) and a region away from walls in the nozzle expansion (for the low speed flow condition). These are simply representative regimes, and no attempt was made to map the entire flow field at this time.

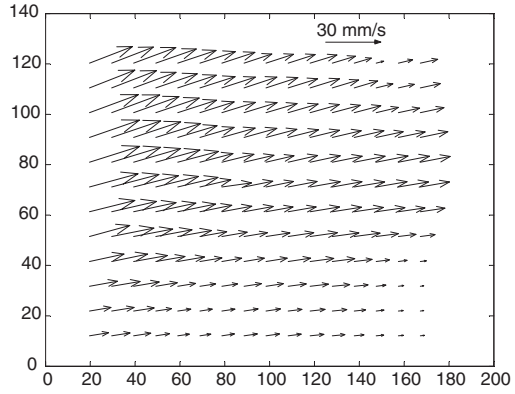

Figure 4. Velocity vectors for a high flow rate case. The lower part of the test area is close to the nozzle wall. The axis coordinates are in microns.

The image pair was analyzed using in-house PIV processing techniques, and selected results were confirmed using well-tested custom microPIV software [**10**]. The in-house PIV data processing techniques are based on the MATLAB-based image analysis software developed by Sveen [**9**] modified to include the cross-correlation signal-to-noise ratio as a criterion during the ensemble averaging of velocity vectors. In processing the average, we first set an acceptable value of signal-to-noise ratio (SNR) and only pick up the vector whose correlation satisfies the SNR threshold participating in the average. The typical number of measurements included in an average is about 40 and only 7% of the total vectors were rejected due to poor SNR. The vector fields for the high speed condition are shown in Figure 4, computed using an interrogation window size of 64 x 64 pixels, and by overlapping the interrogation windows by 75%. The lower axis represents the location of the solid wall where the velocity is zero. The focal place is in the middle of the nozzle, away from either the upper or lower nozzle boundaries. The dynamic range of the system (the ratio of the highest resolved speed to the lowest resolved speed) is limited by the pixel resolution of the images.

SOLID SURFACE MOTION MEASUREMENT

The IR micromotion system can also be used for detection of the position and velocity of a solid feature inside the silicon structure. If the motion of the solid object is harmonic, we can operate in "phase-locked" mode, in which the laser is locked to the frequency of the device (or some precisely control detuned frequency). This has been amply demonstrated using visible light by Freeman [**4**], by our own group, using IR illumination [**5**]. If, however, the motion of the solid object is not harmonic, there is no phase reference and a time-of-flight measurement technique, similar to the PIV technique is necessary. This is demonstrated using the rotation of a microturbine, fabricated as part of the MIT Microengine program [**3**]. The rotor consists of a 4mm turbine disk, which can rotate in a stationary housing (supported by an air bearing). The completed microturbine is a complex device and is comprised of five silicon wafers bonded in a stack with the rotor forming the middle layer. The entire device is encased by silicon and is not accessible to visible light, save for a small access hole, for a fiber-optic speed sensor. One motivation for imaging the rotation is to determine both the speed of rotation and (more importantly) to image the details of any sub-synchronous motion ("whirl"), which can lead to rotor instabilities and ultimately to failure.

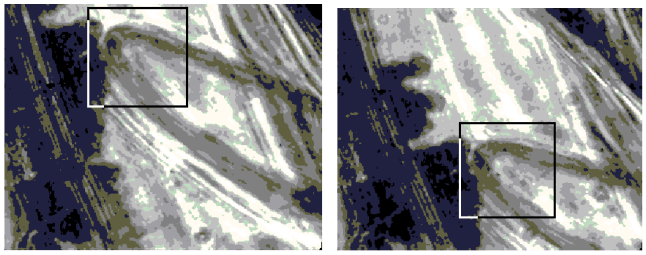

Figure 5. Pair of IR images taken using laser illumination, of a buried microrotor as it spins inside its rotor bearing. The size of each image is 480 by 384 (microns). The square boxes in each frame represent the initial interrogation areas used to compute translation and rotation.

Figure 5 shows a pair of images of the moving rotor taken using the laser illumination while it is spinning at low speed (approximately 5670 RPM). In the time-of-flight (or PIV) mode, the lasers are fired in rapid succession, and in this case the two flashes are separated by 150 microseconds. The motion of the rotor is clearly visible. In order to analyze this image pair both the translation and rotation of image B with respect to image A must be computed. The pictures are first cleaned up by removing dead pixels and overexposed pixels either by thresholding the image (re-assigning pixels that have values that are below or above a given value) or by using a Median filter or an adaptive Wiener filter, both designed to remove high frequencies and "salt and pepper" noise. The images are also equalized so that their intensity distributions are matched.

The velocity of a feature in the image is determined as follows: A first-guess interrogation area (IA) is first selected on each image. This area should contain well-defined features that will be easy to track. Edges and other high-contrast features are most desirable. In addition, features that are highly non-isotropic (i.e. have clear orientation) are preferable in order to compute image rotation. In the example shown above, the leading edge of the rotor blade is selected as the interrogation area. The images are next linearly de-trended, windowed (using a Hamming window) and cross-correlated using an FFT-based cross-correlation routine.

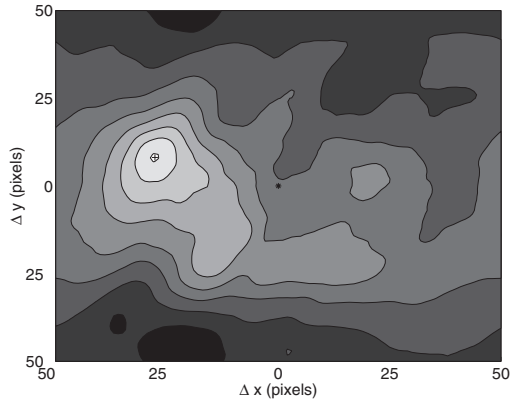

Figure 6. Shaded contour plot of the cross correlation obtained during the (first) translation phase. Note the well-defined maximum indicating the optimal translation.

The cross-correlation for the image pair shown above is presented in Figure 6. Notice that there is a well-defined peak whose position indicates the best-fit translation of the image. This peak is interpolated to sub-pixel accuracy by fitting the cross-correlation near the maximum to a Gaussian surface (with arbitrary orientation and aspect ratio). Using this translation data, Image B is translated using a spline-based subpixel interpolation routine. In addition, a circular ring image is interpolated from the original Cartesian-based pixel grid, again using spline interpolation. A one-dimensional cross-correlation in the azimuthal direction is performed on the ring image to determine the image rotation. As with the translational computation, Gaussian sub-pixel interpolation is used to optimize the rotation between the two images. The azimuthal cross-correlation is performed for several radial values, and the median rotational angle is chosen as the optimal image rotation. Image B is rotated using a bicubic interpolation, and the interrogation areas are re-computed. The entire process is repeated iteratively until no further improvement is observed. Additional details are reported in [**5**]. The results of the completed translation/rotation operation are shown in Figure 7, which shows the previous image pair, superimposed after the optimal translation and rotation. For a perfect image pair, we find that the process is accurate to better than 0.02 pixels and 0.02 degrees, although image-to-image noise does degrade this performance.

CONCLUSIONS

An IR micro-motion system designed to illuminate and measure particle and surface motions inside silicon micromachined devices using infrared wavelengths has been developed and demonstrated. The system has a resolution of approximately 360 nm, although this can be improved by a factor of 2 with high NA optics. Although the resolution is not as good as visible-light microPIV systems (due to both the longer wavelength, the need for larger focal length optics and limits in current IR imaging technologies), it is more than adequate for many micro flows and motions of interest, particularly since other means of interrogation inside the structure are not possible. The system is now being extended to incorporate more sophisticated motion algorithms, as well as to measure instabilities, mixing and reactions inside complex silicon devices.

This work was supported by DARPA and NSF. The authors would like to acknowledge Carl Meinhart and Steve Wereley for many valuable discussions and the use of their PIV code.

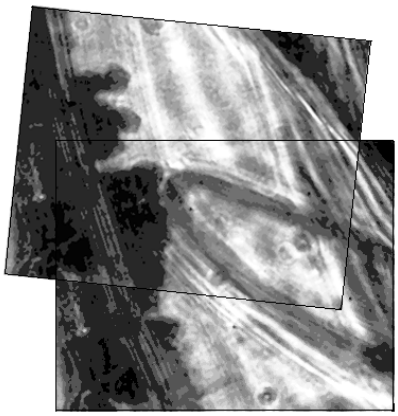

Figure 7. Microrotor image pair, translated, rotated and superimposed, indicating the optimal image shift. In this case Δx = -44.1, Δy = -111.4 (pixels) and Θ = 5.1 degrees.

REFERENCES

1. RJ Adrian (1991) Particle-imaging techniques for experimental fluid mechanics. *Ann. Rev. of Fluid Mech.* **23**: 261-301.
2. M Born & E Wolf (1997). *Principles of Optics.* Sixth Edition. Cambridge University Press, Cambridge.
3. L Fréchette, SA Jacobson, KS Breuer, FE Ehrich, R Ghodssi, R Khanna, C-W Wong, X Zhang, MA Schmidt & AHEpstein. (2000). "Demonstration of a Microfabricated High-Speed Turbine Supported on Gas Bearings" *Proceedings, IEEE Solid State Sensors and Actuators Workshop*. Hilton Head SC.
4. D Freeman (2001) Measuring Motions in MEMS. *Materials Research Soc. Bulletin*. **26**: 4:305-306.
5. KS Breuer, JC Bird, G Han & KJ Westin. (2001). **"**Infrared PIV for Measurement of Fluid and Solid Motion in Micromachined Devices". *Proceedings, ASME IMECE New York, NY. November 2001.*
6. CD Meinhart, ST Wereley & JG Santiago (1999) PIV measurements of a microchannel flow. *Exp. in fluids* **27**: 414-419.
7. CD Meinhart, ST Wereley & MHB Gray (2000) Volume illumination for two-dimensional particle image velocimetry. *Meas. Sci. Technol*. **11**: 809-814.
8. JG Santiago, ST Wereley, CD Meinhart, DJ Beebe & RJ Adrian. (1998). A particle image velocimetry system for microfluids. *Exp. in Fluids* **25**:316-319.
9. JK Sveen (2000) MatPIV 1.4, Mechanics Division, Department of Mathematics, University of Oslo, Norway.
10. ST Wereley. (2000) Personal communication.

MICROSCALE ELECTROLYTIC PROBES, WITH INTEGRATED TEMPERATURE SENSORS, FOR NANO- TO MICRO-LITER FLUID VOLUMES

Dongming He
Assembly Technology Development, Intel Corp.
Chandler, AZ 85224

Mark A. Shannon[1]
University of Illinois at Urbana-Champaign
Urbana, IL 61801

ABSTRACT

Electrolytic conductivity measurements of fluids currently require sample volumes greater than a milliliter. Many applications would benefit from accurate measurements for nano- to microliter sample volumes. However, polarization and non-linear electrode impedance, along with stray impedance's and temperature effects, strongly affect measurements of the solution resistance for microliter and smaller sample volumes. MEMS-based Si electrolytic conductivity probes, down to 50 μm wide, with integrated temperature sensors have been designed and fabricated to mitigates these issues. The accuracy of normal scale probes is achieved with these sensors over 3 orders of magnitude in solution concentration.

INTRODUCTION

Electrolytic sensors can have extensive applications in chemical and biological testing, such as pharmacology, blood and urea analysis, and tissue perfusion measurements. However, conventional conductivity probes are too bulky and blunt for insertion into tissue, and most importantly require relatively large sample volumes to make accurate measurements. In particular, the cell constant, K_c, of the conductivity probe varies with the geometry of the probe *and* the volume being sampled. Thus, as the sample size is reduced for a specific probe size, the measured solution resistance, R_s, does not linearly vary with the conductivity below a critical dimension, and substantial errors can result. Often, the critical dimension to maintain a constant K_c is approximately one order of magnitude larger than the effective electrode spacing, L_{eff}, of the probe. Therefore, the volume occupied by the probe needs to be about 3 orders of magnitude smaller than the sample volume. Currently, for 96 well arrays, probe tips are needed that can accurately sample microliter sample volumes. The much larger 300+ arrays coming on-line need 10 nanoliter sampling! Electrolytic probes with such small dimensions are currently unavailable, and simply reducing their size with designs that have been reported in the literature or are commercially available leads to low sensitivity and large errors in the measurements.

Electrolytic probes used for tissue insertion present another set of challenges. Not only is the volume of solution inherently confined to around the probe tip, but the shape and structure must also allow insertion and sustain relatively large stresses and strains. In addition, electrolytic conductivity is a strong function of temperature, 1-3% per °C for most electrolyte solutions. Since skin temperature can vary on the order of 10°C from the core body temperature and is strongly dependent on depth, the temperature at the point of measurement needs to be known. Ideally, high-aspect ratio electrolytic probes of ~100 μm width are needed, with local temperature compensation. Current methods use needles for extraction and often need several milliliters of fluid. Microscale silicon probes on the order of 100 μm in cross-section are easily insertable, are strong, and can sustain relatively high strains. Microscale probes are also needed that can physically measure the local temperature and concentration in a fluid boundary layer within 100 mm of the surface with minimal flow disturbance. Simply put, new types of microscale electrolytic probes are needed that meet all the above criteria for a wide variety of applications.

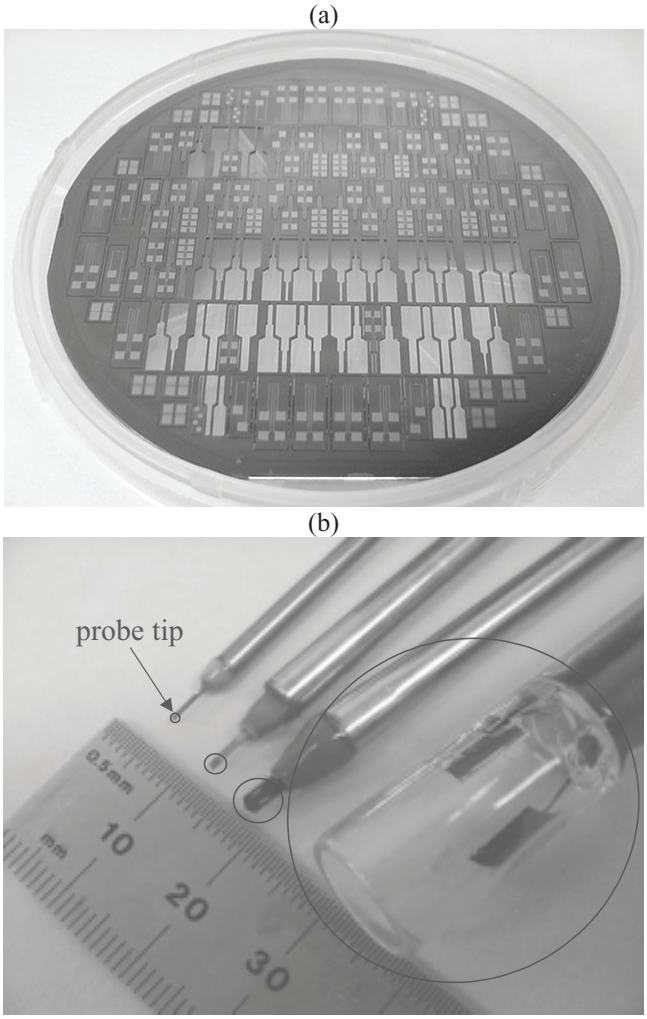

Figure 1. *(a) Photo of a wafer fabricated Si probe tips, with some probes removed from the wafer. Note that the large end accommodates large bond pads for hand soldered leads. Solder-bump pads make the overall size the same as the probe. (b) A photo showing sensors of 500, 1000, and 2000 μm tip width after wire bonding and packaged with stainless tubes, and a commercial 2-electrode conductivity sensor probe.*

[1] Submitting author. Address: 1206 West Green Street, Urbana, IL 61801, USA. Email: mas1@uiuc.edu

0-9640024-4-2/hh2002/$20©2002TRF
DOI 10.31438/trf.hh2002.48

Silicon conductivity sensors have been reported with smooth 2 and 4-electrode probe tips for relatively (~ 1 mL) small volume analysis [**1-5**]. However, smooth Au or Pt microelectrodes have high polarization impedance, making good accuracy difficult if their size is decreased further. In addition, stray capacitance, lead resistance, and high-frequency effects severely limit sensitivity and accuracy as tip sizes drop below ~1 mm. To solve these problems we developed several new design and processing parameters, and fabricated mass-producible, 1 kHz, silicon microelectrolytic sensors with temperature compensation, shown in Fig. 1. These are more than an order of magnitude smaller than other conductivity probes, accurately measuring μL to nL samples. Moreover, the linear conductivity response of the 4-electrode Pt-black sensors ranges over three orders of magnitude, providing better performance than large commercial 2-electrode probes. Therefore, these MEMS-based electrolytic probes offer a viable solution to the vexing problem of nanoliter sample problems, as well as creating insertable probes for tissue and boundary layer flows.

THEORY

Electrolytic conductivity sensors essentially work by measuring the resistance to current flow across electrodes in an ionic solution. Both conduction current and displacement currents can occur at the electrode/solution interface. To avoid chemical reactions associated with conduction current, nearly ideal polarized electrodes [**6**], such as Au and Pt, are often utilized for conductivity measurements with AC excitations to generate a displacement current. However, precise conductivity measurements at the microscale can be strongly affected by polarization impedance, which is a function of the driving frequency, electrolytic concentration and electrical potential. Non-linear impedance effects, such as ion diffusion, chemical reactions, adsorption and desorption of ions at the electrode/solution interface, become more important at high potential and current density, creating a non-constant interfacial impedance during each AC voltage swing. Increasing electrode area and reducing the applied potential help mitigate these effects, but often at the expense of increasing overall device size and increasing operational frequency, both of which acerbate the effect of stray capacitance and non-linear impedance at the microscale.

Figure 2 shows the layout of the sensor electrodes that use four planar electrodes, along with the major dimensions and current paths through the ionic solution. Both the layout of the sensor and the current path, which is affected by the overall geometry and volume of the sample volume, determine the resistance through the solution, which gives a direct measure of the solution conductivity and hence it's ionic concentration. To determine the sensor resistance, R_s, a simplified equivalent circuit of the electrodes is shown in Fig. 3. Each electrode generates a double layer capacitance with the ionic solution, which is a function of the surface potential and ionic concentration, *c*.

The measured solution resistance, R_S, is often set equal to K_C/σ, where K_C is the cell constant that depends on geometry and σ is the solution conductivity to be measured. The main issue for microscale sensors is that K_C can grow rapidly as the size of the sensor is reduced, due to a relative increase in electrode impedance, thereby reducing the accuracy of the measured R_s. Therefore, the electrode layout needs to be designed to reduce K_C, while considering the overall geometry of the probe and the paths that the current take within the solution.

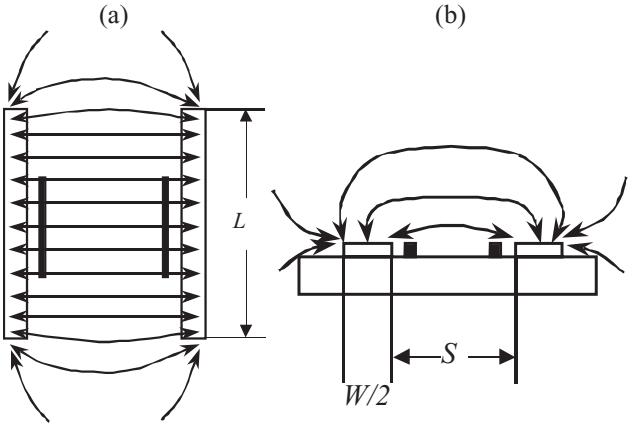

Figure 2. *The top (a) and side (b) view of a planar 4-electrode configuration, showing critical dimensions and current path through a surrounding fluid.*

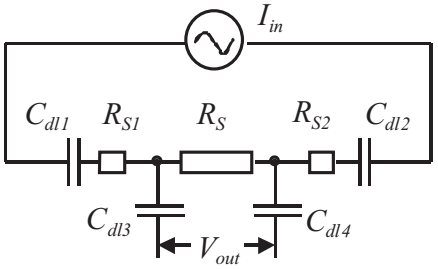

Figure 3. *A circuit representation of the electrode impedences for the 4-electrode sensor in Fig. 2. Note that stray capacitances and resistances of the leads, as well as Z_f, are not included.*

The current flow in Fig. 2 is three-dimensional and requires numerical modeling. However, when $L >> S$ and W then $K_C = (R_{S1}+R_S+R_{S3})\sigma$ can be expressed as

$$K_C = \frac{2\varphi(a)}{L\varphi[(1-a^2)^{\frac{1}{2}}]} \tag{1a}$$

$$\varphi(a) = \int_0^1 \frac{dt}{[(1-t^2)(1-a^2t^2)]^{\frac{1}{2}}} \tag{1b}$$

where φ is the potential, and $a = S/(S+W)$. The results for calculated K_C using Eqn. (1) are 17 to 34% higher than the measured due to neglecting 3-D current flow effects. The 2-D design using Eqn. (1) provides a upper bound on K_C. K_C. ranged from a low of 8.7{cm^{-1}} for 2000 μm wide tip probes to approximately 44 {cm^{-1}} for 50 μm wide tip probes. It should also be noted that polarization impedance scales inversely proportional to the effective electrode surface area (*LW/2* for smooth metal electrodes), and the measured solution resistance scales inversely proportional to *L* if parameter *a* is fixed. This implies that polarization impedance is *more important* for conductivity measurement with microelectrodes than normal scale devices. Therefore, polarization impedance also needs to be considered while limiting K_C in designing smaller electrodes. Leakage currents capacitively coupled through unexposed leads at the sensor tip and the leads going to the amplifier also create stray capacitances and stray resistances. Robust packaging for the sensor tip and fabricating well-insulated leads that are as short as possible from the amplifier are also important to reduce the stray impedances.

EXPERIMENTAL DETAILS

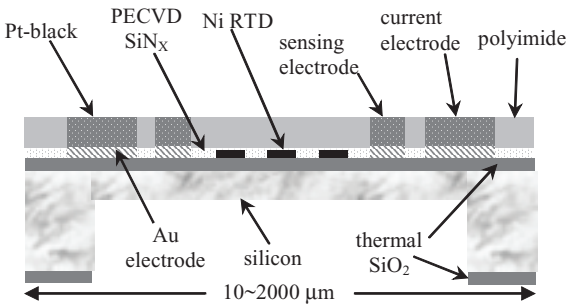

Figure 4. *Cross sectional diagram of 4-electrode sensor probe tip (not to scale). Note that the SiN_x and polyimide passivation layers are needed to achieve the desired performance. In addition, the polyimide layer acts as Pt-black electroplating molds, DRIE mask, and plastic packaging of the tip.*

Figure 4 shows the cross section of a probe tip fabricated by double-sided deep reactive ion etching (DRIE). Each of the layers is deposited on the wafer before etching. Several passivation and isolation layers are added to reduce stray capacitance to the substrate and to the solution. Two layers of PECVD SiN_x are grown on the metal thin-films for passivation of the RTD and leads. A layer of polyimide is applied to improve isolation and to serve as packaging for the probe tip, as well as to provide the mask for double-sided DRIE etching of the wafer. Gold is evaporated and patterned for leads, microelectrodes, and bonding pads to reduce stray resistance. The electrodes are placed over a thinned silicon section to reduce thermal mass and to improve the temperature measurements. Figure 5 shows the top and side view of typical probes made with this method. Probes can be packaged in stainless tubes and wires are bonded to pads and connector pins to facilitate test and handling, as in Fig. 1.

To reduce the effect of polarization impedance, the electrodes are electroplated with Pt-black to increase effective surface area. The effective surface area of an electrode has been reported to increase from hundreds to even one thousand times after Pt-black electroplating [**7**]. In addition, 2 current carrying and 2 sensing electrodes were fabricated to use 4-wire measurements with > 30 MΩ impedance across the sensing electrodes in order to minimize the effect of polarization impedance on the measured potential.

Figure 6. *A 500 µm sensor tip after Pt-black electroplating. Pt is plated within polyimide wells to define the plating mold and to provide additional spacing to reduce solution stray capacitance to the leads. Note that the leads are Au plated to further reduce stray resistances.*

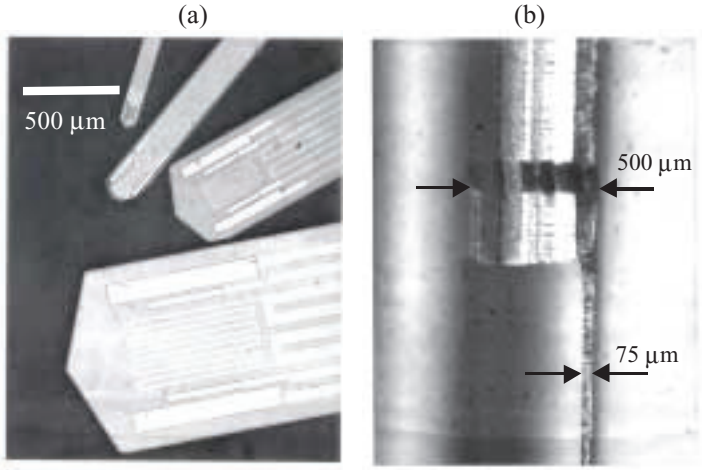

Figure 5*. (a) Sensor probes of 100, 200, 500 and 1000 µm tip width before Pt-black plating. (b) Side view of sensor tip is etched back to about 75 µm.*

RESULTS and DISCUSSION

To provide a means to measure the local temperature of the solution, which is important to achieve accurate conductivity measurements, an integrated thin-film resistive temperature device (RTD) is fabricated directly between the electrodes, as seen in Fig. 5. This location corresponds to the local average temperature for conductivity measurements, even if there is a temperature gradient between the electrodes. Thin-film nickel is deposited and patterned for the RTD due to its higher temperature coefficient of resistance (TCR) than Pt. In the temperature range we are interested in (approximately from -10 to 100°C), pure bulk Ni has a TCR of 6900 ppm per °C, compared with 3900 ppm per °C for pure bulk Pt. The RTD measurements achieved better than 1% accuracy from 0 to 100°C after calibration.

To note the effect of polarization impedance on microscale electrolytic sensors, conductivity measurements for a 200 µm wide sensor probe with 2 and 4-electrodes (with and without Pt-black) are shown in Fig. 7. Note that in Fig. 7(a) the smooth 2-electrode sensors have the largest non-linearity at highest concentrations, which can not be readily observed directly from the resistivity data in Fig. 7(b), but which nevertheless increases the uncertainty in the concentration measurement. By using Pt-black, this uncertainty is decreased to less than 4% with respect to the 95% confidence limit. In addition to reducing uncertainty, Pt-black electrodes also greatly reduces long term drift. Smooth polarized electrodes are very sensitive to fouling and ion absorption, which causes drift in the resistance measurement over time. The increase in area proportionally increases the time over which drift is noticed. However, by using sensing electrodes in a 4-wire configuration, the effect of fouling, etc. on drift is greatly diminished, since the change in impedance at the electrode interface is negligibly small compared to the input impedance of the instrumental amplifier.

As the sensor is reduced below a 100 µm in size, the effect that operation frequency has on the impedance increases in importance. Figure 8 shows the square of the total impedance, Z_{tot}^2 vs. $1/\omega^2$, for different solution concentrations. Note that at lower frequency (higher $1/\omega^2$) the capacitance is approximately constant, but begins to increase as frequency goes much above 10^4 Hz, and thus uncertainty in R_s rapidly grows particularly at higher ionic concentrations. As the inset in Fig. 8 shows, this effect leads to non-linear response in resistivity, taking on a quadratic, rather than linear, form. Therefore, for the smallest sizes, higher order calibrations are required to achieve the highest accuracy.

CONCLUSIONS

Microscale electrolytic probes with integrated temperature sensors were designed and fabricated to measure local conductivity and temperature of ionic solutions [**8**]. The Ni thin-film RTD achieved better than 1% accuracy from 0 to 100°C with a parabolic correlation. Two-electrode conductivity measurements with Pt-black electroplated microelectrodes achieved better than 5% linearity for solutions with conductivity varying from 2 to 180 mS/cm. However, bare 2-electrode measurements suffer from large polarization impedance and drift over time. The polarization impedance decreases hundreds-fold with Pt-black electroplating. Bare 4-electrode measurements also reduce polarization impedance and achieved better than 4% accuracy for the same measurement range for probes above 100 µm tip size. Combining 4 electrode and Pt-black electrodes allows sensors to be fabricated below 100 µm with better than 5% accuracy for a quadratic fit. The 50 µm wide sensor can sense approximately 100 nL sample volume. The lower limit in size appears only to be fabrication limited, to about a 10 µm wide sensor, for a 4 nL sample volume.

ACKNOWLEGEMENTS

This work was supported by DARPA DSO under DABT63-98-C-0053.

REFERENCES

1. W. Olthuis, A. Volanschi, J.G. Bomer, and P. Bergveld, "A new probe for measuring electrolytic conductance", *Sensors & Actuators B 13-14,* 230-233 (1993).
2. N. Kordas, Y. Manoli, W. Mokwa, & M. Rospert, "A CMOS-compatible monolithic conductivity sensor with integrated electrode", *Sensors & Actuators A 43,* 31 (1994).
3. A. Volanschi, W. Olthuis, and P. Bergveld, "Design of a miniature electrolyte conductivity probe using ISFET's in a four point configuration", *Sensors & Actuators B 18-19*, 404-407 (1994).
4. W. Olthuis, W. Streekstra, and P. Bergveld, "Theoretical and experimental determination of cell constants of planar-interdigitataed electrolyte conductivity sensors", *Sensors & Actuators B 24-25*, 252-256 (1995).
5. N.F. Sheppard Jr. and D.J. Mears, "Model of an immobilized enzyme conductimetric urea biosensor", *Biosensors & Bioelectronics 11*, 967-979 (1996).
6. J.O. Bockris and A.K.N. Reddy, Modern Electrochemistry, *Plenum Press* (1970).
7. R.A. Robinson and R.H. Stokes, Electrolyte Solutions, *Butterworths Scientific Publications* (1955).
8. D. He, "Theory, fabrication and characterization of micromachined electrolytic solution conductivity sensors," Ph.D. Dissertation, UIUC, (2001).

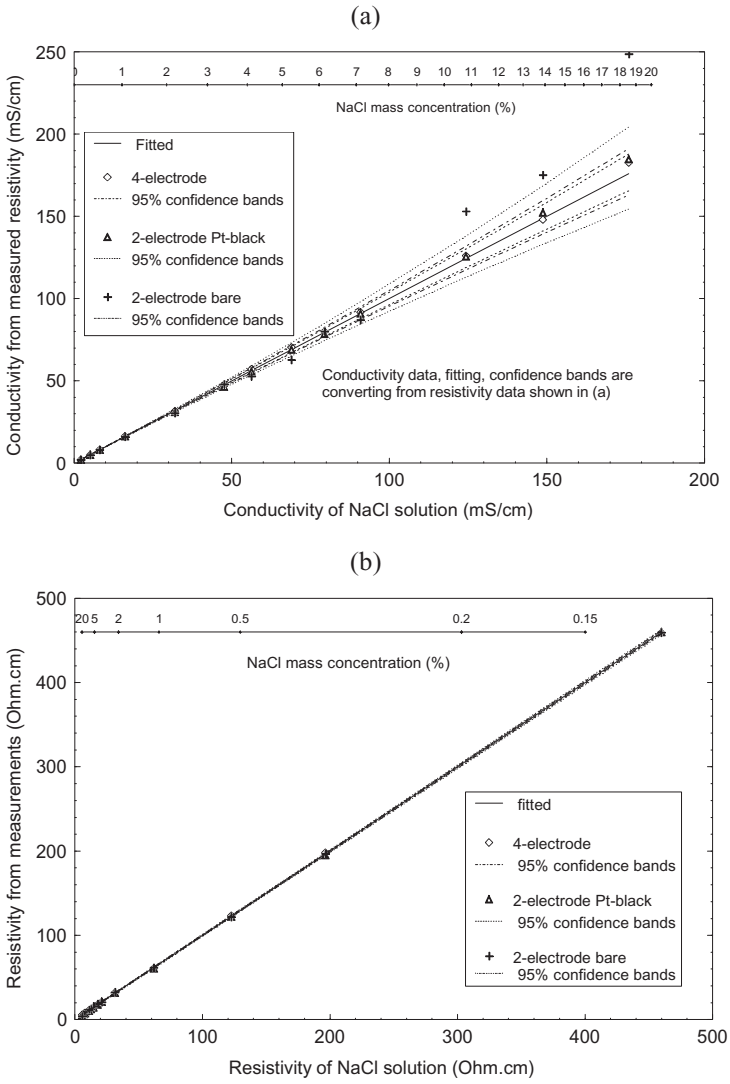

Figure 7*. Experimental results normalized with linear fitting with respect to NaCl solution (a) resistivity and (b) conductivity for three sensor probes: 4-electrode probe without Pt-black, 2-electrode probe with Pt-black, and 2-electrode probe without Pt-black. (data all compensated to 18°C). NaCl molar mass % concentration is also given, so that linearity can be discerned over the entire range with both plots. Note that both Pt-black and 4-wire measurements reduce the non-linearity, extending the linear measurement range.*

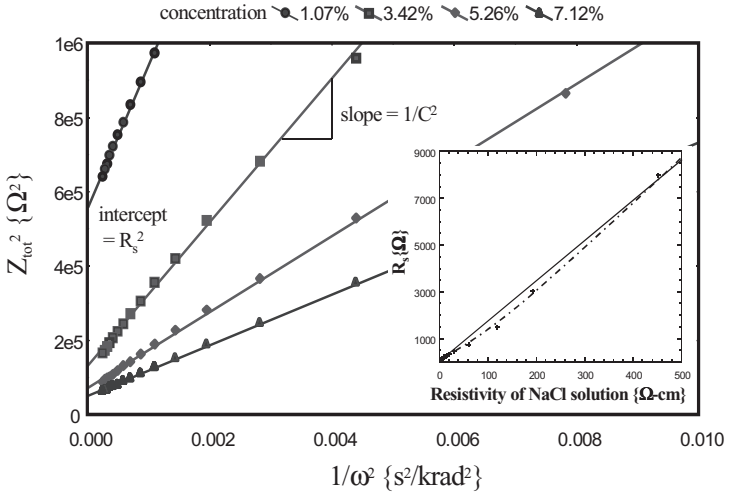

Figure 8. *Impedance for a Pt-black 4-electrode 50 µm sensor tip as a function of frequency, showing the effect of electrode capacitance on the total impedance. Inset shows R_s vs. the solution resistance.*

ACTIVE SOI-BASED NEURAL PROBES

Matthew D. Hills[1], David T. Kewley[2], James M. Bower[2,3], Gregory T. A. Kovacs[1]

(1) Department of Electrical Engineering
Stanford University
Stanford, CA 94305-4075, USA
(2) Computation and Neural Systems
California Institute of Technology
Pasadena, CA 91125, USA

(3) currently with the Research Imaging Center
University of Texas Health Science Center
and the Cajal Neuroscience Center
University of Texas at San Antonio
San Antonio, TX 78249, USA

ABSTRACT

This paper reports *in vivo* recordings from a new integrated, micromachined neural probe. The probes were fabricated by combining a standard CMOS process with a decoupled probe-formation process on silicon-on-insulator wafers. The fabricated probes include thirty-two electrode recording sites with low noise buffering to yield a high signal-to-noise ratio. A subthreshold-biased filtering system to cancel electrode-related offsets is also presented.

INTRODUCTION

Silicon-based probes are a unique tool for neurophysiologists studying the interactions of multiple neurons, where precise electrode placement is critical. Researchers have begun to realize these benefits [**1**] as passive silicon-based, multi-electrode arrays have started to become available to the neurophysiology research community.

Neural probes must be designed to minimize perturbations to the biological system, which requires biocompatible materials and reducing tissue trauma through smooth, low-profile shafts [**2**]. Electrically, the neural probe system must be capable of recording low-level extracellular action potentials, with frequencies of interest ranging from 100Hz-10kHz and amplitudes of 50-500μV, and field potentials, with frequencies of interest from 1Hz-100Hz and amplitudes up to a few mV.

By integrating such probes with circuitry, signal quality can be improved by buffering the signals on-chip, which minimizes parasitic losses due to wiring and packaging and reduces susceptibility to crosstalk and noise pick-up. Early active probe work using PMOS or NMOS processes [**3**,**4**] demonstrated the potential for integrating circuits on the probes. More recent active probe work has shifted towards integrating with a custom CMOS process and has achieved higher yields [**5**]. This custom CMOS process is based upon epitaxial wafers, requires preliminary deep Boron implants to establish the etch stop that defines the probe shape, and requires special care to avoid undercutting the circuitry.

Electrodes exhibit a time-varying drift in the electrode potential [**6**] that can saturate high-gain amplifiers and degrade the performance of differential amplifiers. Conventional recording systems use discrete high-pass filters at the front end to block these offsets. Large capacitors have been integrated on-chip for this purpose [**3**], but this procedure is not area efficient for multiple channels. Other approaches include reset switches, which suffer from feedthrough, and diodes, which are not reliably able to prevent amplifier saturation [**5**].

The probe design presented here addresses these issues through a fabrication procedure that decouples the probe-formation process from the standard CMOS process, and the implementation of electrode offset-cancellation circuitry with low-noise buffering.

SYSTEM DESIGN

The current probes are fork-shaped structures with a full wafer thickness base area and multiple, thin shafts that penetrate the cortex (Figure 1). In designing the active probes, the primary goal was to develop a reliable CMOS-compatible process to facilitate simultaneous recording of a large number of high-quality signals. In order to achieve this, it was necessary to use area-efficient, low-noise buffering circuitry and to develop a probe shaping process that would not require modifications to the underlying circuit process.

Probe Design. The probe formation includes the overall definition of the probe shaping, the electrodes, and the traces. Probe shaping is accomplished through plasma etches stopping on the oxide of a silicon-on-insulator (SOI) wafer. Plasma etching offers flexible control over the probe geometries [**7**], while sidewall smoothness and shape can be controlled by the etch recipe [**8**]. Overall shaft thickness is set by the 25μm device layer, allowing for good rigidity and strength for the 3-5mm shaft lengths. “Bond and etchback” SOI wafers are used to provide the relatively thick device layer and a smooth oxide interface, which translates into a smooth underside on the shafts. Similar probe-shaping methods have recently been reported by several investigators developing passive probes [**9**,**10**].

The recording electrodes were 100μm^2 in area and metallized with evaporated gold. The geometry balances the selectivity of small recording sites [**11**] against the lower source impedances of larger sites, while the gold electrode is resistant to corrosion [**12**] and is readily available for evaporation.

The second metal (aluminum) layer from the CMOS process was used to form the traces along the shafts. By including a dielectric between the trace and electrode, the overall shaft width could be minimized and tetrode geometries could be readily designed. A thick barrier layer of titanium was used between the aluminum traces and gold electrodes to prevent the intermetallic formations of “purple plague.”

Preliminary experiments demonstrated that the silicon substrate can also act as a parasitic electrode. In order to avoid driving this electrode, active probe designs typically tie this substrate potential to the biological reference [**5**]. To minimize possible loading on the system, the substrate was also encapsulated in a silicon nitride dielectric. Due to the difficulty of selectively encapsulating a three-dimensional structure, this was done by relying upon the relative anisotropies of the deposition and etch processes. Such an approach is not well-controlled and would likely have passivation failures, particularly close to the probe tips, but

Travel support has been generously provided by the Transducers Research Foundation and by the DARPA MEMS and DARPA BioFlips programs.

0-9640024-4-2/hh2002/$20©2002TRF
DOI 10.31438/trf.hh2002.49

Solid-State Sensors, Actuators, and Microsystems Workshop
Hilton Head Island, South Carolina, June 2-6, 2002

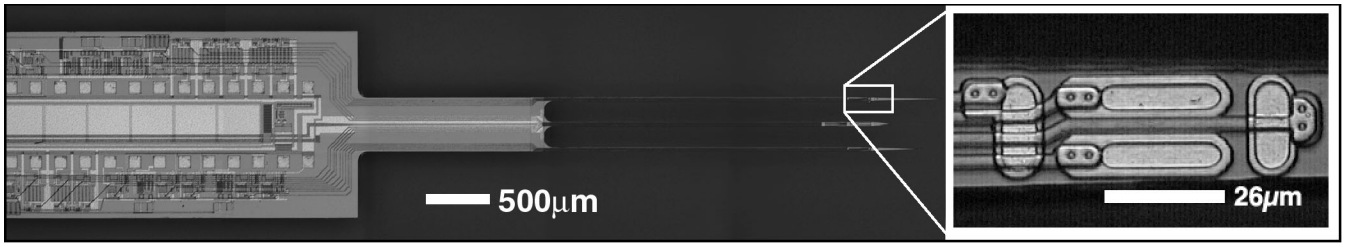

Figure 1. *Micrograph of an active probe with an enlargement of a tetrode recording structure. The large capacitor structure in the center of the circuit area filters the on-chip bias. In the inset, note the narrow shaft width achieved by the multiple metal levels and anisotropic silicon etch.*

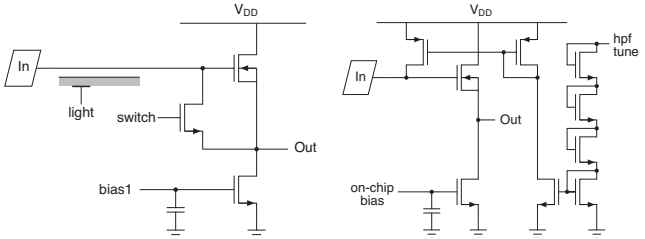

Figure 2. *Schematics of the source-follower circuit (left), and the electrode offset cancellation circuit (right).*

preliminary cross-sections of shafts showed good coverage that would minimize the substrate electrode area.

Light-induced noise was observed in previous work with passive probes and was determined to arise from carrier generation in depletion regions underneath the traces and electrodes [**7**]. This was avoided by utilizing the implants of the CMOS process to dope the shafts and then keep the traces biased so that the shafts remain in accumulation. The coupling could also have been reduced by increasing the dielectric thickness, but with tradeoffs against cross-coupling, shaft cross-sectional area, stress-induced curvature in the shafts, and constraints upon the underlying CMOS process.

To improve upon the handling and packaging issues encountered with earlier probe work [**7**], it was considered important to work with full-wafers throughout the process and to increase the thickness of the base underneath the circuits. The SOI substrate provides both of these features. The oxide layer provides a reliable etch stop for both front-side probe shaping, as well as the back-side release etch. Furthermore, patterning the back side prior to the release etch allows for a thick substrate by which to handle the individual probes and also improves mounting alignment by butting against an edge on the probe mount. After the release etch, the probe bases are still attached to the wafer by tabs that can later be mechanically severed when the probes are ready for packaging. After mounting and wirebonding, the probe bases are encapsulated in an opaque epoxy to protect the bondwires and circuits from the electrolyte and shield the circuitry from light effects.

Circuit Design. For small signals over the bandwidth of interest for neural recording, recording electrodes are typically modeled as high-impedance capacitive sources [**13**]. In order to buffer the signals most efficiently, source followers were used (Figure 2). NFET devices were selected to allow inputs at the positive rail, which was necessary for biasing the biological reference at the substrate potential in the p-well process. With these devices, 1/f noise dominates the circuit noise performance and can be reduced as a function of device area. Techniques for reducing 1/f noise, such as chopper stabilization, introduce problems from clock feedthrough at the high-impedance node. As single-ended designs are sensitive to power-supply noise, the system uses a regulated and filtered battery power supply and the on-chip bias circuit includes a large MOS capacitor to minimize noise on the shared bias line. Other buffer topologies have been demonstrated [**5**] that can improve the PSRR and output resistance, but with typical trade-offs against die area, noise performance, and power.

The electrode offset cancellation is accomplished through a tunable high pass filter formed by the electrode and a variably-biased sub-threshold device (Figure 2). Earlier work [**7**] demonstrated the utility of sub-threshold devices for implementing tunable, low-frequency, high-pass filters between stages to prevent amplifier saturation. The current design moves this to the front of the first stage in order to prevent noise degradation resulting from the dc offsets unbalancing the amplifier input. A similar technique was prototyped [**14**], although implementation required trimming a resistor to compensate for process variations and was not integrated with a probe.

PROBE FABRICATION

The integrated probes were fabricated on 4-inch BESOI wafers with a 25μm thick, $\langle 100 \rangle$ n-type device layer (SiBond L.L.C., Hopewell Junction, NY). Processing proceeded in three phases (Figure 3), and then the probes were mounted on pc boards for use.

Circuit Fabrication. The circuit fabrication followed a standard p-well, poly-gate CMOS sequence [**15**]. The n+ substrate contact was implanted over the shafts as the light shield. The field oxide and first layer of low temperature oxide (LTO) were removed from non-circuit areas during processing by the active and contact etches, respectively. The second 600nm LTO layer was deposited and patterned for vias and with the outline of the probe, so that it would form the dielectric underneath the probe traces. Metal two was sputter-deposited Aluminum 700nm followed by 50nm of titanium, and was patterned with a Cl_2/BCl_3 plasma etch.

Electrode Formation. Metal two was encapsulated by 600nm of PECVD silicon nitride deposited at 350°C. This was patterned using a plasma etch with SF_6 and CF_3Br to clear the contacts for the electrodes and also clear the outline of the probe. To define the electrode areas, a liftoff structure was created using NR8-3000 (Futurrex, Inc., Franklin, NJ), where the undercut necessary for the liftoff was adjusted via the lithography exposure energy. For the electrode, 100nm of titanium, followed by 650nm of gold were deposited by ebeam evaporation. The liftoff was conducted in EMT-130T resist stripper heated to 80°C, and the wafers were then rinsed in a mask cleaner to fully remove residual electrode material from the wafer edges. The 1μm silicon nitride upper dielectric was deposited

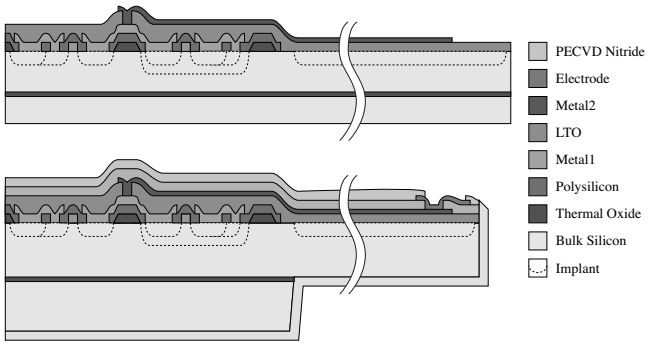

Figure 3. *Cross-sections of probe during processing. The top diagram shows the probe after completion of CMOS through top metal. The bottom diagram shows a cross-section after electrode metallization, passivation, and probe shaping.*

by PECVD at 350°C and then patterned using an SF_6/CF_3Br plasma etch to define the electrode openings, bondpads, and the overall outline of the probe. In order to help protect the dielectrics, a 30nm layer of chromium was sputter deposited and patterned using CR-14 Chromium Etch (Cyantek Corp., Fremont, CA).

Probe Formation. The probe shape was defined using a deep reactive ion etch (DRIE etch) [**8**] that utilized switched SF_6 and C_4F_8 gas flows. As the front-side etch neared completion, the switching ratio was biased to provide more passivation, in order to minimize the lateral etching at the buried oxide layer characteristic of the Bosch etch process [**16**]. The front side of the wafer was then coated with a thick layer of AZP4620 photoresist (Clariant Corp., Somerville, NJ) as protection during the back-side patterning. The back side was patterned with a back-side mask aligner aligning against the front-side stepper-generated fields. This registration was within the ±10μm tolerances in the design layout. The residual oxide and nitride on the back of the wafer were removed using a CHF_3/O_2 plasma etch, and then the back-side silicon was etched using a DRIE etch. The buried oxide was removed with a CHF_3/O_2 plasma etch. After stripping resist and cleaning the wafers, 500nm of silicon nitride was deposited on the back side of the probes. The front side of the wafers was then etched in an SF_6/CF_3Br plasma to remove the substrate-protection nitride that deposited on the probe fronts. The chromium was removed with a quick dip in 50:1 HF to remove chromium oxide, followed by an etch in a 1:1 mixture of acetic acid and CR-14 Chromium Etch, then the probes were rinsed and dried at 150°C.

Mounting. The probes were separated from the wafer by cleaving the tabs to the bulk wafer. A low-stick tape was used underneath the bases to hold them in place. The probes were positioned on the carrier pc boards by butting them against the edge of the alignment groove and bonding with epoxy. Electrical connections were made by wirebonding to the pc board, and the base and wirebond area was encapsulated in Epo-Tek 87GT epoxy (Epoxy Technology, Inc., Billerica, MA).

EXPERIMENTAL RESULTS

After the initial CMOS device verification, the probes were first tested *in vitro* to quantitatively measure system performance and then tested *in vivo* to verify the performance for the intended application. The passive probes created in the same process run

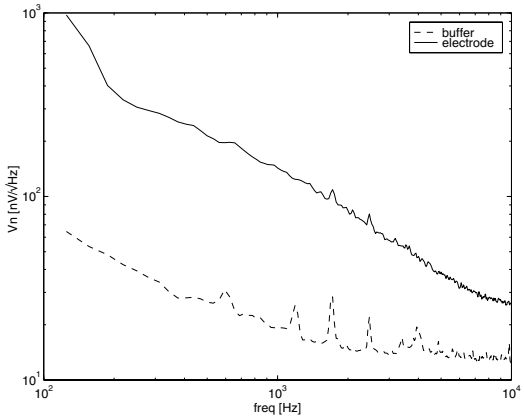

Figure 4. *Spectral plots showing the noise from a buffer with grounded inputs and from a buffer with a 100μm^2 electrode in grounded saline. Note that the electrode noise dominates.*

have been employed for other physiology experiments that have been presented separately [**17**].

Benchtop Testing. The source followers occupy 0.05 mm^2 and dissipate 50μW per channel. Their output impedance is 7kΩ with a grounded input, and 13.4kΩ with a 100μm^2 electrode at the input. 1/f noise is dominant over the 100Hz-10kHz frequency range, with a process Kf_{NMOS}=2.0 10^{-24} V^2F. As shown in Figure 4, the followers alone exhibit a total noise of 1.7 μVrms, while driving the followers through 100μm^2 electrodes in grounded saline gives a total system noise of 11 μVrms.

The electrode offset cancellation circuit performance is demonstrated in Figure 5, and its tuning behavior is shown in Figure 6. The effectiveness of the substrate light protection was assessed by testing sensitivity to laboratory ambient lighting in saline, as shown in Figure 7.

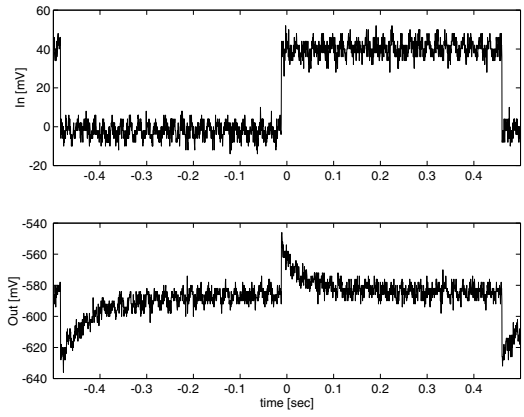

Figure 5. *Response (bottom trace) of the electrode offset compensation circuit to a 50mV step (top trace) applied to a Ag/AgCl electrode in saline. A 10mV high-frequency signal is superimposed on the input for comparison.*

Neural Recordings. The subjects for the physiological tests of the probes were 40-60 day old female albino Sprague-Dawley rats. During each experiment, the animal was anesthetized with ketamine and placed in a stereotaxic rig. Surgery was performed to expose a small area over the parietal cortex, where the probe insertions were

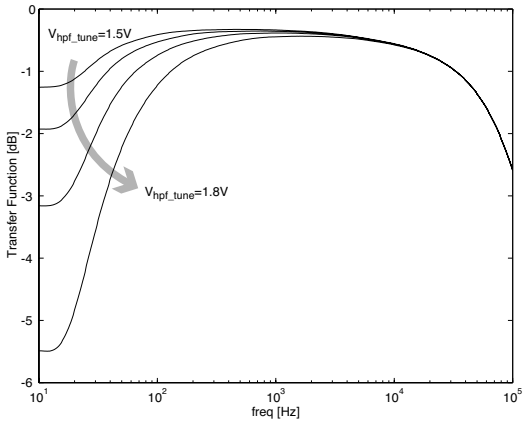

Figure 6. *Transfer function of the electrode offset cancellation circuit showing the tunable high-pass characteristic.*

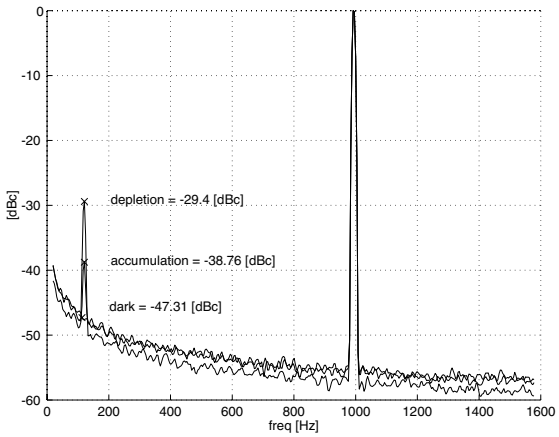

Figure 7. *Spectral output of electrode in saline when under illumination and driven by a Ag/AgCl electrode with a $1mV_{PP}$ at 1kHz signal. The spectra provide a baseline measurment taken in the dark, and then demonstrate the improvement provided by the light protection implant (accumulation) compared to the (depletion) biasing conditions.*

to be performed. Figure 8 shows several channels of spontaneous neural activity recorded from parietal cortex using the active probes. Data was collected using a multi-channel amplifier and data acquisition system [**18**].

The signal quality is comparable to that reported from a custom CMOS process [**5**]. The light protection worked well, as the experiments were conducted in laboratory lighting, although some shielding may still be needed if strong light is used for visual stimulation, as strong microscope lighting over the electrodes produced significant noise. No benefit of the substrate passivation was immediately apparent from the data collected, suggesting that any benefit would be more likely to affect the system behind the shafts, and out of the immediate area of observation. Cross sections of the probe shafts revealed good coverage in SEMs, although failures would be most likely near the tip, where clean cross sections were difficult to make.

CONCLUSION

We have presented a new method for fabricating active neural probes using a standard CMOS process followed by a decoupled micromachining process and demonstrated their utility for *in vivo* measurements. The electronics on the probe have provided low-noise buffering and demonstrated an effective method for electrode offset cancellation that will be useful for systems designed with on-chip amplifiers. Finally, the substrate light protection implants enable experiments to be conducted in brightly lit conditions. Further work needs to be done to determine whether the substrate encapsulation realizes any benefit for the overall system, and future probe shaping would benefit from improved SOI etching techniques [**16**].

ACKNOWLEDGEMENTS

This work has been funded by the National Science Foundation under grant #PC147129-1. Additional support was provided by the NASA National Biocomputation Center.

REFERENCES

1. G. Buzsáki and A. Kandel, "Somadendritic backpropagation of action potentials in cortical pyramidal cells of the awake rat," J. Neurophysiol., vol. 79, pp. 1587-1591, 1998.

2. D. J. Edell, V. V. Toi, V. M. McNeil, and L. D. Clark, "Factors influencing the biocompatibility of insertable silicon microshafts in cerebral cortex," *IEEE Trans. Biomed. Eng.*, vol. 39, pp. 635-643, 1992.

3. K. Takahashi and T. Matsuo, "Integration of multi-microelectrode and interface circuits by silicon planar and three-dimensional fabrication technology," *Sensors and Actuators*, vol. 5, pp. 89-99, 1984.

4. K. Najafi and K. D. Wise, "An implantable multielectrode array with oon-chip signal processing," *IEEE J. Solid-State Circuits*, vol. SSC-21, pp. 1035-1044, 1986.

5. Q. Bai and K. Wise, "Single-Unit Neural Recording with Active Microelectrode Arrays," *IEEE Trans. Biomed. Eng.*, vol. 48, pp. 911-920, 2001.

6. M. D. Gingerich and K. D. Wise, "An active microelectrode array for multipoint stimulation and recording in the central nervous system," in *Digest Int. Conf. on Solid-State Sensors and Actuators*, pp. 280-283, 1999.

7. D. Kewley, M. Hills, D. A. Borkholder, I. Opris, N. Maluf, C. W. Storment, J. Bower, and G. T. A. Kovacs, "Plasma-etched neural probes," *Sensors and Actuators A*, vol. 58, pp. 27-35, 1997.

8. A. A. Ayón, R. Braff, C. C. Lin, H. H. Sawin, and M. A. Schmidt, "Characterization of a Time Multiplexed Inductively Coupled Plasma Etcher," *J. Electrochem. Society*, vol. 146, pp. 339-349, 1999.

9. K. Cheung, G. Lee, K. Djupsund, Y. Dan, L. P. Lee, "A new neural probe using SOI wafers with topological interlocking mechanisms," in *Proc. 1st Intl IEEE-EMBS Conf. on Microtech. in Med. & Biology*, 2000, pp. 507-511.

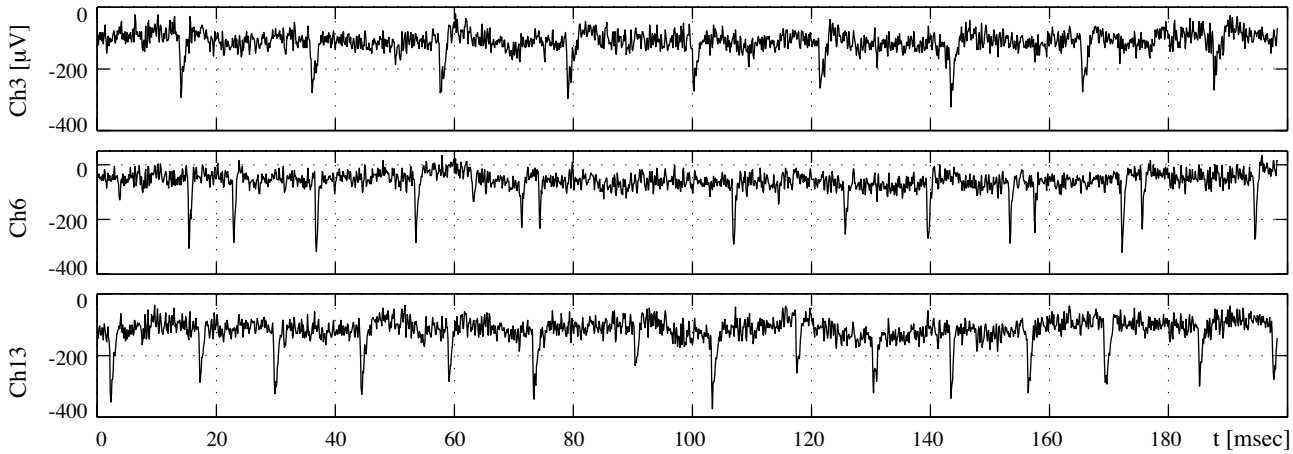

Figure 8. *Recordings of spontaneous neural activity within the parietal cortex. The three traces shown are simultaneous recordings from an active probe in ambient lighting. The top trace was recorded from a site 160µm deeper in the cortex than the electrode corresponding to the central trace, while the bottom trace was from a site displaced 200µm laterally.*

10. P. Norlin, M. Kindlundh, A. Mouroux, K. Yoshida, W. Jensen, and U. F. Hofmann, "A 32-site neural recording probe fabricated by double-sided deep reactive ion etching of silicon-on-insulator substrates," in *Proc. Micromechanics Europe Workshop (MME-2001)*, 2001, pp. 171-174.

11. A. Starr, K. D. Wise, and J. Csongradi, "An Evaluation of Photoengraved Microelectrodes for Extracellular Single-Unit Recording," *IEEE Trans. Biomed. Eng.*, vol. BME-20, pp. 291-293, 1973.

12. K. D. Wise and J. B. Angell, "A low-capacitance multielectrode probe for use in extracellular neurophysiology," *IEEE Trans. Biomed. Eng.*, vol. BME-22, pp. 212-219, 1975.

13. G. T. A. Kovacs, "Microelectrode models for neural interfaces," in *Enabling Technologies for Cultured Neural Networks,* D. A. Stenger and T. M. McKenna, Eds. San Diego:Academic Press, 1994, pp. 121-165.

14. A. Chandran, K. Najafi, and K. Wise, "A New DC Baseline Stabilization Scheme for Neural Recording Microprobes," in *Proc. 1st Joint BMES/EMBS Conf.*, 1999, p. 386.

15. A. Partridge, J. Reynolds, J. Grade, B. Kane, N. Maluf, G. T. A. Kovacs, and T. Kenny, "An integrated controller for tunnel sensors," *IEEE J. Solid-State Circuits*, vol. 34, pp. 1099-1107, 1999.

16. C. Gormley, A. Boyle, V. Srigengan, and S. Blackstone, "HARM processing techniques for MEMS and MOEMS devices using bonded SOI substrates and DRIE," *Proceedings of SPIE*, vol. 4174, pp. 98-110, 2000.

17. W. Freiwald, A. Wannig, A. Kreiter, U. Hofmann, M. Hills, G. T. A. Kovacs, D. Kewley, J. Bower, C. Eurich, and S. Wilke, "Stimulus representation in rat primary visual cortex: multi-electrode recordings and estimation theory," *Neurocomputing*, to be published.

18. K. H. Gilchrist, V. N. Barker, L. E. Fletcher, B. D. DeBusschere, P. Ghanouni, L. Giovangrandi, and G. T. A. Kovacs, "General purpose, field-portable cell-based biosensor platform," *Biosensors and Bioelectronics*, vol. 16, pp. 557-564, 2001.

FLOW-THROUGH MICRO-ELECTROPORATION CHIP FOR GENETIC ENGINEERING OF INDIVIDUAL CELLS

Yong Huang [a] and **Boris Rubinsky** [b]
[a] Bioelectronic Microsystems, Albany, CA94706
[b] Department of Mechanical Engineering, University of California, Berkeley CA 94720

ABSTRACT

We describe a chip that is capable of performing gene transfer in individual biological cells through single cell micro-electroporation. Microfluidic channels are used to handle individual cells in a flow through fashion that yields high electroporation efficiency. Controlled introduction of macromolecules and genetic engineering of an individual cell are demonstrated.

INTRODUCTION

There are many situations, in biology and biotechnology, in which it is desirable to transport across the cell membrane extracellular molecules that are normally cell membrane impermeant. For instance in genetic engineering, gene constructs, that are normally membrane-impermeant, need to be introduced into cells. Conventional methods for gene transfer through the cell membrane include the use of viral vectors, electroporation, liposome fusion and microinjection. These methods are applied to large populations of cells and do not have the capability to selectively manipulate particular cells of interest. Methods that operate on populations of cells are limited in their efficiency because there is no real time control over the events in each individual cell and therefore no real time feedback over the procedure **[1][2]**.

We have developed a micro-electroporation chip **[3][4]**, in which a live cell becomes an integral part of the chip's electrical circuit. The chip facilitates precise control over the process of electroporation in individual cells by measuring in real-time the electrical currents that flow through the cell membrane. This paper expands on our previous work by introducing a new chip design that uses microfluidic structures to precisely handle cells in a flow-through fashion The chip performs electroporation facilitated gene transfer in each cell consecutively. In the chip, cells are transported through a micro channel, whose width is on the same order as the cells, in a single file to the vicinity of a micro hole. The cell near the hole is captured by pressure difference, incorporated in the electrical circuit of the chip, electroporated under controlled conditions, uploaded with the desired genetic material and than released to be replaced by the next cell, consequently yielding virtually 100% gene transfer rate in all the loaded cells.

Using the chip, we introduced a membrane impermeant nucleic acid stain, YOYO-1, into individual prostate adenocarcinoma (ND-1) cells. We performed a quantitative study on the electroporative delivery of macromolecule dyes under different electroporation conditions with fluorescent intensity analysis. Our results suggest that adjusting easily accessible electroporation parameters could regulate the amount of substances introduced into an individual cell. Micro-electroporation was also used to successfully transfect individual ND-1 cells with EGFP (Enhanced Green Fluorescent Protein) genes, and thereby demonstrates the feasibility of single cell level genetic manipulation and engineering.

MICRO-ELECTROPORATION PRINCIPLES

Electroporation is widely used in biotechnology for gene transfer. It employs transient high electrical field to temporarily permeabilize cell membranes by means of forming nanoscale pores in the lipid bilayer membrane**[5][6]**. As a consequence, DNA and other macromolecules, which are normally membrane-impermeant, can be transferred across the electroporated cell membranes **[6][7][8]**. Traditional electroporation technique uses two electrodes to apply high electrical field to a large number of cells in between. This is a trial and error procedure with no real time feedback and control over the electroporation process in individual cells. Therefore, a successful application heavily relies on empirical practice **[7]** and general effectiveness is very low with large variations.

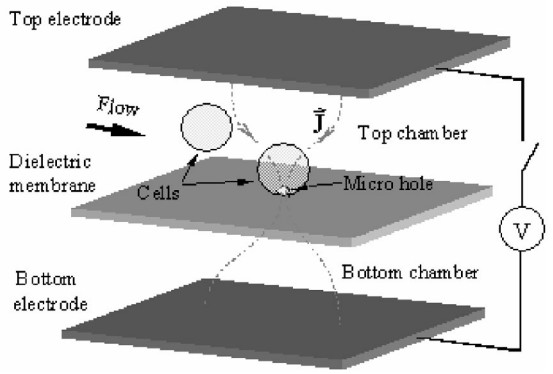

Figure 1. Schematic representation of single-cell level micro-electroporation

It occurred to us that if an electroporated membrane becomes permeable to macromolecules, the pores in the membrane, which allow the transport of macromolecules, should also provide pathways for smaller ions to pass through the membrane; thereby generating measurable transmembrane currents during electroporation as a direct measure on membrane permeability. To measure the small transmembrane current, we came up with a design, shown in Figure 1, in which the electrical current between two electrodes is forced to pass through a micro hole in a dielectric membrane. When a cell is captured in the micro hole by an appropriate pressure gradient, the cell effectively blocks the current path between the two electrodes. Ideally, the transmembrane current is identical with the current flowing between two electrodes, which can be easily measured. Using the transmembrane current as a direct feedback on membrane permeabilization, the electroporation process of the captured cell can be precisely regulated. This controlled single-cell electroporation mode is referred as 'micro-electroporation.' A detailed description of the concepts and procedures of micro-electroporation can be found in references **[3][4]**.

0-9640024-4-2/hh2002/$20©2002TRF
DOI 10.31438/trf.hh2002.50

FLOW-THROUGH CHIP DESIGN AND FABRICATION

Biotechnological applications require the manipulation of large numbers of cells. To this end we have developed a new micro-electroporation chip that can process large numbers of individual cells consecutively in a flow-through fashion. In the chip all cells are transported to the electroporation site in a single line profile through a micro channel whose width is slightly bigger than that of a cell. Once a cell is brought to the vicinity of the micro hole, it is captured by a suction pressure, then micro-electroporated under controlled conditions, uploaded with desired foreign substances such as DNA, and finally released to be replaced by the next cell in the line. Because the micro-electroporation method can achieve 100% electroporation effectiveness on each individual cells, virtually all cells loaded into the chip can be uploaded with the desirable gene constructs. Since the entire process can potentially be controlled by a computer, it is feasible to develop automated micro-electroporation systems for single-cell level genetic manipulation and drug delivery, with high efficiency and throughput.

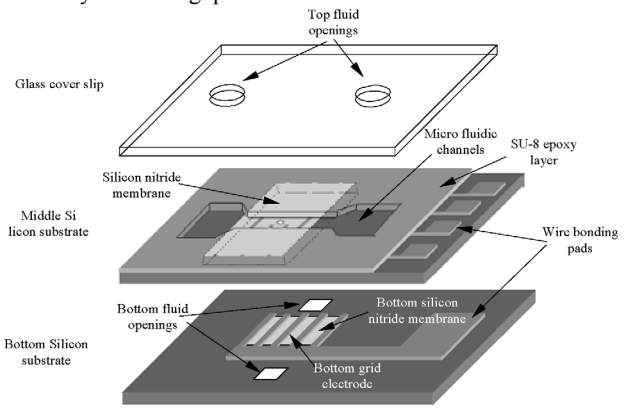

Figure 2. *Construction of a flow-through micro-electroporation chip with microfluidic channels for precise cell transport*

Figure 2 illustrates the construction of the flow-through micro-electroporation chip. The chip consists of two microfabricated silicon substrates and a glass cover slip, bonded together. The bottom and middle substrates form a bottom electroporation chamber that is filled with biological solutions through the bottom fluidic openings. The top electroporation chamber, where cells are loaded, is enclosed by the silicon nitride dielectric membrane and microfluidic structures on the middle substrate, and the cover slip. The central region of the chip is designed to be transparent so as to facilitate the use of light microscopy for visual observation of the cell manipulation process.

The middle silicon device is typically 20mm×10mm×500μm in size. It contains a 1mm×1mm×1μm silicon nitride dielectric membrane with one micro hole, sized between 2μm to 6μm. The hole is etched through the nitride membrane with reactive ion etch. The micro hole provides the only fluidic and electrical connection between the fluid chambers and the electroporation electrodes. The microfluidic channel structures are made of SU-8 thick photoepoxy **[9]**. Figure 3 shows an optical image of a typical design of the flow-through micro-electroporation chip. The fluid channels are typically 30μm deep, 500μm wide at entries and converge to a 30μm wide, 200μm long micro channel near the micro hole region.

The micro channel, whose width is set to be 1.5 times the average diameter of cells used in our experiments, mechanically confines the loaded cells to pass by the micro hole, which is on the channel's centerline, one by one in a single line profile. Filtration structures (not shown) are placed near the entrances of the 30μm wide micro channel to prevent large particles and debris from entering and blocking the channel. At the entrance of the micro channel, there are two auxiliary electrodes that are used to further keep the channel from being blocked by large cells by degenerating the cells with high voltage pulses. Two more 10μm wide auxiliary microelectrodes are placed 10μm away on both sides of the micro hole for cell detection by impedance measurement.

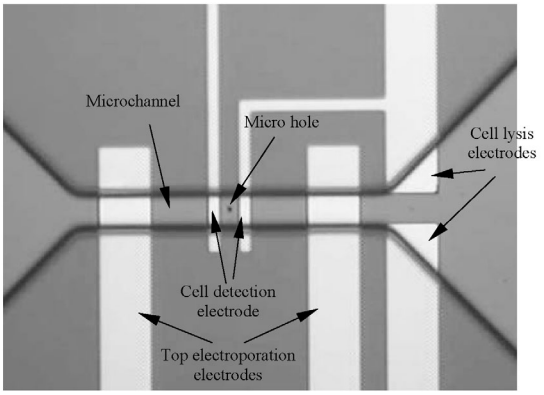

Figure 3.Typical layout of micro hole, microchannel and integrated electrodes on middle layer device

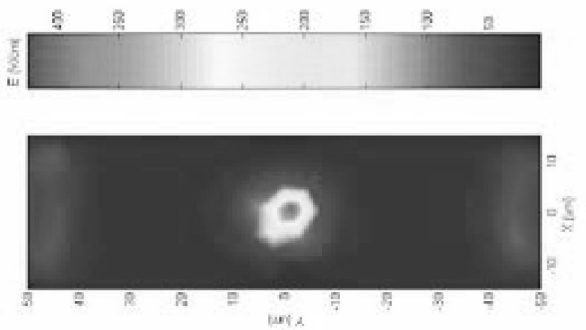

Figure 4*. Electrical field inside a 30μm×30μm micro channel. The illustrated plane is 5μm above the middle dielectric membrane. The micro hole is 3μm in diameter and locates at the channel center. Thickness of the middle dielectric membrane is 1μm. Two 50μm wide thin film electrodes are placed 50μm away from the micro hole. Distance between dielectric membrane and bottom electrode is 500μm. Unit voltage is applied between top and bottom electrodes.*

The top plate electrode in Figure 1 is substituted in our new design by two 50μm wide thin film platinum electrodes that are placed 100μm apart on two sides of the micro hole, as shown in Figure 3. This maintains a symmetric electrical field across the micro-hole. Simulation shows that the position of top electrodes has little influence on the electrical field distribution because most potential drop occurs in the vicinity of the micro hole. Figure 4 shows the simulated electrical field inside the flow-through chip. It is evident that the electrical field inside the channel is highly focused, with strong electrical field in the vicinity of the hole and a negligible field in other regions. This highly concentrated electrical field grants the chip great advantage in performing selective

electroporation only on the cell captured in the micro hole while the nearby cells remain unaffected.

Final sealing of the microfluidic channel is achieved by bonding SU-8 structures to a glass cover with a UV-curable adhesive (NEA121, Norland products). The bonding process we developed produces excellent channel definition, sealing and bonding strength for channels down to 10μm wide. Figure 5 shows the bonding interfaces and a cross-section of a 50μm×20μm rectangular micro channel.

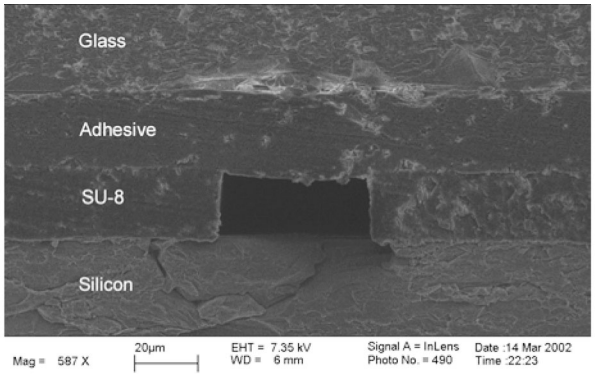

Figure 5. *SEM cross-section image of a sealed* 50μm×20μm *rectangular micro channel and bonding interfaces*

The bottom silicon layer, typically 23mm×10mm×500μm in size, hosts a bottom electrode, fluid openings and wire bonding pads. The bottom electrode is made of an array of thin film platinum lines, with typical width of 20μm, line spacing of 50μm, sitting on top of a 1μm thick transparent silicon nitride supporting membrane. Numerical simulation shows that the electrode geometry induced distortion in electrical field is localized within tens of micrometers from the electrode plane and beyond that, the geometry effects can be ignored and the grid electrode behaves as a plate electrode. The bottom layer is glued to the middle layer with a heat-curable adhesive (NEA121, Norland products). Finally, fluidic ports and tubing are attached to the assembled chip for fluid access.

EXPERIMENT MATERIALS AND METHODS

Human prostate adenocarcinoma cells (ND-1 cell line) are used in our experiments. For each experiment, cells from the confluent monolayer were removed by trypsinisation (trypsin 0.05%, EDTA 0.025%) (Gibco Grand Island, NY) and re-suspended in Dulbecco's PBS (Sigma chemicals, St. Louis, MO) for experimental use.

In order to study the electroporation facilitated transfer of macromolecules, we used the YOYO-1 nucleic acid stain (Molecular Probes, OR). This macromolecule dye cannot pass normal cell membranes. However, when cells are electroporated, the dye molecules can enter the cells and make them fluorescent under excitation. The fluorescent intensity is a measure of how many dye molecules have entered the cells, therefore, the extent of dye transfer can be quantified by fluorescent intensity analysis. Typical YOYO-1 concentration used in our experiments was 1μl/ml. The excitation and emission spectra of YOYO-1 are 491nm and 509nm respectively.

In a typical experiment, ND-1 cell suspension with YOYO-1 dye is injected in the top microfluidic channels of a chip with a syringe. Visually assisted by a microscope (BX60, Olympus), a cell is pulled toward the micro hole along the micro channel, and then captured in the hole by applying a negative pressure in the bottom chamber. Then, an electrical pulse, which induces reversible electroporation in the cell, is applied **[3][4]**. After each pulse, the cells were exposed to UV light to generate a fluorescent image. Images of the fluorescing cell were recorded with a camera (Nikon) on Ektachrome transparency films (Kodak EPN100 Professional), which can accurately record color and intensity information. Subsequently the images were digitalized using a high accuracy transparency file scanner (Cannon FS2710) under the same scanning conditions. Intensity analysis was conducted on the fluorescent images to obtain the fluorescence intensity data for each individual cell. The data was used as the measure of the amount of uploaded fluorescent molecules under different control conditions.

RESULTS AND DISCUSSIONS

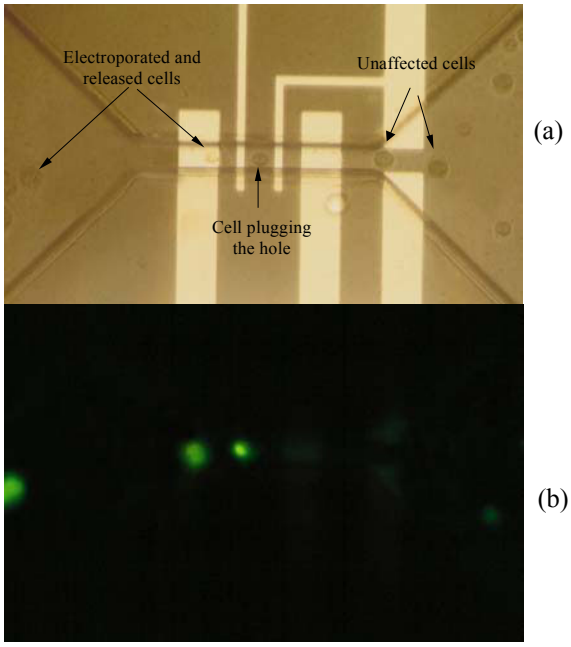

Figure 6. a) Bright field and b)fluorescent images of cells transported to the electroporation site along the micro channel in a single line profile

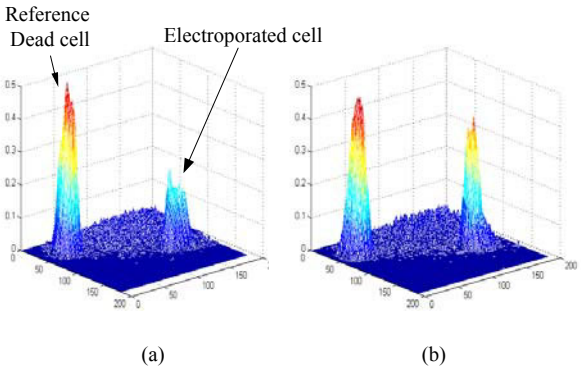

Figure 7. *Fluorescence intensity plots for quantitative analysis of YOYO-1 macromolecule transfer a) after three 10V/100ms electroporation pulses b)after six 10V/100ms electroporation pulses*

Controlled membrane transfer: Experiments have been carried out to study electroporation facilitated macromolecule

transfer across individual cell membranes using the flow-through micro-electroporation chip.

Figure 6 shows typical images obtained from a chip with 3μm micro hole. Figure 6.a is a bright field image taken with a 10X objective that displays all cells in the view field. It can be seen that cells entered the 30μm×30μm micro channel from the left and march through the channel in a single file. A cell in the middle of the channel was trapped in the micro-hole where it was electroporated with a 10V/100ms pulse. The cells to the left of the trapped cell are cells which have been released after being electroporated. It can be clearly seen in Figure 6.b, which is the corresponding fluorescent image, that only the trapped and released cells are fluorescent, indicating uptake of YOYO-1 dyes due to electroporation. The cells to the right which have not yet reached the electroporation site (micro hole) are not visible in the fluorescent image since the YOYO-1 dye has not been introduced inside those cells. This result demonstrates the chip's capability for highly selective single cell electroporation. This capability is due to the concentrated electrical field in the micro-hole vicinity as discussed above. In this particular image, the closest non-fluorescent cell is about 100μm away from the micro-hole electroporation site. However, in other experiments we found that a cell can remain non-fluorescent, *i.e.* not electroporated even when it is in contact with the cell trapped in the hole, which suggests a spatial selectivity resolution of about 10μm.

Figure 7 demonstrates the quantitative analysis of dye transfer with fluorescent intensity analysis. Fluorescent images were obtained using the experimental procedure described above and than converted to intensity images. A dead cell that cannot exclude YOYO-1 dyes was used as a reference. The data from the dead cell is represented by the left plateaus in the intensity plots with average normalized values of 0.43 and 0.47. Figure 7.a corresponds to the image taken after three 10V/100ms electroporation pulse. The average fluorescent intensity of the target cell is 0.14, with a standard variation of 0.02, compared with no measurable intensity before electroporation pulses. This indicates that there is a considerable amount of YOYO-1 inside the cell. Figure 7b shows that as more pulses were applied, at the sixth pulse the average fluorescence intensity of the cell increased to 0.22, with the standard variation of 0.05. This increase in intensity suggests that more YOYO-1 molecules have been introduced into the cells with each electroporation pulse. Because the relation between fluorescent intensity and dye concentration inside the cell is highly non-linear, more studies need to be done before quantitative interpretations of the intensity data can be made.

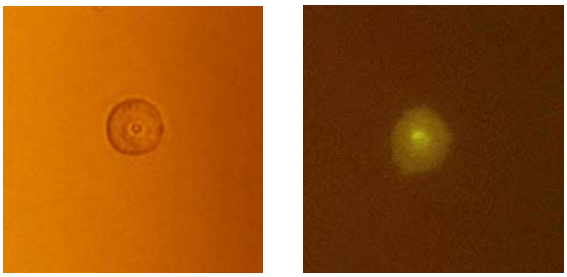

(a) (b)

Figure 8. *in situ gene transfection of individual ND-1 cell with micro-electroporation chip. A 3μm hole chip was used. Enhanced Green Fluorescent Protein (EGFP) gene was electroporatively introduced into the cell by applying two 10V 100ms square pulses, followed by 36 hours of in situ incubation of the cell in cell culture medium at 37℃.. a)bright field image before gene transfection b)fluorescent image of the EGFP transfected ND-1 cell*

Single-cell genetic manipulation: The micro-electroporation chip has the ability to introduce desirable macromolecules into specific individual cells. We have used the micro-electroporation chip, to perform a genetic manipulation on a single ND-1 cell inside the chip. The cell successfully expressed an EGFP gene which was inserted in the cell by micro-electroporation. The detailed protocol is omitted here due to the limited space. This achievement demonstrates that with the micro-electroporation chip, it is feasible to genetically engineer biological cells at the single cell level.

CONCLUSIONS

A new flow-through micro-electroporation chip has been described. The chip can be used for performing controlled electroporation in single cells in a flow-through fashion. Loaded cells are transported to the electroporation site by a microfluidic channel where they are and can be electroporated and permeabilized one by one. This results in a cell loading yield that is virtually 100% manipulation rate. Macromolecules, such as DNA, can be introduced into specific individual cells with the chip. The extent of membrane transfer can be regulated through readily adjustable electroporation parameters. Successful transfection of a ND-1 cell with EGFP gene is demonstrated to validate the feasibility of single-cell genetic manipulation.

ACKNOWLEDGEMENTS

This work is partially supported by NIH under Grant No. 1 R21 RR15252-01.

REFERENCES

1. I. Hapala, "Breaking the barrier: methods for reversible permealization of cellular membranes," *Critical Reviews in Biotechnology* **17**, 105-122, 1997.
2. A. G. Sabelnikov, "Nucleic Acud Transfer Through Cell Membranes: Towards the Underlying Mechanisms." *Prog. Biophys. Molec. Biol.* **62**: 119-152, 1994
3. Y. Huang and B. Rubinsky, "Micro-electroporation: improving the efficiency and understanding of electrical permeabilization of cells," *Biomedical Microdevices* **3**, 145-150, 2000.
4. Y. Huang and B. Rubinsky, "Microfabricated electroporation chip for single cell membrane permeabilization." *Sensors and Actuators: Physical*, **89**, 242-249, 2001.
5. J.C. Weaver, "Electroporation: A general phenomenon for manipulating cells and tissues, " *Journal of Cellular Biochemistry* **51**, 426-435, 1993.
6. E. Newman, A.E Sowers, C. A. Jordan, *Electroporation and electrofusion in cell biology*, Plenum Press, New York, 1989.
7. G. L. Andreason, "Electroporation as a technique for the transfer of macromolecules into mammalian cell lines, " *J. Tiss. Cult. Meth.* **15**, 56-62, 1993.
8. P.F. Lurquin, "Gene transfer by electroporation.", *Molecular Biotechnology* **7**:5-35, 1997
9. H. Lorenz, M. Despont, N. Fahrni, J. Brugger, P. Vettiger, P. Renaud, "High-aspect-ratio, ultrathick, negative-tone near-UV photoresist and its applications for MEMS," *Sensors and Actuators:Physical,* **64**, pp.33-39, 1998.

AN INTEGRATED SURFACE MICROMACHINED CAPACITIVE LATERAL ACCELEROMETER WITH 2μG/√Hz RESOLUTION

Xuesong Jiang, Feiyue Wang, Michael Kraft*, and Bernhard E. Boser
Berkeley Sensor & Actuator Center, University of California at Berkeley
Berkeley, CA 94720-1774
*Department of Electronics and Computer Science, Southampton University
Southampton SO17 1BJ, United Kingdom

ABSTRACT

A capacitive position measurement interface minimizes noise from parasitics in the electromechanical interface and uses correlated double sampling to achieve better than 10^{-3}Å/√Hz displacement resolution. This translates into 2μG/√Hz acceleration resolution when the device is operated in a vacuum.

INTRODUCTION

Surface micromachined accelerometers are finding widespread commercial use [**1,2**] in automotive and industrial applications. However, owing to the small proof-mass, the resolution of present devices is limited to 100μG/√Hz or more. Substantially better performance is achievable with bulk micromachined devices [**3-6**], albeit at the expense of a much larger proof-mass and more expensive fabrication technology.

This paper analyzes the factors governing accelerometer resolution to design a surface micromachined device with a noise floor of 0.75μG/√Hz from electronic sources only. When operated in a vacuum to minimize Brownian noise, 2μG/√Hz acceleration resolution is achievable, which is comparable to the performance of bulk-micromachined parts.

DISPLACEMENT SENSING

A pendular accelerometer consists of a mechanical transducer converting acceleration to displacement followed by a displacement sensor. The resolution of the device is governed by the sensitivity, i.e. the magnitude of the response for a given input, and the noise. It can be improved by either increasing sensitivity, or by lowering the noise.

Transducer sensitivity can be improved by lowering the resonant frequency, as shown by the diagonal line in Figure 2. All else being equal, a device with lower resonant frequency will exhibit better resolution. Since, however, reducing the resonant frequency also lowers the device's tolerance to mechanical shock, practical considerations set an application dependent lower bound on acceptable resonant frequency. The transducer is also responsible for noise. Brownian noise is usually the dominant source, but flicker noise and thermal noise from the electromechanical interface also contribute.

Figure 3 plots the displacement resolution of several accelerometers [**1-14**] to factor out transducer performance. It is interesting to note that alternative detection schemes such as electron tunneling have no apparent performance advantage over capacitive sensors. Another observation from Figure 3 is that the achieved displacement resolution is worse in high precision accelerometers that use a larger proof-mass than those use a smaller mass, indicating that the performance of the high precision accelerometers is fundamentally limited by Brownian motion noise. In order to develop high precision accelerometers with μG/√Hz or sub-μG/√Hz resolution, it is crucial to reduce Brownian noise.

This work uses the switched capacitor sensing technique, which is often associated with increased noise due to folding of

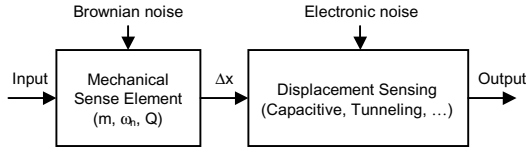

***Figure 1**. Block diagram of a displacement transducer*

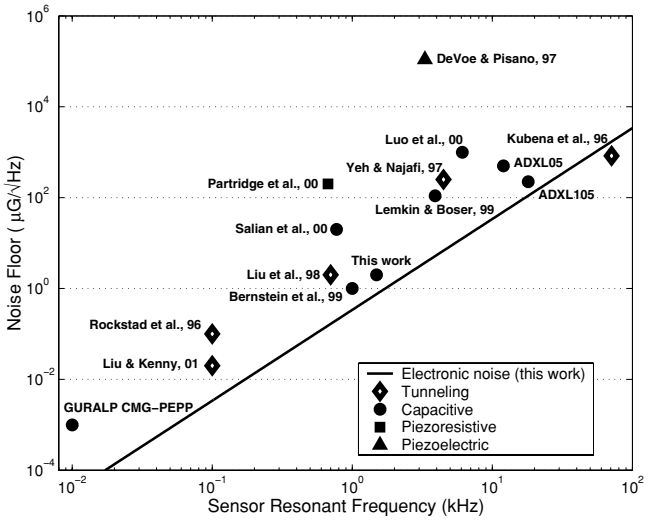

***Figure 2.** Comparison of Noise floor*

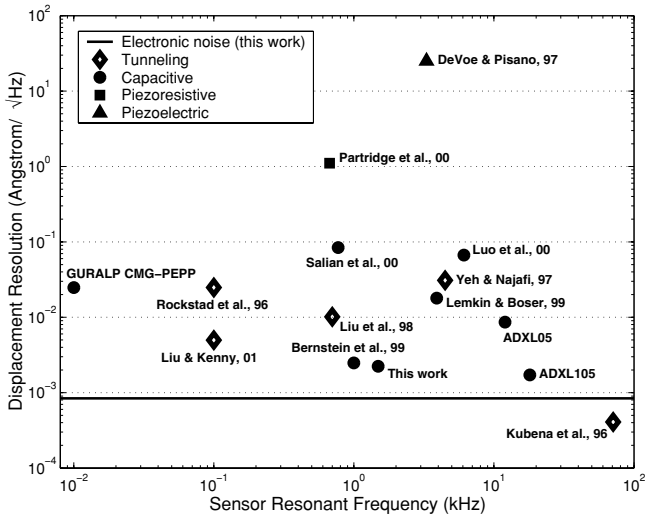

***Figure 3.** Comparison of displacement resolution*

Travel support has been generously provided by the Transducers Research Foundation and by the DARPA MEMS and DARPA BioFlips programs.

broadband thermal noise. However, it is seen in Figure 3 that this work has achieved a better than 10^{-3}Å/√Hz displacement resolution, on par with the best reported results.

ACCELEROMETER DESIGN

The capacitive lateral accelerometer has been designed and fabricated using an integrated MEMS technology with a 6µm-thick mechanical polysilicon layer and 0.8µm transistor feature size for CMOS electronics. Figure 4 shows the die photo of the fabricated device. The complete die size is 3.5mm×3.5mm in which 1.1mm×1.1mm has been specified as the mechanical structure area. The 920µm×880µm sense element weighs 3.6µgram. Differential sense capacitors are formed using parallel plate comb fingers. Limit stops are set to prevent snapping of the comb fingers and the proof mass is allowed to displace a maximum of +/-1µm from its resting position before hitting the limit stops. A thin conductive polysilicon layer underneath the proof mass is electrically connected to the proof mass through the suspension anchors and it has the same potential as that of the proof mass. Consequently, there will be no electrostatic force between the proof mass and the shield layer even when the potential on the proof mass alternates between two different potentials during sensor operation.

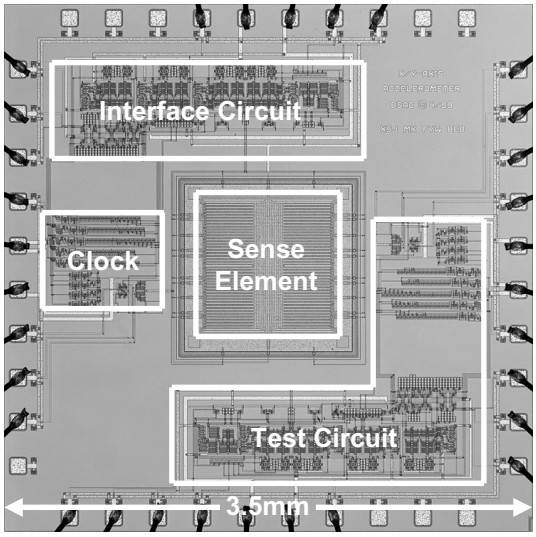

Figure 4. *Die photo*

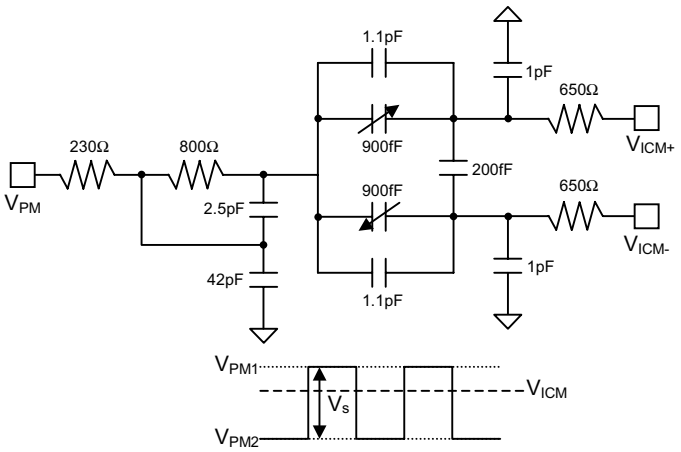

Figure 5. *Electromechanical interface model*

Considerations have been put on reducing parasitic capacitances and parasitic resistances caused by the polysilicon wirings in the mechanical sense element, which is essentially a distributed RC network. The lumped electrostatic interface model shown in Figure 5 has been used in the design of the displacement sensing interface circuit. Most of the parasitic resistances are due to the polysilicon wirings from the fixed sense comb fingers to the CMOS circuitry. The parasitic resistances due to parallel plate sense comb fingers are negligible because these sense comb fingers are connected in parallel. Most parasitic capacitances are due to the anchor capacitances and the wirings through the ground polysilicon layer. The capacitance across the differential sense comb fingers is minimized by maximizing the gap between the adjacent comb fingers.

The accelerometer operates as an open-loop sensor. The sensor outputs are differential analog signals. Open loop sensing enables direct measurement of the individual noise contributions, which can also be used to characterize sensor dynamics. A better understanding of the open-loop sensor helps in designing a closed-loop sensor.

Depending on the mechanical design, the sensor can be mechanical noise dominated or electronic noise dominated. In this design, number of sense fingers has been designed to maximize performance in vacuum. For a sensor operating in air, fewer sense combs should be used.

A fully differential switched capacitor interface circuit has been designed to measure the sense capacitance mismatch in response to acceleration signals. The voltage on the proof mass alternates between V_{PM1} and V_{PM2} at a 50% duty cycle in each sampling period. The correlated double sampling technique similar to that reported in [**15**] is used to reject 1/f noise, $k_B \cdot T / C$ noise due to reset switches, amplifier offset and switch charge injection.

The differential analog outputs of the sensor are converted to a single-ended analog output using an instrumentation amplifier on the test board. The lateral accelerometer has been tested on a shaker table excited by a signal generator. The shaker table generates a vibration perpendicular to the table surface. A reference accelerometer has also been mounted on the shaker table to calibrate the measurement results. To prevent the resonant frequencies of the test board from affecting the measurement results, the test board has been attached tightly to a rigid mounting block. The device has been tested in air as well as in vacuum.

NOISE CHARACTERISTICS IN AIR

A comprehensive analysis of all noise sources is essential to maximizing resolution. To gain more insight, we have developed techniques for measuring individual noise contributions separately.

Periodic spikes were observed in the differential analog outputs. These spikes are caused by inductive coupling between the bond wires and capacitive coupling of the digital/clock signals. Since the energy of these spikes is at frequencies no less than the sampling frequency of the sensing circuit, the effect of these spikes on sensor noise performance is negligible.

A HP35665A dynamic signal analyzer was used to characterize the sensor output noise and the output noise spectrum was obtained after averaging 100 measurements. Figure 6 shows three results, all taken at the atmospheric pressure.

The top trace ($V_s = 4.5V$) exhibits a characteristic 2nd order roll-off for frequencies above the resonant frequency of the sensor, which is at approximately 1.5kHz. It includes all noise sources and

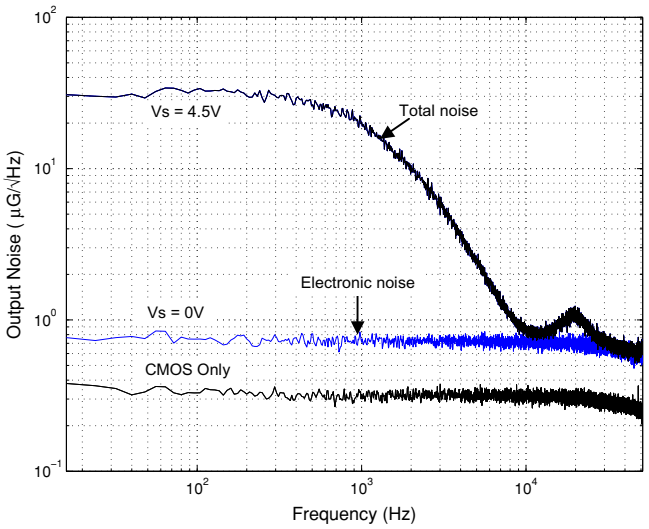

***Figure 6**. Output noise spectra*

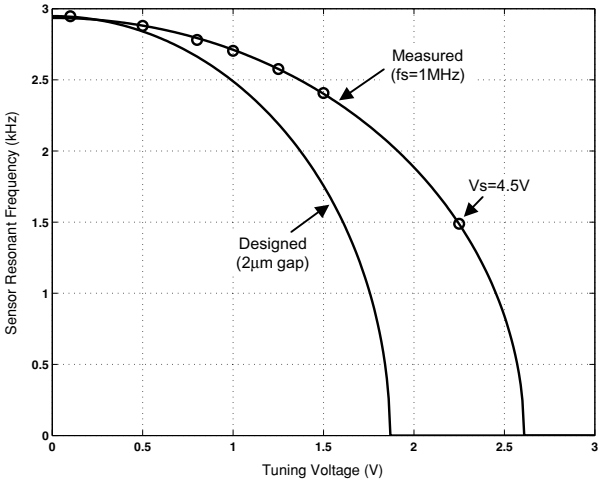

***Figure 7**. Frequency tuning effect*

is dominated by Brownian noise (32μG/√Hz). It underscores the need for operation in vacuum. The mechanical sense element is found over-damped in air with $Q = 0.44$. Using the measured ω_n and Q , the Brownian noise floor at atmospheric pressure is calculated to be 32μG/√Hz, which confirms the accuracy of the noise measurement. It is already known that the output Brownian noise is shaped by the sensor transfer function. If Brownian noise is the dominant noise source, the output noise spectrum reflects the sensor transfer function. Hence, characterization of the accelerometer output noise is equivalent to characterization of the sensor dynamics. 330μm long and 2μm wide parallel plate sense comb fingers were designed to maximize the ratio of sense capacitance to parasitic capacitance. For a certain sense capacitance, fewer anchors are needed using longer comb fingers and hence less parasitic capacitance, at the expense of lower finger resonant frequency. The resonant frequency of sense comb fingers was designed to be 25kHz. However, an over-etch of about 0.3μm in device fabrication reduces the comb finger width and lower their resonant frequency to about 20kHz. Brownian motion noise of these comb fingers is mechanically amplified near the finger resonance and the displacement of the sense comb fingers is picked up by the displacement sensing electronics. In the plot, Brownian motion noise of comb fingers appears at around 20kHz.

The electronic noise can be measured separately when no sense step voltage ($V_s = 0V$) is applied across the sense capacitors and corresponds to 0.75 μG/√Hz. At frequencies below approximately 10kHz, Brownian noise is the dominant noise source. Electronic noise dominates above 10kHz. Due to correlated double sampling, the electronic noise has a white spectrum and the 1/f noise corner is below 1Hz. The droop of electronic noise at frequencies above 30kHz is caused by low-pass filtering provided by the on-chip output buffer. The overall sensor bandwidth is limited by the sensor dynamics.

For reference, the result from an electronic circuit (*CMOS only*) where the mechanical structure has been replaced with fixed poly-poly capacitors is also included to evaluate the effect of mechanical parasitics on electronic noise. About 6dB noise degradation induced by parasitics is observed. The result is better understood by considering the electromechanical interface model shown in Figure 5. The 650Ω wiring resistance adds noise directly to the capacitive sense interface and parasitic capacitances reduce the signal-to-noise ratio by attenuating the signal from the 900fF sense capacitances.

Correlated double sampling eliminates $k_B \cdot T / C$ of the reset switches effectively. Without correlated double sampling, the reset switches at the inputs of the C/V converter contribute $k_B \cdot T / C$ noise equivalent of 2.5μG/√Hz. With correlated double sampling, the electronic noise is mainly due to thermal noise of the C/V converter, which is equivalent to 0.7μG/√Hz.

TEST RESULTS IN VACUUM

When the sensor operates in vacuum, Brownian motion noise is reduced at low frequencies and mechanically amplified near the sensor resonant frequency. The Brownian noise peak in the output noise spectrum of the vacuum test has been used to measure the sensor resonant frequency and to evaluate the electrostatic frequency tuning effect. During our test, it has been found that when Q is too high, the output amplifier overloads and the output becomes a square wave signal with a frequency corresponding to the sense resonant frequency, hence feedback is required for a robust operation in vacuum. In order to bring Brownian noise down to a comparable level of the electronic noise, a Q of better than 1000 is needed.

Because of the use of parallel plate sense comb fingers, the voltage drop across the sense capacitors generates electrostatic frequency tuning effect. This can be exploited to dynamically reduce the resonant frequency, and hence increase the sensitivity, of the device, without reducing the shock resistance when the device is off. For this purpose, the voltage applied to the sense fingers is separated into a common-mode part, V_{tune} , controlling the resonant frequency, and a differential part, V_s , that sets the magnitude of the sense pulse and hence sensitivity of the interface.

It can be seen from Figure 5 that the sense step voltage V_s is given by $V_s = V_{PM2} - V_{PM1}$. Since the potential on the proof mass switches between V_{PM1} and V_{PM2} at a 50% duty cycle, the frequency tuning voltage V_{tune} is given by

$$V_{tune} = \sqrt{0.5 \cdot [(V_{PM1} - V_{ICM})^2 + (V_{PM2} - V_{ICM})^2]} .$$

Note that V_s and V_{tune} can be adjusted independently. Figure 7 shows the measured frequency tuning effect with $|V_{PM1} - V_{ICM}| = |V_{PM2} - V_{ICM}|$, which corresponds to

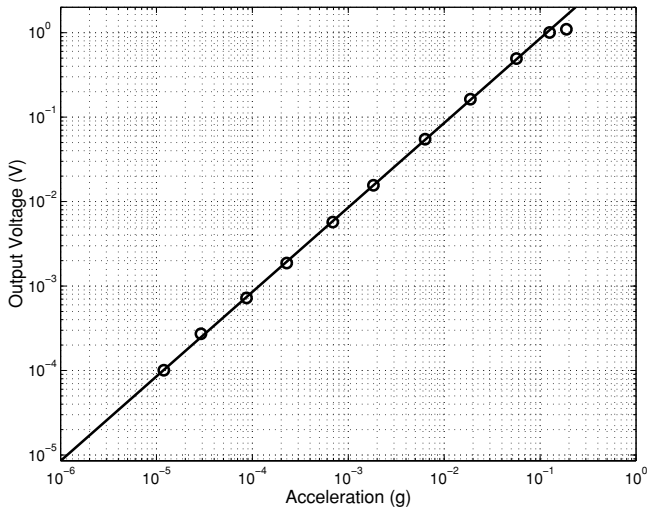

***Figure 8**. Measured accelerometer output response (Acceleration signal at 55Hz and Vs=4.5V)*

$V_{tune} = 0.5 \cdot V_s$. The frequency tuning effect depends on the comb finger gap. The sense comb finger gap has been extracted to be 2.3μm instead of the designed value of 2μm. This result has been verified using SEM. Figure 8 shows the sensor output response to acceleration signals at 55Hz. The test was conducted in vacuum with $V_s = 4.5V$ and $V_{tune} = 0.5 \cdot V_s$. The full-scale range of the device is 125mG and the sensitivity is 8.55V/G under this test setup. Parameters of the lateral accelerometer are summarized in Table1.

***Table 1**. Summary of parameters (Vs = 4.5V unless specified)*

Parameters	Measured
Proof mass	3.6μgram
Mechanical Resonant frequency (Vs = 0V)	2.93kHz
Tuned Resonant frequency	1.488kHz
Quality factor Q	0.44
Sense capacitance	900fF
Sensitivity	8.55V/G
Full scale range	125mG
Comb finger gap	2.3μm
Brownian noise floor in air	32μG/√Hz
Electronic noise floor	0.75μG/√Hz
Measured noise floor in vacuum	2μG/√Hz
Displacement resolution	2.3×10^{-3}Å/√Hz

CONCLUSIONS

An integrated surface micromachined capacitive lateral accelerometer that resolves 2μG/√Hz in a vacuum is presented. Displacement resolution is used to decouple the strong correlation between the achieved acceleration resolution and the sensor resonant frequency. Alternative sensing schemes, such as electron tunneling, have no apparent performance advantage over capacitive sensing. Individual noise contributions are identified experimentally. Better than 10^{-3}Å/√Hz displacement resolution is demonstrated.

ACKNOWLEDGEMENT

The authors would like to thank Joseph I. Seeger and Vladimir Petkov for technical discussion, Analog Devices, Inc. for device fabrication and DARPA for funding this project under agreement F30602-97-2-0266.

REFERENCES

1. ADXL105 datasheet, *http://www.analog.com*

2. ADXL05 datasheet, *http://www.analog.com*

3. J. Bernstein, R. Miller, W. Kelley, and P. Ward, "Low-Noise MEMS Vibration Sensor for Geophysical Applications", *Journal of Microelectromechanical Systems*, Vol. 8, No. 4 (1999) pp.433-8

4. C.-H. Liu, A. M. Barzilai, J. K. Reynolds, A. Partridge, T. W. Kenny, J. D. Grade, and H. K. Rockstad, "Characterization of a High-Sensitivity Micromachined Tunneling Accelerometer with Micro-g Resolution", *Journal of Microelectromechanical Systems*, Vol. 7, No. 2 (1998) pp.235-44

5. C.-H. Liu and T. W. Kenny, "A High-Precision, Wide-Bandwidth Micromachined Tunneling Accelerometer", *Journal of Microelectromechanical Systems*, Vol. 10, No. 3 (2001) pp.425-33

6. H. K. Rockstad, T. K. Tang, J. K. Reynolds, T. W. Kenny, W. J. Kaiser and T. B. Gabrielson, "A Miniature, High-Sensitivity, Electron Tunneling Accelerometer", *Sensors and Actuators A* 53 (1996) pp.227-31

7. R. L. Kubena, G. M. Atkinson, W. P. Robinson and F. P. Stratton, "A New Miniaturized Surface Micromachined Tunneling Accelerometer", *IEEE Electron Device Letters*, Vol. 17, No. 6 (1996), pp.306-8

8. C. Yeh and K. Najafi, "A Low-Voltage Tunneling-Based Silicon Microaccelerometer", *IEEE Transactions on Electron Devices*, Vol. 44, No.11, (1997), pp.1875-82

9. M. Lemkin and B. E. Boser, "A Three-Axis Micromachined Accelerometer with a CMOS Position-Sense Interface and Digital Offset-Trim Electronics", *IEEE Journal of Solid-State Circuits*, Vol. 34, No. 4 (1999), pp.456-68

10. H. Luo, G. K. Fedder and L. R. Carley, "A 1mG Lateral CMOS-MEMS Accelerometer", *Proceedings IEEE Thirteenth Annual International Conference on Microelectromechanical System*, (2000), pp.502-7

11. *http://www.guralp.demon.co.uk*, GURALP CMG-PEPP

12. A. Salian, H. Kulah, N. Yazdi, Guohong He and K. Najafi, "A High-Performance Hybrid CMOS Microaccelerometer", *Technical Digest. Solid-State Sensor and Actuator Workshop*, Hilton Head Island, SC (2000)

13. D. L. DeVoe and A. P. Pisano, "Surface Micromachined Piezoelectric Accelerometers (PiXLs)", *Journal of Microelectromechanical Systems*, Vol. 10, No. 2 (2001), pp.180-6

14. A. Partridge, J. K. Reynolds, B. W. Chui, E. M. Chow, A. M. Fitzgerald, L. Zhang, N. I. Maluf, and T. W. Kenny, "A High-Performance Planar Piezoresistive Accelerometer", *Journal of Microelectromechanical Systems*, Vol. 9, No. 1 (2000), pp.58-66

15. X. Jiang, J. I. Seeger, M. Kraft, and B. E. Boser, "A Monolithic Surface Micromachined Z-Axis Gyroscope with Digital Output", *Digest of Technical Papers, 2000 Symposium on VLSI Circuits*, Hawaii (2000), pp.16-19

NEW PLASTIC MICROINJECTION MOLDING TECHNIQUE FOR EXTREMELY TALL PLASTIC MICROSTRUCTURES USING REMOTE INFRARED RADIATION HEATING METHOD

Sanghyo Kim, Ramachandran Trichur, Gregory Beaucage* and Chong H. Ahn
Microsystems and BioMEMS Lab, *Dept. Material Science and Engineering,
University of Cincinnati,
Cincinnati, OH 45221-0030
Byung H. Kim
Dept. Mechanical and Industrial Engineering,
University of Massachusetts,
Amherst, MA 01003-2210

ABSTRACT

Microfabrication methods using polymers are becoming increasingly popular as low-cost and high volume production alternative to silicon or glass-based MEMS technologies. In this paper an innovative plastic microinjection molding technique using rapid thermal processing (RTP) for the fabrication of high aspect ratio plastic microstructures is reported. This technique focuses on decreasing the cycle time of injection molding of high aspect ratio microstructures and at the same time to achieve better fill and reproducibility of the micromold. In this work the RTP process has been implemented and characterized using Cyclic olefin copolymers (COC), Polycarbonate (PC) and Poly methyl methacrylate (PMMA) and high aspect ratio plastic structures (taller than 100μm) such as plastic micro needles and fluidic micro channels have been realized.

INTRODUCTION

Micro electro-mechanical Systems (MEMS) technology has been applied to the field of biomedical engineering and related field in recent years and there is an increasing demand for miniaturization of various systemic components of biochip. There also have been intense activities to reduce fabrication cost and to increase volume of production to make biochemical detection systems commercially available, so polymer micro fabrication is becoming increasingly important **[1]**.

Microinjection molding is a technique to fabricate precision microstructures using polymers at low cost and high volumes. However, fabrication of high aspect ratio (HAR) plastic microstructures has been considered as one of the most difficult tasks to accomplish without compromising in cycle time **[2,3]**, because of the difficulty of injection fill-depth control at low molding block temperatures as shown in Figure 1. A complete fill of the high aspect ratio features in the mold cavity is almost impossible to achieve without sufficiently increasing the molding block temperature **[4]**, to successfully achieve the flow of the polymer inside the mold cavity. This will lead to a huge increase in cycle time as the mold has to undergo heating and cooling cycle every time when a plastic part is made.

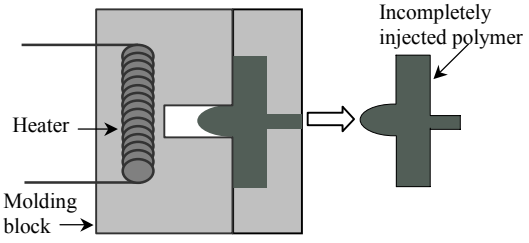

Figure 1. *Illustration of an incompletely injected polymer part due to premature cooling inside the mold cavity.*

In this paper an innovative technique of rapid thermal processing is discussed, where complete fill of the high aspect ratio features in the micro mold disk is achieved without compromising in cycle time, by increasing only the surface temperature of the mold insert by infrared radiation to the melting temperature of the plastic, rather than heating the bulk of the molding block.

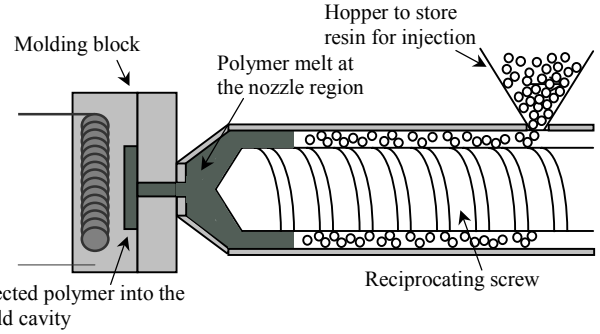

Figure 2. *Schematic diagram of an injection molding machine with molding block.*

INJECTION MOLDING PROCESS

The schematic of an injection molding machine is shown in Figure 2. With this machine the plastic is melted and then injected into the cavity of a closed mold, whose shape is transferred to plastic microstructures on cooling down. Inside the mold cavity the resin continues to flow and fill the mold cavity till the polymer cools down to a highly viscous melt, where the flow stops, and the part can be ejected. In order to ensure good flow properties during injection, thermoplastics with low or medium viscosity are preferred **[5].** So the filling of the mold cavity and subsequently the micro patterns depend on viscosity of polymer melt, injection speed, molding block temperature and the nozzle temperature of the injection unit.

Thus, to achieve a good fill inside the high aspect ratio micro cavities in the mold cavity the molding materials are often processed at their maximum processing temperatures at the injection nozzle region. This ensures lower viscosity and better flow inside the mold cavity. Also the choice of a polymer with lower melt flow index (lower viscosity) and use of higher injection speeds help to achieve better filling inside the mold cavity.

The molding block is normally heated to an elevated temperature (below glass transition temperature of the injected polymer) to help uniform flow of polymer throughout the mold cavity and to prevent abrupt cooling of the polymer melt, which can drastically change its physical properties like mechanical strength, hardness, etc. But, in order to obtain better fill of the high aspect ratio structures inside the mold disk, the tool

Travel support has been generously provided by the Transducers Research Foundation and by the DARPA MEMS and DARPA BioFlips programs.

temperature can be raised even higher (above the glass transition temperature), but this drastically increases the cycle time to injection mold one single plastic part, which increases the manufacturing costs and also decreases throughput.

Thus, the reduction of cycle time is one of the most important issues that need to be addressed to achieve commercially viable and low cost micro structured plastic products. By the use of the rapid thermal processing technique, the cycle time is kept constant as of the conventional injection molding process, but a better fill of the high aspect ratio mold features can be achieved without heating the molding block to above glass transition temperatures.

MOLD FABRICATION

We have developed a new replaceable mold disk technique for the fabrication of the replaceable micro mold disk inserts for injection molding **[6]**. In this technique, the high aspect ratio microstructures are fabricated on a separate circular nickel disk about 3 inches in diameter and 1.5 mm in thickness. The disk is inserted in the molding block, as shown in Figure 3. This reduces many complexities of mold fabrication such as fabrication cost, handling, etc. The mold disk can be taken out from the molding block and be replaced with any other pattern without replacing the whole molding block. The replaceable mold disk technique also can go well with existing microfabrication techniques, which allows the replaceable disk molding technique to be a highly economically viable technique.

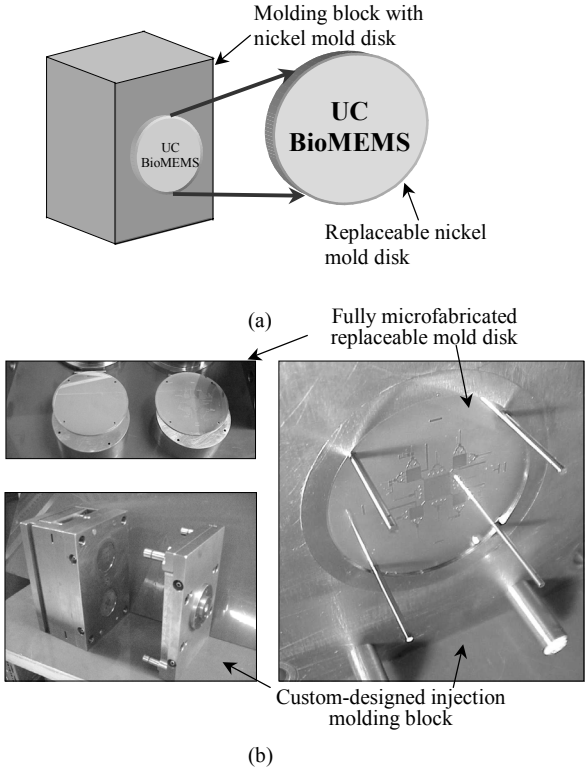

***Figure 3**.Injection molding block: (a) schematic of the molding block with the replaceable mold disk and (b) photographs of the custom designed molding block with the replaceable Ni mold disk and the fabricated microstructures in the Ni mold disk insert.*

An essential step in the fabrication of the micro mold insert is surface preparation of nickel substrate, where the nickel substrate is lapped flat and parallel and polished using a polishing machine. The process summary is schematically described in Figure 4.

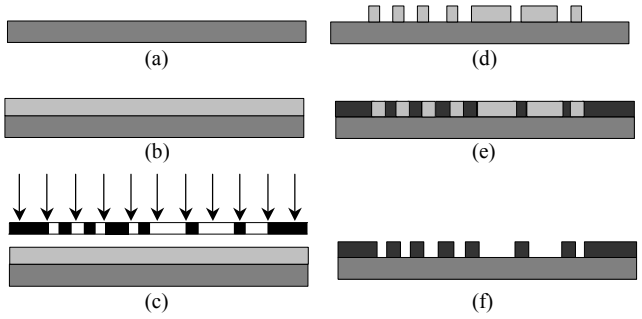

***Figure 4.** Schematic of microfabrication steps for the fabrication of Ni mold disk: (a) flat and parallel polished Ni substrate; (b) spin coated SU 8 on Ni substrate; (c) U-V exposure; (d) patterned SU 8 on nickel after developing; (e) electroplated nickel structures; and (f) final nickel mold disk with electroplated microstructures.*

RAPID THERMAL PROCESS FOR INJECTION MOLDING

From the previous discussions, it is clear that to get a good fill of the polymer inside the mold disk cavity, the nozzle temperature should be near to the maximum processing temperature of the polymer and higher injection speeds and higher holding pressure should be used. But any attempt to increase the molding block temperature will drastically increase the cycle time of operation of the injection molding process.

In the rapid thermal process, the "surface" of a Ni mold disk is heated with IR radiation using a high power halogen lamp. The radiation from the IR source is focused to the surface of the Ni disk and the surface temperature of the replaceable Ni micromold disk reaches a temperature higher than the nozzle temperature in a few seconds. Then, the molding block is closed and the molten plastic is injected from the nozzle at high injection speeds. When the molten plastic enters the mold cavity, it experiences an isothermal environment. The melt temperature and the Ni mold disk surface temperature will be the same at the instant when the plastic is injected. So there will be no heat transfer taking place inside the cavity for a very small period of time and the surface heat of the Ni mold disk will help the plastic to be in a state of low viscosity. As a result of this, complete filling of the mold disk cavity can be achieved without any considerable increase in the cycle time of operation of the injection mold machine.

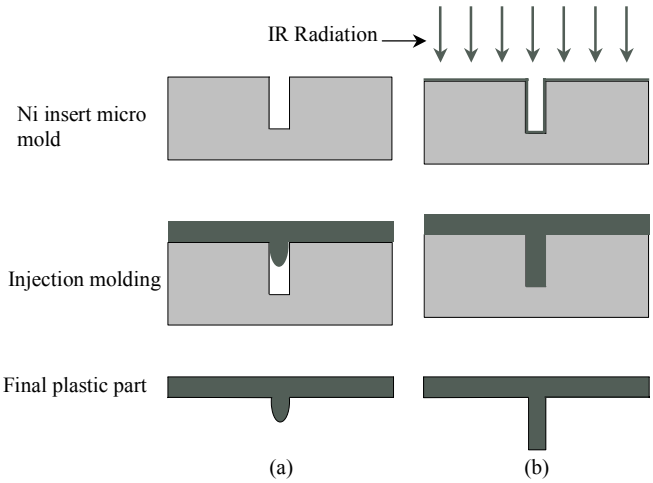

***Figure 5.** Comparison of the molding processes: (a) conventional molding and (b) rapid thermal processing.*

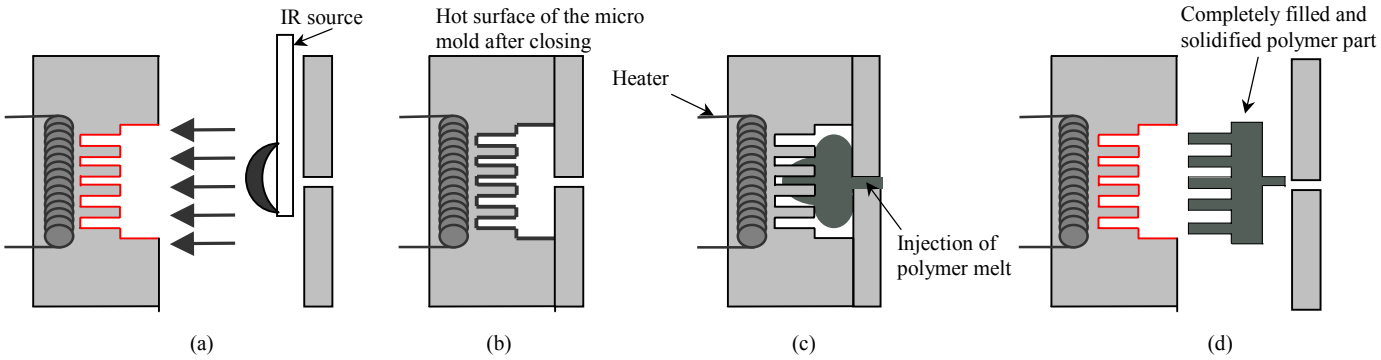

Figure 6. *Schematic description of injection molding using rapid thermal process (a) surface heating of the mold disk using IR source; (b) closure of molding block; (c) filling phase of the injected polymer; and (d) complete filling, solidification and ejection of the final polymer part.*

A comparison of the two processes and the differences of the fill depth in the final plastic microstructure are described in Figure 5. An illustration of the complete cycle of the rapid thermal process is summarized in Figure 6. The cycle time is almost similar to the conventional molding process, since only the surface of the micromold is heated, it reduces any need to heat and cool the whole molding block every time when a plastic part is made. Thus, the process using RTP with infrared radiation provides more economical and feasible source for large-scale production.

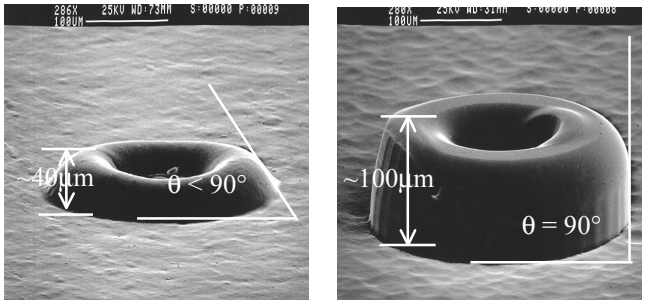

Figure 7. *Comparison of the SEM pictures of microneedles: (a) without RTP process and (b) with RTP process.*

SEM pictures of the actual microneedle structures are shown in Figure 7. The advantage of using the RTP process can be easily understood from the pictures. The shape of the microstructure without the RTP process is that of a partially filled micro cavity, where the plastic has solidified before complete filling of the mold cavity. The height of the structure is around 40 µm and the sidewall profile has angle of around 45°. But the picture Figure 7 (b) of the microneedle fabricated using the RTP process shows complete filling of the mold and good replication of the microstructure in the mold cavity. The height of the plastic structure is around 100 µm, which is the depth of the micro cavity in the mold and the sidewall also has an angle of almost 90°, ensuring exact replication of the mold cavity. A picture of the microchannels fabricated using the rapid thermal process is shown in Figure 8, achieving complete replication of the mold.

A temperature profile of the surface of the Ni mold disk with respect to the exposure time to the IR radiation is shown in Figure 9. It can be seen from the graph that the surface temperature of the Ni mold disk can be raised from the molding block temperature to around 350 °C in less than 20 seconds. This ensures that the heat needed to maintain the flow of the polymer inside the micro mold disk cavity is attained quickly and the heat is dissipated quickly when the lamp is turned off, so the need for a cooling system is naturally averted.

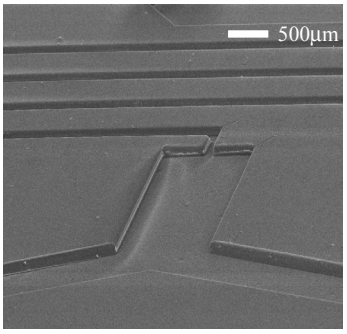

Figure 8. *SEM picture of microchannels in plastic substrate fabricated by RTP process showing complete replication of the mold.*

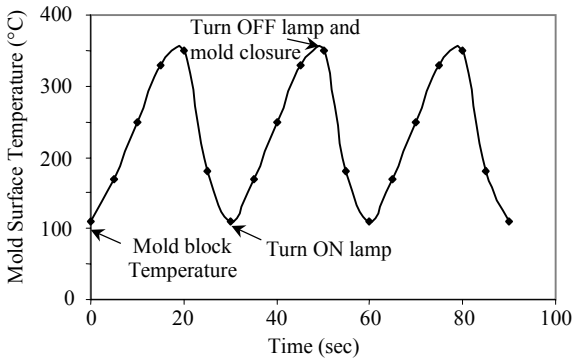

Figure 9. *Surface temperature cycle of the Ni mold surface during IR radiation on the mold surface.*

RESULTS AND DISCUSSION

The rapid thermal process (RTP) was characterized for three different polymers such as Cyclic olefin copolymer (COC), Poly methyl methacrylate (PMMA) and Polycarbonate (PC). The RTP injection molding was performed on these three polymers with various injection speeds from 10 cc/sec to 70 cc/sec in steps of 20 cc/sec. The IR radiation exposure time was also varied from 10 secs to 2 minutes for all the polymers and for various injection speeds. The molding block temperature was fixed at two points, room temperature and maximum debinding temperature for each polymer, and the injection was performed at various speeds at these two temperatures. The RTP parameters were varied when the molding block was at debinding temperature of each polymer.

The results of experiment are plotted in Figure 10 for the polymers PMMA, PC and COC respectively. From the results, the

maximum injection fill depth is achieved in most cases at around 40 seconds of IR radiation exposure time, which makes the cycle time of the injection mold machine around 90 seconds.

From the figures, complete fill of the mold has been never achieved at lower injection speeds, less than 30 cc/sec, irrespective of the process and 100% fill has been achieved at speeds greater than 30 cc/sec and at exposure times around 40 seconds.

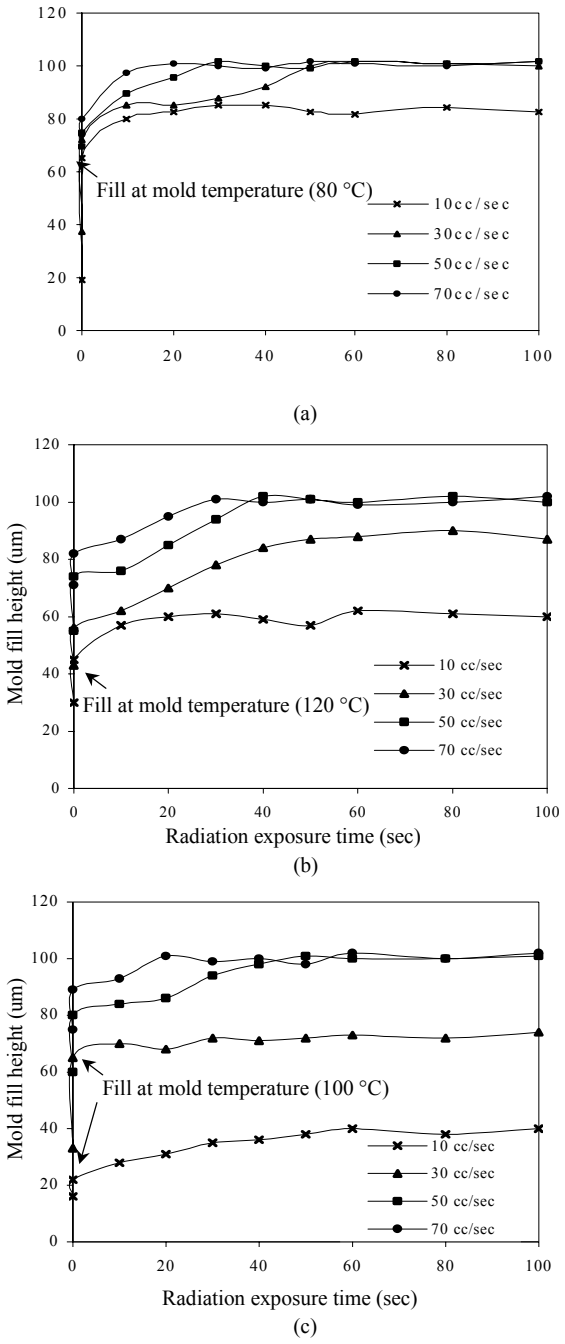

Figure 10. *Measured injection fill depth at various IR exposure time, flow rates and molding block temperature: (a) Poly methyl methacrylate (PMMA); (b) Polycarbonate (PC); and (c) Cyclic olefin copolymer (COC).*

The process can be greatly improved by including a thermal shield between the replaceable Ni mold disk and the molding block, since there is a huge temperature gradient between the disk surface and the molding block surface. Use of higher-powered IR source can greatly help to reduce the cycle time.

CONCLUSION

In this work, an innovative injection molding technique using rapid thermal process has been proposed, implemented and characterized using Cyclic olefin copolymer (COC), Polycarbonate (PC), and Poly methyl methacrylate (PMMA). The obtained results clearly revealed the advantages of the rapid thermal process. The cycle time for the full process was around 90 seconds. This process time clearly shows the advantage of the rapid thermal process over the conventional high aspect ratio injection molding, where the cycle time required was several minutes.

Thus the injection molding technique using the rapid thermal process is a favorable alternative to the conventional high aspect ratio injection molding and the cycle time can be greatly reduced, thereby reducing the injection molding costs and increasing the throughput of the process. The rapid thermal process allows the plastic micromachining using injection molding a commercially viable and economically feasible process for high volume production, which provides plastic biochips and biochemical detection systems to the end user at low cost.

ACKNOWLEDGEMENT

This research was fully supported by a DARPA grant under contract AF F30602-00-1-0569 from the *BioFlips* program, DoD, USA.

REFERENCES

[1] H. Becker and U. Heim, "Hot embossing as a method for the fabrication of polymer high aspect ratio structures", *Sensors and Actuators (*2000), 130-135.

[2] M. S. Despa, K. W. Kelly and J. R. Collier, "Injection molding of polymeric LIGA-HARMS", *Microsystem Technologies* (1999), 60-66.

[3] V. Piotter, T. Hanemann, R. Ruprecht, and J. Hau□elt, "Injection molding and related techniques for fabrication of microstructures", *Microsystem Technologies* (1997), vol.3, 129-133.

[4] V. Piotter, R. Ruprecht, W. Bacher and J. H. Hausselt, "Injection molding of microstructures using filled and unfilled thermoplastics", *proc. of the SPIE* (1995), vol.2639, 146-57.

[5] V. Piotter, T. Gietzelt, T. Hanemann, R. Ruprecht, and J. Hausselt, "Materials for molding processes in microsystem technology", *proc. Micro Materials* (2000), 274-277.

[6] J. W. Choi, S. Kim, R. Trichur, H. J. Cho, A. Puntambekar, R. L. Cole, J. Simkins, S. Murugesan, K. Kim, J. B. Lee, G. Beaucage, J. H. Nevin, and C. H. Ahn, "A plastic micro injection molding technique using replaceable mold-disks for disposable microfluidic systems and biochips", *proc. of μTAS* (2001), 411-412.

MICROCANTILEVERS FOR THERMAL NANOIMAGING AND THERMOMECHANICAL SURFACE MODIFICATION

William P. King, Thomas W. Kenny, and Kenneth E. Goodson
Department of Mechanical Engineering, Stanford University
Stanford, CA 94305-3030
Michel Despont, Urs Duerig, Mark Lantz, Hugo Rothuizen, Gerd Binnig, and Peter Vettiger
IBM Research Division, Zurich Research Laboratory
Rueschlikon, Switzerland, CH-8803

ABSTRACT

This paper reports recent advancements in the development of a microelectromechanical systems (MEMS) based data storage system that uses an array of heated atomic force microscope (AFM) cantilevers to write, read, and erase nanometer-scale data bits in thin polymer film. The cantilever tip contacts the polymer and induces highly local heating and melting to form data bit indentations with a radius of curvature near 20 nm. The same cantilever can be used to thermally detect the presence of previously written bits through operation as an anemometer. This paper reports detailed measurement of cantilever heating for understanding and improving reading and writing operation, improved understanding of the bit formation process that makes possible data density near 0.9 Tbit/in^2, the realization of a single-bit erasing process that employs the highly local melting in the polymer during data writing, and detailed measurement of the thermal reading process. The controlled writing, reading, and erasing of data bits reported in this paper complete the basic technological requirements for the development of a data storage system.

INTRODUCTION

The ultimate limits of magnetic data storage technology will be governed by thermal limits on magnetic data bit size [**1**,**2**] and mechanical positioning of the reading and writing heads [**2**]. It is at present unclear what technological path will overcome these limitations and permit data densities of 1 Tbit/in^2 and beyond. Approaches to overcome media-induced limits on large data densities include perpendicular recording [**3**], recording on patterned media [**3**], and thermally-assisted recording [**4**]. MEMS-based data storage could help overcome mechanical alignment and packaging issues through systems integration [**5**]. Furthermore, MEMS-based data storage approaches that use scanning probes [**6**,**7**] could help overcome mechanical registration and tracking issues. This paper reports progress in the development of a MEMS data storage system based on scanning probes.

Thermomechanical data storage uses a heated, scanning atomic force microscope (AFM) cantilever tip to melt indentations into a polymer film [**7**-**10**]. Bit detection is possible by measuring temperature changes of the heated cantilever as it scans over a previously written surface [**7**-**10**]. Figure 1 shows a schematic of thermomechanical writing and thermal reading. Fig. 2 shows images of fabricated cantilevers. A complete data storage system will reliably and deliberately write, read, and erase data bits. A data density of 400 Gb/in^2 [**8**] has been the maximum data density reported for thermomechanical data storage. The previously reported erasing scheme heated the entire chip to melt and reflow the polymer bit indentations and thus forcing a 100% erase of the media. Recent improvements in understanding heat transfer during reading and writing allow further increases in data density, [**11**,**12**] improved sensitivity in data reading, [**10**] and design of a single-bit erase. We have recently reported design of cantilevers [**10**] and cantilever arrays [**12**] for data writing and reading. This paper reports further developments: increased data density by a factor of 2.5 to near 1 Tbit/in^2, single-bit erasing, and quantitative data reading.

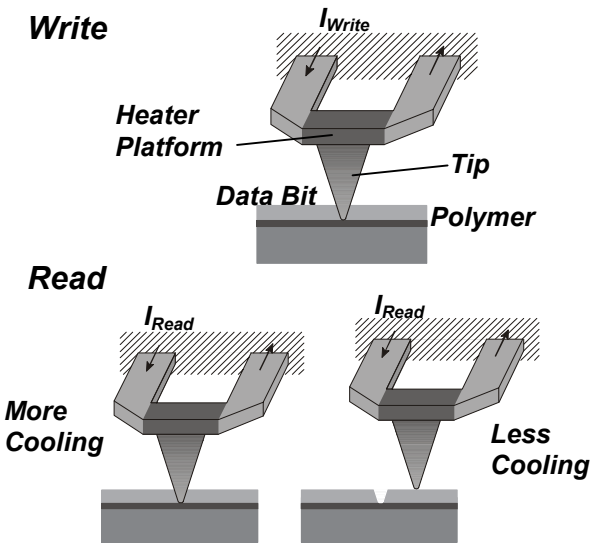

Figure 1. *Thermomechanical data writing and reading.*

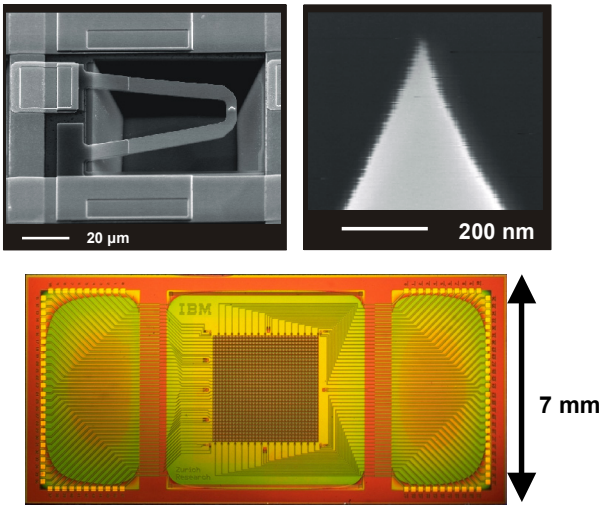

Figure 2. *Scanning electron microscope images of the cantilever, cantilever tip, and a photograph of the cantilever array. Fabrication details are reported in [**13**].*

0-9640024-4-2/hh2002/$20©2002TRF
DOI 10.31438/trf.hh2002.53

CANTILEVER OPERATION

Previous measurement [**9**] and modeling [**10**-**12**] have shown that cantilever heater temperature and the power dissipated in the cantilever govern the size and shape of the data bits and the sensitivity of thermal reading. In order to monitor the power dissipated in the cantilever and the temperature in the cantilever heater platform, the cantilever with resistance R_C is always operated in series with a resistor, R_S, shown in Fig. 3. Cantilever characterization and bit writing measurements are made with just the cantilever and a single series resistor. Also shown in Fig. 3 is a feedback control circuit used for thermal reading operation. The amplifier holds the bridge voltage $V_0 = V_{OFFSET}$ for a 'constant voltage' type operation. A voltage pulse of duration t and amplitude $V_+ - V_0$ is applied to the cantilever, where typical values are 1 – 100 μs and 0 – 3 V. The output of the control circuit is the cantilever voltage integrated over some integration time t_i. The integration time is the time over which the cantilever electrical response is measured, and is not necessarily the cantilever heating time. The cantilever cools after each cantilever heating event, and the circuit resets for the next measurement.

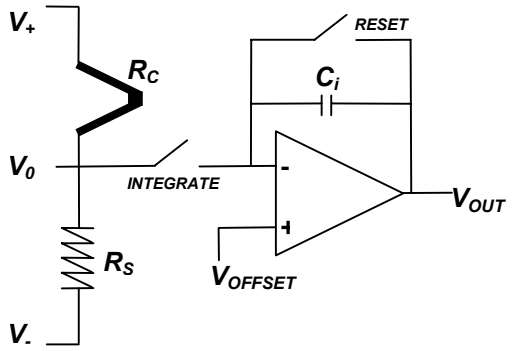

Figure 3. *Schematic of cantilever driving circuit.*

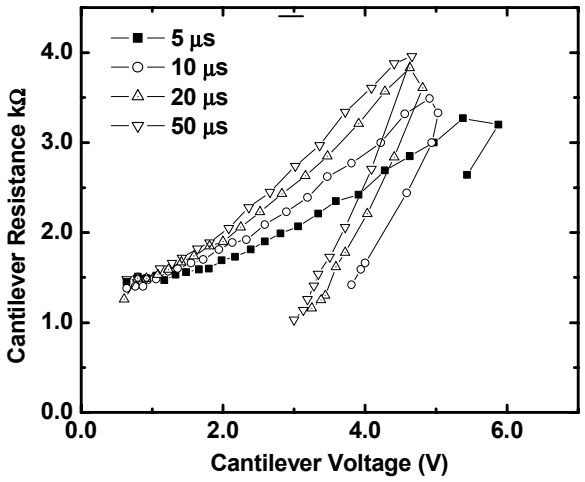

Figure 4. *Cantilever electrical resistance at the end of short voltage pulses.*

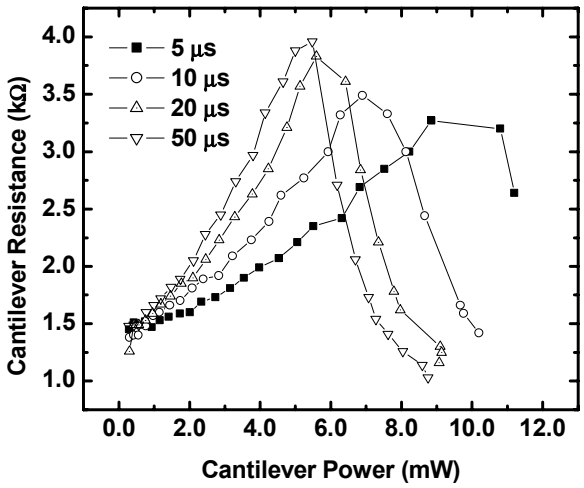

Figure 5. *Power dissipated in cantilever at the end of short voltage pulses.*

Figure 4 shows the cantilever electrical resistance at the end of short electrical pulses for a range of cantilever voltages and heating times and R_S = 3 kW. The 'corner' effect is due to intrinsic carrier generation at high temperatures. Heat diffuses along the length of the cantilever in approximately 20 μs, which accounts for the large change in R-V characteristics at less than 20 μs. Figure 5 shows the cantilever electrical resistance as a function of power dissipated in the cantilever. For long heating times, the cantilever power increases linearly with the cantilever heater temperature.

DATA BIT WRITING AND ERASING

Modeling [**11**,**12**] and measurement [**9**] of data bit writing has identified the spread of heat in the polymer layer as the fundamental limit on data bit density. Figure 6 shows a topographic map of thermomechanically written data bits. The sharp depressions below the polymer surface are the bit centers. The ring surrounding each is the polymer displaced during writing, more clearly shown in Fig. 7.

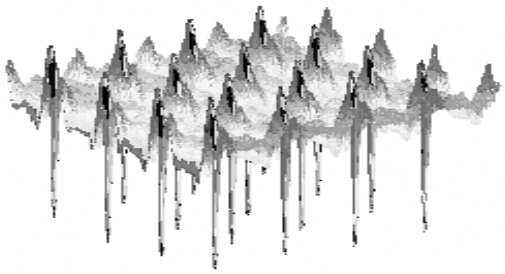

Figure 6. *Field of thermomechanically written data bits. The deep centers of the bits and the conservation of mass pileup ring around the bits are clearly noticeable. The z-axis is unconditioned thermal reading signal and the field is 3 μm X 3 μm in size..*

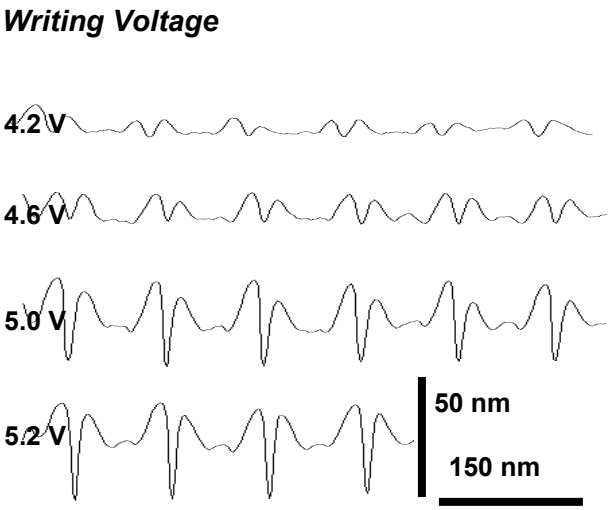

Figure 7. *Line scan across six data bits written at four different writing conditions. The cantilever tip loading force was 30 nN, the writing time was 10 μs. Again, the bit centers and pileup rings are clear.*

Modeling and simulation of heat transfer in the polymer layer during data bit formation shows that heat spreads away from the tip, softening a radial heat-affected zone near the tip [**11**,**12**]. Our hypothesis is that the dimensions of the pileup ring structure surrounding each bit are in fact the dimensions of melted polymer in proximity to the heated tip. Thus, bits written very close to each other or within the pileup ring of a previously written bit will influence the shape of neighbor bits.

To test this hypothesis, we perform an experiment where bits are written at increasing spatial periodicity. Figure 8 shows the results. As the bits are written successively closer together, they begin to melt and deform neighbor bits. For the highest spatial periodicity, the writing nearly eliminates previous bits. The ultimate data density of this technology will therefore depend upon the bit periodicity limited by this highly local melting. For the tip shape, polymer thickness, and writing conditions in Fig. 8, there is a maximum data density of 0.9 Tbit/in^2.

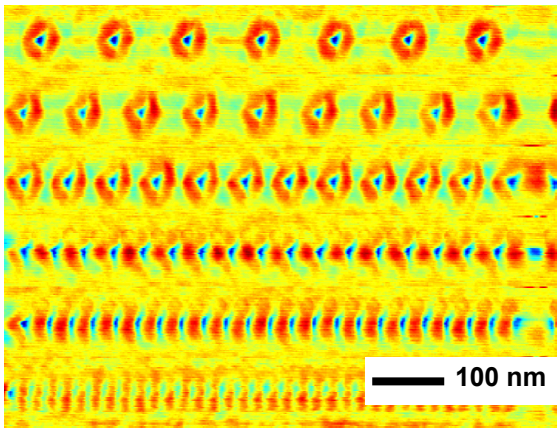

Figure 8*. Data bits written with varying spatial periodicity. The melting of the polymer near each bit limits bit proximity. For these writing conditions, the limit on bit pitch is approximately 30 nm, which corresponds to 0.9 Tbit/in^2.*

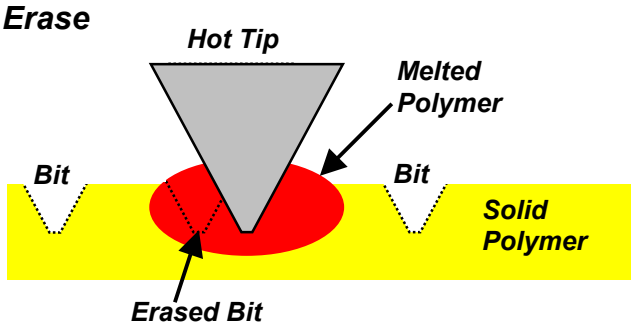

Figure 9*. Concept schematic of data bit erasing. As the melted polymer region increases in size and spreads away from the tip, the melting acts to erase nearby bits.*

While local melting limits data density, it offers an opportunity for local erasing. Previous erasing schemes [**1**,**3**] employed global erasing where the whole polymer substrate was heated to melt and reflow the entire polymer media substrate. The highly local melted near the heated tip during bit formation allows for local erasing, illustrated in Fig. 9.

Figure 10 shows images of bits written and then erased on the same location on the polymer data substrate. Erasing is accomplished by over-writing with a 15 nm bit pitch along the line of the written bits. As erasing requires over-writing, one bit will always be left at the end of a line of erased bits. This bit could be used to store information, depending upon its location, or be ignored, depending upon the data encoding scheme used.

Figure 11 shows line scans across the center line of the written/erased bits. We have demonstrated more than 10^5 write-erase cycles with no measurable change in the required writing conditions or the data reading signal. However, it should be noted that mechanical wear of the tip [**14**] and relaxation of the polymer data bits at high temperatures and long times [**15**] will impact the operation of a data storage device over its lifetime.

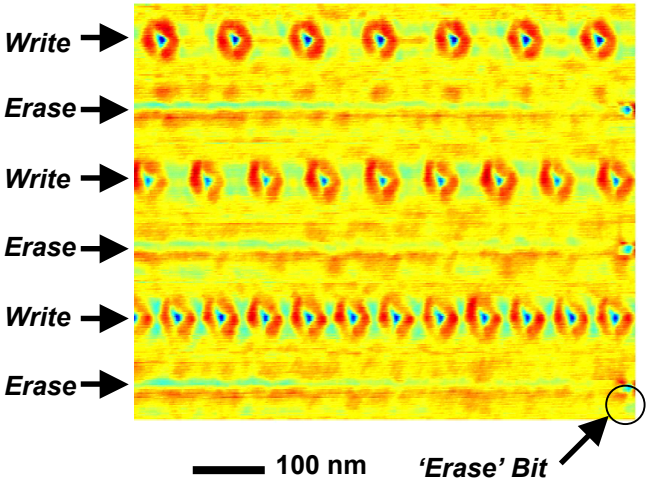

Figure 10. *Three lines of successive writing and erasing on the same polymer 'real estate'. The erased regions were made by overwriting with a dense bit pitch of 15 nm. As erasing requires multiple writes, the last erase write remains as a single 'erase' bit at the end.*

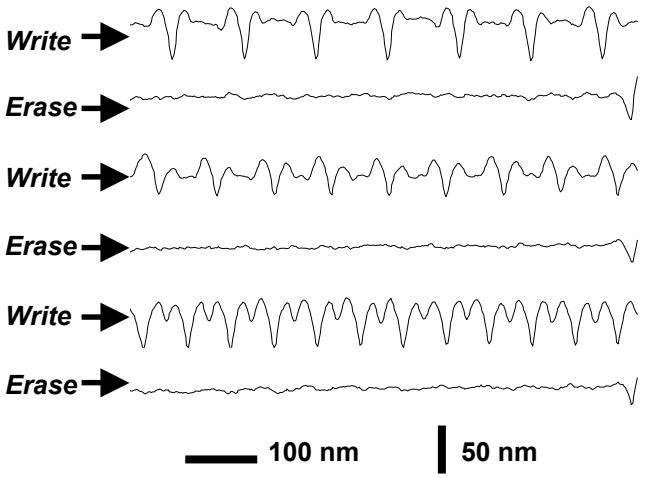

Figure 11. *Line scans of the three lines of successive writing and erasing shown in Fig. 10.*

THERMAL READING

Previous approaches to thermal data reading reported cantilever sensitivity in the range of 0.001 nm^{-1} for a near steady-state reading operation [**8**-**10**]. While offering interesting opportunities for nanometer-scale sensing, a steady-state type operation where the cantilever is constantly heated is not practical for a data storage system. This paper reports a thermal data reading technique that measures the cantilever response to short electrical pulses, which is a function of the thermal impedance between the cantilever and the substrate. The control circuit of Fig. 3 integrates the cantilever reading signal over the heating pulse, thus increasing the cantilever signal over that of the steady-state reading technique. This pulsed-heating reading technique also allows for integration with digital circuitry, which is necessary for a data storage system.

The cantilever reading sensitivity is the dependence of the measured cantilever electrical signal on feature height of the polymer data substrate. The cantilever electrical and thermal properties, as well as the integration. The $\Delta R/R$ cantilever sensitivity is measured for reading of data bits of depth 50 nm. The difference between measured maximum and minimum signals yields the quantity ΔR, and the measured signal at the neutral polymer surface gives the denominator R. In pulsed-heating operation, the cantilever signal integration yields a gain of

$$G = \frac{t_i}{\left(R_C^{-1} + R_S^{-1}\right)^{-1} C_i}$$

Where G is gain, and C_i is the capacitance of the integration capacitor, shown in Fig 3. For typical integration times of 5 – 50 µs, values for R_L and R_S of ~ 3 kΩ, and C ~ 100 pF, typical values for G are in the range 50-500. All of the measurements shown here for pulsed-heating reading are normalized with respect to G so that they may be compared with the steady-state reading, for which G=1.

All of the images and data in this paper are made at an integration reset time of 3 kHz, which is sufficiently long for the cantilever to cool, and for the cantilever scanner to move over the polymer. For all of the measurements here, integration time t_i is equal to half the heating time, made over the second half of the heating pulse.

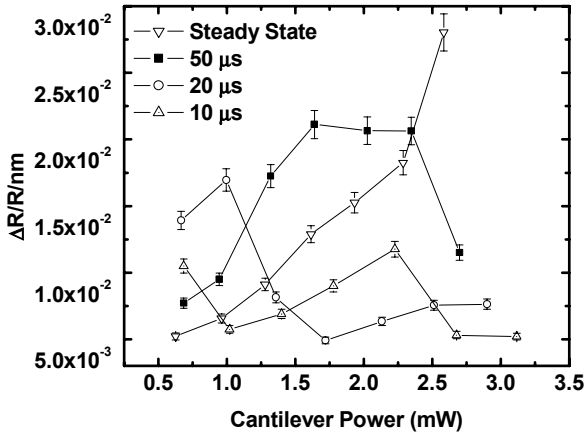

Figure 12. *Cantilever reading sensitivity as a function of heating power and reading time.*

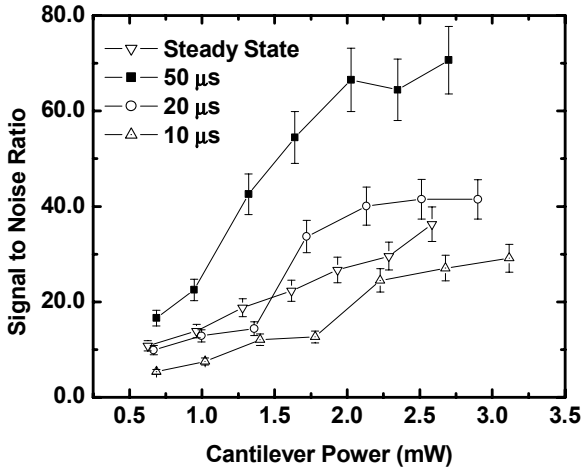

Figure 13. *Signal-to-noise ratio (SNR) of thermal reading of 50 nm data bits as a function of heating power and reading time.*

Calibration of the thermal impedance measurement allows quantitative measurement of the vertical features of Figs. 8 and 10. Figure 12 shows the cantilever sensitivity as a function of heating power and time. The cantilever $\Delta R/R$ vertical sensitivity is as high as 0.003 nm^{-1} in steady state operation, requiring 2.5 mW of power. The cantilever is more sensitive for longer times as the cantilever relaxes to thermal equilibrium. While increased power increases sensitivity in steady state operation, it does not always correspond to increased sensitivity in pulsed operation. Close comparison of Figs. 4 and 5 with Fig. 12 helps explain this result. The slopes of the R-V and the R-P curves are much steeper for longer heating times than shorter heating times. Furthermore, for heating times of less than ~ 20 µs, the cantilever legs do not heat substantially and therefore do not assist in the thermal reading process.

Figure 13 shows the cantilever signal-to-noise (SNR) characteristics for measuring 50 nm data bits, with SNR as high as 70. The signal is calculated as for Fig 12, and the noise is the root-mean-squared noise measured as the cantilever scans over the unmodified polymer substrate. The dominant noise sources are the cantilever and the media, with instrumentation noise measured as comparatively small. Pulses of ~20 µs or longer are required to

achieve SNR better than steady-state operation, as this is the time required for heat to diffuse the length of the cantilever.

CONCLUSIONS

This paper uses improved understanding of the heat transfer processes during thermomechanical data bit writing to achieve data density of 0.9 Tbit/in2, demonstrate local data bit erasing, and measure figures of merit for the thermal data reading process.

Along with previously reported design [5,6], fabrication [3], and operation [1,6] of cantilevers and cantilever arrays, the controlled writing, reading, and erasing of data bits reported in this paper complete the basic technological requirements for the development of a data storage system.

Future work will explore the optimization of tip shape, heating time, heating temperature, loading force, and polymer thickness. There are also interesting opportunities in using the cantilever for nanoscale thermal processing, manufacturing, and materials characterization at the nanometer scale. The very high thermal data reading sensitivity suggests that there may be applications for sub-nanometer displacement sensing.

ACKNOWLEGEMENTS

WPK appreciates the support of IBM Zurich Research Laboratory and the IBM Graduate Research Fellowship Program. The authors further thank B. Gottsmann and P. Seidler of IBM Zurich Research, T. Albrecht of IBM Almaden Research, and B. Chui of Stanford University.

REFERENCES

1. E. Grochowski and R. F. Hoyt, "Future Trends in Hard Disk Drives," *IEEE Transactions Magnetics*, *32,* 1850 (1996).

2. D. A. Thompson and J. D. best, "The Future of Magnetic Data Storage Technology," *IBM Journal of Research and Development*, *44,* 311 (2000).

3. J. Lohau, A. Moser, C. T. Rettner, M. E. Best, and B. D. Terris, "Writing and reading perpendicular magnetic recording media patterned by a focused ion beam," *Applied Physics Letters, 78,* 990 (2001).

4. J. J. M. Ruigrok, R. Coehoorn, S. R. Cumpson, and H. W. Kesteren, "Disk recording beyond 100 Gb/in.^{2}: Hybrid Recording?," *Journal of Applied Physics, 87,* 5389 (2000).

5. L. R. Carley, J. A. Bain, G. K. Fedder, D. W. Greve, D. F. Guillou, M. S. C. Lu, T. Mukherjee, S. Santhanam, L. Abelman, and S. Min, "Single-Chip Computers with Microelectromechanical Systems-Based Magnetic Memory," *Journal of Applied Physics*, *87,* 6680 (2000).

6. H. J. Mamin, R. P. Ried, B. D. Terris, and D. Rugar, "High-Density Data Storage Based on the Atomic Force Microscope," *Proceedings of the IEEE*, *87,* 1014 (1999).

7. P. Vettiger, M. Despont, U. Drechsler, U. Dürig, W. Häberle, M. Lutwyche, H. E. Rothuizen, R. Stutz, R. Widmer, and G. Binnig, "The "Millipede" - More than one thousand tips for future AFM data storage," *IBM Journal of Research and Development*, *44,* 323 (2000).

8. G. Binnig, M. Despont, U. Drechsler, W. Häberle, M. Lutwyche, P. Vettiger, H. J. Mamin, B. W. Chui, and T. W. Kenny, "Ultrahigh-Density Atomic Force Microscopy Data Storage with Erase Capability," *Applied Physics Letters*, *76,* 1329 (1999).

9. G.L.W. Cross, M. Despont, U. Drechsler, U. Dürig, P. Vettiger, W.P. King, and K.E. Goodson, "Thermomechanical Formation and Thermal Sensing of Nanometer-Scale Indentations in PMMA Thin Films for Parallel and Dense AFM Data Storage," in Fundamentals of Nanoindentation and Nanotribology II, Materials Research Society Symposium Proceedings Vol. 649, 2001.

10. W. P. King, T. W. Kenny, K. E. Goodson, G. L. W. Cross, M. Despont, U. Durig, H. Rothuizen, G. Binnig, and P. Vettiger, "Atomic Force Microscope Cantilevers for Combined Thermomechanical Data Writing and Reading," *Applied Physics Letters*, *78,* 1300 (2001).

11. W. P. King and K. E. Goodson, "Modeling and Simulation of Nanometer-Scale Thermomechanical Data Bit Formation," Proceedings of the ASME National Heat Transfer Conference, Anaheim, CA, (2001).

12. W.P. King, PhD Thesis, Stanford University (2002).

13. M. Despont, J. Brugger, U. Drechsler, U. Dürig, W. Häberle, M. Lutwyche, H. Rothuizen, R. Stutz, R. Widmer, H. Rohrer, G. K. Binnig, and P. Vettiger, "VLSI-NEMS Chip for Parallel AFM Data Storage," *Sensors and Actuators A*, *80,* 100 (2000).

14. B. D. Terris, S. A. Rishton, H. J. Mamin, R. P. Ried, and D. Rugar, "Atomic Force Microscope-Based Data Storage: Track Servo and Wear Study," *Applied Physics A*, *66,* S809 (1998).

15. U. Dürig, G. Cross, M. Despont, U. Drechsler, W. Haberle, M. I. Lutwyche, H. Rothuizen, R. Stutz, R. Widmer, P. Vettiger, G. K. Binnig, W. P. King, and K. E. Goodson, ""Millipede" : an AFM data storage system at the frontier of nanotribology," *Tribology Letters, 9*, 25 (2002).

MEMS MICRO-MECHANICAL LOGIC GATES FOR MECHANICAL COMPUTING IN MACHINE ONLY ENVIRONMENTS

Paul E. Kladitis
Air Force Institute of Technology (AFIT)
Department of Electrical and Computer Engineering
2950 P Street
Wright-Patterson AFB OH 45433-7765
Tel: 937-255-3636 ext. 4595, Fax: 937-656-4055, Email: paul.kladitis@afit.edu

ABSTRACT

With respect to microsystems, environments such as harsh radiation, harsh temperature, or limited space may preclude the use of microelectronics and associated power supply for the purposes of sensor to actuator signal processing. For these situations, this work proposes the idea of performing the signal processing computation mechanically. To this end, this work presents novel MEMS micro-mechanical logic gates for mechanical computing. Micro-sized mechanical NAND, NOR, inverting logic gates, static memory cells, and optically readable outputs are developed, fabricated, and tested. A mechanical logic circuit, with the Exclusive-OR (XOR) function, is constructed from three mechanical NAND gates and demonstrated.

INTRODUCTION

In 1889, Charles Babbage invented his decimal based mechanical computer capable of all basic arithmetic operations including solving simultaneous equations, functions, and finding roots – example schematics are shown in Figure 1 [**1**]. Although Babbage's "Analytical Engine" was the size of a room, it probably had beneficial qualities such as being impervious to radiation and being able to operate at high temperatures. With the advent of Micro-Electro-Mechanical Systems (MEMS), machines can be created that are on the order of size of a human red blood cell. It now may be a worthwhile idea to design mechanical computers to take the place of equivalent functioning electrical computers in harsh environments where electronics will fail, such as radioactive or high temperature. Furthermore, there may be situations where the computation between microsensor and microactuator can be implemented mechanically, in a more convenient manner, than implementation by integrated electronics and power supply.

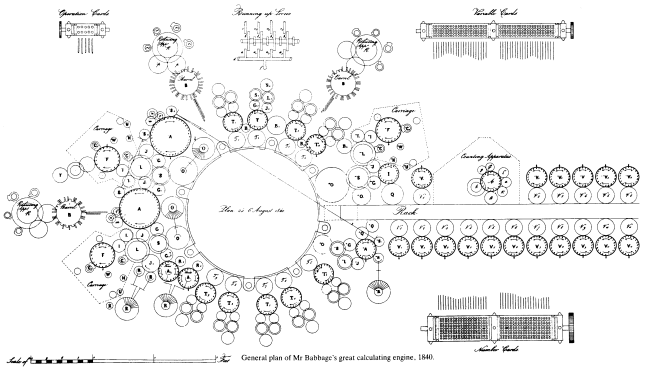

Figure1. *Schematics of Babbage's "Analytical Engine" 1889 [1].*

The art and science of mechanical computing has been around for a long time, as exemplified by Babbage's analytical engine or National Cash Register Co.'s (NCR) mechanical cash registers, Figure 2 [**2**]. In fact, mechanical computing is as ancient as mankind itself. Furthermore, electrical devices are just as ancient, and both have been used, where appropriate, throughout the ages. Figure 3 shows pictures of a fossilized analog computer [**3**] complete with complex gearing, including differential gears, found in the Aegean Sea, and ancient batteries found near Baghdad [**4**], both dated as early as 1000 BC.

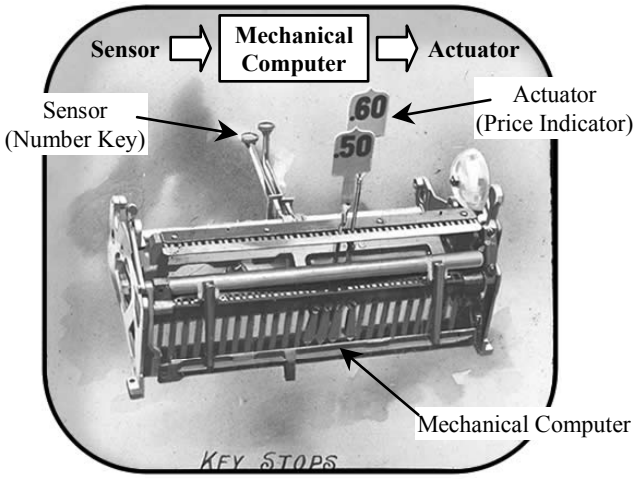

Figure 2. *A "Magic Lantern" image of part of an 1891 NCR cash register [2].*

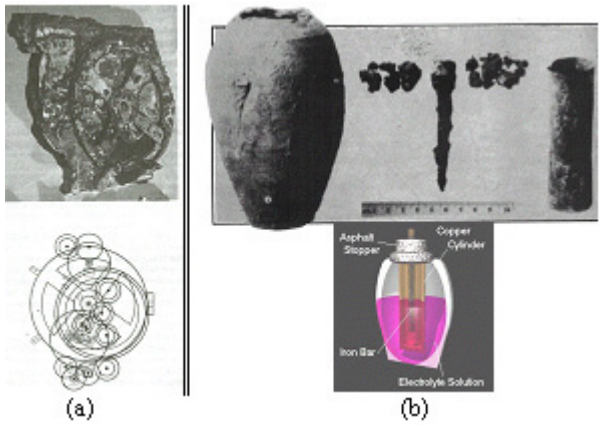

Figure 3. *(a) Photograph of an analog computer including a sketch of x-ray photographs revealing complex gearing [3]. (b) Photograph of ancient battery and components including a depiction of a reconstructed battery [4], both dated at ≈ 1000 BC.*

Mechanical computing can be categorized into analog computing and digital computing. This work demonstrates logic gates in mechanical form – a digital computing component. Electrical logic gates transform high and low electrical inputs into high or low electrical outputs. Mechanical logic (m-logic) gates transform motions at the inputs to motion at the output. This idea stands in contrast to the MEMS AND gate developed by Hirata et

0-9640024-4-2/hh2002/$20©2002TRF
DOI 10.31438/trf.hh2002.54

al. [**5**], where electrical signals are inputs and electrostatically actuated plates perform switching to provide electrical signal outputs. Similarly, the MEMS static RAM (SRAM) of Halg [**6**] also uses electrostatically actuated mechanical actuators to preserve an electrical state. Other work related to MEMS electro-mechanical digital computing can be found in [**7 – 9**]. This work deals with non-electrical mechanical movements only.

Mechanical logic functions are also not a new idea; some early examples include Lull's logic wheels [**10**]. Lull (1274 AD), a monk, designed turning wheels where the position of the wheel compared two ideas, where the ideas are abbreviated in Latin and printed on the wheel. Pastore's syllogism machine (1868) operates in two states: true if the wheels and belts all turn and false if the wheels can not turn [**10**], see Figure 4.

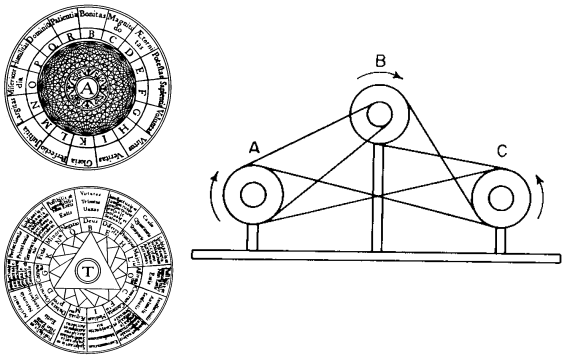

Figure 4. ***(a)*** *Lull's logic wheels 1274, (b) Pastore's syllogism machine 1868 [**10**].*

Presently, the idea of mechanical logic has been revived in the hopes of building super computers using atoms and molecules (nano-compting) [**11 – 13**]. Richard Feynman discussed the concept of atomic digital computing using "reversible logic gates," that is, gates where the output can be "undone." Given the output, the states at the input, that created the output in the first place, are recreated [**14**].

Although the m-logic gates in this work are not reversible, these gates may be, in some way, a step towards realizing nano-computing systems of the future. Similarly, in 1943, the Navy's theoretical engineers (from MIT) proposed an all–electronic device, requiring 70,000 gas tubes, for decrypting the German's 4-rotor Enigma Machine's coded messages, used by U-Boats in the Atlantic Ocean. However, Dayton, Ohio's Joseph R. Desch (1907 - Aug. 3, 1987), at NCR, realized that the gas tubes would generate too much heat to operate reliably. Desch chose to design and build the electro-mechanical NCR "Bombe," shown in Figure 5.

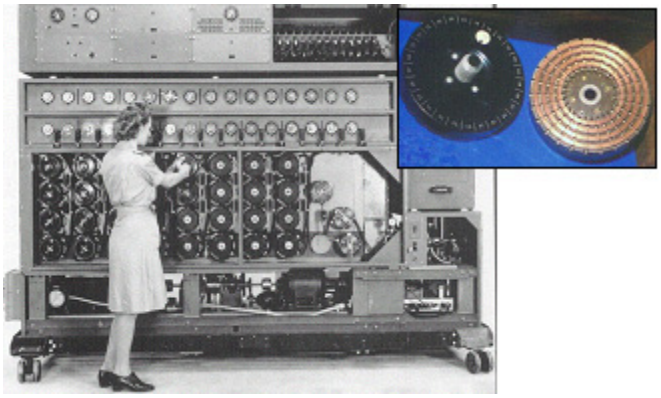

Figure 5. *NSA Photograph of an NCR Bombe. A U.S. Navy WAVE (Women Accepted for Voluntary Emergency Service) is seen, possibly setting an initial position, on one of the rotors. Inset shows a close view of a rotor. Pictures courtesy of Jerry Proc.*

The NCR Bombe "…helped win the battle for control of the Atlantic Ocean. During the war, this project was second only to the atom bomb in terms of national security and secrecy." [**2**] The NCR Bombe, since recent declassification, is now noted as an important step towards modern computing [**2, 15, 16**].

THEORY AND DESIGN

In this research, micro-sized mechanical NAND (m-NAND), NOR (m-NOR), inverting logic gates (m-inverter), static memory cells (m-RAM), and optically readable outputs are developed, fabricated, and tested. Figure 6 depicts an m-NAND gate in its four different states – states also indicated in the inset "truth table".

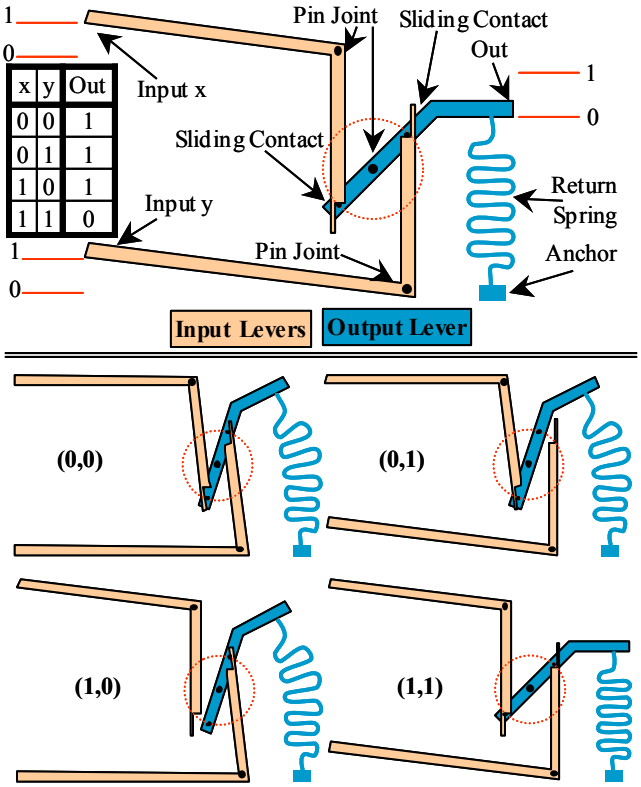

Figure 6. *Depiction of an m-NAND gate, a NAND "truth table," and depictions of the m-NAND's four different states (x,y).*

The design of the m-logic circuits has a one-to-one correspondence with the existing design methodology of electronic combinational and sequential digital logic circuits. The only difference in design concept is as follows: an electronic logic gate requires either 0 V or 5 V inputs and provides a logical 0 V or 5 V output; the m-logic gate's inputs are levers that require either "down" or "up," and the output lever provides a logical "down" or "up". The Boolean algebra, used in design, is still the same, where 0 = "down" and 1 = "up".

The simplest m-logic gate, the m-inverter, is simply a lever. The m-inverter is depicted in Figure 7. An m-inverter can also be created by physically connecting the inputs of the m-NAND together as one input.

The output of an m-logic circuit can be used as actuation or can be read optically. Furthermore, the state of an output can be preserved, in effect, making static memory (m-SRAM). However, a mechanism to disconnect the input of the m-SRAM from the rest of the circuit, until a memory update occurs, may be necessary.

Figure 8 shows the concept of mechanical m-SRAM and optical output where the output (a mirror) is optically covered ("down") or uncovered ("up"). For the memory, a simple spring lever can be used to preserve a "down" or "up" state until forced to change otherwise. The m-SRAM is not demonstrated in this work.

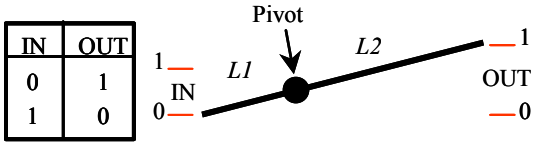

Figure 7. *Depiction of an m-inverter where L1 is the distance from the tip of the input to the pivot, and L2 is the distance from the tip of the output to the pivot.*

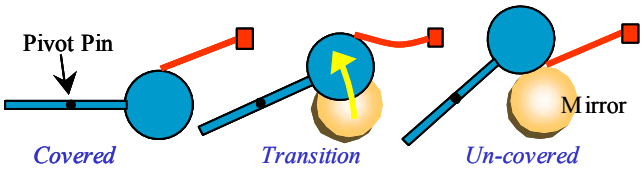

Figure 8. *Depiction of m-SRAM and optical output.*

FABRICATION AND EXPERIMENTAL DETAILS

Figure 9 (a) shows a scanning electron micrograph (SEM) of a fabricated and released m-NAND, and (b) shows an m-NOR. The sliding contacts are implemented in a slightly different manner than depicted in Figure 6. Figure 10 shows a captured video image of an m-NOR with optical output.

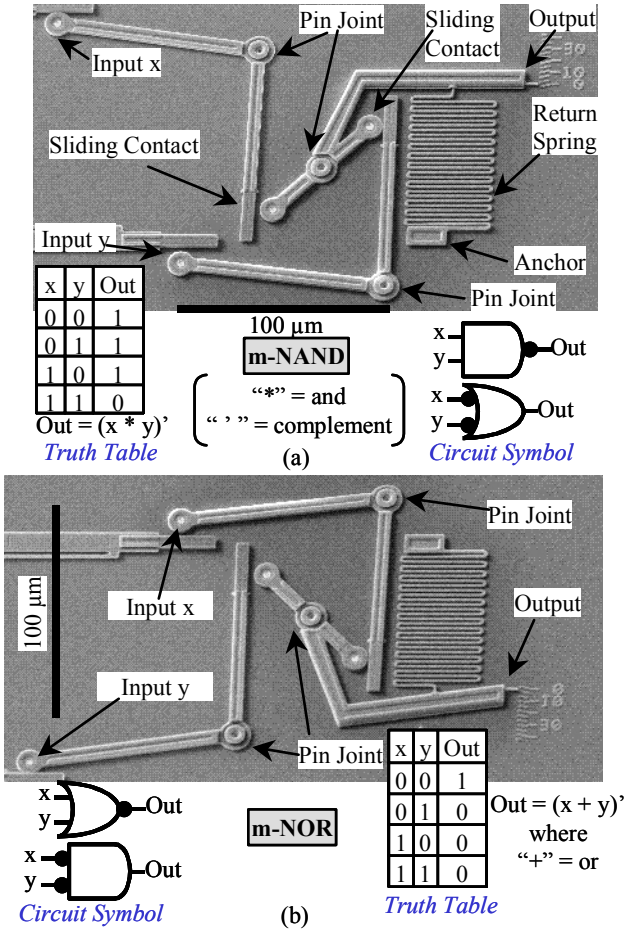

Figure 9. *SEM of a fabricated and released (a) m-NAND and (b) m-NOR, and respective truth tables and circuit symbols.*

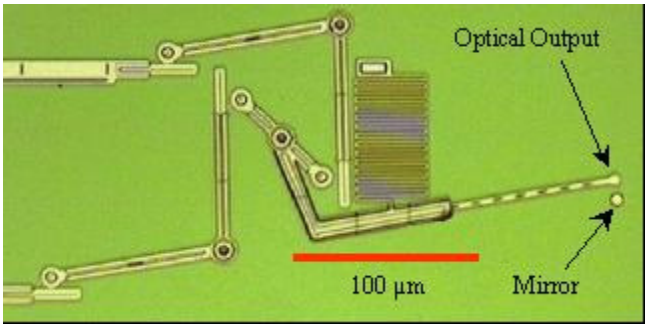

Figure 10. *Video image of an m-NOR with optical output.*

The mechanical logic circuits were fabricated using the MUMPs polysilicon surface micromachining process [**17**], which has two releasable polycrystalline silicon structural layers: poly1 and poly2, poly2 being the upper layer. The input and output levers are made from a stacked combination of poly1 and poly2. The pin caps of the pin joints are made from poly2. The return spring is made from poly1. Each link, of the 28-link return-spring, is 66 µm long and has a cross sectional area of 2 µm × 2µm.

The position of the return-spring connection to the output lever, and length of the output lever, can be varied to achieve a required input actuation force for a desired output deflection, respectively. The following discussion assumes an arbitrary output lever deflection (at the return-spring attachment) of 10 µm. The reaction force of 16- to 21-link springs, stretched 10 µm, was modeled using finite element analysis (FEA). The force required to stretch the 16-link spring was predicted to be 6.94 µN. From beam theory approximations of the spring, corroborated by FEA, the force required (*F*) to stretch an *n*-link spring is $F = 6.94\ \mu N \times 16/n$. Therefore, the restoring force of the 28 link spring when stretched 10 µm, for the m-gates depicted in Figures 9-11, is approximately 6.94 µN × 16/28 = 3.97 µN. Since the lever arm of the spring attachment point is twice as long as the input force lever arm, the force required at a single input, of the m-logic gates, is approximately 2 × 3.97 µN = 7.94 µN. The input lever distance required to deflect the spring attachment point by 10 µm is 10 µm / 2 = 5 µm.

The m-logic circuits were released and tested by mechanically manipulating the inputs with probes and observing the outputs under a microscope. Figure 11 shows a sequence of captured video images of a mechanical Exclusive-OR (m-XOR) circuit composed of 3 m-NANDs – just as the electronic XOR would be. The m-XOR in Figure 11 (a) is in a nonsense state since inputs x' and y' are not set appropriately. In Figure 11 (b) – (e), the m-XOR inputs are appropriately sequenced through the four input states by deflecting the input levers with probes. Down arrows indicate deflected (zero/down state) inputs in Figure 11 (b) – (e).

DISCUSSION

The m-logic circuits suffer from displacement fan-out and force fan-out. Force fan-out is where the output force diminishes due to increasing levels of logic gates thereby increasing pivot and sliding contact friction points and the number of return springs that the input force must overcome. Displacement fan-out is where the output displacement diminishes with increasing number of logic gate levels. Displacement fan-out occurs because the m-gates are surface micromachined, and due to the fabrication process, must have a finite space between the sliding contacts and at the pin joint. These finite spaces add up with each level of logic gates. The m-inverter can be used to compensate for either type of fan-out, but not both. The output displacement is *L2/L1* times the input displacement, while output force is *L1/L2* times the input force.

The dotted-line circles, in Figure 11 (a), indicate the location of the interface sliding contacts between the first level of m-NANDs and the second level output m-NAND. Before release, the output levers of the first level of m-NANDs are initially located below the inputs to the second level m-NAND. To prime the circuit for proper operation, the output levers of the first level of m-NANDs have to be manually (using micromanipulators) lifted to the other side of the second level m-NAND inputs as shown in Figure 11.

Plans for future work includes the following: investigate solutions for optimizing gate design by reducing fan-out and gate size; develop logic level interconnections that do not require manual assembly; demonstrate analog mechanical computing components such as differentiators, integrators, and ALUs; fabrication mechanical computing circuits in SiC; and confirm operation of SiC and polysilicon mechanical computing circuits while in radiation and high temperature harsh environments.

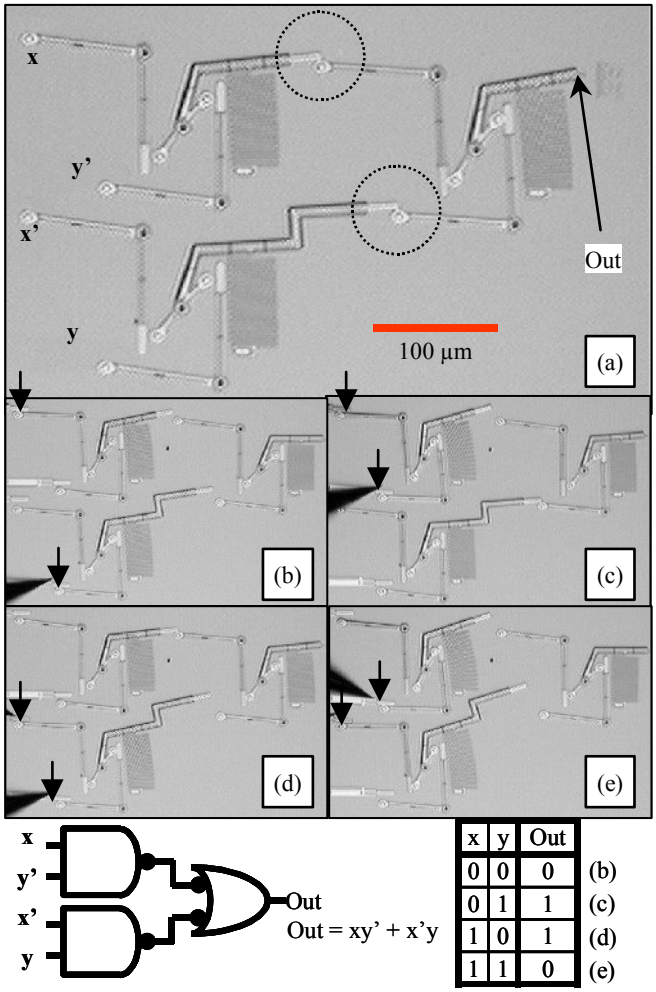

Figure11. *Captured video images of an m-XOR circuit composed of 3 m-NANDs. The states (b) – (e) of the m-XOR are indicated to the right of the truth table. Arrows indicate inputs being deflected.*

CONCLUSIONS

This work presented an overview of mechanical computing and the design and implementation of m-NANDs, m-NORs, optical output, and the implementation of an m-XOR. The concept of the m-inverter and m-SRAM were presented. M-logic gate shortcomings and future work were presented in the Discussion section. Micro m-logic circuits provide a complete non-electronic paradigm for logical computing and may serve as an alternative to radiation hard electronics or electrical sensors and control circuits for high temperature applications. Furthermore, simple mechanical computing, instead of electronic control, between sensor and actuator on a micro platform (robot, satellite, UAV, thruster system), may save space, energy, and be a simpler and straightforward means of implementing control.

ACKNOWLEDGMENTS

The mechanical logic gate idea was conceived, fabricated, and demonstrated by the author, in 1999, while working on a Doctor of Philosophy degree at the University of Colorado at Boulder. Dr. Victor Bright and Dr. Y. C. Lee provided funding for the fabrication. Thanks!

REFERENCES

[1] M. Campbell-Kelly, *The Works of Charles Babbage*, Pickering & Chatto, London, 1989.
[2] The National Cash Register Co. (NCR) archives of The Montgomery County Historical Society, 224 North St. Clair Street, Dayton, Ohio 45402, Phone: 937-228-6271, Fax: 937-331-7160, E-mail: MCHS@Daytonhistory.org.
[3] D. Chittick, *The Puzzle of Ancient Man*, Creation Compass, 1997.
[4] P. T. Keyser, "The Purpose of the Parthian Galvanic Cells," *Journal of Near Eastern Studies*, vol. 52, no. 2, p. 98, 1993.
[5] A. Hirata, K. Machida, H. Kyuragi, and M. Maeda, "A Micromechanical Switch as the Logic Elements for Circuits in Multi Chip Module on Si (MCM-Si)," *Proceedings of the 12th IEEE International Conference on MEMS*, pp. 582-587, 1999.
[6] B. Halg, "On a Nonvolatile Memory Cell Based on Micro-Electro-Mechanics," *Proceedings of the IEEE Conference on MEMS*, pp. 172-176, 1990.
[7] E. J. J. Kruglick and K. S. J. Pister, "MEMS Relay Based Digital Logic Systems," *10th International Conference on Solid-State Sensors and Actuators: Transducers'99*, pp. 818-821, 1999.
[8] R. Yeh, R. A. Conant, and K. S. J. Pister, "Mechanical Digital-to-Analog Converters," *International Conference on Solid-State Sensors and Actuators: Transducers'99*, pp. 998-1001, 1999.
[9] H. Toshiyoshi, D. Kobayashi, M. Mita, G. Hashiguchi, H. Fujita, J. Endo, and Y. Wada, "Micro Electro Mechanical Digital-to-Analog Converter," *10th International Conference on Solid-State Sensors and Actuators: Transducers'99*, pp. 994-997, 1999.
[10] M. Gardner, *Logic machines and diagrams*, McGraw-Hill, 1958.
[11] E. Fredkin and T. Toffoli, "Conservative Logic," *International Journal of Theoretical Physics*, vol. 21, nos. 3/4, pp. 219-253, 1982.
[12] E. K. Drexler, *Nanosystems*, John Wiley & Sons, 1992.
[13] R. C. Merkle, "Two types of mechanical logic," *Nanotechnology*, vol. 4, pp. 114-131, 1993.
[14] R. Feynman, "Infinitesimal Machinery (transcription of 1983 speech)," *Journal of Microelectromechanical Systems*, vol. 2, no. 1, pp. 4-14, March 1993.
[15] J. DeBrosse, "Enigma," *The Dayton Daily News*, An 8 part series beginning February 25, 2001.
[16] Center for Cryptologic History, "The Bombe: prelude to modern cryptanalysis," National Security Agency (NSA), Fort George G. Meade, MD, OCLC number: 35657417, 1990.
[17] D. A. Koester, R. Mahadevan, A. Shishkoff, and K. W. Markus, *MUMPs™ Design Handbook*, Revision 4.0, Cronos Integrated Microsystems, 3021 Cornwallis Road, Research Triangle Park, NC 27709, May 1999.

A 5V CLOSED-LOOP SECOND-ORDER SIGMA-DELTA MICRO-G MICROACCELEROMETER

Haluk Kulah, Arvind Salian[*], Navid Yazdi[**], and Khalil Najafi

Center for Wireless Integrated Microsystems
University of Michigan, Ann Arbor, MI 48109-2122
email: haluk.kulah@umich.edu

ABSTRACT

A closed-loop hybrid accelerometer subsystem consisting of an all-silicon μg capacitive microaccelerometer and a CMOS interface circuit is presented. Microaccelerometer sensitivities are 1.3pF/g and 6pF/g for 2x1mm^2 and 4x1mm^2 doubly-supported bridge structures, and 20pF/g for a cantilever-supported structure, respectively. The calculated mechanical noise floor for the 2x1mm^2 bridge device is 0.39μg/√Hz in atmosphere. The circuit has a 95dB dynamic range, a low offset of 370μV and can resolve better than 75aF. The complete module operates from a single 5V supply and has a measured sensitivity of 430mV/g with a noise floor of 15μg/√Hz in open-loop. The subsystem is operated in closed-loop and can resolve better than 100μg/√Hz for signal frequencies up to 15 Hz, and better than 2μg/√Hz for signal frequencies higher than 15Hz.

INTRODUCTION

Accelerometer systems with micro-g resolution and high precision are needed in navigation/guidance, microgravity measurements, tilt control, platform stabilization, and position sensing [1]. The sensor should have high sensitivity, low temperature sensitivity, and good long-term stability. In order to obtain a large dynamic range and reduce sensitivity to variations in accelerometer mechanical characteristics (mass size, spring constant), closed-loop operation based on force feedback is required. In addition, a digital output is desired in many applications. Our group has previously reported a high-performance silicon microaccelerometer [2], and its open-loop operation using a switched-capacitor readout circuit [3]. In this paper, we report the closed-loop operation of the accelerometer system as a second-order sigma-delta modulator using only a single 5V supply.

THE ACCELEROMETER SYSTEM

To increase accelerometer sensitivity, a large proof mass, compliant suspensions, and large capacitance sensitivity are needed. When operated in open-loop, such an accelerometer will have a limited dynamic range and bandwidth. To increase the dynamic range, the accelerometer can be operated in closed-loop by applying an electrostatically-generated force feedback signal that maintains the proof mass in null position. Recently, Σ-Δ modulation control loops have been used in microaccelerometers to achieve force-rebalancing and obtain a direct digital output [3, 4]. A 2nd-order Σ-Δ modulator, with two integrators, one mechanical and one electrical, not only provides a digital output, but also relaxes the accuracy requirements on the analog circuits.

The general form of a Σ-Δ modulator is shown in Figure 1. The Σ-Δ loop has a low pass transfer function represented by H(s). This low pass characteristic moves most of the quantization noise to higher frequencies out of the input signal band. The high frequency shaped noise is removed from the converted signal by the low pass digital filter following the Σ-Δ modulator loop. In an electromechanical Σ-Δ modulator, H(s) is realized by the low pass transfer function of the sensor. The oversampling ratio in electromechanical modulators is typically very large. Hence sufficiently low quantization noise is achievable with a one-bit digital-to-analog converter (DAC) and quantizer; therefore, the DAC block and the nonlinearity errors of the quantizer are reduced.

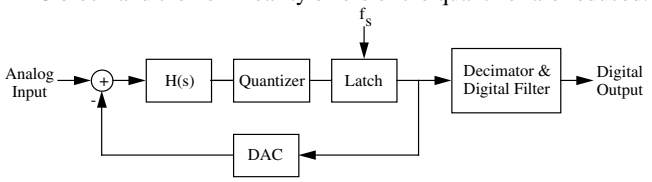

Figure 1: *General oversampling sigma-delta data converter.*

The electrostatic force-feedback for the accelerometer is provided by the high frequency pulse-width modulated (PWM) digital output stream of the electromechanical Σ-Δ modulator. Therefore the closed-loop accelerometer has all the advantages of an oversampled Σ-Δ data converter as well as direct digital output, very wide dynamic range, extended linearity, less stringent precision requirements of the circuit blocks, and larger bandwidth. All these advantages are achieved in an oversampled Σ-Δ modulator by trading-off resolution in the time domain with resolution of the various circuits. The relatively small bandwidth (1kHz), high precision (μg's) and wide dynamic range (18-19b) requirements of our application, make this trade-off very rewarding.

The accelerometer system consists of the sensor and the interface chip. The sensor structure utilizes the whole wafer thickness to attain a large proof mass with integrated polysilicon electrodes above/below it [2]. These electrodes are stiffened by embedding vertical stiffeners in them to allow force rebalancing of the proof mass. Damping holes are formed in the electrodes to obtain a desired damping coefficient for stable operation. Figure 2 shows the device SEM with a 2x1mm^2 proof mass.

In force-rebalanced accelerometers with a large proof mass, a further challenge is maintaining low-voltage operation since the required feedback force has to be large enough to bring the proof mass to null position. In the system reported here, this is accomplished by using a single 5V supply, and by limiting the movement of the proof mass using bushings formed between the electrodes and proof mass as illustrated in Figure 3.

The electrostatic feedback force is a linear function of the output voltage and is linearized by applying differential force on top and bottom electrodes. Assuming that the proof mass

[*] Now with: *Motorola Inc*., Phoenix, AZ
[**] Now with: *Corning Intellisense Corp.*, Wilmington, MA 01887

0-9640024-4-2/hh2002/$20©2002TRF
DOI 10.31438/trf.hh2002.55

displacement is negligible in closed-loop operation, if the circuit applies V_0+V/2 on the top and V_0-V/2 on the bottom electrodes, the differential electrostatic force can be expressed as:

$$F_{e-diff} = F_{e-top} - F_{e-bottom} \approx \frac{\varepsilon_0 A}{d^2} V_0 V \qquad \text{Eq. 1}$$

where A is the electrode area and d is the gap distance between the electrode and the proof mass. It can be shown that the full-scale feedback acceleration is:

$$a_{fs} = \frac{1}{9.8} \times \frac{1}{m} \times \frac{T_f}{T} \times \left(\frac{\varepsilon_0 A}{d^2} V_0 V \right) \qquad \text{Eq. 2}$$

where T_f /T is the ratio of feedback duration over the full readout cycle, and m is the proof mass. For m=2.2mg,T_f/T=3/8, A=1.4mm^2 (effective electrode area after taking the damping holes into account), d=1.5µm and V=2V_0=5volts, the maximum feedback acceleration is 1.2g. In other words, this system can force-rebalance such a large proof mass by a single 5V supply.

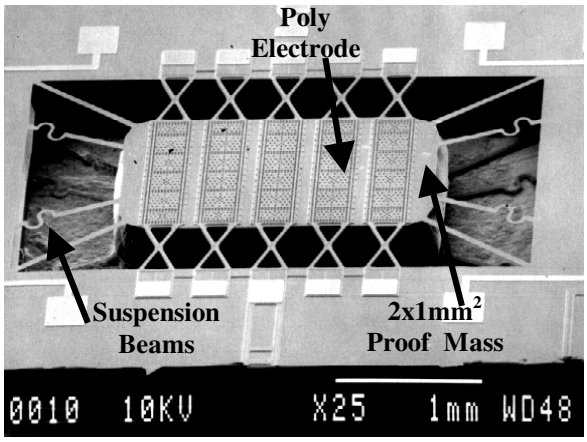

Figure 2. *SEM of a device with 2mm x 1mm proof mass.*

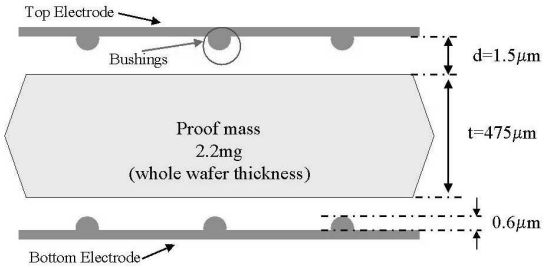

Figure 3: *Cross sectional view of the accelerometer showing the electrodes, proof mass and bushings.*

The microaccelerometer is interfaced with capacitive readout circuitry to detect the capacitance change and to operate the sensor in open-loop or force-rebalance the proof mass in closed-loop. Figure 4 shows the block diagram of the interface circuit [5]. Two fixed reference capacitors are used to form a balanced full-bridge with the sensor capacitive half-bridge, and the sensor top and bottom electrodes are used as the input nodes to the chip front-end. A switched-capacitor readout circuit is utilized to sense the capacitance change. This is because of the large parasitic capacitance associated with the hybrid packaging approach, and because of the large zero-acceleration sense capacitance associated with the accelerometer.

In addition to the switched-capacitor readout circuit, the interface chip incorporates two other important circuits. First, the start-up circuit pulls the proof mass to null position halfway between the two electrodes. At start-up, the proof mass is touching the bushings on the bottom electrodes, and hence the gap distance is approximately 2.4µm. Because of the larger gap and in order to ensure that sufficient electrostatic force is available to bring the mass into null position, a start-up circuit is designed and used. This circuit stops the readout clock and applies a constant feedback voltage of 5 volts on the suitable electrode. The 5V electrostatic signal can overcome the gravitational force of about 1.5g from the proof mass. The design of the start-up circuit has to be such that the proof mass does not oscillate.

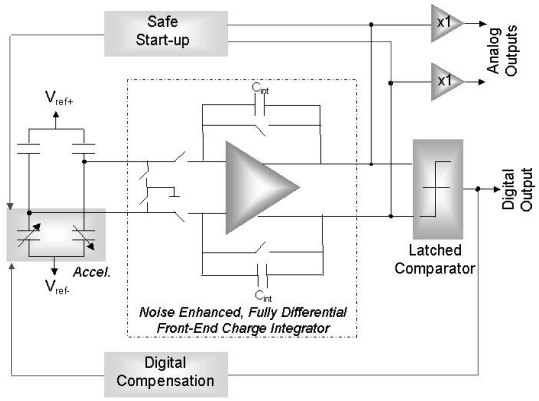

Figure 4: *Block diagram of the interface sigma-delta chip.*

Second, a digital feedback loop and digital compensation block are incorporated to provide a PWM signal to the proof mass and electrodes for force feedback operation. The digital compensation block implements a lead compensator to ensure the loop stability of the system, which degrades as the Q of the accelerometer increases. Electromechanical simulations have been performed to verify the stability of the system with an accelerometer Q of up to eight. Since the Q of the accelerometer implemented in our system is less than 1, the lead compensation circuit is usually not needed in normal operation. This lead compensator is realized by pulse-width modulating the feedback bit, which works quite effectively with the continuous time mechanical low pass transfer function. This approach provides better linearity without any need to implement the digital compensator in the forward signal path.

TEST SETUP & RESULTS

Figure 5 shows the z-axis hybrid subsystem with the sensor and the circuit assembled onto a PC board and mounted inside a standard DIP package. The sensor and the interface circuit are packaged close to each other to minimize parasitics. The hybrid system can operate in both open-loop and closed-loop.

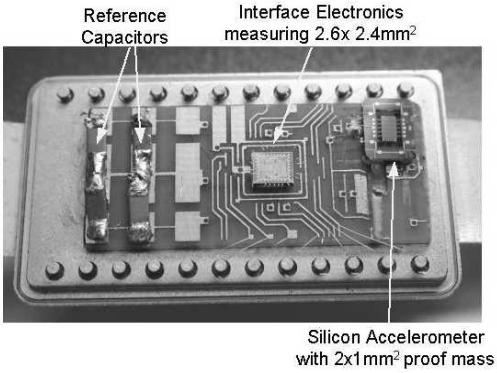

Figure 5: *Hybrid packaged accelerometer and the interface chip in a standard 24-pin IC package.*

Open-Loop Tests:

The open-loop tests were done on a dividing head, in a 1g gravitational field, by changing the acceleration on the sensor from -1g to +1g. While changing the applied acceleration, both top and bottom capacitances were measured, as well as the analog output voltage of the interface electronics. Figure 6 shows the measured capacitance sensitivity for a 2x1mm^2 bridge-type z-axis accelerometer. As the figure shows, the variations of the top and bottom capacitances are perfectly symmetric with an offset of 8pF which is due to the difference in top and bottom gap distances. The offset is fabrication related and can be compensated in the test setup by using proper capacitance values while forming the full bridge. Measured sensitivities are 1.3pF/g and 6pF/g for 2x1mm^2 and 4x1mm^2 doubly-supported bridge structures, and 20pF/g for a cantilever-supported structure, respectively.

The packaged accelerometer system is mounted on a PC board that includes sample-and-hold and low-pass-filter circuits to reduce the test setup related noise.

Figure 7 shows a measured open-loop sensitivity of 430mV/g. The noise floor is measured using a dynamic signal analyzer HP3561. Figure 8 shows the measured output noise spectrum of the complete module with a DC input of 1g, which shows a noise floor of –100.3dB. This indicates that the current system is capable of resolving about 15µg/√Hz.

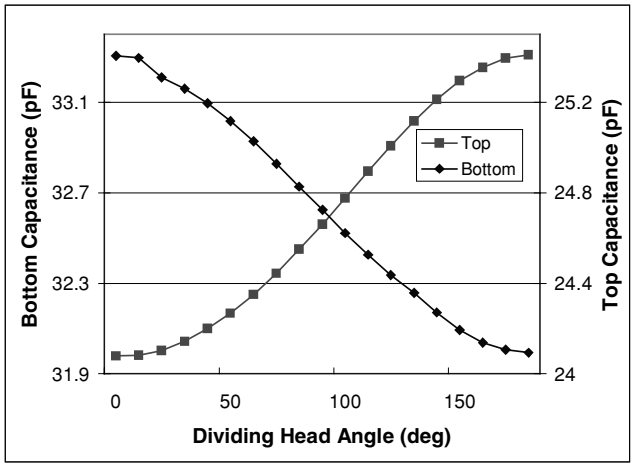

(a)

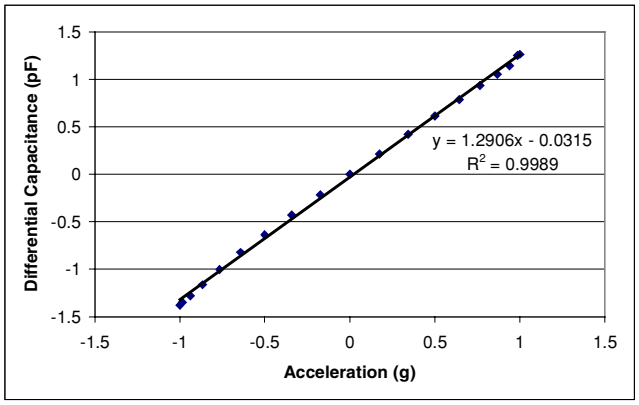

(b)

Figure 6: *Measured capacitance sensitivity for the device with 2x1mm^2 proofmass indicating a sensitivity of 1.3pF/g. (a) Top and Bottom electrodes capacitance variation for 180 degree rotation in earth's gravitational field. (b) Differential capacitance variation between –1 and +1g.*

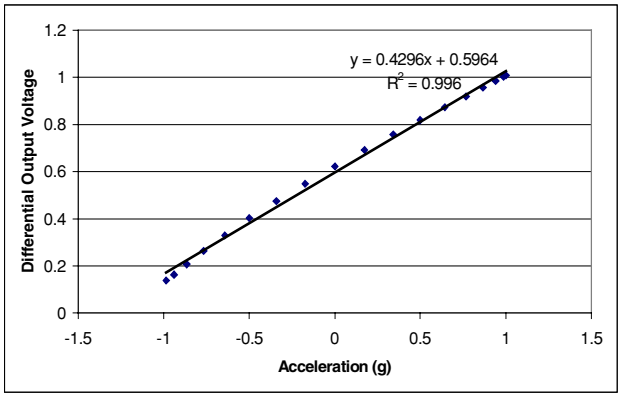

Figure 7*: Measured open loop results for the subsystem with 2x1mm^2 full-bridge type device. Overall sensitivity is 430mV/g.*

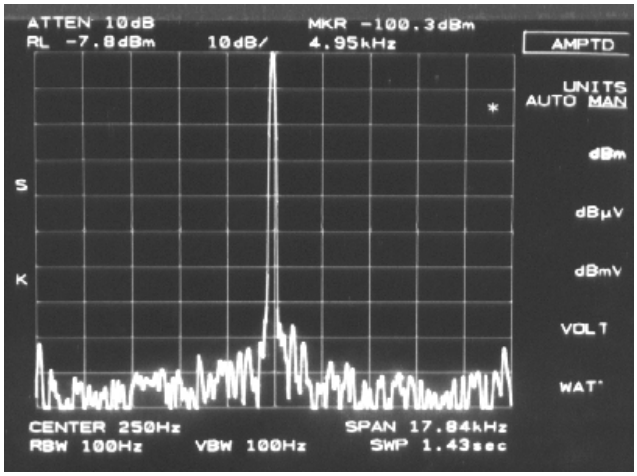

Figure 8: *Noise measurement for the sub system indicating a resolution of 15µg/√Hz.*

Closed-Loop Tests:

Since the interface electronics uses a high oversampling sigma-delta modulation technique, the PWM output bit stream has to be processed to obtain an interpretable signal. This is realized by transferring the digital output to a computer by means of a data acquisition board, and processing the signal (decimating and digital filtering). A sinc^3 filter, FIR filter, decimator and D/A converter have been implemented in MATLAB for this purpose. The closed-loop test setup uses a shaker table, a data acquisition board and LABVIEW and MATLAB programs specifically written for this purpose.

The entire system has been operated closed-loop and the functionality of the system has been verified through extensive tests. Figure 9 shows the decimated PWM digital outputs for (a) pure 1g DC input and (b) 0.25g sinusoidal input acceleration on top of a 1g DC. As the figure shows, the applied input acceleration is recovered successfully. Note that in Fig. 9(a), the only applied acceleration is the 1g gravitational field. The output voltage is constant, except for variations due to noise generated in the system and/or picked up from the environment.

The recorded digital data was signal processed and the Fourier transform of the extracted signal was taken. Figure 10 shows the Fourier transform of the extracted signal for 1g DC bias up to a frequency of 20Hz. As the figure shows, three regions can be identified. Up to a frequency of about 6Hz the noise is slightly less than 100µg/√Hz. From 6Hz to 16 Hz, the noise reduces to about 2µg/√Hz and is constant after that. So, the overall resolution

depends on the bandwidth and the range of frequencies of interest. The reasons for the higher noise at lower frequencies are not known yet.

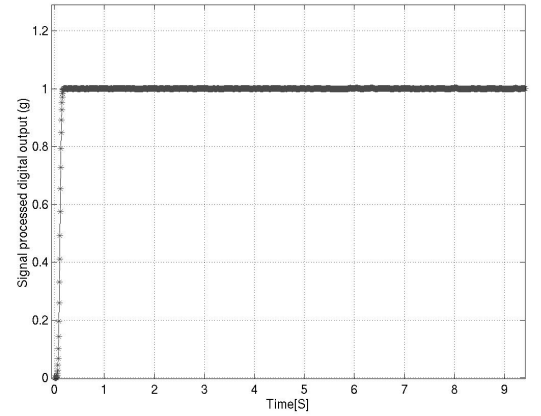

(a)

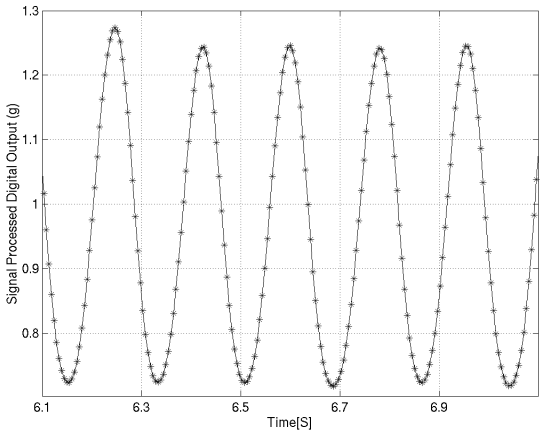

(b)

Figure 9: *Closed-loop measurement results for the hybrid sensor subsystem: (a) for 1g DC input acceleration, (b) for 0.25g sinusoidal input acceleration on top of 1g DC input.*

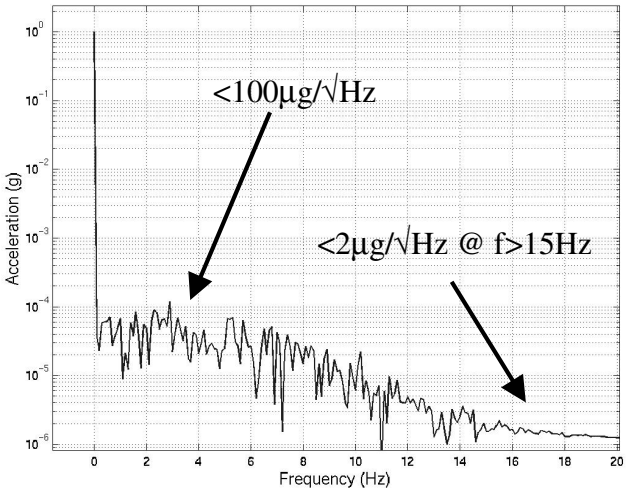

Figure 10: *Closed-loop noise measurement results for 2mm x 1mm bridge structure under 1g DC bias. Notice that the noise floor is less than 100µg/√Hz.*

CONCLUSIONS

A high performance µg accelerometer with high sensitivity, low noise, and closed-loop operation is presented. The accelerometer and the interface electronics operates as a 2nd order electromechanical Σ-Δ modulator. Measured sensitivities are 1.3pF/g and 6pF/g for 2x1mm^2 and 4x1mm^2 doubly supported bridge structures, and 20pF/g for a cantilever-supported structure respectively. The calculated mechanical noise floor for the device is 0.39µg/√Hz at atmosphere. The circuit has a 95dB dynamic range, a low offset of 370µV and can resolve better than 75aF. The complete module has a measured sensitivity of 430 mV/g and a noise floor of 15µg/√Hz in open-loop. The closed loop operation of the system has been achieved for the first time and it has been shown that it results in a resolution better than 100µg/√Hz with a dynamic range of 82dB.

Table 1*. Summary of the circuit/sensor performance*

Sensor Parameters	
Sensitivity	1.3pF/g (2x1mm^2 bridge) 6pF/g (4x1mm^2 bridge) 20pF/g (2x1mm^2 cant.)
Mechanical Noise	0.39µg/√Hz
Interface IC Parameters	
Sampling clock	200kHz
Power dissipation	<6.6mW @ 5V
Capacitance sensitivity	0.3-1.1V/pF (adjustable)
Noise floor	85 µV/√Hz @ 1.1V/pF
Offset	2.7mV (370µV w/ chopper stab.)
Sensor and Interface Module	
Sensitivity	430mV/g
Open-loop resolution	~15µg/√Hz (measured)
Full scale range	±1.2g with 5V supply
Closed-loop MDS	100µg/√Hz

ACKNOWLEDGMENTS

The authors acknowledge the help of Mr. Junseok Chae, Mr. Brendan Casey, Mr. Robert Gordenker, and the staff of WIMS. This work has been supported by DARPA under contract F30602-98-2-0231. Travel support has been provided by the Transducers Research Foundation and by the DARPA MEMS and DARPA BioFlips programs.

REFERENCES

1. N. Yazdi, F. Ayazi, and K. Najafi, "Micromachined Inertial Sensors," *Proc. IEEE,* vol. 86, no. 8, pp. 1640-1659, Aug.1998.
2. N. Yazdi, K. Najafi, "An All-Silicon Single-Wafer Micro-g Accelerometer with a Combined Surface and Bulk Micromachining Process," IEEE/ASME JMEMS, vol. 9, no. 4, pp. 1-8, Dec. 2000.
3. A. Salian, H. Kulah, N.Yazdi, G. He, and K. Najafi, "A High-Performance Hybrid CMOS Microaccelerometer," In Tech. Dig. Solid-State Sensors and Actuators Workshop, Hilton Head Island, SC, USA, pp. 285-288, June 2000.
4. C. Lu, M. Lemkin, and B. Boser, "A monolithic surface micromachined accelerometer with digital output," IEEE J. Solid-State Circuits, vol. 30, no. 12, pp. 1367-1373, Dec. 1995.
5. N. Yazdi and K. Najafi, "An Interface IC for A Capacitive Silicon µg Accelerometer," Tech. Digest, 1999 IEEE ISSCC'99, Feb. 1999.

FINE ZNO PATTERNING WITH CONTROLLED SIDEWALL-ETCH-FRONT SLOPE

Jae Wan Kwon and Eun Sok Kim
Department of EE-Electrophysics, University of Southern California
Los Angeles CA, 90089-0271

ABSTRACT

This paper describes a wet etching technique that solves the major difficulty of fine patterning a c-axis oriented polycrystalline ZnO film. The technique, for the first time, allows the ZnO film to be etched (1) with controlled etch rate ratio between the vertical and horizontal etch rates and (2) with controlled etch-front slope. The ratio between the vertical and horizontal etch rates is as high as 20 to 1, while the angle between the sidewall etch-front surface and the substrate surface can be electrically controlled between 73° and 106°. And ZnO films can now be patterned to fine features (even sub-μm level) by a wet etchant.

INTRODUCTION

Piezoelectric Zinc Oxide (ZnO) is one of most widely used piezoelectric thin films for MEMS, bulk and surface acoustic-wave resonators, acousto-optic devices, etc. [1]. For device miniaturization and/or performance enhancement, fine delineation of a ZnO film to sub-micron level is often needed. However, when a polycrystalline ZnO film is patterned by various acids and bases such as HCl, H_2SO_4, HNO_3, and H_3PO_4, it is well known that the lateral etch rate is at least several times higher than the vertical etch rate, and the etching produces a large undercut as shown in Fig. 1. The extremely high lateral etch rate in the various wet etchants has been a major difficulty for the size reduction and/or performance improvement of ZnO-based microdevices.

In some cases, the etch-front slope of 30 – 40^o downward with respect to the wafer plane (as shown in Fig. 2) has been observed. This peculiar etch-front slope indicates that the lateral etching rate is higher near the ZnO/substrate interface, due to more columnar structure of the ZnO film at the beginning stage of the ZnO film deposition [1].

Among the various etchants for ZnO, 5% ammonium chloride (NH_4Cl) in water at the temperature range of 55°C ~ 60°C is an etchant that does not attack Aluminum, silicon and silicon oxide [2], but produces the large unwanted undercuts as shown in Fig. 1. The etching rate by 5% NH_4Cl is heavily dependent on temperature: particularly, when the etchant temperature is below 20°C, the NH_4Cl hardly etches ZnO. However, with a higher concentration of NH_4Cl in water at a temperature below 20°C and with convective flow of the etchant, we find that we can control the vertical and horizontal etch rates as well as the etch-front slope.

We use two important properties of the NH_4Cl as an etchant for fine ZnO patterning. One is the heavy dependency of the etch rate upon the etchant temperature and the other one is that NH_4Cl is an electrolyte that is capable of producing a galvanizing flux (for batteries, for example). When a direct current is applied to a pair of copper electrodes immersed in aqueous NH_4Cl, water molecules are reduced at the cathode ($2H_2O + 2e^- = H_2 + 2OH^-$), producing H_2 gas that produces convective flow in the etchant.

The newly invented technique for fine ZnO patterning is illustrated in Fig.3. Two copper plates are arranged in parallel, and act as a cathode and an anode for electrical current through 20% NH_4Cl solution in an etching jar whose temperature is kept below

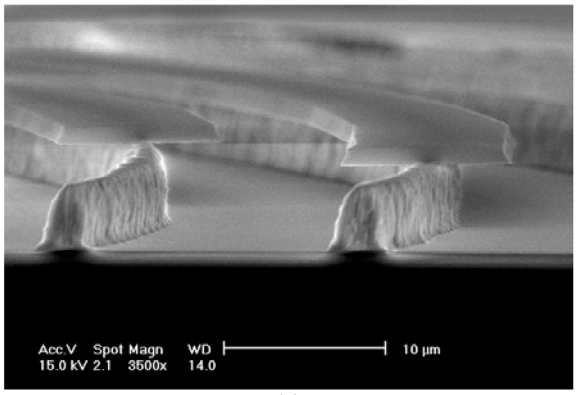

(a)

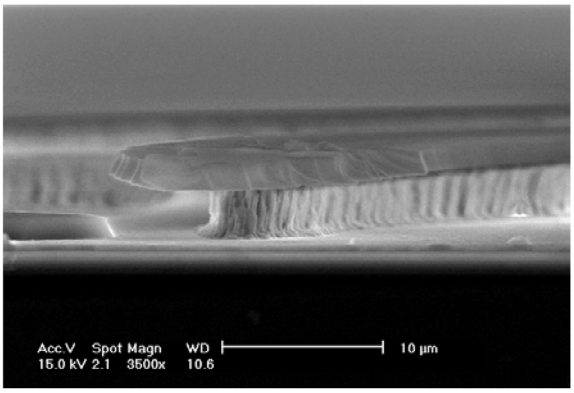

(b)

Figure 1. *SEM pictures showing large lateral undercuts by various etchants: (a) after 16.5 min in NH_4Cl at 55^{o}C, (b) after 3.5 min in CH_3COOH: H_3PO_4: H_2O (1:1:30).*

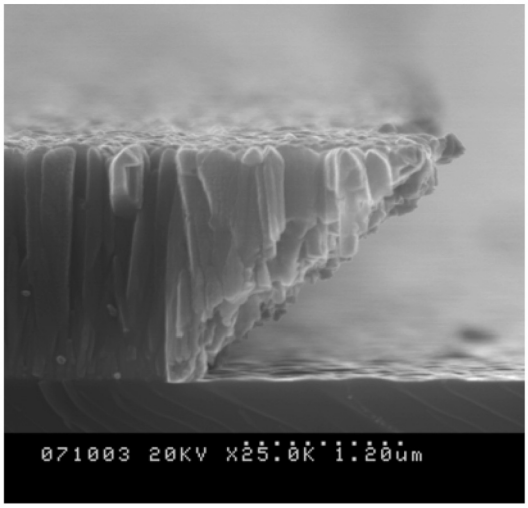

Figure 2. *SEM picture of the etch front of a 2μm thick ZnO on Si_xN_y when etched in the CH_3COOH: H_3PO_4:H_2O (1:1:30).*

0-9640024-4-2/hh2002/$20©2002TRF
DOI 10.31438/trf.hh2002.56

20°C. The etch sample is 5μm thick sputter-deposited, c-axis oriented ZnO film on a SiN coated silicon wafer with patterned photoresist acting as an etch mask, and is attached to the anode copper plate as shown in Fig.3.

EXPERIMENTS AND OBSERVATIONS

Experiment #1

We have tested with small samples (1cm by 1cm) and large samples (3"-diameter wafer). Various current values are applied between the anode and the cathode with a DC potentiometer.

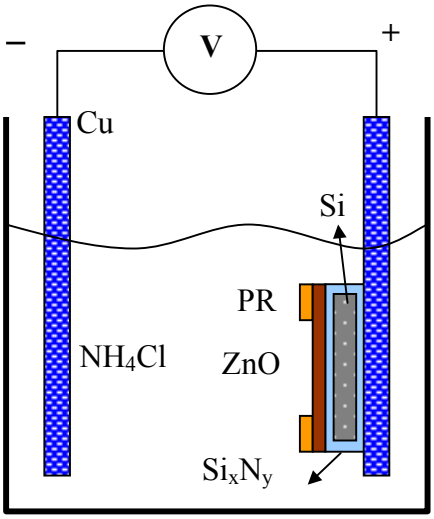

Figure 3. *A newly invented technique to fine pattern ZnO film with negligible lateral undercut and controlled sidewall-etch-front slope.*

We observe that as the etching proceeds, the surface of the cathode copper plate becomes coated with black layer of zinc and copper compound and dark brown precipitates, and also hydrogen gas bubbles form all over the cathode. The electrolyte becomes blue color because of copper ion generated by electrolysis from the cathode.

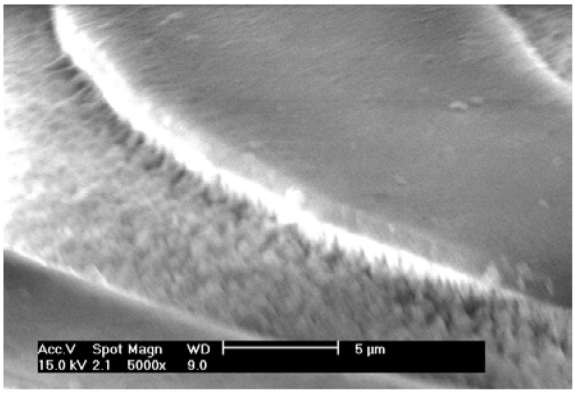

Figure 4. *SEM picture taken after some ZnO etching to show the roughness of the etched ZnO surface, which indicates the directional nature of the etching.*

During the etching process, at the anode, there is a strong chemical reaction in the vertical direction, as shown in Fig. 4, in which we see very rough etch-front on the exposed area compared to photoresist etch mask area. The dominant vertical etching can also be seen very clearly in Fig. 5. Vertically standing pieces of ZnO columnar structure represent that there is very little etching in the lateral direction comparing to the etching in the vertical direction. Figure 6 shows the shape of etch front right beneath the photoresist etch mask after the ZnO etching is done. The etch front is very vertical and perpendicular to the substrate and the corner beneath photoresist is very sharp.

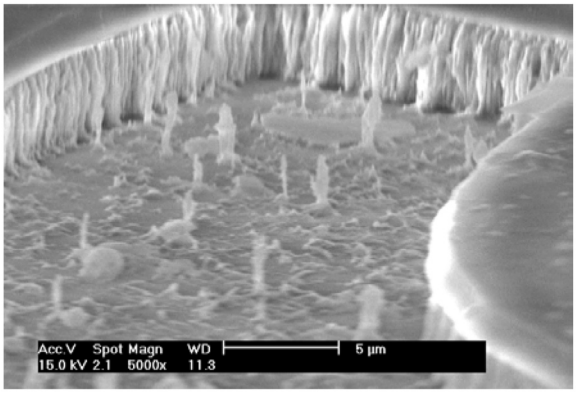

Figure 5. *SEM picture taken near the end of ZnO etching to show vertically standing ZnO pieces: the ZnO sidewall is almost vertical and is hardly etched.*

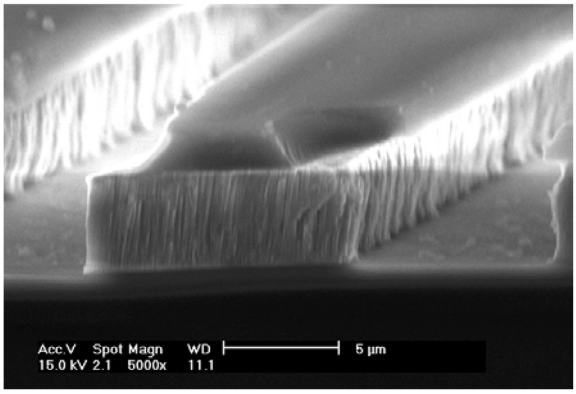

Figure 6. *SEM picture of a patterned ZnO with partially removed photoresist.*

With the new etching technique, we can now control the angle of the etch front (with respect to the substrate surface) from acute angle to obtuse angle by varying the applied current values in the etchant, as shown in Fig. 7. From the cross-sectional views, we see that the slope of the sidewall etch-front can be controlled to a wide range with the applied electrical current. With a low current of 75mA, the etch front is sloped at an acute angle with respect to the substrate surface (Fig. 7a). But when the current is increased to 300mA, the etch-front surface and the substrate surface meet at an obtuse angle (Fig. 7c), similarly to the case shown in Fig. 2. Table 1 summarizes the etching characteristics as a function of the applied current. With the current of 150mA, not only minimum undercut is found, but also the etch-front is straight and perpendicular to the substrate face as shown in Fig. 7b.

This etching technique is very useful not only for fine patterning piezoelectric ZnO films, but also for covering steps of etched ZnO films. For instance, we can intentionally produce a sidewall-etch-front as shown in Fig. 7a (or even more obliquely inclined etch-front) to cover a relatively tall step of ZnO with thin Al film.

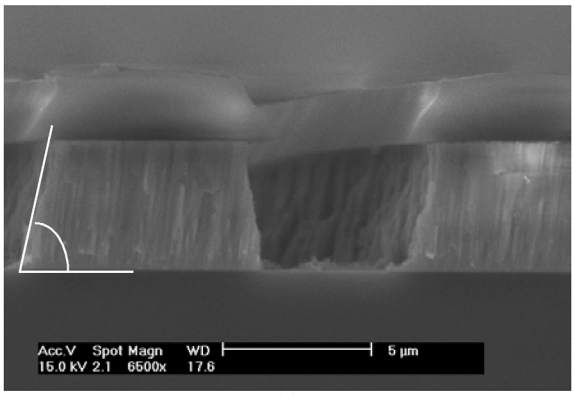

(a)

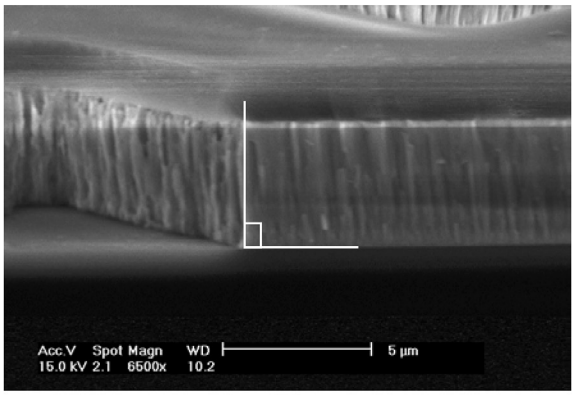

(b)

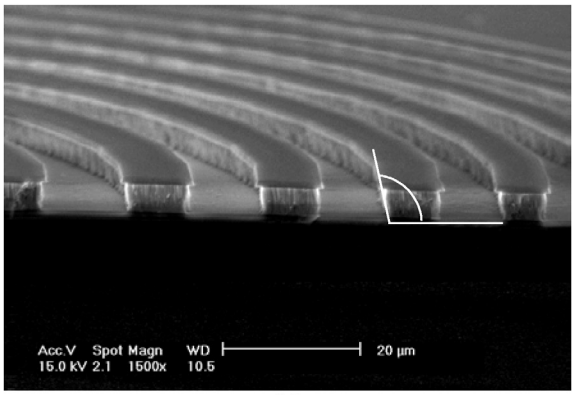

(c)

Figure 7. *SEM pictures showing various sidewall-etch-front angles under various etching conditions (i.e., electrical current between the anode and cathode): (a) 73^o ~78^o at 75 mA (b) 90^o at 150 mA (c) 100^o ~106^o at 300 mA.*

Table 1. *Summary of Etching Characteristics as a Function of Electrical Current Used during Etching.*

Electrical Current During Etching	Lateral Undercut (µm per 5µm vertical etching)	Sidewall-etch-front Slope (degree)	Vertical Etching Rate (µm/min)
75 mA	0.4	73~78	0.19
100 mA	0.3	85~90	0.21
150 mA	0.25	90	0.27
300 mA	0.4	100~106	0.4

To characterize the etching uniformity over a large area, we have tested with a 3-inch wafer in an etching apparatus similar to but larger than the one shown in Fig. 3. The etch sample is again 5µm thick sputter-deposited, c-axis oriented ZnO film on a SiN coated silicon wafer with patterned photoresist acting as an etch mask, and is attached to the anode copper plate similar to Fig.3. Though a larger amount of electrical current (700mA) is applied, after 30 minutes of etching, we observe that the etching uniformity over the large area is not as good as that over the small sample. We notice that the etching rate is significantly higher near the top of the wafer than the bottom, when the wafer is placed vertically up in the etching jar, as illustrated in Fig. 8.

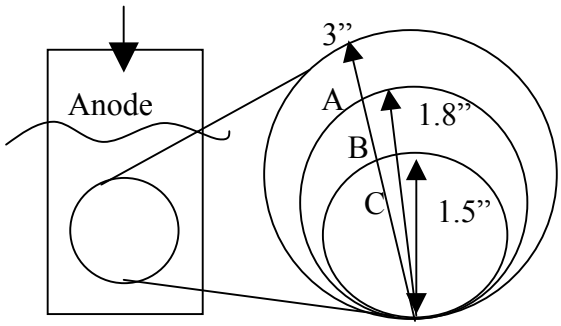

Region A: The 5µm thick ZnO is completely etched.
Region B: About 3 ~ 4.5µm (of the 5 µm) thick ZnO is etched.
Region C: Only about a half of the 5µm thick ZnO is etched.

Figure 8. *Illustration of a 3”wafer sample test for30 minutes in the test setting #1 and of the etching uniformity over the large area.*

To resolve the non-uniformity issue, we coated the whole wafer with gold film, and opened it with square holes for the areas where we wanted the ZnO to etched. This is to ensure that the anode electrical current flows on the wafer surface, and the ratio between the non-conductive etch surface and the conductive anode surface is similar to that for the small sample test condition. We deposited Au film after an adhesion promoter, Cr, on top of ZnO film, and lifted-off the Au film to produce 1cm by 1cm square openings as shown in Fig. 9. The conductive surface was connected electrically to the large anode copper plate. Thus made wafer was supposed to behave a number of small samples arranged and attached on a large anode copper plate.

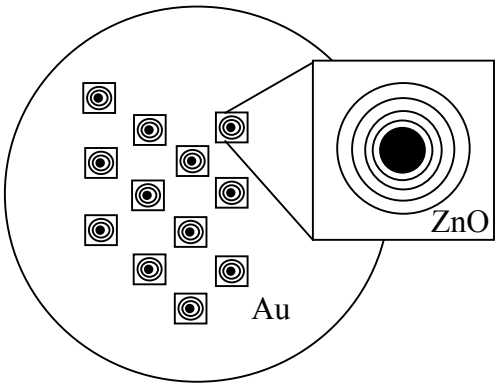

Figure 9. *Illustration of a wafer covered by Au film except the square openings, where a photoresist is patterned into circular annular rings for the ZnO etching test.*

As the ZnO film in the wafer shown in Fig. 9 was etched in the 20% NH_4Cl solution, the Au surface became mottled. In

addition, we observed that not only the color of the ZnO layer changed but also the etch rate became slower, indicating that the Au was reacting slowly in the etchant and ZnO.

Experiment #2

In the large sample test in the experiment #1, we observe that the etching is faster near the top than near the bottom of the wafer (Fig 8). At the same time we notice that there are hydrogen gas bubbles generated near the cathode, which tend to float toward the top portion of the liquid, possibly explaining why the etch rate is different at different vertical levels in the etching jar. Thus, we suspect that the poor etching uniformity over a large sample area is due to a convection flow caused by the movement of the hydrogen gas bubbles (that are electrolytically generated at the cathode).

Hence, we have carried out another experiment as illustrated in Fig. 10, in order to improve the etching uniformity, exploiting the convection flow by the hydrogen gas bubbles. From this experiment, we find that the uniformity is significantly improved on both small and large sample area. In the case of a 3" wafer sample, we now get an etching uniformity of better than 80% over the whole 3" diameter area. The hydrogen gas bubbles are generated very uniformly at the cathode, move upward at a uniform speed, and impinge upon the whole sample area. This moderate floating movement of the gas bubbles generates a convection flow in the etchant, and seems to produce the anisotropic (i.e., vertical-etching dominated) etching characteristic. The number of the gas bubbles depends on the applied current values, and so the magnitude of convection flow can be electrically controlled. With 700mA current, the etch rate (0.47μm/min) with 0.7μm undercut is obtained while the etching proceeds 5μm vertically.

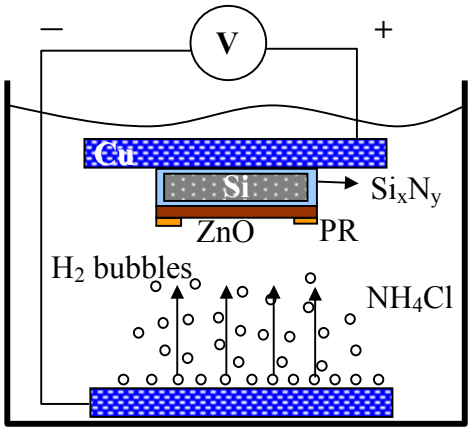

Figure 10. *Illustration of the test setting for exploiting the convective flow of the hydrogen gas bubbles produced at the cathode.*

Experiment #3

To confirm that the vertical-etching-dominated etching characteristic is due to a convection flow of the etchant, we have tested a small sample in the etchant being agitated strongly at various stirring rate. The sample surface faces perpendicularly to the etch flow direction as shown in Fig. 11. At first, the flow speed is set at a similar speed with the convection flow speed in the experiment #2. In this case, the vertical etch rate is about a half that obtained in the experiment #2, but the lateral undercut rate is two times that in the experiment #2. We find that the vertical and lateral etch rates are proportional and inversely proportional to the flow speed, respectively. And with a faster flow speed, we can obtain etch rates similar to the rates in the experiment #2 (both the vertical and lateral etch rates). In the case of a large sample (such as a 3" wafer), a large container and a stirrer would be needed.

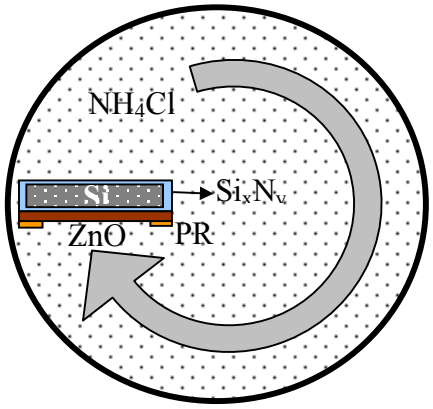

Figure 11. *Illustration of the experiment confirming that the anisotropic etching characteristics by the 20% NH_4Cl solution is due to convective flow of the etchant.*

DISCUSSION

Among all the different experiments described here, the best etching technique for fine patterning of ZnO films is the one used in the experiment #2 (Fig. 10), since it gives best etch uniformity and highest etch rate, and also is easiest to set up. However, with the experiment #2, the gas bubbles tend to stick and grow on the surface of the sample. The ultrasonic agitation has been proven to be helpful in preventing the bubbles from staying on the sample surface. The exact etching mechanism is not yet fully understood, but the anisotropic etching effect in an aqueous NH_4Cl with a convective flow due to electrolytically generated hydrogen gas bubbles has been clearly observed.

CONCLUSION

We have newly developed a wet etching technology for fine patterning of ZnO thin film with controlled etch-front slope. The new technique is very useful not only for fine patterning piezoelectric ZnO films, but also for covering steps of etched ZnO films.

ACKKNOWLEDGEMENTS

This material is based upon work supported by Defense Advanced Research Projects Agency under contract #N66001-00-C-8094 and NSF CAREER Award #ECS00-96092

Travel support has been generously provided by the Transducers Research Foundation and by the DARPA MEMS and DARPA BioFlips programs.

REFERENCES

[1] K.C. Lou, X. Zhu, H. Lakdawala and E.S. Kim, "Study on Etch Front of Piezoelectric ZnO Film and New Step Coverage Technique," IEEE International Ultrasonics Symposium (Toronto, Canada), October 5-8, 1997, pp. 565~568.

[2] S.-C. Chang, D.B. Hicks, and R.C. Laugal, "Pattering of Zinc Oxide Thin Films," IEEE Solid-State Sensor and Actuator Workshop, Hilton Head, SC, June 21-25, 1992. pp. 41 –45.

VERTICAL MICROLENS SCANNER FOR 3D IMAGING

Sunghoon Kwon, Veljko Milanovic,† and Luke P. Lee
Berkeley Sensor and Actuator Center
Department of Bioengineering, University of California, Berkeley, CA 94720
†Adriatic Research Institute, Berkeley, CA 94704-1029

ABSTRACT

We have designed, fabricated, and demonstrated a static vertical microlens scanner with large static displacement and low (<10V) driving voltage, using silicon-on-insulator (SOI) technology. The unique isolated vertical combdrive sets and the coupled-torsion flexure design provides for both upward and downward piston motions and the low driving voltage. Single-directional devices demonstrate maximum static downward displacement of 8 μm at 10 *Vdc* actuation voltage. Bi-directional devices demonstrate vertical actuation from -6.5 μm to +9 μm also at sub-10 *V*. The devices have mechanical resonant frequencies near 400 Hz, and when operated at resonance, a vertical displacement of up to 55 μm peak-to-peak is achieved at up to 7 V_{rms}. The lens motion shows near pure piston motion with very small tilt angle of less than 0.034° and the compensation of the tilt using an isolated comb bank is demonstrated.

INTRODUCTION

Three dimensional (3D) raster scanning of focused light is a basic function for many photonic applications because one can focus light on arbitrary points located in 3D space. A miniaturized 3D raster scanning module with low power and low cost can enable very challenging and exciting optical MEMS applications such as high throughput 3D imaging with array of MEMS microscopes [**1**], retinal displays [**2**], free space optical communication networks with micro motes [**3**], and 3D MEMS memory [**4**]. Advancement of miniaturized optical components provided by optical MEMS is a very promising solution to implement miniaturized, cost effective 3D raster scanning module.

We have been developing miniaturized 3D raster scanning module, which can be fit into 1 mm^3 as a key part of micro confocal imaging array for lab-on-a-chip applications. The diagram for transmissive scanning using three microlens scanner is shown in Fig. 1. High-speed 3D raster scanning of focus can be implemented in shortest optical path only normal to substrate by stacking independent transmissive microlens scanners. While light is passing through each scanner moving in orthogonal direction at different speed, light is steered as well as focused. Successful 2D raster scanning at a focal plan has been demonstrated by stacking of two lateral combdrive actuated microlens [**1**].

However, vertical actuation of microlens is necessary to complete 3D raster scanning by varying effective focal length of whole system. Pure out of plane piston motion of a microlens can control beam divergence, and set the focal plane to desired level without moving sample. Furthermore, importance of vertical microlens actuator is clear when we consider the light emitting and sensing direction of a solid state light source and a detector such as VCSEL and photodiode, and desired hybrid integration between

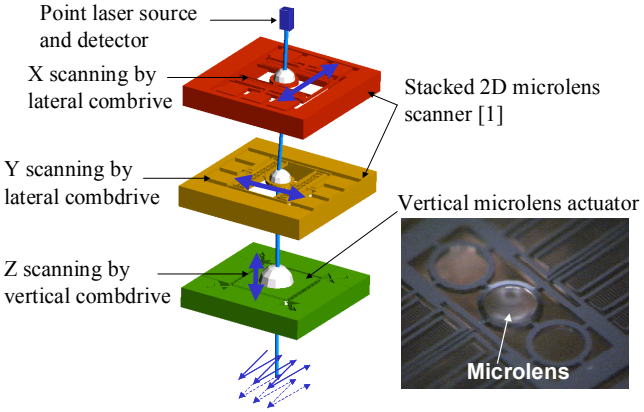

Figure 1. Conceptual diagram of 3D transmissive raster scanner.

silicon MEMS based microoptical components and III/V compound based solid state light sources. Vertical combdrive actuator with limited displacement has been reported using combined bulk and surface micromachining [**5**]. Because the device layer thickness determines the maximum displacement of vertical comb drive, thick device layer such as SOI is favorable to achieve large vertical displacement. However, the trade-off between large displacement and driving voltage limits the performance of such devices due to the high vertical spring constant in high aspect ratio structure.

In this paper, we present the design, fabrication and characterization of SOI vertical actuators with integrated microlenses for 3D imaging application. The features such as large vertical displacement with sub-10 volt actuation via isolated vertical comb banks and a symmetric coupled torsion flexure, and tilting correction capability to pure vertical motion are described with a key enabling multi-level beam SOI-MEMS fabrication technology.

DESIGN CONSIDERATIONS

The desired vertical actuation of microlens for hand-held 3D imaging should meet following important requirements: linear force generation in overall dynamic range for controllability, low power consumption, large static and dynamic vertical displacement for large scanning range, pure piston motion to minimize aberration from lens tilting, and compensation capability for possible lens tilting to minimize optical aberrations. Electrostatic vertical comb drive can meet the first two requirements if it has pre-engagement, [**5**] i.e. some fabricated overlap of upper and lower comb fingers. Vertical comb actuator for our specification should have such pre-engagement for constant force over the range of motion and high aspect ratio for large displacement and optical flatness. Because our 3D imaging application demands at

Contact email address: lplee@socrates.berkeley.edu

This work is funded by DARPA BioFlips program. Travel support has been generously provided by the Transducers Research Foundation and by the DARPA MEMS and DARPA BioFlips programs.

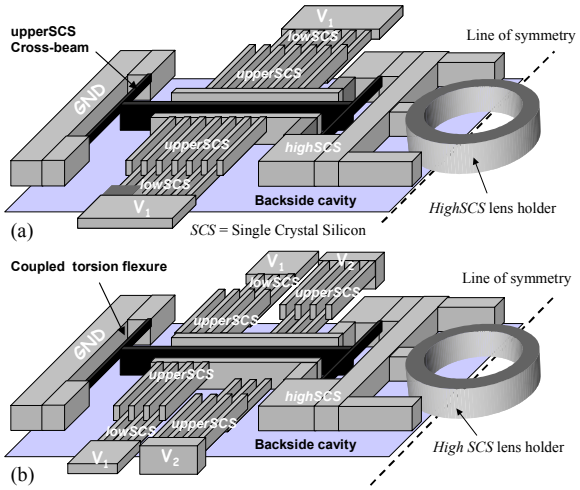

Figure 2. Schematic of one side of the high aspect ratio vertical actuator based on isolated vertical combdrives for : (a) unidirectional, and (b) bi-directional piston motion

minimum 10 μm of static displacement range and comb finger pre-engagement for best control, previously demonstrated vertical comb drives [**2**],[**5**] do not satisfy both requirements. Furthermore, independently controllable comb banks via isolation are favorable to compensate possible lens tilting due to the mismatch from fabrication, and also for the first time to allow actuation both up and down, thereby doubling the total static scanning range. The isolated high aspect ratio vertical comb drive with pre-engagement can be ideal solution for these requirements.

The schematic of one side of the high aspect ratio vertical actuator based on isolated vertical combdrives for unidirectional and bi-directional piston motion is shown in Fig. 2. The devices consist of three major units: isolated comb banks, a symmetric coupled torsion flexure, and a thick lens frame. This is an exact analogy to lateral comb drive actuators so that one can design a vertical combdrive exactly same way as a lateral combdrive. The electrostatic force generated by vertically defined comb drives pull the thick lens holder downward or upward. The two symmetric coupled torsional flexures on both sides of the lens holder transform the torsion of the beam to pure piston motion of the lens.

The isolated comb bank is defined over three different design layers which denote single-crystal-silicon (SCS) beams etched at different vertical levels: *highSCS*, *lowSCS* and *upperSCS* [**6**] as depicted in Fig. 3(a). The *highSCS* layer, the full thickness SOI device-layer beam, is used for rigid structures such as lens holder and connecting beams. The lower comb fingers are defined in the *lowSCS* layer. And compliant torsional flexures and upper comb fingers are defined in the *upperSCS*. *LowSCS* and *upperSCS* layer can have arbitrary thickness due to timed etching. We chose the goal for thickness of both layers to be 3/5 of full device layer thickness, such that there is 1/5 thickness of overlap (for comb finger pre-engagement,) as shown in Fig. 3a. Because all these three different layers are in SOI device layer, the isolation between comb banks is achieved, which leads to independent actuation between comb fingers for bi-directional motion and tilting compensation. In the Fig. 2(b), the schematics shows four isolated combdrive sets with control voltages V_1 ,V_2 . Opposite end of device is controlled by V_3 ,V_4 . Normal upward motion is powered by V_2 ,V_4 while downward motion is powered by V_1 ,V_3 . Tip/tilt compensation is possible with independent control of V_1 - V_4. Applying additional compensation DC voltage to the other side of line of symmetry can compensate the tip/tilt in the line of symmetry axis.

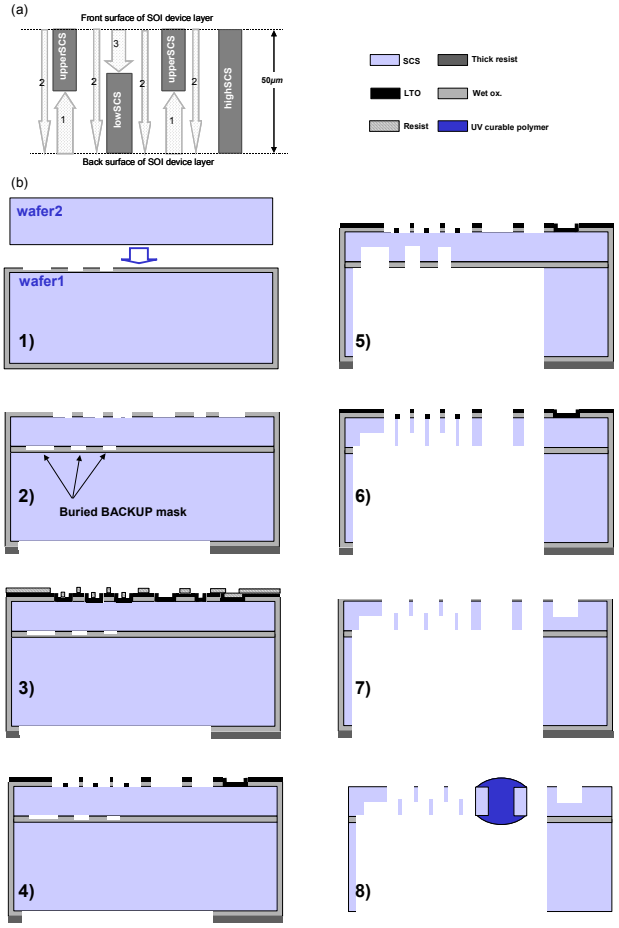

Figure 3. Fabrication process: (a) Conceptual diagram showing order of etching, and (b) detailed fabrication step for masking layer(1-4), etching (5-7), and lens fabrication (8).

The symmetric coupled torsion flexures enables low voltage performance by substituting the difficult out-of-plane bending of high aspect ratio thick beams with more compliant torsion. If we compare the compliance of our coupled torsion flexure with conventional double folded flexures, the coupled torsion flexure can be more than 80 times compliant than the double folded with the same length. The compliance ratio between the conventional bending type and this coupled flexure is a strong function of aspect ratio. As aspect ratio increases the proposed coupled torsion flexure becomes more compliant than the bending type, which makes it attractive in high aspect ratio SOI MEMS. This unique design provides minimum lateral instability and tilting of the lens holder while allowing low-voltage piston motion. And finally the ring shape lens holder is defined in the thick *highSCS* layer for integration of microlenses. The inner and outer diameters of ring shape lens holder are design parameters related with required numerical aperture and entrance pupil size.

FABRICATION

The fabrication process for a vertical microlens scanner is outlined in Fig. 3. The three design layers explained in the previous section are conceptually depicted in Fig. 3(a). In addition to these three layers, the backside of the device was opened to allow an optical window for the microlens, large piston motion, and dry releasing of the device. Such a multilevel beam SOI-MEMS process has been demonstrated for laterally driven torsional micromirror applications [**6**]. In that process the minimum possible pattern size for the *Backup* mask layer (which

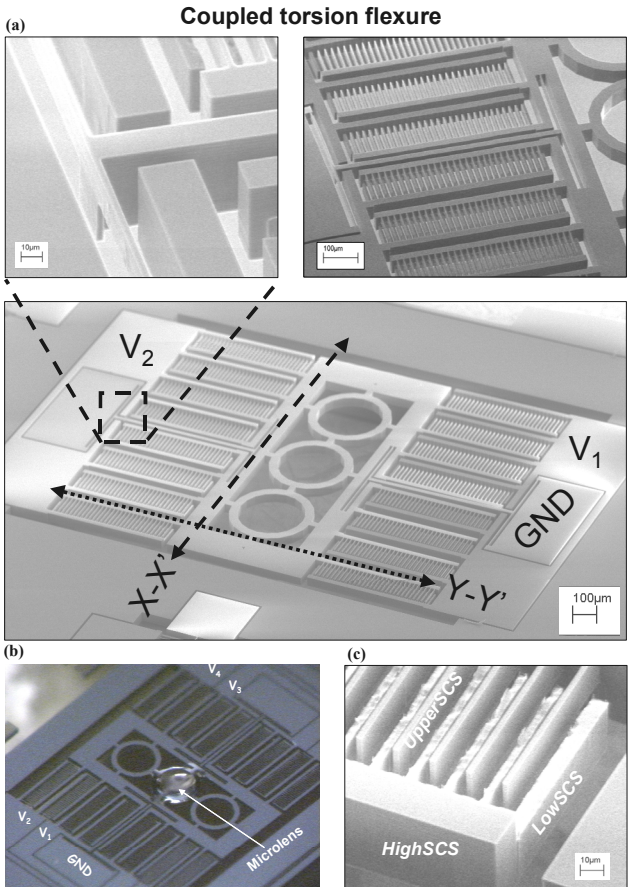

Figure 4. SEM and picture for fabricated vertical microlens scanner: (a) SEM of unidirectional device, (b) Microscopic picture of bi-directional device with polymer lens, (c) self aligned vertical comb fingers.

undercuts device SOI from the backside to create *UpperSCS* beams) was limited to tens of μm because the mask was applied to the SOI wafer backside and mapped to the SOI isolation oxide by a long DRIE. Therefore, it was impossible to place upper and lower beams (here used as upper and lower comb-fingers) within ~20 μm. The advanced version of that process, utilized in this work, performs pre-etching of the backup mask in buried isolation oxide layer during SOI wafer bonding, enables more accurate definition of *upperSCS* features as well as minimum feature distance between various beam types. Namely, in the advanced process, all the critical, beam-defining masks are prepared from the topside using the wafer-stepper for accurate alignment. Another advancement over the previous process is the mask self-alignment, which is critical capability for useful vertical comb-drive based devices. We utilize a single photoresist mask to align both the *upperSCS* and *LowerSCS* etch-defining oxide masks, as shown in Fig. 3(b).

The devices were fabricated in the Berkeley Microlab using Adriatic Research Institute multilevel beam SOI-MEMS technology. The detailed fabrication steps are as follows: 1) 2 μm of thermal oxide is deposited to the first double polished wafer and backup mask is patterned into the oxide layer. Another wafer is thermally bonded and grinded to desired device layer thickness, 50 μm. 2) 1.4 μm of thermal oxide is deposited and the first front side mask for *highSCS* and backside mask for defining optical window and releasing device. This frontside mask is actually bigger than the desired *highSCS* to allow alignment margin to next layer. 3) 600 nm of LTO is deposited and the mask for *lowSCS* and *highSCS* is patterned to resist layer, which means both lower and upper comb fingers are self aligned in same mask [**7**], which prevents the critical alignment step. All pattern size is desired size in this step. 4) LTO and Thermal oxide is etched by same self-align resist mask from 3). Now all masks making step is done. 5) Large backside window for optical window is opened by DRIE, followed by the 20μm thinning of *upperSCS* layer from the backside using buried backup mask. 6) *HighSCS* and *lowSCS* are etched from the front also by DRIE, followed by remaining thin LTO timed etching by RIE. 7) *LowSCS* is thinned by the front side DRIE. The design rule includes the possible lateral etching of *lowSCS*. 8) UV curable polymer droplet is applied to *highSCS* ring shape lens holder and surface tension induces perfect lens shape as previously characterized in [**1**]. Exposure to ultra violet solidifies the polymer droplet on 300 μm lens holder in diameter. The fabricated unidirectional and bi-directional devices are shown in Fig. 4(a) and (b). The X-X' line in the figure matches with the line of symmetry in Fig. 2. The self-aligned vertical comb fingers, which 0.1 μm accurate alignments is accomplished easily using the self-align method, are shown in Fig. 4(c).

RESULTS AND DISCUSSION

Static and dynamic characteristic of the vertical microlens actuator is measured using a laser vibrometer. Figure 5(a) shows the downward static vertical displacement for both unidirectional and bi-directional design. Figure 5(b) shows the upward vertical motion for bi-directional device. The devices have large vertical displacement upto ±10 μm at sub-10V driving voltage. This low voltage actuation is owing to compliant coupled torsion flexure as well as high density vertical comb banks enabled by buried design of the coupled flexure, which allows more area for comb drives. The maximum displacement at 388Hz in resonance was above 50 μm and the scanning range control using linear amplitude modulation is possible as shown in Fig. 5(c). The frequency

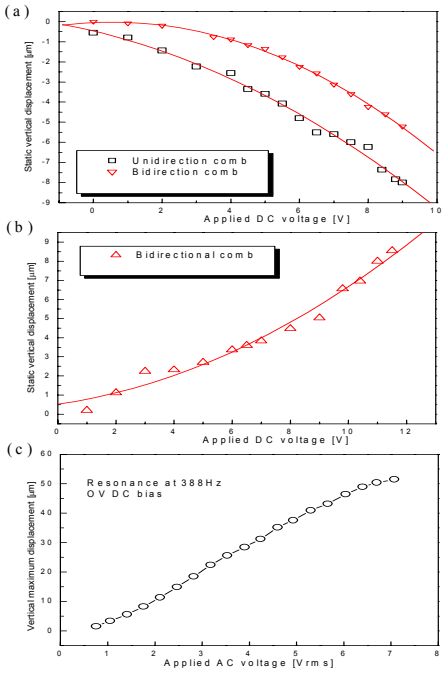

Figure 5. Static and dynamic characterization of the devices: (a) static DOWNWARD vertical deflection of both the single-directional and the bi-directional device, (b) UPWARD vertical deflection of the bi-directional device, and (c) peak-to-peak dynamic deflection at 388 Hz.

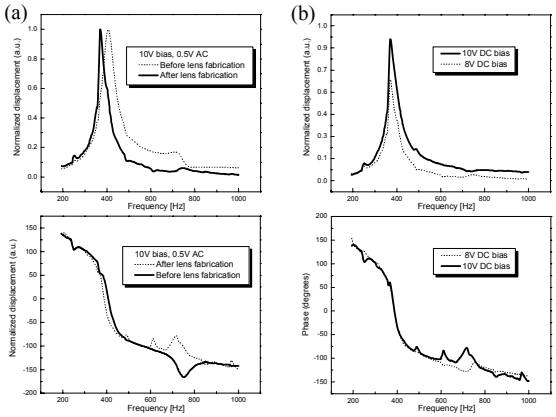

Figure 6. Frequency response of vertical microlens actuator : (a) before and after lens fabrication , and (b) DC bias effect on resonance frequency.

responses for before and after lens fabrication along with DC vias effect are measured using a laser vibrometer and a lock-in amplifier as shown in Fig. 6. Resonance frequency decreased by only 10% by increased mass from lens. Also the DC bias effect on resonance frequency was less than 5% if we compare the frequency response for 10V and 8V DC bias.

The tilting of lens plate during the actuation is measured for estimating possible degree of optical aberration using interferometric profiler. The measured tilt of X-X' axis and Y-Y' axis denoted in Fig. 7(a) is shown in Fig. 7(a). Basically the device has maximum tilting of 0.034° during piston motion in Y-Y' axis, and X-X' axis has one tenth of tilting compared with Y-Y'axis. This small tilting angle is negligible for most of applications, however, the compensation to zero tilt is also possible by using

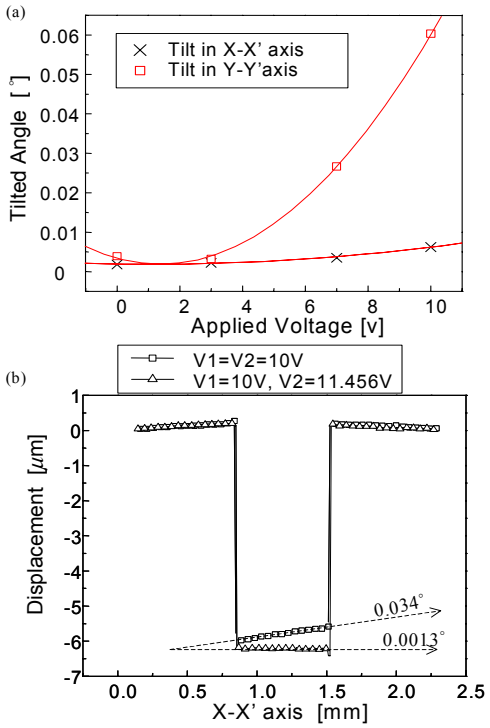

Figure 7. Tilt compensation experiment result showing: (a) Tilt of lens plate for symmetric driving voltage, and (b) tilt compensation by asysmetric driving voltage. Tilt reduced from 0.034° *to* 0.0013° *after compensation.*

asymmetric driving using featured isolated comb banks. To demonstrate the compensation capability using our isolated comb bank, which is one of the major advantage of our process, we tried to compensate the X-X' axis tilting by applying asymmetric voltage to either side of line of symmetric. In other word, by applying asymmetric voltage to V_1, and V_2 indicated in Fig. 4(a). The compensation result is shown in Fig. 7(b) by acquiring profile along with Y-Y'axis. The rectangle profile is symmetric actuation with 10V and the tilt of lens frame was 0.034°. The tilt is compensated to 0.0013° using asymmetric actuation voltages of 10 V and 11.456 V in either side of isolated comb banks, which are the electrodes V1 and V2, respectively. Theoretically, the perfect tilting compensation is possible using this technique.

CONCLUSIONS

We have demonstrated low voltage and large static displacement vertical actuators with integrated microlenses on high aspect ratio silicon-on-insulator (SOI). Due to the coupled torsion flexure and isolated vertical comb banks, low voltage pure vertical piston motion of microlens is demonstrated. The developed device is not only key part for our continueing effort for micro confocal microscope array but also attractive to hybrid integration of photonic devices.

REFERENCES

1. S. Kwon, and L. Lee, "Stacked Two Dimensional Microlens Scanner for Micro Confocal Imaging Array", *15th Annual IEEE International MEMS 2002 Conference*, 1/20-24/02, Las Vegas (2002), pp 483-486.

2. R. Conant, J. Nee, K. Lau, and R. Muller, "A Flat High-Frequency Scanning Micromirror," ", *Technical Digest of the 2000 Solid-State Sensor and Actuator Workshop*, Hilton Head Isl., SC, 6/4- 6/8, Transducer Research Foundation, Cleveland (2000)

3. B. Warneke, M. Last, K. Liebowits, and K.S.J. Pister, "Smart Dust: Communicating with a Cubic-Millimeter Computer", Compueter Magazine, January 2001, pp.44-51.

4. Y. Kawata, **"**Three-dimensional Memory", *Proceedings of the SPIE - The International Society for Optical Engineering*, vol.4081, SPIE-Int. Soc. Opt. Eng, 2000. p.76-85.

5. Yeh, J.-L. A., Hui, C.-Y., and Tien, N. C., "Electrostatic Model for an Asymmetric Vertical Combdrive*"*, *Journal of Microelectromechanical systems*, Vol. 9, No. 1, Mar. 2000.

6. V. Milanovic, M. Last, and K.J.S. Pister, "Torsional Micromirrors with Lateral Actuators", *Transducers'01 – Erosensors XV conference*, Muenchen, Germany, Jun. 2001.

7. U. Krishnamoorthy, O. Solgaard, "Self-Aligned Vertical Comb-drive Actuators for Optical Scanning Micromirrors," *Optical MEMS'01*, Okinawa, Japan, Sep. 2001.

HIGH-FREQUENCY ACTUATION WITH SILICON ELECTROOSMOTIC MICROPUMPS

Daniel J. Laser, Kenneth E. Goodson, Juan G. Santiago, and Thomas W. Kenny
Department of Mechanical Engineering, Stanford University
Stanford, California 94305

ABSTRACT

Electroosmotic micropumps manufactured on silicon substrates using standard micromachining processes can generate pressures of 6 kPa and flow rates of 13 µL/min at 400 V. We present a novel micromachined silicon electroosmotic micropump structure that dramatically reduces die size requirements. We have investigated the prospects for using electroosmotic micropumps in microscale fluidic actuation by integrating a silicon membrane structure into the pump system. By monitoring the velocity of the membrane using a laser vibrometer, we have characterized the micropump's pressure response on timescales below 100 milliseconds. The silicon electrosmotic micropumps studied are found to have a finite pressure response within 10 ms of power activation. Maximum pressure generation, however, appears to take place on a much longer timescale.

INTRODUCTION

Low-voltage electroosmotic micropumps can be fabricated using silicon micromachining in a relatively straightforward manner. The ready integration of micromachined silicon electroosmotic micropumps with other micromachined components makes microactuation a potential application of these micropumps.

Actuator response time is a critical figure of merit for microscale device actuation applications. For micromachined electrostatic comb drive actuators, this response time is generally limited by inertia and is on the order of 1 millisecond or less **[1,2]**. In contrast, the response time of a fluidic actuator can be limited by a wide range of factors, including the inertia of the fluid, the finite velocity with which a pressure wave propagates through the fluid medium, and, for devices that rely on electric-field-mediated pumps such as electroosmotic pumps, electrochemical effects. In microfluidic actuators, gas bubbles in the fluid and mechanical compliance of fixturing and tubing are a source of volume capacitance that can reduce response time.

To evaluate the usefulness of silicon electroosmotic micropumps for microactuation, we have fabricated very simple microactuators with integrated electroosmotic micropumps. The actuated component is a circular silicon nitride membrane located at the center of an annular electroosmotic micropump, as shown in Figure 1. The design of this device is intended to minimize the impact on response time of finite pressure wave propagation velocity, system volume capacitance, and the membrane's mechanical properties. The system can therefore be used to determine the lower limit on the response time of a microactuator driven by the annular electrosmotic micropump.

ELECTROKINETICS AND ELECTROOSMOTIC FLOW

Electroosmotic pumps generate fluid flow and pressure through the application of an electrical potential across a stationary, fluid-filled structure (Figure 2). They are among a family of devices that take advantage of the electric double layer that typically forms at a liquid-solid interface **[3]**. Structures used for electroosmotic pumping must have pore-like features within a few orders of magnitude of the size of the electric double layer, which is generally less than a micron. Electrosmotic pumps made from sintered glass frits have been reported that generate pressures of 250 kPa and flow rates of 7 mL/min **[4]**.

SILICON ELECTROOSMOTIC MICROPUMP DESIGN AND PERFORMANCE

Channels with the micron-scale dimensions appropriate for electroosmotic pumping may be readily fabricated using silicon micromachining, but the silicon substrate limits the electrical potential that can be applied during pump operation to approximately 500 V, even with thin-film insulation **[5]**. Burgreen and Nakache found that the average velocity of electroosmotic flow generated between two wide parallel surfaces by the application of an axial electric field E_x is:

$$\bar{v} = -\frac{h^2}{3\mu}\frac{dp}{dx} + \frac{\varepsilon\zeta}{\mu}E_x\left[1 - G(\alpha, \kappa h)\right]$$

where h is one-half the separation distance between the two pumping surfaces, μ is the fluid viscosity, dp/dx is the pressure gradient counter to the flow, ε is the fluid permittivity, ζ is the zeta potential, α is an ionic energy parameter, and G is a correction term for the thickness of the double layer **[6]**. Electroosmotic pumps made by etching a 5 cm wide, 1.5 µm deep, 500 µm long channel in a silicon substrate, coating the substrate with silicon nitride, and sealing with an anodically bonded borosilicate glass cover generate pressures of 2 kPa and flow rates of 5 µL/min at 500 volts **[7, 8]**, compared to 150 kPa and 15 µL/min for a glass micropump with a similar design operating at 3 kV **[9]**. The difference in the performance of these pumps is attributable to the different zeta potentials of silicon nitride and glass as well as to the difference in applied voltage. Both pumps occupy an area of approximately 5 cm^2 on the substrate, including the etched channels required to transport fluid to and from the pumping channel.

To improve the flow rate generated by the silicon electroosmotic micropump relative to its size, we plasma etch 3 µm wide slots in the silicon substrate to a depth of approximately 100 µm. Subsequent conformal deposition of approximately 0.65 µm of silicon nitride reduces the slot width to 1.7 µm. Spacing the slots every 10 µm yields a 20x improvement in flow area per unit substrate surface area over the previous design. By arranging the 360 slots in an annular configuration as shown in Figures 1(a) and (b), we have produced a micropump with a flow area of approximately 7.2 x 10^4 μm^2 that fits on a 1 cm x 2 cm die. Fabrication of the micropump is completed by anodically bonding a Pyrex 7740 wafer to the top side of the silicon wafer by applying

0-9640024-4-2/hh2002/$20©2002TRF
DOI 10.31438/trf.hh2002.58

Solid-State Sensors, Actuators, and Microsystems Workshop
Hilton Head Island, South Carolina, June 2-6, 2002

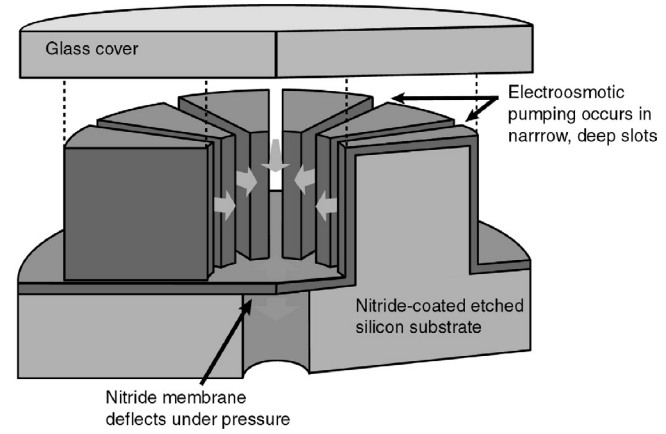

(a)

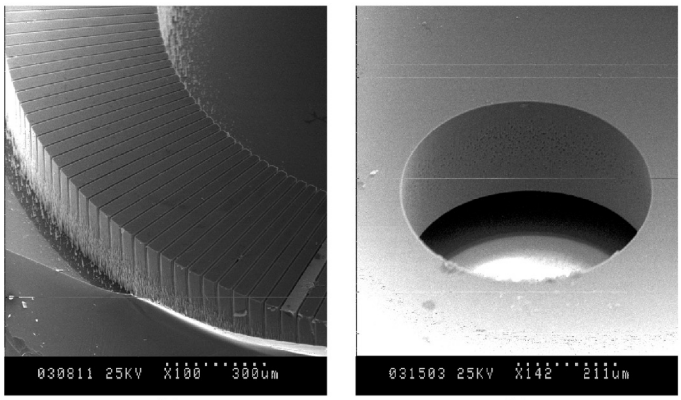

(b) (c)

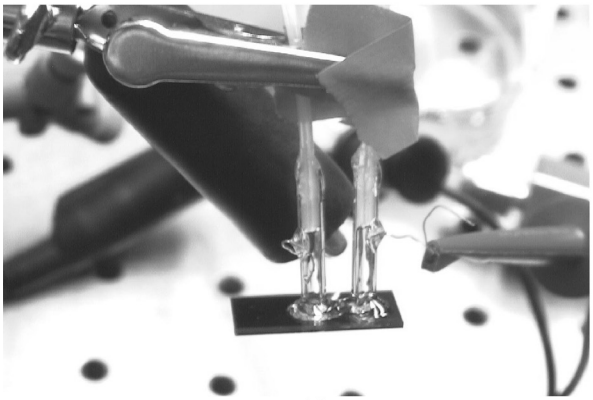

(d)

Figure 1. *Structure of microactuator with integrated electoosmotic micropump. (a) Section perspective illustration. The pump structure is defined by a deep-etched circular interior well and a concentric deep-etched annular well. Narrow slots etched radially in the pump structure connect the inner well and the outer annulus. A layer of silicon nitride insulates the surfaces of the inner well, outer annulus, and slots and forms the membrane. (b) Electron micrograph of the top side of the silicon substrate showing a portion of etched annular pump structure. Although the interior well, exterior well, and slots are all etched simultaneously, the slots etch to a lesser depth because of the feature size dependency of the DRIE process. (c) Electron micrograph of the back side of the silicon showing the released circular membrane at the bottom of the etched cavity. (d) Microactuator with external tubing attached for fluid and electrical connections. Holes drilled in the borosilicate glass cover provide access to the interior. The microactuator measures 1 cm x 2 cm x 1mm.*

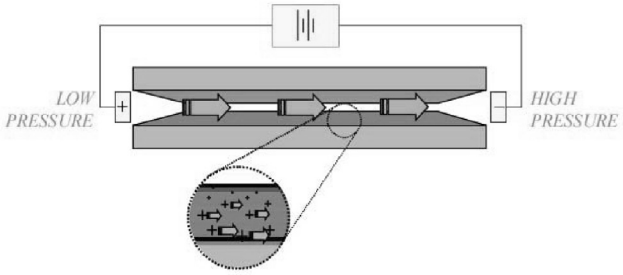

Figure 2. *Electroosmotic flow between closely-spaced, flat, parallel surfaces. An externally-applied electric field acts on mobile ions near the surfaces. Viscous interaction generates flow of the bulk liquid.*

a potential difference of 1200 volts across the two wafers for 30 minutes at 350°C. The devices are then diced and access holes drilled in the glass cover using a diamond-tipped drill bit. Fluid and electrical connections are made through 2 cm glass capillary segments attached to the micropump using UV-cured epoxy. This micropump generates a maximum pressure of 6 kPa and a maximum flow rate of 13 µL/min at 400 V. Power consumption is less than 150 mW. The pressure-flow rate characteristics of the pump, found by measuring compression of room air in a closed capillary, are plotted in Figure 3. The margin of error with this measurement technique is approximately +/- 0.25 kPa.

MICROACTUATOR DESIGN, FABRICATION, AND TESTING

The annular electroosmotic pump described above is converted to an actuator by releasing a circular area of the silicon nitride coating at the center of the interior well using a backside plasma etch, as shown in Figures 1(a) and (c). Devices with membrane diameters of 250 µm and 500 µm have been fabricated. A 300 angstrom layer of gold with a 50 angstrom chrome adhesion layer is evaporatively deposited on the back side of each die to increase the reflectivity of the nitride membrane. The yield of the

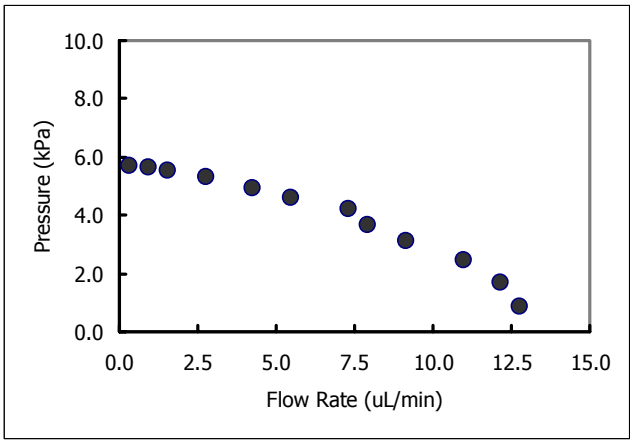

Figure 3. *Pressure/flow rate performance of silicon electroosmotic micropump with 360 2 µm wide slots in an annular configuration. Working fluid is 0.5 mM borate buffer and applied potential is 400 V.*

microactuator fabrication process is approximately 75%, with the lost yield mostly due to exposure issues with thick resist lithography.

The velocity of the membrane during operation is monitored using a laser vibrometer **[10]**. Pump current is monitored during testing using a series reference resistor. Data is collected using a 1.5 GHz digital oscilloscope. The use of the vibrometer to conduct measurements of membrane velocity—where the membrane is within a millimeter of each of the radially-arrayed pump slots micropump—affords a unique capability for resolving the high-speed temporal response of the microactuator (and, in turn, of the micropump). We found that noise limited the vibrometer's velocity resolution to a few hundred nanometers per second during microactuator testing. A finite element model indicates that applying a 6 kPa differential pressure—the maximum generated by the electroosmotic micropump at 400 V—will result in a steady-state maximum membrane displacement of over 1 µm for the 250 µm diameter membrane and over 6 µm for the 500 µm membrane. In our experience, a portion of the steady-state pressure developed by electroosmotic micropumps arises on a timescale of hundreds of seconds. Such response times are associated with membrane velocities of 10 nm/sec or less—velocities below the resolution limit of the vibrometer in our setup. Because of this limitation, the work presented here addresses only the fast (<100 millisecond) transient response of the microactuator.

A further limitation on the accuracy of our measurements is imposed by vibrometer laser focusing and alignment issues. The velocity measured by the vibrometer is the average velocity of the region of the membrane illuminated by the laser—a circular area with a diameter of approximately 20 µm. Using a micrometer stage, we are able to focus the laser within an estimated 25 µm of the center of the membrane. The finite spot size of the laser and potential misalignment of the laser with the center of the membrane can be expected to result in underestimation of the membrane maximum displacement by as much as 20%.

EXPERIMENTAL RESULTS AND ANALYSIS

The microactuators were tested by applying a 400 V_{p-p} sinusoidal input with a 200 V offset to the pump at frequencies

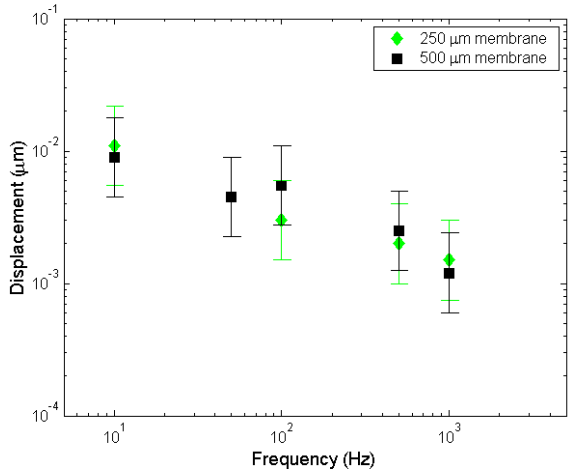

Figure 4. *Membrane displacement amplitude for a 400 V_{p-p} sine wave input (200 V offset) applied to the electroosmotic micropump. Data reflects the average amplitude measured over at least 256 cycles.*

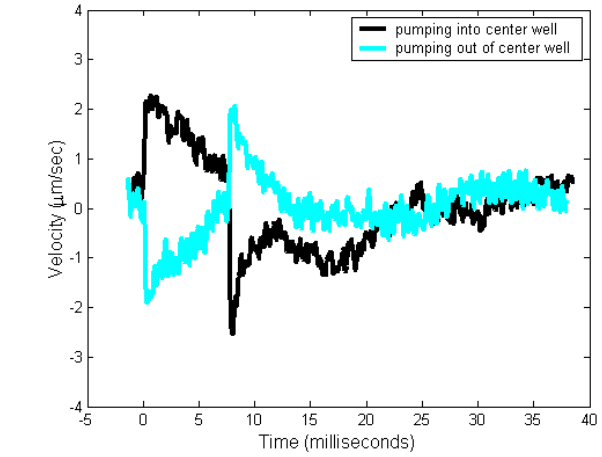

(a)

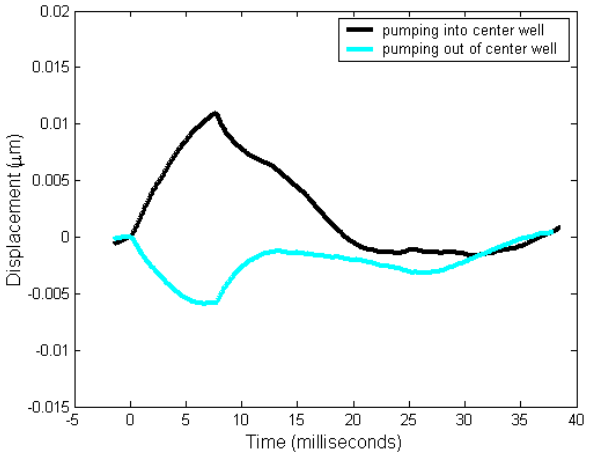

(b)

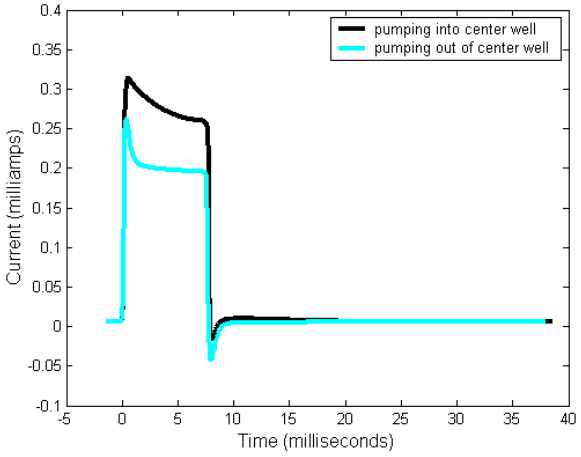

(c)

Figure 5. *Bidirectional response of a 500 µm microactuator to a 25 Hz, 400 volt square-wave input with a duty cycle of 20%. Data is averaged over 1,280 cycles. Plots show (a) membrane velocity; (b) membrane displacement (found by integrating velocity), and (c) current through the micropump. Positive velocities and displacements correspond to outward deflection of the membrane.*

ranging from 10 Hz to 1 kHz. At each frequency, data for at least 256 cycles was acquired and averaged to reduce noise in the measurement. Displacement data was calculated by integrating the velocity measured by the vibrometer. The measured velocity represents the average velocity of the portion of the membrane area illuminated by the vibrometer. Membrane displacement amplitude is plotted as a function of frequency in Figure 4.

Figure 5 shows the response of a 500 μm diameter actuator to a 25 Hz square wave input with a 20% duty cycle at 400 volts. This test was performed for both pumping into the center well (causing the membrane to deflect outward) and out of the center well (causing the membrane to deflect inward). Data was accumulated over 1,280 cycles to reduce noise. The response is qualitatively the same in both directions, although the magnitude of the membrane's outward deflection is larger than its inward deflection.

The measured frequency response and partial step response indicate that electroosmotic microactuators operated closed-loop could be used for applications requiring frequency response into the kilohertz range. The membrane appears to reach only a small fraction of its steady-state displacement in the first eight milliseconds after the voltage is turned on, however, suggesting that the open-loop bandwidth of the device is below 10 Hz. Finite element analysis indicates that the first resonant frequencies of both the 250 μm and the 500 μm membranes are above 100 kHz, so the microactuator response is not believed to be limited by the membrane dynamics. The relatively long timescale apparently required for the pressure generated by the electroosmotic pump to reach its maximum value has been observed in other studies of electroosmotic pumping **[11]** and is not well understood at this time. Fixturing and tubing leading from the actuator to an external valve may be a source of volume capacitance in the microactuator; as currently designed, the microactuator can not be sealed off directly at the die level because of the need to purge electrolytic gas bubbles between experiments. Gas bubbles in the liquid may also be a source of volume capacitance. Gas bubbles arise not only from electrolysis at the electrodes, but also from degassing (e.g., due to increased temperature which reduces solubility) and, in extreme cases, boiling in or near the pump structure. This may be particularly prominent in zero-net-flow conditions that prevent convective transport of heat out of the pump structure.

CONCLUSIONS

Micromachined silicon electroosmotic pumps combine the reliability and effectiveness of electroosmotic pumping with the ease of fabrication and ready integration with other micromachined components afforded by silicon micromachining. We have successfully fabricated a simple microactuator driven by an integrated electroosmotic micropump. Tests of the microactuator suggest that electroosmotic micropumps might be suitable for use in applications requiring actuator bandwidth as high as 1 kHz, although operation at lower frequencies may be required to produce a quasi-static microactuator response.

REFERENCES

1. W.C. Tang, T.C.H. Nguyen, and R.T. Howe, "Laterally Driven Polysilicon Resonant Microstructures," *Sensors and Actuators*, 20, (1989), pp. 25-32.

2. J.D. Grade, H. Jerman, and T.W. Kenny, "A Large-Deflection Electrostatic Actuator for Optical Switching Applications," *Technical Digest of the 2000 Solid-State Sensor and Actuator Workshop*, Hilton Head Isl., SC, Transducer Research Foundation, Cleveland (1994), pp. 97-100.

3. R. J. Hunter, Zeta Potential in Colloid Science, Academic Press, Inc., San Diego (1981).

4. S. Yao, D.E. Huber, J. Mikkelsen, Jr., and J.G. Santiago, "A Large Flowrate Electrokinetic Pump with Micron Pores," *Proceedings of the 2001 ASME International Mechanical Engineering Congress and Exposition*, New York, NY, November 11-16, 2001.

5. D. J. Harrison, P. G. Glavina, and A. Manz, "Towards Minitaturized Electrophoresis and Chemical Analysis Systems on Silicon: An Alternative to Chemical Sensors," *Sensors and Actuators B*, 10 (1993), pp. 107-116.

6. D. Burgreeen and F. R. Nakache, "Electrokinetic Flow in Ultrafine Capillary Slits," *J. Phys. Chemistry* 68, 5 (1964), pp. 1084-1091.

7. D. Laser, S. Yao, C. Chen, J. Mikkelson, K. Goodson, J. Santiago, and T. Kenny, "A Micromachined Low-Voltage Silicon Parallel-Plate Electrokinetic Pump," *Proceedings of the 11th International Conference on Solid-State Sensors and Actuators (Transducers '01),* Munich, Germany (2001).

8. D.J. Laser, K.E. Goodson, J.G. Santiago, and T.W. Kenny, "Impact of Pumping Surface Separation Distance on Micromachined Silicon Electroosmotic Pump Performance," *Proceedings of the 2001 ASME International Mechanical Engineering Congress and Exposition*, New York, NY (2001).

9. C. Chen, S. Zeng, J. Mikkelsen, and J. Santiago, "Development of a Planar Electrokinetic Micropump," *Proceedings of the 2000 ASME International Mechanical Engineering Congress and Exposition*, Orlando, Florida (2000).

10. Polytec OFV 502 fiber interferometer with an OFV 3001 vibrometer controller, Polytec PI, Inc., Tustin, California.

[11] S. Yao, S. Zeng, and J.G. Santiago, "Transient Performance and Load-Change Response of Porous Glass Electroosmotic Pumps," submitted to the 2002 ASME International Mechanical Engineering Congress and Exposition, New Orleans, LA.

CHEMICAL AND BIOLOGICAL DIAGNOSTICS USING FULLY INSULATED ULTRACOMPLIANT THERMAL PROBES

M.-H. Li[1], J.-H. Lee[1], F. Cerrina[1], A.K. Menon[2], and Y. B. Gianchandani[1,3]
[1]Department of Electrical and Computer Engineering, University of Wisconsin, Madison, WI 53706
[2]Department of Biochemistry, University of Wisconsin, Madison, WI 53706
[3]EECS Department, University of Michigan, Ann Arbor, MI 48109

ABSTRACT

This paper reports on the detection of nano-scale chemical variations in photosensitive polymers and biological variations in ovarian cancerous tumor cells that have been accomplished for the first time using scanning thermal probes that we have developed. A probe of 250 µm length, 50 µm width, and 3 µm thickness has a measured spring constant of 0.082 N/m. Lateral spatial resolution of <50 nm, topographic resolution of <1 nm and thermal resolution of <1.2 mK are demonstrated. Wet scanning capability, which widens the possibility of biochemical applications, is also demonstrated for the first time. The structure, fabrication, and assembly of the probe and the interface circuit used for these experiments are described.

I. INTRODUCTION

We are developing ultra compliant thermal probes for critical applications in ULSI lithography research. These include, specifically, mapping the latent image of exposed but undeveloped photoresist (PR) to measure photo-acid generation and diffusion independently from the developing step [1]. Thermal probes have also been used for data storage and other applications [2,3]. Since they offer sub-surface mapping capability, thermal probes also facilitate studies of intra-cellular features in bio-related research. To fulfill our need for these applications, probes must have low spring constant to prevent damaging the soft materials, and provide spatial resolution <100 nm. In addition, to permit scanning in aqueous environments, complete electrical insulation is necessary. Wet aqueous scans are particularly challenging because of enhanced parasitic thermal losses, the need for complete electrical insulation, and the impact of surface tension on the ultra compliant probes. These requirements can not be fulfilled by using the commercially available wire probe which is made of bent bare wires, and has a high spring constant (5 N/m), limited spatial resolution, and no particular isolation [4].

We have previously reported thermocouple or bolometer probes fabricated by 6-7 mask surface micromachining processes using polyimide as the shank material, and the application of these probes for temperature mapping, sub-surface imaging, and the measurement of glass transition temperature in photoresists [5,6]. This paper reports on applying these probes to ULSI lithography research, particularly for mapping the latent image of exposed but undeveloped PR to measure photo-acid generation (PAG) and diffusion independently. Wet scanning capability, which widens the possibility of biochemical applications, is also demonstrated for the first time. This paper also describes changes that have been made to older versions of this probe to help achieve these capabilities.

II. FABRICATION

The basic structure of the probe is similar to that reported in [5,6], with a thin film bolometer sandwiched between two layers of polyimide, forming a cantilever. At one end of the cantilever the metal thin film protrudes through an opening in lower polyimide layer, where it is molded into a pyramidal tip by a notch that was anisotropically wet-etched into the substrate. The tip and a portion of the probe shank are then released from the substrate by etching an underlying sacrificial layer. The released length is then folded over to extend past the die edge for clearance and held in place by an adhesive (Fig. 1). Typical dimensions of the probes after assembly are 250 µm length, 50 µm width, and 3 µm thickness with Cr/Au (200/2000 Å) for the tip and lead, which provides bolometer resistance about 60 Ω.

The present manifestation of the probe (Fig. 2) differs from the ones reported in the past [5,6] in important ways. It includes a thin film of gold (Cr/Au: 200/4000 Å) which holds the flipped over probe by a thermocompression bond. This method retains the flatness of the probe and significantly increases yield. This layer also serves as a mirror to permit simultaneous operation of the probe as an AFM. The revised process also provides a tip diameter of about 50 nm by sharpening the notch used as its mold by non-uniform oxide growth [7]. For operation in aqueous environments, the bond pads and bond wires are covered with a thin layer of polyimide (PI2613™), leaving the scanning tip as the only exposed metallic surface (Fig. 3).

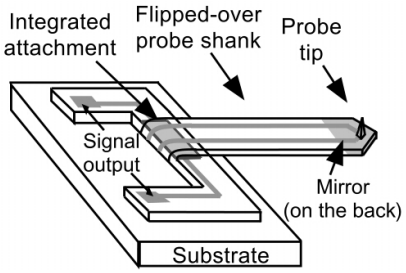

Fig. 1: Schematic of the ultracompliant polyimide thermal probe.

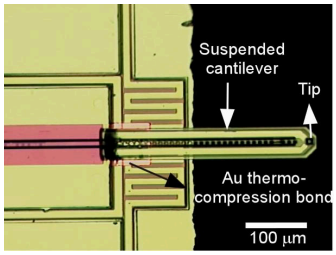

Fig. 2: A 250 µm long probe flipped over the die edge and held down with a gold thermocompression bond.

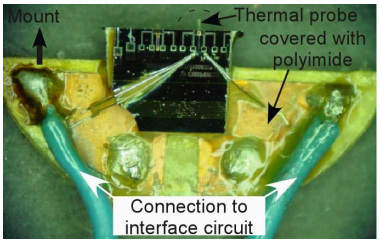

Fig. 3: A mounted scanning thermal probe with the base covered with a polyimide (PI2613™) layer for working in aqueous environments.

0-9640024-4-2/hh2002/$20©2002TRF
DOI 10.31438/trf.hh2002.59

Solid-State Sensors, Actuators, and Microsystems Workshop
Hilton Head Island, South Carolina, June 2-6, 2002

III. OPERATION AND DESIGN OPTIMIZATION

Figure 4 shows an interface circuit used to sense the probe resistance change as it scans across the sample surface. It includes a Wheatstone bridge, two gain stages providing combined amplification of 10^4, and a low pass filter with cutoff frequency of 1 KHz to reduce noise. The output voltage (V_{out}) is plotted in thermal scans.

The probe tip temperature change (ΔT_P) can be calculated from the output voltage change (ΔV_{out}), which is:

$$\Delta T_P \cong \Delta V_{out} \cdot (R_1 + R_P)^2 / (10^4 \cdot V_S \cdot R_1 \cdot R_P \cdot TCR) \quad (1)$$

A ΔV_{out} of 100 mV corresponds to a ΔT_P of 5.657 mK calculated using the voltage and resistance values shown in Fig. 4, and the measured temperature coefficient of resistance (TCR) of 3640 ppm/K for the Cr/Au bolometer. The full scale ΔT_p is indicated for all thermal scans presented in this paper. Before a scan, this circuit is adjusted to balance the Wheatstone bridge with the probe in contact with the sample by adjusting the control resistor (R_c) to make the resistance ratio of R_c/R_2 equal to R_P/R_1 so that the output voltage is as close as possible to 0V.

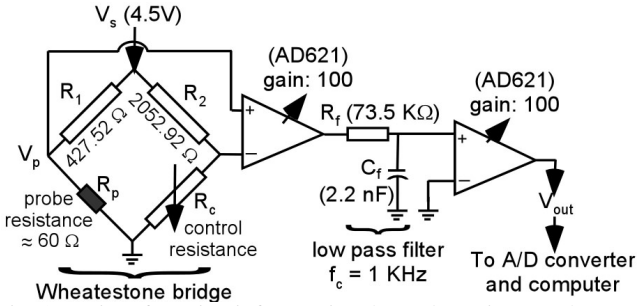

Fig. 4: An interface circuit for sensing the probe resistance change.

In scanning a Si wafer with an ultra-thin photoresist layer of thickness comparable to the scan tip diameter, the heat transfer between the probe tip and silicon substrate can be modeled as that through a cylinder. The heat loss (P_s) to the silicon substrate can be expressed as:

$$P_s = (T_p - T_0) \cdot A_0 \cdot k_s / H \quad (2)$$

where T_p is the probe tip temperature, A_0 is the tip-sample contact area, k_s is the thermal conductivity of photoresist, and H is the photoresist thickness. The silicon substrate is a large heat sink, effectively with a fixed temperature T_0. The thermal conductance image obtained from V_{out} contains both topographic and thermal conductivity information. A purely topographic image is produced simultaneously by monitoring the deflection of the probe cantilever as in a conventional AFM. It is often useful to compare these images for sub-surface and material property information.

IV. MEASUREMENT RESULTS

The spring constant of a 250 μm long, 50 μm wide, and 3 μm thick probe shank measured by using a built-in function in the Topometrix™ scanning system is 0.082 N/m, which is about 10× and 50× lower compared those reported in [2,4]. This allows contact mode scanning of soft materials such as photoresist patterns with feature size of 500 nm easily even without *z*-direction feedback (Fig. 5). The output voltage drops as the probe is scanned across the higher thermal conductivity material (silicon), because the heat loss from the tip to sample increases, which reduces the tip temperature, and the corresponding probe resistance.

Figure 6 shows the topographic and thermal images of exposed but undeveloped UV113™ photoresist patterned with critical dimension of 70 nm and 200 nm pitch. Comparing the topographic and thermal images of partial developed UV113™ photoresist sample (Fig. 7), it is evident that the thermal probe has a lateral spatial resolution of <50 nm. The topographical resolution is <1 nm. The interface circuit is sensitive enough to detect a tip temperature change only 1.13 mK.

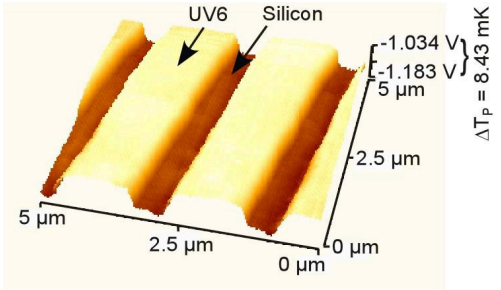

Fig. 5: Thermal image of developed UV6™ photoresist sample with thickness of 350 nm. No *z*-direction feedback.

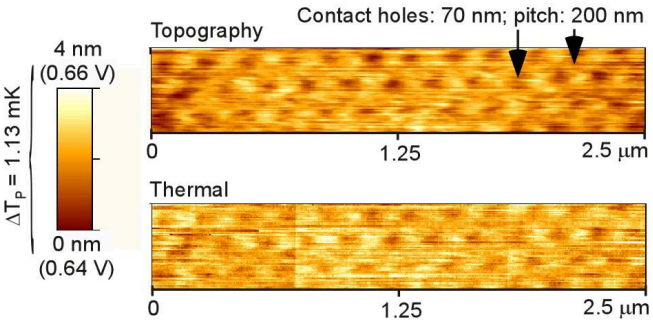

Fig. 6: Topographic (top) and thermal (bottom) images of exposed but undeveloped UV113™ photoresist contact holes of 70 nm.

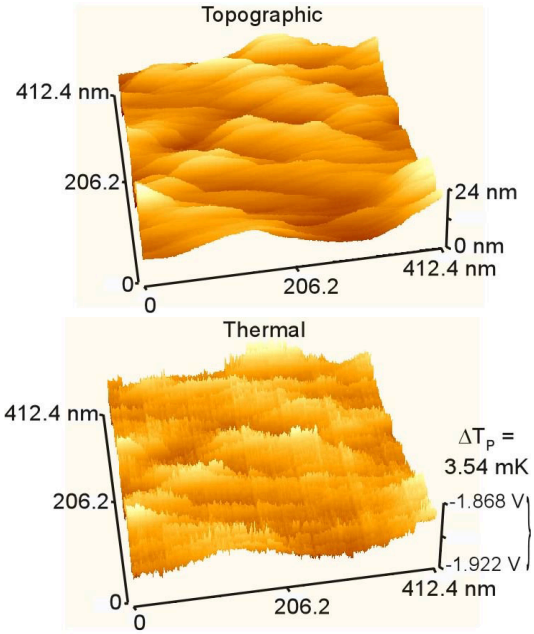

Fig. 7: Topographic (top) and thermal (bottom) images of partial developed UV113™ photoresist sample show the thermal probe has spatial resolution of sub-50 nm.

The positive tone chemically amplified photoresist UV6™ by Shipley, which is suitable for ultra-narrow ULSI linewidths, behaves as shown in Fig. 8 [8]. Unlike standard PR and PMMA, a photoacid generated by exposure permits thermolysis of the backbone polymer during the post exposure bake (PEB), which changes the solubility of the exposed regions of the resist and

releases isobutylene. The photoresist thickness decreases in exposed areas where released isobutylene is evaporated during PEB. It is, therefore, important to control the PEB conditions to suppress the acid diffusion for critical dimension control when using chemical amplification resist systems.

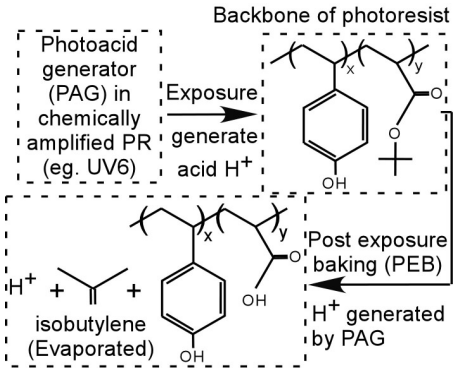

Fig. 8: In UV6™, PAG acid deprotects the backbone during PEB for subsequent dissolution in the developer

Figure 9 shows the topographic and thermal linear scans of a trench in exposed but undeveloped Shipley UV6™ photoresist. As the duration of the 130°C PEB increases from 45 s to 360 s, both the topographic height change (Δh) and ΔV_{out} increase. However, the most significant change in Δh occurs in the 45-90 s period, whereas the most significant change in ΔV_{out} occurs in the 180-360 s period. As noted above, the Δh is due to the release of isobutylene and depends on the acid concentration and the reaction rate of photoresist backbone deprotection. The "v" shape profiles of exposed regions are due to the Gaussian distribution of the e-beam source of dose profile, and hence, the acid concentration [1]. As the PEB time increases, the "v" shape profile widens due to the acid diffusion. However, since the acid diffusion constant, which depends on the process conditions [9], is only about 50 nm^2/s for UV6™ [10], this change is very small (~10 nm) [11], particularly when compared to the 500 nm width of the exposed portion. Since the recommended PEB condition for 130 °C is 90 s, the longer PEB times may deplete the photoresist backbone, minimizing subsequent changes in topography. In contrast, other chemical changes may lead to the ΔV_{out} increase during the 180-360 s period.

The thermal probe was also used to scan HeLa line ovarian cancer tumor cells which are widely used in cell research [12]. The optical and thermal images of the nucleus of a HeLa cell fixed to a glass slide while undergoing mitosis are compared in Fig. 10. Since the topographic variation in such a sample is much larger than the thermal conductivity difference of the organelles within it, the thermal image is very similar to the topography map. Comparing the topographic (AFM) and thermal images of a layer of HeLa cells (Fig. 11), it is evident that the thermal image can provide more details.

Figure 12 shows thermal 2D and linear scans of metal lines on a Si substrate in an aqueous environment. Deformation of the ultracompliant probe by meniscus forces is prevented by immersing the entire mounting platform in the water along with the sample. The variation in metal films is clearly detectable despite the fact that these scans were performed without *z*-axis feedback. This is possible because of the ultra compliant nature and high thermal isolation offered by the probe. Operation in aqueous environments facilitates observation of metabolic activity in living cells.

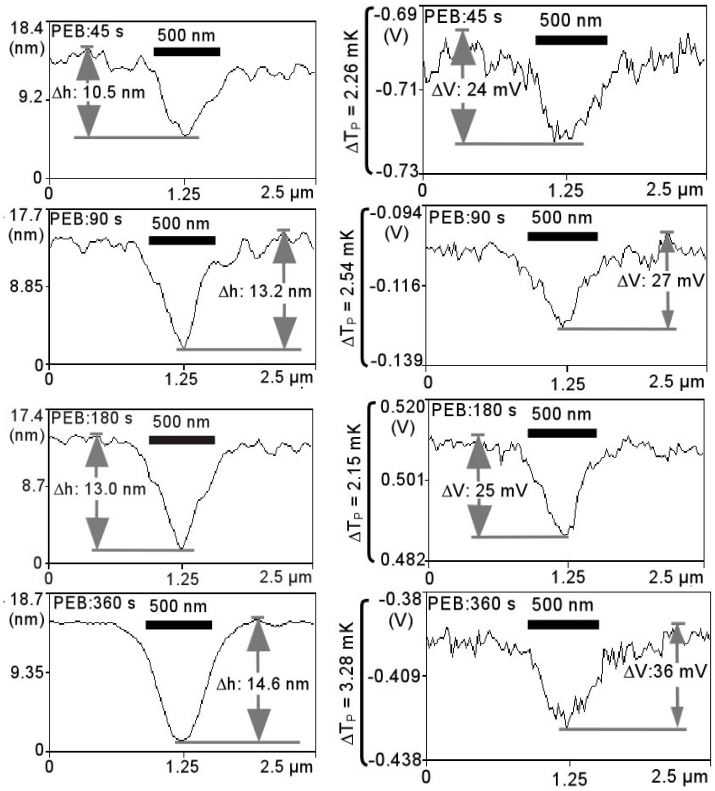

Fig. 9: Topographic (left) and thermal (right) line scans of a latent image in UV6™ with varying PEB time at 130°C.

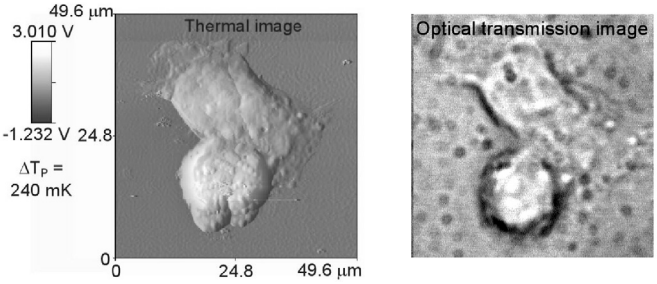

Fig. 10: Thermal (left) and optical (right) images of the nuclei HeLa tumor cells on a glass slide.

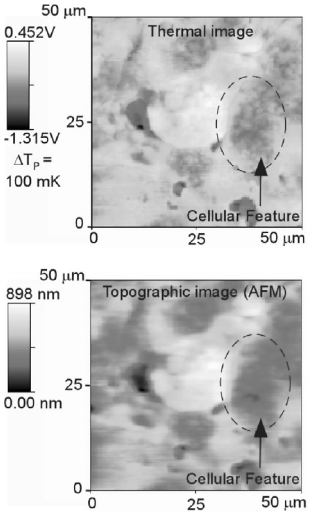

Fig. 11: Thermal (upper) and topographic (lower) images of a layer of HeLa tumor cell on a glass cover slide. The thermal image shows more cellular details.

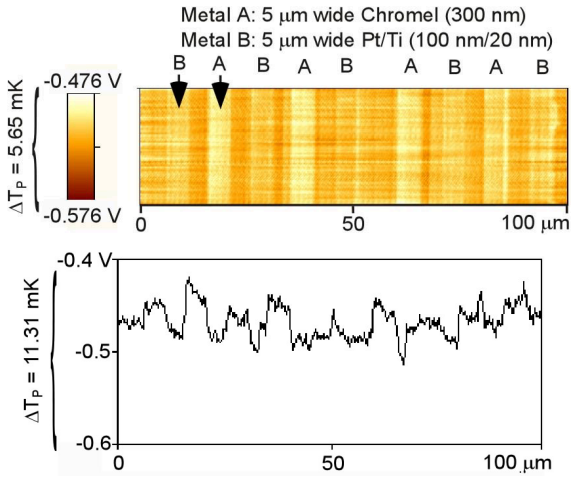

Fig. 12: Area (upper) and linear (lower) thermal scans of metal stripes on a Si substrate obtained without *z*-direction feedback with the probe and sample immersed in water.

V. CONCLUSION

This effort has addressed the development and applications of a polyimide shank thermal probe fabricated by a 6-mask process. These probes are assembled with the help of a thermocompression bond between thin films that greatly improves yield. A coating of polyimide over the pads and wire bonds after assembly permits its operation in aqueous environments. Typical probe dimensions are 250 μm length, 50 μm width, and 3 μm thickness. The probe is ultra-compliant with a spring constant of 0.082 N/m, which can be further reduced by changing the material and/or dimensions. It can be operated without *z*-direction feedback, even when scanning soft materials. The probe offers lateral spatial resolution of <50 nm, topographical resolution of <1 nm, and tip temperature resolution of <1.2 mK. The probe has been used to scan exposed but undeveloped photoresist samples, to study the acid diffusion in photoresist during post-exposure bake, and to image fixed HeLa cells. Scans of thin film metals demonstrated its usefulness while operating in a liquid medium. A summary of its operating limits is presented in Table I.

Table I: Performance summary for the polyimide probe.

Tip Diameter	≈50 nm
Lateral Spatial Resolution	<50 nm
Topographical resolution	<1 nm
Input Referred Circuit Noise (1 KHz BW)	<2 μV
ΔR Resolution	<0.25 mΩ
Tip Temperature Resolution	<1.2 mK
Detectable Thermal Conductance Change	1×10^{-11} W/K (1%)
Detectable Thermal Conductivity Change	2×10^{-3} W/m·K (1%)

ACKNOWLEDGEMENTS

The authors thank Dr. Leo Ocola for supporting the UV113™ photoresist sample, and Dr. Saulius Vainauskas for providing HeLa cell samples. This work was funded in part by the Semiconductor Research Corporation contract # 98-LP-452.005. The Center for NanoTechnology, University of Wisconsin-Madison, is supported in part by DARPA/ONR grant # MDA 972-00-1-0018, and # MDA 972-99-1-0013. The Synchrotron Radiation Center, University of Wisconsin-Madison, at which some of the experimental facilities are located, is operated under NSF award # DMR-0084402. Partial travel support was provided by the Transducers Research Foundation and the DARPA MEMS and BioFlips programs.

REFERENCES

[1] L.E.Ocola, D.Fryer, P.Nealey, J.dePablo, F.Cerrina, and S. Kämmer, "Latent image formation: Nanoscale topography and calorimetric measurements in chemically amplified resists," *J. Vac. Sci. Technol. B*, 14(6), pp. 3974-9, 1996.

[2] P.Vettiger, et al., "The "Millipede"-More than one thousand tips for future AFM data storage," *IBM J. Res. Develop.*, 44(3), pp. 323-40, 2000.

[3] A.Majumdar, "Scanning thermal microscopy," *Annu. Rev. Mater. Sci.*, 29, pp. 505-85, 1999.

[4] TM Microscopes, www.tmmicro.com, probe model# 1615-00.

[5] M.-H.Li, J.J.Wu, Y.B.Gianchandani, "Surface micromachined polyimide scanning thermocouple probes," *J. Microelectromech. Sys.*, 10(1), pp. 3-9, 2001.

[6] M.-H. Li, Y.B. Gianchandani, "Microcalorimetry applications of a surface micromachined bolometer-type thermal probe," *J. Vac. Sci.Technol. B*, 18(6), pp. 3600-3, 2000.

[7] S.Akamine, C.F.Quate, Low temperature thermal oxidation sharpening of microcast tips, *J. Vac. Sci. Technol. B*, 10(5), pp. 2307-10, 1992.

[8] H.Ito, "Chemically amplified resists: past, present, and future," *SPIE* Vol. 3678, pp. 2-12, 1999.

[9] T.Itani, H.Yoshino, S.Hashimoto, M.Yamana, N.Samoto, K. Kasama, "A study of acid diffusion in chemically amplified deep ultraviolet resist," *J. Vac. Sci. Technol. B*, 14(6), pp. 4226-8, 1996.

[10] D.Kang, E.K.Pavelchek, C.Swible-Keane, "The accuracy of current model descriptions of a DUV phtotresist," *SPIE*, vol. 3678, pp. 877-90, 1999.

[11] T.H.Fedynyshyn, J.W.Thackeray, J.H.Georger, M.D. Denison, "Effect of acid diffusion on performance in positive deep ultraviolet resists," *J. Vac. Sci. Technol. B*, 12(6), pp. 3888-94, 1994.

[12] R.L.Warters, O.L.Stone, "Histone protein & DNA synthesis in HeLa cells after thermal shock," *J. Cell. Phys.*, 118, pp. 153-60, 1984.

A HIGH TUNING-RATIO SILICON-MICROMACHINED VARIABLE CAPACITOR WITH LOW DRIVING VOLTAGE

Zhihong Li, and Norman C. Tien
Berkeley Sensor & Actuator Center and Department of Electrical and Computer Engineering,
University of California, Davis, CA 95616.

ABSTRACT

A bulk-micromachined variable capacitor, in which the gap distance between parallel plates is adjusted by comb-drive actuators, has been developed. This capacitor possesses the merits of parallel-plate capacitors and comb-drive actuation without their demerits. Therefore, this device has high tuning range and low tuning voltages with a small footprint and stiff springs, resulting in lower mechanical noise sensitivity and high tuning speed. The initial fabricated devices demonstrate a 5:1 tuning ratio at 20V with 8.46pF maximum capacitance.

INTRODUCTION

Variable capacitors have wide applications in RF circuits for wireless communications such as low-noise voltage-controlled oscillators (VCO's) and high dynamic range filters. Micromachined variable capacitors are very attractive due to their advantages of low parasitics, large voltage swing and high Q [1-8]. The main objectives for a micromachined variable capacitor are to achieve low driving voltage, high tuning ratio, and low mechanical noise sensitivity.

Micromachined variable capacitors generally fall in two categories —those that vary the area and those that vary gap [2, 3]. Often, gap-tuning capacitors are constructed from two surface-micromachined electrostatically-actuated parallel plates. One drawback of this method is that the movable plate can only be actuated one-third of the initial gap distance; beyond this value, the two plates will snap together. In this case, the maximum theoretical tuning ratio is only 1.5:1. In practice, the tuning range can be even lower because of electrical overshoot or mechanical shock. Although techniques that increase the tuning range have been reported [4, 5], they often do not have tuning ratios large enough for many RF applications, and furthermore, have increased process complexity.

Most area-tuning capacitors utilize comb drives as the actuation component and another set of comb fingers as the capacitor [3, 8]. This type of capacitor has no theoretical limitation on the tuning range, because the driving force of comb drives is independent of displacement [9, 10]. However, the capacitance per unit area of comb fingers is typically smaller than parallel plates because of larger gap distances. In addition, the actuation voltage is larger for the same tuning ratio because larger displacement is required. A larger capacitance can be obtained by increasing the device area, while the driving voltage can be lowered by increasing the device area and decreasing the stiffness of springs. However, the larger mass and lower stiffness will lead to higher mechanical noise sensitivity and lower tuning speed because of the decreased resonant frequency.

In this paper, we present a bulk-micromachined variable capacitor that employs comb drive actuators to laterally displace parallel plate capacitors. This device is realized via a simple single-crystal-silicon process performed on glass substrate. This process allows the fabrication of high performance devices on a low loss substrate.

DEVICE DESIGN

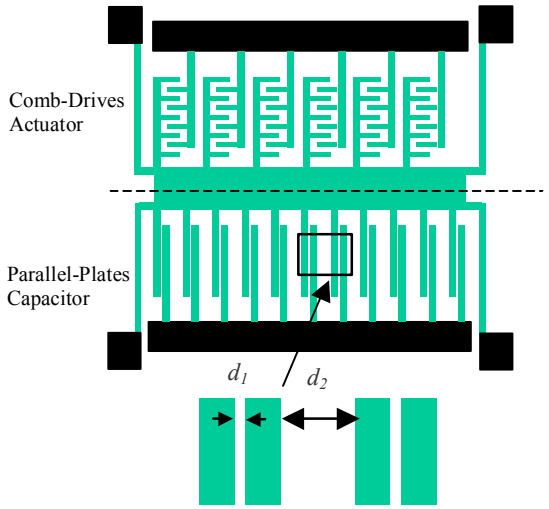

Fig. 1 The schematic view of the variable capacitor with parallel plates as capacitors and comb drives providing the tuning.

Fig.1 shows a schematic view of our designed capacitor. In this capacitor, comb drives provide actuation by the well-known equation [9, 10]

$$F = \frac{\partial C}{\partial x}\frac{V^2}{2} = n\frac{h\varepsilon_0}{g}V^2 \qquad (1)$$

where n is the number of the fingers in the tuning structure, g is the gap between comb fingers, h is thickness of the structures and V is the applied voltage. It can be seen that the driving force is independent of the displacement. Therefore, the undesired "pull in" effect is avoided and a high tuning ratio can be realized.

The parallel plates, which have larger capacitance per unit area, are utilized as the capacitor in the structure. The capacitance as a function of the distance between parallel plates is described as

$$C = \frac{n_1\varepsilon_0 A}{d_1 - \Delta d_1} \qquad (2)$$

where n_1 is the number of pairs of parallel plates, d_1 and Δd_1 are the distance and distance change between the plates, A is the area

0-9640024-4-2/hh2002/$20©2002TRF
DOI 10.31438/trf.hh2002.60

Solid-State Sensors, Actuators, and Microsystems Workshop
Hilton Head Island, South Carolina, June 2-6, 2002

of the plates. Compared to the comb-finger capacitors (where the overlap is changed), the parallel plate element requires a smaller displacement to achieve the same tuning ratio, and therefore requires a lower actuation voltage. As shown in the outlined box in Fig. 1, the movable plate (finger) in a parallel plate capacitor cell and the fixed plate in the adjacent cell form a parasitic capacitor with distance d_2. When d_1 decreases under the applied voltage, d_2 will increase. Consequently, the capacitance and capacitance change will deviate from equation (2). Similarly, a parasitic capacitor is also formed in the actuation section, which will decrease the actuation force. The effect is considered in our models, however it will not be discussed in detail here. To minimize the effect, d_2 is designed to be much larger than d_1.

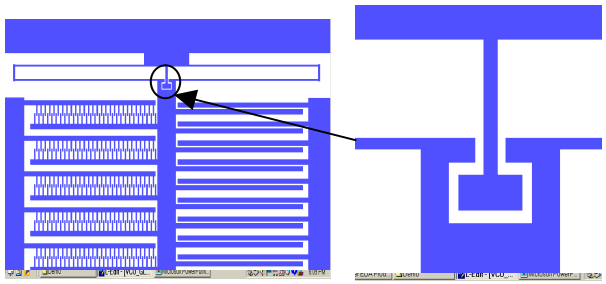

Fig. 2 A layout of our capacitor

Fig. 2 shows a layout of our capacitor. Though the gap between capacitor plates can be precisely controlled by comb drives, the plates may still touch due to mechanical shock or a voltage overshoot. A mechanical stop was designed to protect the parallel plates from shorting or failing because of stiction. The mechanical stop limits the minimum gap between the plates to be 0.5µm in our design, but it can be made smaller. The maximum tuning ratios for the capacitors with the initial gaps of 2µm, 3µm, 4µm and 5µm are 4:1, 6:1, 8:1 and 10:1, respectively, though there is no theoretical limitation if the mechanical stop is not present.

For comparison, we also designed a variable capacitor with parallel-plate actuators and parallel-plate capacitors (shown in Fig. 3, and designated the Type I capacitor), and a variable capacitor with a comb-drive actuator and comb-finger capacitors (shown in Fig. 4, and designated the Type II capacitor).

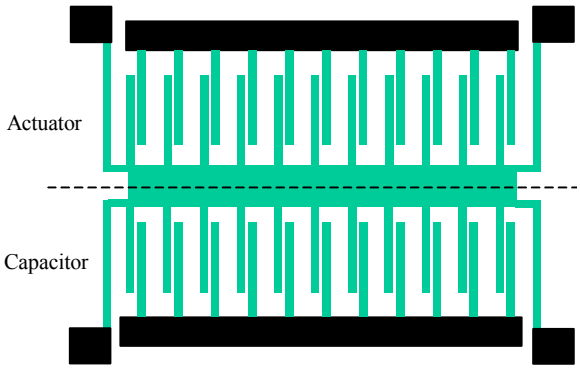

Fig.3 The schematic view of a gap-tuning capacitor with parallel plate actuator and parallel plate capacitor (Type I).

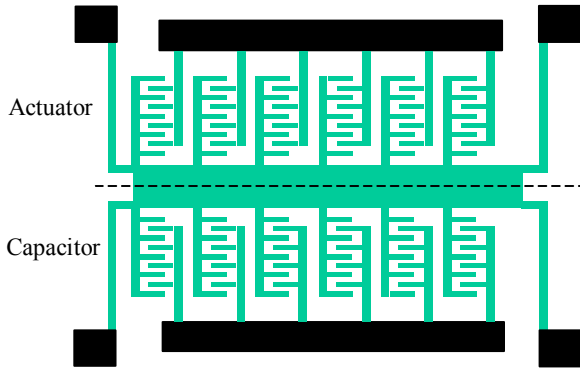

Fig.4 The schematic view of an area-tuning capacitor with comb-drives actuator and comb-finger capacitor (Type II)

FABRICATION

The capacitor is fabricated in a single layer of bulk micromachined single-crystal silicon that sits on a glass wafer. This simple process flow combines wafer bonding and DRIE (Deep Reactive Ion Etch) technologies (shown in Fig. 5). The process started with (100) heavily n-doped 4" silicon wafers. Shallow trenches approximately 4 µm in depth were either dry etched by DRIE or wet etched with KOH (Fig. 5(a)). The silicon and glass wafers were anodically bonded in a 1000V, 400°C and 1atm. ambient (Fig. 5(b)), in a Karl Suss wafer bonder. Silicon wafers were thinned to the desired thickness by wet etching with KOH (Fig. 5(c)). The thickness depends on structure specifications and process capability (about 50µm in our experiments). Finally, the structures were released by DRIE, and an aluminum layer was sputtered on the silicon structures to decrease series resistance and increase Q (Fig. 5(d)).

Compared to surface micromachining, bulk micromachining technology allows the creation of high-aspect-ratio single-crystalline-silicon structures, enabling the fabrication of devices with high electrical and mechanical performance. Employing a glass substrate instead of a silicon one, will significantly reduce the parasitic capacitances due to the substrate for the variable capacitors.

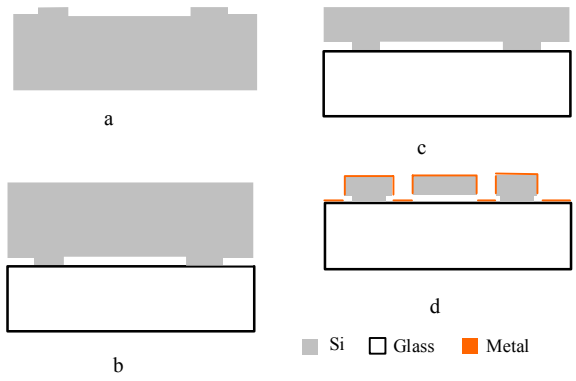

Fig. 5 The fabrication process of the variable capacitor. (a) etching a shallow trench, (b) anodic boding with Pyrex glass, (c) Thinning the silicon wafer, and (d) DRIE and sputtering metal.

RESULTS AND DISCUSSION

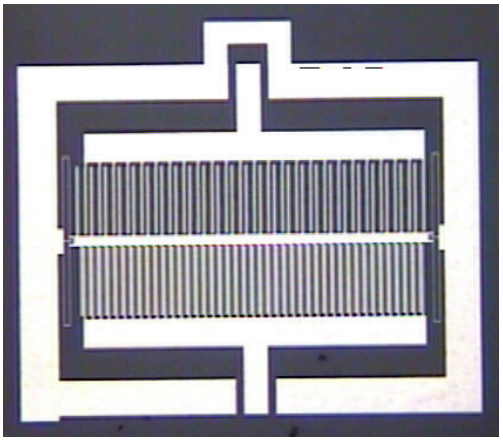

(a)

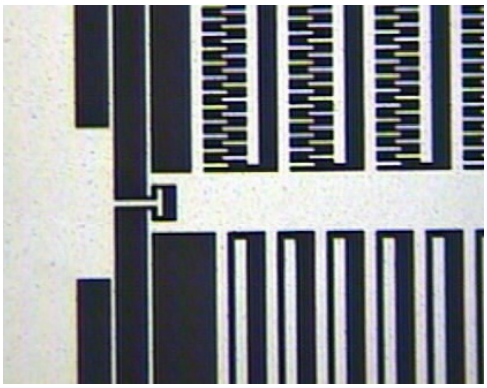

(b)

Fig.6 Micrographs of our variable capacitor: (a) entire device, and (b) a close-up view.

Fig. 6 shows micrographs of a fabricated variable capacitor. The space between the comb fingers is 3μm. The width of the comb fingers and springs are also 3μm. The gaps between the parallel plates, d_1, are 4μm and 5μm in different designs, and d_2 is 15μm, at least 3 times d_1.

Fig. 7 presents the calculated and measured capacitance as a function of actuation voltage for our capacitor with different gap distances between plates (2, 3, 4 and 5μm, respectively.) In our experiments, only capacitors with gaps of 4μm and 5μm were initially fabricated. The values of the capacitors with gaps of 4μm and 5μm are 2.0pF and 1.67pF at 0V, respectively. According to the discussion in the previous section, the designed tuning ratios are limited from 4:1 to 10:1 by a mechanical stop. However, the calculated tuning ratios are slightly less than those values, because of the parasitic capacitors that were included in our calculations with MATLAB. The measured maximum tuning ratio for the capacitor with a starting gap of 5μm is about 5:1, with a capacitance of 8.46pF at 20V. For the capacitor with a starting gap of 4μm, the measured maximum capacitance is 8.23pF at 18V. These tuning ratios area smaller than designed, probably due to the gap of the fabricated mechanical stop being smaller than the design values because of lithography and etch bias. It was observed that the minimum space between the plates is approximately 1μm instead of 0.5μm.

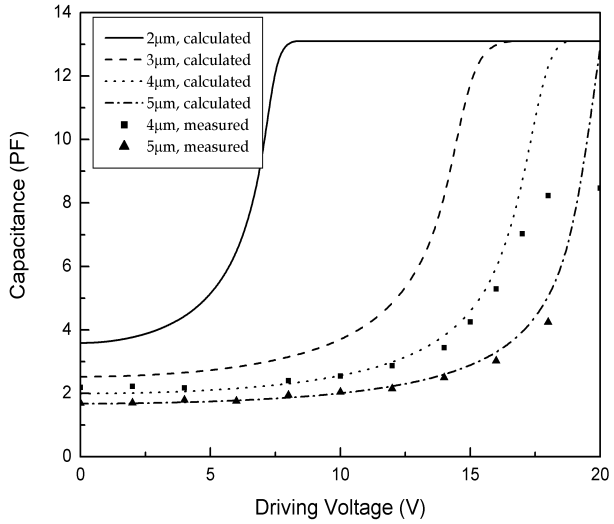

Fig. 7 The calculated and measured capacitances of our devices with different gaps between plates. For the capacitor with 2μm gap, the width and space of comb-drives are also 2μm, while others are 3μm.

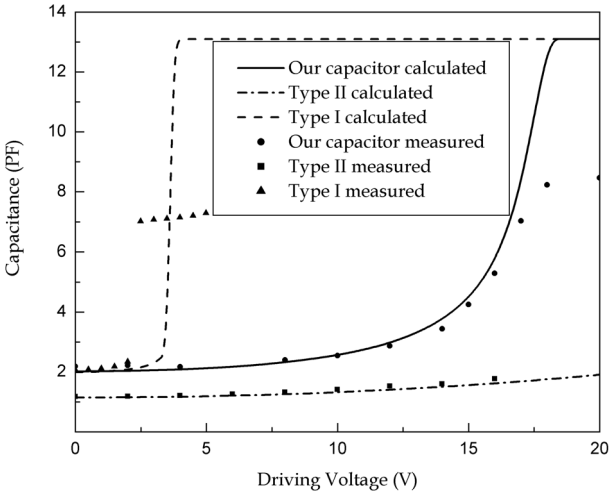

Fig.8 The comparison of calculated and measured capacitances for our capacitor, Type I and Type II capacitors. The gap between parallel plates is 4μm, and the width and space of comb-drives are 3μm.

Fig.8 shows a comparison of our capacitor with Type I and Type II capacitors, where the gap between parallel plates is 4μm and the starting overlap of comb fingers is 5μm. Our capacitor has larger capacitances at 0V, 2.0pF, compared to the Type II capacitor, which had a capacitance of 1.14pF. The maximum measured capacitance of our capacitor is 8.23pF with tuning ratio of 4.1:1 at 18V, while the capacitance of the Type II capacitor at 18V is only 1.8pF with tuning ratio of 1.6:1. It can be seen that our capacitor has higher initial capacitance and requires significantly lower driving voltages to achieve same tuning ratio

when compared to the Type II capacitor. The Type I capacitor has the same capacitance as our capacitor at 0V, but the maximum measured capacitance is only 2.4PF with a tuning ratio of 1.2, after which the plates are pulled in and snap together. The maximum measured tuning ratio is even lower than the theoretical value, 1.5:1, because of mechanical noise or electrical overshoot. The results show that our capacitor has much higher tuning range than the Type I capacitor.

Table.1 compares the requirements of our capacitor and a Type II capacitor for given specifications of 2.5pF initial capacitance and 5:1 tuning range at 15V. It can be seen that the device area of our capacitor is less than half that of the Type II capacitor. Therefore, our capacitor allows for higher level of integration. The spring stiffness of our capacitor, 7.44N/m, is much higher than that of the Type II capacitor, which was 1.74N/m. As a result, our capacitor has lower mechanical noise sensitivity. In addition, shorter and/or wider springs will decrease series resistance and parasitic inductance, resulting in a higher Q as well as a higher self-resonant frequency. The resonant frequency of our capacitor, 2.17kHz, is three times that of the Type II capacitor, which was 0.707kHz. Therefore, our capacitor is capable of operating higher tuning speeds. We did not calculate the performance for the Type I capacitor, since it could not meet the tuning ratio the requirements.

CONCLUSION

We developed a variable capacitor in which the actuation is provided by comb drives and parallel plates are used for the capacitors. This capacitor has both the advantages of parallel-plate capacitors and the benefits found with comb-drive actuation. The comb drives allow for a high tuning ratio without the undesired "pull in" effect present with parallel plate actuators. In addition, the parallel plates provide a large capacitance per unit area and enable lower driving voltages than comb finger capacitors because a shorter displacement is required for an equivalent tuning ratio. This device requires a smaller area, has stiffer springs and a higher resonant frequency, which result in denser integration, low series resistance, low parasitic inductance, low mechanical noise sensitivity and high tuning speed.

ACKNOWLEDGEMENT

The authors would like to thank Prof. Kan of Cornell University who provided test instrumentation, Dr. Zengtao Liu of Cornell University for help in measurement and Mr. Xiaosong Tang for assistance in the fabrication. Fabrication was done in the Cornell Nanofabrication Facility.

REFERENCE

1. C. T.-C. Nguyen, L. P. B. Katehi and G. M. Rebeiz, "Micromachined Devices For Wireless Communications," Proc. IEEE, vol. 86, no. 8, 1998, pp. 1756-68
2. J. J. Yao, "RF MEMS from a device perspective," J. Micromech. Microeng. 10 (2000), R9-R38
3. J. J. Yao, S. T. Park, R. Anderson and J. DeNatale, "High Tuning Ratio MEMS-Based Tunable Capacitors For RF Communications", Proc. Solid-state Sensor and Actuator Workshop, Hilton Head Island, 1998
4. A. Dec and K. Suyama, "Micromachined Electro-Mechanically Tunable Capacitors And Their Applications For RF IC's" IEEE J. Solid-State Circuits, vol. 35, no. 8, 2000, pp. 1231-37
5. J. Zou, C. Liu, J. S-. Aline, J. Chen, S.-Mo Kang, "Development Of A Wide Tuning Range MEMS Tunable Capacitor For Wireless Communication Systems", IEDM 2000, 2000, p403-406.
6. D. J. Young and B. E. Boser, "A Micromachined Variable Capacitor For Monolithic Low-Noise VCOs," in Proc. IEEE Solid-State Sensors Actuators Workshop, Hilton Head, SC, 1996, pp. 86–89
7. D. J. Young, J. L. Tham, and B. E. Boser, A Micromachine-Based Low Phase-Noise GHz Voltage-Controlled Oscillator for Wireless Communications, The 10th International Conference on Solid- State Sensors and Actuators (Transducers'99), Sendai, Japan, 1999, P1386
8. J. J. Yao, S. T. Park, and J. DeNatale, "A Low Power/Low Voltage Electrostatic Actuator For RF MEMS Applications," Proc. Solid-state Sensor and Actuator Workshop, Hilton Head Island, 2000, pp. 246-49
9. A. L. Pisano, and Y. H. Cho, " Mechanical Design Issues in Laterally-driven Microstructures", Sensors and Actuators, A21-23, 1990, 1060-1064
10. W. C. Tang, T.-C. H. Nguyen, M. W. Judy, and R. T. Howe, "Electrostatic-Comb Drive Of Lateral Polysilicon Resonators," Sensors Actuators, vol. A21, pp. 328–331, Feb. 1990.

Table.1. The device requirements for our capacitor and the Type II capacitor given equivalent specifications. The initial overlap of the comb fingers is 5μm.

Devices	Specifications				Requirements		
	Feature Size	Initial Capacitance	Tuning Ratio	Driving Voltage	Device Area	Spring Stiffness	Resonant Frequency
Ours	3μm	2.5pF	5:1	15V	1.5mm^2	7.44N/m	2.17kHz
Type II	3μm	2.5pF	5:1	15V	3.3mm^2	1.74N/m	0.707kHz

A NOVEL MICROMACHINED GLOW PLUG FOR ULTRAHIGH TEMPERATURE IGNITION APPLICATIONS

Li-Anne Liew, Victor M. Bright, and Rishi Raj
Center for Advanced Manufacturing and Packaging of Microwave, Optical and Digital Electronics (CAMPmode),
Department of Mechanical Engineering, University of Colorado at Boulder
Boulder, Colorado 80309-0427; http://mems.colorado.edu

ABSTRACT

This paper presents the design, fabrication and testing of a micro glow plug for ultrahigh temperature ignition applications. The device was fabricated from a novel refractory ceramic known as polymer-derived silicon carbon-nitride, which has been shown to possess outstanding mechanical robustness, corrosion resistance, and thermal shock resistance at temperatures exceeding 1000 ^{o}C. The micro glow plug has been shown to achieve temperatures of at least 1200 ^{o}C, with a response time of less than 1 second and with a power consumption of 3 Watts. In addition, the micro glow plug was used to ignite thermite in both chip-scale and macro-scale reactions.

INTRODUCTION

Glow plugs are temperature ignition devices commonly employed in diesel and natural gas engines [1]. Figure 1 shows a photograph of conventional, commercially available glow plugs and a schematic of the glow tip (the hot section) which typically consists of three components: a heating element, encasing material, and an outer sheath. The major figures of merit for glow plugs are achievable temperature (1200 ^{o}C), response time, power consumption, and cost.

Several drawbacks are associated with these devices: Three different materials and manufacturing processes are required to fabricate the glow tip thus driving up device cost. The device is large (due to the manufacturing processes used) yet the entire heating element heats up to the maximum temperature (1200 ^{o}C), leading to high power consumption (20-100 Watts) and slow response (5-10 seconds).

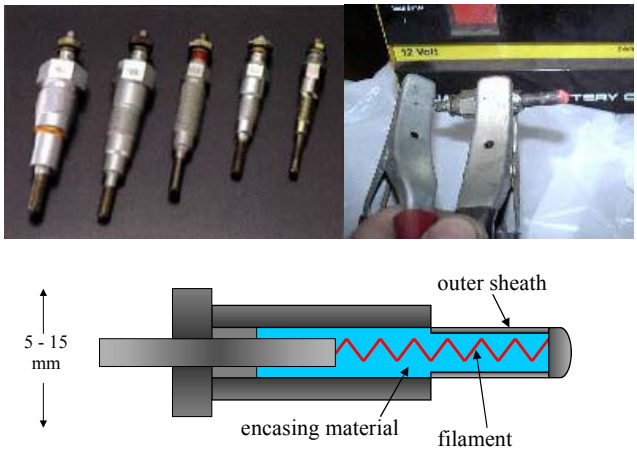

Figure 1. Above: Photographs of conventional diesel glow plugs, typical length 30-50 mm. Photos courtesy of Robert Bosch Corp. (http://www.bosch.com). Below: Schematic of the major components of a glow plug.

Temperature ignition in diesel engines (or any other high-temperature ignition applications for that matter) is therefore a prime application that could benefit from the reduced size, response time and power consumption offered by microsystems. However, until now no MEMS technology existed that could fulfill this need because the materials in the traditional MEMS infrastructure – silicon, polymers, metals and even many ceramics – cannot remain operational when temperatures exceed 1000 ^{o}C in oxidizing environments.

Our group has developed a technology to fabricate MEMS from a novel refractory material called silicon carbon nitride [2] (SiCN). SiCN is a new class of amorphous polymer-derived bulk ceramics that remain mechanically stable to temperatures exceeding 1500 ^{o}C [2] and which exhibit excellent oxidation and creep resistance at those temperatures [2]. Our previous work has resulted in functional but commonplace devices such as electrostatic actuators [3] and thermal actuators [4] that were simply reproduced in SiCN since our focus was microfabrication.

Now, however, this marriage of a novel refractory material with an appropriate microfabrication technology has produced a revolutionary new concept in harsh environment applications (such as high-temperature ignition) that will enable Microsystems to enter markets previously untouched by MEMS.

In this work, a Micro Glow Plug was designed and fabricated from polymer-derived SiCN. When compared to conventional glow plugs, the MGP exhibits faster response time and lower power consumption. The MGP was successfully used to ignite thermite, a solid-state explosive with ignition temperature of 1200 ^{o}C, in both chip-scale and macro-scale reactions, and therefore would also be a potential candidate for diesel engine applications where ignition temperatures are similar.

DESIGN AND FABRICATION OF SiCN MICRO GLOW PLUG

Figure 2 shows a schematic and a scanning electron micrograph of a micro glow plug (MGP). The device consists of a single U-shaped layer of SiCN of thickness 30-300 microns. The tip cross sectional area is designed to be 10 times smaller than that of the wider arms, thus the circular electrical contact pads remain relatively cool while the tip glows upon passing a current through the device. This eliminates one problem found in conventional glow plugs, which is the need to insulate the electrical contacts while operating temperatures are achieved. Furthermore, because of its small size the MGP's response is almost instantaneous, and the device consumes very little power. In addition, only one material is required versus the three material needed to make a conventional glow plug, and the manufacturing is through a photolithography-based batch process therefore the manufacturing cost is significantly lower than that for the conventional devices.

The fabrication of SiCN MEMS is detailed elsewhere [3, 4]. Basically, the fabrication comprises two major processes – a polymer process whereby polymeric structures in the shape of

0-9640024-4-2/hh2002/$20©2002TRF
DOI 10.31438/trf.hh2002.61

MGPs are fabricated from a liquid precursor, and then a ceramic process that consists of heating the polymer in a furnace to the pyrolysis temperature, at which the polymer decomposes into the amorphous SiCN ceramic.

The polymer micromachining process may be accomplished by two separate routes [4] – casting in micromolds fabricated from SU8™ photoresist (from Micro Chem Corp), or by direct photopolymerization. The fabricated polymer structures are then removed from the substrate since they undergo 30% linear shrinkage during pyrolysis. This lack of substrate places a lower design limit on the size of the devices, since each component has to be assembled using manual pick and place. Thus, typical device dimensions range from tens of microns to hundreds of microns.

The polymeric components are then placed in a hot isostatic press (HIP, model AIP 6-30H from American Isostatic Presses) in a nitrogen atmosphere and pyrolyzed at 1000 °C for 4 hours. The polymer structure decomposes into a black-colored amorphous alloy of silicon, carbon and nitrogen. This ceramic is electrically insulating, hence the ceramic structures are then annealed at 1400 °C within the HIP to initiate nanocrystallization of electrically-conductive phases. X-ray diffraction strongly suggests that these nanophases are SiC. Room-temperature DC resistivity of 2-5 Ohm-cm has been measured for material samples processed through this micromachining route [4].

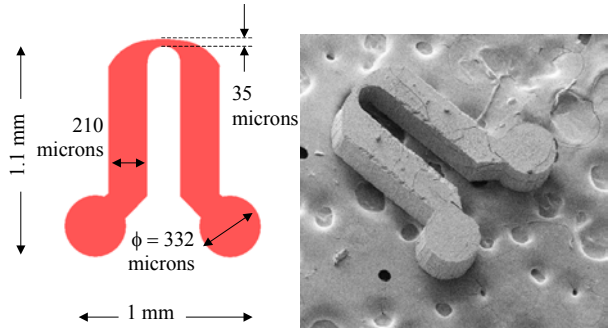

Figure 2. Schematic and scanning electron micrograph of the SiCN Micro Glow Plug (MGP).

Once the polymer MGP structures have been micromachined, they are packaged for testing. For probe-station testing, the devices were simply mounted on alumina substrates with epoxy. For ignition testing, the MGPs were packaged by attachment to photolithographically-patterned alumina substrates using silver paste, and then wirebonded to a commercial 14-pin ceramic dual-in-line package (from Spectrum Semiconductor). Wires were then soldered to the pins on the package.

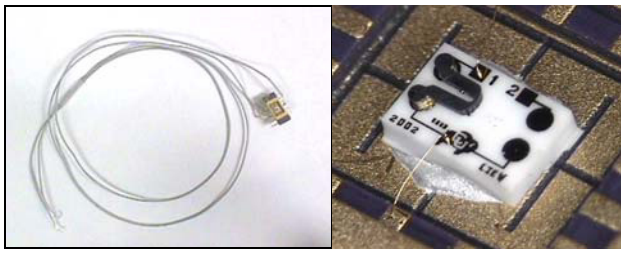

Figure 3. Left: MGP packaged for ignition testing. Right: close-up photograph of the package, showing a MGP mounted on an alumina substrate.

DEVICE TESTING

Electrical Testing

The MGPs were mounted individually on alumina plates using non-conductive epoxy so that the glow tip was suspended over the edge of the substrate for thermal isolation. The alumina substrates were then placed under a probe station and electrical probes were placed on the MGP's circular bond pads. The resistance throughout the MGPs ranged from 200-800 Ohms unactuated, depending on the device thickness.

The majority of devices tested in this work exhibited resistance of around 500 Ohms when unactatued. A constant DC current was then applied to the MGPs until the tips were glowing brightly. The first signs of glowing was observed at 20 mA, with white glow being achieved at 30-35 mA. Upon application of DC current, the response time to achieve white glow is less than 1 second from a "cold" start. Since in most ignition applications the devices would be operated in DC mode, and this response time is significantly faster than conventional glow plugs, more accurate measurements of response time were not done at this stage of the work. Furthermore, the power consumption (typically 2-5 Watts) is significantly lower than that of conventional glow plugs due to the small size. Figure 4 shows photographs of a MGP in the off- and on state.

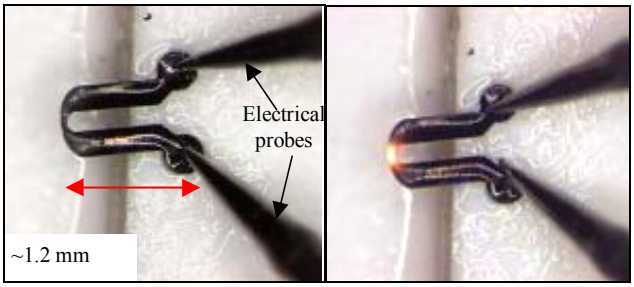

Figure 4. Micro Glow Plug in the "off" state (left) and the "on" state (right), upon application of 30 mA of DC current.

As the glow tip remains heated continuously, various microstructural changes occur within the material over time which cause the resistance to increase until the device fails, i.e. ceases to conduct current. The dominant failure mechanism is believed to be oxidation of the SiCN from the extremely high temperatures (modeled at above 1500 °C) generated from the continuous induced heating, or from crack propagation.

The time to failure for several MGPs was measured for varying levels of applied DC current, the results being shown in Figure 5. Close-up SEMs of the glow tip following failure are shown in Figure 6, showing both an oxidation layer as well as cracks. Given the size of the cracks and the fact that the oxidation forms a layer rather than the core of the material, cracking was probably the cause of failure in this particular device. What temperature does the glow tip achieve during operation? Due to the small dimensions and high temperature of the glow tip, direct temperature measurements using pyrometers or thermocouples is technically difficult. While more sophisticated measurement techniques could be developed, the approach sought here was to indirectly measure the temperature by using the device to ignite or melt various materials whose melting or ignition temperatures are well documented. This would give a lower limit on the device temperature achieved during operation. This is described in the next section.

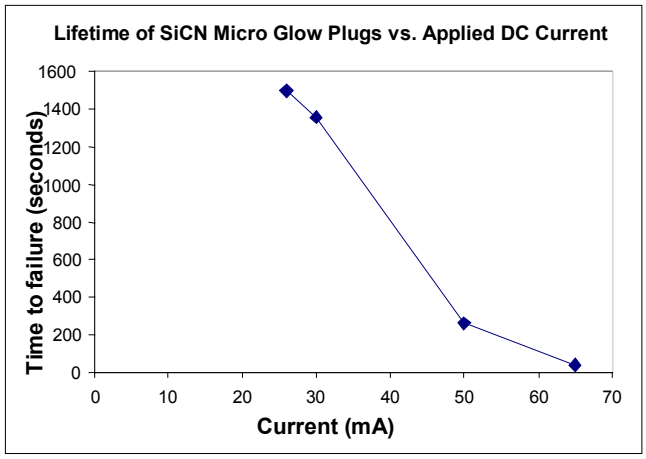

Figure 5. Micro Glow Plug lifetime as a function of applied DC current. The lines connecting the data points are to enhance clarity and do not represent intermediate data values.

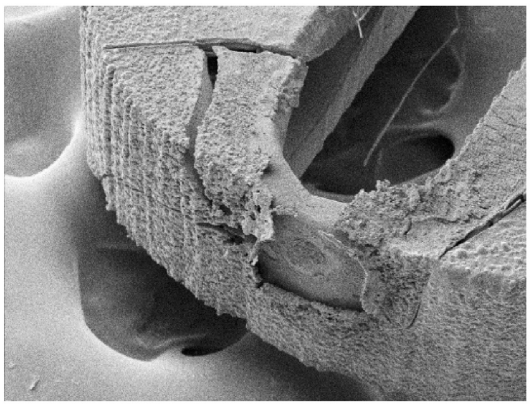

Figure 6. Scanning electron micrograph of a MGP tip following failure after. The thickness of this device is about about 200 microns.

Ignition Testing

In addition to the operational testing described in the previous section, the MGPs were also used to melt or ignite various materials. The purpose of these tests was twofold: to indirectly measure the temperature of the glow tip given the difficulties in direct measurement of such a small high-temperature region, and to demonstrate the functionality of the MGPs as high-temperature ignition devices.

The MGPs were used to ignite thermite [5]. Thermite is a solid-state explosive that has an ignition temperature of about 1200 ^{o}C. Due to this high ignition temperature, thermite is commonly ignited with a strip of burning magnesium ribbon or other vigorous reactions. The thermite reaction itself is highly exothermic, producing temperatures above 2000 ^{o}C. Uses of thermite include welding (known as the Goldschmidt process) and in military incendiary weapons.

In this experiment, thermite was made by mixing Fe_2O_3 with Al powder in a 3:1 ratio. When the temperature of the mixture is raised to above 1200 ^{o}C (the ignition temperature), an oxidation-reduction reaction occurs resulting in molten iron:

$$2Al(s) + Fe_2O_3 \rightarrow Al_2O_3(l) + 2Fe(l)$$

Two variations of the thermite ignition experiments were done: a chip-level reaction and a larger scale reaction utilizing a greater mass of thermite. Both types of reactions were carried out using one MGP at a time.

In the chip-level ignition experiment, 5 milligrams of thermite was placed on the substrate within the package cavity so that the entire MGP and substrate were covered with thermite. The purpose was to demonstrate a chip-scale thermite reaction that would otherwise be inaccessible by conventional ignition means) due to the small size scale of MEMS. Potential applications of such chip-scale thermite-type reactions could be as very powerful micro thrusters or micro power generators, given the violent nature of the thermite reaction. Figure 7 shows photographs of the reaction as captured on a digital video camera at 30 frames per second. Not shown are two intermediate frames of the reaction in which the extreme intensity of the light from the reaction saturated the camera, thereby producing no image. Figure 8 shows photographs of the MGP before and after the chip-scale reaction. After the reaction, all the gold on the alumina substrate, the surrounding area of the package cavity, and the wirebonds had melted and most of the package cavity was filled with the reaction byproducts – solidified iron and gold, and aluminum oxide. Shock waves generated from the reaction scattered some of the powder on the periphery of the chip, thus the package cavity also contained some unreacted thermite. Due to the small amount of thermite used – comparable to the weight of the MGP itself (which is ~ 0.2 milligrams) - the MGP remained intact and operational following the reaction. Therefore, for chip-scale reactions the thermal shock resistance and high-temperature stability of the MGP have been proven in operation, and the possibility of harnessing thermite reactions for MEMS-scale applications has been demonstrated.

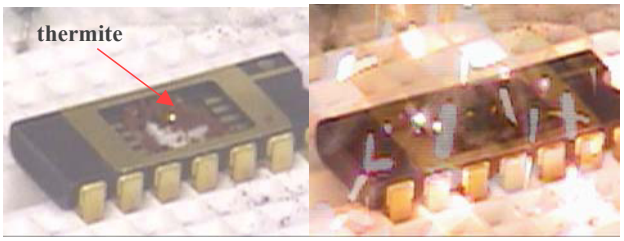

Figure 7. Chip-scale thermite reaction initiated by Micro Glow Plug. (a) MGP starting to glow, (b) ignition! The sequence took about 200 msec.

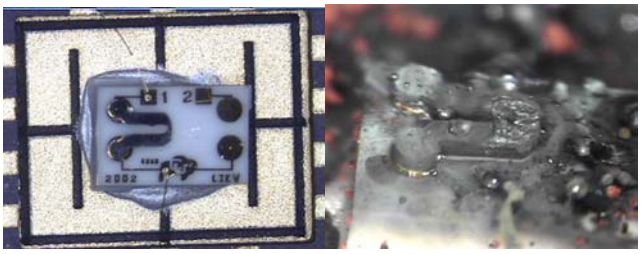

Figure 8. Micro Glow Plug before and after chip-scale reaction.

The MGP was then used to ignite 5 grams of thermite. This is 1000 times as much thermite as was used in the chip-scale reaction, and 25,000 times the mass of the MGP itself. Wires were soldered to the pins on the ceramic package, and the package was placed within a beaker (both glass and plastic beakers were used) and buried in the thermite. Due to the self-propagating nature of

the thermite reaction, a single MGP operating at 25 mA was able to fully ignite all of the thermite, completely engulfing the ceramic package in molten iron. Figure 9 shows video stills of the reaction in the plastic beaker. There was no trace of the MGP or the ceramic package following this reaction. The MGP could have decomposed, been obscured by the molten slag, or been flung some distance from the reaction site by the pressure generated by the reaction (see Figure 10). Figure 10 is a video still showing the extent of the reaction within a 30-mL glass beaker initiated by a single MGP. (Not shown are subsequent video stills in which the glass beaker and then the aluminum plate on which it was placed shattered from the extreme thermal shock.)

Figure 9. Micro Glow Plug igniting 5 grams of thermite in a plastic beaker.

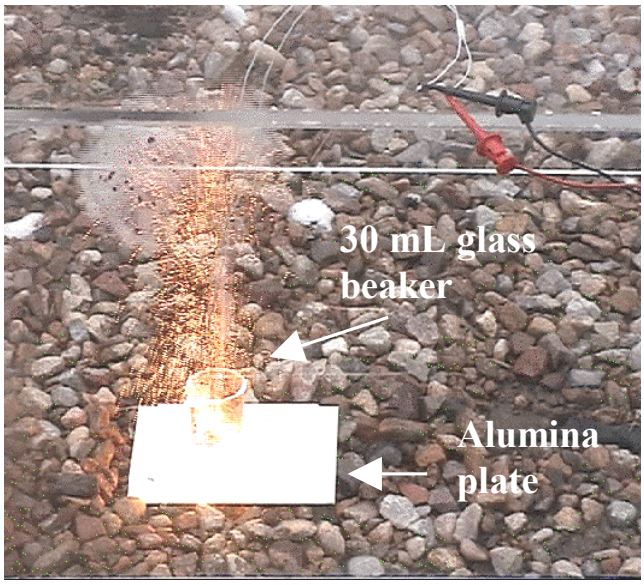

Figure 10. Larger view of thermite reaction within a glass beaker.

Therefore, the thermite experiments demonstrate the successful use of the MGP as a high-temperature igniter, at both the chip-scale and at the macro-scale. In the macro-scale experiments the MGP successfully ignited thermite 25,000 times its own mass – indicating its applicability to conventional diesel engine applications - but was then destroyed/engulfed by the reaction it initiated; however, in the chip-scale reaction where the amount of thermite used was only ten times the mass of the device itself, the MGP remained intact and functional following the reaction, suggesting the potential of harnessing the power of thermite-type reactions for micro-scale applications such as in micro thrusters.

This device therefore offers benefits to an application outside of the current MEMS industry (ignition in diesel engines), as well as enabling the integration of high-ignition temperature explosives into new MEMS-scale applications.

SUMMARY AND CONCLUSIONS

A Micro Glow Plug was designed and fabricated from polymer-derived SiCN ceramic. As summarized in Table 1, the MGP exhibits lower power consumption, faster response and less manufacturing complexity compared to conventional glow plugs while achieving the same operating temperature. The MGP was successfully used to ignite thermite (ignition temperature 1200 ^{o}C) in chip-scale and macro-scale reactions. This device therefore represents a new class of harsh environment micro devices that have the potential to penetrate markets previously untouched by MEMS.

	Conventional Glow Plugs	**SiCN Micro Glow Plug**
Size	Length 30-50 mm	Length 1.1 mm
Temperature	1200 ^{o}C	1200 ^{o}C
Power Consumption	100 Watts	3 Watts
Response Time	5-10 seconds	< 1 second
Fabrication Complexity	3 materials 3 processes	1 material 1 process

Table 1. Comparison between conventional glow plugs and SiCN Micro Glow Plug.

ACKNOWLEDGEMENTS

This work is sponsored by the Defense Advanced Research Projects Agency (DARPA) and U.S. Air Force under contract #F30602-99-2-0543. The authors would also like to thank Dr. R.A. Saravanan, Mr. Chris Yakacki, Ms. Samantha Watson and Mr. Seth Frader-Thompson (University of Colorado, Dept. of Mechanical Engineering) for valuable assistance in various aspects of this work.

REFERENCES

[1] M.L. Willi, B.G. Richards, "Design and Development of a Direct Injected, Glow Plug Ignition-Assisted, Natural Gas Engine," *Journal of Engineering For Gas Turbines and Power-Transactions of the ASME* 117 Vol. 4, pp. 799-803, 1995.

[2] L. An, R. Riedel, C. Konetschny, H.-J. Kleebe, R. Raj, , "Newtonian Viscosity of Amorphous Silicon Carbonitride at High Temperature*," Journal of the American Ceramic Society*, Vol. 81, pp. 1349 – 52, 1998

[3] L.A. Liew, Y. Liu, R. Luo, T. Cross, L. An, V. M. Bright, M. L. Dunn, J. W. Daily and R. Raj, "Fabrication of SiCN MEMS By Photopolymerization of Pre-Ceramic Polymer," *Sensors and Actuators*, vol. A-95, no. 2-3, pp. 120-134, 2002.

[4] L.A. Liew, V.M. Bright, M.L. Dunn, J.W. Daily and R. Raj, "Development of SiCN Ceramic Thermal Actuators*," Proceedings of the 15th Annual International Conference on Micro Electromechanical Systems (MEMS2002)*, pp. 590-593, Las Vegas, Nevada, Jan 20-24, 2002.

[5] A. C. Davies, The Science and Practice of Welding , 8th ed. Cambridge University Press, New York, 1984.

LARGE-AREA ELECTROSTATIC-VALVED SKINS FOR ADAPTIVE FLOW CONTROL ON ORNITHOPTER WINGS

Matthieu Liger, Nick Pornsin-Sirirak, Yu-Chong Tai
Caltech Micromachining Laboratory
Electrical Engineering Department, California Institute of Technology
Pasadena, CA 91125
Steve Ho and Chih-Ming Ho
Mechanical and Aerospace Engineering
University of California
Los Angeles, CA 90095

ABSTRACT

This paper presents the design and fabrication of wafer-sized parylene skins with integrated electrostatic valves used for real-time adaptive airflow control on ornithopter wings. For the first time, we report successful aerodynamic control in both lift and thrust using MEMS **active-valved** wings. By distributing electrostatic valves, the pressure distribution on the wings can be controlled during flapping. The valved wings were tested in a low-speed wind tunnel to measure influence on aerodynamic performance. It was found the lift and thrust generated by the wings in flapping motion can increase by 18% when the valves are actuated.

INTRODUCTION

In a previous study in our group, MEMS-technology parylene wings with titanium alloy were fabricated and tested in flapping motion in a low-speed wind tunnel [1]. Aerodynamic study of the flapping-flight shows that performance is highly dependent on the formation of the unsteady leading-edge vortex. Therefore, pressure distribution control on the wings can be used to achieve optimal aerodynamic performance. Distributed valve actuators on the wings can provide such control. This concept is illustrated in Figure 1. In order to be integrated on flexible parylene MEMS wings, these valve actuators need to be light and flexible as well. Thus, we developed a wafer-sized parylene actuator "skins" technology. In [2] we used that technology to demonstrate that the performance of flapping flight can be greatly increased by integrating "passive" check-valves onto the parylene wings. The ultimate goal in our study, hence this work is to fabricate active valved-skins to dynamically control the wing's pressure loading. In this paper, we present a flexible electrostatic valved-skin using parylene technology. Aerodynamic test results of valved-wings will be discussed, as well as encountered challenges and possible future work.

DESIGN AND FABRICATION

The design and process-flow of the electrostatic valved-skins is based on a low-temperature multi-layer parylene technology incorporating metal electrodes. The skins are made of 4 parylene layers with sandwiched metal electrodes between the first and second layers and between the third and fourth layers. The valves feature 500μm diameter vent-holes that can be closed by tethered valve caps. The vent-holes are 1.28mm apart from each other.. Square-shaped valve caps were used in order to maximize the electrostatic actuation area. The square caps are 1.02mm long. When no voltage is applied between the top and bottom electrodes, the valves act like passive check-valves. When the pressure on the upper side of the valve is higher than the pressure on the bottom side, the differential pressure pushes the cap down to close the vent-hole. Therefore, the non-actuated valve is a pneumatic equivalent of a diode, allowing airflow in one direction only. The minimum pressure required to close the valves in that mode was calculated to be about 1Pa. On the other hand, when voltage is applied between the top and bottom electrodes, the generated electrostatic pressure pulls the valve cap, thus closing the vent-hole regardless of the differential pressure between the top and bottom sides. A 4-inches wafer-sized skin contains 107 dies, and each dies contains 5x5 valves. Figure 2 shows the fabrication process flow. We start the process by spinning an AZ4400 photoresist sacrificial layer, approximately 3μm thick. To avoid having solvent bubbles during the subsequent thermal cycles of the process, this photoresist layer needs to be hardbaked at 120°C for 45 minutes on a hot plate. Then a 1000Å-thick aluminum layer is evaporated. This layer will be used as an etch-stop during the first etching of parylene, to avoid damaging the sacrificial layer. The first layer of parylene-C is then deposited with a thickness of 4μm. To enhance adhesion of the next metal layer, the parylene surface is roughened with low-power oxygen plasma. The bottom

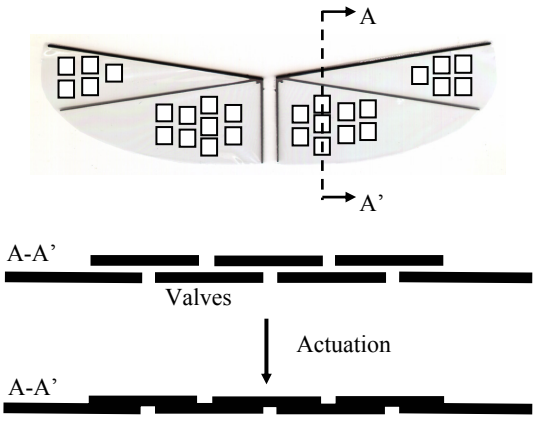

Figure 1: ***Integrated actuator MEMS wings concept***

Travel support has been generously provided by the Transducers Research Foundation and by the DARPA MEMS and DARPA BioFlips programs

Chrome/Gold/Chrome is then evaporated (100Å/ /1500Å/100Å). Chrome is used as a buffer layer between parylene and gold to enhance adhesion. After patterning the bottom electrode, the surface is treated with a 5% A-174 silane solution to improve adhesion between the top chrome and the next parylene. The second layer of parylene (2µm) is then deposited, providing electrical insulation of the bottom electrode (a). A 3500Å amorphous silicon layer sputtering follows the parylene deposition. This silicon layer is used for anti-stiction purposes [3]. The silicon is patterned a first time and is used as a mask to etch the vent hole into the first and second parylene layers. Parylene etching is done by oxygen plasma. The silicon is then patterned a second time to its final shape (b). A 9µm-thick AZ4620 photoresist sacrificial layer is then spun and patterned (c). The third parylene layer (2µm), top electrode (Cr/Au/Cr: 100Å/1500Å/100Å), and fourth parylene (4µm) are deposited and patterned (d). The photoresist sacrificial layers are then released in acetone using an ultrasonic bath. The photoresist release is immediately followed by a SAM elf-Assembled Monolayer) coating (e) [4]. This coating makes the parylene surfaces more hydrophobic, increasing the contact angle from 78° to 120° [5]. The samples are then rinsed and dried. At this point of the process some of the valves caps are stuck on the bottom parylene layer (e) due to meniscus force and the low Young's modulus of Parylene (about 4.5GPa). A BrF3 gas is used to etch away the amorphous silicon layer [6], thus releasing the stuck caps (f). The wafer-sized skin is then cut from the wafer (which was unaffected by the whole process and can used for a subsequent run). Figure 3 shows a fabricated skin (4" diameter).

Several challenges had to be overcome during the development of the fabrication process. First, due to the arge difference in linear thermal expansion coefficients of silicon and parylene ($2.6*10^{-6}$ and $3.5*10^{-5}$ K^{-1} respectively) the sputtered silicon film has compressive stress, resulting in wrinkles. To reduce this problem the parylene surface is roughened in low-power oxygen plasma and annealed in a convection oven at 110°C for 15 minutes. Lower sputtering power was also found to reduce the compressive stress in the film. Another critical step is the thick sacrificial photoresist layer. The AZ4620 layer has to cover the step made by the vent-hole otherwise the second and the third parylene layers will fuse together and prevent the valves from opening. Finally, another

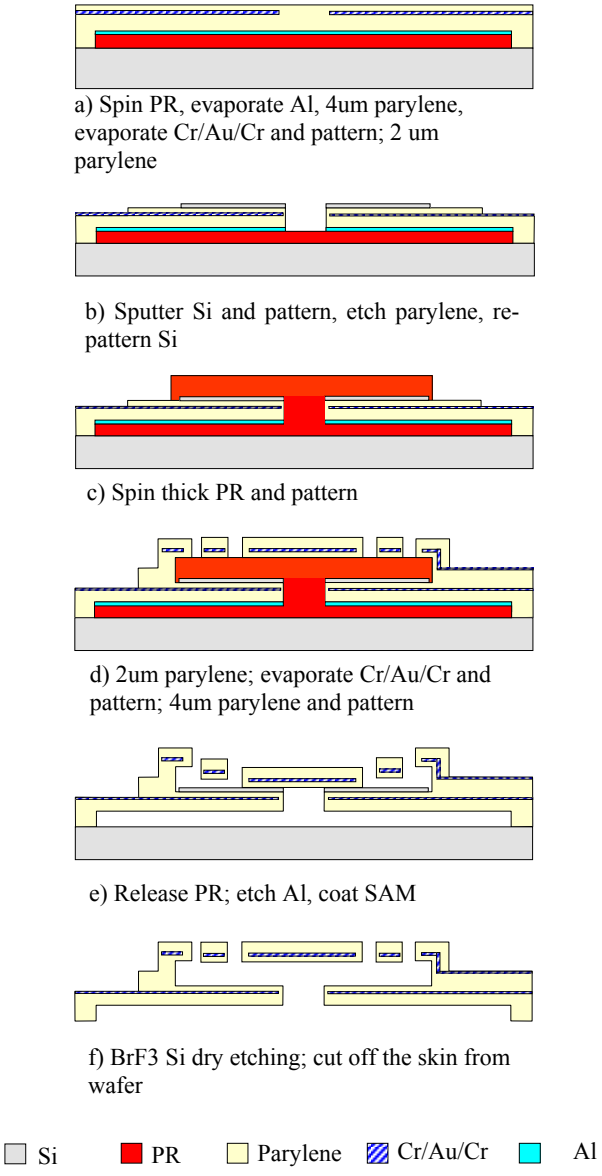

Figure 2: ***Process Flow***

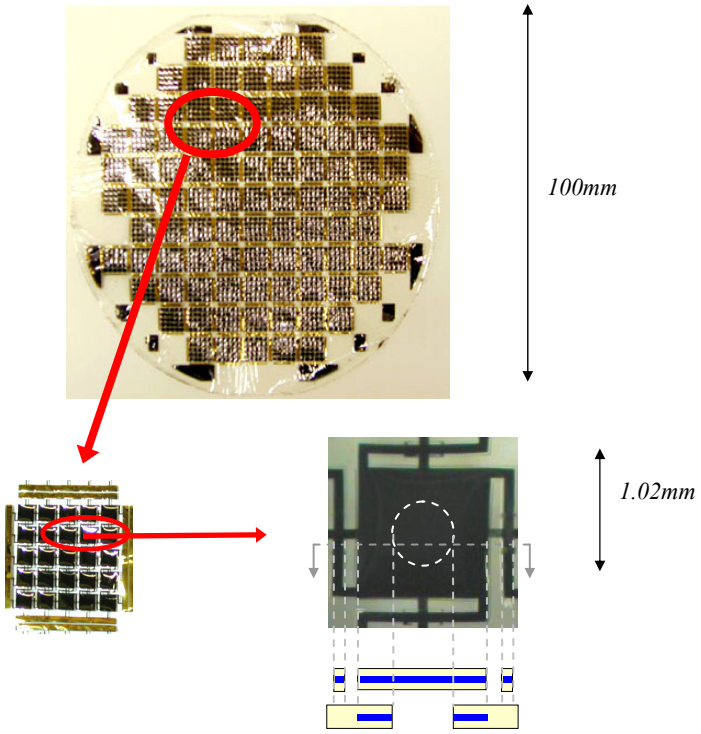

Figure 3: ***Fabricated Skin, Die close-up and valve close-up***

Electrostatic Valve Actuators

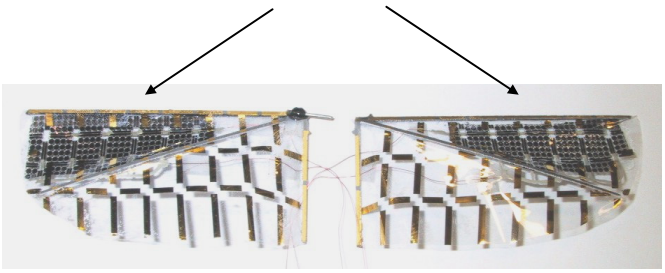

Figure 4: ***MEMS valved-wing***

processing challenge appeared when etching thick (>5μm) layers of parylene. A black residue of unknown composition tends to be formed on the parylene surface preventing further etching. Reducing the pressure of oxygen (from 400mT to 200mT) can solve this problem.

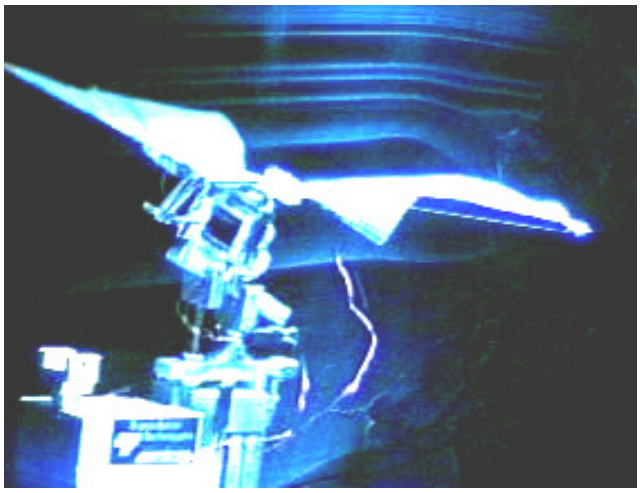

*Figure **5: Wind-Tunnel Testing***

RESULTS AND DISCUSSION

First, actuation tests of the valves were performed under microscope. The pull-in voltage was measured to be around 200V. This is much more than what is expected from a simple theoretical calculation. Several phenomena might be responsible for this. The effective gap is greater than the designed gap, which is given by the AZ4620 layer thickness (8μm). This is due to the flexibility of the skin, which cannot be made perfectly flat. Moreover, stresses in the top electrode results in curling of the valve caps and tethers. Another explanation for this high pull-in voltage could be charging effects in the parylene layers reducing the effective electric field [7].

The valves were tested in a load deflection setup. It was observed that with an applied voltage of 200V, the valves can withstand a differential pressure of 2kPa while keeping the vent-holes sealed.

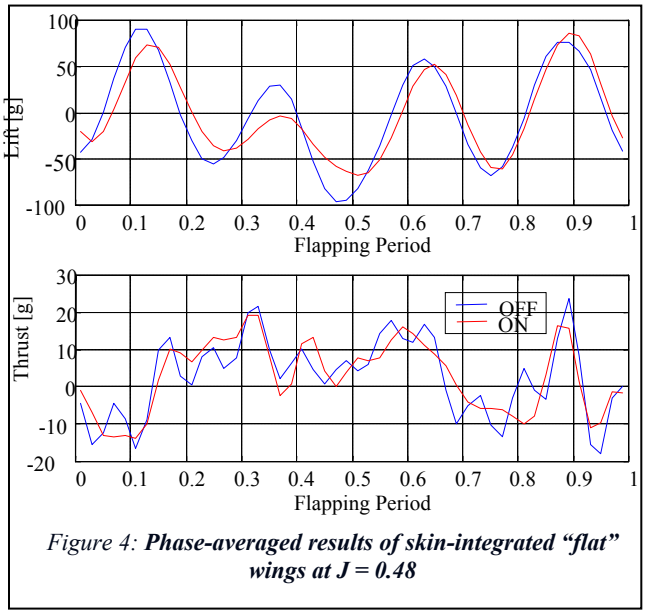

*Figure 4: **Phase-averaged results of skin-integrated "flat" wings at J = 0.48***

This is much greater than the pressure loading during flapping which is on the order of 40 Pa The parylene active valves were then integrated onto parylene MEMS wings (about 80 valves per wing) and tested in a low-speed wind tunnel (0-10m/s). The wings were flapped at 20Hz by an electric motor while load cells connected to the transmission measure instantaneous lift and thrust. The lift and thrust are piled-up over one single flapping

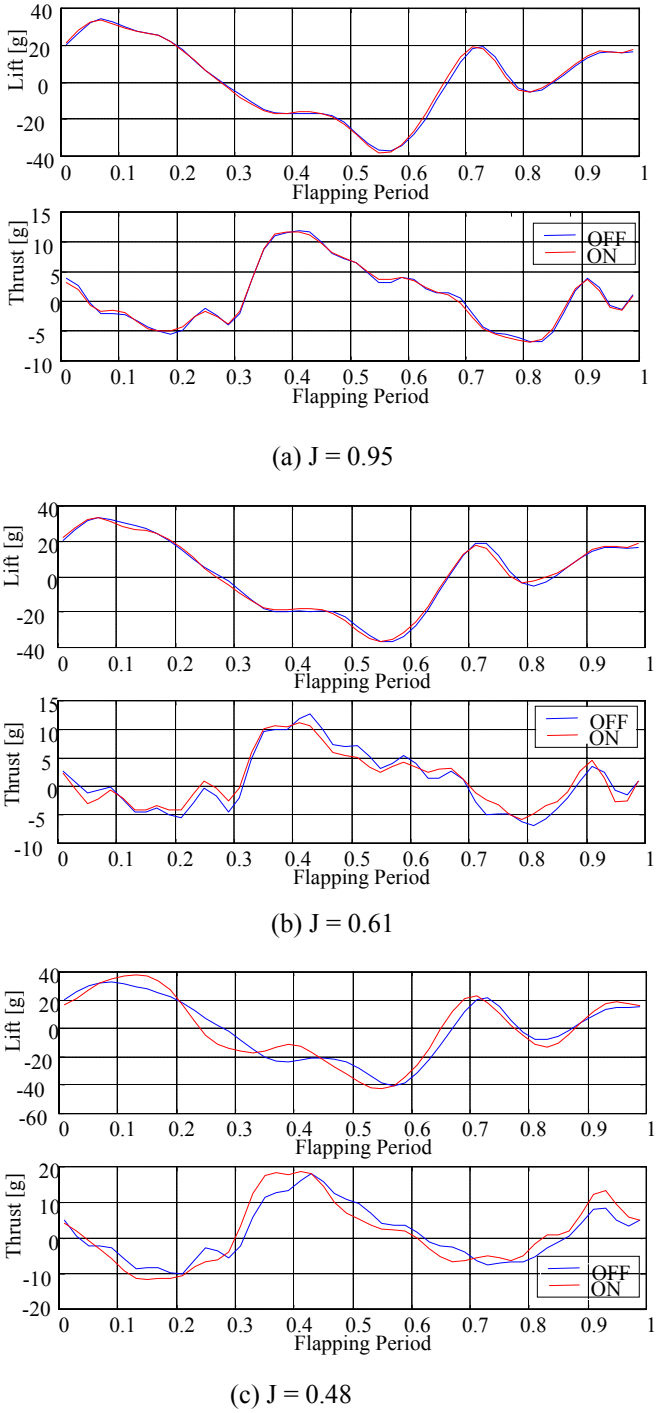

*Figure 5: **Phase-averaged results of skin-integrated "cambered" wings at various advance ratios.** Note that aerodynamic effect is bigger for smaller J*

	ON	OFF
Lift [g]	-1.21	-1.42
Thrust [g]	2.69	2.54

*Table **1: Time-averaged lift and thrust of skin-integrated "flat" wings at J = 0.48***

	ON	OFF
J = 0.48	0.14	-0.01
J = 0.61	0.99	0.94
J = 0.95	1.43	1.42

(a) Lift [g]

	ON	OFF
J = 0.48	1.17	1.00
J = 0.61	1.04	0.88
J = 0.95	0.76	0.80

(b) Thrust [g]

*Table 2: **Time-averaged lift and thrust of skin-integrated "cambered" wings at various advance ratios***

cycle, giving a phase-averaged history. Tests were performed under different advance ratios, angles of attack, and wind speeds. The advance ratio J is a dimensionless number to indicate the unsteadiness of airflow and is given by:

$$J = \frac{U}{2\Phi fb}$$

where U, □, f, and b are wind speed, stroke angle, flapping frequency, and wing length (half wingspan), respectively. J>1 indicates an steady regime whereas J<1 indicates an unsteady regime. We also investigated the effect of the camber of the wings. Figures 4 and 5 show the phase-averaged lift and thrust histories for flat and cambered wings, with several advance ratios, and with the actuators turned ON and OFF. Tables 1 and 2 give the time-averaged values of lift and thrust for flat and cambered wings with actuators turned ON and OFF. The given time-averaged values are obtained by integrating the phase-averaged history over the whole cycle. As can be seen, in every configuration the time-averaged lift and thrust are increased when the actuators are turned on. It is also observed that the effect of the active-valves is greater for more unsteady airflow regime (i.e. lower values of J). This result was expected because, as explained before, the aerodynamic performances of flapping flight arise from unsteady effects. It is clear that consistent control results have been achieved when the actuators were switched between ON and OFF states. Up to 18% of lift and thrust can be gained by actuating the valves when J=0.45. Finally, it can be noticed that the valves' effect is more pronounced for cambered wings than for flat wings.

CONCLUSIONS

We have used our parylene actuators-skin technology to successfully demonstrate the effect of integrated active microvalves on aerodynamic performance of MEMS wings in flapping motion. When used in unsteady airflow regime, the active valves can increase the time-averaged values of lift and thrust by 18%. Future work includes selective actuation of the valves and sensors integration on the skins.

ACKNOWLEDGEMENTS

This project is supported by DARPA (DABT63-98-C-0005) and the NSF Engineering Research Center at Caltech. Travel support has been generously provided by the Transducers Research Foundation and by the DARPA MEMS and DARPA BioFlips programs.

REFERENCES

[1] T. N. Pornsin-Sirirak, S.W. Lee, H. Nassef, J. Grasmeyer, Y.-C. Tai, C. -M. Ho, M. Keennon, "MEMS Wing Technology for a Battery-Powered Ornithopter," *Proceedings of the 13th IEEE International Conference on MEMS (MEMS'00)*, Miyazaki, Japan, Jan. 23-27, 2000, pp. 799-804.

[2] T. Nick Pornsin-Sirirak, M. Liger, Y.-C. Tai, S. Ho, C.-M. Ho, " Flexible Parylene-Valved Skin for Adaptive Flow Control," *," Proceedings of the 15th IEEE International Conference on MEMS (MEMS '02)*, Las Vegas, U.S.A., Jan 20-24, 2001, pp101-104

[3] T. J. Yao, X. Yang, and Y. -C. Tai, "BrF_3 Dry Release Technology for Large Freestanding Parylene MEMS," *Digest of Technical Papers of the 11th International Conference on Solid-State Sensors and Actuators (Transducers '01)*, Munich, Germany, June 10-14, 2001, pp. 652-655.

[4] R. Maboudian, "Self-Assembled Monolayers as Anti-Stiction Coatings for Surface Microstructures," *Digest of Technical Papers, The 10th International Conference on Solid-State Sensors and Actuators (Transducer'99),* Vol 1, Sendai, Japan, June 7-10, 1999, pp. 22-25.

[5] T. Nick Pornsin-Sirirak, "*Parylene MEMS Technology*", PhD Thesis, California Institute of Technology, 2002, pp 114.

[6] X. Q. Wang, X. Yang, K. Walsh, and Y. C. Tai, "Gas-Phase Silicon Etching with Bromine Trofluoride," *Digest of Technical Papers, The 9th International Conference on Solid-State Sensors and Actuators (Transducers '97)*, Vol. 2, Chicago, IL, June 16-19, 1997, pp. 1505-1508.

[7] T.J. Yao, K. Walsh and Y.C. Tai,"Dielectrics Charging Effects on Parylene Electrostatic Actuators" *Proceedings of the 15th IEEE International Conference on MEMS (MEMS '02)*, Las Vegas, USA, Jan. 20-24 2002, pp 614-617.

A HIGH-POWER MEMS ELECTRIC INDUCTION MOTOR

Carol Livermore, Anthony Forte, Theodore Lyszczarz, Stephen D. Umans, Jeffrey H. Lang
Department of Electrical Engineering and Computer Science, Microsystems Technology Laboratories, and Lincoln Laboratory
Massachusetts Institute of Technology
Cambridge, MA 02139

ABSTRACT

An electric induction micromotor was designed and built for high-power operation. Operated at partial actuating voltage, the motor has demonstrated an air gap power in excess of 20 mW and torque of 3.5 μNm at speeds in excess of 55,000 rpm. The device builds on an earlier micromotor demonstrated by Frechette *et al.* [**1**]. The high power of the present motor is enabled by its low-loss, high voltage electrical stator, which also offers improved efficiency. The development of this electromechanical device is an important enabling step not only for Watt-scale micromotors, but also for the development of micro electrical generators. This paper presents the motor's design, the fabrication process that was created to meet its stringent design requirements, and its performance to date.

INTRODUCTION

Applications for Power MEMS range from generating portable electrical power, to propelling micro-scale vehicles, to driving miniature devices like pumps or fans. However, the substantial power handling potential of such devices is accompanied by substantial challenges in their development. High power also implies high levels of other characteristics, such as voltages, currents, temperatures, frequencies, or speeds.

A team at MIT is developing a family of Power MEMS devices for applications like those described above [**2**]. The device described here is an electric induction micromotor designed to convert electrical power into mechanical power at the Watt level. To function at these power levels, the motor is designed to operate at high voltages (about 300 V), high electrical frequencies (a few MHz), and high rotational speeds (greater than 1 Mrpm). These same design requirements, coupled with low electrical losses, would enable a micro-scale electrical generator. The purpose of the present work is to demonstrate that a micro-scale machine can be designed and fabricated to meet these specifications, and to characterize its performance over a range of operating conditions.

DEVICE DESIGN

The motor's actuating principle is electric induction, which is illustrated in Figure 1. The motor has two fundamental components, a spinning rotor disk and a fixed stator plate. Covering the stator surface is an array of radial electrodes, arranged like spokes on a wheel, which are excited with ac voltages to create a traveling wave of potential along the stator surface. Facing the stator is the spinning rotor, which is coated with a thin film of a poorly conducting material. The stator and rotor are separated by a 3 μm air gap. The electric potential on the stator induces image charges in the rotor film. As the stator excitation travels along, the image charges follow, conducting through the rotor film. By design, the conductivity of the rotor film is low enough that the rotor charges lag behind the stator excitation. This generates a tangential electric field that pulls on the rotor charges to create a torque, thereby converting electrical power into mechanical power. Further description and models of electric induction machines may be found in [3] and [4]. A micro-scale electric induction motor has the potential to operate at higher power density than would a macro-scale electric machine because the small gap between rotor and stator can sustain higher electric fields without electrical breakdown than could a larger gap.

The motor's rotor and actuating mechanism are integrated into a micromachined silicon static structure. The complete motor comprises a stack of five silicon wafers; a schematic cross-section of the device is shown in Figure 2. Two of the wafers are patterned with thick and thin films to create the motor's actuating elements, the electrical stator and the electrical rotor. The electrical stator is a planar array of 786 radial electrodes wired into six phases by a separate layer of interconnections, forming 131 pole pairs. On the side of the rotor facing the stator, the spinning rotor disk houses a thin layer of moderately boron-doped polysilicon, which serves as the rotor film. The back side houses a set of turbine blades; these can be driven with compressed air to characterize the rotational performance of the device in the absence of electrical excitation. In related applications, blades could form the working part of a compressor or pump, or turbine blades could drive rotation of the disk for electrical power generation. The wafers are deep-etched to define the freely moving, 4.2 mm diameter, 550 μm thick rotor, along with its system of supporting gas bearings and auxiliary fluid systems. In operation, the rotor is supported both axially and in-plane on films of externally pressurized air that are injected into narrow gaps between the rotating and stationary components. Such bearings have previously been demonstrated to support rotation of a similar microdevice at speeds well over 1 Mrpm [**5**].

Achieving high-power, low-loss motor performance depends on maximizing the capacity to convert electrical power to mechanical power and maximizing efficiency. Analytical system modeling was used to examine the tradeoffs among operating point, conversion capacity, ease of fabrication, and losses in the device and electronics. The results show that minimizing stray capacitance between the electrical components and the substrate is critical both for power conversion capacity and to minimize electrical losses. To meet this requirement, the design calls for

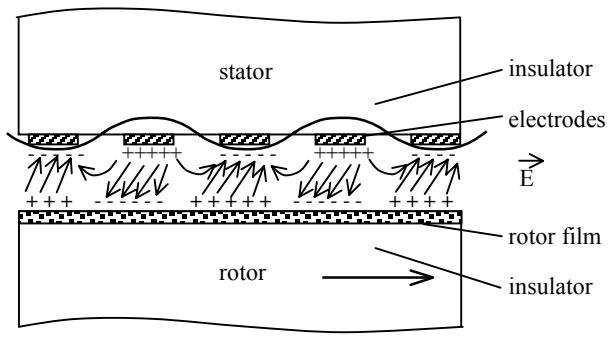

Figure 1. *Schematic diagram of motor operation. A traveling wave of potential on the stator electrodes induces image charges in the rotor film; the resulting tangential electric field spins the rotor.*

0-9640024-4-2/hh2002/$20©2002TRF
DOI 10.31438/trf.hh2002.63

Solid-State Sensors, Actuators, and Microsystems Workshop
Hilton Head Island, South Carolina, June 2-6, 2002

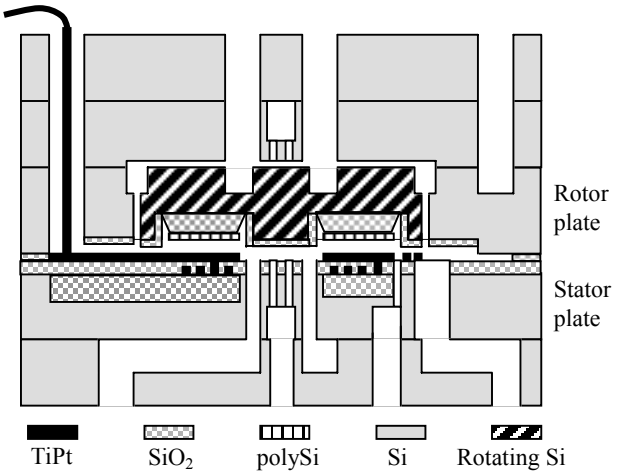

Figure 2. *Cross-sectional schematic diagram of motor showing its five constituent through-etched wafers. Also shown is the integration of the electrical stator and rotor into the stack.*

electrical insulating layers that are tens of micrometers thick. The thick insulators reduce parasitic capacitance and the losses associated with reactive power flowing through them. However, depositing and patterning such films complicates fabrication and makes wafer bonding more difficult. Second, modeling shows that it is imperative to be able to sustain high electric fields of about 10^8 V/m at high frequencies between components separated by several micrometers without suffering electrical breakdown. The higher design frequencies enable higher power, and output power increases as the square of the operating voltage. However, this demands cleanliness and smooth line edges on the electrical stator; defects contribute to early failure from electrical breakdown. In addition, the electrodes and interconnects must be fabricated of a low-resistivity metal to minimize resistive electrical losses. This requirement must be balanced against the thermal and chemical stability that the microfabrication process demands.

FABRICATION

The rotor and fluid flow paths are defined in the device's five constituent silicon wafers by double-sided, aligned deep reactive ion etching. This portion of the fabrication is similar to the process described in [**5**]. Figure 3 shows a photograph of dies from each of the five wafer levels; only four dies are visible because two of the levels are already wafer bonded together. The device is designed to use fusion bonding for the final assembly. However, the device described here was instead assembled at the die level by clamping the individual dies together in an aluminum/acrylic package. The o-rings that create sealed fluidic connections between the outer ports of the device and the inner surface of the package also provide compression to minimize leakage between plates. This provides an experimental advantage: the device can be disassembled for inspection, cleaning, or to perform diagnostics.

The design requirements of low losses and high electrical fields primarily impact the fabrication of the electrical rotor and the electrical stator. While the rotor fabrication process is similar to that used in [**1**], the stator fabrication process is significantly different. For this reason, the emphasis here will be on the stator fabrication process.

Both stator and rotor elements are fabricated on 10 to 20 µm thick oxide layers to minimize stray capacitance of the electrical elements to the substrate. To minimize wafer bow while maintaining a planar wafer surface, the thick oxide layers are limited to isolated oxide islands that are embedded in the silicon substrate. A cross-section of an embedded oxide island in the stator is shown in Figure 4A. The island concept has been demonstrated previously [**6**], but in the present stator, the islands are fabricated by a different and direct technique. Thick oxides are deposited in etched recesses in a silicon substrate using a liftoff process, producing a nearly planar oxide surface. To achieve this, 20 µm deep pits are first etched in the silicon substrate. An aluminum layer with micrometer-scale thickness is deposited and patterned to cover the upper silicon surface but not inside the pits; this serves as the sacrificial layer for the liftoff step. Next, 20 µm of TEOS is deposited over the wafer surface. Liftoff is accomplished by a prolonged HCl etch; the field oxide breaks off neatly, leaving micrometer-scale stubs at the pit edges. If necessary, the stubs may then be minimized by CMP.

The stator electrodes and interconnections are fabricated as two interconnected 0.3 µm thick platinum levels with titanium adhesion layers. Each stator electrode is 900 µm long, tapers from 11 µm to 4 µm wide, and is separated from its neighboring electrodes by just 4 µm. The two platinum layers are fabricated by a liftoff process on top of the thick oxide islands in the silicon substrate, as shown in Figure 4. The upper platinum layer forms the stator's electrodes; a separate underlying layer of platinum interconnection rings groups the electrodes into six phases. The electrodes and interconnects are separated by a 1 µm thick layer of TEOS oxide. Electrical contact between the two layers is established by via contacts etched in the interlayer oxide. The low resistivity of the platinum electrodes and interconnects helps to minimize electrical losses. In addition, their very smooth, lifted-off edges have been experimentally demonstrated to consistently resist electrical breakdown up to the design point of nearly 10^8 V/m at MHz frequencies.

EXPERIMENTAL RESULTS

The motor's performance is characterized as a function of stator excitation voltage and frequency. The hydrostatic gas bearings are first pressurized to float the rotor on a film of air; the stator is then excited with a traveling wave of electric potential to actuate the motor. A fiber optic sensor is inserted into a port in the device to monitor the passage of deep-etched features on the rotor. A spectrum analyzer processes the sensor's output to yield the motor's rotational speed. The motor operates at no load; its speed

Figure 3. *Fabricated die levels of the micro-motor. The electrical stator is second from the left, and both sides of the rotor are shown below.*

is set by the balance between the motor's actuating torque and the viscous drag on the spinning rotor. The viscous torque is measured as a function of rotational speed. The motor's torque and power are then extracted from the measured rotational speed using the experimentally determined load line.

The motor's load line is measured by abruptly removing the stator excitation and monitoring the rotor's deceleration with the optical speed sensor. From these data and the known rotor inertia, we can extract the decelerating viscous torque. This yields a fixed viscous torque constant of $(5.6 \pm 1) \times 10^{-4}$ μN·m·s plus a constant 0.2 ± 0.01 μN·m component of the torque that reflects mechanical rubbing of a piece of debris in one of the thrust bearings.

Figure 5 plots the motor's torque and power measured as a function of electrical frequency for a fixed stator excitation voltage of 45 V_{peak}. The solid lines are fits of a model [**3**,**4**] to the data, with the rotor film conductivity and motor gap as adjustable parameters. The measured torque and power both peak at about

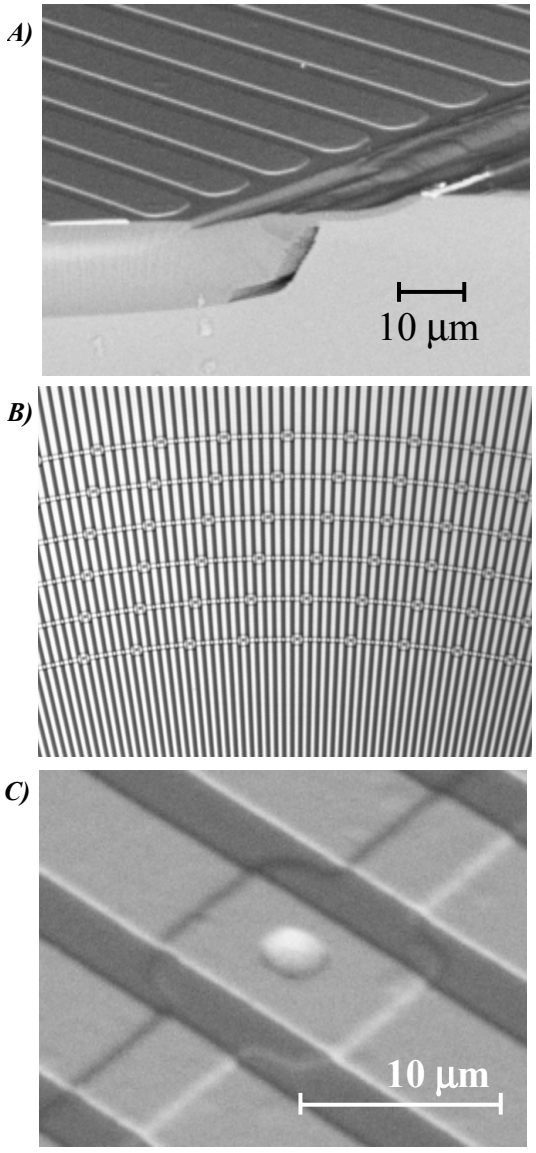

Figure 4. *A) SEM micrograph of stator cross-section, showing electrodes on a recessed oxide island. B) Optical micrograph of the stator structure, showing electrodes connected by interconnection rings. C) SEM micrograph of electrodes and interconnection ring, connected by an electrical via.*

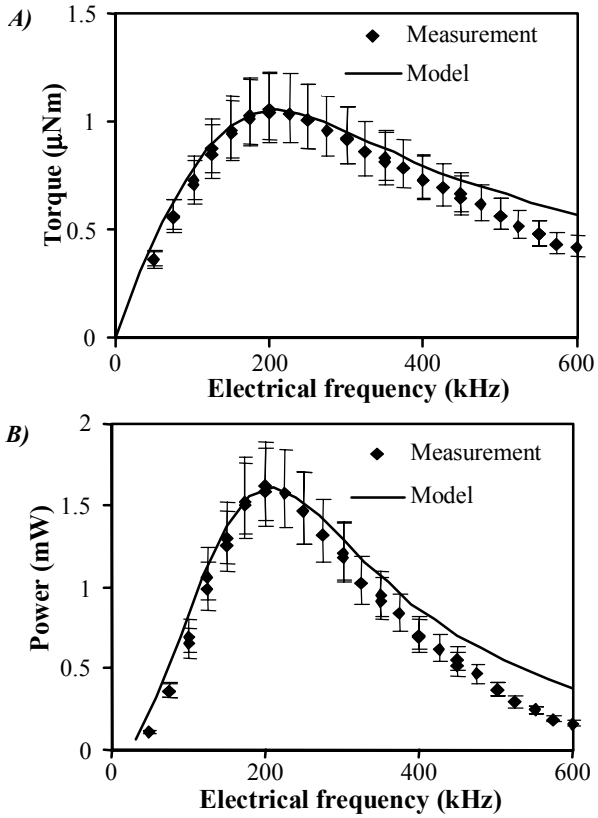

Figure 5. *A) Measured motor torque and B) measured motor power as a function of electrical excitation frequency at a fixed stator excitation voltage of 45 V.*

200 kHz. The peak frequency reflects the resistivity of the moderately doped polysilicon film on the rotor surface, and corresponds to a rotor film sheet conductance of 1.2 nS/square. This is lower than the target conductance of 3 nS/square for this device and likely reflects the omission of high temperature wafer bonding anneals that would promote grain growth in the polysilicon film. The film resistivity impacts the device's maximum possible power output; optimal power is obtained when the rotor film resistivity is well matched to a MHz-range operating frequency.

The peak amplitudes of the measured torque and power reflect the gap between the rotor and stator; more power is converted across a smaller air gap. The data correspond to a motor gap of 1.85 μm. This is smaller than the design value of 3 μm, enabling more power, and it is consistent with the as-fabricated device geometry and the measured viscous torque. Using these values for motor gap and rotor film resistivity, measured and predicted values of torque and power match well.

Figure 6 plots the motor's torque and power measured as a function of the amplitude of the actuating voltage at a fixed electrical frequency of 200 kHz. The torque starts to increase quadratically with voltage, as expected; the trend has an inflection point because the rotor speed cannot exceed the relatively low synchronous speed of the stator excitation at 200 kHz. The maximum measured torque is 3.5 μNm at a speed of over 55,000 rpm for an excitation voltage of 95 V_{peak}. The maximum air gap power attained exceeds 20 mW, corresponding to a power density of 16 kW/m^3. The solid line is the device performance calculated from the model using the motor gap and rotor film resistivity

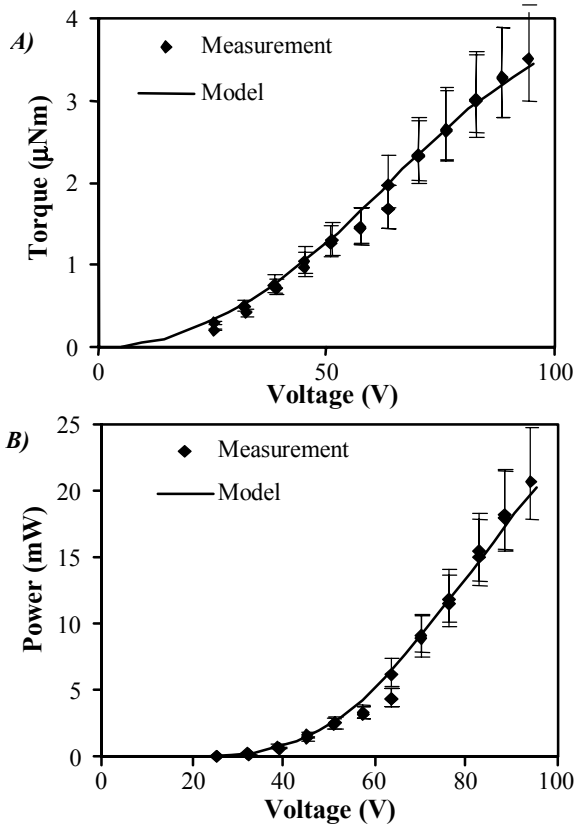

Figure 6. *A) Measured motor torque and B) measured motor power as a function of stator excitation voltage at a fixed stator excitation frequency of 200 kHz.*

determined above. Using the same parameters, the data again agree well with theory.

The maximum actuating voltage in these tests was not limited by electrical breakdown, but rather by the high rotational speeds that are necessary to balance a large actuating torque against viscous drag under no-load operating conditions. In the experiments to date, speed has been limited to ensure an opportunity to characterize devices fully at lower power levels before risking bearing failure or structural damage at higher speeds, which have affected other devices. However, the stators' demonstrated ability to withstand design fields suggests that the motors will be able to attain design voltage and power levels as well.

This micromotor compares well with macro-scale magnetic integral horsepower industrial motors on performance metrics like the shear stress on the rotor and the ratio of this shear stress to the normal pressure. The maximum shear stress attained so far by our electric motors is about 210 N/m^2, at approximately half of the design electric field. If these results are scaled up to full field, as tests on the electrical stators indicate should be possible, the shear stress would be about 800 N/m^2, as compared with about 7,000 N/m^2 for a typical integral horsepower magnetic induction machine [7]. The ratio of shear stress to normal pressure attained in our electric motors so far is about 2%, comparable to the typical magnetic induction machine described above. The micromotor's ability to harness the available energy density in its air gap is comparable to that of a macro-scale magnetic machine.

CONCLUSIONS

An electric induction micromotor designed for high-power operation was fabricated. Operated at partial actuating voltage, the motor demonstrated an air gap power in excess of 20 mW and torque of 3.5 μNm at speeds in excess of 55,000 rpm. This was enabled by the development of low-loss, high-voltage electrical stators, which have been demonstrated to successfully sustain design voltages in experiments. The electrical isolation of stator components from the rest of the device was accomplished by the incorporation of thick islands of oxide that were embedded in the silicon substrate. These islands were formed by a liftoff technique that enabled automatic and nearly complete planarization of the island oxide with the surrounding silicon surface.

ACKNOWLEDGMENTS

We gratefully acknowledge the contributions of A. Ayon, A. Epstein, L. Fréchette, A. Hoelke, P. Maki, S. Nagle, S. Senturia, C. J. Teo, and P. Warren. The devices were fabricated at MIT Lincoln Laboratory and in MIT's Microsystems Technology Laboratories. This work was supported by DARPA TTO, the Army Research Office, and the Army Research Laboratory, managed by Dr. R. Rosenfeld, Dr. T. Doligalski, and Mr. J. Hopkins respectively. The Lincoln Laboratory portion of this work was sponsored by the Defense Advanced Research Project Agency under Air Force Contract F19628-00-C-0002. Opinions, interpretations, conclusions, and recommendations are those of the authors and not necessarily endorsed by the Department of Defense.

REFERENCES

1. L.G. Frechette, S.F. Nagle, R. Ghodssi, S. D. Umans, M.A. Schmidt, J. Lang, "An Electrostatic Induction Micromotor Supported on Gas-Lubricated Bearings*," Technical Digest of the 14th IEEE International Conference on Micro Electro Mechanical Systems*, Interlaken, Switzerland, 1/21-25/01, IEEE (2001), pp. 290-3.

2. A.H. Epstein et al., "Micro-Heat Engines, Gas Turbines, and Rocket Engines – The MIT Microengine Project," AIAA Paper 97-1773*, 28th AIAA Fluid Dynamics Conference*, Snowmass Village, CO, June 29-July 2, 1997.

3. S.F. Bart and J.H. Lang, "An analysis of electroquasistatic induction micromotors," *Sensors and Actuators, 20*, 97 (1989).

4. S.F. Nagle, *Analysis, Design, and Fabrication of an Electric Induction Micromotor for a Micro Gas-Turbine Generator*, Ph.D. Thesis, Massachusetts Institute of Technology, October 2000.

5. L.G. Frechette, S.A. Jacobson, F.F. Ehrich, R. Ghodssi, R. Khanna, C.W. Wong, X. Zhang, K.S. Breuer, M.A. Schmidt, and A.H. Epstein, "Demonstration of a Microfabricated High-Speed Turbine Supported on Gas Bearings", *Technical Digest of the 2000 Solid-State Sensor and Actuator Workshop*, Hilton Head Isl., SC, 6/4-8/00, Transducer Research Foundation, Cleveland (2000), pp. 43-47.

6. R. Ghodssi, L.G. Frechette, S.F. Nagle, X. Zhang, A.A. Ayon, S.D. Senturia, and M.A. Schmidt, "Thick Buried Oxide in Silicon (TBOS): An Integrated Fabrication Technology for Multi-Stack Wafer-Bonded MEMS Processes," *Proceedings of the 10th International Conference on Solid-State Sensors*, Sendai, Japan, June 1999.

7. T.J.E. Miller, *Switched-Reluctance Motors and Their Control*, Oxford University Press (1993).

CLOSED-LOOP CONTROL OF A PARALLEL-PLATE MICROACTUATOR BEYOND THE PULL-IN LIMIT

Michael S.-C. Lu* **and Gary K. Fedder*†**

*Department of Electrical and Computer Engineering and †The Robotics Institute
Carnegie Mellon University, Pittsburgh, PA 15213-3890

ABSTRACT

In this paper, we present a controller design for servoing the position of a parallel-plate electrostatic microactuator beyond its open-loop instability point. Controller design considers nonlinearities from both the parallel-plate actuator and the parallel-plate position sensor, to ensure robust stability within the feedback loop. Desired transient response is achieved by a pre-filter added in front of the feedback loop to shape the input command. The microactuator is characterized by static and dynamic measurements, with a spring constant of 0.17 N/m, mechanical resonant frequency of 12.4 kHz, and effective damping ratio from 0.55 to 0.35 for gaps between 2.3 to 2.65 µm. The minimum input-referred noise capacitance change is measured at a gap of 5.5 µm, corresponding to a minimum input-referred noise displacement of 0.2 nm/√Hz. Results of the servo test show excellent agreement with design specifications (Rise time < 2 ms, overshoot = 0, and settling time < 5 ms) for the intended application as a magnetic probe tip actuator for data storage. Actuator displacement servoed as far as 55% of the gap is measured, which surpasses the static pull-in limit of one-third of the gap.

INTRODUCTION

For many years a well-known yet challenging problem for MEMS researchers interested in electrostatic actuation has been to extend the travel range of parallel-plate type electrostatic microactuators beyond the pull-in instability of one-third of the gap. Several open-loop methods have been proposed, including curved electrode design [**2**], "leveraged bending" method [**3**], and actuator redesign by adding a series feedback capacitance [**4**][**5**] to actuators. Those methods achieve large displacement at the cost of higher actuation voltage. Additional drawbacks of the series capacitor approach include: (1) actuator displacement is limited by parasitic capacitances, and (2) undesirable charge accumulated at the floating high-impedance node between actuated and series capacitances requires constant reset by a switch. Switch turn-off leads to charge injection into the actuated capacitor, which can be destabilizing if actuated capacitance is only several femtofarads. Successful measurements showing displacement as large as 88% and 60% of initial gap have been reported by [**3**] and [**4**], respectively. For applications which require accurate position servo under plant uncertainties and disturbances, closed-loop feedback has been analyzed [**6**]. Yet no measurement of this approach has been reported to the author's knowledge.

Research work presented in this paper originates from development of a probe-based magnetic micro disk drive [**1**] in Carnegie Mellon University. In the envisioned system, arrays of tip actuators are fabricated by a conventional CMOS process with integrated circuits for feedback control and data channels. By the parallel-plate electrostatic servo, actuators are controlled in parallel to the magnetic media atop for data read and write. Each actuator is nonlinear, and becomes unstable as it reaches the pull-in point and beyond. We select design of a linear time-invariant (LTI) controller over a nonlinear or a linear time-varying (LTV) controller for its easier implementation by analog circuits. By linearization, stability analysis is performed in the frequency domain in order to maximize the phase and gain margins.

BLOCK DIAGRAM

The feedback system block diagram is illustrated in Figure 1, which has two transfer functions to be designed. One is the controller, C(s), for achieving robust stability within the loop, and the other is the pre-filter, F(s), which shapes the input command for the feedback loop to achieve desired output performance. The controlled plant consists of the parallel-plate electrostatic actuator and the parallel-plate capacitive position sensor.

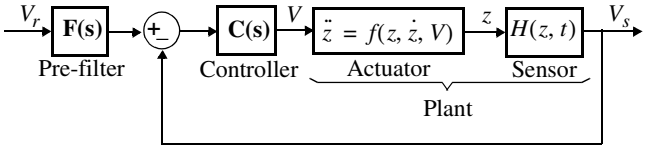

Figure 1. *Two degree-of-freedom feedback system configuration.*

DEVICE FABRICATION

Devices are fabricated by the AMS (Austria Micro System) 0.5 µm three-metal-two-poly CMOS process, followed by post-CMOS micromachining steps described in [**8**]. First, an anisotropic reactive-ion oxide etch (RIE) with CHF_3/O_2 plasma defines the structural sidewalls with the top metal layer used as an etch-resistant mask. The etch rate is 424 Å/min. Next, an deep reactive-ion silicon etch is performed in an inductively-coupled-plasma etcher at an etch rate of 2.9 µm/min. Finally microstructures are released from the substrate by an isotropic silicon etch at 1 µm/min. The process flow is illustrated in Figure 2.

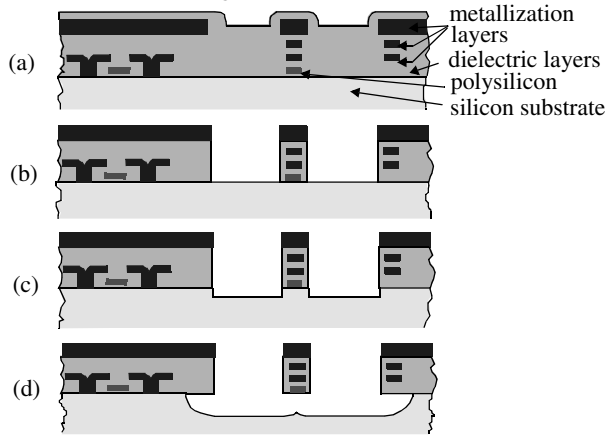

Figure 2. *Cross section of the CMOS-MEMS process flow. (a). After CMOS processing. (b). After anisotropic dielectric reactive-ion etch for definition of structural sidewalls. (c). After anisotropic silicon etch. (d). After isotropic silicon etch for structural release.*

0-9640024-4-2/hh2002/$20©2002TRF
DOI 10.31438/trf.hh2002.64

PLANT

The dynamic equation of a conventional parallel-plate microactuator is described by

$$m\ddot{z} + b\dot{z} + kz = \frac{\varepsilon_o A V^2}{2(g-z)^2} \quad (1)$$

where m is the mass, b is the squeeze-film damping coefficient, k is the spring constant, ε_o is the permittivity of free space, A is the parallel-plate area, and V is the applied voltage. The gap, g, and displacement, z, are defined at the center of the actuated capacitance. A released microactuator is illustrated in Figure 3. It has two anchored springs, which carry actuation and sensing signals individually to avoid feedthrough. An external electrode is placed on top (not shown in the graph) of the actuator to establish the initial gap and the actuated and sensing capacitances. The actuation and sensing plates are mechanically connected, but electrically isolated from each other.

A schematic representation of the entire feedback system is illustrated in Figure 4. The position sensing is achieved by a single-ended capacitive bridge with modulation/demodulation, followed by a low-pass filter to remove the 1x and 2x carrier frequency terms. The sensed output after the low-pass filter is

$$V_s(z) = A_v A_d V_m \left(\frac{C_{s1}(z) + C_{s2}(z)}{C_{s1}(z) + C_{s2}(z) + C_i} - \frac{C_{s1o} + C_{s2o}}{C_{s1o} + C_{s2o} + C_i} \right) \quad (2)$$

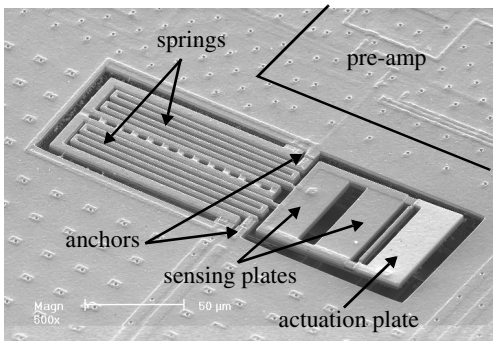

Figure 3. *SEM of the released microactuator fabricated by CMOS-MEMS process.*

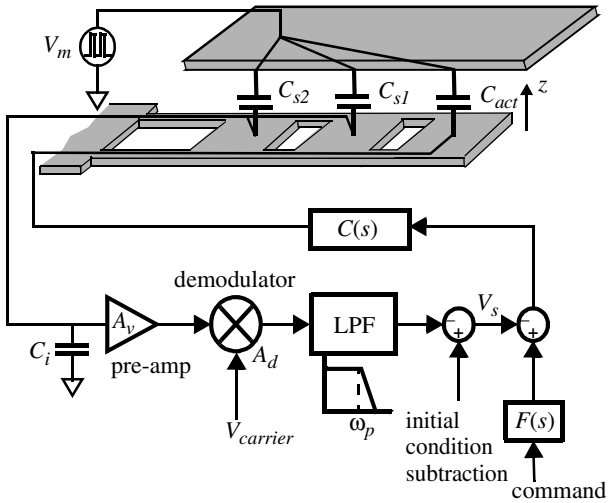

Figure 4. *Schematic representation of the feedback control system.*

where A_v is the pre-amp gain, A_d is the demodulator gain, C_i is the pre-amp input capacitance, and C_{s1o}, C_{s2o} are the initial sensing capacitances. The displacements of the sensing plates are obtained by finite-element simulations [**10**] with given actuation plate displacements z to account for the cantilever rotation. Substituting the displacements into the sensing capacitances gives

$$C_{s1}(z) = \varepsilon_o A/(g - 0.84z), \; C_{s2}(z) = \varepsilon_o A/(g - 0.67z) \quad (3)$$

The capacitive sensor gain at an operating point $z = Z_o$ is defined by differentiation of the sensed output with respect to the displacement. By including the dominant pole ω_p from the low-pass filter, the sensor transfer function at $z = Z_o$ is

$$H(s)\big|_{Z_o} = \frac{(dV_s/dz)_{Z_o}}{1 + s/\omega_p} = \frac{G(Z_o)}{1 + s/\omega_p} \quad (4)$$

Plant parameters used for controller design are: $m = 3 \times 10^{-11}$ kg, $k = 0.17$ N/m, $A_v = 10$, $A_d = 5$, $A = 1600$ µm^2, $g = 3$ µm, and $\omega_p = 120$ kHz. The squeeze-film damping coefficient b is computed between 1.8×10^{-6} and 1.1×10^{-3} N·s/m at gaps between 3 µm and 0.2 µm by simulations [**7**].

CONTROLLER DESIGN

Consider a small variation of Δz and Δv around the operating point (Z_o, V_o), the linearized actuator dynamics is derived by expanding the electrostatic force in the Taylor's series with the higher-order terms omitted:

$$m\Delta\ddot{z} + b\Delta\dot{z} + \left(k - \frac{\partial F_e}{\partial z}\bigg|_{z_o,\, V_o} \right) \Delta z = \frac{\partial F_e}{\partial V}\bigg|_{Z_o,\, V_o} \Delta v \quad (5)$$

where

$$\frac{\partial F_e}{\partial V}\bigg|_{Z_o,\, V_o} = \frac{2kZ_o}{V_o}, \quad (6)$$

and

$$\frac{\partial F_e}{\partial z}\bigg|_{Z_o,\, V_o} = \left(\frac{2\alpha}{1-\alpha} \right) k \quad (7)$$

where $\alpha = Z_o/g$. Combining the transfer function of the linearized actuator and the capacitive sensor in (4) gives the linearized plant

$$P(s) = \frac{G(Z_o) \cdot \left(\frac{2kZ_o}{V_o} \right)}{\left(\frac{s}{\omega_p} + 1 \right) \left(ms^2 + bs + \left(\frac{1-3\alpha}{1-\alpha} \right) k \right)} \quad (8)$$

Rewriting (8) using the resonant frequency $\omega_n = \sqrt{k/m}$ and the damping ratio $\xi = b/(2\sqrt{km})$, and multiplying the plant with a proportional-gain controller $C(s) = K_p$ gives the open-loop transfer function

$$L(s) = \frac{K}{\left(\frac{s}{\omega_p} + 1 \right) (s^2 + 2\xi_e \omega_e s - \omega_e^2)} \quad (9)$$

where

$$K = K_p G(Z_o) \left(\frac{2Z_o}{V_o} \right) \omega_n^2 \quad (10)$$

and the effective resonant frequency and the effective damping ratio due to the spring-softening effect are

$$\omega_e = \sqrt{\frac{3\alpha-1}{1-\alpha}}\omega_n, \quad \xi_e = \sqrt{\frac{1-\alpha}{3\alpha-1}}\xi \tag{11}$$

The magnitude and phase of $L(j\omega)$ are given by

$$|L(j\omega)| = \frac{K}{\sqrt{1+\omega^2/\omega_p^2}\sqrt{(\omega^2+\omega_p^2)^2+(2\xi_e\omega_e\omega)^2}} \tag{12}$$

and

$$\angle L(j\omega) = -\pi + \tan^{-1}\left(\frac{2\xi_e\omega_e\omega}{\omega^2+\omega_e^2}\right) - \tan^{-1}\left(\frac{\omega}{\omega_p}\right) \tag{13}$$

Substituting the phase margin ϕ and the unity-gain frequency $\omega = \omega_\phi$ into (13) gives

$$\frac{2\xi_e\omega_e\omega_\phi}{\omega_\phi^2+\omega_e^2} = \frac{\tan(\phi)-\frac{\omega_\phi}{\omega_p}}{1+\tan(\phi)\cdot\frac{\omega_\phi}{\omega_p}} \tag{14}$$

Equating $\angle L(j\omega)$ to $-\pi$ at the upper gain-margin frequency $\omega = \omega_g$ yields

$$\omega_g = \sqrt{\omega_e(2\xi_e\omega_p-\omega_e)} \tag{15}$$

Then substituting (15) into (12) gives the upper gain margin

$$G_H = \left(\frac{K}{2\xi_e\omega_p\omega_e(1+2\xi_e\omega_e/\omega_p-\omega_e^2/\omega_p^2)}\right)^{-1} \tag{16}$$

Equating $|L(j\omega)|$ to one at $\omega = \omega_\phi$ yields

$$K = \frac{\sqrt{\omega_\phi^2+\omega_p^2}\sqrt{(\omega_\phi^2+\omega_e^2)^2+(2\xi_e\omega_e\omega_\phi)^2}}{\omega_p} \tag{17}$$

By replacing $\omega = 0$ and (17) into (12), the lower gain margin is given by

$$G_L = \sqrt{\left(\frac{\omega_\phi}{\omega_p}\right)^2+1}\sqrt{\left(\frac{\omega_\phi^2}{\omega_e^2}+1\right)^2+\left(\frac{2\xi_e\omega_\phi}{\omega_e}\right)^2} \tag{18}$$

To find the maximum phase margin, $\angle L(j\omega)$ is differentiated with respect to ω at $\omega = \omega_\phi$. The resultant unity-gain frequency is the solution of the following quartic equation:

$$(-\omega_p-2\xi_e\omega_e)\omega_\phi^4+(-2\xi_e\omega_p^2\omega_e-2\omega_p\omega_e^2-4\xi_e^2\omega_p\omega_e^2 + 2\xi_e\omega_e^3)\omega_\phi^2+(2\xi_e\omega_p^2\omega_e^3-\omega_p\omega_e^4) = 0 \tag{19}$$

Given values of ω_p/ω_e and ξ_e according to the ratio of Z_o/g, ω_ϕ is first solved from (19). Then maximum phase margin, upper and lower gain margins and the controller K_p are computed by (14), (16), (18), and (10). Calculated maximum phase margins with respect to the actuator displacement are plotted in Figure 5. Since a LTI controller will be implemented, selected controller should give reasonable phase and gain margins at each displacement. The final design of the controller and pre-filter are:

$$C(s) = 17 \text{ and } F(s) = \frac{1}{1+s/1800} \tag{20}$$

with the resultant phase margins shown in Figure 5.

CHARACTERIZATION

For static measurement, a d.c. voltage is incrementally applied to the actuator, and an a.c. modulation voltage is applied to the top electrode for capacitive sensing. The spring constant of the actuator is extracted from the displacement-voltage characteristic in Figure 6 at 0.17 N/m, and the input capacitance C_i is computed at 333 fF from measurements.

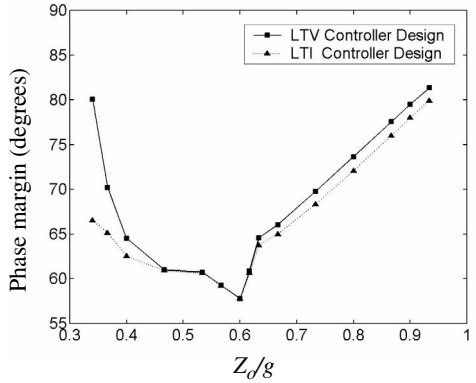

Figure 5. *The maximum phase margin corresponding to the actuator displacement.*

The actuator resonant frequency is measured electronically by the Agilent 4395A spectrum/network analyzer, which gathers readout signal from the demodulator output to construct the actuator frequency response. The resonant frequency decreases as a result of the spring-softening effect from the increasing d.c. bias. Both experimental and NODAS simulation results [**9**] are shown in Figure 7, in which the actuator resonant frequency is found at 12.4 kHz. From the resonant peak of the measured frequency response, effective damping ratio is calculated between 0.55 to 0.35 for gaps between 2.3 to 2.65 μm.

Measured frequency response of the sensing pre-amp has a closed-loop gain of ten and the corner frequency at 6.3 MHz. The minimum input-referred noise voltage is measured at 1.1 μV/√Hz,

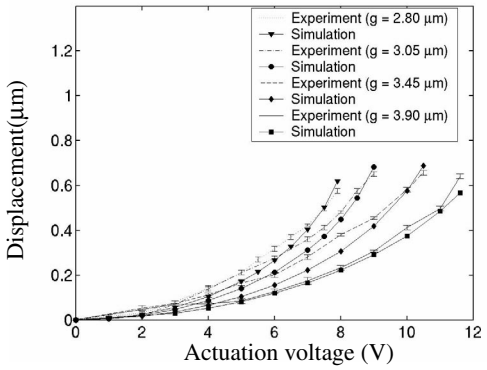

Figure 6. *The static displacement-voltage characteristic measures the actuator spring constant at 0.17 N/m.*

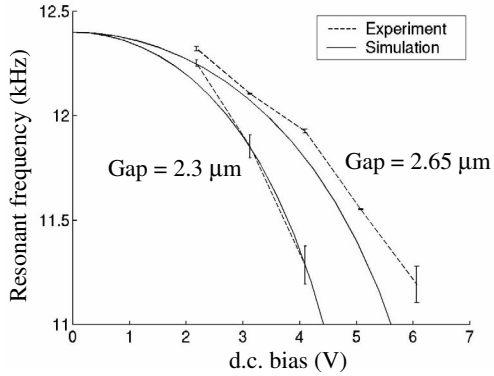

Figure 7. *Measured resonant frequency and its shift due to the electrostatic spring-softening effect.*

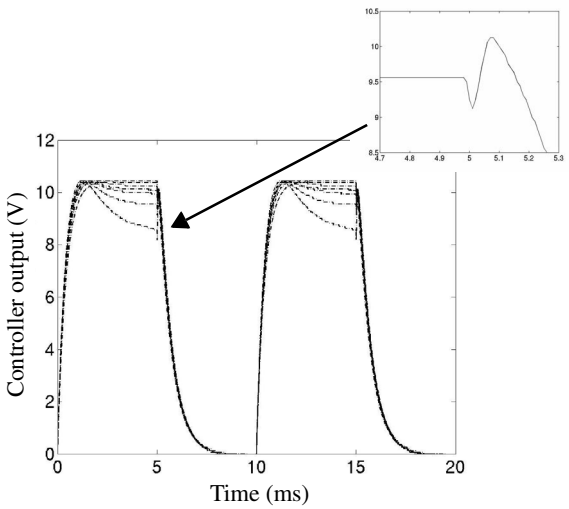

Figure 8. *Measured controller output waveforms when displaced plate enters pull-in region and beyond. The inset illustrates its waveform when the input command turns from high to low.*

which is equal to a minimum input-referred noise capacitance change and a minimum input-referred noise displacement of 0.25 aF/√Hz and 0.2 nm/√Hz, respectively.

CLOSED-LOOP POSITION SERVO

The input command is a square waveform at 100 Hz with the minimum set at zero. A series of controller outputs is measured when the actuator moves across the pull-in instability and beyond, as shown in Figure 8. The decrease of controller output after the pull-in voltage (10.44 V) reduces the stored charge on the plate in order to stabilize the actuator in the unstable regime. As the input command changes from high to low, the controller output first decreases, and then increases as the actuator retracts back to the rest position to maintain stability, as shown by the inset in Figure 8. The actuator displacements, as depicted in Figure 9, are extracted from the measured sensor output voltage waveforms. A maximum displacement of 55 % the gap (g = 3.25 µm) is illustrated, with the rise time less than 2 ms, the settling time less than 5 ms, and no overshoot.

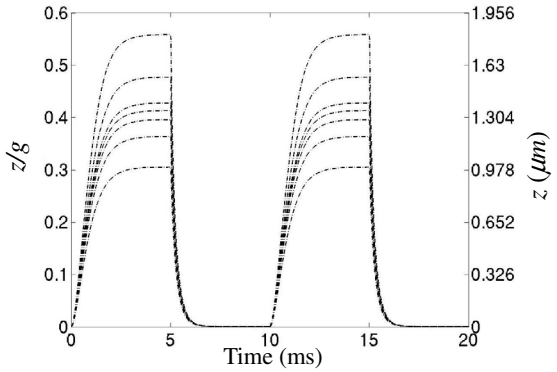

Figure 9. *Transient response of the actuator displacement. (g = 3.25 µm).*

DISCUSSION AND CONCLUSION

Controller design and the closed-loop implementation for the parallel-plate capacitor servo are discussed. With a proportional-gain controller, nonlinearities of the actuator and capacitive sensor are considered. Actuator displacement servoed as far as 55 % of the initial gap is demonstrated. The maximum servo range is limited due to the following reasons: (1) structural curl of the fabricated actuator results in tilted plates and thus reduced damping coefficient, which leads to decrease of the phase margin, and (2) the implemented loop bandwidth is limited by the use of low-pass filtering after the demodulator. Hence no phase-lead compensation can be attempted for the phase loss. From the controller design standpoint, use of a LTI controller facilitates the implementation but is less versatile than other alternatives such as a nonlinear controller and a LTV controller, in terms of bandwidth efficiency and attainable gain and phase margins. Those types of controllers remain interesting research topics for the future.

ACKNOWLEDGEMENT

This work is sponsored by the Defense Advanced Research Project Agency (DARPA) under agreement number F306029820239.

REFERENCES

1. L. R. Carley, J. A. Bain, G. K. Fedder, D. W. Greve, D. F. Guillou, M. Lu, T. Mukherjee, S. Santhanam, L. Abelmann, and S. Min, "Single-chip computers with microelectromechanical system-based magnetic memory", *Journal of Applied Physics*, vol. 87, no. 9, pt. 1-3, (2000), pp. 6680-6685.
2. R. Legtenberg, J. Gilbert, S. D. Senturia, and M. Elwenspoek, "Electrostatic curved electrode actuators", *J. of Microelectromechanical Systems*, vol. 6, no.3, (1997), pp. 257-265.
3. E. S. Hung and S. D. Senturia, "Extending the travel range of analog-tuned electrostatic actuators", *J. of Microelectromechanical Systems*, vol. 8, no.4, (1999), pp. 497-505.
4. E. K. Chan and R. W. Dutton, "Electrostatic micromechanical actuator with extended range of travel", *J. of Microelectromechanical Systems*, vol. 9, no.3, (2000), pp. 321-328.
5. J. I. Seeger, B. E. Boser, "Dynamics and control of parallel-plate actuators beyond the electrostatic instability", *Proc. Transducers'99*, Sendai, Japan, (1999), pp. 474-477.
6. P. B. Chu, K. S. Pister, "Analysis of closed-loop control of parallel-plate electrostatic microgrippers", in *Proc. IEEE int. conf. Robotics and Automation*, San Diego, CA, (1994), pp. 820-825.
7. S. Vemuri, G. K. Fedder, and T. Mukherjee, "Low-order squeeze film model of simulation of MEMS devices," *International conference on Modeling and Simulation of Microsystems*, San Diego, CA, pp. 205-208, 2000.
8. G. K. Fedder, S. Santhanam, M. L. Reed, S. C. Eagle, D. F. Guillou, M. Lu, and L. R. Carley, "Laminated high-aspect-ratio microstructures in a conventional CMOS process", *Sensors and Actuators A (Physical)*, vol. A57, no. 2, (1997), pp. 103-110.
9. G. K. Fedder, Q. Jing, "A hierarchical circuit-level design methodology for microelectromechanical systems," *IEEE Trans. on Circuits and Systems II: Analog and Digital Signal Processing*, vol.46, no.10, (1999), pp. 1309-1315.
10. ABAQUS manual, version 6.2, Hibbitt, Karlsson & Sorensen, Inc., (2001).

A MICROFABRICATED ELECTROCHEMICAL OXYGEN GENERATOR FOR HIGH-DENSITY CELL CULTURE ARRAYS

Michel M. Maharbiz, William J. Holtz, Sahar Sharifzadeh, Jay D. Keasling†, Roger T. Howe
Berkeley Sensor & Actuator Center, 497 Cory Hall
†Dept. of Chemical Engineering, 401 Latimer Hall
University of California at Berkeley, Berkeley, CA 94720

ABSTRACT

We present a microfabricated electrolytic oxygen generator for use in high-density miniature cell culture arrays. The generator consists of Ti/Pt electrodes patterned at the narrow end of conical hydrophilic silicone microchannels filled with electrolyte. Surface tension forces arising from the conical microchannel geometry push generated gas away from the electrodes and down the microchannel. This bubble motion draws fresh electrolyte from an adjacent reservoir onto the electrodes. The oxygen dosage can be precisely controlled in each generator by pulse width modulation of the electrode potential. We demonstrate devices capable of continuously providing for a wide range of oxygen demands (0-200mmol/g DCW/hr) and operating for days. We also present data on corrosion conditions. We investigate pre-cure silicone additives as an alternative to plasma surface modification to obtain hydrophilic silicone surfaces. Additionally, we assay for the presence of reactive oxygen species (ROS) in aqueous medium bubbled with generated gas.

INTRODUCTION

There are an increasing number of areas where miniaturization of cell culture reactors can provide significant benefits over standard reactor or "shake flask" type incubation methods. Cell culture reactors are commonly used for optimization of some metric (such as growth rate or product yield) as a function of reactor settings (pH, oxygen, medium composition, etc.) [**1**]. Traditional-size cell culture reactors are large (>1L) and expensive (>$1000); this usually limits the number of parallel experiments performed in these optimal parameter searches [**2**].

Specifically, the recent completion of several microbial genomes allows the development of novel antibacterial and antifungal drugs targeted to specific genes. A large cultivation parameter space must be explored to determine the function of novel genes, the optimal culture conditions for a desired bioconversion, or the most appropriate cultivation conditions for a previously unculturable microorganism. Given the large numbers of organisms that have been sequenced, unknown genes in each of those organisms, and previously unculturable organisms, a high-throughput cultivation device would allow rapid exploration of the cultivation parameter space.

Dissolved oxygen is a crucial parameter in microbial and eukaryotic cell cultures [**3**]. Not only do different species require vastly different oxygen conditions to thrive, but minute changes in available oxygen affect many of the metabolic pathways of the cell. Traditional methods of oxygen control usually involve bubbling oxygen or ambient gas through the cell culture suspension [**4**]. The specific methods vary considerably, but all make use of an external gas supply and standard plumbing and gas flow devices. Such a system would likely include pumps, valves, a gas reservoir (or an ambient air filter), and a network of fluidic channels. To control the amount of oxygen in each reactor in a high-density microarray, a complicated micro-fluidic system could be fashioned. *In-situ* electrochemical generation of oxygen in each well eliminates the need for complicated micro-fluidics by converting a voltage (current) directly into a known rate of oxygen generation. The oxygen dosage can thus be precisely controlled independently in each well.

Silicone is gaining popularity as a MEMS material, especially for fluidic or biological applications. This is due to its elastic properties, ease of deposition, and biocompatibility[**5,6**]. Most commercially available silicones are hydrophobic, but in many applications this is not desirable. The use of hydrophilic block co-polymer silicones blended with a hydrophobic silicone was investigated to determine the resulting contact angles and their stability over time.

THEORY OF OPERATION

Design

The basic design schematic is shown in top view in Figure 1. A set of interdigitated electrodes lie at the narrow end of a electrolyte-filled conical hydrophilic microchannel. An appropriate potential applied between the interdigited electrodes immersed in electrolyte generates gaseous oxygen (and hydrogen). The wide end of the channel opens into the biological medium. As a gas bubble is generated at the electrodes, it shifts towards the wider end to minimize surface tension. As the bubble travels towards the wide end of the channel, fresh electrolyte is brought onto the electrodes from an adjacent reservoir and another bubble can be formed. Un-reacted electrolyte slugs separate the bubbles in the channel and are transported into the biological suspension along with the gas. The amount of oxygen produced can be controlled by pulse width modulation of the potential. This potential is applied for a period such that the bubble is large enough to span the width of the channel, yet is only a fraction of the channel's length.

There are two mechanisms that cause the bubble to move down the channel. If the channel walls are hydrophilic and diverge from each other, then there will exist opposite but unequal forces on each end of the bubble. These forces result from the difference in channel cross section at each end of the bubble and a difference in the component of the surface tension force in the direction of the channel axis[**7**].

The most illustrative example is that of a channel with radial cross-section. Although the fabricated channels have rectangular cross-sections and different contact angles on different faces, a more complicated analysis obscures the basic mechanism. The surface tension at an end of the bubble can be set equal to the pressure difference across the gas/liquid interface:

$$2\pi R_1 \sigma \cos(\theta - \phi) = \Delta p \pi R_1^{\,2} \quad (1)$$

$$2\pi R_2 \sigma \cos(\theta + \phi) = \Delta p \pi R_2^{\,2} \quad (2)$$

Where R_1 and R_2 are the radii of the conical channel at the bubble's wider and narrower ends respectively, Δp is the pressure difference across the air/liquid interface, σ is the surface tension, ϕ is the angle between the channel wall and the channel axis, and θ is the contact angle of the channel wall. These equations can be used to find the magnitude of the forces on each of the bubble ends:

$$F_1 = 2R_1 \pi \sigma \cos(\theta - \phi) \quad (3)$$

$$F_2 = 2R_2 \pi \sigma \cos(\theta + \phi) \quad (4)$$

These forces are in opposite directions, so the total force in the direction of the wide end of the channel is:

Travel support was generously provided by the Transducers Research Foundation and the DARPA MEMS and DARPA BioFlips programs.

$$F_{net} = 2\pi\sigma[R_2\cos(\theta+\phi) - R_1\cos(\theta-\phi)] \quad (5)$$

Additionally, the conversion of liquid to gas at the electrolysis site results in a net volume expansion that pushes gas and electrolyte away from the electrodes. This expansion moves fluid down the channel rather than back into the reservoir because of the larger orifice size to the channel, which results in less opposing surface tension.

Hydrophilic channel walls are crucial for proper movement of bubbles from the generation site to the exit site at the end of the channel. It is well documented that silicone made hydrophilic by surface treatment with an O_2 plasma reverts to a hydrophobic state over time [**8**]. An alternate method of modifying the silicone is to add a few percent (by weight) of a hydrophilic silicone before curing [**9**]. We present data on bulk co-polymer additives that result in stable, hydrophilic silicones.

Electrolysis

Electrolytic gas generation in micro-channels has previously been investigated for various valve actuators[**10,7**]. The electrolysis of water with noble metal electrodes produces hydrogen and oxygen [**11**]:

$$2H_2O \rightarrow O_2(g) + 4H^+(aq) + 4e^- \quad (\text{anode, } E^0 = -1.229V) \quad (6)$$

$$4H_2O + 4e^- \rightarrow 2H_2(g) + 4OH^-(aq) \quad (\text{cathode, } E^0 = -0.828V) \quad (7)$$

The steady-state half-cell potentials are given in Eqs. 6, 7 ; these assume the anode environment has become acidic and the cathode environment has become basic.

Note that equal amounts of hydroxyl radicals and protons are produced. If the electrodes are spaced far from each other, this will lead to noticeable changes in solution pH. Bohm, et al used this fact to design a microtitration system [12]. Interdigitating closely-spaced electrodes ensures radical recombination and avoids undesirable pH gradients.

Several aspects of electrolyte composition must be considered. Firstly, the electrolyte employed in the bubbler must be pH-neutral and biologically compatible. As the exiting bubbles are separated by electrolyte slugs, a small amount of electrolyte enters the growth medium during bubbler operation.

Additionally, the electrolyte must be free of certain ions that may compete with the electrolysis reactions in Eqs. 6,7. The anodic evolution of chlorine, for example, has been shown to dominate the oxygen evolution reaction in saline solutions.

$$2Cl^- \rightarrow Cl_2 + 2e^- \quad (\text{anode, } E^0 = -1.360V) \quad (8)$$

In the case of chlorine, although Eq. 6 is thermodynamically favored slightly over Eq. 8 at low pH, oxygen has a much higher over-potential than chlorine at current densities >100mA/cm^2 with conventional metal electrodes. Therefore, more chlorine than oxygen will be generated in this regime. Trace metal concentrations can also sometimes undergo transitions that can potentially compete with the oxygen reaction. We have found 1M phosphate buffer to work efficiently while producing no detectable aqueous by-products. It is therefore crucial that the complex growth medium present in the environment outside the bubbler not be allowed to enter into the microchannel as this may result in oxygen production not being the dominant reaction.

Lastly, as gas evolution is directly proportional to current flow between the electrodes, the electrolyte must be sufficiently concentrated to support the currents of interest. Assuming no competing reactions, one molecule of O_2 is generated for every 4 electrons (Eq. 6). Typical oxygen consumption rates for *E. coli* are about 40 mmol /g Dry Cell Weight/hour [**3**]. The total current needed to supply this demand per volume of biomass is then,

$$I = 40\cdot10^{-3}\frac{molO_2}{gDCW\cdot hr}\cdot\rho\cdot N_A\cdot\frac{4e^-}{O_2}\cdot\frac{q_e}{e^-} = \mathbf{4.3}\frac{\mu\mathbf{A}}{\mu L} \quad (9)$$

where ρ=1 g/l is a typical biomass density [**3**], N_A=6.023·10^{23} molecules/mole is Avogadro's number, q_e=1.609·10^{-19} C is the electron charge. As discussion of bubble column gas transfer is beyond the scope of this paper, we will assume the generated gas is fully utilized by the biomass above the bubbler chip[**4**].

Given the well-known oxygen overpotential at metal electrodes and the above current requirement, it is often necessary to operate at potentials in excess of the thermodynamic half-cell potentials for the anode and cathode reactions. As we increase the potential drop across the electrodes, other reactions come into play at the electrode surfaces. Of particular interest are reactions that generate reactive species with aqueous lifetimes greater than a few seconds as these could be potentially anti-microbial if exhausted into the biomass.

We can calculate the rate of electrolyte consumption from the desired oxygen production rate. The electrolyte reservoir must then be large enough to supply electrolyte for the maximum operational lifetime.

$$V_{consumed} = 80\frac{molO_2}{hr\cdot\mu l}\cdot V\cdot\frac{2H_2O}{O_2}\cdot\frac{18g}{mol}\cdot\rho_w = \mathbf{288}\frac{\mathbf{nl}}{\mathbf{hr}} \quad (10)$$

where ρ_w is the density of water and V=200μL is the volume of the biomass.

Corrosion

To control oxygen generation, the operating potential is pulsed at frequencies varying from 0.1 – 2.0 Hz. Direct application of these pulse trains forces the electrodes to continuously alternate polarization during operation. Alternating current polarization has been shown to lead to corrosion and roughening of noble metal electrodes [**13**]. Specifically, those noble metals which readily dissolve hydrogen, such as platinum and palladium, exhibit rapid corrosion rates. Hoare showed that hydrogen-dissolving electrodes absorb evolved hydrogen when negatively polarized and expel hydrogen when positively polarized [**13**]. The resulting movement of the hydrogen atoms resulted in break-up of the electrode surface, leading to roughening and eventual degradation.

Corrosion of noble metal electrodes can be avoided by alternating between a fixed operating potential and an unbiased, or 'floating' condition during operation. This can be readily accomplished by applying the desired pulse train via a relay. During the applied pulse, the electrodes see a fixed potential; on the pulse's falling edge, the relay opens and the electrodes are allowed to float. This eliminates the alternating polarization and thus the motive force for the hydrogen absorption while maintaining the same actuation signal.

MATERIALS AND METHODS

Fabrication

The devices are fabricated on 4" silicon wafers (Fig. 2). A silicon nitride deposition (6000 Å) is followed by an n-type polysilicon deposition (1.5μm, 10 Ω/□). The polysilicon is patterned into traces and passivated with a second silicon nitride deposition. 5x5μm vias are cut into the nitride and Ti (500 Å) and Pt (2000 Å) layers are sputtered and patterned over the vias into 10x10μm electrodes using a lift-off process. Resist (SJR 5740) is spun 50μm thick and patterned to form a mold for channels. Wafers are then dipped in Sylgard Prime Coat and allowed to dry for 4 hours. Room temperature vulcanizing (RTV) silicone (Dow-Corning 734) is spun onto the wafer (150μm thick) and cured at room temperature. The wafer is then subjected to UV light to expose the buried resist. The wafer is diced into 1cm x 1cm chips. A 2mm x 1cm trench is cut in the center of the chip; this trench is

perpendicular to the channels thus providing the fluidic connection between the channel and the biological suspension. The photoresist is removed by immersion in developer with ultrasonic agitation for 60min. For devices requiring surface modification, the chip is exposed to a 50W O_2 plasma at 600mT (Technics PEII-A); this yields hydrophilic silicone surfaces. The completed chip can then be filled by capillary action when immersed in electrolyte for a few seconds. Each chip contains 13 identical electrolytic gas generators.

Contact angle experimental setup

Silicone samples for contact angle measurements were prepared by dipping pre-cleaned glass slides (Fisherbrand 12-550A, 25 x 75 x 1mm) into 50 mL test tubes filled with uncured silicone. Additives were hand-mixed into the silicone before dipping the slides. The samples were degassed in a vacuum chamber for 20 min. and allowed to dry while suspended from one end. This method generated samples with silicone on all surfaces of the glass slide; a small (<1mm) edge bead formed at the bottom end of the slide while drying. Dow-Corning 734 (RTV) silicone was used. Additives used in this paper are GE Silicones SF1488 (40-60 cstks), Gelest DBE-712 (20 cstks, 600MW) and Gelest DBE-224 (400 cstks, ~10,000MW); all are dimethylsiloxane-ethylene oxide block copolymers. A Kruss G10 goniometer with computer video capture and a KSV Sigma701 tensiometer were used for contact angle measurements. Goniometer contact angles were determined by curve fitting on a captured image using a circle-fitting algorithm provided by the software.

Reactive Oxygen Species (ROS) Quantification

Soft plastic centrifuge tubes (United Scientific Products, 1.5 mL flattop, MCT-150) were roughly cut at the narrow end to leave a ~2mm hole. The tubes were then cleaned in isopropanol and blown dry. The large mouth the tubes were bonded to completed bubbler chips using RTV silicone (Dow-Corning 734) and allowed to cure overnight. The tubes were then filled with 1.5 mL phosphate buffer (1M). An indigo trisulfonate colorimetric assay (modified from Standard Method 4500-O_3B [14]) was used to quantify the steady-state ROS concentration in the buffer as follows. Indigo trisulfonate discolors in the presence of reactive oxygen species. During each experiment, the 13 bubblers on the chip were operated simultaneously to generate gas into a filled tube. After 1 hour of operation, 1.2 mL of phosphate buffer was quickly removed and added to 0.3 mL of indigo trisulfonate solution II [14]. Optical densities were measured at a wavelength of 600nm with a path length of 1cm; all measurements were taken with DI water as a blank ($O.D._{600}$=0). A series of controls were made with 1.2 mL of virgin phospate buffer and 0.3 mL of indigo trisulfonate; mean and standard deviation between controls was calculated with measurements from 10 control samples. ROS concentrations were calculated from $O.D._{600}$ as per [**14**].

In a separate experiment, the 13 bubblers on the chip were operated simultaneously to generate gas into a tube filled with pH indicator dyes to visualize pH gradients (either 10:1 H_2O:Alizarin Red S [pH 5-8] or 10:1 H_2O:Bromophenol Blue [pH 3-5]). pH measurements were also made in a Horiba Twin pH meter following recommended calibration procedures over the course of 2 hours.

RESULTS AND DISCUSSION

Figure 3a-d shows the bubbler under normal operation. A minimum delay of 0.5s between potential pulses was found sufficient to allow the bubble time to exit the electrode area. With a 3.3V, 0.5s on, 0.5s off pulse, each bubbler has a maximum oxygen generation rate of 30nL/s. Shorter off-time results in pulses being applied while there is still gas over some electrodes. Additionally, as bubbles lose velocity near the mouth of the channel, smaller delays between pulses leads to gas coalescence and significantly larger exiting bubbles. In the extreme of a constant potential being applied, the generated gas coalesces completely and soon fills the entire channel, including the electrode area; gas generation drops significantly as only a few electrodes are covered with electrolyte.

Exiting bubble size was strongly dependent on silicone contact angle. In channels with hydrophobic contact angles, exiting bubbles remained trapped at the channel mouth. Bubbled gas then inflated the trapped bubble until the buoyancy force overcame surface tension (usually resulting in bubbles with diameters >2mm). A delay of more than 12 hours between oxygen plasma modification and operation resulted in devices which exhibited this behaviour. This motivated our search for time-stable hydrophilic silicones.

Corrosion

As discussed above, application of an AC potential directly to the electrodes results in rapid corrosion of the electrodes. Figure 4 shows the effect of corrosion on electrode surface. Figure 5 shows bubbler lifetime degradation. As Ti/Pt electrodes disintegrate, the amount of current through the bubbler drops. Actuation through a relay results in no appreciable corrosion; bubblers have been operated continuously for up to 24 hours with no detectable drop in current (data not shown). Operational lifetimes are currently limited by the size of our reservoir.

Reactive oxygen radicals (ROS)

Presence of reactive oxygen species was measured using an indigo trisulfonate colorimetric assay (Methods, above). Table 1 shows the results of representative experiments. At our operating potentials, the $O.D._{600}$ variation between controls was greater than that of the sample; this limits the measurement resolution of our current set-up to ~100 μg/L (100ppb). This is mainly due to our small sample size; additionally, we are restricted to small (1cm) optical path lengths for the optical measurement. Ozone concentrations >10 μg/L (10ppb) have been shown to affect *E. coli* metabolism [**15,16,17**]. *E. coli* suspension cultures grow successfully on gas generated by our chips in both rich and minimal medium (data not shown).

Table 1

Optical Density at 600nm wavelength ($O.D._{600}$)			
Controls (std. dev)	Controls (mean)	4.0V 60 min.	5.5V 60 min.
0.013	0.419	0.442	0.384

No pH changes were detected in pH measurement and indicator dye experiments (DI water, nominal pH 6.9±0.2).

Silicone Contact Angles

Silicone surfaces are usually made hydrophilic by oxygen plasma or acid surface modification [**18,19**]. It is well documented that surface modified silicone rapidly loses its hydrophilic nature (usually ~1-2 days) [**8,20**]. Recently, blends of polydimethylsiloxane (PDMS) silicone and amphipathic siloxane copolymers (such as polyethylene oxide) have been suggested as a way of obtaining hydrophilic silicones [**9**]. In an effort to develop time-stable hydrophilic silicones, an RTV silicone was mixed with different concentrations of dimethylsiloxane-ethylene oxide block copolymer and allowed to cure. Contact angles were then measured with a goniometer. Interestingly, we noted that water drops initially showed a hydrophobic profile but relaxed over ~5sec into a stable hydrophilic profile. Table 2 shows blends used and initial contact angles; goniometer data taken over 3 weeks indicated contact angles were stable (data not shown).

Table 2

Blend (% by weight)	Goniometer Contact Angle (quasi-static)
3% DBE-712	35º
6% DBE-712	20º
1% SF1488	45º
3% SF1488	70º
3% DBE-224	55º

Tensiometer data was then taken on identical samples in order to shed light on the observed dynamic aspects of the contact angle. Modified silicone samples were lowered and raised into 150 mL of DI water at 10mm/min over a 10mm section of sample to obtain advancing and receding contact angles. After 10 successive dips, the surface tension of the liquid was measured with a platinum standard plate (provided with the tensiometer) at 20mm/min (Figure 6) and the water was replaced with fresh DI water. The tensiometer data suggests the block copolymer additive leeches into the water over time, changing its surface tension and thus the measured contact angle. Additionally, the surface tension of 15 mL of water extracted from the bottom of the tensiometer beaker was essentially that of pure DI water (data not shown); this further indicates that the leeched co-polymer is sequestered almost exclusively at the air-water interface. Figure 7 shows tensiometer contact angle data over 30 days for bulk modified silicone as well as O_2 plasma surface modified silicone; no aging effect other than that attributed to copolymer leeching was observed. Since the coplymer leeching appears to be a diffusion process, this data suggests microchannels could be patterned whose surface properties change strongly as a function of fluid velocity.

Electrolyte interface

In order to test the separation of electrolyte from the biological suspension, 10µm polystyrene beads were placed in the destination solution and their motion filmed. In the course of 30 minutes of observation, 4 beads were able to enter the channel. These beads were able to travel up the channel a distance approximately equal to the length a bubble occupies in the channel. None of the beads reached the electrolysis site as the bubbles were much shorter than the channel. Each of these beads got caught in the air/water interface of a bubble and this prevented them from moving further down the channel. The trapped beads were then pushed towards the channel end via the movement of the interface. The caught beads were not cleanly ejected from the channel, but instead their position oscillated along the channel axis as they were released from one interface only to be pulled back into the channel and caught on another interface. All 4 of the beads that made it into the channel eventually broke out of the oscillation and were ejected from the channel within minutes.

The motion of the bubbles resulted in the movement of nearby beads into a formation. (Fig. 8) As bubbles exited the channel, they pushed the nearby beads in the solution away from the channel orifice. Due to the low Reynolds number at this length scale, beads that did not come in direct contact with the bubble, but were within ~3 bubble diameters of the channel end, could be seen moving in response to a bubble exiting the channel. The bubble briefly remained attached to the end of the channel until the buoyancy force was greater than the surface tension force holding it down. When the bubble broke free, water moved in to fill the space, and the surrounding beads were pulled in towards the channel end. The repetition of this process resulted in an arc-shaped pile of beads forming at a distance of 1 bubble diameter from the channel orifice center.

CONCLUSION

We successfully microfabricated and tested an electrolytic oxygen generator for use in high-density miniature cell culture arrays. A single generator chip can support oxygen consumption rates >100mmol/DCW/hr and operate for lifetimes in excess of a day. Additionally, the copolymer silicones investigated suggest interesting properties applicable to a broad class of microfluidic devices.

ACKNOWLEDGEMENTS

This work was funded by grants from the Department of Energy and the Defense Advanced Research Projects Agency (DARPA). The authors would like to thank Bill Flounders for excellent advice and references on polymers, Ron Wilson for the scanning electron micrography, and the staff of the U.C. Berkeley Microfabrication Laboratory.

REFERENCES

[1] A. Lübbert and S. B. Jørgensen, "Bioreactor performance: a more scientific approach for practice," *Journal of Biotechnology*, Volume 85, Issue 2, 13 February 2001, Pages 187-212.

[2] P.F. Stanbury, A. Whitaker, S.J. Hall, *Principles of Fermentation Technology*, 2nd Ed., Butterworth Heinemann, 1999.

[3] B. Atkinson, F. Mavituna, eds. *Biochemical Engineering and Biotechnology Handbook*, 2nd ed., New York: Stockton, 1991.

[4] H. W. Blanch, D. S. Clark, *Biochemical Engineering*, New York: Marcel Dekker, 1997.

[5] D Cornelius, C. Monroe, "The Unique Properties of Silicone and Flourosilicone Elastomers," *Polymer Engineering and Science*, vol. 25, no. 8, pp. 467-473.

[6] S.R. Quake and A. Scherer, "From Micro- to Nanofabrication with Soft Materials," *Science*, vol. 290, 24 Nov. 2000, pp. 1536-1540.

[7] A. Papavasiliou, *Bubble-Actuated Planar Microvalves*, PhD Dissertation, UC Berkeley, 2001, pp 27-30.

[8] H. Hillborg, J. F. Ankner, U. W. Gedde, G. D. Smith, H. K. Yasuda and K. Wikström, "Crosslinked polydimethylsiloxane exposed to oxygen plasma studied by neutron reflectometry and other surface specific techniques," *Polymer*, Volume 41, Issue 18, August 2000, Pages 6851-6863.

[9] R Hill ed., *Sillicone Surfactants*, New York: Marcel Dekker, 1999.

[10] P.F. Mann, C. H. Mastrangelo, M.A. Burns, D.T. Burke, "Microfabricated capillarity-driven stop valve and sample injector," *Proceedings of the Micro Electro Mechanical Systems (MEMS '98) Symposium*, Heidelberg, Germany, 1998, pp. 45-50.

[11] R. P. Petrucci, *General Chemistry*, MacMillan Publishing, New York, 1982.

[12] S. Bohm, W. Olthuis, P. Bergveld, "A flow-through cell with integrated coulometric pH actuator," *Sensors and Actuators B (Chemical)*, vol.B47, (no.1-3), Elsevier, 30 April 1998. pp.48-53.

[13] J.P. Hoare, "Some effects of alternating current polarization on the surface of noble metal electrodes," *Electrochemica Acta*, vol. 9, no. 5, May 1964, pp. 599-605.

[14] Standard Method 4500-O_3A*, Standard Methods for the Examination of Water and Wastewater*, 18th Ed., New York, American Public Health Association, 1992, pp. 4-105 to 4-107.

[15] N.K.Hunt, B.J.Mariñas, "Inactivation of *Escherichia Coli* with ozone: chemical and inactivation kinetics," *Water Research*, vol. 33, no. 11, 1999, pp. 2633-2641.

[16] N.K. Hunt, B. J. Mariñas, "Kinetics of *Escherichia Coli* with ozone," *Water Research*, vol. 31, no. 6, 1997, pp. 1355-1362.

[17] I. R. Komanapalli, J. B. Mudd, B.H.S. Lau, "Effect of ozone on metabolic activities of Escherichia Coli K-12," *Toxicology Letters*, vol. 90, 1997, pp. 61-66.

[18] D.C. Duffy, J.C. McDonald, O.J.A. Schueller, G.M. Whitesides, "Rapid Prototyping of Microfluidic Systems in Poly(dimethylsiloxane," *Analytical Chemistry*, vol. 70, no. 23, Dec. 1, 1998, pp.4974-4984.

[19] M.K. Chaudhury, G.M. Whitesides, "Direct measurement of interfacial interactions between semispherical lenses and flat sheets of poly(dimethylsiloxane) and their chemical derivatives," *Langmuir*, vol. 7, no. 5, May 1991, pp. 1013-1025.

[20] D.C. Duffy, O.J.A. Schueller, S.T. Brittain, G.M. Whitesides, "Rapid prototyping of microfluidic switches in poly(dimethyl siloxane) and their actuation by electro-osmotic flow," *Journal of Micromechanics and Microengineering,* vol. 9, 1999, pp. 211-217.

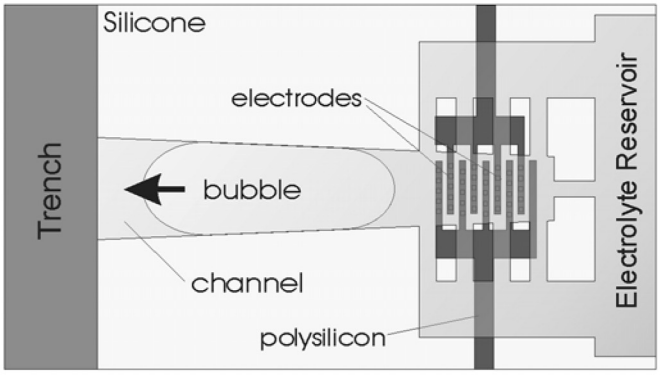

Figure 1: Schematic top view of bubbler.

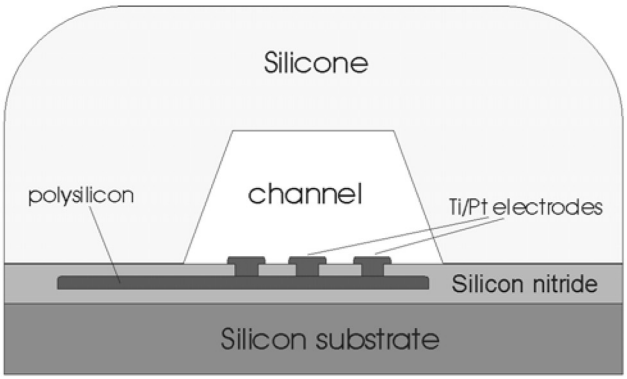

Figure 2: Process cross-section after removal of photoresist.

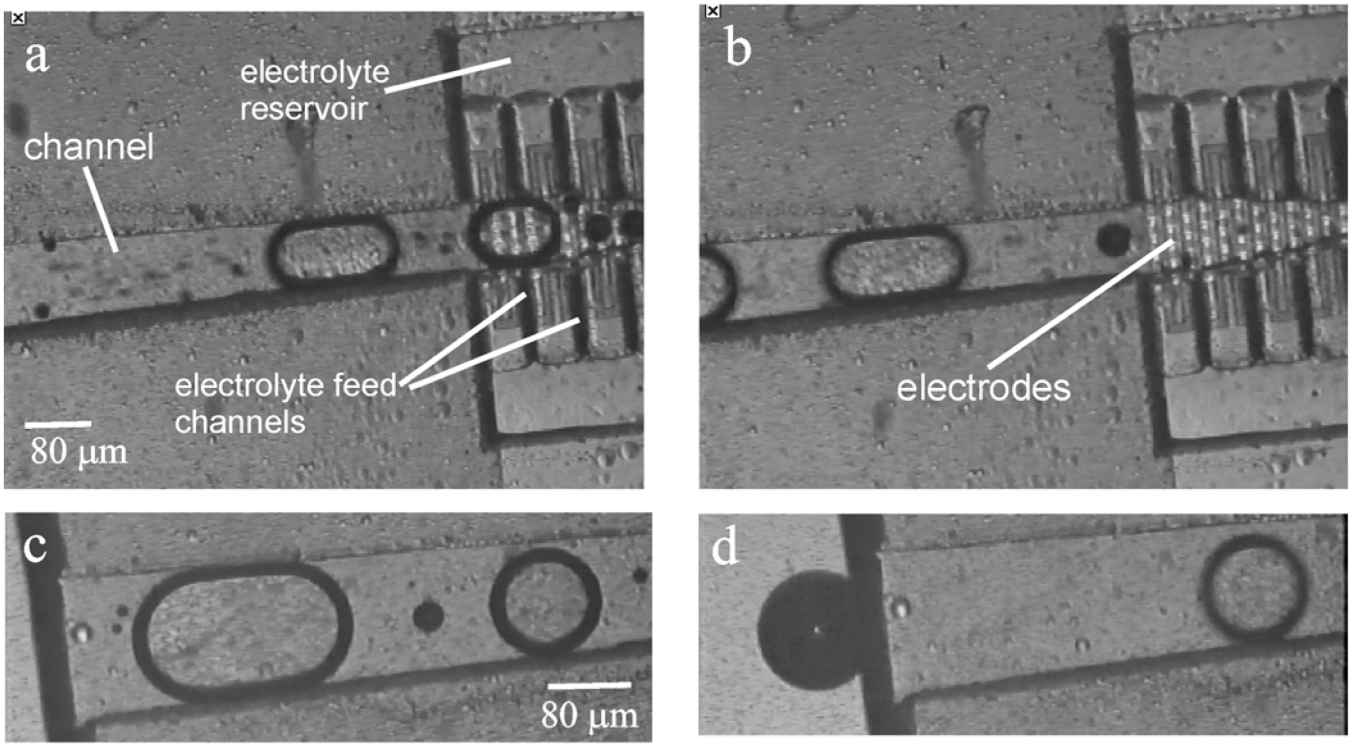

Figure 3: Bubbler in operation. a) Bubble is formed over electrodes. b-c) Bubble travels down conical microchannel. d) Bubble is exhausted into medium (becoming spherical). A voltage pulse train of the right frequency generates a continuous bubble train.

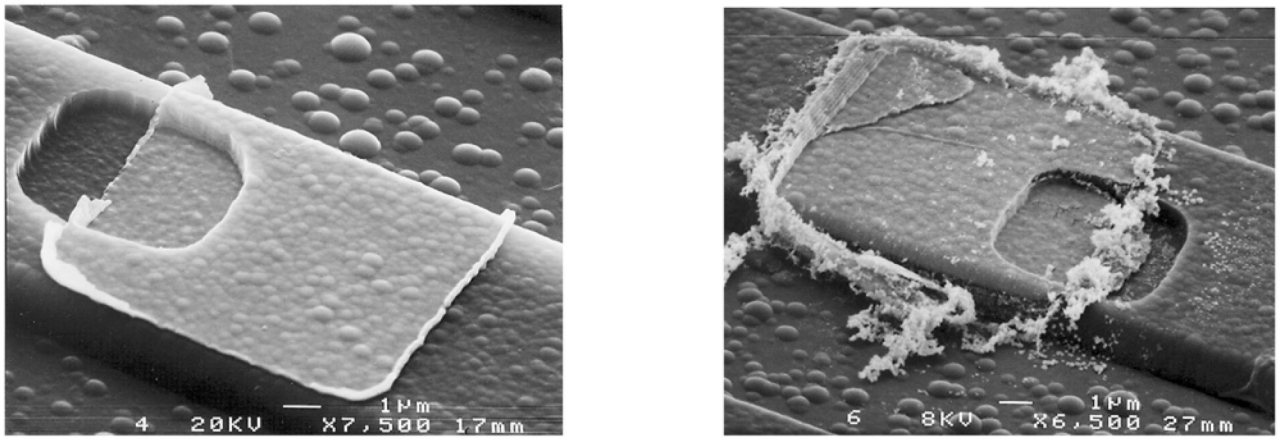

Figure 4: Electrode Corrosion due to AC excitation in electrolyte. A 0-5V, 1 Hz square wave was applied for 1 hour, 1M phosphate buffer, pH = 7.2 was used as the electrolyte. a) Excitation through relay (no corrosion). b) Excitation without a relay (corroded anode). The lithographic misalignment between the metal and via layers on this wafer did not appear to have any effect on bubbler operation.

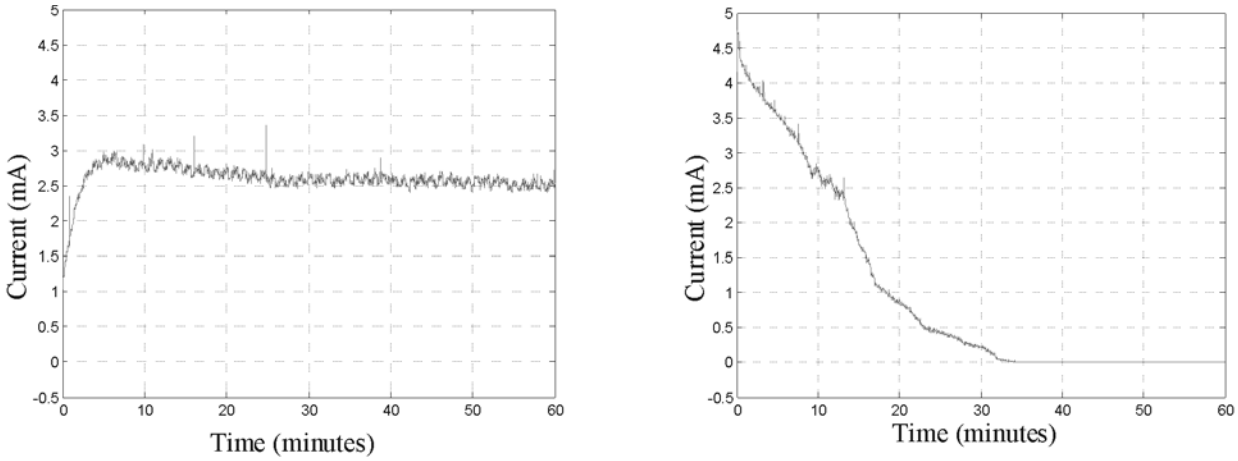

Figure 5: Effect of corrosion on oxygen generator lifetime. A 0-5V, 1 Hz square wave was applied for 1 hour; 1M phosphate buffer, pH = 7.2 was used as the electrolyte. a) Excitation through relay (no corrosion). b) Operation without relay results in gradual corrosion of Ti/Pt electrode; this both reduces operating lifetime and introduces bacteriocidal Ti/Pt contaminants into exit stream..

Figure 6: *(right)* Surface tension of water vs. number of silicone sample immersions into water. 10mm of sample were immersed at 10mm/min into 150mL DI water. Surface tension of pure water is 71 mN/m at STP.

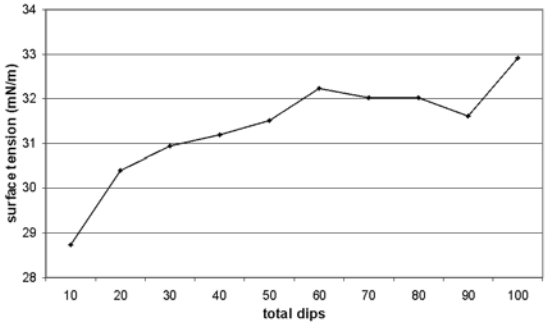

Figure 7a,b: *(below)* Contact angle aging data for modified silicones. Measurements were taken every 2 days for 27 days. 10mm of sample were immersed at 10mm/min into 150mL DI water. Data presented for 1% SF1488 / 734 blend.

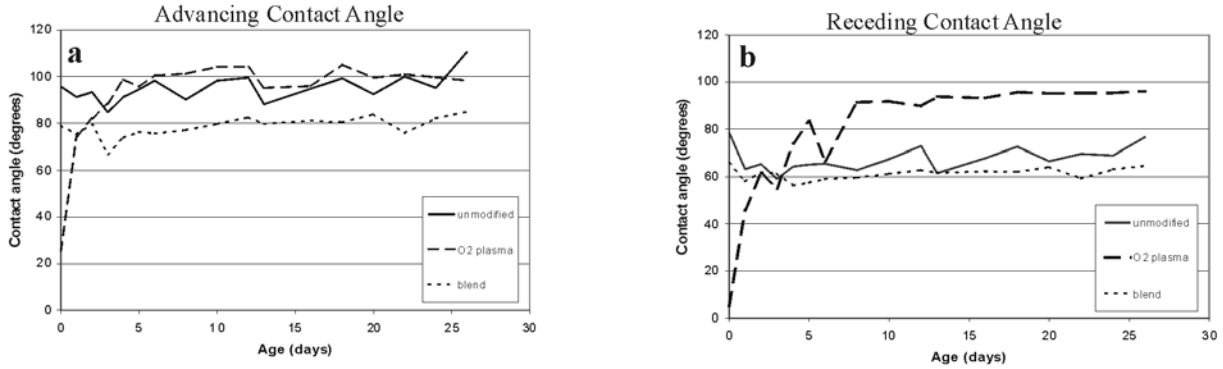

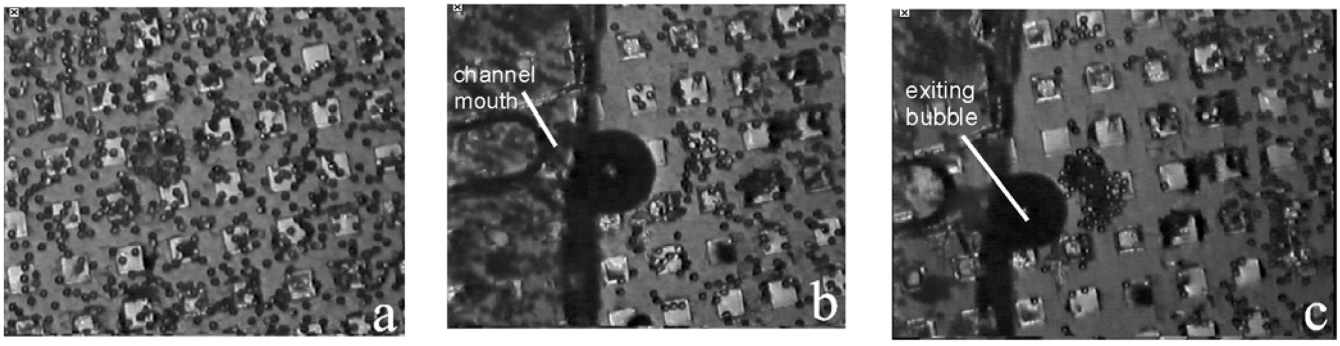

Figure 8: Channels isolate electrodes/electrolyte from foreign particles in surrounding medium. Chips pre-filled with 1M phosphate buffer were immersed in water containing 10μm beads. Any beads that entered the channel were trapped by the gas-liquid interface formed by exiting bubbles; additionally, the liquid motion caused by the exiting bubble aggregated nearby beads at a distance approximately equal to the exiting bubble diameter.
a) Density of unperturbed beads on substrate surface. **b)**Bead arrangement at channel mouth, t=10min.
c) Bead density at channel mouth, t =30min.

PRECISION FABRICATION OF HIGH-SPEED MICRO-ROTORS USING DEEP REACTIVE ION ETCHING (DRIE)

Norihisa Miki, Chiang Juay Teo, Linhvu Ho, and Xin Zhang[†]

Gas Turbine Laboratory, Massachusetts Institute of Technology, Cambridge, MA 02139, USA
[†]Department of Manufacturing Engineering and Fraunhofer USA Center for Manufacturing Innovation, Boston University, Boston, MA 02215, USA

ABSTRACT

High-speed silicon micro-rotors require high-precision fabrication via Deep Reactive Ion Etching (DRIE) so as to minimize the rotor imbalance which limits the maximum operational speed. Etch variation of DRIE process culminates in a difference in the blade height and thus rotor imbalance. A Fourier transform of the etch non-uniformity along the rotor circumference revealed the global effect across the wafer and the local etch variation depending on the concentration or proximity of the patterned geometry. The global etch non-uniformity which results in rotor imbalance could be alleviated to 0.25 % across a rotor of 4.2 mm diameter by optimizing the plasma chamber pressure. The manufacturing processes presented herein are readily applicable to the constructions of other high-speed rotating micro-structures containing intricate geometries and large etched areas.

INTRODUCTION

Rotating micromachinery must spin at high rotating speeds to achieve high power densities, exploiting high-precision bearings and rotors made possible through deep reactive ion etching (DRIE) and multi-stack wafer-level bonding [1], [2]. We have reported DRIE profile control of highly anisotropic, narrow silicon trenches (10-20 µm wide, 300-500 µm deep) [3] and several critical issues involved in the multi-stack silicon direct bonding of the wafers with intricate geometries and large etched areas [4].

Our high-speed microdevice (referred as a "microbearing rig"), consisting of the rotor, bearings, and associated plumbing, is constructed from five DRIE'd silicon wafers precision aligned and fusion bonded into a stack (Figure 1). The rotor is a planar disk with radial turbine blades on one side. It is supported by hydrostatic and/or hydrodynamic gas thrust bearing axially and hydrostatic gas journal bearing radially. Figure 2 depicts the SEM image of the rotor with 22 outer stator blades and 20 inner rotor blades. A typical whirl response curve of a rotor with a certain imbalance is plotted in Figure 3. Whirl amplitude is defined as the distance between the geometric center of the rotor and the journal bearing. Collision occurs when the whirl amplitude exceeds the journal clearance. Below the natural frequency, the rotor spins at its geometric center, which is termed as subcritical operation; above the natural frequency, the rotor rotates about its center of mass, which is termed as supercritical operation [5]. The whirl amplitude during supercritical operation corresponds to the rotor imbalance, which refers to the distance between the geometric center and the center of mass. Rotor imbalance precludes performance of high-speed rotating structures; the maximum peak response near the natural frequency increases with the imbalance, resulting in higher likelihood of rotor collision with the surrounding wall. Higher imbalance also promotes instability, reduces the range of stable operation, and thus limits the maximum operational speeds.

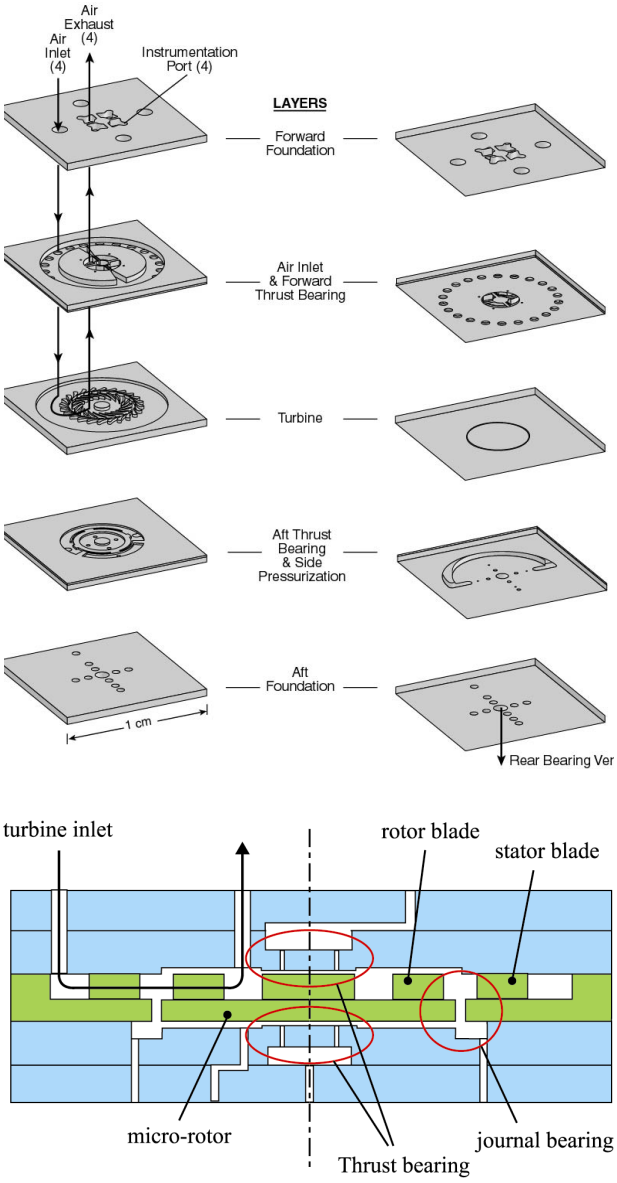

Figure 1. *An exploded schematic showing the detailed wafers involved in the microbearing rig. The left column shows the top view, the right column the view from the bottom, and the lower the cross section. The design speed of the 4.2 mm diameter rotor is 2.4 million RPM.*

0-9640024-4-2/hh2002/$20©2002TRF
DOI 10.31438/trf.hh2002.66

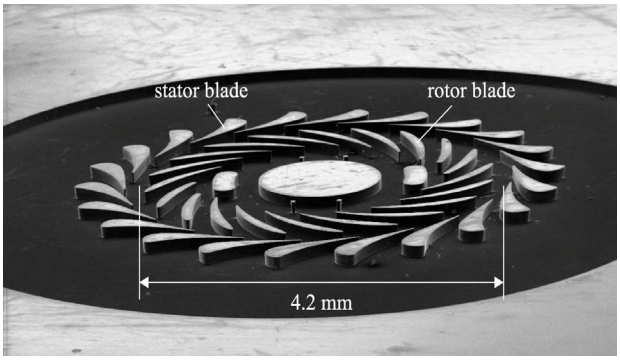

Figure 2. *SEM image of a 4.2 mm diameter by 500 μm thick rotor with radial turbine blades on one side (the other side may consist of an electric motor or generator). There are 22 outer stator blades and 20 inner rotor blades fabricated by DRIE. The blade height is 150 μm.*

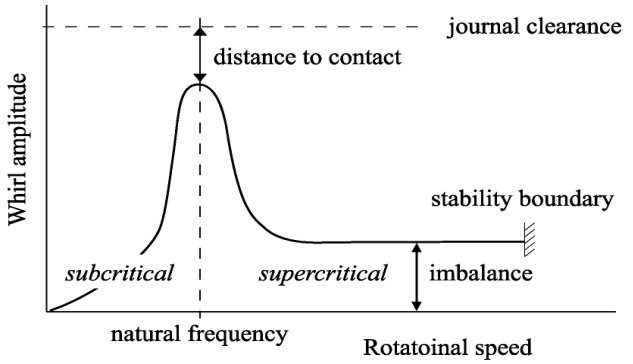

Figure 3. *Whirl response of a rotor. The whirl amplitude during supercritical operation represents the rotor imbalance.*

One of the major contributors to rotor imbalance is the DRIE etch non-uniformity. The etch variation during the DRIE process culminates in a difference in blade height and thus rotor imbalance. This paper addresses radical DRIE uniformity innovation across 4.2 mm diameter by 450 μm thick rotors; the ultimate goal is to attain a sufficiently low imbalance level of the rotor so as to achieve the design speed of 2.4 million rpm. The DRIE process was performed using a Surface Technology Systems Multiplex ICP.

EXPERIMENTS

Twelve dies can fit on to one stack of four-inch wafers, as depicted in Figure 4(a). Dies 4, 5, 8, and 9 are identified as center dies, whereas the remaining dies are termed as edge dies. The etch depth is quantified by the maximum depth in the region enclosed by the two adjacent rotor blades and stator blades, such as the area a_1 surrounded by rotor blades #1 and #2 and the closest stator blade as illustrated in Figure 4(b).

Locally, the etch variation depends on the concentration or proximity of the patterned geometry as illustrated in Figure 5. The contour map illustrates the shallower etch depth with the smaller distance to the contiguous features. However, given the symmetric layout of the features, i.e., even numbers of both stator and rotor blades, the local etch variation is identical for diametrically

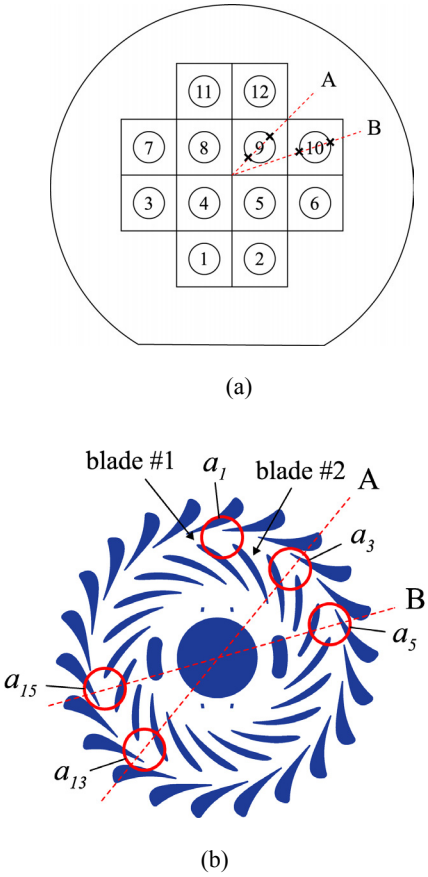

Figure 4. *(a) The location of the dies and (b) the measurement sites.*

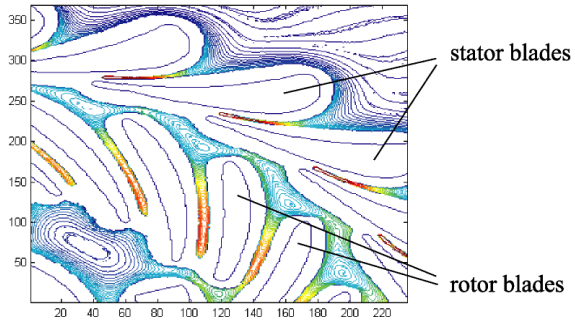

Figure 5. *Measured contours showing DRIE etch variation in a micro-rotor.*

opposite points on the rotor and thus does not contribute to the rotor imbalance.

Globally, DRIE typically causes the center dies having shallower etches by ~10% than the edge dies. This is the consequence of a non-uniform etch rate across the wafer. The global etch variation is evaluated from the difference in etch depths corresponding to the two regions which are nearest and furthest from the center of the wafer. For example, the difference in etch depths are measured in regions a_3 and a_{13} for die #9 and in regions a_5 and a_{15} for die #10. A global etch non-uniformity translates as shown in Figure 6, at the die-level, into a difference in the blade height from one side of the rotor to the other, resulting in the

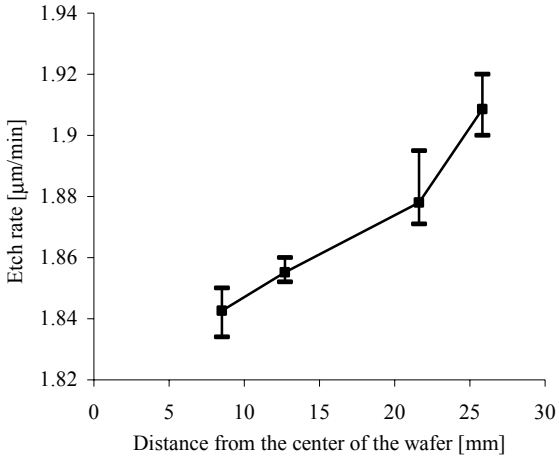

Figure 6. *Etch rate variation across the wafer. The etch rates in the regions closest and furthest from the center of the wafer were measured for the 4 center dies and 4 edge dies (die #1, 6, 7, 12). The left two and the right two represents the global etch non-uniformity across the center dies and the edge dies respectively. The etch rate increases with the distance from the center of the wafer. The etching conditions were: 105 sccm of SF_6 (13 seconds active cycle, 0.5 seconds overlap, 9 W of electrode power and 750 W of coil power), 40 sccm of C_4F_8 (11 seconds active cycle, 6 W of electrode power and 600 W of coil power). The APC angle was set at 62 degrees. After 30 minutes of etching, the wafer was rotated through 180 degrees, followed by another 45 minutes of etching, culminating in 150 μm high blades.*

misalignment between the geometric center and the center of mass, i.e. imbalance.

Figure 7 illustrates the etch depth along the circumference of two different rotors. The etch depth of the area a_1 corresponds to the datum at the position of 0 degrees. The variation of the etch depth is considered to be the combination of the global and local effects. A Fourier transform was performed to segregate local variations from global contributions (Figure 8). The first harmonic corresponds to the global etch variation, whereas the second harmonic results from the local etch variation due to the symmetric feature arising from the even numbers of rotor and stator blades. The edge die and the center die measured herein involve global etch variations of 5.1 μm and 1.4 μm, respectively.

The imbalance originating from the etch variation was estimated assuming a linear relationship between the global etch non-uniformity and the distance from the center of the wafer. Figure 9 indicates that the imbalance, which is the distance between the geometric center and the center of mass of the rotor, increases almost linearly with the global etch uniformity. For example, a global etch variation of 3 % results in a rotor imbalance of 2.7 μm. Figure 10 illustrates the whirl response of a rotor with a global etch variation of 3 %. The curved line is a fitted line to the typical whirl response curve shown in Figure 3. In the supercritical region above the natural frequency of 35000 rpm, the whirl amplitude representing rotor imbalance was about 3 μm. This fact indicates that the global etch non-uniformity produced via DRIE process is the dominant factor for rotor imbalance and hence, the performance of high-speed rotors depends on the precision fabrication.

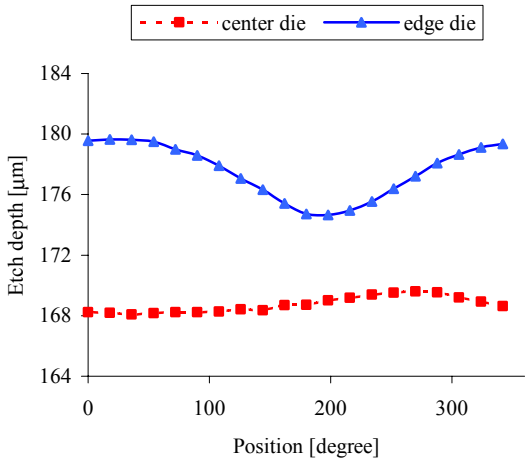

Figure 7. *The etch depth along the periphery of the rotor. Plotted along the abscissa is the angular position on the rotor defined in a clockwise manner, with the data point at 0 degrees depicting the maximum etch depth in region a_1. The etching conditions were identical to those described in the caption of Figure 6.*

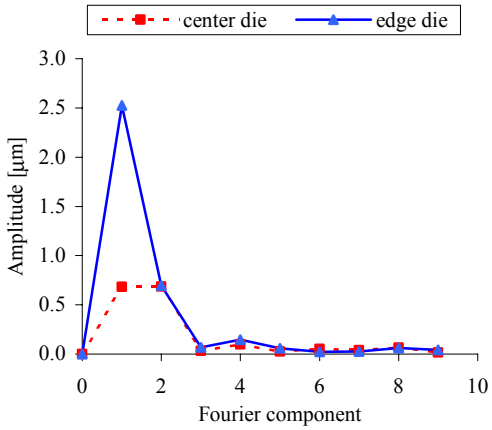

Figure 8. *The Fourier spectrum of the etch variation along the periphery of the rotor. The first Fourier component represents the global etch non-uniformity which is a function of the distance from the center of the wafer, while the local etch variation depending on the concentration and proximity of the features appears as the second Fourier component since the number of stator and rotor blades are both even and thus the features are symmetric.*

We constructed solutions by regarding the uniformity as having a dependence on (i) the availability of etching species and (ii) the efficient removal of etching byproducts that dissociate and redeposit. As an example, given that the diffusivity of the etching species depends on the etching conditions, we demonstrated approaches to improve etching uniformity by dynamically changing the plasma chamber pressure that is controlled by the automatic pressure control valve (APC) positioning. The plasma chamber pressure increases with the APC angle. Figure 11 depicts the ratio of the etch variation normalized by the etch depth, with respect to the APC angle. The etch non-uniformity was minimized at an APC angle of 55 degrees for both center and edge dies, resulting in the etch variation of 0.25 % and 0.5 % for center dies and edge dies, with corresponding estimated rotor imbalance of 0.2 μm and 0.4 μm for center dies and edge dies respectively.

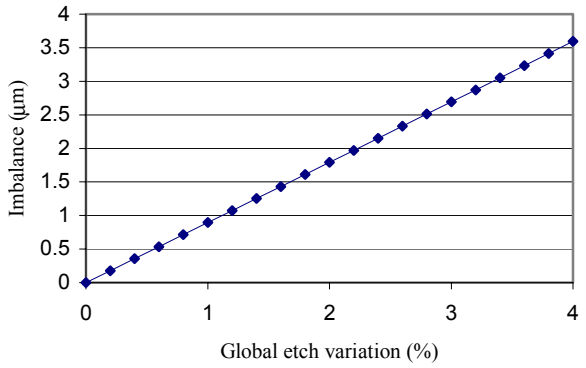

Figure 9. *Imbalance caused by the global etch variation. The estimation was conducted with the average blade height of 150 µm and the total thickness of 450 µm.*

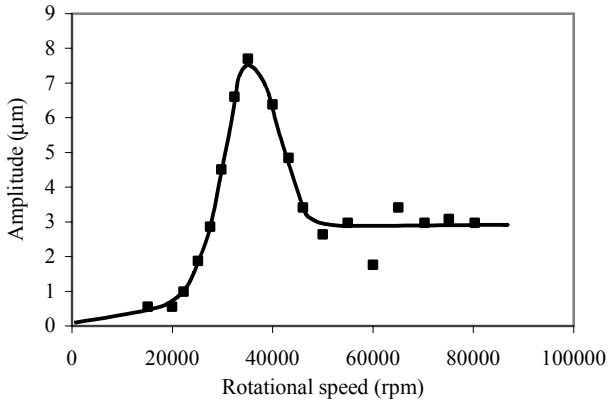

Figure 10. *Whirl response of a rotor with a global etch variation of 3 %. The whirl amplitude in the supercritical region is about 3 µm.*

CONCLUSIONS

This paper discusses the etch non-uniformity of DRIE process, which introduces the imbalance on high-speed micro-rotors and limits their performance. The etch variation measured along the periphery of the rotor was the combination of both global and local effects, which could be segregated via Fourier transformation. The imbalance due to the global etch non-uniformity was estimated for the micro-rotor with symmetric features. The comparison to the experimental results revealed the large dependency of the micro-rotor performance on the precision fabrication. The global etch variation depending on the etching conditions was minimized at an APC angle of 55 degrees. This well-balanced rotor with an estimated imbalance of 0.2 µm will be packaged and tested. The manufacturing processes presented herein are readily applicable to the constructions of other high-speed rotating micro-structures and other micro-devices which require precise fabrication and contain intricate geometries and large etched areas.

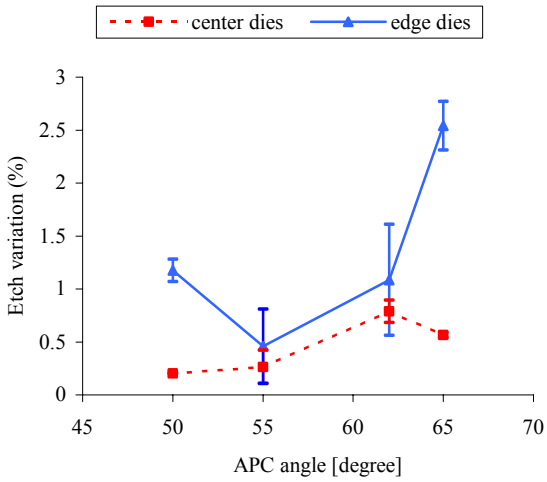

Figure 11. *The global etch variation of the center and edge dies with respect to the APC angle. Except the APC angle, the etching conditions were identical to those described in the caption of Figure 6. It can be deduced that an optimal APC angle of 55 degrees culminates in a high yield of well-balanced rotors; these highly precise rotors, with 0.4 µm imbalance and 0.25 % global etch variation, have been repeatedly spun at 1.4 Mrpm.*

ACKNOWLEDGEMENTS

This work is supported by the Army Research Office (DAAH04-95-1-0093) under Dr. R. Paur and by DARPA (DAAG55-98-1-0365, DABT63-98-C-0004) under Dr. R. Nowack and Dr. J. McMichael respectively.

REFERENCES

1. A.H. Epstein and S.D. Senturia, "Macro Power from Micro Machinery," *Science, Vol. 276*, 1211 (1997).
2. L.G. Frechette, S.A. Jacobson, K.S. Breuer, F.F. Ehrich, R. Ghodssi, R. Khanna, C.W. Wong, X. Zhang, M.A. Schmidt, and A. Epstein, "Demonstration of a Microfabricated High-Speed Turbine Supported on Gas Bearings," *Hilton Head Solid-State Sensors and Actuators Workshop*, Hilton Head Island, SC, June (2000), pp. 43-47.
3. A.A. Ayon, X. Zhang, and R. Khanna, "Ultra Deep Anisotropic Silicon Trenches Using Deep Reactive Ion Etching (DRIE)," *Hilton Head Solid-State Sensors and Actuators Workshop*, Hilton Head Island, SC, June (2000), pp. 339-342.
4. N. Miki, X. Zhang, R. Khanna, A.A. Ayon, D. Ward, and S.M. Spearing, "A Study of Multi-stack Silicon-direct Wafer Bonding for MEMS Manufacturing," The 15th IEEE International Conference on Micro Electro Mechanical Systems, Las Vegas, Nevada, January (2002), pp. 407-410.
5. D. Childs, "Turbomachinery Rotordynamics: phenomena, modeling and analysis," John Wiley, 1993

OPTICAL ACTUATION OF MICROFLUIDICS BASED ON OPTO-ELECTROWETTING

Pei Yu Chiou and Ming C. Wu
Department of Electrical Engineering, University of California at Los Angeles
Los Angeles, CA 90095-1594, USA

Hyejin Moon and Chang-Jin Kim
Department of Mechanical and Aerospace Engineering,
University of California at Los Angeles
Los Angeles, CA 90095-1594,USA

Hiroshi Toshiyoshi
Institute of Industrial Science, University of Tokyo, Japan

ABSTRACT[1]

Optical actuation of liquid droplets has been experimentally demonstrated for the first time using a novel opto-electrowetting principle. The opto-electrowetting (OEW) surface is realized by integrating a photoconductive material underneath a two-dimensional array of electrowetting electrodes. Contact angle change as large as 40° has been achieved when illuminated by a light beam with an intensity of 65 mW/cm^2. A micro-liter droplet of deionized water has been successfully dragged by a 4-mW laser beam across a 1cm x 1cm OEW surface. The droplet speed is measured to be 7 mm/sec. Light actuation enables complex microfluidic functions to be performed on a single chip without encountering the wiring bottleneck of two-dimensional array of electrowetting electrodes.

INTRODUCTION

Surface tension is a dominant force for liquid handling and actuation in microscale. Several mechanisms have been proposed to control surface tension, including thermocapillary [1], electrowetting [2], and light-induced surface tension change [3]. Among them, the electrowetting mechanism has received increasing interests because of its fast switching response and low power consumption. The surface tension between the liquid-solid interface is modified by external electric field, which reduces the contact angle. Examples of electrowetting-based microfluidic systems include optical switches [4], digital microfluidic circuits [5] and liquid lenses with variable focal length [6].

Transport of liquid in droplet forms offers many advantages. It eliminates the need for pumps and valves, has no moving parts, and is free of leak and unwanted mixing. For Lab-on-a-Chip applications, several fluidic functions, such as liquid injection, transportation, mixing, and separation, need to be integrated on a single chip. This has been achieved by Cho, *et al.,* recently [5]. For a general purpose fluidic chip that is capable of manipulating *multiple* droplets simultaneously requires a two-dimensional array of electrodes to control the local surface tension. However, this results in a large number of electrodes that presents a challenge for control and packaging of such chips. The problem becomes even more severe as the droplet size scales down. Though the number of electrodes can in principle be reduced by integrating address decoders on the chip, similar to the memory access circuits, this will significantly increase the cost of the chip.

Travel support has been generously provided by the Transducers Research Foundation and by the DARPA MEMS and DARPA BioFlips programs.

In this paper, we report on a novel mechanism for light-actuation of liquid droplets. This is realized by integrating a photoconductive material underneath the electrowetting electrodes. We called this mechanism "opto-electrowetting". We have successfully fabricated a prototype chip with 1 cm x 1 cm area. A micro-liter droplet has been successfully transported to any location on the chip. This approach completely eliminates the wiring bottleneck of conventional electrowetting schemes. This concept is extendable to nano-liter droplets (or smaller) and simultaneously manipulation of multiple droplets.

PRINCIPLE OF OPTO-ELECTROWETTING

Figure 1(a) shows the general electrowetting mechanism. A droplet of polarizable and conductive liquid is placed on a substrate with an insulating layer between the liquid and the electrode. When an external voltage is applied, the surface tension at the solid-liquid interface is modified and the contact angle changes. The voltage dependence of the contact angle is described by Eq. (1):

$$\cos[\theta(V_A)] = \cos[\theta(0)] + \frac{1}{2}\frac{\varepsilon}{d\gamma_{LV}}V_A^{\,2} \qquad (1)$$

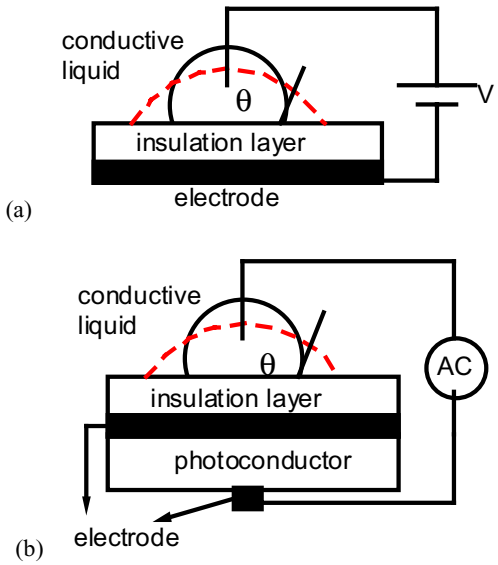

Figure.1 *(a) Conventional electrowetting under DC bias, and (b) opto-electrowetting with an integrated photoconductor under AC bias.*

0-9640024-4-2/hh2002/$20©2002TRF
DOI 10.31438/trf.hh2002.67

where V_A , d , ε , and γ_{LV} are applied voltage, thickness of insulating layer, dielectric constant of the insulating layer, and the interfacial tension between liquid and vapor, respectively. If an AC voltage is applied, V_A is replaced by the root-mean-square (RMS) voltage [7].

Figure 1(b) shows the concept of the proposed opto-electrowetting (OEW) mechanism. A photoconductive material is integrated under the electrode of conventional electrowetting circuit. The electrical impedance of the liquid, insulator, and photoconductor are serially connected. From Eq. (1), the contact angle change of the droplet on this OEW surface is determined by the voltage drop across the insulating layer.

The frequency of the AC voltage is adjusted such that the impedance of the photoconductor dominates in the absence of light (dark state). Through the voltage divider, most of the voltage drops across the photoconductor and there is very little voltage across the insulating layer. Therefore, the contact angle remains the same as the equilibrium value. Upon illumination of light, the conductivity of the photoconductor increases by several orders of magnitude due to electron-hole pair generation. The impedance of the photoconductive layer becomes much smaller than that of the insulation layer. As a result, most of the voltage drop is now across the insulating layer. The contact angle is therefore reduced by light illumination.

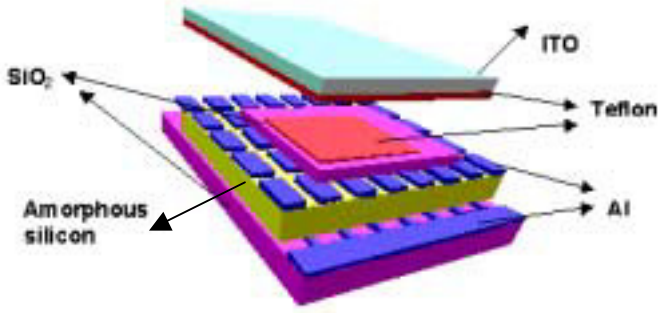

Fig.2 *Schematic structure of the opto-electrowetting (OEW) device. A photoconductive material (amorphous Si) is integrated with a matrix electrode array to realize OEW mechanism.*

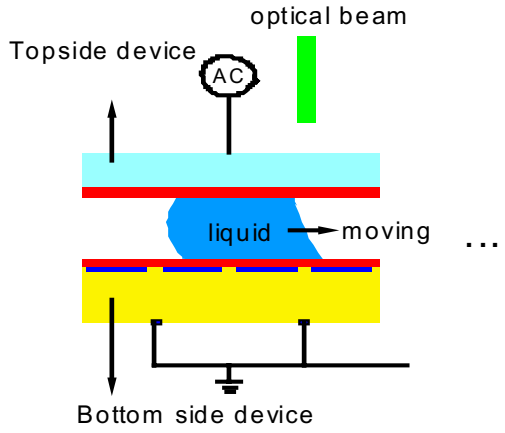

Fig.3 *Principle illustrating light actuation of liquid droplets.*

Figure 2 shows the schematic of the OEW device proposed in this paper. The liquid droplet is sandwiched between a top hydrophobic surface and a bottom OEW surface. The topside is a transparent conductive indium-tin-oxide (ITO) glass coated with 20 nm of Teflon. The OEW structure is realized by integrating a 2-D array of electrowetting electrodes on a photoconductive material. In our current design, twenty thousand electrodes with areas of 50μm × 100μm are employed over a total chip area of 1 cm^2. The photoconductive material employed here is amorphous silicon. It is deposited by plasma-enhanced chemical vapor deposition (PECVD). The electrodes are then covered by a 0.9-μm-thick SiO_2 and a 20-nm-thick Teflon. The Al electrode below the photoconductor has a grid pattern to reduce parasitic capacitance.

The moving principle and the equivalent circuit of this device is presented in Fig. 3 and 4, respectively. An AC voltage is applied between the top ITO electrode and the bottom Al grid. The voltage drop across the insulator and the electrode is controlled by light. Shining an optical beam on one edge of the liquid droplet decreases the contact angle and creates a pressure difference between two ends of the droplet, as shown in Fig. 3. This forces the droplet to follow the movement of the optical beam. Liquid droplet does not move for DC voltage bias because all the voltage drops across the insulating layer on every electrode even without light illumination. The contact angle on both ends of the droplet decreases and no pressure difference is created.

According to the equivalent circuit in Fig. 4, every electrode is connected in parallel. Voltage drop across the SiO_2 on top of each electrode is a function of AC frequency and photoconductivity.

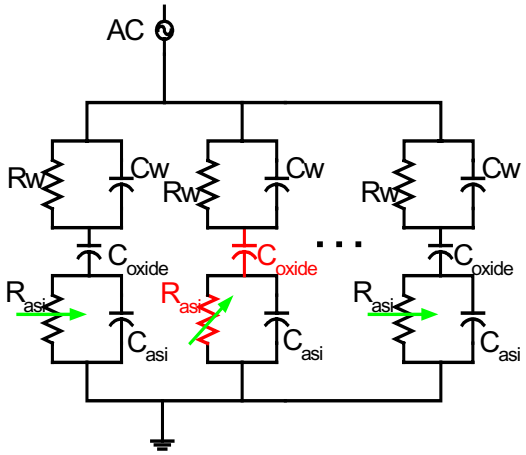

R_w , C_w: resistance and capacitance of water
C_{oxide}: capacitance of between liquid and electrode
R_{asi} , C_{asi}: resistance and capacitance of amorphous Si

Fig.4 *Equivalent circuit of the opto-electrowetting device. Under light illumination, the voltage drop across the photoconductor decreases while the voltage drop across SiO_2 increases.*

CONTACT ANGLE MEASUREMENT UNDER LIGHT ILLUMINATION

To effectively change the contact angle by light, the photoconductor needs to satisfy the following criteria:

(1) Low dark conductivity. This ensures the voltage will not drop across the insulator in the dark.

(2) Short electron-hole pair recombination time. This will shorten the switching time
(3) Visible light response. Low cost visible light sources (either diode lasers or light-emitting diodes) are readily available.

Amorphous silicon satisfies all three criteria. It has a dark conductivity of 10^{-8} S/cm, an electron-hole pair recombination time of ~ a microsecond, and is responsive to visible light. Figure 5(a) shows the experimental setup for measuring the photoconductivity. Two coplanar Al electrodes form Ohmic contacts with amorphous silicon. White light source with uniform intensity is used for measuring the photoconductivity.

The relationship between the photoconductivity and light intensity is shown in Fig. 6. The conductivity increases by 80 times under illumination of light with an intensity of 65 mw/cm^2.

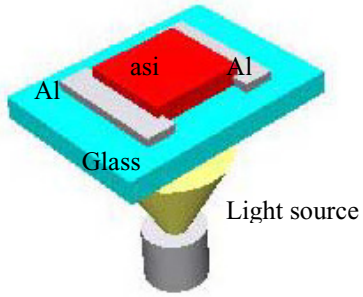

(a)

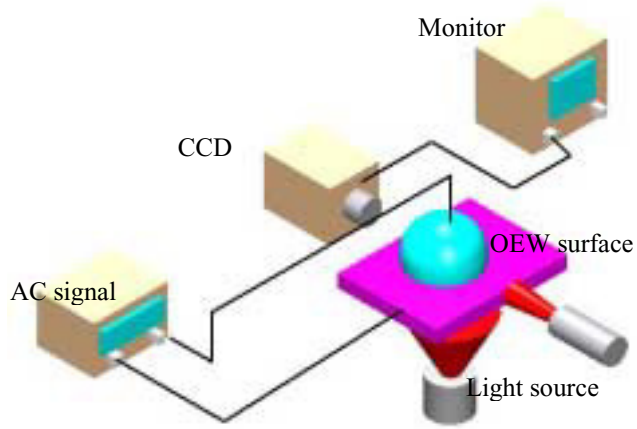

(b)

Fig.5 *Experimental setup for (a) photoconductivity measurement, and (b) contact angle measurement on opto-electrowetting (OEW) surface.*

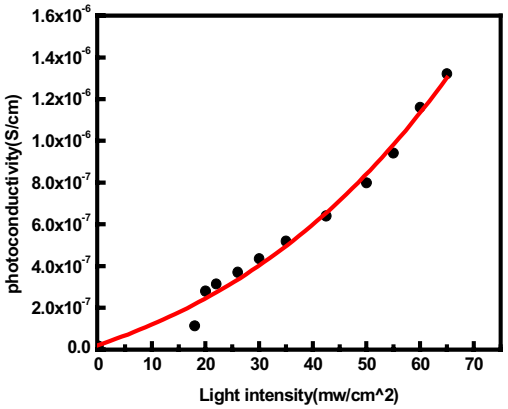

Fig.6 *Photoconductivity versus light intensity for amorphous silicon..*

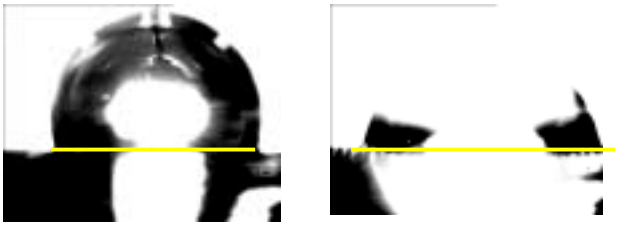

Fig.7 *Side-view profiles of the droplet with and without light illumination.*

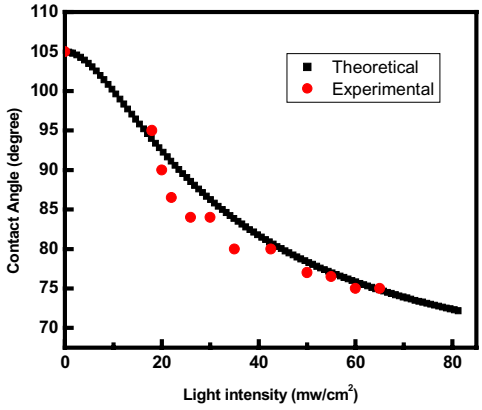

Fig.8 *Contact angle change under light illumination*

To measure the contact angle change, an OEW surface is manufactured on a glass substrate. The thickness of the amorphous silicon layer is the same as the sample used in the photoconductivity measurement. The experimental setup is shown in Fig. 5(b). The liquid used here is DI water. A CCD camera is used to image the side-view profile of the droplet. A 500 Hz, 100 Volt AC signal is applied. Figure 7 shows the side-view profiles of the droplet in the dark and under light illumination of 65mw/cm^2 intensity. The theoretical calculation and experiment result are shown in Fig. 8. In our theoretical calculation, the conductivity of water is assumed to be 10^{-6} S/cm and photoconductivity is

assumed to have linear relationship with light intensity. In this device, the contact angle saturates at around 75 degrees. This saturation comes from the limitation of electrowetting.

EXPERIMENTAL DEMONSTRATION OF LIQUID TRANSPORT BY LIGHT

Figure 9 shows the photograph and microscope picture of the OEW device. The chip area is 1 cm x 1 cm, and the Al electrode area is 50 μm x 100 μm. Over 20,000 electrodes have been fabricated on the OEW surface. To demonstrate light actuation, a droplet with a diameter of 2 mm is sandwiched between a Teflon-coated ITO glass and an OEW surface with a gap of 0.5 mm. A 4-mw laser at 532 nm wavelength is used to drag the liquid droplet. The droplet is successfully moved across the 1cm x 1 cm surface by the laser beam. A droplet speed of 7mm/s was observed. Figure 10 shows four snap shots from the video recording of liquid transport.

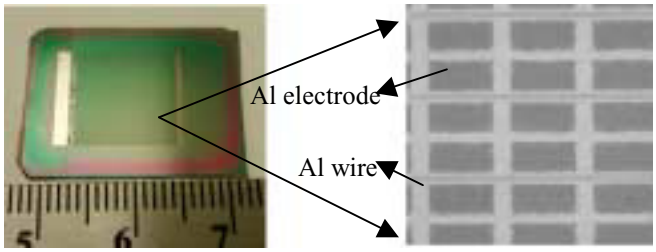

Fig.9 *Photograph and microscope picture of the OEW device.*

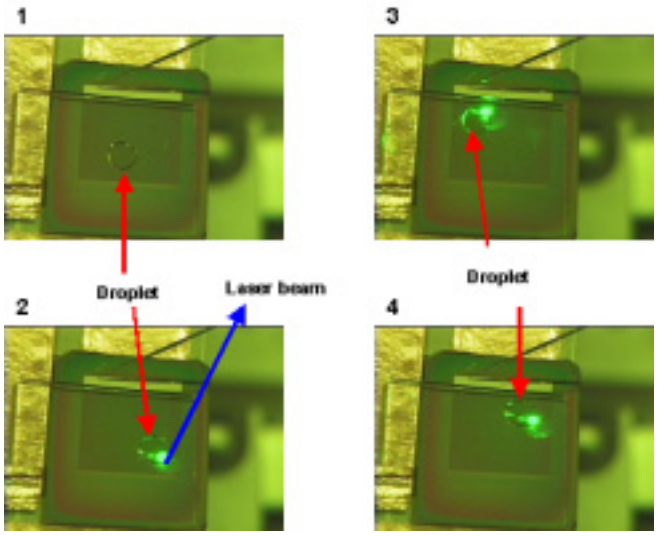

Fig.10 *Example of liquid transport across a 1cm×1cm OEW area actuated by an optical beam.*

CONCLUSION

A novel opto-electrowetting (OEW) mechanism has been proposed to move liquid droplets by light. This mechanism, combining electrowetting with light response of photoconductors. The light actuation enables a large number of electrowetting electrodes to be addressed without wiring bottlenecks. Experimentally, over twenty thousand electrodes have been integrated on a 1cm×1cm area and only a single bias is needed for the entire device. Amorphous silicon is chosen to be the photoconductive material because of its properties of low dark conductivity, photoconductivity at visible wavelength, and short electron-hole pair recombination time. Under an AC bias voltage, the contact angle of the liquid droplet on this OEW surface is a function of light intensity. A 40 degrees contact angle change has been experimentally observed between dark and 65mw/cm^2 light illumination. The contact angle decreasing saturates at 75 degree in the OEW surface due to the wetting limitation of electrowetting. Movement of liquid droplet at 7 mm/sec across the entire surface has been successfully demonstrated using a 4 mW laser beam.

ACKNOWLEDGMENTS

The authors would like to thank Sagi Mathai and Jui-Che Tsai for assisting our measurement, Pamela Peterson for valuable discussions of fabrication process, and professor Chih-Ming Ho for valuable discussions. This project is supported in part by DARPA Optoelectronics Center through CHIPS (Center for Heterogeneously Integrated Photonics) under contract # MDA972-00-1-0019.

REFERENCES

1. T.A. Sammarco, M.A. Burns, "Thermocapillary pumping of discrete drops in microfabricated device," *AIChE* J. 45 (2) (1999) 350-366.

2. Pollack, M.G.; Fair, R.B.; Shenderov, A.D., "Electrowetting-based actuation of liquid droplets for microfluidic applications," *Applied Physics Letters*, vol.77, (no.11), AIP, 11 Sept. 2000. p.1725-6.

3. Kunihiro Ichimura, Sang-Keun Oh, and Masaru Nakagawa, "Light-Driven Motion of Liquids on a Photoresponsive Surface," *Science* 2000 June 2; 288: 1624-1626

4. G.Beni, S. Hackwood, J. L. Jackel, "Continuous electrowetting effect", *Appl. Phys. Lett.* 40 (10) (1982) 912-914.

5. S. K. Cho, S. K. Fan, Hyejin Moon, Chang-Jin Kim, "Towards digital microfluidic circuits: creating, transporting, cutting, and merging liquid droplets by electrowetting-based actuation," *Technical Digest. MEMS 2002. 15th IEEE International Conference on Micro Electro Mechanical Systems, page 32-35.*

6. Sunghoon Kwon, Luke P. Lee, "Focal lengthcontrol by microfabricated planar electrodes-based liquid lens(uPELL)," *Digest of Technical Papers ,Transducers '01 Eurosensors XV 11th International Conference on Solid-State Sensors and Actuactors,, page 1348-1351.*

7. Vallet, M.; Vallade, M.; Berge, B. "Limiting phenomena for the spreading of water on polymer films by electrowetting," *European Physical Journal B*, vol.11, (no.4), EDP Sciences; Springer-Verlag, Oct. 1999. p.583-91.

MULTIELECTRODE MICROPROBES FOR DEEP-BRAIN STIMULATION FABRICATED USING A NOVEL 3-D SHAPING ELECTROPLATING PROCESS

Paulo S. Motta and Jack W. Judy
Electrical Engineering Department, University of California, Los Angeles
Los Angeles, CA 90095, USA

ABSTRACT

This paper describes a novel 22-mm-long multi-channel microelectrode suitable for deep-brain stimulation in rodents. The platinum electrodes and conducting interconnects are insulated by silicon nitride and the mechanical support is provided by a 3-D electroplated biocompatible metallic structure. The shape of the probe has been designed to provide sufficient mechanical stiffness for accurate targeting of deep-brain regions while minimizing tissue damage. The probe thickness and width are smoothly tapered from the 200-µm-wide and 150-µm-thick shank to the 10-µm-thick probe tip. The electrical and mechanical properties of the electrode array have been tested and show an impedance of 4.5 kΩ at 10 kHz.

INTRODUCTION

For nearly half a century [1], microprobes have been used in many different applications to study neuronal tissues and even to restore neuronal function[2]. Although much of this work has been performed in the cortex (*i.e.*, the outer 1-mm-thick layer of the brain that is responsible for processing sensory and motor information as well as learning and memory), an exciting field of research is the recording and stimulation of deep-brain regions (*i.e.*, the thalamus located more than 2 cm below the cortex). The thalamus acts as the emotional center of the brain and provides fine adjustments to the motor system. In fact, it has been shown that deep-brain stimulation (DBS) of the subthalamic nucleus can eliminate the tremors associated with Parkinson's disease [3-4].

An ideal DBS stimulation system has the following characteristics: all materials exposed to the surrounding environment are biocompatible; the stimulating parameters are such that irreversible reactions (*e.g.*, hydrolysis or dissolution) do not occur at the electrode sites; the probe geometry provides a stiff structure to penetrate biological tissues; the tip should be narrow enough to cause the least amount of damage.

The microprobes of stimulators are typically either insulated wires or microfabricated electrode arrays. Insulated metal microwires have long been used in electrophysiology to record and stimulate neural tissue. Microwires are inexpensive, have a wide shank that is easy to handle, possess a sharp tip to minimize tissue damage, and is smoothly tapered in width and thickness to provide the stiffness needed to penetrate neural tissue deeply without bending. The major drawback of microwires is that only one electrode is available per wire. Previously reported multielectrode microprobes have been produced using the following processes and materials to form the probe shank: (1) deeply diffused p+ wells in single crystal silicon [5], (2) the upper single-crystal silicon layer of silicon-on-insulator (SOI) wafers [6], and (3) uniformly electroplated metal [7]. In all of these probe fabrication processes, the resulting shank either has a uniform thickness – except right at the tip – or has an abrupt two-stage thickness with a thin region near to the tip and a thicker region away from the tip to facilitate easy handling. We report here a microprobe that combines the advantages of traditional microwires (*i.e.*, tapered width and thickness) with those of microfabrication (*i.e.*, multiple electrodes per shank) that enable a long probe to be stiff yet minimizes tissue damage upon insertion.

Multielectrode microprobes uniquely suited for deep-brain stimulation in rats have been produced using a simple low-cost batch-fabrication process. The fabricated probes have a length greater than 20 mm and have both a thickness and a width that can be varied smoothly from the dimensions of the tip (~10 µm) to that of the shank (~150 µm).

The complete fabrication process consists of metal traces insulated by LPCVD (bottom) and PECVD (top) silicon nitride, which forms the thin-film electrode array and interconnects. A metal seed layer is then patterned so that a 3-D structure that supports the electrode array can be formed by electroplating Figure 1.

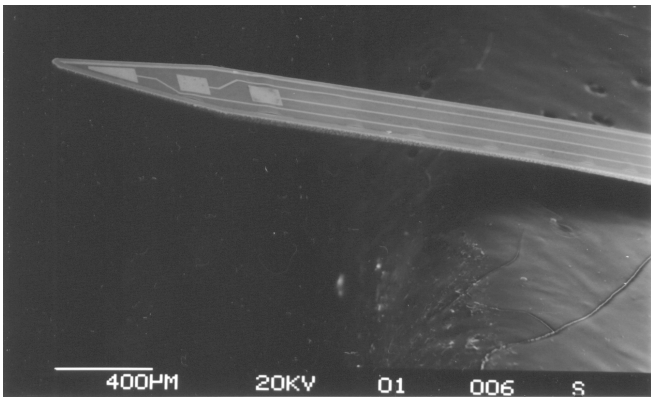

Figure 1. Released probe with 3 electrode sites.

PROBE DESIGN

The intended application largely dictates many of the probe design parameters: length, width, thickness, stiffness, and number of electrodes. For example, the length of cortical electrodes only needs to be ~1 mm [5], whereas deep-brain stimulation-probes must be approximately 10 times longer (*e.g.*, ~10 mm in rats to reach the STN) plus several millimeters to allow the probe to interface with the stimulation circuitry and packaging.

Since the DBS system design for rats requires an overall probe length of 22 mm, the mechanical stiffness of microprobes is important for accurately targeting small deep-brain regions (*e.g.*, the rodent STN is $1.0\times0.5\times0.5\ mm^3$). Cross sections of microfabricated probes are usually rectangular, semicircular, or a combination of both. To illustrate the impact of a ten-fold increase in the beam cross-section geometry, the theoretical stiffness of semicircular cross section is calculated and plotted as a function of beam length (Figure 2). For simplicity, beams with a constant cross section are considered in Figure 2. For semicircular cross sections, the beam stiffness k_{SC} is given by [8]

0-9640024-4-2/hh2002/$20©2002TRF
DOI 10.31438/trf.hh2002.68

Solid-State Sensors, Actuators, and Microsystems Workshop
Hilton Head Island, South Carolina, June 2-6, 2002

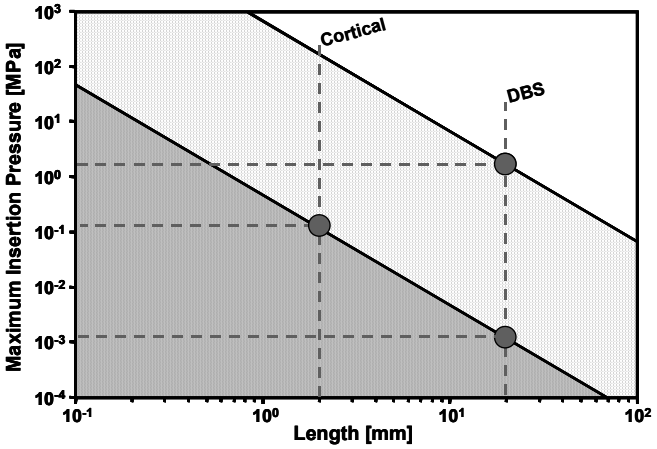

Figure 2. Plot of maximum theoretical insertion pressure as a function of probe length for those with a typical cortical and DBS probe cross sections.

$$k_{SC} = \frac{E \cdot r^4}{3 \cdot l^3} \quad ,$$

with elastic modulus E, semicircular radius r, and length l. The buckling strain ε of a beam fixed on one end is given by

$$\varepsilon = \frac{\pi^2 \cdot I}{A \cdot l^2} = \frac{P}{E} \quad ,$$

with semicircular cross sectional area A, moment of inertia I and insertion pressure P. The maximum insertion pressure before probe buckling takes place can be calculated for each probe geometry

$$P = \frac{\pi^2 \cdot E \cdot I}{A \cdot l^2} \quad .$$

We see that the stiffness has a cubic dependence on length and will drop off rapidly as l is increased. Since DBS probes are ~10 times longer than cortical probes, they are 1000 times less stiff for a given cross section. However, increasing the width and thickness by a factor of 10 will increase the stiffness by a factor of 10^4 for a given probe length. The net result is that even though DBS probes are 10 times longer than cortical probes, they can be 10 times stiffer. Furthermore, if the cortical probes were made as long as a DBS probes, while keeping the cross sectional area unchanged, they would be able to withstand only 3 orders of magnitude less insertion pressure than DBS probes.

Besides being stiff enough to withstand insertion forces and tissue inhomogeneity, the microelectrode must cause the least amount of tissue damage at the active end (*i.e.*, the tip). Thus the thicker and wider DBS probes must smoothly taper to a sharp tip. Other desired probe characteristics are biocompatibility and increased electrode count. Chronic probes must be made of biocompatible materials to avoid rejection of the probe by the host tissue. The greater the number of electrodes available, the larger the number of stimulation patterns possible and the greater the capability of the stimulation system.

Although microwires have been shown to be biocompatible and have a tapered geometry that enables a stiff probe that causes minimum damage, only one electrode is available per microwire. Microfabricated probes provide a high electrode count but the processes used to produce them do not allow for the tapered geometry ideally suited for DBS applications. A microprobe technology that combines the best of microwires and microfabricated probes is needed to address DBS applications, such a Parkinson's disease, epilepsy, etc.

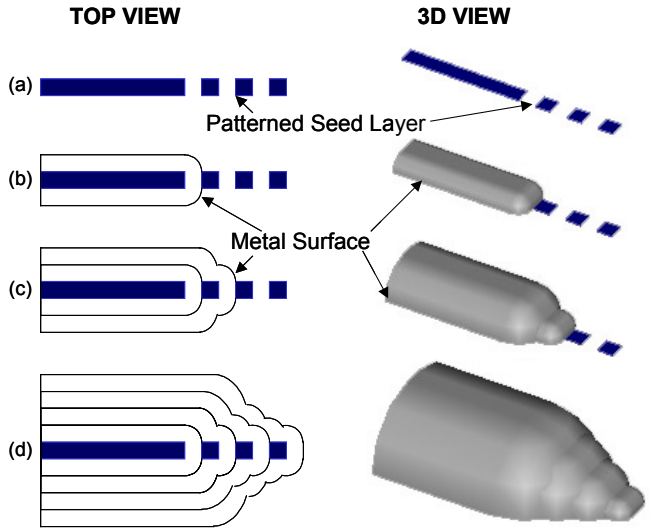

Figure 3. Schematic diagram illustrating (a) patterned seed layer before plating, (b) after the isotropically grown electrodeposit shorts to the first, (c) second, (d) all adjacent patterned seed layer regions.

3-D SHAPING ELECTROPLATING PROCESS

The microfabrication technique reported here uses electroplating to create customizable 3-D structures. Electroplating requires the presence of a seed layer, upon which the electrodeposit is formed. Usually the seed layer is continuous and a plating mold is used to determine the final shape of the electrodeposited film (*i.e.*, through-mask plating). This method leads to sidewalls that mimic that of the plating mold and often results in vertical sidewalls and sharp corners, that are undesirable in chronic implants.

By using a patterned seed layer (*i.e.*, temporarily electrically isolated regions of the seed layer), sidewalls with a slope of 1 or less can be achieved [9]. The electrodeposit grown on a patterned seed layer rounds sharp edges. As the electrodeposit grows vertically and horizontally from one region of patterned seed layer, adjacent regions of patterned seed layer become electrically connected due to the lateral growth. Subsequent deposition will then commence on these newly connected regions as well as the previously plated structures. As illustrated in Figure 3, this process allows for the fabrication of tapered probes which will reduce the amount of tissue damage at the stimulation site while retaining the targeting accuracy needed for long probes.

FABRICATION

The DBS mutlielectrode microprobes reported here consists of four parts: insulating layer, interconnects, electrode sites, and mechanical supporting layer. Silicon nitride deposited by LPCVD and PECVD serves as the insulating layer between the interconnects and supporting layer as well as a chemical barrier between the interconnects and surrounding tissue and fluids. Electrode sites and interconnects are made of platinum, which was chosen for its biocompatibility and charge delivery capability. The mechanical layer made of electroplated nickel and gold provides the probe with the desired level of stiffness. Starting with a <100>-oriented 100-mm-diameter p-type silicon wafer, 100 nm of low-stress LPCVD silicon nitride is deposited to serve as the first insulating layer. This layer is then patterned to define the electrode openings (100×100 μm^2) and the probe shank width. To avoid

spurious metal deposition during the electroplating step, a 100-nm-thick layer of thermal silicon dioxide is grown. Since the previously patterned nitride serves as an oxidation barrier, the silicon dioxide only grows in the openings where silicon was exposed (Figure 5a).

In order to be able to release the microprobes from the silicon substrate, openings on the backside of the wafer must be created for the bulk release etch. In the next step, 10 nm of Cr, 150 nm of Pt, and another 10 nm of Cr are deposited via electron-beam evaporation, to form the probe interconnect and electrode sites (Figure 5b). Using wafer curvature techniques, the stress of the evaporated metal layer is measured to be 933.5 MPa tensile and its sheet resistance is 1.112 Ω/sq. The chromium layers serve as adhesion layers between the insulating layers and the platinum interconnect.

The top insulation layer, a 500-nm-thick silicon nitride layer, is then deposited by PECVD. The purpose of this layer is to electrically isolate the electrodes and interconnects from the mechanical supporting layer. Once the top insulator is patterned, a platinum line that surrounds the probe becomes exposed. This feature will be used during the plating of the mechanical supporting layer to completely seal in the non-biocompatible parts of the probe (*i.e.*, Cr, Ni), as shown in Figure 5c.

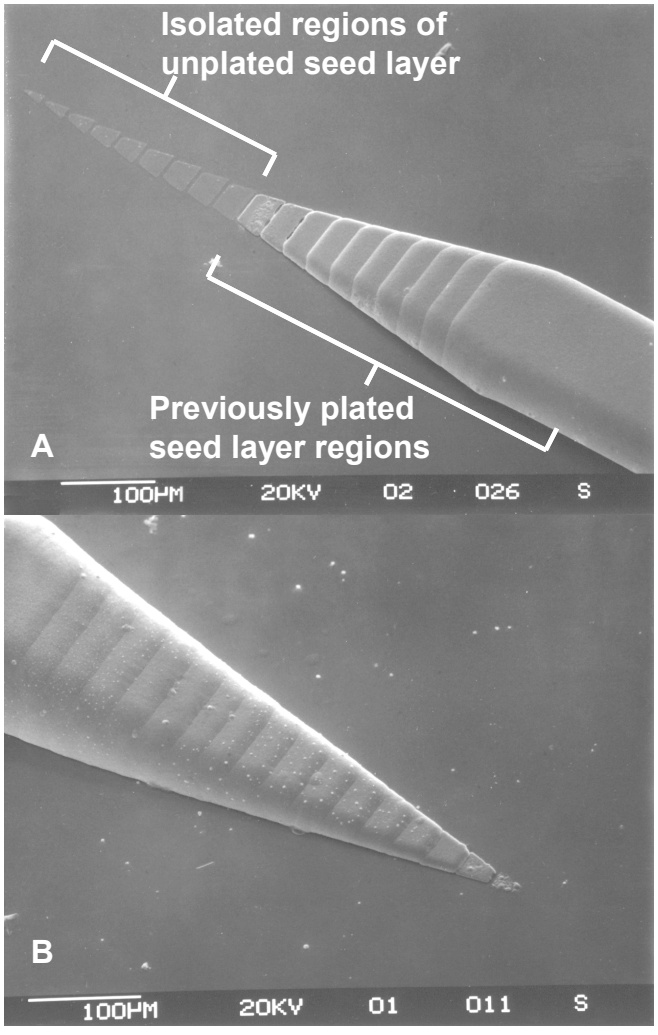

Figure 4. (a) Partially completed 3-D probe plating process.(b) Fully plated tapered probe

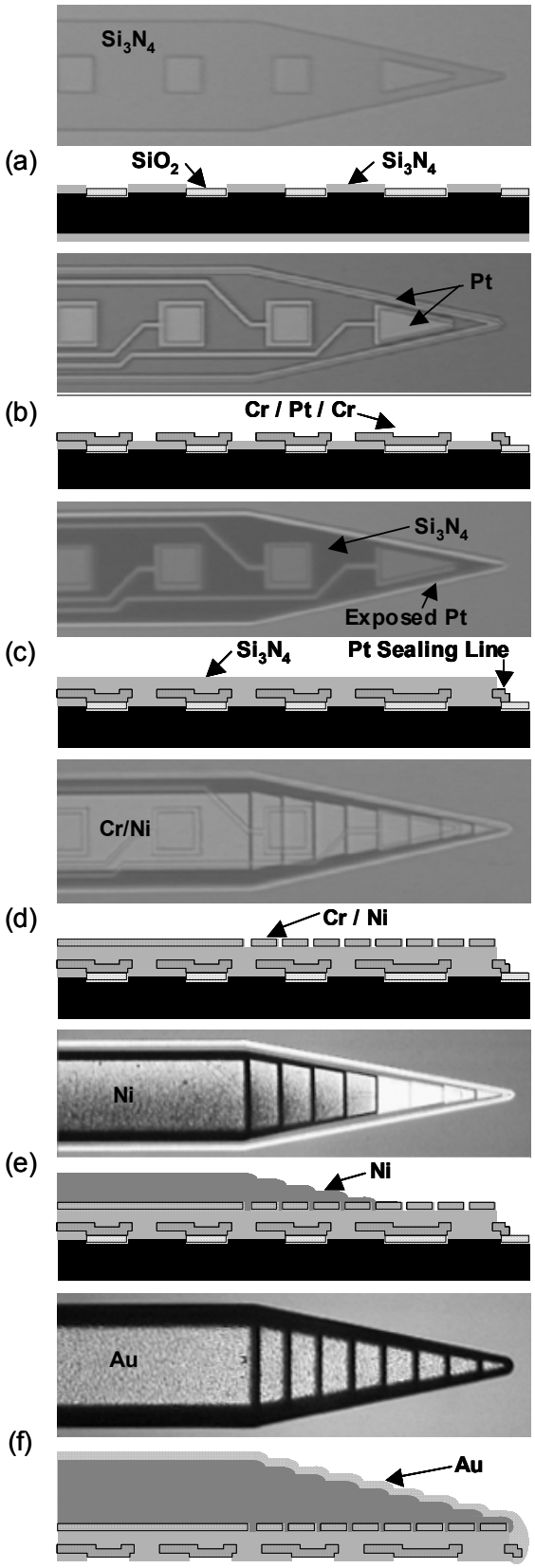

Figure 5. Fabrication process: (a) first insulating layer, (b) interconnect and electrode, (d) second insulating layer, (d) patterned seed layer, (e) electroplated probe shown half way through plating process, (f) plated probe release from substrate.

The next few steps are used to construct the mechanical supporting layer of the probe. Importantly, the in-plane shape of the probe, as defined by the etched nitride layers, will be retained and the thickness of the mechanical layer will be thin at the tip but gradually becoming thicker and stronger at the other end. To accomplish this 3-D geometry, a patterned seed layer made of 10 nm of Cr (adhesion layer) and 100 nm of Ni (seed layer) is deposited by electron-beam evaporation on top of the second nitride layer (Figure 5d). As the electrodeposit forms on the region of the patterned seed layer connected to the plating power supply, the film plates upwards and outwards (Figure 4e). When a neighboring island of isolated seed layer is reached, plating commences over this newly connected surface (Figure 4a).

By linking a series of seed layer islands of different shapes and sizes the thickness and width of the resulting shank can be controlled over a wide range. In our process we use electroplated nickel for strength and a subsequent layer of electroplated gold for biocompatibility (Figure 5e).

In the absence of a plating mold, the effective electroplating area for a patterned seed layer deposit increases with time. Since it is desirable to maintain a constant plating current throughout the formation of the mechanical layer, a program was written in Visual Basic to control the power supply (Agilent E3634A) via an RS-232 interface. The current was increased every minute at increments of ~150 μA. After the plating steps are finished, the probes are released in KOH at 70°C for 15 hours. The overall probe structure consists of platinum electrodes, conductive traces, silicon nitride insulation layers and an electroplated metal shank.

EXPERIMENTAL CHARACTERIZATION

The microelectrode probes were tested electrically and mechanically. The series resistance of the electrode interconnect is 3.4 kΩ. No shorting was observed between channels and the electroplated mechanical supporting layer. The electrode impedance was tested in artificial cerebral spinal fluid (*i.e.*, a sodium chloride-based saline solution) at room temperature. The impedance value of a typical electrode site is 4.5 kΩ at a frequency of 10 kHz. The electrode was also stimulated with a biphasic charge-balanced 200-μs-wide pulse at 180 Hz, with an amplitude of 1 mA. At currents higher than 1.5 mA, hydrolysis was observed at the electrode site. Initial mechanical testing showed that when inserted into simulated brain tissue the probes did not bend nor buckle and were able to be inserted accurately.

CONCLUSIONS

A 22-mm-long multi-channel microprobe electrode array has been designed for DBS application. The design attempts to minimize damage to surrounding tissue while providing sufficient stiffness for this long microprobe to target small brain regions. The DBS microprobe was produced with a low-cost batch-fabrication process that includes a novel 3-D plating process to shape the mechanical supporting layer of the probe into a tapered geometry similar to conventional microwires. Each microfabricated DBS probe has multiple electrodes that can be used to target and tailor the stimulus. These microprobes have the potential to significantly impact DBS research, such as the investigation of treatments for Parkinson's Disease and its debilitating symptoms. In principle, this approach to multielectrode microprobe fabrication could also be combined with integrated circuits, in a batch or assembled process.

ACKNOWLEGMENT

The authors would like to thank Andy Hung for his assistance with the electrochemical testing and the UCLA Applied MEMS laboratory. This work is supported by the NIH-funded UCLA Morris K. Udall Center for Parkinson's Disease Research under grant NS38367.

REFERENCES

1. P. D. Wall, W. S. McCulloch, J. Y. Lettvin, and W. H. Pitts, "The terminal arborization of the cat's pyramidal tract determined by a new technique", *Yale Journal of Biological Medicine*, *28*, (1956).

2. F. T. Hambrecht and J. B. Reswick,, United States, Rehabilitation Services Administration, and National Institute of Neurological and Communicative Disorders and Stroke, *Functional electrical stimulation applications in neural prostheses* New York: M. Dekker, (1977).

3. J. G. Nutt, S. L. Rufener, J. H. Carter, V. C. Anderson, R. Pahwa, J. P. Hammerstad, and K. J. Burchiel, "Interactions between deep brain stimulation and levodopa in Parkinson's disease," *Neurology*, *57*, 10 (2001).

4. J. S. Yeomans, *Principles of brain stimulation* New York: Oxford University Press, (1990).

5. K. Najafi, "Solid-state microsensors for cortical nerve recordings," *IEEE Engineering in Medicine and Biology Magazine*, *13*, 3 (1994).

6. K. Cheung, L. Gun, K. Djupsund, D. Yang, and L. P. Lee, "A new neural probe using SOI wafers with topological interlocking mechanisms," *1st Annual International IEEE-EMBS Special Topic Conference on Microtechnologies in Medicine and Biology* (2000).

7. Y. Sugai, F. Asa, Y. Okada, T. Yokoshima, T. Momma, T. Osaka, and T. Ito, "Formation of microprobe using nickel electrodeposition," *Electrochemistry*, *67*, 12 (1999).

8. W. C. Young, R. G. Budynas, and R. J. Roark, *Roark's Formulas for stress and strain*, 7th ed ed. New York: McGraw-Hill, (2001).

9. A. Maciossek, SPIE, Semicond.Equipment & Mater.Int, and NIST, "Electrodeposition of 3D microstructures without moulds," *Proceedings of the SPIE - The International Society for Optical Engineering*, *2879*, (1996).

A NOVEL MEMS TUNABLE CAPACITOR BASED ON ANGULAR VERTICAL COMB DRIVE ACTUATORS

Hung Nguyen, Dooyoung Hah, Pamela R. Patterson, Wibool Piywattanametha, Ming C. Wu
Department of Electrical Engineering
University of California, Los Angeles, CA 90095, U.S.A.

Rumin Chao
National Cheng Kung University
TAIWAN

ABSTRACT

We report on the design, fabrication, and measurement of a novel MEMS (MicroElectroMechanical System) tunable capacitor with angular vertical comb-drive (AVC) actuators. The AVC allows continuous rotation and therefore large tuning ratio without pull-in. The device fabrication process is relatively simple, consisting of a single deep reactive ion etching step followed by release and out-of-plane assembly of the angular combs. We also report a new 3-D self-assembly process using reflowed Dow Chemical's BCB (Cyclotene) hinges, which are more robust than conventional photoresist hinges. The use of glass substrate has greatly reduced parasitic capacitances. A tuning ratio of 4.2 has been achieved with 10-μm-thick device layer. Our theoretical simulation shows that larger tuning ratio can be achieved with thicker device layers and further optimization of the design.

INTRODUCTION

MEMS (MicroElectroMechanical System) tunable capacitors have recently garnered significant interest due to their inherent performance advantages over conventional solid-state varactors; They generally exhibit larger tuning range and higher quality factor, Q, by reason of lower resistive and insertion losses.

Most MEMS tunable capacitors employ gap-closing electrostatic actuation, which offers relatively short response times and requires low power with little or no heat generation **[1]**. However, gap-closing actuators also suffer from some fundamental limitations. These actuators exhibit a pull-in phenomenon at one third of the gap distance between conductors, which limits the tuning ratio to 1.5 (50%).

There have been several attempts to overcome this theoretical limit via modifications to the gap-closing design **[2]**. Nevertheless, the tuning ratios achieved are still very modest. The use of comb drive actuators has made it possible to achieve a very large tuning ratio **[3]**. While lateral comb drives do not suffer from pull-in, the capacitance tuning relies on the lateral motion of the movable fingers. Hence, the tuning ratio is limited by the maximum separation of these fingers and their overall lengths. In this paper, we propose a novel MEMS tunable capacitor based on angular vertical comb-drive (AVC) actuators **[4]**. Unlike conventional comb-drives that have limited lateral displacements and require larger area for higher tuning, AVCs have the potential for larger tuning range through rotation. This reduces the dependence on the device size. A tuning ratio of 4.2 has been successfully achieved. We have also performed detailed theoretical simulation of the AVC tunable capacitor. Our theory shows that larger tuning ratio can be achieved with optimized device structures.

Travel support has been generously provided by the Transducers Research Foundation and by the DARPA MEMS and DARPA BioFlips programs

DESIGN PRINCIPLE

Figure 1 shows the schematics of the AVC tunable capacitor at zero bias (maximum capacitance) and actuated (minimum capacitance) configurations. The MEMS tunable capacitor utilizes two sets of interdigitated comb fingers to vary the capacitance. The shorter suspended DC comb fingers are set at an initial angle prescribed by the design. With a voltage bias between the suspended and fixed fingers, the electric field pulls the suspended fingers towards the fixed fingers, which in turn, rotates the longer RF fingers that are located at the opposite end of the device. The change in the overlapping area of the RF comb fingers due to the rotation tunes the total capacitance.

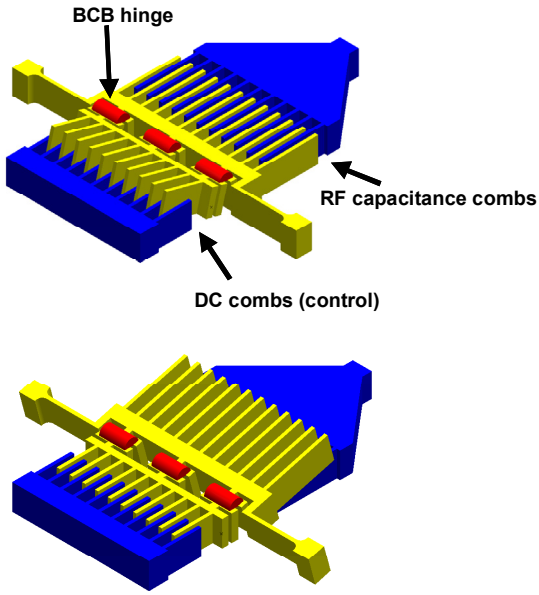

Figure 1. Schematic of tunable capacitor at maximum capacitance (top) and minimum capacitance (bottom).

For small initial tilt angles, the AVC actuator exhibits continuous rotation just like conventional lateral comb drives in lateral translation. When the initial tilt angle exceeds a critical angle, electrostatic pull-in between the tilted comb and the fixed comb starts to appear. This critical angle depends on the geometry of the device. Careful consideration of the device

dimensions are taken to avoid the pull-in phenomenon. Equation (1) describes the condition for which pull-in can occur.

$$PI(\theta) = \frac{\partial C}{\partial \theta} - \theta \frac{\partial^2 C}{\partial \theta^2} \quad (1)$$

where C is the capacitance of the actuator combs and θ is the angle of rotation. Equation (1) is derived from the equilibrium equation between the electrostatic and restoring mechanical torques. To avoid pull-in, Eq. (1) must be positive for all angles. The equation can be rewritten in terms of comb finger dimensions to determine the maximum finger lengths for actuator combs, as shown in Eq. (2):

$$l_{\max} = \frac{3}{2} \frac{t_{finger}}{\theta_{initial}} - l_{offset} \quad (2)$$

where l_{max} is the maximum allowed overlapped finger length of DC comb without pull-in and l_{offset} is the distance from the axis of rotation to base of the DC moving fingers. The device thickness, which in this case is 10 μm, is represented by t_{finger}. From Eq. (2) and the predetermined reflow angle $\theta_{initial}$, optimal dimensions for the tunable capacitor for maximum tuning range can be found. It should be pointed out that the RF comb fingers can be much longer than the DC fingers, unlike in lateral comb-drive devices where RF fingers needs to be shorter. This is utilized to increase the capacitance and to optimize the tuning ratio. The only limit on the length of RF fingers is lateral bending and stiction of the fingertips.

FABRICATION

Figure 2 shows the details of the fabrication process flow. The tunable capacitor is fabricated on glass substrate to reduce parasitic capacitance. We have chosen borofloat glass (BSG) substrate because its faster etch rate and . This greatly facilitates the releasing step. The silicon device layer from an silicon-on-insulator (SOI) wafer is bonded face down to the BSG substrate by anodic bonding. Prior to bonding, the SOI and the glass wafers are thoroughly cleaned and dehydrated to ensure intimate contact between the wafers. The wafers are then anodically bonded at 400° C and 700V (Fig. 2(a)). Bonding times vary depending on applied voltage. Lower voltages require longer bonding time but produces a more effective bonding and fewer voids. The thermal expansion coefficient (TEC) of BSG is also well matched to that of Si below 400°C, which greatly reduces the stress on the silicon device layer. The SOI substrate is subsequently removed by a combination of mechanical and chemical etches (Fig. 2(b)). The exposed buried oxide is also etched in a diluted solution of buffered hydrofluoric acid (BOE). Once the SOI substrate and buried oxide layer are removed, the 10-μm-thick silicon film is patterned and deep reactive ion etched (DRIE) to form the device structure (Fig. 2(c)). Next, photosensitive BCB (Cycotene) hinges are patterned to physically connect the suspended RF and DC fingers (Fig. 2(d)). Without curing the BCB hinges, the glass substrate is then etched in 49% hydrofluoric acid to release the suspended fingers (Fig. 2(e)). Release time is approximately six minutes. The hinges are then cured at 400 degrees in a nitrogen overpressured oven for twenty minutes. The movable DC comb fingers are assembled to an initial angle above the substrate plane (Fig. 2(f)). At the same time the high temperatures removes excess solvent from the release. The final process step involves the metallization over the entire sample with 2500 Å of sputtered aluminum for better conductivity. Sputtered aluminum provides better step coverage particularly at the sidewalls of the 10-μm-thick comb fingers.

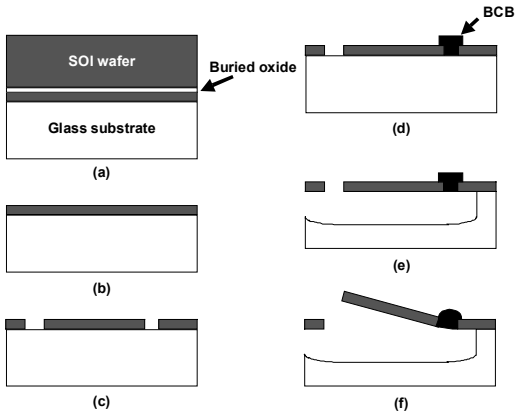

Figure 2. Fabrication process flow.

The combination of high temperature and HF exposure causes the BCB hinges to reflow. The reflow process allows automatic assembly of the DC fingers to an initial reflow angle. Limiters included on the hinge design limits the rotation to approximately 10 degrees. A similar process had been done with conventional photoresist **[5]**. However, BCB is far more attractive due to its chemical and thermal stability **[6]**. Unlike conventional photoresist, uncured BCB can withstand prolonged exposure to HF and solvents without evidence of delaminating or degradation. A scanning electron micrograph (SEM) of the device including the suspended fingers upon release and assembly is shown in Fig. 3.

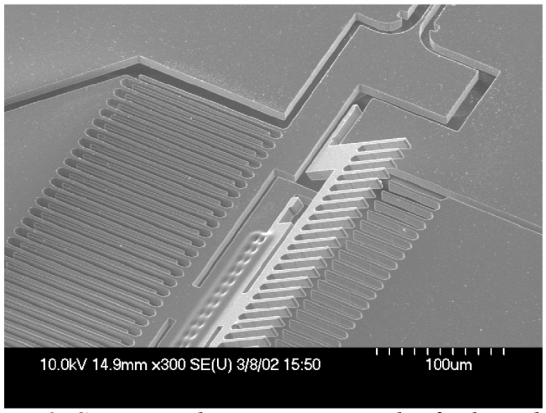

Figure 3. Scanning electron micrograph of released and assembled comb fingers.

EXPERIMENTAL RESULTS

Our initial design for the MEMS tunable capacitor exhibited a tuning ratio of 1.67. While this value exceeded the theoretical limit of 1.5 for parallel plate capacitors, the performance was far from satisfactory. After detailed examination, we have concluded that the smaller than expected tuning ratio is due to the sagging of the suspended comb fingers along the length of the device. The sagging results in finite overlap of the RF comb fingers at maximum rotation.

In our second-generation devices, we shorten the length and increase the width of the torsion spring. Since the bending spring constant is inversely proportional to the cube of the length, this greatly reduces the sagging with slight increase of actuation voltage. Figure 4 shows the interferometric image of the modified device at maximum bias. The DC movable fingers are now aligned with the fixed fingers without any evidence of sagging. The residue overlapping capacitance between RF fingers is greatly reduced. This leads to a 262% increase in the tuning ratio to 4.2.

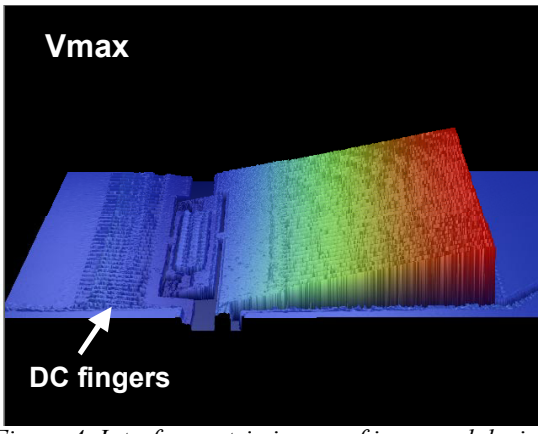

Figure 4. Interferometric image of improved device at maximum voltage. The RF fingers are rotated upward.

The capacitance and the S parameters are measured with a Hewlett Packard network analyzer 8510C and a high frequency coplanar waveguide probe with ground-signal-ground configuration. The measurements are calibrated for two-port measurements. Maximum capacitance at zero bias is measured at 1.34 pF. At maximum voltage, the capacitance is reduced to 0.32 pF. Figure 5 shows the capacitance-versus-voltage (CV) measurement of the tunable capacitor. As expected, the device does not show signs of pull-in. The capacitance reduces continuously as the voltage increases to 60 V. Beyond 60 V, the capacitance saturates and decreases very slowly. The S11 parameters are shown in Fig. 6 at the minimum and the maximum capacitance, respectively. The quality factor Q is measured by extrapolating the impedance values with respect to frequency from the network analyzer. The quality factor, Q, is measured to be 71 and 8.7 at 1 GHz for minimum and maximum capacitances, respectively.

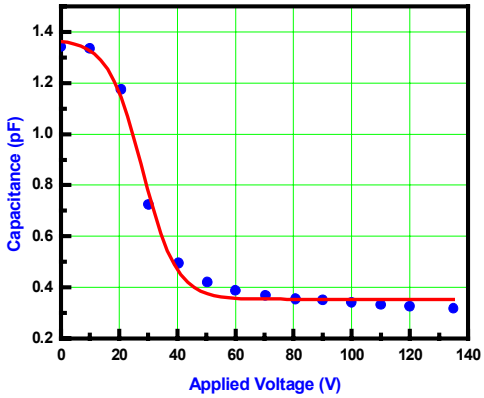

Figure 5. C-V measurement of the tunable capacitor.

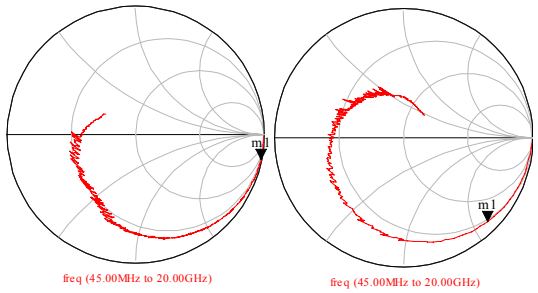

Figure 6. Smith chart showing S11 at (left) minimum and (right) maximum capacitance

The transfer curve that corresponds to the C-V measurement is shown in Fig. 7. It shows the angles of both the DC and RF comb fingers. The suspended DC fingers have an initial reflow angle of 8 degrees. Maximum rotation of 3 degrees occurs at 60 V. In principle, full rotation (8°) should be reached at sufficiently high voltage for AVC actuators. A close examination of the device operation under microscope reveals that the rotating structure hits an intruding beam at 3°, thus preventing the fingers from further rotation. By modifying the design, we believe larger rotation angle can be achieved.

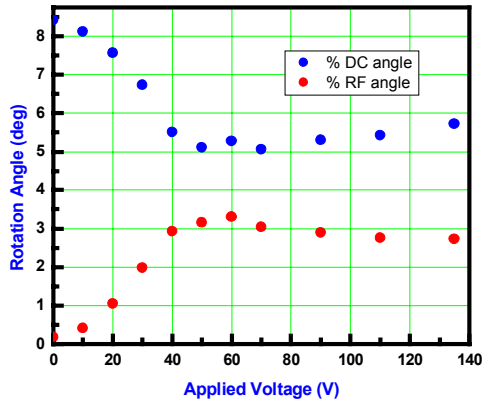

Figure 7. Transfer curve of RF and DC fingers with varying bias voltage.

We have performed theoretical modeling of the AVC tunable capacitor to investigate various parameter ranges for optimizing its performance. We found that the most effective way to increase the tuning ratio and reducing voltage is to increase the device layer thickness. Similar trend is also observed in tunable capacitors with lateral comb drive actuators. Borwick, et. al have shown that increasing the device thickness from 30 µm to 80µm raises the tuning range to from 3 to 8 **[7]**. Migration towards thicker silicon film allows for larger tuning ratios as maximum capacitance between the comb fingers is increased compared to the fringe capacitance when the comb fingers are separated. Figure 8 shows the maximum tuning ratio for a 25-µm-thick device with 10 degree initial tilt angle. It is possible to obtain a tuning ratio of at least 15 for a given finger length. As with the tuning ratio, the quality factor can be improved with the use of highly resistive SOI wafers to reduce resistive loss from the silicon device layers.

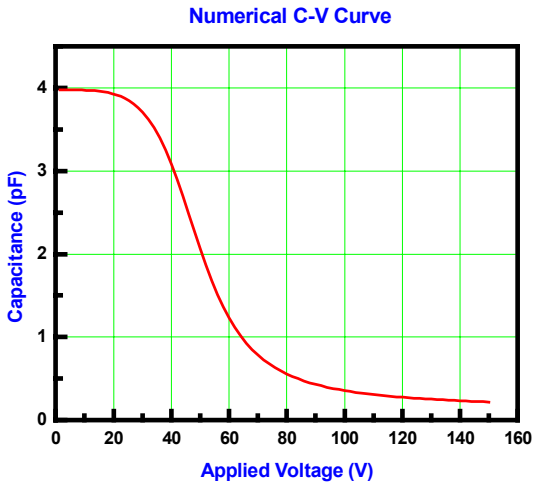

Figure 8. Theoretic C-V curve for 25-μm-thick tunable capacitor

CONCLUSION

We have proposed and successfully fabricated a novel MEMS tunable capacitor with angular vertical comb-drive (AVC) actuators. Continuous tuning without pull-in has been successfully achieved. A tuning ratio of 4.2 has been measured at 1 GHz for a 10-μm-thick device. This is larger than that of lateral comb drive devices with similar device layer thickness. Larger tuning ratio and high Q value can be achieved with thicker device layers.

AKNOWLEDGMENT

The authors would like to thank Drs. Robert Y. Loo, Jim Shaffner, Dan Sivenpiper, and Greg Tangonan of HRL for their valuable discussions. Special thanks also goes to Sagi Mathai and Sanjeev Murthy of UCLA for their assistance in microwave measurements.

This project is supported in part by HRL Laboratories under the University of California MICRO program, and the DARPA Contract N66001-99-C-8635. Travel support has been provided by the Transducers Research Foundation and by the DARPA MEMS and DARPA BioFlips programs.

REFERENCES

1. Dec, A.; Suyama, K., *"A 1.9-GHz CMOS VCO with micromachined*, vol.35, (no.8), IEEE, Aug. 2000. p.1231-7.
2. Jun Zou; Chang Liu; Schutt-Aine, J.; Jinghong Chen; Sung-Mo Kang, ***"****Development of a wide tuning range MEMS tunable capacitor for wireless communication systems."* International Electron Devices Meeting 2000
3. Yao, J.J.; Park, S.; Anderson, R.; DeNatale, J., *"A low power/low voltage electrostatic actuator for RF MEMS applications."* Solid-State Sensor and Actuator Workshop, Hilton Head Island, SC, USA, 4-8 June 2000.
4. P. Patterson, D. Hah, H. Chang, H. Toshiyoshi, M.C. Wu, *"An Angular Vertical Comb Drive Actuator for Scanning Micromirrors",* 2001 International Conference on Optical MEMS, Okinawa, Japan,p.25.
5. Syms, R.R.A.; Gormley, C. V; Blackstone, S.**, "***Improving yield, accuracy and complexity in surface tension self-assembled MOEMS,"* Sensors and Actuators A (Physical), vol.A88, (no.3), Elsevier, 5 March 2001. p.273-83.
6. Tuantranont, A.; Bright, V.M.; Zhang, J.; Zhang, W.; Neff, J.A.; Lee, Y.C. *"Optical beam steering using MEMS-controllable microlens array"* Solid-State Sensor and Actuator Workshop, Hilton Head Island, SC, USA, 4-8 June 2000.
7. R.Borwick, P. Stupar, J. DeNatale, R. Anderson, C. Tsai, and K. Garrett, "*A High Q, Large Tuning Range, Tunable Capacitor for RF Applications,*" MEMS 2002, Las Vegas, NV, USA

Single-Crystal Silicon HARPSS Capacitive Resonators with Submicron Gap-Spacing

Seong Yoel No, Akinori Hashimura, Siavash Pourkamali, and Farrokh Ayazi
School of Electrical and Computer Engineering
Georgia Institute of Technology, GA 30332-0250
E-mail: ayazi@ece.gatech.edu, Tel: (404) 894-9496, Fax: (404) 894-4700

ABSTRACT

This paper reports on the fabrication and characterization of single crystal silicon (SCS) in-plane capacitive resonators with submicron gap spacing using the HARPSS process. The resonating element is made out of single crystal silicon and the drive and sense electrodes are made out of trench-refilled polysilicon, hence yielding an all-silicon microresonator with potentially better temperature and long-term stability. The capacitive gap is defined by a sacrificial oxide layer, which can be potentially reduced to the ten's of nanometer range (700nm reported in this paper). Quality factor as high as 67,000 was measured in 1mTorr vacuum for the 40kHz fundamental resonance frequency of a clamped-clamped beam SCS HARPSS resonator. A 510µm long, 5.5µm wide, 20µm thick clamped-clamped beam resonator was operated in its third resonance mode at 1MHz and demonstrated a Q of 11,000 under vacuum. Electrostatic tuning characteristics of the resonators have been measured and reported.

1. INTRODUCTION

MEMS resonators are a potential candidate to replace current off-chip frequency selective mechanical components such as crystal, ceramic and SAW devices in wireless communication systems. High quality factors, small size and compatibility with IC integration are the major advantages of the silicon MEMS resonators over their counterparts. Extension of the frequency range of capacitive MEMS resonators into the low GHz range requires process technologies that can yield 10-100 nanometer capacitive gap spacings in between the high quality factor (Q) resonating structure and the drive and sense electrodes [**1**].

A number of poly and single crystalline silicon resonators have been reported in literature [**2-7**]. Polysilicon capacitive resonators with submicron gap spacing have been demonstrated with metal electrodes that result in a thermal mismatch [**2**]. Single crystal silicon (SCS) is a more attractive structural material for microresonators compared to polysilicon due to its inherent high mechanical quality factor and independence from various process parameters. However, single crystal silicon resonators reported previously in literature had either complex non-capacitive sense and drive mechanisms [**4**], large capacitive gaps [**5**], or low quality factor [**6**]; such issues may compromise design flexibility and limit the high frequency applications of the microresonators.

This paper reports, for the first time, the implementation of high–Q single crystal silicon resonators with submicron gap spacing using an enhanced and modified version of the HARPSS process. The in-plane resonating element is made out of single crystal silicon and the drive and sense electrodes are made out of trench-refilled polysilicon, hence yielding an all-silicon microresonator. Measurement results on the Q and tuning characteristics of the fabricated beam resonators in the fundamental and third order modes are presented.

2. RESONATOR FABRICATION

The HARPSS process [**7**] has been previously used to make thick polysilicon resonators [**7,8**]. In this paper, the HARPSS process is modified to implement single crystal silicon resonating structures with trench-refilled poly electrodes. The schematic diagram of an in-plane clamped-clamped beam resonator fabricated through the HARPSS process is shown in Fig. 1.

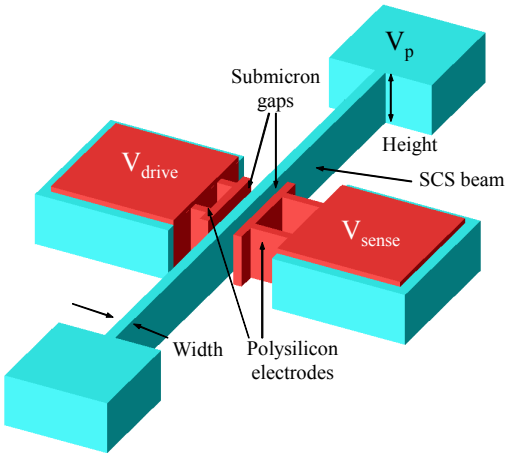

Figure 1. *HARPSS clamped-clamped beam SCS resonator*

The fabrication process flow is shown in Fig. 2. The SCS resonating beam is defined by two adjacent high aspect-ratio trenches that are 2 to 5µm wide and up to 100µm deep. The trenches are etched in an inductively-coupled plasma (ICP) deep reactive ion etching (DRIE) system using the Bosch process. The height of the trenches determines the height of the resonator. A thin conformal layer of sacrificial LPCVD high-temperature oxide is then deposited and trenches are consequently refilled with doped LPCVD poly to form the vertical electrodes. The lateral gap spacing is defined by the thickness of the deposited oxide layer, and thus can be scaled down to the ten's of nanometer range [**1**].

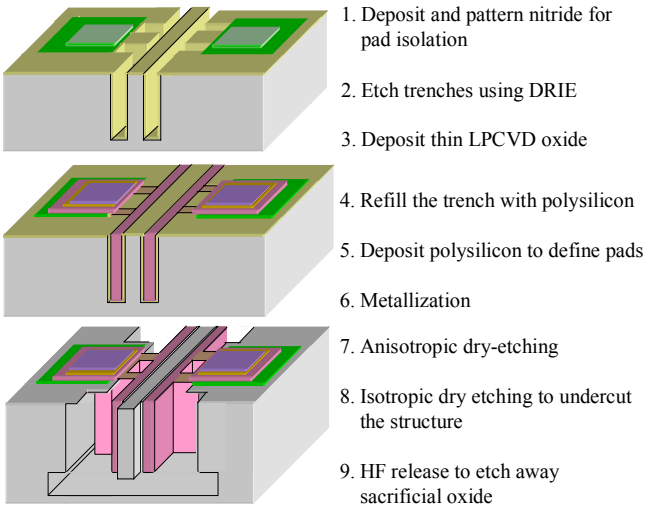

Figure 2. *Process flow for HARPSS single crystal silicon beam resonators.*

0-9640024-4-2/hh2002/$20©2002TRF
DOI 10.31438/trf.hh2002.70

Solid-State Sensors, Actuators, and Microsystems Workshop
Hilton Head Island, South Carolina, June 2-6, 2002

The resonator is released from the silicon substrate using a dry silicon etch in SF_6 plasma, consisting of an anisotropic followed by an isotropic etch to undercut the structures. Finally, the sacrificial oxide is removed in a HF:H_2O (1:1) solution. Fig. 3 shows the SEM picture of a fabricated clamped-clamped beam resonator with a length of 510µm, width of 6.5µm, height of 20µm, and a capacitive gap of 700nm. Figures 4 and 5 are the SEM pictures of the beam electrodes area, showing the single crystal beam, the polysilicon electrodes and the submicron gap.

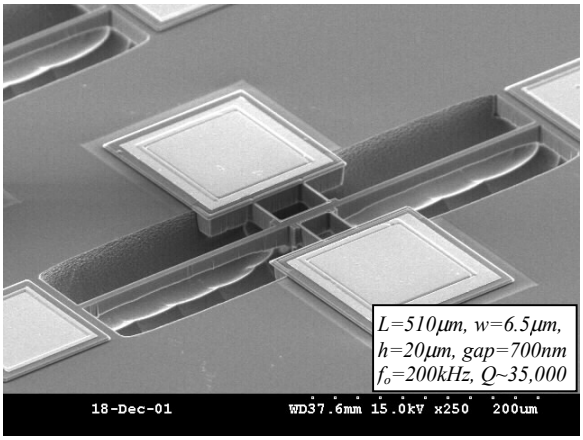

Figure 3. *A 510µm long, 6.5µm wide, 20µm tall clamped-clamped beam HARPSS SCS resonator with a gap spacing of 700nm.*

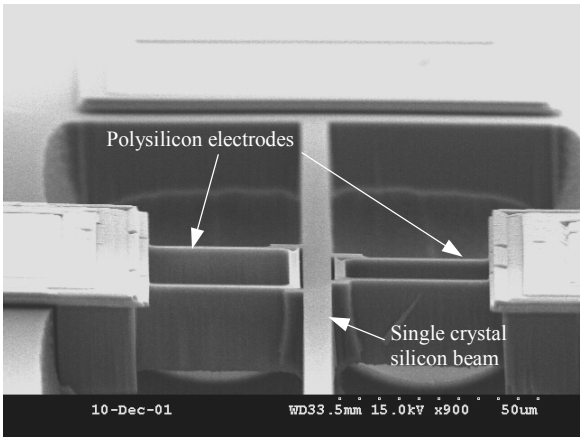

Figure 4. *SEM of the electrode area showing the polysilicon electrodes as tall as the beam separated by submicron gaps.*

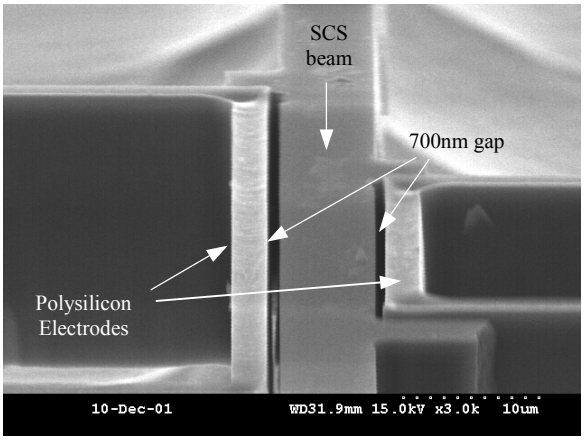

Figure 5. *Close-up view of the electrode area showing the 700 nm gap spacing.*

Disk resonators have also been fabricated using the above process to obtain higher resonance frequency. The SEM picture of a 20µm diameter SCS disk resonator fabricated using the HARPSS process is shown in Fig. 6. Characterization and measurement results for the disk resonators will be reported in the future.

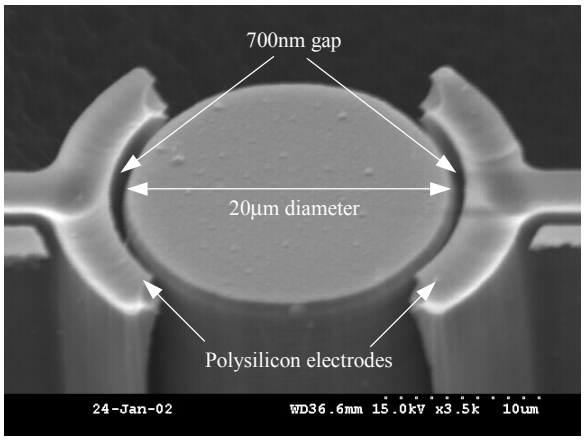

Figure 6*. SEM picture of a 20µm in diameter SCS disk resonator with polysilicon electrodes.*

In this process, the trenches define: 1) the boundary of the resonating structure, and 2) the polysilicon electrodes. At the end of the process, all the polysilicon inside the trenches should be removed, except for the electrode area. Two methods were investigated, as shown in Fig. 7(a) and (b), to separate the polysilicon in the electrode area from the areas that only define the boundary of the resonator. The first method is to physically disconnect the polysilicon electrode by using discontinuous trenches and etch away the polysilicon inside the trenches that define the boundary of the resonator. However, this method creates "stubs" on the sides of the beam as shown in the SEM of Fig. 7(a), introducing residual extra mass. FEM simulations using ANSYS have shown that these stubs do not alter the resonance frequency significantly. The size of these stubs can be controlled by characterizing the isotropic release etch. The alternative method is to use a continuous trench to define the boundary of the resonator and reduce the width of the trench in certain areas. As shown in Fig. 7(b), the narrow trench (located in between the regular size trenches) is primarily filled by the sacrificial oxide.

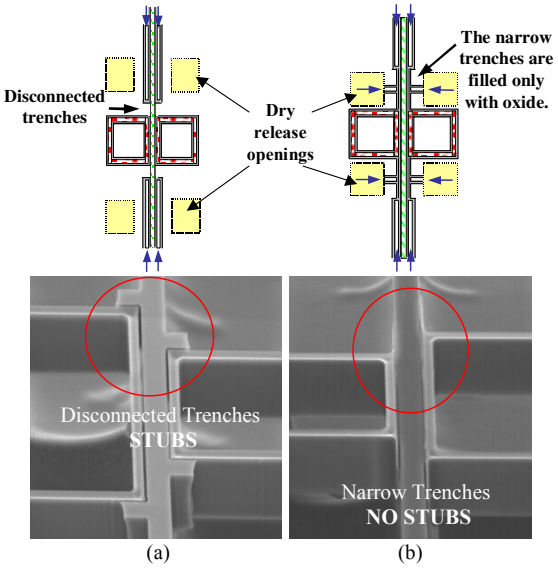

Figure 7*. Diagram and SEM of the separation methods using a) disconnected trenches, b) narrow trenches.*

Due to the presence of voids in the middle of oxide-filled narrow trenches, a thin residual poly line may be formed, connecting the electrode trench-refilled poly to the boundary poly. This parasitic poly will be subsequently etched away during the isotropic etch step of the release process.

3. MEASUREMENT RESULTS

Prototypes of the fabricated SCS beam resonators were tested under vacuum in a two-port configuration using an Agilent 4395A network analyzer. A low noise JFET source-follower with a gain stage was used to interface with the resonators. The sensing interface circuit was built on a printed circuit board (PCB) using surface mount components and the MEMS resonator chip was mounted on the board and wire-bonded. The PCB was placed in a custom vacuum system, which kept the pressure less than 1mTorr.

Fig. 8 shows the plot of a typical frequency response taken from the network analyzer, showing a Q of 62,000 at 49 kHz for a 1100µm long, 7.5µm wide and 20µm tall SCS clamped-clamped beam resonator under 1mTorr vacuum. The summary of the measured Q values for the beam resonators with fundamental frequencies ranging from 41.5kHz to 530 kHz is given in Fig. 9. A Q of ~20,000 was measured for the 0.5MHz beam resonator.

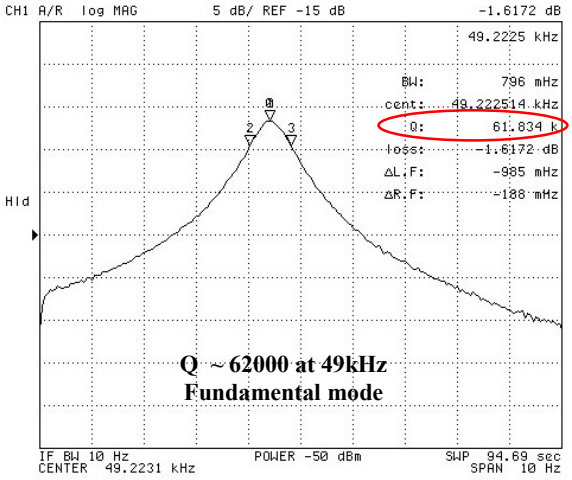

Figure 8. *Response of a 1100µm long, 7.5µm wide, 20µm tall HARPSS SCS beam resonator, showing a Q of ~62000 at 49kHz.*

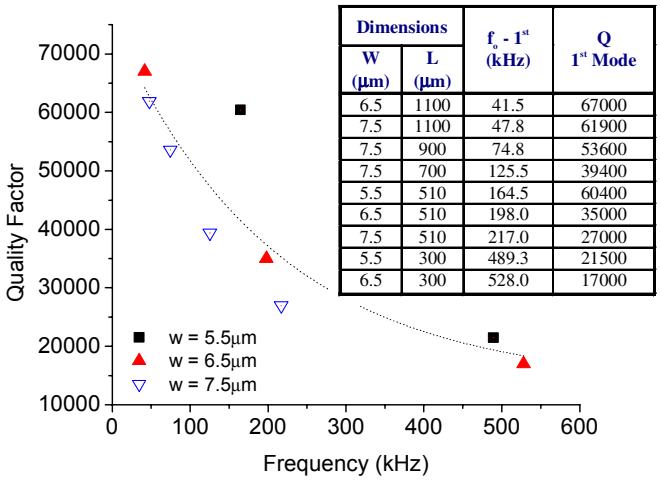

Dimensions W (µm)	Dimensions L (µm)	f_o - 1st (kHz)	Q 1st Mode
6.5	1100	41.5	67000
7.5	1100	47.8	61900
7.5	900	74.8	53600
7.5	700	125.5	39400
5.5	510	164.5	60400
6.5	510	198.0	35000
7.5	510	217.0	27000
5.5	300	489.3	21500
6.5	300	528.0	17000

Figure 9. *Plot of measured Q vs. measured fundamental resonance frequencies of SCS beams. Q decreases with increasing frequency.*

Fig. 10 shows the comparison between the measured and theoretical frequency tuning characteristics for a 300µm long, 6.5µm wide resonator by changing the DC polarization voltage (*Vp*). The mismatch is mainly due to fabrication uncertainties in defining the dimensions of the structure, which alter the overall stiffness. The resonance frequency changed from 505kHz to 450kHz by changing the polarization voltage by more than 40V (the calculated pull-in voltage was 56V), providing a large electrostatic tuning range (~10%).

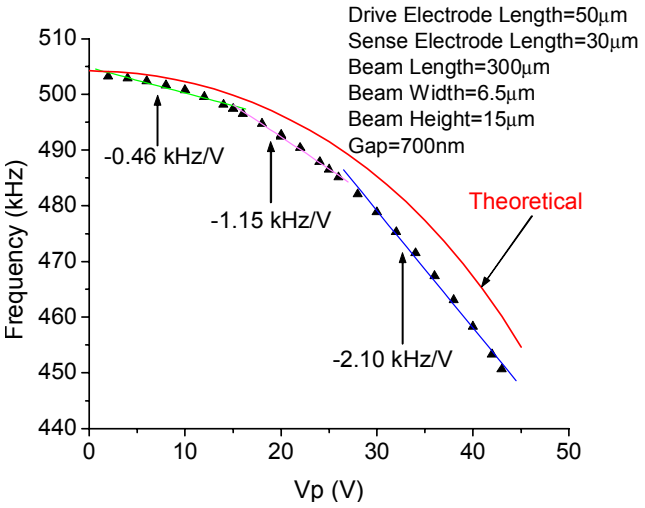

Figure 10. *Plot of the resonance frequency vs. polarization voltage for a 300µm long, 6.5µm wide beam resonator.*

3.1 Third flexural resonance mode

In order to achieve higher operating frequencies, a few of the clamped-clamped beam resonators were actuated in their third flexural mode and the quality factors were measured. The second mode could not be actuated due to the midway position of the drive electrode. A Q of 10,700 was measured at 1.03MHz for the third resonance mode of a 510µm long, 5.5µm wide SCS beam resonator (the 1st mode is at 165kHz). Figure 11 shows the measured resonance peak for this mode (the anti-resonance peak is due to the parasitic feedthrough capacitance), and provides a summary of the Q measurement results for the 3rd mode of the beam resonators with other dimensions.

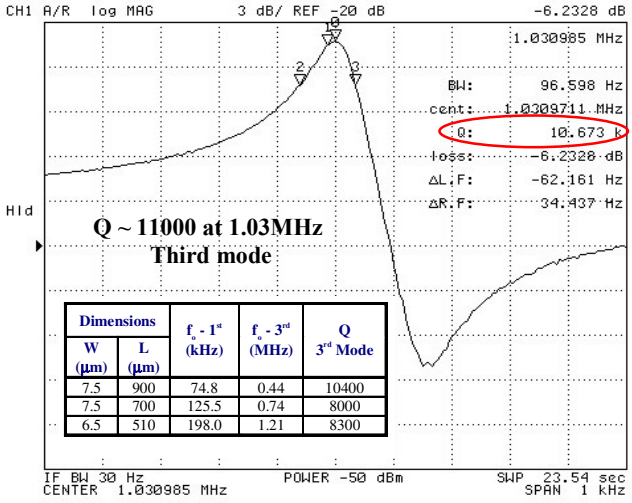

Dimensions W (µm)	Dimensions L (µm)	f_o - 1st (kHz)	f_o - 3rd (MHz)	Q 3rd Mode
7.5	900	74.8	0.44	10400
7.5	700	125.5	0.74	8000
6.5	510	198.0	1.21	8300

Figure 11. *Plot of Q (~10,700) for a clamped-clamped SCS beam resonator operating in its 3rd flexural mode at 1 MHz.*

3.2 Loss Mechanisms

Several possible loss mechanisms have been investigated by researchers including the thermoelastic damping (TED), support, and surface related loss mechanisms [**5**,**9-11**]. Using the TED relationships for beam resonators reported in references [**9**] and [**10**], a minimum Q of 11,000 occurs at frequencies of 4.8, 3.3 and 2.1MHz for SCS beam widths of 5.5, 6.5, and 7.5µm, respectively. Figure 12 shows the plots of calculated Q_{TED} along with the Q measurement results for 5.5µm and 7.5µm wide SCS beam resonators. Although the measured Q values for each beam-width seem to follow the trend predicted by the TED loss (Q decreases with increasing frequency), there is a substantial offset associated with the measured Q values (a factor of 2-3 less than Q_{TED}).

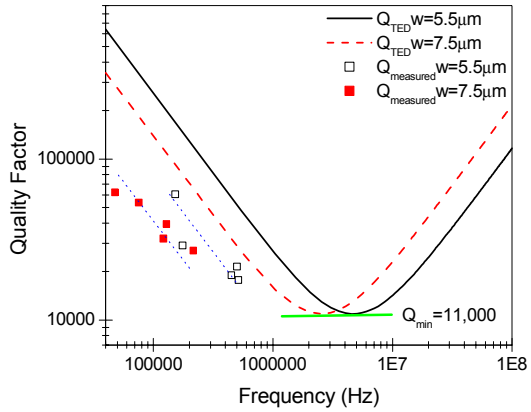

Figure 12. *Q vs. frequency showing the measured quality factor and calculated Q_{TED} for beam-widths of 5.5µm and 7.5µm.*

The observed offset cannot be due to excessive support loss. For the beam resonators, the support loss is proportional to the third power of the length to width ratio $(l/w)^3$ [**11**]. The length to width ratios are greater than 40 (l/w>40) for all the beam resonators studied in this paper, suggesting much larger $Q_{support}$ values than what was measured. However, the surface loss could very well be a major source of dissipation for the resonators reported here. Figure 13 shows the sidewall of a prototype beam resonator, showing significant surface roughness that is indeed present in all of the beam resonators due to the un-optimized DRIE process used in fabrication. The DRIE process can be easily optimized to eliminate the striation on the sidewall and increase the Q. As reported in reference **[5],** the losses associated with surface roughness can be significantly reduced by growing a thin oxide and subsequently removing it.

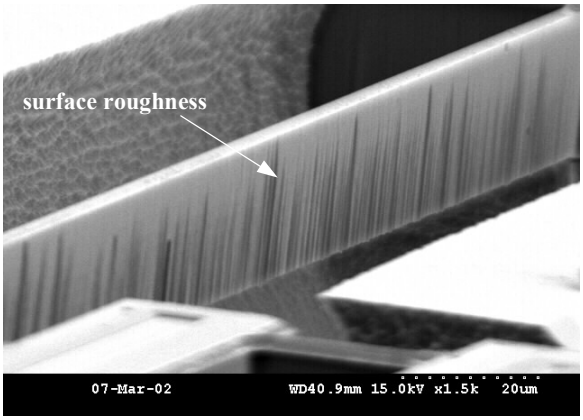

Figure 13. *SEM of the sidewall of a SCS resonator. The vertical "striation" is caused by unoptimized DRIE etch conditions.*

4. CONCLUSIONS

All-silicon high-Q capacitive micromechanical resonators with submicron gap-spacing utilizing single crystal silicon as the resonating element and polysilicon as the electrodes have been reported. The resonators were fabricated using the HARPSS process and uniform capacitive gaps of 0.7µm are demonstrated. Quality factors as high as 67,000 for the 1st mode at 40kHz, and 11,000 for the 3rd mode at 1MHz have been measured for clamped-clamped SCS beam resonators. Investigation of various loss mechanisms revealed that the measured quality factor follows the behavior predicted by the TED loss mechanism with an offset. The reason for the offset is believed to be due to the excessive surface roughness of the SCS beam. Optimization of the DRIE process is expected to reduce the surface roughness and increase the Q. Future work will report on confirmation of the above as well as characterization of the UHF SCS HARPSS resonators.

Acknowledgements

This work was supported by DARPA under contract # DAAH01-01-1-R004. Authors would like to thank Gavin Ho for providing the 3D diagram as well as discussion on TED loss, and the staff at the Georgia Tech Microelectronics Research Center for their assistance.

REFERENCES

1. S. Y. No and F. Ayazi, " The HARPSS Process for Fabrication of Nano-Precision Silicon Electromechanical Resonators", *IEEE Conf. on Nanotechnology*, 10/28-30/01, (2001), pp.489-494.

2. W.-T. Hsu, et al., "Q-Optimized Lateral Free-Free Beam Micromechanical Resonators", *Int. Conf. On Solid-State Sensors and Actuators (Transducer'01)*, Munich, Germany, 6/10-14/01, (2001), pp. 1110-1113.

3. C. Bourgeois et al., "Design of Resonators for the Determination of the Temperature Coefficients of Elastic Constants of Monocrystalline Silicon", *1997 IEEE Int. Freq. Control Symp.*, Orlando, Fl. 5/28-30/97, (1997) pp.791-799.

4. K. Petersen, et al., "Resonant Beam Pressure Sensor Fabricated with Silicon Fusion Bonding", *6th Int. Conf. on Solid State Sensors and Actuators, (Tranducer'91)*, San Francisco, CA, 6/24-28/91, (1991), pp.664-667.

5. R. E. Mihailovich, and N. C. MacDonald, "Dissipation measurements of vacuum-operated single-crystal silicon microresonators", *Sensors and Actuators A ,50*, 199, (1995).

6. T. Mattila et al. "14MHz Micromechanical Oscilaltor", *11th Int. Conf. on Solid-State Sensors and Actuators, (Transducer'01),* Munich, Germany, 6/10-14/01, (2001), pp.1102-1105.

7. F. Ayazi and K. Najafi, "High Aspect-Ratio Combined Poly and Single-Crystal Silicon (HARPSS) MEMS Technology", *JMEMS, 9(3)*, 288, (2000).

8. F. Ayazi and K. Najafi, "A HARPSS Polysilicon Vibrating Ring Gyroscope," *JMEMS*, June 2001, pp. 169-179.

9. T. V. Roszhart, "The Effect of Thermoelastic Internal Friction on the Q of Micromachined Silicon Resonators*", IEEE Solid State Sensor and Actuator Workshop*, Hilton Head, SC, 6/4-7/90, (1990), pp.489-494.

10. R. Lifshitz and M. L. Roukes, "Theromoelastic damping in micro- and nanomechanical systems", *Phy. Rev. B.*, 61(8), 5600, (2000).

11. K. Y. Yasumura et al., "Quality Factors in Micron- and Submicron-Thick Cantilevers", *JMEMS, 9(1)*, 117, (2000).

ANGULAR RATE GYROSCOPE WITH DUAL ANCHOR SUPPORT

Gary J. O'Brien[*,+], David J. Monk[+], and Khalil Najafi[*]

[*]University of Michigan
Center for Wireless Integrated Microsystems
1301 Beal Ave
Ann Arbor, MI 48109-2122

[+]Motorola Inc.
Sensor Products Division
Sensor Development Engineering Group
Tempe, AZ 85284

ABSTRACT

A low-cost high yield surface micromachined gyroscope is presented with a decoupled drive and sense proof mass. A dual anchor approach is described using folded beam springs and a torsion post to significantly reduce the drive proof mass out of plane deflection while maintaining a comparatively low rotational mechanical restoring force. The Z-axis (vertical) proof mass suspension spring constant was increased from 7.86 [N/m] to 251[kN/m] with the addition of the central torsion post. Vertical stiction was eliminated from the design using the dual anchor scheme for the proof mass and a triply clamped beam approach for the fixed electrostatic drive/sense beams. The increase in the Z-axis spring constant of the fixed triply clamped beams is greater than 128X as compared to singly clamped cantilever beams of equal length. In addition, a differential capacitance measurement scheme is presented which rejects undesired proof mass linear acceleration error at the sensor. The sense mode resonant frequency was measured at 44.96 [kHz] with a quality factor Q of 225 in a 3 mtorr ambient. Angular rate resolution was measured at 3.8 [deg/s] in a 20 [Hz] bandwidth.

INTRODUCTION

During the past decade a great deal of research has been performed on MEMS based vibratory gyroscopes for intended use in automotive and inertial navigation applications. Angular rate sensors (gyroscopes) have been implemented using vibrating rings [**1**,**2**], prismatic beams [**3**], tuning forks [**4**-**6**], and torsion [**7**,**8**] oscillation. Significant capacitance based measurement error for the tuning fork and torsional rate gyroscopes is caused by undesired mechanical and electrostatic coupling with the proof mass drive and sense modes. Mechanical decoupling of the drive and sense modes using a torsion beam spring has been previously demonstrated [**8**] with significant reduction of undesirable nonlinear rate output characteristics reported. The Dual Anchor Angular Rate (DAART) sensor, shown in Figure 1, utilizes torsion oscillation with mechanically decoupled drive and sense proof mass modes using a modified torsion spring as shown in Figure 2. The dual anchor design significantly increases the Z-axis spring constant while maintaining a comparatively low rotational mechanical restoring force about the Z-axis. This is accomplished using a 2μm diameter torsion post anchored to the substrate in addition to folded beam springs which suppress precession of the proof mass during rotational (torsion) oscillation, as shown in Figure 3. A 21% increase in the theoretical folded beam spring mechanical restoring force is attributed to inclusion of the torsion post anchor proof mass displacement around the z-axis. Neglecting the proof mass stiffness, the z-axis system spring constant is significantly improved from 7.86 [N/m] to 251[kN/m], with the torsion post included.

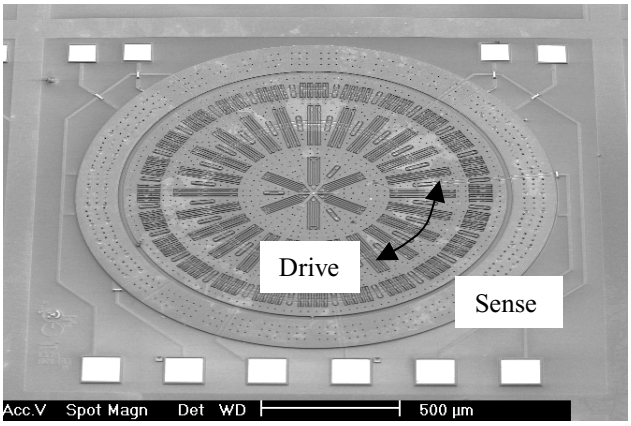

***Figure 1**. DAART Sensor Decoupled Inner Drive and Outer Sense Ring Proof Mass*

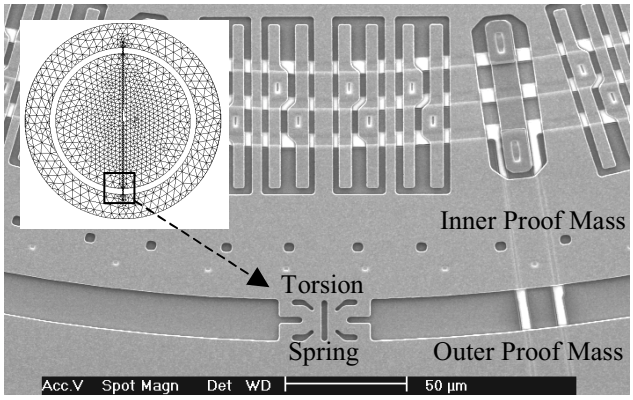

***Figure 2**. Decoupled Inner Drive and Outer Sense Proof Mass Torsion Spring*

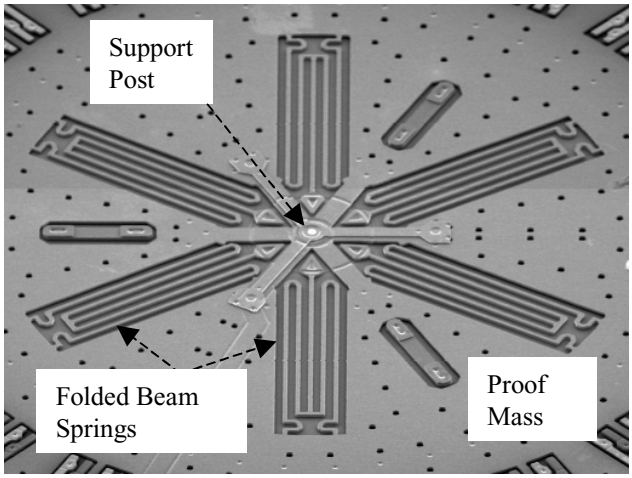

***Figure 3**. DAART Sensor Central Spring Suspension*

0-9640024-4-2/hh2002/$20©2002TRF
DOI 10.31438/trf.hh2002.71

SENSOR OPERATION

The torsional drive and sense modes are intentionally mismatched to reduce quadrature error [**6**] during excitation. The inner ring is electrostatically driven at the resonant frequency of the outer sense proof mass, providing the coupling energy for Coriolis acceleration measurement. Vibratory gyroscopes sense angular rate based on the Coriolis acceleration measurement defined by the cross product of the mass velocity *v*, and the rotation rate *Ω*, as given by Eq. 1.

$$a_{Coriolis} = 2v \times \Omega \qquad (1)$$

The outer proof mass is segmented into quadrants where the effective mass is approximately half the total mass. Coriolis force is defined by the product of the effective outer proof mass *m* and Coriolis acceleration as given by Eq. 2.

$$F_{Coriolis} = 2mv \times \Omega \qquad (2)$$

The Coriolis force couple causes a rotation of the outer sense ring for a counter clockwise rotation as shown in Figure 4.

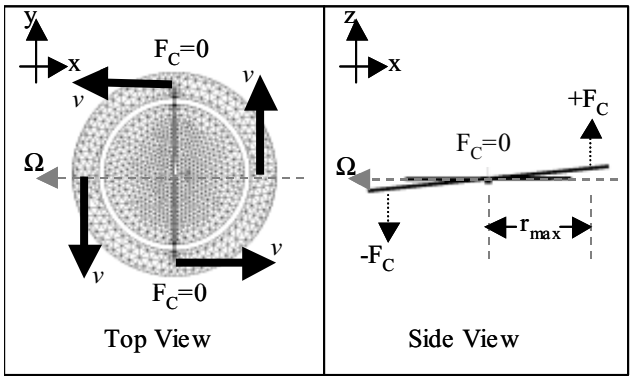

Figure 4. *Outer Proof Mass Coriolis Force Couple*

The velocity is a sinusoidally varying function of the applied driving voltage versus time as given by Eq. (3), where θ_{max} represents the maximum proof mass angular displacement, ω is the drive voltage frequency, and *t* is time.

$$\theta(t) = \theta_{\max} \sin(\varpi t) \qquad (3)$$

Using the small angle approximation, the angular displacement is converted to a linear displacement as given by Eq. 4, where r_{max} represents the distance measured from the proof mass center point to the mid point on the outer sense proof mass ring.

$$y_{\max} = \theta_{\max} r_{\max} \qquad (4)$$

The angular displacement is converted to linear displacement along the y-axis, as given by Eq. 5, where the y_{max} represents the maximum displacement.

$$y(t) = \frac{y_{\max}}{2} \sin(\varpi t) \qquad (5)$$

The velocity of the outer ring is defined by the time dervative of the position vector given by Eq. 6.

$$\frac{dy(t)}{dt} = \frac{y_{\max}}{2} \varpi \cos(\varpi t) \qquad (6)$$

The peak velocity of the 44.96 [kHz] excited outer proof mass is 0.155 [m/s], with a corresponding Coriolis acceleration of 0.021 [m/s^2] for a 3.8 [deg/s] angular rate vector application as shown in Figure 4.

Parallel plate actuator arrays, as shown in Figure 5, were used to increase electrostatic force as compared to comb drive actuation for a fixed applied voltage at the expense of reduced proof mass deflection. The maximum proof mass linear deflection measured at the outer sense mass is approximately 1.1 [μm].

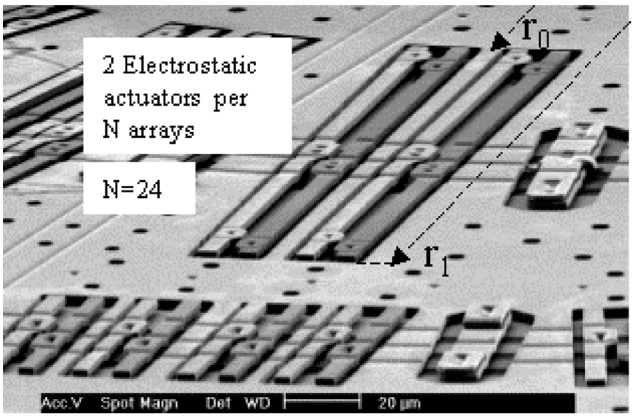

Figure 5. *Parallel Plate Electrostatic Actuator Arrays*

The capacitance of the actuator array [**9**] is defined by Eq. 7., where *T* is the thickness of the proof mass, g_0 is the initial gap spacing, and r_0 and r_1 are measured distance from the proof mass center to inner and outer electrode radii as shown in Figure 5.

$$C(\theta) = \frac{2N\varepsilon_0 T}{\theta} \ln\left(\frac{g_0 - \theta r_0}{g_0 - \theta r_1}\right) \qquad (7)$$

The angular derivative of the actuator array capacitance is given by Eq. 8.

$$\frac{dC(\theta)}{d\theta} = \frac{\varepsilon_0 T}{\theta}\left[\frac{r_1(g_0 - \theta r_0) - r_0(g_0 - \theta r_1)}{(g_0 - \theta r_0)(g_0 - \theta r_1)} - \frac{1}{\theta}\ln\left(\frac{(g_0 - \theta r_0)}{(g_0 - \theta r_1)}\right)\right] \qquad (8)$$

The electrostatic torque generated by the parallel plate actuator arrays is defined by the angular derivative of the potential energy as given by Eq. 9, where V_θ represents the applied voltage amplitude.

$$\frac{dU_{cap}(\theta)}{d\theta} = \frac{1}{2}\frac{dC(\theta)}{d\theta} V_\theta^2 \qquad (9)$$

Drive voltage amplitude was less than 4.6 [Volts] during sinusoidal proof mass excitation.

A cross section of a triply clamped beam used in the parallel plate electrostatic actuator array is shown in Figure 6.

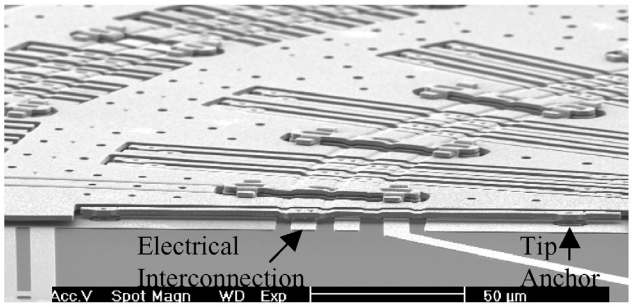

***Figure 6**. Electrostatic Actuator Array Triply Clamped Beam Cross Section*

Previous designs were anchored near the beam center at the underlying electrical polysilicon interconnection resulting in an 8X overall increase in the vertical spring constant as compared to cantilever beams of equal length, as shown in Figure 7.

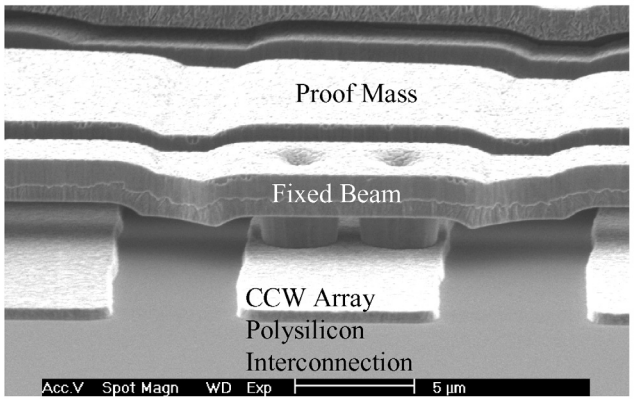

***Figure 7**. Centrally Anchored Parallel Plate Actuator Beams*

However, vertical stiction [**10**] was observed in arrays with beam lengths greater than 160µm during the sacrificial oxide etch process sequence. Centrally anchored beams shorter than 160µm were able to resist vertical stiction during processing and comprise the inner drive proof mass outer electrostatic actuator array as shown in Figure 5. Centrally anchored beams greater than 160µm in length were modified with tip support posts anchored to the substrate, as shown in Figure 8, to eliminate stiction by increasing the vertical spring constant by 128X as compared to simply supported cantilever beams of equal length.

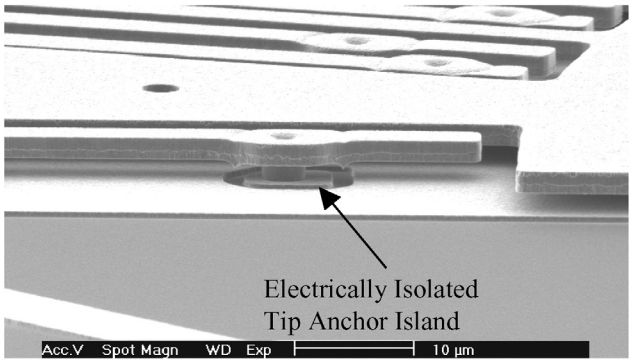

***Figure 8**. Triply Clamped Beam Tip Anchor Support*

SENSE ELECTRODE CONFIGURATION

Undesirable electrostatic coupling attributed to fringing electric field lines terminating on the top surface of the capacitive sensor [**11**] are eliminated using the differential capacitance electrode configuration as shown in Figure 9.

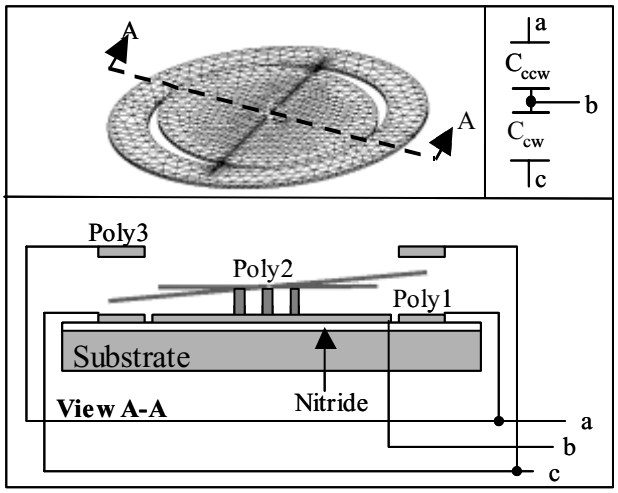

***Figure 9**. Differential Capacitance Electrode Configuration*

Each differential electrode covers one quarter of the outer proof mass area as shown in Figure 10.

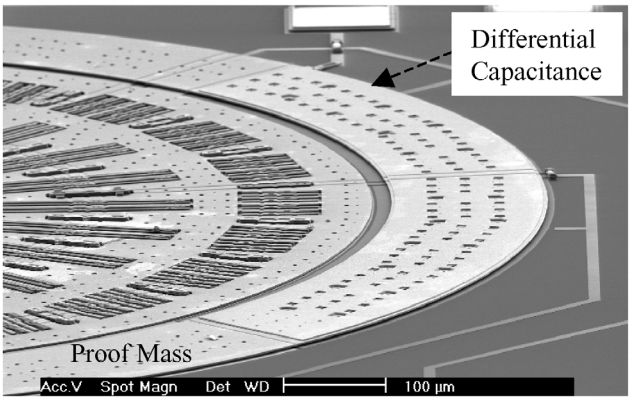

***Figure 10**. Differential Capacitance Sense Electrode*

Detail of the differential capacitance sense electrode is shown in Figure 11.

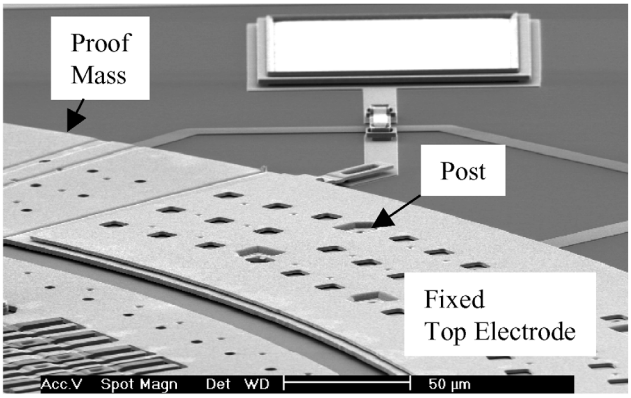

***Figure 11.** Differential Capacitance Sense Electrode Detail*

EXPERIMENTAL RESULTS

The resonant frequency of the sense proof mass mode was measured at 44.96 [kHz] in a 3 [mtorr] ambient using an HP 8751 Network Analyzer as shown in Figure 12.

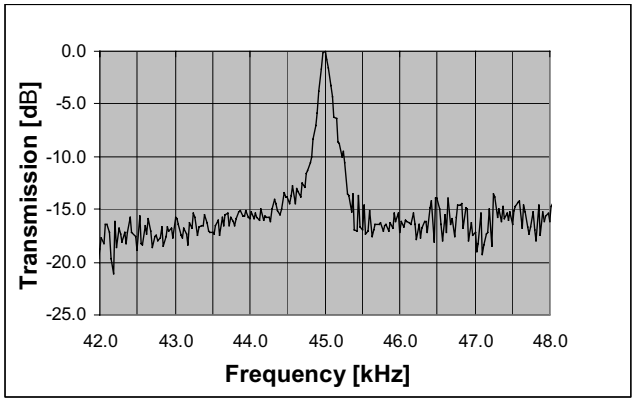

Figure 12. *Sense Mode Resonant Peak @44.96 [kHz], Q=225*

The quality factor Q=225 was extracted from the sense mass resonant frequency measurement, as given by Eq. 10, where the high and low –3dB frequency measurements were 45.02 [kHz] and 44.82 [kHz] respectively.

$$Q = \frac{F_0}{F_{-3dB\_HI} - F_{-3dB\_LO}} \qquad (10)$$

Angular rate resolution was measured in a 3 [mtorr] ambient as 3.8 [deg/sec] in a 20 [Hz] bandwidth, as shown in Figure 13, representing an 8.1 [mV/deg/sec] sensitivity.

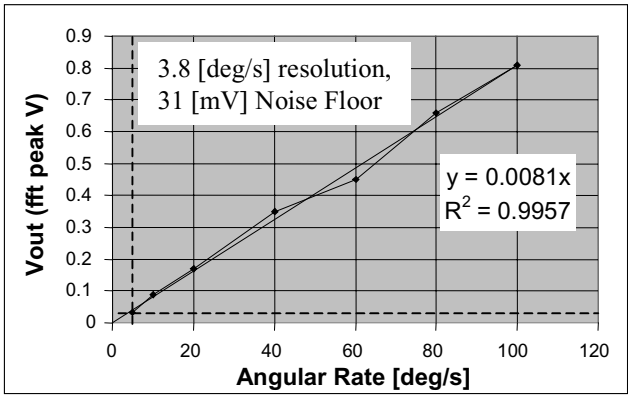

Figure 13*. Angular Rate Measurement*

CONCLUSION

We have demonstrated a low-cost high yield surface micromachined gyroscope with a decoupled drive and sense proof mass. A dual anchor approach is described using folded beam springs and a torsion post to significantly reduce undesired drive proof mass out of plane deflection while maintaining a comparatively low rotational mechanical restoring force. The Z-axis (vertical) proof mass suspension spring constant was increased from 7.86 [N/m] to 251 [kN/m] with the addition of the central torsion post. Interleaved springs attached at least two different radii can be used to supress precession of the central proof mass in lieu of the central torsion post. The interleaved support spring design scheme typically increases Z-axis spring constant by 2X while increasing the rotational spring constant by only 5-10%. Vertical stiction was eliminated from the design using the dual anchor scheme for the proof mass and a triply clamped beam approach for the fixed electrostatic drive/sense beams. The increase in the Z-axis spring constant of the fixed triply clamped beams is greater than 128X as compared to singly clamped cantilever beams of equal length. The parasitic capacitance of the fixed beam electrostatic arrays referenced to the silicon substrate is increased less than 16% due to the tip anchor inclusion. In addition, a differential capacitance measurement scheme is presented which rejects undesired proof mass linear acceleration error at the sensor. The differential capacitance electrode configuration also shields the sensor from fringing electrostatic fields allowing for increased angular rate sensitivity. The sense mode resonant frequency was measured at 44.96 [kHz] with a quality factor Q of 225 in a 3 [mtorr] ambient. Angular rate resolution was measured at 3.8 [deg/s] in a 20 [Hz] bandwidth with an 8.1 [mV/deg/s] sensitivity.

REFERENCES

1. M. W. Putty, and K. Najafi, “A Micromachined Vibrating Ring Gyroscope”, Solid State Sensors and Actuators, Hilton Head, pp. 213-217, 1994.
2. A. Ayazi, and K. Najafi, “Design and Fabrication of a High Performance Polysilicon Ring Gyroscope”, IEEE Micro Electromechanical Systems, pp. 621-626, 1998.
3. P. Greiff, B. Boxenhorn, T. King, and L. Niles, “Silicon Monolithic Gyroscope”, Solid State Sensors and Actuators, Transducers 91, pp. 966-968, 1991.
4. J. Bernstein, S. Cho, A. T. King, A. Kourepenis, P. Maciel, and M. Weinberg, “A Micromachined Comb-Drive Tuning Fork Rate Gyroscope”, IEEE Micro Electromechanical Systems, pp. 143-148, 1993.
5. M. Lutz, W. Golderer, J. Gerstenmeier, J. Marek, B. Malhofer, and D. Shubert, “A Precision Yaw rate Sensor in Silicon Micromachining”, Solid State Sensors and Actuators, Transducers 97, pp. 847-850, 1997.
6. W. A. Clark, and R. T. Howe, “Surface Micromachined Z-Axis Vibratory Rate Gyroscope”, Solid State Sensors and Actuators Workshop, Hilton Head, pp. 283-287, 1996.
7. T. Juneau, A. Pisano, and J. H. Smith, “Dual Axis Operation of a Micromachined Rate Gyroscope”, Solid State Sensors and Actuators, Transducers 97, pp. 883-886, 1997.
8. W. Geiger, B. Folkmer, J. Merz, H. Sandmaier, and W. Lang, “A New Silicon Rate Gyroscope”, IEEE Micro Electromechanical Systems, pp. 615-620, 1998.
9. G. J. O’Brien, D. J. Monk, and L. Lin, “MEMS Cantilever Beam Electrostatic Pull-in Model”, SPIE MEMS, Vol. 4593, pp. 31-41, 2001.
10. C. H. Mastrangelo and C. H. Hsu, “Mechanical Stability and Adhesion of Microstructures Under Capillary Forces –Part 1: Basic Theory”, Journal of MicroElectromechanical Systems, Vol. 2, No. 1, 1993.
11. W. Tang, M. G. Lim, and R. T. Howe, “Electrostatic Comb Drive Levitation and Control Method”, Journal of Micro Electromechanical Systems, Vol. 1, No. 4, 1992.

Integrated Microsystems for Microfluidics/BioMEMS: Cellular Sample Handling and Analysis

Murat Okandan, Paul Galambos, Seethambal S. Mani, David Salas, Gil Benavides, Harold Stewart, David Sandison, Jay Jakubczak

Sandia National Laboratories, P.O. Box 5800 MS 1080 Albuquerque, NM 87185

Abstract

SUMMiT™ technology has evolved over the last decade into one of the most capable surface micromachining technologies [**1**]. Our current technology development efforts are aimed at integration of microfluidic, mechanical, optical and electrical/electrochemical capabilities in this technology base.

Technology

Standard SUMMiT™ technology provides five polysilicon layers that are independently patterned that allows the creation of intricate structures. This allows the designers to have a very flexible design space; however, there are designs which require the creation of electrically insulated chambers and/or mechanical structures. To address these new device and application requirements, we have made modifications to the baseline SUMMiT™ technology, shown in Fig.1, which enable the creation of insulator lined, transparent microfluidic channels/ cavities along with complex mechanical, optical and electrical structures (Fig.2) [**2**].

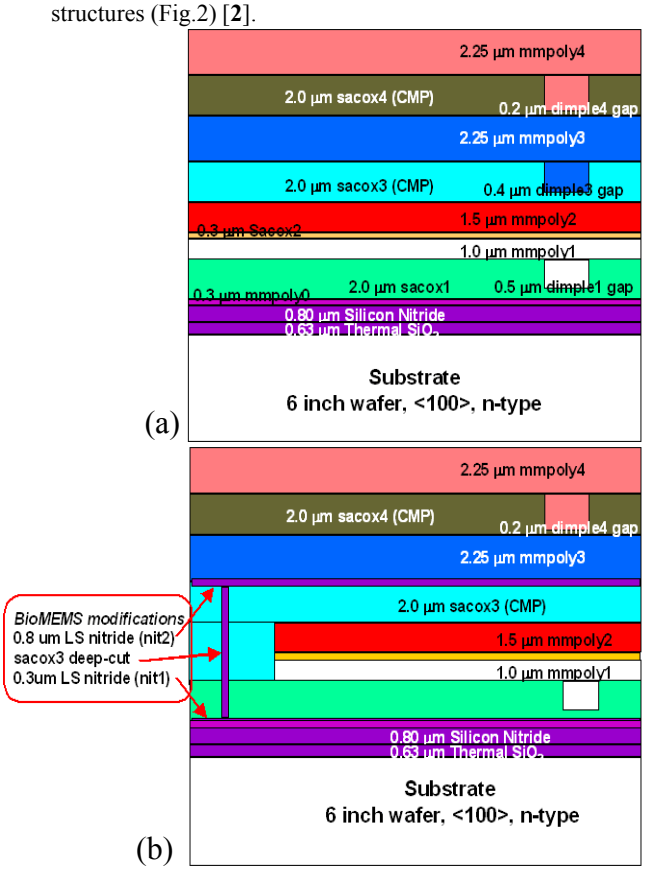

Figure 1. (a) Standard SUMMiT™ layers and (b) modified flow. Incorporation of low stress silicon nitride layers allows the creation of complex microfluidic/mechanical structures with optical access and the ability to create almost any arbitrary field inside these structures. Electrodes that are in contact with the fluid inside the channel allow direct (electrochemical) access to the microenvironment.

Devices

The microsystem components fabricated include valves (Fig.3), an accumulator (Fig.4), pumps (Fig.5), channels (Fig.6) and a microtransfection device (Fig.7) [**3**] as technology demonstration prototypes. These devices are also geared towards being the base components in a microfluidic/BioMEMS design toolbox.

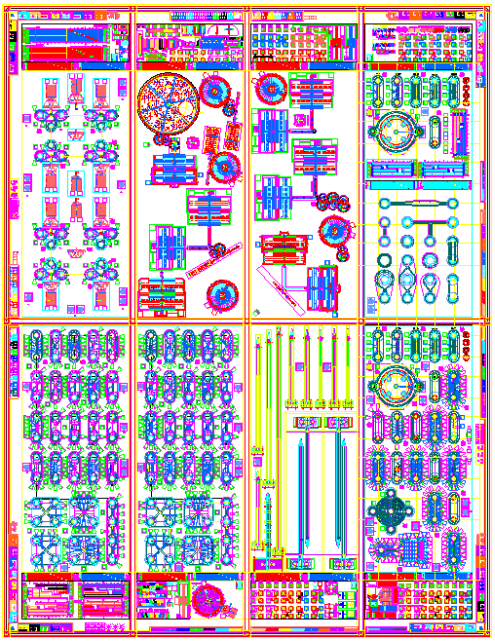

Figure 2. Reticle set of prototype devices (channels, electrodes, pumps, valves, microtransfection device) fabricated using the modified flow.

Valves are critical in many different sample/fluid handling systems. The first prototypes we have fabricated are flapper valves that open in the forward direction and close in the opposite direction. By designing the seats and flaps in subsequent polysilicon layers, check valves that function both in and out of plane directions have been realized. We are currently fabricating electrostatically actuated valves that will allow gating and proportional flow control functions.

Some of the preliminary data for a check valve is also shown in Figure 3. This valve was pressurized in the reverse direction (flow coming out of plane), and after the pressure was equalized on both sides of the valve, the syringe pump was started in the forward direction (flow into the plane). The valve did not open immediately, a pressure difference of 10mbar was required to open the valve which translates to a force of 7.5nN/um^2 at the valve seat/flap interface.

Similar pressure vs. time data is also given for an accumulator structure in Figure 4. This structure was formed by a 500um diameter, 0.6um high cavity. The top of the structure is formed by a 0.8um thick silicon nitride layer. The pressurization and discharge of air from this cavity (through a surface micromachined channel) is shown in the figure.

0-9640024-4-2/hh2002/$20©2002TRF
DOI 10.31438/trf.hh2002.72

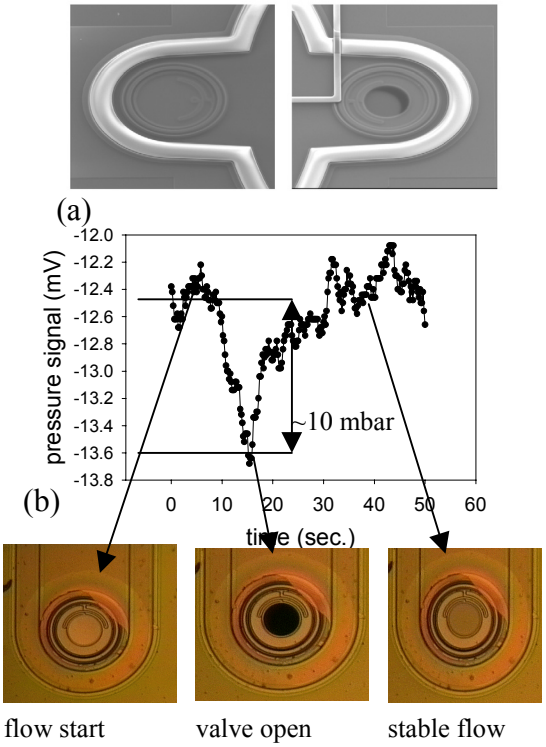

Figure 3.(a) Inlet and outlet valves constructed using polysilicon layers. Polysilicon springs provide the restoring force for the valves. Outer diameter of the valve structure is 135um, and the valve height is 3um. (b) Flow testing of a valve with the nitride layer removed to allow access to the ambient. The valve was over-pressurized in the reverse direction, the valve opened after a pressure difference of 10mbar was reached in the forward direction (which translates to 7.5nN/um^2 at the valve seat).

The valves shown above are incorporated into the membrane pump design in Figure 5. Inlet and outlet ports are on the left and right sides of the circular structure, which are connected through Bosch etched holes and the valves sit on top of these connection ports. Etch release holes (four circular

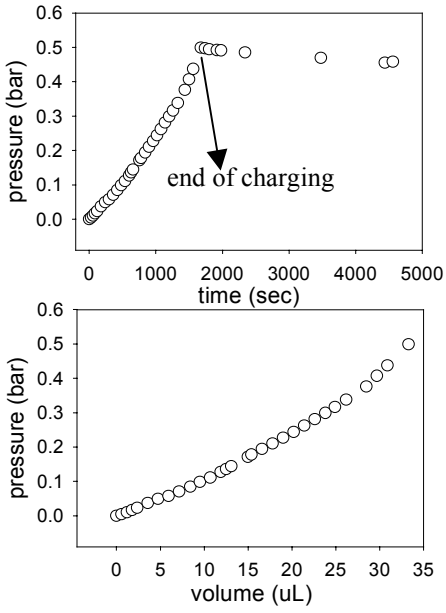

Figure 4. Accumulator. A built-in pressurized fluid storage structure - this chamber consists of a 500um diameter , 0.6um (initial) height region covered by a 0.8um silicon nitride membrane. This chamber was connected to a surface channel to route the chemical of interest into a manipulation chamber. Data shown was taken while charging this chamber with air at flow rate of 1.2 uL/min. After the charging was stopped, flow through the 1nL volume channel was observed as the pressure dropped.

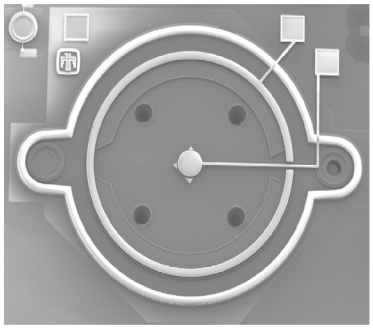

Figure 5. A membrane pump realized using the modified flow. Inlet/outlet valves are inside the cavity and actuation electrodes are placed above the silicon nitride layer (1mm diameter, 6um above the surface).

openings in the middle) are formed during the same process step and are sealed by the fixture/package that holds the chip.

Some of the most interesting and promising features in surface/photo/electro-chemistry also start becoming dominant and/or feasible in the scale of the devices described here. Several devices have been designed and fabricated to investigate these effects (Figure 6). Electokinetic pumping, dielectrophoretic separations, travelling wave setups, magnetic particle manipulations and electrochemical modification of the electrodes/channel contents are some of the concepts that are being addressed by these designs.

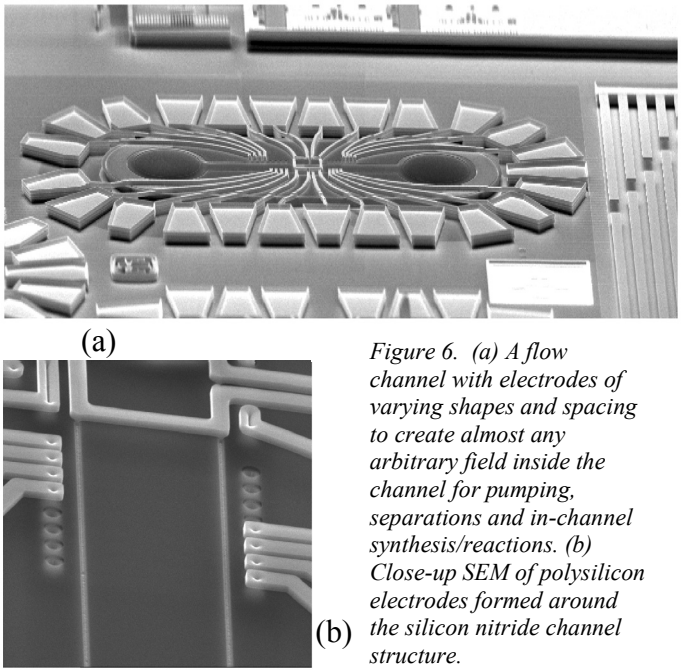

Figure 6. (a) A flow channel with electrodes of varying shapes and spacing to create almost any arbitrary field inside the channel for pumping, separations and in-channel synthesis/reactions. (b) Close-up SEM of polysilicon electrodes formed around the silicon nitride channel structure.

The microtransfection device was also designed and fabricated to demonstrate the integration capabilities offered by this technology (Figure 7). In this device, microfluidic, electrical/electrochemical, optical and mechanical components are integrated to perform manipulations on individual cells in a continuous flow fashion. Cells enter the device through one of the Bosch etched connections from the back of the wafer, travel through the manipulation section which has the electrostatically actuated mechanical manipulator and a second fluid entry/exit port, and exit the device on the other side. All of the structure is enclosed by nitride, which allows optical access, electrical insulation and through a passage, mechanical coupling to the actuator that is placed outside of the fluid flow.

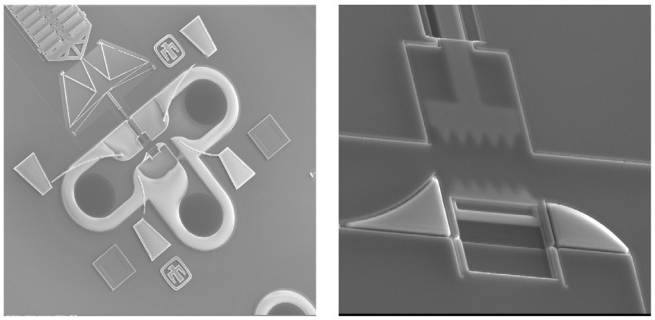

Figure 7. Microtransfection device which shows the integration of microfluidic channels, mechanical/ electrical structures and optical access. The mechanical manipulator is actuated by a high performance comb drive coupled with a displacement multiplier. Electrodes are positioned before and after the manipulation section. Mechanical manipulation is intended to temporarily disrupt the cellular membrane allowing delivery of large molecules into the cell that would normally be excluded. The last figure shows bovine red blood cells flowing through the manipulation region.

Another device that has been designed to manipulate individual cells is the patch clamp array (Figure 8). In this device, cell localization regions are defined by holes etched in the nitride layer, and the vacuum applied through the cavity below is used to capture cells. Silicon substrate behind the cell localization region has been removed to provide optical access for transmission/reflection and fluorescence microscopy with multiple electrodes for simultaneous electrical measurements and manipulations. Devices with further enhancements that involve incorporation of new mechanical structures for coupling to the cells are currently being designed and fabricated.

A critical part of the overall system integration involves packaging and assembly of components such as the ones described here. The methodology we are pursuing for integration is best illustrated by its analogy to the current microelectronic systems; the channels that are formed in plastic or glass integration substrates are analogous to the printed circuit boards and the integrated microfluidic devices are analogous to the integrated circuits, performing specialized functions. The packaging methodology will be very dependent on the final function – for example, an environmental sensor will have to interface with the ambient, requiring specialized collection/sample delivery options. We are pursuing several options in generating these packaging systems, including polymers, plastics and injection molded structures (Fig.9) [**6**].

Conclusions

Microsystems are expected to play a key role in the impending global technology revolution [**7**]. The completion of the human genome project has signaled the start of the hard part of this work: figuring out the details of the cellular machinery that is encoded by the genome and the overall "system" view starting with proteins, leading to cells, tissue, organs and finally the whole organism. The devices and the technology described here are aimed at providing the next generation of tools for the

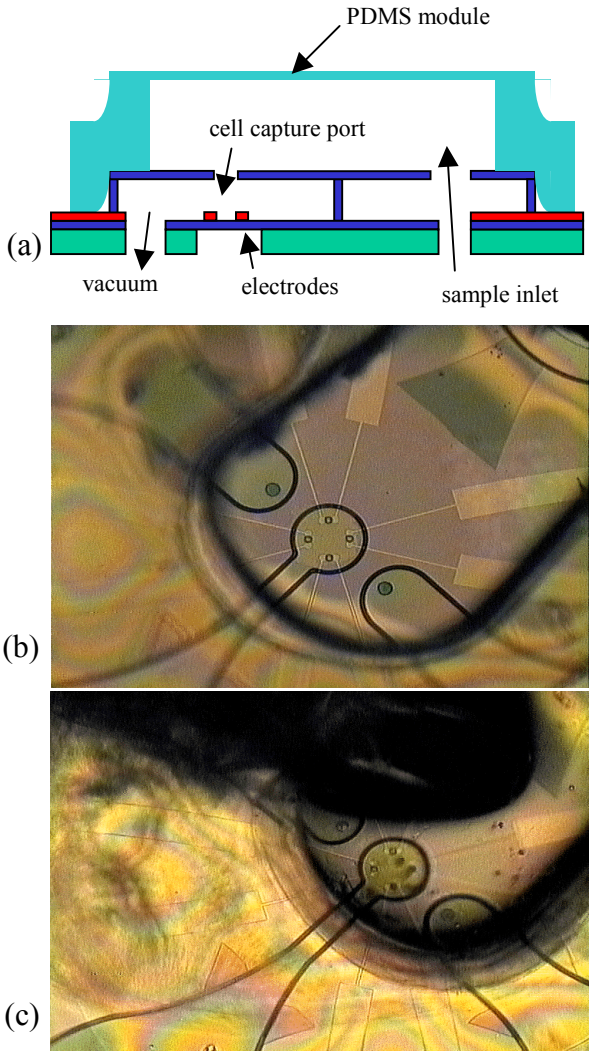

Figure 8. (a) Cross section of the patch clamp array. (b) Cell localization structure with a PDMS cage to hold the sample fluid. Four cell capture regions are visible with two electrodes below each hole in the center . The two larger holes are for fluid delivery/extraction and there is a larger sample delivery port on the top right portion of the device. (b) Red blood cells are being delivered into the device and are captured on the holes with the flow out of the lower left port. Silicon substrate behind the cell localization region has been etched to provide through-device optical access. Impedance based measurements for detecting cell capture and modification, electrochemical modification of electrodes/cells, multiple sample introduction/removal and fluorescence based measurements are currently under way.

biological and medical sciences in pursuit of these goals, starting with tools for measurement and manipulation of a single cell.

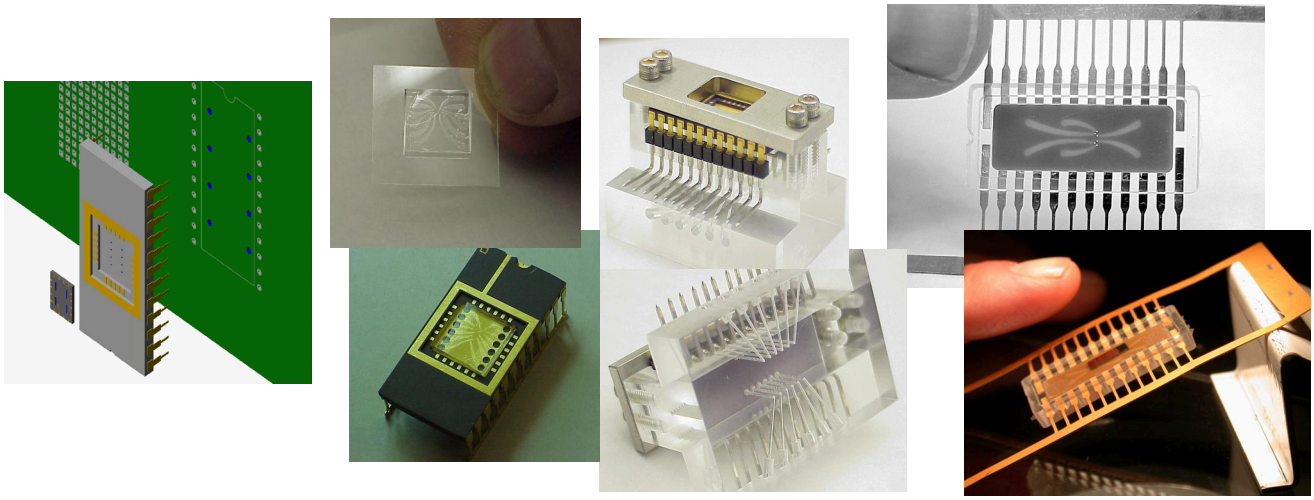

Figure 9. Packaging approach involving the microdevice, polymer/plastic based fanout part, molded or ceramic package and the circuit-board with fluidic and electrical interconnects.

Acknowledgements

We would like to acknowledge the MESA staff at Sandia National Laboratories for fabrication of the devices presented in this paper.

Sandia is a multiprogram laboratory operated by Sandia Corporation, a Lockheed Martin Company, for the United States Department of Energy under Contract DE-AC04-94AL85000.

References

[1] see www.mems.sandia.gov for bibliography

[2] Development of surface micromachining technologies for microfluidics and BioMEMS, M. Okandan, P. Galambos, S. Mani, J. Jakubczak, Proceedings of SPIE, vol.4560, pg.133-139, 2001

[3] Surface micromachined cell manipulation device for transfection and sample preparation, M.Okandan, P. Galambos, S. Mani, J. Jakubczak, Proceedings of uTAS 2001, pg.305-306

[4] Microfabricated electroporation chip for single cell membrane premeabilization, Y. Huang, B. Rubinsky, Sensors and Actuators A, v.89, pg.242-249, 2001

[5] Holding forces of single-particle dielectrophoretic traps, J. Voldman, R.A. Braff, M. Toner, M. Gray, M. Schmidt, Biophysical Journal, v.80, pg.531-541

[6] Precision alignment packaging for microsystems with multiple fluid connections, P. Galambos, G. Benavides, M. Okandan, M. Jenkins, D. Hetherington, 2001 ASME IMECE

[7] The Global Technology Revolution, Bio/Nano/Materials Trends and Their Synergies with Information Technology by 2015, P.S. Anton, et.al., RAND (www.rand.org/publications/MR/MR1307)

A DISPOSABLE CAPILLARY MICROPUMP USING FROZEN WATER AS SACRIFICIAL LAYER

Li-Wei Pan, Yu-Chuan Su, Sha Li and Liwei Lin
Berkeley Sensor and Actuator Center
Mechanical Engineering, University of California at Berkeley
Berkeley, CA 94720-2120

ABSTRACT

A disposable capillary micropump has been successfully demonstrated by a one-mask microfabrication process using frozen water as the sacrificial layer. The micropump consists of two fluidic chambers (source and drain) and a 6.5mm-long, 5μm-thick, naturally formed microchannel for capillary reaction. This prototype capillary micropump requires no electrical power and provides a maximum flow rate of 2nL/min with an operation volume of 10nL in 30 minutes. The surface tension reaction force between the liquid sacrificial layer and the surrounding channel materials controls the heights of the microfluidic components such as chambers and channels naturally. Using water as the sacrificial layer has the advantage of simple and clean processing. As such, this self-primed process and the self-powered micropump may have great potentials in bio-medical applications, including disposable devices.

INTRODUCTION

It have been well documented that micropumps generally require high electrical power to operate and complicated manufacturing process to fabricate [1] Self-powered micropumps that are fabricated by very simple processing steps are attractive, especially, in the area of disposable applications. For example, emerging biological assays such as single molecule studies of DNA and cell adhesion analyses required a system that can provide non-pulsatile flows at extremely low velocity. Previously micropumps driven by the evaporation of water have been developed but the fabrication processes are complicated [2,3]. This work presents a new fabrication technology by using frozen water as a clean and easily removable sacrificial layer in the fabrication process for the first time. The water sacrificial technique can provide smooth and continuous surfaces such that the dead volume can be reduced and the efficiency can be enhanced. This novel technology can also provide the encapsulation of liquid that has the potential for drug delivery applications.

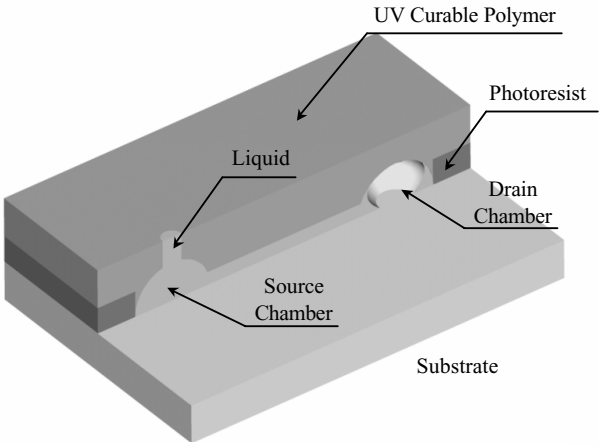

Fig. 1: The schematic drawing illustrating the working principle of the capillary micropump.

WORKING PRINCIPLE

The working principle of the micropump is illustrated in Fig. 1. The whole device is composed of a source and a drain chamber and a long serpentine-shape microchannel. These components are fabricated on top of a hydrophilic surface. In the prototype demonstration, silicon wafer with a layer of thermal oxide has been used as the substrate. A photoresist layer is deposited and

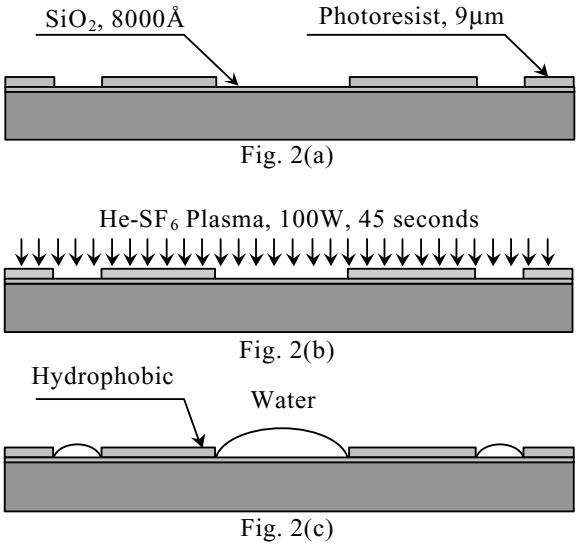

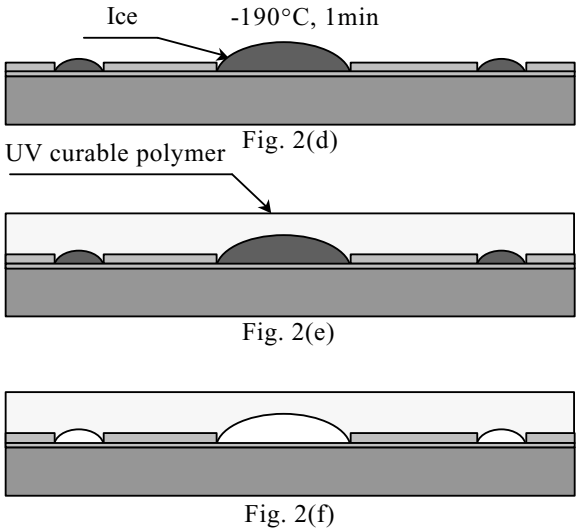

Fig.2: Fabrication sequence of the disposable capillary micropump using frozen water as the sacrificial layer

0-9640024-4-2/hh2002/$20©2002TRF
DOI 10.31438/trf.hh2002.73

patterned to define the chambers and channel areas as shown in Fig. 1 and UV-curable polymer is used to cover and seal the whole system. The critical process step is conducted by placing the sacrificial liquid onto the chamber and channel areas selectively utilizing the property of hydrophilic and hydrophobic surfaces for selective positioning. The sacrificial liquid is then frozen by lowering the substrate temperature to below the freezing temperature for the sacrificial liquid such that UV-curable polymer can be easily placed on top the solid surface. When the substrate temperature is increased, the frozen sacrificial solid becomes liquid again. The sacrificial liquid may evaporate completely to the environment or be kept inside the microstructures depending on the applications and the selection of polymers. In the micropump application as demonstrated in this work, water is used as the sacrificial layer and is driven out completely to complete the process either naturally or by placing the device into an oven to speed up the drying process.

Figure 2 shows the fabrication sequence of the prototype micropump. The process starts with growing a 0.8μm-thick silicon dioxide on a clean silicon wafer. A 9μm-thick photoresist (Shipley STR 1075) layer is patterned to define the microchannels and fluid reservoirs as shown in Fig. 2(a). A plasma process is applied to make the surface of the photoresist hydrophobic [4] (Fig. 2(b)). Water is then poured onto the wafer and is automatically and selectively placed into the microchannels and reservoirs as shown in Fig. 2(c). The naturally formed water areas have different heights and shapes depending on the geometry of channels and the properties of hydrophobic/hydrophilic surfaces and working liquid. The substrate is then immersed into a liquid nitrogen bath for 1 minute and liquid water is transformed as solid ice as shown in Fig. 2(d). The ice serves as the sacrificial layer when a 250μm-thick UV curable polymer is coated and cured as illustrated in Fig. 2(e). The water is driven out either naturally after a few days or by putting in an oven for a few hours to complete the process as shown in Fig. 2(f). Working liquid is supplied through a fluidic port opened at the source chamber. The hydrophilic surface inside the microchannel drags water automatically (self-prime) to the drain chamber by means of surface tension force as an operating capillary micropump.

Figure 3 is the cross sectional view of the fabricated micropump showing the source and drain chambers of 90μm and 204μm in height, respectively. The source chamber is defined by a square area of 600 μm in width and the drain chamber is defined by a circular area of 1250μm in diameter. As a result, the surface

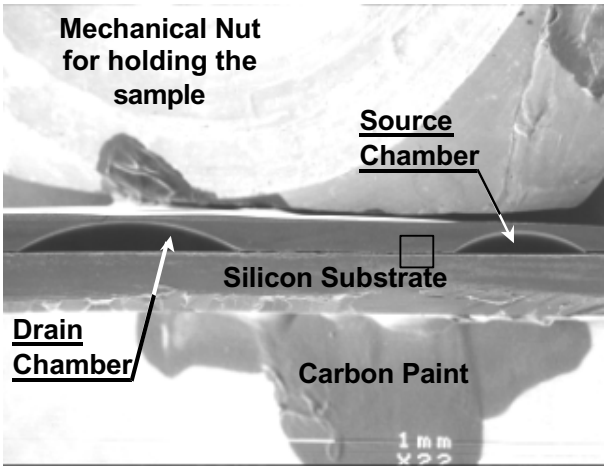

Fig. 3: The SEM microphoto showing the cross-sectional view of microchambers.

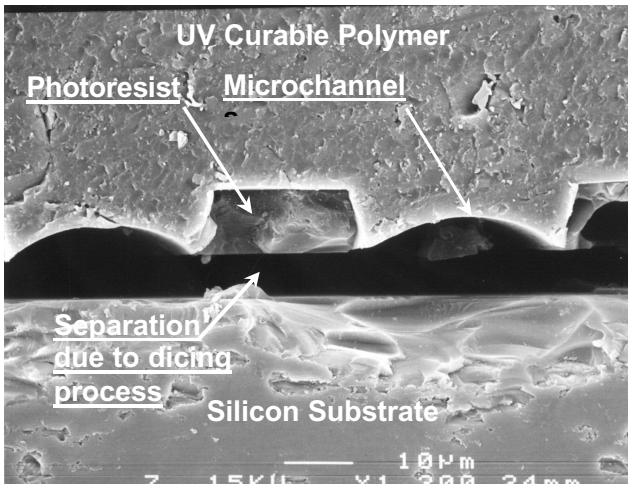

Fig. 4: The close view SEM microphoto of Fig. 2 showing the microchannels.

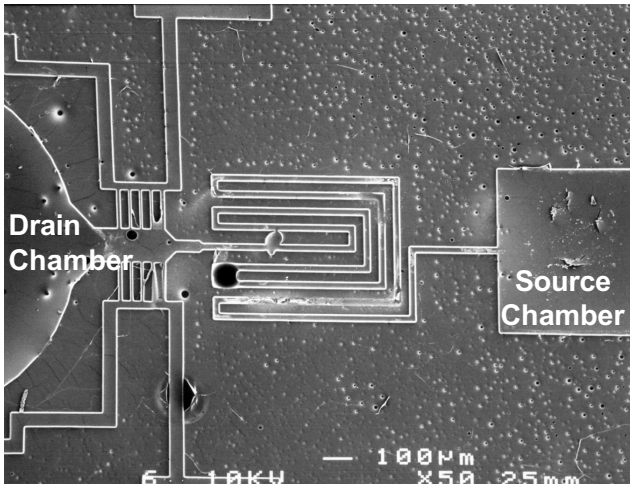

Fig. 5: The SEM microphoto showing the overview of the micropump.

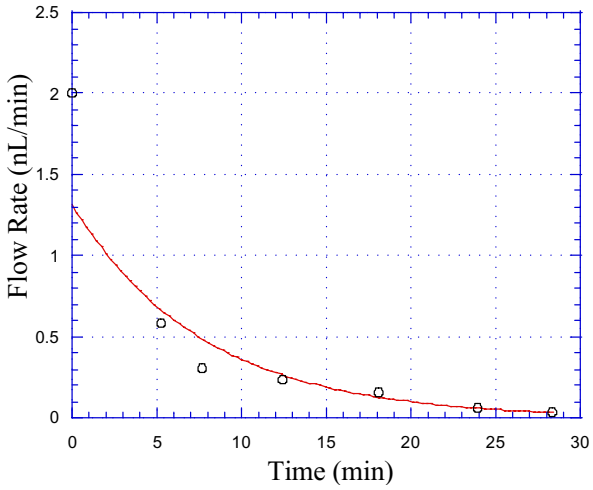

Fig. 6: Measured flow rate of the one-mask, disposable capillary micropump.

tension force of the water droplets controls the height of these chambers naturally in the manufacturing process. The designated box area in Fig. 3 is enlarged and shown in Fig. 4, where the polymer layers (both photoresist and UV-curable polymer) are observed to be separated with the silicon substrate during the wafer dicing process. However, the shape of the two microchannels and the photoresist between them can be clearly observed. The sidewall of the microchannels seems to be hydrophobic that prevents penetration of the sacrificial water. The estimated height of the microchannels is 5μm while the width is 20μm. Figure 5 shows the top SEM microphoto of the whole structure and the total length of the microchannel is 6.5mm as shown. The micropump operates when a hole is poked open and liquid is poured into the source chamber. Capillary force drives the liquid toward the drain chamber at a high flow rate of about 2nl/min initially.

Figure 6 is the measured flow rate of the micropump. It is suggested that flow rate decreases gradually until the capillary driving force is balanced by the air bubble pressure inside the drain chamber.

DISCUSSIONS

Using frozen water as sacrificial layer faces several key challenges. First, the process is sensitive to the conditions of environment such as temperature, humidity and airflow speed. In the prototype demonstration, none of these factors have been carefully controlled or maintained. The fabrication results are expected to improve if these factors can be controlled and optimized in the manufacturing environment. Temperature below freezing temperature (0ºC for water) can keep the sacrificial liquid in the solid form for the next processing steps and liquid nitrogen appears to be an overkill that caused cracking of photoresist and polymer. Therefore, it is desirable that the process can be conducted at a temperature just below the freezing point without abrupt temperature changes in the process.

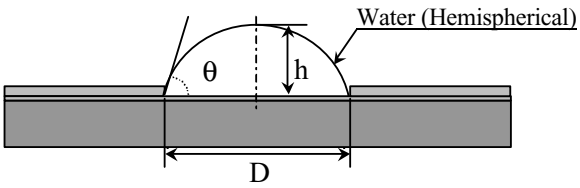

Fig. 7: The schematic drawing illustrates the model for microchamber and channel height design.

Design rules

The naturally formed micro chambers and channels are decided by the balance of surface tension force. Because the maximum feature size in the prototype micropump is in millimeter scale, surface tension force is about at least 10 to 100 times larger than the gravitational force and water droplets can be regarded as hemispherical shapes as shown in Fig. 7 [5] and the height of the droplet, h, can be described as:

$$h = D\left[\frac{1-\cos\theta}{2\sin\theta}\right] \qquad (1)$$

where D is the characteristic length of the opening area (diameter for a circular opening area and width for a rectangular opening area) and θ is the contact of water to air and silicon dioxide interface. In this work, the heights of the source and drain chambers are calculated as 83μm and 173μm respectively and the height of the microchannel is calculated as 3μm. These numbers are calculated based on the assumption that the contact angle of water and air-silicon dioxide interface is 31 degrees at room temperature. Since the micro chambers and channels are created during the transition of solid ice to liquid water and a new contact angle of water and UV curable polymer-silicon dioxide interface will be generated. Experimentally, the contact angle is measured by dicing the micro chamber right through the center as shown in Fig. 8 and the contact angle is measured as 43 degrees. Therefore, the heights of these microstructures are expected to be higher than the prediction using room temperature contact angle data. Based on Eq. 1, the calculated heights of the source and drain chamber used in this work are 118μm and 246μm, respectively, and the height of the microchannel is calculated as 4μm. These numbers are slightly higher than the experimental data.

The new contact angle may tend to increase the liquid volume in micro chambers and channels and may cause local distortions of the shapes of microstructures. The detail physical reaction requires further investigations. However, keeping the processing temperature just below frozen temperature during the curing process of UV-curable polymer may help alleviate this problem. .

Chamber/Channel Shapes and Surface

The top UV curable polymer is detached from silicon substrate for surface analysis by etching away the photoresist layer in IPA (Isopropanol Alcohol). Figure 9 and 10 are SEM microphotos of microchambers and microchannels from the UV curable polymer surface. Cracks are observed on the surface due to abrupt processing temperature change of liquid nitrogen bath. Small cavities are also observed and they were formed due to the release of solvent gas from the photoresist and/or trapped and frozen water droplets from the environment after the liquid nitrogen bath [6]. These cracks and cavities may be eliminated or minimized by choosing appropriate photoresit together with optimized UV baking process and environmental control.

Figure 10 shows the close view of the marked box in Fig. 9 and two different shapes of microchannels (Type A and B) are identified. Type-A shape is formed when sacrificial water behaves like the schematic drawing in Fig. 2(e). Since the sacrificial water is confined at the intersection of the silicon dioxide layer and the sidewall of photoresist, a shallow microchannel shape is the result

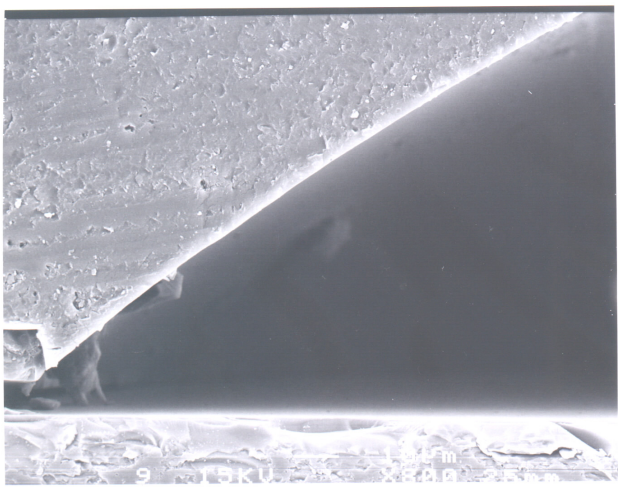

Fig. 8: The cross sectional microphoto showing the contact angle between water, UV curable polymer and silicon dioxide surface.

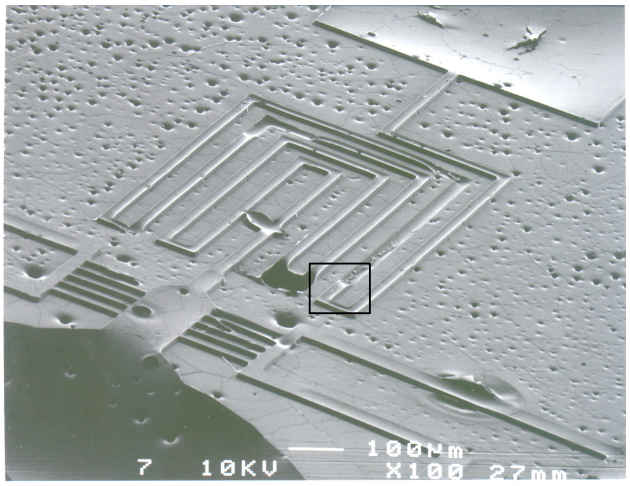

Fig. 9: SEM microphoto showing the microchannels formed by the ice sacrificial layer after removing silicon substrate.

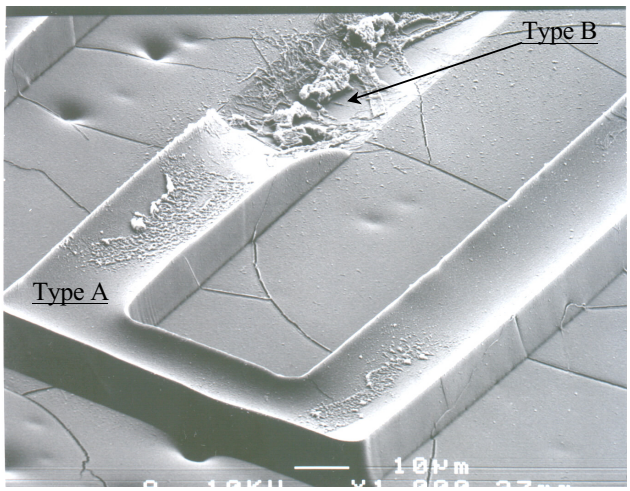

Fig. 10: The close view of the designated box area in Fig. 9.

and type-A shape is formed as shown in Fig. 10. On the other hand, it is observed that the sacrificial water can also fill either partially or completely the sidewalls of the microchannel such that the resulting microchannel shape can go from completely type-A to completely type-B as shown in Fig. 10. Type-B channel happens when the sacrificial water completely fills up the microchannel and the reverse of the channel shape after removing the photoresisit layer as shown in Fig. 10. Experimentally, a wide range of channel shapes from completely Type-A to completely Type-B has been observed in the same manufacturing process along a short piece of microchannel. The fundamental physics behind the various shapes of the microchannels require further investigations. However, it is believed that hydrophobic or hydrophilic surfaces of the photoresist sidewalls, the contact angle of wafer between different surfaces of photoresist, silicon dioxide and UV curable polymer at various temperature and the dynamic responses of the sacrificial water during the manufacturing process are key factors to be studied.

The internal surface of the microchannel formed by the water sacrificial layer is examined by SEM microphoto as shown in Fig. 10. Because there is no mechanical contact during the channel formation process, the surface is expected to be smooth as seen in the figure. Some particles are observed on the micro channel surface probably due to the contamination during the testing process. This smooth surface can minimize the resistance to the fluid flow.

CONCLUSIONS

A capillary micropump is fabricated utilizing frozen water as the sacrificial layer in the microfabrication process. This one-mask process is capable of making microfluidic components such as microchannels and reservoirs with variable heights as controlled by the contract angle of the sacrificial liquid and surrounding channel materials and the lithography-defined open areas. A prototype micropump driven by capillary forces is fabricated and tested as a demonstration vehicle. It has been measured that the micropump can provide a maximum flow rate of 2nL/min with an operation volume of 10nL in 30 minutes. The heights of microchambers and microchannels can be designed by the contact angle of liquid and the size of opening areas. Controlled processing environment near the freezing temperature of sacrificial liquid is suggested to improve the yield of the process.

ACKNOWLEDGEMENTS

The authors would like to thank Mr. Ron Wilson for taking SEM pictures and Hyuck Choo and Jeonggi Seo of BSAC for valuable discussions. These devices were fabricated in the UC-Berkeley Microfabrication lab. This project is supported in part by a DARPA/MTO/BioFlips grant.

REFERENCES

1. M. Esashi, S. Shoji and A. Nakano, “Normally closed microvalve and micropump fabricated on a silicon wafe,” *Sensors and Actuators*, vol.20, (no.1-2), p.163-9, 15 Nov. 1989.
2. V. Namasivayam, K. Handique, D.T. Burke, R.G. Larson, M.A. Burns, “Microfabricated valveless pump for delivering nonpulsatile flow,” *Proceedings of the SPIE- The international Society for Optical Engineering*, vol. 4177, p.220-8, 2000.
3. N. Goedecke and A. Manz, “Towards Evaporation-Driven HPLC on a Chip: An Alternative Transport Process for Micro Analysis Systems,” *Proceedings of Micro Total Analysis Systems 2001*, p. 375-6, 2001.
4. J. Seo and L.P. Lee, “Self-Assembly Templates by Selective Plasma Surface Modification of Micropatterned Photoresist,” *Proceedings, IEEE. Micro Electro Mechanical Systems,* Las Vegas, U.S.A., p. 192-5, 2002.
5. A. Adamson, “Physical Chemistry of Surfaces”, John Wiley & Sons, 4th edition, 1982.
6. C.S Hunag, B.Y Tsui, H.H Shieh, and R. Mohondro, “A novel UV baking process to improve DUV photoresist hardness.”,,*Proceedings of International Symposium on VLSI Technology Systems and Applications, Taipei, Taiwan,* p.135-8., 1999.

MEASUREMENT SYSTEM FOR LOW FORCE AND SMALL DISPLACEMENT CONTACTS

Beth L. Pruitt, Woo-Tae Park, Thomas W. Kenny

Dept. of Mechanical Engineering, Stanford University,

Stanford, CA 94305, pruitt@stanford.edu

ABSTRACT

In order to further miniaturize electrical contacts for novel IC packaging methods and MEMS scale relays, combined measurements of the electrical and mechanical properties of thin film metallization used in low-force contacts is required. Comprehensive data to design these low-force electrical contacts is lacking because no system is readily available for measuring forces, displacements, and electrical resistance at the levels of interest. A new measurement system is designed to characterize the low force behavior of thin gold films by flexibly varying these conditions and implementing an interferometer. This new MEMS/Materials characterization system is capable of measuring displacements and deformations down to 0.1Å, contact forces from mN to nN, and contact resistance from mΩ to kΩ, and represents the first complete system capable of simultaneous measurements of all these parameters.

INTRODUCTION

The rapid development of integrated circuits requires denser packaging for higher integration. As the line width and pitch for interconnects and packaging pads shrink, the size of electrical contacts for packaging must also decrease to accommodate smaller packages and minimize the number of redistribution layers and the area required to transition to external or off-chip connections. For these reasons, the electronics packaging and testing industry is developing new methods to decrease the size of electrical contacts. One approach is the MicroSpring™ interconnect developed by Formfactor, Inc. and shown in Figure 1. Shrinking the size and force applied by these interconnects while maintaining good electrical contact is desirable. MicroSprings™ are used in probe cards for testing or can be integrated directly on the wafer to act as both the first and second level interconnect for packaging. To make these pressure-mated low force interconnects reliable, complete data for electrical and mechanical properties of contacts made with thin-film metallization are required.

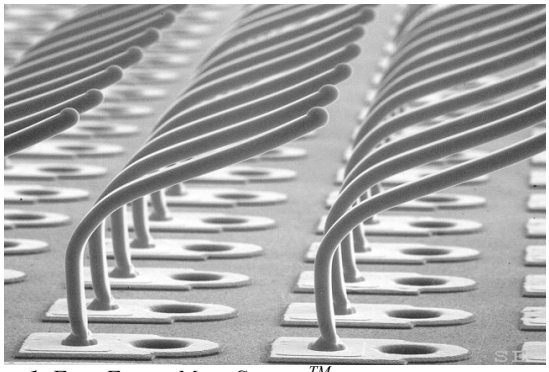

Figure 1. *FormFactor MicroSprings™.*

Low force and small area contacts have been studied previously for very specific applications and materials systems. From the previous work, thin film properties have been found to vary substantially from bulk properties. Discrete results for a single device configuration, load, and material choice are reported for MEMS relays [**1-4**] or limited sets of thin films[**5-7**]. The majority of low force contact data available utilized force balance systems without continuous and synchronous data collection and is from bulk materials[**8-12**].

This paper presents a unique measurement system, as shown schematically in Figure 2, for evaluating thin film contacts and allows easy variation of loading, displacement, and current during the test. Forces are measured on a piezoresistive cantilever [**13**], which is stepped into contact with a sphere metallized identically to the contact pad on the cantilever. Stepwise displacement is controlled with a piezoelectric actuator with a theoretical resolution of 1nm and range of 100µm. The contact displacement is directly measured with an interferometer shown in Figure 3 and discussed later[**14**]. The materials tested in the initial experiments were thin films of evaporated gold with varied thickness[**15**]. Additonal tests with variation of thin film properties through manufacture method have since been conducted with improved accuracy in the revised experimental setup.

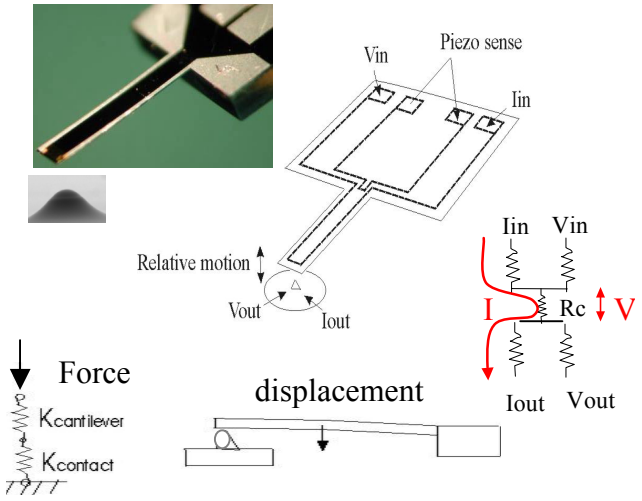

Figure 2. *Piezoresistive cantilever and metallized contact sphere top pictured left. Measurement schematic depicts relationship to mechanical and electrical models used to extract force, displacement, and contact resistance (Rc=V/I) from the measurement.*

Travel support has been generously provided by the Transducers Research Foundation and by the DARPA MEMS and DARPA BioFlips programs.

EXPERIMENT

Design and Characterization of Cantilevers

Piezoresistive cantilever sensors were fabricated in order to measure force and contact resistance simultaneously. Cantilever geometry (width, length and thickness) and doping level/pattern were optimized to measure the desired force range (mN~nN). The sensor and the spherical contact "tip" are metallized with plated, sputtered and evaporated gold of varied thickness. Two aluminum traces on the cantilever along with the two electrical leads at the tip enable 4-wire contact resistance measurement when the sensor makes contact with the tip. The resonant frequency, effective spring constant, and calibration factor for voltage to force transformation is derived by mechanically resonating the cantilever and measuring tip displacement and piezoresistor voltage. The transformations are made using linear beam theory. Details of design and fabrication are discussed in a previous paper**[13]**. The contact geometry investigated is a sphere on flat because it is easily modeled, controlled, and characterized. Glass and polystyrene spheres of 50 and 100μm diameter were potted in photoresist spun on a 4-inch wafer for use as contact tips of different compliance. This process creates a spherical tip protruding from a concave sloped shoulder that enables uniform metallization, also shown in Figure 2. The tips are subsequently metallized with varying thickness of gold using different manufacturing methods.

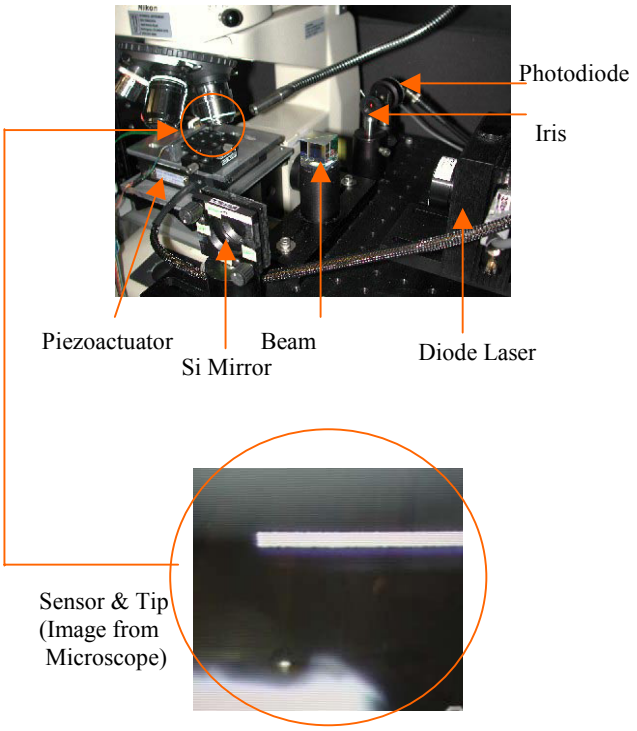

Figure 3. *Measurement system incorporates a customized piezoresistive cantilever to measure force, PolytecP-731 2-axis nanopositioner and E515 closed loop controller with capacitive feedback to apply displacements, and a free space Michelson interferometer for measuring contact displacement.*

The noise spectrum of the piezoresistive force sensor is shown in Figure 4; the noise floor of 80pN at 1Hz is not limiting. Resolution is limited more by drift over the course of a full loading and unloading cycle. However, good resolution during contact initiation allows characterization of small force mechanical properties.

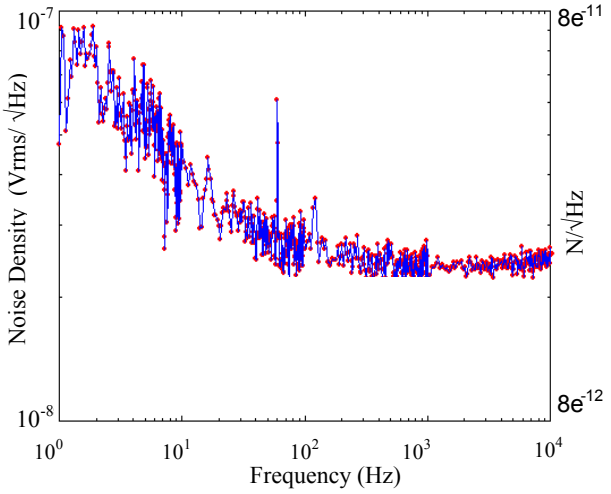

Figure 4. *Noise data for piezoresistor is collected on an HP89410A vector signal analyzer. The piezoresistor noise over the frequency range 10^{-1} to 10^{5} is dominated by 1/f noise below 1kHz. Noise at 1Hz is less than 0.1uV/√Hz or 80pN/√Hz.*

Contact Resistance Measurements

Experiments conducted with the first experimental setup provided some baseline guidance for improvement and data on the effect of cleaning procedures[**15**]. In the revised setup, contact resistance was investigated with varying manufacture methods. Gold films were manufactured by evaporation, sputtering, hard gold plating, and soft gold plating

Figure 5 shows a set of data from films of different manufacture methods. The contact resistance is measured as a function of applied force during the applied loading. For the parameters of deposition used, evaporated gold provides a lower contact resistance than the other films. This difference in behavior is correlated with microstructure and surface roughness. From the figure, we can quantify the adhesion force of each film. It is 20μN for evaporated gold, 60μN for hard plated gold, and 600μN for sputtered gold.

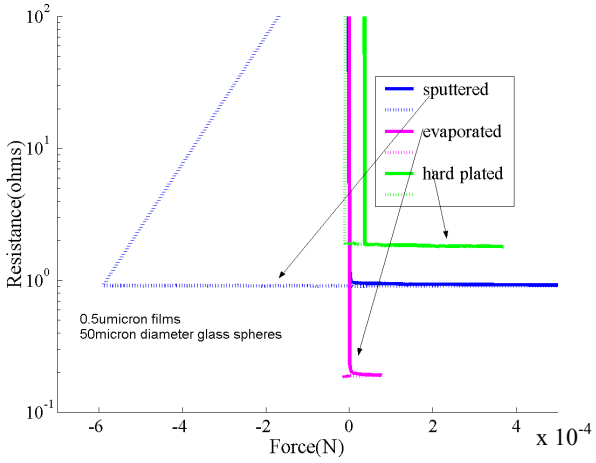

Figure 5. *Contact tests on 50μm diameter glass contact spheres, 0.5μm gold film deposited by sputtering, evaporating, or hard plated gold. The solid line represents the loading data and the dashed line is unloading.*

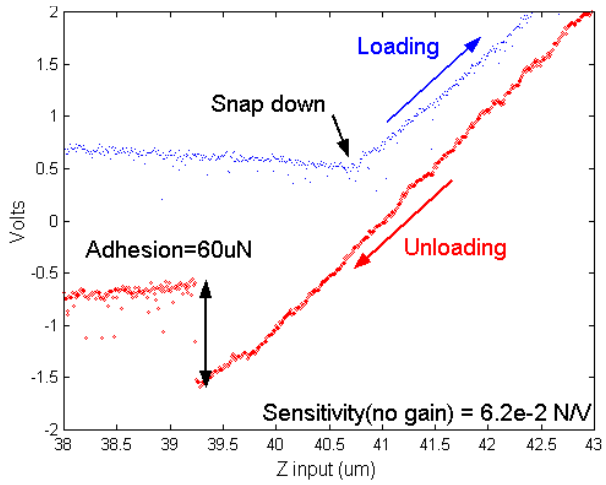

Figure 6. *PiezovoltageX1000 vs. input position for 1800Å evaporated gold film. Force is extracted from the piezoresistive cantilever calibration and features like pull off adhesion and snap down can be extracted. These are correlated with applied current, film thickness, material properties, and substrate type.*

In Figure 6, the snap down force and adhesion force are clearly visible by zooming in data from piezovoltage vs. input displacement.

Contact Displacement Measurement

"Contact displacement" as shown in Figure 7 is the amount of the total deformation of the tip and the cantilever when force is applied to the contact. The elastic property of thin films can be characterized by measuring the contact displacement along with the corresponding force data. Nanoindentation is the appropriate method for extracting material properties, however it does not have the capabilities to measure electrical properties concurrently. In order to directly measure contact displacement, a Michelson interferometer is incorporated to the existing measurement system**[14]**. The configuration of the interferometer is shown in Figure 8. The back of the cantilever sensor replaces one the mirrors of a typical Michelson interferometer to measure the movement of the cantilever.

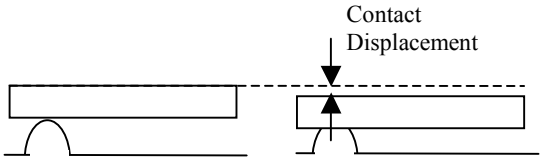

Figure 7. *Definition of a "contact displacement". In the figure, the contact area is exaggerated, however the gold films on both sides are deformed during contact.*

The movement of the cantilever produces a sinusoidal wave of intensity at the detector until the cantilever makes contact with the tip. Because the signal is a sinusoidal wave, the sensitivity is not a constant. The sensitivity of the interferometer as a contact displacement sensor depends on the position of the instant of contact relative to the sinusoidal sensitivity curve. If the contact is at the maxima or minima of the sine wave, the sensitivity will be zero. The maximum sensitivity will be halfway between maxima and minima. In order to get maximum sensitivity, the contact must occur in that region. However, it is impossible to predict the contact point at the start of the test, and not every contact test will yield usable interferometer data.

Figure 9 is the noise spectrum of the interferometer with a stationary cantilever. There are some high peaks between 10 and 100Hz, which is due to some random mechanical noise of the system. In spite of some random noise of the system we can see that the noise at 1Hz is less than 1mV/√Hz, therefore combining with the sensitivity obtained from Figure 10, the theoretical noise floor is less than 10^{-1}nm/√Hz at 1Hz for a typical measurement.

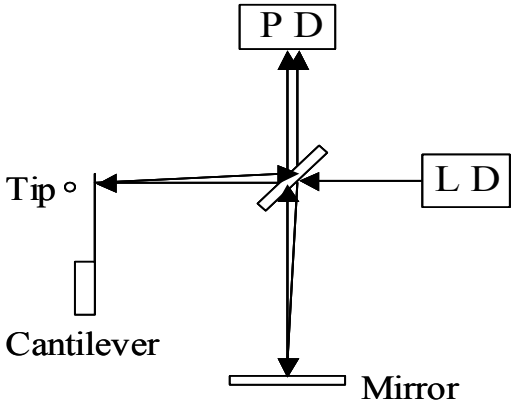

Figure 8. *Schematic of free space Michelson interferometer and displacement measurement back. A Hitachi HL6312G 635nm laser diode (LD) with Melles-Griot 06DLD163 controller and Thorlabs PDA500 amplified GaAsP photo diode (PD) are used with a prism beam splitter, polished Si mirror, to measure fine displacement of the surface of the Si cantilever over the first several microns of contact.*

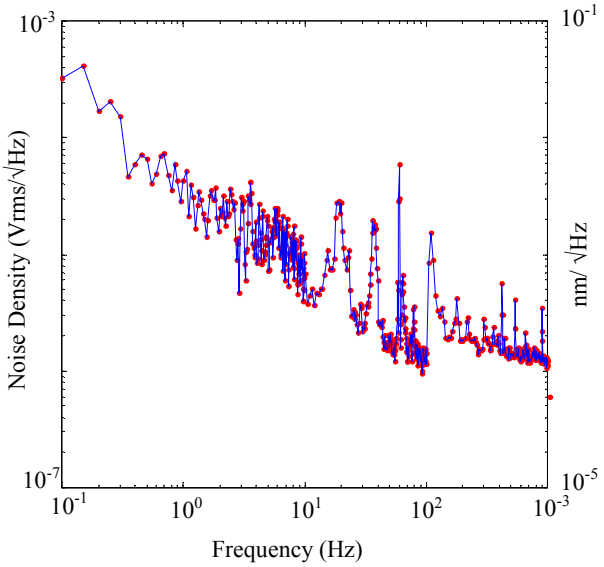

Figure 9*. Noise data for interferometer are collected on an HP89410A vector signal analyzer.*

Figure 10 shows a set of data from a contact of a silicon cantilever (K=72.1 N/m) on a polystyrene sphere with evaporated gold films. Although the movement of the piezoelectric actuator is not ideal and produces vibration, we can get an accurate measurement by averaging data.

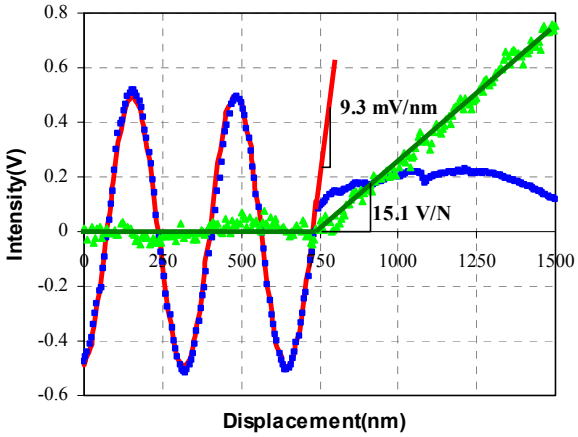

Figure 10. *Data from contact of a silicon cantilever on a polystyrene sphere with 0.5 μm evaporated gold films. The sinusoidal trace is the interferometer data with a curve fit, the linear flat to ramp trace is the piezovoltage with gain 1000.*

From the data points shown in square dots in the figure, a sine curve is carefully fitted. The next step is to find the actual contact point by extrapolating the curve before contact and the curve after the contact. Differentiating the fitted curve at the contact point produces the sensitivity of the interferometer. In the figure, a sensitivity of 9.25mV/nm was obtained by this method. The last step is to divide the voltage change by the sensitivity to get the displacement of the corresponding force. From this set of data, it can be shown that at a force of 5μN, the measured contact displacement is 4.8nm. The contact displacement of the polystyrene sphere on a silicon flat surface is predicted from Hertzian elastic theory for the mutual approach of distant points in the solid as

$$\delta = \frac{a^2}{r} = \left(\frac{9P^2}{16rE^{*2}} \right)^{1/3} \quad (1)$$

where,

$$E^* = \frac{1-\nu_1^2}{E_1} + \frac{1-\nu_2^2}{E_2}$$

δ = mutual approach of distant points on two sides of the contact (m)
a = radius of Hertzian elastic contact area(m)
r= radius of the sphere(m)
P= load(N).

Using the properties given in Table 1 and (1), the predicted displacement is 4.3nm. The difference in displacements is attributed to the deformation of the gold films.

	Modulus, E (Pa)	Poisson's ratio, ν
silicon	2.00E+11	0.23
polystyrene	1.68E+09	0.33

Table 1. *Bulk properties of substrate materials.*

CONCLUSIONS AND FUTURE WORK

This new MEMS/Materials characterization system is capable of simultaneously measuring small displacements and deformations, six orders of magnitude in the force regime between typical atomic force microscope (AFM) cantilevers and conventional methods, and six orders of magnitude in contact resistance. When combined with materials data like focused ion beam sections for microstructure, AFM scans for surface roughness, and nanoindentation measurements for hardness, this system enables the understanding of thin film electrical contact behavior in the low force regime. Further investigation of materials properties and variation of contact parameters is underway to provide design rules for low force, thin film gold contacts.

ACKNOWLEDGMENTS

This work was supported through Formfactor, Inc., the Hertz Foundation Fellowship, and the Alliance for Innovative Manufacturing at Stanford. Assistance and advice from Kenny group members and staff at Formfactor and Stanford is gratefully acknowledged. Travel support has been generously provided by the Transducers Research Foundation and by the DARPA BioFlips programs.

REFERENCES

1. D. Hyman and M. Mehregany, "Contact physics of gold microcontacts for MEMS switches", *Proceedings of the Forty-Fourth IEEE Holm Conference on Electrical Contacts*, IEEE: New York, NY, USA (1998), pp. 325.
2. E. J. J. Kruglick and K. S. J. Pister, "Lateral MEMS microcontact considerations", *J. Microelectromech. Syst. (USA)*, *8*(3) 264-271 (1999).
3. P. M. M. Zavracky, Nicol E.; Morrison, Richard H.; Potter, David, "Microswitches and microrelays with a view toward microwave applications", *Int J RF Microwave Comput Aided Eng*, *9*(4) 338-347 (1999).
4. J. Schimkat, "Contact measurements providing basic design data for microrelay actuators", in *Sens. Actuators A, Phys. (Switzerland), Sensors and Actuators A (Physical)*. (1999).
5. S. Hannoe and H. Hosaka, "Electrical characteristics of micro mechanical contacts", *Microsystem Technologies*, *3*(1) 31-5 (1996).
6. S. C. Bromley and B. J. Nelson, "Performance of microcontacts tested with a novel MEMS device", *Electrical Contacts, Proceedings of the Annual Holm Conference on Electrical Contacts*, pp. 122-127 (2001).
7. J. Beale and R. F. Pease, "Limits of high-density, low-force pressure contacts", *IEEE Transactions on Components, Packaging, and Manufacturing Technology, Part A*, *17*(2) 257-62 (1994).
8. M. Antler, "Tribological Properties of Gold For Electric Contacts", *IEEE Transactions on Parts, Hybrids and Packaging*, (1973).
9. R. Holm and E. Holm, "Electric contacts; theory and application". 4th completely rewritten ed., Berlin, New York,: Springer-Verlag. xv, 482 (1967)
10. W. C. Oliver, R. Hutchings, and J. B. Pethica, "Measurement of Hardness At Indentation Depths As Low As 20 Nanometres", *ASTM Special Technical Publication*, (1985).
11. M. D. Pashley and J. B. Pethica, "The role of surface forces in metal-metal contacts", in *J. Vac. Sci. Technol. A, Vac. Surf. Films (USA)*. (1985).
12. S. P. Sharma, "Some notes on the physics of contact adhesion", *Insulation/Circuits*, *23*(11) 41-5 (1977).
13. B. Pruitt, A. Partridge, M. Bartsch, *et al.* "Design of piezoresistive cantilevers for low force electrical contact measurements", *IMECE: 2000 International Mechanical Engineering Congress and Exposition,* Orlando, FL, (2000).
14. E. Hecht and A. Zajac, "Optics", Reading: Addison-Wesley (1974).
15. B. Pruitt, D.-H. Choi, J. Florando, *et al.* "Low force electrical contact measurements using piezoresistive cantilevers to characterize thin-film metallization", *Transducers '01/EuroSensors XV,* Munich, Germany, Springer (2001), pp. 1032-35.

A NEW APPROACH FOR DISPERSION CONTROL IN NANOFLUIDIC CHANNELS

R. Qiao and N. R. Aluru

Beckman Institute for Advanced Science and Technology
University of Illinois at Urbana-Champaign, Urbana, IL 61801

ABSTRACT

Turns and bends, such as an L-turn or a U-turn, in micro and nanofluidic channels can induce significant dispersion leading to a low efficiency electrophoretic separation process. It has been shown that turn-induced dispersion can be lowered by optimizing the geometry of the turns. In this paper, we propose a new approach for controlling turn-induced dispersion in nanofluidic channels. The approach is based on the idea of locally controlling the ζ-potential at turns and bends. An optimization algorithm was developed to search for the optimal configuration of the ζ-potential near turns. Results for an L-turn and a U-turn show that the dispersion can be lowered significantly by a ζ-potential variation near the turn.

INTRODUCTION

There has been growing interest in developing miniaturized fluidic devices for transport, separation and detection of bio-samples. In many of these devices, capillary electrophoresis is used for sample separation, and electroosmosis is used for sample transport. In several cases, both these processes occur together. Prior studies have shown that a longer channel can improve the separation efficiency. In applications like lab-on-a-chip where the device size is very small, turns must be introduced to integrate a long channel within the small area of a single chip. However, it has been found that such turns could induce serious dispersion, which may negate the effect of using a long channel.

Griffiths et. al. **[1]** and Molho et. al. **[2]** suggested the development of optimized turns to minimize the dispersion. In both these works, numerical methods were used to find the optimal geometrical configuration of the turns. Experimental results show that such an approach is feasible **[2]**. However, fabrication of the optimized geometry may not always be possible because of manufacturing as well as other considerations. In this work, we propose to control the turn-induced dispersion by introducing a localized ζ-potential variation. In this method, the ζ-potential on channel walls near the turn is controlled and the turn geometries are not altered. This approach provides an alternative when optimized turn geometry is difficult to implement in practice. Though flow control using localized ζ-potential variations has been difficult in the past, recent results suggest that it is possible to use such an approach. For example, it was reported in **[4]** that a localized ζ-potential control (through surface patterning) can be employed to produce nonaxial flow in microchannels.

MATHEMATICAL MODEL

Fluid flow due to electrical potentials, also referred as electroosmotic transport, is described by the Laplace equation, the Poisson-Boltzmann equation and the incompressible Navier-Stokes equations. A detailed description of the electroosmotic transport model can be found in **[3]**. The model includes:

$$\nabla^2 \phi = 0 \tag{1}$$

$$\nabla^2 \Psi = \frac{1}{\lambda_D^2} \frac{RT}{F} \sinh\left(\frac{F\Psi}{RT}\right) \tag{2}$$

$$\nabla \cdot \boldsymbol{u} = 0 \tag{3}$$

$$\mu \nabla^2 \boldsymbol{u} - \nabla P + \boldsymbol{F} = 0 \tag{4}$$

$$\boldsymbol{F} = \varepsilon \nabla \phi \nabla^2 \Psi \tag{5}$$

The Laplace equation (1) describes the potential in the electrokinetic geometry because of applied potentials and the Poisson-Boltzmann equation (2) describes the potential (Ψ) in the device because of the ζ-potential at the solution-capillary interface. Equations (3) and (4) describe the fluid flow in the device because of the applied and ζ-potential. Specifically, equation (3) is the incompressible continuity equation and equation (4) is the Stokes equation. In equation (4), $\boldsymbol{F}$ is the body force, the definition of which is given in equation (5). The mathematical model stated in equations (1) – (5) along with the appropriate boundary conditions describes the two-dimensional electroosmotic problem.

In some previous works (e.g. **[1]** and **[2]**), a potential flow is assumed and fluid velocity in electroosmotic flow is assumed to be proportional to the gradient of the applied electric field. This has been justified under several assumptions, of which the most important one may be that the ζ-potential in the entire system must be uniform. Because we intentionally introduce non-uniform ζ-potentials on the wall near turns, a full set of flow and electrokinetic equations (1)-(5) need to be solved to obtain the flow field instead of using the simpler potential flow theory.

Dispersion can be caused by both advection and diffusion **[1]**. In this paper, for simplicity, we consider only the dispersion caused by advection and neglect the diffusion-induced dispersion. The approach can, however, be extended in a straightforward manner to account for diffusion. When diffusion is taken into account, the optimization approach introduced here need not be changed, though the optimal configuration of the ζ-potential on the wall might change. The dispersion is calculated by tracking particles released at the upstream of the turn. The path of these particles is obtained by integrating:

$$\frac{\partial \mathbf{x}}{\partial t} = \mathbf{u} \tag{6}$$

where $\boldsymbol{u}$ is the velocity computed by solving equations (1)-(5). Here, we assume that the velocity of the particles is the same as the local fluid velocity.

NEW CONTROL STRATEGY: LOCALIZED ZETA-POTENTIAL VARIATION

In nanodiameter channels, turns can induce serious dispersion. Shown in Figure 1 is the distribution of particles after passing an L-shaped turn. These particles were released at the upstream of the turn with the same position in the *x*-direction. It can be seen that a serious dispersion occurs as the particles go through the 90° turn.

0-9640024-4-2/hh2002/$20©2002TRF
DOI 10.31438/trf.hh2002.75

Solid-State Sensors, Actuators, and Microsystems Workshop
Hilton Head Island, South Carolina, June 2-6, 2002

The dispersion stems from the fact that the particles near the inner channel wall travel a shorter distance compared to the particles near the outer channel wall. The differing velocity of the particles also contributes to the dispersion. An important observation in Figure 1 is that the particles are no longer in the symmetrical position with respect to the centerline of the channel after they have gone through the L-shaped turn.

One approach to minimize such dispersion is to make the particles travel approximately the same distance as they go through the turn. An alternative approach is to alter the velocity of the particles such that particles travelling longer distances move faster and particles moving shorter distances move slower. A combination of the two approaches can also be employed to minimize the dispersion. An example of the first approach is the work described in **[1]** and **[2]**, where the geometry of the turn is optimized such that the particles travel approximately the same distance at roughly the same velocity.

We propose a new method in which by varying the ζ-potential at the inner wall of the turn, we can change both the migration paths of these particles as well as their velocities without changing the geometry of the turn. By varying ζ-potential, we change the electric field, which in turn alters the migration path and the velocity of the particles. Thus, by controlling the ζ-potential on the inner wall near the turn, the particle dispersion can be minimized.

In this research, we have developed a two-stage control strategy to minimize the particle dispersion. The control scheme is illustrated in Figure 2 for an L-turn. In the first stage, the ζ-potential near the turn is controlled such that the particles are at a symmetrical position with respect to the centerline of the channel after they have passed the turn. In the second stage, the ζ-potential is controlled such that the particle dispersion is minimized. For an L-shaped turn, the second control step implies that the vertical position (*y*-coordinate) of the particles is approximately the same.

Figure 3 shows the position of the particles after passing the turn when only the first stage control is employed. It can be seen that the particle profile is almost symmetric with respect to the centerline of the channel. However, the particles near the channel wall lag behind the particles in the central portion of channel, indicating that the dispersion is still very high. Such a situation can be improved by employing the second stage control. Figure 4 shows the position of the particles after passing the turn. Note that the dispersion is much less than that observed in Figure 1. Even in Figure 4, the particles very near the wall still lag behind the particles in the central portion of channel. This can be explained by the fact that if a particle is within or near the Debye layer (the Debye length is set to be 2.5nm), it has a smaller velocity compared to a particle that is in the central portion of the channel. Even in a straight channel, where there is no bend or a turn, such dispersion, where the particles in the Debye layer lag behind the particles in the central portion of the channel, is observed. Figure 5 shows the streamlines near the turn when the two-stage control is applied. It can be seen that though the geometry of the turn is not altered, the migration path of the particles is changed.

APPROACH

The approach used to minimize the particle dispersion is discussed in this section. In particular, the objective functions developed for each of the control steps are described. For the L-shaped channel example discussed in the previous section, for the first control-step, where the objective is to make the particle profile symmetric with respect to the center line of the channel, the following objective function is employed:

$$F_1 = \sum_{i=1}^{n} \left| w_i (y_i - y_{2n+1-i}) \right| \tag{7}$$

In the development of equation (7), *2n* particles are assumed to be released from the upstream of the channel. y_i refers to the *y*-coordinate of the *i*th particle after the particle has gone through the turn (see Figure 2). Note that in equation (7), the first particle is assumed to be the particle closest to the lower or the bottom channel wall and the *2n*th particle is the particle closest to the top or the upper channel wall. w_i is the weight attached to each particle. As demonstrated in Figure 3, minimization of equation (7) leads to a symmetric particle profile as the particles go through the turn. The minimization of equation (7) can be accomplished by employing a standard optimization algorithm **[5]**.

The objective of the second control step is to minimize the dispersion or scatter between the particles. The objective function for the second control step is taken to be:

$$F_2 = \sum_{i=1}^{2n} w_i \frac{\left| y_i - \bar{y} \right|^2}{2n} \tag{8}$$

w_i is again the weight assigned to each particle. $\bar{y}$ is the mean vertical position of all the particles and y_i is the *y*-coordinate of the *i*th particle.

Equations (7) and (8) can be minimized by treating the ζ-potential at each mesh point on the channel wall as a control parameter. While this may yield the best results, it may not be a very practical situation. Hence, we use the following parameters as control variables to minimize the dispersion in an L-shaped turn:

1. For the first control step, it is assumed that the ζ-potential varies linearly within the control region i.e. ζ-potential varies linearly on *OA* and *OB* (see Figure 2). The ζ-potential at points *A* and *B* is assumed to be ζ_0 (ζ_0 is the known uniform ζ-potential on the channel walls when no control strategy is applied) and the ζ-potential at point *O* is the unknown. The length of the regions *OA* and *OB* is assumed to be the same and the ζ-potential variation on *OA* and *OB* is as shown in Figure 6. The two unknowns to be determined are the ζ-potential at point *O* and the length of region *OA* or *OB*. These unknowns are determined by minimizing equation (7). The ζ-potential at point A and the length of *OA* determined by the optimization algorithm are shown in Figure 7.

2. For the second control step, we assume that the length of the region *BD* or *B'D'* is equal to the width of the channel and the ζ-potential is constant on *BD* or *B'D'*. The unknown in this case is the constant ζ-potential on *BD* or *B'D'* and this can be computed by minimizing equation (8). We chose the length of *BD* to be the width of the channel just to keep the approach simple. It is, of course, possible to treat the length of *BD* also as an unknown. The optimal ζ-potential on *BD* (and *B'D'*) is determined to be $1.3\zeta_0$.

The results for the L-turn suggest that the ζ-potential need to be controlled only at positions very close to the turn, e.g. a few channel widths of the turn. Figure 4 suggests that these control strategies are effective in significantly lowering the dispersion.

RESULTS AND DISCUSSION

The two-stage control approach can be applied to minimize dispersion in other electrokinetic geometries e.g. a U-turn. Shown in Figure 8 is a sketch of the control strategy used for a U-turn.

Similar to an L-turn channel, we have assumed that the ζ-potential distribution on *o-a* and *o'-b* is linear and the ζ-potential along *o-o'* and *b-c* is constant. In addition, the length of the second stage control region (line *b-c* and *b'-c'* in Figure 8) is set to be the channel width. Using the algorithm described above, the optimal configuration of the ζ-potential can be found. Figure 9 shows the dispersion of the particles before the control strategy was applied and Figure 10 shows the dispersion of particles after the control strategy was enforced. It can be seen that the dispersion has been lowered significantly with the two-step control strategy.

One important issue behind the control strategies described here is whether one can manipulate the ζ-potential in the way that the optimization algorithm has suggested? Changing the ζ-potential on the channel walls has been difficult in the past, but recently there has been a lot of work done that makes it possible to change the ζ-potential at walls in a desired way. Various techniques such as altering buffer pH, adding buffer additives, coating of channel wall and applying external voltages across the channel wall have been proposed. Of these approaches, coating of channel wall and applying external voltages can be used to change the ζ-potential on the walls locally. Flow control by coating the channel wall has been reported recently **[4]**. Important progress has also been made in controlling the ζ-potential by applying external voltages. The ζ-potential can now be changed by applying low external potentials (a few hundred volts), whereas in the past this required very high external voltages **[6]**.

CONCLUSIONS

In this paper a novel technique is introduced to control the dispersion induced by turns in nano-channel systems. In the proposed technique, ζ-potential on the wall near the turn is controlled to minimize the dispersion, and the geometry of the turn is not altered. An optimization algorithm has been developed to search for the optimal ζ-potential distribution. Our results on dispersion control in an L-turn and U-turn suggest that:

1. The dispersion caused by the presence of a turn can be lowered significantly by locally altering the ζ-potential distribution at the turn.
2. To minimize the dispersion, ζ-potential need to be altered only within a few channel widths near the turn.

Though the discussion is focused on nano-channel systems, the technique can be applied to dispersion control in micro-channel systems. In addition, the motion of particles due to diffusion, which is neglected in this paper, can be accounted for in a straightforward manner. When diffusion is taken into account, typically, a different ζ-potential distribution is necessary to minimize the particle dispersion.

ACKNOWLEDGMENT

This work was supported by a grant from DARPA under agreement number F30602-98-2-0718. Travel support has been generously provided by the Transducer Research Foundation and by the DARPA MEMS and DARPA BioFlips programs.

REFERENCES

1. S.K. Griffiths and R.H. Nilson. "Low-dispersion turns and junctions for microchannel systems", *Anal. Chem.*, 73, 2 (2001).
2. J. Molho, A.Herr and et al, "Optimization of turn geometries for microchip electrophoresis", *Anal Chem.*, 73, 6, (2001).
3. M. Mitchell, R.Qiao and N.Aluru. "Meshless analysis of steady-state electro-osmotic transport", *Journal of Microelectomechanical Systems*, 9 (2000).
4. A.D. Stroock, M.Wech and et al, "Patterning electro-osmotic flow with patterned surface charge", *Phys Rev Lets*, 84, 15 (2000).
5. M.T. Heath. "Scientific computing: an introductory survey", WCB/McGraw-Hill, 1997.
6. N.A. Polson and M.A. Hayes. "Electroosmotic flow control of fluids on capillary electrophoresis microdevice using an applied external voltage", *Anal. Chem.*, 72, 5 (2000).

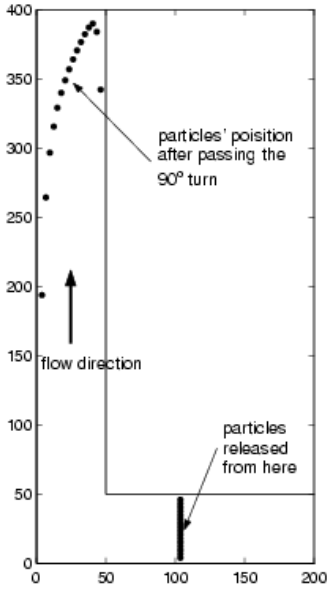

Figure 1. Distribution of particles after passing the 90° turn.

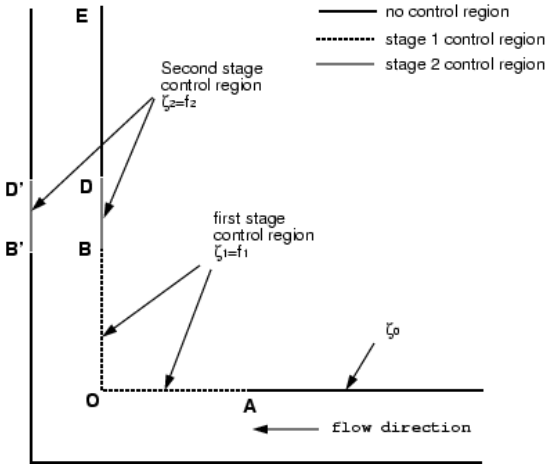

Figure 2. Two-stage control strategy to minimize the particle dispersion in a 90° turn.

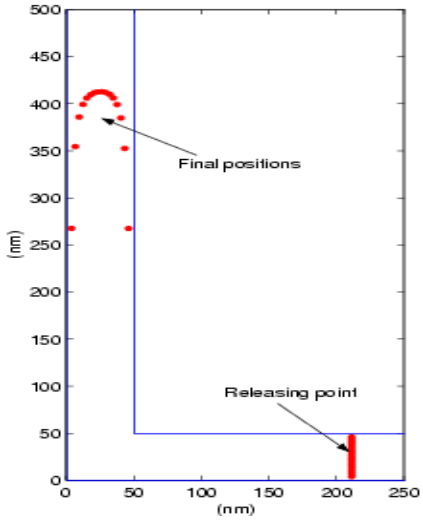

Figure 3. Distribution of particles after passing through the 90° turn. Only first stage control is enforced. Observe that the particle positions are fairly symmetric about the centerline of the channel.

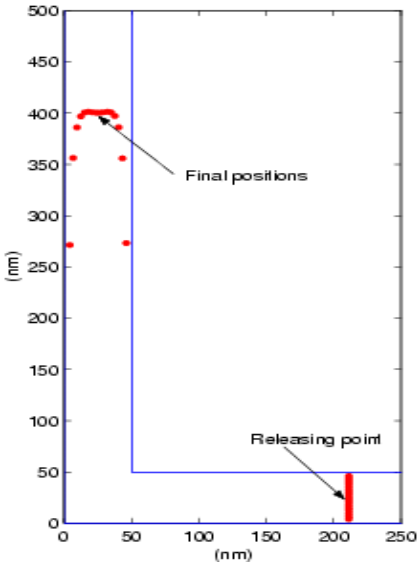

Figure 4. Distribution of particles after passing through the 90° turn. Both first and second stage control are enforced. Observe that the particle dispersion is significantly lowered.

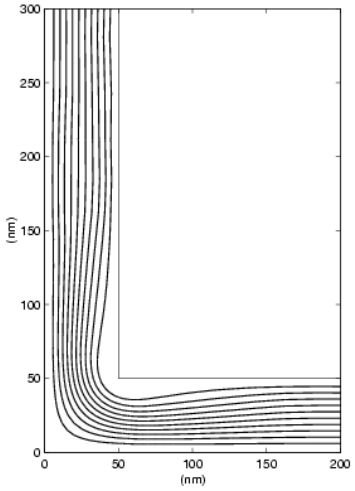

Figure 5. Plot of streamlines when the two-stage control approach is employed for an L-turn.

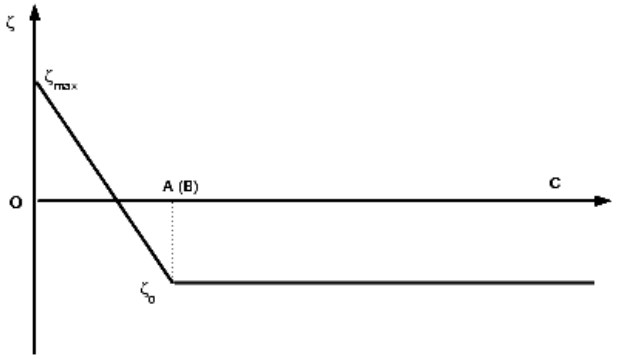

Figure 6. Linear ζ-potential distribution is assumed on OA and OB. Positions of points O, A, B and C are as shown in Figure 2.

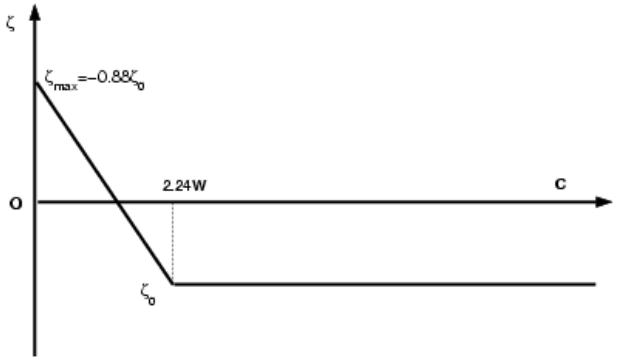

Figure 7. Optimized ζ-potential distribution on patch OA or OB. W is the width of the channel.

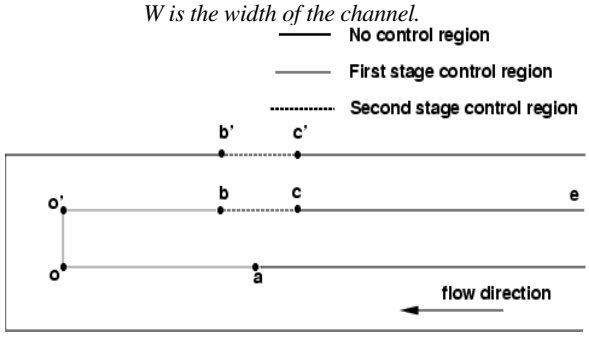

Figure 8. Sketch of a two-stage control strategy to minimize dispersion in a U-turn.

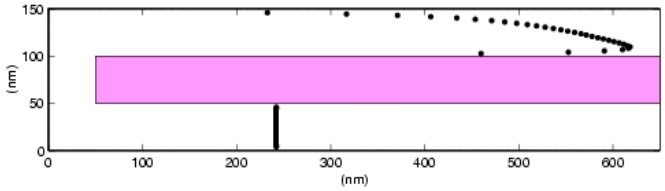

Figure 9. Distribution of particles after passing through a U-turn. No control algorithm was applied.

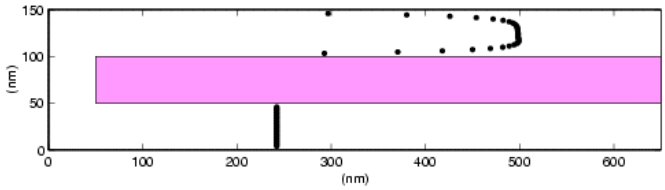

Figure 10. Distribution of particles after passing through a U-turn. A two-step control strategy as described in Figure 8 is applied.

HIGH-RESOLUTION ELECTROMETER WITH MICROMECHANICAL VARIABLE CAPACITOR

Patrick S. Riehl, Karen L. Scott, Richard S. Muller and Roger T. Howe
Berkeley Sensor & Actuator Center, Department of EECS, University of California
Berkeley, CA 94720-1774

ABSTRACT

We have designed, fabricated, and operated an electrometer with a noise-equivalent resolution of 535 electrons rms (86 aC). The electrometer incorporates a silicon resonator that acts as a variable capacitor and is fabricated using a new self-assembly process that demonstrates for the first time the integration of low-noise, low-leakage JFETs with SOI structures. The resolution of the measurements made with the electrometer thus far has been limited to 9500 electrons (1.5 fC) because of a large quiescent charge on the input, generated by JFET gate current. At 1.5 fC, the MEMS electrometer charge resolution is an order of magnitude better than those quoted for the best commercial instruments. Improvements that should lead to higher resolution are proposed.

INTRODUCTION AND THEORY

For over a century, scientists have used electrometers, instruments that measure electric charge, to study a variety of phenomena. Electrometers are used in mass spectrometers, scanning tunneling microscopes, and airborne-particle detectors, to name a few applications.

In 1947, researchers built an electrometer with a resolution of 4 fC (25,000 electrons). **[1]** Although recent research projects have demonstrated charge sensors with subelectron resolution using cryogenics **[2]** or magnetically levitated rotors **[3]**, there has been limited progress in developing practical electrometers for use in instrumentation. (The best commercial electrometer we are aware of is the Keithley 6514, which has a resolution of 10 fC) A fundamental difficulty in making a sensitive, low-frequency, solid-state electrometer is the high level of *1/f* noise associated with a dc measurement. In voltage amplifiers, *1/f* noise can be eliminated using the technique of chopper stabilization, typically implemented using MOS switches. MOS switching is not, however, well suited to electrometry because subthreshold leakage in the off-transistors and switch-charge injection impose a lower limit on the detectable charge value.

The instrument we describe uses the principle of input-capacitance modulation, which was also employed in the "vibrating-reed electrometer" of Palevsky et al. **[1]** To illustrate this technique, consider the basic electrometer circuit of Fig. 1. The charge to be measured, Q, is collected on a variable capacitor, C_V and a parasitic capacitor, C_P. The resulting dc voltage is

$$V = \frac{Q}{C_P + C_V}. \qquad [1]$$

If we let C_V vary sinusoidally, according to

$$C_V = C_0 + \hat{C}\cos\omega t, \qquad [2]$$

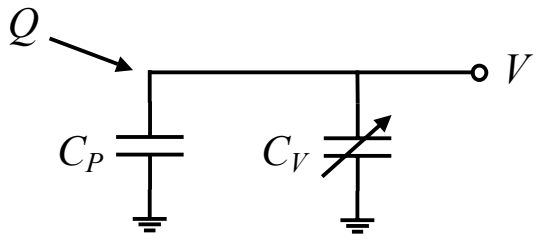

Fig. 1: *Basic input capacitance modulation circuit*

we expect to find a component of V at the modulation frequency ω. By performing a power-series analysis of Eqs. 1 and 2, we find the magnitude of this variation, normalized to the input charge:

$$\frac{\hat{V}}{Q} = \frac{\hat{C}}{(C_0 + C_P)^2}. \qquad [3]$$

Like the dc voltage, the modulated voltage is linearly proportional to input charge. However, the signal-to-noise ratio of the modulated voltage is typically orders-of-magnitude higher because of reduced *1/f* noise. Using synchronous detection at the modulation frequency, we can perform a charge measurement with a lower noise floor. If ω is sufficiently high, the effects of *1/f* noise are negligible.

Equation 3 implies that to obtain maximum signal the electrometer should have a large variable capacitance and small dc capacitances ($C_0 + C_p$). Large parasitic capacitances reduce the signal magnitude severely because of their contribution to the squared term in the denominator. Silicon micromachining allows one to fabricate air-gap variable capacitors with a high relative-capacitance change and a low parasitic capacitance, compared to macroscale devices. Thus, MEMS technology provides the means to build considerably improved electrometers that function according to well-established principles.

FABRICATION

The electrometer requires a technology that combines large capacitance variation, low parasitic capacitance, and low-noise, low-leakage transistors. A two-chip solution in which the variable capacitor and input transistor are located in separate packages performs poorly because of the large parasitic capacitances associated with the packages and interconnects. An integrated process combining CMOS and MEMS provides low parasitic capacitance, but this performance gain is cancelled out to some degree by the poor noise properties of the technology. CMOS transistors are characterized by relatively high *1/f* noise—electrometers invariably use a JFET input stage for this reason.

Our fabrication process includes a fluidic self-assembly step to conductively bond low-noise, low-leakage JFETs to high-aspect-ratio SOI structures. Since the backside of the JFET serves

Travel support has been generously provided by the Transducers Research Foundation and by the DARPA MEMS and DARPA BioFlips programs.

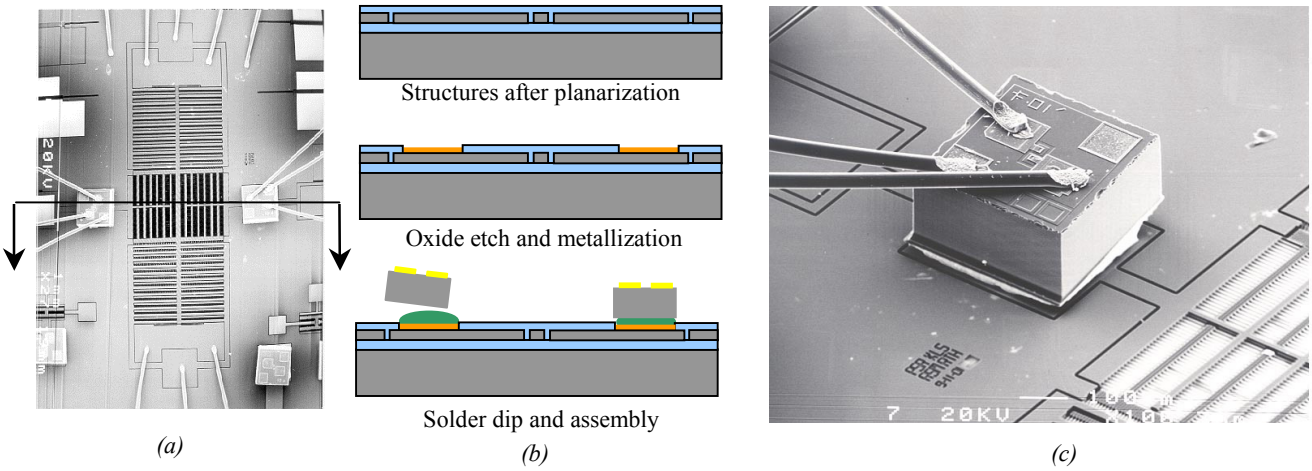

Fig. 2: *Illustrations of the electrometer chip. (a) Scanning electron micrograph of a functional electrometer with indicated line for process-flow cross section. (b) Process-flow cross sections. (c) Assembled and wirebonded JFET on SOI substrate. Wirebonding to the gate of the JFET is not necessary for the operation of the system, but a bond was made here for diagnostic purposes.*

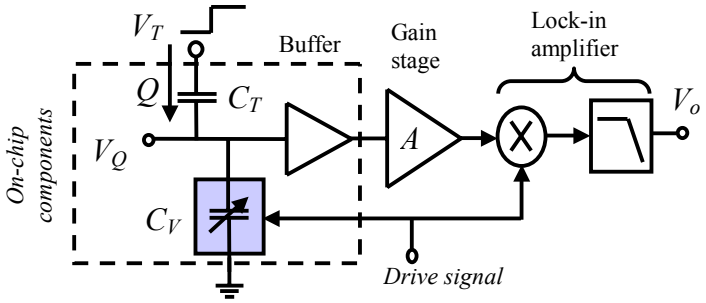

Fig. 3: *Electrometer block diagram.*

as a gate connection, it can be directly connected to a MEMS structure without introducing package parasitics.

The completed device with its corresponding cross section and process flow are shown in Figure 2. The starting SOI wafer has a 50-µm single-crystal silicon layer to be used for micromechanical structures, a 2-µm-thick sacrificial oxide layer, and a 500-µm handle layer. After patterning with 1-µm OCG 825 G-line photoresist, the structural layer was defined using a Surface Technology Systems (STS) deep reactive-ion etcher. **[4]**

Trenches were refilled and the wafer was planarized with PSG, deposited by LPCVD. The phosphorus was driven in and the film densified for 1 hour at 1050 °C. Lift-off, with 9-µm STR 1075 G-line photoresist, was used to define the JFET-gate electrical interconnects. The metallization used was Cr/Ni/Au (10nm/100nm/120nm) with the nickel layer acting as a diffusion barrier between the gold and silicon. The wafer was then covered with 2-µm G-line photoresist and diced. The gold pads were coated with a low-T solder (LMA-117, Small Parts Inc.), consisting of lead, tin, bismuth, cadmium, and indium by immersing the chips in the molten alloy at 70 °C through a DI water and acetic acid interface, pH 3. **[5]** The chips were soaked in concentrated HF for 7 minutes to release the structures. The dice were then rinsed with DI water to remove residual HF and placed into a 70 °C solution of DI water and acetic acid, pH 3, which inhibits oxide formation on the solder. A fluidic self-assembly process developed by Srinivasan **[6]** was used to align and bond the JFETs to the SOI structures. Assembly and self-alignment take place when the gold-plated underside of the JFET comes into contact with the molten alloy on the substrate site. After assembly, the dice were cooled to room temperature, rinsed with DI water, and dried using critical-point drying. Wirebonds were made to the source and drain of the JFETs, as well as to electrodes on the SOI structure. Measured resistances for the solder bonds are less than 5 Ω. The mechanical stability of the solder bonds is sufficient to withstand wirebonding using an ultrasonic wedge bonder (Westbond 7400).

ELECTROMECHANICAL DESIGN

Fig. 3 shows a block diagram of the electrometer system. In this prototype, charge is injected through a test capacitor C_T by applying a step voltage at V_T. The impedance of C_T was measured separately to calibrate the system. The charge accumulates on variable capacitor C_V, implemented by a micromechanical resonator. The resonator is driven by an external signal, which is also used as the reference frequency for the lock-in amplifier. A JFET source follower allows the voltage at V_Q to be buffered off-chip. Following the buffer, a low-noise instrumentation amplifier applies gain. A lock-in amplifier (Stanford Research Systems SRS850) performs the synchronous detection as well as storing and displaying the data. Only the input capacitor, the variable capacitor and the input transistor of the buffer are included on-chip in this implementation.

Resonator Design

The variable capacitor was implemented using an electrostatically driven lateral resonator in the SOI layer. The main drawback of this implementation is the possibility of coupling of the drive signal into the sense circuitry. Driving the structure in ambient air requires ac voltages of a few volts. Since the charges we wish to measure may only generate microvolts on the sense capacitor, it is necessary to take care to prevent any coupling from taking place. We use several methods to reduce this feedthrough, including shielding, differential drive and sense, and harmonic sensing.

Harmonic sensing refers to the technique of making the charge measurement at a harmonic of the drive frequency, rather than at the drive frequency itself. Since we need only sense in a narrow bandwidth around the sense frequency, the feedthrough at the drive frequency can be rejected by filtering. This technique has been used in an electrostatic voltmeter. **[7]** We devised a geometry of comb fingers that generates a sense voltage at twice

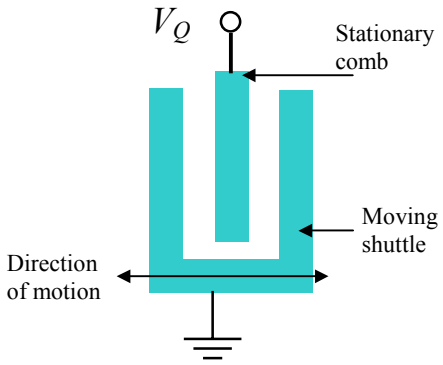

Fig. 4: *Balanced transverse comb*

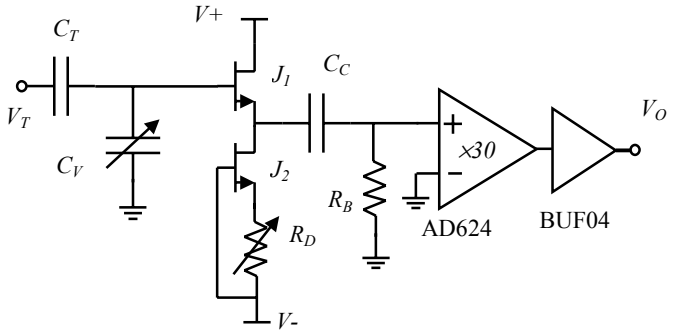

Fig. 5: *Electrometer circuit schematic*

the frequency of motion of the structure, the balanced transverse comb arrangement shown in Fig. 4. Due to the nonlinearity of the two opposing parallel-plate capacitors, each cycle of motion of the resonator generates two maxima and two minima of C_V. The resulting voltage at V_Q contains a component at twice the motional frequency when a charge is applied to C_V.

An overhead SEM of the resonator is shown in Fig. 2(a). We apply antisymmetric ac waveforms to the two opposing drive electrodes. Due to the symmetry of the structure, the effect of these two signals cancels out at the charge nodes.

Circuit design

Fig. 5 shows the circuit schematic for the electrometer. Table 1 gives the component values for the circuit. Although the system was designed with the option for differential circuits, the effectiveness of our other feedthrough-rejection mechanisms allowed us to use single-ended circuits for the measurements in the following section.

The source-follower circuit uses two JFETs (InterFet part#2N4117), an on-chip input device (*J1*) and an off-chip current source (*J2*). The output of the buffer is ac-coupled to the instrumentation amplifier to protect it from out-of-range voltages. The instrumentation amplifier is configured for a gain of 30. Its output is connected to an analog buffer to drive external loads. All of the components described are enclosed in a grounded metal box with BNC feedthroughs for critical signals.

EXPERIMENTAL RESULTS

The following methodology was used to make charge measurements using the prototype electrometer.

Using a dc potential of 15 V on both drive electrodes added to antisymmetric 5 Vp-p ac waveforms, we are able to drive the resonator with an amplitude of 2.7 µm, half of the gap spacing. The resonator has a measured resonant frequency of 2.6 kHz and a quality factor of 0.75. (Mechanical measurements were taken using the computer microvision system. **[8]**) Since the system is overdamped, it is advantageous to drive at a frequency below resonance. A drive frequency of 700 Hz was used.

Component	Value
C_T	156 fF
C_V	9 pF + 0.42 pF×cosωt
R_D	0-10 kΩ, 5 kΩ nom.
C_C	18 nF
R_B	22 kΩ
$V+/V-$	+6V/-6V

Table 1: *Electrometer circuit component values*

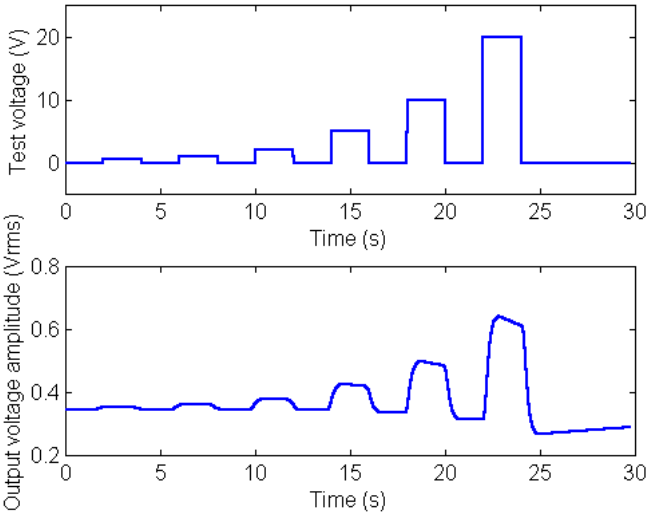

Figure 6: *Step-voltage series applied to test capacitor (top) with corresponding lock-in output trace (bottom).*

A known quantity of charge was injected onto the input by applying a step voltage on the input capacitor using a programmable voltage source (Keithley 2400 Sourcemeter). The output of the system was monitored using the lock-in amplifier. The signal at twice the drive frequency (1400 Hz) was selected. The raw data were analyzed in MATLAB to determine the step height ΔV_0 associated with each input charge ΔQ. An example data trace is shown in Fig. 6. After a positive V_T step, the input charge decays exponentially toward the equilibrium (starting) value with a time constant of roughly 15 s, hence the apparent shift in baseline signal when the opposite step voltage is applied.

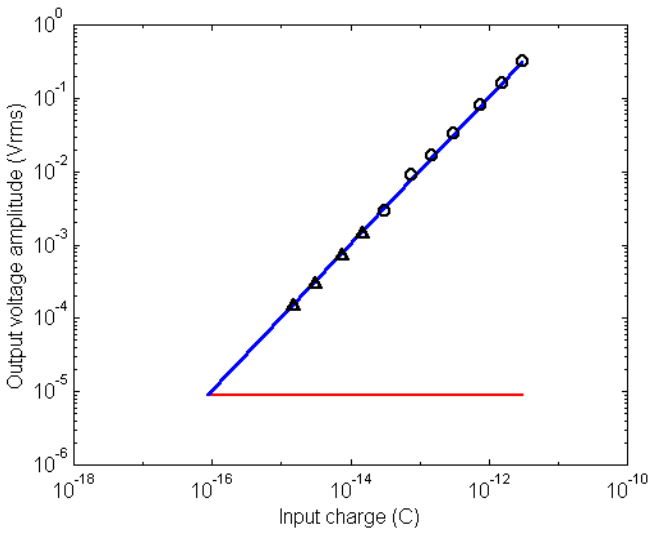

Figure 7: *Measured data from the electrometer with linear fit and noise floor in a 3.1 Hz bandwidth.*

A range of charge measurements is plotted in Fig. 7. The smallest charge measured was 1.5 fC (9500 electrons) and the largest was 3 pC (19,000,000 electrons). The circles and triangles represent measurements taken using different lock-in-amplifier settings. The series represented by circles used a lock-in bandwidth of 1 Hz and a full-scale voltage of 1V. The series represented by triangles used a 3.1 Hz bandwidth and 50 mV full-scale. The maximum relative error of the entire series with respect to a linear fit is less than 15%.

Also plotted on Fig. 7 is the noise floor of the lower-range measurement, which was determined using a dynamic signal analyzer, and confirmed by observing the lock-in amplifier trace with no drive voltage applied. The input-equivalent voltage-noise density is 166 nV/√Hz. This corresponds to an input-equivalent charge of 86 aC (535 electrons) in the 3.1 Hz lock-in bandwidth.

The dominant limitation on the present system is that, in equilibrium, a quiescent charge of 4.5 pC is present on the input node. This charge is the result of the gate-leakage current of the JFET, which balances the leakage current to ground at an input voltage of 0.5 V. The presence of this charge generates a quiescent signal of 0.35 mVrms at the system output. This signal limits the gain we are able to use in the instrumentation amplifier and the lock-in amplifier. As a result, because the data-acquisition system has a limited dynamic range, we are not able to measure charges on the order of the noise floor. Data series 2 (triangles) was taken by initially applying a large negative pulse to V_T to clear the quiescent charge. We were then able to make small-charge measurements using a high-gain setting before the input charge returned to equilibrium. The leakage rate prevented the accurate measurement of any smaller charges.

In addition to the dc component of charge leakage, there is a random component. The rms random leakage current in a 1-minute measurement was 20 fA. The majority of this noise is at frequencies lower than 1 Hz.

The feedthrough signal at the sense frequency is less than 13 μV at the output. This signal is equivalent to a constant 120 aC (752 electrons) at the input. We measured this voltage when applying zero dc bias to the resonator, so that in theory no motion would occur. It is not clear whether the observed signal is, in fact, due to feedthrough, or due to motion of the structure because of a slight force imbalance between the opposing drive combs. In either case, feedthrough is not a limiting factor on sensitivity in the present measurement range.

CONCLUSIONS

The electrometer reported here has a higher measured resolution than that of the best available commercial instrument. Moreover, our noise analysis indicates that the measured performance can be improved. The present system should be capable of resolving 20 electrons in a 1 Hz bandwidth if only electronic thermal noise sources were present. In order to achieve this performance, we will have to identify and eliminate extraneous noise sources and solve the leakage problem. We believe that the quiescent charge can be cancelled using another JFET connected so as to apply an equal and opposite leakage current. Differential operation should also help with the quiescent-charge problem, as well as reject any common-mode feedthrough signals. We have in hand an electrometer fabricated in an integrated CMOS/MEMS process that addresses these issues. Tests are underway to determine the sensitivity of this system.

ACKNOWLEDGEMENTS

Thanks to Ron Wilson (UCB) for SEM work, Lixia Zhou (UCB) for a critical donation of materials, and Dr. Stephen Fuerstenau (JPL) and Dr. Norm Madden (LBNL) for the initial inspiration for this project, and subsequent consultations.

REFERENCES

1. H. Palevsky, R. Swank, and R. Grenchik, "Design of Dynamic Condenser Electrometers", *Review of Scientific Instruments*, *18*, 298 (1947).

2. A. N. Cleland and M. L. Roukes, "A nanometer-scale mechanical electrometer", *Nature*, *392*, 160 (1998).

3. J. C. Price, W. Innes, S. Klein, and M. Perl. "Rotor electrometer: New instrument for bulk matter quark search experiments", *Rev. Sci. Inst.*, *57*, 2691, (1986).

4. M. Madou. *Fundamentals of Microfabrication*. CRC Press, Boca Raton, FL, (1997).

5. U. Srinivasan, "Fluidic Microassembly Using Patterned Self-Assembled Monolayers and Capillary Forces", PhD Dissertation, University of California, Berkeley, (2001).

6. U. Srinivasan, D. Liepmann, R.T. Howe, "Microstructure to substrate self-assembly using capillary forces", Journal of Microelectromechanical Systems, *10-1*, 17-24 (2001).

7. D. P. Loconto and R. S. Muller, "High-sensitivity micromechanical electrostatic voltmeter", Proceedings of the 7th International Conference on MEMS, Yokohama (1993).

8. D. M. Freeman, A. J. Aranyosi, M. J. Gordon, and S. S. Hong, "Multidimenional Motion Analysis of MEMS Using Computer Microvision," *Tech. Dig. Solid-State Sensor and Actuator Workshop*, Hilton Head, SC, Transducers Research Foundation, Cleveland, 150-155 (1998).

INTEGRATION OF "ON-CHIP" ELECTROCHEMICAL DETECTION IN A MICROFABRICATED CAPILLARY ELECTROPHORESIS DEVICE

Thomas J. Roussel, Jr[1]. and Robert S. Keynton
Department of Mechanical Engineering, University of Louisville
Louisville, KY 40292

Mark M. Crain, Vijay Bathlagundu, Douglas J. Jackson, John A. Conklin, Rekha Pai, John F. Naber, and Kevin M. Walsh
Department of Electrical and Computer Engineering, University of Louisville
Louisville, KY 40292

Jayadeep Gullapalli and Richard P. Baldwin
Department of Chemistry, University of Louisville
Louisville, KY 40292

ABSTRACT

The purpose of this effort has been to develop a self-contained, transportable capillary electrophoresis (CE) with electrochemical (EC) detection analysis system, which contains all electrodes "on-chip" and employs specially made, miniaturized CE and EC supporting electronics. A novel fabrication process that produced recessed platinum electrodes was developed to form the CE/EC device from two patterned ultra-flat glass substrates. The electrodes in the bottom substrate were formed by a self-aligned etch and deposition technique using a photholithographic lift-off process. The top substrate was etched to form the microchannels (20 µm deep x 50 µm wide [avg]) and thermally bonded to the bottom substrate. The CE/EC experiments were performed using 0.02M phosphate buffer (pH 6) and a buffer/analyte solution (2.2 mM dopamine, 2.3 mM catechol) with an applied voltage of 250V, which was delivered by a custom electronics unit interfaced to a laptop computer equipped with data acquisition software. Detection limits (S/N = 3) were found to be 4.3 µM for dopamine and 4.4 µM for catechol. A linear response was observed up to 2200 µM and 2300 µM for dopamine and catechol, respectively. Overall, the analytical performance of our CE/EC device is comparable to previously reported hybrid lab-on-a-chip devices with external CE and/or EC electrodes.

INTRODUCTION

Lab-on-a-chip detection schemes have most often utilized laser induced fluorescence (LIF) delivered in an off-chip format where the detection system itself is significantly larger than the chip. Electrochemical (EC) detection is more ideally suited to an on-chip format as demonstrated by an increasing number of capillary electrophoresis (CE) paired with EC detection applications for microchip devices [1-11]. However, in virtually all cases, both the EC detection electrodes crucial to sensitivity and selectivity and the CE driving electrodes have been conventional in size and design, consisting of manually positioned wire electrodes inserted into the chip. Our lab-on-a-chip efforts have been directed toward the development of self-contained and transportable CE/EC analysis systems that (a) incorporate all the required electrodes directly on the chip (Figure 1) and (b) utilize miniaturized CE and EC supporting electronics that are designed especially for the purpose of supporting our microchip platforms.

FABRICATION

A novel fabrication process that yielded recessed platinum electrodes was developed to form the CE/EC device from two photolithographically patterned ultra-flat glass substrates (pre-coated Soda Lime glass photomasks - Cr layer and AZ1518 photoresist). The electrodes on the bottom substrate were formed by creating 0.3 µm recessions in the glass, using the existing chrome/photoresist layer as a masking layer with a self-aligned etch in a 6:1 BOE solution at 25 °C for 30 seconds. This step was

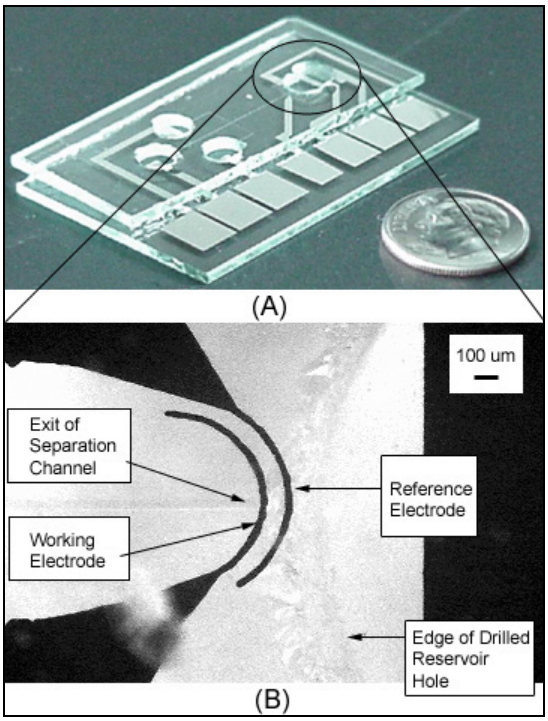

Figure 1. *Photographs of (A) entire CE/EC microchip and (B) magnified (30x) top view of the EC cell and electrodes.*

[1] **"*Travel support has been generously provided by the Transducers Research Foundation and by the DARPA MEMS and DARPA BioFlips programs.*"**

followed by sputter deposition of Ti as an adhesion layer (t = 10 nm) followed by Platinum (t = 300nm). The final electrode design was realized with a photolithographic liftoff process. The microchannels (20 µm deep x 50 µm wide [average]) were created with wet chemical etching using a 6:1 BOE solution at room temperature for 30 minutes. The capillary system design consisted of a "balanced-cross", in that each arm was 1 cm in length with two arms bent at 90° to facilitate placement on the 3.5 cm x 5.0 cm final substrate. Subsequently, thermal fusion bonding was used to mate the two substrates and hermetically seal the capillary system. A 3°C per minute ramp up to and down from the bonding temperature of 620°C was critical to ensure that thermal stresses introduced into the glass substrates were not large enough to fracture either part. The slight recession of the electrodes beneath the surface of the glass dramatically affected the yield of the fabrication process by allowing a more conformal bond between the two glass surfaces. This step also aids in electrically isolating the electrode traces from one another. The strategic design and placement of the EC detection electrodes contributed strongly to the microchip performance.

EXPERIMENTAL DETAILS

EC and CE experiments were performed with 0.020M pH 6.0 phosphate buffer and a buffer/analyte solution sample (2.2 mM dopamine, 2.3 mM catechol; Figure 2). An applied separation voltage of 250 V was delivered by a custom-made miniaturized electronics unit interfaced to a laptop computer equipped with both a control interface for the microchip system as well as data acquisition software for collecting EC detection data [12-14]. Amperometric EC detection was conducted with a three-electrode potentiostat included in the electronics designed for this system, which was powered by a single 9V battery [14-15]. The sensitivity of the EC detection system was performed via testing with known concentrations of the samples described previously; then each sample was diluted to a lesser concentration and tested again. This was repeated until the sample could no longer be detected by the system.

Short-term (Figure 3) and long-term (Figure 4) repeatability and stability studies of our CE/EC devices were conducted. The short-term studies involved repeating the same set of experiments for an extended period of time, while holding all controllable factors (temperature, applied injection and separation voltages, EC potential voltage, etc.) constant. The volumes of solutions in the capillary-end reservoirs were maintained at a constant level because these small volumes (~ 150 µl) tend to evaporate fast, and evaporation could affect the repeatability data. In all cases, a series of experiments did not last long enough to deplete any reservoir of either buffer solution or sample. Additionally, electrolysis of the buffer solution, which usually leads to bubble generation and, in turn, experimental failure, was not observed. The long-term studies examined experimental data spread over days and weeks, comparing results from situations where the experimental factors were the same or similar.

RESULTS

The detection limit (S/N = 3) was found to be 4.3 µM and 4.4 µM for dopamine and catechol, respectively, at an applied potential of +0.75V (vs. Pt). Linear responses up to 2200 µM (r-squared = 0.9991) and 2300 µM (r-squared = 0.9959) were observed for both dopamine and catechol, respectively. These

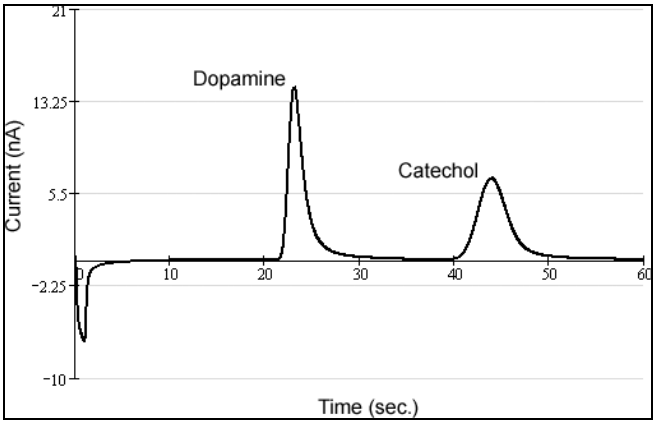

Figure 2. *Sample electropherogram obtained for dopamine (2.2 mM) and catechol (2.3 mM) in pH 6 phosphate buffer for "optimum" microchip configuration. Conditions: CE separation voltage = 250 V; EC potential =+0.75 V vs. Pt reference electrode.*

findings are comparable to other studies that utilized non-integrated electrodes [6, 10, 11]. As shown in Figure 3, the repeatability study showed nearly identical peak heights between successive experiments. These experiments were conducted without cleaning the system between successive injection/separations. The results suggest that the system injects a very precise and repeatable volume of sample (~ 125 pL). Additionally, any buildup of unreacted analyte in the detection reservoir can be neglected, at least over a handful of experiments, in that the unused sample in the detection reservoir did not appear to affect the results. The long-term stability tests demonstrated similar migration times and peak currents for dopamine throughout the time period investigated (8 months of studies) and the microchips included in the study show no signs of deterioration. Figure 4 represents a typical collection of results spanning roughly sixty days. In these experiments, new solutions of buffer and sample, with identical composition, were used. The plots indicate that the repeatability of the EC detection is consistent and highly predictable.

Several design characteristics were found to significantly affect the analytical performance of the on-chip EC electrodes: (1) the distance between the EC working electrode and the CE channel exit, which was directly responsible for the sensitivity and response of the EC detection circuitry; (2) the formation of a "shelf" restricting the height of the detection reservoir in the vicinity of the working electrode, which minimized the initial diffusion of the analyte plug upon exiting the separation channel; and, (3) the material and position of the reference electrode, which helps to accurately control the potential applied to the working electrode The peak current observed for dopamine was plotted as a function of the applied potential to generate a series of "hydrodynamic voltammograms" (Figure 5) for comparison with cyclic voltammetry data. These plots illustrate the EC detector response to a range of applied oxidation potentials and indicate optimal operating potential. In three-electrode potentiostats, the output of the working electrode will exhibit these unique 's'-curves and are traditionally used to establish an optimal oxidation potential for the EC detection system with detection electrodes of a particular chemical makeup. These curves, however, are also

influenced by the chemical makeup of the reference electrode. To explore this effect, the microfabricated Pt reference electrode was converted in situ to an Ag/AgCl electrode to evaluate electrode material effects. As is shown in the changes between curves A and B in Figure 5, there is a noticeable and expected shift in the 's'-curve after the in-situ modification, indicating that the modification to Ag/AgCl was successful.

CONCLUSIONS

For the first time, traditional photolithographic processes have been used to incorporate both CE high voltage and EC detection electrodes directly onto the microchip platform. The analytical performance of the microfabricated devices, in both the hydrodynamic voltammogram results and the sensitivity of the system, is comparable to previously reported hybrid lab-on-a-chip devices with external CE and/or EC electrodes. The increasing demand for on-chip micro-systems to perform multiple analyses from a single sample injection has been corroborated by the short-term results presented, enhancing the ability to do quantitative analyses with an ever-decreasing quantity of original sample. The long-term repeatability results are quite surprising, considering that some devices have undergone several hundreds of experiments and are still producing nearly identical results.

ACKNOWLEDGEMENTS

This work was supported by the National Science Foundation XYZ-on-a-chip program under grant # CTS-9980831 and by the Department of Energy under grant # 46411101095.

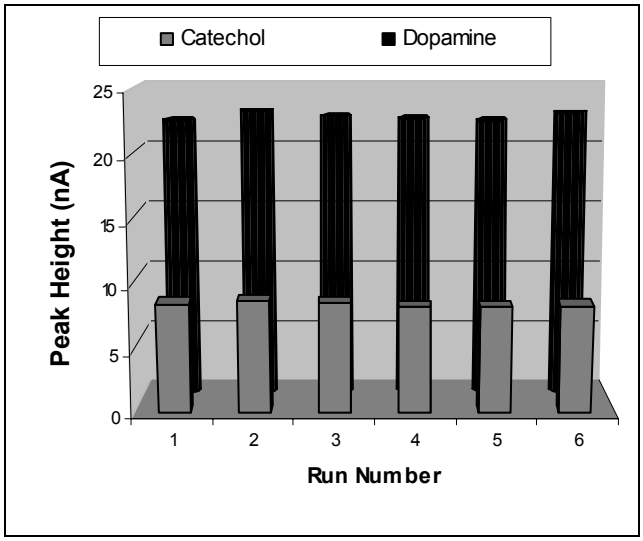

Figure 3. *Dopamine and catechol peak currents for a series of 6 sequential injections. Conditions as in Figure 2.*

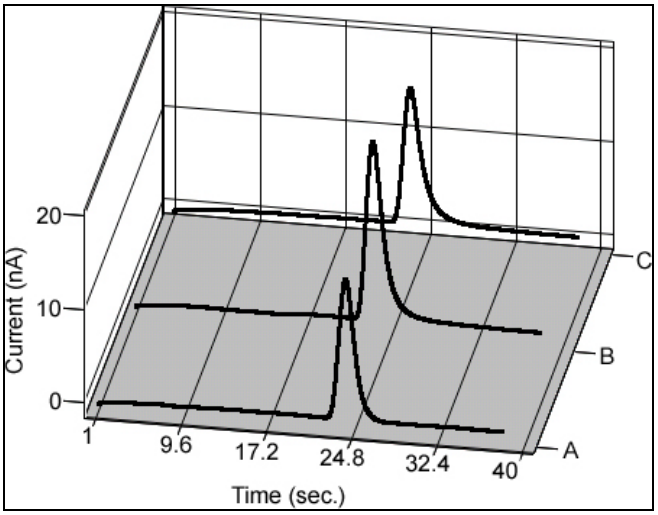

Figure 4. *Electropherograms observed for dopamine (2.2 mM) with same microchip device on (A) 7/18/01, (B) 9/18/01, and (C) 9/26/01. Conditions as in Figure 2.*

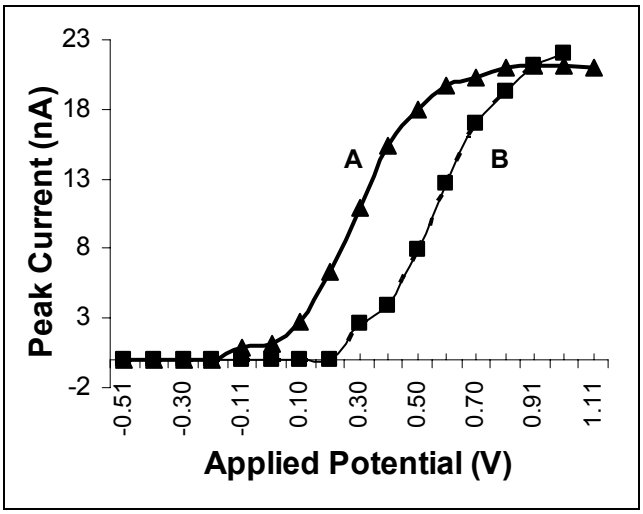

Figure 5. *Two hydrodynamic voltammograms of (A) dopamine with Pt pseudo-reference electrode, and (B) dopamine with in-situ modified Ag/AgCl reference electrode.*

REFERENCES

1. J. Wang, B. Tian, and E. Sahlin, "Integrated Electrophoresis Chips/Amperometric Detection with Sputtered Gold Working Electrodes", *Analytical Chemistry,* 1999, *71*(17), pp. 3901-3904.

2. J. Wang, B. Tian, and E. Sahlin, "Micromachined Electrophoresis Chips with Thick-Film Electrochemical Detectors", *Analytical Chemistry,* 1999, *71*(23), pp. 5436-5440.

3. J. Wang, M. P. Chatrathi, and B. Tian, "Microseparation Chips for Performing Multienzymatic Dehydrogenase/Oxidase Assays: Simultaneous Electrochemical Measurement of Ethanol and Glucose", *Analytical Chemistry*, 2001, *73(6)*, pp. 1296-1300.

4. J. Wang, M. P. Chatrathi, A. Mulchandani and W. Chen, "Capillary Electrophoresis Microchips for Separation and Detection of Organophosphate Nerve Agents", *Analytical Chemistry*, 2001, *73(8)*, pp. 1804-1808.

5. C. S. Henry, M. Zhong, S. M. Lunte, M. Kim, H. Bau, and J. J. Santiago, "Ceramic Microchips for Capillary Electrophoresis-Electrochemistry", *Anal. Commun.,* 1999, *36*, pp. 305-307.

6. R. S. Martin, A. J. Gawron, S. M. Lunte, and C. S. Henry, "Dual-Electrode Electrochemical Detection for Poly(dimethylsiloxane)-Fabricated Capillary Electrophoresis Microchips", *Analytical Chemistry*, 2000, *72(14)*, pp. 3196-3202.

7. A. J. Gawron, R. S. Martin, and S. M. Lunte, "Fabrication And Evaluation of a Carbon-Based Dual-Electrode Detector for Poly(dimethylsiloxane) Electrophoresis Chips", *Electrophoresis*, 2001, *22*, pp. 242-248.

8. J. S. Rossier, M. A. Roberts, R. Ferrigno, and H. H. Girault, "Electrochemical Detection in Polymer Microchannels", *Analytical Chemistry*, 1999, *71(19)*, pp. 4294-4299.

9. J. S. Rossier, A. Schwarz, F. Reymond, R. Ferrigno, F. Bianchi, and H. H. Girault, "Microchannel Networks for Electrophoretic Separations", *Electrophoresis*, 1999, *20*, pp. 727-731.

10. J. S. Rossier, R. Ferrigno, and H. H. Girault, "Electrophoresis with Electrochemical Detection in a Polymer Microdevice", *Journal of Electroanalytical Chemistry*, 2000, *492 (1)*, pp. 15 - 22.

11. M. A. Schwarz, B. Galliker, K. Fluri, T. Kappes, and P. C. Hauser, "A Two-Electrode Configuration for Simplified Amperometric Detection in a Microfabricated Electrophoretic Separation Device", *Analyst*, 2001, *126*, pp. 147-151.

12. D. J. Jackson, J. F. Naber, T. J. Roussel, Jr., V. Bathlagundu, M. M. Crain, R. Pai, J. A. Conklin, R. P. Baldwin, R. S. Keynton, and K. M. Walsh, manuscript in preparation for Analytical Chemistry.

13. D. Jackson, J. Naber, R. Baldwin, K. Walsh, R. Keynton, M. Crain, T. Roussel, and M. Diaconu, "A Compact Battery Powered High Voltage Power Supply for Capillary Electrophoresis Using Microchip Capillaries", *Proceedings of the Pittsburgh Conference on Analytical Chemistry and Applied Spectroscopy (PITTCON 2001)*, #116, 2001.

14. V. Bathlagundu, D. Jackson, J. Naber, R. Baldwin, K. Walsh, R. Keynton, M. Crain, T. Roussel, M. Diaconu, "A Portable Battery Powered Electrochemical Detection Circuit With a 1000 Volt CE Power Supply for Microchip Capillaries", *Proceedings of the Fourteenth Biennial University/ Government/ Industry Microelectronics Symposium*, pp. 197-200, 2001.

15. D. Jackson, J. Naber, R. Baldwin, K. Walsh, R. Keynton, M. Crain, T. Roussel, and M. Diaconu, "A Portable Battery Powered Electrochemical Detection Circuit", *Proceedings of the Pittsburgh Conference on Analytical Chemistry and Applied Spectroscopy (PITTCON 2001)*, #1345, 2001.

PARALLEL-PLATE DRIVEN OSCILLATIONS AND RESONANT PULL-IN

Joseph I. Seeger and Bernhard E. Boser
Berkeley Sensor & Actuator Center
University of California, Berkeley, CA 94720-1774

ABSTRACT

This work characterizes parallel-plate actuators for oscillations near the mechanical resonant frequency and amplitudes comparable to the actuator gap. Specifically, we show that at resonance, the structure can move beyond the well-known pull-in-limit but is instead limited to 56% of the gap by "resonant pull-in." Above the resonant frequency, the structure is not limited by pull-in and can theoretically oscillate across the entire gap. We develop a describing function model, which includes an amplitude-dependent model for electrostatic spring tuning, to predict the steady-state frequency response. These results are verified experimentally.

INTRODUCTION

Many MEMS applications, such as gyroscopes, scanning mirrors, and filters, are based on vibrating mechanical structures. In many designs, there is a specific vibration frequency that is desired. However, in order to maximize the vibration amplitude, the mechanical structure must be vibrated at its resonant frequency. Because the resonant frequency varies due to fabrication tolerances, temperature, and age, it is desirable to tune the resonant frequency to match the desired frequency. Several techniques have been presented for tuning the resonant frequency of a mechanical structure, including thermal [**1**] and electrostatic comb designs [**2,3,4**].

Among those approaches, parallel-plate, electrostatic electrodes have been most widely used for frequency tuning as well as actuation. Because they are nonlinear, parallel-plate actuators generally are used in applications where the motion is much smaller than the gap. For example, it is well known that, at low frequencies, parallel-plate actuators are limited to deflections less than one-third of the gap before the actuator will snap [**5**]. We are interested in using parallel-plate electrodes to vibrate a gyroscope proof-mass (Figure 1) at its resonant frequency to achieve large-amplitude motion while tuning the resonant frequency to reduce drift. This work characterizes parallel-plate actuators for oscillations near the mechanical resonant frequency and amplitudes comparable to the gap. Specifically, we show that at resonance, the structure can move beyond the well-known pull-in-limit but is instead limited by "resonant pull-in." Above the resonant frequency, the structure can move more than the resonant pull-in limit. We develop a describing-function model, which includes an amplitude-dependent model for electrostatic spring tuning, to predict the steady-state frequency response.

DEVICE MODEL

A parallel-plate driven structure is shown in Figure 1. It is modeled by a lumped mass, m, supported by a suspension with spring constant, k, and subject to viscous damping, b. The natural resonant frequency of the structure is defined as $\omega_n=\sqrt{(k/m)}$, and the quality factor is defined as $Q=m\omega_n/b$.

Figure 2 shows a schematic of the actuator including the digital drive electronics. The electrodes on either side of the structure are switched between ground and voltage V_d. Using the parallel-plate approximation, the net electrostatic force applied to the proof-mass is

$$F_{el}(x,D)\approx\begin{cases}+\dfrac{C_oV_d^2}{2d}\dfrac{1}{(1-x/d)^2}, & (D=1)\\ -\dfrac{C_oV_2^2}{2d}\dfrac{1}{(1+x/d)^2}, & (D=0)\end{cases}, \qquad (1)$$

where x is the proof-mass displacement, d is the nominal size of the gap, $C_0=\varepsilon A/d$ is the nominal parallel-plate capacitance of the actuator, A is the electrode area, ε is the permittivity of the fluid (air in our case) in the gap, and D is the digital signal that selects which electrode is activated.

RESONANT PULL-IN

At low excitation frequencies, pull-in occurs if the negative spring constant, due to the parallel-plate actuator, exceeds the mechanical spring constant. This occurs if the drive voltage exceeds the pull-in voltage. For drive voltages less than the pull-in voltage, the resonant frequency is lowered by the electrostatic spring but is not reduced to zero, as in the case of pull-in. Nevertheless, at resonance, there can be an instability, called

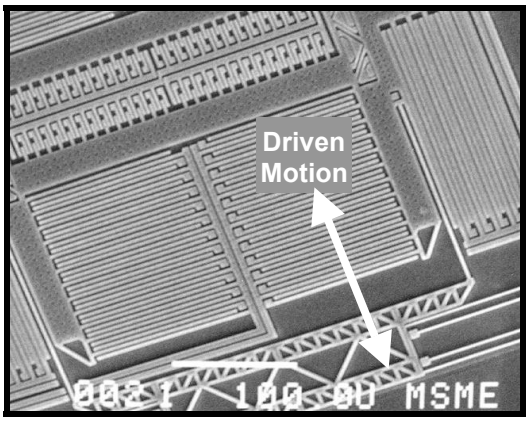

Figure 1. *Parallel-plate driven, gyroscope proof-mass*

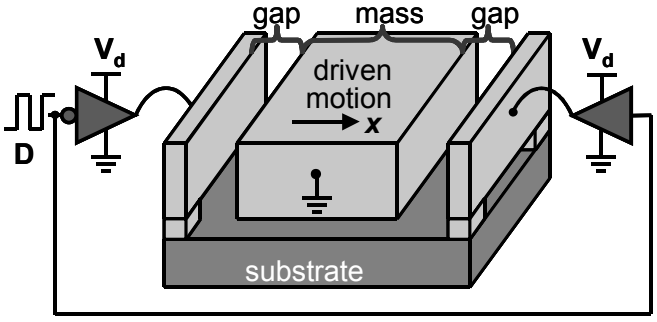

Figure 2. *Actuator schematic*

Travel support has been generously provided by the Transducers Research Foundation and by the DARPA MEMS and DARPA BioFlips programs.

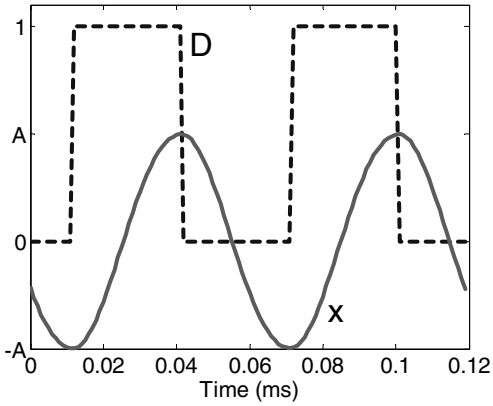

Figure 3. *Drive voltage and position waveforms at resonance*

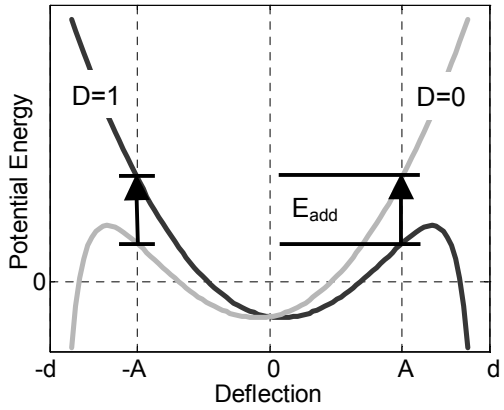

Figure 4. *Potential energy vs. deflection*

resonant pull-in, that causes the structure amplitude to build up and then snap against one of the fixed electrodes. This instability depends on the energy provided by the parallel-plate actuator.

Figure 3 illustrates voltage and position waveforms at resonance. For half of the oscillation period, the drive voltage is constant. During this time, the potential energy can be written as the combination of spring potential energy and electrostatic potential energy:

$$PE(x,D)=\frac{1}{2}kx^2-\begin{cases}\dfrac{C_0V_d^2}{2}\dfrac{1}{(1-x/d)}, & (D=1)\\ \dfrac{C_0V_d^2}{2}\dfrac{1}{(1+x/d)}, & (D=0)\end{cases} \qquad (2)$$

This function is plotted in Figure 4. At resonance, the drive signal, D, switches at the peak deflection, $x=\pm A$. When D switches, the potential energy of the system increases. The change in potential energy represents the energy that is provided by the electrostatic actuator in one half-cycle:

$$E_{add}(A)=PE(A,0)-PE(A,1)=C_0V_d^2\frac{A/d}{1-(A/d)^2}. \qquad (3)$$

As the structure moves, energy is removed by the mechanical damping and by the electrical resistance in the wiring and structure. The electrical resistance, R, can be ignored if it is much smaller than the equivalent resistance of the damper:

$$R << b/(C_0'V_d)^2, \qquad (4)$$

where C_0' is dC/dx evaluated at $x=0$. In most designs, the wiring and structure resistance is significantly smaller than the equivalent

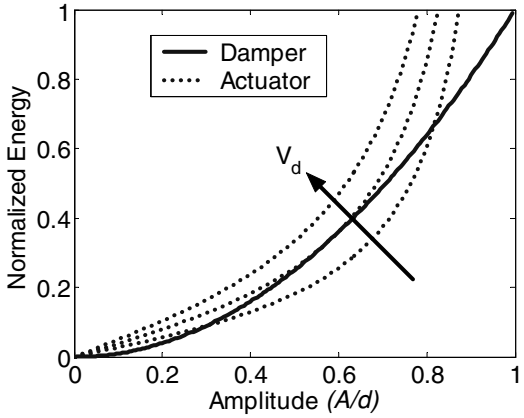

Figure 5. *Energy added and energy removed vs. amplitude*

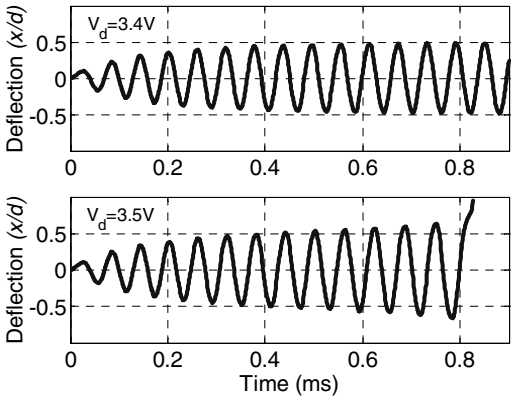

Figure 6. *Transient simulations. The lower plot illustrates resonant pull-in and the upper plot is stable.*

resistance. Thus, it can be assumed that the energy lost is due to the mechanical damping. At resonance, the motion of the structure will be approximately sinusoidal with amplitude A, and the energy dissipated by the damper in one half-cycle will be

$$E_{lost}=\frac{\pi}{2}\omega_{tun}bA^2=\frac{\pi}{2}\frac{k\omega_{tun}}{Q\omega_n}A^2, \qquad (5)$$

where ω_{tun} is the tuned resonant frequency. The tuned resonant frequency, ω_{tun}, is lower than the natural resonant frequency, ω_n, because of the negative-spring effect of the parallel-plate actuator.

The energy added, Eq. (3), for three different voltage sources and the energy removed by a damper, Eq. (5), are illustrated in Figure 5. Amplitudes where the energy added equals the energy lost correspond to steady-state oscillations. For low voltages, there are two non-zero intersections. The largest amplitude solution is unstable. A slight increase in amplitude causes more energy to be added than is dissipated, which in turn causes the amplitude to increase further. The other solution is stable; a slight increase in amplitude causes more energy to be dissipated than is provided. For voltages greater than V_{rpi}, there are no non-zero solutions. In this case, the oscillation amplitude builds up until the structure snaps against one of the electrodes. Figure 6 shows simulation results of resonant excitation for $V_d < V_{rpi}$ and for $V_d > V_{rpi}$.

The steady-state oscillation amplitude can be found from the condition, $E_{add}=E_{lost}$. Thus,

$$\frac{A}{d}\left(1-\left(\frac{A}{d}\right)^2\right)=\frac{2C_0V_d^2}{\pi kd^2}\frac{Q\omega_n}{\omega_{tun}} \qquad (6)$$

As will be shown in the next section, ω_{tun} has a slight dependence on A. However, if ω_{tun} is approximated as constant, it can be shown that the maximum stable amplitude, at the tuned resonant frequency, is

$$A_{\max} \approx d/\sqrt{3} \approx .56d\,. \tag{7}$$

This amplitude occurs at the resonant-pull-in voltage

$$V_{rpi} = \sqrt{\frac{\pi}{Q\sqrt{27}}\frac{\omega_{tun}}{\omega_n}\frac{kd^2}{C_o}}\,, \tag{8}$$

which also depends on the tuned resonant frequency. If the frequency dependence is ignored, and the dc pull-in voltage is substituted into Eq. (8), the resonant-pull-in voltage can be expressed as

$$V_{rpi} \le V_{pi}\sqrt{\frac{2}{Q}}\,, \tag{9}$$

where

$$V_{pi} = \sqrt{\frac{8}{27}\frac{kd^2}{C_0}}\,. \tag{10}$$

Thus, for $Q>2$, resonant pull-in will occur at a lower voltage than DC pull-in.

DESCRIBING FUNCTION MODEL

In this section, a model is developed to predict steady-state oscillation amplitudes over a wide range of excitation frequencies. The preceding energy analysis could be easily extended to off-resonance excitation, but it does not account for the negative spring effect of the parallel-plate actuator. The negative spring effect motivates the describing function approach [**6**].

Figure 7 shows a nonlinear block diagram of a parallel-plate driven, vibrating structure. Because the electrostatic force has a nonlinear dependence on position, both the steady-state oscillation—if there is one—and the steady-state force will be periodic but not sinusoidal. In general, an exact solution requires a computer simulation. However, if Q is sufficiently high and the driving frequency is near or above the mechanical resonant frequency ($\omega \ge \omega_n/2$), the motion can be approximated by a single sinusoid because the harmonic components will be attenuated by the structure dynamics.

Assuming that $x=A\cos(\omega t)$ and that D lags the deflection by phase, ϕ, the electrostatic force, from Eq. (1), can be represented by its Fourier components:

$$F_{el}(\omega t) = F_{dc} - k_{el}A\cos(\omega t) - b_{el}A\sin(\omega t) + \mathrm{K} \tag{11}$$

where

$$k_{el}(A,\phi) = \frac{-1}{\pi A}\int_0^{2\pi} F(\tau)\cos(\tau)d\tau$$
$$b_{el}(A,\phi) = \frac{1}{\pi A}\int_0^{2\pi} F(\tau)\sin(\tau)d\tau \tag{12}$$

The average force, F_{dc}, on the structure is zero. The second term is the component that is in phase with position and represents the spring force. The third term is in phase with velocity and represents the energy added by the actuator. Assuming that the mass only responds to the dc and fundamental component, the harmonic terms are neglected.

At resonance ($\phi=-90°$),

$$k_{el}(A,-90°) = -\frac{C_0V_d^2}{d^2}\frac{1}{\left(1-(A/d)^2\right)^{1.5}} \tag{13}$$

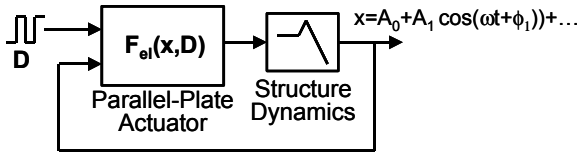

Figure 7. *Nonlinear block diagram*

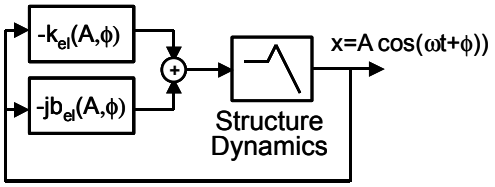

Figure 8. *Block diagram including describing function elements*

$$b_{el}(A,-90°) = -\frac{C_0V_d^2}{d^2}\frac{2}{\pi}\frac{1}{(A/d)}\frac{1}{1-(A/d)^2}\,. \tag{14}$$

For small oscillation amplitudes ($A\approx 0$) the electrical spring constant is identical to the well-known parallel-plate spring constant. The energy provided, in one half-cycle, by the negative damping term ($E_{add}=-\pi b_{el}A^2/2$) matches Eq. (3).

Figure 8 shows the same block diagram from Figure 7 except that the nonlinear, electrostatic-force block has been replaced by the amplitude and phase dependent terms in Eq. (12). From the block diagram, two equations can be derived: the frequency equation,

$$\left(\frac{\omega}{\omega_n}\right)^2 = 1 + \frac{k_{el}(A,\phi)}{k}\,, \tag{15}$$

and the energy equation,

$$-\frac{b_{el}(A,\phi)}{k} = \frac{1}{Q}\frac{\omega}{\omega_n}\,. \tag{16}$$

Using a numerical method, equations (15) and (16) can be solved for amplitude and frequency as a function of phase. The results are discussed in the next section.

The spring and energy terms are plotted in Figure 9 and Figure 10. Resonant pull-in occurs if $db_{el}/dA < d\omega/dA$. At resonance, db_{el}/dA becomes negative at 56% of the gap. At $\omega=\omega_n$, $k_{el}=0$, and $db_{el}/dA>0$ for all amplitudes. Thus, the model predicts that vibration at the natural resonant frequency will be stable over the entire gap.

RESULTS AND DISCUSSION

The parallel-plate behavior was verified experimentally using the gyroscope structure in Figure 1. The structure is 2.25μm thick. The resonant frequency was designed to be 10kHz. The nominal drive capacitance is 70fF with a 2μm gap. The structure oscillates at atmospheric pressure.

Using the Computer Microvision system, designed at MIT [**7**], the frequency response of the structure was measured for different drive voltages. The results are shown in Figure 11 along with the results of the describing function model. The model data fit the measured results for a resonant frequency, f_n=9.3kHz, $Q=5.3$, and $C_0/(kd^2)=0.0088$, or equivalently $V_{pi}=5.8V$. According to equation (9), the resonant-pull-in voltage, $V_{rpi}<3.56V$. Combining equations (8), (13), and (15) predicts $V_{pi}=3.42V$ because the resonant frequency is tuned to $\omega_{tun}=0.9\omega_n$.

In Figure 11, there are curves for three different drive voltages: $3.0V$, $3.4V$, and $4.5V$. For the curves corresponding to $V_d=3V$ and $V_d=3.4V$, the motion is stable for all frequencies, and

the amplitude is limited to less than ~56% of the gap. Notice that the resonant frequency is lower for the *3.4V* drive voltage. As predicted in the resonant pull-in section, there are also unstable solutions, but these oscillations are unobservable without feedback.

For the curve corresponding to the largest drive voltage, there are three distinct frequency ranges: 1) In the lower frequency range, there are stable amplitudes that are limited to less than half of the gap. The solutions in the upper half of the curve are unstable and require feedback to be achieved. If the voltage is increased further, the maximum stable amplitude at low frequencies tends to the dc pull-in limit, one-third of the gap. 2) In the midband range, there are no solutions, stable or unstable. In this region, the energy provided always exceeds the energy removed by the damper, and the structure snaps. 3) In the high frequency range, there is one solution for every frequency. In this frequency range, there is no pull-in limit, and it is possible for the structure to achieve a stable amplitude greater than 56% of the gap. In fact, we recorded a 1.4μm amplitude vibration across the 2μm gap at 9kHz.

There are two non-idealities that might affect the parallel-plate actuator. The first is nonlinear damping due to squeeze-films [**8**]. However, for the test structure, in which the thickness and the gap are comparable, the data does not indicate that the damping depends on position. The second issue is electrostatic fringing fields. The fringing fields might introduce errors in the energy and spring terms, but they do not change the qualitative behavior.

CONCLUSION

Parallel-plate actuators that are driven near the resonant frequency can move more than the dc pull-in limit of one-third of the gap. However, actuators that are driven at the tuned resonant frequency, are instead limited to 56% of the gap due to resonant pull-in. Above the tuned resonant frequency, it is possible to oscillate more than 56% of the gap. If the structure is driven at the natural resonant frequency, the vibration theoretically should be able to span the entire gap. Using the describing-function model we can predict the steady-state amplitudes for excitation frequencies above $\omega_n/2$. If feedback is used, it should be possible to stabilize the normally unstable oscillation amplitudes to achieve a wide range of operating frequencies at low voltages.

ACKNOWLEDGMENT

This research was funded by DARPA under agreement F30602-97-2-0266.

REFERENCES

1. R.R.A. Syms, "Electrothermal Frequency Tuning of Folded and Coupled Vibrating Micromechanical Resonators," *J. MEMS.*, 2, **7** (1998), pp. 164-171.
2. S.G. Adams, F.M. Bertsch, K.A. Shaw, P.G. Hartwell, F.C. Moon, and N.C. MacDonald, "Capacitance Based Tunable Resonators," *J. Micromech. Microeng.*, **8** (1998), pp. 15-23.
3. K. Lee and Y. Cho, "A Triangular Electrostatic Comb Array for Micromechanical Resonant Frequency Tuning," *Sensors and Actuators*, **A 70** (1998), pp. 112-117.
4. W. Ye, S. Mukherjee, and N.C. MacDonald, "Optimal Shape Design of an Electrostatic Comb Drive in Microelectromechanical Systems," *J. MEMS.*, 1, **7** (1998), pp.16-26.
5. Y. Nemirovsky and O. Bocobza-Degani, "A Methodology and Model for the Pull-In Parameters of Electrostatic Actuators," *J. MEMS.*, 4, **10** (2001), pp. 601-615.
6. J-J.E. Slotine, *Applied Nonlinear Control*, Prentice-Hall, 1991
7. D.M. Freeman, A.J. Aranyosi, M.J. Gordon, and S.S. Hong, "Multidimensional Motion Analysis of MEMS Using Computer Microvision," *Tech. Dig. Solid-State Sensor and Actuator Workshop*, Hilton Head, SC, Transducers Research Foundation, Cleveland (1998), pp.150-155.
8. J. B. Starr, "Squeeze-film damping in solid-state accelerometers," *IEEE Solid-State Sensor and Actuator Workshop*, Hilton Head Island, SC, June 1990, p.44-7.

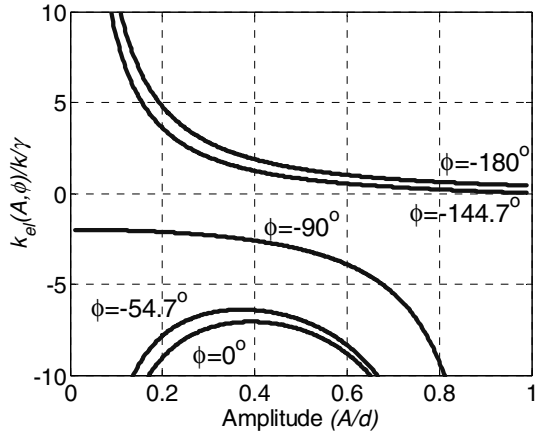

Figure 9. *Spring component versus amplitude; $\gamma=(C_0V_d^2)/(2kd^2)$.*

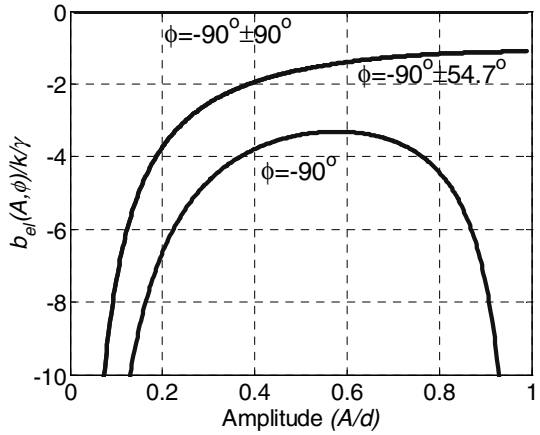

Figure 10. *Energy component versus amplitude; $\gamma=(C_0V_d^2)/(2kd^2)$.*

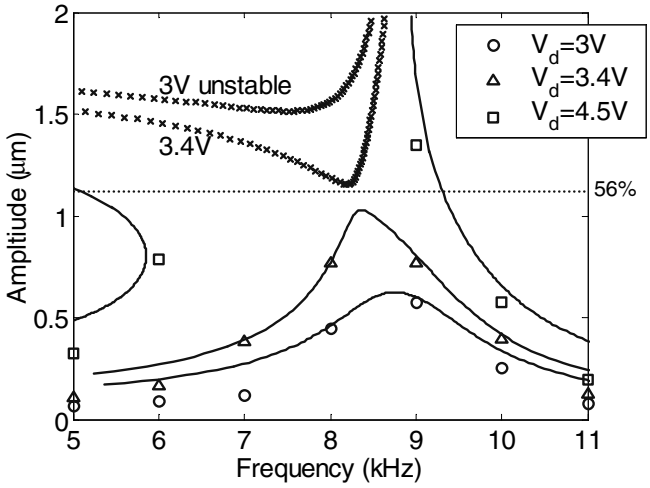

Figure 11. Describing function model and measured frequency response

Batch Fabricated Inline Microfluidic Valve

P. Selvaganapathy, E. T. Carlen and C. H. Mastrangelo
Center for Wireless Integrated Microsystems
Department of Electrical Engineering and Computer Science
University of Michigan, Ann Arbor, MI 48109-2122, USA.

ABSTRACT

A normally open electrothermally actuated inline microvalve that has been developed, fabricated and tested with liquids is presented. The inline valve is surface micromachined on top of flexible microfluidic channels using a low temperature fabrication process; therefore it is suitable for integration with microfluidic networks requiring actuation of a large number of valves under electrical control. Complete closure of sealed microchannels has been observed with power as low as 40 mW. Response times of 15 msec have been measured. Breakdown of the inline valve occurs at an upstream pressure of 23 psig.

INTRODUCTION

Emerging microfluidic systems involve the integration and automation of many individual steps performed in macroscale biochemical analysis [1,2,3]. This requires the ability to control precisely and efficiently the transport of reagents and samples throughout different parts of the system. Typically these systems require many valves operating simultaneously or in sequence. Therefore, the valve actuators must be small operating with low power, and must integrate easily with the system components.

Over the past decade, there has been wide variety of actuation mechanisms and methods employed for construction of microvalves including electrostatic, magnetic, piezoelectric, bimorph and thermopneumatic actuation [1]. Some of these techniques employ bulk micromachining and anodic bonding, making the valves large, out of plane and difficult to integrate in large scale in microfluidic systems.

In this paper, we present a simple microfluidic valve that is easily integrated with other fluidic components on the same die. Thermopneumatic actuation was chosen for this valve because it holds several advantages over other actuation schemes. Most actuation methods provide either large displacements or large forces. Shape memory alloys provide both large actuation and displacements but can be difficult to integrate and do not conform to the shape of the channel [4]. Thermopneumatic actuation provides both large displacements (2-10 μm) and forces (~1N), and with the recent published method [5] for batch fabrication compatible with microfluidic systems, is ideal for this application. The thermopneumatic actuators used as the active elements of the microvalves presented here are based on the phase change expansion of a sealed surface micromachined patch of paraffin.

DEVICE DESIGN

The actuation mechanism depends on a thermally triggered phase change in the paraffin actuation material resulting in a volumetric expansion. Paraffin is a linear hydrocarbon mixture of alkanes of varying chain lengths, with high volumetric expansion upon phase change from solid to liquid. It also has other desirable properties such as, low thermal and electrical conductivity, low viscosity in liquid phase and stability through numerous phase change cycles. Typically volumetric expansion between 10-30% can be achieved when heated at temperatures ranging from 65-150°C, depending on the melting temperature of the material. Figure 1 shows the pressure-volume-temperature (PVT) characteristics of the paraffin material used in the devices (bonding wax, Logitech Ltd, (0CON-175) with a melting temperature of 72°C.

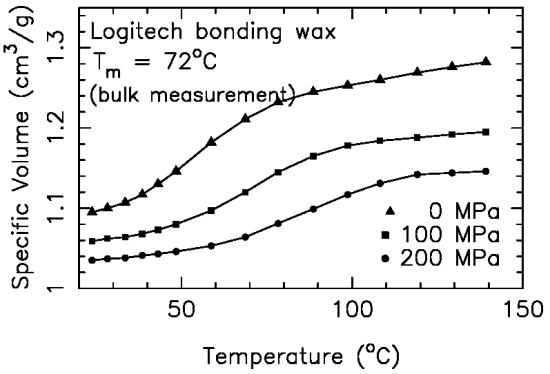

***Figure 1**: PVT of Logitech 0CON-175 bonding wax*

Figure 2 shows the top view of the inline valve with a paraffin microactuator. Figure 2a shows a microchannel with a reduced section and heaters on either side of the reduced section. The cross sectional dimension of the microchannel is 10 μm x 100 μm (height x width). In the reduced section the dimensions are

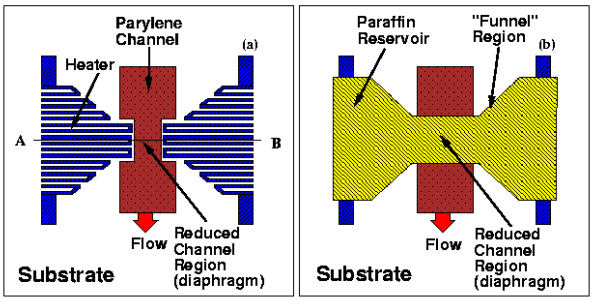

***Figure 2**: Top view of the microactuator*

1 μm x (10-50) μm. The top of this microchannel is constructed from thin (0.2 μm) parylene, acting as a diaphragm for paraffin actuation in the reduced section. The heaters on both sides of the channel are patterned and used to melt the paraffin. Figure 2b shows the paraffin micromachined on top of the heaters and the reduced section. The paraffin is then sealed with a thick (3-4 μm) parylene layer. The paraffin layer has this unique shape in order to funnel the melted paraffin from the reservoir onto the reduced

0-9640024-4-2/hh2002/$20©2002TRF
DOI 10.31438/trf.hh2002.79

channel region providing hydraulic advantage for maximizing diaphragm deflection. Figure 3 shows a perspective schematic of the valve.

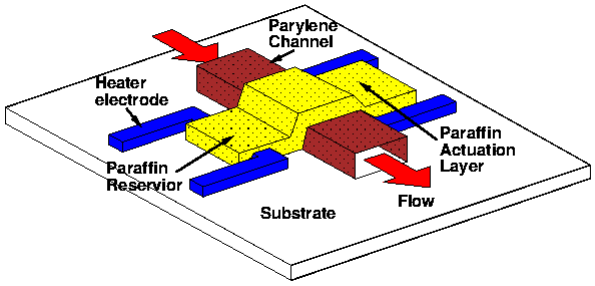

***Figure 3**: 3-D schematic view of the valve.*

The paraffin patch overlaps the reduced region of the microchannel. When the heaters melt the paraffin in the reservoirs it flows into the reduced channel section deflecting the thin diaphragm closing the channel. In order to maximize the deflection, the paraffin reservoir is enclosed by a thick (10 µm) Ni electroplated layer as shown in Figure 4. The Ni layer prevents the expansion of the paraffin chamber upwards and concentrates the expansion to the diaphragm in the reduced channel region as well as improving the heat transfer to the paraffin. The change in the cross section of the channel at the reduced height channel region is shown in Figure 4.

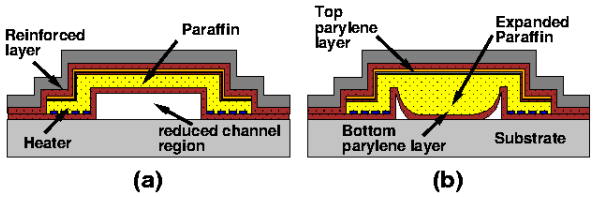

***Figure 4**: Cross section of reduced channel region during off and on states*

FABRICATION

The entire microfluidic system including inline valve and microchannel was fabricated using a low temperature process (<90°C). Figure 5 shows a simplified process flow. Inlet holes to the microchannels were patterned in UV definable glass substrates (Foturan, Schott Corp.). Patterning the Foturan substrates required UV (312 nm) exposure (~2 J/cm^2 energy density for a through wafer patterning) followed by heat treatment, which reached 600°C for 1 hour. During the heat treatment the substrate surface became rough and required surface refinishing. The substrates are then planarized with a 20 µm calcined aluminum oxide slurry (0CON-012, Logitech, Ltd.) for 1 hour and polished with an alkaline colloidal silica slurry (SF1 0CON-140, Logitech, Ltd.) for 1 hour. The wafer was then cleaned using a piranha clean recipe (H_2SO_4:H_2O_2, 1:1) for 20 mins to remove organic residue on the surface. Next, the sacrificial channel except the reduced region and reservoir areas are formed by spin-casting a 10 µm-thick photoresist (AZ 9260, Clariant) layer followed by softbake 65°C for 1 hr), exposure (5mW/cm^2 for 110 sec.), and development (1:4 AZ400K (Clariant):DI H_2O for 3 mins). The reduced height region was formed by spin casting photoresist layer 1 µm thick (SC 1813, Shipley, Corp.) followed by softbake (65°C for 1 hour), exposure (5mW/cm^2 for 20 sec.), and development (MF319, Shipley, Corp). This layer defines the height and the width of the reduced region. The width varied from 10 µm to 50 µm for various devices in the die. The entire substrate was then coated with the bottom parylene layer 3 µm thick.

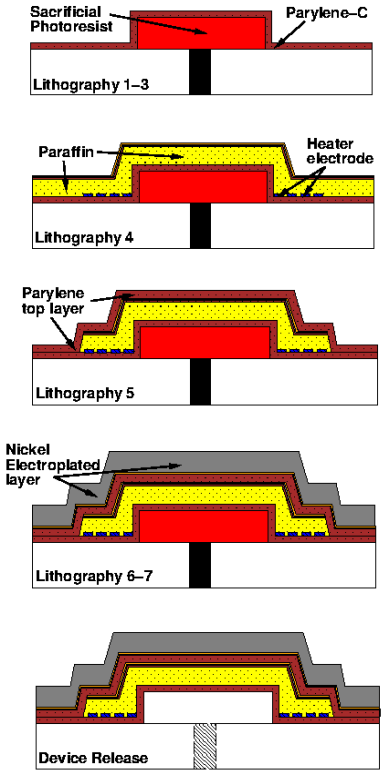

***Figure 5**: Fabrication process flow for microvalve*

Next, SiO_2 /Cr/Al (10/30/500nm) layers were sputter coated on the wafer. The Cr/Al layers were then patterned and wet etched forming the actuator heaters. The SiO_2 layer was then removed in the field areas. Paraffin is then thermally evaporated and covered with the parylene/Cr/Au (500/50/300nm) etch mask materials. The Cr/Au layers are patterned and parylene/paraffin films were removed using a CF_4:O_2 RIE step. The second parylene layer, 3-4 µm thick, was then vapor deposited and patterned. A Ti/Au (50/500nm) seed layer for the electrodeposited nickel reinforcing layer was then sputter coated on the sample. A thick photoresist electroforming mold was then spin cast and patterned. A 10 µm thick nickel reinforcement layer was then electrodeposited. After the nickel deposition was complete, the photoresist mold was removed with acetone and the exposed Ti/Au areas are wet etched.

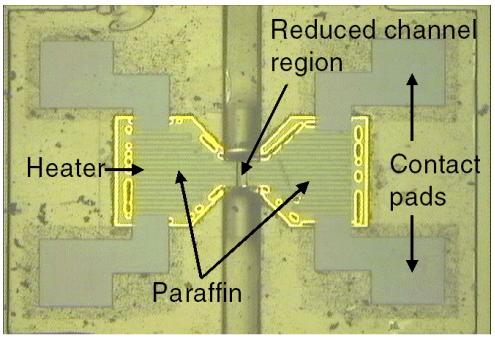

***Figure 6**: Optical photograph of the backside of the valve*

The Foturan glass substrates were then wet etched (10:1 DI H2O: HF (49%)) forming the inlet holes while at the same time dicing the wafer. Finally, the sacrificial photoresist was removed in an acetone bath for 2 hrs.

Figure 6 shows the backside view through the glass substrate of the fabricated valve. The heaters along with the paraffin on top of them can be clearly seen. Figure 7a shows an SEM photograph of the microvalve along with the microchannel and reservoir. Figure 7b shows a closer view of the microvalve from which the reservoir and the reduced channel region can be clearly delineated.

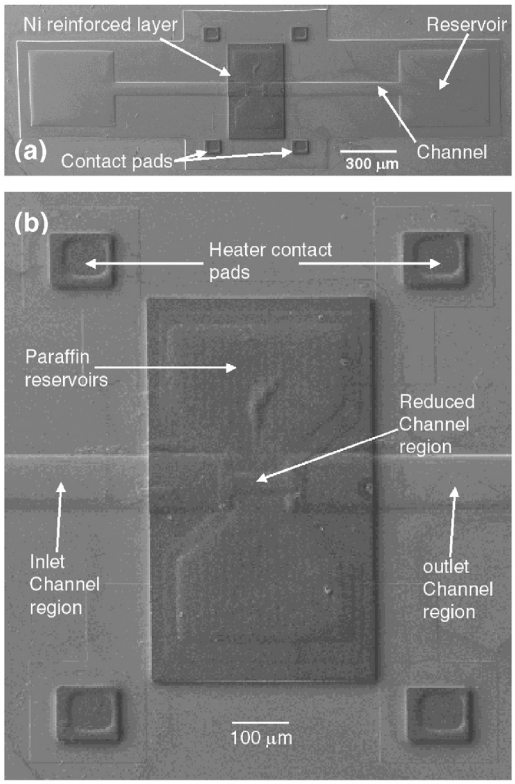

***Figure 7**: SEM photograph of a) valve channel system and b) closeup of the microvalve*

EXPERIMENTS

The inline devices were mounted on a custom made microfluidic test fixture shown in Figure 8. The fixture consists of four tapered channels having a gradient in diameter from 1 mm on the outside connecting to an external fluidic system to 500 μm on the inside connecting to the reservoirs on the die. A silicone rubber O-ring was placed between the fixture and the die. A top plate was used to clamp the die firmly against the O-ring and fixture. This provides a good fluidic seal between the fixture and the die. The top plate has an opening that allows electrical contact of the heaters for testing.

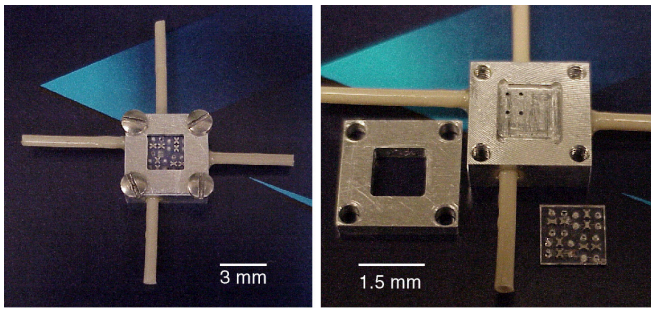

***Figure 8**: Fixture used to connect the devices to macroscale fluidic control and measurement system a) assembled b) disassembled*

The fixture along with the device were then attached to the fluidic control and measurement system. A schematic of the system is shown in Figure 9. A syringe pump (BAS MD 1001) was used to force the liquid into the microfluidic channel with a controlled pressure control at the inlet channel region. A pressure transducer (Omega PX4600) was used to monitor the pressure at the inlet region. The pressure transducer's output was recorded using a computer.

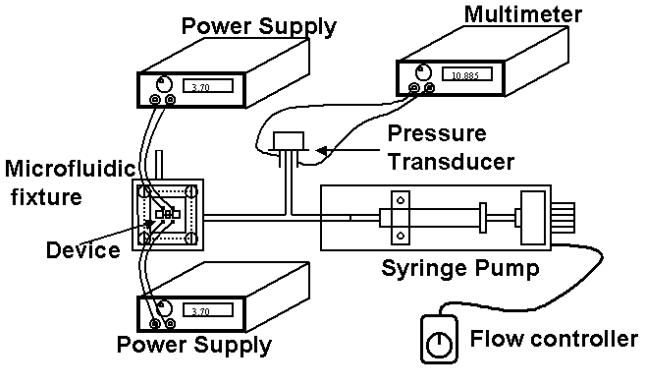

***Figure 9**: Schematic of the pressure control and monitoring system used for characterization of the valve*

The following methodology was used to test the characteristics of the valve. Initially the liquid was pumped through the system into the microchannel and out of the fixture. The valve was then closed, and the pressure in the upstream side of the valve, as monitored by the transducer was allowed to rise to the desired level. The syringe pump is stopped and the power supplied to the heaters was reduced gradually until the valve breaks allowing the liquid to flow through. This produces an accurate measurement of the power required to hold a particular pressure differential across the valve. The liquid used in all the cases was DI water.

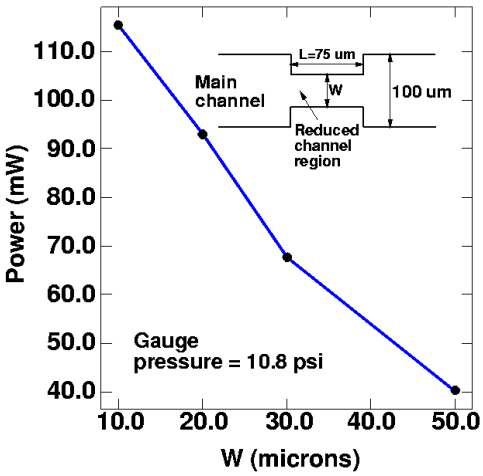

***Figure 10**: Power required to close a microchannel with variation in reduced channel width*

Several devices with varying reduced channel dimensions from 10 µm to 50 µm were constructed and tested. The height (1 µm) in each case was the same. The pressure at the upstream end was maintained at 10.8 psig and the minimum power required for closing of the valve was measured. The result presented in Figure 10 shows that as the channel width increases the power required to close the valve decreases. An increase in channel width places the supports of the diaphragm farther apart making the diaphragm deflect more for the same pressure. Since the pressure generated on the diaphragm from the expanded paraffin is correlated to the electrical power, more power is required to close channels with smaller widths.

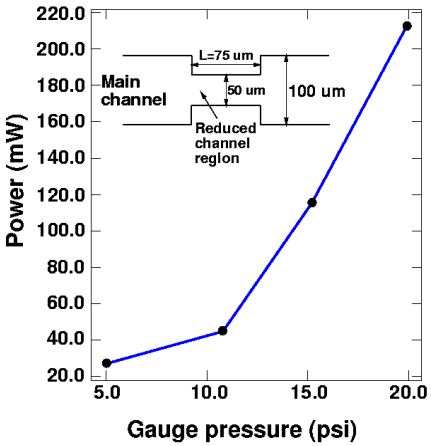

***Figure 11**: Power required to close a microchannel variation in upstream pressure.*

Figure 11 shows measurements of the power required to close a microchannel with 50 µm reduced channel width for different upstream pressures. It shows that higher power is required for closing channels with higher upstream pressure. Figure 12 shows the transient response of the valve when it opens. Typically the cooling of the molten paraffin determines the response time of the valve, which can be indirectly correlated using the opening characteristics. The valve closing required 50 mW of power, and the upstream pressure was maintained to be slightly above 10 psig. The valve opened in about 15 ms.

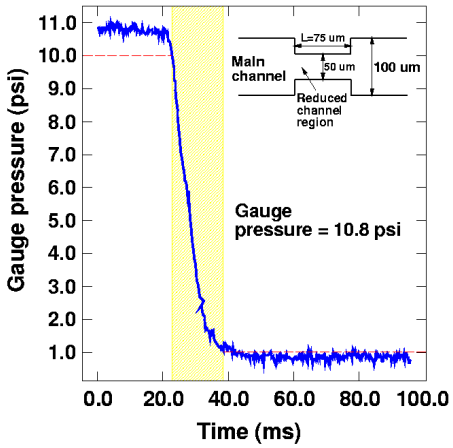

***Figure 12**: Transient response of the upstream pressure to valve opening*

One dimensional steady state and transient simulations on the device were performed using ABAQUS FEM software. The temperature at the surface of the electroplated Nickel was also measured using an IR camera (Inframetrics, Inc. SC 1000) for varying power. This measurement was used in simulations to determine the heater surface temperature with respect to the power delivered to the heaters as shown in Figure 13. Figure 13 shows that phase change occurs at power as low as 30 mW. Furthermore simulations were performed, to determine the transient response of the device at various heater temperatures, which matched experiments. The inline valve device was found to undergo structural failure above 23 psig. The failure occurred either due to the loss of adhesion between the parylene channel reservoirs when the upstream pressure is increased or due to the loss of adhesion between the top and bottom layers of parylene of the paraffin reservoir due to expansion of paraffin at above 300 mW. This caused a leakage of paraffin outside its reservoir.

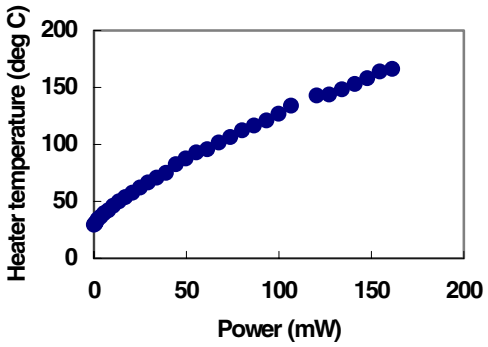

***Figure 13**: Simulated heater temperature vs. power delivered*

CONCLUSIONS

In this paper we presented the design, fabrication and testing of an electrothermally actuated, normally open, inline microvalve for microfluidic applications. Actuation was performed by a thin paraffin layer as a thermally activated phase change material. The novel construction uses the top layer of the flexible parylene channel as the diaphragm, which is actuated by the expansion of a paraffin reservoir. The valve is constructed using a simple, low temperature fabrication process. The inline valve device is especially suitable for microfluidic systems where a large number of valves are required under electrical control.

ACKNOWLEDGEMENTS

This work is supported by DARPA grant under contract F30602 - 98-2-0197

REFERENCES

[1] S. Shoji and M. Esashi, "Microflow devices and systems," J. Micromech. Microeng., vol. 4, pg. 157-171,1994.

[2] M. A. Burns et al., "An integrated nanoliter DNA analysis device," Science, vol. 282, pg. 253-258, 1998

[3] D. J. Harrison, et al., "Capillary electrophoresis and sample injection systems integrated on a planar glass chip," Anal. Chem., vol.64, pg. 1926-1932, 1992.

[4] P. Krulevitch, et al., "Thin film shape memory alloy microactuators," JMEMS, vol. 5, pg. 270-281, 1996.

[5] E. T. Carlen and C. H. Mastrangelo, "Simple, high actuation power, thermally activated paraffin microactuator," Transducers'99, vol. 2, pg. 1364-1367, 1999.

A SEPARATOR-ANALYZER FLOWMETER FOR COMPLEX LIQUIDS IN MICROFLUIDIC SYSTEMS

Shramik Sengupta *, Babak Ziaie [#,*] and Victor H Barocas *
Departments of Biomedical Engineering* and Electrical and Computer Engineering [#]
University of Minnesota (Twin Cities)
Minneapolis, MN 55455

ABSTRACT

The measurement and control of the flow rate of fluids containing charged macro-molecular species (such as proteins) and particles is required for a number of applications, such as controlled drug delivery and micro-scale bioreactors. The flow rates that need to be measured for such systems can be as small as picoliters per second (microliters per day). We are developing a novel flow meter, called the separator-analyzer flow meter (or SAF meter), to measure the flow rate of suspensions laden with protein or other charged macromolecules or particles. The SAF meter consists of a channel that splits into two parts and then recombines. A pair of electrodes is positioned before the channel bifurcation. When a DC potential is applied across this pair of electrodes, the charged species in the mixture are dragged toward one electrode, and the solutions flowing into the two arms downstream differ in the concentration (separator). This difference in concentrations is inversely proportional to the flow rate of the original mixture. The concentration difference can be measured optically or electrochemically (analyzer). Based on the input to the separator (strength of the applied electric field), and the output from the analyzer (concentrations in the two arms), it is possible to obtain the flow rate of the solution or suspension (and consequently the amount of charged species). A milli-scale prototype has been fabricated and has been used to measure flow rates from 25-75 μl/minute.

INTRODUCTION

In Biomedical Microsystems (Bio-MEMS), the fluid handled is typically a suspension of particles and macromolecules. (e.g., cell lysate, and protein or DNA solutions) **[1]**,**[2]**. In many applications, the quantity of interest is often the mass-flow-rate of the solute. Besides, the flow rates that are typically encountered (micro-liters per day to micro-liters per second) imply that a different set of physical phenomena (diffusion, viscosity and electro-kinetic effects) become significant at these micrometer scales. This renders many of the techniques commonly used for flow sensing in the macro-scale **[3]** ineffective, and new techniques for measuring flow rates need to be developed. For any new flow sensor to be successful as an "on chip" device, it is also important that it be fabricated using the same techniques that are used for fabricating the rest of the system. Thus, building a flow sensor using standard micro-fabrication techniques would be a significant advance toward the development of an independent microfluidic system that incorporates pumps, flow sensors and circuit logic to implement feedback or optimal control strategies.

In this work, we present a new design for a flow sensor targeted to measure the flow rates of macromolecular solutions in channels. The geometry of this device is simple enough to allow fabrication using standard micro-fabrication processes. In addition, it takes into account (and makes use of) diffusion and electrophoresis, physical phenomena that become important at micrometer length scales.

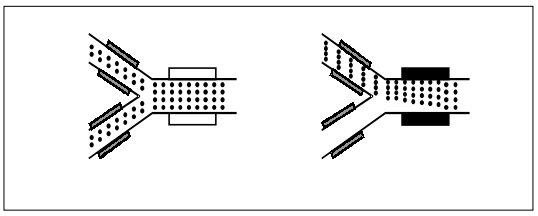

***Figure 1**: Schematic diagram showing the operating principle of the SAF meter. With no voltage applied to the separator (left panel) the concentration is unaffected. With a DC voltage to applied the separator (right panel) the charged species are steered.*

PRINCIPLE OF OPERATION

Figure 1 schematically demonstrates the operating principle of the Separator-Analyzer Flow (SAF) meter. As seen in this figure, the flow sensing system consists of two parts, a main (undivided) channel and a pair of smaller channels. The smaller channels subsequently merge again (not shown in picture). A pair of electrodes is positioned across the channel just prior to the bifurcation. As long as no DC voltage is applied across these electrodes, the particles move with the fluid and are distributed equally between the two branch channels. However, if a constant DC voltage is applied, some of the particles in the fluid are dragged toward one electrode and the concentrations in the two fluid streams are different [Figure 1(right panel)]. If we assume plug flow for the fluid in the channel, then the difference in concentration is given by the equation

$$\frac{\Delta C}{2C_0} = \frac{\mu_e EL}{W}\left(\frac{1}{< V_x >}\right) \qquad (1)$$

where, ΔC = Difference of the concentrations in the two branch arms,
C_0 = Concentration in the main channel,
μ_e = Electrophoretic mobility of the particles,
$<V_x>$ = Average velocity of the fluid in the main channel,
L = Length of the separator electrodes, and
W = Half-width of the separator channel.

Travel support has been generously provided by the Transducers Research Foundation & the DARPA MEMS & DARPA BioFlips Program.

We refer to this mode of operation of the sensor as the Constant Field Mode. It may be noted that there is a certain minimum velocity that can be measured. If the velocity is too low (or the field is too strong), all the particles are dragged down to the lower arm. Thus, another way to operate this device would be to control the electric field in such a way that the critical electric field (needed to keep all the particles in the lower arm) can be measured. In this case, the critical electric field (E_c) is given by the relation

$$E_C = \left(\frac{W}{L \mu_e} \right) < V_x > \qquad (2)$$

As evident from equations (1) and (2), the ability to measure flow is contingent upon the ability to measure the concentration of the particles in the suspension (or at the very least being able to distinguish between a suspension and a "clear" solvent). This can be done using various analytical techniques that can be broadly divided into two groups, optical and electrical. Measurement of absorbance could be a suitable optical technique for the analyzer since the absorbance of a protein solution at 280 nm is proportional to the concentration of the protein in the solution. **[4]**. This approach would be well suited to a static array of devices that could be scanned by a mounted laser, for example; but measuring absorbance "on chip" would be a considerable challenge. In addition, it is known that differences in the concentration of proteins in solution will cause the solutions to exhibit different dielectric constants (ε_r) **[5]**, providing another potential concentration measurement tool. Electrodes placed across the solutions flowing through the two arms of the analyzer will then act like the plates of a parallel-plate capacitor, whose capacitance (C) is given by

$$C = \varepsilon_0 \varepsilon_r (A/d) \qquad (3)$$

where, ε_0 is the permitivity of free space, A is the surface area of the analyzer electrode and d is the distance between the two electrodes. Thus, capacitance measurements may also be used in the analyzer. It may be noted that while the separator electrodes must be placed along the sidewalls of the channels, the analyzer electrodes can be placed either along the sidewalls or on the top and bottom of the channel.

DESIGN ISSUES

The purpose of the design exercise for this device is to specify a range of channel and electrode dimensions over which it will function and provide the corresponding minimum and maximum flow rates that can be measured. If operated in the constant field mode, the minimum measurable velocity is obtained when $\Delta C/2C_o = 1$ (corresponding to all the particles in the lower arm). Thus,

$$<Vx>_{min} = (\mu_e L / W) \qquad (4)$$

While the electrostatic force supplied by the DC field tries to bring all the particles toward one side of the channel, diffusion tries to homogenize the solution across the width of the channel. If we set the characteristic time for diffusion ($= W^2/2D$; where D is the diffusivity of the particle in the solution) to be ten times larger than the characteristic time for electrophoretic migration ($= w/ \mu_e E$), the least measurable flow rate (Q_{min}) is given by the relation

$$Q_{min} = 40\ D\ L\ (h / W) \qquad (5)$$

where h is the height of the channel. We would ideally like Q_{min} to be as small as possible. Of the quantities in the above expression *D* (the diffusivity of the protein) is beyond our control. The ratio of the channel height by width is determined by the etching technology used, (h/W) ratios of ~1 or lower can be obtained using isotropic etchants like HF/HNO_3, whereas more specialized anisotropic etching techniques will be required to obtain significantly higher values. The limit to how small the length of the electrode (L) can get is determined by the minimum feature size that can be drawn on the photolithography mask (5 microns in our case). Figure 2 shows how the minimum measurable flow rate varies for a solution of hen egg white lysozyme ($D = 7.5 \times 10^{-7}$ cm^2/s **[6]**) as a function of these two sets of parameters.

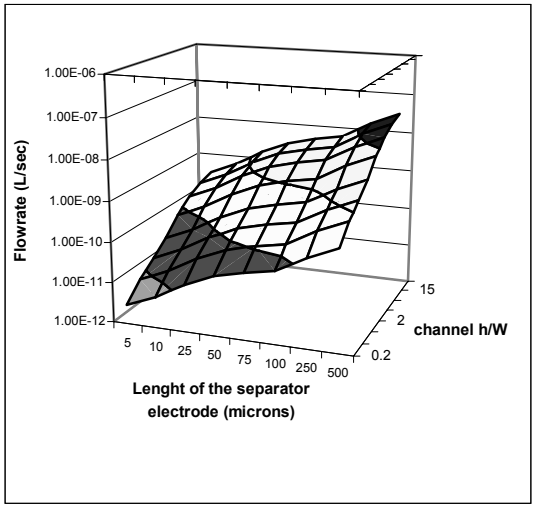

***Figure 2**: Plot of the minimum measurable flow-rate for a solution of lysozyme as a function of the channel and electrode parameters.*

Once the hardware parameters have been chosen based on the minimum measurable flow rate, raising the field strength causes the surface plot in figure 2 would be shifted upward, thus allowing for the measurement of higher flow rates. The resolution of the measurement of the flow rate is a function of the resolution of the measurement of the concentration difference in the analyzer. As indicated by Figure 2, to measure a low flow rate, one would prefer a channel that is shallow but wide. However, to get a better sensitivity out of our (capacitive) analyzer, one would like the plates to be wide and distance between them to be low (see equation 3). Hence, we would prefer to place the electrodes of the analyzer on the top and bottom of the channels.

MILLISCALE PROTOTYPE

Although the goal of our work is to fabricate a micro-scale flow sensor capable of measuring flow rates as low as pico-liters per second (micro-liters per day), in order to verify the novel principle of operation experimentally, we first made a milli-scale prototype capable of measuring higher flow rates (of the order of micro-liters per hour) using the same principle. A picture of the prototype is shown in Figure 3. It was made out of commercially available UV-curable epoxy on top of a glass wafer. The top surface of the device

is made out of Plexiglas, with holes drilled in for fluidic inlets and outlets. As seen in the picture, it consists of a main channel (1mm wide) that splits into two branches (500 μm wide). All channels are 250 micron deep. The strip of platinum placed just prior to the bifurcation is 250 microns thick, and 1mm wide. Thus, the effective length of the separator electrode is 1 mm. The channels do not recombine, nor is there analyzer built into the device. However, the fluid in the two arms may be collected for off-line analysis.

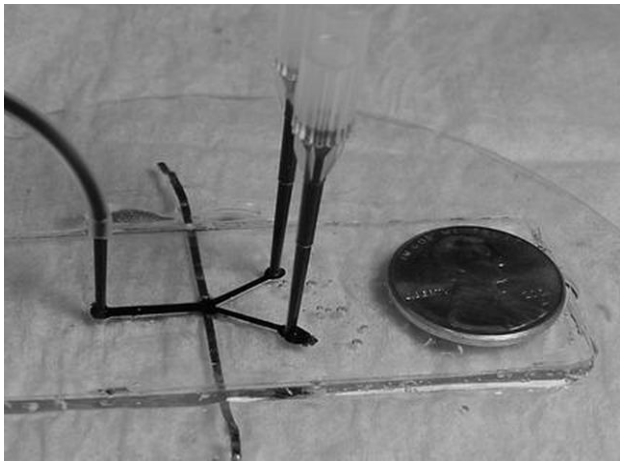

***Figure 3**: Picture of the milli-scale prototype used for conducting proof-of-concept experiments.*

PROOF-OF-CONCEPT EXPERIMENTS

A set of experiments was conducted using the prototype shown above to experimentally verify the principle of operation of the SAF meter. The experimental protocol used is schematically illustrated in Figure 4.

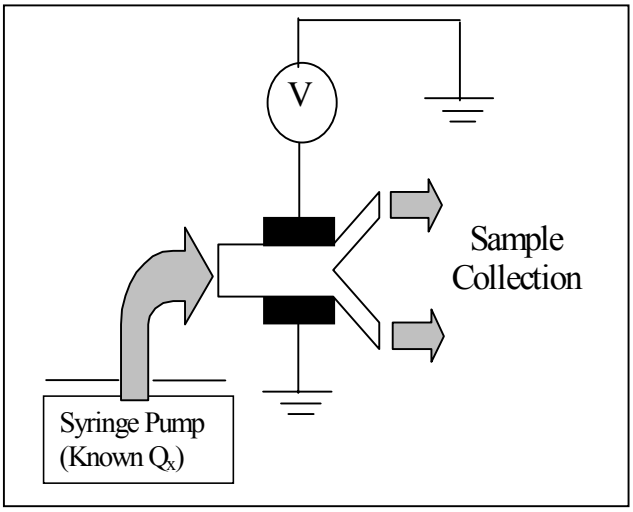

***Figure 4**: Schematic representation of the experimental protocol used to conduct proof-of -concept experiments.*

As seen in the figure, we use a syringe pump to deliver known flow rates of a standard solution of Bovine Serum Albumin (BSA) in DI water. At the same time, a known DC potential difference is applied across the electrodes, and the fluid coming out of the two channels are collected. The concentration of BSA in the collected samples is measured by measuring the optical density (OD) of suitable dilutions of these samples at 280 nm. The degree of separation ($\Delta C/2C_0$) can be obtained from the measured concentrations.

RESULTS

Table 1 (below) summarizes our results for a set of imposed flow rates and applied voltages. It reports the mean (and standard deviation, n = 3 to 5) values of the degree of separation calculated from individual sets of observed concentrations. It may also be noted that only those observations were used for which the mass balance closed to within ±5%.

	25 μl / min	50 μl / min	75 μl / min
5 Volts	0.1033 (0.020)*	0.0689 (0.003)	0.0479 (0.007)*
10 Volts	0.1986 (0.027)	0.1077 (0.011)	0.0838 (0.020)
15 Volts	0.3399 (0.004)	0.1236 (0.019)*	0.1124 (0.015)*

***Table 1**: Observed values of ($\Delta C/2C_0$) as a function of known values of flow rate (Q) and applied voltage (V) [* indicates the mean and standard deviation of five observations. (as opposed to that of three, for other cases)]*

Equation (1) may be rewritten in terms of the applied voltage and imposed flow rate, as opposed to the electric field strength and the average velocity, respectively. On doing this, equation (1) assumes the form

$$\frac{\Delta C}{2C_0} = \frac{\mu_e LH}{W}\left(\frac{V}{Q}\right) \qquad (6)$$

Thus, if the obtained values of ($\Delta C/2C_0$) are plotted against the ratio of the applied voltage and imposed flow rate, then the points must lie on a straight line, the slope of which will be a function of the dimensions of the channel and the electrode and the electrophoretic mobility of the protein. In Figure 5, we plot the (mean) values shown in Table1 against the ratio of the applied voltages and imposed flow rates. A straight line is then fitted through the points, and the equation of the straight line (along with the R^2 value of the fit) is also displayed in the figure.

The high value for the R^2 indicates that the experiments are in accordance with the theory. Also, equation (6) predicts that the slope of the line should be equal to ($\mu_e LH/W$). Using the known values of the dimensions of the channel and the electrode, and the numerical value of the slope obtained from the fit, one may indirectly measure the electrophoretic mobility of the protein (equivalent to our flow measurement strategy). Performing the above exercise with the current data yields a value of -17.8×10^{-5} cm^2 V^{-1} s^{-1} for the electrophoretic mobility of the protein (BSA) in DI water at a pH of 7. (The negative sign indicates that the protein has a net negative charge at that pH.) The corresponding value in literature **[7]** was found to be - 12×10^{-5} cm^2 V^{-1} s^{-1}. Thus our mathematical model, while qualitatively valid, seems to be lacking in the ability to

correctly predict the degree of separation based on the flow rate (or vice-versa). Although tolerances in the dimensions of the separator would have contributed to the observed error, we believe that the main source of error lies in the primitive fluid flow model that we used and the assumption of a uniform electric field.

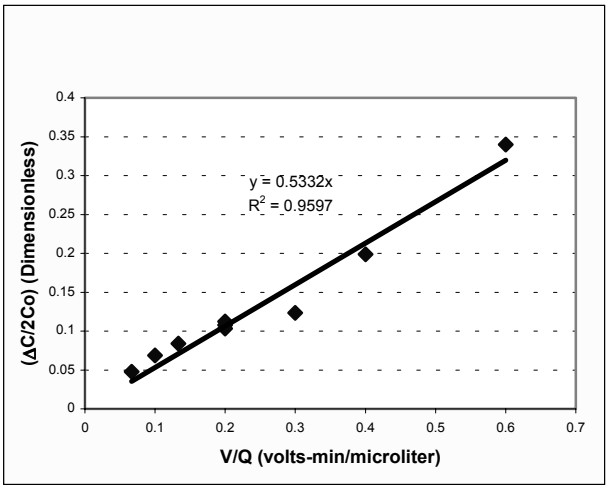

***Figure 5**:Plot of ($\Delta C/2C_0$) vs. (V/Q)*

CONCLUSIONS

In this work, we have proposed a novel method of measuring the flow rates of charged suspensions. The basic idea, i.e. that the degree of separation achieved by electrophoresis of the dissolved or suspended charged species in a direction perpendicular to the fluid flow could be used as a predictor for the flow rate of the fluid, was borne out by experiments conducted on a milli-scale prototype. Further, it may be noted that the SAF meter contains no moving parts, and that it specifically takes into account physical phenomena predominant at the micro-scale (such as electrophoresis and diffusion). These features make it ideal for incorporation into micro-fluidic systems. Besides, should the need arise, the SAF meter may also be calibrated as a mass-flow meter (for the suspended/dissolved species) since we measure concentrations to calculate the flow rate.

ONGOING AND FUTURE WORK

As may be obvious from the data presented, our experiments thus far have covered only a part of the possible values for the degree of separation (viz. from zero to one) that can be effected by the separator. We are currently conducting experiments similar to the ones described (but with different flow-rates and applied voltages) to make our demonstration more complete. Our technique at present also lacks an inbuilt (on-line) analyzer. We are currently building a milli-scale prototype of the analyzer to demonstrate the ability to measure protein concentrations using electrical techniques. Once this is done, smaller versions of the SAF meter (capable of measuring lower flow-rates) will be (micro)fabricated. The sensors thus fabricated will also have to be tested and characterized.

Acknowledgements

This work has been supported by a University of Minnesota Graduate School Grant in Aid (to VHB). We also gratefully acknowledge guidance received from Dr. Antonio Baldi and experimental help being received from Brett Hautala and Sarah Setiawan.

REFERENCES

1. D.L.Polla et al., "Microdevices in Medicine", *Annual Reviews of Biomedical Engineering*, 2 (2000), pp. 571-576

2. I. Walther, B. van der Schoot, M. Boillat, O Muller, and A Cogoli, "Microtechnology in space bioreactors", *Chimia*, 53,3 (1999) pp 75-80

3 N. Cheremisinoff, Applied Fluid Flow Measurement, M. Decker, New-York, 1979.

4 F.M. Ausubel et al. Current Protocols in Molecular Biology, John Wiley and Sons, 2001

5. N. Nandi and B. Bagchi, "Anomalous dielectric relaxation of aqueous protein solutions", *The Journal of Physical Chemistry A*, 102, 43, (1998), pp. 8217-82221

6. S. Beretta, G. Ghirico, and G. Baldini, "Short-range interactions of globular proteins at high ionic strength", *Macromolecules* 33, 23, (2000) pp 8663-70.

7. N.G. Douglas, A.A. Humffray, H.R.C. Pratt, and G.W. Stevens, "Electrophoretic Mobility of proteins and protein mixtures" *Chemical Engineering Science* 50, 5 (1995) pp.743-754

Polymer based Actuator for nozzle-diffuser Pumps in Plastic Microfluidic Systems

P. Sethu and C. H. Mastrangelo

Center for Wireless Integrated Microsystems
Department of Electrical Engineering and Computer Science
University of Michigan
Ann Arbor, MI 48109

ABSTRACT

Plastic casting is an inexpensive technique for fabrication of disposable microfluidic systems for various biochemical applications. Pumps are critical for these systems and have a wide variety of applications including transport, mixing, cooling and creating pressure differences. In this paper we discuss the fabrication of a valve-less nozzle-diffuser pump integrated within a plastic microfluidic system. The pump uses thermal actuation, making use of the large volumetric expansion of a wax patch when it transitions from a solid to liquid phase. Testing of fabricated devices show maximum flow rates of 70 nl/min and generation of pressure heads of up to 1400 Pa.

INTRODUCTION

Miniaturized systems for biochemical assays [1] significantly reduce cycle times, reagent costs and labor intensity. Plastic microfabrication techniques have been extensively used to build inexpensive analysis systems since most of these systems are targeted for single use applications. Commonly used techniques include injection molding, hot embossing and casting. Plastic casting has been shown to be an inexpensive technique capable of producing high-resolution features like channels and reservoirs that are required to construct these systems. Different materials like PDMS [2], Epoxies [3], Acrylics, etc. have been used for casting. We use epoxies to cast our systems since they provide a rigid platform and have high glass transition temperatures that allow for conventional photolithography to pattern electrodes and heaters.

Pumps in microfluidic systems are essential for fluid transport but also have other applications like mixing, cooling and pressure generation. Pumping is achieved using different actuation mechanisms like electrohydrodynamic, electrokinetic, mechanical displacement and bubble generation, which have all been miniaturized and used for pumping in glass and silicon based microsystems. Ideally we would like pumps to be inexpensive, simple to fabricate and easy to integrate within a plastic microfluidic system with high flow rates and pressure generation at relatively low power. For most bioassay applications bubble generation and local heating of the liquid are undesirable.

We have developed a wax-based actuator similar to the actuator developed by Carlen et. al. [4] that makes use of the large volumetric expansion of wax when it transitions from solid to liquid phase to generate large volume displacement that can be used to pump liquids. The fabrication technique is simple and inexpensive and these actuators can be mass fabricated on cast epoxy substrates. The actuator is used in a nozzle-diffuser [5] arrangement in series to generate a net fluid flow. The pump uses relatively low power and there is no bubble generation and operates at low temperatures (< 65°C at the surface of the wax patch).

The device is fabricated using epoxy casting. The channel structure is cast on one substrate and the wax actuator is fabricated using a screen-printing technique on another substrate. Both the substrates are then bonded together using an adhesive bonding technique.

THEORY

Nozzle-diffuser pumps are built by coupling a nozzle, pumping chamber and diffuser together in series. The volume of fluid in the pumping chamber is periodically varied using an oscillating pressure (actuator). The kinetic energy of the fluid (velocity) is converted to potential energy (pressure) in both the nozzle and diffuser, but the efficiency of this process is much greater in the diffuser direction thus discharging more fluid through the diffuser. If Q_d is the discharge through the diffuser and Q_n the discharge through the nozzle then an increase in the chamber volume causes $|Q_d| > |Q_n|$ and a decrease in the chamber volume causes $|Q_d| < |Q_n|$ resulting in a net pumping action (Fig 1.).

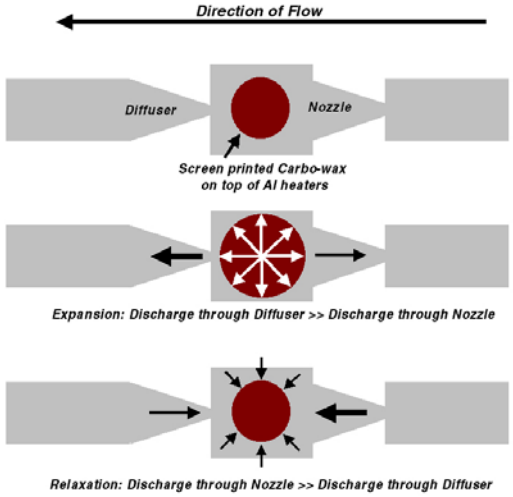

Figure 1. *Principle of operation of nozzle-diffuser pumps and fluid flow with increasing and decreasing chamber volume*

The pressure differences across the nozzle and diffuser are given by:

$$\Delta P_d = \frac{\rho v_d^2 \xi_d}{2} \quad \text{and} \quad \Delta P_n = \frac{\rho v_n^2 \xi_n}{2}$$

0-9640024-4-2/hh2002/$20©2002TRF
DOI 10.31438/trf.hh2002.81

where:

ΔP_d and ΔP_n = Pressure difference across the diffuser and nozzle
ξ_d and ξ_n = Pressure loss coefficients for the diffuser and nozzle
v_d and v_n = Average velocities at the diffuser and nozzle

If ξ_d is less than ξ_n then pumping will occur in the direction of the diffuser [6]. These pumps cannot generate large pressure and are suitable for low-pressure fluidic systems.

And the volume flow rate is given by:

$$Q = 2Vf \frac{[(\xi_n/\xi_d)^{1/2} - 1]}{(\xi_n/\xi_d)^{1/2} + 1}$$

where:

Q = Volume flow rate
V = Volume variation per cycle
f = pulse frequency

FABRICATION

The device is fabricated using plastic casting as shown in Figure 2. The substrate with the channels, reservoirs, pumping chamber and the nozzle-diffuser geometry is made using epoxy EPOTEK 301-2 FL (fig 2.a) which is a clear optical grade epoxy (> 97% light transmission), low viscosity (125 cpS at 100 rpm) and glass transition temperature T_g = 65^{O}C. A stamper with 50 μm tall negative replicas of the channels, chamber and nozzle-diffuser geometry is formed by etching a silicon wafer using a deep RIE process (SF_6 160 sscm, C_4F_8 80 sscm O_2 13 sscm, coil power 800W, platen power 600W). The stamper is then vapor deposited with a 1 μm thick parylene layer, which serves as a release layer to aid separation of the cured plastic from the stamper. The silicon stamper is sandwiched with a Teflon O-ring (2 mm thick) and flat polypropylene disc in an aluminum mold. The epoxy resin is injected into the sandwich and maintained at 80^{0}C for 3 hours and then the cured plastic is released. Access holes for channels and electrodes are drilled using a micro drill press

A second epoxy substrate is made by casting using EPOTEK –314 a clear, high temperature epoxy (T_g = 150^{O}C). This epoxy is essential since metal heaters and contacts are patterned on the surface using conventional photolithography techniques and the plastic must be able to withstand temperatures of up to 110^{O}C. This substrate is made using the same technique but a blank silicon wafer with a 1 μm thick parylene layer is used instead of the etched stamper. The released substrate is then vapor deposited with a 0.5 μm thick parylene layer to improve adhesion of metals to the surface. Then metal layers Cr/Al (500 A^o/ 2000 A^o) are evaporated onto the substrate and heaters and contacts are patterned using photolithography.

The wax patches are made using a screen-printing process. The screen-printing process uses a 15 μm thick stencil screen made of aluminum with precision cut openings for printing. The plastic substrate (EPOTEK 314) with the patterned heaters is then mounted on the screen printer and the openings on the screen and the heaters on the substrate are aligned and the screen is locked in position. The wax used is Poly ethylene Glycol, MW 8000 (PEG 8000, DOW Chemical Co.) which is a water-soluble carbowax

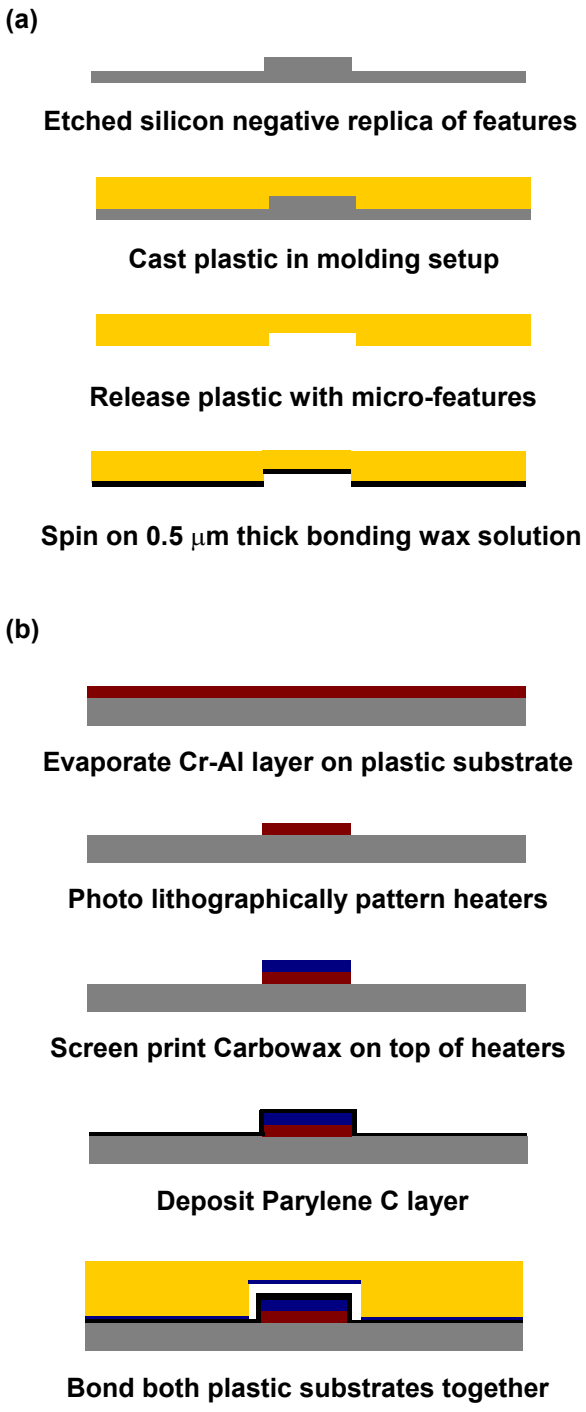

Figure 2 (a) and (b). *Shown is the process flow for fabrication of the channel structure and wax actuator respectively. The two substrates are then bonded using an adhesive*

with a melting point of 65^{O}C and a volumetric expansion of 30% on transition from solid to liquid. The wax is melted by heating to 80 ^{O}C and then screen-printed using a teflon squeegee (2kPa pressure, 8 ft/min speed). The substrate is released and placed in an oven at 65 ^{O}C for 3 minutes for the wax to re flow and to obtain a smooth surface. The contacts for the heaters are masked using

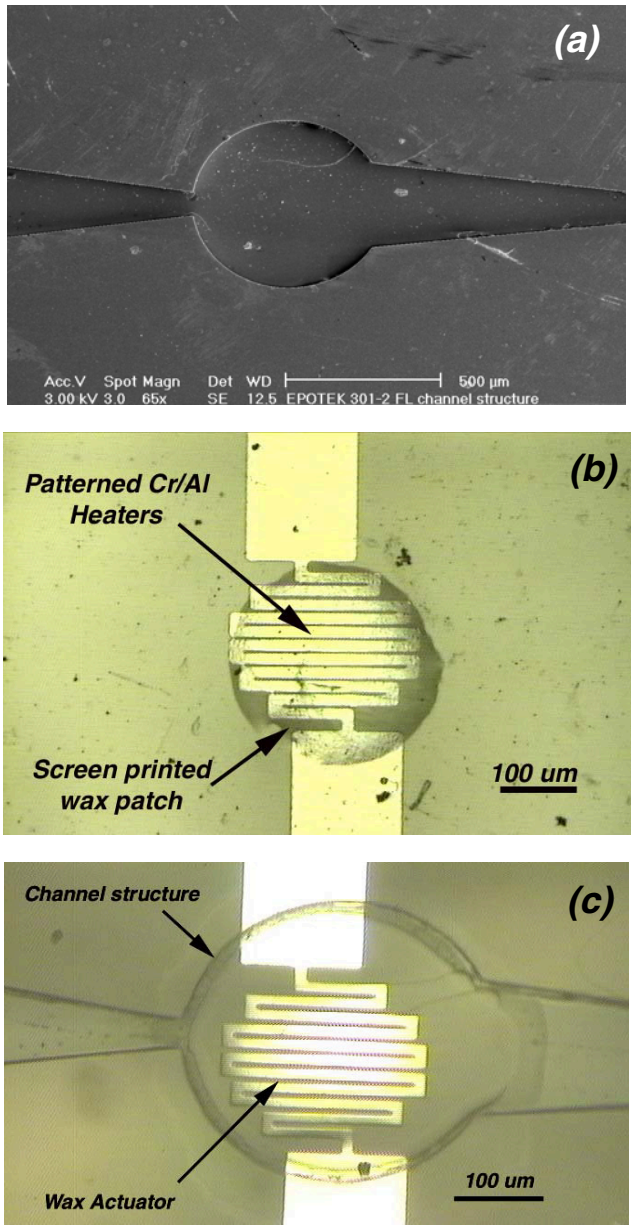

Figure 3. (a) *Pictures show SEM of EPOTEK 301-2 FL substrate with chamber, channel and nozzle-diffuser geometry, (b) wax actuator on EPOTEK 314 substrate and (c) bonded nozzle-diffuser pump respectively.*

masking tape and the substrate is coated with 4 µm thick parylene C layer. Figure 3.b. shows a picture of 15 µm tall wax actuator.

The EPOTEK 301-2 FL substrate with the channels and nozzle-diffuser geometry is spin coated with a 0.5 µm thick layer of bonding wax solution (Blanchard bonding wax dissolved 1:1 by weight in acetone) and then aligned and bonded to the EPOTEK 314 substrate with the wax actuator using a laminator with the rollers at 60 ^{o}C, speed of 2 ft/min and gauge of 4 mm. The access holes for the electrodes are filled with conductive epoxy and cured at room temperature for 18 hours. Figure 3.c. shows a picture of the bonded device. The pumping chamber is 500 µm in diameter with diffuser angle of 30 ^{o} and channel widths of 400 µm.

EXPERIMENTAL DETAILS

Tests were performed first on the fabricated wax actuator to obtain the deflection heights under different applied voltages. Individual dies with the fabricated actuator were wire bonded to a PC board and the PC board was setup under a ZYGO optical surface profilometer. The surface of the actuator corresponding to the different applied voltages was imaged.

Experiments were also performed to calculate the flow rate and pumping pressure. Flow rate calculations were performed by introducing 3 µm diameter beads into the pumping liquid (water) and observing the time taken by the particle to travel a fixed distance. In order to eliminate pressure effects a channel design as shown in figure 4.a. was used. The system is filled with the pumping liquid with particles and then the outlet ports are sealed to eliminate pressure effects. The liquid flows in a circular fashion as shown in the picture and by observing the path traced by the particle flow rate is calculated for different applied voltage and pulse frequency. A second experiment was performed to calculate pumping pressure. The channels were redesigned to allow for a column of air to be trapped as shown in figure 4.b. The column is placed after the diffuser and the compression of air in the column due to pumping pressure for an applied voltage and different pulse frequencies is calculated.

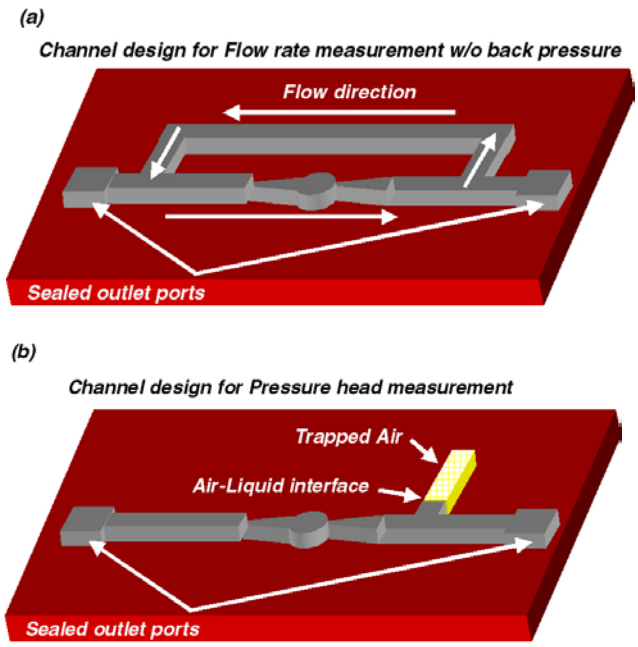

Figure 4. *Channel design for calculation of (a) flow rate with zero back pressure and (b) pumping pressure.*

RESULTS AND DISCUSSION

The surface profiles obtained due to deflection of the membrane on expansion of wax at different applied voltages is shown in figure 5. Voltages up to 5V were applied and a maximum deflection of 25 µm was obtained at 5V. The deflecting 4 µm parylene C membrane containing the wax failed at higher voltages due to high stress produced on wax expansion.

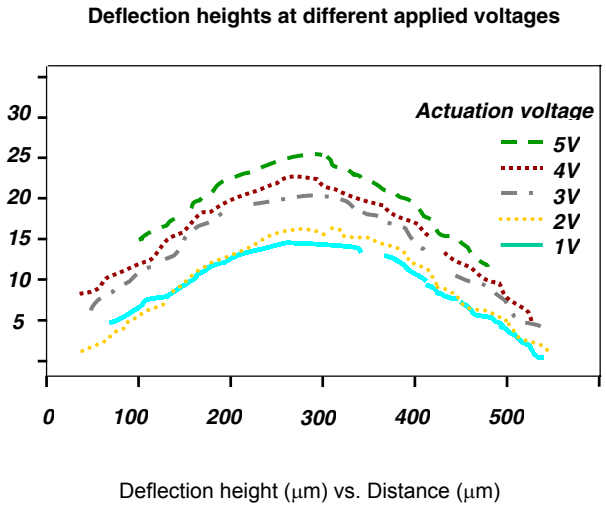

Figure 5. *Optical profiles of the deflection heights of the wax actuator surface obtained at different voltages using a ZYGO optical surface profilometer.*

Flow rate measurements were done using the setup as shown in figure 4(a) and the particle flow velocities were measured for different applied voltages and pulse frequencies. Volume flow rates were calculated and plotted (figure 6) and maximum flow rates of 70 nl/min was obtained at an applied voltage of 5V and pulse frequency of 1 Hz. The wax-based actuator operates best at lower frequencies (0.5 Hz – 1.5 Hz). This is due to the slow response time of the carbowax. High frequencies result in low volumetric expansion and hence low volume displacement because the heat generated due to the pulse is not sufficient to melt the entire wax patch.

Experiments were performed to calculate the pumping pressure that can be generated using the nozzle-diffuser pump. The setup used was as shown in figure 4(b). The channels were filled with fluid and air was trapped in a column, which is located just past the diffuser. The pump was operated at 5V and the pulse frequency was varied. The pressure generated was calculated from the data obtained for height of the trapped air column. Maximum pumping pressure of 1400 Pa was obtained at a frequency of 1 Hz. Results are plotted in figure 7.

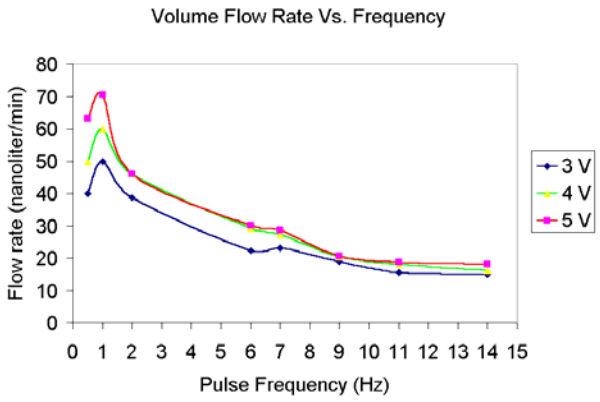

Figure 6. *Volume flow rates obtained at different pulse frequencies for different applied voltages*

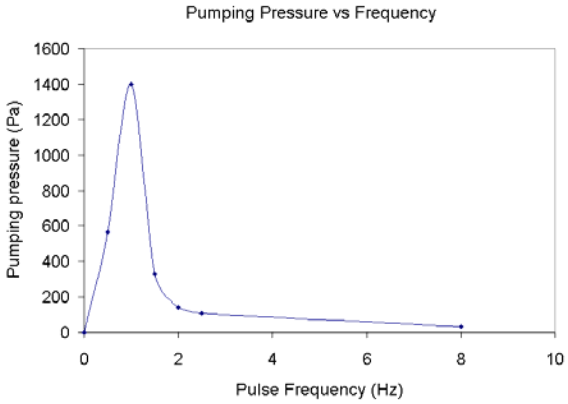

Figure 7. *Pumping pressure generated at 5V plotted for different pulse frequencies*

CONCLUSIONS

We have developed a simple technique for fabrication and integration of low cost actuators within a disposable plastic microfluidic system for nozzle diffuser pumps. The pump operates at relatively low power and has maximum flow rates of about 70 nl/min and pumping pressures of 1400 Pa, which makes it attractive for applications like fluid transport, cooling and mixing in microfluidic systems.

ACKNOWLEDGEMENTS

This research work was supported by DARPA MEMS program under the contract F30602-98-2-0197.

REFERENCES

1. M. A. Burns, et. al., "An integrated nanoliter DNA analysis device", *Science, 282,* 253-258, (1998).

2. E. Kim, et. al., "Polymer microstructures formed by molding in capillaries", *Nature, 376,* 347, (1996).

3. P. Sethu, et. al., "Fabrication of Genetic Analysis Microsystems using Plastic Microcasting", *Technical Digest of the 2000 Solid-State Sensor and Actuator Workshop*, Hilton Head Isl., SC, pp. 175 – 179, (2000).

4. E. T. Carlen and C. H. Mastrangelo, "Simple, High Actuation Power, Thermally Activated Paraffin Microactuator", *International conference on Solid-State Sensors and Actuators (Transducers 99)*, Japan, 2, 1364-1367, (1999).

5. E. Stemme and G. Stemme, "A Valveless Diffuser/Nozzle based Fluid Pump", *Sensors and Actuators*, A339, pp. 159-167. (1993).

6. Olsson, et. al., "Valve-Less Planar Pumps fabricated using thermoplastic replication", *Technical Digest of the 10th annual workshop of Micro Electro Mechanical Systems*, Nagoya, Japan, pp. 305 – 310, (1997).

INTERFACE THERMAL CONDUCTANCE FOR MICROACTUATED DEVICES

Woo-Bin Song and Joseph J. Talghader
Department of Electrical and Computer Engineering, University of Minnesota
Minneapolis, MN 55455

ABSTRACT

In this paper, the thermal contact conductance (TCC) of actuated (snapped-down) interfaces is characterized, perhaps for the first time. The TCC of a typical polysilicon/nitride interface brought together by electrostatic actuation is about 6.0 W/(K-cm^2) in air and 9.5 W/(K-cm^2) under vacuum. For every device tested, the TCC is higher in vacuum than in air. This is in stark contrast to the behavior of bulk interfaces and may be the result of decreased solid-solid contact area in air caused by the pressure of the interstitial fluid. It is also found that the TCC increases with electrostatic pressure, as expected from bulk theory, but appears to be largely unaffected by monolayer surface treatments.

INTRODUCTION

The thermal contact conductance is the most critical parameter in the study of heat transfer across interfaces. While the TCC has been exhaustively studied for interfaces in microelectronics packaging**[1]**, the TCC of MEMS interfaces has not been explored, perhaps because standard measurement techniques are difficult to apply in surface micromachining. Despite this, the design of many micromachined devices such as AFM thermal probes**[2]** and uncooled IR detectors**[3]** could be significantly improved by understanding their TCCs. In addition, recent work has shown the possibility of creating micromechanical devices with electronically tunable thermal conductance**[4]**, where the tuning range would be greatly extended with the high TCCs measured here.

Theoretical models for the TCC indicate that there are two primary paths for heat conduction between two interfaces at room temperature**[5]**: one is solid-solid conduction through the contact points, and the other is conduction through an interstitial material, if there is one. Measurements of macroscopic interfaces have shown that TCCs measured in vacuum are significantly lower than those measured with an interstitial gas, usually air**[6]**. This behavior is typically attributed to the additional conduction paths offered by the air. To date, the modeling and experimentation for the TCC have been developed for interfaces that have surface roughness on the order of a micron or so. Little or no data appears to exist on the TCC of interfaces with roughness multiple orders of magnitude less than this value. However, the mechanical interface between a micromachined device and its underlying substrate, as shown in Fig. 1, may have surface roughness on the order of a few nanometers or less. In this paper, it is shown that the TCC of micromechanical interfaces is extremely high compared to traditional interfaces and is decreased by the presence of air, in contrast to measurements on larger, rougher interfaces. The data suggests that trapped interstitial gas at nanometer roughness serves primarily to reduce the solid-solid contact area, overwhelming its traditional role in providing alternate conduction paths.

BACKGROUND

Given the experimental difficulties of mechanically handling very small devices, measurements of the TCC of microstructures cannot be performed in the same way as is done on the macroscale. Large samples are often measured using a mechanical press that brings two cylindrical bars together with a specified force**[7-9]**. The bars are often contained within a vacuum chamber so that the interface can be tested under vacuum in order to isolate a value for the solid-solid conductance in the absence of the interstitial gas. Heat is applied to one cylinder and a series of thermocouples measure the temperature along the axial direction of the bars.

For micromachined structures, one does not have direct mechanical control of the interface, but rather one must move it indirectly through the application of a voltage (assuming electrostatic actuation). A technique commonly used to calculate the thermal conductance of bolometers**[10]** and micromirrors**[11]** can be modified to obtain the TCC of actuated interfaces. Consider a square microstructure supported by two long thin beams, as shown in Fig. 1. The microstructure is designed such that the plate has a moderate resistance and the beams have negligible resistance. If a current flows through the device, then the dissipated power is $P_{in} = I^2R$. The resistance, R, depends on temperature via the equation, $R=R_0[1+\alpha\Delta T]$, where R_0 is initial resistance at ambient temperature, α is the temperature coefficient of resistance (TCR), and ΔT is the difference in temperature between the device and its surroundings. If the microstructure is designed so that its supports are of uniform cross-section, then the heat dissipated out of the structure will be $P_{out}=G\Delta T$, where G is the thermal conductance in W/K. In steady-state, $P_{in}=P_{out}$, and we can write the expression,

$$\frac{1}{R} = \frac{1}{R_0} - \frac{\alpha}{G} I^2 \qquad (1),$$

which relates the slope of 1/R vs. I^2 to the thermal conductance of a microstructure. By designing a microstructure to have very low thermal conductance when suspended above the surface of a substrate, one can make the TCC the dominant heat transfer mechanism when the device is actuated. The measurement of G is then a probe of TCC. An image of the apparatus used in these measurements is shown in Fig. 2.

EXPERIMENT AND DISCUSSION

The test structures used to measure the TCC are fabricated in a standard surface micromachining process. First a 500nm silicon nitride layer is deposited on top of a silicon substrate followed by 1500nm of silicon dioxide, which is patterned and etched to form anchor points for a 750nm thick doped polysilicon layer. The polysilicon is etched into square plates supported by two 24μm wide beams. The beams vary in length from 50μm to 150μm, and the plates vary in size from 150μm to 200μm square. The support beams are coated with gold to insure that the vast majority of the device resistance occurs in

0-9640024-4-2/hh2002/$20©2002TRF
DOI 10.31438/trf.hh2002.82

Solid-State Sensors, Actuators, and Microsystems Workshop
Hilton Head Island, South Carolina, June 2-6, 2002

the plate. The various geometric and material parameters for the structures are shown in Table I.

If a plate in air is not actuated, the thermal conductance, G, is dominated by air conduction. For example, a 200μm square plate in air as shown in Fig. 1 has a measured conductance of 1.77×10^{-4} W/K. Under vacuum, a structure is dominated by conduction through the support arms. Fig. 4 shows that the vacuum conductance for a 200μm plate with 75μm supports in vacuum is 1.77×10^{-5} W/K. When a structure is snapped-down, the thermal conductance is dominated by the TCC, as seen by the greater than an order of magnitude change in both air and vacuum in Figs. 3 and 4. The magnitude of the TCCs in air and vacuum are about $6.0\text{x}10^{4}$W/(K-m^2) and $9.5\text{x}10^{4}$W/(K-m^2), respectively. Other samples can vary by as much as a factor of 2 from these values but the air/vacuum trend is always the same. All of these numbers are significantly greater than that seen with traditional interfaces, even compared to metal-metal structures**[6,8,9,12]**. The pressure of the contact can be extracted from the applied voltage at actuation, which corresponds to a force of $F=\varepsilon AV^2/d^2$, where F is the force, ε is the dielectric constant of silicon nitride, A is the contact (plate) area, V is the applied voltage, and d is the gap spacing defined by the thickness of the silicon nitride insulator. A typical value for an applied voltage of 65V is about 1MPa. The samples show a monotonic increase in TCC with pressure in both vacuum and air, as expected from bulk theory.

In addition to providing quantitative data for the TCC, Figs. 3 and 4 show the surprising result that the TCC is higher when the structures are actuated in a vacuum. This behavior is very different from bulk interfaces where the TCC decreases in vacuum. For any given test structure, it is found that the TCC is smallest when the device is snapped down in air, increases if the vacuum chamber is pumped out with the device snapped down, and increases still further if the structure is then released and re-actuated. An example is shown in Table 2. Fig. 6 shows results for the TCC vs. increasing pressure where the pressure is applied electrostatically by increasing the voltage after snap-down. The TCC increases continuously with pressure as expected from theory.

Based on these observations, we propose that this behavior is due to trapped air in the small interstitial voids, whose primary contribution to the TCC is reduced solid-solid contact area rather than the provision of an efficient alternate conduction path. In-use stiction studies provide some independent support for this explanation. While very few of the test structures become stuck to the substrate during repeated actuation in air, this behavior occurs to the majority of devices actuated in vacuum. Since stiction is related to the Van der Waals interactions of contact points at the interface, the difference in stiction for an individual device suggests a difference in solid-solid contact area.

One probable origin of these behaviors is the relative surface roughness of the interfaces. As mentioned in the introduction, most previous TCC studies have been done on samples with surface roughness on the order of 0.1 to 10μm. The roughness of the samples used in this study is on the order of a few nanometers. For example, the structure whose data is shown in Figures 3 and 4 has a roughness of 8nm, as measured by optical interferometry. It is interesting to speculate that the contact area and TCC at such small roughnesses may be dominated more by the energy and viscosity of the interfacial fluid than by the topography of the interface itself.

CONCLUSIONS

The TCC of micromechanical interfaces has been measured electronically, using the change in resistance with current as a probe of the underlying thermal conductivity. From these measurements it is found that the TCC of microactuated interfaces, which have a film roughness on the order of nanometers, is significantly higher than seen in rougher macroscopic interfaces. Surface treatments, such as self-assembling monolayers, had little effect on the TCC. In addition, the TCC of micromachined completely differently in the presence of an interstitial gas (air), namely the conductance increases as the interstitial gas is removed from the interface. Measurements suggest that the air reduces the solid-solid contact area, superseding its traditional role in providing an alternative conduction path.

REFERENCES

1. See for example, A. D. Kraus and A. Bar-Cohen, *Thermal Analysis and Control of Electronic Equipment*, McGraw-Hill, 1983, pp. 199-214.
2. W. P. King, T.W. Kenny, K.E.Goodson, et. al., "Atomic force microscope cantilevers for combined thermomechanical data writing and reading," *Applied Physics Letters*, *78*, 1300, (2001).
3. R. A. Wood, "Monolithic silicon microbolometer arrays," Ch. 3 in *Uncooled Infrared Imaging Systems and Arrays*, Ed. P. W. Kruse, and D. D. Skatrud, *Semiconductors and Semimetals*, vol. 47, Academic Press, New York, 1997, pp. 43-121.
4. R.N. Supino and J. J. Talghader, "Electrostatic control of microstructure thermal conductivity," *Applied Physics Letters*, *78*, 1778, (2001).
5. S. M. S. Wahid, and C. V. Madhusudana, "Gap conductance in contact heat transfer*", International Journal of Heat and Mass Transfer*, *43,* 4383 (2000).
6. J. J. Salgon, F. Robbe-Valloire, J. Blouet, and J. Bransier, "A mechanical and geometrical approach to thermal contact resistance," *International Journal of Heat and Mass Transfer, 40*, 1121 (1997).
7. L. S. Fletcher, P. A. Smuda, and D. A. Gyorog, American Institute of Aeronautics and Astronautics Journal, *7*, 1302 (1969).
8. K. E. Parmenter and E. Marschall, "Influence of surface preparation on thermal contact conductance of stainless steel and aluminum," *Experimental Heat Transfer, 8*, 195 (1995).
9. E. G. Wolff and D. A. Schneider, "Prediction of thermal contact resistance between polished surfaces," *International Journal of Heat and Mass Transfer, 41*, 3469 (1998).
10. P. Eriksson, J. Y. Andersson, and G. Stemme, "Thermal Characterization of Surface-Micromachined Silicon Nitride Membranes for Thermal Infrared Detectors," *Journal of Microelectromechanical Systems***,** *6,* 55, (1997).
11. R. N. Supino and J. J. Talghader, "Average optical power monitoring in micromirrors," *IEEE Journal of Selected Topics in Quantum Electronics, 8*, 1 (2002).
12. T. Aikawa and W. O. Winer, "Thermal contact conductance across Si_3N_4-Si_3N_4 contact," *Wear, 177*, 25 (1994).

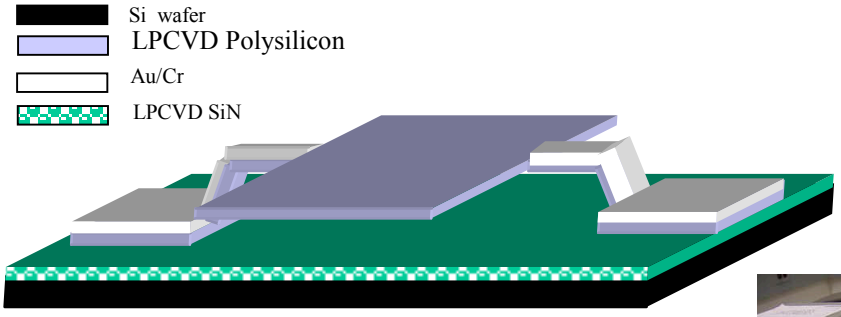

(a)

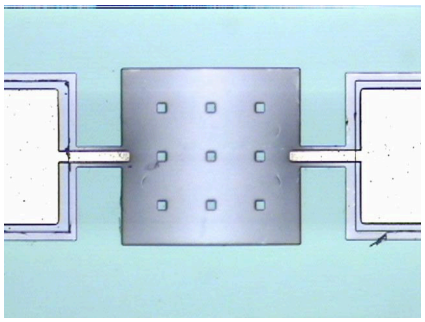

(b)

Fig. 1 – Diagram(a) and optical micrograph(b) of a test structure used in this study to measure thermal contact conductance.

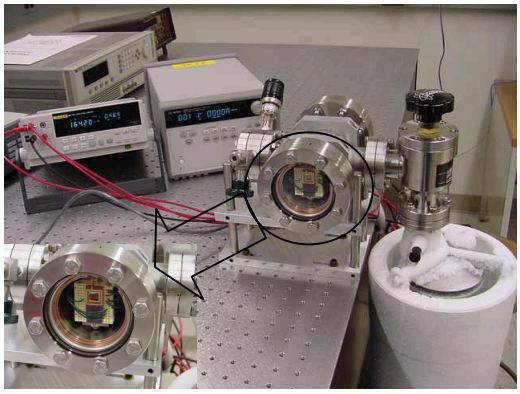

Fig. 2 – Image of vacuum system used to measure TCC. The optical window allows optical measurements to be made in addition to electrical ones.

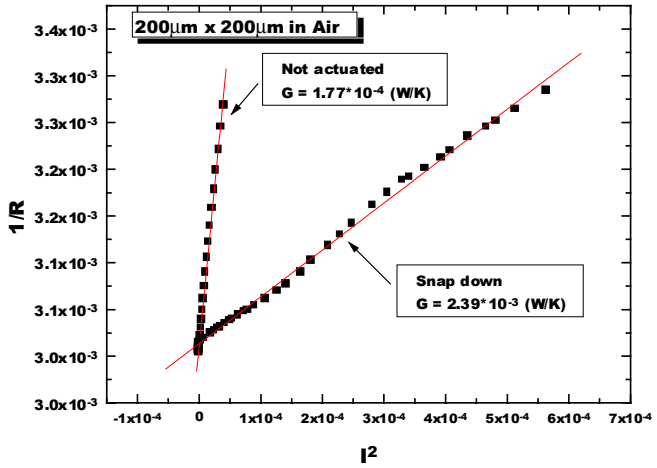

Fig. 3 – 1/R vs, I^2 for a test structure in air. The relatively flat curve is the measurement for the unactuated device, while the steeply sloped curve is for the snap-down condition. The slope of the lines is inversely proportional to the thermal conductance. Note that the TCC measured in this manner (G under snap-down) is more than an order of magnitude greater than typical values seen with bulk metal interfaces. At least part of this difference is likely due to the extreme flatness (<2nm) of the polysilicon and nitride surfaces.

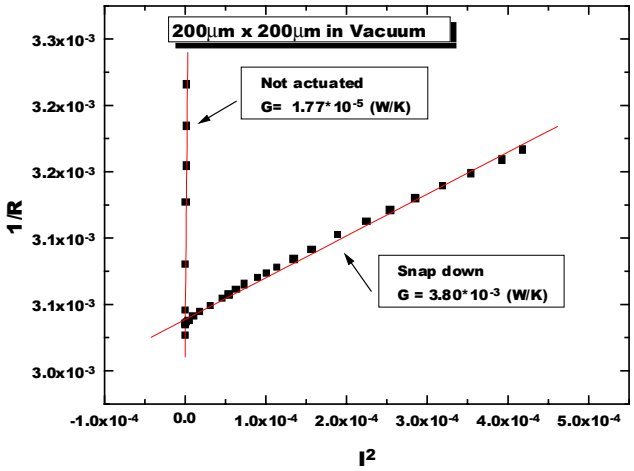

Fig. 4 - 1/R vs, I^2 for the test structure in Fig. 3 in vacuum. The relatively flat curve is the measurement for the unactuated device, while the steeply sloped curve is for the snap-down condition. Note that the TCC in vacuum (G under snap-down) is significantly higher than the TCC in air from Fig. 3. This behavior is different from that of bulk interfaces. It implies that the interstitial fluid in actuated MEMS devices reduces the solid-solid contact area of the polysilicon-nitride interface. The alternate conduction path provided by the air is not efficient enough to overcome the reduction in contact area.

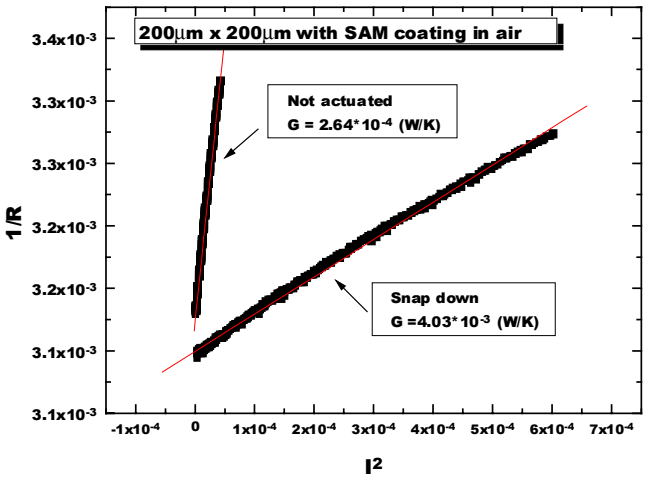

Fig. 5 - 1/R vs, I^2 for a SAM-coated test structure in air. The relatively flat curve is the measurement for the unactuated device, while the steeply sloped curve is for the snap-down condition. The snap-down voltage is 50V. The TCC measured for this device (and others) falls within the range of typical TCCs measured for devices without the SAM.

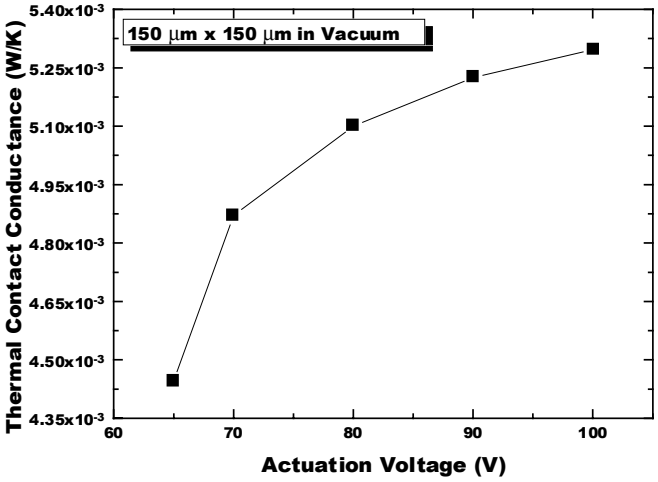

Fig. 6 – Thermal conductance vs. actuation voltage for a test structure in vacuum. All of the applied voltages are greater than the snap-down condition. The increased voltage across the insulator causes increased attractive force, so this curve is an indirect measurement of the TCC vs. pressure.

Parameter	Value
Size of Mirror	200 µm x 200 µm and 150 µm x 150 µm
Thickness of Mirror	0.75 µm
Length of supporting arm	75 µm and 100 µm
Width of supporting arm	24 µm
Air Gap Spacing	1.5 µm
Thermal Conductivity of Polysilicon (G)	0.29 W/(cm-K)
Thermal Conductivity of dry air at 20°C	0.0002564 W/(cm-K)
Density of Polysilicon	2.3 g/cm^3
Specific heat of Polysilicon	0.92 J/(g-K)
Temperature Coefficient of Resistance (á)	-0.12% (K^{-1})
Resistance (R), Basic Resistance (R_0) at T_0, and Current (I)	

Table 1 – Parameters and variable definitions used in this study.

Thermal Contact Conductance of 150 µm x 150 µm mirror (unit: W/K)	
In Air with the mirror snapped down	2.69 x 10^{-3}
In pumping out with the mirror snapped down	2.94 x 10^{-3}
In vacuum, released and re-actuated	3.10 x 10^{-3}

Table 2 – TCC of a 150µm x 150µm test structure in air and in vacuum. The test structure is first snapped-down and measured in air. While still snapped down, the vacuum chamber is pumped out (to below 50mTorr) and allowed to stabilize. The TCC is then remeasured and found to be higher. The device is released and then reactuated, and the TCC is found to be yet higher. These measurements may be explained if some interstitial fluid (air) is trapped under the device by the actuation and then released when the actuation voltage is removed. The effect is even larger for larger area devices.

MICRO-POWER WIRELESS TRANSMITTER WITH PRINTED BATTERY FOR MEMS SENSING AND COMMUNICATION APPLICATIONS

Michael Suster, Darrin J. Young, and Wen H. Ko
Department of EECS, Case Western Reserve University
Cleveland, Ohio 44106

ABSTRACT

A micro-power tunnel-diode-based LC-tuned oscillator architecture is proposed for MEMS sensing and wireless data transmission applications. The prototype sensing and transmitting module employs a MEMS capacitive pressure sensor performing pressure to frequency conversion and a miniature on-board loop serving as the inductor for the LC tank and also a transmitting antenna. The system achieves a reliable telemetry performance over a distance of three meters with a total power consumption of 65 μW. Printed zinc-air batteries have been demonstrated as a power supply for the prototype system. The battery provides an output voltage around 1.4 V and can sustain a continuous telemetry operation over five hours.

INTRODUCTION

Low power miniature wireless sensor communication network is critical for biomedical implants and various industrial applications. A number of wireless modules have been developed to provide data telemetry capabilities for MEMS sensors used for biomedical implants [1, 2, 3, 4, 5, 6, 7, 8]. In these applications, sensors such as pressure sensors, strain gauge transducers, etc. are interfaced with active electronic circuits that convert the sensing information to frequency [3, 8] or to voltage [4, 5, 6, 7], which is further digitized before wireless transmission. Passive RF powering and telemetry schemes are commonly implemented with inductive coupling coils, which, however, result in a limited telemetry distance on the order of several inches [1, 3, 4, 5, 8, 9]. Active transmitters employing RF oscillators achieve an enhanced telemetry distance but with the penalty of excessive power dissipation [7]. Therefore, it is highly desirable to develop and demonstrate low power miniature sensing and data transmission systems achieving an enhanced telemetry distance. In this paper, we report a 65 μW wireless sensor communication module achieving a telemetry distance of three meters, suitable for various biomedical and industrial applications.

MEMS SENSOR AND TRANSMIITER

Figure 1 presents the proposed architecture, which consists of a tunnel-diode-based LC-tuned oscillator transmitter employing a MEMS capacitive pressure sensor interfaced with an on-board loop inductor also functioning as a transmission antenna, attractive for system implementation. The negative resistance of the tunnel diode under a proper bias condition compensates the tank loss, thus developing an oscillation. The oscillator output frequency is determined by the LC tank resonance. The MEMS capacitive pressure sensor thus converts the pressure information to a capacitance change resulting in the oscillator output frequency variation, which can be detected by an external receiver. This pressure to frequency modulation scheme is attractive for achieving a reliable data transmission compared to other amplitude modulation techniques.

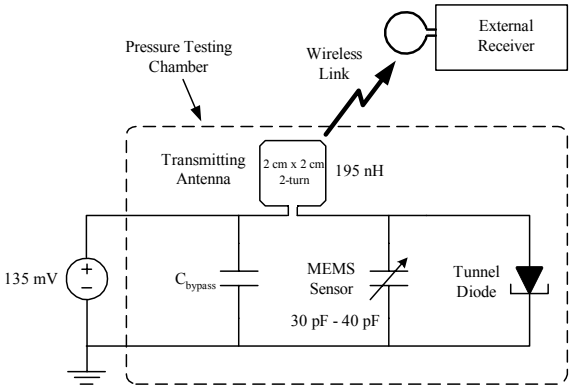

Figure 1. *Wireless Transmitter Architecture*

Figure 2 shows a typical I-V characteristic of a commercial germanium tunnel diode employed in the current prototype design.

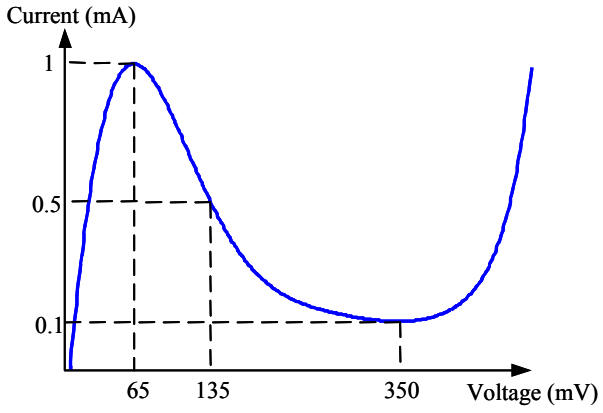

Figure 2. *Tunnel Diode I-V Curve*

A DC supply voltage around 135 mV is typically needed to bias the diode thus significantly minimizing the power dissipation, a key advantage over other conventional electronic oscillator designs. The device consumes an

0-9640024-4-2/hh2002/$20©2002TRF
DOI 10.31438/trf.hh2002.83

average DC current of 0.5 mA, hence 65 µW power dissipation. A reduced power consumption is expected through using small-current diodes. Silicon tunnel diodes can also be used for implementing the prototype system and are attractive for potential integration with silicon-based MEMS pressure sensors, achieving further system miniaturization.

Figure 3 shows a photo of the MEMS sensor and transmitter prototype system.

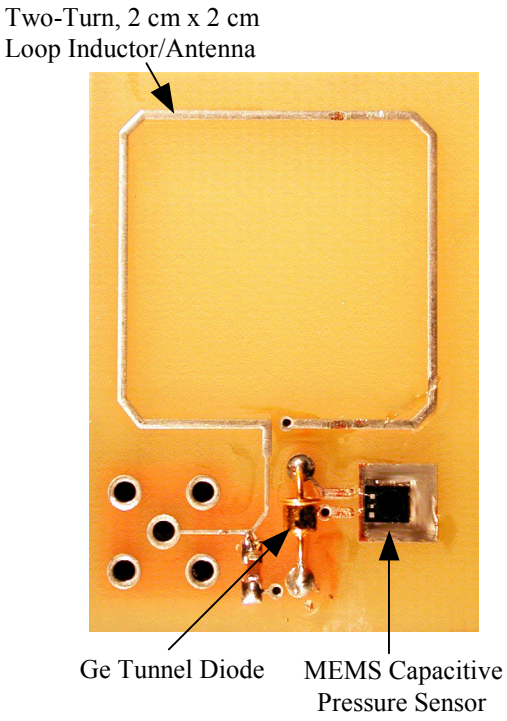

Figure 3. *Photo of Prototype System*

It consists of a MEMS pressure sensor interfaced with a discrete germanium tunnel diode and an on-board square loop inductor through wire bonding. A MEMS touch-mode capacitive pressure sensor [10] is employed as a demonstration vehicle for the current prototype. Figure 4 presents a simplified cross-section view of the device with detailed fabrication process outlined in [10].

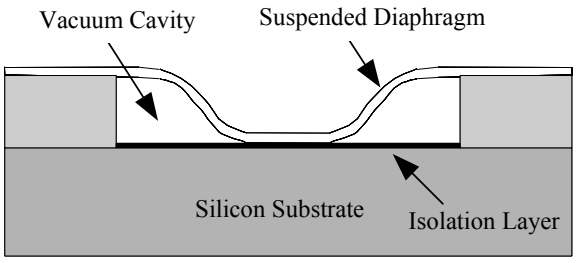

Figure 4. *Sensor Cross-Section View*

The sensor consists of an edge-clamped silicon diaphragm over a vacuum cavity. The diaphragm deflects under an increasing external pressure and touches the substrate causing a linear increase in sensor capacitance value beyond the touch point pressure. Figure 5 shows a typical device characteristic response between the capacitance value and applied pressure.

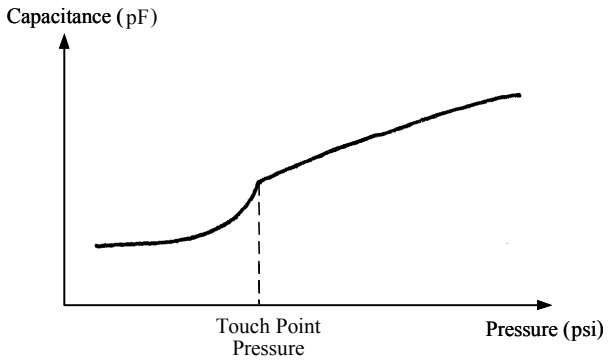

Figure 5. *MEMS Pressure Sensor Characteristic*

A MEMS pressure sensor consisting of a circular diaphragm with a diameter of 0.8 mm, shown in Figure 6, exhibits a touch point pressure of 8 psi and capacitance values ranging from 30 pF at 2 psi to 40 pF at 32 psi (absolute pressures), a useful range for biomedical applications.

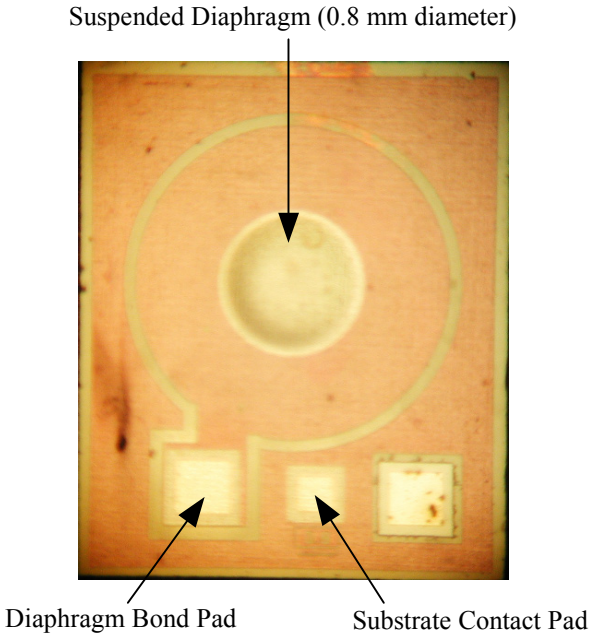

Figure 6. *MEMS Pressure Sensor*

This device is interfaced with a two-turn, 2 cm x 2 cm on-board square loop providing 195 nH inductance value to form the LC tank circuit as illustrated in Figures 1 and 3. The loop is also used as a transmission antenna for data telemetry. The current loop size is constrained by the operating frequency around 50 MHz, limited by the large resistive loss of the pressure sensor. Increased operating frequencies can be achieved with redesigned high-Q capacitive sensors thus reducing the loop dimension, attractive for system miniaturization. High-Q capacitive

sensors and loop inductors are also critical for minimizing bias current required for tunnel diodes, crucial for low power applications.

EXPERIMENT RESULTS

Figure 7 shows the experiment setup for the wireless sensor communication module.

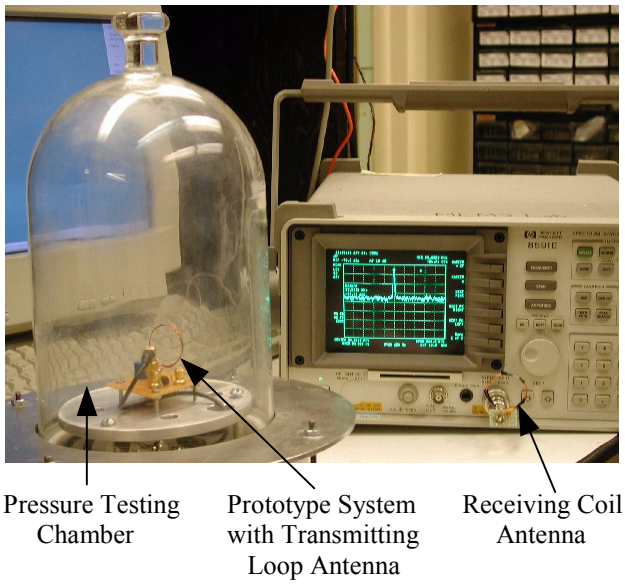

Figure 7. *Experiment Setup*

The prototype system is positioned inside a pressure test chamber. Wound wire coil loops were used for the early designs and are shown here for illustration purpose. A spectrum analyzer is used as an external receiver with a receiving loop antenna, similar to the transmission one, tuned to the nominal operating frequency and connected to the input port through a buffer. The oscillator operates around 53.5 MHz at 1 atm. Its frequency varies from 55.3 MHz to 51.1 MHz through pressure increase from 3 psi to 33 psi (absolute pressures), as shown in Figure 8.

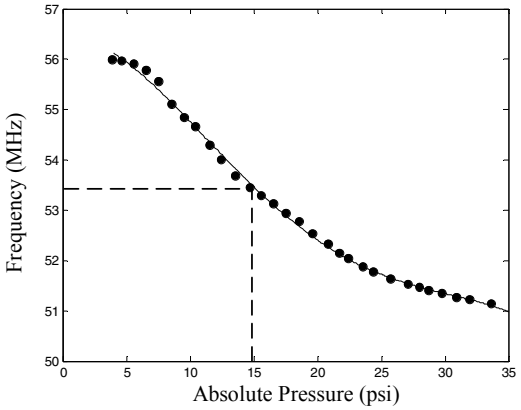

Figure 8. *Oscillator Frequency Versus Pressure*

Figure 9 presents the received power versus telemetry distance under 1 atm, indicating that the spectrum analyzer can receive incoming signal with an SNR of at least 10 dB over a distance of three meters.

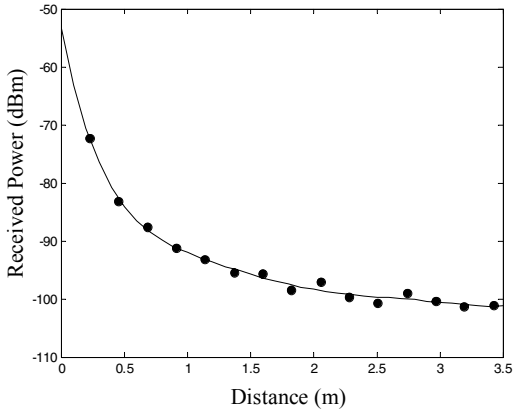

Figure 9. *Received Power Versus Distance*

Figure 10 shows a corresponding received power spectrum at that distance. An extended communication range is expected through using a more sensitive receiver.

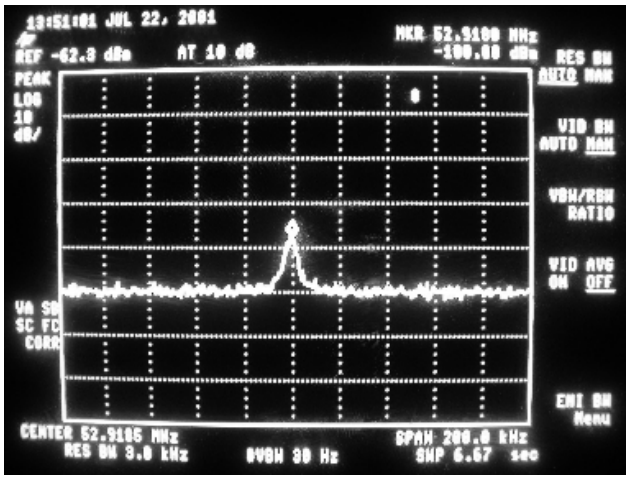

Figure 10. *Received Power Spectrum*

Further system miniaturization has also been explored by replacing the MEMS capacitive sensor with a high-Q fixed-value capacitor. An increased operating frequency of 80 MHz has been obtained with a two-turn, 0.5 cm x 0.5 cm on-board square loop inductor. The system achieves a telemetry distance of 0.7 meters with the same power dissipation.

A long-term frequency drift of 25 KHz over a few days has been observed in the prototype, limiting the system resolution. An improved design employing sensor electronic interface and analog to digital conversion circuits combined with a tunnel-diode-based frequency-shift-keying (FSK) oscillator transmitter will be considered in the future to achieve a low-power high-resolution performance.

Printed zinc-air batteries, designed and fabricated by the Chemical Engineering Department at CWRU, have been demonstrated as a power supply for the prototype system. The battery, consisting of stacked layers of electrodes and electrolyte with a dimension of approximately 2.5 cm x 2.5 cm x 1 mm, provides an output voltage around 1.4 V and can sustain a continuous operation of wireless module over five hours. A bias network, shown in Figure 11, is designed to properly bias the tunnel-diode oscillator transmitter [11].

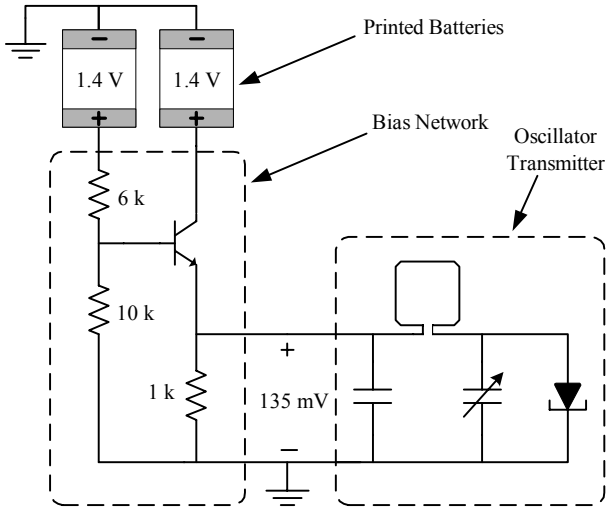

Figure 11. *Oscillator Transmitter with Printed Battery Bias Network*

The thick film printing process is attractive for potentially implementing the batteries on the wireless module substrate, miniaturizing overall system size. The oscillator power dissipation can be further minimized through using a low duty cycle clock to activate the transmission system for small bandwidth signals. This technique will increase the system operation time by orders of magnitude.

CONCLUSION

Tunnel-diode-based oscillator transmitter is attractive for low-power MEMS sensing and telemetry applications. The prototype wireless sensing and communication module achieves a three-meter telemetry distance with 65 μW power dissipation. The proposed architecture can also serve as a low-power telemetry platform for general sensing and wireless communication applications. Printed zinc-air batteries are capable of powering the prototype design over five hours and can be potentially implemented on the wireless module substrate to achieve system miniaturization.

ACKNOWLEDGMENT

The authors would like to thank Professor Chung-Chiun Liu of the Chemical Engineering Department at Case Western Reserve University for supplying the printed zinc-air batteries. This work is partially supported by NASA under Glennan Microsystem Initiative. Travel support has been generously provided by the Transducers Research Foundation and by the DARPA MEMS and DARPA BioFlips programs.

REFERENCES

[1] W-H Ko and M-R Neuman, "Implant Biotelemetry and Microelectronics," *Science*, Vol.15, No. 3773, pp. 351-360, April, 1967.

[2] W-H Ko, E.Yon, S. Mabrouk and J. Hynecek, "Taped-on Heart Rate and Electrocardiogram Telemetry Transmitters," *J. of Asso. for Advancement of Med. Instrumentation*, Vol.5, No.5, pp268-272, 1971.

[3] S. Chatzandroulis, D. Tsoukalas, and P. A. Neukomm, "A miniature Pressure System with a Capacitive Sensor and a Passive Telemetry Link for Use in Implantable Applications," *Journal of MicroElectroMechanical Systems*, Vol. 9, No. 1, pp. 18-23, March, 2000.

[4] D. Dudenbostel, K-L Krieger, C. Candler, and R. Laur, "A New Passive CMOS Telemetry Chip To Receive Power and Transmit Data For A Wide Range of Sensor Applications," *1997 International Conference on Solid-State Sensor and Actuators*, pp. 995-998, June, 1997.

[5] C. Hierold, et al, "Implantable Low Power Integrated Pressure Sensor System For Minimal Invasive Telemetric Patient Monitoring," *Proceeding of MEMS 98*, pp. 568-573, January, 1998.

[6] Q Huang and M. Oberle, "A 0.5-mW Passive Telemetry IC for Biomedical Applications," *IEEE Journal of Solid-State Circuits*, Vol. 33, No. 7, pp. 937-946, July, 1998.

[7] J-B Begueret, M. R. Benbrahim, Z. Li, F. Rodes, and J-P Dom, "Converters Dedicated to Long-Term Monitoring of Strain Gauge Transducers," *IEEE Journal of Solid-State Circuits*, Vol. 32, No. 3, pp. 349-356, March, 1997.

[8] K. Stangel, S. Kolnsberg, D. Hammerschmidt, B. J. Hosticka, H. K. Trieu, and W. Mokwa, "A Programmable Intraocular CMOS Pressure Sensor System Implant," *IEEE Journal of Solid-State Circuits*, Vol. 36, No. 7, pp. 1094-1100, July, 2001.

[9] M. A. Fonseca, J. M. English, M. von Arx, and M. G. Allen, "High Temperature Characterization of Ceramic Pressure Sensors," *Proceedings of the 11th International Conference on Solid-State Sensors and Actuators,* pp. 486-489, June, 2001.

[10] W. H. Ko and Q. Wang, "Touch Mode Capacitive Pressure Sensors," *Sensors and Actuators* 75 (1999), pp. 242-251.

[11] W. F. Chow, *Principles of Tunnel Diode Circuit*, Wiley, New York, 1964.

QUALITY FACTOR ENHANCEMENT OF *IN SITU* ANNEALING CANTILEVERS

A. Tewary, K.Y. Yasumura†, T.D. Stowe‡, T.W. Kenny
Department of Applied Physics and Department of Mechanical Engineering,
Stanford University
*Stanford, CA 94305**

D. Rugar
IBM Almaden Research Center
San Jose, CA 95120

ABSTRACT

Ultrathin cantilevers with force resolution in the aN/$\sqrt{Hz}$ range have been used in a variety of microscopy experiments to detect extremely small forces. Such cantilevers face a fundamental limit to their ability to detect small forces: thermomechanical noise. For ultrathin cantilever structures, improvement of the Q is vital to the improvement of force resolution. Heat treatments to remove surface contaminants have demonstrated improvements in the room temperature Q. In order to utilize this treatment in actual experiments, *in situ* self-annealing single-crystal silicon cantilevers have been fabricated. With 100 mW of applied power, 0.25 μm thick "self-annealing" cantilevers have demonstrated a three-fold improvement in their room temperature Q. By integrating the thermal noise spectrum of the cantilevers while they are being annealed, it is deduced that the cantilever is heated to 1000±100 K.

I. INTRODUCTION

Ultrathin single crystal silicon cantilevers have been used to demonstrate attonewton force resolution [1]. The force resolution of these cantilevers is limited by thermomechanical noise. This noise is a result of the cantilever being in thermal equilibrium with its surroundings. The stronger the coupling to the surrounding heat bath, the larger the force noise of the cantilever oscillator. For a cantilever of width w, length l, and thickness t at a temperature T, the minimum detectable force is given by

$$F_{min} = \sqrt{\frac{wt^2}{lQ}}\sqrt{k_B T B}(E\rho)^{1/4} \qquad (1)$$

where Q is the quality factor of the oscillator, k_B is Boltzman's constant, B is the measurement bandwidth, E is the Young's modulus of the cantilever material, and ρ is the cantilever mass density. Because of this geometrical dependence on force resolution, effort has focused on creating smaller oscillators while maintaining high Q. Prior work on arrays of silicon and silicon nitride cantilevers has shown, however, that Q is linearly dependent on t and independent of w and l [2–4]. Such behavior indicates that surface loss mechanisms dominate the Q of micron to submicron-thick cantilever structures with resonance frequencies in the 1-10 kHz have exhibited quality factors of 10^4 [5]. High frequency, 2000 Å-thick paddle-shaped oscillators with resonance frequencies in the 1-10 MHz range have exhibited quality factors of 10^3 [6]. This result is consistent with the observed reduction in quality factor with decreasing oscillator dimensions.

Annealing has been shown by Wang to improve the quality factor of surface micromachined polysilicon resonator structures for use in rf MEMS devices by a factor of six [7]. Integrated heating paths in surface micromachined polysilicon comb-drive resonators were used to improve the Q and to frequency trim the resonators. Additionally, Chui [8] has shown that applying heating power as little as 1 mW can heat a micromachined cantilever designed for use in thermomechanical data storage to a temperature of 800 °C in vacuum causing the cantilever to glow in the visible wavelength range. The use of *in situ* annealing techniques have also been used to desorb surface oxides [9] and to repair damage in silicon due to implantation induced damage [10].

In complex experiments where the cantilevers being used require alignment to other experimental features such as magnets, optical fibers, or microstrip resonators this can present numerous problems if the quality factor is allowed to degrade before the cantilever can be aligned. Additionally, some experiments may be conducted over time scales of days or possibly weeks. It would be impractical to open up the measurement chamber, apply additional heat treatments to the cantilever, and then realign the cantilever to the optical fiber interferometer and experimental system. An ideal method to heat the cantilevers and to prevent adsorbates from recollecting on the cantilever surface would be to heat them within the vacuum chamber just prior to using them. This can be accomplished through the use of *in situ* "self-annealing" cantilevers.

II. SELF-ANNEALING CANTILEVERS

The *in situ* annealing cantilevers used in these experiments were fabricated at the Stanford Nanofabrication Facility. Figure 1 shows an SEM of a self-annealing cantilever made from single-crystal silicon. The cantilever is connected to the substrate silicon die by two legs. In order to measure the cantilever motion, a target paddle is located between the cantilever legs to which an optical fiber interferometer is aligned. Included into the cantilever design is a current path and two heater regions. The current paths on the cantilever lead to large bonding regions on the cantilever substrate die. Wirebonding to this region allows a current to flow through the cantilever's two heater regions. Figure 2 shows a side view of an annealing cantilever. In this figure the overhanging region of the substrate is clearly visible. This overhang is used to thermally and mechanically isolate the heater regions and the cantilever from the rest of the support die. The two openings in the substrate also help to thermally, electrically, and mechanically isolate the cantilever structure. A closer view of the cantilever base and substrate region is also shown in Fig. 2. The cantilever leg is 0.25 μm thick, 200 μm long, and 2 μm wide while the heater region is ~4 μm thick at its thickest region. The cantilever resonance frequency is 5.3 kHz and is clamped at the overhanging substrate.

*Travel support for A.Tewary has been generously provided by the Transducers Research Foundation and by the DARPA MEMS and DARPA BioFlips programs.; †Now at Iolon Inc., San Jose, CA 95131; ‡Now at Light Connect, Inc., Newark, CA 94560

0-9640024-4-2/hh2002/$20©2002TRF
DOI 10.31438/trf.hh2002.84

Solid-State Sensors, Actuators, and Microsystems Workshop
Hilton Head Island, South Carolina, June 2-6, 2002

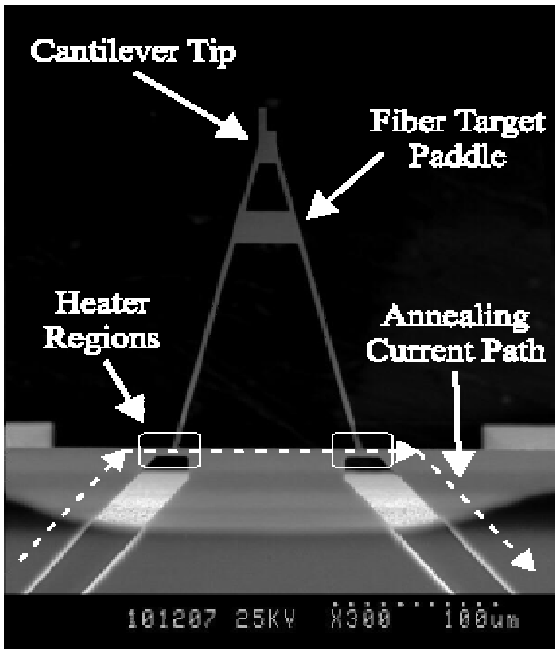

FIG. 1: *SEM of a self-annealing cantilever. These cantilevers have a targeting paddle to which the fiber optic interferometer is aligned. Also shown is a current path and two resistive heater regions that warm when an annealing current is applied to the cantilever.*

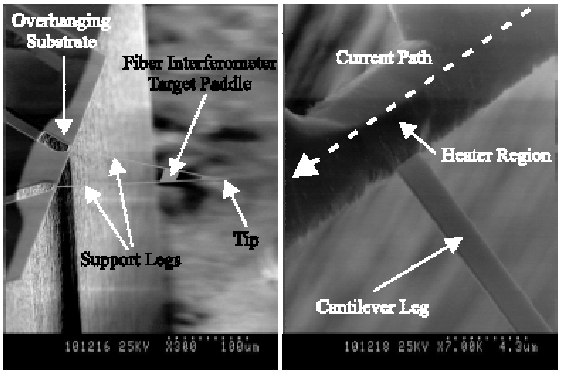

FIG. 2: *Side view SEM of an annealing cantilever. The thick overhanging substrate is mechanically isolated from the cantilever, and allows the cantilever to be thermally isolated from the substrate. Also shown is a close-up view of one of the heater regions at the base of a cantilever leg.*

The heater regions on the ledge were implanted with boron to a density of $10^{15} - 10^{16}$ cm^{-3}. The cantilever current path was doped to a density of 10^{19} cm^{-3}. A detailed description of the fabrication sequence can be found in Stowe [11].

In order to measure the cantilever motion a 1310 nm optical fiber interferometer was used [12]. This interferometer had a measured displacement resolution of 2×10^{-3} Å$/\sqrt{Hz}$. Dissipation measurements were performed using a ring-down technique in which the cantilevers were excited into motion using a self-oscillation circuit. This circuit filtered, amplified, and phase shifted the cantilever's thermal noise signal and then fed this signal to a piezoelectric stack. A current source is used to provide the annealing current to the cantilever under study.

When applying the annealing current to the self-annealing cantilever, care must be taken to avoid thermally shocking the cantilever. The annealing current cannot be turned on and off in a binary fashion to the desired current level. Instantaneously switching on or off the current results in crack formation at the base of the cantilever that causes the resistance to increase and the cantilever leg to burn out. In order to prevent thermally shocking the cantilever, the current source was programmed to provide a gentle rise, current plateau, and then a gentle decrease in the annealing current.

III. CANTILEVER TEMPERATURE DETERMINATION

Only a small volume of silicon is warmed when applying the annealing current, thus a direct temperature measurement of the cantilever sample stage will not produce an accurate temperature measurement of the self-annealing cantilever.

In order to obtain a measurement of the cantilever temperature during the high temperature anneal, the thermal noise motion of the cantilever is measured by integration of the thermal noise spectrum of the cantilever [13, 14]. From the equipartition theorem, the amount of thermal energy per mode of a simple harmonic oscillator is $\frac{1}{2}k_BT = \frac{1}{2}k\left\langle x^2\right\rangle$ where k_B is Boltzman's constant, T is the cantilever temperature, k is the cantilever spring constant, and x is the cantilever displacement. Thus, by first measuring the thermal noise displacement at room temperature (300 K), estimates of the cantilever temperature at higher temperatures can be made because $T_1/T_2 = \left\langle x_1^2\right\rangle / \left\langle x_2^2\right\rangle$. The estimates of the cantilever temperature obtained using this method have an uncertainty of $\pm 100K$. Experiments were performed to anneal the cantilevers at progressively higher temperatures and measure the new resonance frequency and quality factor after the cantilever has been allowed to cool back down to room temperature.

In order to be sure that the temperature that is measured at the base of the cantilever accurately represents the temperature of the entire cantilever, calculations of the estimated thermal conductance of the cantilever can be made. The cantilever shown in Fig. 1 will have power lost due to thermal conduction from the heater regions to the die substrate and from blackbody radiation to its surroundings. It can be shown, however, that the conductance through the overhanging substrate dominates the cantilever equilibrium temperature [15]. Because the experiment is performed in vacuum, thermal convection will not be considered. If an annealing current is applied to the cantilever such that 100 mW of power is applied at the heater regions heat will flow through the overhanging support to the larger substrate die. From Fig. 1 estimates of the geometry of the conductance path can be obtained. A more accurate calculation would require finite element analysis, but for this purpose it will be shown that estimates are sufficient. The heater region of the cantilever has a thickness of 4 μm, an estimated length of 10 μm to the overhanging substrate region, and a width of 4 μm. Because there are two leg regions the estimated thermal conductance of the annealing cantilever from the heater region to the substrate die is given by

$$G = 2\kappa\frac{tw}{l} \tag{2}$$

where κ is the thermal conductivity of silicon at elevated temperatures (at 1000 K, $\kappa \sim 30$ W/m/K), t is the thickness of the overhanging substrate region, w is the width of the conductance path, and l is the length of the conductance path. With the above values for the annealing cantilever, $G = 9.6 \times 10^{-5}$ W/K. If 100 mW of annealing power is applied to the heater regions of the cantilever, the estimated total temperature rise would be $\Delta T = P/G$ =1040 K. This is in good agreement with the

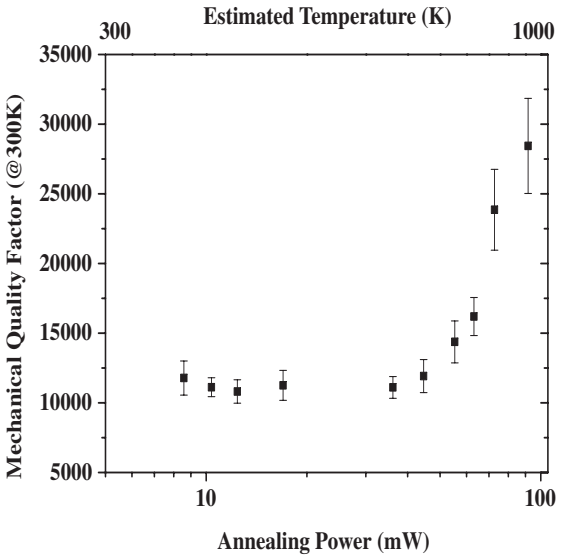

FIG. 3: *Room temperature Q after application of an annealing current for a 200 μm-long cantilever. The cantilever temperature at the highest annealing power was estimated to be* 1000±100 *K. This temperature was determined by integrating the cantilever thermal noise.*

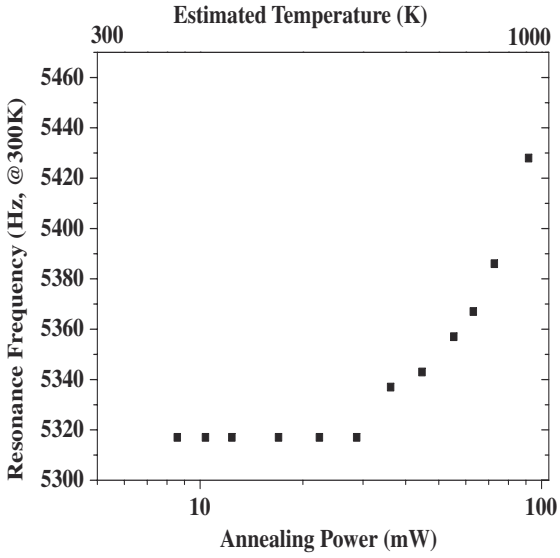

FIG. 4: *Room temperature cantilever resonance frequency for a 200 μm-long cantilever, after application of an annealing current that heats the cantilever to the temperature T. The cantilever temperature at the highest annealing power was estimated to be* 1000±100 *K. This temperature was estimated by integrating the cantilever thermal motion.*

temperature increase measured from the thermal noise motion for the self-annealing cantilevers.

IV. ANNEALING EXPERIMENTS

Figure 3 shows a plot of cantilever Q versus annealing power for the 200 μm-long cantilever that is shown in Fig. 1. The Q measurements were obtained after the cantilever cooled back down to room temperature after each anneal. The values plotted each represent an average of 10 measurements and the error bars are calculated from the standard deviation. A plot of room temperature frequency after that cantilever has been heated at a certain power is shown in Fig. 4. The annealing soak time was 10 minutes for each data point in Figs. 3 and 4. In this plot, the high temperature was measured by integration of the thermal noise spectrum. The final data point corresponds to an estimated temperature of 1000±100 K.

In Fig. 3 it is seen that the Q does not start to increase until ∼40 mW of annealing power is applied. This increase in the Q coincides with a large frequency jump (∼20 Hz) observed in the room temperature frequency of the cantilevers. The presence of adsorbed contaminants on the surface of the cantilever causes the resonance frequency to decrease because they add mass to the entire system. Thus, the removal of these contaminants reduces the mass of the system and causes the observed frequency increase when 40 mW of annealing power is applied. The increase in Q and f are not due solely to the removal of water from the cantilever surfaces. Even though water is removed during the high temperature anneals, it quickly recollects onto the cantilever surface after the annealing current is removed. The easily removed adsorbed contaminants, however, do not quickly return to the cantilever surface resulting in a higher Q value. Possible surface adsorbates include organics introduced in the processing of the cantilevers or during exposure to the laboratory atmosphere. It is not until 100 mW of annealing power is applied to the cantilever that a three-fold improvement in Q is seen. This applied annealing power corresponds to a temperature of 1000±100 K, as obtained from the integration of the thermal noise motion. Such high temperatures can begin to desorb oxide from the surface of the silicon cantilevers [9, 16].

After the initial annealing experiments, the cantilever was exposed to air then replaced in the vacuum chamber. After the exposure to air, the Q returned to its pre-annealed value. However, the resonance frequency was 14 Hz less than the pre-annealed value. Because the spring constant k and the thickness t are related such that $k \propto t^3$ and the mass m and the thickness are related such that $m \propto t$, the resonance frequency change is expected to depend linearly with cantilever thickness, since $\omega = \sqrt{k/m} \propto t$. It is therefore expected that as the surface oxide is removed, the thickness of the silicon would decrease thereby resulting in a reduction of the cantilever resonance frequency.

The annealing experiments were conducted on cantilevers of different lengths. Although the experiments were conducted on cantilevers of varying initial quality factors, strong trends are evident. In each case in which the cantilever temperature reached ∼ 1000 K, the Q was enhanced. Furthermore, the resonant frequency of each cantilever was increased by ∼ 3%, which is consistent with mass-loading materials being removed from the surface of the cantilever. The enhanced Q and the resonance frequency shifts were observed in cantilevers that had been stored in air and in cantilevers that had been stored in a dry nitrogen gas environment. Effects of annealing on the Q and resonance frequency for a 350 μm-long cantilever are shown in Fig. 5 and Fig. 6, and for a 300 μm-long cantilever are shown in Fig. 7, and Fig. 8. Both of these cantilevers are 0.25 μm thick and 2 μm wide, and each has a heater region that is ∼4 μm thick. The Q values plotted represent an average of 10 measurements and the error bars are calculated from the standard deviation. The results indicate that the improvements in quality factor by approximately a factor of three can be seen in cantilevers with varying initial values of Q and resonant frequency.

Arai has studied similar cantilever systems. Arai performed *in situ* annealing of a silicon piezoresistive cantilever to remove tip contaminants and oxide layers that can reduce image quality when used in an AFM [9]. The piezoresistive AFM cantilever was heated by passing mA level current through the

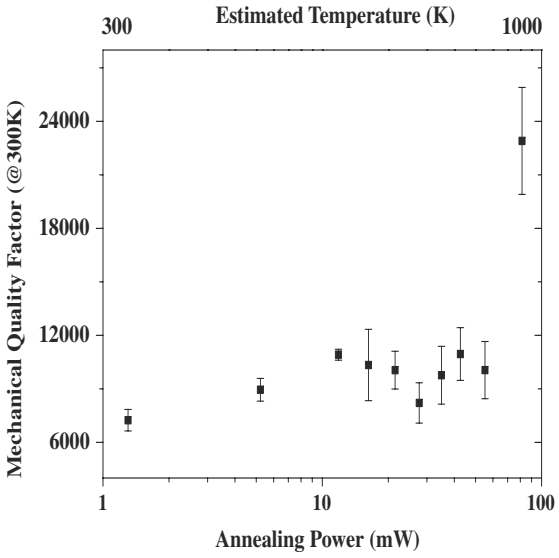

FIG. 5: *Room temperature Q vs. Power for 350 μm-long cantilever. The cantilever temperature at the highest annealing power was estimated to be* 1000±100 *K. The Q increased from its initial value of ∼7000 to a final value of ∼22000 with the anneal. This cantilever was stored in a dry nitrogen gas environment and had minimal exposure to the laboratory atmosphere. Since additional contaminants were not introduced on the surface, the initial Q is high.*

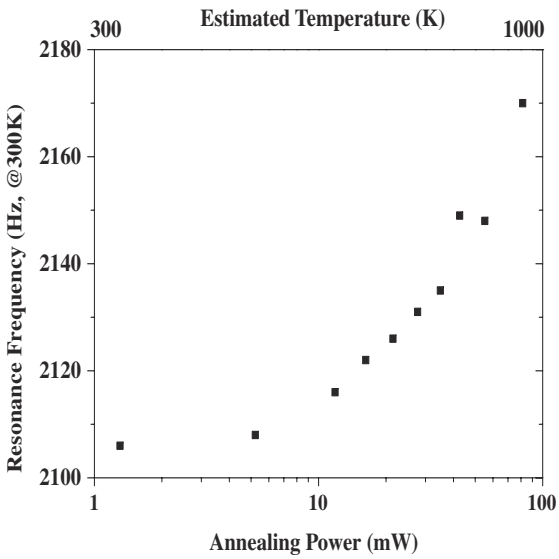

FIG. 6: *Room temperature Resonance Frequency vs. Power for 350 μm-long cantilever. The cantilever temperature at the highest annealing power was estimated to be* 1000±100 *K.*

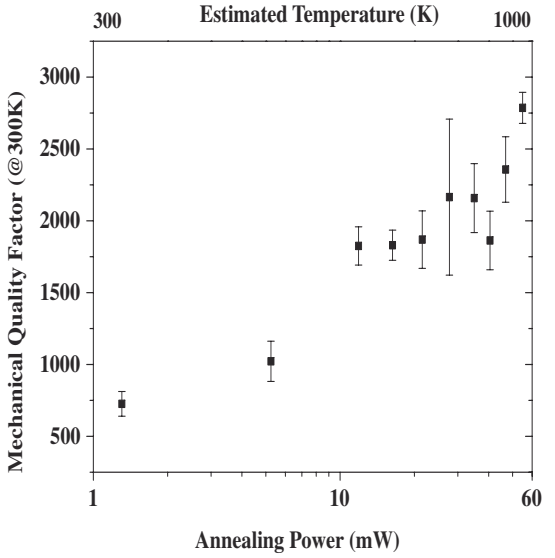

FIG. 7: *Room temperature Q vs. Power for 300 μm-long cantilever. The cantilever temperature at the highest annealing power was estimated to be* 1000±100 *K. The Q increased from its initial value of ∼700 to a final value of ∼2700. This cantilever was exposed to the laboratory atmosphere for an extended period of time, which may have contributed to the high level of contamination on the surface.*

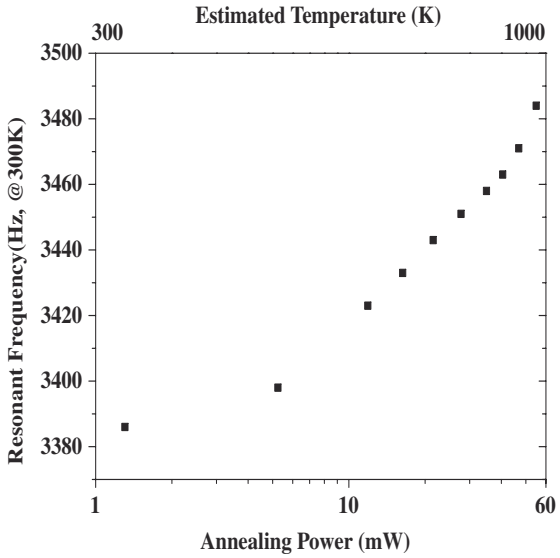

FIG. 8: Room temperature Resonance Frequency vs. Power for 300 μm-long cantilever. The cantilever temperature at the highest annealing power was estimated to be 1000±100 K.

resistive regions of the cantilever heating it up to 650 °C. The cantilever temperature was measured using an optical pyrometer with an uncertainty of ±50 K. Arai's experiments were performed at a vacuum chamber pressure of 8×10^{-11} torr. Auger electron spectroscopy of the cantilever tip shows that a new cantilever will release Si, C, and O in measureable quantities. After annealing at 650 °C for 1 hour both the C and O peaks were removed from the Auger spectra. Although information is not given on how long the cantilever surface remains clean for further oxide and contaminant collection, Arai was able to demonstrated improved AFM spatial resolution after surface treatment. In order to demonstrate control over surface oxide formation, a new oxide surface layer was grown by heating the cantilever to 650 °C in an O_2 environment with a pressure of 5×10^{-5} torr. Subsequent Auger spectra analysis showed that an oxide reformed in this manner could be removed by re-annealing the cantilever in the UHV vacuum chamber.

Yang has also studied the effect of *in situ* heating of single-crystal silicon cantilevers in vacuum [17]. Yang has demonstrated that significant improvement in Q can be obtained when heating a silicon cantilever in vacuum to 1000 °C for 30 seconds.

Yang used x-ray photoelectron spectroscopy to show that annealing at 1000 °C removed both C and O-based materials from the cantilever surface.

V. CONCLUSIONS

In situ "self-annealing" cantilevers are a novel method to improve the understanding of the surface-related dissipation mechanisms present in ultrathin cantilevers. Our results indicate that the removal of contamination from the surface of the cantilever produces significantly enhanced Q values. However, the removal of easily adsorbed surface contaminants does not appear to significantly influence the quality factor. It is not until temperatures of $\sim$1000 K are applied that there is a three-fold improvement in the room temperature quality factor for cantilevers with varying initial values of Q and resonant frequency. Our results, and the results of others in the literature, strongly suggest the removal of the oxide from the surface of the cantilever enhances the quality factor.

Possible future experiments include performing these same measurements in a UHV vacuum system in order to be able to control the removal of surface materials in a more precise manner. The addition of residual gas analysis systems would allow determination of the exact contaminant materials liberated from the cantilever surface during the high temperature anneals. Additionally, the use of forming gases to provide additional passivation and surface stability can be used to extend the lifetime of the improved quality factors.

ACKNOWLEDGEMENTS

This work has been supported by the National Science Foundation CAREER Award (CMR-9971414) and the National SciencE Foundation Instrumentation for Materials Research Program (DMR 9504099). This work also made use of the National Nanofabrication Users Network facilities funded by the National Science Foundation under award number ECS-9731294.

[1] T. Stowe, K. Yasumura, T. Kenny, D. Botkin, K. Wago, and D. Rugar, Appl. Phys. Lett. **71**, 288 (1997).
[2] D. Carr, S. Evoy, L. Sekaric, H. Craighead, and J. Parpia, Appl. Phys. Lett. **75**, 920 (1999).
[3] K. Yasumura, J. Chiaverini, T. Kenny, and D. Rugar, Transducers 1999 pp. 540–544 (1999).
[4] K. Yasumura, T. Stowe, E. Chow, T. Pfafman, T. Kenny, B. Stipe, and D. Rugar, IEEE J. Microelectromech. Syst. **9**, 117 (2000).
[5] K. Yasumura, T. Stowe, E. Chow, T.Pfafman, T. Kenny, and D. Rugar, Solid-State Sensors and Actuator Workshop, Hilton Head, South Carolina, June 8-11, 1999 pp. 65–70 (1998).
[6] S. Evoy, D. Carr, L. Sekaric, A. Olkhovets, J. Parpia, and H. Craighead, J. Appl. Phys. **86**, 6072 (1999).
[7] K. Wang, A. Wong, W. Hsu, and C.-C. Nguyen, Transducers 1997 pp. 109–112 (1997).
[8] B. Chui, *AFM cantilevers for thermomechanical data storage, Ph.D. Dissertation* (1999).
[9] T. Arai and M. Tomitori, Appl. Phys. A **66**, S319 (1998).
[10] L. Csepregi, E. Kennedy, J. Mayer, and T. Sigmon, J. Appl. Phys. **49**, 3906 (1978).
[11] T. Stowe, *Extending the lower limits of force detection using micrommachined silicon cantilevers, Ph.D. Dissertation* (2000).
[12] D. Rugar, H. Mamin, and P. Guethner, Appl. Phys. Lett. **55**, 2588 (1989).
[13] Y. Martin, C. Williams, and H. Wickramasinghe, J. Appl. Phys. **61**, 4723 (1987).
[14] J. Hutter and J. Bechhoefer, Rev. Sci. Instrum. **64**, 1868 (1993).
[15] K. Yasumura, *Energy Dissipation mechanisms in microcantilever oscillators with application to the detection of small forces, Ph.D. Dissertation* (2001).
[16] U. Hashim, S. Shaari, and B. Majlis, ICSE '98 Proc. pp. 213–216 (1998).
[17] J. Yang, T. Ono, and M. Esashi, Appl. Phys. Lett. **77**, 3860 (2000).

ANALOG TUNABLE GRATINGS WITH NANOMETER RESOLUTION

Chee Wei Wong, Wei-Chuan Shih, Yong Bae Jeon, Salil Desai,
Dennis Freeman, Sang-Gook Kim, and George Barbastathis
Massachusetts Institute of Technology, Cambridge, MA 02139

ABSTRACT

We have designed analog tunable diffractive gratings with period tunable to within fraction of a nanometer and diffracted angular changes on the order of 1 μradian. We deform the gratings in both electrostatic and piezoelectric actuator designs, and demonstrate period changes of order 2 nm, with limitation from measurement noise. Fabrication processes and results are presented. Actuator characterization and experimental measurements for both devices suggest applications in optical telecommunications and microspectroscopy.

INTRODUCTION

We here present a tunable MEMS grating which permits analog control over the diffraction angle, accomplished by analog deformation of the grating structure in the lateral direction. Prior work on digitally tunable gratings involves individual control of each grating beam or a set of beams (such as in the Grating Light Valve [1] and Polychromator [2]). Work on analog tunable gratings involves either thermal actuation [3,4], or vertical and lateral movement of two vertically stacked grating structures [4]. Compared to these tunable grating implementations, our device concept trades deflection range for angular resolution. Applications for high-resolution analog tunable gratings include microspectrometers, external cavity tunable lasers, and thermal compensators for wavelength multiplexer-demultiplexers. In this paper, we describe two implementations: electrostatic and piezoelectric. The piezoelectric design is better suited for applications requiring smaller tuning range and ultra-fine tunability of below 1 nm. The electrostatic design, on the other hand, is appropriate for broader range and coarser tunability.

CONCEPTS AND DESIGN

Analog tunability of our grating devices is achieved by lateral actuation forces on the grating structure, either by electrostatic comb-drives or thin-film piezoelectric actuators, as illustrated in Figure 1. By contrast, for the digital design, the tuning is achieved by pulling some of the grating beams downwards by electrodes beneath the grating. Intensity modulation is realized by controlling the beam height. The tuning resolution is limited to the beam width (approximately 1 μm). Theoretically our devices, given the lateral actuated deformation, can have resolution three orders of magnitude better than the digital versions. In the electrostatic device, the grating is comprised of suspended beams supported by flexures. In the piezoelectric device, the grating is deposited onto a thin sub-micron membrane, from which the membrane is deformed to create the desired grating period change.

Figure 2a illustrates the design schematic of the electrostatic device. Two comb-drive actuators [5] deform the periodic structure. The structure is composed of grating bars in the center window and flexures which connect each bar. The flexures determine the stiffness of the entire structure. The suspended structure is attached to the silicon substrate through four anchors.

The stiffness of the flexure can be estimated by a general formula $k=Ew^3t/L^3$, where k is the effective spring constant for one period, E the Young's modulus of the material, t the thickness of the structure, w the width of the flexure beam, and L the length of the folded beam. The flexure stiffness is selected based on a trade-off: low tuning voltage (<30V) requires the device to be compliant, while the device should be sufficiently stiff so as to avoid modal resonance. Additional, the comb-drive actuators draw essentially no current; therefore, it operates with minimal power requirements. While the comb-drives deliver small force, usually limited to μN or less, the structure could be designed to be adequately complaint. The force can be estimated as $F=-N\varepsilon tV^2/2g$, where *N* is the number of finger pairs, ε is the permittivity of air, t is the thickness of the structure, g is the gap distance between two adjacent fingers, and V is the applied voltage. The minimum grating period is set by the resolution of the available lithography tool. Since the flexures on the sides of the grating must be defined, we find the minimum grating pitch is, at best, 4 times the design rule for 75% duty cycle or 6 times the design rule for 50% duty cycle.

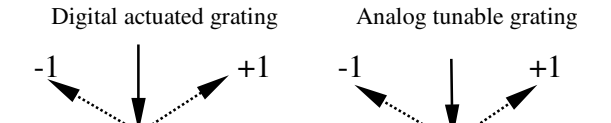

Figure 1. *Actuation concept of an analog tunable grating, permitting analog control of diffraction angle.*

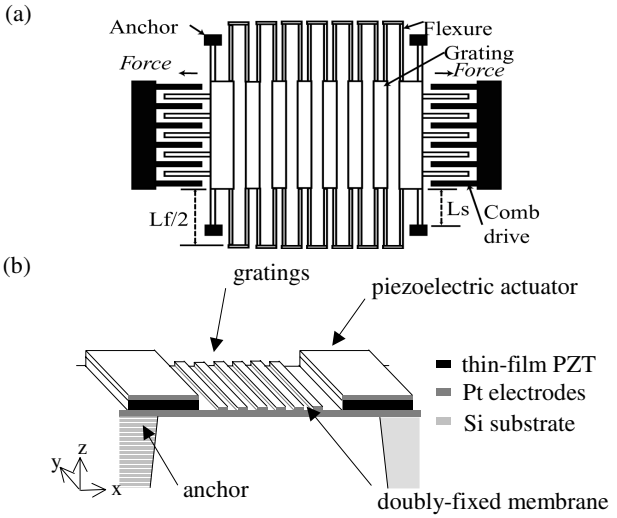

Figure 2. *Design schematic: (a) Electrostatic comb-drive actuation, (b) Piezoelectric thin-film actuation.*

For the piezoelectric device, the driving force is provided via the deposited thin-film lead zirconate titanate (PZT) actuators. Application of an electric field across the PZT film effects shrinkage of the film in the lateral direction, due to reorientation of the crystallographic domains. The membrane is correspondingly strained. The period of the diffraction grating, which is deposited onto the membrane, is thus progressively tuned and a linear response to the applied voltage due to the small strain range of less

Travel support has been generously provided by the Transducers Research Foundation and by the DARPA MEMS and DARPA BioFlips programs.

0-9640024-4-2/hh2002/$20©2002TRF
DOI 10.31438/trf.hh2002.85

than 1%. The doubly-hinged membrane design configuration, shown in Figure 2b, minimizes out-of-plane displacements of the gratings from either residual stress or the actuated piezoelectric films.

The in-plane x-deflection δ_x prediction, along the grating period axis, begins with a piezoelectric bimorph model [6] as

$$\delta_x = \frac{d_{31} E_{pzt} A V_a}{t_{pzt} k_x} \quad , \qquad (1)$$

where k_x is the effective axial stiffness = $\sum_i E_i A_i / L$, d_{31} the piezoelectric coupling coefficient, E_i the material Young modulus, A_i the cross-sectional area, V_a the applied voltage, t_{pzt} thickness of PZT layer, and L the x-dimension beam length. Boundary conditions are then applied, with symmetry across the center of the membrane, and the solution reached iteratively. We note for an isotropic wide membrane, $E_i \rightarrow E_i / (1- \upsilon_i^2)$ and $d_{31} \rightarrow d_{31} (1+ \upsilon_i)$, where υ_i is the material Poisson's ratio. For our doubly-fixed membrane design parameters (d_{31} = - 100 pC/N, E_{pzt} = 90 GPa, t_{pzt} = 0.5 µm, and L = 450 µm), our analytical and finite-element Coventorware models are in agreement to within 0.5%. Both predict a 250 nm x-axis displacement of the membrane with a single actuator at 10 V applied and suggest a 1.83 nm grating period change (0.046% strain), assuming strain uniformity across the membrane. For a 632.8 nm laser on a 4 um grating period, this corresponds to an angular change of 72 µradian for the first diffracted order.

Moreover, the finite-element model, calibrated against our experimental results, provides a numerical estimate on the slight bow in the membrane, at 0.94 µm raise against the edges of a 232 µm bow length. Approaching the diffracted image as the Fourier transform of the binary phase grating in the Fraunhofer regime [7], we estimate a decrease in first order diffraction efficiency to about 4.4% when actuated at 10V. In terms of mechanical resolution, however, the fine voltage control of the piezoelectric material suggests the resolution of a grating period change below a nanometer and angular change below a microradian. Out-of-plane membrane displacement, asymmetrical rotation of the membrane when actuated, thermal disturbances, modal vibrations, and optical detection techniques will limit the finest achievable resolution of the total membrane displacement.

FABRICATION

The fabrication process for the electrostatic device is depicted in Figure 3. It starts with an SOI (Silicon On Insulator) wafer with a 20 µm thick device layer and a 2 µm thick buried oxide. First we etch through the device layer with DRIE (Deep Reactive Ion Etching) technology. The advantage of using DRIE is that it allows us to obtain grating beams and flexures that are 20 µm thick in the vertical direction. This increases the vertical stiffness of the structure and avoids potential stiction problems during the releasing step. The design also includes lateral bumps to ensure that no lateral stiction occurs either. More importantly, the device is essentially free of residual stress because the main structure, i.e., the device silicon layer, is not formed by thin-film deposition. Since the buried oxide behaves essentially like a good etch stop, our design also avoids potential problems due to the loading effect (i.e., etching non-uniformity due to different exposed areas) which shows up almost in any etching process. The DRIE process is followed by an HF etching step to release the moving parts. Since the lateral dimension of the moving parts is much smaller than that of the fixed parts, we have large process latitude during the time-control releasing process. After releasing, we deposit an aluminum film to form the electrodes and the reflective surface on the gratings. Figures 4 shows images of the fabricated electrostatic device.

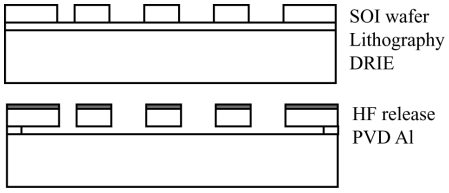

Figure 3. *Electrostatic device fabrication process flow.*

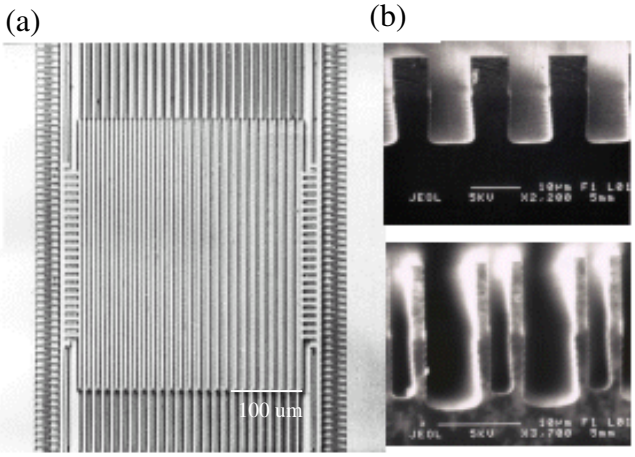

Figure 4. *Tunable electrostatic grating: (a) under optical microscope at 130X magnification, (b) SEM cross-sections of the gratings (top) and the flexures (bottom) on test sample.*

Fabrication process of the piezoelectric analog tunable grating, shown in Figure 5, involves both surface and bulk micromachining to improve device yield. First, a 200 nm silicon nitride layer is deposited via PECVD and then patterned to form a hard-mask for a later KOH backside etch. A 220 nm Pt/Ti layer is then evaporated on the substrate and patterned to create the bottom electrode via lift-off, instead of RIE, to facilitate fabrication process repeatability. Sol-gel PZT is subsequently spun-on and annealed in repeated individual steps to create a high-quality PZT layer with 0.5 µm thickness. PZT hillock and crack formation issues were resolved with fine-tuning of the Pt/Ti bottom electrode and PZT fabrication conditions. The piezoelectric layer is successfully patterned via an economic wet-etch technique [8] and the top electrode deposited with a second 220 nm Pt/Ti evaporation and lift-off procedure. The diffractive grating is next separately created with a 160 nm Pt lift-off with 2 µm minimal linewidth features. The doubly-hinged membrane is then defined with a 445 um KOH backside etch, and released with a 5 µm Si RIE.

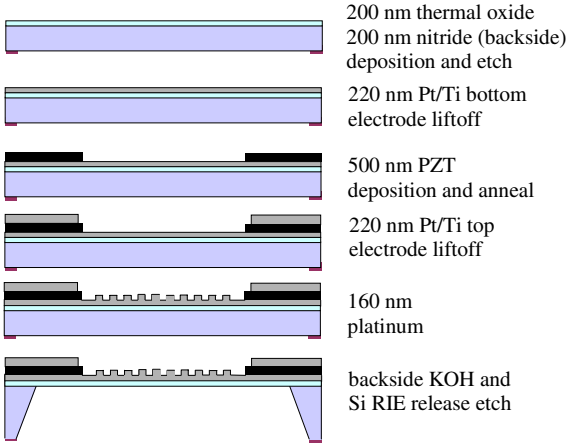

Figure 5. *Piezoelectric device fabrication process flow.*

The fabricated device is shown in Figure 6. The completed PZT has a predominant perovskite phase aided by good adhesion between the bottom Pt/Ti electrode, the SiO_2 diffusion barrier, and the substrate. The average grain size of the PZT film is on the order of 0.1 µm. Ferroelectric characterization, Figure 7, suggests a excellent dielectric constant of above 1200 and a dielectric loss below 0.05. Fatigue lifecycle experiments suggest operation above 10^{10} cycles under a 5 V rectangular pulse-train signal. The power consumption of the PZT film at 10 V actuation is gauged at 30 nW, made possible from its high resistivity. The fabricated binary phase grating also has a duty cycle measured as varying between 42 to 66%, depending on the process conditions. First and second order diffraction efficiencies were measured at 7.6% and 5.0% respectively for the fabricated grating, although higher efficiencies could be achieved with better process control.

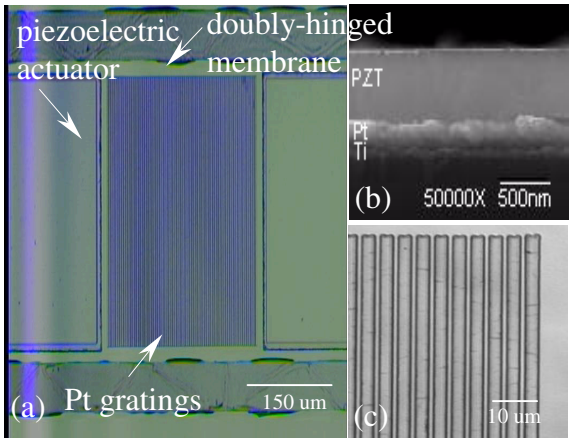

Figure 6. *(a) Piezoelectric-actuated tunable grating under 120X magnification, (b) SEM cross-section image of fabricated PZT actuator on Pt/Ti electrodes, (c) magnified view of Pt gratings with 4 µm period.*

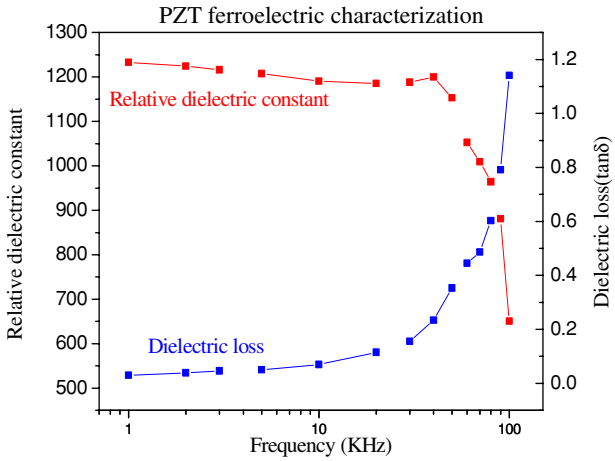

Figure 7. *Ferroelectric response of fabricated PZT film. A relative dielectric constant of 1200 and dielectric loss of less than 0.05 was measured.*

EXPERIMENTAL DESCRIPTION

We measured the angle change versus actuation voltage with two different methods: optical beam steering with image processing, and the computer microvision technique [9], which involves obtaining three-dimensional images of microscopic targets using the optical sectioning property of a light microscope and post-processing the combined images to analyze the images with nanometer precision.

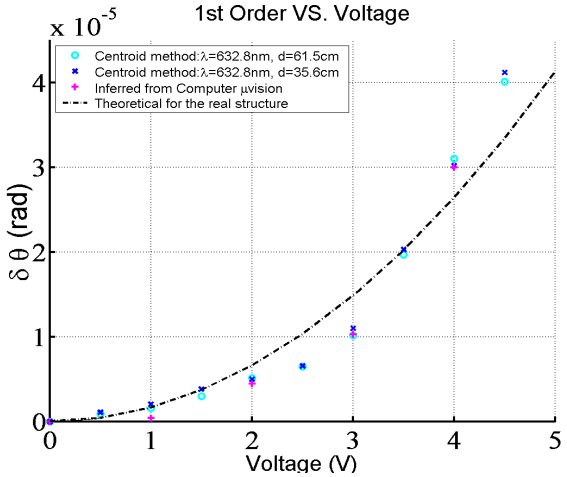

Figure 8. *Diffraction angular change against applied voltage for electrostatic device. The centroid method compares the first-order image centroids before and after actuation.*

The results of the electrostatic device (deflection angle vs. voltage) from two testing setups, Figure 8, match the theory very well. The tuning range is about 0.05 mrad at 5 V and the resolution is roughly an order of magnitude smaller. The measured frequency response, Figure 9, has the first mode at 1-2 KHz due to the very compliant flexure. Figure 10 shows the measured diffraction efficiency over different actuation voltages. Both device design and fabrication process optimizations are underway.

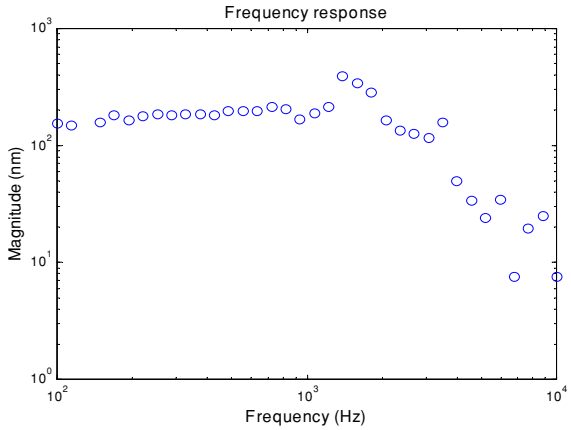

Figure 9. *Frequency response of electrostatic gratings, depicting resonance above operating range. This device has 7 periods.*

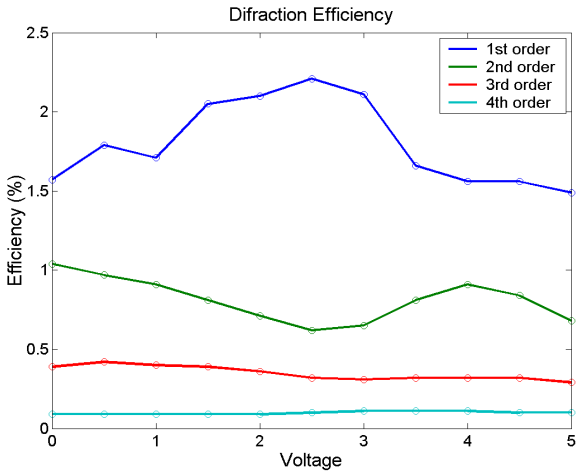

Figure 10. *Diffraction efficiency of electrostatic grating against applied voltage. The efficiency is lower than previously measured values of 12% due to the absence of the reflective metal deposition in this device batch.*

The membrane deformation of the piezoelectric-actuated device, measured with the computer microvision technique [9], demonstrated a 229 ± 2 nm in-plane motion along the membrane length at 9.0 V actuation. This corresponds to an estimated period change of 1.8 nm for this set of devices, assuming uniformity in the membrane strain. Measurements on uniformity suggest a variation of approximately 10% across the gratings. The gratings also show an expected shrinkage in the y-lateral direction due to deformation in the x-lateral direction. The membrane deformation is in agreement with the analytical and finite-element formulation and a more detailed characterization of the d_{31} coefficient will be carried out. In Figure 11, the PZT polarization-electric field hysteresis behavior, due to the domain reorientations, is evident when the membrane is actuated from –10 V to +10 V. This matches with the coercive field from electrical hysteresis

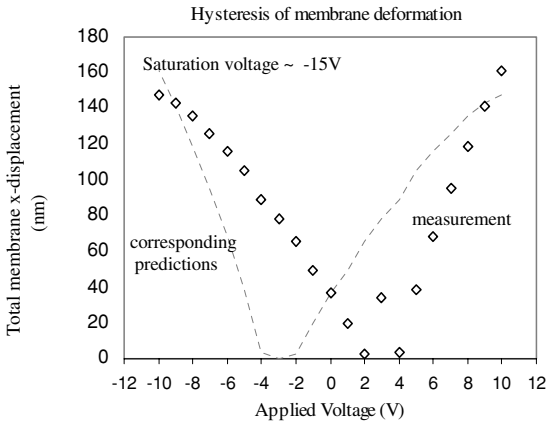

Figure 11. *Deformation pulled with saturation voltage (-15V) and step-wise increased to 10 V (measured with computer microvision [9]). The non-zero displacement at 0 V results from hysteresis in the PZT.*

In addition, the diffraction angles agree well with diffraction theory. More specifically, the angular change of the first diffracted order by applying voltage to one of the two actuators in the design is shown in Figure 12. Comparisons between the optical image centroid processing, mechanical membrane deformation measurements, and theoretical predictions suggest good agreement. At 10 V actuation, the angular change is estimated at 75 μradians for this set of devices. The uncertainty is largely limited to tilt in the membrane when actuated. Future work involves obtaining detailed measurements of the out-of-plane motion and bow of the actuated membrane.

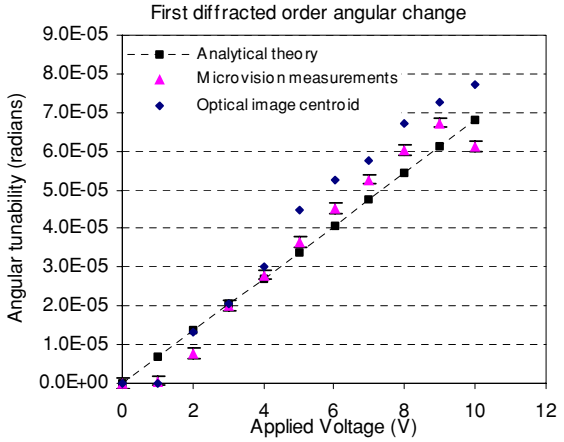

Figure 12. *First order diffracted angular change against applied voltage obtained by optical image centroid processing and mechanical motion measurements. The results are in good*

CONCLUSIONS

We have designed, fabricated, and demonstrated electrostatic and piezoelectric-actuated analog tunable gratings, via mechanical deformation of the grating structure. The expected performance of the electrostatic-actuated device is a wide tunable range of milliradians with resolution of three orders of magnitude smaller at actuation voltage below 30 V with closed-loop control. The piezoelectric-actuated tunable grating, moreover, demonstrates a grating period change on the order of a nanometer, agreeing well with our analytical and finite-element models, and suggests a range up to 0.1 milliradian with resolution on the order of microradians.

ACKNOWLEDGEMENTS

The authors would like to thank Arnab Sinha, Kurt Broderick and Martin Schmidt for their invaluable assistance. The contributions by Gregory Nielson and Carlos Hidrovo are also appreciated. This project is funded by ASML and the National Science Foundation.

REFERENCES

1. R. B. Apte *et al*., "Grating Light Valves for High Resolution Displays," *Solid State Sensors and Actuators Workshop*, Hilton Head, SC, pp.1-6, June 1994.
2. M. B. Sinclair *et al*., "Synthetic Spectra: A Tool for Correlation Spectroscopy," *Applied Optics 36*, No. 15, pp.3342-3348, May 1997.
3. X.M. Zhang and A.Q. Liu, "A MEMS Pitch-tunable Grating Add / Drop Multiplexers", *Optical MEMS 2000 IEEE/LEOS International Conference*, Kauai, HI, pp.25-26, August 2000.
4. D.E. Sene *et al*., "Development and Characterization of Micro-Mechanical Gratings for Optical Modulation", *Proc. of IEEE MEMS Workshop*, San Diego, CA, pp.222-227, February 1996.
5. W. C. Tang *et al*., "Lateral Driven Polysilicon Resonant Microstructures," *Proc. of IEEE MEMS Workshop*, Salt Lake City, UT, pp.53-59, February 1989.
6. M. S. Weinberg, "Working Equations for Piezoelectric Actuators and Sensors", *Jour. of Microelectromechanical Systems*, Vol.8, No.4, pp.529-533, December 1999.
7. J.W. Goodman, *Introduction to Fourier Optics*, McGraw-Hill, San Francisco, CA, pp.63-89, 2nd edition, 1996.
8. W. Liu *et al.*, "Preparation and properties of multiplayer Pb(Zr,Ti)O3 / PbTiO3 thin films for pyroelectric application", *Thin Solid Films*, V371, Issue 1-2, pp.254-258, August 2000.
9. D. M. Freeman *et al*., "Multidimensional Motion Analysis of MEMS using Computer Microvision," *Solid State Sensors and Actuators Workshop*, Hilton Head, SC, pp.150-155, June 1998.

MICROMACHINED VARIABLE CAPACITOR WITH WIDE TUNING RANGE

Zhixiong Xiao, Wuyong Peng, R. F. Wolffenbuttel* and K. R. Farmer
[1]New Jersey Institute of Technology, Microelectronics Research Center,
121 Summit Street- Rm 200, Newark, NJ 07102, USA
[*]Delft University of Technology, ITS/Et, DIMES/ Lab. EI,
Mekelweg 4, 2628 CD Delft, The Netherlands

ABSTRACT

In this paper, ultra-thin silicon wafers, SU-8 bonding and DRIE technology have been combined for the fabrication of a folded spring, dual electrostatic drive, vertical plate variable capacitor device with displacement limiting bumpers. The SU-8 bonding replaces the use of expensive SOI wafers and enables a more flexible design. The thick SU-8 also decreases the parasitic substrate capacitance. Due to the presence of the bumpers, our variable capacitor has two tuning voltage regimes: first a parabolic region that achieves roughly a 290% tuning range, then a linear region that achieves an additional 310%, making the total tuning range about 600%, possibly the largest range reported in the literature to date.

INTRODUCTION

Electronically tunable capacitors are key elements in communications circuits such as voltage controlled oscillators and tunable capacitor filters. Numerous papers address variable capacitors[**1-16**]. In an integrated circuit design, a variable capacitor is usually realized with a reversed p-n junction, which can give a 335% tuning range[**13**]. However, the silicon p-n junction usually has large series resistance plus parasitic capacitance to the substrate. The variable capacitors manufactured with micromachining technology can accommodate large voltage swings so that the phase noise can be improved by allowing a large voltage swing across an LC circuit. This is normally not possible with p-n junction capacitors, where the designer must ensure that the junction does not become forward-biased over the tuning voltage range. Additionally, micro-mechanical capacitors are not expected to respond to microwave frequencies, which are normally 10,000 times higher than their mechanical resonant frequencies. Hence these devices are not expected to produce a large amount of harmonic distortion.

For electrostatic drive variable capacitors fabricated using micromachining processes, Yao, et al., [**13**] have reported a capacitor with a tuning range of 200% based on lateral comb structures on an SOI substrate. Feng, et al., [**16**] have used a thermal actuator in their variable capacitor and achieved a tuning range of 270%. In this paper, ultra-thin silicon wafers, SU-8 bonding and DRIE technology have been combined for the fabrication of a folded spring, dual electrostatic drive, vertical plate device with displacement limiting bumpers. The total tuning range of this variable capacitor is about 600%.

DESIGN AND THEORY

Figure 1 shows a simplified electrical/mechanical schematic of our variable capacitor and LC drive circuit. The device consists of sets of fixed and movable vertical plates, forming separate drive and sense capacitors. Figure 2 shows several microscope images of the fabricated device. In Fig. 2a, two separate drive capacitors are

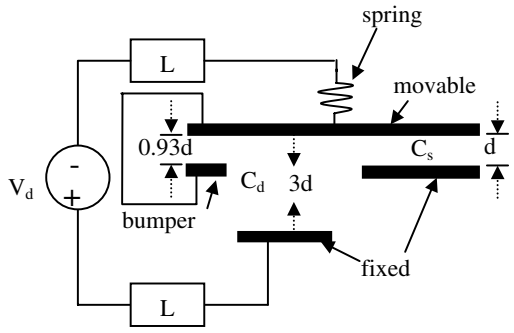

Figure 1. *Electrical/mechanical schematic of micromachined variable capacitor and LC drive circuit. C_d, the drive capacitor, has an electrode spacing that is three times that of C_s, the sense capacitor. L is about 0.1 mH.*

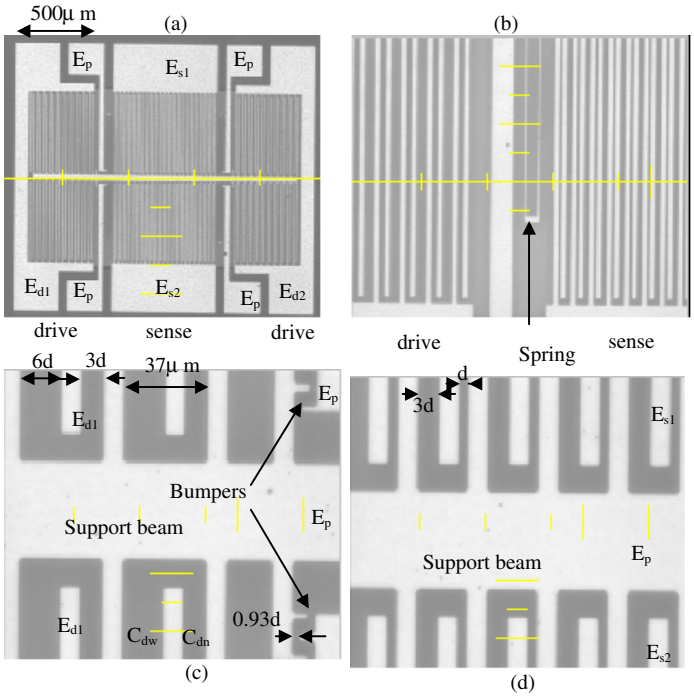

Figure 2. *(a) Top view of fabricated device. The drive voltage is applied between the common electrode E_p and the drive electrodes E_{d1} and E_{d2}. The capacitance is sensed between E_s (shorted E_{s1} and E_{s2}) and the common electrode E_p. The movable fingers are mounted to a center support beam and connected to the E_p electrodes by 4 μ m wide, 730 μ m long, 29.5 μ m thick springs. (b) Close up image showing a portion of the folded spring. (c) Close up image of drive capacitor showing placement of movable fingers with smallest asymmetric electrode spacing 3d=9 μ m and bumper spacing nominally 0.93d=2.8 μ m. The bumpers are always at the same potential. (d) Close up image of sense capacitor showing smallest electrode spacing d=3.0 μ m.*

0-9640024-4-2/hh2002/$20©2002TRF
DOI 10.31438/trf.hh2002.86

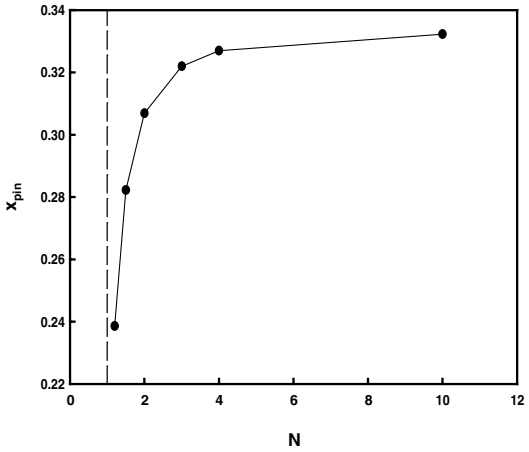

Figure 3. *Fractional displacement at pull-in, x_{pin}, versus drive electrode wide to narrow gap spacing ratio, N>1.*

placed symmetrically on the ends of the structure, and the sense capacitor occupies the center region. The sense and drive capacitors share a common electrode E_p, which is connected through four folded springs to a movable support beam with attached fingers. A portion of a folded spring is shown in Fig. 2b. As shown in Figs. 2c and 2d, C_d and C_s actually consist of wide and narrow air gap capacitances. In both cases, the net capacitance

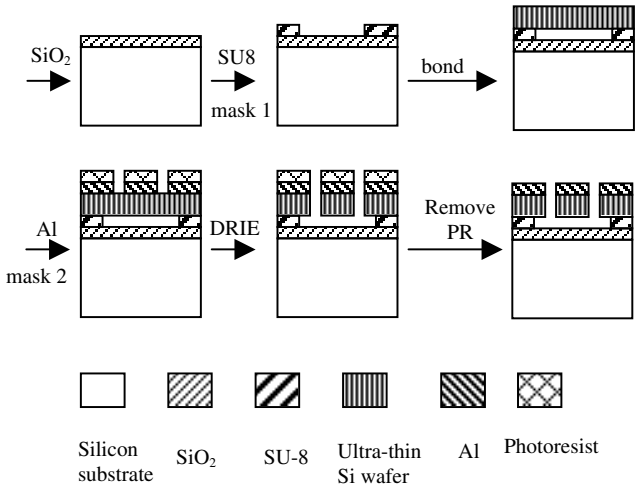

Figure 4. *Two mask process schematic for micromachined variable capacitor*

is strongly dominated by the narrow gap behavior. The narrow drive gap spacing is designed to be three times that of the narrow sense gap so that a maximum sense electrode displacement can be achieved at the lowest possible applied voltage without causing drive electrode pull-in. The 2.8µm long bumpers in Fig. 2c, which are always at the same potential, limit the maximum displacement to less than the full 3µm sense gap distance. Before the electrode E_P contacts the bumpers, the capacitance increases parabolically with increasing applied voltage. After contact, the capacitance increases approximately linearly. This is similar to a previous report in [**17**] where curved electrode actuators were used to extend the travel range.

The voltage for transition from parabolic to linear behavior can be estimated analytically by calculating the drive electrode pull-in voltage, V_{pin}. Balancing the electrostatic and mechanical forces before pull-in gives

$$\frac{\varepsilon_0 V^2 A}{2(d_0-\Delta d)^2}-\frac{\varepsilon_0 V^2 A}{2(Nd_0+\Delta d)^2}=k\Delta d \qquad (1)$$

where N is the wide to narrow gap spacing ratio for the drive electrode, (N.B., N>1) and Δd is the displacement. A, e_0, V and k are the capacitor area, permittivity of free space, applied voltage and spring constant, respectively. An expression for the fractional displacement at pull-in, x=? d_{pin}/d_0, is found by maximizing equation (1). Thus differentiating (1) with respect to displacement, multiplying by ?d, and subtracting (1), gives

$$\frac{1-3x_{pin}}{(1-x_{pin})^3}-\frac{N+3x_{pin}}{(N+x_{pin})^3}=0 \qquad (2)$$

where the normalized displacement at pull-in depends only on N. Figure 3 shows a plot of x_{pin} versus N. Observe that x_{pin} decreases dramatically as N approaches 1. For example, at N=2, x_{pin}=0.3069. When N is infinite, x_{pin}=1/3, which is the well known result for a single parallel plate system.

By substituting x_{pin} into equation (1), the pull-in voltage can be written as

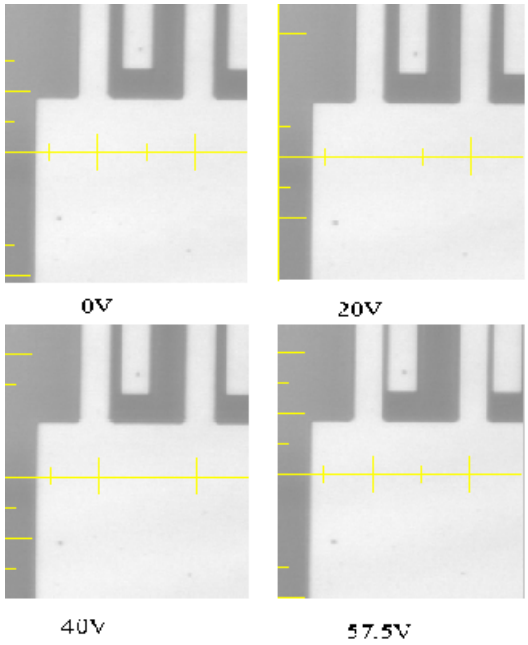

Figure 5. *A portion of the sense capacitor at various drive voltages*

$$V_{pin}=\sqrt{\frac{x_{pin}}{\frac{1}{(1-x_{pin})^2}-\frac{1}{(N+x_{pin})^2}}\frac{2d_0^3 k}{\varepsilon_0 A}} \qquad (3)$$

As discussed in the following section, the analytical results can be compared with simulation results obtained using MEMCAD (now COVENTOR) finite element analysis software. Using this tool, the spring constant for our system is estimated to be about 13 N/m.

FABRICATION AND RESULTS

Figure 4 shows the main fabrication steps. The process starts with SU-8 photolithography on an oxidized silicon wafer to form a cavity. The realized cavity depth is about 22µm at 3000 rpm. An ultrathin silicon wafer[**18**] was bonded to the silicon substrate by SU-8 bonding[**19**] at 105°C, using an EVI 501 universal bonding system. Aluminum was then sputtered onto the bonded wafer stack, and patterned by HP_3O_4 etching at 40° after photolithography. The devices were released by deep reactive ion etching (DRIE) using the BOSCH process in a Unaxis/Plasma-Therm inductively coupled plasma system. Finally, the photoresist was removed using oxygen plasma etching. The aluminum on the structure, besides allowing good external electrical contact, also decreases the device series resistance, improving its Q factor.

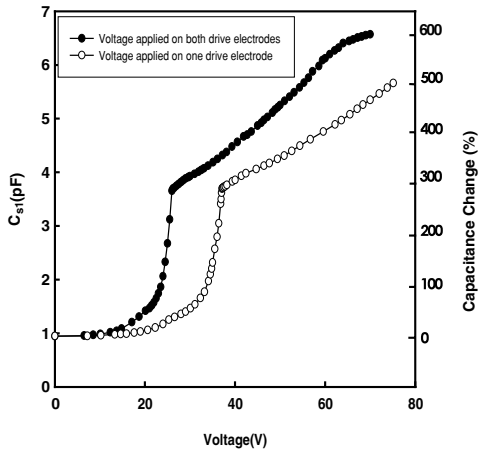

Figure 6. *The measured capacitance C_{s1}, between E_{s1} and E_p (left axis), and the percentage change in capacitance (right axis) versus voltage*

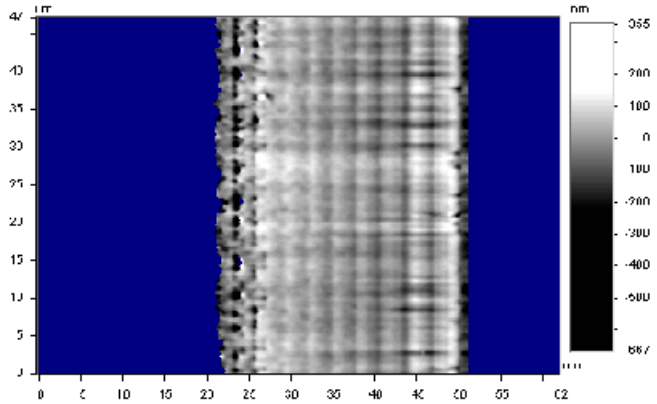

Figure 7. *Optical profile of device sidewall after DRIE etching*

Figure 5 shows sense capacitor photos at 0V, 20V, 40V and 57.5V when voltage was applied on only one drive electrode. As expected, the capacitor electrodes move closer when the voltage increases.

Figure 6 shows the measured sense capacitance value C_s between one sense electrode E_{s1}, and the common electrode, E_p. The figure also shows the percentage change in capacitance. The capacitance is measured using an HP 4284A precision LCR meter. The amplitude and frequency of the testing signal were 5mV and 1MHz, respectively. When voltage is applied on both drive electrodes, the capacitance parabolically increases from 0.945pF at 0V to 3.657pF at 26V, and then increases nearly linearly to 6.57pF at 70V. This corresponds to tuning ranges of 287% at 26V and 595% at 70V. When voltage is applied on one drive electrode, the capacitance increases parabolically from 0.945pF at 0V to 3.696pF at 37.1V, and then nearly linearly to 5.55pF at 75.1V. This corresponds to tuning ranges of 290% at 37.1V and 497.5% at 75.1V. For each measurement, the results are reproducible and without discernable DC hysteresis. In addition, the final displacement appears only to be limited by dielectric breakdown, which exceeds 80V for these devices in air. Figure 7 shows the capacitor sidewall image using a VEECO NT3300 optical profilometer. It shows that the ultrathin silicon wafer is approximately 29.5µm thick. In addition, the image reveals the capacitor surface microroughness induced by the Bosch etching process. The RMS roughness is about 71nm.

Table 1 provides a comparison of the measured transition voltages to analytical and COVENTOR 2001 pull-in simulation results. For completeness, COVENTOR simulation parameters are also given in the table. Good agreement is found for the two cases, when voltage is applied either to only one or to both drive electrodes. Note that the measured transition voltage is slightly higher than the analytical and simulation results, but this can easily be attributed to non-parallel electrodes or other effects neglected in the theory. The possibility of non-parallel electrodes (i.e., a few degree DRIE sidewall slope) is suggested by the observation that the drive electrodes never seen to make full contact at the top surface of the device. While we have achieved a wide tuning range in these capacitors, we note that even with the addition of aluminum, the measured Q factor is only ~100 at 1MHz. We attribute this result to the use of relatively high resistivity, 1–10 Ocm, ultra-thin silicon wafers. We are currently fabricating improved devices using heavily doped silicon, as well as softer springs and improved drive electrodes to lower the drive voltage.

Table 1. *Comparison of measured transition voltage to analytical and COVENTOR simulation results*

	Measured transition voltage	Calculated pull-in voltage	COVENTOR pull-in voltage
Voltage on one electrode	37.1V	35.0V	34.25V
			27 node element for meshing 20583 total nodes convergence ratio=5×10^{-3}
Voltage on both electrodes	26.0V	24.75V	23.91V
			27 node element for meshing 22869 total nodes convergence ratio=5×10^{-3}

CONCLUSIONS

In summary, combining ultra-thin silicon wafers, SU-8 bonding and DRIE, we have designed and fabricated a micromachined variable capacitor that exhibits two tuning regimes, parabolic and linear, and has achieved roughly a 600% tuning range.

ACKNOWLEDGEMENT

This work was supported through the National Science Foundation, awards ECS-9624798 and DMR-9871272, and the New Jersey Commission on Science and Technology through the NJ MEMS Initiative.

REFERENCES

1. R. S. Muller and T. I. Kamins, "Device electronics for integrated circuits", *John Wiley & Sons Inc.,* 1977.
2. F. Svelto, P. Erratico, S. Manzini, and R. Castello, "A metal-oxide-semiconductor varactor", *IEEE Electron Device Letters, 20,* 164-166(1999).
3. C. L. Goldsmith, A. Malczewski, Z. J. Yao, S. Chen, J. Ehmke, and D. H. Hinzel, "RF MEMS variable capacitors for tunable filters", *International Journal of RF and Microwave Aided Engineering, 9(4),* 362-374(1999).
4. D. J. Young, V. Malba, J. J. Ou, A. F. Bernhardt, and B. E. Boser, "Monolithic high-performance three–dimensional coil inductors for wireless communication application", *Tech. Digest, International Electron Devices Meeting, 1997,* pp. 67-70.
5. D. J. Young, V. Malba, J. T. Ou, A. F. Bernhardt, and B. E. Boser, "A low-noise RF voltage-controlled oscillator using on-chip high Q three-dimensional coil inductor and micromachined variable capacitor", *Technical Digest of Solid-State Sensor and Actuator Workshop,* Hilton Head Isl., SC(1998), pp. 128-131.
6. D. J. Young, and W. E. Boser, "A micromachined variable capacitor for monolithic low-noise VCOs in cellular phone application", *Technical Digest of Solid-State Sensor and Actuator Workshop,* Hilton Head Isl., SC(1996), pp. 86-89.
7. M. Steyaert, and J. Craninckx, "1.1 GHz oscillator using bondwire inductance", *Electronics Letters, 30,* 244-245(1994).
8. D. J. Young, J. L. Tham, and B. E. Boser, "A micromachine-based low phase-noise GHz voltage-controlled oscillator for wireless communications", *Proceeding of 10th Solid-State Sensor and Actuators,* Sendai, Japan(*19*99), pp. 1386-1389.
9. A. Dec, and K. Suyama, "Micromachined varactor with wide tuning range", *Electronics Letters, 33,* 922-924(1997).
10. A. Dec, and K. Suyama, "A 1.9GHz micromachined-based low phase noise CMOS VCO", Proceeding of 46th *IEEE International Solid-State Circuits Conference,* San Francisco Marriott. (1999), pp. 80-81.
11. E. S. Hung and S. D. Senturia, "Tunable capacitors with programmable capacitance-voltage characteristic", *Technical Digest of 1998 Solid-State Sensor and Actuator Workshop,* Hilton Head Isl., SC(1998), pp. 292-295.
12. M. Husák, "One-chip integrated resonance circuit with a capacitive pressure sensor", *J. Micromech. Microeng. 7,* 173-178 (1997).
13. J Jason Yao, "RF MEMS from a device perspective", *J. Micromech. Microeng. 10,* R9-R38(2000).
14. A. Dec, and K. Suyama, "Microwave MEMS-Based Voltage-Controlled Oscillators", *IEEE Transactions on Microwave Theory and Techniques, 48,* 1943-1949(2000).
15. J. Zou, C. Liu, J. Schutt-Aine, J. Chen, and S.-M. Kang, "Development of Wide Tuning Range MEMS Tunable Capacitor for Wireless Communication Systems", *Tech. Digest, International Electron Devices Meeting,* San Francisco, CA(2000), pp. 403-406.
16. Z. Feng, H. Zhang, W. Zhang, B. Su, K. Gupta, V. Bright, Y. Lee, "MEMS-based variable capacitor for millimeter-wave applications", *Tech. Digest, Solid-State sensors and Actuators Workshop,* Hilton Head Island, SC(2000), pp. 255-258.
17. R. Legtenberg, J. Gilbert, S. D. Senturia, and M. Elwenspoek, "Electrostatic curved electrode actuators", *IEEE J. of Microelecromechanical Systems, 6,* 257(1997).
18. Ultrathin silicon wafers are available from Virginia Semiconductor, Inc., Fredericksburg, VA.
19. S. K. Sampath, L. St.Clair, Xingtao Wu, D. V. Ivanov, Q. Wang, C. Ghosh and K. R. Farmer, "Rapid MEMS Prototyping using SU-8, Wafer Bonding and Deep Reactive Ion Etching," *Proceedings of the 14th Biennial University/Government/Industry Microelectronics Symposium*, Richmond, VA, 6/18-20/ 2001, p. 158.

A LOW-VOLTAGE TILTABLE MICROPLATFORM USING BENT-BEAM ACTUATION

Yuan Xie and Clark T.-C. Nguyen
Center for Integrated Microsystems
Department of Electrical Engineering and Computer Science
University of Michigan
Ann Arbor, Michigan 48109-2122, U.S.A.

ABSTRACT

A tiltable microplatform for adaptive artificial vision applications has been demonstrated that utilizes special bent-beam electrostatic actuators to achieve DC tilt angles larger than 10^o with actuation voltages less than 20V, and a resonance tilt angle of 19^o when driven to resonance at 33 kHz via a combination of 14V DC, plus 5V AC. This bent-beam actuation mechanism has the further advantage that its physical implementation is out of the way of the microplatform itself, making it amenable to applications where light must pass through the platform and substrate (e.g., adaptive vision).

Keywords: MOEMS, artificial vision, tilt angle, low voltage

I. INTRODUCTION

In the wake of rapid advancements in optical MEMS technology spurred by the telecommunications industry, micromechanical actuation mechanisms capable of generating plate tilt angles on the order of 10^o are now commonplace [1]-[3]. Among the various actuation strategies, vibromotor [1] and bimorph [2] methods stand out as some of the most voltage efficient, requiring 20V AC and 1-2 V (but with considerable power consumption), respectively, to attain tilt angles greater than 10^o in large plates, often for optical scanning applications. However, actuation methods capable of low power, low voltage tilt actuations of plates that allow light to pass through a 3D array of elements are fewer in number [3], and most require excessive power or voltage levels.

One such 3D arrayed application, for which this work is specifically targeted, is the adaptive artificial vision system depicted in Fig. 1, where incoming light is collected, subdivided into a 2D array, collimated, then directed through an array of tiltable microprisms before finally reaching a pixel array. In this system, the microprisms disperse the color content of the incoming light, and by tilting, modulate the colors from pixel to pixel on the detection plane—an operation often required by algorithms for color adaptation in vision systems [4]. Because the change in the angle of light passing through a prism is only a weak function of the prism tilt, tilt angles of 10^o or greater are needed for adequate traversal of colors over adjacent pixels, and such tilts must be accomplished via low voltages and with low power consumption.

This paper describes a new bent-beam electrostatic (i.e., low power) actuation method that achieves DC platform tilts larger than 10^o with actuation voltages less than 20V and resonance tilts up to 19^o at 33 kHz, while offering an implementation structure amenable to applications requiring 3D arrayed transmission-based operation.

II. MICROPLATFORM OPERATION

Figure 2 presents a perspective-view schematic of the demonstrated tiltable microplatform housing a microprism. As shown, the low-stress nitride microplatform itself is suspended via rigid polysilicon suspension beams above a hole in the silicon substrate (as in [3]) that (1) allows light to pass through; and (2) allows unimpeded tilting of the microplatform over very large angles. The suspension beams are actually not anchored to the substrate directly, but rather rest upon the substrate via strategically-placed dimples, around which the suspensions can pivot to affect tilting of the platform. These pivoting suspension beams together with the network of

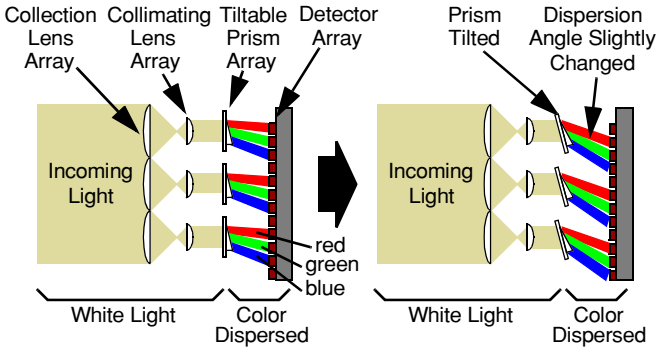

Fig. 1: Schematic of a portion of the adaptive artificial vision application targeted by the tiltable microplatform. Beyond the detector array, vision algorithms are applied to the 2D data via transistor DSP circuits, then fed back to control platform tilting so as to affect color adaptation.

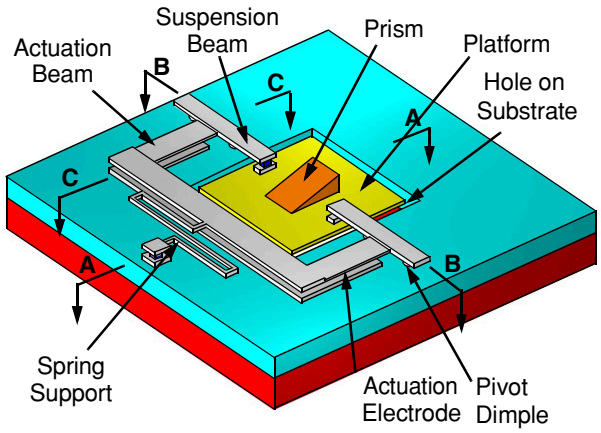

Fig. 2: 3D view of the bent-beam actuated tiltable microplatform

beams attached to them then realize the bent-beam actuation mechanism that makes possible tilting of the platform at such low voltages. As illustrated in Fig. 3, bent-beam actuation is achieved by pulling down a thin doped-polysilicon beam perpendicularly attached to the suspension beam, and bending this thin beam close to the suspension dimple so as to pivot the suspension around an angle defined by the degree of bending in the thin beam. In this work, the thin beam is pulled down electrostatically by applying a suitable voltage to an underlying, nitride-covered (to prevent shorting), doped-polysilicon electrode. The voltage required to achieve a given angle is greatly reduced in this system, because: (1) the pivoting dimple eliminates the need to overcome a torsional stiffness; and (2) once pulled down, portions of the beam near the bend are very close to the underlying electrode, so the electrostatic beam-bending force is larger for a given voltage.

III. BENT-BEAM ACTUATOR DESIGN

To obtain an expression for tilt angle as a function of applied actuation voltage for a bent-beam actuator, an energy method similar to that described in [5] is used, in which the derivative of the total potential energy in the system with respect to distance is set to

Travel support has been generously provided by the Transducers Research Foundation and by the DARPA MEMS and DARPA BioFlips programs.

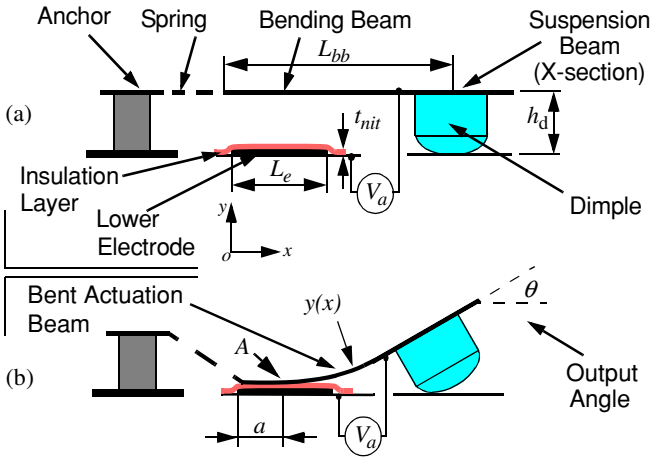

Fig. 3: Schematics describing the mechanism behind bent-beam actuation. (a) Before and (b) after application of the actuation voltage V_a.

zero at equilibrium.

Using this technique, neglecting fringing electric fields and dimple-to-substrate friction, the voltage required to pin the bending beam up to the point *A* in Fig. 3 can be derived and written as

$$V_a(a) = \sqrt{\frac{(12h_d^2 EI)/(L_{bb}-a)^4}{\frac{\varepsilon_{nit}\varepsilon_o W_{bb}}{t_{nit}} + \frac{\varepsilon_o W_{bb}\delta z(a)}{\delta a}}} \qquad (1)$$

where

$$z(a) = (L_{bb}-a)\sqrt{\frac{\varepsilon_{nit}}{h_d t_{nit}}} \cdot \operatorname{atan}\left[(L_e-a)\sqrt{\frac{\varepsilon_{nit}h_d}{t_{int}(L_{bb}-a)^2}}\right] \qquad (2)$$

and where L_{bb} and W_{bb} are the length and the width, respectively, of the bending beam, L_e is the length of the actuation electrode, a is the electrode-to-beam contact length when the bending beam is pinned to the substrate, h_d is the height of the dimple, t_{nit} is the thickness of the insulation layer, E is the Young's modulus of polysilicon, I is the bending moment of the bending beam, ε_{nit} is the dielectric constant of the insulation layer, and ε_o is the permittivity of free space. Using (1) to determine the distance a generated by a given voltage V_a, the tilt angle can then be determined via the expression

$$\theta(a) = \operatorname{atan}\left[\frac{dy(x)}{dx}\right]\Bigg|_{x=L_{bb}} = \operatorname{atan}\left[\frac{2h_d}{L_{bb}-a}\right] \qquad (3)$$

where *y(x)* is the deflection of the beam, approximately parabolic.

IV. FABRICATION PROCESS

The fabrication process for the tiltable microplatform combines surface micromachining with deep RIE and phased lithography, and is very briefly summarized in Fig. 4. The process begins with the growth of a 2µm thermal oxide insulation layer, which is patterned to form sealant vias that later prevent etching of the isolation layer during a final HF release etch step. 1µm of silicon rich (low stress) LPCVD nitride is then deposited at 835°C to fill the sealant vias and to serve as the structural material for the eventual microplatform. Next, 3000Å of LPCVD polysilicon is deposited at 588°C, then $POCl_3$-doped and patterned to form electrodes and electrical interconnect. An 1800Å layer of stoichiometric nitride is then deposited and patterned over the patterned polysilicon to serve as an insulation layer that prevents shorting between the actuation electrodes and suspended polysilicon structures (c.f., Fig. 3). The platform nitride is then patterned and covered by a 3.3µm-thick LPCVD high temperature oxide (HTO) layer, deposited at 920°C, that sets the gap spacing between the actuation electrodes and the bending beams. Next, 3000Å of LPCVD polysilicon is deposited at 588°C, then doped and patterned to form the bending beams.

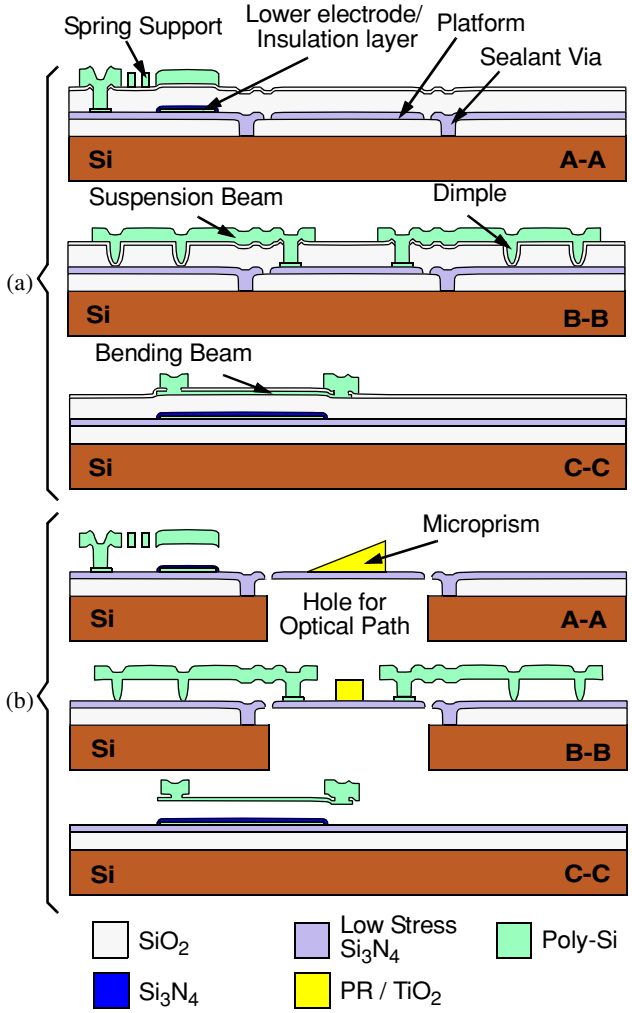

Fig. 4: Cross-sections describing the tiltable microprism process flow at (a) a point just before prism processing; and (b) the end of the process (i.e., final cross-section).

At this juncture, dimple molds are formed by first RIE'ing vias corresponding to dimple locations into the thick sacrificial oxide, then blanket depositing a 1500Å-thick spacer layer of HTO that effectively sets the dimple-to-substrate spacing. This method for forming dimples eliminates the need for the timed etch needed in a previous dimple-formation process [6], and greatly enhances the accuracy to which the dimple-to-substrate gap spacing can be set.

Openings are then etched via RIE into the thin HTO layer above the bending beams and into the thick HTO layer in the field to form attachments between the bending beams and the thicker structural layer making up the platform suspension beams and spring support (c.f., Fig. 2), and to form an anchor to the substrate for the spring support. (Note that this is the only point rigidly attached to the substrate.) The thick structural features are then formed via a 2µm-thick LPCVD, low-stress polysilicon deposition at 588°C, followed by subsequent doping and patterning to form the suspension beams and spring support, and yielding the cross sections of Fig. 4(a).

To form the photoresist microprism on the microplatform, HTO is first removed over the microplatform, and a 2.7µm-thick photoresist layer (AZ1800 series) is spun on. The microprism is then delineated by exposing the photoresist through a gray-scale mask [7] that

Table 1: Bent-Beam Actuated Microplatform Design

Parameter	Value	Units
Microplatform Size	100×90	μm
Bending Beam Length, L_{bb}	94	μm
Bending Beam Width, W_{bb}	18	μm
Bending Beam Thickness, h_{bb}	0.3	μm
Actuation Electrode Length, L_e	83	μm
Dimple Height, h_d	3.45	μm
Electrode Dielectric Thickness, t_{nit}	0.18	μm
Polysilicon Young's Modulus, E	150	GPa

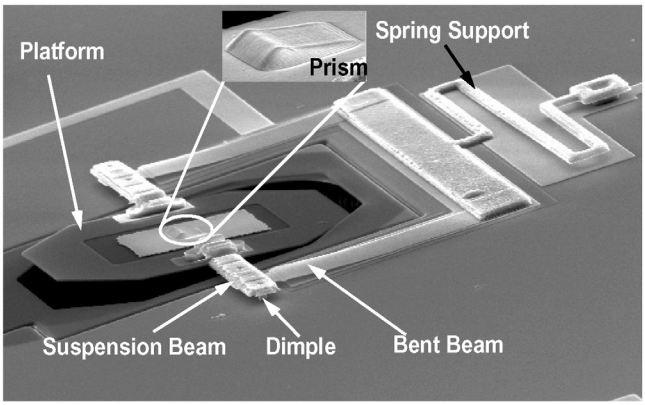

Fig. 5: SEM of a microplatform housing a photoresist microprism with 11V applied actuation voltage. The tilt angle is 7°.

affects a linear variation in exposure intensity over the prism area, effectively exposing a triangular shaped cut into the photoresist thickness. A subsequent development step then removes all exposed photoresist, leaving behind a photoresist microprism.

To allow the passage of light through the microprism, a through-wafer hole is etched from the back side of the wafer using the Bosch process before release. The release etch is finally done using 48.8 wt. % concentrated HF, followed by a supercritical CO_2 drying step to minimize sticking, yielding the cross section of Fig. 4(b), where three levels of suspension—nitride platform, bending beams, and suspension beams—have been achieved in a single planar process.

V. EXPERIMENTAL RESULTS

Bent-beam actuated microplatforms were designed for various actuation voltage ranges using the theory of Section III, then fabricated using the process of Section IV. Table 1 summarizes the design of the device tested for this paper. Figure 5 presents the SEM of a fabricated microplatform housing a photoresist prism under 11V of applied actuation voltage, clearly showing bending of the thin upper beam to achieve a tilt angle of 7°.

Completed microplatforms were tested using three different methods: (1) direct visual observation in air under an optical microscope; (2) observation under an SEM equipped with electrical feedthroughs (c.f., Fig. 5); and for the best accuracy, (3) the optical measurement setup depicted in Fig. 6. In the last of these, the sample under test is mounted on an xyz-stage and a He-Ne (532nm) laser beam is focused on the microplatform using an objective lens with a focal length of 50mm. A microscope is used to align the laser spot to the microplatform (avoiding the prism, for now). The reflection of the laser beam from the platform is projected onto a white screen with a measurement scale, from which the tilt angle of the microplatform can be extracted using trigonometric identities together with the law of reflection. In effect, the position of the laser spot on the screen and the distance between the screen and the device define the tilting angle.

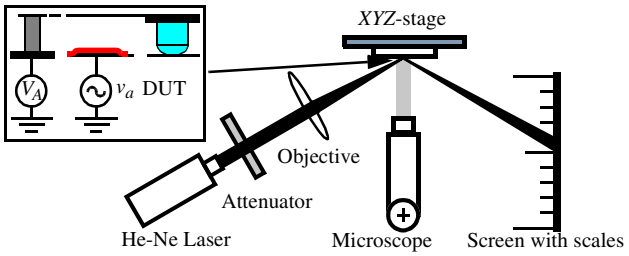

Fig. 6: Test set-up for accurate platform tilt angle measurement.

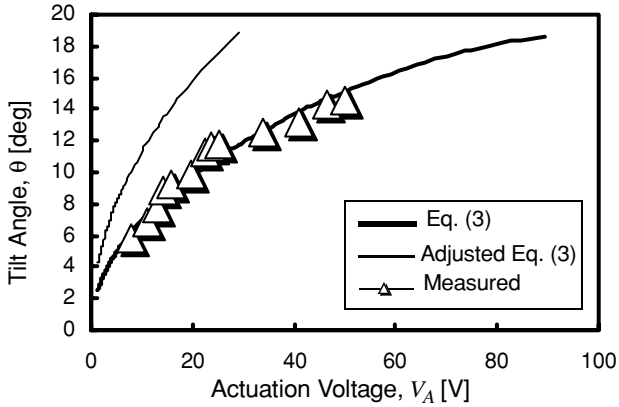

Fig. 7: Measured tilt angle versus actuation voltage for the device of Table 1.

A. Static Behavior

The fabrication yield of tiltable microplatforms with bent-beam actuators was quite good, with virtually all devices surviving the release and supercritical CO_2 drying steps, including and especially the very thin bending beams. Upon initial testing under an optical microscope, all tested devices were found to be operable with no problems for actuation voltages V_A from 0-20V. However, when voltages exceeded 30V, the bending beams of a small subset of the devices became stuck to their actuation electrodes. Once stuck in this manner, probing could only free bending beams for about half the devices. The other half had bending beams that could be moved laterally by probing (so they weren't fused), but that remained pinned to the actuation electrodes, suggesting charging of the nitride dielectric as a possible cause for the observed sticking.

Figure 7 presents a plot of tilt angle versus actuation voltage for the device of Table 1 as measured using the set-up of Fig. 6. The theoretical prediction of (3) is also plotted in Fig. 7 and is seen to be offset from the measured curve, consistently predicting values lower than measured. This mismatch between theory and measurement is caused by a combination of (1) dimple non-ideality, whereby the dimple is not a perfectly rounded pivot, but in fact has a somewhat flat bottom, so pivots along an edge instead; and (2) the finite width of the platform suspension beams. To account for these non-idealities, the "2" in the numerator of the argument of (3) is changed to "1.22", yielding the adjusted curve shown in Fig. 7, which now very closely matches the measured data.

B. Dynamic Behavior

To characterize the dynamic behavior of the device, frequency spectra were obtained by applying a DC voltage to the bending beam, while applying a swept-frequency AC voltage to the lower electrode (c.f., Fig. 6). As the frequency of the AC voltage increases, the laser spot of Fig. 6 begins to blur into a continuous line, as shown in Fig. 8, and reaches a maximum length at the resonance frequency, at which point the platform/suspension system exhibits its largest vibration amplitude.

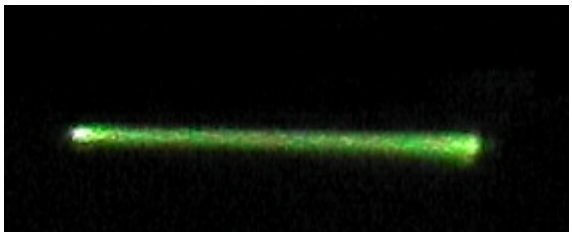

Fig. 8: Reflected laser beam trace during AC measurement.

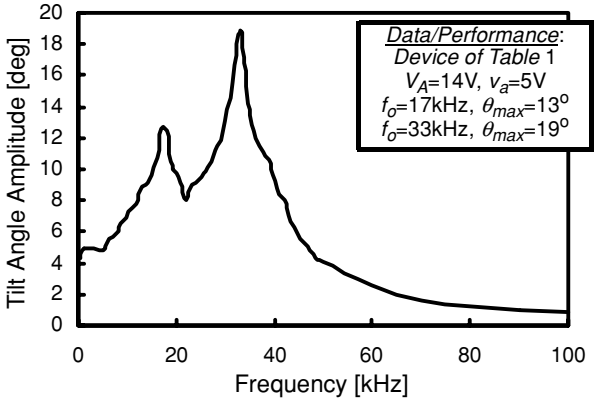

Fig. 9: Measured frequency spectrum of the bent-beam microplatform of Table 1.

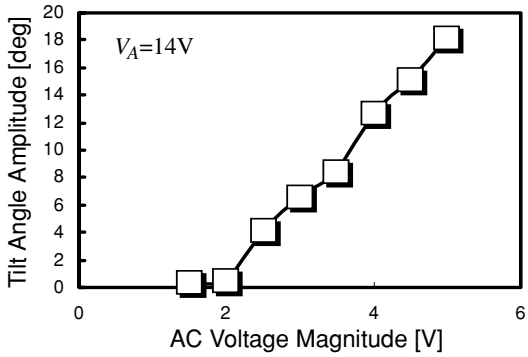

Fig. 10: Tilt angle as a function of AC voltage amplitude for the bent-beam actuated microplatform of Table 1.

Figure 9 presents the measured frequency spectrum for the bent-beam actuated microplatform of Table 1. Here, two resonant peaks are seen, possibly arising from the mechanical filter [8] nature of the overall system, where each of the two bent beams act as resonators coupled loosely by the platform and its suspensions. The lower peak at 17 kHz has a maximum tilt angle around 13°, while the higher peak at 33 kHz has a maximum tilt angle of 19°. Both peak frequencies are quite high compared with frequencies achieved by alternative tilt actuation mechanisms, making bent-beam actuation a strong candidate for high speed optical applications. As expected, the voltages required to tilt at such angles at resonance are much smaller than those needed in static operation. Figure 10 presents a measured plot of tilt angle versus AC voltage amplitude for the device of Table 1 under a constant DC voltage V_A of 14V, showing actuation voltages for this bent-beam actuation method much smaller than for alternative methods.

Figure 11 finally presents measured curves of resonance frequency and resonance tilt angle versus DC bias. Here, an expected strong dependence of resonance tilt angle on DC bias is exhibited. On the other hand, only a weak dependence of resonance frequency on DC bias is observed, which for the higher frequency peak actually increases with DC-bias, suggesting that suspended bending beam length reductions by pinning are slightly more important than

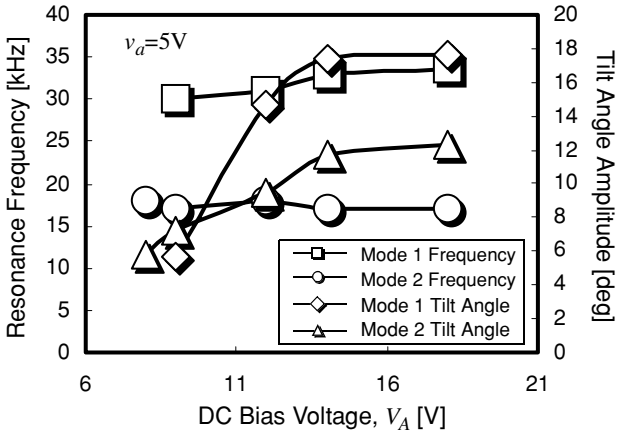

Fig. 11: Resonance frequency and tilt angle as a function of DC voltage for each mode of the device in Table 1.

electrical spring softening [6] for this peak.

VI. CONCLUSIONS

An electrostatic bent-beam actuated tiltable microplatform fabricated using a combined surface micromachining and deep RIE technology has been demonstrated with a measured maximum tilt angle and resonance frequency of 19° and 33 kHz, respectively, obtained using a voltage combination of 14V DC and 5V amplitude AC. Given that the described bent-beam actuation technique is largely electrostatic in nature, the tilt angle-to-voltage/power ratio achieved by the above values represents one of the largest available using MEMS technology, and the numbers demonstrated here can even be bettered by reducing bending beam thicknesses. This, combined with an implementation structure conducive to transmission-based optical signal processing, makes bent-beam actuation a good candidate for 3D arrayed adaptive vision applications. In this regard, the tiltable dispersive microprism function of this device is presently under evaluation.

***Acknowledgment*:** This work was supported under an ARO MURI on an Adaptive Optoelectronic Eye.

References.

[1]M.-H. Kiang, *et al.*, "Surface-micromachined electrostatic-comb driven scanning micromirrors for barcode scanners", *MEMS'96*, San Diego, Feb. 11-15, 1996, pp. 192-197.

[2]M. E. Motamedi, *et al.*, "MOEM scan engine for bar code reading and factory automation", *Proceedings of SPIE*, vol. 3276, *Miniaturized Systems with Micro-Optics and Micromechanics III*, Jan. 24 -30, 1998, San Jose, CA, pp. 66-80.

[3]V. R. Dhuler, *et al.*, "A novel two axis actuator for high speed large angular rotation", *Transducers'97*, Chicago, June 16-19, 1997, pp. 327-330.

[4]D. Berwick, *et al.*, "A chromaticity space for specularity, illumination color- and illumination pose-invariant 3-D object recognition", *Proceedings*, 6th IEEE Int. Conf. on Computer Vision, Bombay, India, 1998, pp. 165-170.

[5]R. Legtenberg, *et al.*, "Electrostatic curved electrode actuators", *JMEMS*, vol. 6, no. 3, pp. 257-265, Sept. 1997.

[6]K. Wang, *et al.*, "VHF free–free beam high-*Q* micromechanical resonators", *JMEMS*, vol. 9, no. 3, pp. 347-360, Sept. 2000.

[7]W. Daschner, *et al.*, "General aspheric refractive micro-optics fabricated by optical lithography using a high energy beam sensitive glass gray-level mask", *J. Vac. Sci. Technol.* B 14(6), pp. 3730-3733, Nov./Dec. 1996.

[8]R. A. Johnson, *Mechanical Filters in Electronics*. New York: Wiley, 1983.

IC-Integrated Flexible Shear-Stress Sensor Skin

Yong Xu, Yu-Chong Tai, Adam Huang*, and Chih-Ming Ho*

MS 136-93, California Institute of Technology, Pasadena, CA 91125, USA

*MAE, University of California, Los Angeles, CA 90024, USA

ABSTRACT

This paper reports the first IC-integrated flexible shear-stress sensor skin. By integrating both bias and signal-conditioning circuitry on-chip, the wiring of the MEMS skin is significantly simplified and reliability is improved. The circuit is first made by a commercial IC foundry (i.e., Mitel) and micromachining is done on the CMOS wafers to form the skins. We further demonstrated the use of the sensor skin by packaging it on a semi-cylindrical aluminum block and tested it in a wind tunnel. In our experiment, the skin has successfully identified both the flow separation and stagnation points. It is believed that the IC-integrated smart skin technology demonstrated here can be applied to many other interesting applications in biomedicine, wearable microsystems, robotics and so on.

INTRODUCTION

Since the emergence of MEMS technology, numerous miniaturized sensors and actuators have been fabricated using techniques originally developed for the integrated circuits industry. Inherently, most MEMS devices are built on rigid substrates. However, for a wide variety of applications, it has long been desirable for sensors, actuators and circuits to be mounted on non-planar surfaces or even on flexible objects such as a human body. For example, we have been working on a new way of controlling the Unmanned Aerial Vehicle (UAV) through the sensing/controlling of the flow separation at the leading edge. This requires distributed sensors mounted on the cylindrical surface of leading edge. Accordingly, we developed flexible shear-stress sensor skins for the UAV project [1]. These skins, however, contained only sensors and required many electrical lead connections. The complete separation-detecting system consisted of the packaged sensor skins, bias board, and data acquisition board and a tremendous number of interconnection cables as shown in Fig. 1.

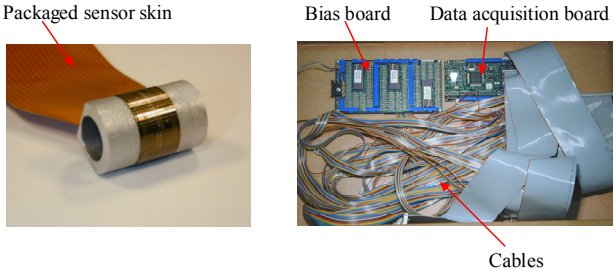

Figure 1 the flow separation detection system based on non-integrated sensor skin.

Therefore, it is highly desirable to develop IC-integrated shear-stress sensor skins with on-skin bias circuits, amplifiers, and multiplexers. By making IC-integrated skin, we can eliminate the bias board and interconnection cables, simplify the design of the data acquisition board, and improve system reliability at the same time. However, the integration of MEMS and ICs onto the same flexible skin is a challenge.

Generally speaking, MEMS-IC integration can be categorized into two groups: hybrid integration and monolithic integration. In the case of hybrid integration, MEMS parts and circuit parts are fabricated separately and then are packaged together by wafer bonding or other packaging technologies. With regard to flexible shear-stress sensor skin, monolithic integration is preferred since hybrid integration does not simplify the packaging process. Based on when MEMS parts are fabricated, monolithic integration can be classified as mixed MEMS-IC process, MEMS-first process (pre-IC or pre-CMOS) and IC-first process (post-IC or post-CMOS). The first approach is best exemplified by Analog Devices' accelerometer, which is fabricated by interleaving and customizing the MEMS manufacturing steps with the IC process [2]. J. H. Smith et al. at Sandia National Laboratories developed a unique MEMS-first process [3]. In this approach, MEMS devices are first fabricated in a trench on the surface of the wafer. The wafer is then planarized and the trench is sealed. The wafer with MEMS is then processed using conventional process. However, it would be highly unlikely for any IC foundry service to modify their IC fabrication process or take pre-processed wafers. Therefore, most monolithic integration is done with the post-IC approach, taking advantages of the widely available CMOS foundry services. For this IC-integrated shear-stress sensor skin, post-CMOS process is chosen for the same reason.

DESIGN

The shear stress is of great importance for many applications such as fluid dynamics monitoring, but obtaining it remains a difficult task largely due to the lack of instrumentation. There are many methods to measure the local wall shear stress, including Stanton tube, direct measurement, thermal method, Preston tube, sub-layer fence and electrochemical technique [4]. Of these approaches, the thermal method is most widely used since it does not interfere with the flow and it offers the possibility of measuring time-varying flows. Conventional thermal shear-stress sensors are typically made by depositing thin-film metal resistors, mostly platinum or nickel, on flat substrates. During operation, the resistor is electrically heated, while the fluid flow cools it down. The input power of the resistor will change with the wall shear stress from the ambient flow field and this change can be readily detected electronically. A large portion of the power is lost to the substrate via thermal conduction. With micromachining technology, a vacuum cavity can be built underneath the resistor to reduce the heat loss to the substrate, thus improving the sensitivity and frequency response of sensor. The basic structure of the micromachined thermal shear stress sensor is a polysilicon resistor sitting on a nitride diaphragm with a vacuum cavity underneath [5, 6]. This is the sensor design used in the non-integrated sensor skin [1].

0-9640024-4-2/hh2002/$20©2002TRF
DOI 10.31438/trf.hh2002.88

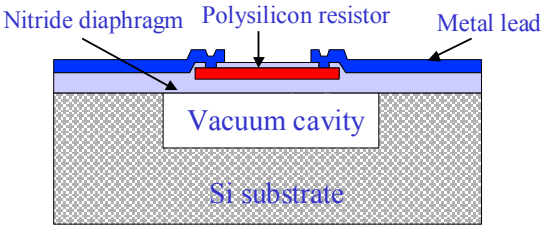

Figure 2 Cross-section of a vacuum insulated thermal shear stress sensor

Due to the limitation of post-CMOS process, this structure cannot be employed here. For this IC-integrated skin, the gate poly of the CMOS process is utilized as the sensing elements of the shear stress sensors. The silicon underneath is etched away to achieve the thermal isolation and a Parylene N layer is deposited as diaphragm. The cross section of the sensor is illustrated in Figure 5 (g).

Figure 3 shows the schematic of the integrated flexible shear-stress sensor skin. The shear-stress sensors, which utilize the gate polysilicon of the CMOS process as the sensing elements, operate in CC mode and are biased by the cascode current mirrors. The output voltage is multiplexed by PMOS switches and addressing circuitry. There are 16 shear stress sensors, which can be exactly accessed by a 4-bit address. An operational amplifier is also implemented to perform on-chip amplification.

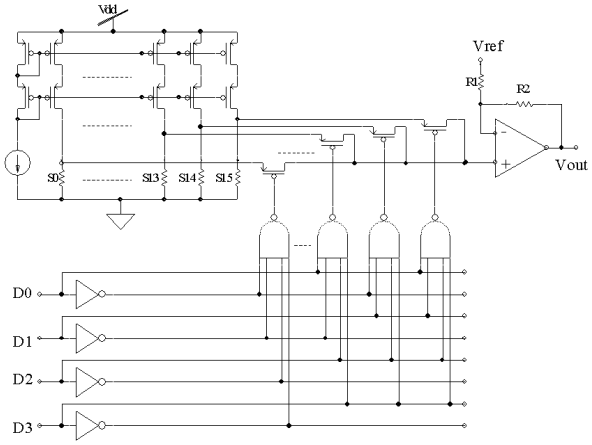

Figure 3 Schematic of the integrated flexible shear stress sensor skin.

FABRICATION

First, the circuits were fabricated by Mitel Semiconductor, which is Canadian CMOS foundry [7]. The gate poly of Mitel process is 320 nm thick, with a temperature coefficient of resistance (TCR) of 0.1% and a sheet resistance of 20Ω per square. Figure 4 shows the 6" wafer back from Mitel.

Then the post-CMOS process was conducted at the Caltech Micromachining Lab. Figure 5 (a) shows the cross section of the wafer back from Mitel. The polysilicon sensing elements are covered by dielectric and metal layers, so the process begins with patterning the metal and dielectric layers at the

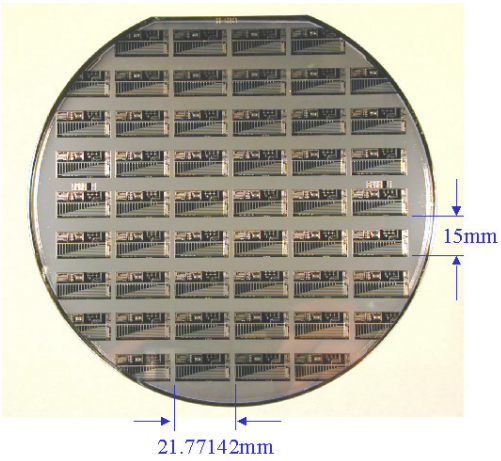

Figure 4 A 6" wafer back from Mitel.

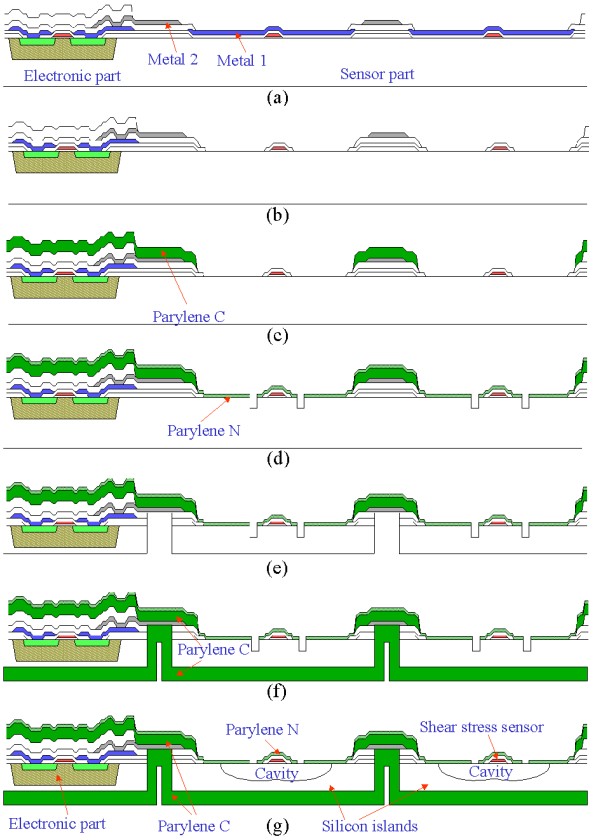

Figure 5 The simplified post-CMOS fabrication process.

sensor area, followed by deposition and patterning of 10 µm Parylene C on front side. Next, 1.5 µm Parylene N is deposited and patterned. Please note that both Parylene C and N are used in this project. Parylene C serves as the mechanical support to encapsulate the silicon islands while Parylene N serves as the diaphragm material to support the sensing element after releasing. There are two major differences between Parylene C and N which lead to their different roles. The first difference lies in the melting temperature. Parylene N has a much higher melting temperature (420 °C) than that of Parylene C (290 °C). Since the poly resistor will be heated up during operation, Parylene N is chosen as the membrane material to ensure the

high temperature compatibility. The second difference lies in the deposition rate. Parylene C has a much higher deposition rate than Parylene N. To provide enough mechanical support, we need approximately 10μm Parylene on both the front and back sides. It is impractical to deposit such a thick layer of Parylene N. The releasing holes for shear-stress sensor are then formed by patterning Parylen N as shown in Figure 5(d). These holes are further etched into the silicon substrate to enhance the BrF3 releasing process.

The process at the backside begins with the thinning down of the wafer. Next the silicon islands are formed by dry etching from the back side. DRIE is used in these two steps. After etching silicon down to the dielectric layer on the front side, pad etchant is used to remove the dielectric layer. Now 10 μm Parylene C is deposited on the wafer back side to sandwich the silicon islands. The final step is to release the polysilicon resistor by BrF3 gas phase etching. The purpose of this step is to achieve good thermal isolation for the sensing element.

The integrated skin cut from the wafer is shown in Figure 6. The silicon islands are clearly seen by shining light from the backside. The metal leads going across the islands can also be clearly observed.

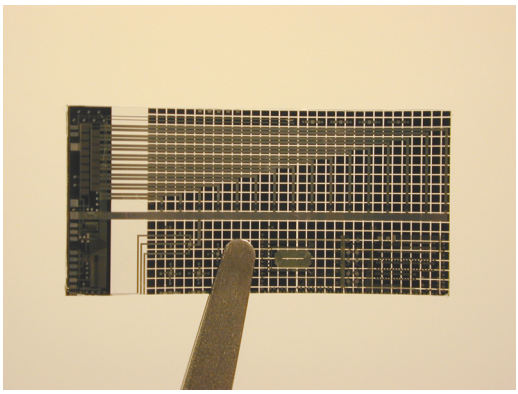

Figure 6 The fabricated IC-integrated skin held in tweezers.

PACKAGING

The sensor skin can be readily mounted on a non-planar surface. Figure 7 shows a single skin packaged on a semi-cylindrical surface of an aluminum block, which is the leading edge of an airfoil. Wire-bonding and conventional soldering were used to connect the sensor skin to the outside instrument. This configuration is adequate for our wind tunnel test. However, for real aircraft wing applications, the edge of the skin that contains the metal pads should be folded underneath the wing surface as in [1].

WIND TUNNEL TEST

The wind tunnel test was carried out in the UCLA wind tunnel lab. The testing set-up is illustrated in Figure 8. The integrated sensor skin was mounted on the top of the semi-cylindrical aluminum block. The definitions of sensor location θ and angle of attack α (AOA) can also be found in this figure. Shear stress distributions at different angles of attack were measured using the on-chip circuitry as shown in Figure 3. Sensor 0 is at the top surface and sensor 15 is at the bottom surface of the aluminum block. Since then angle between adjacent sensors is 12° and the 16 sensors exactly span 180°. It is worth noting that the vertical axis is the normalized output change $\Delta V / V$, where V is the output voltage. The purpose of this normalization is to minimize the non-uniformity of the sensors' shear-stress sensitivity caused by the process variation [8].

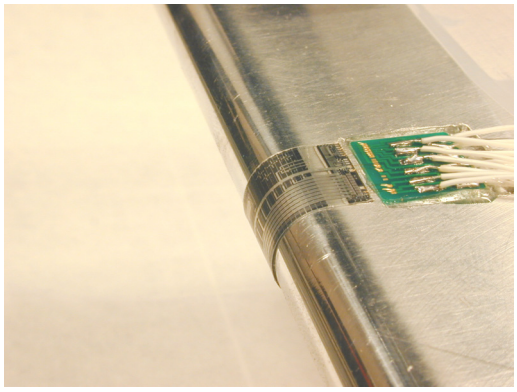

Figure 7 Sensor skins mounted on semi-cylindrical aluminum block

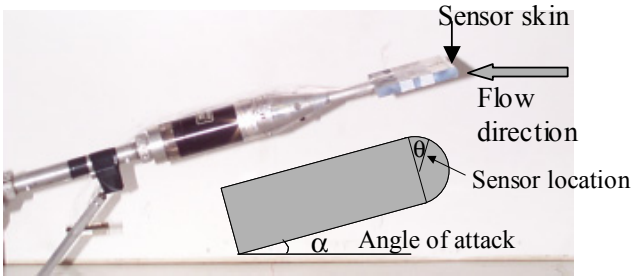

Figure 8 Testing setup in wind tunnel.

The separation point, which is characterized as the place where the shear stress has a sharp jump, can be clearly observed. Interestingly, the stagnation point, where the shear stress has a minimum value in the middle can also be identified. In the case of 0° AOA, the stagnation point is at the sensor 7 (84°), which is exactly as expected. On the other hand, the separation points may be at sensor 0 and sensor 15 or even beyond. In the case of 15° AOA, the separation point is at sensor 2 (24°) while the stagnation point is at sensor 9 (108°). For 30° AOA, the separation point moves to sensor 3 (36°) while the stagnation point moves to sensor 12 (144°).

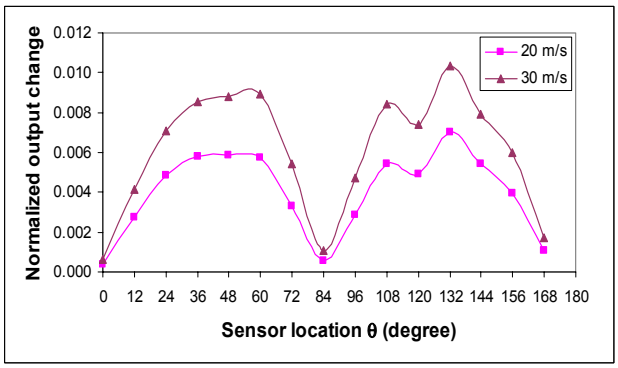

(a) 0° angle of attack

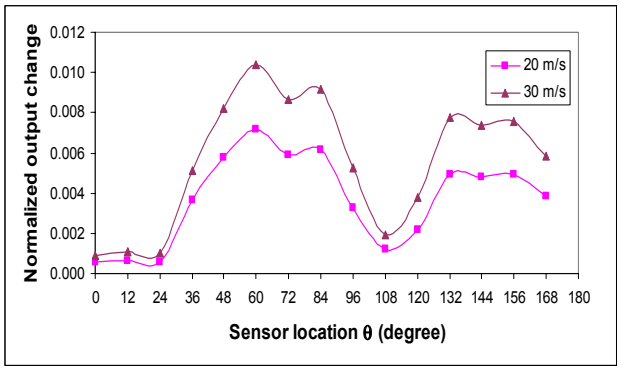

(b) 15° angle of attack

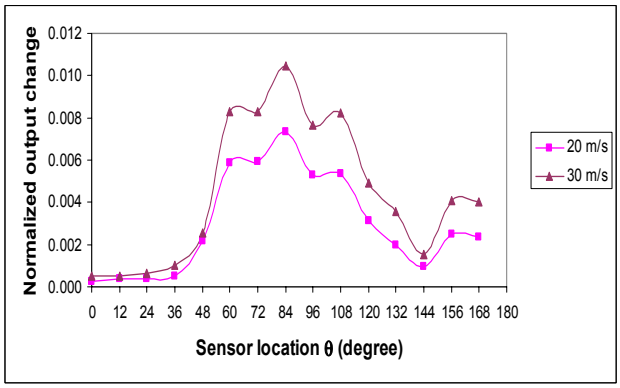

(c) 30° angle of attack

Figure 9 Shear stress distributions at different angles of attack.

DISCUSSION

An IC-integrated shear-stress sensor skin is successfully fabricated. With bias and signal conditioning circuitry integrated on-chip, the packaging and deployment of the sensor skin are significantly simplified and the system reliability is improved. In the wind tunnel test, both separation and stagnation points are detected by the sensor skin.

The IC-integrated smart skin technology demonstrated in this paper may have many other interesting applications. The first example is for the biomedical applications. Many MEMS devices have already been widely employed in biomedicine where miniaturized sensors, actuators and other micro structures are needed. However, the IC-integrated smart skins can further promote us to another level of functionality. As shown in Figure 10, the sensor skin can be mounted on human body like a Band-Aid™. Examples for future applications may include smart skins with sensors capable of monitoring physiological parameters such as glucose and insulin levels. For implantable applications, sensors can be built on flexible substrates to conform to the organ shape or to minimize tissue trauma during patient movement. Smart skins incorporating arrays of tactile, temperature, and other sensors are very helpful to surgical instruments for minimally invasive surgery. The IC-integrated smart skin would also be of great promise for wearable microsystems, robotics and many other research areas.

ACKNOWLEDGEMENTS

This project is supported by DARPA under the Navy contract N66001-97-C-8610 and by the NSF Center for Neuromorphic System Engineering at Caltech. Travel support has been generously provided by the Transducers Research Foundation and by the DARPA MEMS and DARPA BioFlips programs. The help from Justin Boland, Stacey Walker Boland, Matthieu Liger, Jun Xie and Trevor Roper is also highly appreciated.

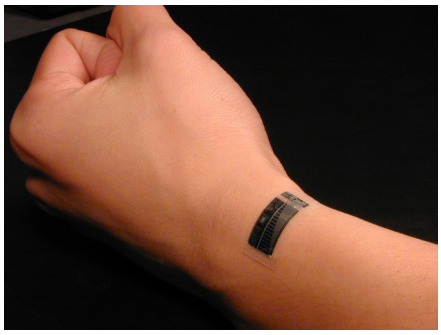

Figure 10 Example of future applications of the smart skin technology.

REFERENCES

[1] F. Jiang, Y. Xu, T. Weng, Z. Han, Y.-C. Tai, A. Huang, C.-M. Ho, and S. Newbern, "Flexible shear stress sensor skin for aerodynamics applications," presented at IEEE International Conference on Micro Electro Mechanical Systems (MEMS), Miyazaki, Japan, 2000.

[2] W. Kuehnel and S. Sherman, "A Surface Micromachined Silicon Accelerometer with on-Chip Detection Circuitry," *Sensors and Actuators a-Physical*, vol. 45, pp. 7-16, 1994.

[3] J. H. Smith, S. Montague, J. J. Sniegowski, J. R. Murray, and P. J. McWhorter, "Embedded micromechanical devices for the monolithic integration of MEMS with CMOS," presented at International Electron Devices Meeting. Technical Digest (Cat. No.95CH35810). IEEE. 1995, 1995.

[4] T. J. Hanratty and J. A. Campbell, "Measurement of wall shear stress," in *Fluid Mechanics Measurements*, R. J. Goldstein, Ed., 2nd ed: Taylor & Francis, 1996, pp. 575-648.

[5] C. Liu, Y. C. Tai, J. B. Huang, and C. M. Ho, "Surface Micromachined Thermal Shear Stress Sensor," presented at ASME International Mechanical Engineering Congress and Exposition, Chicago, IL, 1994.

[6] Y. Xu, F. Jiang, Q. Lin, J. Clendenen, S. Tung, and Y.-C. Tai, "Underwater Shear-Stress Sensor," presented at IEEE International Conference on Micro Electro Mechanical Systems (MEMS), Las Vegas, Nevada, 2002.

[7] "http://www.mitelsemi.com,".

[8] Q. Lin, F. Jiang, X. Wang, Z. Han, Y. C. Tai, J. Lew, and C. M. Ho, "MEMS Thermal Shear-Stress Sensors: Experiments, Theory and Modeling," presented at Solid-State Sensor and Actuator Workshop, Hilton Head Island, SC, 2000.

FLUID DAMPING OF AN ELECTROSTATIC ACTUATOR FOR OPTICAL SWITCHING APPLICATIONS

Kevin Y. Yasumura, John D. Grade, and Hal Jerman
Micromachining Development Group
ioλon Inc.
1870 Lundy Avenue
San Jose, CA 95131-1826

ABSTRACT

A 1×4 optical switch has been fabricated using a micromachined rotary actuator and commercially available miniature optics. This switch features an electrostatic actuator and a separately fabricated out-of-plane mirror. An important characteristic of such a device is its switching speed. Improved switching time can be obtained by damping the fundamental mode of motion to reduce the effect of ringing when the switch output is changed to a different fiber. In addition, damping the motor motion will improve the switch's immunity to externally applied accelerations. One means to passively damp the actuator modes of motion is to use a damping fluid with a viscosity greater than air (190 uP). Switching times of ~1 msec have been obtained for a fluid filled switch with less than 0.5 dB insertion loss.

INTRODUCTION

There are a number of applications that require low port count optical switches. These applications include adding protection and restoration capabilities to an optical network, optical component testing, and network monitoring. Using an optical switch, a failed fiber or transmitter link can be quickly bypassed until it can be repaired. In a component testing application, low port count optical switches can be used to test a series of optical components using the same set of test hardware. This can significantly reduce equipment cost and increase testing throughput. Real-time network monitoring and diagnostic applications are also possible through the use of optical switches. All of these applications can be accomplished using low port count optical switches that can be scaled to higher port numbers if needed.

In long-haul optical networks, all-optical switching provides a means to reduce overall system cost by reducing the number of times light must be converted to an electrical signal and again to an optical signal (OEO conversion). This process is expensive, requiring both a receiver and a transmitter to resend the optical signal. Optical transparency is becoming increasingly important for next generation network system designers as the percentage of node pass-through traffic increases. All-optical switches also have the advantage of being transmission protocol and bit-rate independent.

One version of a low port count optical switch is the 1×4 switch shown in Fig. 1. The switch consists of a micromachined rotary electrostatic actuator, a reflective mirror, a ceramic substrate, a GRIN lens, and an array of optical fibers. This separation of components allows for best-of-class component selection without concern for process compatibility. In addition, such a process allows for improved yield and flexibility in design. Shown in Fig. 1 is a 5 fiber array: 1 fiber is the input fiber (center fiber) and the other four fibers are the switch output fibers. The GRIN lens collimates the input beam from the fiber array and focuses it onto the mirror which is placed so that the axis of rotation is at the focal point of the lens. The light then reflects off of the mirror, passes back through the lens, and is refocused onto one of the output fibers. The actuator selects which output is used by rotating the mirror such that the input beam is reflected toward the selected output fiber. The entire switch package is approximately 1" × 1" × 0.5" including the necessary drive and control electronics.

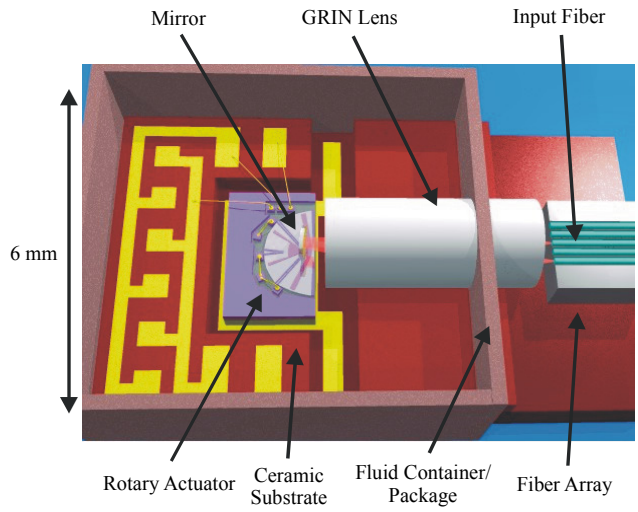

Figure 1. *Diagram of a 1×4 optical switch using a micromachined rotary actuator, a micromachined mirror, a GRIN lens, and a fiber array consisting of the input optical fiber and four output fibers. The switch is fabricated on a ceramic substrate and placed within a small 8 pin DIL package.*

Figure 2 shows a SEM photograph of a rotary actuator with a 12° total rotation range [**1**]. An early, undamped switch of this type was made with less than 0.5 dB insertion loss and with < 5 msec switching times between channels [**2**].

The resonance frequency of the switch actuator as well as its quality factor, Q, limit the optical switching time. In an open-loop system, high Q will produce ringing during a switching event, and it is therefore useful to reduce the Q of the fundamental mode of oscillation. Because device size and cost are important considerations for a commercial product, a reliable yet inexpensive means to damp the motor motion was sought. This work focuses on reduction in quality factor for such a micromachined actuator using a passive, fluid-filled damping approach to improve switching time performance.

OPTICAL SWITCH FABRICATION AND DESIGN

The process for fabricating the micromachined actuator has been described in detail in previous work [**3**]. First, a substrate

0-9640024-4-2/hh2002/$20©2002TRF
DOI 10.31438/trf.hh2002.89

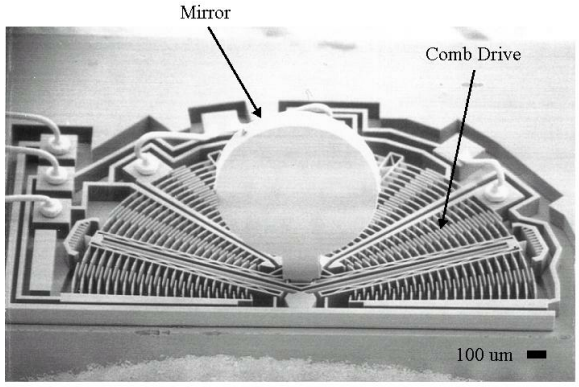

Figure 2. *SEM photograph of a switch actuator and its reflective mirror. The rotary switch motor has a total rotation range of 12 degrees with a maximum applied voltage of 150 V. The actuator die size is 2.8 × 1.8 mm. Two sets of combs rotate the actuator about an axis normal to the die surface (yaw). Applying a voltage to the electrically-isolated silicon substrate allows the mirror to be tilted upwards (pitch) to a maximum of 0.2 degrees with an applied voltage of 80 V.*

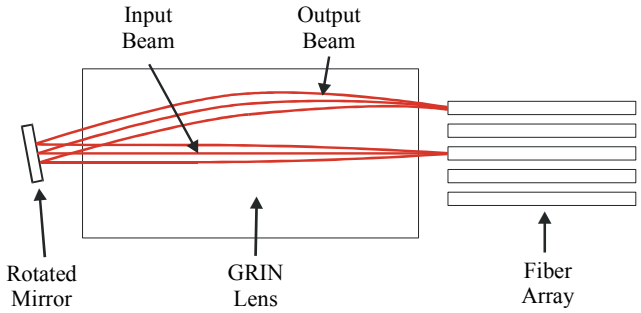

Figure 3. *Diagram of the optical switch in operation. In this figure, the MEMS actuator has been rotated to switch the input light into the upper-most output fiber. The MEMS rotator can be instructed to quickly switch the input light to any of the output fibers.*

silicon wafer is patterned with a 15-um deep cavity. The micromachined actuator will be fabricated above these cavities in the substrate wafer. Next, the device wafer is fusion bonded to the substrate wafer. The wafer stack is then ground and polished to produce the desired total motor thickness (typically 85-um thick). Contact pad metalization is then deposited and patterned. Finally, the motor features are defined using a DRIE process. Figure 2 shows a fabricated motor with its mirror attached. The paddle-shaped mirror is a gold-coated silicon plate with an attachment peg that is inserted into the motor. This mirror can be fabricated using the same process as the actuators. Passive placement of the mirror onto the rotary micromachined actuator using vision-guided robotics can routinely produce < 0.1 degrees of out-of-plane tilt.

In order to drive the actuator, a maximum voltage of 150 V is applied to one of two sets of electrostatic combs. Although the actuator requires a fairly high voltage to move to full angular rotation, the current draw is very small (pA) producing a low power device (nW). One set of combs causes the motor to rotate in the clockwise direction while the opposite set of combs will make the motor rotate in the counter-clockwise direction. The rotation of the actuator allows the switch to steer the incoming light into one of the output fibers. The actuator shown in Fig. 2 has a typical fundamental resonance frequency of 700 Hz allowing it to make rapid transitions between the various output states.

A diagram of the switching process is shown in Fig. 3. In this figure, the micromachined actuator has been rotated such that the incident light coming into the switch from the input fiber is reflected toward the top output fiber. The output fiber can be selected by simply moving the high-speed actuator to a new position. Accurate targeting of the output fiber is crucial to limit the amount of power loss in the switch. A radial beam misalignment of only 1 um from the center of the output fiber core will reduce the coupled power by 0.22 dB assuming purely gaussian beam coupling.

This issue becomes very important if you consider that the fiber cores in the fiber array are not perfectly collinear. The slight misalignment in each fiber is due to core centration error in the fiber itself and variability in the fabrication of the fiber array. Typically, about a 1 um height variation is found in a given fiber array. Figure 4 shows a plot of fiber core center position as a function of height along the y-axis (normal to the plane of the switch ceramic) for a typical array. This figure shows that an actuator that can only rotate (i.e., translate the beam in the x-direction) will not be able to optimally couple light into all of the output fibers. A means to deal with this is to create an actuator that can rotate in the in-plane direction but can also tilt in the out-of-plane direction [**4**]. The micromachined rotary actuator shown in Fig. 2 features this out-of-plane tilting capability. By applying a voltage to the electrically-isolated substrate wafer, the actuator can be attracted toward the substrate. For a typical 15-um deep etch cavity, this will produce a maximum of 0.2 degrees of out-of-plane tilting. This is more than enough motion to allow the actuator to efficiently couple light into all of the output fibers of the fiber array.

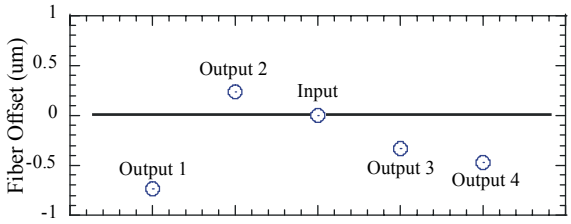

Figure 4. *Plot of the fiber core positions for a typical fiber array. In each fiber array the fiber cores are not perfectly aligned in the y-axis direction potentially causing additional coupling loss. Typical fiber array height variation is 1 um.*

Another issue that is resolved by using an actuator that can rotate about two axes is fiber-crossing during switching events. Instead of simply sweeping across all of the intermediary fibers, such an actuator can raise the beam above the fiber cores, rotate to the desired output fiber, and then tilt the beam back into position for the output fiber. Figure 5 shows a diagram of this type of switching event. By following the non-crossing switching path, the fiber crosstalk can be reduced significantly.

Because of the DRIE process used to fabricate the rotary actuators, high capacitance structures are created. The change in capacitance as the actuator rotates is > 1 pF. This allows for the use of off-chip capacitance circuitry that can be used to infer the position of the rotary actuator during operation. When the switch is fabricated, all of the initial components can be placed passively. The fiber array is the last component to be placed onto the switch. During the placement process, the fiber positions are optimized for coupled power. These optimal coupling voltages are then stored in

the control electronics. Future switching events then use these programmed voltages values together with the capacitance circuitry to provide a degree of closed-loop control for the actuator motion. The out-of-plane actuator motion is open-loop.

The long-term reliability of micromachined devices is often of concern. For the high-aspect ratio MEMS devices used in Iolon Corporation's products, however, excellent motor reliability has been demonstrated. A set of DRIE actuators, similar to the type shown in Fig. 2 has been actuated over 60 billion times with no measurable change in performance.

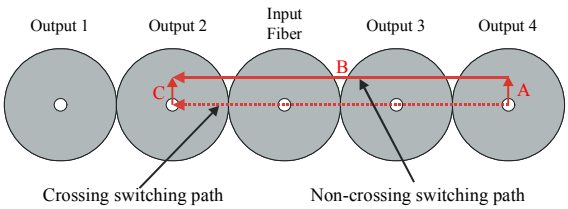

Figure 5. *In addition to being able to deal with the fiber core alignment issue, it is desirable to have a non-crossing switch: i.e., when switching between the different output fibers, light is not inadvertently sent into one of the intermediary fibers. This is shown in the diagram above. In the crossing switching path, light will be sent into output fiber 3 before the beam reaches output fiber 2. This is resolved by having an actuator that can first raise the beam above the fiber core positions (path A), cross over to the desired output fiber (path B), and then tilt the beam down and into the target output fiber core (path C). Note: switching paths are not drawn to scale.*

SWITCH PERFORMANCE & FLUID DAMPING

For MEMS devices fabricated from materials such as silicon, silicon carbide, silicon nitride, and polysilicon, the intrinsic material damping can be very low. Q's greater than 10^3-10^4 can be obtained for silicon micromachined structures operated in vacuum [**5**,**6**]. Such high Q's are of value to improve measurement resolution if used as a resonant sensor. In a switching application, however, high Q produces residual ringing of the device when it is switched between channels. A reduction of Q preferably below 1 is therefore desired. For MEMS devices operated in atmosphere, air damping is usually the dominant damping mechanism [**6**,**7**,**8**,**9**].

The fundamental resonance of the switch actuator shown in Fig. 2 has a measured Q of 20 in air. When compared with intrinsic Q values of single-crystal silicon structures, this is already a large amount of damping. Additional damping, however, is desired in order to reduce the Q further. Because the gap between moving elements is limited by fabrication design rules, additional gas damping via design modifications is difficult to obtain. Another means to increase damping is to fill the actuator package with a damping fluid with a viscosity greater than air (190 uP) [**10**,**11**]. There are a large number of possible fluids that could be used. Gases such as Ne (315 uP viscosity) can produce small amounts of additional damping. An ideal damping fluid would have a viscosity sufficient to bring the Q close to unity but low enough to allow high-speed operation.

The damping fluid must also be nonconductive to allow proper operation of the electrostatic comb drive. Additionally, a liquid will have a dielectric constant higher than air. This will benefit the motor's motion because the force between the actuator combs is proportional to the dielectric constant of the material between the combs. Polar fluids typically have higher dielectric constants.

Two different fluids were tested: a proprietary low-viscosity oil (Cargille 4501) and diethylbenzene (DEB). If the fluid damping is modeled using Stokes flow damping, the Q can be expressed as

$$Q = \frac{g}{\mu A}\sqrt{km},$$

where μ is the fluid viscosity, A is the comb overlap area, k is the motor's suspension stiffness, m is the moving mass, and g is either the boundary layer thickness or the gap between the moving elements [**8**]. The low-viscosity oil has a viscosity of 1.4 cP while diethylbenzene is 0.6 cP (measured using a falling ball viscometer). With the Stokes model, the predicted Q's are 0.25 for the oil and 0.60 for diethylbenzene. Figure 6 shows measured frequency responses in air, in oil, in diethylbenzene, and again in air after the fluid fill tests. The measured and predicted quality factors differ by less than 15%. The pre- and post-air tests produced identical damping results.

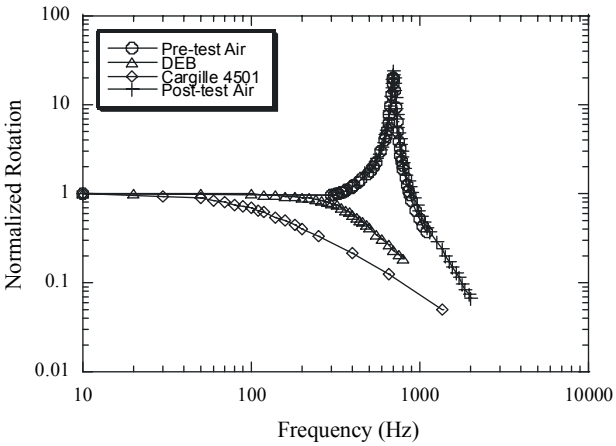

Figure 6. *Frequency response plot of the switch actuator. The motor was measured in air, in a low viscosity oil (Cargille 4501), in diethylbenzene (DEB), and again in air after removal of the fluid damping materials. The introduction of the fluid fill materials has reduced the fundamental Q below 1 in both cases. The motor returned to its initial damping value after removal of the fluid damping materials.*

Figure 7 shows a fiber-switching event with an applied step voltage. Data for switching both in air and in a damping fluid is shown. In air, considerable ringing is observed in the output fiber after the switching event. The fundamental, in-plane Q of the actuator (~20) produces ringing as the motor settles into its new alignment position. A total switching time of > 50 msec was observed under these conditions. By reducing the fundamental Q of the actuator, this ringing response can be removed. Fluid damping the rotary actuator produces a significant improvement in the fiber switching time.

Figure 8 shows a zoomed view of the fiber-switching event in a fluid environment. Diethylbenzene damped the motor's fundamental Q to below 1. This fluid damping enabled switching times of ~1 msec. The drop in power after first light is caused by slight overshoot of the actuator as it switches to the new output fiber.

A secondary benefit of using a fluid-filled damping scheme is the enhancement of the electrostatic force caused by the increased dielectric constant of the fluid material. Because the force created

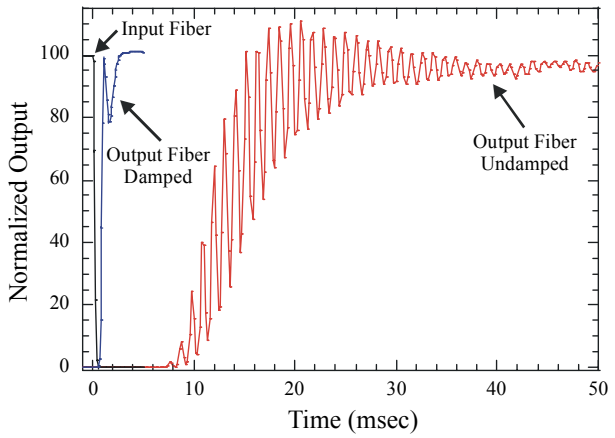

Figure 7. *Fiber switching in air and in a damping fluid (DEB) with an applied step voltage. The ringing observed in air is caused by this step change in drive voltage. The Q of the actuator (20) increases the decay time of the post-transition oscillation, producing switching times > 50 msec. One means to reduce this ringing effect is to reduce the actuator quality factor. After application of the damping fluid, the switching time (and amount of ringing) has been reduced significantly.*

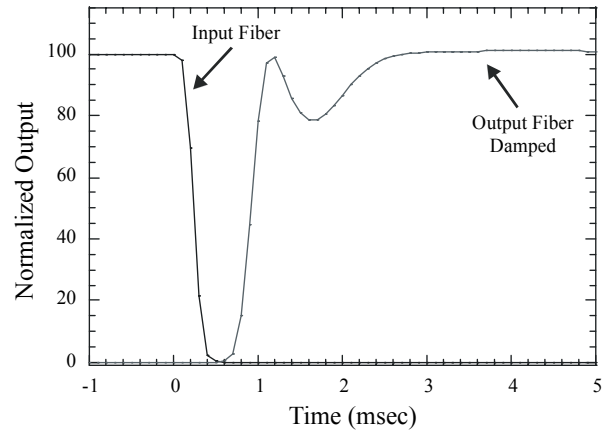

Figure 8. *Fiber switching in diethylbenzene (DEB). The ringing observed in the output fiber when switching in air is dramatically reduced by damping the actuator's fundamental oscillation mode to have a Q less than 1. Note the reduced time scale: the damped switching time is just over 1 msec to first light. The 1 dB power drop is caused by slight rotational overshoot of the switch actuator.*

by the comb drive is proportional to εV^2, where ε is the dielectric constant of the fluid-fill material and V is the applied voltage, the amount of voltage required to drive the actuator to full deflection is reduced. In air, the voltage required to reach full in-plane angular rotation is 150 V. This maximum voltage is reduced when the switch is filled with a fluid damping material. For DEB, the voltage reduction indicated a dielectric constant of 2.44 while for Cargille 4501 the dielectric constant was 3.45. This is a considerable increase in the electrostatic force. Other types of actuator systems could potentially benefit from using such a force-enhancement scheme when actuator size or voltages are limited by experimental or design considerations.

Additional issues with this concept might include possible fluid degradation over time. This is especially important if high optical powers are to be switched using this device. Additionally, the effect of the fluid on the optical surfaces and coatings needs to be investigated to ensure reliable switch operation over the lifetime of the device. Finally, to limit the switch insertion loss, attention to the optical absorption spectrum of the selected fluid material also needs to be investigated.

CONCLUSIONS

A novel method to passively damp an all-optical electrostatic switch actuator has been demonstrated. Q's < 1 have been obtained while simultaneously improving the switching time performance. Switching times of ~1 msec have been obtained for a packaged 1 × 4 microswitch device.

This passive, fluid-based damping technique offers advantages not only to the measured switching time but it should also improve the vibration immunity of the device. The use of nonconductive, high dielectric constant materials also produces an enhancement to the electrostatic force used to actuate the MEMS device. This results in a reduction in the voltage required to move the mirror rotator to full angular deflection.

ACKNOWLEDGEMENTS

The authors would like to thank Al Fennema, Steve Hrinya, Kathy Jackson, Howard Lee, Pei-Fei Li, and Chris Tan at Iolon, Inc. and Sam Wong at TRW Lucas Novasensor for their assistance with fabrication, assembly, and testing.

REFERENCES

1. J.H. Jerman and J.D. Grade, US Patent 6,329,737 B1, "Rotary Electrostatic Microactuator", Dec 11, 2001.
2. J.D. Grade and J.H. Jerman, "MEMS Electrostatic Actuators for Optical Switching Applications", *Optical Fiber Conference*, WX2-1, 2000.
3. J.D. Grade, H. Jerman, and T.W. Kenny, "A large-deflection electrostatic actuator for optical switching applications", *Proc. 2000 Solid-State Sensor and Actuator Workshop, Hilton Head, SC*, pp. 97-100.
4. J.H. Jerman and J.D. Grade, US Patent 6,333,584 B1, "Tiltable Electrostatic Actuator and Method for Using Same", Dec 25, 2001.
5. R.E. Mihailovich and N.C. MacDonald, "Dissipation measurements in vacuum-operated single-crystal silicon microresonators", *Sens. Actuators*, vol. 50, pp. 199-207, 1995.
6. K.Y. Yasumura, *et al.*, "Quality factors in micron- and submicron-thick cantilevers", *Jour. Microelec. Mech. Sys.*, vol. 9, no. 1, pp. 117-125, 2000.
7. W.C. Tang, *et al.*, "Laterally driven polysilicon resonant microstructures", *Proc. IEEE Workshop on Micro. Electro. Mech. Syst., Salt Lake City, UT, U.S.A.*, Feb. 1989, pp. 53-59.
8. Y.H. Cho, *et al.*, "Viscous Energy Dissipation in Laterally Oscillating Planar Microstructures: A Theoretical and Experimental Study", *Proc. IEEE Conf. Of Micro. Elect. Mech. Systems, Ft. Lauderdale, FL*, Feb 1993.
9. F.R. Blom, *et al.*, "Dependence of the quality factor of micromachined silicon beam resonators on pressure and geometry", *J. Vac. Sci. Technol.*, B10, 1, 1992, pp. 19-26.
10. L. Roylance and J. Angell, "A batch fabricated silicon accelerometer", *IEEE Trans. on Elec. Dev.*, vol. ED-26, no. 12, pp. 1911-1917, Dec 1979.
11. J.D. Grade, J.H. Jerman, and J.D. Drake, PCT International Publication number W0 01/95468, "Micromechanical Device With Damped Microactuator", Dec 13, 2001.

Large Area Microfluidic Mixer
Integrated with Linear Fluidic Transporters and Reservoirs

Hongyu Yu and Eun Sok Kim
Department of Electrical Engineering-Electrophysics
University of Southern California
Los Angeles, CA 90089-0271

ABSTRACT

This paper describes a large area (over 100 mm^2) micromixer integrated with long-channel fluidic transporters and reservoirs on a same substrate. Both the micromixer and the linear fluid transporter are built on a PZT sheet with its electrodes patterned to produce self-focused acoustic beams for powerful in-plane liquid motion (through acoustic streaming effect). Self-focusing Acoustic Transducers (SFAT) are sectored and connected in various patterns for a variety of mixing and transport effects, and are set under a silicon, glass or plastic wafer that contains a large area, shallow, mixing chamber. Mixing in a 200 µm deep, 100 mm^2 chamber can be done within 2 seconds.

INTRODUCTION

Lab-on-chip (LOC) with microfluidic processing capabilities has great potential for biomedical applications. Especially, microfluidic systems that can process liquids of tens of µl are greatly needed for many biomedical processing systems. Microfluidic mixing has conventionally been done using heat, electrolysis and electromagnetic force. These methods, however, present some difficulties in any of the following requirements: compatibility with biomedical applications, easiness of integration with LOC system, mixing capability of relatively large volume liquid. It has been reported that focused acoustic waves are effective in generating fluidic motion [1], and a sectored Self-focusing Acoustic-wave Transducer can produce strong in-plane liquid motion for micromixing [2]. Thus, we have used several arrays of sectored SFATs to transport (over tens of mm length) and mix (over hundreds of mm^2) fluids noninvasively. This paper describes the theory, design and experimental results of the fluid mixer integrated with fluidic transporters and reservoirs.

THEORY

SFAT with its electrodes on both faces of a piezoelectric film patterned as shown in Fig.1 focuses acoustic waves through constructive wave interference [3]. When RF power is applied between the electrodes (sandwiching the piezoelectric film) with its frequency corresponding to the thickness mode resonance of the piezoelectric film, strong acoustic waves are generated over the areas covered by the electrodes. With a proper design of the electrode patterns (e.g., a set of annular rings acting as half-wave-band sources), we can achieve wave-focusing effect without any acoustic lens due to the acoustic waves interfering with each other as they propagate in the fluid adjacent to the transducer.

With a set of complete annular rings, the acoustic field is radially symmetrical in the plane of the rings. But when the rings are broken into segments of various angles, the acoustic field becomes nonsymmetrical in the in-plane. The basic cell that we employ for the SFAT fluid driver is a 90° sectored SFAT built on a PZT substrate shown in Fig. 2.

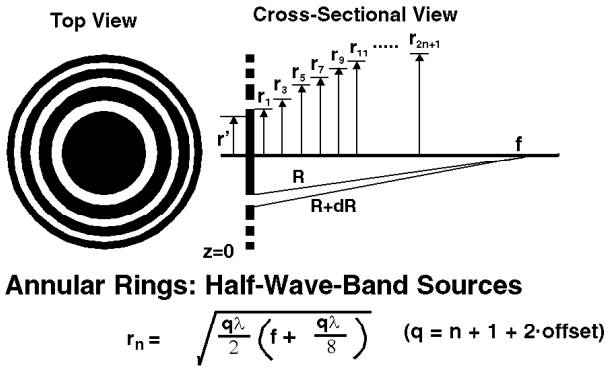

Fig. 1 *The electrode pattern of annular rings on both faces of a piezoelectric plate for self-focusing of acoustic waves.*

A high-intensity acoustic wave propagating in a medium is absorbed and scattered by the medium. The wave attenuation with a high intensity wave is nonlinear, and causes the medium itself to move. This nonlinear acoustic effect is called acoustic streaming.

In a sectored SFAT, the electrode patterns for the top and bottom electrodes are designed to produce large acoustic pressure gradient (especially in the in-plane direction) near the focal points. As the intensified acoustic waves travel in the liquid with accompanying acoustic loss, the acoustic streaming happens, and there exists steady body force in the liquid to drive fluid flow [4].

$$\vec{F}_b = \rho_0 \left\langle \vec{v}_1 \nabla \cdot \vec{v}_1 + (\vec{v}_1 \cdot \nabla)\vec{v}_1 \right\rangle$$

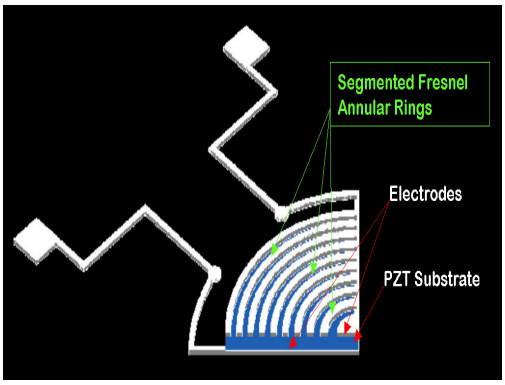

Fig. 2 *A 90° sectored SFAT cell*

0-9640024-4-2/hh2002/$20©2002TRF
DOI 10.31438/trf.hh2002.90

FABRICATION

Figure 3 shows the fabrication process for the sectored-SFAT fluid driver. We use a 192µm thick PZT sheet as the transducer substrate. With the front-to-backside alignment marks, 2.54 µm thick silver electrodes on both sides of the PZT sheet are patterned such that the top and bottom FASA electrodes overlap each other. The silver is etched with 3M HNO_3 in 35 seconds. The fluid chambers are micromachined in silicon substrate using HNA isotropic etching or KOH anisotropic etching. Two kinds of mixing chambers have been fabricated: one in a 400µm thick silicon wafer, the other over a 170µm thick glass or 100µm thick plastic wafer with an etched-through silicon on its top (shown in Fig 4). The mixing chambers, built on a silicon wafer, are fabricated together with linear channels and rectangular reservoirs on a same substrate to produce an integrated microfluidic subsystem, which is then bonded (with about 10µm thick epoxy) to the PZT transducer (Fig.3).

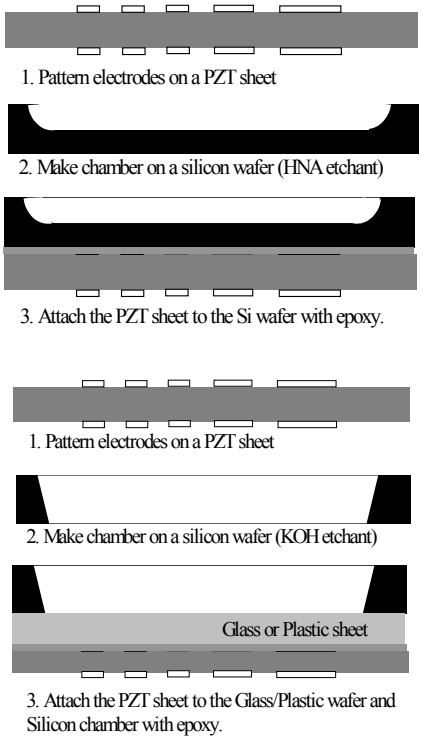

Fig. 3 *Brief fabrication steps for two types of mixing chambers in Si wafer (top three) and Glass or plastic wafer (bottom three).*

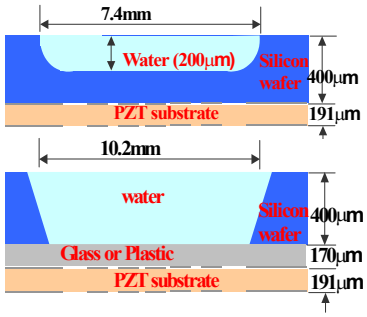

Fig. 4 *Cross sectional views of the two types of mixing chambers.*

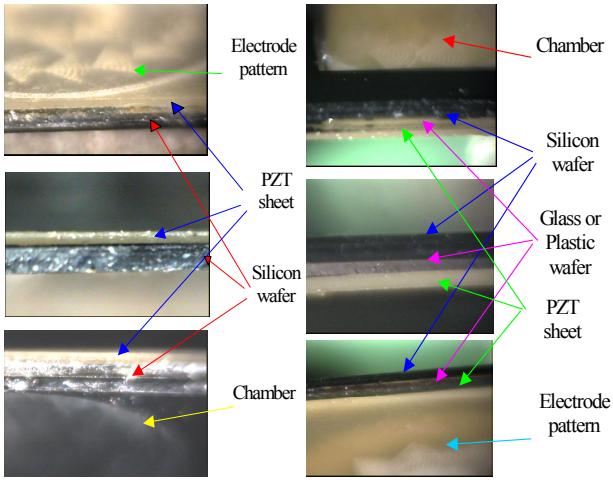

Fig. 5 *Cross-sectional photos of the completed mixers*

EXPERIMENTAL METHOD

The fabricated devices are tested in an apparatus shown in Fig. 6, where a RF square wave (with the frequency around 12 MHz corresponding to the thickness of PZT sheet) is modulated with a sequence of pulses from a function generator before being amplified by an RF amplifier and applied to the device. The peak-to-peak voltage of the RF amplifier output is typically about 40 V, and the electrical field across the PZT substrate is about 10^5 V/m. When we apply a continuous square wave, the series resistance of the electrodes produce significant amount of heat. Thus, we use a pulsed square wave with 30 to 120 Hz pulse repetition frequency and on time of 40 to 100 µs (corresponding to a duty cycle of 0.12% to 1.2%). With this pulsed wave, heating is negligible.

The fluidic subsystem includes a mixer, two linear transporters and rectangular reservoirs. In the rectangular reservoirs, we first place red ink and DI water along with microspheres of 10µm in diameter to facilitate the observation of the liquid flow and mixing trace. Those liquids are transported from the reservoirs to the circular mixing chamber through the connecting fluidic channels by the microfluidic driver [5], and then are mixed together in the mixing chamber by the micromixer.

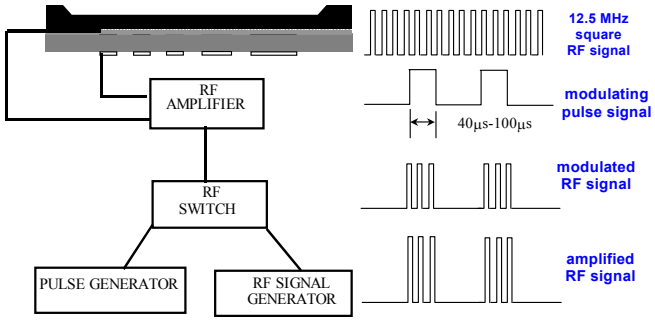

Fig. 6 *Schematic of the test set-up.*

EXPERIMENTAL RESULTS

The top-view photo of the fabricated microfluidic subsystem (with two rectangular reservoirs of 9.4 x 3.4 mm^2 each, 1 mm wide and 8.4 mm long channels, and a circular mixing

chamber of 7.4mm in diameter) is shown in Fig. 7. The micromixer can mix liquids (about 0.2 to 0.4 mm tall) over 100mm^2 area within 2 seconds. To demonstrate the mixing capability, two kinds of liquids (red ink and DI water) with microspheres are stored in the two rectangular reservoirs (on the right-hand side of Fig. 7), driven along the two narrow and long channels (on the middle of Fig. 7) by linear arrays of the sector SFATs, and mixed in the circular chamber (on the left-hand side of Fig. 7) by the micromixer.

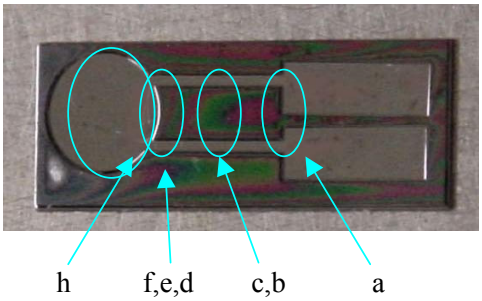

Fig. 7 *Top view photo of the fabricated microfluidic subsystem made in a silicon wafer with PZT sheet.*

The fluids in the subsystem are driven by the sector SFATs, and their flows are captured at the four regions indicated with elliptical circles in Fig. 7 at different points of time (a-h) as follows:

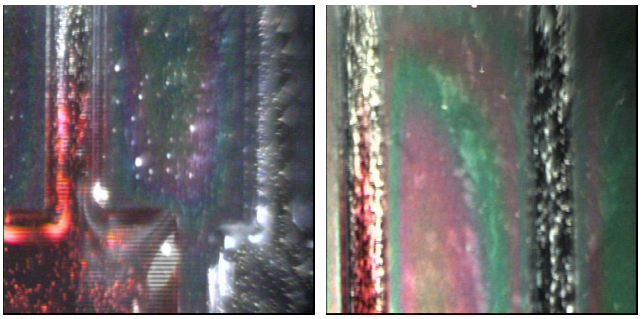

a b

(a) 0.5 sec after electrical pulses are applied to the PZT drivers, the liquids begin to be driven from the rectangular reservoirs at the right hand side (Fig. 7);

(b) 1.2 sec after the turn on of the pulses, the liquids arrive at the channel midpoint;

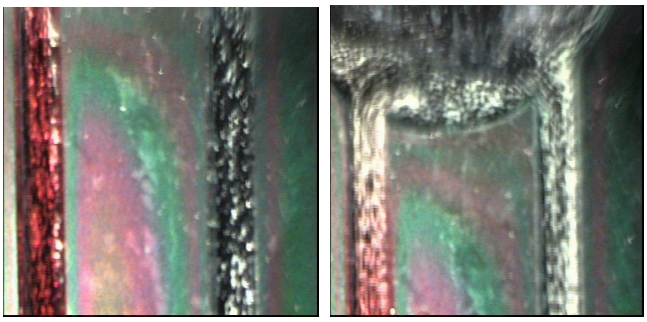

c d

(c) the liquids being continuously transported by two sets of linear array of sector SFATs attached to the microfluidic subsystem;

(d) the liquids being continuously delivered to the mixing chamber by the linear array of sector SFATs.

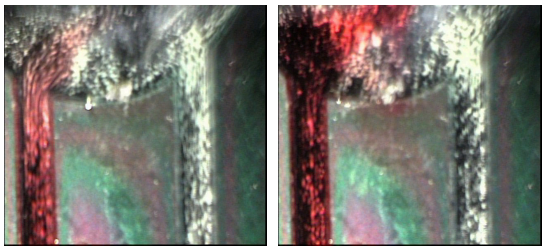

e f

(e) 1.7 sec after the turn on of the pulses, the liquids arrive at the mixing chamber;

(f) start of the mixing;

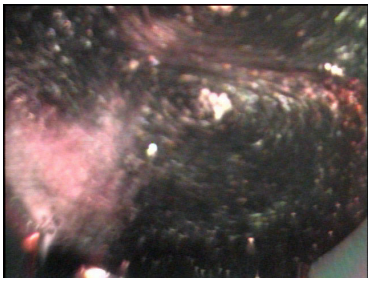

h

(h) 3.2 sec after the power on (it shows the effective mixing of the two liquids).

The mixing speed can easily be controlled by adjusting the pulse duty cycle or the peak voltage level. And different electrode patterns on the SFAT can produce different fluid mixing traces as shown in Fig. 8: in (a) there are 3 “eyes” producing almost random mixing, while in (b) there is only one “eye” in fluid mixing flow which would be good for a directional mixing.

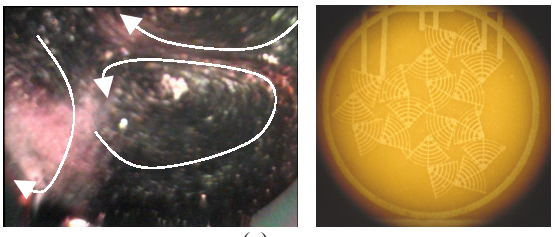

(a)

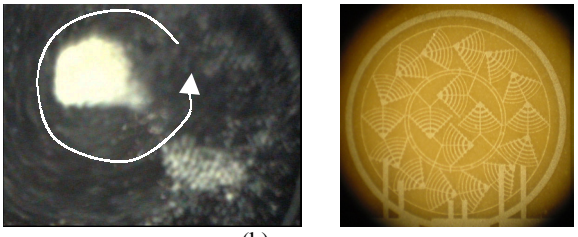

(b)

Fig. 8 *Mixing patterns and the electrode patterns on the SFATs that produce the mixing traces.*

In the experiment, we find the ‘eye’ point is not good for mixing liquids with particles, because the particles come and tend to stay there without moving around. To solve this problem, we adjust the RF frequency so that the liquid mixing trace may be changed. When the frequency is changed a little, such as ±0.1MHz, there is still good mixing effect in the chamber, although the mixing speed is slowed down a little, and at same

time, the liquid mixing trace is changed. The reason for such trace change is that when the frequency is varied, the interference between the waves varies, resulting in a variation in the acoustic wave distribution in the liquid, which changes the body force distribution in the liquid,. When we change the liquid traces by changing the RF frequency, we can force all particles to mixing and avoid the nodal effect by the 'eye' (Fig.9).

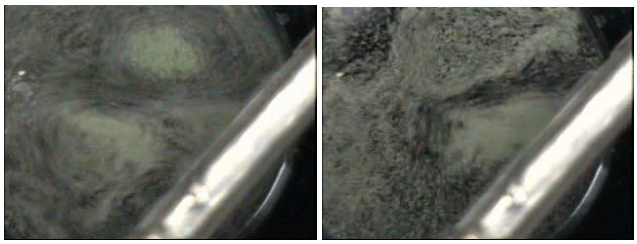

Fig. 9 *Liquid trace changes when the RF frequency is changed by a small amount.*

When the PZT SFAT is glued to a silicon wafer that contains microfluidic channels and chambers, the S11 parameter of the SFAT (without any liquid) is as shown in Fig. 10. There are two peaks in the S11 (due to the micromachined silicon attached to the PZT sheet), which broaden the resonance characteristic. From the S11, we see that there is still at least 30% of the peak power at the frequency ±0.1MHz off from the center frequency. With liquid in the mixing chamber, the drop in the available power (from the peak power as the frequency is varied) would be less due to the mass loading effect by the liquid. Thus, we would still have significant amount of acoustic power available for mixing, even when we vary the RF frequency to change the liquid traces.

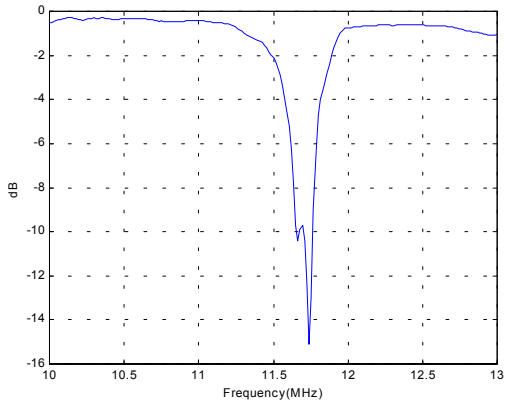

Fig. 10 *S11 parameter of the sector SFAT attached to a silicon wafer with microfluidic channels and chambers.*

In addition to silicon wafer, glass and plastic wafers also have been used as the chamber/channel/reservoir substrate. We get almost same mixing effect on these wafers, although the mixing speeds are slowed down, especially on the plastic wafer, due to more acoustic absorption in the plastic or glass wafer than in a silicon wafer. Figure 11 shows the time sequence of the mixing effect on a plastic wafer.

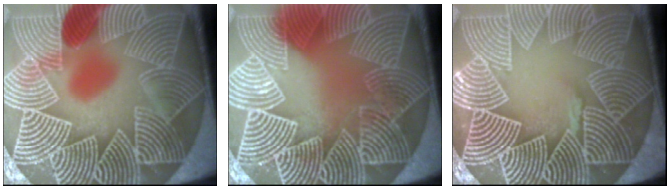

a b c

Fig 11 *Time procession of the mixing: (a) Right after red ink is dropped in the water, (b) 2.4 sec later, (c) 8.6 sec later.*

SUMMARY

In this paper, we describe a large area (over 100 mm^2) micromixer integrated with long-channel fluidic transporters and large reservoirs on a same substrate. The three major microfluidic components are integrated in a micromachined silicon substrate with sector SFATs built on a PZT sheet. The micromixers and linear fluid transporters built on the PZT SFATs produce strong in-plane fluid motion without heat. And we demonstrate a powerful mixing effect over a large surface area. In addition, we demonstrate the integrated microfluidic subsytem over a glass or plastic wafer with silicon sidewalls. The microfluidic subsystem described in this paper integrates three major fluidic components (i.e., micromixer, liquid transporter, and reservoir), and is ready for a stand-alone microfluidic system, once one-way valves are integrated.

ACKNOWLEDGMENT

This material is based upon work supported by Defense Advanced Research Projects Agency under contract #N66001-00-C-8094.

Travel support has been generously provided by the Transducers Research Foundation and by the DARPA MEMS and DARPA BioFlips programs.

REFERENCES

[1]. X. Zhu and E.S. Kim, "Microfluidic Motion Generation with Acoustic Waves," Sensors and Actuators: A. Physical, vol. 66/1-3, pp. 355-360, April 1998.

[2] V. Vivek, Y. Zeng and E.S. Kim, "Novel Acoustic-Wave Micromixer," IEEE International Micro Electro Mechanical Systems Conference, Miyazaki, Japan, January 23-27, 2000, pp. 668-673.

[3] D. Huang and E.S. Kim, "Micromachined Acoustic-Wave Liquid Ejector," IEEE/ASME Journal of Microelectromechanical Systems, vol. 10, pp. 442-449, September 2001

[4]. T. Uchida, T. Suzuki and S. Shiokawa, "Investigation of Acoustic Streaming Excited by Surface Acoustic Waves," 1995 IEEE Ultrasonics symposium pp. 1081-1084.

[5] H. Yu and E.S. Kim, "Noninvasive Acoustic-Wave Microfluidic Driver," IEEE International Micro Electro Mechanical Systems Conference, Las Vegas, Nevada, January 20-24, 2002, pp.125-128.

TWO-DIMENSIONAL CHIP-BASED PROTEIN ANALYSIS USING COUPLED ISOELECTRIC FOCUSING AND CAPILLARY ELECTROPHORESIS

Amy E. Herr, James C. Mikkelsen, Juan G. Santiago, and Thomas W. Kenny
Department of Mechanical Engineering, Stanford University
Stanford, CA 94305-4021

ABSTRACT

A chip-based acrylic microfluidic device that sequentially couples isoelectric focusing (IEF) and capillary electrophoresis (CE) has been designed and demonstrated. To our knowledge, this is the first time such an implementation of on-chip two-dimensional (2-D) electrophoresis has been presented. Both dimensions in this liquid-phase system were characterized using a full-field CCD imaging approach. Commercial ampholytes were used in microchannel-based IEF to sustain a stable pH gradient. Analysis of the concentrating IEF step revealed substantially reduced electroosmotic mobilities, as compared to typical mobilities for acrylic microchannels filled with standard buffer solutions. Due to this residual electroosmotic flow, IEF species were simultaneously rapidly focused and slowly mobilized into intersections. After IEF separation and 100x pre-concentration, voltage switching was used to electrokinetically inject portions of a multi-protein mixture into the second separation, which was ampholyte-based CE. Mobility information was obtained from the second dimension. Results are presented in a 2-D area plot. With optimization, this architecture has the potential to be a basis for high-throughput, high-resolution protein and peptide analysis.

INTRODUCTION

Multi-dimensional separation techniques can be used to attain ultra-high resolution. Typically, two independent separation mechanisms are employed sequentially, each providing a selective displacement along respective separation axes.[**1**] This coupling of techniques allows species that would not necessarily be resolved by either technique to become fully resolved.[**2**] Two-dimensional electrophoresis sequentially couples IEF to CE, thus taking advantage of the demonstrated independence of the two mechanisms. This technique is typically implemented, over a period of hours, using slab-gel and coupled capillary formats; wherein, an IEF step comes to completion, is halted, and a subsequent CE analysis proceeds. The sequential coupling of discrete separation mechanisms is relevant to assays with numerous sample species, as in the case of proteomic analyses[**3**], but has been described as a 'bottleneck' in such work.

During miniaturized IEF, species were simultaneously focused and mobilized, as previously demonstrated.[**4**] Species concentrations were increased by ~100x due to focusing. In chip-based 2-D electrophoresis, the focused species were subsequently electrokinetically injected into the CE dimension and separated based on mobility differences. This microfluidic system opens possibilities for further species manipulation and analysis. Additionally, the low viscosity of the ampholyte solution and the short channel lengths employed in this work substantially decreased the analysis time for both IEF and CE, as compared to a slab-gel approach. Integration of the respective dimensions on a single device is investigated and 2-D results are presented.

EXPERIMENTAL DETAILS

Commercial carrier ampholytes (pH 3 to 10, Bio-Rad Laboratories) were used as the separation media. Catholyte and anolyte were 40 mM sodium hydroxide and 20 mM phosphoric acid, respectively. The sample mixture consisted of green fluorescent protein (180 nM), unpurified FITC-labeled ovalbumin (100 nM), and FITC-labeled dextran (100 nM, MW 10 kDa).

The planar multi-dimensional chips were designed in-house and fabricated by ACLARA Biosciences in poly(methyl methacrylate) using an imprinting and laminating technique similar to that reported in the literature (*w* x *d*: 200 µm x 20 µm).[**5**] Channel geometry was that of a cross-t intersection (Figure 1). Custom fixturing was designed and fabricated in-house to provide wells for inserting platinum electrodes and allow for pressure cleaning of the channels. High voltage was applied and adjusted using a computer-controlled high voltage power supply (Micralyne). Species transport was monitored using standard epifluorescence techniques and a cooled CCD camera (Roper Scientific). A 0.31x demagnifier (Diagnostic Instruments Inc.) increased the field of view. Spatial electropherograms were obtained by binning each CCD image in a direction perpendicular to the particular separation axis.

INTEGRATED DEVICE OPERATION

IEF and CE were controlled by the chemistry (including pH) and applied potential at specific microchannel reservoirs. A uniform ampholyte buffer solution was used as the separation media for all separations performed using the integrated device. The device architecture is depicted in Figure 1. While the ampholytes in the IEF dimension align under an applied axial electric field to form an axial pH gradient (between *A* and *C*) the ampholytes in the CE dimension (*BW*) remain unfocused, behaving as a buffer with a measured pH of 8.

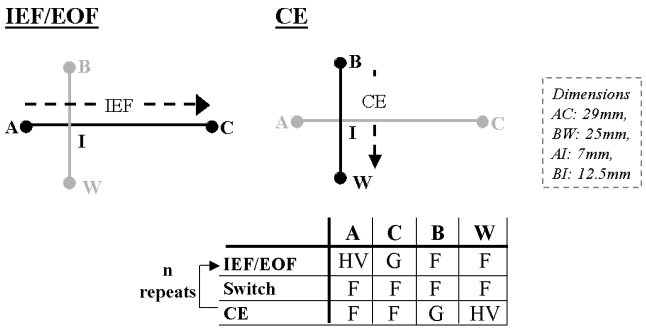

		A	C	B	W
n repeats	IEF/EOF	HV	G	F	F
	Switch	F	F	F	F
	CE	F	F	G	HV

Figure 1. IEF & CE separation modes in the multi-dimensional system. *Reservoirs: A (anolyte), B (buffer), C (catholyte), and W (waste). HV: high voltage, F: floating, G: ground.*

Travel support has been generously provided by the Transducers Research Foundation and by the DARPA MEMS and DARPA BioFlips Programs.

The 2-D separation was conducted by repeating a three step gated injection sequence: (1) an initial IEF/EOF (mobilization) step, (2) switching, and (3) a CE step, (see Figure 1). During IEF, the species focus, separate and essentially form a 'queue' for sampling into the second dimension. Low-dispersion electroosmotic flow mobilizes the queue to the channel intersection that couples the IEF to CE. Once the species of interest arrives at the intersection, the potential is 'switched' off for 3 s, allowing relaxation of pH gradients at the intersection. This is followed by dispensing of the fluid volume at the head of the queue into the CE dimension.

RESULTS AND DISCUSSION

The protein sample was first analyzed using uncoupled, microchip-based 1D IEF and CE. Sample mixture was focused using IEF and the relative location of the peaks was observed. No absolute pI information was acquired. Sample mixture was also subjected to CE analysis and absolute mobility information was obtained. Note that the CE analysis was carried out in unfocused ampholytes. Spatial electropherograms from these analyses are presented in Figure 2.

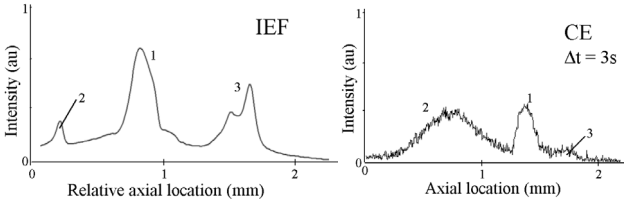

Figure 2. Spatial electropherograms of the independent 1D separations. *IEF is shown in the left image, while CE on an unconcentrated sample is presented in the right image.* $E_{IEF} = E_{CE} = 390$ *V/cm.*

The sample mixture was then analyzed using the coupled IEF-CE separation system. The voltage algorithm described in Figure 1 was employed. Figure 3, shows CCD images of the focused fluorescent species during an IEF-CE sequence. Boxes (dashed lines) highlight the queuing behavior of fluid volumes from IEF into CE.

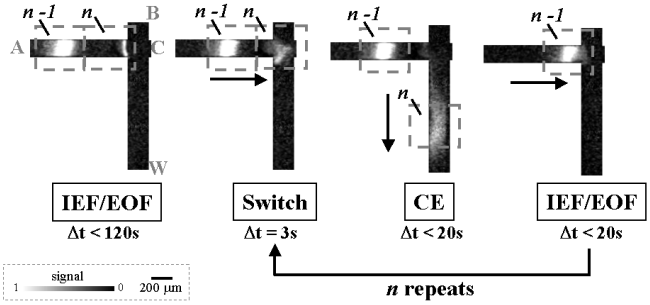

Figure 3. CCD images of queuing and sampling of fluid volumes from the IEF dimension into the CE dimension. *Fluid volume n contains focused FITC-dextran (tight band), while volume n-1 contains focused GFP (wide band). Samples are focused and mobilized during IEF/EOF, switched, and analyzed with CE. This procedure is repeated for all IEF bands. Arrows next to CCD images indicate sample motion. Channels are labeled consistent with Figure 1.* $E_{IEF} = E_{CE} = 390$ *V/cm.*

The intensity information obtained for each of the *n* CE sequences is displayed in a single 2D plot for a given time during the CE analyses (Figure 4). The axes are the spatial coordinates of the respective IEF and CE dimensions. The grayscale indicates the fluorescence intensity at a given location. Four distinct species are observed (labeled 1-4). Each of the species has a distinct pI and electrophoretic mobility. Species 1 and 4 have been oversampled, as the distributions span more than a single CE extraction. This oversampling is important for enhanced resolution. The 2-D plot also shows species (4,5) that are not resolved in the corresponding 1D IEF and CE. Analysis of 20% of the IEF fluid volume was completed in less than five minutes. This is a significant improvement over slab-gel systems that would complete such an analysis in several hours.

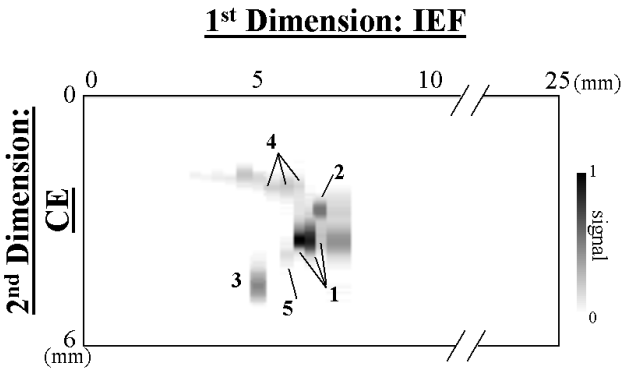

Figure 4. 2D representation of sample assay at Δt = 7s. *The multi-component sample was focused during IEF and extracted into the CE dimension using a gated injection scheme.*

CONCLUSIONS

IEF and CE were fluidically coupled and sequentially implemented using a single integrated microchip device. IEF was employed as an initial separation and pre-concentration step. The concentration increase resulting from the IEF step (100x) made possible a fluorescence-detection based CE separation of the initially dilute samples. In this system, IEF quickly reaches steady state (2 min) and exhibits residual EOF that can be used to provide a low-dispersion means of mobilizing focused sample species towards intersections for sampling into a second dimension. A mixture of proteins was analyzed using the 2-D system and results demonstrate the potential for enhanced performance through on-chip 2-D electrophoresis.

REFERENCES

1. O'Farrell, P.H., "High-Resolution 2-Dimensional Electrophoresis of Proteins." *Journal of Biological Chemistry*, 10, 250 (1975).
2. Giddings, J.C., "Two-Dimensional Separations : Concept and Promise." *Anal. Chem.*, 12, 56 (1984).
3. Wilkins, M.R., et al., "From proteins to proteomes: Large-scale protein identification by two-dimensional electrophoresis and amino acid analysis." *BioTechnology*, 14 (1996).
4. Herr, A.E., et al. "Investigation of a Miniaturized Capillary Isoelectric Focusing (cIEF) System Using a Full-Field Detection Approach", *Solid-State Sensor & Actuator Workshop*. Hilton Head Island, SC USA, Transducers Research Foundation, (2000)
5. Boone, T.D., et al. "Integrated Chemical Analysis on Plastic Microfluidic Devices", *Solid-State Sensors and Actuators Workshop*. Hilton Head, S.C. USA, 6/98, Transducers Research Foundation, (1998) pp.87-92.

NANOELECTROMECHANICAL SILICON CARBIDE RESONATORS FOR ULTRA HIGH FREQUENCY APPLICATIONS

X.M.H. Huang, K.L. Ekinci, and Y.T. Yang
Condensed Matter Physics, California Institute of Technology
Pasadena, California 91125

C.A. Zorman and M. Mehregany
Electrical Engineering and Computer Science
Case Western Reserve U., Cleveland, OH 44106

M.L. Roukes
Condensed Matter Physics, California Inst. of Tech.
Pasadena, California 91125

ABSTRACT

Nanomechanical resonators with fundamental mode resonance frequencies in the Ultra High Frequency (UHF) band were fabricated from single crystalline 3C-SiC thin films epitaxially grown on Si substrates using a combination of electron beam lithography and micromachining techniques. Resonant frequencies of doubly clamped resonator pairs were measured by magnetomotive transduction combined with a balanced bridge readout circuit. Resonant frequencies as high as 632 MHz were recorded.

INTRODUCTION

The rapidly growing interest in RF MEMS has created a need to push the frequencies of micromechanical resonators into the UHF band. Evidence is emerging that polysilicon at best provides limited performance at these frequencies. As a result, recent initiatives are exploring structures made from materials with higher acoustic velocities [**1**-**2**], as well as nanometer-scale dimensions [**3**] to create devices with such frequencies. This paper reports on our latest efforts in developing nanometer-scale, electromechanical resonators using 3C-SiC thin films [**4**], employing a strategy that capitalizes on both a reduction in scale and an increase in acoustic velocity to achieve resonant frequencies in the UHF band.

EXPERIMENTAL DETAILS

The 3C-SiC films used in this work are heteroepitaxially grown on 100 mm-diameter (100) Si wafers in a rf-induction-heated, APCVD reactor [**5**]. SiH_4 and C_3H_8 are used as precursors, and H_2 is used as a carrier gas. The epitaxial process is a two-step, high-temperature (1280◇C) procedure, involving the carbonization of the Si surface in a C_3H_8/H_2 ambient followed by epitaxial growth using SiH_4, C_3H_8, and H_2. The epitaxial growth recipe is optimized for micron-thick films yet produces 50 nm to 250 nm-thick films of sufficient surface quality for e-beam lithography.

Device fabrication utilizes a combination of optical and electron beam lithography techniques. The process begins by using standard photoresist and optical lithography to define the large-area contact pads which consist of a 6 nm-thick Cr adhesion layer and a 80 nm-thick Au film. The substrates are then coated with a PMMA thin film, which is then patterned by electron beam lithography into a Ni lift-off mold that defines the submicron mechanical components of the SiC devices. The patterned Ni mask (~36 nm thick) is transferred to the 3C-SiC layer by electron cyclotron resonance (ECR) etching using a $NF_3/O_2/Ar$ anisotropic etch. The newly patterned 3C-SiC beams are then released by simply etching the underlying Si substrate using an isotropic NF_3/Ar ECR etch. The Ni mask remains on the SiC beams to be used as a conducting layer for device testing. The device structures consist of two identical doubly-clamped beams, as shown in Fig. 1. The beams are roughly 1.25 μm long, 180 nm wide and 75 nm thick.

Travel support for X. Huang has been generously provided by the Transducers Research Foundation and the DARPA MEMS and DARPA BioFlips Programs.

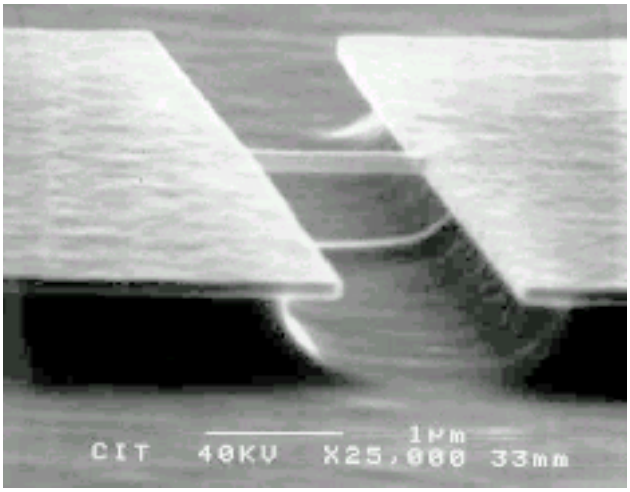

Figure 1. *SEM showing one of the two nominally identical doubly-clamped SiC beams in a device structure. The SiC beam is capped with nickel metallization.*

The test setup is shown in Fig. 2. The size of the beams prohibits use of electrostatic transduction, so magnetomotive transduction is instead employed. Each doubly-clamped beam pair is positioned perpendicular to a strong magnetic field (4 to 8T) in vacuum at cryogenic temperatures. An rf current is passed through the Ni conductor. For rf frequencies away from the mechanical resonances, the induced mechanical motion is minimal and the output at terminal III is ground. When the driving frequency matches the resonant frequency of one of the beams, motion will occur in that beam which induces an emf voltage at terminal III. After proper amplification, the voltage is measured by a network analyzer.

In the language of network analysis, we evaluate the mechanical performance of the device by measuring the frequency dependence of the forward transmission coefficient S_{21} of the network. Information about the mechanical motion is revealed as resonance peaks in the spectra. The in-plane resonances are seen at 615 MHz and 632 MHz, respectively, as shown in Figs. 3, where the frequency dependence of the forward transmission coefficient is plotted. The two resonances have a phase difference of about 180°, as shown in Fig. 4. These data contain information about both the mechanical resonator and the electrical connections. To extract information about the mechanical resonant structure, we subtract the background, which is also a complex-valued function of frequency, by fitting data points taken away from the resonance peaks. After subtracting the background, the amplitude of the resulting function can be plotted to clearly resolve the resonance peaks at 615 MHz and 632 MHz, as shown in Fig. 5.

0-9640024-4-2/hh2002/$20©2002TRF
DOI 10.31438/trf.hh2002.92

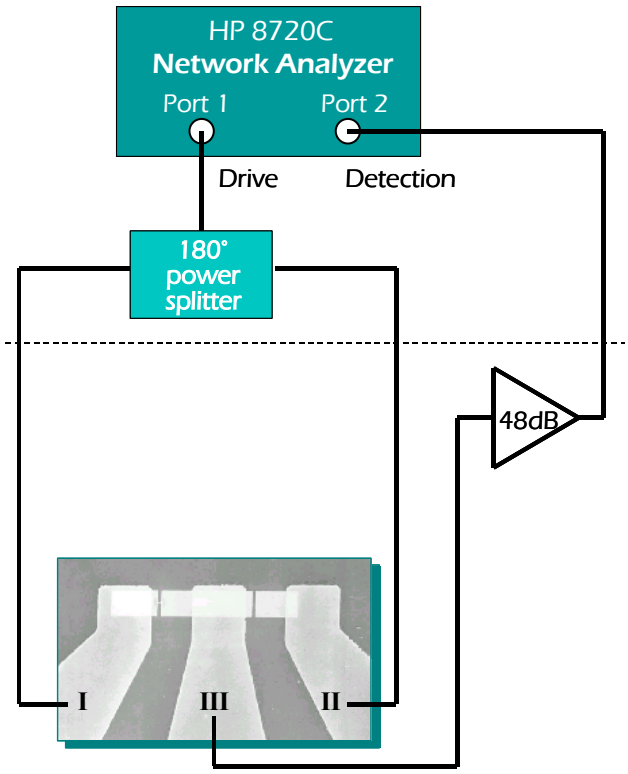

Figure 2. *Schematic of the measurement setup. At the resonant frequency of one of the beams an emf is induced which induces a voltage. This emf voltage affects the power transmitted out from terminal III towards the detector. The power is amplified and detected at Port 2 of the network analyzer. The connections linked to pads I and II are identical from the device to the 180° power splitter, which divides the driving power from Port 1 of the network analyzer into two equal partitions with a phase difference of 180°.*

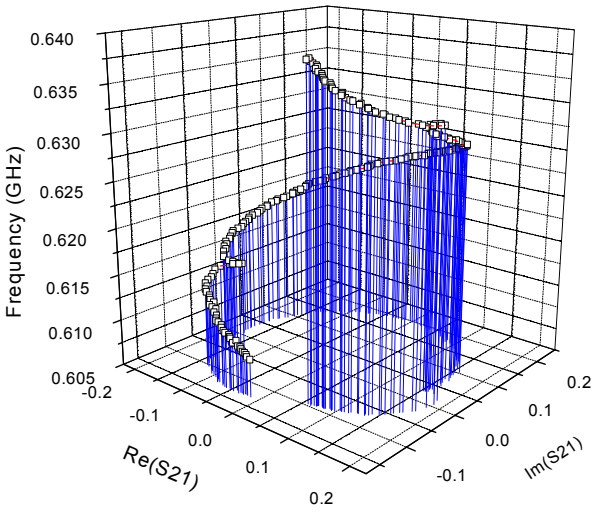

Figure 3. *The frequency dependence of the forward transmission coefficient S_{21} of the network. The magnetic field for the test is 8 T, the driving power is –60dBm and the resolution band width is 10 Hz.*

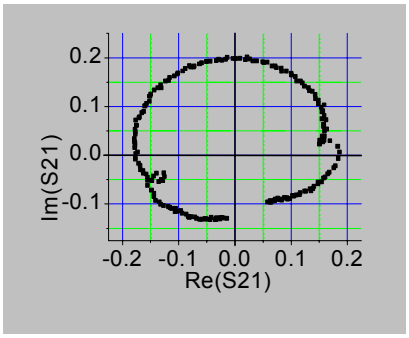

Figure 4. *The projection of the complex function in Fig. 3 onto the S_{21} plane, showing the 180 deg phase difference in the two resonances.*

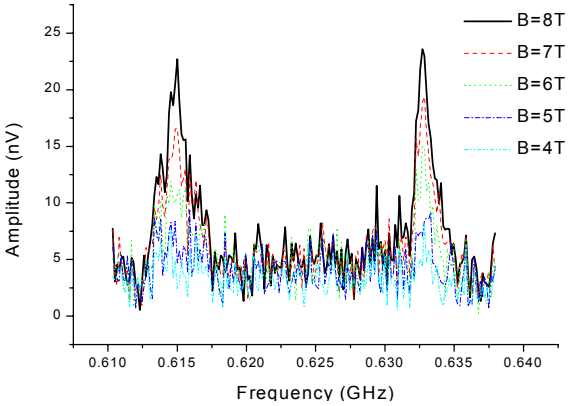

Figure 5. *Signal amplitude referred back to the input of the pre-amplifier. This is obtained by taking modulus after subtracting the background function from the raw data.*

CONCLUSIONS

We have demonstrated the measurement of SiC nanomechanical resonators with fundamental resonance frequencies in the UHF range, with clear promise of accessing the microwave L-band frequencies by the same technique. Exciting opportunities in physics and technology are anticipated from more detailed studies of such frequency bands of mechanical motion, which were inaccessible until now.

Acknowledgements: This work was supported by DARPA MTO/MEMS under grants DABT63-98-1-0012 (Caltech) and DABT63-98-1-0010 (CWRU).

REFERENCES

[1] M. Mehregany, C. Zorman, N. Rajan, and C. Wu, *Proc. IEEE*, **86**, 1594, (1998).

[2] J. Wang, J. Butler, D Hsu, and C. Nguyen, *Tech. Dig. 15th Int. Conf. on MEMS*, 657, (2002).

[3] M. Roukes, Technical Digest – 2000 Solid State Sensor and Actuator Workshop, Hilton Head SC, June 4-8, 2000, p. 367.

[4] Y. Yang, K. Ekinci, X. Huang, L. Schiavone, M. Roukes, C. Zorman, and M. Mehregany, *Appl. Phys. Lett.*, **78**, 162, (2001).

[5] C.A Zorman, A.J. Fleischman, A.S. Dewa, M. Mehregany, C. Jacob, and P. Pirouz, *J. Appl. Phys*, **78**, 5136, (1995).

HIGH VOLTAGE LIMITS FOR ELECTROSTATIC TRANSDUCERS: ON THE ROLE OF AMBIENT PRESSURE AND DEVICE DIMENSION IN MICRODISCHARGES

Chester G. Wilson[1], Amy E. Wendt[1], and Yogesh B. Gianchandani[1,2]
[1]Department of Electrical and Computer Engineering, University of Wisconsin, Madison, WI 53706
[2]EECS Department, University of Michigan, Ann Arbor, MI 48109

ABSTRACT

In order to understand the details of high-field breakdown in microstructures that are vacuum packaged, a series of experiments are used to determine characteristics of microdischarges. It is found that many of these contradict conventional assumptions based upon large scale discharges. When planar microelectrodes are used, Paschen's curve is not followed; the anode and cathode current paths are a strong function of pressure; voltage gradients are supported in the glow region; and the glow region is confined directly over the cathode. It is shown that magnets can be used to further confine the discharge. This information is pertinent for recently reported devices that exploit microdischarges for sensing.

I. INTRODUCTION

Electrostatic sensing and actuation are pervasive in MEMS technology not only because of the wide variety of materials that they accommodate, but also because they are generally power efficient [1-4]. In many cases performance measures such as sensitivity and dynamic range of sensors, or force and displacement of actuators are limited by the highest electric field that can be safely achieved, or voltage bias that can be applied. While there has been an incipient effort to study this phenomena at atmospheric pressure [5], most such devices are packaged in vacuum. In addition, the spatial distribution of the electric field and breakdown current, which are critical parameters for sustained avalanche breakdown, have not been reported in the context of microstructures. By addressing these questions, this paper attempts to establish design guidelines for high field devices. In doing so it also addresses the requirements for sustained arcs and microplasmas which have been successfully used etch silicon wafers and sense chemical impurities in liquids and gases [6,7]. The experiments demonstrate that microdischarges violate many of the assumptions used routinely for larger scale discharges.

II. STRUCTURE AND EXPERIMENT

It is conventionally believed that the breakdown voltage (BV) in a vacuum environment follows the Paschen curve (Fig. 1) which indicates that a minimum voltage is achieved at a particular product of pressure and separation between bias electrodes ($P \bullet d$). This is constrained by fewer collisions at lower pressure and lower collisional energy at higher pressures, both of which necessitate a higher electric field to sustain the avalanche breakdown. However, with most microstructures, multiple path lengths are simultaneously available, which makes the discharge gap a variable, and permits a low BV to be sustained even as the pressure changes from the value that favors the minimum electrode separation (Fig. 1).

In order to measure the spatial distribution of discharge current, a discharge was created between planar thin-film metal electrodes on a glass substrate at various levels of vacuum. Segmented electrodes (Fig. 2) were first used as a cathode, and then as an anode to measure the difference between the bias-dependent trajectory of the positive ions and electrons respectively, in a nitrogen ambient. Figure 3 shows that the cathode current favors longer paths at 1.2 Torr, but at 6 Torr the distribution between the four pads is comparable. In contrast, the same change in pressure results in a more dramatic change in the spatial distribution of anodic current, (Fig 3). This asymmetry is believed to be caused by secondary emission electrons, which are abundant near the cathode, in sustaining microdischarges, as discussed next.

Another important aspect of microdischarges that differs from conventional assumptions is that the glow region is confined to the proximity of the cathodes (Fig 5). This suggests that the ionization events in microplasmas are driven primarily by secondary electrons emitted by the cathodes. In contrast, larger scale plasmas have a glow region that extends between the electrodes, with a prominent dark sheath near the cathode. This phenomenon can be critical to the design of microdischarge-based sensors and display devices that have recently been reported [7-10]. In addition, the voltage in the glow region of large-scale plasmas is nearly constant. Most of the voltage drop is across the sheath near the cathode, which has a diminished electron population. Measurements of the potential distribution of microdischarges were performed using the arrangement shown in Fig 6. In contrast to large scale plasmas, microdischarges show a significant voltage gradient (electric field) in the glow region over the cathode, which ranges from 0.10–0.25 V/μm over 1.2–6 Torr (Fig. 7,8).

By using concentric cylindrical magnets located beneath a planar electrode, we have been able to tailor the shape of the glow region, demonstrating that the microdischarge mechanism can be controlled in a spatially selective manner (Fig 9).

In conclusion, these results demonstrate how breakdown in vacuum varies with design parameters and operating conditions, and that it can be substantially different from conventional assumptions.

ACKNOWLEDGEMENTS

This effort is supported in part by the National Science Foundation, US Geological Survey, and the Sea Grant. Partial travel support for the conference was provided by the Transducers Research Foundation, and by the DARPA MEMS and DARPA BioFlips programs.

REFERENCES

[1] L.J.Hornbeck, "Current status of the digital micromirror device (DMD) for projection television applications, *IEEE IEDM*, 1993, pp. 381-4
[2] B.Gogoi, C.Chuan, C.Mastrangelo, "Force balanced micro-machined pressure sensors," *IEEE T-ED*, 48(8), 8/01, pp. 1575-84
[3] T.Tsuchiya, Y.Kageyama, H.Funabashi, J.Sakata, "Polysilicon vibrating gyroscope vacuum encapsulated in an on-chip microchamber," *Sensors & Actuators,* A90(1-2), 5/01, pp. 49-55
[4] F.Ayazi, H.H.Chen, F.Kocer, H.Guong, K.Najafi, "A HARPSS polysilicon vibrating ring gyroscope," *JMEMS*, 6/01, pp. 169-79
[5] T.Ono, Y.Dong, M.Esashi, "Microdischarge and electric breakdown in a micro-gap," *JM&M,* 10(3) 9/00, pp. 445-51
[6] C.Wilson, Y.Gianchandani, "Silicon micro-machining using in-situ DC microplasmas," *JMEMS* 10(1) 3/01, p. 50-4
[7] J.C.T. Eijkel, H. Stoeri, A. Manz, "A dc microplasma on a chip employed as an optical emission detector for gas chromatography," *Anal. Chem.* 72, 6/00, pp. 2547-2552
[8] C.Wilson, Y.Gianchandani, "LEd-SpEC: Spectroscopic detection of contaminants using glow discharges from liquid microelectrodes," *IEEE MEMS Conf.,* Las Vegas, 1/02, pp. 248-51
[9] G.Jenkins, A.Manz, "Optical emission detection of liquid analytes using a micro-machined D.C. glow discharge device at atmospheric pressure" *•TAS*, 2001, pp. 349-350
[10] S.J.Park, J.Chen, C.Liu, J.G.Eden, "Silicon microdischarge devices having inverted pyramidal cathodes: Fabrication and performance of arrays," *Appl. Phys. Lett.*, (78)4, 1/01, pp. 419-21

0-9640024-4-2/hh2002/$20©2002TRF
DOI 10.31438/trf.hh2002.93

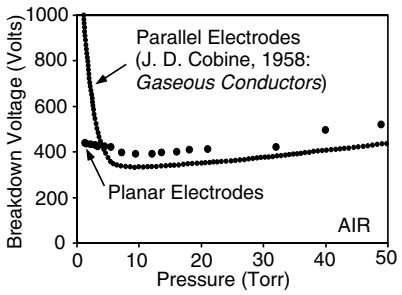

Fig. 1: Paschen voltage breakdown curve for parallel and planar electrodes with 500µm spacing.

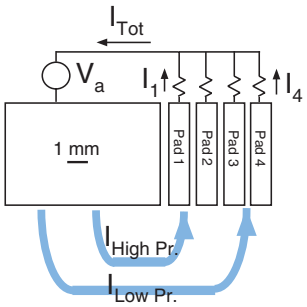

Fig. 2: Planar Ti electrode configuration, patterned on glass to measure cathode current density. Cathode is split into separate paths, where the current is independently measured. Polarity can be reversed to measure anode current density.

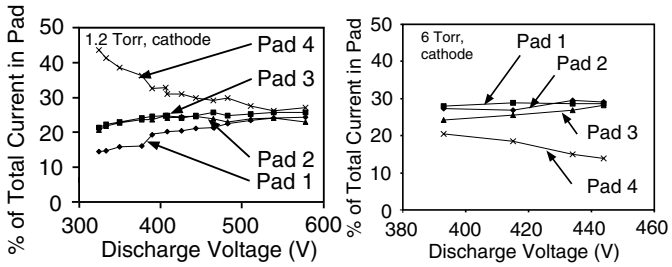

Fig. 3: Normalized current in the cathode electrode for an N_2 microplasma, operated at 1.2 Torr (a-left) and at 6 Torr (b-right).

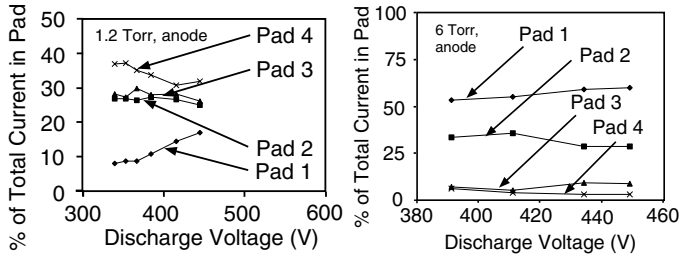

Fig. 4: Normalized current in the anode electrode for an N_2 microplasma, operated at 1.2 Torr (a-left) and 6 Torr (b-right).

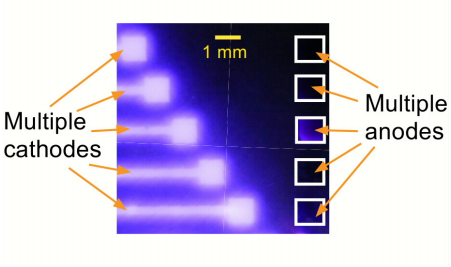

Fig. 5: Air microplasmas with varying electrode spacing show that the glow exists only over the cathode, and is independent of spacing, but dependent upon pressure and power density.

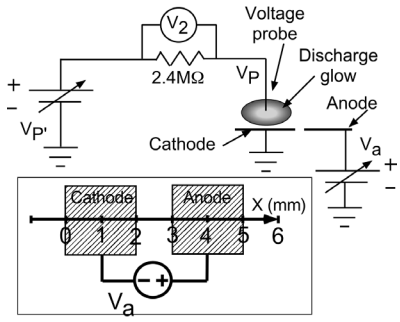

Fig. 6: Plasma floating potential V_P, is measured by varying applied voltage $V_{P'}$ to find the value at which V_2 is zero. The inset shows the dimensions of the planar electrodes.

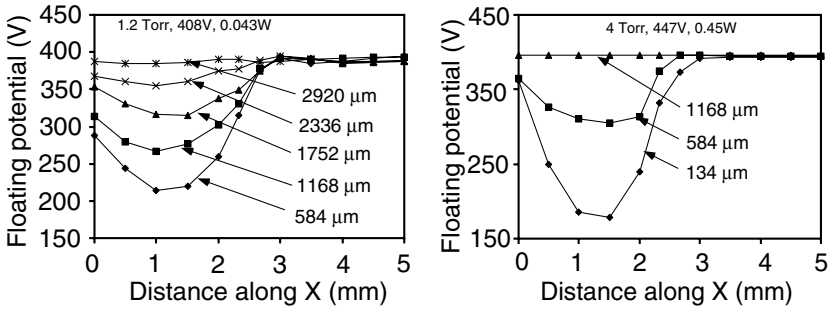

Fig. 7: Floating potential of an N_2 microplasma at 1.2 Torr (a-left) and 4 Torr (b-right), generated by the electrodes shown in Fig. 6. Voltage is measured along X for varying heights over the coplanar electrodes. The plasma becomes more confined at higher pressures.

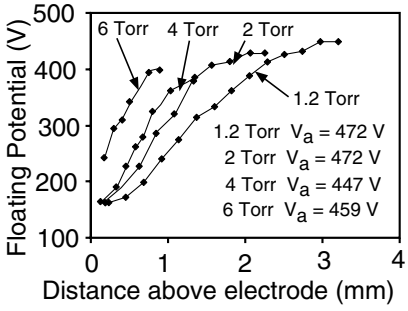

Fig. 8: Floating potential of N_2 microplasmas at varying pressures, as a function of above electrodes at X = 1.2 mm. Glow height decreases and voltage gradient increases w/ increasing pressure.

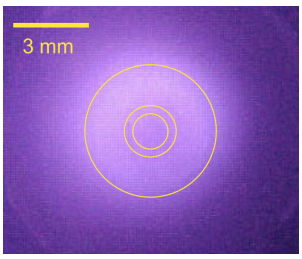

Fig. 9: Microplasma at 1.2 Torr confined using a coaxial magnetic structure.

SELF-ASSEMBLED OUT-OF-PLANE HIGH Q INDUCTORS:

Christopher L. Chua, David K. Fork, Koenraad Van Schuylenbergh, and Jeng-Ping Lu
Palo Alto Research Center, 3333 Coyote Hill Road
Palo Alto, CA 94304

ABSTRACT

We report for the first time self-assembled out-of-plane micro inductors. The resulting Q values are among the highest reported to date.

DEVICE DESCRIPTION AND FABRICATION

Micro-machined out-of-plane inductors with coil axis parallel to the substrate plane have garnered increasing interest [**1**], [**2**] because of their fundamental advantages over conventional in-plane spiral coils. We have developed a new approach for fabricating out-of-plane coils using uncomplicated semiconductor processing technology. The process relies on stress-engineered thin films that are deposited with a built-in stress gradient so that, when patterned and released from their substrate, they curl into a designed radius of curvature. These micro-springs self assemble into three-dimensional scaffolds that we plate with copper (Cu) to form highly conductive coil windings.

It is well known that many refractory metals have a common property of acquiring tensile stress when sputtered at high pressures and compressive stress when sputtered at low pressures. A film that is compressive at the bottom and tensile on the surface can, for example, be realized by simply increasing the ambient pressure during sputtering. When patterned and released, such a stress-graded film will curl up with a radius of curvature [**3**] given by $r = h * Y/\Delta\sigma$, where h is the film thickness, Y the biaxial Young's modulus, and $\Delta\sigma$ the stress difference between the top and bottom of the film.

Figure 1 shows an array of molybdenum-chromium micro-springs that have been released from their substrate. The springs follow a circular trajectory with the given radius. To make out-of-plane inductors, springs are placed in opposite directions so that when released, the spring pairs curl and interlock into each other to form coil windings. Figure 2 shows scanning electron micrographs of the self-assembled springs. A magnified view of the interlocking spring tips is shown in Figure 3. The interlocking connection provides a mechanical catch that prevents paired springs from curling further after they come together. Thus, the coil diameter is determined by mask design rather than by the exact stress profile in the film. Consequently, the coil geometrical properties are largely independent of the film deposition parameters. The assembled devices can be taken in and out of a liquid without breaking apart.

RESULTS

The solenoids are designed with diameters of about 0.6 mm for operation at about 1 GHz - this frequency being chosen for its relevance to wireless communication applications. Figures 4 and 5 show Q-factor plots for coils on glass and coils on silicon, respectively. The silicon wafers have resistivities of 15 to 20 Ω-cm. We obtain quality factors of over 70 at 1 GHz for coils on glass. This value is very close to the hypothetical maximum neglecting proximity effects and sources of losses other than skin effect current constriction in the coil winding. Coils on silicon show quality factors of 35 to 40 at 1 GHz due to substrate eddy currents. These Q values are among the highest reported to date for coils on unaltered silicon wafers.

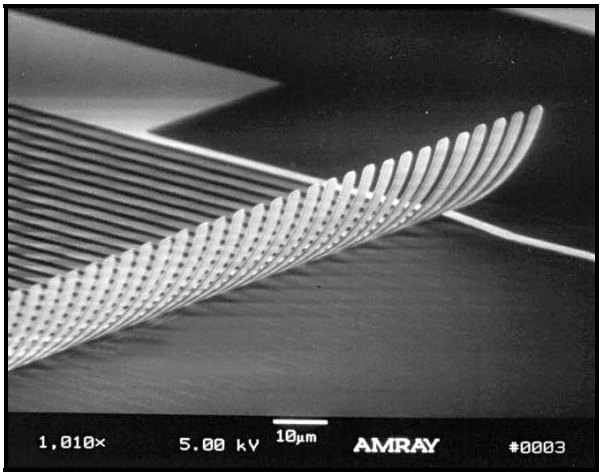

Figure 1. *SEM of an array of released micro-machined springs*

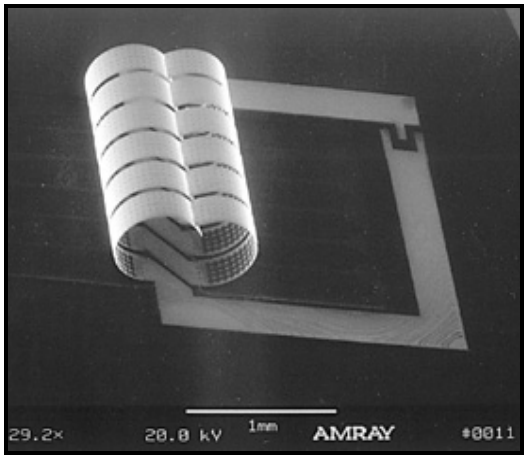

Figure 2. *SEM of an assembled out-of-plane coil before plating*

0-9640024-4-2/hh2002/$20©2002TRF
DOI 10.31438/trf.hh2002.94

Solid-State Sensors, Actuators, and Microsystems Workshop
Hilton Head Island, South Carolina, June 2-6, 2002

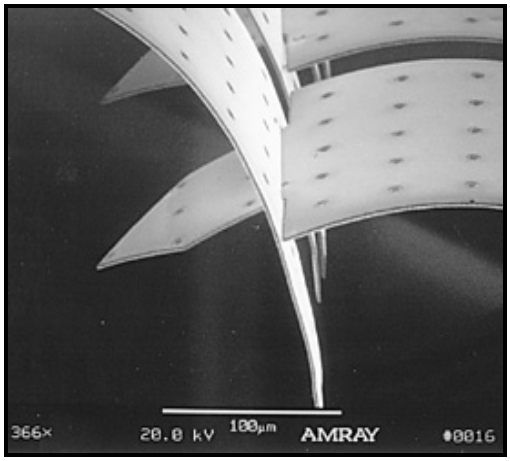

Figure 3. *Magnified image of the interlocking spring tips*

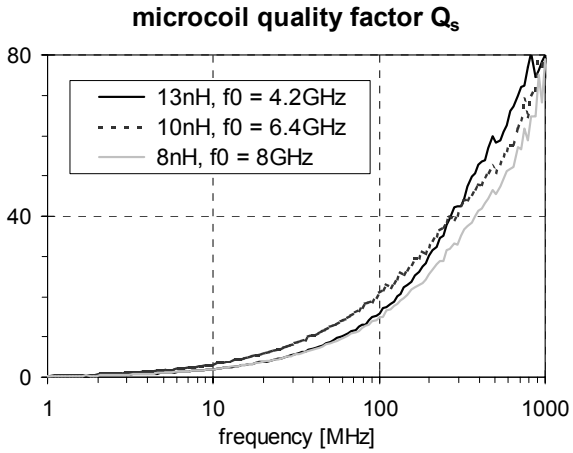

Figure 4. *Quality factors of out-of-plane coils on glass substrates. f_o is the parasitic resonance frequency.*

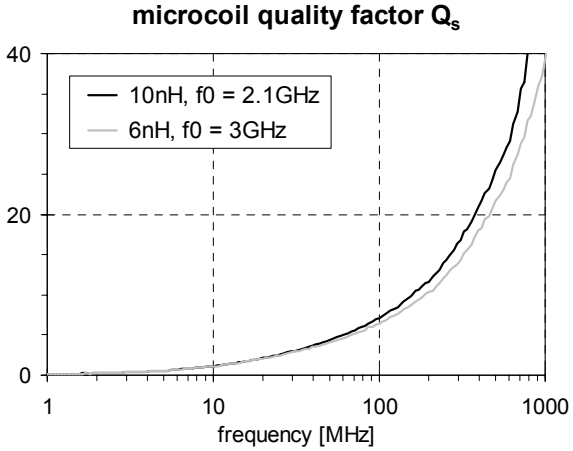

Figure 5. *Quality factors of out-of-plane coils on silicon substrates (resistivities = 15 to 20 Ω-cm). f_o is the parasitic resonance frequency.*

REFERENCES

1. J-B Yoon, B Kim, Y. Choi, and E Yoon, "3-D lithography and metal surface micromachining for RF and microwave MEMs," *IEEE MEMs*, Las Vegas, NV (2002), pp. 673 - 676.

2. D. Young, V. Malba, J. Ou, A. Bernhardt, and B. Boser, "A low noise RF voltage-controlled oscillator using on-chip high Q three-dimensional coil inductor and micromachined variable capacitor," *Tech. Digest, Solid State Sensor and Actuator Workshop*, (1998), pp. 128 - 131.

3. D.L. Smith and A.S. Alimonda, "A new flip-chip technology for high-density packaging," *Proceedings of the 46th Electronic Components and Technology Conference*, Orlando, FL (1996).

RF MEMS BASED ON EPOXY-CORE CONDUCTORS

Yong-Kyu Yoon, Jin-Woo Park, and Mark G. Allen
School of Electrical and Computer Engineering
Georgia Institute of Technology
Atlanta, GA 30332

ABSTRACT

In many RF MEMS applications, currents are confined to the outermost portions of conductors due to the skin effect. Conductors consisting of epoxy cores coated with metal are appropriate to consider for these applications, and in many instances are easier to fabricate than their solid-metal-core counterparts. As an example of this approach, this paper reports a three-dimensional, high-aspect-ratio, high Q-factor, solenoid-type RF inductor. The conductors of this inductor are fabricated using SU8 epoxy cores and subsequent metal electrodeposition. The SU8 core approach allows for relatively simple formation of extremely high aspect ratio columns for inductor sidewalls. In addition, an SU8 bridge fabrication technique has been realized using a double exposure and single develop scheme. A single, vialess metallization is then used to form the conducting paths of the inductor. By combining these techniques, epoxy-core RF inductors have been fabricated and tested. A single turn inductor that is 900μm in height and has a 600μm wide air-core area shows a maximum Q-factor of 84 and an inductance of 1.17nH at 2.6GHz.

INTRODUCTION

Integrated 3-dimensional solenoid type RF inductors with high Q-factor fabricated using MEMS technology have been pursued for several years **[1]**. More recently, these devices have been integrated with CMOS circuits to form functional RF power amplifiers **[2]**. These devices are typically fabricated by plating through photoresist molds. However, the ratio of coil height to turn-to-turn pitch in many of these devices is relatively low due to difficulties in forming and filling extremely small, high aspect ratio via holes. The low profile coil suffers from magnetic flux leakage between relatively wide conductor line spaces, which can result in Q-factor decrease. Increased core height, leading to a geometry closer to an ideal solenoid, should yield more ideal performance. In addition, the previous inductors consisted of three discrete layers: lower electrode, via, and upper electrode. This construction not only leads to an increased number of electrodeposition steps, but also has the potential for increased via resistance and/or mechanical weakness at each interface.

In this paper, a tall solenoid inductor is proposed using SU8 epoxy as a core or backbone structure. This SU8 core is then covered in a single electrodeposition step. This approach differs from the conventional 3-D RF inductor fabrication, which uses via holes followed by via filling. With SU8 material, it is relatively easy to fabricate columns of a given aspect ratio as opposed to vias of the same aspect ratio **[3]**. In addition, metal electrodeposition on the column surface is much easier than via hole filling to obtain void-free and seamless conductor structures.

To fabricate inductors in a single metal deposition step, this column formation technique is combined with a double exposure and single development technique to form laterally-extended bridges on top of columns. Thus, SU8 column and bridge formation followed by metal coating is proposed as a method to realize inductors with high aspect ratio (up to 10:1) interconnect between lower and upper conductors. With this geometry, a large inductance in the same number of turns is obtained, and the device is geometrically closer to an ideal solenoid inductor.

It should be noted that due to the skin effect, as long as the metal coating is large in thickness compared with the skin depth at the operating frequencies of interest, no degradation of conductivity is expected in epoxy-core structures compared with metal-core structures. This approach is therefore also potentially of interest for other RF MEMS applications, such as transformers, switches and antennas.

FABRICATION

The fabrication process is described in Figure 1. In order to selectively coat metal only on the SU8 column, bridge, and bottom electrode definition area, three foundation layers are deposited on a glass substrate; a chromium (100nm thick) electrical contact layer for electroplating; a silicon dioxide (1000nm thick) passivation layer; and a titanium (Ti) / copper (Cu) / titanium (Ti) (30nm / 1000nm / 30nm) sacrificial layer for selective seed layer definition. The Ti/Cu/Ti and silicon dioxide layers are patterned for bottom electrode definition (Figure 1.1). A single SU8 layer is coated and soft baked, where the thickness of the SU8 layer becomes height of the inductor. A large optical dose is applied through the column mask and post-exposure baked at 95°C on a hot plate (Figure 1.2). Prior to development, a small optical dose is applied through the lateral bridge mask, and the structure is post-exposure baked at 95°C in an oven. After this two-step exposure and bake, the SU8 has the desired top bridge portion cross-linked at the top of the cross-linked columns (Figure 1.3). Developing the SU8 leaves the column and bridge. After curing the released structure in a 100°C oven, chromium/gold (20nm/150nm) layers are coated using DC sputtering as the seed layer for subsequent electroplating (Figure 1.4). Removal of the previously-deposited copper and titanium layers leaves the Cr/Au seed layers only on the surface of the SU8 structure and the bottom electrode area. Copper/gold layers are then electroplated in sequence to a thickness of 10-15 microns (Figure 1.5). Removal of the passivation silicon dioxide and initial chromium layer in sequence isolates the structure to complete the process (Figure 1.6). Unlike the SU8 multi-exposure-single-develop technique described in **[4]**, which utilizes anti-reflection coatings in order to control the thickness of the upper portion of the device, the technique described in this paper relies on control of the baking steps to achieve the final structure.

EXPERIMENT AND RESULTS

Fabricated SU-8 core structures prior to metal deposition and after metal coating to form solenoid inductors are shown in Figure 2 upper and lower, respectively. The height of the inductors is approximately 0.5 millimeter and copper and gold are electrodeposited in sequence in the thickness of 14μm and 1μm, respectively, in order to form electrical inductor path. Two single-turn inductors, one 500μm tall with a 600μm core width, and one 900μm tall and 600μm in core width, are shown in Figure 3. They

0-9640024-4-2/hh2002/$20©2002TRF
DOI 10.31438/trf.hh2002.95

Solid-State Sensors, Actuators, and Microsystems Workshop
Hilton Head Island, South Carolina, June 2-6, 2002

have been RF tested, and the obtained inductance and Q-factor as a function of frequency is shown in Figure 4. The 900µm device shows an inductance and a maximum Q-factor of 1.17nH and 84 (at 2.6 GHz), respectively, while the 500µm device shows an inductance and a maximum Q-factor of 0.77nH and 85 (at 2.5 GHz), respectively. The relatively large Q-factors indicate that the RF performance of these devices is not degraded by conductors with epoxy cores compared with solid cores.

CONCLUSION

Epoxy-core fabrication approaches for RF MEMS conductors have been demonstrated. The fabrication advantages of this approach have been utilized to create tall, 3-D solenoid inductors. As predicted by the skin effect phenomenon, high Q-factor is obtained even though the interior core of the devices is nonconducting. This approach may also be of interest for other RF MEMS applications, such as transformers, switches and antennas.

ACKNOWLEDGEMENT

The authors would like to thank Mr. S.-W. Yoon and Prof. J. Laskar of Georgia Tech for their assistance with device measurement, and Mr. Y.-H. Joung and Mr. F. Cros of Georgia Tech for helpful technical discussion. Travel support has been generously provided by the Transducers Research Foundation and by the DARPA MEMS and DARPA BioFlips programs.

REFERENCES

1. Y.J.Kim and M.G.Allen, "Surface Micromachined Solenoid Inductors for High Frequency Applications," *IEEE Trans. CPMT, Part C, vol. 21, No. 1*, pp. 26-33, Jan. 1998.
2. Y.K.Yoon, E.Chen, M.G.Allen, and J.Laskar, "Embedded Solenoid Inductors for RF CMOS Power Amplifier," *Proceeding of Solid-State and Actuators, Transducers'01 EurosensorsXV, Vol. 2*, pp. 1114-1117, 2001
3. H.Lorenz, M.Despont, N.Fahrni, J.Brugger, P.Vettiger, P. Renaud, "High aspect ratio, ultrathick, negative-tone near-UV photoresist and its applications for MEMS," *Sensors and Actuators, Part A, vol. 64*, pp-33-39, 1998
4. F.G.Tseng, Y.J.Chuang, and W.K.Lin, "A Novel Fabrication Method of Embedded Micro Channels Employing Simple UV Dosage control and Antireflection Coating", *Proceedings of IEEE MEMS 2002*, Las Vegas, pp. 69-72, 2002

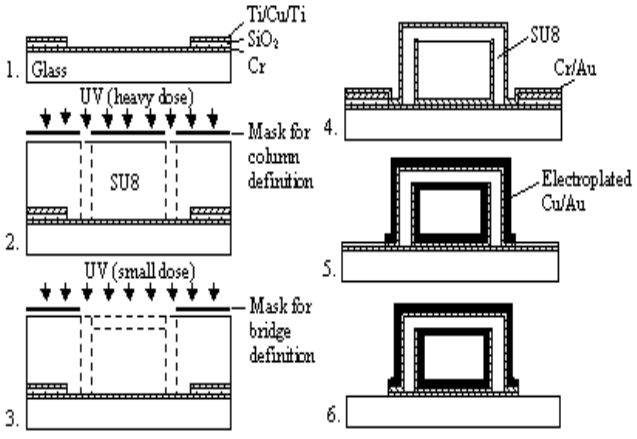

Figure 1. *Fabrication process*

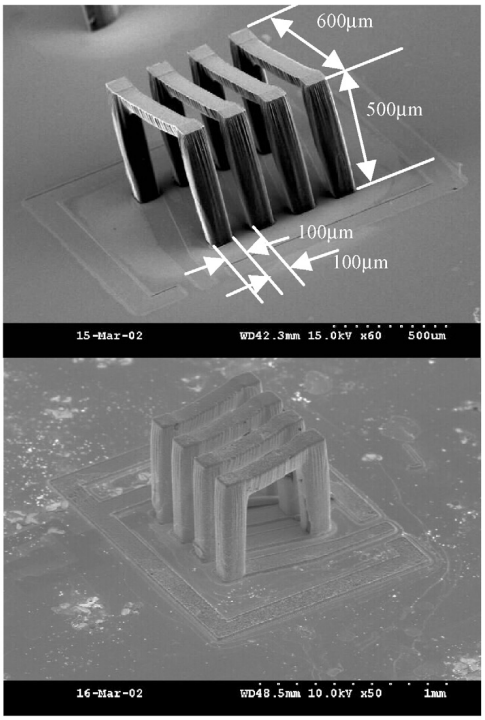

Figure 2. *(Upper) Fabricated SU-8 core structures prior to metal deposition. (Lower) After metal coating to form solenoid inductors. Note that the height of the inductors is approximately 0.5 millimeter.*

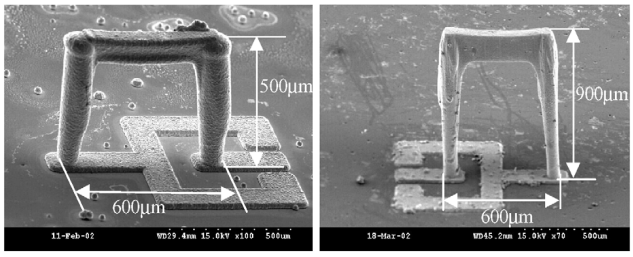

Figure 3. *Single turn inductors; (Left) 500µm device, (Right) 900µm device.*

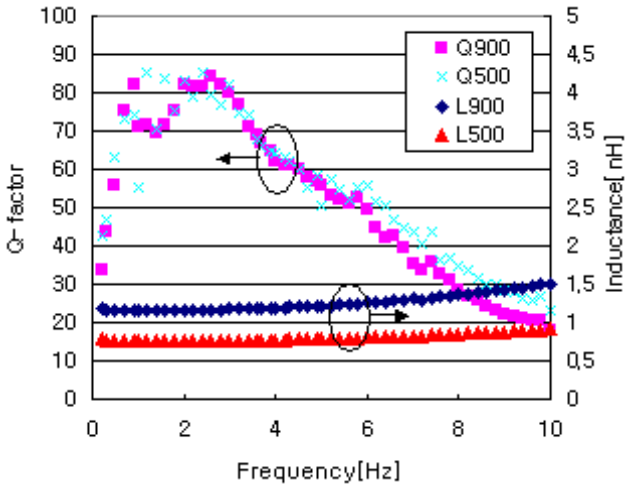

Figure 4. *Inductance and Q-factor for two single turn inductors.*

FABRICATION OF SUPERMEMBRANES AND OTHER STRUCTURES USING ONE-STEP POROUS POLYSILICON FILMS

George M. Dougherty, Albert P. Pisano[1] and Timothy Sands
Department of Materials Science and Engineering and [1]Department of Mechanical Engineering
Berkeley Sensor and Actuator Center, 497 Cory Hall, University of California – Berkeley 94720

ABSTRACT

We have recently developed a simple and controlled process by which fluid-permeable porous polycrystalline silicon (polysilicon) films can be created in a single ten-minute LPCVD deposition, using only standard equipment, with no other processing steps required. The remarkable combination of qualities exhibited by these films, coupled with their great ease of use, allows the easy microfabrication of structures that were never before feasible.

INTRODUCTION

The fabrication of large freestanding membranes, sealed cavities, and similar structures has long been a difficult task for MEMS designers and process developers. Backside wafer through-etching with anisotropic wet etchants, and similar techniques, have generally been required, often with the addition of wafer-to-wafer bonding and other involved processes.

Recently, as a result of extensive materials science investigations [1], we have discovered a process by which polycrystalline silicon (polysilicon) films can be deposited in a porous condition, such that they are permeable to liquid etchant solutions. The phenomenon of "permeable polysilicon" was first observed several years ago [2], but the origin of the permeability and the means of process control were unknown. The recent investigations led to the discovery of a growth regime for polysilicon whereby standard low-pressure chemical vapor deposition (LPCVD) methods result in a polysilicon film that is porous in the as-deposited state, requiring no additional process steps. The process is very simple, requiring only a single ten-minute deposition step under the correct process conditions.

The new One-Step Porous Polysilicon process offers a powerful new tool for microfabrication. Open etch holes, or backside access, are not required in order to release a porous polysilicon film because etch solution can pass through the film itself. As a result, a whole range of microfabricated structures that would have been difficult or impossible to make using traditional micromachining techniques can now be made quickly and easily.

SUPERMEMBRANES

A dramatic example of the capability offered by the new process is the fabrication of unbroken, free-standing membranes of remarkable size ("supermembranes"), only 100 nm thick, aligned over their entire area only 1 micron above the underlying substrate. Such membranes have been produced which are larger than a square centimeter in size. The fabrication requires only the deposition of a porous film over a sacrificial oxide, which is subsequently released though the porous film using HF, a release process which takes less than a minute.

The porous polysilicon process yields films that are inherently almost free of internal residual stress, as described below, and are generally used in a slightly (less than 50 MPa) tensile condition for membrane applications. Perhaps even more important for applications is the fact that they are naturally aligned with high precision over the substrate, separated only by the thickness of the removed sacrificial layer. These membranes immediately suggest new possibilities for acoustic microphones, high-sensitivity pressure sensors, and other MEMS devices. A photo of part of a supermembrane is shown in figure 1.

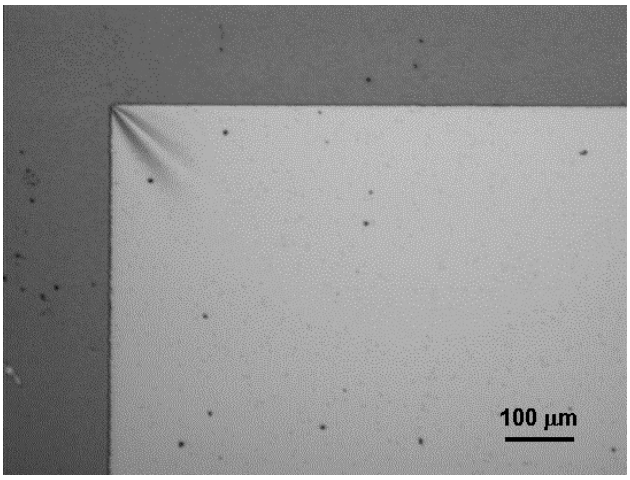

Figure 1. *One corner of a very large (0.9 cm x 1.2 cm) porous polysilicon supermembrane. The pinching or "bedsheeting" visible in the sharp corner is an optical effect seen in released tensile porous polysilicon membranes.*

OTHER EXAMPLE STRUCTURES

The porous polysilicon films are highly conformal, have very low residual stress, and are composed entirely of a standard CMOS material (silicon). They are resistant to stiction, such that many structures with dimensions less than 100 μm can be released without the use of critical point drying or similar techniques. In addition, the pores can be easily sealed with a subsequent layer of silicon nitride, polysilicon, or other material, to produce a hermetically sealed membrane. This process has been used in our laboratory to fabricate micromachined ultrasonic immersion transducers. A wide range of other structures has been fabricated using the films, a selection of which is shown here.

Because the porous films are conformal, almost any sacrificial structure can be coated with a porous layer and then released to yield a hollow structure with walls composed of porous polysilicon. An example of this is shown in figure 2, a broken cross-section of a porous polysilicon cantilever beam. Other examples of new structures that are possible are the dual-lumen microchannel structure fabricated on a silicon dioxide substrate,

Travel support has been generously provided by the Transducers Research Foundation and by the DARPA MEMS and DARPA BIOFlips programs.

shown in figure 3, and the enclosed serpentine flow channel made entirely of porous polysilicon, shown in figure 4. One-Step Porous Polysilicon offers a convenient way of making porous fluidic structures for separation, filtration, and other purposes.

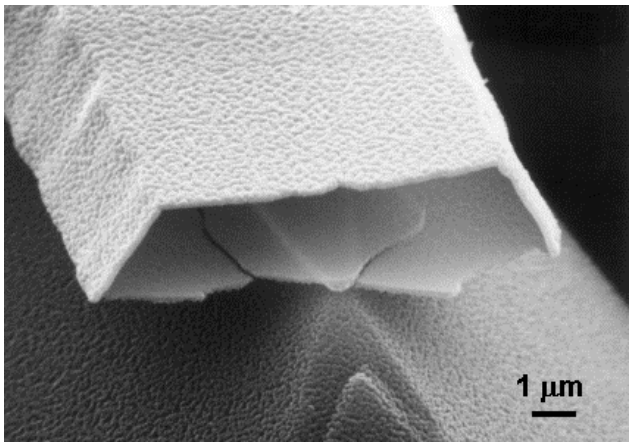

Figure 2. *A porous polysilicon cantilever beam, broken open to show the hollow interior.*

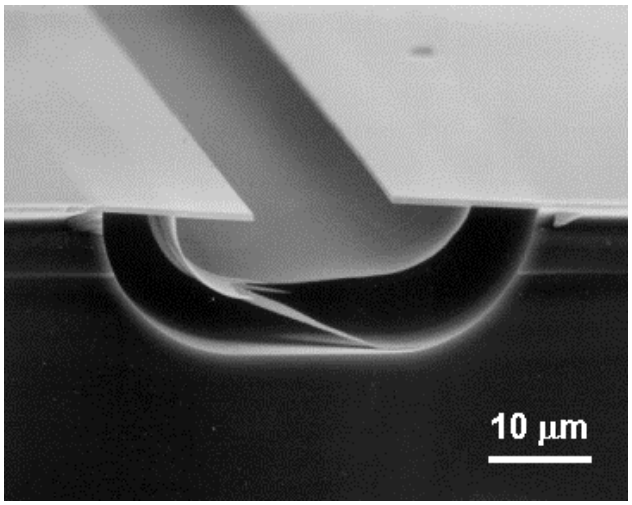

Figure 3. *A microchannel in a silicon dioxide substrate, featuring two interior fluid passages separated by a curved layer of porous polysilicon.*

ONE-STEP POROUS POLYSILICON

The pores in the polysilicon material occur spontaneously during deposition within a narrow process window. The distinctive cobblestone morphology characteristic of the porous films occurs at the transition between a lower temperature deposition regime that yields tensile films, and a higher temperature regime that yields compressive films. By measuring film residual stress using standard wafer-curvature methods, the process is easily tuned and controlled to produce porous films with high yield. Figure 5 is a high magnification SEM photo showing the pores between polysilicon grains, typically ranging from 10 to 50 nm in size. More information on the process is available in reference [1].

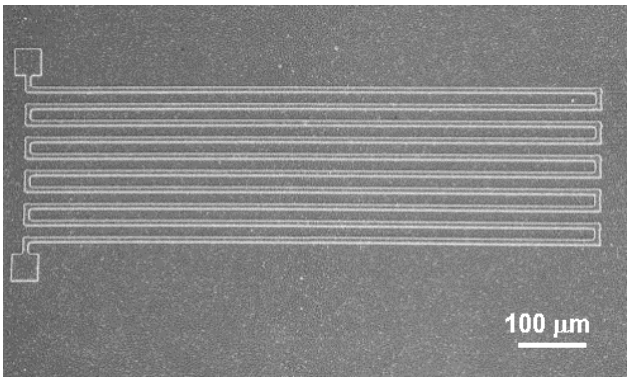

Figure 4. *A serpentine hollow structure with walls made of porous polysilicon. Porous structures of this size can be released without the use of critical point drying or similar special techniques*.

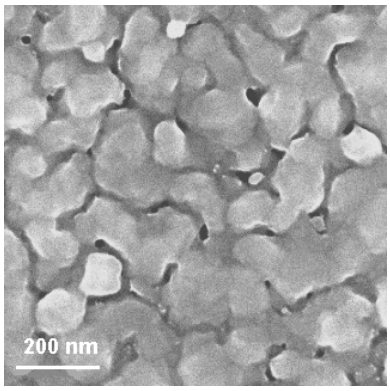

Figure 5. *SEM photo of the structure of a One-Step Porous Polysilicon film, showing the pores between grains.*

CONCLUSION

The One-Step Porous Polysilicon material offers attractive new opportunities for MEMS designers and fabrication process developers. Its combination of properties and its great convenience and ease of use allow the simple and elegant fabrication of a wide range of structures, a few simple examples of which have been presented here.

REFERENCES

1. G.M. Dougherty, T. Sands, and A. Pisano, "The Materials Science of 'Permeable Polysilicon' Thin Films," in Materials Science of Microelectromechanical Systems (MEMS) Devices IV, Materials Research Society vol. 687, Boston, MA, November 2001.

2. L. Lin, K. M. McNair, R.T. Howe, and A.P. Pisano, "Vacuum-encapsulated Lateral Microresonators," Proc. 7th International Conf. On Solid-State Sensors and Actuators (Transducers 93), Yokohama, Japan, June 7-10 1993, pp. 270-3.

Travel support has been generously provided by the Transducers Research Foundation and by the DARPA MEMS and DARPA BIOFlips programs.

1200 Mirror Array Integrated with CMOS for Photonic Switching: Application of Mechanical Leveraging and Torsional Electrostatic Actuation To Reduce Drive Voltage Requirements and Increase Angular Tilt

James H. Smith, Steven S. Nasiri, Janusz Bryzek, Mitch Novack, James B. Starr, Haesung Kwon, Anthony F. Flannery, David L. Marx, Zhenfang Chen, and Elaheh Sigari
Transparent Networks, Inc.
Santa Clara, CA 95050

ABSTRACT

The design, fabrication, and performance of a 1200 mirror array for photonic switching applications are presented. Torsional electrostatic actuators are combined with angular amplifiers derived from 4-bar mechanisms to improve the mechanical performance of the devices to 8° while maintaining the switched drive voltage requirements at 120V. The process technology and the integration of the mirror array with a custom drive ASIC is also discussed briefly. The mirrors are being used in a telecommunication application to form the basis of a 1200 port optical switch.

INTRODUCTION

The basic physics to overcome in electrostatic actuator design is the 2nd order relationship between electric field (applied voltage divided by actuator gap) and the actuation force. So, to maintain force as a constant, the applied voltage must increase linearly with increases in the maximum displacement of the amplifier. In many applications, tens to hundreds of microns of motion are required. This requires very large gaps and subsequently hundreds of volts to drive these devices. A number of innovations have improved upon the basic performance of the parallel plate electrostatic drive including the comb drive [1] and the application of leverage to comb drives [2,3]. Leveraging has also been applied to improve the performance of mechanical sensors [4].

MECHANICAL AND ELECTROSTATIC DESIGN

The tradeoff between force and electrode spacing is a fundamental design issue in mirror arrays for optical switching applications. Since these mirrors are typically 0.5 mm to 2.0 mm in size, the spacing between the platform and the underlying electrode must be considerable to prevent mechanical interference of the platform and the electrode. Also, the parallel plate-like drives (as well as torsional drives) exhibit non-linear behaviors that are difficult to control beyond ~30-40% of the initial gap. This results in gap spacings of 200 microns or more in a typical design. This large spacing drives the actuation voltage requirements to extremely high levels such as 350 V or more.

A concept similar to the mechanical leverage demonstrated in linear actuators can also be applied to achieve angular leverage. Figure 1 illustrates the classical 4-bar linkage mechanism. If the dimensions of the linkages are appropriately chosen, angular amplification can be readily achieved between the linkages ($\Delta\theta_2 > \Delta\theta_1$). With angular amplification, the gap spacing for torsional actuators can be reduced with a subsequent reduction in drive voltage. The classic 4-bar uses pin joints as the pivoting mechanism. To eliminate reliability issues and to enable fabrication, these pin joints are replaced with spring designs to form virtual pivots[5]. Additionally, the suspension of the mirror includes shock/overvoltage/overrange protection and electrostatic shielding.

The Transparent Networks Leveraged Virtual Pivot ™ suspension, first disclosed by Nasiri [6], combines an angular amplifier with a virtual pivot point and torsional actuators to reduce drive voltage as well as improve the angular range of the mirror array. A leverage ratio of 4:1 (illustrated in Figure 2) has enabled the use of 120 V on the drive ASIC while achieving full angular performance of 8°. Although 120V is higher than most CMOS, it is easily within the range of niche CMOS foundries who specialize in custom processes or by stacking of transistors in conventional CMOS foundries. The basic limit to switching voltages on a drive ASIC is the tub to substrate isolation breakdown voltage. This can range from 30 V to over 150V depending upon the particular process. 120V does not require exotic isolation methods such as dielectric isolation nor expensive materials such as SOI.

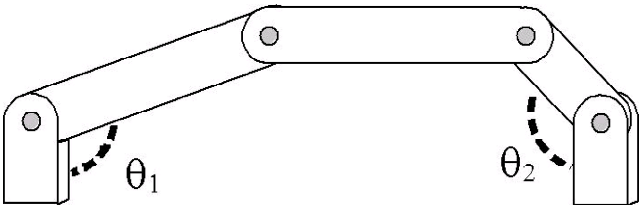

Figure 1. *A basic 4-bar mechanism for mechanical angular amplification. With appropriate choice of geometry, the relationship between the changes in θ_1 and θ_2 can be used to amplify the motions at the respective pin joints.*

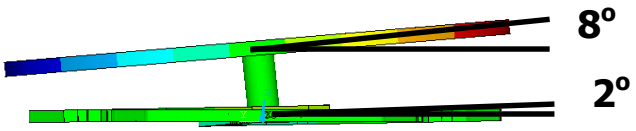

Figure 2. *A compliant version of a 4-bar mechanism is used in the mechanical mirror design to amplify the angular motion movement of the actuators (2°) to achieve a larger angular tilt of the mirror's reflective platform (8°).*

FABRICATION

The mirror fabrication is separated into CMOS fabrication, electrode fabrication, and MEMS fabrication. The MEMS fabrication has both a pre- and post-CMOS portion and includes 8 mask layers. First, CMOS is built in a foundry process. Next, the electrode assembly (a multi-level conductor/dielectric stack) is built on top of the foundry CMOS in a separate foundry operation. Both of these operations use standard foundry operations that support wafer flows in excess of 10,000 wafers per month. A MEMS wafer stack including the mirror and the suspension is pre-built in an unreleased form from two fusion-bonded wafers using DRIE and wafer thinning. The pre-built mirrors, still in wafer form, are bonded using one of two low temperature bonding

0-9640024-4-2/hh2002/$20©2002TRF
DOI 10.31438/trf.hh2002.97

techniques (depending upon application) to the CMOS/electrode array. The completed wafer stack of 3 wafers is post-processed to thin the mirror platform, coat the mirrors with a reflective coating, and release the mirrors resulting in the mirror array shown in Figure 3. The optical coating of the mirror is gold with an adhesion layer / diffusion barrier. A cross-sectional SEM of the mechanical portion of the mirror array is shown in Figure 4.

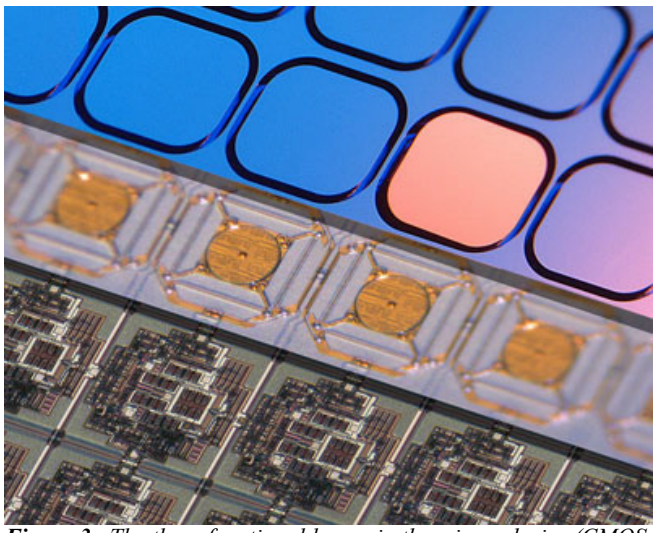

Figure 3. *The three functional layers in the mirror device (CMOS, Electrode, and Mechanical) overlayed to show the structure of the mirror array. The bottom CMOS layer provides high voltage switching (120V); the intermediate Electrode layer provides routing, shielding, and electrodes; the top Mechanical layer provides the optically-reflecting surface and mechanical suspension. For reference, the cell pitch in the photograph is approx. 1 mm.*

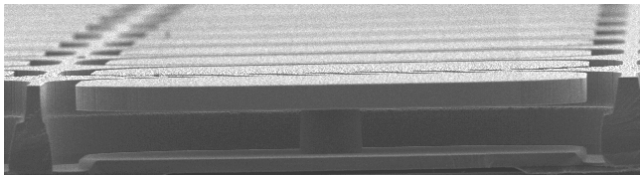

Figure 4. *A cross-sectional SEM of a single cell in the MEMS-portion of the mirror array.*

PERFORMANCE

The demonstration of leveraged actuation through the static performance of the mirror is presented below and was obtained using external drive signals and a passive electrode array. Full dynamic performance of the mirror integrated with its drive ASIC and feedback loop has been demonstrated and will be reported in a subsequent paper.

Figure 5 illustrates the experimentally measured mirror tilt angle vs. drive voltage for one of the initial mirror designs. Simulations of subsequent designs show drive voltage requirements as low as 70V (switched) with tilt angles of 10^{o} through optimization of suspension and electrode design. In all cases, a common negative bias equal to 2/3 of the maximum switched voltage is applied to the MEMS actuator.

In its dynamic configuration within the optical switch, the mirror has demonstrated optical switch closure and stabilization in under 8 ms and an ability to handle 1W of switched optical power.

CONCLUSIONS

The application of leveraged torsional electrostatic actuation to 3-D mirror arrays for photonic switching has been presented. The leveraged mechanical design drops drive voltage requirements to 120 V to achieve an 8^{o} tilt angle. The design of the mirror also hides the suspension beneath the reflecting platform and isolates the packaging and actuation stresses from the reflective platform. This results in extremely close packing density (~90% linear fill) and large angular deflections $>8^{o}$ which aid the performance of high port count, low-loss optical switching systems.

A MEMS fabrication process has been demonstrated using 8 masks that is compatible with CMOS from commonly available foundries. This process uses a pre-built MEMS stack, wafer bonding to CMOS, and post-processing of the final 3-wafer stack to release the structures.

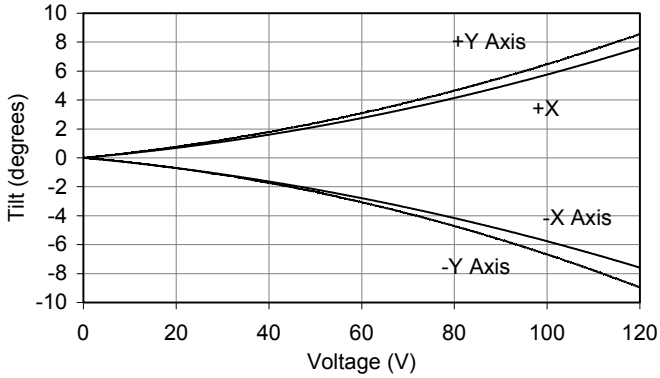

Figure 5. *Static angle as a function of switched voltage for a mirror tilting on two orthogonal axes (X and Y). A constant mirror bias of –90V is used on the mirror array in addition to the switched voltage.*

REFERENCES

1. W. C. Tang, T.-C. H. Nguyen, M. W. Judy, and R. T. Howe, "Electrostatic-comb drive of lateral polysilicon resonators," Sensors and Actuators, vol. A21-23, pp. 328-331. 1990.
2. J. Sniegowski and C. Smith, "An Application of Mechanical Leverage to Microactuation," 8th International Conference on Solid-State Sensors and Actuators, and Eurosensors IX, Proc. TRANSDUCERS '95/Eurosensors IX, Stockholm, Sweden, June 25-29, 1995, Vol. 2, pp. 364-367 (paper 325-PB9).
3. M. Rodgers, et al., "A New Class of High Force, Low-Voltage, Compliant Actuation Systems," Solid-State Sensor and Actuator Workshop, Hilton Head Island, South Carolina, June 4-8, 2000.
4. T. Roessig, R. Howe, A. Pisano, and J. Smith "Surface-Micromachined Resonant Accelerometer," 1997 International Conference on Solid-State Sensors and Actuators, Chicago, IL, June 16-19, 1997, Vol. 2, pp. 859-862.
5. M. Murphy, A. Midha and L. Howell, "The topological synthesis of compliant mechanisms," Mechanism and Machine Theory, 31 (1996) 185-199.
6. S. Nasiri, "Microelectromechanical Mirror and Mirror Array," U.S. patent application 09/779189, Feb. 2001.

ACKNOWLEDGEMENTS

Special acknowledgement is deserved by J. Garate, M. Wang, D. Tactac, and P. Le for the fabrication of these devices. Optical photographs by R. Barnard. Many thanks to C. Ray, N. Maluf, and S. Terry for technical advice. CMOS design by H. Gurcan, D. Skurnik, and R. Sprague to be reported in future publications.

AUTHOR INDEX

KEYWORD INDEX